



*polymers*

# Advances in Biocompatible and Biodegradable Polymers

Volume I

---

Edited by

José Miguel Ferri, Vicent Fombuena Borràs and  
Miguel Fernando Aldás Carrasco

Printed Edition of the Special Issue Published in *Polymers*

# **Advances in Biocompatible and Biodegradable Polymers-Volume I**



# **Advances in Biocompatible and Biodegradable Polymers-Volume I**

Editors

**José Miguel Ferri**

**Vicent Fombuena Borràs**

**Miguel Fernando Aldás Carrasco**

MDPI • Basel • Beijing • Wuhan • Barcelona • Belgrade • Manchester • Tokyo • Cluj • Tianjin



*Editors*

José Miguel Ferri  
Department of Nuclear and  
Chemical Engineering  
Universitat Politècnica  
de València  
Alcoy  
Spain

Vicent Fombuena Borràs  
Department of Nuclear and  
Chemical Engineering  
Universitat Politècnica  
de València  
Alcoy  
Spain

Miguel Fernando Aldás  
Carrasco  
Center of Polymers Applied  
Research (CIAP)  
Escuela Politécnica Nacional  
Quito  
Ecuador

*Editorial Office*

MDPI  
St. Alban-Anlage 66  
4052 Basel, Switzerland

This is a reprint of articles from the Special Issue published online in the open access journal *Polymers* (ISSN 2073-4360) (available at: [https://www.mdpi.com/journal/polymers/special\\_issues/biocompat.biodegrad.polym](https://www.mdpi.com/journal/polymers/special_issues/biocompat.biodegrad.polym)).

For citation purposes, cite each article independently as indicated on the article page online and as indicated below:

LastName, A.A.; LastName, B.B.; LastName, C.C. Article Title. <i>Journal Name</i> <b>Year</b> , <i>Volume Number</i> , Page Range.
--

**Volume 1**

ISBN 978-3-0365-7404-2 (Hbk)

ISBN 978-3-0365-7405-9 (PDF)

**Volume 1-2**

ISBN 978-3-0365-7402-8 (Hbk)

ISBN 978-3-0365-7403-5 (PDF)

© 2023 by the authors. Articles in this book are Open Access and distributed under the Creative Commons Attribution (CC BY) license, which allows users to download, copy and build upon published articles, as long as the author and publisher are properly credited, which ensures maximum dissemination and a wider impact of our publications.

The book as a whole is distributed by MDPI under the terms and conditions of the Creative Commons license CC BY-NC-ND.

# Contents

<b>About the Editors</b> . . . . .	ix
<b>Preface to "Advances in Biocompatible and Biodegradable Polymers-Volume I"</b> . . . . .	xi
<b>Seung-Woon Baek, Jun Hyuk Kim, Duck Hyun Song, Da-Seul Kim, Chun Gwon Park and Dong Keun Han</b> Enhanced Mechanical Properties and Anti-Inflammation of Poly(L-Lactic Acid) by Stereocomplexes of PLLA/PDLA and Surface-Modified Magnesium Hydroxide Nanoparticles Reprinted from: <i>Polymers</i> <b>2022</b> , <i>14</i> , 3790, doi:10.3390/polym14183790 . . . . .	1
<b>Grażyna Korbecka-Glinka, Klaudia Piekarska and Maria Wiśniewska-Wrona</b> The Use of Carbohydrate Biopolymers in Plant Protection against Pathogenic Fungi Reprinted from: <i>Polymers</i> <b>2022</b> , <i>14</i> , 2854, doi:10.3390/coatings11030274 . . . . .	17
<b>Dong Hyun Lee, Eun Kwang Lee, Chae Hyun Kim, Hyung Joong Yun, Young-Joon Kim and Hocheon Yoo</b> Blended Polymer Dry Electrodes for Reliable Electrocardiogram and Electromyogram Measurements and Their Eco-Friendly Disposal Led by Degradability in Hot Water Reprinted from: <i>Polymers</i> <b>2022</b> , <i>14</i> , 2586, doi:10.3390/coatings11030274 . . . . .	45
<b>Jagoda Józwick-Pruska, Krystyna Wrześniewska-Tosik, Tomasz Mik, Ewa Wesółowska, Tomasz Kowalewski and Michalina Pałczyńska, et al.</b> Biodegradable Nonwovens with Poultry Feather Addition as a Method for Recycling and Waste Management Reprinted from: <i>Polymers</i> <b>2022</b> , <i>14</i> , 2370, doi:10.3390/polym14122370 . . . . .	59
<b>Marius Murariu, Yoann Paint, Oltea Murariu, Fouad Laoutid and Philippe Dubois</b> Recent Advances in Production of Ecofriendly Polylactide (PLA)-Calcium Sulfate (Anhydrite II) Composites: From the Evidence of Filler Stability to the Effects of PLA Matrix and Filling on Key Properties Reprinted from: <i>Polymers</i> <b>2022</b> , <i>14</i> , 2360, doi:10.3390/polym14122360 . . . . .	71
<b>Sílvia Baptista, João R. Pereira, Cátia V. Gil, Cristiana A. V. Torres, Maria A. M. Reis and Filomena Freitas</b> Development of Olive Oil and $\alpha$ -Tocopherol Containing Emulsions Stabilized by FucoPol: Rheological and Textural Analyses Reprinted from: <i>Polymers</i> <b>2022</b> , <i>14</i> , 2349, doi:10.3390/polym14122349 . . . . .	93
<b>Aatikah Tareen, Saira Saeed, Atia Iqbal, Rida Batool and Nazia Jamil</b> Biodeterioration of Microplastics: A Promising Step towards Plastics Waste Management Reprinted from: <i>Polymers</i> <b>2022</b> , <i>14</i> , 2275, doi:10.3390/polym14112275 . . . . .	111
<b>Ana Marta Rodrigues, Rita Dias Guardão Franca, Madalena Dionísio, Chantal Sevrin, Christian Grandfils and Maria A. M. Reis, et al.</b> Polyhydroxyalkanoates from a Mixed Microbial Culture: Extraction Optimization and Polymer Characterization Reprinted from: <i>Polymers</i> <b>2022</b> , <i>14</i> , 2155, doi:10.3390/polym14112155 . . . . .	127
<b>Sami Fadlallah, Quentin Carboué, Louis M. M. Mouterde, Aihemaiti Kayishaer, Yasmine Werghi and Aurélien A. M. Peru, et al.</b> Synthesis and Enzymatic Degradation of Sustainable Levoglucosenone-Derived Copolyesters with Renewable Citronellol Side Chains Reprinted from: <i>Polymers</i> <b>2022</b> , <i>14</i> , 2082, doi:10.3390/polym14102082 . . . . .	149

<b>Cátia V. Gil, Ana Teresa Rebocho, Asiyah Esmail, Chantal Sevrin, Christian Grandfils and Cristiana A. V. Torres, et al.</b> Characterization of the Thermostable Biosurfactant Produced by <i>Burkholderia thailandensis</i> DSM 13276 Reprinted from: <i>Polymers</i> <b>2022</b> , <i>14</i> , 2088, doi:10.3390/polym14102088 . . . . .	<b>163</b>
<b>Irina N. Vikhareva, Guliya K. Aminova and Aliya K. Mazitova</b> Development of a Highly Efficient Environmentally Friendly Plasticizer Reprinted from: <i>Polymers</i> <b>2022</b> , <i>14</i> , 1888, doi:10.3390/polym14091888 . . . . .	<b>175</b>
<b>Tristan Hampe, Andreas Wiessner, Holm Frauendorf, Mohammad Alhussein, Petr Karlovsky and Ralf Bürgers, et al.</b> Monomer Release from Dental Resins: The Current Status on Study Setup, Detection and Quantification for In Vitro Testing Reprinted from: <i>Polymers</i> <b>2022</b> , <i>14</i> , 1790, doi:10.3390/polym14091790 . . . . .	<b>191</b>
<b>Quentin Carboué, Sami Fadlallah, Yasmine Werghi, Lionel Longé, Antoine Gallos and Florent Allais, et al.</b> Impact of Bis- <i>O</i> -dihydroferuloyl-1,4-butanediol Content on the Chemical, Enzymatic and Fungal Degradation Processes of Poly(3-hydroxybutyrate) Reprinted from: <i>Polymers</i> <b>2022</b> , <i>14</i> , 1564, doi:10.3390/polym14081564 . . . . .	<b>213</b>
<b>Klementina Pušnik Črešnar, Alexandra Zamboulis, Dimitrios N. Bikiaris, Alexandra Aulova and Lidija Fras Zemljč</b> Kraft Lignin/Tannin as a Potential Accelerator of Antioxidant and Antibacterial Properties in an Active Thermoplastic Polyester-Based Multifunctional Material Reprinted from: <i>Polymers</i> <b>2022</b> , <i>14</i> , 1532, doi:10.3390/polym14081532 . . . . .	<b>229</b>
<b>Marina Vukoje, Rahela Kulčar, Katarina Itrić Ivanda, Josip Bota and Tomislav Cigula</b> Improvement in Thermochromic Offset Print UV Stability by Applying PCL Nanocomposite Coatings Reprinted from: <i>Polymers</i> <b>2022</b> , <i>14</i> , 1484, doi:10.3390/polym14071484 . . . . .	<b>247</b>
<b>Nuttapol Tanadchangsaeng and Anchana Pattanasupong</b> Evaluation of Biodegradabilities of Biosynthetic Polyhydroxyalkanoates in Thailand Seawater and Toxicity Assessment of Environmental Safety Levels Reprinted from: <i>Polymers</i> <b>2022</b> , <i>14</i> , 428, doi:10.3390/polym14030428 . . . . .	<b>269</b>
<b>Shiou Xuan Tan, Hwai Chyuan Ong, Andri Andriyana, Steven Lim, Yean Ling Pang and Fitranto Kusumo, et al.</b> Characterization and Parametric Study on Mechanical Properties Enhancement in Biodegradable Chitosan-Reinforced Starch-Based Bioplastic Film Reprinted from: <i>Polymers</i> <b>2022</b> , <i>14</i> , 278, doi:10.3390/polym14020278 . . . . .	<b>283</b>
<b>Piotr Gruber, Viktoria Hoppe, Emilia Grochowska, Justyna Paleczny, Adam Junka and Irina Smolina, et al.</b> Material Extrusion-Based Additive Manufacturing of Poly(Lactic Acid) Antibacterial Filaments—A Case Study of Antimicrobial Properties Reprinted from: <i>Polymers</i> <b>2021</b> , <i>13</i> , 4337, doi:10.3390/polym13244337 . . . . .	<b>305</b>
<b>Carmelo J. Luis-Pérez, Irene Buj-Corral and Xavier Sánchez-Casas</b> Modeling of the Influence of Input AM Parameters on Dimensional Error and Form Errors in PLA Parts Printed with FFF Technology Reprinted from: <i>Polymers</i> <b>2021</b> , <i>13</i> , 4152, doi:10.3390/polym13234152 . . . . .	<b>319</b>

<b>Anand Utpal Vakil, Natalie Marie Petryk, Ellen Shepherd and Mary Beth B. Monroe</b> Biostable Shape Memory Polymer Foams for Smart Biomaterial Applications Reprinted from: <i>Polymers</i> <b>2021</b> , <i>13</i> , 4084, doi:10.3390/polym13234084 . . . . .	<b>343</b>
<b>Félix Carrasco, Orlando Santana Pérez and Maria Lluïsa Maspoch</b> Kinetics of the Thermal Degradation of Poly(lactic acid) and Polyamide Bioblends Reprinted from: <i>Polymers</i> <b>2021</b> , <i>13</i> , 3996, doi:10.3390/polym13223996 . . . . .	<b>361</b>
<b>Ofek Golan, Hila Shalom, Ifat Kaplan-Ashiri, Sidney R. Cohen, Yishay Feldman and Iddo Pinkas, et al.</b> Poly(L-lactic acid) Reinforced with Hydroxyapatite and Tungsten Disulfide Nanotubes Reprinted from: <i>Polymers</i> <b>2021</b> , <i>13</i> , 3851, doi:10.3390/polym13213851 . . . . .	<b>377</b>
<b>Yuandong Wu, Weishuang Zheng, Yinan Xiao, Beining Du, Xingru Zhang and Min Wen, et al.</b> Multifunctional, Robust, and Porous PHBV—GO/MXene Composite Membranes with Good Hydrophilicity, Antibacterial Activity, and Platelet Adsorption Performance Reprinted from: <i>Polymers</i> <b>2021</b> , <i>13</i> , 3748, doi:10.3390/polym13213748 . . . . .	<b>397</b>
<b>Shan Jiang, Tingting Su, Jingjing Zhao and Zhanyong Wang</b> Biodegradation of Polystyrene by <i>Tenebrio molitor</i> , <i>Galleria mellonella</i> , and <i>Zophobas atratus</i> Larvae and Comparison of Their Degradation Effects Reprinted from: <i>Polymers</i> <b>2021</b> , <i>13</i> , 3539, doi:10.3390/coatings11030274 . . . . .	<b>417</b>
<b>María Aguado, Laura Saldaña, Eduardo Pérez del Río, Judith Guasch, Marc Parera and Alba Córdoba, et al.</b> Polylactide, Processed by a Foaming Method Using Compressed Freon R134a, for Tissue Engineering Reprinted from: <i>Polymers</i> <b>2021</b> , <i>13</i> , 3453, doi:10.3390/polym13203453 . . . . .	<b>431</b>
<b>Shuaikai Ren, Mengjie Wang, Chunxin Wang, Yan Wang, Changjiao Sun and Zhanghua Zeng, et al.</b> Application of Non-Viral Vectors in Drug Delivery and Gene Therapy Reprinted from: <i>Polymers</i> <b>2021</b> , <i>13</i> , 3307, doi:10.3390/polym13193307 . . . . .	<b>449</b>
<b>Tanyaluck Mekpothi, Puttinan Meepowpan, Montira Sriyai, Robert Molloy and Winita Punyodom</b> Novel Poly(Methylenelactide-g-L-Lactide) Graft Copolymers Synthesized by a Combination of Vinyl Addition and Ring-Opening Polymerizations Reprinted from: <i>Polymers</i> <b>2021</b> , <i>13</i> , 3374, doi:10.3390/polym13193374 . . . . .	<b>477</b>





# About the Editors

## **José Miguel Ferri**

Dr. José Miguel Ferri (h-index 14—Scopus) works at the Department of Nuclear and Chemical Engineering of the Escuela Politécnica Superior de Alcoy (EPSA) of the Universitat Politècnica de València, (UPV) Alcoy, Spain. He holds degrees in Technical Engineering, Industrial Mechanical Engineering, and Materials Engineering. He joined the Technological Institute of Materials (ITM) in 2014 as a research technician and obtained an international PhD in engineering and industrial production in 2017. His field of research concerns the development of new metallic materials (Mg foams for the medical sector), polymeric materials (the improvement of the thermal, mechanical, and processing properties of biodegradable polymers), and composite materials (metallic matrices for the electronics and aeronautics sectors and polymeric matrices for the aeronautics and construction sectors).

## **Vicent Fombuena Borràs**

Dr. Vicent Fombuena Borràs (h-index 18—Scopus) works at the Department of Nuclear and Chemical Engineering of the Escuela Politécnica Superior de Alcoy (EPSA) of the Universitat Politècnica de València, (UPV) Alcoy, Spain. He holds degrees in Technical Engineering, Industrial Chemical Engineering, and Materials Engineering. He joined the Technological Institute of Materials (ITM) in 2008 as a research technician and obtained an international PhD in engineering and industrial production in 2012. His research work concerns the implementation of a circular economic model in the polymer industry. He has focused his efforts on obtaining multiple active compounds from seeds and agroforestry residues for application in thermoplastic and thermosetting polymers. He has extensive experience in developing techniques for the chemical, thermal, and mechanical characterization of materials.

## **Miguel Fernando Aldás Carrasco**

Miguel Fernando Aldás Carrasco (h-index 10—Scopus) has been a lecturer and researcher at the Escuela Politécnica Nacional (Quito, Ecuador) since 2008. He actively collaborates with the Centro de Investigaciones Aplicadas a Polímeros (Center of Polymers Applied Research) (CIAP) and the Faculty of Chemical Engineering and Agroindustry. He holds degrees in Chemical Engineering from Escuela Politécnica Nacional (Quito, Ecuador), a Master in Innovative Materials degree from Université Claude Bernard Lyon 1 (Lyon, France), and a Doctorate in engineering from Universitat Politècnica de València (Valencia, Spain). He has worked under the direction of Prof. Juan López Martínez and Dr. Marina P. Arrieta, constituting a portion of the team of researchers at the Materials Technology Institute (ITM-UPV) at the Alcoy campus within the Development of Materials for Sustainable Structures (DEMES) group. His field of research concerns the use of natural additives for biopolymers and biodegradable materials, the development of thermoplastic starch-based materials, the study of the degradation of synthetic and biodegradable plastic materials, and the technology behind processing techniques.



# Preface to "Advances in Biocompatible and Biodegradable Polymers-Volume I"

Among the strategies for reducing the negative effects on the environment effected by the uncontrolled consumption and low potential for the recovery of conventional plastics, the synthesis of new biodegradable and recyclable plastics represents one of the most promising methods for minimizing the negative effects of conventional non-biodegradable plastics. The spectrum of existing biodegradable materials is still very narrow; thus, to achieve greater applicability, research is being carried out on biodegradable polymer mixtures, the synthesis of new polymers, and the incorporation of new stabilizers for thermal degradation, alongside the use of other additives such as antibacterials or new and more sustainable plasticizers. Some studies analyze direct applications, such as shape memory foams, new cartilage implants, drug release, etc.

The reader can find several studies on the degradation of biodegradable polymers under composting conditions; however, novel bacteria that degrade polymers considered non-biodegradable in other, unusual conditions (such as conditions of high salinity) are also presented.

**José Miguel Ferri, Vicent Fombuena Borràs, and Miguel Fernando Aldás Carrasco**

*Editors*



## Article

# Enhanced Mechanical Properties and Anti-Inflammation of Poly(L-Lactic Acid) by Stereocomplexes of PLLA/PDLA and Surface-Modified Magnesium Hydroxide Nanoparticles

Seung-Woon Baek<sup>1,2,3,†</sup>, Jun Hyuk Kim<sup>1,†</sup>, Duck Hyun Song<sup>1</sup>, Da-Seul Kim<sup>1,4</sup>, Chun Gwon Park<sup>2,3,\*</sup> and Dong Keun Han<sup>1,\*</sup>

<sup>1</sup> Department of Biomedical Science, CHA University, 335 Pangyo-ro, Bundang-gu, Seongnam-si 13488, Korea

<sup>2</sup> Department of Biomedical Engineering, SKKU Institute for Convergence, Sungkyunkwan University (SKKU), 2066 Seobu-ro, Jangan-gu, Suwon-si 16419, Korea

<sup>3</sup> Department of Intelligent Precision Healthcare Convergence, SKKU Institute for Convergence, Sungkyunkwan University (SKKU), 2066 Seobu-ro, Jangan-gu, Suwon-si 16419, Korea

<sup>4</sup> School of Integrative Engineering, Chung-Ang University, 84 Heukseok-ro, Dongjak-gu, Seoul 06974, Korea

\* Correspondence: chunpark@skku.edu (C.G.P.); dkhan@cha.ac.kr (D.K.H.)

† These authors contributed equally to this work.

**Citation:** Baek, S.-W.; Kim, J.H.; Song, D.H.; Kim, D.-S.; Park, C.G.; Han, D.K. Enhanced Mechanical Properties and Anti-Inflammation of Poly(L-Lactic Acid) by Stereocomplexes of PLLA/PDLA and Surface-Modified Magnesium Hydroxide Nanoparticles. *Polymers* **2022**, *14*, 3790. <https://doi.org/10.3390/polym14183790>

Academic Editors: José Miguel Ferri, Vicent Fombuena Borràs and Miguel Fernando Aldás Carrasco

Received: 16 August 2022

Accepted: 7 September 2022

Published: 10 September 2022

**Publisher's Note:** MDPI stays neutral with regard to jurisdictional claims in published maps and institutional affiliations.



**Copyright:** © 2022 by the authors. Licensee MDPI, Basel, Switzerland. This article is an open access article distributed under the terms and conditions of the Creative Commons Attribution (CC BY) license (<https://creativecommons.org/licenses/by/4.0/>).

**Abstract:** Poly(L-lactic acid) (PLLA), as a biodegradable polymer, has attracted attention for use as a biomaterial. In order to apply PLLA as a cardiovascular stent, stronger mechanical properties and anti-inflammatory effects against acidic by-products are required. In this study, PLLA/PDLA stereocomplex microparticles (SC) were developed and surface-modified magnesium hydroxide (MH) nanoparticles with oligolactide were combined with these PLLA composites. The SC improved the mechanical properties of the PLLA composites through the formation of stereocomplex structures. The surface-modified MH nanoparticles showed enhanced mechanical properties due to the stereocomplex structures formed by PLLA chains and inhibited inflammatory responses by pH neutralization as a result of MH. Additionally, the MH nanoparticles containing PLLA composites had antibacterial effects and increased the viability of human vascular endothelial cells. This technology is expected to have great potential in the development of PLLA composite materials for the production of various medical devices, such as cardiovascular stents.

**Keywords:** Poly(L-lactic acid); Poly(D-lactic acid); stereocomplex; magnesium hydroxide; biodegradable vascular scaffold; nanoparticles

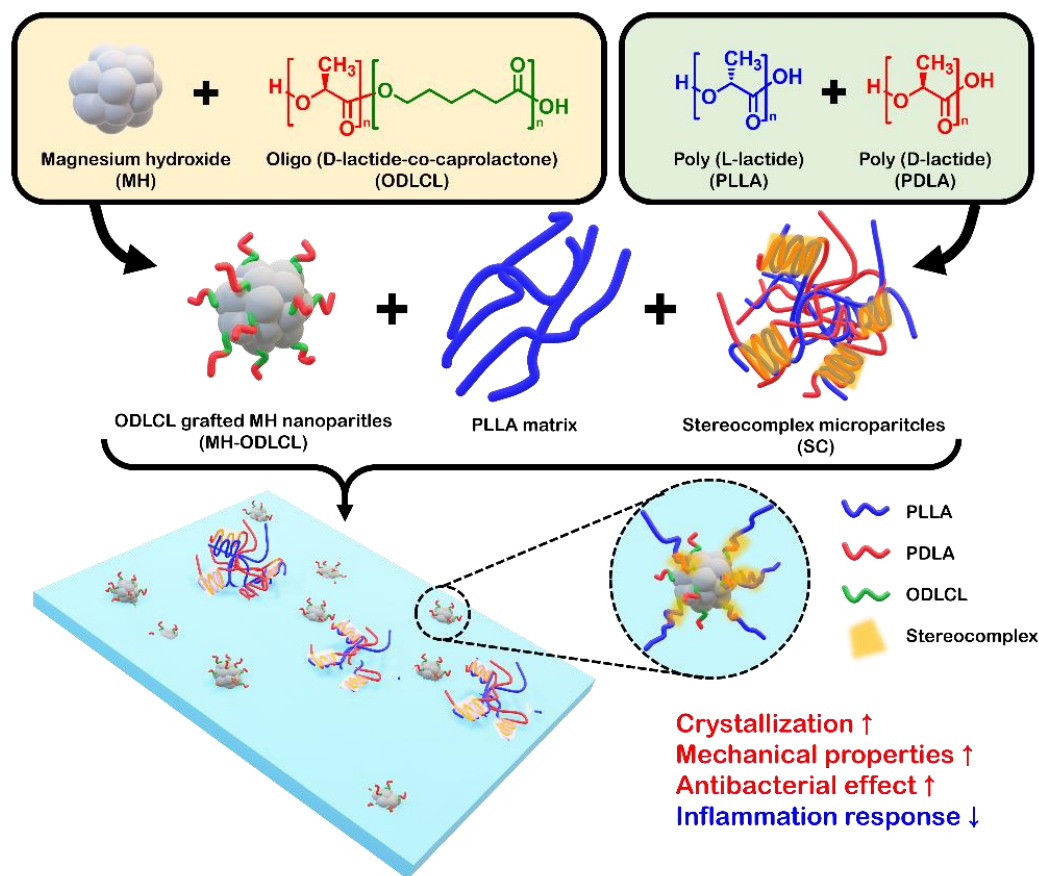
## 1. Introduction

Biodegradable polymers are extensively used in biomedical materials for tissue engineering and regeneration to facilitate the healing process [1–3]. Among them, poly(lactic acid) (PLA) has attracted attention as a biomaterial due to its non-toxicity, elasticity, biodegradability, good mechanical properties, and approval by the FDA. However, the production of certain medical devices, such as cardiovascular stents, requires biomaterials to have strong mechanical properties, and PLA is weaker than metal, resulting in recoil. Many researchers have devoted efforts to enhancing the mechanical properties of PLA. Wang et al. reported on the fabrication of tough PLA composites by adding poly(butylene adipate-co-terephthalate) (PBAT) and using a multifunctional epoxy oligomer as a crosslinker [4]. Deng et al. reported the development of PLA blends including ethylene-acrylic ester-glycidyl methacrylate terpolymers (EGMAs) via reactive blending and crystallization by annealing to obtain super-toughened PLA [5]. However, although the methods described above can improve the mechanical properties of PLA, they can also cause toxicity in the human body. Among the various methods for improving mechanical properties, the formation of stereocomplex structures is a method which allows for excellent biocompatibility.

The stereocomplex structures formed by the mixing of enantiomeric poly(L-lactic acid) (PLLA) and poly(D-lactic acid) (PDLA) increase intermolecular interactions through the formation of hydrogen bonds and dipole–dipole interactions, resulting in tightly packed chains side by side, improving thermal stability, hydrolysis resistance, and mechanical properties [6–8]. Im et al. described the improvement of mechanical properties by in situ self-nucleated polymerization of PLLA using stereocomplex poly(lactide) (SC-PLA) as a nucleating agent [9].

PLLA as polyester is degraded by hydrolysis in the body to produce lactic acid by-products. The lactic acid produced decreases local pH and induces inflammatory responses [10,11]. In our previous studies, the acidic by-products of biodegradable polymers were neutralized using magnesium hydroxide [Mg(OH)<sub>2</sub>, MH] [12–14]. MH is a biocompatible inorganic particle that has been widely used as an antacid agent. The pH-neutralizing effect of MH was found to reduce inflammatory response and improve tissue regeneration. In addition, MH has antibacterial properties [15,16]. Heydarian et al. reported that bacterial infection occurs the expression of pro-inflammatory cytokines, such as interleukin-6 (IL-6), interleukin-8 (IL-8), and tumor necrosis factor- $\alpha$  (TNF- $\alpha$ ), in cells [17]. Unfortunately, the hydrophilic inorganic particles, such as MH, in hydrophobic polymers are aggregated and weaken the mechanical properties of the materials. To overcome these problems, many researchers have studied the surface modification of inorganic particles using ricinoleic acid, stearic acid, polylactic acid, and silane to improve interfacial bonding between PLLA and inorganic particles [18–22]. Previously, we have studied the surface modification of MH using monomers and oligomers of PLLA, such as DL-lactide, oligo(DL-lactic acid) (ODLLA), and oligo-D-lactide- $\epsilon$ -caprolactone (ODLCL) [23,24].

In this study, we fabricated PLLA composites including surface-modified MH nanoparticles and stereocomplex microparticles (SC) which had anti-inflammatory effects and improved mechanical properties. First, the SC, as homocomposites of PLLA and PDLA, were fabricated using an oil-in-water emulsion method. Secondly, based on the findings from our previous studies, the surface of MH was modified with oligo-D-lactide- $\epsilon$ -caprolactone (ODLCL) (MH-ODLCL). ODLCL, a copolymer of D-lactide and  $\epsilon$ -caprolactone, forms a stereocomplex structure due to the domain of D-lactic acid in the matrix of PLLA. Finally, a composite composed of PLLA, SC, and MH-ODLCL was developed by the solvent casting method and hot-pressing for the reduction of inflammatory response and improved mechanical properties (Figure 1). After configuring the PLLA composites, the mechanical properties, degradation behavior, and expression of inflammatory factors were evaluated. These results indicated that the disadvantages of PLLA are mitigated and that the material can be applied in biodegradable vascular scaffolds.



**Figure 1.** A schematic illustration of the preparation of the PLLA composites. The surface of MH was modified with ODLCL, and the SC were fabricated using PLLA and PDLA. The PLLA composites contained surface-modified MH and SC to provide anti-inflammatory effects and improved mechanical properties.

## 2. Materials and Methods

### 2.1. Materials

Poly(L-lactic acid) (PLLA) and poly(D-lactic acid) (PDLA) were obtained from Samyang Biopharmaceutical Corp. (Seongnam-si, Korea). L-Lactide was obtained from DURECT Co. (Cupertino, CA, USA). D-Lactide was supplied by Haihang Industry Co., Ltd. (Jinan, Shandong, China). Magnesium hydroxide,  $\epsilon$ -caprolactone, poly(vinyl alcohol) (PVA,  $M_w \approx 13,000$ – $23,000$ ), tin(II) 2-ethylhexanoate, and 1-octanol were obtained from Sigma-Aldrich (St. Louis, MO, USA). Toluene, chloroform, n-hexane, acetone, and dichloromethane (DCM) were supplied by Daejung Co. Ltd. (Seoul, Korea). IL-6 and IL-8 enzyme-linked immunosorbent assay (ELISA) kits were supplied by R&D Systems (Minneapolis, MN, USA). Phosphate-buffered saline (PBS) tablets were acquired from Thermo Fisher Scientific (Waltham, MS, USA). Proteinase K was obtained from Bioneer Co., Ltd. (Daejeon, Korea).

Gram-negative bacteria (*Escherichia coli* (*E. coli*)) and Gram-positive bacteria (*Staphylococcus saprophyticus* (*S. saprophyticus*)) were supplied by the Korean Collection for Type Cultures (KCTC; Daejeon, Korea). Luria-Bertani broth (LB broth), Luria-Bertani broth with agar (LB agar), nutrient broth, and nutrient agar were obtained from Sigma-Aldrich (St. Louis, MO, USA).

Human coronary artery endothelial cells (HCAECs) and EGM-2 media with an MV bullet kit were obtained from Lonza (Basel, Switzerland). A cell-counting kit (CCK-8) was purchased from Dongin LS (Korea). PBS solution was obtained from Hyclone (GE Healthcare Life Sciences, Logan, UT, USA). All chemicals were laboratory reagent grade and used without purification.



## 2.2. Preparation and Characterization of the Stereocomplex Microparticles (SC)

The SC were fabricated using a homogenization method. PLLA solution (DCM, 2 wt%) was added to 0.5 wt% aqueous PVA solution, followed by homogenization in a homogenizer operating at 10,000 rpm for 10 min (LSM-A, Silverson, Buckinghamshire, England). After that, the DCM was evaporated using an evaporator (N-1300, Eyela, Tokyo, Japan) for 3 h, and the SC were washed under centrifugation.

Field emission scanning electron microscopy (FE-SEM; S-4800, Hitachi, Tokyo, Japan) was used to observe the surface morphologies of the SC at 15 kv with the SE mode at 3.5 k. The samples were coated with platinum using an ion coater at 3 mA for 90 s. The average size and standard deviation of the SC were calculated from more than 500 particles in SEM images using ImageJ software (National Institutes of Health, Bethesda, MD, USA).

Differential scanning calorimetry (DSC; DSC4000, PerkinElmer, Waltham, MA, USA) was used to analyze the thermal behavior of the PLLA, PDLA, and their composites. Under nitrogen conditions, samples of approximately 5 mg were heated from 30 to 250 °C to measure non-isothermal crystallization. They were measured at a heating rate of 10 °C/min. The equation below was used to calculate the final crystallinity of homocrystallites and stereocomplex crystallites ( $X_{c,HC}$  and  $X_{c,SC}$ , respectively):

$$X_c(\%) = \frac{\Delta H_m}{\Delta H_f \omega_f} \times 100$$

where  $\Delta H_m$  stands for the melting enthalpy for crystallization,  $\omega_f$  stands for the weight fraction of PLLA in the PLLA composites, and  $\Delta H_f$  stands for the melting enthalpy for completely crystallized homocrystallites or stereocomplex crystallites (93 or 142 J/g). The equation below was used to calculate the proportion of stereocomplex crystallites ( $f_{SC}$ ) [25]:

$$f_{SC}(\%) = \frac{X_{c,SC}}{X_{c,SC} + X_{c,HC}} \times 100$$

The crystalline structures of the PLLA, PDLA, and SC were examined using X-ray diffraction measurements. An X-ray diffractometer (XRD; D2 phaser, Bruker, Karlsruhe, Germany) and CuK $\alpha$  radiation was used to record the XRD patterns of the samples, and the degrees of crystallinity were estimated using crystalline peak areas. Profiles were recorded with a scattering angle range of  $2\theta = 0\text{--}30^\circ$  and a scan speed of 0.05°/s [26,27].

An attenuated total reflection Fourier transform infrared spectrometer (ATR-FTIR; Spectrum Two FT-IR Spectrometer, Perkin Elmer, Waltham, MA, USA) with a resolution of 4 scans at 1 cm<sup>-1</sup> and scales of 890–970 and 2920–3040 cm<sup>-1</sup> was used to record the infrared spectra of the PLLA, PDLA, and SC.

## 2.3. Synthesis and Characterization of the Surface-Modified Magnesium Hydroxide

The ring-opening polymerization process was used to synthesize the OLLCL and ODLCL. Lactide and caprolactone were mixed in a ratio of 7:3 and then placed into a round beaker flask with toluene. After that, Tin(II) 2-ethylhexanoate and 0.0453 mM of 1-octanol 3.839 mM were added, and the flask was purged with a nitrogen atmosphere. The polymerization occurred at 140 °C for 18 h. The synthesized oligomers were dissolved in chloroform, then precipitated in hexane to remove unreacted monomers and dried.

The oligomer-grafted MH was synthesized by combining the hydroxylate of MH and the carboxylate of the oligomers. The MH and oligomers ( $M_w \approx 7$  k) at a 1:1 ratio were placed into a round beaker flask with chloroform. After chloroform was evaporated at 90 °C for 6 h, the mixture was reacted under vacuum conditions at 150 °C for 15 h. The synthesized MH was washed using a co-solvent of chloroform/acetone (4:6) under centrifugation (7000 rpm, 10 min).

FE-SEM (15 kv, SE mode,  $\times 130$  k) and dynamic laser scattering (DLS; Zetasizer Nano ZS, Malvern Instruments, Worcestershire, UK) were used to observe surface morphologies and sizes. The samples were coated with platinum using an ion coater at 3 mA for

90 s. To observe dispersibility, the MH, MH-OLLCL, and MH-ODLCL were dispersed in chloroform and left for 3 h at room temperature. ATR-FTIR with a resolution of 4 scans at  $1\text{ cm}^{-1}$  and a scale of  $600\text{--}4000\text{ cm}^{-1}$  was used to record the infrared spectra. Thermogravimetric analysis (TGA; TGA 4000, PerkinElmer, Waltham, USA) was used to measure the grafting degree and composition. A mass-temperature curve was recorded under the test temperature range of  $30\text{--}800\text{ }^{\circ}\text{C}$  at a heating rate of  $10\text{ }^{\circ}\text{C}/\text{min}$  under nitrogen conditions.

#### 2.4. Preparation and Characterization of the PLLA Composites

The PLLA composite manufacturing process was divided into two steps. In the first step, the solvent casting method was used to fabricate the PLLA composites. After 5 g of PLLA and 10 phr of oligomer-grafted MH were added to 70 mL of chloroform, the mixture was poured into a Teflon mold, and the solvent was evaporated at room temperature for 24 h. In the second step, a compression molding machine (QM900A, QMESYS, Gyangmyung, Korea) was used for the thermal melting and hot-pressing of the composites. The composites from the previous step and the SC (5 phr) were mixed and then hot-pressed at  $160\text{ }^{\circ}\text{C}$  for 5 min. FE-SEM (15 kv, SE mode,  $\times 500$ ) was used to observe the surface morphologies of the PLLA composites, and energy-dispersive spectroscopy (EDS) connected to the FE-SEM was used to measure the chemical compositions of the specimens. The samples were coated with platinum using an ion coater at 3 mA for 90 s. ATR-FTIR was used to record the infrared spectra of the PLLA composites, and TGA was used to measure the grafting degree and composition of the PLLA composites. The crystalline structures of the PLLA composites were examined via XRD. Profiles were recorded at a scattering angle range of  $2\theta = 0\text{--}40^{\circ}$  and a scan speed of  $0.05^{\circ}/\text{s}$ . The thermal behavior of the PLLA composites was analyzed using a DSC.

#### 2.5. Mechanical Properties

A universal testing machine (UTM; TO-101, Testone, Siheung, Korea) was used to investigate tensile strength, elongation, and Young's modulus, following ASTM standard D638. The PLLA composites were produced as dumb-bell-shaped specimens ( $14 \times 6 \times 2\text{ mm}^3$ ). They were investigated at room temperature under a crosshead speed of  $10\text{ mm}/\text{min}$ .

#### 2.6. Degradation Behavior

To observe degradation behavior, the PLLA composites were fabricated into rectangular shapes ( $10\text{ mm} \times 5\text{ mm}$ ). After each sample was weighed, it was placed in 1 mL of PBS solution at pH 7.4 with proteinase K ( $0.04\text{ mg}/\text{mL}$ ). This experiment was progressed at  $37\text{ }^{\circ}\text{C}$  for 4 days. A digital pH meter (Five Easy Plus, Mettler Toledo, Columbus, OH, USA) was used to evaluate the change in pH at identical times. To measure the remaining mass, a solution of the samples was washed with distilled water 3 times and dried under a vacuum. To measure the remaining mass, the solution of the samples was removed and dried under vacuum for 4 h. The following equation was used to calculate the weight loss of the samples [23]:

$$\text{Weight loss (\%)} = \frac{W_{AD}}{W_{BD}} \times 100$$

where  $W_{BD}$  refers to the weight of the PLLA composites before degradation and  $W_{AD}$  refers to the weight of the PLLA composites after degradation for a certain number of days.

#### 2.7. Antibacterials Assay

*E. coli* were incubated in Luria-Bertani broth (LB broth; L3022, St. Louis, MO, USA, Sigma-Aldrich) and Luria-Bertani broth with agar (LB agar; L2897, St. Louis, MO, USA, Sigma-Aldrich) at  $37\text{ }^{\circ}\text{C}$  with aeration. *S. saprophyticus* were incubated in nutrient broth (70122, St. Louis, MO, USA, Sigma-Aldrich) and nutrient agar (70148, St. Louis, MO, USA, Sigma-Aldrich), also at  $37\text{ }^{\circ}\text{C}$  with aeration. After 16 h, the Gram-negative and Gram-positive bacteria were centrifuged and then resuspended in sterilized 0.85% NaCl solution. The density of the bacteria solution was calculated to be approximately  $104\text{ CFU}$

(colony-forming units)/mL. The PLLA composites were added to 1 mL of the bacterial suspension for antibacterial testing. The composite scaffolds with the bacteria suspension were incubated at 37 °C for 1 day. Then, 100 µL of diluted bacterial suspension with the PLLA composites was spread on agar plates, and the plates were incubated overnight at 37 °C. The bactericidal effects were evaluated in terms of the CFUs using image J.

### 2.8. Cell Viability and Inflammation

HCAECs were grown in an EGM2–MV bullet kit in a humidified atmosphere with 5% carbon dioxide (CO<sub>2</sub>) at 37 °C. HCAECs were seeded at a density of  $5 \times 10^4$  cells/well in a 24–well cell culture plate and treated with degradation product at 60 °C for 21 days. After 24 h, the viability of cells and inflammatory response were determined using a CCK–8 assay kit and an ELISA kit for IL–6 and IL–8, respectively. The processes were conducted according to the provided protocols.

### 2.9. Statistical Analysis

The quantitative results were expressed as means  $\pm$  standard deviations (SDs). #  $p < 0.0001$ , \*\*\*  $p < 0.001$ , \*\*  $p < 0.01$ , and \*  $p < 0.05$  indicate statistically significant differences. Statistical significance was evaluated by one–way analysis of variance (ANOVA) following Tukey’s method, using GraphPad Prism 7.0 software (GraphPad Software Inc., San Diego, CA, USA).

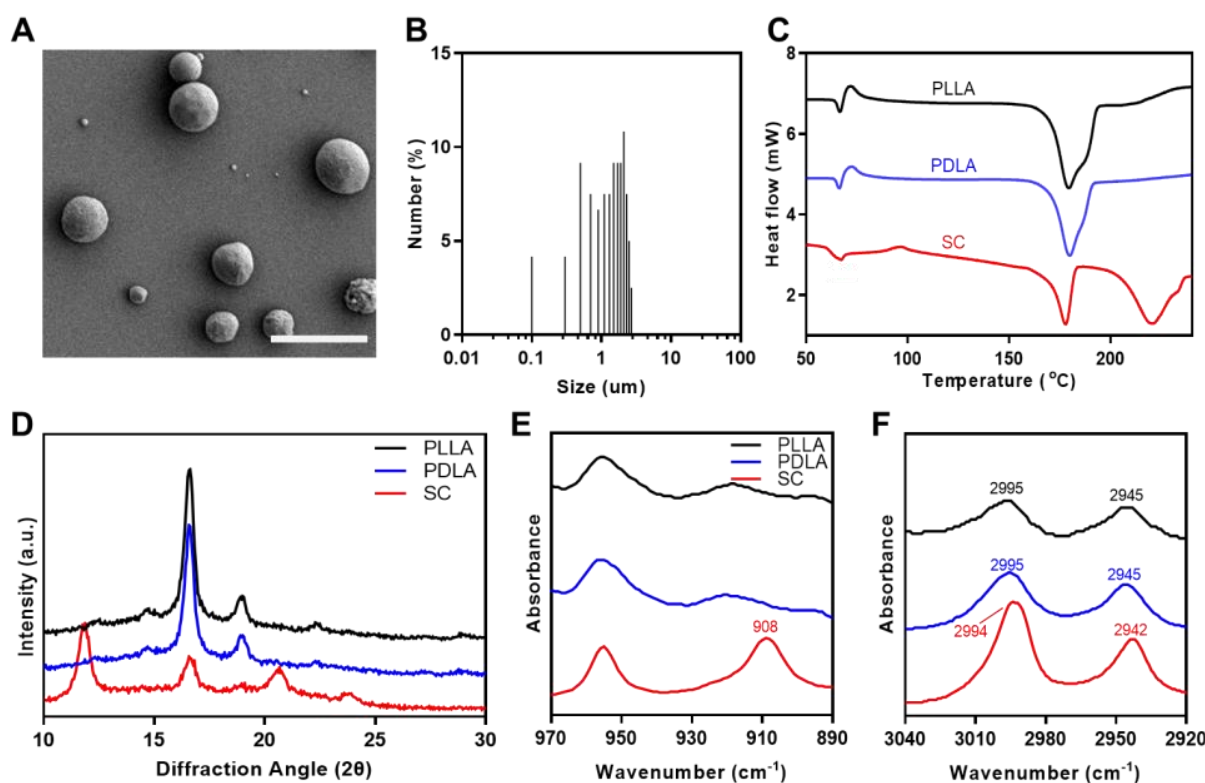
## 3. Results and Discussion

### 3.1. Characterization of the Stereocomplex Microparticles

The stereocomplex microparticles (SC) were fabricated using a homogenizer to provide enhanced mechanical properties in a PLLA matrix. Figure 2A shows an SEM image of the SC. The SC exhibited spherical morphologies and were of various sizes. The average size of the SC measured using SEM imagery was  $1.433 \pm 0.704$  µm (Figure 2B). Figure 2C displays DSC thermograms of a second heating scan of the PLLA, PDLA, and SC. The endothermic peak of homocrystallines of PLLA and PDLA were observed at 179 °C, whereas, for the SC observed the two endothermic homocrystallines and stereocomplex crystallines peaks at 178.21 and 220.28 °C, respectively [28–30]. Table 1 summarizes the corresponding parameters for the DSC thermograms for the PLLA, PDLA, and SC. These results showed a sharp decrease in  $X_{C,HC}$  and formation of  $X_{C,SC}$  and  $f_{sc}$  in the SC. Figure 2D shows XRD patterns for the PLLA, PDLA, and SC. The PLLA and PDLA had large homocrystal peaks at  $2\theta = 16.6$  and  $18.8^\circ$ , while the SC showed large homocrystal peaks at  $2\theta = 16.7^\circ$  as well as stereocomplex crystal peaks at  $2\theta = 11.8, 20.7, \text{ and } 23.9^\circ$  [27,31]. The FTIR spectra for the PLLA, PDLA, and SC are presented in Figures 2E and 2F. As shown in Figure 2E, compared to the PLLA and PDLA, the SC showed FTIR absorption at  $908 \text{ cm}^{-1}$ , indicating  $3_1$ –helical conformations of stereocomplex crystallines in the SC. Figure 2F displayed a low–frequency shift of C–H stretching at  $2995 \text{ to } 2994 \text{ cm}^{-1}$  and  $2945 \text{ to } 2942 \text{ cm}^{-1}$  by hydrogen bond formation between two groups among C–O, C–CH<sub>3</sub>, and C–CH<sub>2</sub> stretching [25].

**Table 1.** Thermal properties of the PLLA, PDLA, and SC.

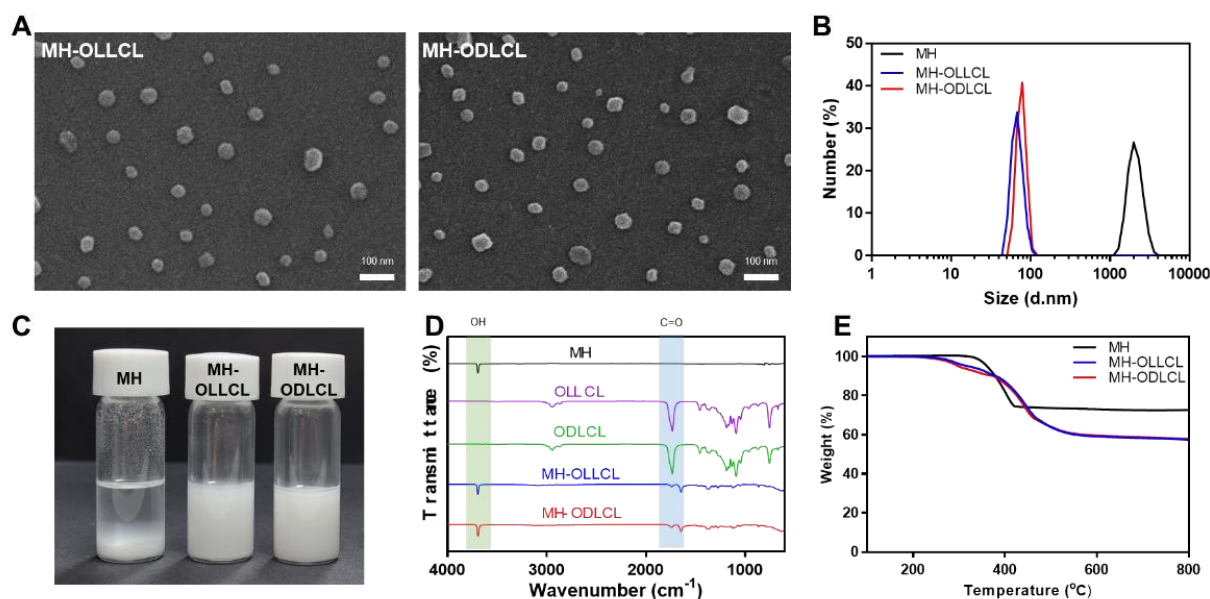
	T <sub>g</sub> (°C)	T <sub>c</sub> (°C)	T <sub>m,HC</sub> (°C)	ΔH <sub>m,HC</sub> (J/g)	T <sub>m,SC</sub> (°C)	ΔH <sub>m,SC</sub> (J/g)	X <sub>C,HC</sub> (%)	X <sub>C,SC</sub> (%)	f <sub>sc</sub> (%)
PLLA	66.68	111.92	179.42	64.49	–	–	69.34	–	–
PDLA	66.62	104.62	179.88	63.08	–	–	67.83	–	–
SC	67.76	112.18	178.21	15.97	220.28	28.84	17.17	20.31	54.19



**Figure 2.** (A) SEM image and (B) size distribution of SC. Scale bar: 5  $\mu\text{m}$ . (C) DSC thermograms, (D) XRD spectra, and (E,F) ATR-FTIR spectra of the PLLA, PDLA, and SC.

### 3.2. Characterization of the Surface-Modified Magnesium Hydroxide Nanoparticles

Figure 3A shows an SEM image of the surface-modified MH nanoparticles (MH-OLLCL and MH-ODLCL). The sizes of both the MH-OLLCL and MH-ODLCL were approximately 40 nm. As shown in Figure 3B, the average sizes of the MH, MH-OLLCL, and MH-ODLCL particles in an organic solvent analyzed by DLS were  $2111 \pm 449.8$ ,  $75.56 \pm 13.24$ , and  $76.93 \pm 10.25$  nm, respectively, which were slightly larger than the sizes determined from the SEM images due to the hydrodynamic volumes of the DLS method. The sizes of the MH-OLLCL and MH-ODLCL were smaller than those of the MHs, because the hydrophilic MHs aggregated in the organic solvent, whereas the surface-modified MH-OLLCL and MH-ODLCL with their hydrophobic oligomers had high stabilities in the organic solvent. Figure 3C shows the dispersion of the MHs, MH-OLLCL, and MH-ODLCL. Compared to the MHs, the surface-modified MH nanoparticles showed stable dispersity. The chemical structures of the synthesized MH-OLLCL and MH-ODLCL were analyzed by ATR-FTIR (Figure 3D). The unmodified MHs had peaks of -OH stretching at  $3699\text{ cm}^{-1}$ . The peaks at  $1760\text{ cm}^{-1}$  of the oligomers (OLLCL and ODLCL) represented the carbonyls of the ester groups. The MH-OLLCL and MH-ODLCL had peaks of shifted ester bonds at  $1644\text{ cm}^{-1}$ , which demonstrated that the OLLCL and ODLCL had been successfully modified on the surface of the MH nanoparticles. Figure 3E shows the amounts of OLLCL and ODLCL grafted on the surface of MHs measured by TGA. The weights of unmodified MH nanoparticles decreased in the temperature range of 280 to  $450\text{ }^{\circ}\text{C}$ , as the MH decomposed to magnesium oxide (MgO). The weight loss for the MHs reached 32.7% at  $700\text{ }^{\circ}\text{C}$ , and the weight losses for the MH-OLLCL and MH-ODLCL were 42.6 and 42.2%, respectively [32]. When the remaining MgO was converted into MH, the amounts of MH-OLLCL and MH-ODLCL were 16.9 and 16.3%, respectively.

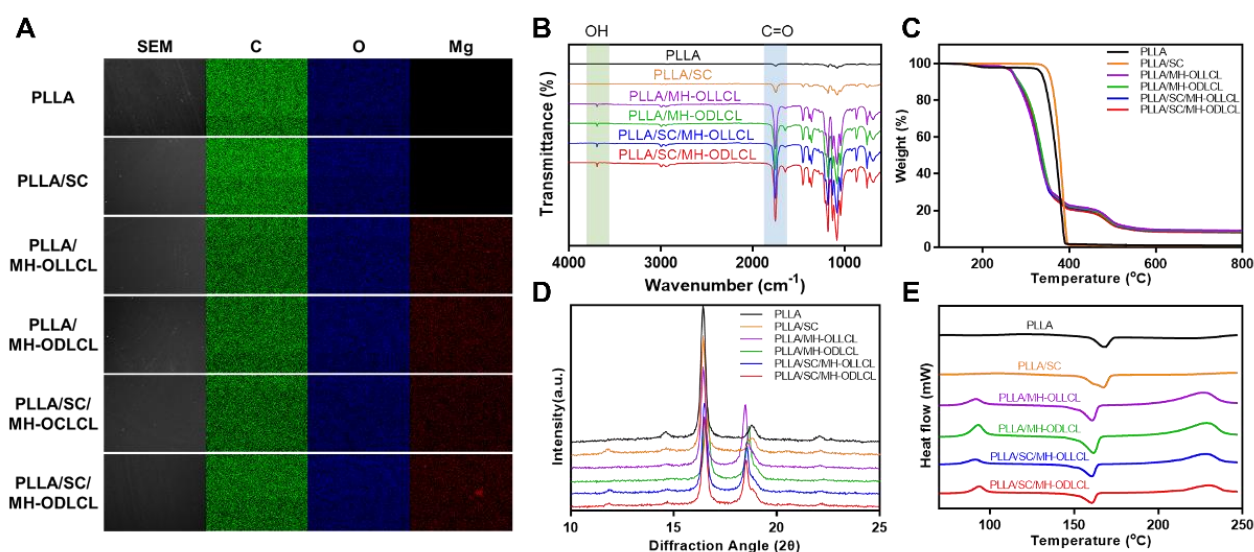


**Figure 3.** Characterization of the surface-modified MHs. (A) SEM images of the MH-OLLCL and MH-ODLCL. Scale bar: 100 nm. (B) Size distribution, (C) optical image of dispersion in an organic solvent, (D) ATR-FTIR spectra, and (E) TGA thermograms of the MHs, MH-OLLCL, and MH-ODLCL.

### 3.3. Characterization of the PLLA Composites

Figure 4A shows SEM images and corresponding EDS mappings for the PLLA, PLLA/SC, PLLA/MH-OLLCL, PLLA/MH-ODLCL, PLLA/SC/MH-OLLCL, and PLLA/SC/MH-ODLCL nanoparticles. All samples displayed smooth and uniform surfaces. The distribution of C, O, and Mg elements in each sample was observed via EDX analysis. The C and O mapping results were similar across all samples. While Mg elements were not detected in the PLLA and PLLA/SC nanoparticles, they were evenly distributed in the PLLA/MH-OLLCL, PLLA/MH-ODLCL, PLLA/SC/MH-OLLCL, and PLLA/SC/MH-ODLCL composites. To further confirm the MH in the PLLA composites, the PLLA, PLLA/SC, PLLA/MH-OLLCL, PLLA/MH-ODLCL, PLLA/SC/MH-OLLCL, and PLLA/SC/MH-ODLCL nanoparticles were measured by ATR-FTIR (Figure 4B). Compared with the PLLA and PLLA/SC composites, the PLLA/MH-OLLCL, PLLA/MH-ODLCL, PLLA/SC/MH-OLLCL, and PLLA/SC/MH-ODLCL nanoparticles had an -OH stretching absorption peak for MH at  $3697\text{ cm}^{-1}$ . The amounts of MH contained in the PLLA composites were measured using TGA thermograms (Figure 4C). The PLLA/MH-OLLCL, PLLA/MH-ODLCL, PLLA/SC/MH-OLLCL, and PLLA/SC/MH-ODLCL composites contained approximately 8% MH. In Figure 4D, to investigate crystallization by the stereocomplex structures, XRD patterns were estimated. The PLLA/SC, PLLA/SC/MH-OLLCL, and PLLA/SC/MH-ODLCL composites containing SC showed weak stereocomplex crystal peaks at  $2\theta = 11.8$  [27,31]. However, a stereocomplex crystal peak was not observed for the PLLA/MH-ODLCL because it was hidden by the strong crystal peak of MH. To further analyze stereocomplex structures, the nonisothermal crystallization and melting behaviors of PLA composites were evaluated by DSC (Figure 4E). Table 2 lists the thermal parameters obtained for the PLLA composites. All samples had  $T_g$  ranges from 55 to 63 °C and a  $T_m$  for homocrystallines of approximately 166 °C. The PLLA/MH-OLLCL, PLLA/MH-ODLCL, PLLA/SC/MH-OLLCL, and PLLA/SC/MH-ODLCL composites containing MH indicated exothermic peaks at the  $T_m$  position for stereocomplex crystallines, since the PLLA/MH showed an exothermic peak at about 230 °C (Figure S1). However, it had a different melting enthalpy by offsetting between the exothermic peak of MH and the endothermic peak of stereocomplex crystallines. The melting enthalpies of the PLLA/MH-OLLCL, PLLA/MH-ODLCL, PLLA/SC/MH-OLLCL, and PLLA/SC/MH-ODLCL composites

were 66.00, 52.49, 32.65, and 32.04 J/g, respectively. The MH-ODLCL had lower melting enthalpies than the MH-OLLCL due to their stereocomplex structures. Compared with the MH-OLLCL and MH-ODLCL, the melting enthalpies of the PLLA/SC/MH-OLLCL and PLLA/SC/MH-ODLCL composites were greatly reduced by the SC. The stereocomplex crystal peak for the PLLA/SC nanoparticles was also not exhibited. Tashiro et al. investigated stereocomplex crystal peaks according to PLLA/PDLA blend samples with various L/D form ratios [33]. They demonstrated that the stereocomplex crystal peak did not appear below a 9/1 ratio. Figure S2 shows ATR-FTIR spectra for the PLLA and PLLA/SC particles which demonstrate the stereocomplex structures of the PLLA/SC nanoparticles. The PLLA/SC showed FTIR absorption at  $908\text{ cm}^{-1}$ , indicating  $3_1$ -helical conformations of stereocomplex crystallines [25]. These results suggest that stereocomplex structures were formed in the PLLA composites by the SC and MH-ODLCL.



**Figure 4.** Characterization of the PLLA composites. (A) SEM image, (B) ATR-FTIR spectra, (C) TGA thermograms, (D) XRD spectra, and (E) DSC thermograms of the PLLA, PLLA/SC, PLLA/MH-OLLCL, PLLA/MH-ODLCL, PLLA/SC/MH-OLLCL, and PLLA/SC/MH-ODLCL composites.

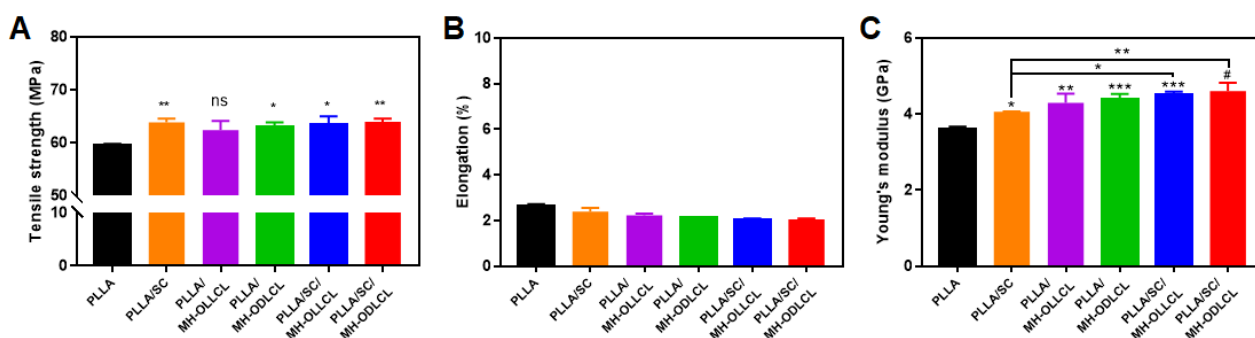
**Table 2.** Thermal properties of the PLLA, PLLA/SC, PLLA/MH-OLLCL, PLLA/MH-ODLCL, PLLA/SC/MH-OLLCL, and PLLA/SC/MH-ODLCL composites.

	$T_g$ (°C)	$T_c$ (°C)	$T_{m,HC}$ (°C)	$\Delta H_{m,HC}$ (J/g)	$X_{C,HC}$ (%)
PLLA	63.37	–	167.03	8.971	9.64
PLLA/SC	55.98	111.98	167.47	28.19	30.31
PLLA/MH-OLLCL	56.51	91.78	160.58	32.46	34.90
PLLA/MH-ODLCL	56.93	93.18	161.38	30.29	32.56
PLLA/SC/MH-OLLCL	55.81	91.32	160.45	27.95	30.05
PLLA/SC/MH-ODLCL	56.32	93.79	160.55	27.45	29.51

### 3.4. Mechanical Properties of the PLLA Composites

The mechanical properties of the PLLA composites were investigated by UTM. Figure 5A shows the tensile strengths of the PLLA composites. The PLLA/MH-OLLCL composite had a similar result to pure PLLA. In contrast, the tensile strength of the PLLA/MH-ODLCL composite increased compared to that of pure PLLA, because the MH-ODLCL formed stereocomplex structures with PLLA chains. The PLLA/SC, PLLA/SC/MH-OLLCL, and PLLA/SC/MH-ODLCL composites, in which stereocomplex structures formed between the SC and PLLA chains, had significantly improved tensile strengths of 63.7, 63.3, and 64.0 MPa, respectively. The elongation of all samples was around 2% (Figure 5B). Surface-modified

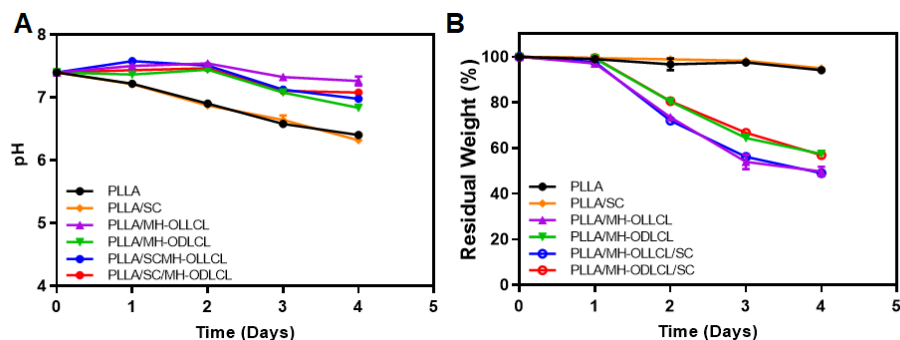
MH and SC in the PLLA composites did not affect elongation. The Young's moduli for the PLLA, PLLA/SC, PLLA/MH-OLLCL, PLLA/MH-ODLCL, PLLA/SC/MH-OLLCL, and PLLA/SC/MH-ODLCL composites were 4.06, 4.30, 4.38, 4.50, and 4.61 GPa, respectively. The inclusion of SC increased the Young's moduli by the formation of stereocomplex structures. The inclusion of surface-modified MH increased interaction between the PLLA chains and the surface-modified MH, resulting in improved Young's moduli. Among the PLLA composites containing surface-modified MH, the PLLA/MH-ODLCL composite showed an enhanced Young's modulus relative to the PLLA/MH-OLLCL composite due to the formation of stereocomplex structures. When both the surface-modified MH and SC were included, the Young's modulus increased further as a result of their synergistic effect, and the PLLA/SC/MH-ODLCL composite had the highest Young's modulus.



**Figure 5.** Mechanical properties of the PLLA, PLLA/SC, PLLA/MH-OLLCL, PLLA/MH-ODLCL, PLLA/SC/MH-OLLCL, and PLLA/SC/MH-ODLCL composites: (A) tensile strength, (B) elongation, and (C) Young's modulus (\*  $p < 0.05$ , \*\*  $p < 0.01$ , \*\*\*  $p < 0.001$ , #  $p < 0.0001$ ).

### 3.5. Degradation Behavior of the PLLA Composites

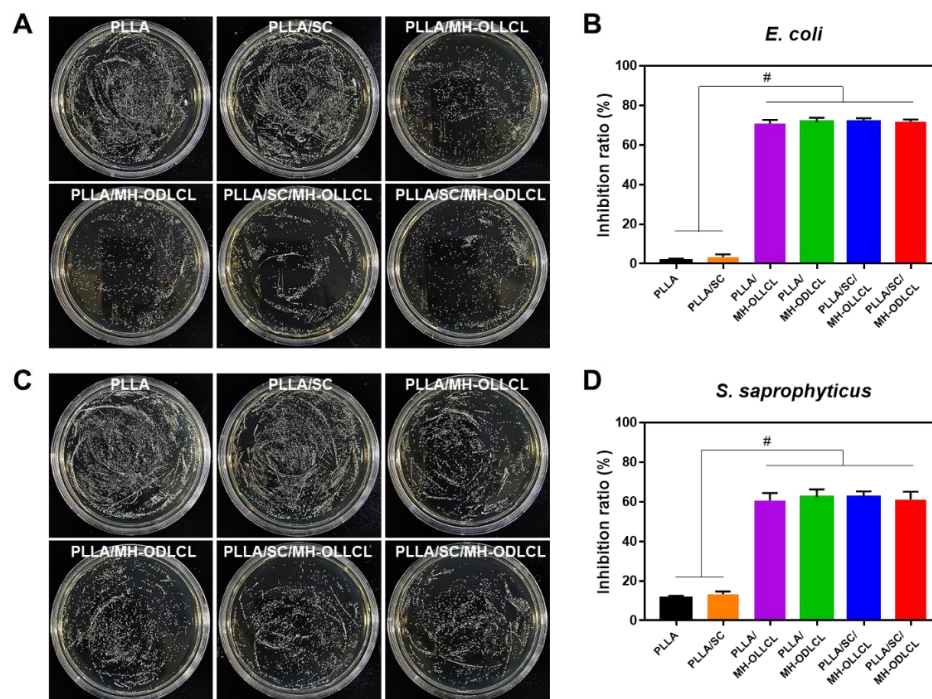
The degradation of the PLLA composites took place under accelerated conditions with proteinase K in PBS solution over 4 days. Figure 6A shows the change in pH values for the PLLA, PLLA/SC, PLLA/MH-OLLCL, PLLA/MH-ODLCL, PLLA/SC/MH-OLLCL, and PLLA/SC/MH-ODLCL composites. The pH values for the PLLA and PLLA/SC continuously decreased during degradation over the 4 days to 6.4 and 6.3, respectively. Meanwhile, the PLLA/MH-OLLCL, PLLA/MH-ODLCL, PLLA/SC/MH-OLLCL, and PLLA/SC/MH-ODLCL composites maintained neutral pHs at 7.22, 6.89, 6.98, and 7.08, respectively, because the MH in the PLLA composites released basic magnesium ions that neutralized the acidic by-products of the PLLA [34]. The residual weights of the PLLA and PLLA/SC did not degrade and were maintained at around 100% over the 4 days. In the PLLA/MH-OLLCL and PLLA/SC/MH-OLLCL composites, the residual weights decreased to 49.73 and 49.23%, respectively, over the 4 days. These results were due to the accelerated degradation, as MH was initially released and water molecules penetrated the MH-released sites. Compared to the PLLA composites containing MH-OLLCL, the PLLA/MH-ODLCL and PLLA/SC/MH-ODLCL composites were slowly degraded due to their being densely packed and their enhanced intermolecular interactions (57.43 and 58.89%, respectively). Thus, the PLLA composites with MH can biodegrade within 24 months to suppress the inflammation that occurs during long-term implantation.



**Figure 6.** Changes in (A) pH value and (B) residual weight during degradation in PBS solution with proteinase K at 37 °C over 4 days for the PLLA, PLLA/SC, PLLA/MH-OLLCL, PLLA/MH-ODLCL, PLLA/SC/MH-OLLCL, and PLLA/SC/MH-ODLCL composites.

### 3.6. Biological Properties of the PLLA Composites

Figure 7 shows results of the investigation of the bactericidal activity of each of the PLLA composites. Antimicrobial activity results for the PLLA and the PLLA/SC, PLLA/MH-OLLCL, PLLA/MH-ODLCL, PLLA/SC/MH-OLLCL, and PLLA/SC/MH-ODLCL composites showed that the Gram-negative bacteria (*E. coli*) were inhibited by 1.72, 3.32, 70.86, 71.66, 71.75, and 71.80%, respectively, and that the Gram-positive bacteria (*S. saprophyticus*) were inhibited by 11.71, 13.33, 60.62, 62.28, 62.35, and 61.07%, respectively. Compared to the PLLA and the PLLA/SC, the PLLA composites containing MH significantly inhibited both *E. coli* and *S. saprophyticus* due to the presence of MH. These results suggest that the PLLA composites containing MH have antibacterial effects, since the adsorption of  $Mg^{2+}$  ions destroys bacterial cell walls and induces cell death [16,35–39].

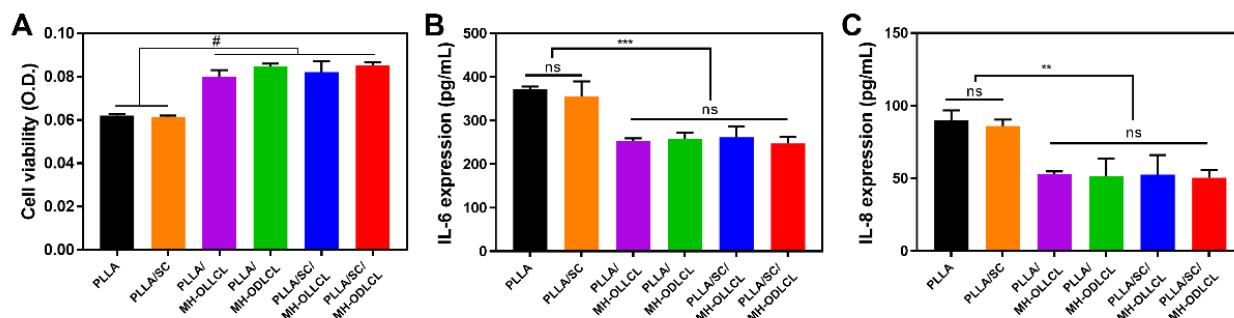


**Figure 7.** The bactericidal activity of each PLLA composite was investigated. Representative images showing the antimicrobial activities against Gram-negative bacteria (*E. coli*; A,B) and Gram-positive bacteria (*S. saprophyticus*; C,D) of the PLLA and the PLLA/SC, PLLA/MH-OLLCL, PLLA/MH-ODLCL, PLLA/SC/MH-OLLCL, and PLLA/SC/MH-ODLCL composites and their respective quantifications (#  $p < 0.0001$ ).



The cell viability of HCAECs was evaluated under treatment with L-lactic acid (L-Lac, 12 mM), the degradation product of PLLA, and with surface-modified MH (Figure S3). The cell viability of HCAECs was reduced to 36% when treated with L-Lac. On the other hand, the L-Lac and surface-modified MH treated groups demonstrated cell viabilities of more than 80%. On the basis of these results, it was demonstrated that the acidic degradation products of PLLA induced damage to HCAECs and that the MH inhibited damage to HCAECs by neutralizing the acidic degradation products.

To investigate the biocompatibility of the PLLA composites in vitro, HCAECs were treated with degradation products obtained under accelerated conditions (Figure 8). Figure 8A shows cell viability at 24 h as quantified by CCK-8. Compared to the PLLA/MH-OLLCL, PLLA/MH-ODLCL, PLLA/SC/MH-OLLCL, and PLLA/SC/MH-ODLCL composites, the cell viability of the PLLA and PLLA/SC decreased due to acidic degradation by-products. On the other hand, cell viability did not decrease for the PLLA composites including MH due to the neutralization of the acidic degradation products by MH. In addition, the release of magnesium ions by dissociated MH affects mitochondrial RNA splicing protein 2 (MRS2) and transient receptor potential cation channel subfamily M member 7 (TRPM7) and maintains the homeostasis of HCAECs [10]. The expression of pro-inflammatory cytokines was investigated using an ELISA kit (Figure 8B,C). Compared to PLLA and PLLA/SC, the PLLA/MH-OLLCL, PLLA/MH-ODLCL, PLLA/SC/MH-OLLCL, and PLLA/SC/MH-ODLCL composites showed decreased expression of IL-6 and IL-8. Consequently, MH significantly prevented noninfectious inflammatory reactions caused by lactic acid derived from PLLA. Riemann et al. reported that an acidic environment leads to pathological gene expression and induces an inflammatory response [34,40].



**Figure 8.** In vitro biocompatibility test of the PLLA and PLLA/MH, PLLA/SC, PLLA/MH-OLLCL, PLLA/MH-ODLCL, PLLA/SC/MH-OLLCL, and PLLA/SC/MH-ODLCL composites. (A) HCAECs cell viability with the degradation product of the PLLA composites treatment for 24 h. The expressions of (B) IL-6 and (C) IL-8 in HCAECs after 24 h, as determined by ELISA (\*\*  $p < 0.01$ , \*\*\*  $p < 0.001$ , #  $p < 0.0001$ ).

#### 4. Conclusions

Among biodegradable polymers, PLLA has attracted attention as a biomaterial due to its non-toxicity, elasticity, biodegradability, and good mechanical strength. However, it is unsuitable for producing items that require high mechanical strength, such as cardiovascular stents, and pH at the implant site in the body is reduced by its degradation products, which induces an inflammatory response. In this study, the composite, including SC and modified MH in PLLA, was successfully prepared for formation of stereocomplex structure and anti-inflammatory effect.

We investigated the formation of stereocomplex structures and the anti-inflammatory effects of SC and surface-modified MH in the PLLA composites. The PLLA composites containing SC and surface-modified MH showed significantly improved mechanical properties due to the existence of stereocomplex structures and inhibited inflammatory responses in vascular endothelial cells. In addition, they recently displayed antibacterial effects that are considered important in biomedical materials [39,41].

There is a limitation to this study. Since it is known that the degradation period of PLLA is more than 24 months, we measured the degradation behavior of PLLA composites using proteinase K under accelerated conditions [42]. When the PLLA was hydrolyzed at 37 °C, the pH value remained neutral for up to 40 weeks and the mechanical strength decreased from 6 months [42,43]. Therefore, it can be inferred that the method using proteinase K quickly passed the period of maintained mechanical strength. In a future study, we plan to degrade the PLLA composites at 37 °C over 2 years to measure their mechanical properties and degradation behavior.

These PLLA composites are expected to be applied in the future as biomaterials in the production of such items as biodegradable vascular scaffolds with improved mechanical properties and reduced cytotoxicity.

**Supplementary Materials:** The following supporting information can be downloaded at: <https://www.mdpi.com/article/10.3390/polym14183790/s1>, Figure S1: DSC thermograms of the PLLA/MH, Figure S2: ATR-FTIR spectra of the PLLA and PLLA/SC, Figure S3: Cell viability of HCAEC in 12 mM L-Lac with surface-modified MH at a concentration of 10 phr for 24 h.

**Author Contributions:** D.K.H. and C.G.P. conceived and supervised the project. S.-W.B. and J.H.K. contributed equally to this work. S.-W.B., J.H.K., D.-S.K., and D.H.S. performed the experiments and analyzed the data. The manuscript was written by S.-W.B., J.H.K., D.-S.K., and C.G.P. All authors have read and agreed to the published version of the manuscript.

**Funding:** This work was supported by the Basic Science Research Program (2020R1A2B5B03002344) and the Bio & Medical Technology Development Program (2018M3A9E2024579) through the National Research Foundation of Korea, funded by the Ministry of Science and ICT (MSIT); a Korea Medical Device Development Fund grant, funded by the Korean government (the Ministry of Science and ICT; the Ministry of Trade, Industry and Energy; the Ministry of Health & Welfare, Republic of Korea); and the Ministry of Food and Drug Safety (202011A05-05); and the Korea Health Technology R&D Project through the Korea Health Industry Development Institute (KHIDI), funded by the Ministry of Health & Welfare, Republic of Korea (HI18C0089).

**Institutional Review Board Statement:** Not applicable.

**Informed Consent Statement:** Not applicable.

**Data Availability Statement:** The data used in this study are presented in the text. Additional information can be made available upon request from the corresponding author.

**Conflicts of Interest:** The authors declare no conflict of interest.

## References

1. Capuana, E.; Lopresti, F.; Ceraulo, M.; La Carrubba, V. Poly-L-Lactic Acid (PLLA)-Based Biomaterials for Regenerative Medicine: A Review on Processing and Applications. *Polymers* **2022**, *14*, 1153. [CrossRef] [PubMed]
2. Arkaban, H.; Barani, M.; Akbarizadeh, M.R.; Pal Singh Chauhan, N.; Jadoun, S.; Dehghani Soltani, M.; Zarrintaj, P. Polyacrylic Acid Nanoplatfoms: Antimicrobial, Tissue Engineering, and Cancer Theranostic Applications. *Polymers* **2022**, *14*, 1259. [CrossRef] [PubMed]
3. Liu, J.; Li, T.; Zhang, H.; Zhao, W.; Qu, L.; Chen, S.; Wu, S. Electrospun strong, bioactive, and bioabsorbable silk fibroin/poly (L-lactic-acid) nanoyarns for constructing advanced nanotextile tissue scaffolds. *Mater. Today Bio* **2022**, *14*, 100243. [CrossRef] [PubMed]
4. Wang, X.; Peng, S.; Chen, H.; Yu, X.; Zhao, X. Mechanical properties, rheological behaviors, and phase morphologies of high-toughness PLA/PBAT blends by in-situ reactive compatibilization. *Compos. Part B* **2019**, *173*, 107028. [CrossRef]
5. Deng, L.; Xu, C.; Wang, X.; Wang, Z. Supertoughened Polylactide Binary Blend with High Heat Deflection Temperature Achieved by Thermal Annealing above the Glass Transition Temperature. *ACS Sustain. Chem. Eng.* **2018**, *6*, 480–490. [CrossRef]
6. Eleuteri, M.; Bernal, M.; Milanesio, M.; Monticelli, O.; Fina, A. Stereocomplexation of Poly(Lactic Acid)s on Graphite Nanoplatelets: From Functionalized Nanoparticles to Self-assembled Nanostructures. *Front. Chem.* **2019**, *7*, 176. [CrossRef]
7. Luo, F.; Fortenberry, A.; Ren, J.; Qiang, Z. Recent Progress in Enhancing Poly(Lactic Acid) Stereocomplex Formation for Material Property Improvement. *Front. Chem.* **2020**, *8*, 688. [CrossRef]
8. Wan, Z.-Q.; Longo, J.M.; Liang, L.-X.; Chen, H.-Y.; Hou, G.-J.; Yang, S.; Zhang, W.-P.; Coates, G.W.; Lu, X.-B. Comprehensive Understanding of Polyester Stereocomplexation. *J. Am. Chem. Soc.* **2019**, *141*, 14780–14787. [CrossRef]

9. Im, S.H.; Jung, Y.; Kim, S.H. In Situ Homologous Polymerization of L-Lactide Having a Stereocomplex Crystal. *Macromolecules* **2018**, *51*, 6303–6311. [[CrossRef](#)]
10. Ko, K.-W.; Choi, B.; Kang, E.Y.; Shin, S.-W.; Baek, S.-W.; Han, D.K. The antagonistic effect of magnesium hydroxide particles on vascular endothelial activation induced by acidic PLGA degradation products. *Biomater. Sci.* **2021**, *9*, 892–907. [[CrossRef](#)]
11. Yang, F.; Niu, X.; Gu, X.; Xu, C.; Wang, W.; Fan, Y. Biodegradable Magnesium-Incorporated Poly(l-lactic acid) Microspheres for Manipulation of Drug Release and Alleviation of Inflammatory Response. *ACS Appl. Mater. Interfaces* **2019**, *11*, 23546–23557. [[CrossRef](#)] [[PubMed](#)]
12. Kim, Y.A.; Chun, S.Y.; Park, S.-B.; Kang, E.; Koh, W.-G.; Kwon, T.G.; Han, D.K.; Joung, Y.K. Scaffold-supported extracellular matrices preserved by magnesium hydroxide nanoparticles for renal tissue regeneration. *Biomater. Sci.* **2020**, *8*, 5427–5440. [[CrossRef](#)] [[PubMed](#)]
13. Ge, Y.; Hu, Z.; Chen, J.; Qin, Y.; Wu, F.; Jin, T. Exenatide Microspheres for Monthly Controlled-Release Aided by Magnesium Hydroxide. *Pharmaceutics* **2021**, *13*, 816. [[CrossRef](#)] [[PubMed](#)]
14. Go, E.J.; Kang, E.Y.; Lee, S.K.; Park, S.; Kim, J.H.; Park, W.; Kim, I.H.; Choi, B.; Han, D.K. An osteoconductive PLGA scaffold with bioactive  $\beta$ -TCP and anti-inflammatory Mg(OH)<sub>2</sub> to improve in vivo bone regeneration. *Biomater. Sci.* **2020**, *8*, 937–948. [[CrossRef](#)]
15. Jang, H.J.; Park, S.-B.; Bedair, T.M.; Oh, M.-K.; Ahn, D.-J.; Park, W.; Joung, Y.K.; Han, D.K. Effect of various shaped magnesium hydroxide particles on mechanical and biological properties of poly(lactic-co-glycolic acid) composites. *J. Ind. Eng. Chem.* **2018**, *59*, 266–276. [[CrossRef](#)]
16. Pan, X.; Wang, Y.; Chen, Z.; Pan, D.; Cheng, Y.; Liu, Z.; Lin, Z.; Guan, X. Investigation of Antibacterial Activity and Related Mechanism of a Series of Nano-Mg(OH)<sub>2</sub>. *ACS Appl. Mater. Interfaces* **2013**, *5*, 1137–1142. [[CrossRef](#)]
17. Heydarian, M.; Schweinlin, M.; Schwarz, T.; Rawal, R.; Walles, H.; Metzger, M.; Rudel, T.; Kozjak-Pavlovic, V. Triple co-culture and perfusion bioreactor for studying the interaction between *Neisseria gonorrhoeae* and neutrophils: A novel 3D tissue model for bacterial infection and immunity. *J. Tissue Eng.* **2021**, *12*, 2041731420988802. [[CrossRef](#)]
18. Kim, J.K.; Go, E.J.; Ko, K.W.; Oh, H.J.; Han, J.; Han, D.K.; Park, W. PLGA Microspheres Containing Hydrophobically Modified Magnesium Hydroxide Particles for Acid Neutralization-Mediated Anti-Inflammation. *Tissue Eng. Regen. Med.* **2021**, *18*, 613–622. [[CrossRef](#)]
19. Shuai, C.; Yu, L.; Feng, P.; Peng, S.; Pan, H.; Bai, X. Construction of a stereocomplex between poly(d-lactide) grafted hydroxyapatite and poly(l-lactide): Toward a bioactive composite scaffold with enhanced interfacial bonding. *J. Mater. Chem. B* **2022**, *10*, 214–223. [[CrossRef](#)]
20. Kamiya, H.; Iijima, M. Surface modification and characterization for dispersion stability of inorganic nanometer-scaled particles in liquid media. *Sci. Technol. Adv. Mater.* **2010**, *11*, 044304. [[CrossRef](#)]
21. Kango, S.; Kalia, S.; Celli, A.; Njuguna, J.; Habibi, Y.; Kumar, R. Surface modification of inorganic nanoparticles for development of organic-inorganic nanocomposites—A review. *Prog. Polym. Sci.* **2013**, *38*, 1232–1261. [[CrossRef](#)]
22. Zhao, Y.; Liu, B.; Yang, J.; Jia, J.; You, C.; Chen, M. Effects of modifying agents on surface modifications of magnesium oxide whiskers. *Appl. Surf. Sci.* **2016**, *388*, 370–375. [[CrossRef](#)]
23. Kang, E.Y.; Park, S.-B.; Choi, B.; Baek, S.-W.; Ko, K.-W.; Rhim, W.-K.; Park, W.; Kim, I.-H.; Han, D.K. Enhanced mechanical and biological characteristics of PLLA composites through surface grafting of oligolactide on magnesium hydroxide nanoparticles. *Biomater. Sci.* **2020**, *8*, 2018–2030. [[CrossRef](#)] [[PubMed](#)]
24. Baek, S.-W.; Song, D.H.; Lee, H.I.; Kim, D.-S.; Heo, Y.; Kim, J.H.; Park, C.G.; Han, D.K. Poly(L-Lactic Acid) Composite with Surface-Modified Magnesium Hydroxide Nanoparticles by Biodegradable Oligomer for Augmented Mechanical and Biological Properties. *Materials* **2021**, *14*, 5869. [[CrossRef](#)] [[PubMed](#)]
25. Ren, Q.; Wu, M.; Weng, Z.; Zhu, X.; Li, W.; Huang, P.; Wang, L.; Zheng, W.; Ohshima, M. Promoted formation of stereocomplex in enantiomeric poly(lactic acid)s induced by cellulose nanofibers. *Carbohydr. Polym.* **2022**, *276*, 118800. [[CrossRef](#)] [[PubMed](#)]
26. Srithep, Y.; Akkaprasa, T.; Pholharn, D.; Morris, J.; Liu, S.-J.; Patrojanasophon, P.; Ngawhirunpat, T. Metronidazole-loaded polylactide stereocomplex electrospun nanofiber mats for treatment of periodontal disease. *J. Drug Deliv. Sci. Technol.* **2021**, *64*, 102582. [[CrossRef](#)]
27. Park, H.-S.; Hong, C.-K. Relationship between the Stereocomplex Crystallization Behavior and Mechanical Properties of PLLA/PDLA Blends. *Polymers* **2021**, *13*, 1851. [[CrossRef](#)]
28. Sun, C.; Zheng, Y.; Xu, S.; Ni, L.; Li, X.; Shan, G.; Bao, Y.; Pan, P. Role of Chain Entanglements in the Stereocomplex Crystallization between Poly(lactic acid) Enantiomers. *ACS Macro Lett.* **2021**, *10*, 1023–1028. [[CrossRef](#)]
29. Gu, T.; Sun, D.-X.; Qi, X.-D.; Yang, J.-H.; Zhao, C.-S.; Lei, Y.-Z.; Wang, Y. Synchronously enhanced thermal conductivity and heat resistance in poly(l-lactide)/graphene nanoplatelets composites via constructing stereocomplex crystallites at interface. *Compos. Part B* **2021**, *224*, 109163. [[CrossRef](#)]
30. Chen, J.; Rong, C.; Lin, T.; Chen, Y.; Wu, J.; You, J.; Wang, H.; Li, Y. Stable Co-Continuous PLA/PBAT Blends Compatibilized by Interfacial Stereocomplex Crystallites: Toward Full Biodegradable Polymer Blends with Simultaneously Enhanced Mechanical Properties and Crystallization Rates. *Macromolecules* **2021**, *54*, 2852–2861. [[CrossRef](#)]
31. Liu, H.; Bai, D.; Du, S.; Li, X.; Bai, H.; Fu, Q. Stereocomplex Crystallization Induced Significant Improvement in Transparency and Stiffness-Toughness Performance of Core-Shell Rubber Nanoparticles Toughened Poly(l-lactide) Blends. *Macromol. Mater. Eng.* **2021**, *306*, 2100021. [[CrossRef](#)]

32. Hsu, J.-P.; Nacu, A. Preparation of submicron-sized Mg(OH)<sub>2</sub> particles through precipitation. *Colloids Surf. A Physicochem. Eng. Asp.* **2005**, *262*, 220–231. [[CrossRef](#)]
33. Tashiro, K.; Kouno, N.; Wang, H.; Tsuji, H. Crystal Structure of Poly(lactic acid) Stereocomplex: Random Packing Model of PDLA and PLLA Chains As Studied by X-ray Diffraction Analysis. *Macromolecules* **2017**, *50*, 8048–8065. [[CrossRef](#)]
34. Bedair, T.M.; Lee, C.K.; Kim, D.S.; Baek, S.W.; Bedair, H.M.; Joshi, H.P.; Choi, U.Y.; Park, K.H.; Park, W.; Han, I.; et al. Magnesium hydroxide-incorporated PLGA composite attenuates inflammation and promotes BMP2-induced bone formation in spinal fusion. *J. Tissue. Eng.* **2020**, *11*, 2041731420967591. [[CrossRef](#)]
35. Arampatzis, A.S.; Kontogiannopoulos, K.N.; Theodoridis, K.; Aggelidou, E.; Rat, A.; Willems, A.; Tsivintzelis, I.; Papageorgiou, V.P.; Kritis, A.; Assimopoulou, A.N. Electrospun wound dressings containing bioactive natural products: Physico-chemical characterization and biological assessment. *Biomater. Res.* **2021**, *25*, 23. [[CrossRef](#)]
36. Irfan, M.; Munir, H.; Ismail, H. Moringa oleifera gum based silver and zinc oxide nanoparticles: Green synthesis, characterization and their antibacterial potential against MRSA. *Biomater. Res.* **2021**, *25*, 17. [[CrossRef](#)]
37. Halbus, A.F.; Horozov, T.S.; Paunov, V.N. Controlling the Antimicrobial Action of Surface Modified Magnesium Hydroxide Nanoparticles. *Biomimetics* **2019**, *4*, 41. [[CrossRef](#)]
38. Balducci, G.; Bravo Diaz, L.; Gregory, D.H. Recent progress in the synthesis of nanostructured magnesium hydroxide. *CrystEngComm* **2017**, *19*, 6067–6084. [[CrossRef](#)]
39. Kim, D.-S.; Lee, J.-K.; Kim, J.H.; Lee, J.; Kim, D.S.; An, S.; Park, S.-B.; Kim, T.-H.; Rim, J.S.; Lee, S.; et al. Advanced PLGA hybrid scaffold with a bioactive PDRN/BMP2 nanocomplex for angiogenesis and bone regeneration using human fetal MSCs. *Sci. Adv.* **2021**, *7*, eabj1083. [[CrossRef](#)]
40. Riemann, A.; Ihling, A.; Thomas, J.; Schneider, B.; Thews, O.; Gekle, M. Acidic environment activates inflammatory programs in fibroblasts via a cAMP-MAPK pathway. *Biochim. Biophys. Acta.* **2015**, *1853*, 299–307. [[CrossRef](#)]
41. Qiao, S.; Wu, D.; Li, Z.; Zhu, Y.; Zhan, F.; Lai, H.; Gu, Y. The combination of multi-functional ingredients-loaded hydrogels and three-dimensional printed porous titanium alloys for infective bone defect treatment. *J. Tissue Eng.* **2020**, *11*, 2041731420965797. [[CrossRef](#)] [[PubMed](#)]
42. Onuma, Y.; Serruys, P.W. Bioresorbable scaffold: The advent of a new era in percutaneous coronary and peripheral revascularization? *Circulation* **2011**, *123*, 779–797. [[CrossRef](#)] [[PubMed](#)]
43. Bartkowiak-Jowska, M.; Będziński, R.; Kozłowska, A.; Filipiak, J.; Pezowicz, C. Mechanical, rheological, fatigue, and degradation behavior of PLLA, PGLA and PDGLA as materials for vascular implants. *Meccanica* **2013**, *48*, 721–731. [[CrossRef](#)]



Review

# The Use of Carbohydrate Biopolymers in Plant Protection against Pathogenic Fungi

Grażyna Korbecka-Glinka <sup>1,\*</sup>, Klaudia Piekarska <sup>2</sup> and Maria Wiśniewska-Wrona <sup>2</sup>

<sup>1</sup> Department of Plant Breeding and Biotechnology, Institute of Soil Science and Plant Cultivation-State Research Institute, Czartoryskich 8, 24-100 Puławy, Poland

<sup>2</sup> Biomedical Engineering Center, Łukasiewicz Research Network-Łódź Institute of Technology, Skłodowskiej-Curie 19/27, 90-570 Łódź, Poland; klaudia.piekarska@lit.lukasiewicz.gov.pl (K.P.); maria.wisniewska-wrona@lit.lukasiewicz.gov.pl (M.W.-W.)

\* Correspondence: gkorbecka@iung.pulawy.pl

**Abstract:** Fungal pathogens cause significant yield losses of many important crops worldwide. They are commonly controlled with fungicides which may have negative impact on human health and the environment. A more sustainable plant protection can be based on carbohydrate biopolymers because they are biodegradable and may act as antifungal compounds, effective elicitors or carriers of active ingredients. We reviewed recent applications of three common polysaccharides (chitosan, alginate and cellulose) to crop protection against pathogenic fungi. We distinguished treatments dedicated for seed sowing material, field applications and coating of harvested fruits and vegetables. All reviewed biopolymers were used in the three types of treatments, therefore they proved to be versatile resources for development of plant protection products. Antifungal activity of the obtained polymer formulations and coatings is often enhanced by addition of biocontrol microorganisms, preservatives, plant extracts and essential oils. Carbohydrate polymers can also be used for controlled-release of pesticides. Rapid development of nanotechnology resulted in creating new promising methods of crop protection using nanoparticles, nano-/micro-carriers and electrospun nanofibers. To summarize this review we outline advantages and disadvantages of using carbohydrate biopolymers in plant protection.

**Keywords:** phytopathogenic fungi; polysaccharides; plant protection; antifungal coatings; seed coating; seed treatments; field applications; pre-harvest treatments; post-harvest treatments; edible coatings

**Citation:** Korbecka-Glinka, G.; Piekarska, K.; Wiśniewska-Wrona, M. The Use of Carbohydrate Biopolymers in Plant Protection against Pathogenic Fungi. *Polymers* **2022**, *14*, 2854. <https://doi.org/10.3390/polym14142854>

Academic Editor: José Miguel Ferri

Received: 1 May 2022

Accepted: 7 July 2022

Published: 13 July 2022

**Publisher's Note:** MDPI stays neutral with regard to jurisdictional claims in published maps and institutional affiliations.



**Copyright:** © 2022 by the authors. Licensee MDPI, Basel, Switzerland. This article is an open access article distributed under the terms and conditions of the Creative Commons Attribution (CC BY) license (<https://creativecommons.org/licenses/by/4.0/>).

## 1. Introduction

Agriculture today faces a challenge of having to produce food for the growing human population, while pests and pathogens constantly reduce the crop. Global estimates of yield losses caused by pests and pathogens in five major food crops (including wheat, rice, maize, potato and soybean) range from 17.2% to 30.0% [1]. Among the pathogens, fungi and oomycetes are considered to be the most destructive [2,3]. Key aspects of biology of these organisms, important from the epidemiological perspective, include broad host ranges, high virulence, high reproductive potential and ability to survive outside the plant host as a saprophyte or durable spores [3]. Fungal and oomycete pathogens pose a growing threat to the global food security because they spread to new areas with trade and transport or due to climate change. Moreover, common agricultural practices do not help to combat epidemics, as genetically uniform crops are grown in large areas in monocultures while their protection relies on single resistance genes in the plants or/and single-target-site fungicides. Selection pressures in such agroecosystems favor prolific variants of fungicide-resistant pathogens which are able to overcome plant resistance [4].

Introduction of first synthetic organic fungicides (thiram, zineb and nabam) in the 1940s initiated a rapid development of the plant protection industry. In the next three decades,

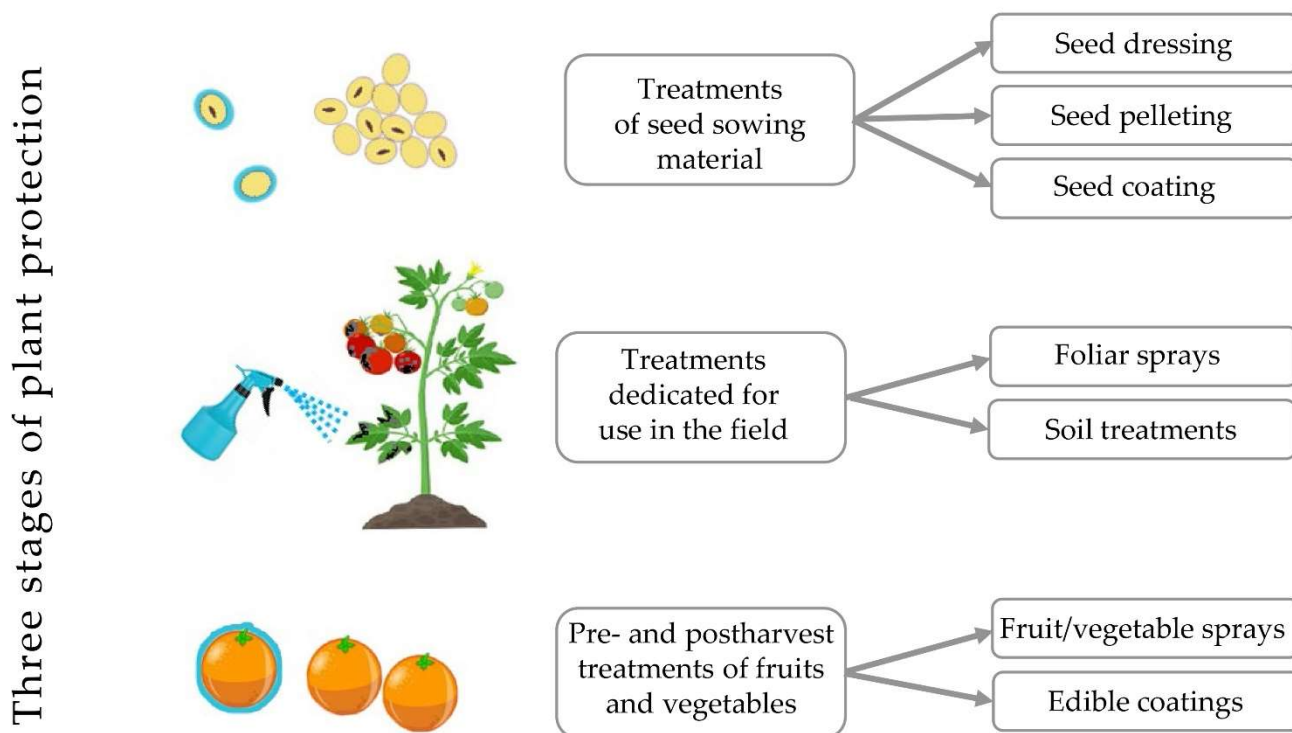
many new active compounds representing major classes of fungicides were produced and applied to plant protection, first to horticultural crops and then to cereals [5]. Soon fungicide treatments became a common practice in agriculture and they were associated with a significant increase in yield, ranging from 14% to 100% depending on the crop [6]. The current list of fungal control agents includes over 230 compounds, and the development of new ones is driven by fungicide resistance management [7,8]. However, widespread usage of pesticides was also associated with the contamination of terrestrial and aquatic ecosystems, toxic effects on non-target organisms and negative impact on human health [9,10]. The growing concerns about these problems have led to introducing regulations concerning safe and efficient use of these agrochemicals and a registration of new active ingredients worldwide [11]. A recent “Farm to Fork Strategy” adopted by the European Commission aims at 50% reduction in the use of chemical pesticides by 2030 [12].

Few alternative approaches were proposed to address the challenge of significant reduction in pesticide use. Lázaro et al. [13] suggested, based on their meta-analysis, that 50% reduction in fungicide use can be achieved by employing decision support systems, which will help the farmers to plan fungicide application based on an observed or a predicted risk of fungal disease. Nevertheless, the agrochemical industry responds to the challenges in plant protection differently-by exploring other two alternative approaches: developing advanced types of fungicides with novel modes of action and improving application of conventional fungicides by means of targeted delivery systems based on encapsulation technology [14]. Another approach is to search for ingredients of safer plant protection formulations among metal/metal oxide nanoparticles, plant extracts, essential oils, antagonistic microorganisms or food additives (e.g., [14,15]).

Carbohydrate biopolymers can also be used to develop plant protection products which will form an alternative to conventional fungicides. These biopolymers can be obtained in large amounts from many natural sources. They are also non-toxic and biodegradable, and therefore suitable for use in organic agriculture. Moreover, they can interact with many hydrophobic and hydrophilic compounds in more complex formulations [16]. There are three functions carbohydrate biopolymers may play in plant protection against pathogenic fungi. Firstly, they may directly interact with fungi by inhibiting spore germination and mycelial growth, what was shown in case of chitosan [17,18]. Secondly, they may act as effective elicitors inducing the plant immune system to cope with pathogens [19]. Thirdly, they may be used as carrier in controlled-release formulations of agrochemicals or other active ingredients [16].

Plants are threatened by fungi at different stages of their growth, hence different types of treatments were developed to ensure efficient plant protection (Figure 1). Firstly, seeds may be colonized by pathogenic fungi or they cope with them during germination in the soil. Therefore, various seed treatments were developed to enhance the quality of seed sowing material and to improve plant emergence in the field [20–22]. Secondly, in the field, plants are exposed to a variety of air- and soil-borne pathogens, hence antifungal formulations are applied in a form of foliar sprays or soil treatments in order to provide adequate protection [23,24]. Finally, ripe fruits and vegetables may be colonized by fungi which decrease their storability and induce decay; therefore, additional plant protection is required before or after harvest and it is frequently applied in a form of edible coatings [25,26].

Here we aim at reviewing recent studies on using carbohydrate polymers in antifungal formulations dedicated for the above-mentioned stages of crop production, for: seed treatments, use in the field and treatments of harvested crops. We will focus on three commonly available biopolymers: chitosan, alginate and cellulose.



**Figure 1.** Stages and forms of antifungal plant protection applications which can be based on carbohydrate biopolymers.

## 2. Chitosan

Chitin is the second most abundant renewable biopolymer in the world [27]. It occurs in marine shellfish, insects, mushrooms and yeast. The highest percentage content of chitin has been observed in shells and tails of crabs, shrimps and lobsters [28]. The best-known derivative of chitin is chitosan, which is a polycationic polymer isolated after the deacetylation of chitin. Chitosan is a linear polymer  $\beta$ -(1 $\rightarrow$ 4)-linked D-glucosamine and N-acetyl-D-glucosamine. Compared to chitin, chitosan is more functional due to its amino based functional groups stretching along the chain [29]. In addition, the protonation intensity of amino groups also plays a vital role in its functionality. Following the process of deacetylation, chitosan can be obtained from the solution in different forms, such as powder, fiber and sponges [30]. The molecular weight (Mw), degree of deacetylation (DA), ionic concentration, pH, the nature of the acid and the distribution of acetyl groups along with the main chain essentially influence the solubility of chitosan. Being a cationic polymer, chitosan displays instability in media with variable pH and ionic strength. This biopolymer has a variety of unique functional characteristics, such as biodegradability, biocompatibility, nontoxicity, antibacterial and antifungal properties. Its biological properties depend on factors such as the DA, Mw, polymerization, viscosity and dissociation constant. It has versatile mechanical properties, which have led to its enhancement of use in different applications such as encapsulation technology and controlled release coatings [31].

The most useful property of chitosan in agriculture is that it can act as a trigger in plant defense against pathogenic microorganisms. In addition, chitosan shows broad-spectrum antimicrobial effects against bacteria, fungi and viruses. Generally, chitosan is more effective against fungi than bacteria and it often exhibits higher inhibition effects on Gram-positive bacteria than Gram-negative bacteria, possibly because Gram-negative bacteria have an outer membrane structure in the cell wall affecting the cellular entry of chitosan [32]. Chitosan is widely used in agriculture in pre- and post-harvest treatments of crops to control microbial infections [18]. Chitosan-induced inhibition was observed in studies focusing on assessment of mycelial growth, sporulation, spore viability and germination and the production of fungal virulence factors. Chitosan has also been applied as a sole



ingredient or composite with other elements especially with metals particles for enhanced anti-fungal effects [33]. For example, silver nanoparticles were incorporated into chitosan and tested the nanocomposite formulation as an anti-fungal agent against *Rhizoctonia solani*, *Aspergillus flavus* and *Alternaria alternata* isolated from chickpea seeds. Importantly from economical point of view, chitosan affects germination and hyphal morphology fungal of pathogens threatening harvested crops (e.g., *Rhizopus stolonifer* and *Botrytis cinerea*) [34]. This polymer also inhibits the growth of many other plant pathogenic and mycoparasitic fungi (such as *Colletotrichum* spp., *Alternaria* spp. or *Trichoderma* spp.). Sensitive fungi show energy-dependent plasma membrane permeabilization by chitosan [35]. As a broad-spectrum fungicide, chitosan has been shown to be effective against several fungal plant pathogens. It can effectively inhibit the development of phytopathogenic fungi at different life-cycle stages. Chitosan has been shown to inhibit infections caused by fungi such as *B. cinerea* or *F. oxysporum* f. sp. *radicis-lycopersici* [36]. The antifungal activity of chitosan on plant depends on the type, concentration and test organism. For example, when effect of two types of chitosan (92.1 kDa and 357.3 kDa) was tested on *Penicillium italicum*, at a concentration of 0.1%—chitosan of lower Mw was more effective in inhibiting fungal growth, while at a concentration of 0.2%—chitosan of higher Mw showed stronger antifungal activity [37].

Chitosan oligosaccharides (COS) are the degraded products prepared by chemical or enzymatic hydrolysis of chitosan or chitin derived mainly from crustacean shells. They are composed of glucosamines linked by  $\beta$ -1,4-glycosidic bonds [38]. The degrees of polymerization of COS are usually 2–20 [39]. In recent years, COS has received a lot of attention due to their physicochemical properties, such as high water solubility, low viscosity, biocompatibility and biodegradability. Furthermore, COS were demonstrated to have various activities in the plant protection such as inducing plant resistance to pathogens, promoting its growth and development and improving the quality and yield of plant products [40].

### 2.1. Chitosan seed Treatments

Antifungal seed treatments provide protection against seed borne or soil borne pathogenic fungi, which can significantly lower seed germination and plant emergence in the field. Chitosan in such treatments is usually applied in a form of solution for seed soaking or coating (Table 1). For example, Silva-Castro et al. [41] searched for an effective method to protect seeds and seedlings of pine trees from *Fusarium circinatum*, a dangerous pathogen threatening pine forests in Spain. They developed seed coating treatments using low and medium Mw chitosan (20 kDa and 60–130 kDa, respectively) and/or propolis ethanolic extract. They applied these treatments to the pine tree seeds inoculated with the pathogen. All coating treatment resulted in improved survival of the *Pinus sylvestris* seedlings under pathogen pressure. However, a low Mw chitosan treatment also had a positive influence on total phenolic content and antioxidant capacity of the seedlings; therefore, this seed treatment was selected as the most beneficial for protection of *P. sylvestris*.

Effectiveness of chitosan against seed borne pathogens was studied in case of *Jatropha curcas*, which is an industrial plant cultivated on many continents. Pabon-Baquero et al. [42] tested effects of chitosan on fungi (*Fusarium equiseti* and *Curvularia lunata*) isolated from ungerminated *J. curcas* seeds. Chitosan applied at different concentrations (0.5–4.0 mg mL<sup>-1</sup>) inhibited mycelium growth and affected sporulation and spore germination of both species in vitro. Application of chitosan on pathogen inoculated seeds reduced the infection and had no negative effect on seed germination.

Seed borne fungi (e.g., *Aspergillus niger*, *Alternaria alternata* and *Rhizopus* sp.) have a negative impact on germination of artichoke seeds leading to significant losses of this crop. Therefore, Ziani et al. [43] tested effects of chitosan seed coatings on germination of this crop. In all treatments, chitosan reduced number of fungi detected on seeds and stimulated the growth of seedlings. Chitosan with lower Mw gave better results, but it was not effective against *Rhizopus*. The combination of chitosan and commercial fungicide

(tetramethylthiuram disulfide) applied at reduced concentrations resulted in a strong antifungal protection, improved germination and seedling growth.

Antifungal activity of chitosan was also tested against a soil borne pathogen, *Fusarium solani*, causing root rot in fenugreek [44]. The inhibitory effect on a mycelium growth, dry biomass, sporulation and fungal spore germination increased with the increasing concentration of chitosan (up to 2 g L<sup>-1</sup>) applied in vitro. The treatment of *F. solani* inoculated seeds resulted in significantly reduced infection rate of seedlings and longer radicle lengths. When tested in pot and field experiments, chitosan application on seeds reduced severity of root rot disease and increased yield. Moreover, it also resulted in stimulation of plant defense mechanisms because increased activity of chitinase and glucanase enzymes was observed in chitosan treated fenugreek plants.

A poor germination of pepper seedlings in wet and cold soil became a motivation to develop a seed treatment for this crop. Chitosan solutions (0.01–0.5%) were used to soak the pepper seeds and then germination parameters were assessed in two different temperature conditions. These treatments accelerated germination at 25 °C and improved seedling emergence in the cold test by 29%. Moreover, they increased activity of chitinase and glucanase in chitosan treated seed/seedlings compared to the untreated ones. Higher activity of these enzymes may indicate stimulation of plant defense mechanisms which may provide protection against fungal diseases [45].

Bio-based seed treatments with essential oils and plant extracts are becoming increasingly more popular due to their natural origin, faster degradation, low environmental impact and higher acceptance of the consumers avoiding chemical fungicides. Chitosan nanoparticles (NPs) with garlic essential oil were prepared by encapsulation method in order to protect the seeds of wheat, oat and barley. The new seed treatment, combining the two components, resulted in a strong antifungal activity against *Aspergillus versicolor*, *A. niger* and *Fusarium oxysporum*, comparable to the effects of standard tebuconazole treatment. Moreover, the new treatment stimulated also seed germination and seedling development what is its additional advantage apart from being an environmentally friendly alternative to chemical fungicides [46].

Attjioui et al. [47] investigated the efficacy of partially acetylated chitosan polymers and chitosan oligosaccharides (COS), applied alone and in combination, in vitro for their antifungal effect against the economically important seed-borne pathogen *F. graminearum*. The results showed that the antifungal activity of chitosan depends on its Mw. The analyzes revealed a dose–response relationship of three chitosans with the same DA (10%) and different Mw. Low Mw polymers were slightly more active than high Mw polymers or COS. However, synergistic effects of the chitosan polymer and COS were also observed on the growth of *F. graminearum*.

The combined treatment of COS and ε-poly-l-lysine had a highly inhibitory effect (inhibition rate exceeding 90%) on the destructive fungus *Botrytis cinerea* causing tomato gray mold [48]. In another study on effects of COS on the same pathogen, high fungal control efficiencies were detected and explained by that fact that COS induce plant disease resistance [49].

## 2.2. Chitosan Treatments Dedicated for Field Application

Chitosan is frequently combined with metal NPs in order to lower their toxicity (Table 2). Antifungal effects of such combination were explored by Dananjaya et al. [50] who searched for an environmentally friendly method of controlling *F. oxysporum* species complex causing infections of a broad range of plant and animals hosts. They developed chitosan NPs and chitosan-silver nanocomposites and compared their impact on the growth of *F. oxysporum* in vitro. Both solutions caused significant inhibition of fungal growth (although this effect was significantly stronger for nanocomposite with silver), and ultra-structural analysis revealed the signs of mycelium damage: higher membrane permeability, disruption of the mycelium surface and cell disintegration. These findings show that chitosan-based NPs and nanocomposites can effectively damage the pathogen and can

be used in fungal control treatments. In another study, chitosan and its nanocomposites with either silver NPs, ZnO or CuO were evaluated as potential antifungal agents against *Fusarium oxysporum* f. sp. *ciceri* causing Fusarium wilt on chickpea. The strongest antifungal effects were recorded for nanocomposites of chitosan with ZnO and CuO in tests performed in vitro and in vivo; these nanocomposites showed also lower toxicity [51].

The impact of NPs containing copper and chitosan on *Curvularia* leaf spot disease and the growth of maize were studied by Choudhary et al. [52]. Cu-CS NPs comprehensively inhibited in vitro mycelial growth of *Curvularia lunata*. Plants treated with this formulation showed lower disease severity compared to the other studied formulations (NPs, bulk chitosan, CuSO<sub>4</sub> and fungicide and water as control). Conclusion drawn from pot and field experiments was that application of Cu-CS NPs unquestionably controls the disease, boosts plant growth and yield.

Tomato plants may be attacked by *Pythium* spp. during early stage of growth, causing seed rot, pre-emergence damping-off, or stem rot symptoms and by *Fusarium oxysporum*, causing the most epidemic vascular wilt and root rot diseases [53]. Elsherbiny et al. [54] examined antifungal activity of chitosan nanocomposites loaded with antioxidants (vanillin and cinnamaldehyde). Samples were prepared by intercalation of chitosan into sodium montmorillonite, polyaniline and incorporation of chitosan/polyaniline/exfoliated montmorillonite. The obtained nanocomposites showed strong inhibitory effects on the linear growth of the target both pathogens even at 50 mg mL<sup>-1</sup> concentration.

Saponines are complex glycosidic compounds which belong to plant secondary metabolites. Fungistatic activities of saponine-rich extracts were demonstrated by Chapagain et al. [55]. In another study, saponin was one of the substances combined in NPs with chitosan in order to enhance its antifungal properties [56]. Other NPs included chitosan, saponin, copper or chitosan combined with copper. The prepared NPs were evaluated for their effect on the growth of three phytopathogenic fungi in vitro. Among the various tested formulations, NPs comprising of chitosan and copper were found the most effective at 0.1% concentration and showed 60–90% growth inhibition of the tested fungi and a maximum (87.4%) inhibition rate on *Alternaria alternata* spore germination. Pure chitosan NPs at the same concentration showed the strongest effect on mycelial growth of *Macrophomina phaseolina*. Therefore, chitosan-based NPs with or without copper can be used for plant protection in the future [56].

In another study, chitosan-pectin NPs encapsulated with carbendazim were produced. The method of ionotropic gelation was used, and the experiment focused on fungicide release in vitro and bio-efficacy. Characterization of the synthesized NPs showed that the size of the NPs encapsulated with carbendazim was 70–90 nm, the encapsulation efficiency was 99.2% and the Zeta potential was 50.2 mV. The nanoformulation showed 100% inhibition of test fungi against *Fusarium oxysporum* and *Aspergillus parasiticus*. Carbendazim nanoformulation requires less fungicide and therefore it is a more environmentally friendly method of controlling phytopathogenic fungi. This nanoformulation showed a greater efficacy at a lower concentration compared to the top commercial form of the fungicide against the target species [57].

### 2.3. Pre- and Post-Harvest Crop Protection Based on Chitosan

Chitosan represents a model plant protection biopolymer which is sustainable for control of post-harvest decay of fresh fruits and frequently used for this purpose (Table 3). One of the most important causes of harvested fruit decay is *Penicillium expansum* responsible for blue mold. Madanipour et al. [58] assessed the effect of post-harvest chitosan application in combination with licorice ethanol extract on shelf-life of apple fruits. Chitosan-licorice edible coating inhibited *P. expansum* growth and reduced post-harvest decay rate. In general, chitosan was more effective when combined with licorice extract. The results of this research support the idea that coating may be a safe alternative method to prolong shelf-life and reduce post-harvest losses of apple and maybe other fruits in storage time. In another study, infections caused by mold fungi were controlled by chitosan combined with essential

oils (EOS), which are also known for their antifungal activity [59]. The effectiveness of chitosan-based films integrated with the EOS from *Mentha piperita* L. or *Mentha × villosa* Huds was evaluated in cherry tomato fruits. Main antimicrobial compounds present in these essential oils are rotundifolone and menthol. They belong to monoterpenes and have the ability to disorganize the membrane structure, resulting in depolarization and morphological alterations, interfering with fungal metabolism. The obtained films were edible and effectively controlled infection caused by fungi such as *Penicillium expansum*, *Botrytis cinerea*, *Rhizopus stolonifera* and *Aspergillus niger*.

Postharvest decay of table grapes is causing significant losses of the crop attributed to pathogenic fungi, such as *Botrytis cinerea*. In a process of searching for alternative to sulfur dioxide fumigation of grapes, Shen and Yang [60] developed edible coatings for these fruit using chitosan in combination with salicylic acid, which is a phytohormone promoting plant resistance. The coatings made of both ingredients induced the activities of phenylalanine ammonia lyase, chitinase,  $\beta$ -1, and 3-glucanase, and reduced the decay of table grapes by inhibiting the growth of *B. cinerea*. A composite coating formulation containing 1% chitosan-salicylic acid successfully decreased the respiration rate and delayed changes in weight loss, measurement of total soluble solids, titratable acidity and total phenolic content and sensory attributes of table grapes during storage. The amino group of chitosan interacts with the carbonyl group of salicylic acid to form a conjugate molecule [60]. Another eco-friendly plant protection method for the same purpose was developed by Youssef et al. [61]. They utilized chitosan nanoparticles (CS NPs), silica nanoparticles (SN NPs) and chitosan-silica nanocomposites (CS-SNs) and tested their impact on *B. cinerea* growth inhibition in vitro and in vivo, on two grape cultivars 'Italia' and 'Benitaka'. In vitro tests showed that compared to control, CS NPs, SN NPs and CS-SNs reduced fungal growth by 72, 76 and 100%, respectively. After natural infection, at the end of cold storage, application of CS-SNs was also the most effective treatment; it reduced the development of gray mold by 59–83%, depending on cultivar. Since these nanocomposites had no negative effect on fruit quality, they are a promising alternative to fungicides controlling gray mold on grapes.

NPs with chitosan were used in another study aiming at protecting bell peppers from mold fungi. Gonzalez-Saucedo et al. [62] combined them with an extract obtained from leaves of nanche (*Byrsonima crassifolia*). Antifungal activity of the obtained NPs was confirmed in in vitro tests by recording up to 100% growth inhibition of *Alternaria alternata*. Edible coatings with these NPs sprayed on bell peppers before harvest reduced infections and improved storability of the crop; after storage reduced weight loss and better physicochemical features of peppers were observed.

One of the very complex edible coatings was developed for controlling green mold in harvested oranges [63]. It consists of chitosan integrated with phenolics-rich pomegranate peel extract and a biocontrol agent (*Wickerhamomyces anomalus*). The strongest effectiveness against *Penicillium digitatum* was observed in case of coating combining all of the above-mentioned components what confirmed synergistic effect of their activity.

Table 1. Examples of antifungal seed treatments based on carbohydrate biopolymers (chitosan, alginate or cellulose) or their derivatives.

Form of Application	Chemical Composition of the Seed Treatment Formulation *			Target Pathogen(s) (Plant Disease)	Effects of the Treatment	Ref.
	Carbohydrate Polymer or Its Derivative	Other Components				
Seed coating	CS (low and medium Mw)	propolis extract, Tween 80, Halloysite		<i>Fusarium circinatum</i> (pre- and post-emergence damping off in pine seedlings)	All coatings significantly reduced the post-emergence mortality of <i>Pinus sylvestris</i> seedlings inoculated with <i>F. circinatum</i> ; coating with low Mw chitosan also had a positive influence on total phenolic content and antioxidant capacity of the seedlings.	[41]
Seed coating	CS			Fungi isolated from <i>Jatropha curcas</i> seeds: <i>Fusarium equiseti</i> , <i>Curularia lunata</i>	Inhibited mycelium growth, sporulation and spore germination in vitro; improved germination of <i>J. curcas</i> seeds inoculated with <i>F. equiseti</i> or <i>C. lunata</i> .	[42]
Seed coating	CS	Fungicide: tetramethylthiuram disulfide; Span 80		seed borne fungi on artichoke seeds e.g., <i>Rhizopus</i> sp., <i>Aspergillus</i> sp.	Stimulated formation of an abundant root system, reduced fungal infection of seeds/seedlings, but <i>Rhizopus</i> sp. is effectively inhibited only by the fungicide.	[43]
Seed treatment	CS	HCl, NaOH		<i>Fusarium solani</i> (root rot disease on fenugreek)	Significantly reduced growth, sporulation, dried biomass and spore germination of <i>F. solani</i>	[44]
Seed treatment	CS	Fungicide: Benomyl [methyl 1-(butylcarbamoyl)-2-benzimidazole], acetic acid		Soil borne pathogens threatening pepper seeds	Improved the germination at 25 °C, higher emergence in cold test, increased activity of chitinase and glucanase in chitosan-treated seeds compared to the untreated ones.	[45]
Seed treatment	CS	CS-Garlic EO NPs, sodium tripolyphosphate		<i>Fusarium oxysporum</i> , <i>Aspergillus versicolor</i> , <i>Aspergillus niger</i> (Fusarium head blight, wilt and root rot on cereals)	Synergistic effect of CS NPs and garlic EO resulting in a strong antifungal activity; stimulated germination and seedling growth.	[46]
-	COS	-		<i>Fusarium graminearum</i> (crown/root rot, Fusarium head blight in cereals)	Antifungal effects against <i>F. graminearum</i> , affected conidia germination and caused ultrastructural modifications of fungi	[47]

Table 1. Cont.

Form of Application	Chemical Composition of the Seed Treatment Formulation *		Target Pathogen(s) (Plant Disease)	Effects of the Treatment	Ref.
	Carbohydrate Polymer or Its Derivative	Other Components			
Spray	COS	$\epsilon$ -poly-L-lysine	<i>Botrytis cinerea</i> (tomato gray mold)	Strong antifungal, synergistic effect of application of two bio-fungicides in combination, inhibition rate of <i>B. cinerea</i> > 90% in vitro, effective protection of the plants in vivo	[48]
Spray, seed treatment	COS	TEMPO, NaBr, NaOCl, NaOH, HCl	<i>B. cinerea</i>	Effective control <i>B. cinerea</i> on tomatoes and better antifungal activity, significant growth stimulation of cucumber seedlings	[49]
Seed treatment	AG	<i>Bacillus subtilis</i> , bentonite, starch and titanium dioxide NPs	<i>Rhizoctonia solani</i> (seed decay and damping-off of bean seedlings)	The application of encapsulated <i>B. subtilis</i> on inoculated bean seeds provided stronger disease inhibition compared to free bacteria. It also increased the parameters of vegetative growth of bean plants.	[64]
Seed treatment	AG	Three strains of <i>Streptomyces</i> spp.	<i>Ganoderma boninense</i> (Basal stem rot disease on oil palms)	<i>S. palmiae</i> CMU-AB204T strain exhibited the strong antifungal activity in vitro. It was also the most effective in suppressing the disease on oil palm seedlings in vivo.	[65]
Seed treatment	AG	Ag NPs, aldehyde	<i>Colletotrichum lagenarium</i> , <i>Sclerotinia sclerotiorum</i> , <i>C. gloeosporioides</i> , <i>F. solani</i> , <i>Sphaeropsidales</i> , <i>R. solani</i>	Nanopesticide with a broad-spectrum antifungal activity in vitro. No negative effects on seed germination were detected.	[66]
Seed treatment	AG	Silica NPs, EOS from: <i>Cymbopogon citratus</i> , <i>Syzygium aromaticum</i>	<i>Gaeumannomyces graminis</i> var. <i>tritici</i>	The rate of disease control was >20% higher than in control when tested on wheat	[67]
Seed coating	EC, HEC, MC	sodium lignosulfonate, lauryl sulfate	storage fungi e.g., <i>Aspergillus niger</i> (seed deterioration in storage)	After few months of storage: lower moisture content of the seeds, higher germination percentage, higher emergence in the field and lower fungal infestation.	[68]

Table 1. Cont.

Form of Application	Chemical Composition of the Seed Treatment Formulation *		Target Pathogen(s) (Plant Disease)	Effects of the Treatment	Ref.
	Carbohydrate Polymer or Its Derivative	Other Components			
Seed treatment	CMC	Biocontrol microorganisms: <i>Bacillus cereus</i> , <i>Trichoderma harzianum</i>	<i>F. graminearum</i> (cereal damping-off complex)	Reduced disease severity after seed treatment with biocontrol in controlled conditions.	[69]
Seed coating	CMC	Fungicides: difenoconazole, fludioxonil FSC, LAE-9, NNO, polyacrylamide, ethylene glycol, gelatin, pigment	<i>Rhizoctonia cerealis</i> (Sharp eyespot of wheat)	Reduced severity sharp eyespot disease in the field.	[70]
Electrospun seed coating	CDA nanofibers	Pesticides (abamectin, fluopyram) acetone, dimethyl acetamid	soil borne fungi e.g., <i>Alternaria</i> spp. (soil borne diseases of soybean)	Laboratory tests showed: slow release of pesticides in water environment and growth inhibition of <i>A. linariae</i> by fluopyram released from nanofibers.	[71]
Electrospun seed coating	CA nanofibers	Cu <sup>2+</sup> , gelatin surfactant (Tween80), acetic acid	<i>Fusarium oxysporum</i>	Promoted seed germination in diseased media, increased seedling biomass.	[72]

\* Abbreviations: CS—Chitosan, Mw—molecular weight, AG—Alginate, COS—Chitosan oligosaccharides, EOS—Essential oils, CMC—Carboxymethyl cellulose, MC—Methyl cellulose, EC—Ethyl cellulose, HEC—Hydroxyethyl cellulose, CA—Cellulose acetate, CDA—Cellulose diacetate, TEMPO-2,2,6,6-Tetramethylpiperidine-1-oxyl, NPs—Nanoparticles.

### 3. Alginate

Alginates are naturally occurring polymers showing low toxicity, good biocompatibility and biodegradability [73]. Excellent gelling and thickening properties as well as low production cost and good availability make them easy to develop and use. One of the most important and commonly utilized features of these polysaccharides is the ability to undergo ionotropic gelation, which is gel formation process occurring upon the contact with divalent cations. The gelation mechanisms of alginate very often act according to the model, known as egg-box, where the Ca-binding sites show a mirror symmetric conformation [74].

Alginates are obtained by extracting alginic acid in alkaline solutions from brown algae. Alginic acid consists of  $\beta$ -D-mannuronic (M) and  $\alpha$ -L-guluronic (G) residues linked by a  $\beta$ -1,4-glycosidic bond. The ratio of the participation of M and G and their distribution in the chain determines their gelation. For example, alginates derived from *Laminaria hyperbore* are characterized by an enrichment of the density of guluronic fragments (G) compared to alginates derived from *Acophyllum nodosum* or *Laminaria japonica*. Alginates have found application in many industrial sectors such as biomedical, pharmaceutical, tissue engineering and agriculture [75,76].

These polysaccharides can be combined with a wide range of substances, such as phytohormones, amino acids, fatty acids and microelements, and used in agriculture as organic fertilizers, delivery systems, seed treatments and edible coating films for vegetable and fruits. For example, alginates with chitosan and other substances were used in soybean seed coatings [77,78]. Alginate coatings have also been reported to be good oxygen barriers and to reduce the natural microflora counts [79]. Moreover, they stimulate the growth of aerial parts and the root system of plants and increase their resistance to pathogens [80].

Alginates were commonly used for encapsulation of microorganisms [81]. Biofertilizers, namely *Rhizobium* (Gram -), and biocontrol agents, such as *Pseudomonas* (Gram -) and *Trichoderma*, have been well established in the field of agricultural practices for many decades [82]. The use of conventional liquid or solid formulations in agricultural areas causes many problems, mainly due to the poor viability of the microorganisms during storage and field application. Encapsulation technology helps to overcome these problems. This form of immobilization of microorganisms results in extended shelf-life and controlled release of microorganisms from the preparations, which increases the effectiveness of their use in the field [73,83].

Alginate oligosaccharides (AOS), which are degradation products of alginate, show more attractive biological activity due to their low molecular weight [84,85]. AOS exhibit excellent potential for agricultural applications because they promote plant growth, alleviate growth inhibition under abiotic stress, induce defense responses in plant and extend a shelf-life of harvested crops [86,87].

#### 3.1. Alginate Seed Treatments

Sodium alginate is often utilized in encapsulation process because of its excellent features, such as appropriate morphology, fiber size, porosity, degradation and swelling ratio [88]. This polymer was used to develop an innovative encapsulation system for delivery of biocontrol bacteria *Bacillus subtilis* (Vru1). The formulation contained also bentonite, starch and titanium dioxide NPs [64]. The purpose of encapsulation was to protect the bacteria from harmful environmental conditions and strengthen their survival rate so that they could provide an effective control of *Rhizoctonia solani* infection on bean plants. Greenhouse tests of different variants of control treatments on fungal inoculated bean seeds showed that encapsulation enhanced antifungal effects of *B. subtilis*, because it led to stronger disease inhibition compared to treatment with free bacteria. The application of encapsulated *B. subtilis* has also significantly increased the growth of bean plants. Therefore, the developed nanocapsules with biocontrol bacteria are a potential alternative for sustainable agriculture.

Alginate was also used in a new method to control oil palm disease, which was meant to be an alternative to pesticide treatments [65]. The oil palm trees are frequently damaged



by the fungal infection (basal stem rot disease) caused by *Ganoderma boninense*. The selected three strains of biocontrol bacteria *Streptomyces* spp. exhibited the strongest degree of anti-*G. boninense* activity in vitro. Therefore, the effectiveness of these microorganisms on suppressing the disease symptoms was tested in vivo on oil palm seedlings using spore immobilized in alginate beads. Formulation with *S. palmae* CMU-AB204T strain resulted in the lowest disease severity and the highest degree of plant vigor. Therefore, this strain can be used as biocontrol agent protecting palm trees from basal stem rot disease [65].

Xiang et al. [66] developed a new high-performance nanopesticide with a broad-spectrum antifungal activity. It is comprised of silver NPs synthesized from aldehyde modified sodium alginate (SA-AgNPs). The synthesized SA-AgNPs showed a strong antifungal activity against the following pathogens: *Colletotrichum lagenarium*, *Sclerotinia sclerotiorum*, *C. gloeosporioides*, *Fusarium solani*, Sphaeropsidales and *Rhizoctonia solani*. This activity was associated with the impact of SA-AgNPs on fungal membrane permeability, soluble protein synthesis, destruction of DNA structure and inhibition of its replication. The new SA-AgNPs showed no inhibition of seed germination hence their phytotoxicity was excluded.

Essential oils (EOS) obtained from *Cymbopogon citratus* and *Syzygium aromaticum* were used against *Gaeumannomyces graminis* var. *tritici*, an aggressive pathogen causing a take-all disease of wheat. To provide a controlled delivery of the EOS, they were encapsulated into mesoporous silica NPs and then sodium alginate was used to keep these NPs around the seeds. Effects of this formulation were compared to the effects of pure EOS both in vitro and in vivo. Encapsulating of EOS successfully increased their stability in the environment, allowed their controlled release and reduced fungicidal dose. Results confirmed compatibility of alginate with natural fungicidal compounds and its positive impact on effectiveness of the whole formulation [67].

### 3.2. Alginate Treatments Dedicated for Field Application

Alginates were used in slow-release systems with Bosphorus (formerly nicobiphen) which is a broad-spectrum fungicide that is safe for plants. It can inhibit the respiration of fungi by binding to the enzyme succinate dehydrogenase in fungal mitochondria. To control the fungicide release rate, a slow-release boscalid composition for the treatment of gray mold was patented. The authors used bentonite, cationic surfactant and sodium alginate solution for dispersion as agent for controlling cucumber Botrytis [89]. In another study, agar and alginate beads containing thiram, were produced in order to slow down the release of active fungicide in vitro and in soil. The amount of active ingredient available for leaching and volatilization was decreased from the beads and the availability of the fungicide in the soil was prolonged. The release of thiram decreased with increasing alginate concentration in the feed from 1% to 2.5% (w/v), which explained the progressive shrinkage of the alginate spheres, which in turn led to an increase in Ca<sup>2+</sup> alginate cross-link density and a decrease the size of the pores. A slower release of thiram in soil compared to in vitro conditions what was explained by the occlusion of the ball surface by soil particles slowing diffusion, and also by dissolved soil water, which can also delay pesticide displacement [90].

The alginate oligosaccharides (AOS) combined with *Meyerozim guilliermondii* have been studied as a possible physiological biocontrol against *Penicillium expansum* infection of pears. Blue mold caused by *P. expansum* was significantly inhibited by the developed formulation in concentration of 5 g L<sup>-1</sup>, while it did not affect the growth and reproduction of *M. guilliermondii* in vitro or in vivo on pears [91].

### 3.3. Pre- and Post-Harvest Crop Protection Based on Alginate

Coating films on fruits and vegetables with preservative compounds slow down ripening and senescence due to formation of a modified atmosphere around the fruits and vegetables thereby reducing the respiration rate [92]. These coatings are made of edible material which provides a moisture barrier and prevents solute movement from the food [93]. They can be made of biodegradable raw material, such as polysaccharides,

and serve as a primary packaging which is directly in contact with the fruit, wrapping it to form a gas and moisture barrier, improving the mechanical property, reducing the microbial load, keeping the sensory properties intact while prolonging the shelf-life [94]. Fruit and vegetable coatings based on alginates can exhibit all these qualities and they may be combined with diverse active ingredients (Table 3). For example, Xu et al. [95] described the inclusion of cyclolipopeptides (CL) from *Bacillus subtilis* in the production of an easily removable alginate coating for preserving blueberries. The obtained CL-alginate coatings provided strong antifungal properties and kept blueberries fresh during 20 days of cold storage. Fungal contamination of the coated fruits was reduced to  $2.5 \times 10^3$  cfu g<sup>-1</sup> and it was at least 10 times lower compared to uncoated control. Moreover, the coating resulted in higher firmness, reduced respiratory rate and reduced weight loss in the stored blueberries.

Essential oils (EOS) are hydrophobic concentrated liquids derived from aromatic plants. They contain a multitude of bioactive compounds such as antimicrobial and antioxidant, and can be used as preservative for fruits. Therefore, they may be used to maintain the quality and shelf-life of fresh-cut fruits. Fresh-cut papaya pieces were treated with alginate based edible coatings containing thyme and oregano EOS, which constituted the lipid component of the coating. Increasing concentration of essential oil resulted in extended shelf-life and a higher moisture retention capacity of the samples. However, the strong smell of essential oils, caused a negative reaction from the sensory panel. Nevertheless, positive effects of the coatings include reduced weight loss, retarded pH changes, reduced respiration rate and delayed senescence. The reduced microbial growth may be due to the incorporation of essential oil as well as due to the modified atmosphere created by the coating [96]. Similar alginate-based coatings combined with EOS were shown to extend self-life of fruits and reduce the counts of microorganisms in case of raspberries, fresh-cut apples and pineapples [97–99] (Table 3). Another study described the use of an alginate/vanillin combination to improve the quality and safety of table grapes. The pre-harvest spray and post-harvest fruit coating was applied to three grape varieties. Alginate treatments effectively prevented weight loss and firmness loss of the fruit. Moreover, alginate/vanillin coating provided a significant reduction in yeast-mold growth. In addition, it maintained the nutritional and sensory quality of grapes, preserved functional properties (such as phenolic content and antioxidant activity) and extended their shelf-life by diminishing fungal decay [100].

Alginate-based coatings of fruits can be enriched with plant extracts in order to enhance their antifungal properties. For example, rhubarb (*Rheum rhaipanicum* L.) extract, known for its antifungal and antiseptic activity, was combined with sodium alginate in a coating for peach preservation [101]. Alginate coatings (1% sodium alginate) reduced weight loss, firmness loss and respiratory rate and resulted in higher nutritional value of the stored coated fruits compared to uncoated control fruits. Moreover, a significantly lower decay index was recorded for alginate-coated fruit previously inoculated with *Penicillium expansum*, which was explained by reduced gas exchange inhibiting growth of molds which are aerobic. However, all of the above-mentioned positive effects of alginate coating were significantly enhanced by addition of rhubarb extract, therefore a coating combining both components was recommended as a treatment prolonging shelf-life of peach fruits.

The addition of nanomaterials can also enhance the antifungal activity of the alginate coatings. Jiang et al. [102] reported the efficacy of a composite alginate/nano-Ag coating in reducing the counts of different groups of microorganisms on coated shiitake mushrooms after the cold storage for 16 days compared with the uncoated control.

The addition of ZnO nanoparticles in different concentrations to sodium alginate-coatings resulted in the enhanced shelf-life of cold stored strawberries by preventing the loss of weight, sensory attributes and the reduction in ascorbic acid, total phenols and total anthocyanins content. The nano-coating, which was the most effective in reducing the counts of yeast, molds and aerobic bacteria in cold stored strawberries, comprised 1.5% sodium alginate and ZnO nanoparticles at the concentration of 1.25 g L<sup>-1</sup> [103].

Zhuo et al. [104] demonstrated that AOS treatment improved resistance to post-harvest decay and quality in kiwifruit (*Actinidia deliciosa* cv. ‘Bruno’). The results showed that in vitro AOS did not inhibit the growth of *Botrytis cinerea*, which is the causal agent of gray mold in kiwifruit, but they reduced the incidence of gray mold and diameter of lesions of kiwifruit during storage.

**Table 2.** Examples of antifungal treatments dedicated for field application and based on carbohydrate biopolymers (chitosan, alginate or cellulose) or their derivatives.

Form of Application	Chemical Composition of the Seed Treatment Formulation *		Target Pathogen(s) (Plant Disease)	Effects of the Treatment	Ref.
	Carbohydrate Polymer or Its Derivative	Other Components			
-	CS	CS NPs, CS-Ag NCs, AgNO <sub>3</sub> , TPP, NaOH, Na <sub>5</sub> P <sub>3</sub> O <sub>10</sub>	<i>Fusarium oxysporum</i>	Reduced fungal growth in vitro, morphological and ultrastructural changes in of the mycelium	[50]
Soil application	CS	CS-Ag CS-CuO, CS-ZnO	<i>F. oxysporum</i> f. sp. <i>Ciceri</i> (Wilt disease of chickpea)	Nanocomposites of chitosan combined with CuO or ZnO provided the most effective protection against wilt disease and promoted growth of chickpea plants	[51]
Seed treatment, foliar application	CS	CS-Cu NPs	<i>Curvularia lunata</i> , (Curvularia leaf spot disease of maize)	Lower disease severity observed in maize in pot and field experiments, plant growth stimulation.	[52]
Seedling treatment	CS	vanilin, cinnamaldehyde, polyaniline, sodium montmorillonite	<i>Pythium</i> spp. <i>Fusarium oxysporum</i> (root rot, pre-emergence damping off in tomato plants)	Strong inhibitory effect on the linear growth of both target pathogens, reduced disease incidence under greenhouse conditions	[54]
-	CS	CS-Saponin NPs, CS-Cu NPs, TPP	<i>Alternaria alternata</i> , <i>Macrophomina phaseolina</i> , <i>Rhizoctonia solani</i> ,	Compared to CS-Saponin NPs, CS-Cu NPs were more effective and caused fungal growth inhibition in vitro of 89.5%, 63.0% and 60.1% in case of <i>A. alternate</i> , <i>M. phaseolina</i> and <i>R. solani</i> , respectively.	[56]
Encapsulation	CS	CS-pectin NPs, fungicide: carbendazim	<i>F. oxysporum</i> , <i>Aspergillus parasiticus</i>	100% inhibition of tested fungi. Carbendazim nanoformulation showed greater efficacy at a lower concentration compared to the top carbendazim and commercial form against target species	[57]
Foliar spray	CS	CS-Cu NPs, CuSO <sub>4</sub> , fungicide: Bavistin	<i>Curvularia lunata</i> (Curvularia leaf spot in maize)	Significant defense response and control of the disease in maize.	[52]
Encapsulation	AG	Fungicide: Bosphorus -(formerly nicobiphen); bentonite	<i>Botrytis. cinerea</i> (gray mold on cucumber)	Broad-spectrum fungicide inhibits the respiration of fungi by binding to the enzyme succinate dehydrogenase in fungal mitochondria.	[89]
Encapsulation	AG beads	Fungicide: thiram	various fungi	Slower release the active fungicide in vitro and in the soil.	[90]
Spray	AOS	<i>Meyerozyma guilliermondii</i>	<i>Penicillium Expansum</i> (blue mold on pears)	The results showed that AOS (5 g/L) combined with <i>M. guilliermondii</i> significantly reduced blue mold decay incidence and lesion diameter in pears.	[91]
Encapsulation	EC	Fungicide: fluazinam; gum arabic, emulsifier	<i>B cinerea</i> (gray mold on cucumber)	In vitro tests: stronger inhibitory effect on <i>B. cinerea</i> . In the field experiment: slower degradation after spraying plants and no phytotoxic effects on plants in case of encapsulated fungicide compared to fungicide suspension.	[105]
Nano- carriers	fatty acid cellulose ester	Fugicides: captan, pyraclostrobin	<i>Neonectria ditissima</i> , <i>Phaeoacremonium minimum</i> (Apple Canker and Esca disease of grapevine)	In vitro tests: pesticide release in contact with cellulolytic fungi and fungal growth inhibition	[106]

Table 2. Cont.

Form of Application	Chemical Composition of the Seed Treatment Formulation *		Target Pathogen(s) (Plant Disease)	Effects of the Treatment	Ref.
	Carbohydrate Polymer or Its Derivative	Other Components			
Nano- carriers	HPC	Fungicide (pyraclostrobin); silica NPs	<i>Magnaporthe oryzae</i> (rice blast)	Fungicide release induced either by low pH or cellulase. Prolonged photostability and reduced cytotoxicity of the fungicide delivered in nanocarriers compared to commercial formulations.	[107]
Micro-spheres	Copolymer: CS, CMC	EOS: citral	<i>B. cinerea</i> (gray mold in solanaceous crops)	Antifungal activity in vitro and reduced disease incidence in tomato tested in vivo	[108]
Electrospun membrane	CA	5-chloro-8-hydroxyquinolinol, polyethylene glycol, acetone	<i>Phaeoconiella chlamydospora</i> , <i>Phaeoacremonium aleophilum</i> (Esca on grapevine)	Membranes prevent fungal spore penetration of plant tissues wounded by pruning procedure	[109]

\* Abbreviations: CS—Chitosan, AG—Alginate, AOS—Alginate oligosaccharides, EOS—Essential oils, CMC—Carboxymethyl cellulose, HPC—Hydroxypropyl cellulose, CA—Cellulose acetate, NPs—Nanoparticles.

#### 4. Cellulose

Cellulose is the most abundant carbohydrate biopolymer in nature. It is produced by plants in a photosynthesis process and it plays an important, structural role in these organisms. Cellulose can be obtained from plant material, such as wood, cotton, flax, water plants, grasses, agricultural residues and from bacteria belonging to few genera. However, the main sources of this polymer for commercial production are wood and cotton [110,111].

Cellulose consists of long chains of beta (1-4)-glycosidically linked glucose units. It is insoluble in water and common organic solvents. Cellulose can be converted into a variety of derivatives with different functionalities through etherification or esterification [111]. Cellulose ethers commonly used in agriculture include: methyl cellulose (ME), ethyl cellulose (EC), hydroxyethyl cellulose (HEC), hydroxypropyl cellulose (HPC), hydroxypropyl methylcellulose (HPMC) and carboxymethyl cellulose (CMC). These derivatives are characterized by higher solubility in water and/or organic solvents compared to cellulose. Their properties allow for using them as thickeners, binders or coating agents in formulations applied as foliar sprays, seed treatments or edible films on food products.

Among esters, the most important compounds include cellulose acetates (cellulose acetate—CA; cellulose diacetate—CDA) which are tasteless, nontoxic, relatively stable in storage, insoluble in water and easily biodegradable [111], which make them suitable for use in organic agriculture and food production. Moreover, they are suitable substrates for production of electrospun nanofibers, which can be used in biodegradable membranes and coatings of plant material for the targeted delivery of agrochemicals [112].

Cellulose derivatives are commonly used in plant protection applications as binders and carriers of active ingredients and biocontrol agents. However, they can also form biodegradable membranes and coatings of plant material, which can form a protective physical barrier from the environment.

##### 4.1. Cellulose Seed Treatments

Seed coating procedure requires using liquid substances which will bind solid materials and active ingredients to the seed surface. These liquids, called binders, are responsible for integrity and durability of the coating during its application and after drying [113]. Cellulose ethers are relatively frequently used for this purpose. Pedrini et al. [114] reviewed 127 publications on seed coating methods and found that at least one of the five cellulose ethers (MC, EC, HEC, HPC and CMC) was used in approximately 20% of non-commercial seed coatings with a known composition.

Polymeric coatings without active ingredients can act as physical barrier preventing moisture from entering the seeds during storage thereby preventing development of fungi and deterioration of the seeds. Such seed treatments are particularly important in countries

where seeds are stored in the conditions of a high temperature and a high moisture, which are highly detrimental for the stored seeds. Kumar et al. [68] tested effects of various polymer seed coatings on storability of soybean seeds. Some of the coatings included in their study consisted of MC, EC or HEC. After six months of storage, coated seeds showed lower moisture content and higher emergence in the field compared to uncoated control seeds. Coating with cellulose derivatives resulted also in lower percentage of seeds infected with storage fungi, such as *Alternaria alternata*, *Aspergillus niger*, *Curvularia lunata*, *Dreschlera halodes*, *Fusarium moniliformae*, *Cladosporium* spp. and *Penicillium* spp.

CMC can be used as base for formulations containing microorganisms. For example, Viji et al. [115] used this cellulose ether in formulations containing biocontrol agent-bacterial strains of *Pseudomonas aeruginosa*. Foliar sprays using these formulations effectively reduced the gray leaf spot disease in perennial ryegrass. In another study, the same polymer was combined with biocontrol microorganisms in seed treatment formulation protecting wheat against *Fusarium graminearum* [69].

CMC is often used in seed coatings containing fungicides. Such coatings consist usually of several components. Ren et al. [70] optimized the coating formulation for protection of germinating wheat seeds from soil borne diseases. They tested effects of few polymers on the emergence and growth of wheat seedlings and concluded that best results are obtained for CMC combined with polyacrylamide. Therefore, these two polymers were selected as binders for the seed coating delivering fungicides: difenoconazole and fludioxonil FSC designed for control of sharp eyespot disease in wheat.

Pesticides delivered in the seed coating protect germinating seeds only for a short time if they are rapidly released to the environment. Many soil-borne pathogens may threaten seeds, seedlings and young plants; therefore, a more sustained release of plant protection agents from the coating would be desirable. A choice of polymer for the coating seems to be an important decision in this context. Farias et al. [71] chose CDA for developing a new nanofiber coating for soybean seeds. In contrast to other electrospinnable polymers such as polyvinylpyrrolidone (PVP) and polyvinyl alcohol (PVA), CDA is hydrophobic in nature. Laboratory tests of the new nanofibers with abamectin or fluopyram, showed that only 5.5–25% of the total content of these pesticides was released during 2 weeks of soaking in the water. Nanofibers spun directly on the soybean seeds had no detrimental effects on seed germination. Moreover, in vitro tests with fluopyram loaded nanofibers showed also that the released fungicide caused a significant growth inhibition of *Alternaria lineariae*.

Recently, Xu et al. [72] used a method of electrospinning two biopolymers (CA and gelatin) to produce a copper ( $\text{Cu}^{2+}$ ) loaded nanofiber seed coating for protection against soil borne diseases. They avoided using toxic organic solvents (such as acetone or dimethyl acetamide), therefore their solution is more environmentally friendly. Interestingly, they showed that the kinetics of  $\text{Cu}^{2+}$  release from nanofibers can be altered by using different proportions of two biopolymers and adding a surfactant. The effectiveness of new seed treatments was tested in greenhouse experiments in which coated seeds of lettuce and tomato were germinated in *Fusarium oxysporum* infected media. The nanofiber coating clearly improved germination rate and plant growth under pathogen pressure.

#### 4.2. Cellulose Treatments Dedicated for Field Application

CMC and EC were used as controlled release matrices for delivery of insecticides and herbicides [116]. However, recent publication of Liu et al. [105] showed that EC microcapsules with fungicide can be effectively used as plant protection against *Botrytis cinerea* causing gray mold (Table 2). This form of delivery of plant protection agent assures prolonged release and slower degradation in the environment. Moreover, encapsulation of the fungicides reduces the toxic effects on cucumber plants treated in the field.

Encapsulation of fungicides using derivatives of cellulose has one more important advantage. Many fungal pathogens of plants produce cellulase—an enzyme degrading cellulose. Therefore, nanocarriers with fungicides made of this polysaccharide will quickly disintegrate in contact with such fungi and release their cargo where it is the most needed.

Machado et al. [106] produced such nanocarriers using fatty acid cellulose ester and fungicides for plant protection against severe trunk diseases of apple trees and grapevine caused by cellulase producing fungi *Neonectria ditissima* and *Phaeoacremonium minimum*. They showed in laboratory tests that the growth of both pathogens is greatly inhibited by fungicides provided in nanocarriers. In contrast, in case of fungus which is unable to produce this enzyme (*Cylindrocladium buxicola*), the effect on inhibition of the fungal growth was much smaller, because it depended only on diffusion of the fungicide from the nanocarriers.

Fungal infection exposes plant cell not only to cell wall degrading enzymes such as cellulase but also to lower pH. Therefore, Gao et al. [107] constructed nanocarriers using HPC and hollow mesoporous silica nanoparticles which release fungicide in response to either of the two stimuli.

Plant protection products comprised of nanocarriers can deliver not only fungicides but also antimicrobial substances of natural origin, such as plant essential oils. Ma et al. [108] demonstrated that hydrogel microspheres made of chitosan and CMC can be loaded with citral, which increases bioavailability of this highly volatile and unstable compound. The obtained microspheres with citral showed antibacterial activity in vitro and antifungal properties in vivo in tomato plants. They reduced incidence of the disease caused by *Botrytis cinerea*.

Another form of plant protection application was developed for grapevine protection against fungi causing esca, a damaging disease caused mainly by two species of fungi: *Phaeoconiella chlamydospora* and *Phaeoacremonium aleophilum*. In order to prevent fungal infections of the wounds formed during pruning procedure, Spasova et al. [109] produced a protective antifungal membranes using electrospinning technology. Membranes build using CA or CA and polyethylene glycol (PEG) were combined with antifungal agent: 5-chloro-8-hydroxyquinolinol. Laboratory tests of both types of membranes showed a quicker release of the pesticide from CA/PEG membrane, what was explained by a higher wettability of this material. Antifungal effect of the obtained membranes was confirmed in vitro by showing the growth inhibition of *P. chlamydospora* and *P. aleophilum*.

#### 4.3. Post-Harvest Crop Protection Based on Cellulose

Cellulose ethers such as MC, CMC, HPC and HPMC are widely produced and used in edible coatings of various fruits and vegetables. They bind the coating to the surface of the product, provide moisture and create a barrier for gas exchange [26]. Out of the above-mentioned ethers, CMC is the most important for industry and commonly used in food production, also in edible coatings of fruit and vegetables. Antifungal effects of CMC coatings can be inferred from studies which test effects of coating on decay and quality of fruits after storage. For example, Kumar et al. [117] coated guava fruit with various CMC solutions (0–2.0 g L<sup>-1</sup>). After 12 days of storage at ambient temperature, coating with CMC at the intermediate concentration (1.5 g L<sup>-1</sup>) resulted in the lowest percentage of decayed fruit and best fruit quality compared to other coating treatments. In another study, Baswal et al. [118] compared effects of several coatings consisting of CMC, chitosan or beeswax on decay and quality of mandarin fruits after 75 days of cold storage. The best protection was provided by CMC coating (2.0 g L<sup>-1</sup>), which retained its integrity during the whole storage period. It was the most effective in maintaining fruit quality parameters, while reducing fruit decay and activity of cell wall degrading enzymes.

Next generation of edible coatings consist of polymeric matrix combined with functional and bioactive compounds which enhance the quality of the coated product and bring additional benefits to the health of the consumers [26]. For example, CMC was combined with probiotic bacteria *Lactobacillus plantarum* in edible coating created to extend a shelf-life of strawberries [119]. The bacteria remained viable on the surface of coated fruit for 15 days of cold storage and they helped to reduce the growth of yeast and molds probably due to competitive interaction with these microorganisms. The coating treatments with higher amounts of *L. plantarum* (5.76–9.80 × 10<sup>13</sup> cfu mL<sup>-1</sup>) were the most effective

in reducing fruit decay and the counts yeast and molds compared to uncoated control. CMC coating without bacteria also resulted in a reduction in fruit decay and the counts of detrimental microorganisms but its effects were intermediate compared to control and the above-mentioned *L. plantarum* coatings.

Antifungal properties of the polysaccharide coatings can be also enhanced by addition of plant extracts. It was shown in *in vitro* tests that extract of *Impatiens balsamina* L. stems inhibited growth of *Penicillium* molds responsible for postharvest infections of citrus fruits. Therefore, Chen et al. [120] added this extract to edible coatings of tangerine fruits based on CMC. The complex coating that was obtained included also additional substances which functioned as antioxidant, plasticizer, moisturizer, and antiseptic. Further analyses involved comparing effects of three treatments including uncoated control, CMC coating without additional substances and the complex coating described above. After 100 days of cold storage, the lowest decay rate and weight loss were recorded for fruits treated with the complex coatings. These measures for fruits coated only with CMC showed intermediate values. The complex coating resulted in the highest nutritional quality of the fruits (Table 3). Moreover, antioxidant and defense-related enzymes reached the highest activities for this treatment.

Tesfay et al. [121] isolated pathogenic three fungi from avocado fruits, namely *Colletotrichum gloeosporioides*, *Alternaria alternata* and *Lasiodiplodia theobromae*, and showed *in vitro* that their growth can be inhibited by extracts obtained from moringa (*Moringa oleifera* Lam.) plants or seeds. Therefore, they added these extracts to CMC to obtain antifungal coatings for avocado fruits. The new coatings improved storability of avocado fruits and their antifungal properties were confirmed *in vivo*. Inoculation of coated and uncoated fruits with *C. gloeosporioides* and *A. alternata* showed that the coating significantly reduced the disease incidence and severity. Therefore, the new coating treatments are suitable as organic postharvest treatment for avocado fruit.

Edible coatings based on HPMC were used for coating fruit and vegetables, but they were frequently combined with preservatives classified by EU regulations as food additives which are generally recognized as safe. Valencia-Chamorro et al. [122] developed such a coating for cold stored oranges and tested its antifungal properties in fruit which was first inoculated with *P. digitatum* or *P. italicum* and then coated with HPMC in combination with one or two preservatives and hydrophobic components. After cold storage, the coating had no negative effect on the fruit quality and its antifungal properties were confirmed. The most effective coating, containing potassium sorbate and sodium propionate, controlled development of green and blue mold on the inoculated fruit. A similar coating was developed for cherry tomatoes by Fagundes et al. [123]; however, this study aimed at controlling two important pathogens *Botrytis cinerea* and *Alternaria alternata*. A range of *in vitro* tests allowed to select the most effective preservative to control these fungi. HPMC-lipid coatings containing the selected preservatives were used in *in vivo* experiments to coat pathogen inoculated tomatoes. The coating in this case had also curative properties as the disease incidence and severity were significantly reduced although these effects were stronger in case of experiment with *A. alternata*.

**Table 3.** Examples of antifungal coatings of fruits and vegetables based on carbohydrate biopolymers (chitosan, alginate or cellulose) or their derivatives.

Fruit or Vegetable	Chemical Composition of the Coating *		Fungi Responsible for Crop Decay	Effects of the Coating	Ref.
	Carbohydrate Polymer or Its Derivative	Other Components			
Apple	CS	licorice extract	<i>Penicillium expansum</i>	CS-licorice coating inhibited <i>P. expansum</i> growth, reduced postharvest decay rate and weight loss of apples.	[58]
Cherry tomato	CS	EOS from <i>Mentha</i> spp.	<i>P. expansum</i> , <i>Botrytis cinerea</i> , <i>Rhizopus stolonifera</i> , <i>Aspergillus niger</i>	CS-EOS combination strongly inhibited mycelial growth and spore germination of target fungi. CS-EOS coatings reduced decay of inoculated tomato fruits and preserved quality of the stored fruit	[59]
Grapes	CS	salicylic acid, glacial acetic acid, NaOH	<i>B. cinerea</i>	Compared to pure CS coatings, coatings based on CS-salicylic acid conjugate were the most effective at promoting plant resistance, reducing fruit decay while improving their storability	[60]
Grapes	CS NPs	Silica NPs	<i>B. cinerea</i>	Compared to both types of NPs, CS-silica nanocomposites were the most effective in inhibiting <i>B. cinerea</i> growth in vitro and in vivo. No negative impact on fruit quality was observed.	[61]
Bell pepper	CS NPs	<i>Byrsonima crassifolia</i> extract	<i>Alternaria alternata</i>	CS NPs inhibited <i>A. alternata</i> growth up to 100% in vitro; when used in edible coatings in vivo they reduced the counts of microorganisms, decreased weight loss and improved quality of peppers after storage.	[62]
Orange	CS	pomegranate peel extract, <i>Wickerhamomyces anomalus</i>	<i>Penicillium digitatum</i>	Coatings combining CS, pomegranate peel extract and <i>W. anomalus</i> showed the strongest antifungal effect in vivo (synergistic effect of the three components confirmed)	[63]
Blueberry	AG	Cyclolipopeptides from <i>Bacillus subtilis</i>	<i>Aspergillus niger</i>	Compared to uncoated control, coated fruit showed >10× lower fungal contamination, reduced respiratory rate and weight loss during cold storage	[95]
Papaya	AG	Thyme and oregano EOS, Tween 80	not specified	Coatings reduced weight loss of fresh-cut fruit, retarded pH changes, reduced respiration rate thus delayed senescence	[96]
Apple	AG	EOS: lemongrass, oregano, vanillin; apple puree	<i>Listeria innocua</i>	Coatings with EOS inhibited the growth of <i>L. innocua</i> inoculated on apple pieces as well as psychrophilic aerobic bacteria, yeasts and molds	[99]
Pineapple	AG	EOS: lemongrass, glycerol, sunflower oil, ascorbic acid, citric acid	yeast and molds	Reduced weight loss, respiration rate, total counts of microorganisms, yeast and molds during storage	[97]
Raspberry	AG	EOS: citral and eugenol, ascorbic acid	yeast and molds	Improved storability, nutritional and sensory quality of fruits, growth inhibition of molds, yeasts and aerobic mesophilic microorganisms (compared to uncoated control)	[98]
Grapes	AG	vanillin, glycerol	<i>B. cinerea</i>	Maintained nutritional quality, sensory quality and extended the shelf-life of grapes, reduced growth of yeasts and molds	[100]
Peach	AG	rhubarb extract	<i>P. expansum</i>	Reduced weight loss, firmness loss, respiratory rate and higher nutritional value compared to uncoated control fruits; reduced decay index recorded for coated fruit which were previously inoculated with <i>P. expansum</i> .	[101]
Shiitake mushrooms	AG	Nano-Ag	bacteria, yeasts and molds	Enhanced shelf-life, higher physicochemical and sensory quality, reduced weight loss, lower counts of different groups of microorganisms.	[102]



Table 3. Cont.

Fruit or Vegetable	Chemical Composition of the Coating *		Fungi Responsible for Crop Decay	Effects of the Coating	Ref.
	Carbohydrate Polymer or Its Derivative	Other Components			
Strawberry	AG	ZnO NPs	not specified	Enhanced shelf-life, reduced loss of weight, texture quality and the content of the ascorbic acid, total phenols and anthocyanins.	[103]
Kiwifruit	AOS	-	<i>B. cinerea</i>	AOS did not inhibit the growth of <i>B. cinerea</i> in vitro, but reduced the incidence of gray mold and diameter of lesions of kiwifruit during storage.	[104]
Guava	CMC	-	not specified	Reduced decay and weight loss of fruits; higher firmness; better sensory attributes; higher sugar, ascorbic acid and phenol contents; higher titratable acidity	[117]
Mandarin	CMC	-	<i>Penicillium italicum</i>	Best results compared to chitosan and beeswax coatings: reduced decay and weight loss of fruits; higher juice content and firmness of the fruits; lower activity of cell wall degrading enzymes; higher titratable acidity; higher ascorbic acid and carotenoids contents	[118]
Strawberry	CMC	probiotic bacteria: <i>Lactobacillus plantarum</i> , glycerol		Reduced counts of yeast and molds and reduced percentage of decayed fruits after cold storage (better results compared to control and compared to pure CMC coating); reduced weight loss, slower deterioration of ascorbic acid and phenolic compounds.	[119]
Tangerine	CMC	ethanol extract of <i>Impatiens balsamina</i> L. stems, citric acid, sucrose ester, calcium propionate, glycerol	<i>Penicillium</i> spp.	Improved results compared to pure CMC coating: lowest decay and weight loss after cold storage; highest total soluble solid, titratable acid, total sugar and ascorbic acid contents; highest activity of antioxidant and defence-related enzymes	[120]
Avocado	CMC	Moringa plant extracts	<i>Colletotrichum gloeosporioides</i> , <i>A. alternata</i> , <i>Lasiodiplodia theobromae</i>	Reduced decay and weight loss of the stored fruit higher firmness of the fruit; reduced ethylene production and respiration rate; confirmed antifungal effect in fungal inoculation in vivo test.	[121]
Orange	HPMC	food preservatives, shellac, beeswax, glycerol, stearic acid	<i>P. digitatum</i> , <i>P. italicum</i>	Lower incidence and severity of the disease observed on <i>Penicillium</i> sp. inoculated fruit (compared to inoculated and uncoated control). The most effective coating contained potassium sorbate and sodium propionate. Coating had no adverse effects on fruit quality.	[122]
Cherry tomato	HPMC	food preservatives	<i>B. cinerea</i> , <i>A. alternata</i>	Positive effect on the fruit quality and antifungal properties of coatings were confirmed.	[123]

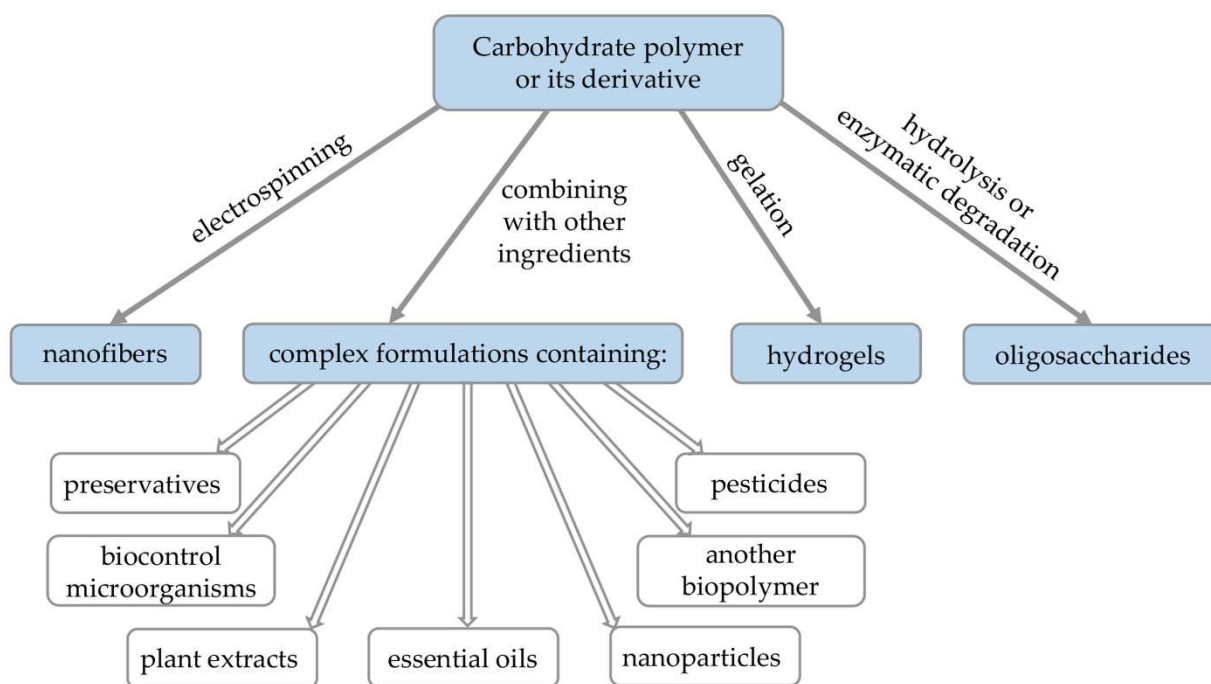
\* Abbreviations: CS—chitosan, AG—alginate, AOS—alginate oligosaccharides, EOS—essential oils, CMC—carboxymethyl cellulose, HPMC—hydroxypropyl methylcellulose, NPs—nanoparticles.

## 5. Advantages and Disadvantages of Carbohydrate Biopolymers Used in Plant Protection

Cellulose, chitosan and alginate are the most common carbohydrates in nature. Moreover, cellulose and chitosan can be obtained from waste material from agriculture, wood processing or crustacean shells produced by food industry. High availability is probably the most important advantage of carbohydrates considered in this review. Moreover, since these polymers are of natural origin, there are a lot of microorganisms in the environment which are able to decompose them, therefore they are highly biodegradable and suitable for organic agriculture. In addition, non-toxicity makes these biopolymers safe for the consumers and non-target organisms in the environment.

During preparation of plant protection formulations carbohydrate biopolymers can be subjected to a variety of different processes such as chemical modification, electrospinning, hydrolysis and gelation. Moreover, since they have the ability to interact with many

hydrophobic and hydrophilic compounds, they are often combined with other ingredients in composites or complex formulations (Figure 2, Tables 1–3).



**Figure 2.** Alternative modification methods of carbohydrate polymers which can be used in the process of preparing antifungal plant protection formulations.

Carbohydrate biopolymers can be used in the process of encapsulation of biocontrol microorganisms in order to protect them from harmful environmental conditions and prolong their viability [64,83]. Similar solution can be used for delivering agrochemicals or volatile active ingredients (essential oils). In this case biopolymers extend activity of encapsulated compounds and ensure their slow release to the crops, thereby increasing efficiency of plant protection and reducing environmental impact of the used agrochemicals [14,16,108]. Moreover, polysaccharides in a form of hydrogels provide additional positive effect of increased water retention in the soil therefore they may help to alleviate effects of drought stress on plants [16]. Another advantage of carbohydrate biopolymers is that the products of their hydrolysis or enzymatic degradation (oligosaccharides) may act as elicitors stimulating plant defense mechanisms [19]. Chitosan, alginate and cellulose derivatives have a film forming capacity. Therefore, they are suitable as coatings for seeds or harvested fruits, which may reduce fungal growth even if they act as passive barrier [26].

Despite these advantages, carbohydrate biopolymers are not commonly utilized in plant protection due to a number of reasons. Firstly, they can be easily degraded by widespread microorganisms which is a disadvantage in the context of a short shelf-life of plant protection products based on these compounds. In order to maintain the biochemical properties and bioactivity of the biopolymer-containing product, it should also contain a preservative reducing a microbial growth. For example, a commercial plant protection product, Beta-chikol<sup>®</sup>, based on chitosan lactate, had a chlorhexidine digluconate added for this purpose (Wiśniewska-Wrona—pers. comm).

Secondly, carbohydrate biopolymers are obtained from various sources which are naturally quite variable. A source organism, its geographic origin and the time of harvest affect the content and chemical structure of these polymers [19]. The extraction and purification techniques of these polysaccharides are not fully standardized and contribute to the variability of the end product [124]. As a result, the commercially available carbohydrate biopolymers have broadly specified physico-chemical characteristics and tests of their bioactivity do not always yield reproducible results ([19], Wiśniewska-Wrona—unpublished

data). The high level of structural heterogeneity and polydispersity of these polymers make it difficult to provide a proven information on their efficiency, safety for the consumers and the environment, which is a huge disadvantage when going through the approval and commercialization process [125].

Thirdly, purification of carbohydrate polymers from natural raw materials is not very efficient and can be costly. For example, the traditional method of producing chitosan on an industrial scale from crustacean shell waste involves few chemical treatments in order to remove proteins, mineral salts and pigments. Then chitosan is obtained by hydrolysis of acetamide groups by severe alkaline treatment. The whole process is considered to be expensive and laborious; it also harmful to the environment as it requires using harsh chemicals and generates high amounts of wastes [126]. However, due to the growing demand on this polymer worldwide the global market of chitosan is developing dynamically, therefore alternative sources of this polymer (fungi, insects) and more sustainable production methods are being explored [127,128].

When comparing the three biopolymers included in the review among each other, we can point few clear differences in terms of their properties and applications. Chitosan is frequently treated as antifungal agent because of its proven direct antifungal activity, although it is also rather expensive compared to the other two polymers. Alginate is frequently combined with biocontrol bacteria and fungi, because due to its hydrophilic nature this polymer increases survival of these microorganisms. Cellulose is valued as the cheapest and commonly available resource. Although it cannot be used without modification because of its low solubility in water and lack of functional groups, therefore esters and ethers of this polymer are usually used.

## 6. Future Perspectives and Challenges

As we outlined in the introduction, the widespread use of chemical fungicides had a negative impact on environment, non-target organisms and human health. The growing concerns about these issues have led to the implementation of regulations restricting the use of these agrochemicals. For example, the current “Farm to Fork Strategy” aims at a significant reduction in pesticides use by 2030. Apart from regulatory framework, the consumers’ demand on healthier agricultural products provided a motivation to develop organic agriculture and stimulated development of plant protection products based on natural alternatives to chemical pesticides. As we showed in this review, carbohydrate biopolymers such as chitosan, alginate, cellulose or their derivatives, are suitable for this purpose because of their above-mentioned advantages including nontoxicity, biocompatibility and biodegradability. A lot of recently published studies showed that these compounds are versatile resources for producing plant protection formulations effective against pathogenic fungi because they can act as antifungal compounds, effective elicitors, carriers or matrices for controlled release of active ingredients. The growing interest in reducing the use of chemical pesticide may provide a motivation to improve and standardize production methods of carbohydrate biopolymers and to overcome commercialization barriers for the plant protection products containing these compounds.

Antifungal activity of the formulations based on carbohydrate biopolymers is usually lower or comparable to standard fungicidal treatments [46,51]. However, it can be enhanced by developing complex, more effective formulations which combine these biopolymers with other antifungal agents (Figure 2). Rapid development of nanotechnology opened possibilities of creating new promising forms of plant protection products based on nanoparticles, nano-/micro-carriers and electrospun nanofibers. However, there is a recognized need to evaluate these solutions for their safety and toxicity before they are introduced for use in agriculture [16].

The three carbohydrate biopolymers were successfully used to develop natural plant protection methods for various stages of plant production. As we showed in numerous examples, each of the three biopolymers can be used in treatments dedicated for seed sowing material, field applications and protection of harvested fruits and vegetables.

**Author Contributions:** Conceptualization and writing—original draft, G.K.-G., K.P. and M.W.-W.; writing—review and editing, G.K.-G. and K.P. All authors have read and agreed to the published version of the manuscript.

**Funding:** This research received no external funding.

**Institutional Review Board Statement:** Not applicable.

**Informed Consent Statement:** Not applicable.

**Data Availability Statement:** Not applicable.

**Conflicts of Interest:** The authors declare no conflict of interest.

## References

- Savary, S.; Willocquet, L.; Pethybridge, S.J.; Esker, P.; McRoberts, N.; Nelson, A. The global burden of pathogens and pests on major food crops. *Nat. Ecol. Evol.* **2019**, *3*, 430–439. [[CrossRef](#)] [[PubMed](#)]
- Bebber, D.P.; Gurr, S.J. Crop-destroying fungal and oomycete pathogens challenge food security. *Fungal Genet. Biol.* **2015**, *74*, 62–64. [[CrossRef](#)] [[PubMed](#)]
- Fisher, M.C.; Henk, D.A.; Briggs, C.J.; Brownstein, J.S.; Madoff, L.C.; McCraw, S.L.; Gurr, S.J. Emerging fungal threats to animal, plant and ecosystem health. *Nature* **2012**, *484*, 186–194. [[CrossRef](#)] [[PubMed](#)]
- Fones, H.N.; Bebbler, D.P.; Chaloner, T.M.; Kay, W.T.; Steinberg, G.; Gurr, S.J. Threats to global food security from emerging fungal and oomycete crop pathogens. *Nat. Food* **2020**, *1*, 332–342. [[CrossRef](#)]
- Russell, P.E. A century of fungicide evolution. *J. Agric. Sci.* **2005**, *143*, 11–25. [[CrossRef](#)]
- Gianessi, L.P.; Reigner, N. The importance of fungicides in U.S. crop production. *Outlooks Pest Manag.* **2006**, *17*, 209–213. [[CrossRef](#)]
- Corkley, I.; Fraaije, B.; Hawkins, N. Fungicide resistance management: Maximizing the effective life of plant protection products. *Plant Pathol.* **2022**, *71*, 150–169. [[CrossRef](#)]
- Fungicide Resistance Action Committee. FRAC Code List 2021: Fungal Control Agents Sorted by Cross Resistance Pattern and Mode of Action. Available online: <https://www.frac.info> (accessed on 20 April 2022).
- Carvalho, F.P. Pesticides, environment, and food safety. *Food Energy Secur.* **2017**, *6*, 48–60. [[CrossRef](#)]
- Zubrod, J.P.; Bundschuh, M.; Arts, G.; Bruhl, C.A.; Imfeld, G.; Knabel, A.; Payraudeau, S.; Rasmussen, J.J.; Rohr, J.; Scharmüller, A.; et al. Fungicides: An overlooked pesticide class? *Environ. Sci. Technol.* **2019**, *53*, 3347–3365. [[CrossRef](#)]
- Russell, P.E. The development of commercial disease control. *Plant Pathol.* **2006**, *55*, 585–594. [[CrossRef](#)]
- European Commission. *Communication from the Commission to the European Parliament, the Council, the European Economic and Social Committee and the Committee of the Regions: A Farm to Fork Strategy for a Fair, Healthy and Environmentally-Friendly Food System*; European Commission: Brussels, Belgium, 2020; Volume COM(2020) 381 final.
- Lázaro, E.; Makowski, D.; Vicent, A. Decision support systems halve fungicide use compared to calendar-based strategies without increasing disease risk. *Commun. Earth Environ.* **2021**, *2*, 224. [[CrossRef](#)]
- Tleuova, A.B.; Wielogorska, E.; Talluri, V.; Stepanek, F.; Elliott, C.T.; Grigoriev, D.O. Recent advances and remaining barriers to producing novel formulations of fungicides for safe and sustainable agriculture. *J. Control. Release* **2020**, *326*, 468–481. [[CrossRef](#)] [[PubMed](#)]
- Palou, L.; Ali, A.; Fallik, E.; Romanazzi, G. GRAS, plant- and animal-derived compounds as alternatives to conventional fungicides for the control of postharvest diseases of fresh horticultural produce. *Postharvest Biol. Technol.* **2016**, *122*, 41–52. [[CrossRef](#)]
- Campos, E.V.R.; de Oliveira, J.L.; Fraceto, L.F.; Singh, B. Polysaccharides as safer release systems for agrochemicals. *Agron. Sustain. Dev.* **2015**, *35*, 47–66. [[CrossRef](#)]
- Lopez-Moya, F.; Suarez-Fernandez, M.; Lopez-Llorca, L.V. Molecular mechanisms of chitosan interactions with fungi and plants. *Int. J. Mol. Sci.* **2019**, *20*, 332. [[CrossRef](#)] [[PubMed](#)]
- Xing, K.; Zhu, X.; Peng, X.; Qin, S. Chitosan antimicrobial and eliciting properties for pest control in agriculture: A review. *Agron. Sustain. Dev.* **2015**, *35*, 569–588. [[CrossRef](#)]
- Zheng, F.; Chen, L.; Zhang, P.F.; Zhou, J.Q.; Lu, X.F.; Tian, W. Carbohydrate polymers exhibit great potential as effective elicitors in organic agriculture: A review. *Carbohydr. Polym.* **2020**, *230*, 115637. [[CrossRef](#)]
- Korbecka-Glinka, G.; Wiśniewska-Wrona, M.; Kopania, E. The use of natural polymers for treatments enhancing sowing material. *Polimery* **2021**, *66*, 11–20. (In Polish) [[CrossRef](#)]
- Lamichhane, J.R.; You, M.P.; Laudinot, V.; Barbetti, M.J.; Aubertot, J.N. Revisiting sustainability of fungicide seed treatments for field crops. *Plant Dis.* **2020**, *104*, 610–623. [[CrossRef](#)]
- Mancini, V.; Romanazzi, G. Seed treatments to control seedborne fungal pathogens of vegetable crops. *Pest Manag. Sci.* **2014**, *70*, 860–868. [[CrossRef](#)]
- Gossen, B.D.; Peng, G.; Wolf, T.M.; McDonald, M.R. Improving spray retention to enhance the efficacy of foliar-applied disease- and pest-management products in field and row crops. *Can. J. Plant Pathol.* **2008**, *30*, 505–516. [[CrossRef](#)]

24. Panth, M.; Hassler, S.C.; Baysal-Gurel, F. Methods for management of soilborne diseases in crop production. *Agriculture* **2020**, *10*, 16. [[CrossRef](#)]
25. Davies, C.R.; Wohlgemuth, F.; Young, T.; Violet, J.; Dickinson, M.; Sanders, J.W.; Vallieres, C.; Avery, S.V. Evolving challenges and strategies for fungal control in the food supply chain. *Fungal Biol. Rev.* **2021**, *36*, 15–26. [[CrossRef](#)]
26. Panahirad, S.; Dadpour, M.; Peighambaroust, S.H.; Soltanzadeh, M.; Gullon, B.; Alirezalu, K.; Lorenzo, J.M. Applications of carboxymethyl cellulose- and pectin-based active edible coatings in preservation of fruits and vegetables: A review. *Trends Food Sci. Technol.* **2021**, *110*, 663–673. [[CrossRef](#)]
27. Khoushab, F.; Yamabhai, M. Chitin research revisited. *Mar. Drugs* **2010**, *8*, 1988–2012. [[CrossRef](#)]
28. Pawlowska, A.; Stepczynska, M. Natural biocidal compounds of plant origin as biodegradable materials modifiers. *J. Polym. Environ.* **2022**, *30*, 1683–1708. [[CrossRef](#)]
29. Kurita, K. Chitin and chitosan: Functional biopolymers from marine crustaceans. *Mar. Biotechnol.* **2006**, *8*, 203–226. [[CrossRef](#)] [[PubMed](#)]
30. Elieh-Ali-Komi, D.; Hamblin, M.R. Chitin and chitosan: Production and application of versatile biomedical nanomaterials. *Int. J. Adv. Res.* **2016**, *4*, 411–427.
31. Martau, G.A.; Mihai, M.; Vodnar, D.C. The use of chitosan, alginate, and pectin in the biomedical and food sector-biocompatibility, bioadhesiveness, and biodegradability. *Polymers* **2019**, *11*, 1837. [[CrossRef](#)] [[PubMed](#)]
32. Malerba, M.; Cerana, R. Chitosan effects on plant systems. *Int. J. Mol. Sci.* **2016**, *17*, 996. [[CrossRef](#)]
33. Kaur, P.; Thakur, R.; Choudhary, A. An in vitro study of the antifungal activity of silver/chitosan nanoformulations against important seed borne pathogens. *Int. J. Sci. Technol. Res.* **2012**, *1*, 83–86.
34. Verlee, A.; Mincke, S.; Stevens, C.V. Recent developments in antibacterial and antifungal chitosan and its derivatives. *Carbohydr. Polym.* **2017**, *164*, 268–283. [[CrossRef](#)] [[PubMed](#)]
35. Palma-Guerrero, J.; Huang, I.C.; Jansson, H.B.; Salinas, J.; Lopez-Llorca, L.V.; Read, N.D. Chitosan permeabilizes the plasma membrane and kills cells of *Neurospora crassa* in an energy dependent manner. *Fungal Genet. Biol.* **2009**, *46*, 585–594. [[CrossRef](#)] [[PubMed](#)]
36. Rabea, E.I.; Badawy, M.E.T.; Stevens, C.V.; Smagghe, G.; Steurbaut, W. Chitosan as antimicrobial agent: Applications and mode of action. *Biomacromolecules* **2003**, *4*, 1457–1465. [[CrossRef](#)]
37. Chien, P.J.; Chou, C.C. Antifungal activity of chitosan and its application to control post-harvest quality and fungal rotting of Takan citrus fruit (*Citrus tarkan Hayata*). *J. Sci. Food Agric.* **2006**, *86*, 1964–1969. [[CrossRef](#)]
38. Muanprasat, C.; Wongkrasant, P.; Satitsri, S.; Moonwiriyakit, A.; Pongkorpsakol, P.; Mattaveewong, T.; Pichyangkura, R.; Chatsudthipong, V. Activation of AMPK by chitosan oligosaccharide in intestinal epithelial cells: Mechanism of action and potential applications in intestinal disorders. *Biochem. Pharmacol.* **2015**, *96*, 225–236. [[CrossRef](#)]
39. Mourya, V.K.; Inamdar, N.N.; Choudhari, Y.M. Chitooligosaccharides: Synthesis, characterization and applications. *Polym. Sci. Ser. A* **2011**, *53*, 583–612. [[CrossRef](#)]
40. Yuan, X.B.; Zheng, J.P.; Jiao, S.M.; Cheng, G.; Feng, C.; Du, Y.G.; Liu, H.T. A review on the preparation of chitosan oligosaccharides and application to human health, animal husbandry and agricultural production. *Carbohydr. Polym.* **2019**, *220*, 60–70. [[CrossRef](#)]
41. Silva-Castro, I.; Diez, J.J.; Martin-Ramos, P.; Pinto, G.; Alves, A.; Martin-Gil, J.; Martin-Garcia, J. Application of bioactive coatings based on chitosan and propolis for *Pinus* spp. protection against *Fusarium circinatum*. *Forests* **2018**, *9*, 685. [[CrossRef](#)]
42. Pabon-Baquero, D.; Velazquez-del Valle, M.G.; Evangelista-Lozano, S.; Leon-Rodriguez, R.; Hernandez-Lauzardo, A.N. Chitosan effects on phytopathogenic fungi and seed germination of *Jatropha curcas* L. *Rev. Chapingo Ser. Cienc. For. Am.* **2015**, *21*, 241–253. [[CrossRef](#)]
43. Ziani, K.; Ursua, B.; Mate, J.I. Application of bioactive coatings based on chitosan for artichoke seed protection. *Crop Prot.* **2010**, *29*, 853–859. [[CrossRef](#)]
44. Ghule, M.R.; Ramteke, P.K.; Ramteke, S.D.; Kodre, P.S.; Langote, A.; Gaikwad, A.V.; Holkar, S.K.; Jambhekar, H. Impact of chitosan seed treatment of fenugreek for management of root rot disease caused by *Fusarium solani* under in vitro and in vivo conditions. *3 Biotech* **2021**, *11*, 290. [[CrossRef](#)] [[PubMed](#)]
45. Samarah, N.H.; Al-Quraan, N.A.; Massad, R.S.; Welbaum, G.E. Treatment of bell pepper (*Capsicum annuum* L.) seeds with chitosan increases chitinase and glucanase activities and enhances emergence in a standard cold test. *Sci. Hort.* **2020**, *269*, 109393. [[CrossRef](#)]
46. Mondejar-Lopez, M.; Rubio-Moraga, A.; Lopez-Jimenez, A.J.; Martinez, J.C.G.; Ahrazem, O.; Gomez-Gomez, L.; Niza, E. Chitosan nanoparticles loaded with garlic essential oil: A new alternative to tebuconazole as seed dressing agent. *Carbohydr. Polym.* **2022**, *277*, 118815. [[CrossRef](#)] [[PubMed](#)]
47. Attjioui, M.; Gillet, D.; El Gueddari, N.E.; Moerschbacher, B.M. Synergistic antimicrobial effect of chitosan polymers and oligomers. *Mol. Plant Microbe Interact.* **2021**, *34*, 770–778. [[CrossRef](#)]
48. Sun, G.Z.; Yang, Q.C.; Zhang, A.C.; Guo, J.; Liu, X.J.; Wang, Y.; Ma, Q. Synergistic effect of the combined bio-fungicides epsilon-poly-L-lysine and chitooligosaccharide in controlling grey mould (*Botrytis cinerea*) in tomatoes. *Int. J. Food Microbiol.* **2018**, *276*, 46–53. [[CrossRef](#)]
49. Gao, K.; Zhan, J.; Qin, Y.K.; Liu, S.; Xing, R.E.; Yu, H.H.; Chen, X.L.; Li, P.C. Synthesis and effects of the selective oxidation of chitosan in induced disease resistance against *Botrytis cinerea*. *Carbohydr. Polym.* **2021**, *265*, 118073. [[CrossRef](#)]

50. Dananjaya, S.H.S.; Erandani, W.; Kim, C.H.; Nikapitiya, C.; Lee, J.; De Zoysa, M. Comparative study on antifungal activities of chitosan nanoparticles and chitosan silver nano composites against *Fusarium oxysporum* species complex. *Int. J. Biol. Macromol.* **2017**, *105*, 478–488. [[CrossRef](#)]
51. Kaur, P.; Duhan, J.S.; Thakur, R. Comparative pot studies of chitosan and chitosan-metal nanocomposites as nano-agrochemicals against fusarium wilt of chickpea (*Cicer arietinum* L.). *Biocatal. Agric. Biotechnol.* **2018**, *14*, 466–471. [[CrossRef](#)]
52. Choudhary, R.C.; Kumaraswamy, R.V.; Kumari, S.; Sharma, S.S.; Pal, A.; Raliya, R.; Biswas, P.; Saharan, V. Cu-chitosan nanoparticle boost defense responses and plant growth in maize (*Zea mays* L.). *Sci. Rep.* **2017**, *7*, 9754. [[CrossRef](#)]
53. Mohammed, B.L.; Hussein, R.A.; Toama, F.N. Biological control of Fusarium wilt in tomato by endophytic rhizobacteria. *Energy Procedia* **2019**, *157*, 171–179. [[CrossRef](#)]
54. Elsherbiny, A.S.; Galal, A.; Ghoneem, K.M.; Salahuddin, N.A. Novel chitosan-based nanocomposites as ecofriendly pesticide carriers: Synthesis, root rot inhibition and growth management of tomato plants. *Carbohydr. Polym.* **2022**, *282*, 119111. [[CrossRef](#)]
55. Chapagain, B.P.; Wiesman, Z.; Tsrur, L. In vitro study of the antifungal activity of saponin-rich extracts against prevalent phytopathogenic fungi. *Ind. Crop. Prod.* **2007**, *26*, 109–115. [[CrossRef](#)]
56. Saharan, V.; Mehrotra, A.; Khatik, R.; Rawal, P.; Sharma, S.S.; Pal, A. Synthesis of chitosan based nanoparticles and their in vitro evaluation against phytopathogenic fungi. *Int. J. Biol. Macromol.* **2013**, *62*, 677–683. [[CrossRef](#)] [[PubMed](#)]
57. Sandhya, Kumar, S.; Kumar, D.; Dilbaghi, N. Preparation, characterization, and bio-efficacy evaluation of controlled release carbendazim-loaded polymeric nanoparticles. *Environ. Sci. Pollut. Res. Int.* **2017**, *24*, 926–937. [[CrossRef](#)] [[PubMed](#)]
58. Madanipour, S.; Alimohammadi, M.; Rezaie, S.; Nabizadeh, R.; Khaniki, G.J.; Hadi, M.; Yousefi, M.; Bidgoli, S.M.; Yousefzadeh, S. Influence of postharvest application of chitosan combined with ethanolic extract of liquorice on shelflife of apple fruit. *J. Environ. Health Sci. Eng.* **2019**, *17*, 331–336. [[CrossRef](#)] [[PubMed](#)]
59. Guerra, I.C.D.; de Oliveira, P.D.L.; Pontes, A.L.D.; Lucio, A.; Tavares, J.F.; Barbosa, J.M.; Madruga, M.S.; de Souza, E.L. Coatings comprising chitosan and *Mentha piperita* L. or *Mentha x villosa* Huds essential oils to prevent common postharvest mold infections and maintain the quality of cherry tomato fruit. *Int. J. Food Microbiol.* **2015**, *214*, 168–178. [[CrossRef](#)] [[PubMed](#)]
60. Shen, Y.F.; Yang, H.Q. Effect of preharvest chitosan-g-salicylic acid treatment on postharvest table grape quality, shelf life, and resistance to *Botrytis cinerea*-induced spoilage. *Sci. Hortic.* **2017**, *224*, 367–373. [[CrossRef](#)]
61. Youssef, K.; de Oliveira, A.G.; Tischer, C.A.; Hussain, I.; Roberto, S.R. Synergistic effect of a novel chitosanisilica nanocomposites-based formulation against gray mold of table grapes and its possible mode of action. *Int. J. Biol. Macromol.* **2019**, *141*, 247–258. [[CrossRef](#)]
62. Gonzalez-Saucedo, A.; Barrera-Necha, L.L.; Ventura-Aguilar, R.I.; Correa-Pacheco, Z.N.; Bautista-Banos, S.; Hernandez-Lopez, M. Extension of the postharvest quality of bell pepper by applying nanostructured coatings of chitosan with *Byrsonima crassifolia* extract (L.) Kunth. *Postharvest Biol. Technol.* **2019**, *149*, 74–82. [[CrossRef](#)]
63. Kharchoufi, S.; Parafati, L.; Licciardello, F.; Muratore, G.; Hamdi, M.; Cirvilleri, G.; Restuccia, C. Edible coatings incorporating pomegranate peel extract and biocontrol yeast to reduce *Penicillium digitatum* postharvest decay of oranges. *Food Microbiol.* **2018**, *74*, 107–112. [[CrossRef](#)] [[PubMed](#)]
64. Saberi-Rise, R.; Moradi-Pour, M. The effect of *Bacillus subtilis* Vru1 encapsulated in alginate—Bentonite coating enriched with titanium nanoparticles against *Rhizoctonia solani* on bean. *Int. J. Biol. Macromol.* **2020**, *152*, 1089–1097. [[CrossRef](#)]
65. Sujarit, K.; Pathom-aree, W.; Mori, M.; Dobashi, K.; Shiomi, K.; Lumyong, S. *Streptomyces palmae* CMU-AB204 (T), an antifungal producing-actinomycete, as a potential biocontrol agent to protect palm oil producing trees from basal stem rot disease fungus, *Ganoderma boninense*. *Biol. Control* **2020**, *148*, 104307. [[CrossRef](#)]
66. Xiang, S.Y.; Ma, X.Z.; Shi, H.; Ma, T.; Tian, C.L.; Chen, Y.; Chen, H.T.; Chen, X.; Luo, K.; Cai, L.; et al. Green synthesis of an alginate-coated silver nanoparticle shows high antifungal activity by enhancing its cell membrane penetrating ability. *ACS Appl. Bio Mater.* **2019**, *2*, 4087–4096. [[CrossRef](#)]
67. Sattary, M.; Amini, J.; Hallaj, R. Antifungal activity of the lemongrass and clove oil encapsulated in mesoporous silica nanoparticles against wheat's take-all disease. *Pest. Biochem. Physiol.* **2020**, *170*, 104696. [[CrossRef](#)] [[PubMed](#)]
68. Kumar, J.; Nisar, K.; Arun Kumar, M.B.; Walia, S.; Shakil, N.A.; Prasad, R.; Parmar, B.S. Development of polymeric seed coats for seed quality enhancement of soybean. *Indian J. Agric. Sci.* **2007**, *77*, 738–743.
69. Dal Bello, G.M.; Monaco, C.I.; Simon, M.R. Biological control of seedling blight of wheat caused by *Fusarium graminearum* with beneficial rhizosphere microorganisms. *World J. Microbiol. Biotechnol.* **2002**, *18*, 627–636. [[CrossRef](#)]
70. Ren, X.X.; Chen, C.; Ye, Z.H.; Su, X.Y.; Xiao, J.J.; Liao, M.; Cao, H.Q. Development and application of seed coating agent for the control of major soil-borne diseases infecting wheat. *Agronomy* **2019**, *9*, 413. [[CrossRef](#)]
71. Farias, B.V.; Pirezada, T.; Mathew, R.; Sit, T.L.; Opperman, C.; Khan, S.A. Electrospun polymer nanofibers as seed coatings for crop protection. *ACS Sustain. Chem. Eng.* **2019**, *7*, 19848–19856. [[CrossRef](#)]
72. Xu, T.; Ma, C.X.; Aytac, Z.; Hu, X.; Ng, K.W.; White, J.C.; Demokritou, P. Enhancing agrichemical delivery and seedling development with biodegradable, tunable, biopolymer-based nanofiber seed coatings. *ACS Sustain. Chem. Eng.* **2020**, *8*, 9537–9548. [[CrossRef](#)]
73. Bashan, Y.; de-Bashan, L.E.; Prabhu, S.R.; Hernandez, J.P. Advances in plant growth-promoting bacterial inoculant technology: Formulations and practical perspectives (1998–2013). *Plant Soil* **2014**, *378*, 1–33. [[CrossRef](#)]
74. Cao, L.; Lu, W.; Mata, A.; Nishinari, K.; Fang, Y. Egg-box model-based gelation of alginate and pectin: A review. *Carbohydr. Polym.* **2020**, *242*, 116389. [[CrossRef](#)] [[PubMed](#)]

75. Nair, M.S.; Tomar, M.; Punia, S.; Kukula-Koch, W.; Kumar, M. Enhancing the functionality of chitosan- and alginate-based active edible coatings/films for the preservation of fruits and vegetables: A review. *Int. J. Biol. Macromol.* **2020**, *164*, 304–320. [[CrossRef](#)]
76. Percival, S.L.; McCarty, S.M. Silver and alginates: Role in wound healing and biofilm control. *Adv. Wound Care* **2015**, *4*, 407–414. [[CrossRef](#)] [[PubMed](#)]
77. Jarecki, W. Soybean response to seed coating with chitosan + alginate/PEG and/or inoculation. *Agronomy* **2021**, *11*, 1737. [[CrossRef](#)]
78. Jarecki, W.; Wietecha, J. Effect of seed coating on the yield of soybean *Glycine max* (L.) Merr. *Plant Soil Environ.* **2021**, *67*, 468–473. [[CrossRef](#)]
79. Amanatidou, A.; Slump, R.A.; Gorris, L.G.M.; Smid, E.J. High oxygen and high carbon dioxide modified atmospheres for shelf-life extension of minimally processed carrots. *J. Food Sci.* **2000**, *65*, 61–66. [[CrossRef](#)]
80. Zhang, Y.H.; Liu, H.; Yin, H.; Wang, W.X.; Zhao, X.M.; Du, Y.G. Nitric oxide mediates alginate oligosaccharides-induced root development in wheat (*Triticum aestivum* L.). *Plant Physiol. Biochem.* **2013**, *71*, 49–56. [[CrossRef](#)]
81. Jung, G.; Mugnier, J.; Diem, H.G.; Dommergues, Y.R. Polymer-entrapped rhizobium as an inoculant for legumes. *Plant Soil* **1982**, *65*, 219–231. [[CrossRef](#)]
82. Heo, K.R.; Lee, K.Y.; Lee, S.H.; Jung, S.J.; Lee, S.W.; Moon, B.J. Control of crisphead lettuce damping-off and bottom rot by seed coating with alginate and *Pseudomonas aeruginosa* LY-11. *Plant Pathol. J.* **2008**, *24*, 67–73. [[CrossRef](#)]
83. John, R.P.; Tyagi, R.D.; Brar, S.K.; Surampalli, R.Y.; Prevost, D. Bio-encapsulation of microbial cells for targeted agricultural delivery. *Crit. Rev. Biotechnol.* **2011**, *31*, 211–226. [[CrossRef](#)] [[PubMed](#)]
84. Ali, A.; Khan, M.M.A.; Uddin, M.; Naeem, M.; Idrees, M.; Hashmi, N.; Dar, T.A.; Varshney, L. Radiolytically depolymerized sodium alginate improves physiological activities, yield attributes and composition of essential oil of *Eucalyptus citriodora* Hook. *Carbohydr. Polym.* **2014**, *112*, 134–144. [[CrossRef](#)] [[PubMed](#)]
85. Hu, T.; Li, C.X.; Zhao, X.; Li, G.S.; Yu, G.L.; Guan, H.S. Preparation and characterization of guluronic acid oligosaccharides degraded by a rapid microwave irradiation method. *Carbohydr. Res.* **2013**, *373*, 53–58. [[CrossRef](#)]
86. Hien, N.Q.; Nagasawa, N.; Tham, L.X.; Yoshii, F.; Dang, V.H.; Mitomo, H.; Makuuchi, K.; Kume, T. Growth-promotion of plants with depolymerized alginates by irradiation. *Radiat. Phys. Chem.* **2000**, *59*, 97–101. [[CrossRef](#)]
87. Iwasaki, K.; Matsubara, Y. Purification of alginate oligosaccharides with root growth-promoting activity toward lettuce. *Biosci. Biotechnol. Biochem.* **2000**, *64*, 1067–1070. [[CrossRef](#)]
88. Liakos, I.; Rizzello, L.; Scurr, D.J.; Pompa, P.P.; Bayer, I.S.; Athanassiou, A. All-natural composite wound dressing films of essential oils encapsulated in sodium alginate with antimicrobial properties. *Int. J. Pharm.* **2014**, *463*, 137–145. [[CrossRef](#)]
89. Qu, L.; Wang, H.; Zhu, L.; Duan, X.; Quan, W.; Kong, W. Sustained Release Agent for Controlling Cucumber Botrytis. CN104396958A, 11 March 2015.
90. Singh, B.; Sharma, D.K.; Dhiman, A. Environment friendly agar and alginate-based thiram delivery system. *Toxicol. Environ. Chem.* **2013**, *95*, 567–578. [[CrossRef](#)]
91. Han, J.J.; Zhao, L.N.; Zhu, H.M.; Dhanasekaran, S.; Zhang, X.Y.; Zhang, H.Y. Study on the effect of alginate oligosaccharide combined with *Meyerozyma guilliermondii* against *Penicillium expansum* in pears and the possible mechanisms involved. *Physiol. Mol. Plant Pathol.* **2021**, *115*, 101654. [[CrossRef](#)]
92. Maqbool, M.; Ali, A.; Alderson, P.G.; Mohamed, M.T.M.; Siddiqui, Y.; Zahid, N. Postharvest application of gum arabic and essential oils for controlling anthracnose and quality of banana and papaya during cold storage. *Postharvest Biol. Technol.* **2011**, *62*, 71–76. [[CrossRef](#)]
93. Dhall, R.K. Advances in edible coatings for fresh fruits and vegetables: A review. *Crit. Rev. Food Sci. Nutr.* **2013**, *53*, 435–450. [[CrossRef](#)]
94. Galus, S.; Kadzinska, J. Food applications of emulsion-based edible films and coatings. *Trends Food Sci. Technol.* **2015**, *45*, 273–283. [[CrossRef](#)]
95. Xu, L.L.; Zhang, B.; Qin, Y.H.; Li, F.Y.; Yang, S.J.; Lu, P.P.; Wang, L.; Fan, J.F. Preparation and characterization of antifungal coating films composed of sodium alginate and cyclolipopeptides produced by *Bacillus subtilis*. *Int. J. Biol. Macromol.* **2020**, *143*, 602–609. [[CrossRef](#)] [[PubMed](#)]
96. Tabassum, N.; Khan, M.A. Modified atmosphere packaging of fresh-cut papaya using alginate based edible coating: Quality evaluation and shelf life study. *Sci. Hortic.* **2020**, *259*, 108853. [[CrossRef](#)]
97. Azarakhsh, N.; Osman, A.; Ghazali, H.M.; Tan, C.P.; Adzahan, N.M. Lemongrass essential oil incorporated into alginate-based edible coating for shelf-life extension and quality retention of fresh-cut pineapple. *Postharvest Biol. Technol.* **2014**, *88*, 1–7. [[CrossRef](#)]
98. Guerreiro, A.C.; Gago, C.M.L.; Miguel, M.G.C.; Faleiro, M.L.; Antunes, M.D.C. The influence of edible coatings enriched with citral and eugenol on the raspberry storage ability, nutritional and sensory quality. *Food Packag. Shelf Life* **2016**, *9*, 20–28. [[CrossRef](#)]
99. Rojas-Grau, M.A.; Raybaudi-Massilia, R.M.; Soliva-Fortuny, R.C.; Avena-Bustillos, R.J.; McHugh, T.H.; Martin-Belloso, O. Apple puree-alginate edible coating as carrier of antimicrobial agents to prolong shelf-life of fresh-cut apples. *Postharvest Biol. Technol.* **2007**, *45*, 254–264. [[CrossRef](#)]
100. Takma, D.K.; Korel, F. Impact of preharvest and postharvest alginate treatments enriched with vanillin on postharvest decay, biochemical properties, quality and sensory attributes of table grapes. *Food Chem.* **2017**, *221*, 187–195. [[CrossRef](#)]

101. Li, X.Y.; Du, X.L.; Liu, Y.; Tong, L.J.; Wang, Q.; Li, J.L. Rhubarb extract incorporated into an alginate-based edible coating for peach preservation. *Sci. Hort.* **2019**, *257*, 108685. [[CrossRef](#)]
102. Jiang, T.J.; Feng, L.F.; Wang, Y.B. Effect of alginate/nano-Ag coating on microbial and physicochemical characteristics of shiitake mushroom (*Lentinus edodes*) during cold storage. *Food Chem.* **2013**, *141*, 954–960. [[CrossRef](#)]
103. Emamifar, A.; Bavaisi, S. Nanocomposite coating based on sodium alginate and nano-ZnO for extending the storage life of fresh strawberries (*Fragaria x ananassa* Duch.). *J. Food Meas. Charact.* **2020**, *14*, 1012–1024. [[CrossRef](#)]
104. Zhuo, R.L.; Li, B.Q.; Tian, S.P. Alginate oligosaccharide improves resistance to postharvest decay and quality in kiwifruit (*Actinidia deliciosa* cv. Bruno). *Hortic. Plant J.* **2022**, *8*, 44–52. [[CrossRef](#)]
105. Liu, Q.Z.; Liu, P.Q.; Xu, Y.J.; Wang, B.; Liu, P.F.; Hao, J.J.; Liu, X.L. Encapsulation of fluazinam to extend efficacy duration in controlling *Botrytis cinerea* on cucumber. *Pest Manag. Sci.* **2021**, *77*, 2836–2842. [[CrossRef](#)] [[PubMed](#)]
106. Machado, T.O.; Beckers, S.J.; Fischer, J.; Sayer, C.; de Araujo, P.H.H.; Landfester, K.; Wurm, F.R. Cellulose nanocarriers via miniemulsion allow pathogen-specific agrochemical delivery. *J. Colloid Interface Sci.* **2021**, *601*, 678–688. [[CrossRef](#)] [[PubMed](#)]
107. Gao, Y.H.; Liu, Y.; Qin, X.Y.; Guo, Z.P.; Li, D.L.; Li, C.G.; Wan, H.; Zhu, F.X.; Li, J.H.; Zhang, Z.; et al. Dual stimuli-responsive fungicide carrier based on hollow mesoporous silica/hydroxypropyl cellulose hybrid nanoparticles. *J. Hazard. Mater.* **2021**, *414*, 125513. [[CrossRef](#)] [[PubMed](#)]
108. Ma, H.H.; Zhao, Y.; Lu, Z.J.; Xing, R.L.; Yao, X.M.; Jin, Z.X.; Wang, Y.Y.; Yu, F. Citral-loaded chitosan/carboxymethyl cellulose copolymer hydrogel microspheres with improved antimicrobial effects for plant protection. *Int. J. Biol. Macromol.* **2020**, *164*, 986–993. [[CrossRef](#)]
109. Spasova, M.; Manolova, N.; Rashkov, I.; Naydenov, M. Electrospun 5-chloro-8-hydroxyquinoline-loaded cellulose acetate/polyethylene glycol antifungal membranes against esca. *Polymers* **2019**, *11*, 1617. [[CrossRef](#)]
110. Barhoum, A.; Jeevanandam, J.; Rastogi, A.; Samyn, P.; Boluk, Y.; Dufresne, A.; Danquah, M.K.; Bechelany, M. Plant celluloses, hemicelluloses, lignins, and volatile oils for the synthesis of nanoparticles and nanostructured materials. *Nanoscale* **2020**, *12*, 22845–22890. [[CrossRef](#)]
111. Heinze, T.; ElSeoud, O.A.; Koschella, A. *Cellulose Derivatives: Synthesis, Structure, and Properties*; Springer: Cham, Switzerland, 2018; pp. 1–531. [[CrossRef](#)]
112. Meraz-Davila, S.; Perez-Garcia, C.E.; Feregrino-Perez, A.A. Challenges and advantages of electrospun nanofibers in agriculture: A review. *Mater. Res. Express* **2021**, *8*, 042001. [[CrossRef](#)]
113. Afzal, I.; Javed, T.; Amirkhani, M.; Taylor, A.G. Modern seed technology: Seed coating delivery systems for enhancing seed and crop performance. *Agriculture* **2020**, *10*, 526. [[CrossRef](#)]
114. Pedrini, S.; Merritt, D.J.; Stevens, J.; Dixon, K. Seed coating: Science or marketing spin? *Trends Plant Sci.* **2017**, *22*, 106–116. [[CrossRef](#)]
115. Viji, G.; Uddin, W.; Romaine, C.P. Suppression of gray leaf spot (blast) of perennial ryegrass turf by *Pseudomonas aeruginosa* from spent mushroom substrate. *Biol. Control* **2003**, *26*, 233–243. [[CrossRef](#)]
116. Neri-Badang, M.C.; Chakraborty, S. Carbohydrate polymers as controlled release devices for pesticides. *J. Carbohydr. Chem.* **2019**, *38*, 67–85. [[CrossRef](#)]
117. Kumar, S.; Baswal, A.K.; Ramezani, A.; Gill, K.S.; Mirza, A.A. Impact of carboxymethyl cellulose based edible coating on storage life and quality of guava fruit cv. 'Allahabad Safeda' under ambient storage conditions. *J. Food Meas. Charact.* **2021**, *15*, 4805–4812. [[CrossRef](#)]
118. Baswal, A.K.; Dhaliwal, H.S.; Singh, Z.; Mahajan, B.V.C.; Kalia, A.; Gill, K.S. Influence of carboxy methylcellulose, chitosan and beeswax coatings on cold storage life and quality of Kinnow mandarin fruit. *Sci. Hort.* **2020**, *260*, 108887. [[CrossRef](#)]
119. Khodaei, D.; Hamidi-Esfahani, Z. Influence of bioactive edible coatings loaded with *Lactobacillus plantarum* on physicochemical properties of fresh strawberries. *Postharvest Biol. Technol.* **2019**, *156*, 110944. [[CrossRef](#)]
120. Chen, C.Y.; Peng, X.; Zeng, R.; Wan, C.P.; Chen, M.; Chen, J.Y. Physiological and biochemical responses in cold-stored citrus fruits to carboxymethyl cellulose coating containing ethanol extract of *Impatiens balsamina* L. stems. *J. Food Process. Preserv.* **2017**, *41*, e12999. [[CrossRef](#)]
121. Tesfay, S.Z.; Magwaza, L.S.; Mbili, N.; Mditshwa, A. Carboxyl methylcellulose (CMC) containing moringa plant extracts as new postharvest organic edible coating for avocado (*Persea americana* Mill.) fruit. *Sci. Hort.* **2017**, *226*, 201–207. [[CrossRef](#)]
122. Valencia-Chamorro, S.A.; Perez-Gago, M.B.; del Rio, M.A.; Palou, L. Effect of antifungal hydroxypropyl methylcellulose (HPMC)-lipid edible composite coatings on postharvest decay development and quality attributes of cold-stored 'Valencia' oranges. *Postharvest Biol. Technol.* **2009**, *54*, 72–79. [[CrossRef](#)]
123. Fagundes, C.; Perez-Gago, M.B.; Monteiro, A.R.; Palou, L. Antifungal activity of food additives in vitro and as ingredients of hydroxypropyl methylcellulose-lipid edible coatings against *Botrytis cinerea* and *Alternaria alternata* on cherry tomato fruit. *Int. J. Food Microbiol.* **2013**, *166*, 391–398. [[CrossRef](#)]
124. Garcia-Vaquero, M.; Rajauria, G.; O'Doherty, J.V.; Sweeney, T. Polysaccharides from macroalgae: Recent advances, innovative technologies and challenges in extraction and purification. *Food Res. Int.* **2017**, *99*, 1011–1020. [[CrossRef](#)]
125. Bouissil, S.; Pierre, G.; El Alaoui-Talibi, Z.; Michaud, P.; El Modafar, C.; Delattre, C. Applications of algal polysaccharides and derivatives in therapeutic and agricultural fields. *Curr. Pharm. Des.* **2019**, *25*, 1187–1199. [[CrossRef](#)] [[PubMed](#)]
126. Kaur, S.; Dhillon, G.S. The versatile biopolymer chitosan: Potential sources, evaluation of extraction methods and applications. *Crit. Rev. Microbiol.* **2014**, *40*, 155–175. [[CrossRef](#)] [[PubMed](#)]



127. Tyliszczak, B.; Drabczyk, A.; Kudlacik-Kramarczyk, S.; Sobczak-Kupiec, A. Sustainable Production of Chitosan. In *Sustainable Production: Novel Trends in Energy, Environment and Material Systems*; Krolczyk, G.M., Wzorek, M., Krol, A., Kochan, O., Su, J., Kacprzyk, J., Eds.; Springer: Cham, Switzerland, 2020; Volume 198, pp. 45–60.
128. Stasinska-Jakubas, M.; Hawrylak-Nowak, B. Protective, biostimulating, and eliciting effects of chitosan and its derivatives on crop plants. *Molecules* **2022**, *27*, 2801. [[CrossRef](#)] [[PubMed](#)]

## Article

# Blended Polymer Dry Electrodes for Reliable Electrocardiogram and Electromyogram Measurements and Their Eco-Friendly Disposal Led by Degradability in Hot Water

Dong Hyun Lee <sup>1,†</sup>, Eun Kwang Lee <sup>2,†</sup>, Chae Hyun Kim <sup>1,†</sup>, Hyung Joong Yun <sup>3</sup>, Young-Joon Kim <sup>1,\*</sup> and Hocheon Yoo <sup>1,\*</sup>

<sup>1</sup> Department of Electronic Engineering, Gachon University, 1342 Seongnam-daero, Seongnam 13120, Korea; danny99hodam@gachon.ac.kr (D.H.L.); chrabbit27@naver.com (C.H.K.)

<sup>2</sup> Department of Chemical Engineering, Pukyong National University (PKNU), Busan 48513, Korea; ekleee@pknu.ac.kr

<sup>3</sup> Advance Nano Research Group, Korea Basic Science Institute (KBSI), Daejeon 34126, Korea; hjyun@kbsi.re.kr

\* Correspondence: youngkim@gachon.ac.kr (Y.-J.K.); hyoo@gachon.ac.kr (H.Y.)

† These authors contributed equally to this work.

**Abstract:** To increase the human lifespan, healthcare monitoring devices that diagnose diseases and check body conditions have attracted considerable interest. Commercial AgCl-based wet electrodes with the advantages of high conductivity and strong adaptability to human skin are considered the most frequently used electrode material for healthcare monitoring. However, commercial AgCl-based wet electrodes, when exposed for a long period, cause an evaporation of organic solvents, which could reduce the signal-to-noise ratio of biosignals and stimulate human skin. In this context, we demonstrate a dry electrode for a poly(3,4-ethylenedioxythiophene):poly(styrenesulfonate) (PEDOT:PSS)-based blended polymer electrode using a combination of PEDOT:PSS, waterborne polyurethane (WPU) and ethylene glycol (EG) that could be reused for a long period of time to detect electrocardiography (ECG) and electromyography (EMG). Both ECG and EMG are reliably detected by the wireless real-time monitoring system. In particular, the proposed dry electrode detects biosignals without deterioration for over 2 weeks. Additionally, a double layer of a polyimide (PI) substrate and fluorinated polymer CYTOP induces the strong waterproof characteristics of external liquids for the proposed dry electrodes, having a low surface energy of 14.49 mN/m. In addition, the proposed electrode has excellent degradability in water; it dissolves in hot water at 60 °C.

**Keywords:** electrocardiography; electromyography; PEDOT:PSS; degradability; polymer electrode

**Citation:** Lee, D.H.; Lee, E.K.; Kim, C.H.; Yun, H.J.; Kim, Y.-J.; Yoo, H. Blended Polymer Dry Electrodes for Reliable Electrocardiogram and Electromyogram Measurements and Their Eco-Friendly Disposal Led by Degradability in Hot Water. *Polymers* **2022**, *14*, 2586. <https://doi.org/10.3390/polym14132586>

Academic Editors: José Miguel Ferri, Vicent Fombuena Borràs and Miguel Fernando Aldás Carrasco

Received: 7 May 2022

Accepted: 21 June 2022

Published: 26 June 2022

**Publisher's Note:** MDPI stays neutral with regard to jurisdictional claims in published maps and institutional affiliations.



**Copyright:** © 2022 by the authors. Licensee MDPI, Basel, Switzerland. This article is an open access article distributed under the terms and conditions of the Creative Commons Attribution (CC BY) license (<https://creativecommons.org/licenses/by/4.0/>).

## 1. Introduction

To ensure the world's aging population has the right to individual life, neurological diseases, cardiovascular diseases, etc. are becoming notable social issues. As a result, many studies have been carried out to develop high-performance electrocardiograph (ECG) and electromyograph (EMG) sensors that can efficiently obtain biosignals from the surface of the human body. Especially, a non-invasive biopotential electrode is well known for its key contribution as a component of a biopotential acquisition system from a human being due to its fast measurement setup on the surface of the human body without leaving a scar. Robust and reliable biosignal acquisition is strongly dependent on the characteristic of biopotential electrodes, such as adhesion, wet-degradability, conductivity and micro-/macroscopic morphology.

So far, much work on the development of biopotential electrodes has been carried out in terms of material properties and mechanical flexibility to record biosignals. Commercially, wet-type electrodes (typically, Ag/AgCl) have been widely utilized because of their high conductivity and conformability to human skin [1–3]. However, electrolytes

of the wet-type electrodes are diffused into the subcutaneous area of the human body, and organic solvents of the wet-type electrodes evaporated over a long period of time. Thus, this would cause skin irritation and significant decays of the signal-to-noise ratio of biosignals, respectively. Instead, the fabrication of dry-type electrodes was intensively investigated using a thin metal [4–7], a carbon nanotube (CNT) [8–11], polymer–metal particle composites [12], graphene [13–17] and conductive polymers, such as poly(3,4-ethylenedioxythiophene):poly(styrenesulfonate) (PEDOT:PSS) [18–20].

Major technological issues in the fabrication of biopotential electrodes are mechanical robustness and reliability for long-term biosignal recording. A previously reported study fabricated organogel-based strain-insensitive conductors using PEDOT:PSS, polyacrylamide (AAm) and ethylene glycol (EG) [18]. Excessive ions and impurities in PEDOT:PSS were eliminated via dialysis. In addition, EG, which has a high boiling point (197 °C), scarcely evaporated at room temperature, so organogel-based PEDOT:PSS maintained the compositional ratio over a long time. Biocompatible PEDOT:PSS electrode was fabricated by blending a waterborne polyurethane (WPU) and D-sorbitol, which is a food additive used in various fields such as cosmetic lotions, creams, toothpastes and food additives [20]. The fabricated dry-type PEDOT:PSS electrodes exhibited excellent electrical conductivity, strong adhesion properties and long-term stability. Complex microstructured and macropillar-shaped biopotential electrodes have been reported by a research group of ETH Zurich, which exhibited low electrical impedance [21]. The complex microstructured electrodes and macropillar-shaped electrodes were fabricated using multiple photolithography and a stencil printing technique, respectively. However, the fabrication of the biopotential electrodes involved multiple steps of the lithographic process and could suffer from the reduction in the fabrication process yield. From these points of view, human-friendly and environmentally friendly biopotential electrodes are highly required, with simple yet robust film formation using conductive polymers.

PEDOT:PSS, a representative high-conductivity polymer, is a polymer mixture composed of conductive PEDOT and insulating PSS. PEDOT:PSS has attracted attention over the decades due to high transmittance in the visible light region and solution processability. PEDOT:PSS can be applied to various electronic devices and display fields, such as wearable devices, transparent electrodes and solar cells [22–24]. Recently, research has been reported to improve the conductivity, thermoelectric characteristics and mechanical flexibility of PEDOT:PSS. Ionic liquids such as butyl-3-methylimidazolium, tetrafluoroborate and 2-methylimidazolium hydrogen sulfate improve the conductivity of PEDOT:PSS [25,26]. In addition, deep eutectic solvents (DES), which are biocompatible, and biodegradable solvents increased the thermoelectric and sensing characteristics of PEDOT:PSS [27,28]. Lastly, the addition of elastomer to PEDOT:PSS leads to high mechanical characteristics [29]. The PEDOT:PSS composite, with improved conductivity, sensing and mechanical characteristics, is a strong potential candidate for use as an electrophysiological epidermal electrode.

In this light, we present waterproof dry-type PEDOT:PSS (WPD) electrodes covered with a commercially available fluorinated polymer (CYTOP), WPU and polyethylenimine (PEI) on a polyimide (PI) substrate to measure human electrocardiography (ECG) and electromyography (EMG). Due to the doubled cover of CYTOP on the electrode structure, a powerful waterproof characteristic was realized on the ECG and EMG electrodes. The waterproof dry electrode sensed biosignals without deterioration over 2 weeks. Moreover, the material constituting the dry electrode had an excellent eco-friendly degradable characteristic to minimize the production of electronic waste. Our proposed PEDOT:PSS-based dry electrode demonstrated a stable ECG and EMG signal recording wirelessly with real-time monitoring.

## 2. Materials and Methods

The PI substrate that acted as a framework to form the proposed electrode was cut to a certain size (2 cm × 2 cm). The standardized PI substrate was sonicated in acetone and isopropyl alcohol (IPA) for 10 min sequentially and then dried with nitrogen gas (99.99%).

After all the residue was removed in an oven at 95 °C for 5 min, the CYTOP solution was diluted 1:5 by CYTOP solvent (CT-SOLV180) and stirred for 6 h. The CYTOP solution with 0.5 mL was coated on the standardized PI substrate at 3000 rpm for 30 s and then annealed with a hotplate at 100 °C for 20 min, and 150 °C for 1 h sequentially in order to remove the CYTOP solvent. A total of 0.5 mL of the PEI solution (Sigma-Aldrich, St Louis, MO, USA) was coated at 3000 rpm for 30 s in the opposite layer of the PI substrate, in which the CYTOP was not coated to form an adhesion layer for selective molding and firm fixation of the PWE solution. The PWE solution was prepared by mixing a PEDOT:PSS solution (Heraeus, Hanau, Germany), WPU (Sigma-Aldrich, St Louis, MO, USA) and ethylene glycol (Sigma-Aldrich, St Louis, MO, USA) overnight (mixing ratio, 6:1:2). The WPU solution was prepared by stirring overnight at a ratio of 10:1, using deionized water as a solvent. The prepared PWE solution was drop-cast on the coated PEI layer and then, a 110 °C annealing process was performed in an oven. The drop-casting process of the PWE solution and annealing process using the oven was repeated 4 times (total of 2500 mL: 500 mL, 500 mL, 750 mL, 750 mL).

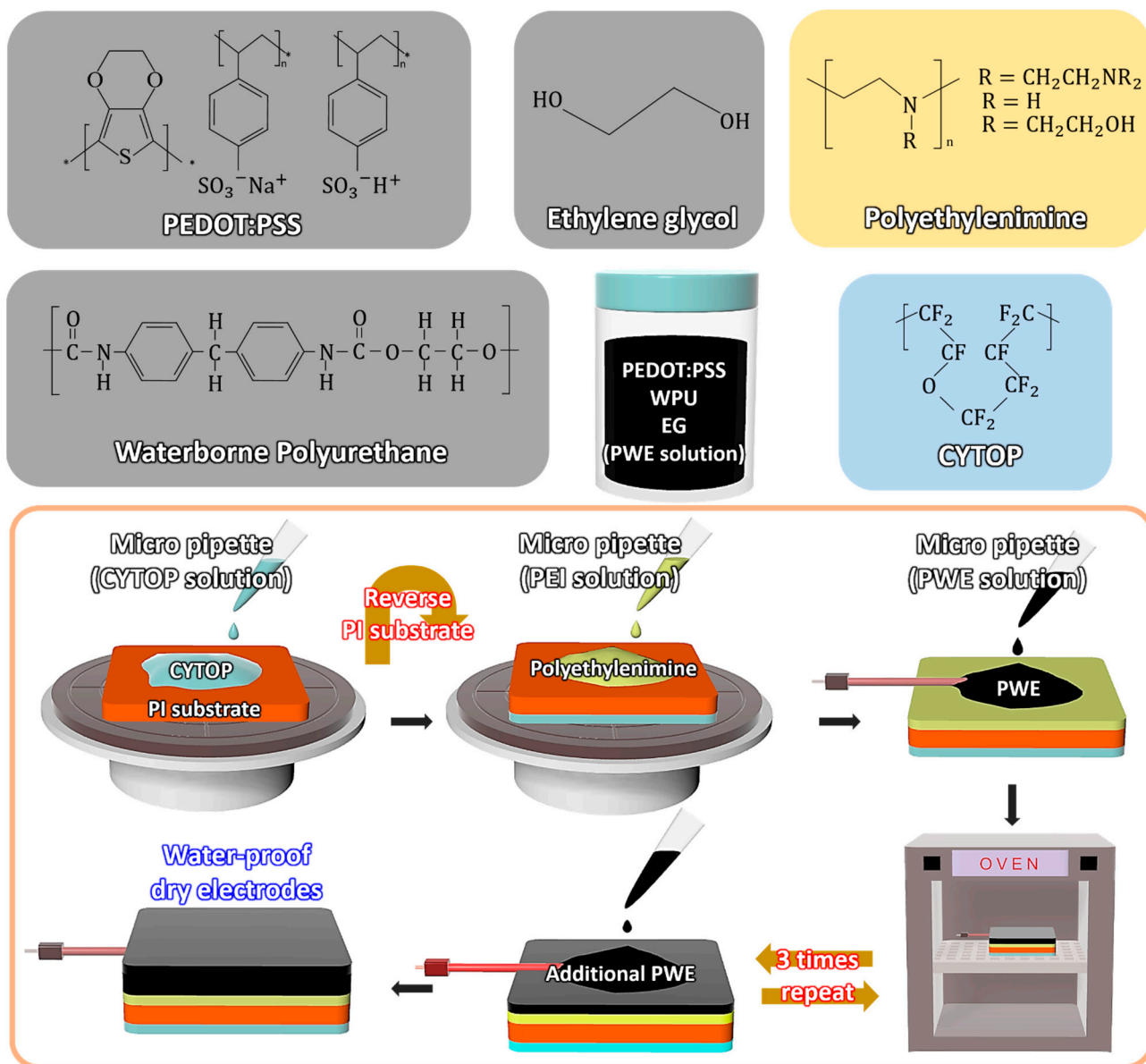
To investigate the chemical structure and the change in the energy level of WPD electrodes, the X-ray photoelectron spectroscopy (XPS) and ultraviolet photoelectron spectroscopy (UPS, AXIS Supra, Kratos, Manchester, UK) measurements were performed and using a monochromatic Al K $\alpha$  ( $h\nu = 1486.6$  eV) source. The morphological properties of the WPD electrodes were characterized by scanning electron microscopy (SEM, S-4700, Hitachi, Tokyo, Japan) and atomic force microscopy (AFM, Park NX10, Park systems, Suwon, South Korea). The image size of AFM was 10  $\mu\text{m} \times 10 \mu\text{m}$ , and the resolution was 0.05 nm. The surface energy was investigated by contact angle measurements (DSA100, KRUSS, Hamburg, Germany) and calculated with KRUSS advanced software.

### 3. Results and Discussion

Figure 1 shows the fabrication process of the proposed waterproof dry electrode and the chemical structures of the materials. The proposed electrode which detects the human biopotential signals such as ECG and EMG was composed of three polymers: PEDOT:PSS [30,31], WPU [32,33] and EG [34]. PEDOT:PSS is a polymer with high conductivity and was used as the main active material of the proposed electrode. In addition, PEDOT:PSS, which has high transmittance in visible light regions and solution processability, has attracted attention in fields such as wearable devices, transparent electrodes and solar cells. However, PEDOT:PSS film is not suitable for reliable contact with moving human skin due to its relatively low physical durability and flexibility. The added WPU provides elasticity and flexibility characteristics to PEDOT:PSS films to minimize the damage to the electrode due to the movement of the human body. In addition, EG provides additional conductivity to the PEDOT:PSS films, allowing the WPD electrode to reliably detect ECG and EMG biopotential signals. The PEI plays the role of the adhesive layer between the blended polymer electrode solution and the PI substrate. Moreover, the hydrophobic CYTOP layer coated on the PI substrate protects the WPD electrode from external liquids. The PI substrate acts as the framework for the WPD electrode and leaves an additional waterproof effect. A detailed description of the fabrication process of the waterproof dry electrode is presented in the Section 2.

The position of the WPD electrodes attached to the human body for detecting the ECG and EMG biopotential signals and the shape of the waveform are shown in the 3D illustration (Figure 2a,b). There were two-electrode and three-electrode systems for detecting ECG and EMG biopotential signals, respectively. The two-electrode system was composed of positive and negative electrodes, whereas the three-electrode system added a reference electrode to set the biopotential standard. It is noted that a blue-wired electrode indicates positive and negative electrodes, while a yellow electrode indicates a reference electrode. Figure 2c and d show the front side and back side photography of the fabricated WPD electrode, respectively. In addition, the WPD electrode with flexible and elastic

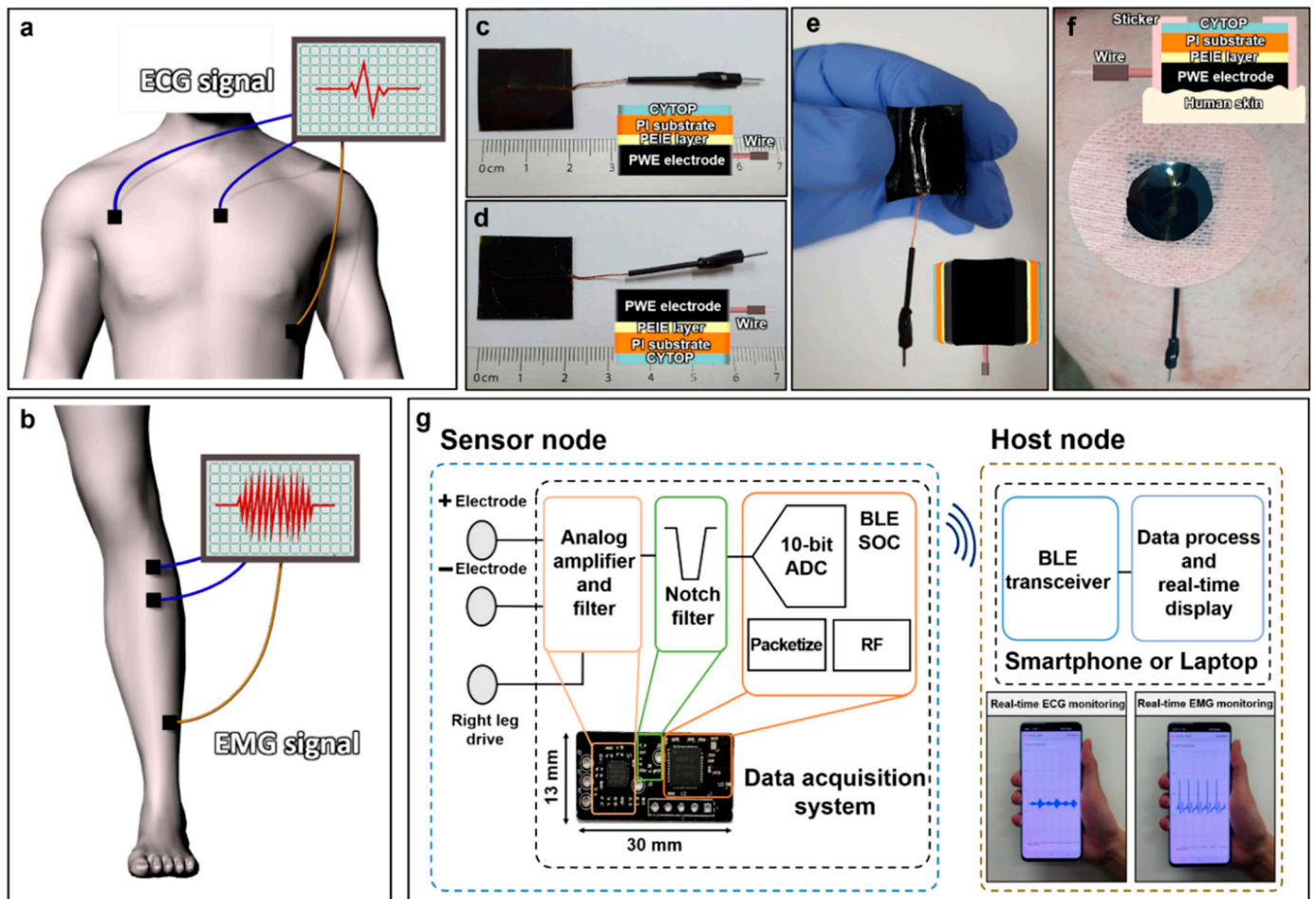
characteristics by the PI substrate is shown (Figure 2e). Figure 2f shows the WPD electrode was attached to real human skin using a medical sticker to detect the biopotential signals.



**Figure 1.** The 3D illustration of the waterproof dry-type PEDOT:PSS (WPD) electrode fabrication process and chemical structure of constituent materials.

Figure 2g is a block diagram of a real-time monitoring system to obtain ECG and EMG biopotential signals. The system was divided into two sub-systems: the sensor node and the host node. In the sensor node, there was a 180 kΩ resistor placed between the WPD electrode and the amplifier to ensure that the current flow never exceeded 10 μA. The analog amplifier and filter block conditioned the biosignal acquired from the WPD electrode with a voltage gain of 60 dB (AD8232, Analog Devices). An instrumentation amplifier initially amplified the signal from the WPD electrodes and attenuated common-mode signals. An active filter conditioned the signal with a second-order high-pass and a low-pass active filter to eliminate unnecessary motion artifacts and high-frequency noise. The active filter was designed with a passband from 0.34 Hz to 41 Hz and 40.17 Hz to 727 Hz for ECG and EMG, respectively. A right leg drive circuit was used to further improve the common-mode rejection. To eliminate powerline noise caused by general consumer electronics, a Twin-T

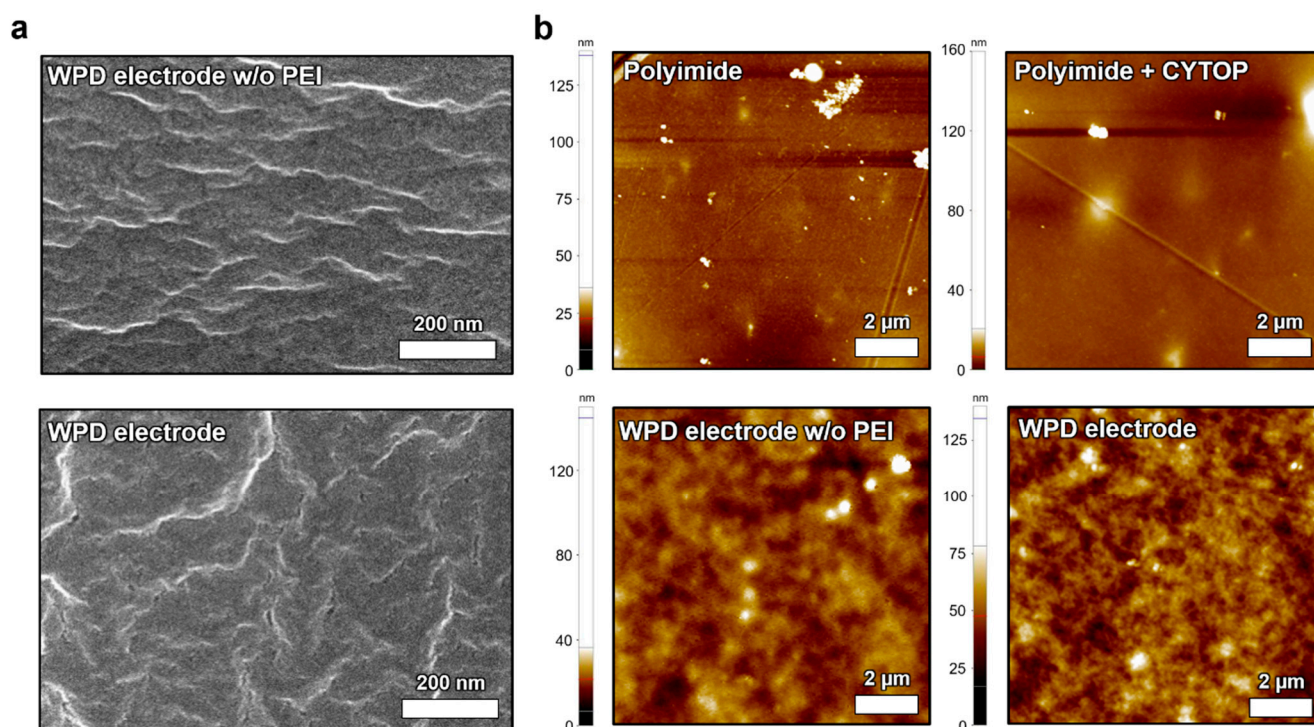
notch filter block was implemented. The biosignals were then sampled at 12 bits with a sampling rate of 7 kSps using the Analog-to-Digital Converter (ADC) embedded in the Bluetooth low-energy system-on-chips (BLE SoC, nRF52832, Nordic Semiconductor). The sampled data were collected in a buffer and transmitted from a burst mode to the host node every 24 ms. This sensor node sub-system was manufactured in a printed circuit board (PCB) with a size of 13 mm x 30 mm. The wirelessly transmitted data were received by the host node, which could either be a smartphone or a personal computer, where the data were displayed in real time by a custom-made software application.



**Figure 2.** The ECG and EMG biopotential signal detecting system, and the wireless real-time monitoring system. The 3D illustration of 2-electrode systems and 3-electrode systems for detecting human ECG and EMG biopotential signals. Blue electrode: positive and negative electrodes, yellow electrode: reference electrode. (a) The position of WPD electrodes attached to a human chest to detect the ECG biopotential signals; (b) the position of WPD electrodes attached to a human right leg to detect the EMG biopotential signals; the photography of the fabricated WPD electrodes; (c) the front side of the WPD electrodes; (d) the back side of the WPD electrodes; (e) the flexibility of the WPD electrodes; (f) the WPD electrodes attached to a real human body; (g) the block diagram of a real-time monitoring system.

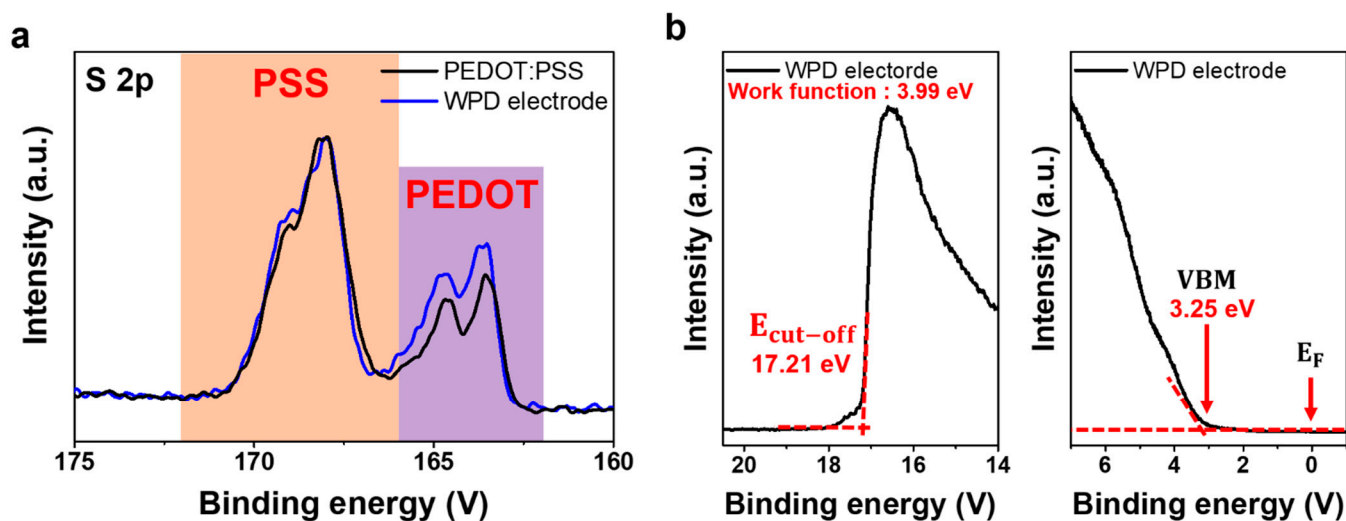
SEM measurement was used for the analysis of WPD electrodes (Figure 3a). SEM images of the WPD electrode layer without PEI and the WPD electrode layer were captured. The wrinkles were observed on the surfaces of both dry electrodes fabricated using the drop-casting process. AFM measurement was conducted to analyze the surface properties of the proposed WPD electrode layer with or without the PEI layer and, additionally, the presence or absence of CYTOP on the PI substrate was confirmed (Figure 3b). The

roughness of the PI substrate and the PI substrate on CYTOP was 6.96 nm and 7.13 nm, respectively. In addition, the roughness of the WPD electrode layer without PEI was 7.45 nm, whereas it increased to 15.44 nm when the PEI layer was added. The surface was not smooth, due to the two types of WPD electrodes produced via drop-casting. Lastly, the presence of the PEI layer increased the contact surface area with human skin with additional roughness, allowing for stable ECG and EMG biopotential signal detection [35].



**Figure 3.** The morphological analysis of the WPD electrodes. The SEM surface image of (a) the WPD electrode layer without PEI and WPD electrode layer; the AFM surface image of (b) the PI substrate, CYTOP coated PI substrate, WPD electrode layer without PEI and WPD electrode layer.

XPS was performed to shed light on the chemical structure of the WPD electrodes. Figure 4a shows the S 2p spectra of PEDOT:PSS and WPD electrodes. The PEDOT chain peak occurred in the range of binding energy of 162 to 166 eV and the PSS chain peak occurred in the range of binding energy of 166 to 172 eV (Figure 4b) [36,37]. The PEDOT chain peak intensity of WPD increased more than PEDOT:PSS, which indicated an improvement in conductivity [38]. Sheet resistance measurement was performed to investigate the conductivity of PEDOT:PSS and WPD electrodes (Supplementary Figure S1). The measured sheet resistance of PEDOT:PSS and WPD electrodes was equal to 10.67  $\Omega$  and 1.158  $\Omega$ , respectively. The sheet resistance of the WPD electrode was improved by EG. The EG enhanced the conductivity of PEDOT:PSS by removing the insulating PSS chains from PEDOT:PSS. Figure 4b shows the UPS spectra of the WPD electrode with the optimized composition ratio. The valence band maximum (VBM) and the cut-off of the WPD electrode were plotted as 17.21 eV and 3.25 eV, respectively. As a result, the WPD electrode had a work function of 3.99 eV, which was reduced by 0.85 eV, compared to the work function of the pure PEDOT:PSS of 4.84 eV (Supplementary Figure S2). The optical bandgaps of PEDOT:PSS and WPD electrodes were calculated using the Tauc plot method (Supplementary Figure S3). The optical bandgaps of the WPD electrode and the PEDOT:PSS electrode were 5.13 eV and 5.12 eV, respectively. The 0.01 eV energy bandgap change between the PEDOT:PSS electrode and the WPD electrode was negligible. When WPU and EG were added to PEDOT:PSS to fabricate WPD electrodes, the Fermi level increased by 0.85 eV, while the energy band was maintained unchanged.

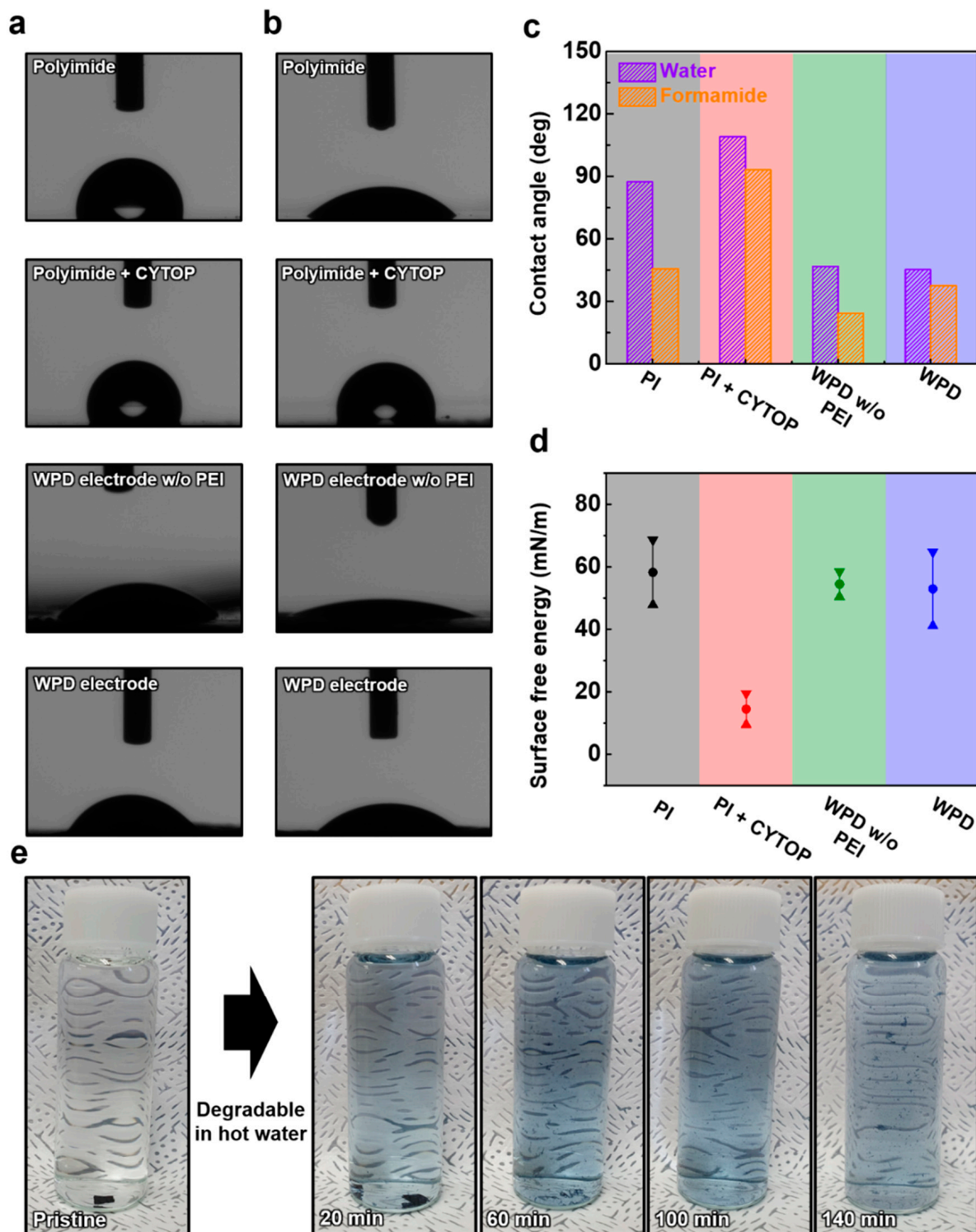


**Figure 4.** (a) The XPS analysis of the PEDOT:PSS and the WPD electrode; (b) the UPS analysis of the optimized WPD electrode.

The contact angle analysis was performed for the hydrophobic characteristics of a CYTOP-coated PI substrate and the investigation of the surface energy with the WPD electrode layer. The deionized water (DI water) and formamide were used to measure the contact angle and surface energy (Figure 5a,b). Figure 5c shows the histogram graph of the contact angle with deionized water and formamide. When CYTOP was coated on the PI substrate, the contact angle increased from  $87.35^\circ$  to  $109.09^\circ$  in DI water and also increased from  $45.73^\circ$  to  $93.16^\circ$  in formamide. Additionally, the contact angle characteristics of the WPD electrode without the PEI layer and the WPD electrode were analyzed. The contact angle between the WPD electrode without the PEI layer and the WPD electrode by DI water changed from  $46.86^\circ$  to  $45.22^\circ$ , and the difference of 1.64 degrees was negligible. On the other hand, the contact angle at formamide changed from  $24.37^\circ$  to  $37.47^\circ$ , and the difference was  $13.1^\circ$ . Additionally, the surface energy of four types of samples (PI substrate, CYTOP-coated PI substrate, WPD electrode without PEI layer and WPD electrode) was analyzed. The surface energy of the PI substrate and the CYTOP-coated PI substrate was  $58.22$  mN/m and  $14.49$  mN/m, respectively. On the other hand, the surface energy of the WPD electrode without the PEI layer and the WPD electrode was  $58.53$  mN/m and  $52.96$  mN/m, respectively. As a result, the PI substrate that prevented the physical penetration of external liquids and the CYTOP with strong hydrophobicity prevented the decomposition of the WPD electrode by liquid. [39,40]. To demonstrate the eco-friendly disposal of the proposed WPD electrodes, a degradability test was performed. Figure 5e shows photography of the WPD electrode immersed in DI water at  $60^\circ\text{C}$ . The WPD electrode that was ultrasonicated had totally degraded, leaving tiny fragments after 140 min. This shows that PEDOT, WPU and EG composing the WPD electrode all have the characteristics of being degradable by water, and that degradability proceeds easily with external stimuli.

Additionally, degradability tests of the WPD electrodes immersed in cold water were performed (Supplementary Figure S4). The WPD electrodes immersed in cold water ( $22^\circ\text{C}$ ) were degradable in 600 min, with the exception of small fragments. The degradable rate of WPD electrodes in cold water was about 460 min slower than in hot water. The observed result indicates that hot water at  $60^\circ\text{C}$  activates the chemical reaction of the WPD electrode, causing it to degrade quicker [41].

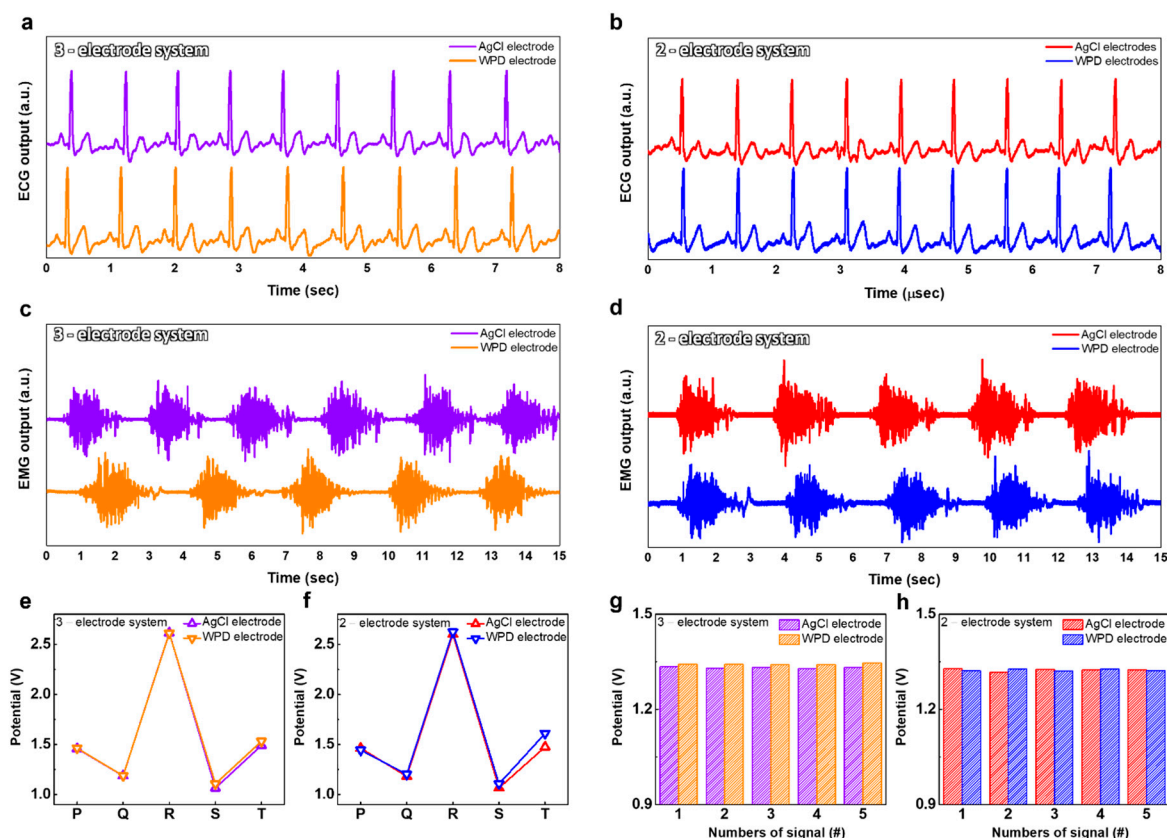




**Figure 5.** The analysis of contact angle. (a) The image of contact angle with deionized water; (b) the image of contact angle with formamide; (c) the histogram graph of contact angle with deionized water and formamide; (d) the graph of surface energy; (e) photography of degraded the WPD electrode over time.

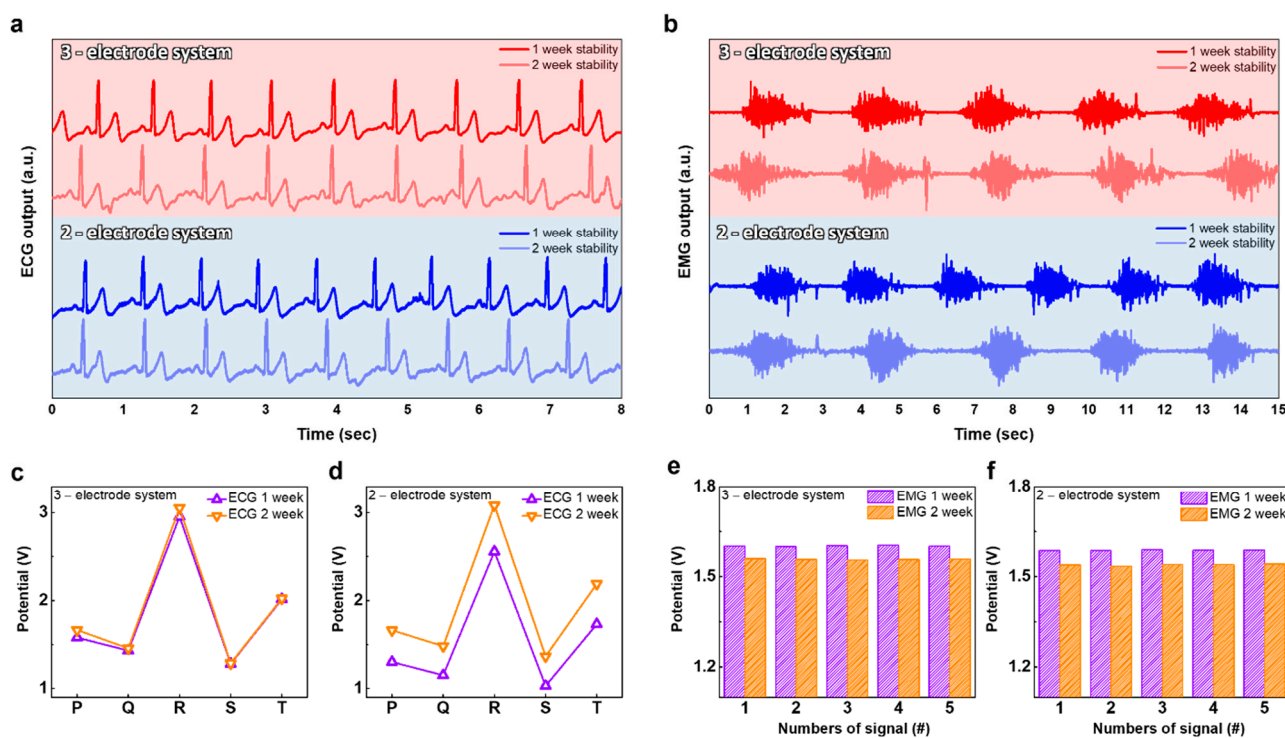
The ECG and EMG biopotential signals were confirmed using the proposed WPD electrode. The ECG and EMG biopotential signals were received from the chest and left leg, respectively. Additionally, the medical sticker was used to immobilize the electrodes with human skin. We compared it with a commercial AgCl-based electrode to prove the

superiority of the WPD electrode in the detection of ECG and EMG biopotential signals. The ECG and EMG biopotential signals were measured using both the three-electrode system and the two-electrode system (Figure 6a–d). The ECG biopotential signal measured with the WPD electrodes clearly defined the peaks of the PQRST. The ECG could be identified by the repetitive P wave, QRS complex and T wave. The P wave and QRS complex were generated by atrial depolarization and ventricular depolarization, respectively. In addition, the T wave was caused by the repolarization of the ventricles. [42] Additionally, the EMG biopotential signals, which represent the movement of human muscle, were defined and gathered using the miniaturized monitoring system. In addition, we also plotted the PQRST peak of the ECG waveform measured with the WPD electrodes, compared to a commercial AgCl-based electrode used to investigate the ability to discriminate the waveform of the ECG measured (Figure 6e,f). In the three-electrode system, the change in the PQRST biopotential signal of ECG detected with WPD electrodes averaged 16 mV. In addition, the biopotential of the T peak, detected with the two-electrode system using the WPD electrode, was measured to be more than 130 mV higher than the commercial AgCl-based electrode, which proves that the ECG biopotential signals are measured more clearly with the WPD electrode. Figure 6f,g show the quantified EMG biopotential signals that plotted the five waveforms. The EMG biopotential signal change in the three-electrode system was measured to 10 mV, whereas the two-electrode system was measured to 6 mV. As a result, the WPD electrode and the commercial AgCl-based electrode show similar capabilities for detecting ECG and EMG biopotential signals. Note that the voltage readings were based on the amplification and filtering process of the sensor node.



**Figure 6.** The biopotential signals of ECG and EMG with the WPD electrodes and commercial AgCl-based electrodes. (a) The ECG biopotential signals in 3-electrode system; (b) the ECG biopotential signals in 2-electrode system; (c) the EMG biopotential signals in 3-electrode system; (d) the EMG biopotential signals in 2-electrode system; (e) the PQRST peak in 3-electrode system; (f) the PQRST peak in 2-electrode system; (g) the quantified EMG biopotential signals in 3-electrode system; (h) The quantified EMG biopotential signals in 2-electrode system.

Next, we investigated the proposed electrode's robustness by reusing the same WPD electrode for 2 weeks. The ECG and EMG biopotential signal measurements were performed utilizing reused WPD electrodes at 1-week intervals (Figure 7a,b). The ECG and EMG biopotential signals were clearly detected by the reused WPD electrodes. As a result, the WPD electrode showed superior performance in detecting ECG and EMG biosignals over two weeks. We also plotted the PQRST peaks of the ECG biopotential signal detected with the reused WPD electrodes at 1-week intervals (Figure 7c,d). The ECG biopotential detected by the two-electrode system presented a 101 mV insignificant difference biopotential at the R peak. On the other hand, in the ECG biopotential signals measured with the three-electrode system, the peak intensity differed by an average of 402 mV. The plotted EMG biopotential signal intensity decreased as the number of reuses of the WPD electrode increased (Figure 7e,f). The EMG averaged biopotential signals measured with the two-electrode system and the three-electrode system had a difference of 44 mV and 47 mV, respectively. Again, the biopotential readings were obtained from the sensor node described in Figure 2.



**Figure 7.** The robustness of the WPD electrodes. (a) Repeatability tests for 2 weeks with the WPD electrode for ECG biopotential signals; (b) repeatability tests for 2 weeks with the WPD electrode for EMG biopotential signals; the biopotential signal detected for 2 weeks at intervals of 1 week; (c) the PQRST peak in 3-electrode system; (d) the PQRST peak in 2-electrode system; (e) the quantified EMG biopotential signals in 3-electrode system; (f) the quantified EMG biopotential signals in 2-electrode system.

#### 4. Conclusions

In summary, we presented waterproof dry-type PEDOT:PSS (WPD) ECG and EMG electrodes protected from external liquid using a double layer of a polyimide (PI) substrate and fluorinated polymer CYTOP. The morphological characteristics and chemical composition ratios of WPD electrodes were investigated through XPS, UPS, SEM and AFM analysis. Additionally, the waterproofing effect of the PI substrate and CYTOP layer was verified using the contact angle analysis. The WPU and EG improved the flexibility and additional conductivity characteristics in the proposed WPD electrodes, respectively. The WPD electrode clearly detected ECG and EMG biopotential signals using the two-electrode

system and the three-electrode system. In addition, the WPD electrode and the commercial AgCl-based wet electrodes showed similar performances in detecting ECG and EMG biopotential signals. The proposed WPD electrode verified the robustness of the electrode by detecting ECG and EMG biopotential signals for 2 weeks. Our study can be applied to dry biopotential electrodes research regarding the reliable detection of biosignals in an external humid atmosphere.

**Supplementary Materials:** The following supporting information can be downloaded at: <https://www.mdpi.com/article/10.3390/coatings11030274/s1>, Supplementary Figure S1: Sheet resistance of PEDOT:PSS electrode and the proposed WPD electrode. Supplementary Figure S2: The UPS analysis of the PEDOT:PSS. Supplementary Figure S3: Optical bandgap of the PEDOT:PSS electrode and the proposed WPD electrode shown in the Tauc plot method. Supplementary Figure S4: Photography of WPD electrode degradable performance over time immersed in cold water.

**Author Contributions:** Conceptualization, D.H.L., E.K.L., C.H.K., Y.-J.K. and H.Y.; methodology, D.H.L. and C.H.K.; validation, D.H.L. and C.H.K.; formal analysis, D.H.L., C.H.K., H.J.Y. and Y.-J.K.; investigation, D.H.L., E.K.L., C.H.K., H.J.Y., Y.-J.K. and H.Y.; writing—original draft preparation, D.H.L., E.K.L. and C.H.K.; writing—review and editing, E.K.L., Y.-J.K. and H.Y.; supervision, Y.-J.K., and H.Y.; funding acquisition, Y.-J.K., and H.Y. All authors have read and agreed to the published version of the manuscript.

**Funding:** This research was supported by the National Research Foundation of Korea (NRF) grant funded by the Korean Government (MSIT) (NRF-2020M3A9E4104385) and a Research Grant of Pukyong National University (2022) in 202203500001.

**Institutional Review Board Statement:** The study was conducted in accordance with the Declaration of Helsinki and approved by the Institutional Review Board (or Ethics Committee) of Gachon University (protocol code 1044396-202109-HR-205-01).

**Informed Consent Statement:** Informed consent was obtained from all subjects involved in the study.

**Acknowledgments:** Human EMG and ECG measurements were performed according to the experimental regulations approved by Institutional Review Board Committee of Gachon University (IRB No. 1044396-202109-HR-205-01). The volunteers obtained informed consent prior to the experiment and complied with the research regulations.

**Conflicts of Interest:** The authors declare no conflict of interest.

## References

- Polk, B.J.; Stelzenmuller, A.; Mijares, G.; MacCrehan, W.; Gaitan, M. Ag/AgCl microelectrodes with improved stability for microfluidics. *Sens. Actuators B Chem.* **2006**, *114*, 239–247. [\[CrossRef\]](#)
- East, G.A.; Del Valle, M.A. Easy-to-make Ag/AgCl reference electrode. *J. Chem. Educ.* **2000**, *77*, 97. [\[CrossRef\]](#)
- Fernandez, M.; Pallas-Areny, R. Ag-AgCl electrode noise in high-resolution ECG measurements. *Biomed. Instrum. Technol.* **2000**, *34*, 125–130.
- Zhou, W.; Song, R.; Pan, X.; Peng, Y.; Qi, X.; Peng, J.; Hui, K.S.; Hui, K.N. Fabrication and impedance measurement of novel metal dry bioelectrode. *Sens. Actuators A Phys.* **2013**, *201*, 127–133. [\[CrossRef\]](#)
- Meng, Y.; Li, Z.B.; Chen, X.; Chen, J.P. A flexible dry micro-dome electrode for ECG monitoring. *Microsyst. Technol.* **2015**, *21*, 1241–1248. [\[CrossRef\]](#)
- Shahandashti, P.F.; Pourkheyrollah, H.; Jahanshahi, A.; Ghafoorifard, H. Highly conformable stretchable dry electrodes based on inexpensive flex substrate for long-term biopotential (EMG/ECG) monitoring. *Sens. Actuators A Phys.* **2019**, *295*, 678–686. [\[CrossRef\]](#)
- Lee, S.; Yoon, J.; Lee, D.; Seong, D.; Lee, S.; Jang, M.; Choi, J.; Yu, K.J.; Kim, J.; Lee, S. Wireless epidermal electromyogram sensing system. *Electronics* **2020**, *9*, 269. [\[CrossRef\]](#)
- Chlaihawi, A.A.; Narakathu, B.B.; Emamian, S.; Bazuin, B.J.; Atashbar, M.Z. Development of printed and flexible dry ECG electrodes. *Sens. Bio-Sens. Res.* **2018**, *20*, 9–15. [\[CrossRef\]](#)
- Jung, H.-C.; Moon, J.-H.; Baek, D.-H.; Lee, J.-H.; Choi, Y.-Y.; Hong, J.-S.; Lee, S.-H. CNT/PDMS composite flexible dry electrodes for long-term ECG monitoring. *IEEE Trans. Biomed. Eng.* **2012**, *59*, 1472–1479. [\[CrossRef\]](#)
- Bansal, M.; Gandhi, B. IoT Based Smart Health Care System Using CNT Electrodes (for Continuous ECG Monitoring). In Proceedings of the 2017 International Conference on Computing, Communication and Automation (ICCCA), Greater Noida, India, 5–6 May 2017; pp. 1324–1329.

11. Lee, J.H.; Nam, Y.W.; Jung, H.-C.; Baek, D.-H.; Lee, S.-H.; Hong, J.S. Shear induced CNT/PDMS conducting thin film for electrode cardiogram (ECG) electrode. *BioChip J.* **2012**, *6*, 91–98. [[CrossRef](#)]
12. La, T.; Qiu, S.; Scott, D.K.; Bakhtiari, R.; Kuziek, J.W.P.; Mathewson, K.E.; Rieger, J.; Chung, H. Two-layered and stretchable e-textile patches for wearable healthcare electronics. *Adv. Healthc. Mater.* **2018**, *7*, 1801033. [[CrossRef](#)]
13. Yapici, M.K.; Alkhidir, T.; Samad, Y.A.; Liao, K. Graphene-clad textile electrodes for electrocardiogram monitoring. *Sens. Actuators B Chem.* **2015**, *221*, 1469–1474. [[CrossRef](#)]
14. Lou, C.; Li, R.; Li, Z.; Liang, T.; Wei, Z.; Run, M.; Yan, X.; Liu, X. Flexible graphene electrodes for prolonged dynamic ECG monitoring. *Sensors* **2016**, *16*, 1833. [[CrossRef](#)]
15. Kabiri Ameri, S.; Ho, R.; Jang, H.; Tao, L.; Wang, Y.; Wang, L.; Schnyer, D.M.; Akinwande, D.; Lu, N. Graphene electronic tattoo sensors. *ACS Nano* **2017**, *11*, 7634–7641. [[CrossRef](#)]
16. Das, P.S.; Hossain, M.F.; Park, J.Y. Chemically reduced graphene oxide-based dry electrodes as touch sensor for electrocardiograph measurement. *Microelectron. Eng.* **2017**, *180*, 45–51. [[CrossRef](#)]
17. Karim, N.; Afroj, S.; Malandraki, A.; Butterworth, S.; Beach, C.; Rigout, M.; Novoselov, K.S.; Casson, A.J.; Yeates, S.G. All inkjet-printed graphene-based conductive patterns for wearable e-textile applications. *J. Mater. Chem. C* **2017**, *5*, 11640–11648. [[CrossRef](#)]
18. Lee, Y.; Kang, H.; Gwon, S.H.; Choi, G.M.; Lim, S.; Sun, J.; Joo, Y. A strain-insensitive stretchable electronic conductor: PEDOT: PSS/acrylamide organogels. *Adv. Mater.* **2016**, *28*, 1636–1643. [[CrossRef](#)]
19. Stauffer, F.; Thielen, M.; Sauter, C.; Chardonens, S.; Bachmann, S.; Tybrandt, K.; Peters, C.; Hierold, C.; Vörös, J. Skin conformal polymer electrodes for clinical ECG and EEG recordings. *Adv. Healthc. Mater.* **2018**, *7*, 1700994. [[CrossRef](#)]
20. Zhang, L.; Kumar, K.S.; He, H.; Cai, C.J.; He, X.; Gao, H.; Yue, S.; Li, C.; Seet, R.C.-S.; Ren, H. Fully organic compliant dry electrodes self-adhesive to skin for long-term motion-robust epidermal biopotential monitoring. *Nat. Commun.* **2020**, *11*, 4683. [[CrossRef](#)]
21. Park, M.; Park, Y.J.; Chen, X.; Park, Y.; Kim, M.; Ahn, J. MoS<sub>2</sub>-based tactile sensor for electronic skin applications. *Adv. Mater.* **2016**, *28*, 2556–2562. [[CrossRef](#)]
22. Tseghai, G.B.; Mengistie, D.A.; Malengier, B.; Fante, K.A.; Van Langenhove, L. PEDOT: PSS-based conductive textiles and their applications. *Sensors* **2020**, *20*, 1881. [[CrossRef](#)] [[PubMed](#)]
23. Ouyang, J. “Secondary doping” methods to significantly enhance the conductivity of PEDOT: PSS for its application as transparent electrode of optoelectronic devices. *Displays* **2013**, *34*, 423–436. [[CrossRef](#)]
24. Hu, L.; Song, J.; Yin, X.; Su, Z.; Li, Z. Research progress on polymer solar cells based on PEDOT: PSS electrodes. *Polymers* **2020**, *12*, 145. [[CrossRef](#)]
25. Döbbelin, M.; Marcilla, R.; Salsamendi, M.; Pozo-Gonzalo, C.; Carrasco, P.M.; Pomposo, J.A.; Mecerreyes, D. Influence of ionic liquids on the electrical conductivity and morphology of PEDOT: PSS films. *Chem. Mater.* **2007**, *19*, 2147–2149. [[CrossRef](#)]
26. Ahmad, Z.; Azman, A.W.; Buys, Y.F.; Sarifuddin, N. Mechanisms for doped PEDOT: PSS electrical conductivity improvement. *Mater. Adv.* **2021**, *2*, 7118–7138.
27. Zhu, Z.; Liu, C.; Shi, H.; Jiang, Q.; Xu, J.; Jiang, F.; Xiong, J.; Liu, E. An effective approach to enhanced thermoelectric properties of PEDOT: PSS films by a DES post-treatment. *J. Polym. Sci. Part B Polym. Phys.* **2015**, *53*, 885–892. [[CrossRef](#)]
28. Prathish, K.P.; Carvalho, R.C.; Brett, C.M.A. Highly sensitive poly (3, 4-ethylenedioxythiophene) modified electrodes by electropolymerisation in deep eutectic solvents. *Electrochem. Commun.* **2014**, *44*, 8–11. [[CrossRef](#)]
29. Seyedin, M.Z.; Razal, J.M.; Innis, P.C.; Wallace, G.G. Strain-responsive polyurethane/PEDOT: PSS elastomeric composite fibers with high electrical conductivity. *Adv. Funct. Mater.* **2014**, *24*, 2957–2966. [[CrossRef](#)]
30. Shi, H.; Liu, C.; Jiang, Q.; Xu, J. Effective approaches to improve the electrical conductivity of PEDOT: PSS: A review. *Adv. Electron. Mater.* **2015**, *1*, 1500017. [[CrossRef](#)]
31. Kayser, L.V.; Lipomi, D.J. Stretchable conductive polymers and composites based on PEDOT and PEDOT: PSS. *Adv. Mater.* **2019**, *31*, 1806133. [[CrossRef](#)]
32. Li, P.; Du, D.; Guo, L.; Guo, Y.; Ouyang, J. Stretchable and conductive polymer films for high-performance electromagnetic interference shielding. *J. Mater. Chem. C* **2016**, *4*, 6525–6532. [[CrossRef](#)]
33. Yu, F.; Xu, X.; Lin, N.; Liu, X.Y. Structural engineering of waterborne polyurethane for high performance waterproof coatings. *RSC Adv.* **2015**, *5*, 72544–72552. [[CrossRef](#)]
34. Bohne, D.; Fischer, S.; Obermeier, E. Thermal, conductivity, density, viscosity, and Prandtl-numbers of ethylene glycol-water mixtures. *Ber. Bunsenges. Phys. Chem.* **1984**, *88*, 739–742. [[CrossRef](#)]
35. Yun, I.; Jeung, J.; Lim, H.; Kang, J.; Lee, S.; Park, S.; Seong, S.; Park, S.; Cho, K.; Chung, Y. Stable bioelectric signal acquisition using an enlarged surface-area flexible skin electrode. *ACS Appl. Electron. Mater.* **2021**, *3*, 1842–1851. [[CrossRef](#)]
36. Zhang, W.; Zhao, B.; He, Z.; Zhao, X.; Wang, H.; Yang, S.; Wu, H.; Cao, Y. High-efficiency ITO-free polymer solar cells using highly conductive PEDOT: PSS/surfactant bilayer transparent anodes. *Energy Environ. Sci.* **2013**, *6*, 1956–1964. [[CrossRef](#)]
37. Rafique, S.; Roslan, N.A.; Abdullah, S.M.; Li, L.; Supangat, A.; Jilani, A.; Iwamoto, M. UV-ozone treated graphene oxide/PEDOT: PSS bilayer as a novel hole transport layer in highly efficient and stable organic solar cells. *Org. Electron.* **2019**, *66*, 32–42. [[CrossRef](#)]
38. Mengistie, D.A.; Wang, P.-C.; Chu, C.-W. Effect of molecular weight of additives on the conductivity of PEDOT: PSS and efficiency for ITO-free organic solar cells. *J. Mater. Chem. A* **2013**, *1*, 9907–9915. [[CrossRef](#)]

39. Walser, M.P.; Kalb, W.L.; Mathis, T.; Brenner, T.J.; Batlogg, B. Stable complementary inverters with organic field-effect transistors on Cytop fluoropolymer gate dielectric. *Appl. Phys. Lett.* **2009**, *94*, 36. [[CrossRef](#)]
40. Chae, J.B.; Kwon, J.O.; Yang, J.S.; Kim, D.; Rhee, K.; Chung, S.K. Optimum thickness of hydrophobic layer for operating voltage reduction in EWOD systems. *Sens. Actuators A Phys.* **2014**, *215*, 8–16. [[CrossRef](#)]
41. Mofokeng, J.P.; Luyt, A.S. Morphology and thermal degradation studies of melt-mixed poly (lactic acid)(PLA)/poly ( $\epsilon$ -caprolactone)(PCL) biodegradable polymer blend nanocomposites with TiO<sub>2</sub> as filler. *Polym. Test.* **2015**, *45*, 93–100. [[CrossRef](#)]
42. Hurst, J.W. Naming of the waves in the ECG, with a brief account of their genesis. *Circulation* **1998**, *98*, 1937–1942. [[CrossRef](#)]



## Article

# Biodegradable Nonwovens with Poultry Feather Addition as a Method for Recycling and Waste Management

Jagoda Jóźwik-Pruska \*, Krystyna Wrześniewska-Tosik, Tomasz Mik, Ewa Wesołowska, Tomasz Kowalewski, Michalina Pałczyńska, Damian Walisiak and Magdalena Szalczyńska

Łódź Institute of Technology, Łukasiewicz Research Network, 90-570 Lodz, Poland; krystyna.wrzesniewska-tosik@lit.lukasiewicz.gov.pl (K.W.-T.); tomasz.mik@lit.lukasiewicz.gov.pl (T.M.); ewa.wesolowska@lit.lukasiewicz.gov.pl (E.W.); tomasz.kowalewski@lit.lukasiewicz.gov.pl (T.K.); michalina.palczynska@lit.lukasiewicz.gov.pl (M.P.); damian.walisiak@lit.lukasiewicz.gov.pl (D.W.); magdalena.szalczynska@lit.lukasiewicz.gov.pl (M.S.)

\* Correspondence: jagoda.jozwik-pruska@lit.lukasiewicz.gov.pl; Tel.: +48-423070827

**Abstract:** Geotextiles are used for separation, drainage, filtration and anti-erosion protection sealing, as well as to improve plant vegetation conditions. The research objective of this study was to verify the influence of the addition of poultry feathers on accelerating the biodegradation of nonwovens in cultivated soil. The tests were carried out in laboratory conditions and were based on the assessment of weight loss. The experiments confirmed the positive effects of the presence of waste that was rich in keratin on the time required for the biodegradation of the tested materials (the period of biodegradation was 8–24 weeks). Additionally, the influence of the biodegradation of the tested materials on the ecotoxicity was investigated and showed no negative effects on the microbiological activity ( $10^6$  cfu). The research also included the determination of the carbon to nitrogen ratio of the test medium (blank, 12–14:1; with feather addition, 19–20:1). A statistical analysis revealed a correlation between the mechanical properties and the period of biological decomposition. This research was an important step for the management of poultry feather waste in agricultural applications. The tested materials could be seen an alternative that meets all ecological criteria, which seems to be a golden solution that not only allows the delivery of important nutrients to the soil, but also manages waste in an environmentally safe manner.

**Keywords:** biodegradation; keratin; feather; poultry waste; nonwovens

**Citation:** Jóźwik-Pruska, J.; Wrześniewska-Tosik, K.; Mik, T.; Wesołowska, E.; Kowalewski, T.; Pałczyńska, M.; Walisiak, D.; Szalczyńska, M. Biodegradable Nonwovens with Poultry Feather Addition as a Method for Recycling and Waste Management. *Polymers* **2022**, *14*, 2370. <https://doi.org/10.3390/polym14122370>

Academic Editors: José Miguel Ferri, Vicent Fombuena Borràs, Miguel Fernando Aldás Carrasco and Dimitrios Bikiaris

Received: 11 April 2022

Accepted: 7 June 2022

Published: 11 June 2022

**Publisher's Note:** MDPI stays neutral with regard to jurisdictional claims in published maps and institutional affiliations.



**Copyright:** © 2022 by the authors. Licensee MDPI, Basel, Switzerland. This article is an open access article distributed under the terms and conditions of the Creative Commons Attribution (CC BY) license (<https://creativecommons.org/licenses/by/4.0/>).

## 1. Introduction

According to the Organisation for Economic Cooperation and Development (OECD), “biodegradation” is the process of the decomposition of organic substances by microorganisms into simpler substances, such as carbon dioxide, water and ammonia [1,2]. The microorganisms require energy and oxygen, carbon, phosphorous, sulphur, nitrogen, calcium, magnesium and other elements to grow and reproduce. Organic substances are oxidised into carbon dioxide and water through an exothermic process and the obtained energy is partially used by the microorganisms and the rest is lost as heat. The process can be especially observed in composting. Biodegradation can be conducted both under aerobic and anaerobic conditions [3]. Bacteria, fungi, insects, worms and many more organisms participate in the breakdown of various materials. Biodegradation is essential for nature and the whole ecosystem because it provides the opportunity to decrease waste and produce nutrients that are crucial for the growth of new life [4,5]. Recently, biodegradability has become a requirement for materials that are used in everyday life and is one of the essential features for evaluating their sustainability [4].

A wide range of tests can be applied to examine the biodegradability of a product. The choice of method refers to the type and properties of each sample. The biodegradation process is conducted mainly in water, soil and compost environments [6]. The estimation of



biodegradability is mainly based on a calculation of weight loss or by an evaluation of the production of CO<sub>2</sub>. Each method has its own advantages and disadvantages. Estimation on the basis of released CO<sub>2</sub> only relates to the measured and calculated theoretical carbon content of the sample. In the method that is based on the weight loss calculation, there is the risk of losing microscopic parts of the sample. Nevertheless, in our opinion, the second method provides a more complete picture of the degradation process and the behaviour of the sample over time (influence on the structure, surface, disintegration ability, etc.).

Chemical fibres are manufactured for various purposes, including textiles and agriculture. The worldwide production of fibres is growing every year. The literature reports that the global production output of chemical fibre (organic and synthetic) industry has reached 80.9 million metric tons [7]. Synthetic polymers are the most commonly used materials to produce manmade fibres. Due to the fact that they are not biodegradable, their application needs to be limited and products should be reused to a limited extent. The resistance of these materials to biological breakdown is crucial because of environmental pollution. Their build-up in the environment results in the release of toxic pollutants, which then influence living organisms within the soil and water [4].

The importance of fibre-reinforced composites in the manufacture of a wide range of industrial products is still increasing. Special interest is focused on the replacement (full or partial) of synthetic polymers with biopolymers, including keratin. This polymer can be obtained from sheep wool, poultry feathers, horn, nails and many other sources. Its chemical properties allow for the use of keratin as a thermoset material, which can be linked to other polymers [8–11]. Biodegradability, biocompatibility and fire-retardant capability are among the valuable properties of keratin [8].

It should be highlighted that according to the regulations of the European Parliament [12], the promotion of harmonious and sustainable economic growth should be carried out with respect for the natural environment. The modern approach to environmental protection enforces the creation and implementation of new technologies, especially those that contribute to the elimination of pollution at the source.

In a leading company on the Polish market, the amount of waste in the form of feathers is 6 tons per day, which is processed into industrial flour. The European Union (EU) has banned its use in fodder, which has caused a problem with the legitimacy of processing feathers that are a by-product of slaughter into industrial meal.

The processing of keratin-rich feathers allows us to obtain diverse thermoplastic biocomposites and translates into improvements in economic returns for the poultry industry. The composition of feather keratin is based on small protein molecules (molecular weights of 10–30 kDa). Extensive internal bonding results in thermal and mechanical stability [13]. Undeniably, its low cost and natural abundance makes feather keratin a valuable material for the production of biodegradable polymers for various applications [8].

The literature has reported the incorporation of feather keratin in various synthetic polymers, such as polypropylene (PP) and polyethylene (PE) [14,15]. Cheng et al. [16] investigated the possibility of incorporating feather fibres into polylactic acid (PLA). Other researchers combined feathers with polyurethane [11,17].

The biodegradation of fibres starts with changes in their structures or compositions. Chemical changes can be examined by the application of Fourier transform infrared spectroscopy (FTIR) or infrared spectroscopy. Degradation can be also estimated by visual observations and microscopy [4,18]. According to the European Standard EN 14995 Plastics—Evaluation of Compostability—Test scheme and specifications (2009) [19], the biodegradation process of a sample cannot exceed 24 weeks. The progress of decomposition is estimated and calculated on the basis of weight loss. While the biodegradability of various textiles is a desirable feature, sometimes the final product design requires sufficient resistance to degradation in order to provide long-term use [4]. Yet, the safety of use should be examined.

Poultry feathers are a by-product of animal origin, which are obtained during poultry slaughter. There are about 33 plants and 100 slaughterhouses operating within the poultry

industry in Poland, of which Cedrob S.A. is Poland's largest. Cedrob S.A. belongs to the Cedrob Group, which also includes Gobarto S.A. (the leading pig meat producer) and Cedrob Passau GmbH (the Cedrob Group's representative on the German market).

The further processing of feathers into poultry meal is realised by Utilisation Plants, which was used as a protein additive for industrial feeds until 2004. After the introduction of the Regulation of the European Parliament and Council (EC) No. 999/2001, the ban on its use in livestock nutrition has caused a problem with the reasonableness of processing of feathers, among other materials, from slaughter into industrial meal. The only other uses of such meal are possibly as organic fertiliser for field fertilisation or as an addition to incineration in industrial boiler rooms. Both applications have no economic or environmental justification and can cause environmental and health hazards.

In response to the need to manage feather waste, the Team of Keratin Composites from the Łukasiewicz Research Network, Institute of Biopolymers and Chemical Fibres, aimed to develop innovative feather-based nonwovens that are characterised by additional functionalities and advantages, which are derived from the use of feather keratin, such as tailor-made biodegradation that is adjusted to the crop duration, the input of organic nitrogen into the soil, zero waste at their end of life and cost-competitive materials. The nonwovens that are obtained by the needle punching method consist of wool and feather-based keratin fibres and can be used for agricultural applications. This method has now been patented (P.430284 (19 June 2019) "Method for producing fluffy composite nonwoven fabric"). In this context, the main objective of this study was to create a concept for a waste management method for the by-products of animal production that is desirable from the point of view of economics and social effects through the exploitation of underutilised waste, in order to obtain added value raw materials for the agricultural sector, such as feather-based nonwovens. The technology of the designed solution assumes that the share of waste material in the form of feathers is at a level of about 50%.

There are many reasons why developed nonwovens are suitable for agricultural use:

- They are safe for the environment and human health by ensuring a reduction in biomass waste, in the form of feathers, that is deposited and pollutes the environment;
- The developed innovative nonwovens are made of biodegradable raw materials of natural origin;
- We have the ability to control the time of microbial decomposition by adjusting the share of feather fractions in the nonwovens;
- They have high efficiency with low financial outlay (i.e., the market price of the developed products is much lower than that of fossil-based products due to the fact that they are made from waste materials);
- Nonwovens that are made from natural waste resources can be used soil improvement agents because they contain significant amounts of fertilising ingredients within their structure, which can then be used to meet the nutritional needs of crops.

The paper presents the results of the biodegradation of keratin-based nonwoven fabrics in a soil environment and the influence of their mechanical properties on the process. The influence of the composition (feather amount) on the susceptibility of the material to biodegradation was examined and a statistical analysis was performed.

## 2. Materials and Methods

This study was carried out on two groups of protective nonwovens with the addition of keratin fibres in the form of feathers from a poultry slaughterhouse (i.e., Cedrob S.A., Ciechanów, Poland, which is Poland's largest poultry producer).

The technology of the designed solution assumed the share of waste material, in the form of feathers, in the nonwovens to be at the level of about 50%. The percentage content of feathers in the nonwovens was estimated on the basis of a weight study: the difference in weight of the nonwoven containing the feathers and that of the reference nonwoven (without feathers). The first group was composed of Trevira bico "type 256" and the second was of Trevira bico "type 453". Additionally, the reference samples, without

feathers, were examined and were marked as “0”. The nonwovens were designed and intended to cover the grassy-bean mixture on difficult terrains (new dumps, heaps, railway embankments, ski slopes, etc.), on which obtaining a good sodding is very difficult. Table 1 presents the compositions of the samples that were tested. Table 2 presents selected mechanical properties of the materials. The SEM photo-documentation can be found in the Supplementary Material (Table S1).

**Table 1.** The compositions of the tested nonwovens.

Group	Nonwoven	Feather Amount (%)	Wool Amount (%)	Trevira Bico	
				Amount (%)	Type
I	Nonwoven I	0	90	10	256
		38.5	55	6	
	Nonwoven II	0	90	10	
		34.8	58	7	
	Nonwoven III	0	90	10	
		44.4	50	6	
II	DA I/1	30.0	63	7	453
		0	90	10	
	DA I/1 and 2	32.0	61	7	
		0	90	10	
	DA I/2	40	54	6	
		0	90	10	
DA II/2	40.0	54	6		
	0	90	10		

**Table 2.** The mechanical properties of the tested materials ( $\pm$  SD).

Group	Nonwoven	Feather	Base Weight (g/m <sup>2</sup> )	Thickness (mm)	Tensile Strength in the Horizontal Direction (N)	Tensile Strength in the Vertical Direction (N)	Tear Resistance in the Horizontal Direction (N)	Tear Resistance in the Vertical Direction (N)
			EN 29073-1:1994	EN ISO 9073-2:2002	EN 29073-3:1994	EN 29073-3:1994	EN ISO 9073-4:2002	EN ISO 9073-4:2002
I	Wool I	+	78.2 $\pm$ 2.3	1.33 $\pm$ 0.06	1.11 $\pm$ 0.22	2.02 $\pm$ 0.43	1.80 $\pm$ 0.08	1.22 $\pm$ 0.04
		-	48.1 $\pm$ 4.5	1.13 $\pm$ 0.05	1.18 $\pm$ 0.60	2.68 $\pm$ 0.57	2.26 $\pm$ 0.30	1.45 $\pm$ 0.36
	Wool II	+	158.0 $\pm$ 7	2.04 $\pm$ 0.08	3.91 $\pm$ 1.07	10.20 $\pm$ 2.60	5.18 $\pm$ 0.39	4.94 $\pm$ 0.31
		-	103.0 $\pm$ 10.0	1.75 $\pm$ 0.08	4.89 $\pm$ 1.84	7.22 $\pm$ 1.09	5.89 $\pm$ 0.91	3.21 $\pm$ 0.35
	Wool III	+	284.0 $\pm$ 8.0	2.83 $\pm$ 0.18	31.9 $\pm$ 12.1	27.20 $\pm$ 2.20	31.2 $\pm$ 6.3	15.4 $\pm$ 2.2
		-	158.0 $\pm$ 12.0	2.11 $\pm$ 0.07	14.90 $\pm$ 2.40	40.00 $\pm$ 5.1	18.90 $\pm$ 3.20	23.50 $\pm$ 6.1
II	DA I/1	+	103.0 $\pm$ 6	1.62 $\pm$ 0.12	0.36 $\pm$ 0.11	0.70 $\pm$ 0.15	1.06 $\pm$ 0.56	0.52 $\pm$ 0.46
		-	86.0 $\pm$ 4.00	1.76 $\pm$ 0.13	0.58 $\pm$ 0.05	1.14 $\pm$ 0.27	1.43 $\pm$ 0.51	0.65 $\pm$ 0.12
	DA I/1 and 2	+	116.0 $\pm$ 13.0	1.70 $\pm$ 0.14	0.44 $\pm$ 0.05	0.92 $\pm$ 0.16	1.17 $\pm$ 0.36	0.38 $\pm$ 0.20
		-	70.9 $\pm$ 3.80	1.56 $\pm$ 0.12	0.56 $\pm$ 0.10	1.01 $\pm$ 0.21	1.02 $\pm$ 0.30	0.64 $\pm$ 0.57
	DA I/2	+	101.0 $\pm$ 14.0	1.75 $\pm$ 0.15	0.34 $\pm$ 0.07	1.44 $\pm$ 1.29	1.38 $\pm$ 0.04	0.43 $\pm$ 0.12
		-	86.0 $\pm$ 4.00	1.76 $\pm$ 0.13	0.58 $\pm$ 0.05	1.14 $\pm$ 0.27	1.43 $\pm$ 0.51	0.65 $\pm$ 0.12
DA II/2	+	144 $\pm$ 0.16	2.14 $\pm$ 0.13	0.69 $\pm$ 0.14	1.70 $\pm$ 0.46	1.94 $\pm$ 0.32	0.85 $\pm$ 0.34	
	-	90.8 $\pm$ 5.00	1.93 $\pm$ 0.15	0.72 $\pm$ 0.12	2.42 $\pm$ 0.51	2.74 $\pm$ 0.68	0.67 $\pm$ 0.14	

The biodegradation tests were carried out at the laboratory scale. For the experiments, samples taken from nonwovens that were produced at a quarter-technical scale were used. Each 5  $\times$  5 cm sample was tested in triplicate under the conditions of repeatability and reproducibility. For each final result, the components of the uncertainty of the measurement were determined. The method used has been validated. Cotton (100%) was used as reference material. According to the available standards, biodegradable materials should achieve 90% decomposition within a maximum period of 24 weeks.

The biodegradability tests were conducted in soil under the controlled conditions of temperature (30  $\pm$  2  $^{\circ}$ C) and humidity (60–75%). The start of each test was preceded by an examination of the microbiological activity of the medium (soil) in order to ensure appropriate conditions ( $\geq 10^6$  cfu). The samples were placed in research reactors that were filled with the test soil and then stored in a heat chamber, which enabled the control and maintenance of the set environmental parameters (temperature and humidity). The

incubation process was carried out at a constant temperature for a maximum period of 24 weeks with the daily humidity control of the test medium. Within the designated periods, the progress of the biodegradation process in aerobic conditions was controlled. Photo-documentation was also obtained. Additionally, ecotoxicity tests were conducted and showed the influence of the decomposition of the developed nonwovens on the microbiological activity of the microorganisms inhabiting the soil. This research was carried out in accordance with the accredited research procedure of the “Assessment of the influence of natural and synthetic materials on soil microflora”, which was developed on the basis of the relevant international standards (EN ISO 7218:2008; EN ISO 11133; EN ISO 11133:2014-07/A1; EN ISO 4833-1:2013-12; EN ISO 19036:2020-04).

The mechanical properties were also tested according to the relevant international standards (PN-EN ISO 9073-2:2002; PN-EN 29073-1:1994; PN-EN 29073-3:1994; PN-EN ISO 9073-4:2002).

Due to the complexity and heterogeneity of the research materials, it was not possible to describe the reaction stoichiometry in detail. Nevertheless, the research included the determination of the carbon to nitrogen ratio within the test medium during the biodegradation process. The aim was to control the C:N ratio and verify that it was not negatively influenced by the sample decomposition.


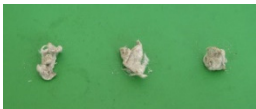



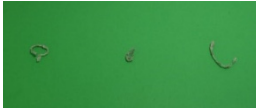
The data were then statistically evaluated using a statistical analysis package (StatSoft, Poland STATISTICA, version 9.0.). The Shapiro–Wilk test was used to check for the normal distribution of the results. When the results were non-parametric, the Mann–Whitney *U* test was used to determine any differences between the results in both groups. The level of statistical significance was defined as  $p < 0.05$ . A correlation analysis was also performed.

### 3. Results

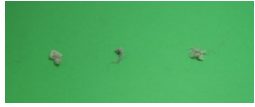
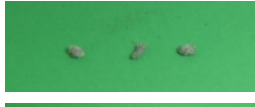
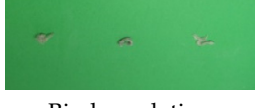
The mechanical properties of the studied materials were tested. Table 2 presents the obtained results.

The biodegradation degree (mass loss) was calculated for the tested groups of nonwovens. The level of mass loss varied considerably between these groups. After 24 weeks, the level of biodegradation in Group I reached an average of  $89.6\% \pm 2.67$ , while in the Group II, all samples reached 100% within 8–24 weeks. Table 3 presents the photo-documentation of the progress of the process for selected samples. The application of the Shapiro–Wilk test showed that the hypothesis regarding the data being normally distributed could be rejected ( $p < 0.05$ ). The differences between the levels of mass loss of the two groups were found after performing a Mann–Whitney *U* test. Considering a difference in the *p*-value of  $< 0.05$  to be statistically significant, the compositions of the nonwovens had an influence on their biodegradability.

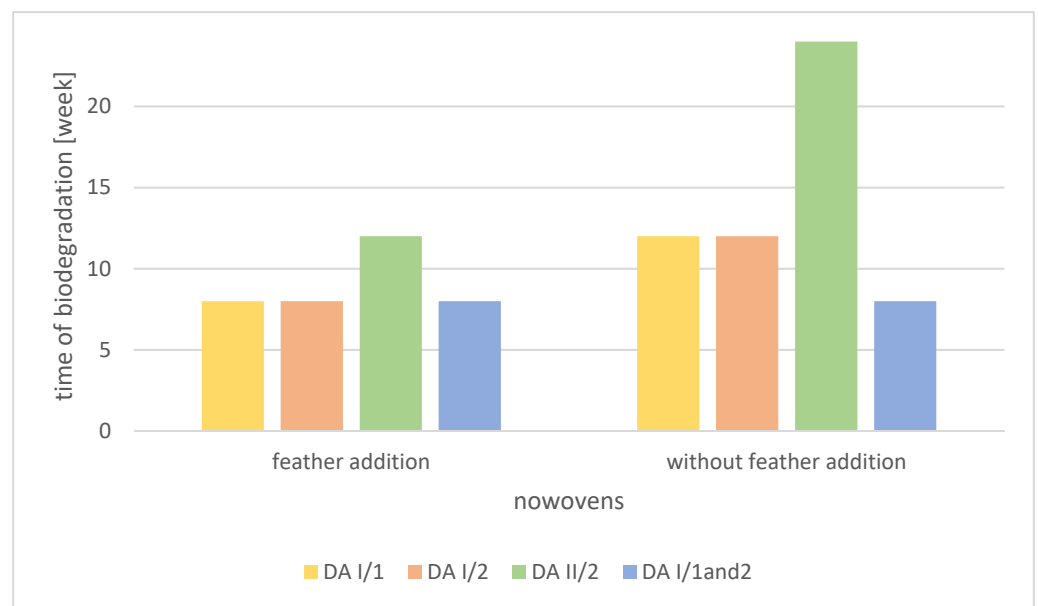
**Table 3.** The photo-documentation of the biodegradation process (Sample DA II/2).

	DA II/2 “0”	DA II/2
1 Week		
4 Weeks		
8 Weeks		

**Table 3.** *Cont.*

	DA II/2 "0"	DA II/2
12 Weeks		
16 Weeks		Biodegradation 100%
20 Weeks		
24 Weeks	Biodegradation 100%	

For the samples from Group II, a detailed analysis of the effects of the addition of poultry feathers on biodegradation was performed. Figure 1 presents the ratio of the biodegradation times of the materials.



**Figure 1.** The biodegradation times of the samples, with and without the addition of feathers, for the samples in Group II.

In order to present the differences between the selected features of the tested samples in Group II, an ANOVA test was performed (Table 4).

**Table 4.** The results obtained by the ANOVA test for the samples in Group II.

		Feather	
		No	Yes
Week of Biodegradation	Mean	14	9
	SD *	6.93	2.00
	Min.	8	8
	Max.	24	12
	Median	12	8

Table 4. Cont.

		Feather	
		No	Yes
Tensile Strength in the Horizontal Direction	Mean	0.61	0.46
	SD *	0.07	0.16
	Min.	0.56	0.34
	Max.	0.72	0.69
	Median	0.58	0.40
Tensile Strength in the Vertical Direction	Mean	1.42	1.19
	SD *	0.66	0.46
	Min.	1.01	0.70
	Max.	2.42	1.70
	Median	1.14	1.18
Tear Resistance in the Horizontal Direction	Mean	1.65	1.39
	SD *	0.75	0.39
	Min.	1.02	1.06
	Max.	2.74	1.94
	Median	1.43	1.28
Tear Resistance in the Vertical Direction	Mean	0.65	0.54
	SD *	0.01	0.21
	Min.	0.64	0.38
	Max.	0.67	0.85
	Median	0.65	0.47

SD \*, standard deviation.

A correlation analysis was also performed in order to present the interdependencies between the selected properties of the materials. Correlations between the mechanical properties and the degree of the mass loss/time of biodegradation were checked ( $p < 0.05$ ) and the obtained results are presented in Table 5.

**Table 5.** The relationships between the metrological parameters and the biodegradability/biodegradation times of samples in Groups I and II (correlation matrix; correlation coefficient).

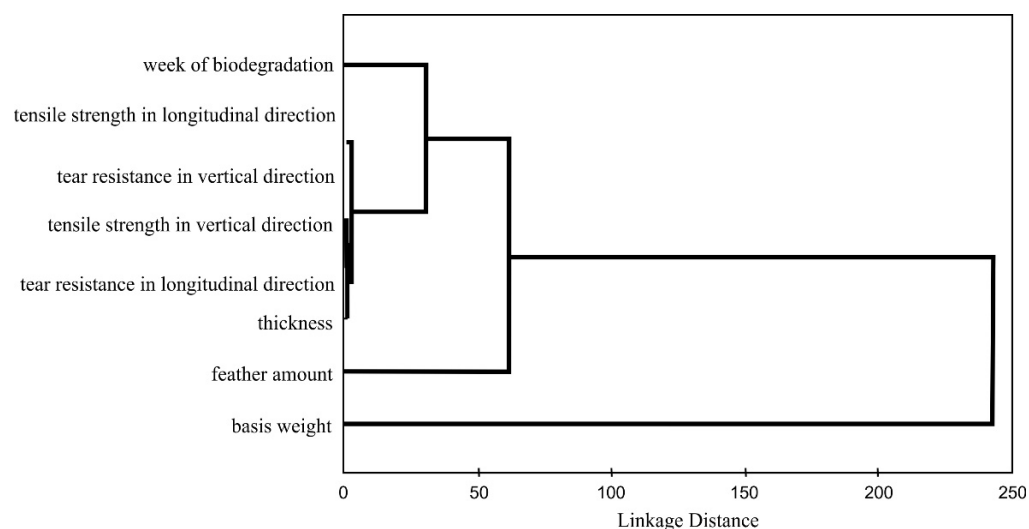
	Group	Feather Addition	Thickness	Tensile Strength in the Horizontal Direction	Tensile Strength in the Vertical Direction	Tear Resistance in the Horizontal Direction	Tear Resistance in the Vertical Direction
Biodegradability (%)	I	0.24	−0.16	0.12	−0.10	0.19	−0.05
Weeks of Biodegradation	II	−0.62	0.54	<b>0.74</b>	<b>0.87</b>	<b>0.94</b>	0.45

**bold:** values for which the hypothesis ( $H_0$ ; value of the coefficient in the correlation is 0) can be rejected.

In order to illustrate the relationships between the examined features, a cluster analysis was performed for the samples in Group II (Figure 2). The test organised items (features) into groups, or clusters, on the basis of how closely associated they were.

The determination of the carbon to nitrogen ratio in the test medium was determined during the biodegradation process. The obtained results showed differences between the blank sample of soil and the samples of soil during/after the decomposition of samples. While the C:N ratio for the blank sample of soil was constant throughout the trial (12–14:1), the ratios were higher for the media in which the samples were buried (19–20:1), especially during the first weeks of the trial.

The main aim of the ecotoxicity tests was to investigate the influence of the nonwovens, with and without feathers addition, on the microbiological activity of the tested substrate (soil). The conducted tests showed no toxic effects on the microorganisms. This testing was very important due to the essential role of microorganisms in the biodegradation process.



**Figure 2.** The biodegradation times of the samples, with and without the addition of feathers, in Group II.

#### 4. Discussion

The literature reports that chicken feathers have unique properties. The barb is a protein fibre that has high flexibility, low density and a good spinning length. The rachis has low rigidity and low density. These features make chicken feather barbs a good composite for manufacturing textile products, either on their own or in structural interactions with other fibres [20].

Natural fibres are divided into three main groups, based on their origin: plant (cellulose) fibres, animal (protein) fibres and mineral fibres. Their compositions (cellulose/protein content) influence their mechanical properties and the biodegradation process [21–23]. The main medium for the decomposition of polymer waste is soil, which is characterised by varied biodiversity [24]. The time required for the biodegradation of bioplastics depends on the substrate properties [22].

Recently, interest in geotextiles within environmental engineering has been increasing. Both synthetic and biodegradable materials are used. Separation, drainage, filtration, anti-erosion protection sealing and improvements in plant vegetation conditions are among their most important functions. Biopolymers and natural fibres could replace synthetic materials in up to 50% of applications [22]. This is very promising, especially as synthetic fibres are usually not subject to biological degradation. It should be highlighted that due to the growth in consumer and industrial demand for environmentally friendly products, the use of raw materials that are obtained from natural sources has increased significantly. The replacement of synthetic materials, such as PP and polyester, with natural biopolymers (e.g., poly(lactic)acid) is essential because of the amount of waste that is produced due to consumption. According to the US Environmental Protection Agency, 14.3 million tons of textiles were discarded in 2012. It should be pointed out that only 15.7% of this waste was recovered [25]. Recently, geotextiles that are made from synthetic fibres have been considered more critically. A great emphasis is now placed on the application of natural fibres, or biofibres, from renewable sources [26]. Chicken feather-based geotextile materials seem to be a promising solution within agriculture due to the properties of keratin. The feather fibre can preserve soil, increase moisture content and decrease the compaction of soil [26,27].

The study described in this paper showed the great potential of nonwovens that are made with the addition of feathers, especially in that they are biodegradable. The use of feather waste in the production of nonwovens as agricultural products could be the perfect solution for the management of hazardous waste while simultaneously enriching the natural environment. The literature reports [28] that chicken feather fibres can be used

as a cheap raw material for nonwoven production. Yet, due to poor length, they need to be combined with other material during the production process.

The main purpose of the biodegradation tests was to demonstrate the impact of the material on the environment. Due to the huge problems with the management of post-consumer waste, the ability to biodegrade is a desirable feature for materials. The process also provides nutrients that are crucial for the growth of new life.

The literature reports that the rate of biodegradability of various materials depends on the nature of the polymer and the structure of the fibres [29]. Our obtained results showed no influence of the presence of feather addition on the biodegradation process in Group I (correlation coefficient = 0.24). Different results were obtained for Group II (correlation coefficient =  $-0.46$ ;  $p < 0.05$ ). Here, it could be seen that in most cases, the addition of feathers shortened the degradation time of the nonwoven fabrics. It could be assumed that the chemical compounds that are present in feathers (mainly keratin) had a positive effect on the activity of the soil microorganisms, thereby accelerating the biodegradation time of the whole sample.

It should be highlighted that animal remains that are rich in  $\alpha$ -keratin are relatively quickly biodegraded by keratinolytic microorganisms, which use native keratin as a source of C, N, S and energy. The mechanisms of degradation are not fully known [27,29–31]. One of the initial theories was presented by Raubitschek [32], but this was discarded after the discovery of keratinase [33,34]. Other theories pointed to, inter alia, enzymatic keratin digestion by keratinolytic enzymes and the sulphuric amino acid metabolism of microorganisms as the basis of decomposition [35–37].

A wide range of bacteria, actinomycetes and filamentous fungi have been characterised as keratinolytic microorganisms. Special attention should be paid to bacteria belonging to the genus *Bacillus*, such as *B. subtilis*, *B. pumilus*, *B. cereus*, *B. coagulans*, *B. licheniformis* or *B. megatherium* [28,35]. The type of microorganism is not the only factor that is essential for the degradation of materials. Their activity and the properties of the material itself (ecotoxic effects) are also extremely important. The conducted ecotoxicity tests showed no negative influence of the decomposition of the materials on microbial activity and allowed us to establish the ecological characteristics of the tested materials.

Tesfaye et al. [20], on the basis of mechanical properties, assumed that feathers could be applied in geotextiles and road construction applications, as well as the textile industry, energy industry (as insulation materials) and packaging industry. Agriculture application is of special interest because of the water-holding capacity of the feather fibres, which could improve the moisture content of soil. According to scientific reports, feather composting is a safe, sanitary and cost-effective technology that could allow us to obtain products (compost) that could then be used as fertilisers. Their decomposition in soil environments results in an increase in carbon (C), nitrate nitrogen (N-NO<sub>3</sub>) and sulphur sulphate (S-SO<sub>4</sub>) concentrations, which are easily absorbed by plants [5,36–38]. Our study was in accordance with the literature data (C:N ratio).

The mechanical properties of materials influence the times of biodegradation. It could be concluded that higher values of tensile strength and tear resistance reflected the ability of microorganisms to resist the decomposition of the nonwoven fabrics. Simultaneously, it should be pointed out that higher amounts of feather addition shortened the biodegradation times. The nonwovens are supposed to protect seeds, prevent soil from washing off, limit the impact of rainfall on soil aggregates and inhibit rainwater runoff. The tensile strength of the nonwovens could be a deciding factor in its long-term durability and service life. Hence, good tensile strength is a necessary parameter for them. The base weights of the nonwovens are also important. A heavier material would press the seeds into the soil, cover them and improve conditions for seedling germination and development.

The cluster analysis showed that there was a strong linkage between the mechanical properties. This group of features was associated with the number of weeks of biodegradation. In turn, this cluster was connected to the feather amount.



Jin et al. [39] tested nonwoven fabrics (PE/PP) with the addition of duck feather fibres. Their study revealed the good mechanical properties and sorption capacity of the bicomponent, indicating its potential application as a material for textile dyeing effluent treatment. Soekoco et al. [40] applied chicken feather waste to the production of nonwoven insulator material. The obtained material, which was based on PP, showed higher tensile strength values than commercial insulator material.

There is little evidence in the literature regarding the biodegradability of nonwovens with the addition of feather waste. Mrajji et al. [41] investigated the effects of nonwoven structures on the mechanical, thermal and biodegradability properties of feather-based nonwoven materials that were reinforced by polyester composites. The obtained results showed that the introduction of feather waste into the matrix slightly reduced the degradation process time. This confirmed that the type of polymer and the structure of the fibre have a great influence on the rate of biodegradation.

Interest in the implementation of feather waste in the production of nonwovens is still increasing. Casadesús et al. [42] proposed a method for the management of feather waste in the production of sound-absorbing nonwoven materials. The authors investigated the environmental impacts of the solution using life cycle analysis (LCA) methodology and the utility aspect. The obtained results showed that higher amounts of feathers lowered the environmental impacts while simultaneously satisfying acoustic properties. Vilchez et al. [33] proposed a simple and straightforward method to produce nonwovens with feather additions and (nano)cellulose fibres. The fabricated materials had good mechanical properties and seemed to meet the ecological criteria. The literature [28,42,43] reports that the use of feathers in nonwoven fabrics could find applications for erosion control purposes, especially in areas that have been denuded of vegetation and soil stabilisation is desired.

The developed nonwovens that could be used for agricultural applications are characterised by new functionalities, such as biodegradability that can be adjusted ad hoc to the type and duration of the crop and soil enrichment from the inflow of organic nitrogen. Nonwovens that only contain ingredients of natural origin are a valuable source of nutrients for plants. The flow of organic nitrogen into the soil comes from the biodegradation of the feathers.

## 5. Conclusions

The tested materials in both groups differed significantly. The positive effects of feather addition on the time of the biodegradation of the nonwovens in Group II were shown. Moreover, a correlation between the selected mechanical properties and the time of biodegradation was noticed. It could be concluded that the addition of feather waste affects the mechanical properties of the materials. The addition of feathers makes the product more susceptible to the action of microorganisms, releases C and N into the soil, shortens the biodegradation time and allows for waste management. The presented results of biodegradation and ecotoxicity confirmed the legitimacy of implementing this type of technology on a large scale. The biodegradable nonwovens that were tested and described in this paper seem to meet all criteria for eco-friendly agricultural products and have great potential for commercial use

## 6. Patents

P.430284. (19 June 2019) “Sposób wytwarzania puszystej włókniny kompozytowej”.

**Supplementary Materials:** The following supporting information can be downloaded at: <https://www.mdpi.com/article/10.3390/polym14122370/s1>, Table S1: SEM photo-documentation of the samples.

**Author Contributions:** Conceptualisation, J.J.-P., K.W.-T. and T.M.; methodology: J.J.-P. and M.S.; writing—original draft preparation, J.J.-P. and M.S.; writing—review and editing, J.J.-P., M.S. and E.W.; visualisation, J.J.-P.; supervision, J.J.-P., K.W.-T., T.M. and E.W.; project administration, K.W.-T.; funding acquisition, K.W.-T.; project Leader and contributed to the final discussion of the results,

K.W.-T.; participation in feather-based nonwoven manufacturing, T.M., E.W., T.K., M.P. and D.W. All authors have read and agreed to the published version of the manuscript.

**Funding:** This research was funded by the EU through the Regional Development Fund under the Intelligent Development Operational Programme National Centre for Research and Development. (grant number: POIR.04.01.04-00-0059/17).

**Institutional Review Board Statement:** Not applicable.

**Informed Consent Statement:** Not applicable.

**Data Availability Statement:** Not applicable.

**Acknowledgments:** The investigations presented were carried out as a part of the research project EkoPióro POIR.04.01.04-00-0059/17: “Development of innovative protective nonwovens with addition of feathers”. The project is co-financed by the European Union through the European Regional Development Fund under the Intelligent Development Operational Programme.

**Conflicts of Interest:** The authors declare no conflict of interest.

## References

1. OECD. Glossary of Statistical Terms. 2021. Available online: <https://stats.oecd.org/glossary/detail.asp?ID=203> (accessed on 17 February 2021).
2. United Nations. Glossary of Environment Statistics. In *Studies in Methods*; Series F; United Nations: New York, NY, USA, 1997.
3. Poznyak, T.I.; Chairez Oria, I.; Poznyak, A.S. *Ozonation and Biodegradation in Environmental Engineering*, 1st ed.; Elsevier Inc.: Amsterdam, The Netherlands, 2019; pp. 353–388. [\[CrossRef\]](#)
4. Rana, S.; Pichandi, S.; Parveen, S.; Fangueiro, R. Biodegradation Studies of Textiles and Clothing Products. In *Roadmap to Sustainable Textiles and Clothing. Textile Science and Clothing Technology*; Muthu, S., Ed.; Springer: Singapore, 2014.
5. Urbanek, A.K.; Rymowicz, W.; Mirończuk, A.M. Degradation of plastics and plastic-degrading bacteria in cold marine habitats. *Appl. Microbiol. Biotechnol.* **2018**, *102*, 7669–7678. [\[CrossRef\]](#)
6. Fernández, L. Chemical Fibers Global Production 2000–2019. Available online: <https://www.statista.com/statistics/271651/global-production-of-the-chemical-fiber-industry/> (accessed on 17 February 2022).
7. Shavandi, A.; Ali, M.A. Keratin based thermoplastic biocomposites: A review. *Rev. Environ. Sci. Bio.* **2019**, *18*, 299–316. [\[CrossRef\]](#)
8. Shavandi, A.; Carne, A.; Bekhit, A.A.; Bekhit, A.E.-D.A. An improved method for solubilisation of wool keratin using peracetic acid. *J. Environ. Chem. Eng.* **2017**, *5*, 1977–1984. [\[CrossRef\]](#)
9. Shavandi, A.; Silva, T.H.; Bekhit, A.A.; Bekhit, A.E.-D.A. Keratin: Dissolution, extraction and biomedical application. *Biomater. Sci.* **2017**, *5*, 1699–1735. [\[CrossRef\]](#) [\[PubMed\]](#)
10. Wrześniewska-Tosik, K.; Ryszkowska, J.; Mik, T.; Wesołowska, E.; Kowalewski, T.; Pałczyńska, M.; Sałasińska, K.; Walisiak, D.; Czajka, A. Composites of Semi-Rigid Polyurethane Foams with Keratin Fibers Derived from Poultry Feathers and Flame Retardant Additives. *Polymers* **2020**, *12*, 2943. [\[CrossRef\]](#) [\[PubMed\]](#)
11. 2021/2004(INI); European Parliament Resolution of 11 March 2021 on the European Semester for Economic Policy Coordination: Annual Sustainable Growth Strategy. European Parliament: Brussels, Belgium, 2021.
12. Poole, A.J.; Church, J.S.; Huson, M.G. Environmentally sustainable fibers from regenerated protein. *Biomacromolecules* **2009**, *10*, 1–8. [\[CrossRef\]](#) [\[PubMed\]](#)
13. Barone, J.R. Polyethylene/keratin fiber composites with varying polyethylene crystallinity. *Compos. Part A Appl. Sci.* **2005**, *36*, 1518–1524. [\[CrossRef\]](#)
14. Barone, J.R.; Gregoire, N.T. Characterisation of fibre–polymer interactions and transcrystallinity in short keratin fibre–polypropylene composites. *Plast. Rubber Compos.* **2006**, *35*, 287–293. [\[CrossRef\]](#)
15. Bertini, F.; Canetti, M.; Patrucco, A.; Zoccola, M. Wool keratin-polypropylene composites: Properties and thermal degradation. *Polym. Degrad. Stab.* **2013**, *98*, 980–987. [\[CrossRef\]](#)
16. Cheng, S.; Lau, K.-t.; Liu, T.; Zhao, Y.; Lam, P.-M.; Yin, Y. Mechanical and thermal properties of chicken feather fiber/PLA green composites. *Compos. B Eng.* **2009**, *40*, 650–654. [\[CrossRef\]](#)
17. Aranberri, I.; Montes, S.; Wesołowska, E.; Rekondo, A.; Wrześniewska-Tosik, K.; Grande, H.-J. Improved Thermal Insulating Properties of Renewable Polyol Based Polyurethane Foams Reinforced with Chicken Feathers. *Polymers* **2019**, *11*, 2002. [\[CrossRef\]](#) [\[PubMed\]](#)
18. Călin, M.; Constantinescu-Aruxandei, M.D.; Alexandrescu, E.; Răut, I.; Doni, M.B.; Arsene, M.-L.; Oancea, F.; Jecu, L.; Lazăr, V. Degradation of keratin substrates by keratinolytic fungi. *Electron. J. Biotechnol.* **2017**, *28*, 101–112. [\[CrossRef\]](#)
19. *European Standard EN 14995*; Plastics—Evaluation of Compostability—Test Scheme and Specifications. CEN: Brussels, Belgium, 2009.
20. Tesfaye, T.; Sithole, B.; Ramjugernath, D.; Chunilall, V. Valorisation of chicken feathers: Characterisation of physical properties and morphological structure. *J. Clean. Prod.* **2017**, *149*, 349–365. [\[CrossRef\]](#)

21. Kakonke, G.; Tesfaye, T.; Sithole, B.; Ntunka, M. Production and characterization of cotton-chicken feather fibres blended absorbent fabrics. *J. Clean. Prod.* **2020**, *243*, 118508. [[CrossRef](#)]
22. Marczak, D.; Lejcuś, K.; Misiewicz, J. Characteristics of biodegradable textiles used in environmental engineering: A comprehensive review. *J. Clean. Prod.* **2020**, *268*, 122129. [[CrossRef](#)]
23. Faruk, O.; Bledzki, A.K.; Fink, H.-P.; Sain, M. Biocomposites reinforced with natural fibers: 2000–2010. *Prog. Polym. Sci.* **2012**, *37*, 1552–1596. [[CrossRef](#)]
24. Emadian, S.M.; Onay, T.T.; Demirel, B. Biodegradation of bioplastics in natural environments. *Waste Manag.* **2017**, *59*, 526–536. [[CrossRef](#)]
25. Nam, S.; Slopek, R.; Wolf, D.; Warnock, M.; Condon, B.D.; Sawhney, P.; Gbur, E.; Reynolds, M.; Allen, C. Comparison of biodegradation of low-weight hydroentangled raw cotton nonwoven fabric and that of commonly used disposable nonwoven fabrics in aerobic Captina silt loam soil. *Text. Res. J.* **2015**, *86*, 155–166. [[CrossRef](#)]
26. Kumar, N.; Das, D. Nonwoven geotextiles from nettle and poly(lactic acid) fibers for slope stabilization using bioengineering approach. *Geotext. Geomembr.* **2018**, *46*, 206–213. [[CrossRef](#)]
27. Montes-Zarazúa, E.; Colín-Cruz, A.; Pérez-Rea, M.d.L.L.; de Icaza, M.; Velasco-Santos, C.; Martínez-Hernández, A.L. Effect of Keratin Structures from Chicken Feathers on Expansive Soil Remediation. *Adv. Mater. Sci. Eng.* **2015**, *2015*, 1–10. [[CrossRef](#)]
28. George, B.R.; Bockarie, A.; McBride, H. Utilization of Turkey Feather Fibers in Nonwoven Erosion Control Fabrics. *Nonwoven Ind.* **2003**, 45–52. [[CrossRef](#)]
29. Kornilowicz-Kowalska, T.; Bohacz, J. Biodegradation of keratin waste: Theory and practical aspects. *Waste Manag.* **2011**, *31*, 1689–1701. [[CrossRef](#)] [[PubMed](#)]
30. Kunert, J. Thiosulphate esters in keratin attacked by dermatophytes in vitro. *Sabouraudia* **1972**, *10*, 6–13. [[CrossRef](#)] [[PubMed](#)]
31. Broda, J.; Przybyło, S.; Kobiela-Mendrek, K.; Biniaś, D.; Rom, M.; Grzybowska-Pietras, M.J.; Laszczak, R. Biodegradation of sheep wool geotextiles. *Int. Biodeter. Biodegr.* **2016**, *115*, 31–38. [[CrossRef](#)]
32. Casadesús, M.; Álvarez, M.D.; Garrido, N.; Molins, G.; Macanás, J.; Colom, X.; Cañavate, J.; Carrillo, F. Environmental impact assessment of sound absorbing nonwovens based on chicken feathers waste. *Resour. Conserv. Recycl.* **2019**, *149*, 489–499. [[CrossRef](#)]
33. Vilchez, V.; Dieckmann, E.; Tammelin, E.; Cheeseman, C.; Lee, K.-Y. Upcycling poultry feathers with (nano)cellulose: Sustainable composites derived from non-woven whole feather preforms. *ACS Sustain. Chem. Eng.* **2020**, *8*, 14263–14267. [[CrossRef](#)]
34. Yadav, S.; Khosla, B. Biodegradation of poultry feather waste by keratinase producing *Bacillus cereus* strain isolated from poultry farms waste disposal site. *CSCEE* **2021**, *4*, 100114. [[CrossRef](#)]
35. Li, Q. Progress in Microbial Degradation of Feather Waste. *Front. Microbiol.* **2019**, *10*, 2717. [[CrossRef](#)]
36. Kirwan, K.; Wood, B.M. Recycling of materials in automotive engineering. In *Advanced Materials in Automotive Engineering*; WMG, University of Warwick: Cambridge, UK, 2012; pp. 299–314.
37. Bohacz, J.; Kornilowicz-Kowalska, T. Nitrogen and sulfur transformations in composts containing chicken feathers. *Compost Sci. Util.* **2009**, *17*, 180–188. [[CrossRef](#)]
38. Bohacz, J.; Kornilowicz-Kowalska, T. Changes in enzymatic activity in composts containing chicken feathers. *Biores. Technol.* **2009**, *100*, 3604–3612. [[CrossRef](#)]
39. Jin, X.; Lu, L.; Wu, H.; Ke, Q.; Wang, H. Duck Feather/Nonwoven Composite Fabrics for Removing Metals Present in Textile Dyeing Effluents. *J. Eng. Fibers Fabr.* **2013**, *8*, 155892501300800. [[CrossRef](#)]
40. Soekoco, A.S.; Ichwan, M.; Hananto, A.; Mustafa, D. *Application of Chicken Feather Waste as a Material of Nonwoven Insulator*; AIP Publishing LLC: Melville, NY, USA, 2018.
41. Mrajji, O.; Wazna, M.E.; Samouh, Z.; Bouari, A.E.; Cherkaoui, O.; El Moznine, R. The effect of nonwoven structure on thermomechanical properties of feather waste reinforced polyester composite. *J. Ind. Text.* **2020**, 152808372094773. [[CrossRef](#)]
42. Zhang, W.; Yangk, X.; Li, C.; Liang, M.; Lu, C.; Deng, Y. Mechanochemical activation of cellulose and its thermoplastic polyvinyl alcohol ecomposites with enhanced physicochemical properties. *Carbohydr. Polym.* **2011**, *83*, 257–263. [[CrossRef](#)]
43. Mrajji, O.; Wazna, M.E.; Boussoualem, Y.; Bouari, A.E.; Cherkaoui, O. Feather waste as a thermal insulation solution: Treatment, elaboration and characterization. *J. Ind. Text.* **2019**, *50*, 1674–1697. [[CrossRef](#)]

## Article

# Recent Advances in Production of Ecofriendly Polylactide (PLA)–Calcium Sulfate (Anhydrite II) Composites: From the Evidence of Filler Stability to the Effects of PLA Matrix and Filling on Key Properties

Marius Murariu <sup>1,\*</sup>, Yoann Paint <sup>1</sup>, Oltea Murariu <sup>1</sup>, Fouad Laoutid <sup>1</sup> and Philippe Dubois <sup>1,2,\*</sup>

<sup>1</sup> Laboratory of Polymeric and Composite Materials, Materia Nova Materials R&D Center & UMons Innovation Center, 7000 Mons, Belgium; yoann.paint@materianova.be (Y.P.); oltea.murariu@materianova.be (O.M.); fouad.laoutid@materianova.be (F.L.)

<sup>2</sup> Laboratory of Polymeric and Composite Materials, Center of Innovation and Research in Materials and Polymers (CIRMAP), University of Mons (UMons), 7000 Mons, Belgium

\* Correspondence: marius.murariu@materianova.be (M.M.); philippe.dubois@umons.ac.be (P.D.); Tel.: +32-65-554976 (M.M.); +32-65-373000 (P.D.); Fax: +32-65-373054 (P.D.)

**Abstract:** The melt–mixing of polylactide (PLA) with micro- and/or nanofillers is a key method used to obtain specific end-use characteristics and improvements of properties. So-called “insoluble” CaSO<sub>4</sub> (CS) β-anhydrite II (AII) is a mineral filler recently considered for the industry of polymer composites. First, the study proves that AII made from natural gypsum by a specifically thermal treatment is highly stable compared to other CS forms. Then, PLAs of different isomer purity and molecular weights (for injection molding (IM) and extrusion), have been used to produce “green” composites filled with 20–40 wt.% AII. The composites show good thermal and mechanical properties, accounting for the excellent filler dispersion and stability. The stiffness of composites increases with the amount of filler, whereas their tensile strength is found to be dependent on PLA molecular weights. Interestingly, the impact resistance is improved by adding 20% AII into all investigated PLAs. Due to advanced kinetics of crystallization ascribed to the effects of AII and use of a PLA grade of high L-lactic acid isomer purity, the composites show after IM an impressive degree of crystallinity (DC), i.e., as high as 50%, while their Vicat softening temperature is remarkably increased to 160 °C, which are thermal properties of great interest for applications requiring elevated rigidity and heat resistance.

**Keywords:** poly(lactic acid); PLA; biocomposites; mineral filler; calcium sulfate; natural gypsum; anhydrite II; melt–mixing; thermal and mechanical properties; crystallization; Vicat softening temperature; injection molding and extrusion; technical applications

**Citation:** Murariu, M.; Paint, Y.; Murariu, O.; Laoutid, F.; Dubois, P. Recent Advances in Production of Ecofriendly Polylactide (PLA)–Calcium Sulfate (Anhydrite II) Composites: From the Evidence of Filler Stability to the Effects of PLA Matrix and Filling on Key Properties. *Polymers* **2022**, *14*, 2360. <https://doi.org/10.3390/polym14122360>

Academic Editors: José Miguel Ferri, Vicent Fombuena Borràs and Miguel Fernando Aldás Carrasco

Received: 29 April 2022

Accepted: 5 June 2022

Published: 10 June 2022

**Publisher’s Note:** MDPI stays neutral with regard to jurisdictional claims in published maps and institutional affiliations.



**Copyright:** © 2022 by the authors. Licensee MDPI, Basel, Switzerland. This article is an open access article distributed under the terms and conditions of the Creative Commons Attribution (CC BY) license (<https://creativecommons.org/licenses/by/4.0/>).

## 1. Introduction

The high interest and progress in the production of biosourced polymers such as polylactide or poly(lactic acid) (PLA), is connected to a large number of factors, including the increase in requests for more environmentally sustainable products, the development of new biobased feedstocks and larger consideration of the techniques of recycling, increase in restrictions for the use of polymers with high “carbon footprint” of petrochemical origin, particularly in applications such as packaging, automotive, electrical and electronics industry, and so on [1–8].

Nowadays, when looking for a sustainable society and environmentally friendly products, the market turns to more “durable” applications, therefore important demands can be expected for new biomaterials which clearly offer multiple benefits to customers. Still, for many applications, the carbon footprint of products can be reduced by replacing “fossil carbon” with “renewable carbon” [9].

PLA, a biodegradable polyester produced from renewable resources, is one of the key bioplastics with the largest market significance due to its properties (high tensile strength and rigidity, good flexural strength, optical transparency) [2]. Due to its very interesting properties, PLA is currently receiving considerable attention for traditional applications such as packaging [10], as well as the production of textile fibers [11,12], and it also finds higher added value for durable/technical [9,13] and biomedical applications [14].

Regarding the use of PLA in durable applications, unfortunately, its application is somewhat limited because this biopolyester suffers from some shortcomings, e.g., poor thermal resistance, low heat distortion temperature and rate of crystallization, as well as rather high sensitivity to hydrolysis, whereas specific end-use properties are required. Therefore, at this time, an impressive number of studies concerning the production of novel PLA (nano)composites characterized by improved characteristics, such as better processability, enhanced mechanical properties and thermal resistance, flame retardancy, tailored electrical properties, longer durability to allow PLA utilization in applications requiring higher added value, have been undertaken. To reach the end-user demands, the properties of PLA can be tuned up by combining the polyester matrix with different dispersed phases: micro- and nano-fillers, reinforcing fibers, impact modifiers, plasticizers, other polymers, and various types of additives. Following different objectives, PLA has already been melt-mixed with  $\text{CaCO}_3$  [8,15], talc [16,17], kaolin [18],  $\text{BaSO}_4$  [19], and other mineral fillers, typically used in the industry of polymer composites.

It is worth mentioning that composites of PLA with  $\text{CaSO}_4$  (CS), as anhydrite or hydrated forms, have been primarily used in the field of biomedical applications for bone reparation and production of implant materials [20–23]. CS is considered as an uncommon biocompatible material which is completely resorbed following its implantation [21]. Nevertheless, few studies were devoted to the utilization of synthetic CS whiskers to reinforce polyvinyl chloride (PVC) [24,25], polypropylene (PP) [26,27], and polycaprolactone (PCL) [28]. Furthermore, in response to the demands for enlarging PLA applications while reducing its production cost, it has been previously disclosed by us and our collaborators that PLA can be effectively melt-blended with adequately thermally treated synthetic gypsum [29–32], a by-product directly issued from the lactic acid (LA) production process [33–35]. PLA can be successfully melt-blended with previously calcinated gypsum at 500 °C, so called  $\beta$ -anhydrite II (AII), which is less sensitive to moisture [2,32]. From the perspective of “green chemistry”, as well as economics, CS was considered a logical filler choice for PLA cost reduction due to its availability as a waste stream from LA production [36]. Moreover, as for other mineral-filled polymers, the addition of a third component into PLA-AII compositions, i.e., plasticizers [30], impact modifiers [32,37], clays [38], flame retardants (FRs) [2], other additives, has been considered to obtain composites with specific end-use properties. For more information on this topic, we suggest a short insight on the case study presented in a review published by us concerning the production and properties PLA composites [2].

Nevertheless, nowadays, the producers of natural gypsum are currently looking for new markets by proposing CS derivatives, such as AII, for new applications of higher added value, e.g., in the industry of polymer composites, paints, coatings, etc. Regarding so-called “insoluble” anhydrite (CS AII), somewhat regrettably, this filler is less known by potential users. Therefore, the information regarding the utilization of stable CS (AII) for reinforcing polymers is very limited compared to other mineral fillers (talc,  $\text{CaCO}_3$ , kaolin, etc.), whereas the nature of CS derivatives or the necessity of thermally treatments at high temperature to produce stable fillers was much less studied [27,39]. There is also a misunderstanding connected to the quick absorption of water or high sensitivity to moisture, which is specific to CS hemihydrate ( $\text{CaSO}_4 \cdot 0.5\text{H}_2\text{O}$ ) and to “soluble” anhydrite (i.e., AIII). Consequently, this confusion is detrimental for the utilization of stable forms of CS (i.e., AII) in melt-blending applications with polymers requiring fillers characterized by high thermal stability and low absorption of water/moisture. Accordingly, it is necessary to find additional methods to prove the stability and added value of AII as filler. To the best

of our knowledge, the potential of this filler has not been identified sufficiently, therefore, further prospects are required to reveal its beneficial effects for different purposes.

On the other hand, the earlier studies realized by us and our collaborators [2] were mostly limited to a specific PLA from the first generation (i.e., an amorphous PLA matrix, not available commercially today) and to the use of synthetic gypsum by-product as obtained directly from the LA process. Today, various PLA grades are available, characterized by different molecular weights, L-lactic acid isomer purity, as well as the presence of special additives, paving the way for new possibilities in applications [2,3]. In addition, it is known that the choice of PLA matrix is of high importance when following different techniques in processing (injection molding (IM), extrusion, 3D printing, etc.), aspects less considered in the previous studies. Still, as already mentioned, PLA is often in an amorphous state after any processing step, such as extrusion or IM, showing limited or poor heat resistance (low heat distortion temperature (HDT)). In fact, this is a kind of ‘Achilles’ heel’, limiting PLA use in engineering/technical applications [40]. This parameter (i.e., the degree of crystallinity (DC)) is particularly essential to control the PLA degradation rate, thermal resistance, as well as mechanical, optical, and barrier properties. The adequate choice of PLA matrix, and the combination with a filler that can increase the crystallization rate of PLA, could open the way to better performing composites designed for engineering applications requiring resistance at high temperature.

Based on the prior art, the main goal of this study is to present recent experimental results and advances regarding the properties of mineral-filled biocomposites produced with CS AII made from natural gypsum and using PLA matrices of different molecular weights and isomer purity, mainly intended for processing by IM or extrusion. This will allow determining that the adequate choice of the PLA matrix is of key importance from the perspective of the application. Moreover, because CS AII is less known as a performant filler, one additional goal is to increase the interest in its utilization by experimentally proving its stability under harder testing conditions, such as following mixing in water as slurry. Regarding the PLA-AII composites, the study is focused on the characterization of their morphology and evidence for enhancement and tuning of thermal and mechanical properties connected to the nature of PLA and amounts of filler. However, it reveals some unexpected performances for special compositions, i.e., a remarkable increase in both DC and Vicat softening temperature (VST). Due to their properties, these “green” composites are of potential interest for utilization in the biomedical sector (e.g., via 3D printing) as biodegradable/rigid packaging and in technical applications requiring rigidity, heat resistance, and dimensional stability.

## 2. Materials and Methods

### 2.1. Materials

Three distinct PLA grades were investigated in the frame of the experimental program to consider different applications of and techniques for processing:

1. PLA 4032D (supplier: NatureWorks LLC, Blair, NE, USA), is a PLA of high molecular weight and melt viscosity designed for the extrusion of films and the realization of PLA blends. It is characterized by low D-isomer content (1.4%) and a melting temperature ( $T_m$ ) in the range of 155 to 170 °C and is abbreviated as PLA1.
2. PLA2: PLA 3051D is an IM grade for realization of products requiring low HDT (supplier NatureWorks LLC) characterized by higher D-isomer content (i.e., 4.3%) and a  $T_m$  in the range of 150 to 165 °C, according to the technical sheet of the supplier.
3. PLA3: PLA Luminy L105 (supplied by Total Corbion PLA (actually, TotalEnergies Corbion), Gorinchem, The Netherlands) is characterized by high L-isomer purity (L-isomer  $\geq 99\%$ , and implicit by very low content of D-isomer,  $<1\%$ ) and  $T_m$  of ca. 175 °C. PLA3 is a high flow PLA for spinning and IM, allowing the production of items with thin walls.

Table 1 shows the rheological information (i.e., melt flow rate (MFR) values) and the results of molecular characterizations by gel permeation chromatography (GPC), also

referred to as size-exclusion chromatography (SEC) obtained using Agilent 1200 Series GPC-SEC System (Agilent Technologies, Santa Clara, CA, USA) and chloroform (at 30 °C) as the solvent ( $M_w$  being the weight-average molar mass expressed in polystyrene equivalent, the dispersity being the  $M_w/M_n$  ratio between the weight- and number-average molar masses).

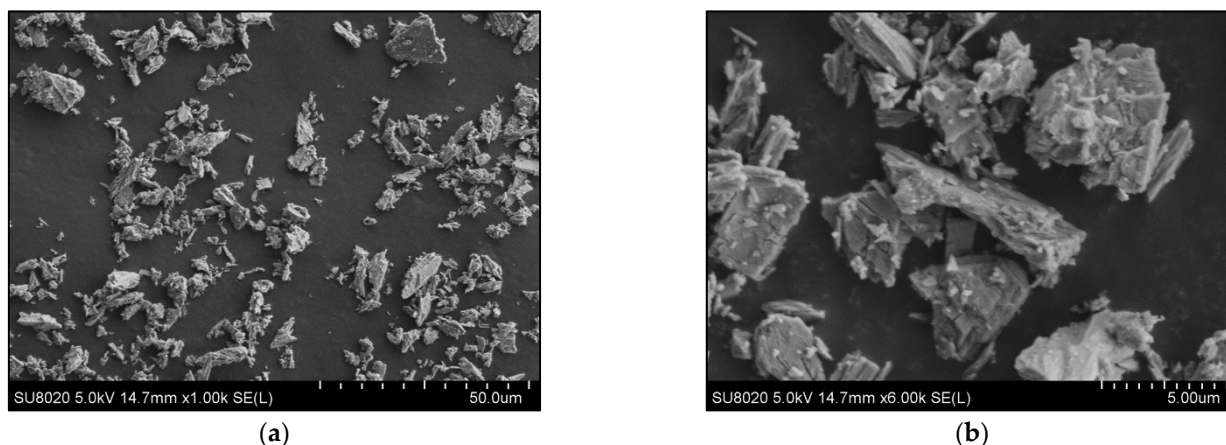
**Table 1.** Characteristics of PLAs used as the polymer matrix.

PLA Matrix	$M_w$	$M_w/M_n$ (Dispersity)	D-Isomer, %	MFR *, g/10 min
PLA1	209,000	2.0	1.4	7
PLA2	182,000	2.0	4.3	10–25
PLA3	133,000	1.9	<1.0	70

\* Values indicated by supplier: Melt Flow Rate (MFR) measurements at 210 °C, 2.16 kg.

CaSO<sub>4</sub> β-anhydrite II (CS AII) delivered as “ToroWhite” filler was kindly supplied by Toro Gips S.L. (Spain). According to the information provided by supplier, these products are obtained from selected food and pharma grades of high purity natural gypsum. They are characterized by high whiteness/lightness ( $L^*$ ), AII being an alternative of choice as a white pigment (TiO<sub>2</sub>) extender. Color measurements performed in the CIELab mode (illuminate D65, 10°) with a SpectroDens Premium (TECHKON GmbH, Königstein, Germany) have evidenced the high lightness of AII, i.e.,  $L^*$  of 95.8. Samples of CS dihydrate were also obtained from the same supplier for specific comparative tests (vide infra).

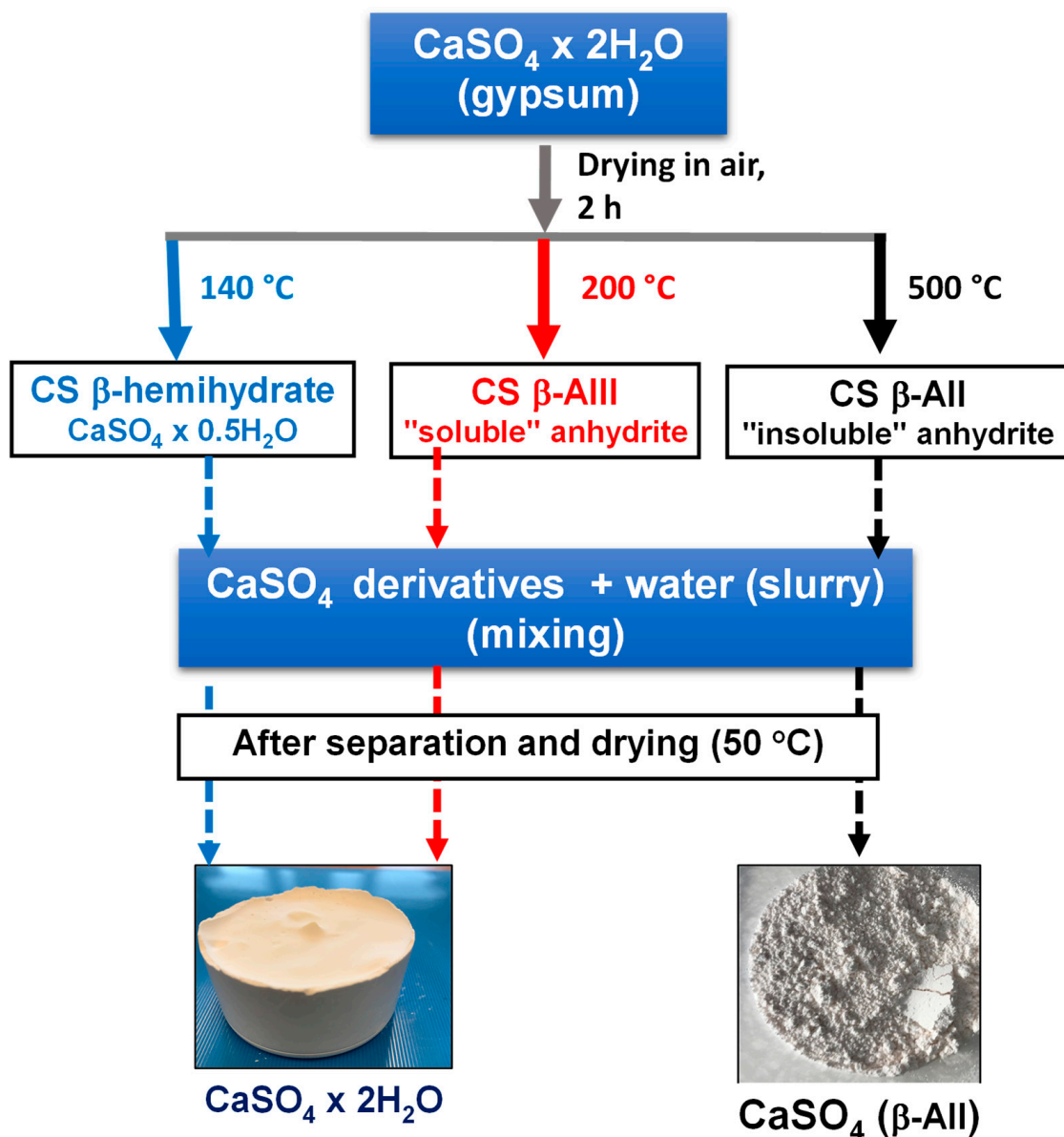
Figure 1a,b show selected SEM pictures to illustrate the morphology of AII filler used in this study for melt-blending with PLAs. The granulometry of AII sample was characterized by Dynamic Light Scattering (DLS) using a Mastersizer 3000 laser particle size analyzer (Malvern Panalytical Ltd., Malvern, UK), the microparticles having a  $D_{v50}$  of 5.4 μm and a  $D_{v90}$  of 14.9 μm.



**Figure 1.** (a,b) SEM micrographs (SE mode) at different magnifications of CS AII microparticles.

## 2.2. Specific Methods and Analyses to Demonstrate the Stability of AII as Filler

To evidence the distinct characteristics of AII, CS dihydrate was thermally treated during 2 h at different temperatures (140 °C, 200 °C, and 500 °C) in a Nabertherm B400 furnace (Nabertherm GmbH, Lilienthal, Germany) to obtain different forms of CS, respectively, CS hemihydrate, CS β-anhydrite III (AIII), and CS β-anhydrite AII (Figure 2). Then, the so-produced samples were characterized using TGA and XRD techniques. Furthermore, to test the stability of AII even after immersion in water, AII powders were mixed as a slurry (20%) in demineralized water for 24 h. The solid fraction (AII) was separated by sedimentation and centrifugation, maintained 24 h under a fume hood at room temperature (RT), and then dried under vacuum at low temperature (50 °C) for 2 h to remove the residual moisture.



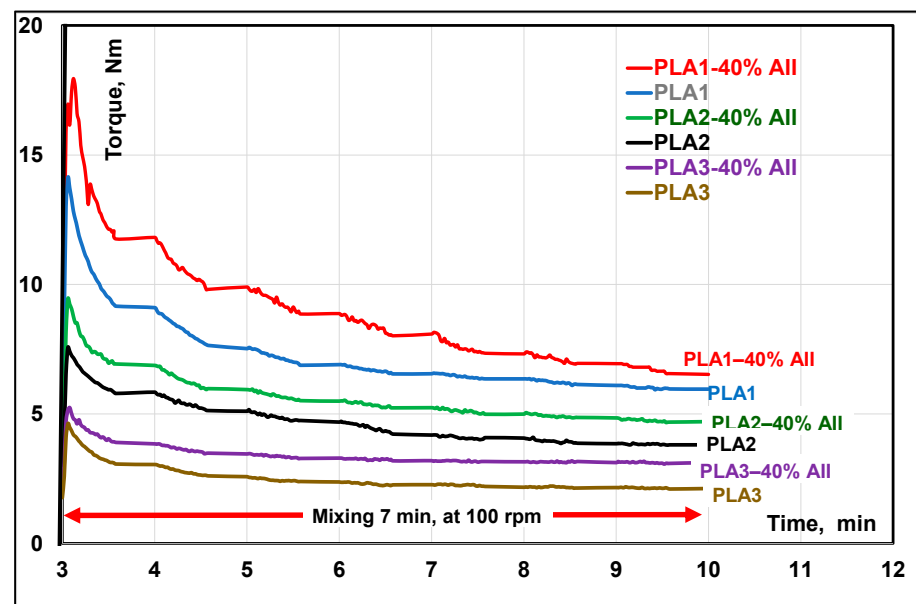
**Figure 2.** Experimental attempts to evidence the stability of CS  $\beta$ -AII by comparison to CS  $\beta$ -hemihydrate and CS  $\beta$ -AIII.

On the other hand, for sake of comparison, similar experiments were performed with CS (hemihydrate) and AIII, but these fillers were found to be extremely sensitive to water [41], leading to the formation of solid “blocky” structures of CS dihydrate (Figure 2).

### 2.3. Preparation of PLA-AII Composites

All materials were carefully dried at 70 °C overnight to limit PLA degradation during processing at high temperature due to the presence of moisture. Starting from dry-mixed PLAs and CS (AII) blends, PLA composites were obtained by melt-compounding each of the three polyester matrices with 20% and 40 wt.% AII at 200 °C, using a Brabender bench scale kneader (Brabender GmbH & Co. KG, Duisburg, Germany) equipped with “came” blades (conditions of processing: feeding at 30 rpm for 3 min, followed by 7 min melt-mixing at 100 rpm). The evolution of mechanical torque during the melt-mixing of PLAs and PLA–AII composites was followed and considered as primary rheological information (Figure 3).





**Figure 3.** Comparative evolution of torque during melt-mixing of PLAs and PLA-AII composites using Brabender internal mixers.

In the subsequent step, the materials recovered after the melt-compounding process (after cooling in nitrogen liquid) were ground with a Pulverisette 19 (Fritsch GMBH, Idar-Oberstein, Germany), whereas the specimens for mechanical characterizations were obtained by IM, using a DSM micro injection molding (IM) machine (now Xplore, Sittard, The Netherlands), using the following processing conditions: temperature of IM = 200 °C, mold temperature = 70 °C. For the sake of comparison, neat PLAs were processed using similar conditions as with the mineral filled composites. Throughout this contribution, all percentages are given as weight percent (wt.%).

#### 2.4. Methods of Characterization

(a) Thermogravimetric analyses (TGA) were performed using a TGA Q50 (TA Instruments, New Castle, DE, USA) by heating the samples under nitrogen or air from room temperature (RT) up to a max. 800 °C (platinum pans, heating ramp of 20 °C/min, 60 cm<sup>3</sup>/min gas flow rate).

(b) Differential Scanning Calorimetry (DSC) measurements were accomplished by using a DSC Q200 from TA Instruments (New Castle, DE, USA) under nitrogen flow. In the case of PLAs and PLA composites, the procedure was as follows: first heating scan at 10 °C/min from 0 °C up to 200 °C, isotherm at these temperature for 2 min, then cooling by 10 °C/min to −20 °C, and finally, a second heating scan from −20 to 200 °C at 10 °C/min. The first scan was used to erase the prior thermal history of the polymer samples. The events of interest linked to the crystallization of PLA during DSC cooling scan, i.e., the crystallization temperatures ( $T_c$ ) and the enthalpies of crystallization ( $\Delta H_c$ ), were quantified using TA Instruments Universal Analysis 2000 software (Version 3.9A (TA Instruments—Waters LLC, New Castle, DE, USA)). Noteworthy, all data were normalized to the amounts of PLA from the samples. The thermal parameters were also evaluated in the second DSC heating scan and abbreviated as follows: glass transition temperature ( $T_g$ ), cold crystallization temperature ( $T_{cc}$ ), enthalpy of cold crystallization ( $\Delta H_{cc}$ ), melting peak temperature ( $T_m$ ), melting enthalpy ( $\Delta H_m$ ), and final DC ( $\chi$ ). The DC (degree of crystallinity) was determined using the following general equation:

$$\chi = \frac{(\Delta H_m - \Delta H_{cc})}{\Delta H_m^0 \times W_{PLA}} \times 100 (\%)$$

where  $\Delta H_m$  and  $\Delta H_{cc}$  are the enthalpies of melting and of cold-crystallization, respectively,  $W$  is the weight fraction of PLA in composites, and  $\Delta H_m^0$  is the melting enthalpy of 100% crystalline PLA considered 93 J/g [42]. Notable, the DC was calculated by subtracting the enthalpy of cold crystallization ( $\Delta H_{cc}$ ) and of pre-melt crystallization (if it was evidenced on DSC curves), from the enthalpy of melting ( $\Delta H_m$ ).

To have information about the DC of specimens produced by IM, the properties of PLA and PLA-AII composites of interest were evaluated following the first DSC scan. The DSC technique was also used to evidence the transformation of gypsum by heating to 400 °C (the limit of instrument).

(c) Mechanical testing: Tensile tests were performed with a Lloyd LR 10K bench machine (Lloyd Instruments Ltd., Bognor Regis, West Sussex, UK) according to the ASTM D638-02a norm on specimens-type V at a crosshead speed of 1 mm/min. For the characterization of Izod impact resistance, a Ray-Ran 2500 pendulum impact tester and a Ray-Ran 1900 notching apparatus (Ray-Ran Test Equipment Ltd., Warwickshire, UK) were used according to ASTM D256 norm (method A, 3.46 m/s impact speed, 0.668 kg hammer). For both tensile and impact tests, the specimens produced by IM were previously conditioned for at least 48 h at  $23 \pm 2$  °C under relative humidity of  $50 \pm 5\%$ , and the values were averaged over minimum five measurements.

(d) DMA (Dynamic Mechanical Analysis) were performed on rectangular specimens ( $60 \times 12 \times 2$  mm<sup>3</sup>) obtained by IM (DSM micro-IM machine) using a DMA 2980 apparatus (TA Instruments, New Castle, DE, USA) in dual cantilever bending mode. The dynamic storage and loss moduli ( $E'$  and  $E''$ , respectively) were determined at a constant frequency of 1 Hz and amplitude of 20  $\mu$ m as a function of temperature from  $-20$  °C to 140 °C, at a heating rate of 3 °C/min.

(e) Vicat softening temperature (VST) measurements were performed according to ASTM D1525, using HDT/Vicat 3-300 Allround A1 (ZwickRoell GmbH & Co, Ulm, Germany) equipment. The samples with thickness of 3.2 mm were rectangular shaped ( $12 \times 10$  mm<sup>2</sup>). All samples were evaluated under a load of 1000 g and at a heating rate of 120 °C/h using minimum 3 specimens.

(f) Scanning Electron Microscopy (SEM) analyses on the PLA samples, previously cryofractured at a liquid nitrogen temperature, were performed using a Philips XL scanning electronic microscope (Eindhoven, Netherlands) at various accelerated voltages and magnitudes. For better information and easy interpretation, the SEM was equipped for both secondary (SE) and back scattered electrons (BSE) imaging. Reported microphotographs represent typical morphologies as observed at, at least, three distinct locations. SEM analyses of AII microparticles were performed at different magnifications in the SE mode (5 kV accelerated voltage). SEM analyses were also performed on the surfaces of selected specimens fractured by tensile or impact testing.

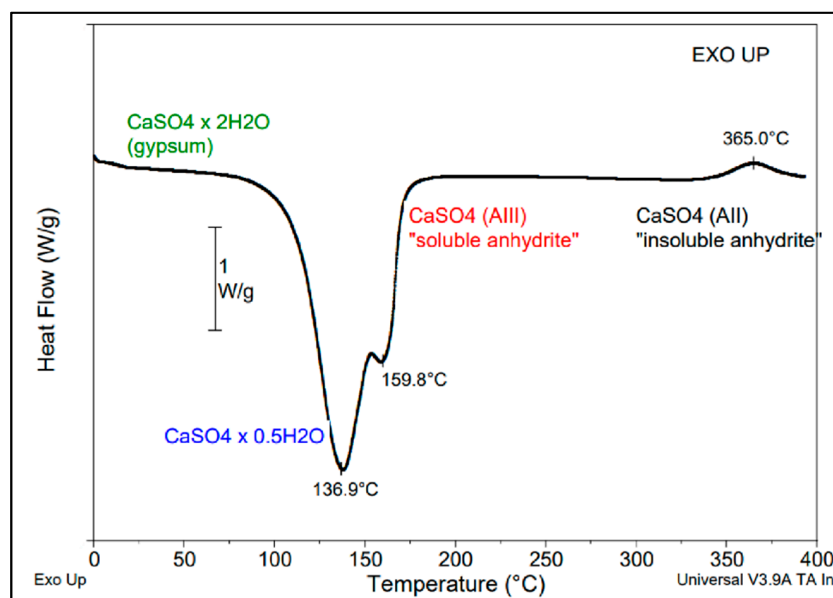
(g) X-ray diffraction (XRD) characterization: The morphological analysis of CS powders by X-ray diffraction was performed on a Siemens D5000 diffractometer (Siemens AG, Munich, Germany) using Cu K $\alpha$  radiation (wavelength, 1.5406 Å) at RT, for  $2\theta$  from 10° to 90° (scanning step 0.026).

### 3. Results and Discussion

#### 3.1. New Evidence of CS AII Stability as Filler for the Industry of Polymer Composites

It is a noteworthy reminder that CS is available in several forms: dihydrate—CaSO<sub>4</sub>·2H<sub>2</sub>O (commonly known as gypsum), hemihydrate—CaSO<sub>4</sub> 0.5H<sub>2</sub>O (Plaster of Paris, stucco, or bassanite), and different types of anhydrite [43–45]. The dehydration of gypsum (CS dihydrate) above 100 °C at low pressure (vacuum) or under air at atmospheric pressure, favors  $\beta$ -CS hemihydrate formation. An increase in the temperature to about 200 °C allows producing so called  $\beta$ -anhydrite III ( $\beta$ -AIII)—which is not stable, whereas calcination at temperatures higher than 350 °C (e.g., at 500–800 °C in an industrial process) allows obtaining stable  $\beta$ -anhydrite II (abbreviated as AII). The CS phases obtained by progressive dehydration and calcination of gypsum at higher temperatures are in the following

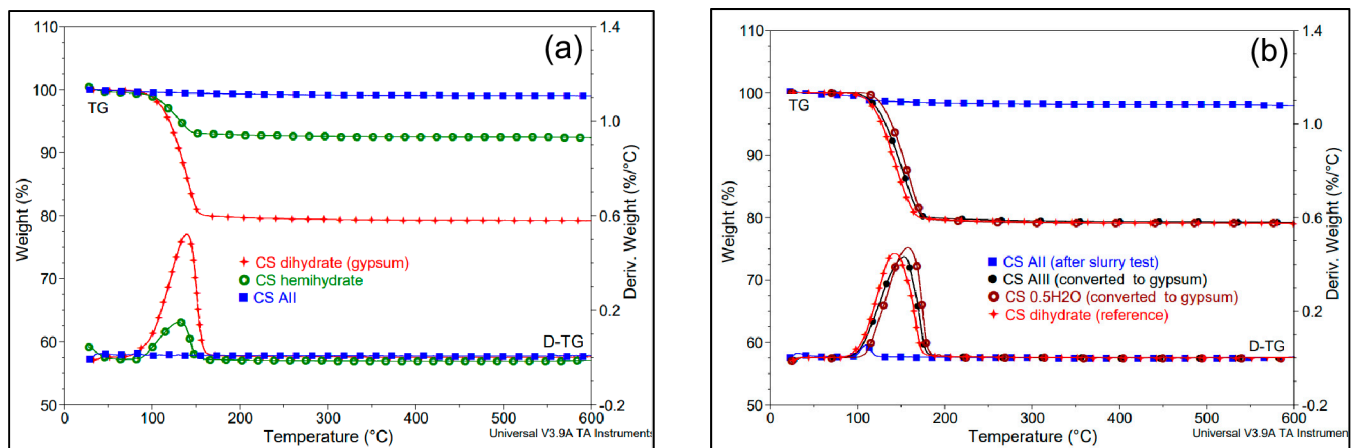
order [43]: dihydrate  $\rightarrow$  hemihydrate  $\rightarrow$  anhydrite III  $\rightarrow$  anhydrite II  $\rightarrow$  anhydrite I (at temperatures higher than 1180 °C). DSC is a powerful tool of analysis that can be considered to evidence the thermal transformations of CS dihydrate during heating (Figure 4). Accordingly, in the first step, the gypsum was transformed at about 140 °C in  $\beta$ -CS hemihydrate. When the hemihydrate was heated at higher temperature it was converted into “soluble” anhydrite—AIII (endothermal process, a shoulder was observed at about 160 °C on DSC curve), and above 350 °C, “insoluble” anhydrite ( $\beta$ -AII) was generated, as evidenced by the exothermal transformation on DSC curves.



**Figure 4.** Thermal transformations of CS dihydrate as revealed by DSC heating to 400 °C (DSC method, 10 °C/min).

To allow the use of CS in the production of polymer composites (e.g., based on polyesters, such as PLA), we restate that it is of prime importance to dry (dehydrate) the CS dihydrate or hemihydrate prior melt-compounding, or the use of stable anhydrite forms is required, keeping in mind the importance of minimizing free moisture. Indeed, PLA is stable in the molten state provided that it is adequately stabilized and dried to have a maximum acceptable water content of 250 ppm, or even below 50 ppm, in the case of processing at high temperature [3]. Moreover, following a comparative study, it has been reported elsewhere that synthetic  $\beta$ -AII (made from gypsum from the LA production process), is much better suited for melt-blending with PLA than  $\beta$ -AIII, which is by far too sensitive to atmospheric water absorption [29]. Indeed, AIII has a dramatically quick uptake of water, which was evidenced at the start of the thermogravimetric analyses, thus its rapid transformation to CS hydrated forms can be assumed. Moreover, in the case of AIII analyzed by XRD, it was reported that the high humidity triggered an instant transformation into CS hemihydrate (bassanite) [46]. Accordingly, due to its instability, AIII is not recommended for melt-blending with polymers with high sensitivity to degradation by hydrolysis during processing at high temperature.

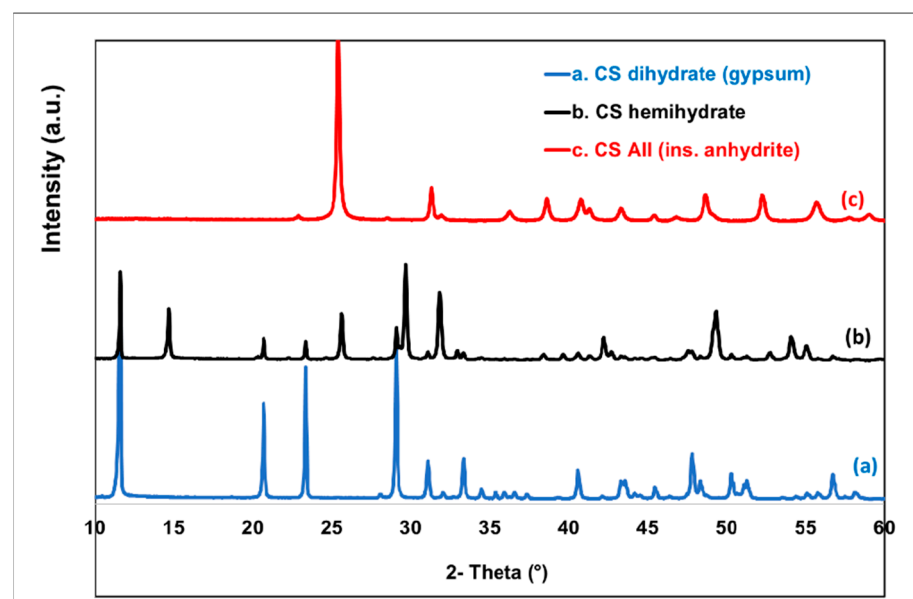
Figure 5a shows the comparison of thermogravimetric analyses (TG) of CS derivatives produced from natural gypsum by thermal treatments at different temperatures. AII showed a particularly good thermal stability in all ranges of temperature (with a weight loss lower than 1% by heating to 600 °C). On the contrary, CS dihydrate and CS hemihydrate record a weight loss of 20–21% and 6–7%, respectively, in the dehydration process step (below 200 °C).



**Figure 5.** (a,b) Comparative TG and D-TG traces (20 °C/min, under N<sub>2</sub>). (a) CS hydrated forms (dihydrate and hemihydrate) and AII; (b) samples recovered after the slurry tests: CS (AII) after 24 h mixing in water as slurry; CS (AIII) converted to gypsum; CS hemihydrate converted to gypsum; CS dihydrate (reference).

The comparative TGAs of the recovered products after the slurry tests (Figure 5b) evidence only some low content of superficial water/moisture in the sample labelled “AII”, without fully excluding the presence of some traces of sub-hydrates. On the other hand, the total rehydration with the formation of gypsum in the case of CS hemihydrate and of AIII, was confirmed by the high amount of water lost during heating (21–22%).

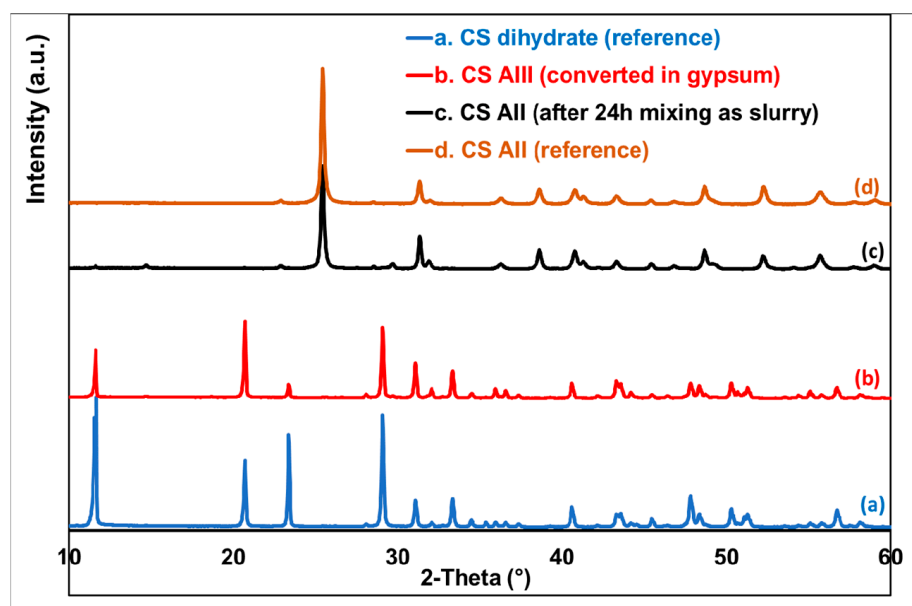
Interestingly, the XRD technique is also largely used to evidence the differences between the various CS derivatives [46]. Figure 6 shows the comparative XRD patterns of products obtained following the transformation of gypsum at different calcination temperatures (see experimental section) to obtain  $\beta$ -CS hemihydrate and  $\beta$ -AII. AIII was not included here due to its sensitivity to moisture and its quick transformation into hydrated forms. For CS dihydrate (gypsum), five major diffraction peaks, i.e., (020), (021), (130), (041), and (−221), have been reported elsewhere [47]. Positions (2 $\theta$ ) of these peaks were confirmed in the present study, respectively, at 11.6°, 20.7°, 23.4°, 29.1°, and 31.1°, whereas additional XRD peaks were observed at higher 2 $\theta$  angle.



**Figure 6.** XRD patterns of CS AII and of CS hydrated forms.

The diffractogram of  $\beta$ -CS hemihydrate featured specific peaks at  $2\theta \approx 14.7, 25.6, 29.7,$  and  $31.9^\circ$  [48]. The presence of a supplementary peak at  $2\theta \approx 11.6$  (seen also for CS dihydrate) is reasonably ascribed to the inherent absorption of moisture, leading to traces of other CS hydrated forms. After the dehydration and thermal treatments (i.e., at  $500^\circ\text{C}$ ) of gypsum (monoclinic crystal system), the crystalline structure of the obtained CS  $\beta$ -anhydrite II (AII) was different, i.e., orthorhombic [49]. It was characterized by only one intense peak at  $2\theta \approx 25.4^\circ$  and a number of smaller ones at higher scattering angles [31].

On the other hand, Figure 7 shows the results of XRD analyses of selected samples recovered after the slurry tests. Accordingly, the following was found: when mixing in water only AII was stable, keeping its original crystalline structure as evidenced by the same XRD peaks, while the other CS forms (such as AIII and CS hemihydrate) were rehydrated to gypsum (CS dihydrate).



**Figure 7.** XRD patterns to evidence the stability of AII following the slurry tests.

These new results respond to the current questions asked by potential users requiring evidence of AII stability following contact with moisture/water. AII exhibited the closest packing of ions, which makes it highly dense and strong, whereas the absence of empty channels means it reacts slowly with water [43].

By considering its overall properties (high thermal stability, whiteness, low hardness (Mohs), very low solubility/rate of rehydration, others), AII can be considered a promising natural filler for the industry of polymer composites.

### 3.2. Characterization of PLA–AII Composites

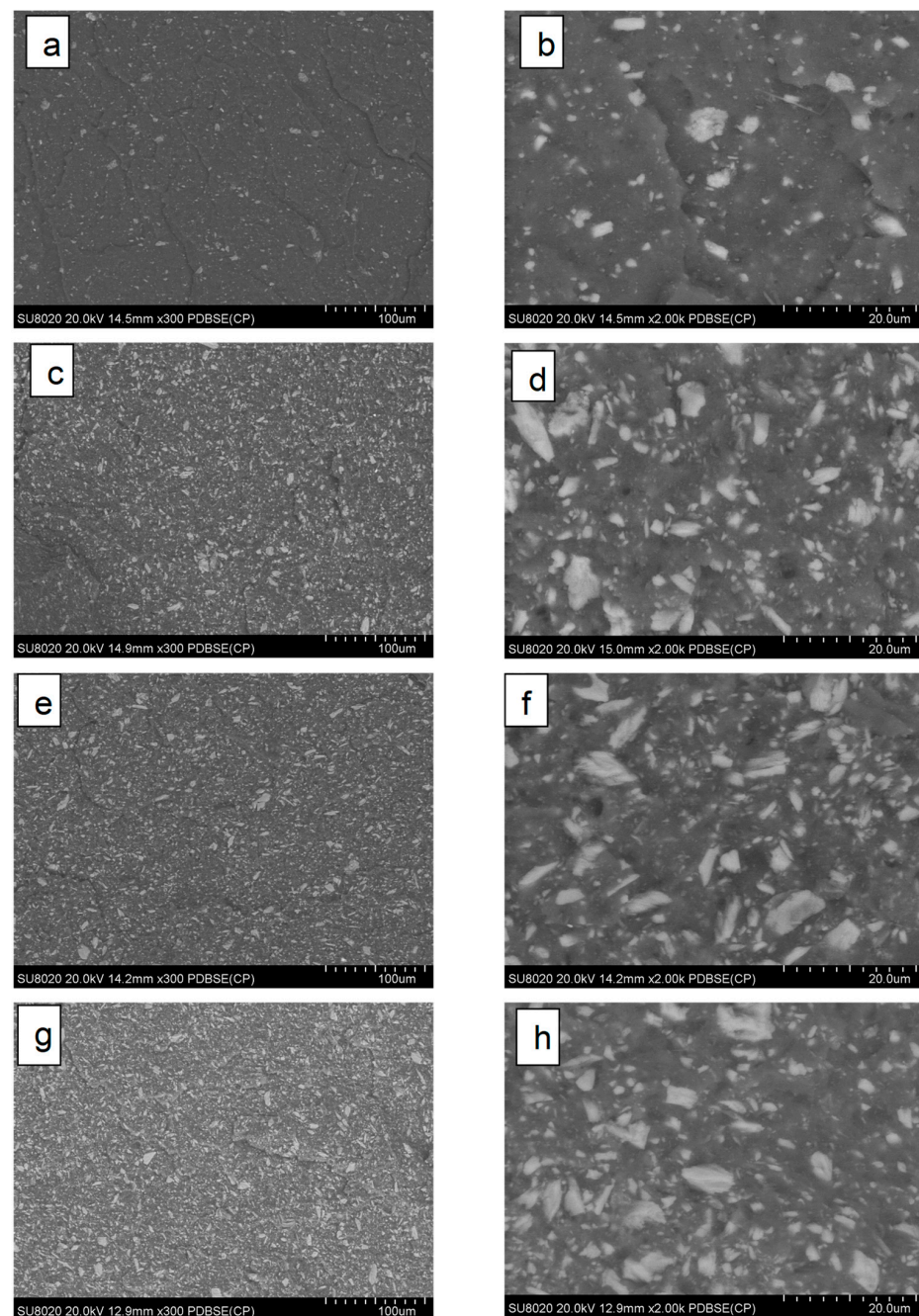
First, it is important to point out that the results discussed hereinafter concern the use of AII without any surface treatments, whereas the PLAs used as polymer matrices are characterized by different molecular weights ( $M_{WPLA1} > M_{WPLA2} > M_{WPLA3}$ ) and rheology, to allow adapted melt processing techniques (e.g., extrusion or IM). Furthermore, for PLA2 and PLA3 (PLA grades of high fluidity designed for IM), the attention will be focused on the differences linked to the purity in L-lactic acid enantiomer.

By considering the evolution of torque values during melt mixing process as primary rheological information, in all cases the addition of filler (AII) into PLA led to the increase in mechanical torque/melt viscosity. Furthermore, the torque was clearly determined by the molecular weights of PLAs (see Figure 3, experimental part) and the following order was seen by melt-mixing at the temperature of  $200^\circ\text{C}$ : PLA1–40% AII > PLA1 > PLA2–40% AII > PLA2 > PLA3–40% AII > PLA3.

### 3.2.1. Morphology of PLA-AII Composites

After the grinding process, the microparticles of AII used for this study had a volume median diameter of  $\sim 5 \mu\text{m}$  (analysis of granulometry by DLS). The particulate filler was characterized by a low aspect ratio, whereas a shared morphology, i.e., particles with irregular shape and fibrillar/flaky aspect due to the cleavage of CS layers, was evidenced by SEM (Figure 1, section Materials).

Regarding the morphology of composites, for better evidence of filler distribution through PLA matrix, SEM imaging was performed using back scattered electrons (BSE) to obtain a higher phase contrast. Figure 8a–h shows representative SEM-BSE images of cryofractured surfaces of PLA–AII composites with 20–40% filler.



**Figure 8.** (a–h) SEM–BSE pictures at low and high magnification of cryofractured surfaces of PLA–AII composites having different PLA matrices: (a,b) PLA1–20% AII; (c,d) PLA1–40% AII; (e,f) PLA2–40% AII; (g,h) PLA3–40% AII.

Well-distributed/dispersed particles, with various geometries and quite broad size distribution were evidenced at the surface of cryofractured specimens. A cryofracture characterizing moderate, but effective adhesion between filler (AII) and PLA, can be assumed by considering the overall SEM images, but also considering the mechanical performances of composites. It is worth a reminder that such quality of dispersion was obtained without any previous surface treatment of filler. However, better individual particles dispersion was easily obtained at lower filler content (20% AII) (Figure 8a,b), whereas at high filling (40 wt.%), the presence of some aggregates/some zones with poorer dispersion was not totally excluded. Furthermore, it is difficult to conclude that following the melt-compounding with internal mixers led to important differences regarding the morphology of composites (i.e., in relation to the type of PLA matrix and the rheology of blends, which is essentially determined at similar amounts of filler by the molecular weights of PLA).

### 3.2.2. Thermogravimetric Analysis (TGA)

The results of thermal characterizations by TGA (Table 2) allow concluding that the addition of AII into different PLAs primarily leads to composites characterized by similar or better thermal properties than those of neat polymers processed under similar conditions. Interestingly, following the comparison of processed PLAs, PLA1 showed better thermal characteristics than PLA2 and PLA3. This difference was also seen in the case of composites, and it is reasonably ascribed to the higher molecular weights of PLA1. An increase in the onset of thermal degradation ( $T_{5\%}$ , temperature corresponding to 5% weight loss) and of maximum decomposition temperature ( $T_d$ , from max. D-TG) was found as a general tendency by filling PLAs with up to 40% AII. However, more spectacular changes were observed when PLA2 or PLA3 was used as the polymer matrix. Furthermore, from the D-TG curves, it is observed that the rate of thermal degradation (wt.%/°C) at the temperature corresponding to the max. rate of degradation was much reduced/delayed in the case of composites, in quite good correlation with the amounts of filler. The enhancement of thermal stability by filling PLA with AII is a key-property in the perspective of processing and further application of such materials. For additional insight, the comparative TG and D-TG curves of neat PLAs and PLA-(20–40)% AII composites are shown in the Supplementary Material Figure S1a–c.

**Table 2.** Thermal parameters of PLAs and PLA-AII composites as determined by TGA.

Sample	Onset of Thermal Degradation ( $T_{5\%}$ ), °C	Temp. at Max. Rate of Degradation, °C (From D-TG)	Max. Degradation Rate, wt.%/°C (From D-TG)
PLA1	341	376	2.7
PLA1–20% AII	345	382	2.2
PLA1–40% AII	342	378	1.7
PLA2	317	362	2.1
PLA2–20% AII	320	372	2.2
PLA2–40% AII	330	377	1.7
PLA3	320	369	2.5
PLA3–20% AII	330	370	2.1
PLA3–40% AII	335	378	1.5

### 3.2.3. Differential Scanning Calorimetry (DSC)

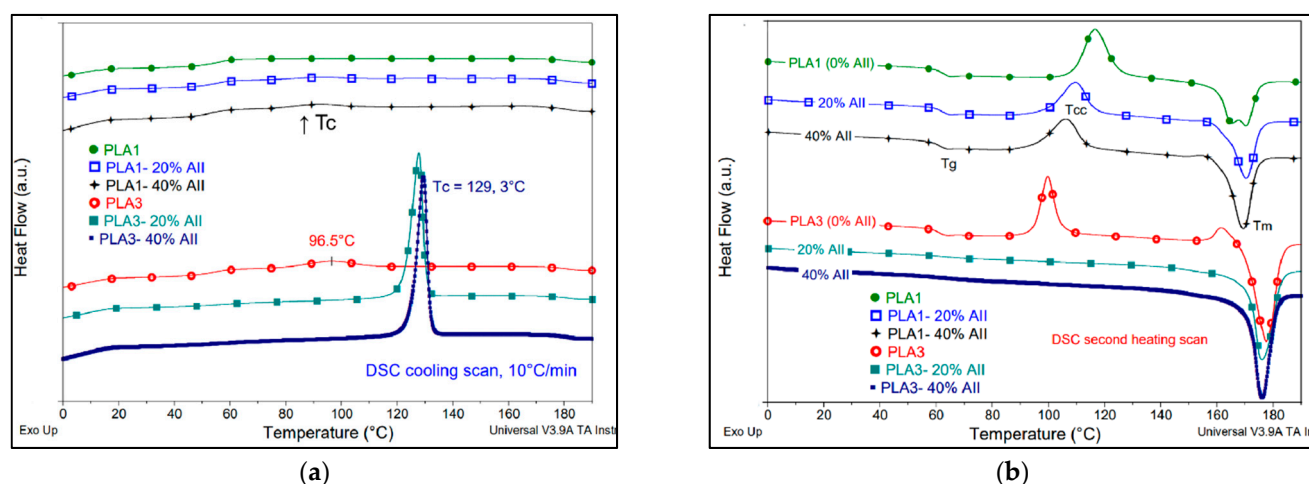
It is generally recognized that the PLAs of higher L-isomer purity (less than 1% D-isomer) are characterized by higher kinetics of crystallization, properties that can be improved in the presence of nucleating agents, to allow the utilization in applications requiring high HDT [50]. In contrast, PLA resins of higher D-isomer content (4–8%) are more suitable for thermoformed, extruded, and blow molded products, since they are

more easily processed when the crystallinity is lower [3]. First, from the DSC analyses (Table 3 and Figure 9a,b) it was observed that the addition of AII had beneficial effects on the crystallization of PLA, distinctly evidenced for PLA1 and especially for PLA3 as a polymer matrix.

**Table 3.** Comparative DSC results of neat PLAs and PLA–AII composites obtained using different PLA grades as polymer matrix (second DSC heating scan, by 10 °C/min).

Sample (%, by Weight)	T <sub>g</sub> (°C)	T <sub>cc</sub> (°C)	ΔH <sub>cc</sub> (J g <sup>-1</sup> )	T <sub>m</sub> * (°C)	ΔH <sub>m</sub> (J g <sup>-1</sup> )	χ * %
PLA1	63	116	35.4	166; 170	37.1	1.8
PLA1–20% AII	62	109	26.2	170	37.8	12.5
PLA1–40% AII	61	106	27.4	169	45.4	19.4
PLA2	61	135	1.6	154	2.3	0.8
PLA2–20% AII	61	133	5.7	153	6.5	0.9
PLA2–40% AII	62	133	3.5	153	5.3	1.9
PLA3	61	100 (161)	28.9 (5.2)	177	62.7	30.8
PLA3–20% AII	ND **	-	-	176	55.7	59.9
PLA3–40% AII	ND	-	-	176	55.3	59.5

\* χ-DC as calculated by subtracting ΔH<sub>cc</sub> from ΔH<sub>m</sub> and by considering an enthalpy of 93 J/g for 100% crystalline PLA; ND: \*\* not detectable on DSC curve.



**Figure 9.** (a,b). Comparative DSC curves of neat PLAs (PLA1 and PLA3) and those of PLA1–AII and PLA3–AII composites obtained during (a) cooling and (b) second DSC heating (10 °C/min).

Moreover, the DSC curves obtained during cooling and second heating scans clearly revealed that the association of AII with PLA3 of high L-isomer purity ( $\geq 99\%$ ) characterized by medium molecular weights (macromolecular chains with increased mobility during cooling process), yielded to composites characterized by surprising kinetics of crystallization and a high DC. In fact, the DC remarkably increased from 31% (neat-PLA3 processed) to about 60% in composites (PLA3–(20–40)% AII). Moreover, the effect of the filler was also significant using PLA1 as the matrix (PLA of higher molecular weights, D-isomer = 1.4%), the composites being characterized by better/moderate crystallization ability, determined by the level of filler: the DC of PLA1 (1.8%) increased in composites up to about 20%.

Still, using PLA2 with higher D-enantiomer content (4.3%), there were no important changes in crystallinity (Table 3 and Figure S2 from the Supplementary Material). The DC of neat PLA2 and of composites remained very low (DC < 2%) and only were slightly affected by the amount of filler. Regarding the cold crystallization process recorded in the second DSC scan, PLA2 had a lower crystallization ability (T<sub>cc</sub> determined at high

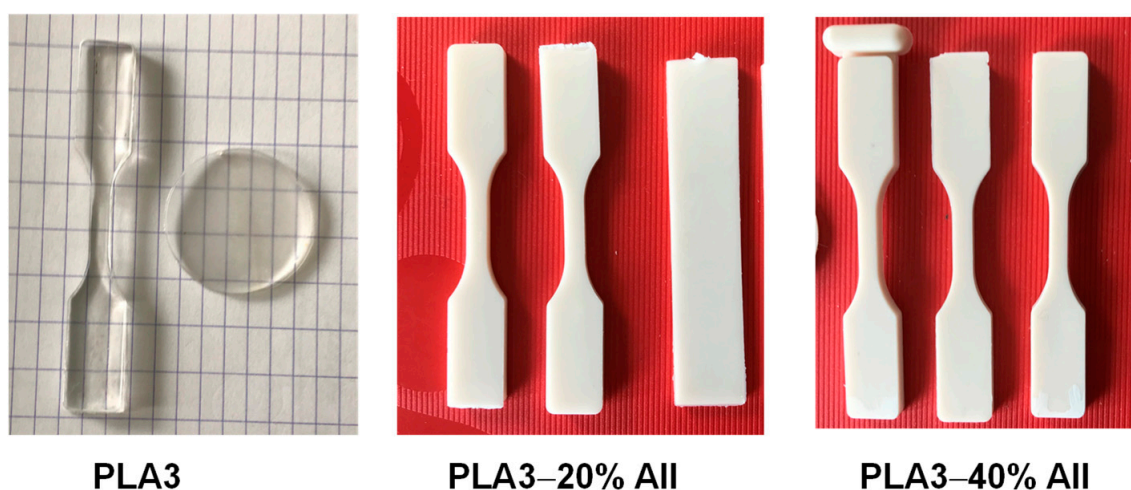


temperatures, i.e., 133–135 °C), whereas for PLA1 samples,  $T_{cc}$  decreased with the amount of filler, from 116 °C to 106 °C. However, by comparing the neat PLAs and their respective composites, for most of the samples, there was no significant modification of glass transition and melting temperatures ( $T_g$  and  $T_m$ ).

In relation to the results of DSC characterizations, it was once more proved that the highest kinetics of crystallization/DC are obtained by reducing the molecular weights of PLA and using PLA of higher L-enantiomer purity [51], i.e., for PLA3. Still, the addition of AII into PLA3 leads to composites of interest for technical applications (by considering the overall performances of composites), because they show a superior DC, properties reasonably ascribed to the nucleating effects of filler and inherent characteristics of the polymer matrix.

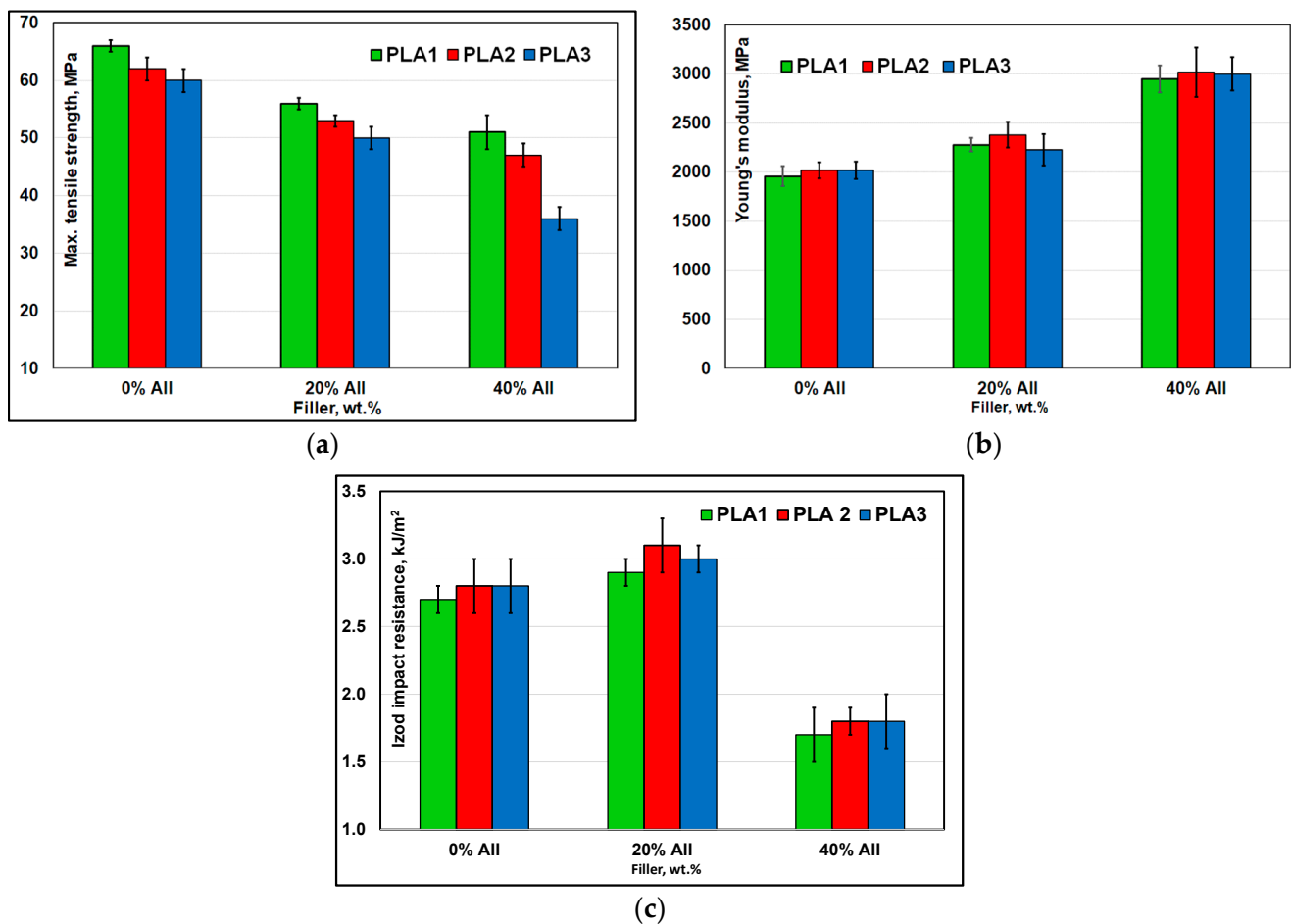
### 3.2.4. Mechanical Characterizations

The specimens for mechanical testing (Figure 10) were produced by IM (see experimental section). The strength of particulate-filled polymer composites depends, to a great extent, on the properties of the matrix, the interfacial adhesion between the matrix and dispersed phase, the filler shape, size, and amount [52]. Noteworthy, comprehensive studies regarding the interfacial adhesion between the PLA and microfiller (AII) have been realized using different techniques by the research group of Pukánszky B. and collab. [53].



**Figure 10.** Selected pictures to illustrate the aspect of specimens of PLA and PLA–AII composites produced by IM.

Figure 11a–c summarizes the results of mechanical characterizations of neat PLAs and their respective composites filled with 20–40% AII. For composites, the tensile strength gradually decreased with the loading of filler, e.g., adding 20% AII, from 60–66 MPa (neat PLAs) to 50–56 MPa for composites, values which are of real interest for engineering applications. In contrast, Young's modulus (Figure 11b) was significantly enhanced (from  $\approx 2000$  MPa, neat PLAs) to a value of about 3000 MPa by filling with 40% AII, without any significant influence linked to the nature of PLAs. Moreover, when we compared the values of tensile strength ( $\sigma$ ) of neat PLAs and PLA–AII composites, it was observed that they followed the same order ( $\sigma_{PLA1} > \sigma_{PLA2} > \sigma_{PLA3}$ ) as that of molecular weights ( $M_{wPLA1} > M_{wPLA2} > M_{wPLA3}$ ). Accordingly, at high filling (40% AII), it is worth noting the tensile strength of composites obtained using PLA1 and PLA2 as matrix (51 MPa and 47 MPa, respectively). As expected, all PLAs had low nominal strain at break (about 5%), values that decreased to 2–3% for composites.



**Figure 11.** (a–c). Comparative mechanical characterizations of PLAs with different amounts of filler: (a) Maximum tensile strength; (b) Young's modulus; (c) Izod impact resistance (notched specimens).

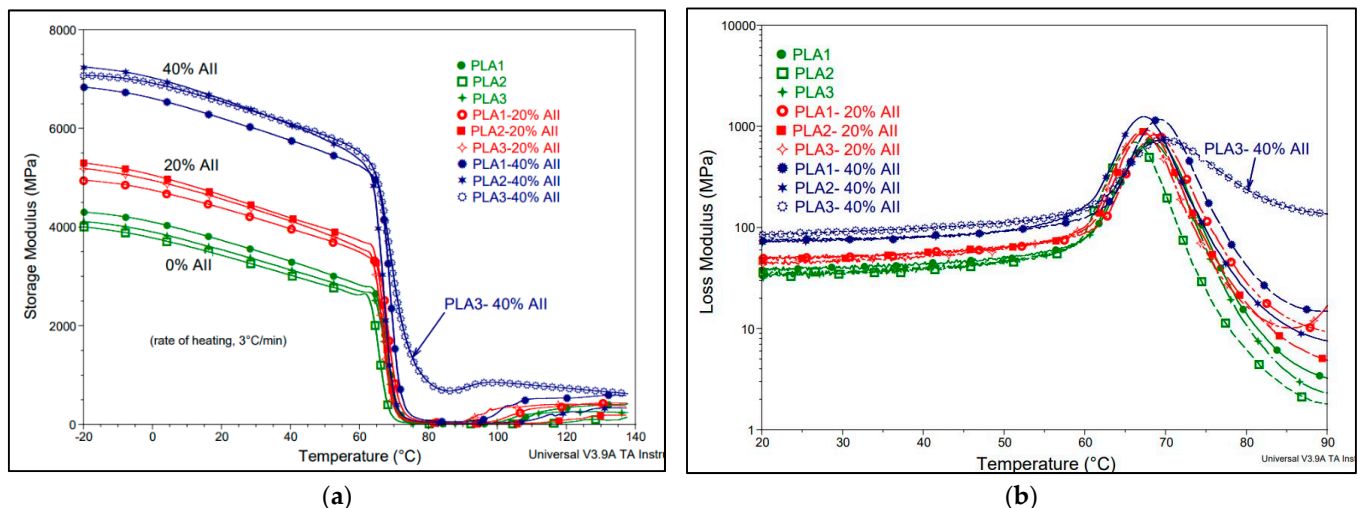
Regarding the impact resistance, it has been reported in the literature that in some cases, well dispersed particulate fillers, at optimal loadings or having specific surface treatment, can contribute to the increase in impact properties [54,55]. Interestingly, the Izod impact resistance of composites (Figure 11c) was slightly improved by incorporating 20% AII in each of the three studied PLAs, whereas a further increase in filler content to 40% led to an important reduction in this parameter. In the case of PLA–20% AII composites, it is once more proved that well distributed/dispersed rigid/particulate microparticles can contribute to the dissipation of impact energy by reducing the crack propagation by different mechanisms (e.g., by crack-bridging [56] or crack pinning, which require certain adhesion between polymer and filler; whereas the debonding at matrix–particle interface is also for consideration as mechanism [48]). However, additional SEM images performed on fractured samples by tensile or impact testing (Supplementary Material, Figures S3 and S4) suggested that at the interface zone (PLA matrix–filler) were seen both regions, accounting for the good/moderate adhesion due to the maintaining of intimate physical contact between constituents after the mechanical solicitation (which explains the noticeable tensile properties), and zones of debonding or shear yielding, traditionally ascribed to a toughening mechanism with rigid particles, with contribution in reducing the cracking and in dissipating the energy of impact solicitation [37,54,55].

On the other hand, at higher filling (i.e., 40 wt.%), due to the inherent presence of more heterogeneous (mechanically weak) regions, e.g., aggregates of microparticles, they may act as stress concentrators, causing a decrease in tensile and impact resistance. Therefore, for applications in which the impact strength is a key-concern, these composites need to be modified to fulfil the industry requirements [2]. Modification of filler (AII) by special

surface treatments or/and the addition of a third component into PLA–AII composites, i.e., a plasticizer [55], an impact modifier [37,57], etc., can represent alternatives of choice for better impact resistance performances.

### 3.2.5. Dynamic Mechanical Analysis (DMA)

DMA has been used to provide information about the performances of PLA–AII composites in a broad temperature range (i.e., from  $-20\text{ }^{\circ}\text{C}$  to  $140\text{ }^{\circ}\text{C}$ ). Figure 12a,b shows the evolution of storage and loss modulus ( $E'$  and  $E''$ , respectively) of neat PLAs and their composites as a function of the temperature. In correlation with AII percentage,  $E'$  increased distinctly in the low-temperature glassy region for all composite samples (Figure 12a), trends that are like those recorded for the evolution of Young’s modulus in tensile tests, highlighting the reinforcing effect of filler. This increase is ascribed to considerable interfacial properties, allowing the stress transfer at low deformations, which finally is expressed in the enhancements of  $E'$  and Young modulus with filler content [48]. Undeniably, as it is revealed as key example in Table 4, at the temperature of  $60\text{ }^{\circ}\text{C}$  (very close to  $T_g$ ), the loading of filler was responsible for the level of  $E'$ , apparently without some influence linked to the nature of PLA matrix.  $E'$  was twofold increased for PLA composites filled with 40% AII compared to the unfilled PLAs.



**Figure 12.** (a,b). Dependencies of (a)  $E'$  (storage modulus) and (b)  $E''$  (loss modulus) vs. temperature: neat PLAs compared with PLA–AII composites.

**Table 4.** Effects of AII addition on the values of storage modulus ( $E'$ ) at the temperature of  $60\text{ }^{\circ}\text{C}$  for different PLA matrices.

AII Content →	0%	20%	40%
↓ PLA Matrix	↓ Storage Modulus ( $E'$ ), GPa		
PLA1	2.8	3.5	5.2
PLA2	2.6	3.7	5.4
PLA3	2.7	3.6	5.5

Figure 12b shows the evolution of  $E''$  (loss modulus) as a function of temperature. The results showed that the composites were characterized by slightly higher  $E''$ , determined by the filler loading, an increase assigned to the contribution of the mechanical loss generated in the interfacial regions [48]. However, the max. peak of  $E''$  ascribed to the  $T_g$  zone was only slightly changed, from  $66\text{--}68\text{ }^{\circ}\text{C}$  for the neat PLAs to max.  $70\text{ }^{\circ}\text{C}$  upon AII filling, results that are in good agreement with DSC data.

Still, due to the highly filling and increased crystallinity at higher temperatures (i.e., in the range  $80\text{--}140\text{ }^{\circ}\text{C}$ ), PLA3-40% AII composites showed the most important enhancements

of both,  $E'$  and  $E''$ . As demonstrated under dynamic solicitation by DMA, melt-blending of PLA with AII offers the possibility to produce PLA composites for applications requiring enhanced mechanical rigidity and higher temperature of utilization.

### 3.2.6. Vicat Softening Temperature (VST)

It is generally assumed that the fillers can be effective reinforcement phases leading to the improvement in specific thermal properties, such as HDT and VST, mostly in semi-crystalline polymers (polyethylene (PE), PP, polyamide (PA), etc.). The VSTs of neat PLAs were around 62–63 °C (Figure 13), whereas the addition of 20–40% filler into PLA1 and PLA2 led only to a slight increase in VST to about 65 °C. On the other hand, somewhat unexpectedly, when considering the melt processing conditions (the temperature of the mold was around 70 °C, without any additional annealing process to obtain higher crystallinity), the most remarkable enhancements were obtained for PLA3–AII composites, i.e., an increase in VST to 160 °C, primarily ascribed to the high level of crystallinity. In fact, the IM tests highlighted that the association PLA3 with AII leads to PLA composites characterized by remarkable crystallization kinetics, that allows the production of items with high DC. Indeed, the comparative DSC analyses performed on IM specimens (Supplementary Material, Figure S5a–c), confirmed the high DC (49–53%) of PLA3–AII composites, results that are in good agreement with those presented in the section thermal characterizations (DSC).

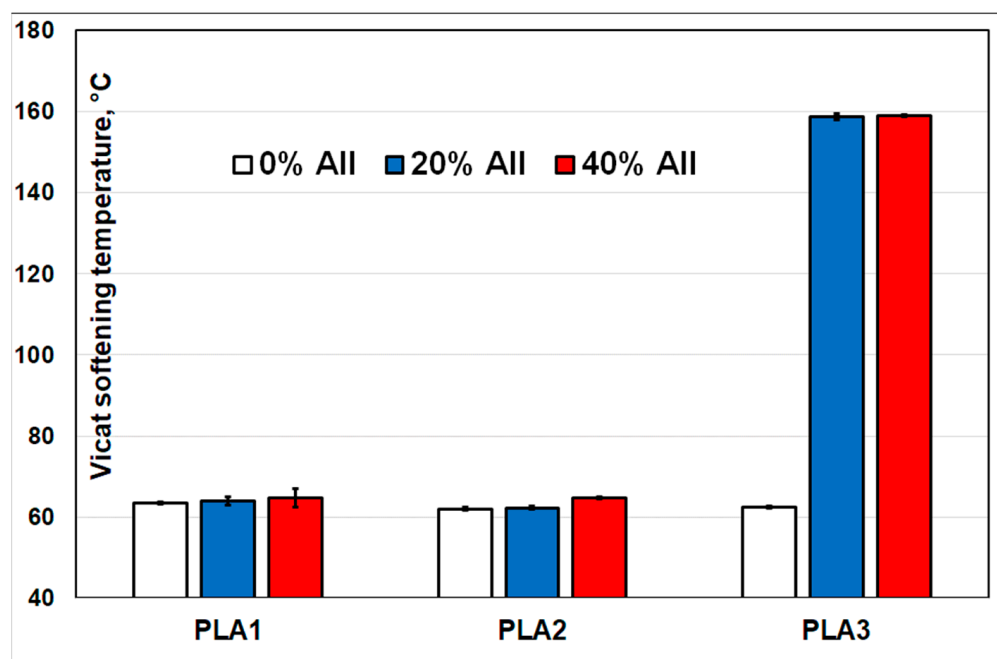


Figure 13. Vicat softening temperature (VST) of PLAs with different amounts of filler.

Before concluding, it is important to mention that the composites concerned in this study need further optimization by taking into account the constraints imposed by application (e.g., the amount of filler is a key-parameter), and this it is expected to be realized following their production in higher quantities using for melt-compounding twin-screw extruders. Moreover, in the frame of forthcoming contributions, it will be important to reconfirm the performances of composites using optimized processing conditions (extrusion, IM, etc.) and also to determine other characteristics of interest (flexural strength, HDT, rheological behaviour and MFI, evolution of molecular parameters as function of the residence time at high temperature and shear, etc.). Furthermore, the studies on crystallization mechanisms using alternative techniques of investigation (polarized light microscopy (POM), XRD, etc.), are of further concern.

#### 4. Conclusions

The study provides answers to current requests regarding the production of environmentally friendly materials using PLAs as a matrix (biosourced and biodegradable) and the utilization of mineral fillers such as CS  $\beta$ -AII made from natural gypsum.

New tests and specific characterizations were performed to prove the stability of AII as produced by the calcination of gypsum at high temperature (i.e., 500 °C), in comparison to other CS derivatives. Characterized by excellent thermal stability and low absorption of moisture/water of rehydration, so called “insoluble” AII is stable, maintaining its crystal structure even after mixing in water as slurry. Moreover, the overall results confirmed that CS  $\beta$ -AII is a filler of real interest for the industry of polymer composites.

PLAs of different L-lactic acid isomer purity and molecular weights (as supplied for distinct processing techniques) were used to produce by melt-compounding composites filled with 20–40% AII. The addition of filler leads to composites characterized by enhanced thermal stability and increased rigidity (Young’s modulus), determined by the amount of filler. Interestingly, PLA impact resistance was not decreased when up to 20% filler was added, whereas the ultimate strength properties were dependent on the molecular characteristics of PLA matrix, keeping a similar order (PLA1 > PLA2 > PLA3). The values of tensile strength (e.g., 50–56 MPa, for PLA–20% AII composites) are of real interest for engineering applications. Melt-blending PLA with AII leads to two-fold enhancement of storage modulus (at 60 °C) and offers the possibility to use PLA in applications requiring enhanced mechanical rigidity and/or higher temperature of utilization. The good thermo-mechanical properties are ascribed to the fine distribution and dispersion of AII within PLA matrix, and favorable interfacial interactions between components.

Advanced kinetics of crystallization linked to the addition of AII were evidenced by DSC for PLA3 of high L-isomer purity ( $\geq 99\%$ ) and lower molecular weights. Still, following the IM processing, the properties of crystallization remain impressive in the case of PLA3 filled with 20–40% AII (DC of about 50%), whereas a VST of 160 °C was attained on IM specimens (only 63 °C for the neat PLA). By considering the overall performances (tensile strength, stiffness, VST, other specific properties), these composites are proposed for development/production at larger scale, as a quick answer to current requests for the use of PLA-based products in engineering applications. Nevertheless, by the carefully choosing the PLA matrix, these “green” mineral filled (AII) composites can be designed for processing by IM, extrusion, thermoforming, and 3D printing.

**Supplementary Materials:** The following supporting information can be downloaded at: <https://www.mdpi.com/article/10.3390/polym14122360/s1>, as Supplementary Material: Figure S1a–c. TG and D-TG curves of neat PLAs and PLA–(20–40)% AII composites (under air, 20 °C/min): (a) PLA1 and PLA1–AII; (b) PLA2 and PLA2–AII; (c) PLA3 and PLA3–AII composites; Figure S2: Comparative DSC curves of neat PLA2 and those of PLA2–AII composites, as obtained during second DSC heating (10 °C/min).; Figure S3: SEM images (SE mode) of PLA–AII composites performed on the fractured surfaces obtained after tensile testing.; Figure S4: SEM images (SE mode) of PLA1–(20–40)% AII composites performed on fractured surfaces obtained by impact testing.; Figure S5a–c. Comparative DSC analyses on injection molded specimens of PLA and PLA–AII composites assessing for the higher degree of crystallinity (DC) of PLA3–AII composites (first DSC scan, 10 °C/min).

**Author Contributions:** Data curation, M.M. and O.M.; Formal analysis, M.M., Y.P. and O.M.; Funding acquisition, M.M. and F.L.; Investigation, M.M., Y.P. and O.M.; Supervision, P.D.; Writing—original draft, M.M.; Writing—review & editing, M.M., F.L. and P.D. All authors have read and agreed to the published version of the manuscript.

**Funding:** This research was funded by Toro Gips S.L. (Barcelona, Spain), grant “TOROGYPS”, and by the Materia Nova R&D Center using internal funding.

**Institutional Review Board Statement:** Not applicable.

**Informed Consent Statement:** Not applicable.

**Data Availability Statement:** Not applicable.

**Acknowledgments:** The authors wish to thank Toro Gips S.L. (Barcelona, Spain) for supplying ToroWhite (CS) samples and for accepting the publication of the scientific results obtained in the frame of the TOROGYPS project. Special thanks are addressed to Erdem Kütükçü and Ludwig Soukup from Toro Gips S.L. for the kind collaboration and fruitful discussions regarding ToroWhite products. The authors are also grateful to all scientific partners involved in the FEDER - INTERREG III (FRANCE-WALLONIE-FLANDRE Program) MABIOLAC project (FW-1.3.17) for the initial contribution to the development of the topics linked to this study.

**Conflicts of Interest:** The authors declare no conflict of interest. The funders gave their agreement for the publication of scientific results, and they had no role in the design of the study; in the collection, analyses, or interpretation of data; in the writing of the manuscript.

## References

- Babu, R.P.; O'Connor, K.; Seeram, R. Current progress on bio-based polymers and their future trends. *Prog. Biomater.* **2013**, *2*, 8. [[CrossRef](#)] [[PubMed](#)]
- Murariu, M.; Dubois, P. PLA composites: From production to properties. *Adv. Drug Deliv. Rev.* **2016**, *107*, 17–46. [[CrossRef](#)] [[PubMed](#)]
- Lim, L.T.; Auras, R.; Rubino, M. Processing technologies for poly(lactic acid). *Prog. Polym. Sci.* **2008**, *33*, 820–852. [[CrossRef](#)]
- Bai, H.; Deng, S.; Bai, D.; Zhang, Q.; Fu, Q. Recent advances in processing of stereocomplex-type polylactide. *Macromol. Rapid Commun.* **2017**, *38*, 1700454. [[CrossRef](#)]
- Chow, W.; Teoh, E.; Karger-Kocsis, J. Flame retarded poly(lactic acid): A review. *Express Polym. Lett.* **2018**, *12*, 396–417. [[CrossRef](#)]
- Wróblewska-Krepsztul, J.; Rydzkowski, T.; Borowski, G.; Szczypiński, M.; Klepka, T.; Thakur, V.K. Recent progress in biodegradable polymers and nanocomposite-based packaging materials for sustainable environment. *Int. J. Polym. Anal. Charact.* **2018**, *23*, 383–395. [[CrossRef](#)]
- Rezvani Ghomi, E.; Khosravi, F.; Saedi Ardahaei, A.; Dai, Y.; Neisiany, R.E.; Foroughi, F.; Wu, M.; Das, O.; Ramakrishna, S. The life cycle assessment for polylactic acid (PLA) to make it a low-carbon material. *Polymers* **2021**, *13*, 1854. [[CrossRef](#)]
- Aframehr, W.M.; Molki, B.; Heidarian, P.; Behzad, T.; Sadeghi, M.; Bagheri, R. Effect of calcium carbonate nanoparticles on barrier properties and biodegradability of polylactic acid. *Fibers Polym.* **2017**, *18*, 2041–2048. [[CrossRef](#)]
- Tripathi, N.; Misra, M.; Mohanty, A.K. Durable polylactic acid (PLA)-based sustainable engineered blends and biocomposites: Recent developments, challenges, and opportunities. *ACS Eng. Au* **2021**, *1*, 7–38. [[CrossRef](#)]
- Auras, R.; Harte, B.; Selke, S. An overview of polylactides as packaging materials. *Macromol. Biosci.* **2004**, *4*, 835–864. [[CrossRef](#)]
- Yang, Y.; Zhang, M.; Ju, Z.; Tam, P.Y.; Hua, T.; Younas, M.W.; Kamrul, H.; Hu, H. Poly(lactic acid) fibers, yarns and fabrics: Manufacturing, properties and applications. *Text. Res. J.* **2020**, *91*, 1641–1669. [[CrossRef](#)]
- Avinc, O.; Khoddami, A. Overview of Poly(lactic acid) (PLA) fibre. *Fibre Chem.* **2009**, *41*, 391–401. [[CrossRef](#)]
- Nagarajan, V.; Mohanty, A.K.; Misra, M. Perspective on polylactic acid (PLA) based sustainable materials for durable applications: Focus on toughness and heat resistance. *ACS Sustain. Chem. Eng.* **2016**, *4*, 2899–2916. [[CrossRef](#)]
- DeStefano, V.; Khan, S.; Tabada, A. Applications of PLA in modern medicine. *Eng. Regen.* **2020**, *1*, 76–87. [[CrossRef](#)]
- Kim, H.S.; Park, B.H.; Choi, J.H.; Yoon, J.S. Mechanical properties and thermal stability of poly(l-lactide)/calcium carbonate composites. *J. Appl. Polym. Sci.* **2008**, *109*, 3087–3092. [[CrossRef](#)]
- Yu, W.; Wang, X.; Ferraris, E.; Zhang, J. Melt crystallization of PLA/talc in fused filament fabrication. *Mater. Des.* **2019**, *182*, 108013. [[CrossRef](#)]
- Fowlks, A.C.; Narayan, R. The effect of maleated polylactic acid (PLA) as an interfacial modifier in PLA-talc composites. *J. Appl. Polym. Sci.* **2010**, *118*, 2810–2820. [[CrossRef](#)]
- Ge, X.; Chang, M.; Jiang, W.; Zhang, B.; Xing, R.; Bulin, C. Selective location of kaolin and effects of maleic anhydride in kaolin/poly( $\epsilon$ -caprolactone)/poly(lactic acid) composites. *Appl. Clay Sci.* **2020**, *189*, 105524. [[CrossRef](#)]
- Yang, J.N.; Xu, Y.X.; Nie, S.B.; Cheng, G.J.; Tao, Y.L.; Zhu, J.B. Morphological structure, impact toughness, thermal property and kinetic analysis on the cold crystallization of poly(lactic acid) bio-composites toughened by precipitated barium sulfate. *Polym. Degrad. Stab.* **2018**, *158*, 176–189. [[CrossRef](#)]
- Utami, D.P.; Sunarso; Eriwati, Y.K.; Triaminingsih, S.; Indrani, D.J.; Innawaty, D. Improvement of bone filler materials using granular calcium sulfate dihydrate-gelatin-polycaprolactone composite. In *Key Engineering Materials*; Trans Tech Publications Ltd.: Bach, Switzerland, 2020; Volume 829, pp. 63–68.
- Thomas, M.V.; Puleo, D.A. Calcium sulfate: Properties and clinical applications. *J. Biomed. Mater. Res. Part B Appl. Biomater.* **2009**, *88*, 597–610. [[CrossRef](#)]
- Saroia, J.; Wang, Y.; Wei, Q.; Lei, M.; Li, X.; Guo, Y.; Zhang, K. A review on 3D printed matrix polymer composites: Its potential and future challenges. *Int. J. Adv. Manuf. Technol.* **2020**, *106*, 1695–1721. [[CrossRef](#)]
- Gao, C.; Gao, J.; You, X.; Huo, S.; Li, X.; Zhang, Y.; Zhang, W. Fabrication of calcium sulfate/PLLA composite for bone repair. *J. Biomed. Mater. Res. Part A* **2005**, *73*, 244–253. [[CrossRef](#)] [[PubMed](#)]

24. Zhang, S.H.; Gan, W.J.; Sun, W.X.; Ling, C.J.; Wang, X.; Li, Q.F. Study on structures and properties of CaSO<sub>4</sub> whiskers/PVC composites. *Adv. Mater. Res.* **2011**, 335–336, 234–239. [[CrossRef](#)]
25. Ma, P.; Chen, H.; Zhang, Q.; Wang, J.; Xiang, L. Preparation of hierarchical CaSO<sub>4</sub> whisker and its reinforcing effect on PVC composites. *J. Nanomater.* **2018**, 2018, 7803854. [[CrossRef](#)]
26. Dong, F.; Liu, J.; Tan, H.; Wu, C.; He, X.; He, P. Preparation of calcium sulfate hemihydrate and application in polypropylene composites. *J. Nanosci. Nanotechnol.* **2017**, 17, 6970–6975. [[CrossRef](#)]
27. Saujanya, C.; Radhakrishnan, S. Structure and properties of PP/CaSO<sub>4</sub> composite part iii: Effect of the filler grade on properties. *J. Mater. Sci.* **2000**, 35, 2319–2323. [[CrossRef](#)]
28. Liu, J.; Ren, L.; Wei, Q.; Wu, J.L.; Liu, S.; Wang, Y.; Li, G. Microstructure and properties of polycaprolactone/calcium sulfate particle and whisker composites. *Polym. Compos.* **2012**, 33, 501–508. [[CrossRef](#)]
29. Murariu, M.; Da Silva Ferreira, A.; Degée, P.; Alexandre, M.; Dubois, P. Polylactide compositions. Part 1: Effect of filler content and size on mechanical properties of PLA/calcium sulfate composites. *Polymer* **2007**, 48, 2613–2618. [[CrossRef](#)]
30. Murariu, M.; Da Silva Ferreira, A.; Pluta, M.; Bonnaud, L.; Alexandre, M.; Dubois, P. Polylactide (PLA)–CaSO<sub>4</sub> composites toughened with low molecular weight and polymeric ester-like plasticizers and related performances. *Eur. Polym. J.* **2008**, 44, 3842–3852. [[CrossRef](#)]
31. Pluta, M.; Murariu, M.; Alexandre, M.; Galeski, A.; Dubois, P. Polylactide compositions. The influence of ageing on the structure, thermal and viscoelastic properties of PLA/calcium sulfate composites. *Polym. Degrad. Stab.* **2008**, 93, 925–931. [[CrossRef](#)]
32. Murariu, M.; Ferreira, A.D.S.; Duquesne, E.; Bonnaud, L.; Dubois, P. Polylactide (PLA) and highly filled PLA—calcium sulfate composites with improved impact properties. In *Macromolecular Symposia*; WILEY-VCH Verlag: Weinheim, Germany, 2008; Volume 272, pp. 1–12. [[CrossRef](#)]
33. Mecking, S. Nature or petrochemistry?—Biologically degradable materials. *Angew. Chem. Int. Ed.* **2004**, 43, 1078–1085. [[CrossRef](#)] [[PubMed](#)]
34. Narayanan, N.; Roychoudhury, P.K.; Srivastava, A. L (+) lactic acid fermentation and its product polymerization. *Electron. J. Biotechnol.* **2004**, 7, 167–178.
35. Vink, E.T.H.; Davies, S. Life cycle inventory and impact assessment data for 2014 Ingeo™ polylactide production. *Ind. Biotechnol.* **2015**, 11, 167–180. [[CrossRef](#)]
36. Sobkowicz, M.J.; Feaver, J.L.; Dorgan, J.R. Clean and green bioplastic composites: Comparison of calcium sulfate and carbon nanospheres in polylactide composites. *CLEAN—Soil Air Water* **2008**, 36, 706–713. [[CrossRef](#)]
37. Pluta, M.; Murariu, M.; Dechief, A.-L.; Bonnaud, L.; Galeski, A.; Dubois, P. Impact-modified polylactide–calcium sulfate composites: Structure and properties. *J. Appl. Polym. Sci.* **2012**, 125, 4302–4315. [[CrossRef](#)]
38. Murariu, M.; Bonnaud, L.; Yoann, P.; Fontaine, G.; Bourbigot, S.; Dubois, P. New trends in polylactide (PLA)-based materials: “Green” PLA–calcium sulfate (nano)composites tailored with flame retardant properties. *Polym. Degrad. Stab.* **2010**, 95, 374–381. [[CrossRef](#)]
39. Ramos, F.J.H.T.V.; Mendes, L.C. Recycled high-density polyethylene/gypsum composites: Evaluation of the microscopic, thermal, flammability, and mechanical properties. *Green Chem. Lett. Rev.* **2014**, 7, 199–208. [[CrossRef](#)]
40. Harris, A.M.; Lee, E.C. Improving mechanical performance of injection molded PLA by controlling crystallinity. *J. Appl. Polym. Sci.* **2008**, 107, 2246–2255. [[CrossRef](#)]
41. Singh, N.B.; Middendorf, B. Calcium sulphate hemihydrate hydration leading to gypsum crystallization. *Prog. Cryst. Growth Charact. Mater.* **2007**, 53, 57–77. [[CrossRef](#)]
42. Yoo, H.M.; Jeong, S.-Y.; Choi, S.-W. Analysis of the rheological property and crystallization behavior of polylactic acid (Ingeo™ biopolymer 4032D) at different process temperatures. *e-Polymers* **2021**, 21, 702–709. [[CrossRef](#)]
43. Wirsching, F. Calcium sulfate. In *Ullmann's Encyclopedia of Industrial Chemistry*, 2012th ed.; Wiley-VCH Verlag GmbH & Co. KGaA: Weinheim, Germany, 2012; Volume 6, pp. 519–550.
44. Fatu, D. Kinetics of gypsum dehydration. *J. Therm. Anal. Calorim.* **2001**, 65, 213–220. [[CrossRef](#)]
45. Lushnikova, N.; Dvorkin, L. Sustainability of gypsum products as a construction material. In *Sustainability of Construction Materials*, 2nd ed.; Khatib, J., Ed.; Elsevier: Amsterdam, The Netherlands, 2016; Chapter 25; pp. 643–682.
46. Seufert, S.; Hesse, C.; Goetz-Neunhoeffler, F.; Neubauer, J. Quantitative determination of anhydrite III from dehydrated gypsum by XRD. *Cem. Concr. Res.* **2009**, 39, 936–941. [[CrossRef](#)]
47. Inoue, M.; Hirasawa, I. The relationship between crystal morphology and XRD peak intensity on CaSO<sub>4</sub>·2H<sub>2</sub>O. *J. Cryst. Growth* **2013**, 380, 169–175. [[CrossRef](#)]
48. Pluta, M.; Murariu, M.; Da Silva Ferreira, A.; Alexandre, M.; Galeski, A.; Dubois, P. Polylactide compositions. II. Correlation between morphology and main properties of PLA/calcium sulfate composites. *J. Polym. Sci. Part B Polym. Phys.* **2007**, 45, 2770–2780. [[CrossRef](#)]
49. Beaugnon, F.; Quiligotti, S.; Chevreux, S.; Wallez, G. On the monoclinic distortion of β-anhydrite CaSO<sub>4</sub>. *Solid State Sci.* **2020**, 108, 106399. [[CrossRef](#)]
50. Aliotta, L.; Cinelli, P.; Coltelli, M.B.; Righetti, M.C.; Gazzano, M.; Lazzeri, A. Effect of nucleating agents on crystallinity and properties of poly (lactic acid) (PLA). *Eur. Polym. J.* **2017**, 93, 822–832. [[CrossRef](#)]
51. Müller, A.J.; Ávila, M.; Saenz, G.; Salazar, J. Chapter 3 Crystallization of PLA-based materials. In *Poly(Lactic Acid) Science and Technology: Processing, Properties, Additives and Applications*; The Royal Society of Chemistry: London, UK, 2015; pp. 66–98.

52. Liang, J.-Z. Toughening and reinforcing in rigid inorganic particulate filled poly(propylene): A review. *J. Appl. Polym. Sci.* **2002**, *83*, 1547–1555. [[CrossRef](#)]
53. Imre, B.; Keledi, G.; Renner, K.; Móczó, J.; Murariu, M.; Dubois, P.; Pukánszky, B. Adhesion and micromechanical deformation processes in PLA/CaSO<sub>4</sub> composites. *Carbohydr. Polym.* **2012**, *89*, 759–767. [[CrossRef](#)]
54. Zuiderduin, W.C.J.; Westzaan, C.; Huétink, J.; Gaymans, R.J. Toughening of polypropylene with calcium carbonate particles. *Polymer* **2003**, *44*, 261–275. [[CrossRef](#)]
55. Aliotta, L.; Cinelli, P.; Coltelli, M.B.; Lazzeri, A. Rigid filler toughening in PLA-calcium carbonate composites: Effect of particle surface treatment and matrix plasticization. *Eur. Polym. J.* **2019**, *113*, 78–88. [[CrossRef](#)]
56. Meng, Q.; Wang, T. An improved crack-bridging model for rigid particle-polymer composites. *Eng. Fract. Mech.* **2019**, *211*, 291–302. [[CrossRef](#)]
57. Liu, H.; Zhang, J. Research progress in toughening modification of poly(lactic acid). *J. Polym. Sci. Part B Polym. Phys.* **2011**, *49*, 1051–1083. [[CrossRef](#)]





## Article

# Development of Olive Oil and $\alpha$ -Tocopherol Containing Emulsions Stabilized by FucoPol: Rheological and Textural Analyses

Sílvia Baptista<sup>1,2,3</sup>, João R. Pereira<sup>1,2</sup>, Cátia V. Gil<sup>1,2</sup>, Cristiana A. V. Torres<sup>1,2</sup>, Maria A. M. Reis<sup>1,2</sup> and Filomena Freitas<sup>1,2,\*</sup>

<sup>1</sup> Associate Laboratory i4HB—Institute for Health and Bioeconomy, School of Science and Technology, NOVA University Lisbon, 2829-516 Caparica, Portugal; silvia.baptista@73100.pt (S.B.); jra.pereira@campus.fct.unl.pt (J.R.P.); cv.gil@campus.fct.unl.pt (C.V.G.); c.torres@fct.unl.pt (C.A.V.T.); amr@fct.unl.pt (M.A.M.R.)

<sup>2</sup> UCIBIO—Applied Molecular Biosciences Unit, Department of Chemistry, School of Science and Technology, NOVA University Lisbon, 2819-516 Caparica, Portugal

<sup>3</sup> 73100, Lda. Edifício Arcis, Rua Ivone Silva, 6, 4<sup>o</sup> Piso, 1050-124 Lisboa, Portugal

\* Correspondence: a4406@fct.unl.pt; Tel.: +351-212948357

**Citation:** Baptista, S.; Pereira, J.R.; Gil, C.V.; Torres, C.A.V.; Reis, M.A.M.; Freitas, F. Development of Olive Oil and  $\alpha$ -Tocopherol Containing Emulsions Stabilized by FucoPol: Rheological and Textural Analyses. *Polymers* **2022**, *14*, 2349. <https://doi.org/10.3390/polym14122349>

Academic Editors: José Miguel Ferri, Vicent Fombuena Borràs and Miguel Fernando Aldás Carrasco

Received: 30 April 2022

Accepted: 6 June 2022

Published: 9 June 2022

**Publisher's Note:** MDPI stays neutral with regard to jurisdictional claims in published maps and institutional affiliations.



**Copyright:** © 2022 by the authors. Licensee MDPI, Basel, Switzerland. This article is an open access article distributed under the terms and conditions of the Creative Commons Attribution (CC BY) license (<https://creativecommons.org/licenses/by/4.0/>).

**Abstract:** Biobased raw materials like natural polysaccharides are increasingly sought by the cosmetic industry for their valuable properties. Such biodegradable and usually non-cytotoxic biopolymers are commonly used in skin-care products as rheological modifiers, bioemulsifiers and/or bioactive ingredients. FucoPol is a natural polysaccharide with reported biocompatibility, emulsion-forming and stabilizing capacity, shear-thinning behavior and bioactivity (e.g., antioxidant capacity, wound healing ability) that potentiate its utilization in skin-care products. In this study, olive oil and  $\alpha$ -tocopherol containing emulsions were stabilized with FucoPol. Although the presence of  $\alpha$ -tocopherol negatively impacted the emulsions' stability, it increased their emulsification index (EI). Moreover, FucoPol outperformed the commercial emulsifier Sepigel® 305, under the tested conditions, with higher EI and higher stability under storage for 30 days. The formulation of FucoPol-based emulsions with olive oil and  $\alpha$ -tocopherol was studied by Response Surface Methodology (RSM) that allowed the definition of the ingredients' content to attain high emulsification. The RSM model established that  $\alpha$ -tocopherol concentration had no significant impact on the EI within the tested ranges, with optimal emulsification for FucoPol concentration in the range 0.7–1.2 wt.% and olive oil contents of 20–30 wt.%. Formulations with 25 wt.% olive oil and either 0.5 or 2.0 wt.%  $\alpha$ -tocopherol were emulsified with 1.0 wt.% or 0.7 wt.% FucoPol, respectively, resulting in oil-in-water (O/W) emulsions. The emulsions had similar shear-thinning behavior, but the formulation with higher FucoPol content displayed higher apparent viscosity, higher consistency, as well as higher firmness, adhesiveness and cohesiveness, but lower spreadability. These findings show FucoPol's high performance as an emulsifier for olive oil/ $\alpha$ -tocopherol, which are supported by an effective impact on the physicochemical and structural characteristics of the emulsions. Hence, this natural polysaccharide is a potential alternative to other emulsifiers.

**Keywords:** polysaccharide; FucoPol; response surface methodology; oil-in-water emulsions; rheology; texture

## 1. Introduction

The cosmetics industry's interest in moving towards sustainability has significantly increased the incorporation of natural polymers into cosmetic formulations. Among those, many polysaccharides have properties similar to non-biodegradable synthetic polymers, which makes them environmentally friendly alternative raw materials [1,2]. Specifically, bacterial polysaccharides can be used in formulations as moisturizing agents, thickeners,



as the aqueous phase, at o:w weight ratios of 3:2 and 2:3. The emulsification index (EI, %) and the emulsification stability (ES, %) were determined by the following equations [22]:

$$EI = \frac{h_e}{h_T} \times 100 \quad (1)$$

$$ES = \frac{\text{Final EI}}{\text{Initial EI}} \times 100 \quad (2)$$

where  $h_e$  (mm) is the height of the emulsion layer, and  $h_T$  (mm) is the overall height of the mixture after emulsification. Initial and final EI are the values measured at 24 h and after 720 h (30 days), respectively.

Emulsions with olive oil (o:w weight ratio of 3:2) were also prepared with Sepigel<sup>®</sup> 305, a commercial emulsifier, at concentrations of 0.1 and 0.5 wt.%. An active ingredient,  $\alpha$ -tocopherol, was added to the oil phase at different concentrations (0.0, 2.0, and 5.0 wt.%) and emulsions stabilized with FucoPol or Sepigel<sup>®</sup> (0.5 and 1.0 wt.%) were prepared with olive oil at an o:w weight ratio of 3:2.

#### 2.4. Factorial Design of Experiments

Response surface methodology (RSM) [23] was applied to determine the best formulation to prepare olive oil and  $\alpha$ -tocopherol emulsions stabilized with FucoPol. A five-level three-variable central composite design (CCD) was applied, consisting of seventeen runs, with eight factorial points, six axial points, and three central points (Table 1).

**Table 1.** Independent variables and their levels used in the response surface design.

Independent Variables	Coded Variable	Factor Level				
		$-\alpha$	$-1$	$0$	$1$	$\alpha$
FucoPol (wt.%)	A	0.00	0.30	0.80	1.30	1.64
Olive oil (wt.%)	B	13.18	20.00	30.00	40.00	46.82
$\alpha$ -tocopherol (wt.%)	C	0.00	1.00	2.50	4.00	5.02

The central points are used to determine the experimental error and the reproducibility of the data. The independent variables are coded to have low and high levels of  $-1$  and  $+1$ , respectively. The axial points  $-\alpha$  and  $+\alpha$  were fixed at 1.682 from the central point and make the design rotatable. The mathematical relationship between the independent variables can be approximated by the second-order polynomial model equation:

$$Y = \beta_0 + \sum_{i=1}^n \beta_i x_i + \sum_{i=1}^n \sum_{j=1}^n \beta_{ij} x_i x_j + \sum_{i=1}^n \beta_{ii} x_i^2 \quad (3)$$

where  $Y$  is the predicted response;  $x_i$  are the independent variables ( $n = 3$ ). The parameter  $\beta_0$  is the model constant;  $\beta_i$  are the linear coefficients;  $\beta_{ii}$  are the quadratic coefficients, and  $\beta_{ij}$  are the cross-product coefficients [24]. A full factorial design of experiments was drawn up using the Design-Expert (Design-Expert<sup>®</sup> software package from Stat-Ease Inc.). The validated model was plotted in a three-dimensional graph and a surface response that corresponds to the best emulsification was generated. Analysis of variance (ANOVA) was used to determine the regression coefficients of individual linear, quadratic, and interaction terms.

#### 2.5. Characterization of the Emulsions

##### 2.5.1. Type of Emulsion

The method described by Kavitate et al. [22] was used to determine the type of emulsion. A droplet of the test emulsion was placed onto Whatman<sup>™</sup> filter paper (0.2  $\mu\text{m}$ , GE Healthcare Life Sciences, Munich, Germany) and its ability to disperse on the surface was evaluated.

### 2.5.2. Microscopic Observation

The emulsions were stained with Nile Blue (a lipophilic dye), as described by Martins et al. [25]. Briefly, 10  $\mu\text{L}$  of the emulsion were stained with 1% (*v/v*) Nile Blue A (Sigma-Aldrich, Darmstadt, Germany) and observed in a Zeiss Imager D2 epifluorescence microscope (Carl Zeiss, Oberkochen, Germany), with a magnification of 40 $\times$  through ZEN lite software (Carl Zeiss, Oberkochen, Germany).

### 2.5.3. Viscoelastic Properties

The emulsions' rheological properties were studied using an MCR 92 modular compact rheometer (Anton Paar, Graz, Austria), equipped with a PP50/S parallel plate geometry (diameter 50 mm) and a P-PTD 200/AIR Peltier plate to keep the measurement temperature constant at 25  $^{\circ}\text{C}$ . A steady-state flow ramp was used to determine flow curves for shear rates between 0.01 and 1000  $\text{s}^{-1}$ . The flow curves were fitted to the Cross model [16,26]:

$$\eta = \frac{\eta_0}{1 + (\tau \dot{\gamma})^m} \quad (4)$$

where  $\eta$  is the apparent viscosity (Pa.s),  $\eta_0$  is the viscosity at zero shear rate (Pa.s),  $\tau$  (s) is the relaxation time (s), and  $m$  is a dimensionless constant, related to the exponent of power law ( $n$ ) by  $m = 1 - n$  [13,16]. Frequency sweep tests were performed with frequencies ranging from 0.01 to 16 Hz for a constant strain of 0.5% that was well within the linear viscoelastic limit (LVE) evaluated through preliminary amplitude sweep tests.

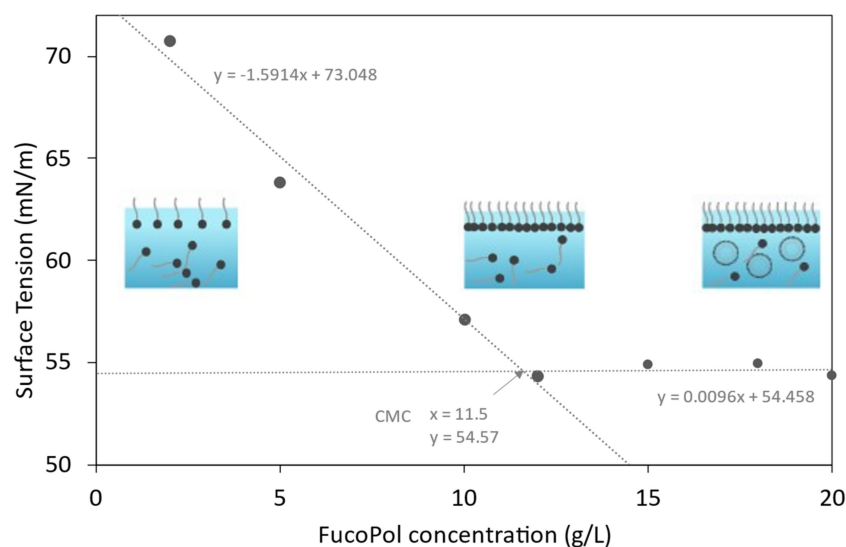
### 2.5.4. Texture Analysis

Texture analysis was performed as described by Tafuro et al. [1]. The firmness, consistency, cohesiveness, and adhesivity of the attained formulations were determined using a texture analyser (TMS-Pro, Food Technology Corporation, Sterling, VA, USA) equipped with a 50 N load cell (Mecmesin, Sterling, VA, USA). The sample was placed in a female conic holder and was compressed 11 mm of depth (which represented a sample deformation of around 70%); this procedure was done twice by a male conic probe at a speed of 2 mm/s. The samples' mechanical parameters were determined from the force–displacement curve: the firmness corresponded to the highest force value attained by the sample during the first compression; the consistency was calculated by the area under the curve of the first compression; the cohesiveness was determined through the ratio of the areas under the curve from the first and the second compressions; and the adhesiveness was determined from the area under the curve from the negative peak attained after the first compression [1,2].

## 3. Results and Discussion

### 3.1. Surface-Active Properties

Figure 1 shows the equilibrium surface tension as a function of FucoPol concentration. Two distinct regions can be identified: up to around 11.5 g/L, there is a reduction of the surface tension with increasing FucoPol concentration, while above such value the surface tension remains constant irrespective of the biopolymer's concentration. FucoPol's critical micelle concentration (CMC) was determined to be approximately 11.5 g/L, given as the point of intersection between the two lines, which correspond to the linear regression of each set of data points [27,28]. This value is considerably higher than those reported for commercial polysaccharides like xanthan and guar gum (approximately 0.15 g/L and 5 g/L, respectively) [29], suggesting a lower thermodynamic stability of the particles system [30]. Nevertheless, FucoPol reduced the surface tension of water from 72 mN/m to 54.6 mN/m at the CMC, a value that is within the range reported for other microbial biosurfactants (34–69 mN/m) [31–33]. Moreover, polymeric biosurfactants, despite not significantly lowering the water's surface tension, are generally more effective in the formation and stabilization of emulsions [31,34].



**Figure 1.** Surface tension of FucoPol solutions at concentrations ranging from 1 to 20 g/L.

### 3.2. Emulsion Forming and Stabilizing Capacity of FucoPol

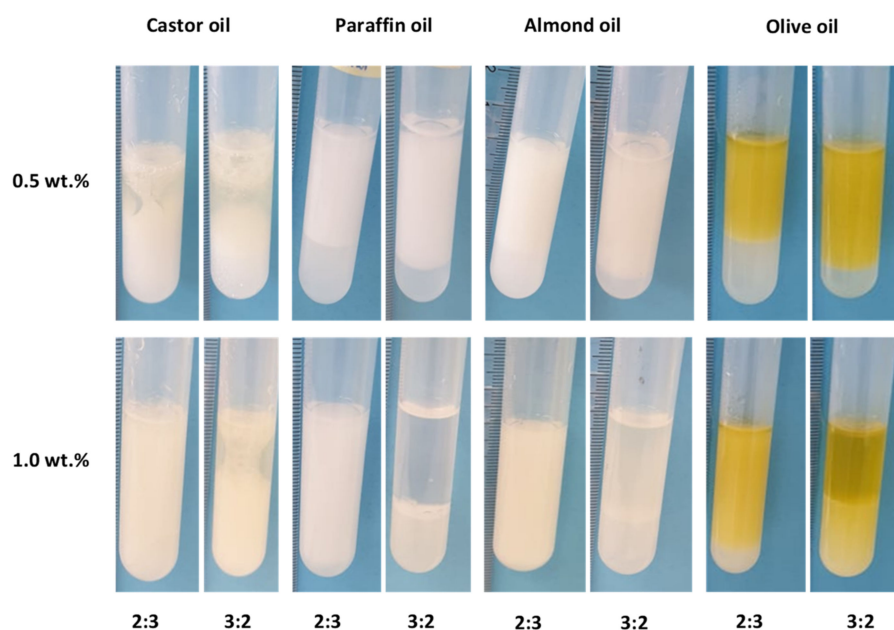
#### 3.2.1. Preparation of FucoPol-Stabilized Emulsions with Different Oils

FucoPol was used to prepare emulsions with four different oils commonly used in cosmetic products' formulations, namely, castor oil [35–38], paraffin oil [39–41], almond oil [42,43] and olive oil [44–48]. Castor oil is a natural oil that acts as an antimicrobial, anti-inflammatory, antioxidant, wound healing, vasoconstrictive [49] and UV-protective agent [50]. Paraffin oil is a petroleum-based derivative that enables the regulation of viscosity in formulations, possessing protective and lubricating properties which prevent skin dehydration [51]. Almond oil, an abundant macro and micronutrients source, is utilized in cosmetics due to its moisturizing and restructuring properties [42]. Olive oil, composed of squalene, phytosterol, tocopherol, vitamins A and E, and fatty acids (oleic and linoleic acids), is indicated for skin applications due to its acidity and soothing effect [16,39,52].

The assays consisted of mixing the biopolymer, at a concentration of 0.5 or 1.0 wt.%, with each oil, at 2:3 or 3:2 weight ratios. As shown in Figure 2, FucoPol efficiently emulsified all the tested hydrophobic compounds, with EI at 24 h (E24) values above 50% (Table 2), which is the criterion for a good emulsifier [53]. For the 2:3 weight ratio, increasing the concentration of the polymer from 0.5 wt.% to 1.0 wt.% resulted in increased E24 for all the tested oils (Table 2). For the 3:2 weight ratio, on the other hand, this was not observed. In fact, for all tested oils, the E24 value decreased except for castor oil (E24 increased from 56 to 100%). All other oils presented negligible emulsification (Figure 2; Table 2). For 0.5 wt.% of FucoPol, increasing the oil ratio from 2:3 to 3:2 resulted in higher E24, except for castor oil.

**Table 2.** Emulsification activity measured at 24 h (E24) and emulsions' stability (ES) for the emulsions stabilized with FucoPol. Data are shown as the average  $\pm$  standard deviation (SD) ( $n = 3$ ).

Oil	FucoPol	E24 (%)		ES (%)	
		2:3	3:2	2:3	3:2
Castor oil	0.5%	70 $\pm$ 3	53 $\pm$ 4	81 $\pm$ 3	77 $\pm$ 4
	1.0%	100 $\pm$ 0	100 $\pm$ 0	20 $\pm$ 0	11 $\pm$ 0
Paraffin oil	0.5%	58 $\pm$ 2	80 $\pm$ 4	87 $\pm$ 5	68 $\pm$ 6
	1.0%	85 $\pm$ 2	6 $\pm$ 0	54 $\pm$ 1	78 $\pm$ 0
Almond oil	0.5%	84 $\pm$ 4	93 $\pm$ 6	50 $\pm$ 3	47 $\pm$ 6
	1.0%	89 $\pm$ 0	0 $\pm$ 0	31 $\pm$ 6	0 $\pm$ 0
Olive oil	0.5%	58 $\pm$ 0	76 $\pm$ 0	85 $\pm$ 2	97 $\pm$ 0
	1.0%	81 $\pm$ 1	56 $\pm$ 0	56 $\pm$ 1	100 $\pm$ 0



**Figure 2.** Emulsions prepared with FucoPol (0.5 or 1.0 wt.%) with castor oil, paraffin oil, almond oil, and olive oil, at o:w weight ratios of 2:3 and 3:2.

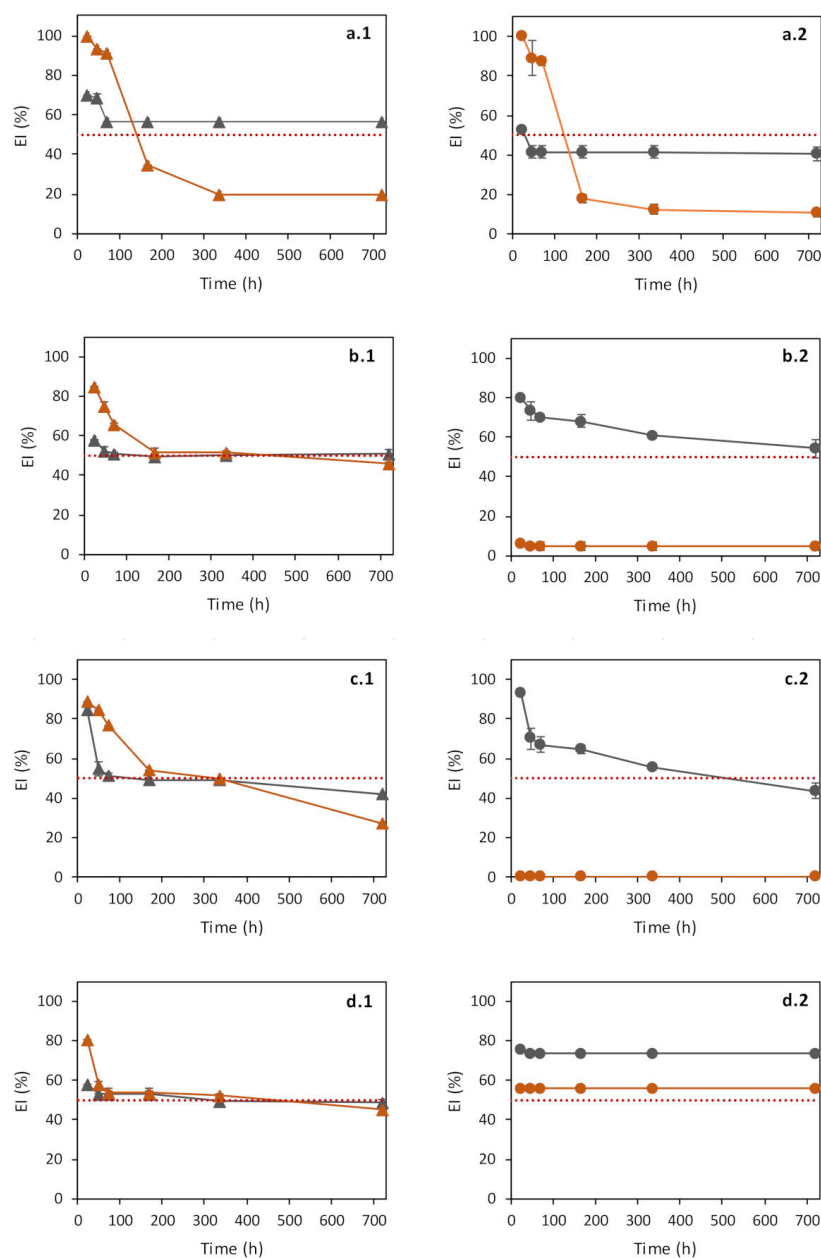
### 3.2.2. Evaluation of Emulsions' Stability

Cosmetic applications require that the emulsions have adequate shelf-life, usually up to six months [47,54–56]. The stability of the emulsions prepared with FucoPol was evaluated at room temperature, by measuring their EI over a period of 720 h (30 days). As shown in Figure 3, FucoPol emulsion stabilizing capacity depended on the o:w weight ratio, as well as on the tested oil. All FucoPol-stabilized emulsions had no detectable changes in odor or color during the storage period.

The least stable sample was the emulsion prepared with castor oil at an o:w weight ratio of 3:2 and a FucoPol concentration of 1.0 wt.% (Figure 3(a.2)). This sample's EI dropped from 100% at 24 h to 18% at 7 days, with an overall ES of 11% (Table 2). Nevertheless, the emulsions prepared with castor oil and 0.5 wt.% FucoPol (Figure 3(a.1,a.2)) were stable for both o:w weight ratios, presenting ES values of  $81 \pm 3\%$  and  $77 \pm 4\%$ , respectively (Table 2).

Most of the emulsions prepared with paraffin oil and almond oil also showed a significant decrease in their EI during the 720 h shelf-life test (Figure 3(b.1–c.2)) with ES values of 0 to 54% (Table 2). Despite the lower E24 values (56–76%), the olive oil/FucoPol emulsions, for both o:w weight ratios tested, showed higher stability (Figure 3(d.1,d.2)), corresponding to ES values of 85–100% (Table 2). Antunes et al. [42] obtained olive oil/FucoPol emulsions in 2:3 and 3:2 (*v/v*) ratios that maintained at least 50% of the initial EI for 9 weeks, which agrees with the results reported in this study.

The results obtained in this study demonstrate that FucoPol is a promising stabilizer for emulsions with any of the tested oils provided the adequate o:w weight ratio and FucoPol concentration are utilized. Castor oil (at the 2:3 weight ratio, 1.0 wt.% FucoPol), paraffin oil (at the 3:2 weight ratio, 0.5 wt.% FucoPol) and olive oil (at the 3:2 weight ratio, 0.5 wt.% FucoPol, and at the 2:3 ratio for either 0.5 or 1.0 wt.% FucoPol) presented high EI and were stable over the 720 h storage period. Given the good results obtained for olive oil and its known biological properties [16,39,52], this oil was chosen for the subsequent studies.



**Figure 3.** Emulsification index (EI%) overtime for emulsions prepared with FucoPol and different hydrophobic compounds: Castor oil (a.1,a.2), paraffin oil (b.1,b.2), almond oil (c.1,c.2) and olive oil (d.1,d.2), for FucoPol concentrations of 0.5 wt.% (gray) and 1.0 wt.% (orange), for o:w weight ratios of 2:3 (left) and 3:2 (right). The red dashed line represents EI (%) = 50. ( $n = 3$ ).

### 3.2.3. Assaying $\alpha$ -Tocopherol as an Additive to the FucoPol-Stabilized Emulsions

The effect of  $\alpha$ -tocopherol, an antioxidant commonly used in cosmetic formulations [57,58], on FucoPol/olive oil emulsions were evaluated by testing different concentrations of this additive on the EI and on the emulsions' stability. According to the risk profile of tocopherols [59], the maximum concentration of  $\alpha$ -tocopherol allowed in cosmetic products is 5 wt.%. Nonetheless, the  $\alpha$ -tocopherol concentration in the skin care cosmetics below 0.2% is sufficient to protect lipids against peroxidation [60]. Therefore,  $\alpha$ -tocopherol at concentrations of 2.0 and 5.0 wt.% were selected for testing as an additive in FucoPol/olive oil emulsions.

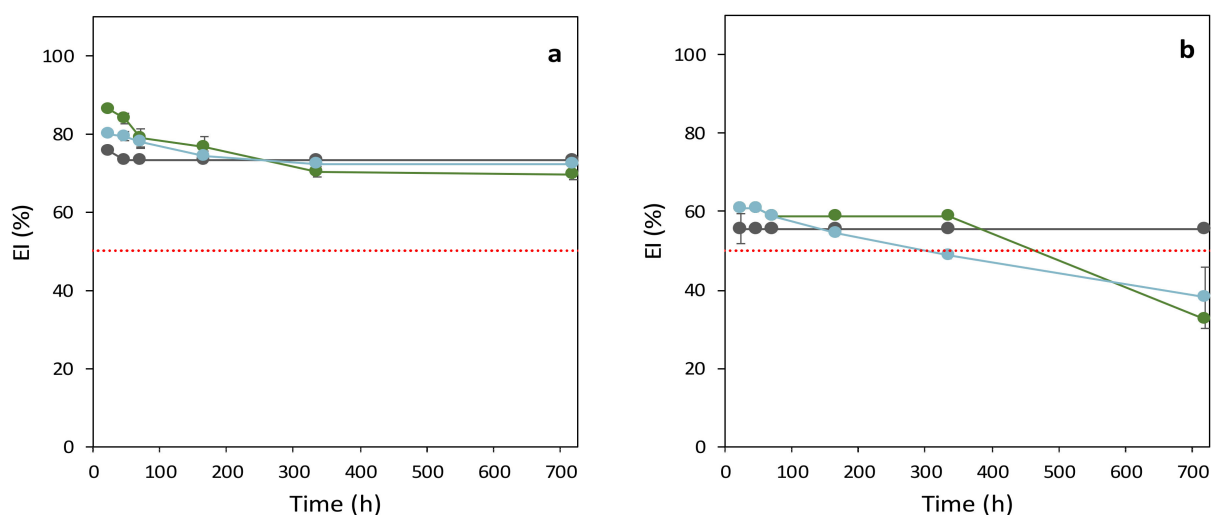
As shown in Table 3, the addition of  $\alpha$ -tocopherol led to an increase in the E24 values for both FucoPol concentrations tested. Compared to the samples with no  $\alpha$ -tocopherol that had E24 values of 76% and 56%, for FucoPol concentrations of 0.5 and 1.0 wt.%,



respectively (Table 3), the addition of  $\alpha$ -tocopherol resulted in higher E24 (80–86% and 61%, respectively). However, the resulting emulsions were less stable, especially for those prepared with 1.0 wt.% FucoPol that had overall ES of 61%, compared to 96% for the sample with no  $\alpha$ -tocopherol (Figure 4, Table 3). For the emulsions prepared with 0.5 wt.% FucoPol, the ES was 82% and 90%, for 2.0 and 5.0 wt.%  $\alpha$ -tocopherol, respectively (Table 3). Despite the observed ES reduction, the sample containing 5.0 wt.%  $\alpha$ -tocopherol had an ES of 90 at 720 h, identical to the sample with no additive (Table 3).

**Table 3.** Emulsification activity at 24 h (E24) and emulsions' stability over a period of 720 h, for the emulsion prepared with FucoPol, olive oil and  $\alpha$ -tocopherol, at 3:2 (*w/w*) ratio. Data are shown as the average  $\pm$  standard deviation (SD) (*n* = 3).

Emulsifier	$\alpha$ -Tocopherol (wt.%)	0.5 wt.% Emulsifier		1.0 wt.% Emulsifier	
		E24 (%)	ES (%)	E24 (%)	ES (%)
FucoPol	0	76 $\pm$ 0	87 $\pm$ 3	56 $\pm$ 0	96 $\pm$ 0
	2.0	86 $\pm$ 1	82 $\pm$ 1	61 $\pm$ 0	53 $\pm$ 5
	5.0	80 $\pm$ 1	90 $\pm$ 1	61 $\pm$ 0	63 $\pm$ 12
Sepigel	0	0 $\pm$ 0	-	49 $\pm$ 0	100 $\pm$ 0
	2.0	0 $\pm$ 0	-	0 $\pm$ 0	-
	5.0	0 $\pm$ 0	-	0 $\pm$ 0	-



**Figure 4.** Emulsification index (EI%) over time for the FucoPol-stabilized emulsions with olive oil and  $\alpha$ -tocopherol, at the 3:2 ratio: FucoPol (0.5 wt.% (a); 1.0 wt.%, (b));  $\alpha$ -tocopherol: 0 wt.%, gray; 2.0 wt.%, green; 5.0 wt.%, blue. The red dashed line represents EI = 50%. (*n* = 3).

#### 3.2.4. Comparison with Sepigel<sup>®</sup> 305

The commercial emulsifier agent Sepigel<sup>®</sup> 305 (also known as Farcosgel) was used to prepare emulsions with olive oil (o:w weight ratio of 3:2), with and without  $\alpha$ -tocopherol, and the results were compared to those of FucoPol's emulsions (Table 3). Sepigel<sup>®</sup> 305 is a synthetic hydrophilic polymer used in cosmetics to provide increased viscosity and stability to the formulation [61]. Sepigel<sup>®</sup> 305 is composed by a blend of polyacrylamide (10–20%), C13–14 Isoparaffin (1–5%), and Laureth-7 (1–5%). In its composition, each compound presents a specific function: the pre-neutralized polyacrylamide polymer is contained within an emulsion, where isoparaffin forms an oily phase and laureth-7 acts as a surfactant [61–63]. The comparison between Sepigel<sup>®</sup> 305 and FucoPol aims to discuss the possibility to replace a widely used chemical agent with a naturally produced polymer in cosmetic formulations. Interestingly, no emulsification was observed for the 0.5 wt.% Sepigel<sup>®</sup> samples and an EI of 49  $\pm$  0% was obtained for 1.0 wt.%, which was, nevertheless, stable for the 720 h shelf-life periods assay. The

addition of  $\alpha$ -tocopherol had a negative impact, and no emulsification was observed for any additive concentration. According to Anchisi et al. [56], Sepigel<sup>®</sup> 305 at concentrations of 1.5–7%, with an oil phase consisting mainly of a fluid oil, resulted in good emulsification for O/W skin creams. Other studies have reported the development of stable emulsions containing this polymer at concentrations higher than 2 wt.% [61–64]. At lower concentrations (<1.5 wt.%), the synthetic hydrophilic polymer was able to stabilize O/W formulations only with the addition of different emulsifying ingredients and emulsion stabilizers [65,66]. These results show the ability of the natural polymer FucoPol to emulsify without the addition of other agents at low concentrations, which becomes an advantage compared to the synthetic polymer Sepigel<sup>®</sup> 305.

### 3.3. Emulsification Optimization by Response Surface Methodology

#### 3.3.1. Response Analysis

Table 4 shows the data for the 17 runs of the CCD. Results show that the emulsification after 24 h ranged from 0.0 to 97.8%. Good emulsification index (E24 > 95%) was obtained in runs 1, 5, 11, 12, 14, 16 and 17, for which FucoPol concentration was 0.8–1.3 wt.%, and the olive oil content was 20–30 wt.%, irrespective of the  $\alpha$ -tocopherol content that varied from 0–5 wt.%. These results suggest that  $\alpha$ -tocopherol concentration has little effect on the E24. Outside those FucoPol and olive oil concentration ranges, E24 of 30.4–78.3% were attained. As expected, no emulsification was obtained in run 15 due to the absence of the bioemulsifier. Moreover, there was also no emulsification for runs 2, 6 and 10.

**Table 4.** Central composite design (CCD) with studied variables (A: FucoPol, B: Olive oil, C:  $\alpha$ -tocopherol), experiment and theoretically predicted values E24.

Run	FucoPol, A (wt.%)	Olive Oil, B (wt.%)	$\alpha$ -Tocopherol, C (wt.%)	E24 (%)	
				Actual Value	Predicted Value
1	0.8	30	2.5	97.8	97.1
2	1.6	30	2.5	0.0	3.0
3	0.3	20	4.0	30.4	26.8
4	0.8	46.8	2.5	78.3	57.3
5	0.8	30	0.0	95.7	100
6	1.3	40	4.0	0.0	19.5
7	0.3	20	1.0	76.1	56.6
8	0.3	40	4.0	69.6	72.7
9	0.8	13.2	2.5	73.9	95.0
10	1.3	40	1.0	0.0	3.6
11	0.8	30	5.0	95.7	90.0
12	0.8	30	2.5	97.7	97.1
13	0.3	40	1.0	69.6	78.7
14	0.8	30	2.5	97.6	97.1
15	0.0	30	2.5	0.0	15.3
16	1.3	20	4.0	95.6	87.0
17	1.3	20	1.0	97.8	94.6

E24 predicted value =  $97.07 - 3.82A - 11.24B - 3.5C - 28.26AB + 5.43AC + 5.98BC - 34.31A^2 - 7.41B^2 - 0.4880C^2$ .

#### 3.3.2. RSM Modelling

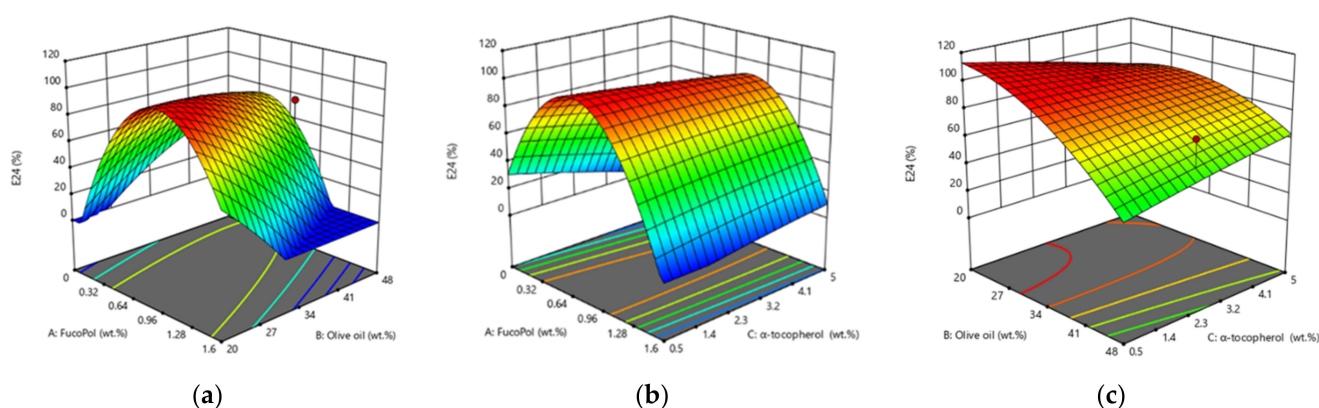
RSM methodology was used to evaluate the effect of each ingredient (FucoPol, olive oil and  $\alpha$ -tocopherol) on the E24 of the emulsions, as well as the combined effect of the variables. ANOVA was used to define the working ranges for each variable resulting in the highest E24 values. The statistical analysis (Table 5) shows that the proposed model was adequate [67]. The quadratic model was found to be significant ( $f$ -value = 18.51 and  $p$ -value = 0.001), and it was supported by an insignificant lack-of-fit ( $p$  = 0.634) toward the response (E24). There is only 0.10% chance that a “Model F-Value” could occur due to noise, meaning that the greater  $f$ -value from unity explains adequately the variation of the data around its mean; in addition, the estimated factor effects are real [68,69]. The  $R^2$  (0.965) was in reasonable agreement with the adjusted  $R^2$  (0.913). The adjusted coefficient of determination indicated that 91.31% of the

variability in the response could be explained by the model. Hence, the quadratic model is an accurate representation of the actual relationships between the response and the variables. The observed precision of 12.19 indicates an adequate signal (ratio > 4 is desirable). The statistical analysis indicates that the proposed model was adequate to predict the ingredients' concentrations to obtain stable emulsions ( $E_{24} > 50\%$ ) [53].

**Table 5.** ANOVA for response surface quadratic model. (SS)—Sum of Squares shows the variance of values; (MS)—Mean Square is the arithmetic mean of the squared differences;  $p$ -value < 0.05 indicate model terms are significant.

Source	SS	MS	$f$ -Value	$p$ -Value	Significance
Model	24,439.63	2715.51	18.51	0.001	Significant
A: FucoPol	199.37	199.37	1.360	0.287	
B: Olive oil	2854.49	2854.49	19.46	0.004	
C: $\alpha$ -tocopherol	167.58	167.58	1.140	0.326	
AB	6390.15	6390.15	43.56	0.001	
AC	236.31	236.31	1.610	0.251	
BC	286.08	286.08	1.950	0.212	
A <sup>2</sup>	14,317.43	14,317.43	97.60	0.0001	
B <sup>2</sup>	0.0002	0.0002	$1.4 \times 10^{-6}$	0.999	
C <sup>2</sup>	72.96	72.96	0.497	0.507	
Lack of Fit	582.37	145.59	0.766	0.634	Not significant
R <sup>2</sup>			0.965		
R <sup>2</sup> adjusted			0.913		
R <sup>2</sup> predicted			0.622		
Adequate precision			12.19		

The response of the RSM was shown as three-dimensional surface graphs (Figure 5, and contour plots resulting in an infinite number of combinations of the FucoPol, olive oil, and  $\alpha$ -tocopherol. The result suggests that FucoPol concentrations between 0.8–1.3 wt.% and olive oil concentrations between 20–30 wt.% reach  $E_{24}$  values above 95.6%. Moreover,  $\alpha$ -tocopherol does not appear to influence the  $E_{24}$  value (Figure 5). Figure 5a shows an inversely proportional interaction between FucoPol and olive oil, whereby  $E_{24}$  value increases with the increase in FucoPol concentration and decrease in olive oil concentration. Figure 5b corroborates the observed inverse proportionality between FucoPol and olive oil concentrations. Lastly, Figure 5c shows higher  $E_{24}$  values for olive oil between 25–30 wt.%.



**Figure 5.** Three-dimensional response surface plot showing the interactive effects of different components on the O/W emulsion. (a) FucoPol and Olive oil (wt.%) with  $\alpha$ -tocopherol fixed at 2.5 wt.%, (b) FucoPol and  $\alpha$ -tocopherol (wt.%) with olive oil fixed at 30 wt.%, (c) olive oil and  $\alpha$ -tocopherol (wt.%) with FucoPol fixed at 0.8 wt.%.

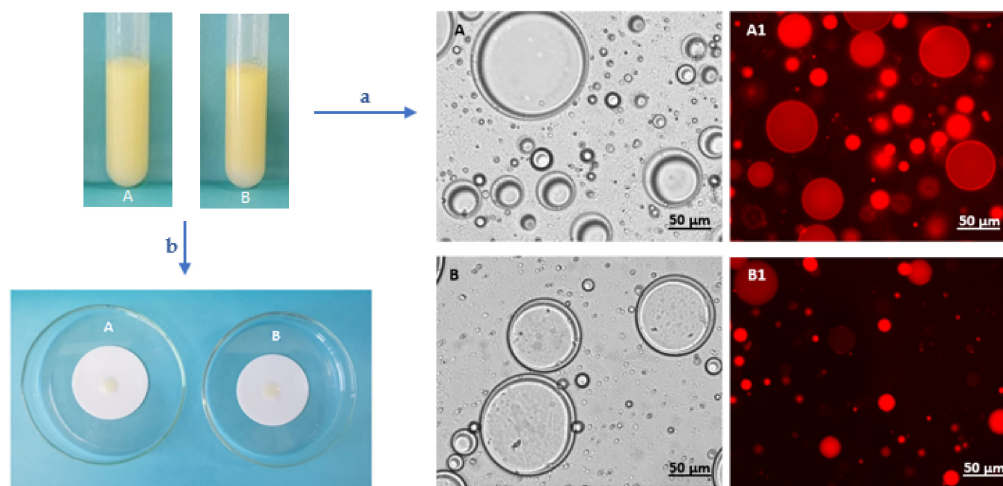
Based on Figure 5, increasing the concentration of FucoPol resulted in emulsions more stable against coalescence, avoiding emulsion phase separation [70]. This is due to FucoPol's ability to allow a specific texture (of increased viscosity) to the formulation and to decrease elasticity-driven creaming of the droplets [3]. FucoPol concentration and olive oil concentration have inversely proportional effects, as shown by the  $p$ -value  $< 0.05$  (Table 5). In this case, linear (B), interaction (AB) and quadratic ( $A^2$ ) are significant model terms on E24 including a positive linear effect ( $p = 0.004$ ) of olive oil and a quadratic effect ( $p = 0.0001$ ) of FucoPol, interacting with himself on the response [67]. This result agrees with results obtained for bacterial cellulose, in which emulsions became more stable as the concentration increased, reaching 1 wt.% [71]. In contrast, for xanthan gum concentrations of 0.12% and 0.2%, emulsions became more stable with 50 wt.% of oil [72–74].

Based on the results obtained in the CCD, two FucoPol-stabilized emulsions were prepared: F1 that comprised 1.0 wt.% FucoPol, 25 wt.% olive oil and 0.5 wt.%  $\alpha$ -tocopherol; and F2 that comprised 0.7 wt.% FucoPol, 25 wt.% olive oil and 2.0 wt.%  $\alpha$ -tocopherol. F1 and F2 yielded E24 values of  $98.0 \pm 0.40\%$  and  $84.7 \pm 0.0\%$ , respectively.

### 3.4. Characterization of the FucoPol-Stabilized Emulsions

#### 3.4.1. Type of Emulsion

The microscopic observation (Figure 6a) of the emulsions showed compartmentalized structures characteristic of O/W emulsions, consisting of dispersed oil droplets in the aqueous phase [75,76]. Furthermore, in the emulsion determination test (Figure 6b), the emulsions' droplets rapidly dispersed on the filter paper, thus confirming their O/W nature [22,77,78]. O/W emulsions represent nearly 65% of the total emulsified products available in the cosmetic industry market due to their sensorial properties [79,80] and are present in several products such as creams and lotions [80,81]. W/O emulsions are commonly used in waterproof products by providing higher hydration to emulsions [80]. However, these emulsions usually are responsible for an oily sensation on the skin, which enhances the consumer preference for O/W emulsified products [82].

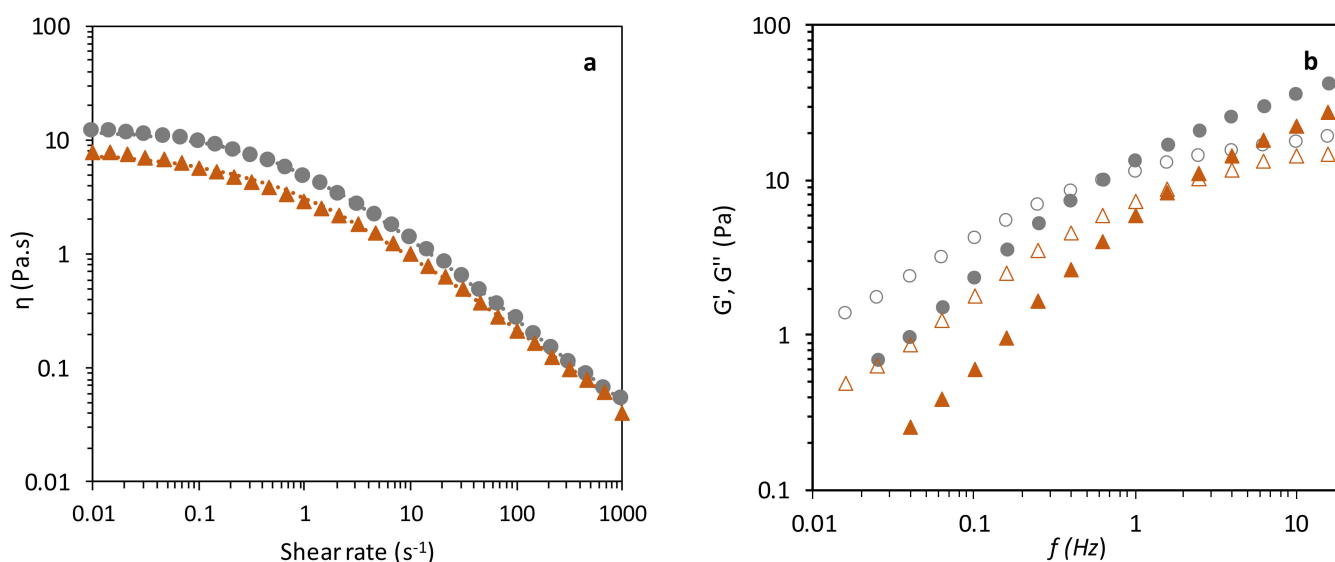


**Figure 6.** (a) Optical microscopic ( $40\times$ ) images of F1 (A) and F2 (B) emulsions; contrast phase and fluorescence after Nile Blue A staining (A1, B1, respectively); (b) emulsion determination test by filter paper wetting.

#### 3.4.2. Viscoelastic Properties

As shown in Figure 7a, both samples presented a shear-thinning behaviour, as the viscosity progressively decreased under increasing shear rates, in agreement with previous studies that reported the same behaviour for FucoPol/olive oil emulsions [16]. This effect is observed when a spherical shape is detangled by polymer chains and the droplets begin to deform, forming an ellipsoidal shape. Moreover, layer formation, due to aggregate breaking into elemental constituents, is concurring with the shear plane, decreasing the overall flow

resistance [1,2,83,84]. This shear-thinning behaviour was observed for emulsions stabilized by other polysaccharides, such as xanthan gum and guar gum [83,85]. Nevertheless, slight differences are noticed between samples, namely, a lower apparent viscosity for the emulsion F2 (Figure 7a, triangles) compared to emulsion F1 (Figure 7a, circles), which was probably due to the lower polymer concentration in F2. FucoPol increased viscosity in the water phase leads to decreased droplets' mobility and collision numbers, which can explain the observed behaviour [86].



**Figure 7.** Rheological profile analysis of FucoPol formulations F1 (circles) and F2 (triangles): (a) viscosity curves as a function of the shear rate, flow curves fitted with Cross model ( $n = 3$ ); (b) elastic  $G'$  (closed) and viscous  $G''$  (open) moduli in the function of frequency.

A non-Newtonian mathematical model, the Cross model, was fitted to the experimental results (Figure 7a) with the resulting parameters given in Table 6. The highest  $\eta_0$  value was observed for emulsion F1 ( $13.92 \pm 2.36$  Pa.s), but the  $\tau$  fitting parameter was similar for both emulsions. The emulsions had an identical degree of shear-thinning as shown by the similar values of  $m$  ( $0.74 \pm 0.00$  and  $0.68 \pm 0.01$ ) [87].

**Table 6.** Cross model parameters estimated for formulations samples:  $\eta_0$ —apparent viscosity of the second Newtonian plateau (Pa.s);  $\tau$ —relaxation time (s);  $m$ —dimensionless constant; Data are shown as the average  $\pm$  standard deviation (SD) ( $n = 3$ ); and textural parameters.

Emulsion	Cross Model Parameters			Textural Parameters			
	$\eta_0$ (Pa.s)	$\tau$ (s)	$m$	Firmness (N)	Consistency (mJ)	Adhesiveness (mJ)	Cohesiveness
F1	$13.92 \pm 2.36$	$1.64 \pm 0.13$	$0.74 \pm 0.00$	0.074	0.088	0.156	0.748
F2	$7.59 \pm 0.04$	$1.72 \pm 0.04$	$0.68 \pm 0.01$	0.074	0.055	0.129	0.688

$$RE = \sum_{i=1}^n (|x_{eI} - i - x_{calc,i}| / x_{exp}) / n \text{ is between } 0.011 \text{ and } 0.019.$$

The mechanical spectra (Figure 7b) of the two FucoPol-stabilized emulsions showed higher loss modulus ( $G''$ ) than storage modulus ( $G'$ ), indicating a liquid-like behaviour [16], with FucoPol viscosity being the dominant property influencing the emulsions' stability [54,88]. The mechanical spectra for the two emulsions are quite similar, with  $G''$  increasing at a higher rate than  $G'$ , with the crossover of dynamic moduli being perceived at a lower frequency (0.6 Hz) for emulsion F1 than for emulsion F2 (1.6 Hz). This indicates that, for emulsion F1, higher viscosity translates into lower energy storage threshold, featuring a  $G' G''$  crossover

at a lower frequency [16,89]. After the crossover point, increasing the frequency displays a solid-like behaviour for both emulsions ( $G' > G''$ ) [54,90].

### 3.4.3. Textural Assessment

As shown in Table 6, the FucoPol-stabilized emulsions F1 and F2 had the same firmness (0.074 N) when perforated 11 mm with a conic probe. The consistency of emulsion F1 was 0.088 mJ, while that of sample F2 was 0.055 mJ. Studies showed that the firmness and energy required to deform a sample are related to the sample's spreadability: high firmness and consistency values indicate a less spreadable sample, whilst lower consistency and firmness values indicate a more spreadable sample [1,2]. Hence, these results show that both samples are very spreadable, presenting low firmness and consistency values. Moreover, emulsion F2 was more spreadable than sample F1 (Table 6). The spreadability (skin cover capacity over time) is crucial in cosmetic emulsion development being a decisive factor for consumers' approval of products [91]. While both samples showed some adhesivity, emulsion F1 (0.156 mJ) seemed to be more adhesive than F2 (0.129 mJ). When a formulation is spread, verifying the material's uniform scattering throughout the applied surface is pivotal to avoid the active substance's accumulation or dissipation and to insure the correct utilization of the formulation [1,2]. Therefore, the cohesiveness was also an important parameter to be observed. Given this, emulsion F1 (0.748) is more cohesive than emulsion F2 (0.688), which concludes that sample F1 has higher firmness, adhesiveness and cohesiveness but is less spreadable than sample F2. These results are concordant with  $\eta_0$  (Pa.s) values (Table 6), where emulsion F1 exhibited higher apparent viscosity ( $13.92 \pm 2.36$  Pa.s) than F2 ( $7.59 \pm 0.04$  Pa.s).

### 3.4.4. Comparative Analysis of the FucoPol-Stabilized Emulsions

F2 emulsion had a slightly higher spreadability value [91], a feature of interest for cosmetic and pharmaceutical applications. Furthermore, at high shear rates (e.g.,  $1000 \text{ s}^{-1}$ , which is representative of a skin spreading process [91]), both F1 and F2 emulsions displayed analogous viscosity (0.05 Pa.s and 0.04 Pa.s, respectively). Such characteristics are found in lotions or light creams [80,82], thus confirming the potential of FucoPol for the development of skin care cosmetic products.

## 4. Conclusions

This study demonstrated the ability of the bacterial polysaccharide FucoPol to emulsify olive oil and  $\alpha$ -tocopherol, outperforming the commercial emulsifier Sepigel®. The resulting O/W emulsions had good viscosity and spreadability, which substantiates its relevance in the development of cosmetic applications. The emulsion textural properties can be modulated by using different FucoPol and  $\alpha$ -tocopherol contents, thus yielding formulations suitable for use in different skin-care products. The intrinsic antioxidant capacity of FucoPol adds to that of  $\alpha$ -tocopherol, which, together with FucoPol's wound-healing ability, render this natural polysaccharide as a valuable biomaterial for cosmetic formulations' development.

**Author Contributions:** Conceptualization, S.B. and F.F.; methodology, S.B., J.R.P. and C.V.G.; investigation, S.B., J.R.P. and C.V.G.; writing—original draft preparation, S.B.; writing—review and editing, M.A.M.R., F.F. and C.A.V.T.; supervision and funding, M.A.M.R. and F.F. All authors have read and agreed to the published version of the manuscript.

**Funding:** This work is financed by national funds from FCT—Fundação para a Ciência e a Tecnologia, I.P., in the scope of the project UIDP/04378/2020 and UIDB/04378/2020 of the Research Unit on Applied Molecular Biosciences—UCIBIO and the project LA/P/0140/2020 of the Associate Laboratory Institute for Health and Bioeconomy—i4HB. C.V.G and J.R.P. acknowledge FCT I.P. for PhD Grants 2021.05798.BD and SFRH/BD/147518/2019, respectively.

**Institutional Review Board Statement:** Not applicable.

**Informed Consent Statement:** Not applicable.

**Data Availability Statement:** Data will be available upon request.

**Conflicts of Interest:** Sílvia Baptista is employed by the company 73100 Lda. The remaining authors declare no conflict of interest.

## References

1. Tafuro, G.; Costantini, A.; Baratto, G.; Busata, L.; Semenzato, A. Rheological and Textural Characterization of Acrylic Polymer Water Dispersions for Cosmetic Use. *Ind. Eng. Chem. Res.* **2019**, *58*, 23549–23558. [[CrossRef](#)]
2. Tafuro, G.; Costantini, A.; Baratto, G.; Francescato, S.; Busata, L.; Semenzato, A. Characterization of Polysaccharidic Associations for Cosmetic Use: Rheology and Texture Analysis. *Cosmetics* **2021**, *8*, 62. [[CrossRef](#)]
3. Baptista, S.; Freitas, F. Bacterial Polysaccharides: Cosmetic Applications. In *PolySaccharides of Microbial Origin*; Oliveira, J., Radhouani, H., Reis, R.L., Eds.; Springer Nature AG: Cham, Switzerland, 2021; ISBN 9783030357344.
4. Gilbert, L.; Picard, C.; Savary, G.; Grisel, M. Rheological and Textural Characterization of Cosmetic Emulsions Containing Natural and Synthetic Polymers: Relationships between Both Data. *Colloids Surf. A Physicochem. Eng. Asp.* **2013**, *421*, 150–163. [[CrossRef](#)]
5. Lochhead, R.Y. The Role of Polymers in Cosmetics: Recent Trends. *ACS Symp. Ser.* **2007**, *961*, 3–56. [[CrossRef](#)]
6. Filipovic, M.; Lukic, M.; Djordjevic, S.; Krstonosic, V.; Pantelic, I.; Vuleta, G.; Savic, S. Towards Satisfying Performance of an O/W Cosmetic Emulsion: Screening of Reformulation Factors on Textural and Rheological Properties Using General Experimental Design. *Int. J. Cosmet. Sci.* **2017**, *39*, 486–499. [[CrossRef](#)]
7. Fialho, L.; Araújo, D.; Alves, V.D.; Roma-rodrigues, C.; Baptista, V.; Fernandes, A.R.; Freitas, F.; Reis, M.A.M. Cation-Mediated Gelation of the Fucose-Rich Polysaccharide FucoPol: Preparation and Characterization of Hydrogel Beads and Their Cytotoxicity Assessment. *Int. J. Polym. Mater. Polym. Biomater.* **2021**, *70*, 90–99. [[CrossRef](#)]
8. Torres, C.A.V.; Marques, R.; Antunes, S.; Alves, V.D.; Sousa, I.; Maria, A.; Oliveira, R.; Freitas, F.; Reis, M.A.M. Kinetics of Production and Characterization of the Fucose-Containing Exopolysaccharide from *Enterobacter* A47. *J. Biotechnol.* **2011**, *156*, 261–267. [[CrossRef](#)]
9. Freitas, F.; Alves, V.D.; Torres, C.A.V.; Cruz, M.; Sousa, I.; João, M.; Ramos, A.M.; Reis, M.A.M. Fucose-Containing Exopolysaccharide Produced by the Newly Isolated *Enterobacter* Strain A47 DSM 23139. *Carbohydr. Polym.* **2011**, *83*, 159–165. [[CrossRef](#)]
10. Concórdio-Reis, P.; Reis, M.A.M.; Freitas, F. Biosorption of Heavy Metals by the Bacterial Exopolysaccharide FucoPol. *Appl. Sci.* **2020**, *10*, 6708. [[CrossRef](#)]
11. Guerreiro, B.M.; Freitas, F.; Lima, J.C.; Silva, J.C.; Dionísio, M.; Reis, M.A.M. Demonstration of the Cryoprotective Properties of the Fucose-Containing Polysaccharide FucoPol. *Carbohydr. Polym.* **2020**, *245*, 116500. [[CrossRef](#)]
12. Concórdio-Reis, P.; Pereira, C.V.; Batista, M.P.; Sevrin, C.; Grand, C.; Marques, A.C.; Fortunato, E.; Gaspar, F.B.; Matias, A.A.; Freitas, F. Silver Nanocomposites Based on the Bacterial Fucose-Rich Polysaccharide Secreted by *Enterobacter* A47 for Wound Dressing Applications: Synthesis, Characterization and in Vitro Bioactivity. *Int. J. Biol. Macromol.* **2020**, *163*, 959–969. [[CrossRef](#)] [[PubMed](#)]
13. Torres, C.A.V.; Ferreira, A.R.V.; Freitas, F.; Reis, M.A.M.; Coelho, I.; Sousa, I.; Alves, V.D. Rheological Studies of the Fucose-Rich Exopolysaccharide FucoPol. *Int. J. Biol. Macromol.* **2015**, *79*, 611–617. [[CrossRef](#)] [[PubMed](#)]
14. Ferreira, A.R.V.; Torres, C.A.V.; Freitas, F.; Reis, M.A.M.; Alves, V.D.; Coelho, I.M. Biodegradable Films Produced from the Bacterial Polysaccharide FucoPol. *Int. J. Biol. Macromol.* **2014**, *71*, 111–116. [[CrossRef](#)] [[PubMed](#)]
15. Ferreira, A.R.V.; Torres, C.A.V.; Freitas, F.; Sevrin, C.; Grandfils, C.; Reis, M.A.M.; Alves, V.D.; Coelho, I.M. Development and Characterization of Bilayer Films of FucoPol and Chitosan. *Carbohydr. Polym.* **2016**, *147*, 8–15. [[CrossRef](#)] [[PubMed](#)]
16. Baptista, S.; Torres, C.A.V.; Sevrin, C.; Grandfils, C.; Reis, M.A.M.; Freitas, F. Extraction of the Bacterial Extracellular Polysaccharide FucoPol by Membrane-Based Methods: Efficiency and Impact on Biopolymer Properties. *Polymers* **2022**, *14*, 390. [[CrossRef](#)] [[PubMed](#)]
17. Guerreiro, B.M.; Silva, J.C.; Lima, J.C.; Reis, M.A.M.; Freitas, F. Antioxidant Potential of the Bio-Based Fucose-Rich Polysaccharide FucoPol Supports Its Use in Oxidative Stress-Inducing Systems. *Polymers* **2021**, *13*, 3020. [[CrossRef](#)]
18. Guerreiro, B.M.; Freitas, F.; Lima, J.C.; Silva, J.C.; Reis, M.A.M. Photoprotective Effect of the Fucose-Containing Polysaccharide FucoPol. *Carbohydr. Polym.* **2021**, *259*, 117761. [[CrossRef](#)]
19. Freitas, F.; Alves, V.; Reis, M.A.M. Bacterial Polysaccharides: Production and Applications in Cosmetic Industry. In *Polysaccharides*; Springer: Cham, Switzerland, 2014; pp. 2017–2043. [[CrossRef](#)]
20. Concórdio-reis, P.; Pereira, J.R.; Torres, C.A.V.; Sevrin, C. Effect of Mono- and Dipotassium Phosphate Concentration on Extracellular Polysaccharide Production by the Bacterium *Enterobacter* A47. *Process Biochem.* **2018**, *75*, 16–21. [[CrossRef](#)]
21. Pansiripat, S.; Pornsunthorntawe, O.; Rujiravanit, R.; Kitiyanan, B.; Somboonthanate, P.; Chavadej, S. Biosurfactant Production by *Pseudomonas aeruginosa* SP4 Using Sequencing Batch Reactors: Effect of Oil-to-Glucose Ratio. *Biochem. Eng. J.* **2010**, *49*, 185–191. [[CrossRef](#)]
22. Kavitate, D.; Balyan, S.; Devi, P.B.; Shetty, P.H. Evaluation of Oil-in-Water (O/W) Emulsifying Properties of Galactan Exopolysaccharide from *Weissella confusa* KR780676. *J. Food Sci. Technol.* **2020**, *57*, 1579–1585. [[CrossRef](#)]
23. Lundstedt, T.; Seifert, E.; Abramo, L.; Thelin, B.; Nystrom, A.; Pettersen, J.; Bergman, R. Experimental Design and Optimization. *Chemom. Intell. Lab. Syst.* **1998**, *42*, 3–40. [[CrossRef](#)]

24. Roosta, M.; Ghaedi, M.; Daneshfar, A.; Sahraei, R.; Asghari, A. Optimization of the Ultrasonic Assisted Removal of Methylene Blue by Gold Nanoparticles Loaded on Activated Carbon Using Experimental Design Methodology. *Ultrason. Sonochem.* **2014**, *21*, 242–252. [[CrossRef](#)] [[PubMed](#)]
25. Martins, D.; Rocha, C.; Dourado, F.; Gama, M. Bacterial Cellulose-Carboxymethyl Cellulose (BC:CMC) Dry Formulation as Stabilizer and Texturizing Agent for Surfactant-Free Cosmetic Formulations. *Colloids Surf. A Physicochem. Eng. Asp.* **2021**, *617*, 126380. [[CrossRef](#)]
26. Alves, V.D.; Freitas, F.; Torres, C.A.V.; Cruz, M.; Marques, R.; Grandfils, C.; Gonçalves, M.P.; Oliveira, R.; Reis, M.A.M. Rheological and Morphological Characterization of the Culture Broth During Exopolysaccharide Production by *Enterobacter* sp. *Carbohydr. Polym.* **2010**, *81*, 758–764. [[CrossRef](#)]
27. Fernandes, R.N.; Simiqueli, A.A.; Vidigal, M.C.T.R.; Minim, V.P.R.; Minim, L.A. Kinetic Stability of the Oil-in-Water Emulsions and Dynamic Interfacial Properties of Mixtures of Sucrose Esters and Polysaccharides. *Food Chem.* **2021**, *357*, 129693. [[CrossRef](#)]
28. Gaudin, T.; Rotureau, P.; Pezron, I.; Fayet, G. Investigating the Impact of Sugar-Based Surfactants Structure on Surface Tension at Critical Micelle Concentration with Structure-Property Relationships. *J. Colloid Interface Sci.* **2018**, *516*, 162–171. [[CrossRef](#)]
29. Garti, N.; Leser, M.E. Emulsification Properties of Hydrocolloids. *Polym. Adv. Technol.* **2001**, *12*, 123–135. [[CrossRef](#)]
30. Breitenbach, B.B.; Schmid, I.; Wich, P.R. Amphiphilic Polysaccharide Block Copolymers for PH-Responsive Micellar Nanoparticles. *Biomacromolecules* **2017**, *18*, 2839–2848. [[CrossRef](#)]
31. Jain, R.M.; Mody, K.; Joshi, N.; Mishra, A.; Jha, B. Production and Structural Characterization of Biosurfactant Produced by an Alkaliphilic Bacterium, *Klebsiella* sp.: Evaluation of Different Carbon Sources. *Colloids Surf. B Biointerfaces* **2013**, *108*, 199–204. [[CrossRef](#)] [[PubMed](#)]
32. Phulpoto, I.A.; Yu, Z.; Hu, B.; Wang, Y.; Ndayisenga, F.; Li, J.; Liang, H.; Qazi, M.A. Production and Characterization of Surfactin-like Biosurfactant Produced by Novel Strain *Bacillus nealsonii* S2MT and It's Potential for Oil Contaminated Soil Remediation. *Microb. Cell Factories* **2020**, *19*, 145. [[CrossRef](#)]
33. Rodríguez-López, L.; López-Prieto, A.; Lopez-Álvarez, M.; Pérez-Davila, S.; Serra, J.; González, P.; Cruz, J.M.; Moldes, A.B. Characterization and Cytotoxic Effect of Biosurfactants Obtained from Different Sources. *ACS Omega* **2020**, *5*, 31381–31390. [[CrossRef](#)] [[PubMed](#)]
34. Sałek, K.; Euston, S.R. Sustainable Microbial Biosurfactants and Bioemulsifiers for Commercial Exploitation. *Process Biochem.* **2019**, *85*, 143–155. [[CrossRef](#)]
35. Bernardi, D.S.; Pereira, T.A.; Maciel, N.R.; Bortoloto, J.; Viera, G.S.; Oliveira, G.C.; Rocha-Filho, P.A. Formation and Stability of Oil-in-Water Nanoemulsions Containing Rice Bran Oil: In Vitro and In Vivo Assessments. *J. Nanobiotechnol.* **2011**, *9*, 44. [[CrossRef](#)] [[PubMed](#)]
36. Patel, V.R.; Dumancas, G.G.; Viswanath, L.C.K.; Maples, R.; Subong, B.J.J. Castor Oil: Properties, Uses, and Optimization of Processing Parameters in Commercial Production. *Lipid Insights* **2016**, *9*, LPI-S40233. [[CrossRef](#)]
37. Chu, C.C.; Nyam, K.L. Application of Seed Oils and Its Bioactive Compounds in Sunscreen Formulations. *JAOCs J. Am. Oil Chem. Soc.* **2021**, *98*, 713–726. [[CrossRef](#)]
38. Maktabi, B.; Liberatore, M.W.; Baki, G. Meadowfoam Seed Oil as a Natural Dispersing Agent for Colorants in Lipstick. *Int. J. Cosmet. Sci.* **2021**, *43*, 484–493. [[CrossRef](#)]
39. Smaoui, S.; Hlima, H.; Jarraya, R.; Kamoun, N.; Ellouze, R.; Damak, M. Cosmetic Emulsion from Virgin Olive Oil: Formulation and Bio-Physical Evaluation. *Afr. J. Biotechnol.* **2012**, *11*, 9664–9671. [[CrossRef](#)]
40. Shkreli, R.; Terziu, R.; Memushaj, L.; Dharmo, K. Formulation and Stability Evaluation of a Cosmetics Emulsion Loaded with Different Concentrations of Synthetic and Natural Preservative. *J. Biol. Stud.* **2022**, *5*, 38–51.
41. Laurent, S. A Study of I-Cyclodextrin-Stabilized Paraffin Oil/Water Emulsions. *J. Soc. Cosmet. Chem.* **1999**, *50*, 15–22.
42. Ahmad, Z. The Uses and Properties of Almond Oil. *Complementary Ther. Clin. Pract.* **2010**, *16*, 10–12. [[CrossRef](#)]
43. Čolić, S.; Zec, G.; Natić, M.; Fotirić-Akšić, M. Almond (*Prunus dulcis*) Oil. In *Fruit Oils: Chemistry and Functionality*; Springer: Cham, Switzerland, 2019; ISBN 9783030124731.
44. Gallardo, V.; Munoz, M.; Ruiz, M.A. Formulations of Hydrogels and Lipogels with Vitamin E. *J. Cosmet. Dermatol.* **2005**, *4*, 187–192. [[CrossRef](#)] [[PubMed](#)]
45. Mota, A.H.; Silva, C.O.; Nicolai, M.; Baby, A.; Palma, L.; Rijo, P.; Ascensão, L.; Reis, C.P. Design and Evaluation of Novel Topical Formulation with Olive Oil as Natural Functional Active. *Pharm. Dev. Technol.* **2018**, *23*, 794–805. [[CrossRef](#)] [[PubMed](#)]
46. César, F.C.S.; Maia Campos, P.M.B.G. Influence of Vegetable Oils in the Rheology, Texture Profile and Sensory Properties of Cosmetic Formulations Based on Organogel. *Int. J. Cosmet. Sci.* **2020**, *42*, 494–500. [[CrossRef](#)] [[PubMed](#)]
47. Nunes, A.; Gonçalves, L.; Marto, J.; Martins, A.M.; Silva, A.N.; Pinto, P.; Martins, M.; Fraga, C.; Ribeiro, H.M. Investigations of Olive Oil Industry By-Products Extracts with Potential Skin Benefits in Topical Formulations. *Pharmaceutics* **2021**, *13*, 465. [[CrossRef](#)]
48. Gorini, I.; Iorio, S.; Ciliberti, R.; Licata, M.; Armocida, G. Olive Oil in Pharmacological and Cosmetic Traditions. *J. Cosmet. Dermatol.* **2019**, *18*, 1575–1579. [[CrossRef](#)]
49. Sandford, E.C.; Muntz, A.; Craig, J.P. Therapeutic Potential of Castor Oil in Managing Blepharitis, Meibomian Gland Dysfunction and Dry Eye. *Clin. Exp. Optom.* **2021**, *104*, 315–322. [[CrossRef](#)]
50. Kaur, C.D.; Saraf, S. In Vitro Sun Protection Factor Determination of Herbal Oils Used in Cosmetics. *Pharmacogn. Res.* **2010**, *2*, 22–25. [[CrossRef](#)]



51. Chuberre, B.; Araviiskaia, E.; Bieber, T.; Barbaud, A. Mineral Oils and Waxes in Cosmetics: An Overview Mainly Based on the Current European Regulations and the Safety Profile of These Compounds. *J. Eur. Acad. Dermatol. Venereol.* **2019**, *33*, 5–14. [[CrossRef](#)]
52. Rodrigues, F.; Pimentel, F.B.; Oliveira, M.B.P.P. Olive By-Products: Challenge Application in Cosmetic Industry. *Ind. Crops Prod.* **2015**, *70*, 116–124. [[CrossRef](#)]
53. Willumsen, P.A.; Karlson, U. Screening of Bacteria, Isolated from PAH-Contaminated Soils, for Production of Biosurfactants and Bioemulsifiers. *Biodegradation* **1996**, *7*, 415–423. [[CrossRef](#)]
54. Kaltsa, O.; Spiliopoulou, N.; Yanniotis, S.; Mandala, I. Stability and Physical Properties of Model Macro- and Nano/Submicron Emulsions Containing Fenugreek Gum. *Food Hydrocoll.* **2016**, *61*, 625–632. [[CrossRef](#)]
55. Kaur, N.; Kaur, M.; Mahajan, M.; Jain, S.K. Development, Characterization and Evaluation of Nanocarrier Based Formulations of Antipsoriatic Drug “Acitretin” for Skin Targeting. *J. Drug Deliv. Sci. Technol.* **2020**, *60*, 102010. [[CrossRef](#)]
56. Anchisi, C.; Maccioni, A.M.; Sinico, C.; Valenti, D. Stability Studies of New Cosmetic Formulations with Vegetable Extracts as Functional Agents. *Farmaco* **2001**, *56*, 427–431. [[CrossRef](#)]
57. Jaiswal, P.V.; Ijeri, V.S.; Srivastava, A.K. Voltammetric Behavior of  $\alpha$ -Tocopherol and Its Determination Using Surfactant + Ethanol + Water and Surfactant + Acetonitrile + Water Mixed Solvent Systems. *Anal. Chim. Acta* **2001**, *441*, 201–206. [[CrossRef](#)]
58. Alayoubi, A.; Kanthala, S.; Satyanarayanajois, S.D.; Anderson, J.F.; Sylvester, P.W.; Nazzal, S. Stability and in Vitro Antiproliferative Activity of Bioactive “ Vitamin E ” Fortified Parenteral Lipid Emulsions. *Colloids Surf. B Biointerfaces* **2013**, *103*, 23–30. [[CrossRef](#)]
59. Fiume, M.M.; Bergfeld, W.F.; Belsito, D.V.; Hill, R.A.; Klaassen, C.D.; Liebler, D.C.; Marks, J.G.; Shank, R.C.; Slaga, T.J.; Snyder, P.W.; et al. Safety Assessment of Tocopherols and Tocotrienols as Used in Cosmetics. *Int. J. Toxicol.* **2018**, *37*, 61S–94S. [[CrossRef](#)]
60. Cieřla, J.; Koczańska, M.; Narkiewicz-Michalek, J.; Szymula, M.; Bieganski, A. Effect of  $\alpha$ -Tocopherol on the Properties of Microemulsions Stabilized by the Ionic Surfactants. *J. Mol. Liq.* **2017**, *236*, 117–123. [[CrossRef](#)]
61. Gonçalves, G.M.S.; Maia Campos, P.M.B.G. Shelf Life and Rheology of Emulsions Containing Vitamin C and Its Derivatives. *Rev. Cienc. Farm. Basica Apl.* **2009**, *30*, 217–224.
62. Daher, C.C.; Fontes, I.S.; de Oliveira Rodrigues, R.; Azevedo De Brito Damasceno, G.; dos Santos Soares, D.; Flávio Soares Aragão, C.; Paula Barreto Gomes, A.; Ferrari, M. Development of O/W Emulsions Containing *Euterpe oleracea* Extract and Evaluation of Photoprotective Efficacy. *Braz. J. Pharm. Sci.* **2014**, *50*, 639–652. [[CrossRef](#)]
63. Infante, V.H.P.; Calixto, L.S.; Maia Campos, P.M.B.G. Physico-Mechanical Properties of Topical Formulations Based on Different Polymers. *Biomed. Biopharm. Res.* **2019**, *16*, 213–222. [[CrossRef](#)]
64. Vanti, G.; Grifoni, L.; Bergonzi, M.C.; Antiga, E.; Montefusco, F.; Caproni, M.; Bilia, A.R. Development and Optimisation of Biopharmaceutical Properties of a New Microemulgel of Cannabidiol for Locally-Acting Dermatological Delivery. *Int. J. Pharm.* **2021**, *607*, 121036. [[CrossRef](#)]
65. Moldovan, M.L.; Ionuț, I.; Bogdan, C. Cosmetic Products Containing Natural Based Emollients for Restoring Impaired Skin Barrier: Formulation and in Vivo Evaluation. *Farmacia* **2021**, *69*, 129–134. [[CrossRef](#)]
66. Bergamante, V.; Ceschel, G.C.; Marazzita, S.; Ronchi, C.; Fini, A. Effect of Vehicles on Topical Application of *Aloe vera* and *Arnica montana* Components. *Drug Deliv.* **2007**, *14*, 427–432. [[CrossRef](#)]
67. Lee, W.C.; Yusof, S.; Hamid, N.S.A.; Baharin, B.S. Optimizing Conditions for Hot Water Extraction of Banana Juice Using Response Surface Methodology (RSM). *J. Food Eng.* **2006**, *75*, 473–479. [[CrossRef](#)]
68. Hamzaoui, A.H.; Jamoussi, B.; M'nif, A. Lithium Recovery from Highly Concentrated Solutions: Response Surface Methodology (RSM) Process Parameters Optimization. *Hydrometallurgy* **2008**, *90*, 1–7. [[CrossRef](#)]
69. Khuri, A.I.; Mukhopadhyay, S. Response Surface Methodology. *Wiley Interdiscip. Rev. Comput. Stat.* **2010**, *2*, 128–149. [[CrossRef](#)]
70. Yu, L.; Li, S.; Stubbs, L.P.; Lau, H.C. Effects of Salinity and Ph on the Stability of Clay-Stabilized Oil-in-Water Pickering Emulsions. *SPE J.* **2021**, *26*, 1402–1421. [[CrossRef](#)]
71. Paximada, P.; Tsouko, E.; Kopsahelis, N.; Koutinas, A.A.; Mandala, I. Bacterial Cellulose as Stabilizer of o/w Emulsions. *Food Hydrocoll.* **2016**, *53*, 225–232. [[CrossRef](#)]
72. Krstonošić, V.; Dokić, L.; Nikolić, I.; Milanović, M. Influence of Xanthan Gum on Oil-in-Water Emulsion Characteristics Stabilized by OSA Starch. *Food Hydrocoll.* **2015**, *45*, 9–17. [[CrossRef](#)]
73. Vélez, G.; Fernández, M.A.; Muñoz, J.; Williams, P.A.; English, R.J. Role of Hydrocolloids in the Creaming of Oil in Water Emulsions. *J. Agric. Food Chem.* **2003**, *51*, 265–269. [[CrossRef](#)]
74. Sun, C.; Gunasekaran, S.; Richards, M.P. Effect of Xanthan Gum on Physicochemical Properties of Whey Protein Isolate Stabilized Oil-in-Water Emulsions. *Food Hydrocoll.* **2007**, *21*, 555–564. [[CrossRef](#)]
75. McClements, D.J. Critical Review of Techniques and Methodologies for Characterization of Emulsion Stability. *Crit. Rev. Food Sci. Nutr.* **2007**, *47*, 611–649. [[CrossRef](#)] [[PubMed](#)]
76. Akbari, S.; Nour, A.H. Emulsion Types, Stability Mechanisms and Rheology: A Review. *Int. J. Innov. Res. Sci. Stud.* **2018**, *1*, 14–21. [[CrossRef](#)]
77. Lata Yadav, K.; Kumar Rahi, D.; Kumar Soni, S. Bioemulsifying Potential of Exopolysaccharide Produced by an Indigenous Species of *Aureobasidium pullulans* RYLF10. *PeerJ PrePrints* **2014**, *2*, e726v1. [[CrossRef](#)]
78. Kavitate, D.; Balyan, S.; Devi, P.B.; Shetty, P.H. Interface between Food Grade Flavour and Water Soluble Galactan Biopolymer to Form a Stable Water-in-Oil-in-Water Emulsion. *Int. J. Biol. Macromol.* **2019**, *135*, 445–452. [[CrossRef](#)]

79. Huber, P. Sensory Measurement-Evaluation and Testing of Cosmetic Products. In *Cosmetic Science and Technology: Theoretical Principles and Applications*; Elsevier Inc.: Amsterdam, The Netherlands, 2017; ISBN 9780128020548.
80. Calvo, F.; Gómez, J.M.; Ricardez-Sandoval, L.; Alvarez, O. Integrated Design of Emulsified Cosmetic Products: A Review. *Chem. Eng. Res. Des.* **2020**, *161*, 279–303. [[CrossRef](#)]
81. Marti-Mestres, G.; Nielloud, F. Emulsions in Health Care Applications—An Overview. *J. Dispers. Sci. Technol.* **2002**, *23*, 419–439. [[CrossRef](#)]
82. Cheng, Y.S.; Lam, K.W.; Ng, K.M.; Ko, R.K.M.; Wibowo, C. An Integrative Approach to Product Development—A Skin-Care Cream. *Comput. Chem. Eng.* **2009**, *33*, 1097–1113. [[CrossRef](#)]
83. Vianna-Filho, R.P.; Petkowicz, C.L.O.; Silveira, J.L.M. Rheological Characterization of O/W Emulsions Incorporated with Neutral and Charged Polysaccharides. *Carbohydr. Polym.* **2013**, *93*, 266–272. [[CrossRef](#)]
84. Tadros, T. Interparticle Interactions in Concentrated Suspensions and Their Bulk (Rheological) Properties. *Adv. Colloid Interface Sci.* **2011**, *168*, 263–277. [[CrossRef](#)]
85. Quintana, J.M.; Califano, A.N.; Zaritzky, N.E.; Partal, P.; Franco, J.M. Linear and Nonlinear Viscoelastic Behavior of Olein-Water Emulsions Stabilized with Polysaccharides. *J. Texture Stud.* **2002**, *33*, 215–236. [[CrossRef](#)]
86. Krstonošić, V.; Dokić, L.; Dokić, P.; Dapčević, T. Effects of Xanthan Gum on Physicochemical Properties and Stability of Corn Oil-in-Water Emulsions Stabilized by Polyoxyethylene (20) Sorbitan Monooleate. *Food Hydrocoll.* **2009**, *23*, 2212–2218. [[CrossRef](#)]
87. Webb, E.B.; Koh, C.A.; Liberatore, M.W. High Pressure Rheology of Hydrate Slurries Formed from Water-in-Mineral Oil Emulsions. *Ind. Eng. Chem. Res.* **2014**, *53*, 6998–7007. [[CrossRef](#)]
88. Rózańska, S.; Broniarz-Press, L.; Rózański, J.; Mitkowski, P.T.; Ochowiak, M.; Woziwodzki, S. Extensional Viscosity of o/w Emulsion Stabilized by Polysaccharides Measured on the Opposed-Nozzle Device. *Food Hydrocoll.* **2013**, *32*, 130–142. [[CrossRef](#)]
89. Cruz, M.; Freitas, F.; Torres, C.A.V.; Reis, M.A.M.; Alves, V.D. Influence of Temperature on the Rheological Behavior of a New Fucose-Containing Bacterial Exopolysaccharide. *Int. J. Biol. Macromol.* **2011**, *48*, 695–699. [[CrossRef](#)]
90. Iqbal, S.; Xu, Z.; Huang, H.; Chen, X.D. Controlling the Rheological Properties of Oil Phases Using Controlled Protein-Polysaccharide Aggregation and Heteroaggregation in Water-in-Oil Emulsions. *Food Hydrocoll.* **2019**, *96*, 278–287. [[CrossRef](#)]
91. Savary, G.; Grisel, M.; Picard, C. Impact of Emollients on the Spreading Properties of Cosmetic Products: A Combined Sensory and Instrumental Characterization. *Colloids Surf. B Biointerfaces* **2013**, *102*, 371–378. [[CrossRef](#)]



## Article

# Biodeterioration of Microplastics: A Promising Step towards Plastics Waste Management

Aatikah Tareen <sup>1</sup>, Saira Saeed <sup>1</sup>, Atia Iqbal <sup>1</sup>, Rida Batool <sup>2</sup> and Nazia Jamil <sup>2,\*</sup>

<sup>1</sup> Department of Microbiology and Molecular Genetics, The Women University Multan, Multan 66000, Pakistan; atikatarin@gmail.com (A.T.); sairasaheed16@yahoo.com (S.S.); atia.iqbal@wum.edu.pk (A.I.)

<sup>2</sup> Institute of Microbiology and Molecular Genetics, University of the Punjab, Lahore 54590, Pakistan; rida.mmg@pu.edu.pk

\* Correspondence: nazia.mmg@pu.edu.pk

**Abstract:** Polyethylene and Polyester materials are resistant to degradation and a significant source of microplastics pollution, which is an emerging concern. In the present study, the potential of a dumped site bacterial community was evaluated. After primary screening, it was observed that 68.5% were linear low-density polyethylene, 33.3% were high-density, and 12.9% were Polyester degraders. Five strains were chosen for secondary screening, in which they were monitored by FTIR, SEM and weight loss degradation trials. Major results were observed for *Alcaligenes faecalis* (MK517568) and *Bacillus cereus* (MK517567), as they showed the highest degradation activity. *Alcaligenes faecalis* (MK517568) degrades LLDPE by 3.5%, HDPE by 5.8% and Polyester by 17.3%. *Bacillus cereus* (MK517567) is better tolerated at 30 °C and degrades Polyester by 29%. Changes in infrared spectra indicated degradation pathways of different strains depending on the types of plastics targeted. Through SEM analysis, grooves, piths and holes were observed on the surface. These findings suggest that soil bacteria develop an effective mechanism for degradation of microplastics and beads that enables them to utilize plastics as a source of energy without the need for pre-treatments, which highlights the importance of these soil bacteria for the future of effective plastic waste management in a soil environment.

**Citation:** Tareen, A.; Saeed, S.;

Iqbal, A.; Batool, R.; Jamil, N.

Biodeterioration of Microplastics: A Promising Step towards Plastics

Waste Management. *Polymers* **2022**, *14*, 2275. <https://doi.org/10.3390/polym14112275>

Academic Editor: José Miguel Ferri

Received: 30 April 2022

Accepted: 27 May 2022

Published: 2 June 2022

**Publisher's Note:** MDPI stays neutral with regard to jurisdictional claims in published maps and institutional affiliations.



**Copyright:** © 2022 by the authors. Licensee MDPI, Basel, Switzerland. This article is an open access article distributed under the terms and conditions of the Creative Commons Attribution (CC BY) license (<https://creativecommons.org/licenses/by/4.0/>).

**Keywords:** micro-pollutants; landfill; soil biota; polyethylene; polyester

## 1. Introduction

After their development over the last hundred years, plastics have been utilized in numerous ways, and are associated with every part of our lives [1]. Regardless of their benefits, issues identified with their wide application cannot be ignored. Most of these plastics are resistant and remain in the earth for generations [2]. According to recent information, worldwide plastic production reached 360 million tons in 2018. Asia is the biggest maker and consumer of the world's plastics. Among worldwide plastic producers, China is the largest (30%), trailed by Europe (17%), and in total 18% are from Canada, Mexico and US [3]. It is appropriate to specify that petrochemical plastics account for over 80% of overall plastic use. For instance, polyethylene terephthalate, polyester, polyethylene, polypropylene, polystyrene, and polyvinyl chloride are the most commonly utilized plastics [4]. Various strategies utilized for plastic waste management are dumping in a garbage lot, burning and reusing. Each of these techniques has its disadvantages; for example, plastics when burnt or incorporated into landfills utilize sources of land, which causes pollution, and limited natural resources are wasted. Currently, limited quantities are reused and this causes a hindrance to the idea of the circular economy; only 9% of plastic has been recycled from the total production of 8.3 bn metric tons since the 1950s [5,6]. It has also been reported that in 1990 Coca-Cola promised to use 25% recycled plastic by 2015, but in 2020 only 11.5% had been recycled [7].

Among the plastics which currently exist, fragmented particles have gained attention and are even more troubling. These are characterized as microplastics (1  $\mu\text{m}$ –5 mm) based on their diverse range [8,9]. Due to the smaller size and wide dispersion of these fragments, it is hard to gather them and remove them subsequently from the environment. In the same way, the speed at which they enter nature outstrips their clearance speed [10]. Besides, microplastics are found in potable water, which may become a danger to well-being [11]. Polyethylene is a generally utilized type of plastic because of its conveyance ability. Nonetheless, because of its saturated linear hydrocarbon chains, and because it can be communicated as  $-\text{CH}_2\text{-CH}_2-$ , PE items are hard to be corrupted by nature [12]. A feasible way-out of this problem is conversion of plastics by microbes. Microbes that have the potential to degrade plastics belong mostly to the phyla Proteobacteria, Firmicutes and Actinobacteria, and most were screened from polluted dumpsites. Studies should concentrate on biodegradation of microplastics focusing on the most well-known contaminants such as polyethylene [13].

Microbial assisted deterioration of polymers by bacteria and fungi has been effectively researched in indigenous habitats, such as soil. For example, *Bacillus* sp., *Rhodococcus* sp. [14], *Pseudomonas aeruginosa* [15], *Zalerionmaritimum* [16], and *Aspergillus clavatus* [17] can utilize plastic polymers as their energy source in cultivation media, therefore causing a decrease in the dry weight of polymers and inciting physical–chemical alterations which include modifications in surface morphologies. Subsequently these microbes form cracks and rough surfaces and produce chemical bonding structures, such as carbonyl groups, ketones and aldehydes [18]. Microorganisms can break down the polymers in two phases, firstly inside them, and then becoming enzymatically dissimilated in order to discharge extracellular proteins, causing chain cleavage in the monomer, which can be used by microorganisms [14]. Microbial species have the ability to change polymers into monomers and, additionally, to dissimilate into carbon dioxide and water. The biodegradation accomplished by microbes is related key characteristic such as the atomic weight and crystallinity of the polymers [19–21].

The aim of the present study is to evaluate the potential of locally isolated strains to degrade plastics with different chemical compositions based on their petrochemical origin. *Alcaligenes faecalis*, *Bacillus* spp. and *Staphylococcus* sp. were isolated from dumps in Multan, with affinity for LLDPE, HDPE and Polyester and with a considerably faster decay rate which is globally needed, especially in developing countries.

## 2. Material and Methods

### 2.1. Polyethylene and Polyester Used in the Current Study

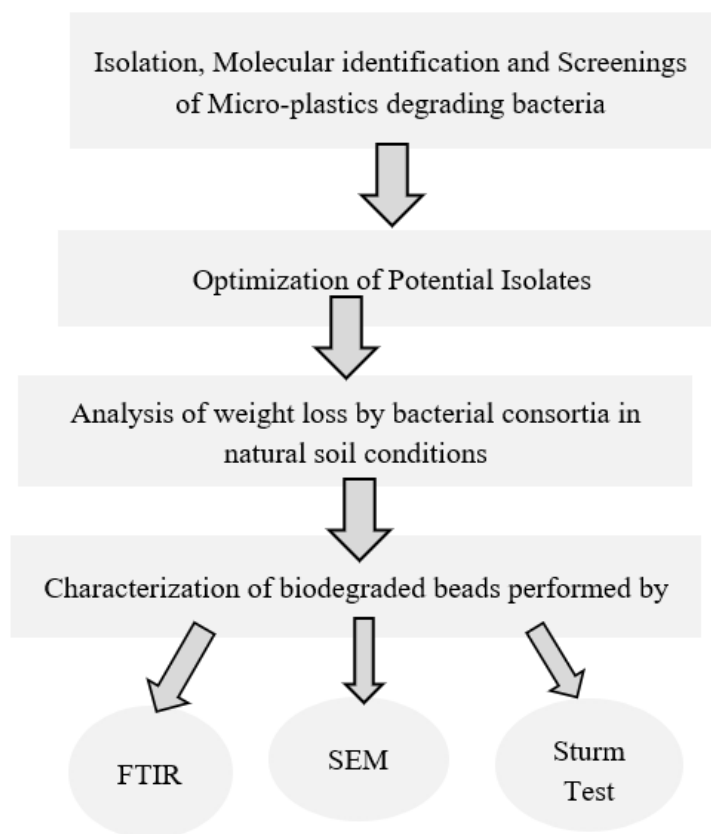
Plastic beads and powders of Linear low-density polyethylene, high-density polyethylene and aromatic Polyester used in the current study were provided by Mehran Plastic Industries Pvt Limited, Karachi, Pakistan. LLDPE, HDPE and polyester (HOROH) and terephthalic acid ( $p\text{-HOOC-C}_6\text{H}_4\text{COOH}$ ) were in the form of fine powders with 99.5% purity. Beads were sterilized, followed by washing with 70% ethanol and drying with filter paper to make them ready-to-use in experimentation.

In this study, biodegradation of microplastics and beads was carried out by soil biota.

### 2.2. Isolation, Identification, and Screening of Bacterial Isolates

Samples of soil (5 g) were collected from different municipal dumpsites in Multan which are heavily contaminated with various plastic waste, in commercial areas. These specified areas were chosen since they had been used as a plastic dump site for a very long time, expanding the likelihood of finding bacteria that has the ability to degrade plastics. By using a conventional serial dilution method, 50  $\mu\text{L}$  from  $10^{-6}$  dilution was spread on a nutrient agar (Sigma Aldrich, Saint Louis, MO, USA) plate infused with 1% of plastic powder for the isolation of plastic degrading bacteria, and for each type of given plastic this procedure was repeated. After 15 days of incubation at 37  $^\circ\text{C}$ , bacteria with distinct zones were selected and sub-cultured for further characterization [10]. Based on morphological

characterization of the bacterial colony after primary screening, Gram-stained slides were observed under light microscope at 40× and 100× for identification. Figure 1 graphically explains the research framework.



**Figure 1.** Schematic diagram of the study.

Secondary screening of isolates was performed by both static and shaking methods using mineral salt medium previously used by Osman et al. [22] supplemented with 5% polyethylene (LLDPE and HDPE) and polyester powder. Isolation of plastic degrading bacteria was verified by streaking the bacteria on 5% concentration solid media, and diameter of zone was observed after 15 days of incubation at 37 °C, while shaking technique involved biodegradation assay and liquid media. After secondary screening, molecular identification was performed by amplification of 16S rRNA gene by using primers 785F 5' (GGA TTA GAT ACC CTG GTA) 3', 27F 5' (AGA GTT TGA TCM TGG CTC AG) 3 from the MacroGen sequencing system. Sequences were analyzed utilizing the BLAST tool from the National Centre for Biotechnology Information (NCBI) (<https://www.ncbi.nlm.nih.gov/> accessed on 25 May 2022) against reference 16S rRNA sequences of type strains and submitted to GenBank. To construct consensus, neighbor joining tree phylogenetic analysis was carried out by using Molecular Evolutionary Genetics Analysis (MEGA) version 7 software (Pennsylvania State University, State College, PA, USA) [23].

### 2.3. Rate of Deterioration by Weight Loss Strategy and the Impact of Temperature and pH on Weight of Plastic

Isolates showing zone of clearance in static secondary screening were further assessed in the degradation study. Each isolate was separately inoculated in flasks containing 20 mL of minimal medium and beads of Polyethylene (LLDPE and HDPE) and Polyester,

separately. The biodegradation study was implemented for a period of 40 days. Analysis was carried out by weight reduction using the following formula [24].

$$\text{Weight loss \%} = \frac{\text{initial weight} - \text{final weight}}{\text{initial weight}} \times 100 \quad (1)$$

Biodegradation study of LLDPE, HDPE and Polyester was performed at different temperature and pH conditions in order to optimize the isolated bacterial cultures in different environmental conditions, for future study. The range of temperature used was 30–45 °C, and the pH was maintained at 4.0 and 8.0 scale. The weight of plastic beads was recorded earlier. Optimization of isolates was carried out for 15 days [25].

#### 2.4. Formulation of Microbial Consortia and Determination of Weight Loss for the Mixture of Plastic Pellets in Local Natural Conditions

An acclimated consortium capable of degrading polyester, high-density and linear low-density polyethylene pellets was developed in the laboratory. A 500 mL flask with nutrient broth (Sigma Aldrich, Saint Louis, MO, USA) inoculated with *Alcaligenes faecalis*, *Streptococcus* sp. and three types of *Bacillus* spp. was utilized for the degradation experiment. Subsequently, the consortium was cultured, until lag phase was developed, for 6 days. A control was set up containing just broth and beads of LLDPE, HDPE and polyester [26], to examine biodegradation of LLDPE, HDPE and Polyester in off-site conditions. The biodegradation of commercially available plastic beads under the attack of bacteria was studied using the soil burial method for an interval of three months. Pre-weighted beads were washed with 70% ethanol and added to soil. Sterilized pellets were added to soil along with nutrient broth and inoculum. Soil selected was clay loam with pH 8.0. The experiment proceeded from March to May, so temperature variations (23 °C to 45 °C) could be noted.

#### 2.5. Analysis of Plastic Beads Degradation by Sturm Test

Plastic degrading bacteria can break down the long chains of polymers into monomers by their different activities, either by oxidation or enzymatic hydrolysis. CO<sub>2</sub> evolved as a result of mineralization of plastics in aerobic conditions. Evolution of CO<sub>2</sub> by bacterial isolates can be assessed by Sturm test applied in a modified way. Pre-weighted beads of LLDPE, HDPE and Polyester were added to a flask containing 5 mL of MSM broth, and then 1 mL of KOH (1M) was added. This was inoculated with 24 h old culture and incubated in a rotatory incubator for 25 days. Aerobic conditions were maintained in the rotatory incubator. After 25 days of incubation, the amount of carbon dioxide generated was calculated in the test and in the control. CO<sub>2</sub> produced as a result of mineralization was trapped in a flask containing KOH. Barium chloride solution BaCl<sub>2</sub> (1M) was added to this flask, and as a result barium carbonate precipitates formed. Precipitates were filtered on filter paper and dried at 50 °C in an oven for an hour. The weight of the precipitates indicates CO<sub>2</sub> generation by test organism as their end product [27].

#### 2.6. Surface Modification Analysis of Plastic Beads by Scanning Electron Microscopy

Degraded beads of aromatic polyester, and linear-low density and high-density polyethylene were set up on an aluminum-disk with a width of 1.2 cm using double sided black colored carbon tape. Sputtering of samples with a thin layer of gold in a vacuum chamber was performed using argon gas and an electric current of approximately 3 mA. Then labelled tests pellets were placed sequentially in the scanning electron microscope chamber and magnification was set to display images at 500×, 1000× and 10,000× with a TESCAN MERA 3 field emission scanning electron microscope [28].

#### 2.7. Structural Changes in Plastic Beads—Analysis by Fourier Transform Infrared Spectroscopy

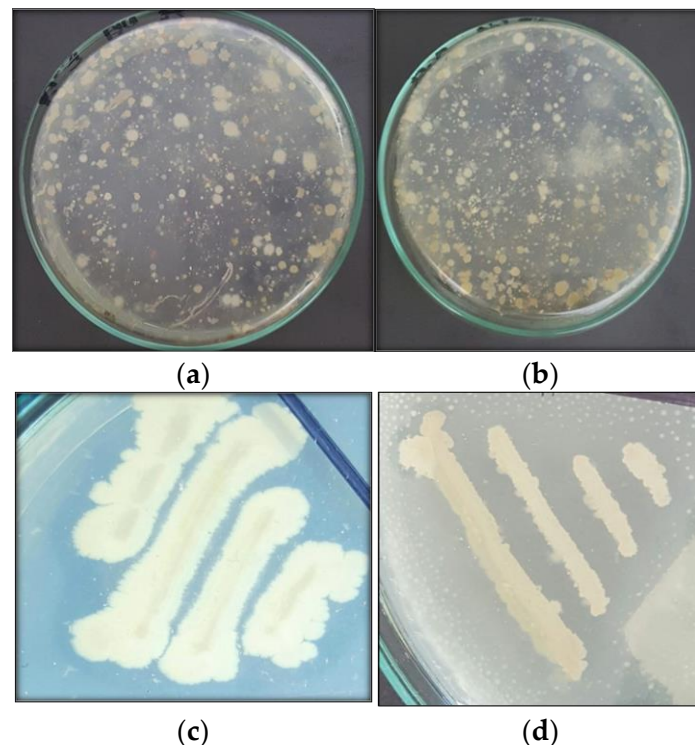
The LLDPE, HDPE and Polyester beads treated with isolated bacteria for 40 days were examined by FTIR. Background noise was eliminated by performing a blank scan in the frequency range of 4000 to 600 cm<sup>-1</sup>. Thus, the samples were scanned in the region

of 400–4000  $\text{cm}^{-1}$  at a resolution of 4  $\text{cm}^{-1}$ . The resultant spectrum included a plot of rate transmittance versus wave number, which was additionally investigated against the respective comparative controls [29].

### 3. Results

#### 3.1. Isolation and Screening of Bacteria with Potential to Degrade Microplastics of LLDPE, HDPE and Polyester

In the present study, isolation of effective polyethylene (LLDPE, HDPE) and aromatic polyester with degrading bacteria from municipal landfill soil was carried out. The dump sites' soil samples were collected from the historic Daulat gate of the city, Northern Bypass, Sher-shah Road and Shujabad Road. Morphologically distinct isolates were used to determine the ability to use plastic as carbon source. The experiments were conducted over a screening series. Primary screening led to the isolation of 54 bacterial isolates. Out of 54 isolates, 37 were considered as linear low-density polyethylene degraders (68.5%), 18 isolates were high-density polyethylene degraders (33.3%) and seven isolates were polyester microfiber degraders (12.9%) as shown in Figure 2. Out of 54 isolates, bacterial isolates which show distinct growth and zone were streaked on 5% concentration of each given type of microplastic and observed after the formation of clear zones. *Alcaligenes faecalis* (SA-5) shows a zone of clearance with 3 mm for polyester microfibers and 1 mm for LLDPE. *Bacillus cereus* (SA-68) shows a 6 mm diameter for LLDPE and a 2 mm for HDPE. *Bacillus* spp. (SB-14) shows a 4 mm diameter for LLDPE and a 0.25 mm for polyester microfibers. Another *Bacillus* spp. (SC-9) shows a 1.5 mm diameter for HDPE and a 3 mm for LLDPE microplastics. *Streptococcus* spp. (SC-56) shows a 5 mm zone diameter for LLDPE and a 0.5 mm diameter for HDPE microplastics. These five isolates show prominent zones and were tested further for biodegradation assay.

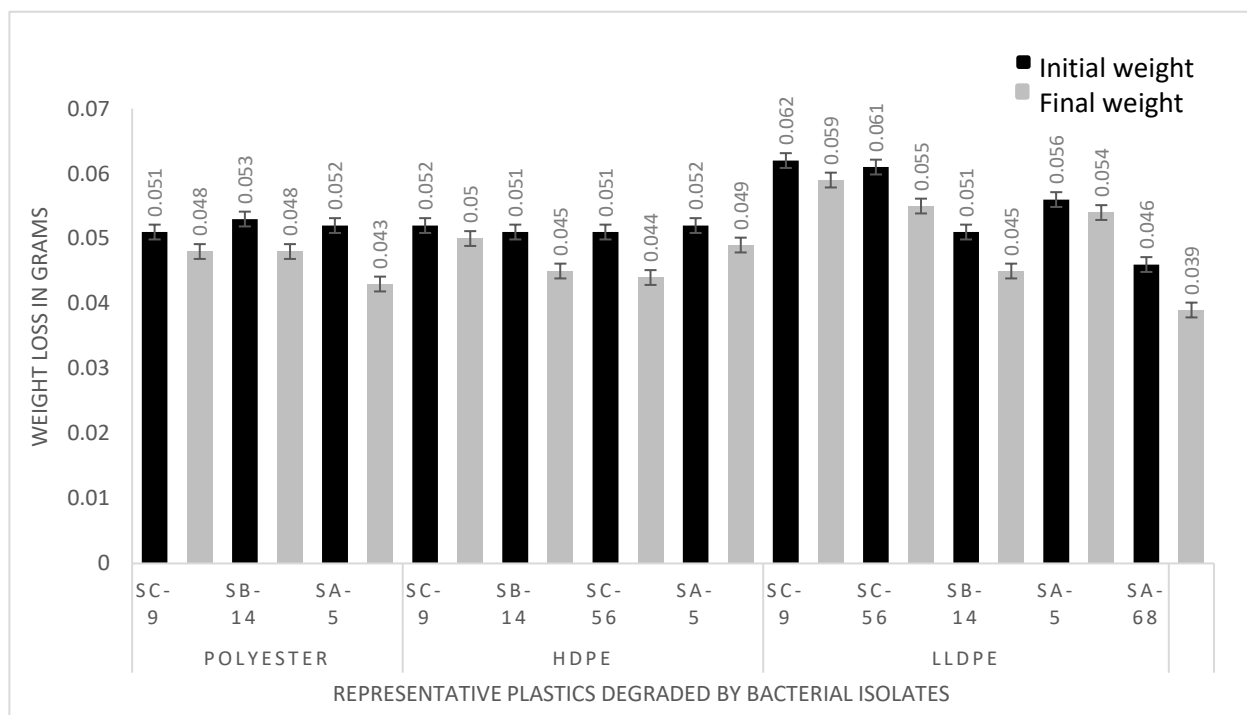


**Figure 2.** (a,b) showing growth of bacterial colonies on LLDPE and HDPE with clear zones, (c,d) showing growth of bacterial isolates on LLDPE and Polyester.



### 3.2. Assessment of the Polyethylene (LLDPE and HDPE) and Polyester Deteriorating Bacteria Based on Weight Loss Percentage in Ex-Situ and Laboratory Conditions

The degradation was determined by calculating the percentage of weight loss in polyethylene and polyester beads by isolated bacteria after 40 days of incubation. Linear low-density polyethylene degraded by SA-5 (*Alcaligenes faecalis*) (MK517568), SA-68 (*Bacillus cereus*) (MK517567), *Bacillus* sp. (SB-14 and SC-9) and *Streptococcus* spp. (SC-56) by 3.5%, 15%, 11.8%, 4.8% and 9.8%, respectively. High density polyethylene was degraded by SA-5 (*Alcaligenes faecalis*) (MK517568) *Bacillus* sp. (SB-14 and SC-9) and *Streptococcus* spp. (SC-56) by 5.8%, 11.7%, 3.8% and 13.7%, respectively. Polyester was degraded by SA-5 *Alcaligenes faecalis* (MK517568), *Bacillus* sp. (SB-14 and SC-9) by 17.3%, 9.4% and 5.8%, respectively. Difference between initial and final weight indicates the significant extent of polyethylene and polyester utilization by the bacteria, as shown in Figure 3. Replicates were used to gain statistical confidence as standard deviation was used, while control (no bacteria) showed zero percentage of degradation, and beads were floating in the media. In the treatment flasks, beads had settled down due to bacterial action.



**Figure 3.** Significant weight reduction in plastic by bacteria—results shown by potential isolates.

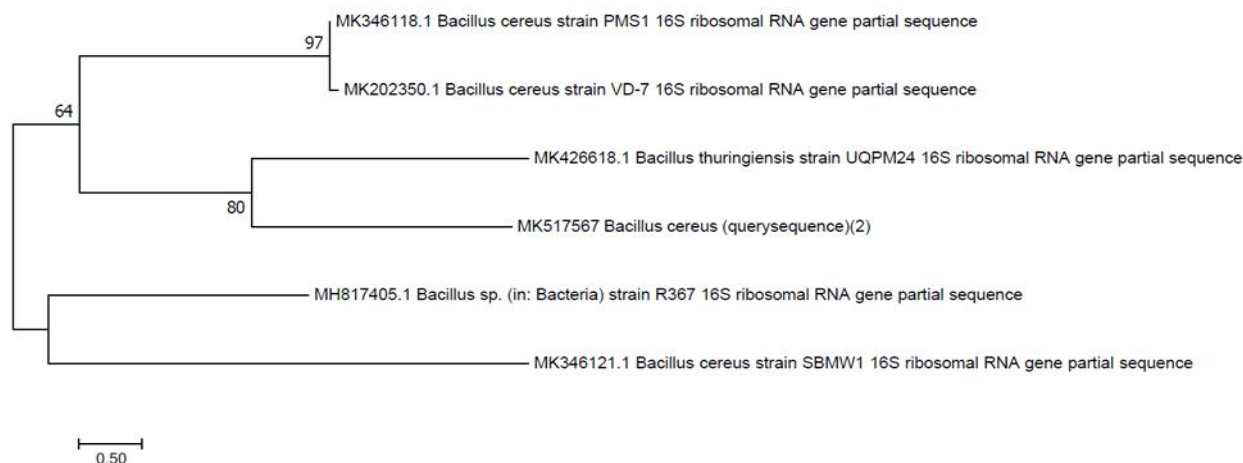
After the biodegradation assay, bacteria were optimized. After 15 days of incubation with continuous shaking, maximum percentage reduction in weight or percentage loss in weight (% WL) of the polyester beads was recorded with *Bacillus cereus* (MK517567) ( $29.4 \pm 0.05$ ) at 30 °C, as the highest weight loss during the experiment. *Alcaligenes faecalis* (SA-5) revealed 6.6% polyester-degradation at 45 °C. Polyester degradation was carried out at 30 °C as well as at 45 °C by both isolates (SA-5 and SA-68), respectively. In addition, 3.5% high density polyethylene degradation was recorded by *Alcaligenes faecalis* (SA-5), and *Bacillus cereus* (SA-68) showed ( $6.6 \pm 0.02$ ) for HDPE. At 30 °C the highest weight loss was observed by *Bacillus cereus* (SA-68) for polyester, along with ( $8.0 \pm 0.02$ ) for LLDPE. *Bacillus* spp. (SB-14 and SC-9) and *Streptococcus* sp. did not show very promising results in changing environmental conditions. SA-5 and SA-68 were considered as promising degraders and were identified by sequencing.

### 3.3. Determination of Weight Loss in Local Natural Conditions by Consortium

The percentage of weight loss in natural conditions was  $4.3 \pm 0.02$ ,  $4.8 \pm 0.02$  and  $2.7 \pm 0.02$  for LLDPE, HDPE and polyester beads after 90 days of incubation, respectively. The weight loss percentage of plastics strips was  $4.8 \pm 0.02$  and  $4.9 \pm 0.02$  for LLDPE and HDPE after 90 days of incubation, respectively. At the end of incubation, plastic strips were easy targets for bacteria compared to beads, and the possible reason for this may be that bacterial strain utilized the released C compounds from plastic strips during the degradation. It is suggested that the result with this type of method was observed for the first time in this region, and will help in the degradation of plastic strips under different environmental conditions.

### 3.4. Characterization and Molecular Identification

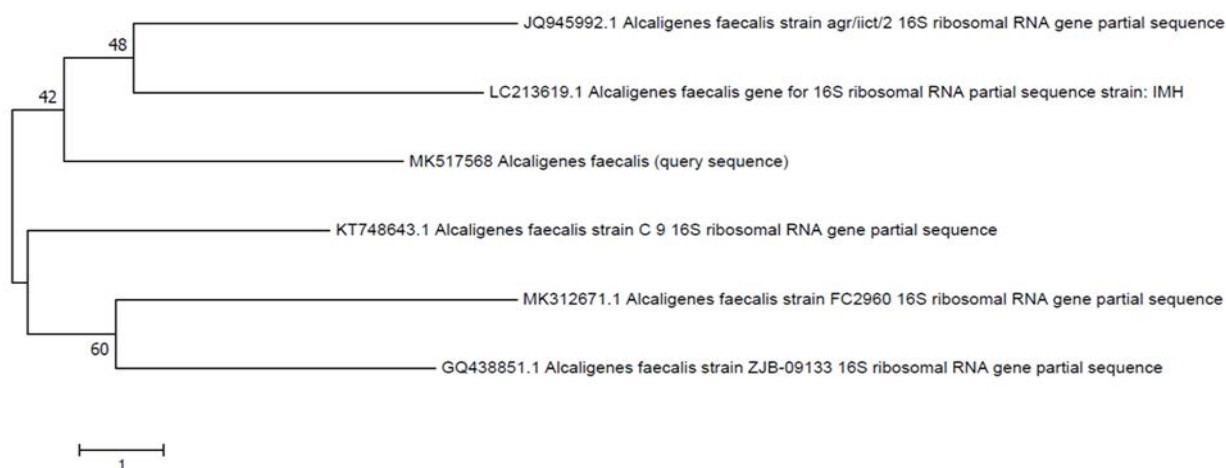
The morphological characteristics of the bacterial isolates were identified by conventional methods. Gram staining of bacterial isolates show that they are Gram-positive rods and cocci. Growth on nutrient media with small, circular, flat, white colored, opaque or translucent colonies with smooth edges was observed on the plates. Biochemical testing revealed that isolates are catalase, indole and MRVP negative, while positive for starch hydrolysis. SB-14 gives a yellow butt and red slant with gas production. Based on the 16S rRNA gene sequencing and biochemical characterization, the bacteria isolated from the site mainly belonged to Bacilli from *Bacillus cereus* and *Alcaligenes*. As inferred by 16S rRNA gene analysis, strain SA-68, showed 99% similarity with corresponding gene sequences of reference strains *Bacillus cereus* SBMW1 and strain SA-5 showed 100% similarity with *Alcaligenes* sp. (KX164437.1), respectively. Phylogenetic trees (Figures 4 and 5) showed that the strain was clustered on separate branches, with reference strains belonging to respective genera. The GenBank nucleotide accession numbers were assigned to strain *Bacillus cereus* SA-68 is MK517567, respectively. Query sequence was designated as *Alcaligenes faecalis* with GenBank accession no. MK517568.



**Figure 4.** Neighbor joining tree of *Bacillus cereus* (MK517567).

### 3.5. Degradation of Plastic Beads Confirmed by CO<sub>2</sub> Production in Sturm Test

Carbon dioxide, evolved as a result of deterioration of polyethylene (LLDPE, HDPE) and polyester by *Alcaligenes faecalis* (SA-5), *Bacillus cereus* (SA-68), *Bacillus* spp. (SB-14 and SC-9) *Streptococcus* sp. (SC-56), was trapped and compared to the amount evolved in the case of biotic control under similar conditions. Evolved carbon dioxide calculated from media inoculated was 0.602 g, 0.427, 0.723, 0.524 and 0.205 g/5 mL CO<sub>2</sub> g<sup>-1</sup> of C, respectively, while the control flask indicated no precipitates.



**Figure 5.** Neighbor joining tree of *Alcaligenes faecalis* (MK517568).

### 3.6. Fourier-Transform Infrared Spectroscopy (FTIR) Analysis

The changes in spectral peaks due to biodegradation were determined using a FTIR (ATR-alpha Bruker) spectrophotometer. The degradation of linear-low density and high-density polyethylene and aromatic polyester was confirmed by the changes in spectra of the FTIR analysis. The pellets without any treatment served as control, and pellets of LLDPE, HDPE and Polyester treated with isolated *Alcaligenes faecalis*, *Bacillus* sp. and *Streptococcus* spp. in MSM broth acted as test. In the case of LLDPE, the results of this study demonstrated that LLDPE pellets showed four peaks in the range from 2900 to 715  $\text{cm}^{-1}$ , at 2913.92, 2846.83, 1462.50 and 718.05. The vibrational mood of peaks was observed in comparison with control, and when LLDPE pellets were treated with *Alcaligenes faecalis* (SA-5), they showed more vibrational shifts than with *Bacillus* spp. (SC-9). The first peak shifted to 2913.83  $\text{cm}^{-1}$  which indicates the C–H stretching of the methyl group, the second peak shifted to 2846.50  $\text{cm}^{-1}$  which indicates the C–H symmetric and asymmetric stretching of methylene (C–H<sub>2</sub>), the third peak shifted to 1462.05  $\text{cm}^{-1}$  which indicates the C=C and replacement of carbonyl bond with amine bond, and the fourth peak shifted to 718.23  $\text{cm}^{-1}$  which indicates the –C=C– stretching and the presence of alkene group as shown in Table 1. For HDPE, the spectral peaks were observed from 2900 to 715  $\text{cm}^{-1}$  when treated with bacterial isolates. The four peaks were observed from control of HDPE at 2913.94 (C–H stretching–CH<sub>3</sub>), 2846.58 (CH stretching–CH<sub>2</sub>), 1461.42 (bending C–H bond of methylene) and 718.23  $\text{cm}^{-1}$  (C–O). In case of treatments with bacterial isolates, the wave number of spectral peaks showed shifts up to 2914.37  $\text{cm}^{-1}$  which indicates the vibrations in the stretching of C=C bond seen in alkanes. The second peak showed shifts to 2846.70  $\text{cm}^{-1}$  which indicates the stretching of C–H bonds in methylene, and the absorbance range of 3000–2800  $\text{cm}^{-1}$  corresponds to C–H stretching and the presence of alkanes. The third peak shifted to 1461.76  $\text{cm}^{-1}$  which indicates the –CH<sub>2</sub> stretching and presence of aromatics, and the band around it also corresponds to bending deformation. The fourth peak shifted to 717.82  $\text{cm}^{-1}$  which indicates the rocking deformation of bonds. For Polyester, two treatments were given for SA-5 and SC-9. as both were showed biodegradation for polyester along with other treatments. The nine spectral peaks were observed in control of polyester at 2024.83 (C–H), 1709.16 (Carbonyl group), 1409.10 (C=C), 1339.65 (CH<sub>3</sub>), 1241.02 (Ar–O–R), 1097.75 (C–O), 1017.93 (C–O), 871.00 (Aromatic ring) and 720.01  $\text{cm}^{-1}$  (Mono-substituted aromatic ring). With treatment, the peak shifted to 1710.84  $\text{cm}^{-1}$  which indicates a change the carbonyl group’s polyester component and thus the cleavage of the ester bond. The other peak shifted to 1408.45  $\text{cm}^{-1}$  which indicates the decrease in intensity of band leads to bond cleavage of C=C. The other band shifted to 1340.04 which indicates CH<sub>3</sub> symmetrical bending. The fourth peak shifted to 1238.19 which indicates the asymmetrical bending of Ar–O–R. The fifth peak shifted to 1088.58 which indicates the bond cleavage of C–O, and 1017.93 (control) shifted to 1016.01 which indicates the bond cleavage of C–O. The peak

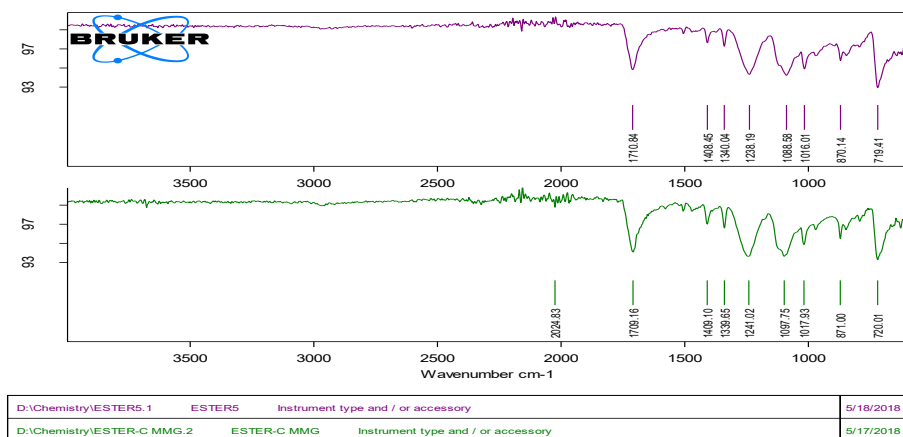
871.00 (control) shifted to 870.14 which indicates the aromatic ring bend out of plane and the peak 720.01 (control) shifted to 719.4 which indicates the stretch of monosubstituted ring. The first peak, which disappeared after treatment with SA-5, indicates that cleavage of C–H bond occurred which shows the formation of new intermediate products, as shown in Figure 6.

**Table 1.** FTIR peaks corresponding to vibrational moods and functional groups of LLDPE and HDPE.

Spectral Peaks Shift in LLDPE				
Peak Number	1	2	3	4
Frequency (cm <sup>-1</sup> )	2913.83	2846.50	1462.05	718.23
Vibrational mood & Functional Group	C–H stretching of methyl group	C–H symmetric and asymmetric stretching of methylene (C–H <sub>2</sub> )	C=C and replacement of carbonyl bond with amine bond	–C=C– stretching and the presence of alkene group

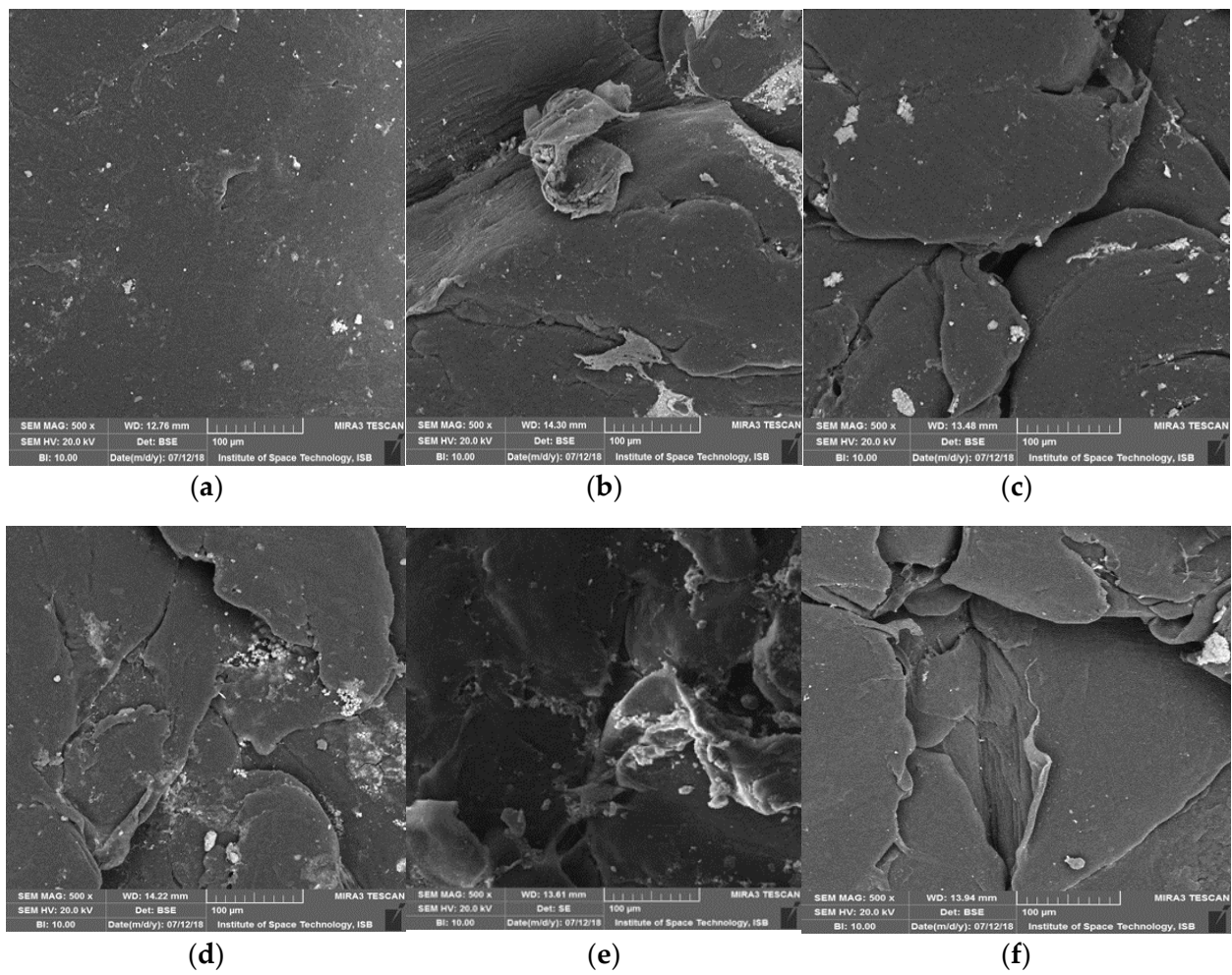
Spectral Peaks Shift in HDPE				
Peak Number	1	2	3	4
Frequency (cm <sup>-1</sup> )	2914.37	2846.70	1461.76	717.82
Vibrational mood & Functional Group	stretching of C=C bond	stretching of C–H bonds in methylene	–CH <sub>2</sub> stretching	C=C– stretching



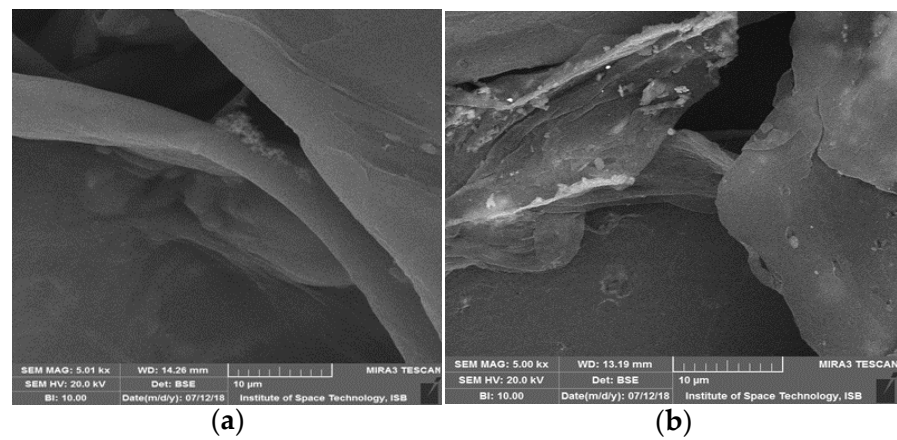
**Figure 6.** Spectral peaks of Polyester indicating the comparison of *Alcaligenes faecalis* (SA-5) with control.

### 3.7. Surface Modifications Confirmed by Scanning Electron Microscopic Analysis

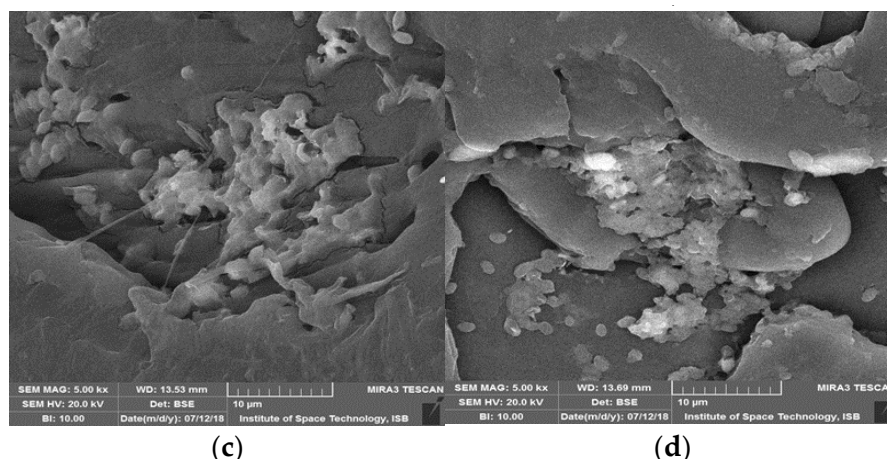
In this study, properties were authenticated with SEM and FTIR analysis. Degradation and morphological changes in polyester, liner-low density and high-density polyethylene pellets after bacterial treatment were analyzed by scanning electron microscopy. As regards the length of all samples, degradation was observed due to the roughness of surfaces and formation of cracks/holes/scions. (Figures 7–9). Bacterial cells attached to surfaces were also visualized on some tested pellets. Scanning electron micrographs revealed that isolates cause localized surface deterioration in the plastic pellets, while the outside of untreated plastics is flawless and smooth even following 40 days of incubation. LLDPE samples’ surface indicates bacterial attachment and bacterial actions on surface as shown at 500×, while HDPE and polyester are shown at 1000 and 10,000× for better understanding.



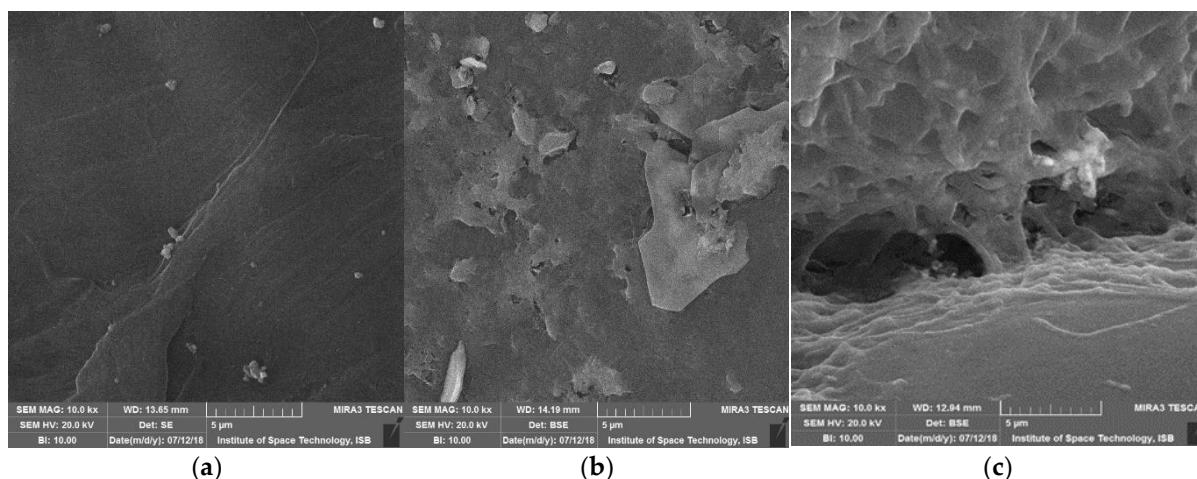
**Figure 7.** SEM captures of LLDPE beads following 40 days of incubation by isolates. (a) Control, (b) SA-5 *Alcaligenes faecalis* treated LLDPE showing bacterial attachment, (c) SA-68 *Bacillus cereus* treated LLDPE showing surface cracks, (d) SB-14 treated LLDPE showing surface erosion, (e) SC-56 treated LLDPE showing granules of bacterial action, (f) SC-9 treated LLDPE showing pith and groove.



**Figure 8.** Cont.



**Figure 8.** SEM captures of HDPE beads following 40 days of incubation by isolates. (a) Control showing no bacteria present, (b) SA-5 *Alcaligenes* treated HDPE showing groove, (c) SB-14 treated HDPE showing bacterial granules, (d) SC-56 treated HDPE showing surface cracks and bacterial attachment.



**Figure 9.** SEM captures of polyester beads following 40 days of incubation by isolates. (a) control-smooth surface, (b) SA-5 *Alcaligenes* treated polyester showing piths, (c) SB-14 treated polyester showing groove, piths and holes.

#### 4. Discussion

Detrimental effects of plastic waste are increasing. Therefore, its elimination from the earth is fundamental. Among thermal, photooxidative, mechanochemical, and catalytic degradation strategies, biodegradation is considered as the best choice for plastic waste degradation on account of the minimal effort required and its eco-accommodating nature [30]. However, detailed characterization of proficient plastic-deteriorating microorganisms and microbial compounds should be completed [31]. Different studies demonstrate the biodegradation of plastics by marine water isolates and rhizosphere samples, but this study isolated bacteria from municipal landfill sites, as these sites are capable of accommodating bacteria with high potential to degrade plastics and remain stable. The current study from Multan, Pakistan isolates 54 bacterial isolates with a potential to degrade different types of microplastics and beads, and to the best of the author's knowledge no previous studies have been found on isolation of these bacteria from this region. Therefore, these indigenously isolated strains can be a valuable input for combating plastic pollution waste. Earlier in 2013 from Islamabad, Pakistan, Shah reported polyester-polyurethane degrading bacteria [32]. Primary screening results on the growth of isolates along with zones on

infused media with plastic powder, and repeated screening with 5% concentration, led to formation of clear zones ranging from 0.25 to 6 mm. Compared to this, in a study conducted from Iraq the zones ranged from 2.5–3.0 mm on 0.1% LDPE infused MSM, which implied that the bacterial colonies engendering a clear zone were capable of degrading polyethylene in minimal media [10]. In the treatment flasks, beads settled down due to bacterial action. Many studies report that film-type plastics required at least two months for biodegradation to occur [33], which is a very long time for testing and makes them unsuitable for identification of new bacterial strains. Alternatively, the surface area of beads is larger than that of plastic films, and the chance of bacterial attachment increases, which may speed up the reaction [34]. To test this, we prescribed 40 days of incubation for beads in liquid media, and both rate of biodegradation and efficiency were improved. The apparent degradation efficiency was assessed by weight loss of beads in MSM, *Bacillus cereus* degraded LLDPE by 15%. *Alcaligenes faecalis* degraded polyester by 17.3% and weight loss for other types of plastic was also noted as mentioned in the appropriate section. Weight reduction may have been due to the different metabolism rate of different species. Different studies have reported that the rate of degradation of polyethylene varied from 1.5 to 13% as according to different assays and types of microbes [35]. Another study from India also supports that *Bacillus* spp. are plastic degraders by using *Bacillus amyloliquefaciens* as LDPE degraders [36]. All these studies indicate that these are degraders for specific types of plastic, but for this study *Alcaligenes faecalis* and *Bacillus cereus* showed the potential to degrade more than a single type of plastic. Weight reduction was also optimized at different environmental conditions in the laboratory and outside, in which *Bacillus cereus* (SA-68) showed maximum tolerance and degraded polyester by 29% weight loss after 15 days of incubation. In another study, optimization of growth media was carried out in which pH of the media containing HDPE gradually decreased after 90 days of incubation from 7.3 to 5% [37]. We optimized bacteria for their growth and potential ability to degrade plastic in different environmental conditions, although different studies use *Alcaligenes faecalis*, *Bacillus* spp. and *Streptomyces* spp. as potential degraders. In another study, *Alcaligenes faecalis* was isolated from PET-treated soil and confirmed as plastic degrader by FTIR analysis [38]. Another study from Iraq used *Streptomyces* spp. as source for pollution control, but suggested it was best as an LDPE degrader isolated from soil [39]. More than these studies, the effectiveness of degradation noticed in this study was comparable to that of LDPE film degraded by mixed microbial cultures of *Bacillus* sp. and *Paenibacillus* sp., in which both bacteria together exhibit at 15% the highest degradation efficiency [36]. Studies have described that plastics can be degraded into monomers, and then these monomers are converted into CO<sub>2</sub> and water. To test this, a Sturm test was performed with a modified procedure. In another study, the process used involved titration with thiosulphate and sodium hydroxide in the presence of barium chloride and KOH. The highest rate of evolution for LDPE was 6.28 g/L and the lowest was 1.19 g/L [27]. Compared to this, the present study involves 0.723/5 mL noted previously. Curiously, the surfaces of pellets were seen to have become uneven and filled with cracks and grooves [10]. After thorough observations in different studies, it has been demonstrated that microorganisms can change not only appearance but functional groups and other characteristics [40]. In this study, these properties were authenticated by SEM and FTIR analysis. Previous studies utilized SEM micrographs as an analytical tool to demonstrate erosions, cavities, and pores formed on plastic films in order to indicate the extent of colonization and degradation [41]. Curiously, authors describe the surfaces of pellets as seen to have become uneven and filled with cracks and grooves [10]. Other studies also confirmed degradation by formation of biofilm on the plastic surface. In the study conducted in 2014 on LDPE degradation by *Bacillus amyloliquefaciens* isolated from municipal solid, SEM analysis revealed that both the strain exhibited adherence and growth with LDPE, used as a sole carbon source [36]. Another study that used a photocatalytic technique for deterioration of polystyrene also indicates that cavities/holes increased in size after the treatment [42]. In the present study it was also observed that cavities or holes were produced in pellets. SEM analysis revealed

surface erosion and bacterial adhesion by giving proof of the deterioration of the plastic beads because of the activity of the bacteria, and ensured the degradation capability of the bacteria. In addition to these analyses, isolated strains efficiently degrade beads and microplastics of various categories of plastic. Hence, the difference in biodegradation rate between LLDPE, HDPE and polyester may be due to the presence of specific enzymes or concentrations of different enzymes required for kinds of different plastic degradation. This demonstrates that, during growth of bacteria, there may be different metabolism rates and uptake of energy from plastic as a source of carbon [34]. PE microplastics can be categorized into HDPE and LDPE. Enzyme based degradation is divided into two steps, extracellular and intracellular. In the first step, LDPE is broken down into shorter chains and in the next is step followed by mineralization into CO<sub>2</sub> and H<sub>2</sub>O as described in the Sturm test. Laccase and Alkane showed that the reaction in polyethylene belong to that of the AlkB family of enzymes, while Laccase is the most commonly reported enzyme responsible for HDPE degradation, and alkane hydrolase for LDPE degradation [13,43]. Other studies also confirmed that manganese peroxidase and laccase enzymes produced by *Bacillus cereus* were involved in the degradation of low-density polyethylene after an incubation of nine weeks followed by confirmation by FTIR [41]. Another study explained that *Alcaligenes faecalis* produced extracellular enzymes such as CMCase, protease, xylanase and lipase, which indicates that the surface of the plastic was attacked by these enzymes after SEM and FTIR analysis [44]. Montazer et al. explain that these secreted bacterial enzymes followed the formation of monomers by the β-oxidation system pathway [45]. Spectral changes indicate the changes in formation of new bands at 1460, 600–700 cm<sup>-1</sup>. Our observations are similar to a previous report in which bands at 2900, 720, 1460 cm<sup>-1</sup> indicated the rocking deformation and stretching of bonds [46]. Another study also explains the degradation of Polyester and observed FTIR peaks, and functional groups observed were similar to the present study as CO (2230–2050 cm<sup>-1</sup>), aliphatic compounds (3140–2640 cm<sup>-1</sup>), carbonyl compounds (1900–1680 cm<sup>-1</sup>) and alkene (940–850 cm<sup>-1</sup>) are identified [47]. In another study, it was observed through FTIR that addition of –OH group to LDPE backbone was due to the activity of bacteria producing enzymes for degradation of plastic [48]. In this study, observations were made which indicate that cleavage in the carbonyl group also suggests plastic degradation. In addition to these analyses, isolated strains efficiently degrade beads and microplastics of various categories of plastic.

## 5. Conclusions

The current investigation demonstrated the degradation of three types of plastic by soil bacteria isolated from municipal landfill sites. Among 54 isolates, *Alcaligenes faecalis* acted as most the promising candidate, but *Bacillus* spp. and *Streptococcus* sp. performed successful degradation, with stability. Bacterial attachment and formation of cracks were well observed via scanning electron microscope. The methods developed may help in future to screen and identify new bacterial strains that have the capability of degrading more than single type of plastic.

**Author Contributions:** Conceptualization, methodology, S.S. and A.T.; software, A.T.; validation, N.J.; formal analysis, A.T. and N.J.; investigation, S.S.; resources, R.B. and N.J.; data curation, R.B.; writing—original draft preparation, N.J.; visualization, S.S.; supervision, A.I.; project administration, A.I.; funding acquisition, R.B. All authors have read and agreed to the published version of the manuscript.

**Funding:** This research received no external funding.

**Informed Consent Statement:** All authors gave their informed consent prior to their inclusion in the study.

**Acknowledgments:** Authors acknowledged by department of Microbiology and Molecular Genetics, The Women University, Multan.

**Conflicts of Interest:** The authors declare no conflict interest.



### Abbreviations

LLDPE	Linear low-density polyethylene
HDPE	High-density polyethylene
SEM	Scanning Electron Microscope
FTIR	Fourier Transform Infrared Spectroscopy

### References

- Zhang, J.Q.; Gao, D.; Li, Q.H.; Zhao, Y.X.; Li, L.; Lin, H.F.; Bi, Q.R.; Zhao, Y.C. Biodegradation of polyethylene microplastic particles by the fungus *Aspergillus flavus* from the guts of wax moth *Galleria mellonella*. *Sci. Total Environ.* **2019**, *704*, 1–29. [[CrossRef](#)] [[PubMed](#)]
- Tiwari, N.; Santhiya, D.; Sharma, J.G. Microbial remediation of micro-nano plastics: Current knowledge and future trends. *Environ. Pollut.* **2020**, *265*, 115044. [[CrossRef](#)] [[PubMed](#)]
- Plastics Europe. *Plastics—The Facts 2020: An Analysis of European Plastics Production, Demand and Waste Data 2019*; Plastics Europe: Brussels, Belgium, 2020.
- Urbanek, A.K.; Rymowicz, W.; Mironczuk, A.M. Degradation of plastics and plasticdegrading bacteria in cold marine habitats. *Appl. Microbiol. Biotechnol.* **2018**, *102*, 7669–7678. [[CrossRef](#)] [[PubMed](#)]
- Geyer, R.; Jambeck, J.R.; Law, K.L. Production, use, and fate of all plastics ever made. *Sci. Adv.* **2017**, *3*, e1700782. [[CrossRef](#)] [[PubMed](#)]
- Chen, Y.; Awasthi, A.K.; Wei, F.; Tan, Q.; Li, J. Single-use plastics: Production, usage, disposal, and adverse impacts. *Sci. Total Environ.* **2020**, *752*, 141772. [[CrossRef](#)] [[PubMed](#)]
- DelemareTangpuori, A.; Harding-Rolls, G.; Urbancic, N.; Banegas Zallio, X.P. *Talking Trash: The Corporate Playbook of False Solutions to the Plastics Crisis*; Changing Markets Foundation: Utrecht, The Netherlands; London, UK, 2020.
- Eerkes-Medrano, D.; Thompson, R.C.; Aldridge, D.C. Microplastics in freshwater systems: A review of the emerging threats, identification of knowledge gaps and prioritisation of research needs. *Water Res.* **2015**, *75*, 63–82. [[CrossRef](#)]
- Gigault, J.; Ter Halle, A.; Baudrimont, M.; Pascal, P.-Y.; Gauffre, F.; Phi, T.-L.; El Hadri, H.; Grassl, B.; Reynaud, S. Current opinion: What is a nanoplastic? *Environ. Pollut.* **2018**, *518*, 1030–1034. [[CrossRef](#)]
- Auta, H.S.; Emenike, C.U.; Fauziah, S.H. Screening of *Bacillus* strains isolated from mangrove ecosystems in Peninsular Malaysia for microplastic degradation. *Environ. Pollut.* **2017**, *231*, 1552–1559. [[CrossRef](#)]
- Novotna, K.; Cermakova, L.; Pivokonska, L.; Cajthaml, T.; Pivokonsky, M. Microplastics in drinking water treatment—Current knowledge and research needs. *Sci. Total Environ.* **2019**, *667*, 730–740. [[CrossRef](#)]
- Das, M.P.; Kumar, S.; Das, J. Fungal-mediated deterioration and biodegradation study of low-density polyethylene (LDPE) isolated from municipal dump yard in Chennai, India. *Energy Ecol. Environ.* **2018**, *3*, 229–236. [[CrossRef](#)]
- Matjašič, T.; Simčič, T.; Medvešek, N.; Bajt, O.; Dreo, T.; Mori, N. Critical evaluation of biodegradation studies on synthetic plastics through a systematic literature review. *Sci. Total Environ.* **2021**, *752*, 141959. [[CrossRef](#)] [[PubMed](#)]
- Auta, H.S.; Emenike, C.U.; Jayanthi, B.; Fauziah, S.H. Growth kinetics and biodeterioration of polypropylene microplastics by *Bacillus* sp. and *Rhodococcus* sp. isolated from mangrove sediment. *Mar. Pollut. Bull.* **2018**, *127*, 15–21. [[CrossRef](#)]
- Jeon, H.J.; Kim, M.N. Functional analysis of alkane hydroxylase system derived from *Pseudomonas aeruginosa* E7 for low molecular weight polyethylene biodegradation. *Int. Biodeterior. Biodegrad.* **2015**, *103*, 141–146. [[CrossRef](#)]
- Paço, A.; Duarte, K.; João, P.; Santos, P.S.M.; Pereira, R.; Pereira, M.E. Biodegradation of polyethylene microplastics by the marine fungus *Zalerionmaritimum*. *Sci. Total Environ.* **2017**, *586*, 10–15. [[CrossRef](#)] [[PubMed](#)]
- Gajendiran, A.; Krishnamoorthy, S.; Abraham, J. Microbial degradation of low-density polyethylene (LDPE) by *Aspergillus clavatus* strain JASK1 isolated from landfill soil. *3 Biotech* **2016**, *6*, 52–57. [[CrossRef](#)] [[PubMed](#)]
- Mukherjee, S.; Chowdhuri, U.R.; Kundu, P.P. Bio-degradation of polyethylene waste by simultaneous use of two bacteria: *Bacillus licheniformis* for production of bio-surfactant and *Lysinibacillus fusiformis* for bio-degradation. *RSC Adv.* **2015**, *6*, 2982–2992. [[CrossRef](#)]
- Gewert, B.; Plassmann, M.M.; MacLeod, M. Pathways for degradation of plastic polymers floating in the marine environment. *Environ. Sci. Processes Impacts* **2015**, *17*, 1513–1521. [[CrossRef](#)]
- Nauendorf, A.; Krause, S.; Bigalke, N.K.; Gorb, E.V.; Gorb, S.N.; Haeckel, M.; Treude, T. Microbial colonization and degradation of polyethylene and biodegradable plastic bags in temperate fine-grained organic-rich marine sediments. *Mar. Pollut. Bull.* **2016**, *103*, 168–178. [[CrossRef](#)]
- Glaser, J.A. Biological Degradation of Polymers in the Environment. In *Plastics in the Environment*; Intech Open: London, UK, 2019. [[CrossRef](#)]
- Osman, M.; Satti, S.M.; Luqman, A.; Hasan, F.; Shah, Z.; Shah, A.A. Degradation of Polyester Polyurethane by *Aspergillus* sp. Strain S45 Isolated from Soil. *J. Polym. Environ.* **2018**, *26*, 301–310. [[CrossRef](#)]
- Ahmad, F.; Anwar, S.; Firdous, S.; Da-Chuan, Y.; Iqbal, S. Biodegradation of bispyribac sodium by a novel bacterial consortium BDAM: Optimization of degradation conditions using response surface methodology. *J. Hazard. Mater.* **2018**, *349*, 272–281. [[CrossRef](#)]
- Mohan, A.J.; Sekhar, V.C.; Bhaskar, T.; Nampoothiri, K.M. Microbial assisted high impact polystyrene (HIPS) degradation. *Bioresour. Technol.* **2016**, *213*, 204–207. [[CrossRef](#)] [[PubMed](#)]

25. Kale, S.K.; Deshmukh, A.G.; Dudhare, M.S.; Patil, V.B. Microbial degradation of plastic: A review. *J. Biochem. Technol.* **2015**, *6*, 952–961.
26. Tsiota, P.; Karkanorachaki, K.; Syranidou, E.; Franchini, M.; Kalogerakis, N. Microbial Degradation of HDPE Secondary Microplastics: Preliminary Results. In *Proceedings of the International Conference on Microplastic Pollution in the Mediterranean Sea*; Springer Water: Cham, Switzerland, 2018; pp. 181–188.
27. Singh, J.; Gupta, K.C. Screening and identification of low-density polyethylene (LDPE) degrading soil fungi isolated from polythene polluted sites around Gwalior City (MP). *Int. J. Curr. Microbiol. Appl. Sci.* **2014**, *3*, 443–448.
28. Dharmalingam, S.; Hayes, D.G.; Wadsworth, L.C.; Dunlap, R.N.; DeBruyn, J.M.; Lee, J.; Wszelaki, A.L. Soil degradation of polylactic acid/polyhydroxyalkanoate-based nonwoven mulches. *J. Polym. Environ.* **2015**, *23*, 302–315. [[CrossRef](#)]
29. Skariyachan, S.; Patil, A.A.; Shankar, A.; Manjunath, M.; Bachappanavar, N.; Kiran, S. Enhanced polymer degradation of polyethylene and polypropylene by novel thermophilic consortia of *Brevibacillus* sps. and *Aneurinibacillus* sp. screened from waste management landfills and sewage treatment plants. *Polym. Degrad. Stab.* **2018**, *149*, 52–68. [[CrossRef](#)]
30. Yogalakshmi, K.N.; Singh, S. Plastic Waste: Environmental Hazards, Its Biodegradation, and Challenges. In *Bioremediation of Industrial Waste for Environmental Safety*; Springer: Singapore, 2020; pp. 99–133.
31. Singh, S.; Rawat, P.S. Biodegradation of Plastic: An Innovative Solution to Safe the Human Health and Environment. In *Handbook of Research on Environmental and Human Health Impacts of Plastic Pollution*; IGI Global: Hershey, PA, USA, 2020; pp. 435–461.
32. Shah, Z.; Krumholz, L.; Aktas, D.F.; Hasan, F.; Khattak, M.; Shah, A.A. Degradation of polyester polyurethane by a newly isolated soil bacterium, *Bacillus subtilis* strain MZA-75. *Biodegradation* **2013**, *24*, 865–877. [[CrossRef](#)] [[PubMed](#)]
33. Yang, Y.; Yang, J.; Wu, W.M.; Zhao, J.; Song, Y.; Gao, L.; Yang, R.; Jiang, L. Biodegradation and mineralization of polystyrene by plastic-eating mealworms: Part 2. Role of gut microorganisms. *Environ. Sci. Technol.* **2015**, *49*, 12087–12093. [[CrossRef](#)]
34. Li, J.; Kim, H.R.; Lee, H.M.; Yu, H.C.; Jeon, E.; Lee, S.; Kim, D.H. Rapid biodegradation of polyphenylene sulfide plastic beads by *Pseudomonas* sp. *Sci. Total Environ.* **2020**, *720*, 137616. [[CrossRef](#)]
35. Park, S.Y.; Kim, C.G. Biodegradation of micro-polyethylene particles by bacterial colonization of a mixed microbial consortium isolated from a landfill site. *Chemosphere* **2019**, *222*, 527–533. [[CrossRef](#)]
36. Das, M.P.; Kumar, S. An approach to low-density polyethylene biodegradation by *Bacillus amyloliquefaciens*. *3 Biotech* **2015**, *5*, 81–86. [[CrossRef](#)]
37. Ojha, N.; Pradhan, N.; Singh, S.; Barla, A.; Shrivastava, A.; Khatua, P.; Bose, S. Evaluation of HDPE and LDPE degradation by fungus, implemented by statistical optimization. *Sci. Rep.* **2017**, *7*, 39515. [[CrossRef](#)] [[PubMed](#)]
38. Markandan, M.; Sepperumal, U.; Rodríguez, L.V.C. Bacterial (*Alcaligenes Faecalis*) Degradation of PET (Poly (Ethylene Terephthalate) Obtained from Old Bottles Wastes. *Acta Microbiol. Bulg.* **2020**, *36*, 145.
39. Soud, S.A. Biodegradation of Polyethylene LDPE plastic waste using Locally Isolated *Streptomyces* sp. *J. Pharm. Sci. Res.* **2019**, *11*, 1333–1339.
40. Jeon, H.J.; Kim, M.N. Biodegradation of poly(l-lactide) (PLA) exposed to UV irradiation by a mesophilic bacterium. *Int. Biodeterior. Biodegrad.* **2013**, *85*, 289–293. [[CrossRef](#)]
41. Sowmya, H.V.; Ramalingappa, M.K.; Thippeswamy, B. Biodegradation of polyethylene by *Bacillus cereus*. *Adv. Polym. Sci. Technol. Int. J.* **2014**, *4*, 28–32.
42. Sarwan, B.; Acharya, A.D.; Kaur, S.; Pare, B. Visible light photocatalytic deterioration of polystyrene plastic using supported BiOCl nanoflower and nanodisk. *Eur. Polym. J.* **2020**, *134*, 109793. [[CrossRef](#)]
43. Ghatge, S.; Yang, Y.; Ahn, J.-H.; Hur, H.-G. Biodegradation of polyethylene: A brief review. *Appl. Biol. Chem.* **2020**, *63*, 27. [[CrossRef](#)]
44. Montazer, Z.; Habibi Najafi, M.B.; Levin, D.B. Challenges with verifying microbial degradation of polyethylene. *Polymers* **2020**, *12*, 123. [[CrossRef](#)]
45. Nag, M.; Lahiri, D.; Dutta, B.; Jadav, G.; Ray, R.R. Biodegradation of used polyethylene bags by a new marine strain of *Alcaligenes faecalis* LNDR-1. *Environ. Sci. Pollut. Res.* **2021**, *28*, 41365–41379. [[CrossRef](#)]
46. Immanuel, O.M.; Ibiene, A.A.; Stanley, H.O. Enhanced biodegradation of polyethylene by fungus isolated from the koluama mangrove swamp in the Niger Delta. *J. Microbiol. Biotechnol. Res.* **2017**, *4*, 1–9.
47. Qiu, T.; Ge, F.; Li, C.; Lu, S. Study of the thermal degradation of flame-retardant polyester GFRP using TGA and TG-FTIR-GC/MS. *J. Therm. Anal. Calorim.* **2022**, *147*, 5743–5760. [[CrossRef](#)]
48. Roy, R.; Mukherjee, G.; Gupta, A.D.; Tribade, P.; Sil, A.K. Isolation of a soil bacterium for remediation of polyurethane and low-density polyethylene: A promising tool towards sustainable cleanup of the environment. *3 Biotech* **2021**, *11*, 29. [[CrossRef](#)] [[PubMed](#)]



## Article

# Polyhydroxyalkanoates from a Mixed Microbial Culture: Extraction Optimization and Polymer Characterization

Ana Marta Rodrigues<sup>1,2</sup>, Rita Dias Guardão Franca<sup>1,2</sup>, Madalena Dionísio<sup>3</sup>, Chantal Sevrin<sup>4</sup>, Christian Grandfils<sup>4</sup>, Maria A. M. Reis<sup>1,2</sup> and Nídia Dana Lourenço<sup>1,2,\*</sup>

<sup>1</sup> Associate Laboratory i4HB—Institute for Health and Bioeconomy, NOVA School of Science and Technology, NOVA University Lisbon, 2829-516 Caparica, Portugal; amsi.rodrigues@campus.fct.unl.pt (A.M.R.); r.franca@campus.fct.unl.pt (R.D.G.F.); amr@fct.unl.pt (M.A.M.R.)

<sup>2</sup> UCIBIO—Applied Molecular Biosciences Unit, Department of Chemistry, NOVA School of Science and Technology, NOVA University Lisbon, 2829-516 Caparica, Portugal

<sup>3</sup> LAQV-REQUIMTE, Department of Chemistry, NOVA School of Science and Technology, NOVA University Lisbon, 2829-516 Caparica, Portugal; madalena.dionisio@fct.unl.pt

<sup>4</sup> CEIB-Interfaculty Research Centre of Biomaterials, University of Liege, B-4000 Liège, Belgium; csevrin@uliege.be (C.S.); c.grandfils@uliege.be (C.G.)

\* Correspondence: nidia.lourenco@fct.unl.pt

**Citation:** Rodrigues, A.M.; Franca, R.D.G.; Dionísio, M.; Sevrin, C.; Grandfils, C.; Reis, M.A.M.; Lourenço, N.D. Polyhydroxyalkanoates from a Mixed Microbial Culture: Extraction Optimization and Polymer Characterization. *Polymers* **2022**, *14*, 2155. <https://doi.org/10.3390/polym14112155>

Academic Editors: José Miguel Ferri, Vicent Fombuena Borràs and Miguel Fernando Aldás Carrasco

Received: 29 April 2022

Accepted: 23 May 2022

Published: 25 May 2022

**Publisher's Note:** MDPI stays neutral with regard to jurisdictional claims in published maps and institutional affiliations.



**Copyright:** © 2022 by the authors. Licensee MDPI, Basel, Switzerland. This article is an open access article distributed under the terms and conditions of the Creative Commons Attribution (CC BY) license (<https://creativecommons.org/licenses/by/4.0/>).

**Abstract:** Polyhydroxyalkanoates (PHA) are biopolymers with potential to replace conventional oil-based plastics. However, PHA high production costs limit their scope of commercial applications. Downstream processing is currently the major cost factor for PHA production but one of the least investigated aspects of the PHA production chain. In this study, the extraction of poly(3-hydroxybutyrate-co-3-hydroxyvalerate) produced at pilot scale by a mixed microbial culture was performed using sodium hydroxide (NaOH) or sodium hypochlorite (NaClO) as digestion agents of non-PHA cellular mass. Optimal conditions for digestion with NaOH (0.3 M, 4.8 h) and NaClO (9.0%, 3.4 h) resulted in polymers with a PHA purity and recovery of ca. 100%, in the case of the former and ca. 99% and 90%, respectively, in the case of the latter. These methods presented higher PHA recoveries than extraction by soxhlet with chloroform, the benchmark protocol for PHA extraction. The polymers extracted by the three methods presented similar PHA purities, molecular weights and polydispersity indices. Using the optimized conditions for NaOH and NaClO digestions, this study analyzed the effect of the initial intracellular PHA content (40–70%), biomass concentration (20–100 g/L) and biomass pre-treatment (fresh vs. dried vs. lyophilized) on the performance of PHA extraction by these two methods.

**Keywords:** PHA extraction; chemical digestion; design of experiments; polymer properties

## 1. Introduction

Polyhydroxyalkanoates (PHA) are biodegradable and biobased polymers produced by bacterial fermentation. PHA accumulate intracellularly as water insoluble inclusion bodies that function as carbon and energy storage [1–3]. The replacement of conventional oil-based plastics by PHA in various segments has been thoroughly discussed due to their similar thermo-physical properties, with PHA offering environmentally friendly advantages, such as biocompatibility, biodegradability and compostability [1,4]. PHA production costs, however, are currently higher than those for oil-derived plastics (EUR 1.18–6.12/kg vs. <EUR 1/kg), which limits their potential to niche-market high value applications [1]. Continuous efforts have been made to reduce PHA production costs by applying mixed microbial cultures (MMC) and waste streams as carbon source for PHA production, as an alternative to pure cultures and the required sterile conditions and expensive substrates. Hence, PHA downstream processing is now the most economically impacting factor in the PHA production chain [1,4].

The best established and most commonly used methods for PHA recovery employ halogenated solvents, such as chloroform. Although these methods often generate superior recovery yields and product purity values, they are environmentally harmful, make use of large volumes of noxious solvents and require excessive energy input, making the recovery process unsustainable and economically unfeasible [4,5]. Thus, research has been leaning toward the development of more environmentally friendly approaches for the extraction and purification of PHA [4].

The use of alkaline compounds, such as sodium hydroxide (NaOH), can be a valid, cost-effective and green alternative to chlorinated compounds for the extraction of PHA [2]. Furthermore, alkaline treatment for PHA recovery has been considered more economically feasible when compared to an organic solvent-based process [6]. Hydroxides cause saponification of the lipids present in the cell wall of the microorganism, leading to increased membrane permeability and release of proteins and non-PHA cell material [7].

Mohammadi et al. (2012) [8] used NaOH to recover PHA (poly(3-hydroxybutyrate-co-3-hydroxyhexanoate), PHBHHx) from lyophilized recombinant *Cupriavidus necator* (PHA content of ca. 38.3%), having tested different NaOH concentrations, digestion times and reaction temperatures. The authors obtained over 96% of PHA recovery and purity by treating lyophilized cells with 0.05 M NaOH at 4 °C for 3 h. The fact that this efficient, simple, non-toxic and environmentally friendly treatment resulted in negligible degradation of the polymer molecular weight (Mw) supports the utilization of alkaline-based methods as an alternative to organic solvents for PHA recovery. Jiang et al. (2015) [3] assessed the feasibility of using NaOH for the extraction and purification of PHA (polyhydroxybutyrate, PHB) from MMC (PHA content of ca. 70%) fed with acetate and compared the results with those obtained from extraction with dichloromethane. These authors verified that the PHA purity in the final product increased when both NaOH concentration and treatment time increased, though PHA recovery decreased in both situations. Applying NaOH at 0.20 M to fresh biomass for 1 h, the authors obtained a PHA purity of 87% and a PHA recovery of 97%. When treatment time was increased to 3 h, PHA purity increased to 92% and PHA recovery was reduced to 94%. The comparison between the results of these alkaline-based methods and the ones obtained with extraction by dichloromethane, 98% of PHA purity and 56% of PHA recovery, suggests that PHA extraction with NaOH might be a viable alternative to extraction with organic solvents.

With the purpose of developing a low-cost extraction method with high PHA recovery to achieve a cost-effective polymer production, Heinrich et al. (2012) [9] studied a simplified method for PHA extraction at large scale from cells of *Ralstonia eutropha* H16 (now reclassified as *Cupriavidus necator*), cultivated with a synthetic carbon/magnesium solution, using sodium hypochlorite (NaClO, 13%, v/v). NaClO is a strong oxidizing chemical that dissolves non-PHA cellular mass (NPCM), while PHA granules remain in the solid form [10]. Very high purities have been reported for PHA extraction with NaClO, but as PHA is not completely insoluble in NaClO, the often-associated decrease in polymer molecular weight after extraction has caused concern when dealing with this chemical [9–12]. In the study by Heinrich et al. (2012) [9], PHA with an average purity of 93% was extracted with a maximum recovery of 87% when the largest extraction volume tested, 50 L, was used. Nevertheless, treatment with NaClO led to a 50–70% decrease in the polymer molecular weight and higher dispersity of the polymer. Villano et al. (2014) [11] recovered PHA (poly(3-hydroxybutyrate-co-3-hydroxyvalerate), PHBV) from fresh MMC, produced using a synthetic mixture of acetic and propionic acids, by operating an extraction reactor using two digestion agents: NaOH (1 M) and NaClO (5% active Cl<sub>2</sub>). In the study by Villano et al. (2014) [11], PHA extraction displayed greater performance when NaClO was used for the digestion of NPCM, as opposed to NaOH, both in terms of polymer recovery (ca. 100%, w/w) and purity (>90%, w/w). The results showed, however, a wide polymer molecular weight distribution, which might be detrimental to the application of the process. Furthermore, treatments using NaClO may be hazardous and not viable for large-scale application due to the risk of formation of toxic halogenated compounds [5].

Until now, most PHA extraction studies have used either pure cultures or MMC produced with synthetic substrates [1]. The present study focused on the optimization of PHA (PHBV) extraction from a MMC (ca. 70% PHA) produced at pilot scale with fruit pulp waste by NPCM digestion with either NaOH or NaClO. Optimization was performed using lyophilized biomass at a set concentration (20 g/L) through a central composite rotatable design (CCRD), a response surface methodology (RSM) design that efficiently seeks the optimum conditions for a multivariate system. RSM involves performing statistically designed experiments, coefficients estimation in mathematical models and response prediction and model accuracy testing [13]. Central composite design, in particular, has been often used for the optimization of conditions from various processes, including chemical and biochemical reactions [14]. In the current study, CCRD was used to determine different combinations of reagent concentration and digestion time to be tested and also to predict the conditions that maximize both PHA purity and recovery. This study also assessed the impact of intracellular PHA content, biomass pre-treatment and biomass concentration on PHA extraction performance and polymer characteristics, including molecular weight, thermal properties and infrared spectra.

## 2. Materials and Methods

### 2.1. Biomass Samples

Four different biomass samples containing the polymer poly(3-hydroxybutyrate-co-3-hydroxyvalerate) (PHBV) were used in the PHA extraction trials, and all were produced in a three-stage process pilot unit plant operated at room temperature. This unit consisted of an acidogenic fermentation stage, performed in an upflow anaerobic sludge blanket (UASB) reactor with a working volume of 60 L; a culture selection stage, performed in a 100 L sequencing batch reactor (SBR) operating under a feast and famine regime; and a PHA accumulation stage, performed in a 60 L fed-batch reactor. The UASB reactor, the SBR and the fed-batch reactor were designed inhouse. Fruit pulp waste was used as feedstock for this production.

The PHA accumulation process was performed with biomass purged from the culture selection SBR and a volatile fatty acid (VFA)-rich stream derived from the UASB. The accumulation reactor worked in pulse feeding mode under nutrient limitation. After accumulation, the different PHA-enriched biomasses were acidified with sulfuric acid (Sigma-Aldrich, Sigma-Aldrich, Burlington, MA, USA), centrifuged and stored at 4 °C before lyophilization.

Biomass A was collected at the end of a PHA accumulation process and had an intracellular PHA content of ca. 70% (31% of 3-hydroxyvalerate, 3HV). This sample was used for the PHA extraction optimization tests and to study the impact of the biomass concentration on the PHA extraction performance. Biomasses B and C were collected at distinct times of a second PHA accumulation process, namely after the first and second feed pulses, and had PHA contents of ca. 35–41% (18% 3HV) and ca. 44–52% (18% 3HV), respectively. Biomass D was collected at the end of a third PHA accumulation and presented a PHA content of ca. 73% (21% 3HV). Biomasses B, C and D were used to study the effect of the intracellular PHA content on PHA extraction. Additionally, to study the effect of biomass pre-treatment on PHA extraction, trials were performed using biomass C, not only lyophilized but also in its fresh state (i.e., only subjected to acidification and centrifugation) and in its dry state (i.e., subjected to acidification, centrifugation and drying at 60 °C for 3.5 days).

### 2.2. PHA Extraction

For the determination of the optimal conditions for PHA extraction from lyophilized PHA-enriched biomass using NaOH (97%, Sigma-Aldrich, Burlington, MA, USA) or NaClO (10–15% active Cl<sub>2</sub>, Acros Organic, Geel, Belgium), biomass was mixed at 20 g/L in 50 mL tubes with 20 mL of NaOH or NaClO solutions, according to the conditions determined by the experimental design (see Section 2.4), and incubated at 200 rpm and 30 °C. After

incubation with NaOH, the suspension was centrifuged at  $9300 \times g$  for 10 min at  $20\text{ }^{\circ}\text{C}$ , the resulting pellet was washed with 40 mL of water and then frozen and lyophilized for 48 h. Regarding digestion with NaClO, 20 mL of water were added to the suspension after incubation and before the first centrifugation to enhance the solid–liquid separation. Afterward, the processing of the pellet was the same as previously described for suspensions, including NaOH. For comparison purposes, conventional PHA extraction with chloroform was performed. In this method, 10 g of lyophilized biomass were subjected to Soxhlet extraction with chloroform (99.5% Sigma-Aldrich, Burlington, MA, USA) at  $80\text{ }^{\circ}\text{C}$  over 48 h, followed by precipitation in ice-cold ethanol (EtOH; 1:10 *v/v*, Fisher Chemical, Waltham, MA, USA), as described by Pereira et al. (2019) [15].

To assess the effect of biomass pre-treatment on PHA extraction performance, lyophilized, fresh and dry biomasses were mixed at 20 g/L in 50 mL tubes with 20 mL of NaOH or NaClO solutions, using the respective determined optimal conditions, and incubated at 200 rpm and  $30\text{ }^{\circ}\text{C}$ . The same experimental conditions were applied to lyophilized biomass with different intracellular PHA contents (biomasses B, C and D) and to lyophilized biomass with the same PHA content (biomass A) but at biomass concentrations of 20, 40, 60, 80 and 100 g/L to analyze the effect of intracellular PHA content and biomass concentration on PHA extraction performance. The processing of the resulting extraction products for both studies followed as described in the first paragraph of the present section.

### 2.3. PHA Content and Composition

PHA content and its composition in biomass and in extraction products were determined by gas chromatography (GC, Trace 1300, Thermo Scientific, Waltham, MA, USA), following a methanolysis method based on the one described by Cruz et al. (2016) [16]. Summarily, the lyophilized samples (1 to 2 mg) were hydrolyzed with 1 mL of 20% (*v/v*) sulfuric acid (Sigma-Aldrich, HPLC grade, Burlington, MA, USA) in methanol (Fisher Chemical, HPLC grade, Waltham, MA USA) and 1 mL of chloroform (Sigma-Aldrich, HPLC grade, Burlington, MA, USA), including heptadecanoate (HD) at 1 g/L, to function as internal standard. The reaction occurred at  $100\text{ }^{\circ}\text{C}$  over 3.5 h. The obtained methyl esters were analyzed in a Restek column (Crossbond, Stabilwax, Bellefonte, PA, USA) at a constant pressure of 14.50 Psi, using helium (Air Liquid, Paris, France) as the carrier gas. The oven temperature program was set as follows:  $20\text{ }^{\circ}\text{C}/\text{min}$  until  $100\text{ }^{\circ}\text{C}$ ;  $3\text{ }^{\circ}\text{C}/\text{min}$  until  $155\text{ }^{\circ}\text{C}$ ;  $20\text{ }^{\circ}\text{C}/\text{min}$  until  $220\text{ }^{\circ}\text{C}$ .

Commercial PHBV (Sigma-Aldrich, 88 mol% 3HB, 12 mol% 3HV, Burlington, MA, USA) was used as standard for the construction of calibration curves that allowed the determination of the mass of both 3HB and 3HV in each sample. The PHA content values were obtained by dividing the mass of PHA (mass of 3HB + mass of 3HV) in each sample by the mass of lyophilized total solids (TS) used for GC analysis, according to Equation (1):

$$\text{PHA Content} \left( \%, \frac{\text{mg}}{\text{mg}} \right) = \frac{\text{PHA}}{\text{TS}} \times 100 \quad (1)$$

To calculate the PHA recovery yield according to Equation (2), it was necessary to determine the PHA mass of both the final extraction product and of the biomass from which the extraction product was obtained ( $\text{PHA}_{\text{final}}$  and  $\text{PHA}_{\text{initial}}$ , respectively).

$$\text{Recovery} \left( \%, \frac{\text{mg}}{\text{mg}} \right) = \frac{\text{PHA}_{\text{final}}}{\text{PHA}_{\text{initial}}} \times 100 \quad (2)$$

### 2.4. Experimental Design and Statistical Validation

RSM was used to assess the optimal conditions for PHA extraction using digestion with either NaOH or NaClO. CCRD was performed to analyze the impact and interaction between the experimental variables ( $X_i$ ), reagent concentration (M for NaOH and % for NaClO) and digestion time (h), and the observed responses, PHA purity (%) and PHA recovery (%). The design applied consisted of nine experiments performed randomly: four

factorial design points at levels  $\pm 1$ ; four experiments of axial level  $\alpha = \pm 1.414$ ; and a central point with three replicates. The experimental values for the two independent variables were established according to the literature [3,6,8,9,11,12,17–21]. The experimental tests for optimization of PHA extraction with NaOH and NaClO were performed as described in Table 1.

**Table 1.** Experimental conditions for the digestion of non-PHA cellular mass (NPCM) with NaOH or NaClO, obtained using a central composite rotatable design (CCRD) of experiments, with reagent concentration (M and % for NaOH and NaClO, respectively) and digestion time (h;  $t_{\text{digestion-NaOH}}$  and  $t_{\text{digestion-NaClO}}$  for digestion with NaOH and NaClO, respectively) as independent variables.

Test	NaOH (M)	$t_{\text{digestion-NaOH}}$ (h)	NaClO (%)	$t_{\text{digestion-NaClO}}$ (h)
1	0.14	0.80	1.90	0.60
2	0.84	0.80	11.10	0.60
3	0.14	4.30	1.90	3.00
4	0.84	4.30	11.10	3.00
5	0.49	2.55	6.50	1.80
6	0.49	2.55	6.50	1.80
7	0.49	2.55	6.50	1.80
8	0.00	2.55	0.00	1.80
9	0.98	2.55	13.00	1.80
10	0.49	0.08	6.50	0.10
11	0.49	5.02	6.50	3.50

The experimental data were fitted to the second-order model presented in Equation (3) to evaluate the system's behavior.

$$Y_p = b_0 + b_1X_1 + b_2X_2 + b_{11}X_1^2 + b_{22}X_2^2 + b_{12}X_1X_2 \quad (3)$$

In Equation (3),  $Y_p$  corresponds to the predicted responses, and  $X_1$  and  $X_2$  are the coded values of the independent variables, namely reagent concentration and digestion time.  $b_0$ ,  $b_i$ ,  $b_j$ ,  $b_{ij}$  ( $i, j = 1, 2$ ) are the coefficient estimates,  $b_0$  being the interception,  $b_1$  and  $b_2$  the linear terms,  $b_{11}$  and  $b_{22}$  the quadratic terms, and the  $b_{12}$  the interaction term. A statistical analysis was performed to evaluate the significance of each source of variation and select an appropriate quadratic model.

Analysis of variance (ANOVA) was used to assess the fit of each model, which was considered an accurate prediction tool when it met the following criteria: a good correlation value ( $R^2 > 0.7$ , acceptable for biological samples [22]) with statistical meaning ( $p$ -value  $< 0.05$ , for a 95% confidence level) and with no lack of fit ( $p$ -value  $> 0.05$ , for 95% confidence level) [23]. Statistics and surface plots analysis provided information on the effect of reagent (NaOH or NaClO) concentration and digestion time on PHA purity and PHA recovery.

### 2.5. PHA Infrared Spectra

Fourier transform infrared (FTIR) spectra of the extracted PHA were collected between 400 and 4000  $\text{cm}^{-1}$ , at room temperature, using a Cary 630 FTIR spectrometer (Agilent Technologies, Santa Clara, CA, USA) with a thermoelectrically cooled dTGS detector and KBr standard beam splitter and equipped with a diamond attenuated total reflectance (ATR) accessory. All spectra were recorded via the ATR method, with a resolution of 1  $\text{cm}^{-1}$  and 16 scans.

### 2.6. PHA Molecular Mass Distribution

The weight average molecular weight ( $M_w$ ), number average molecular weight ( $M_n$ ) and polydispersity index ( $M_w/M_n$ ; PDI) of the extracted PHA were determined by size exclusion chromatography (SEC). For this analysis, 15 mg of each sample was first dissolved in 3 mL of chloroform at room temperature for 18 h. Then, the resultant solutions



were filtered with glass fiber filters 47 mm (PALL, Port Washington, NY, USA) and analyzed by a Waters SEC system (Milford, MA, USA), with support SEC: PLgel 5  $\mu\text{m}$  Guard, 50  $\times$  7.5 mm; PLgel 5  $\mu\text{m}$  104  $\text{\AA}$ , 300  $\times$  7.5 mm; PLgel 5  $\mu\text{m}$  500  $\text{\AA}$ , 300  $\times$  7.5 mm (Polymer Laboratories, Church Stretton, UK). A temperature of equilibration of 30  $^{\circ}\text{C}$  was used, along with a flow rate of 1 mL/min, with degassing, and chloroform as the mobile phase. An amount of 100  $\mu\text{L}$  of each sample was injected in the SEC circuit. The refractive index detector Waters 2410 was used for polymer detection, using the sensitivity 512 and a collect duration of 25 min. Relative molecular weights of the polymers were determined according to the universal calibration method adopting polystyrene standards with molecular weights between 800 Da and 504.5 kDa, and using Waters Millenium SEC software (Milford, MA, USA).

### 2.7. PHA Thermal Properties

Differential scanning calorimetry (DSC) analysis was used to probe the thermal properties of the extracted PHA. This analysis was performed using a differential scanning calorimeter DSC Q2000 (TA Instruments, New Castle, DE, USA). Each sample (approximately 4 mg) was placed in a sealed aluminum pan, perforated to allow water/solvents release. Thermograms were collected in a range of temperatures between  $-90^{\circ}\text{C}$  and  $160^{\circ}\text{C}$ , with heating and cooling steps of  $10^{\circ}\text{C}/\text{min}$  under a nitrogen atmosphere. Two cooling/heating cycles were performed for each sample. The glass transition temperature ( $T_g$ ,  $^{\circ}\text{C}$ ) and the melting temperature ( $T_m$ ,  $^{\circ}\text{C}$ ) were determined as the midpoint of the heat flux step and at the minimum of the endothermic peak, respectively, of the second heating run, due to water or solvent evaporation occurring during the first heating.

## 3. Results

### 3.1. Effects of Reagent Concentration and Digestion Time on PHA Extraction with NaOH/NaClO: Analysis of PHA Purity and Recovery

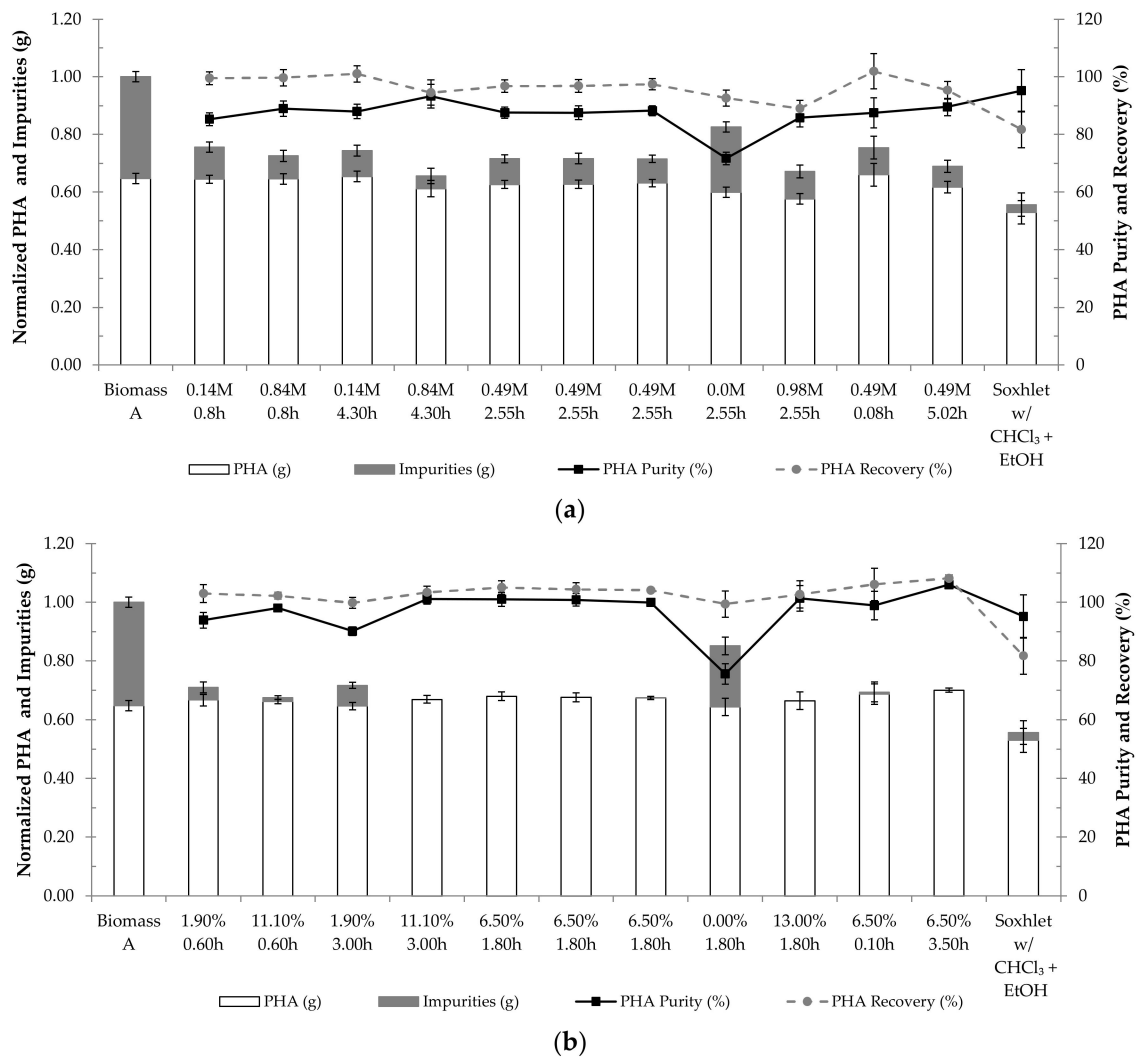
With the aim of obtaining the optimal conditions for PHA extraction through NPCM digestion with NaOH or NaClO, a CCRD with reagent concentration and digestion time as independent variables was used to study the PHA purity and PHA recovery of the extraction products. The results from subjecting biomass A (see Section 2.1), lyophilized biomass with ca. 70% of intracellular PHA content, to different digestion conditions with NaOH and NaClO are presented in Figure 1a,b, respectively.

Regarding PHA extraction with NaOH (Figure 1a), the highest PHA purity,  $93.28 \pm 4.10\%$ , was obtained when the biomass was treated with NaOH at 0.84 M for 4.30 h, and a complete PHA recovery was attained when treatment with NaOH at 0.49 M for 0.08 h was applied. Considering Figure 1b, the final product with the highest PHA purity was obtained, with complete PHA recovery, when the biomass was digested with NaClO at 6.50% for 3.50 h.

ANOVA analysis was used for the two responses (PHA purity and PHA recovery) obtained after digestion with either NaOH or NaClO, and the results are presented in Tables 2 and 3, respectively.

**Table 2.** Analysis of variance (ANOVA) of the central composite design applied to PHA extraction through NPCM digestion by NaOH: significance levels ( $p$ -values) of model and lack of fit, and correlation values ( $R^2$ ) for the responses studied, namely PHA purity and PHA recovery.

	Model $p$ -Value	Lack of Fit $p$ -Value	$R^2$
PHA Purity	0.00	0.98	0.82
PHA Recovery	0.00	0.65	0.93



**Figure 1.** Results of PHA extraction using NaOH (a) and NaClO (b) for each pair of reagent concentration (a) M for NaOH; (b) % for NaClO and digestion time (h) tested. The results are expressed in PHA purity (%), PHA recovery (%), normalized mass of PHA (g) and normalized mass of impurities (g). Biomass A corresponds to the starting biomass with intracellular PHA prior to extraction. The results of the conventional PHA extraction with chloroform (extraction with chloroform in soxhlet, followed by purification in ethanol (EtOH)) are also displayed as “Soxhlet w/CHCl<sub>3</sub> + EtOH”.

**Table 3.** Analysis of variance (ANOVA) of the central composite design applied to PHA extraction through NPCM digestion by NaClO: significance levels (*p*-values) of model and lack of fit, and correlation values (*R*<sup>2</sup>) for the responses studied, namely PHA purity and PHA recovery.

	Model <i>p</i> -Value	Lack of Fit <i>p</i> -Value	<i>R</i> <sup>2</sup>
PHA Purity	0.00	0.06	0.89
PHA Recovery	0.00	0.29	0.80

Tables 2 and 3 demonstrate *R*<sup>2</sup> values greater than 0.7 for PHA purity and PHA recovery obtained after digestion with NaOH and NaClO, respectively. Thus, according to Lundstedt et al. (1998) [22], the second-order model showed an adequate fit for the considered responses. Furthermore, the model and lack of fit *p*-values presented in Tables 2 and 3 demonstrate that the second-order model had significance (*p* < 0.05) for all responses and no evidence of lack of fit (*p* > 0.05).

### 3.2. Optimal Reagent Concentration and Digestion Time for PHA Extraction with NaOH and NaClO

Multiple linear regression (MLR) analysis of the models developed for PHA extraction using NaOH (Table 4) or NaClO (Table 5) provided information regarding the linear, quadratic and interaction effects of NaOH/NaClO concentration and digestion time on PHA purity and PHA recovery.

**Table 4.** Multiple linear regression (MLR) analysis of the polynomial models obtained for PHA extraction through NPCM digestion by NaOH: constants and *p*-values for linear, quadratic and interaction effects of NaOH concentration ([NaOH]) and digestion time (t) for the studied responses, PHA purity and PHA recovery.

Effect	Constant	Linear		Quadratic		Interaction
		[NaOH] ( $X_1$ )	t ( $X_2$ )	[NaOH] × [NaOH] ( $X_1^2$ )	t × t ( $X_2^2$ )	[NaOH] × t ( $X_1X_2$ )
PHA Purity ( $Y_1$ )	−1.134	0.012	0.064	0.020	0.061	0.008
<i>p</i> -Value	$7.572 \times 10^{-18}$	0.387	$8.621 \times 10^{-5}$	0.226	$7.859 \times 10^{-4}$	0.619
PHA Recovery ( $Y_2$ )	89.921	−3.535	−1.104	0.479	1.887	−1.985
<i>p</i> -Value	$6.367 \times 10^{-24}$	$2.742 \times 10^{-7}$	0.003	0.284	$2.332 \times 10^{-4}$	$2.552 \times 10^{-4}$

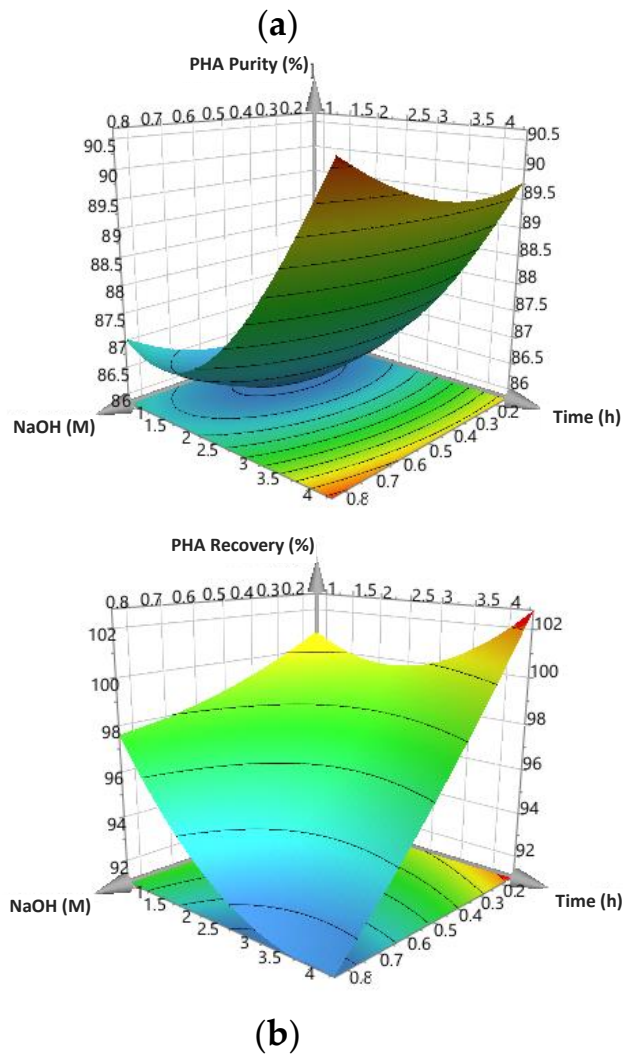
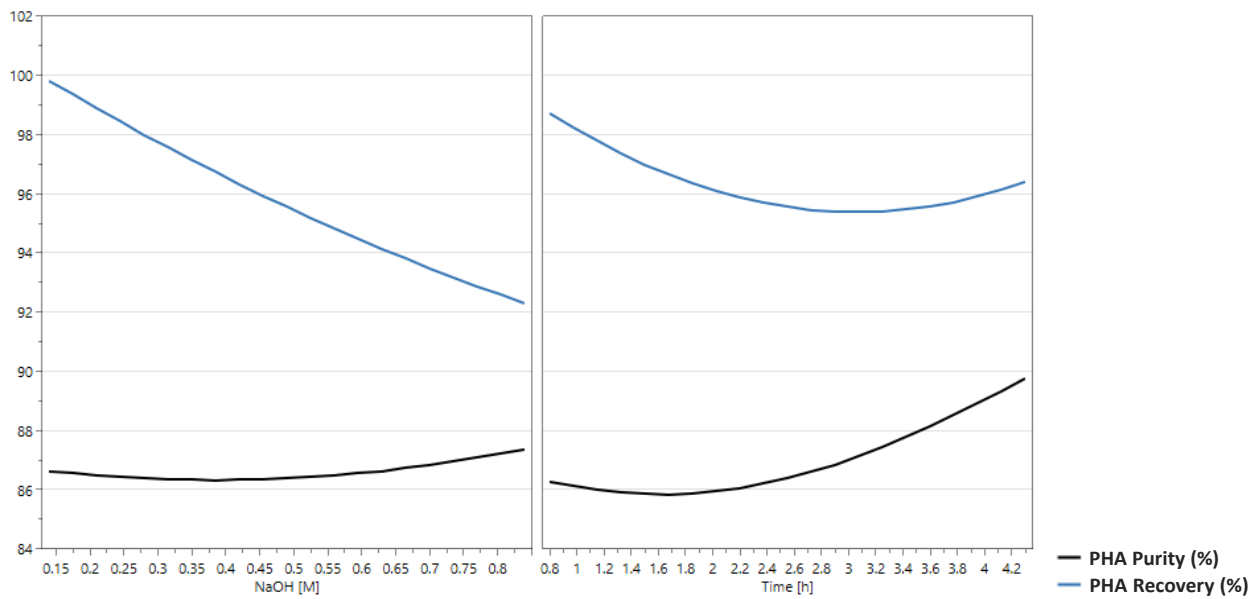
**Table 5.** Multiple linear regression (MLR) analysis of the polynomial models obtained for PHA extraction through NPCM digestion by NaClO: constants and *p*-values for linear, quadratic and interaction effects of NaClO concentration ([NaClO]) and digestion time (t) for the studied responses, PHA purity and PHA recovery.

Effect	Constant	Linear		Quadratic		Interaction
		[NaClO] ( $X_1$ )	t ( $X_2$ )	[NaClO] × [NaClO] ( $X_1^2$ )	t × t ( $X_2^2$ )	[NaClO] × t ( $X_1X_2$ )
PHA Purity ( $Y_1$ )	100.659	7.572	1.367	−6.079	1.686	2.258
<i>p</i> -Value	$6.988 \times 10^{-27}$	$6.672 \times 10^{-9}$	0.119	$1.035 \times 10^{-6}$	0.079	0.100
PHA Recovery ( $Y_2$ )	97.929	2.188	0.728	−2.196	1.202	1.267
<i>p</i> -Value	$5.869 \times 10^{-25}$	$8.157 \times 10^{-4}$	0.160	0.002	0.041	0.088

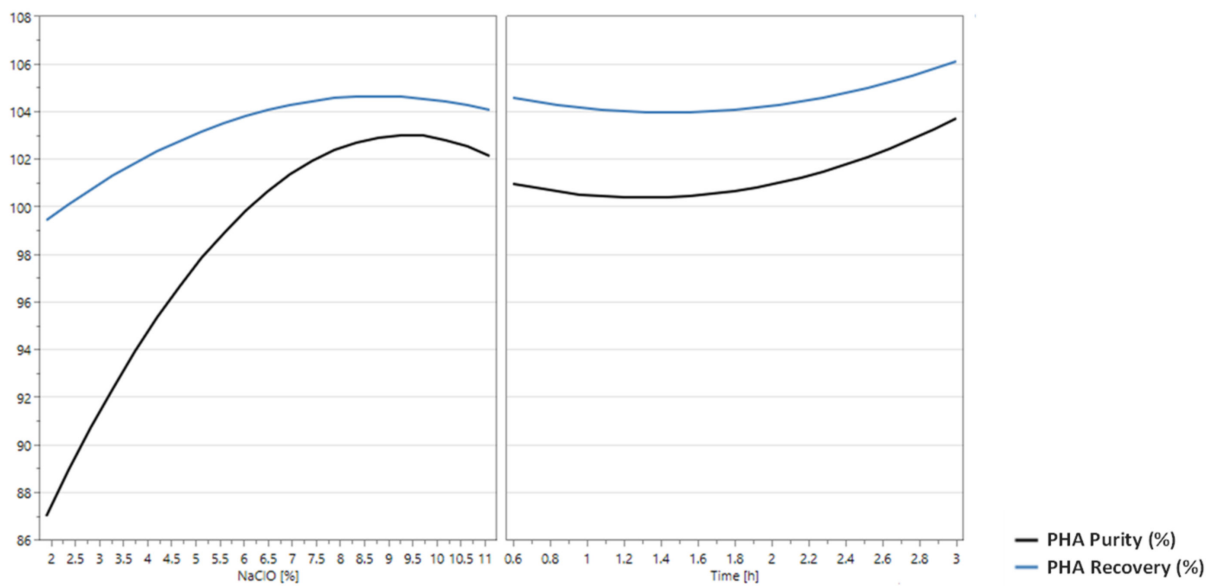
Regarding PHA extraction by NaOH digestion, Table 4 shows that PHA purity was affected primarily by the linear and quadratic terms of digestion time ( $p < 0.05$ ). In terms of PHA recovery, this was mainly influenced by the linear terms of NaOH concentration and digestion time, the quadratic terms of digestion time and also the term of interaction between NaOH concentration and digestion time.

Table 5 shows that in PHA extraction through NaClO digestion, PHA purity was mostly impacted by the linear and quadratic terms of NaClO concentration. As for PHA recovery in this process, this was mainly impacted by the linear and quadratic terms of NaClO concentration, as well as the quadratic term of digestion time.

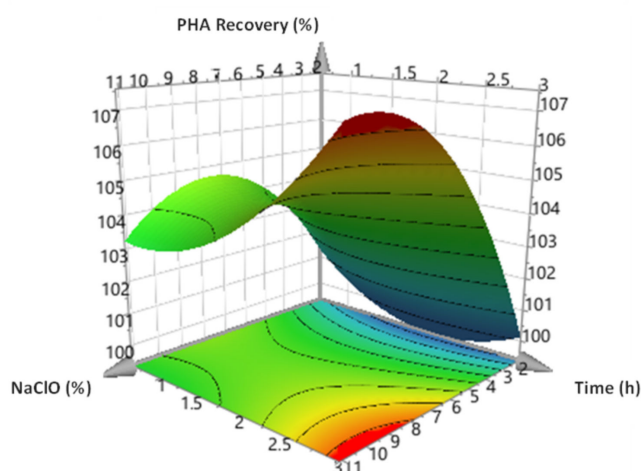
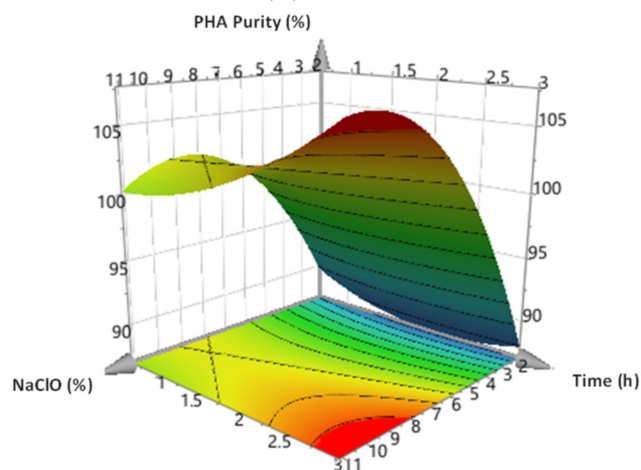
The prediction plots and the 3D surface plots regarding the PHA purity and PHA recovery models for PHA extraction with NaOH and NaClO are presented in Figures 2 and 3, respectively.



**Figure 2.** Prediction plots (a) and 3D surface plots (b) for the models developed for the prediction of PHA purity and PHA recovery considering NaOH concentration and digestion time as independent variables. These models were developed using the experimental PHA purity and PHA recovery values obtained in the CCRD tests for PHA extraction with NaOH.



(a)



(b)

**Figure 3.** Prediction plots (a) and 3D surface plots (b) for the models developed for the prediction of PHA purity and PHA recovery considering NaClO concentration and digestion time as independent variables. These models were developed using the experimental PHA purity and PHA recovery values obtained in the CCRD tests for PHA extraction with NaClO.

Considering Figure 2a, the developed models suggest that PHA purity slightly increases with the increase in NaOH concentration, while PHA recovery substantially decreases. Concerning the effect of the digestion time, PHA content is expected to increase when the reaction time increases, while PHA recovery will tend to decrease.

Observing Figure 2b, it is possible to assess that PHA content should be maximized when biomass is treated with NaOH at a concentration of about 0.8 M and a digestion time of around 4 h. On the other hand, PHA recovery should be highest when NaOH is used at a concentration of ca. 0.2 M and when the digestion has a duration of about 4 h.

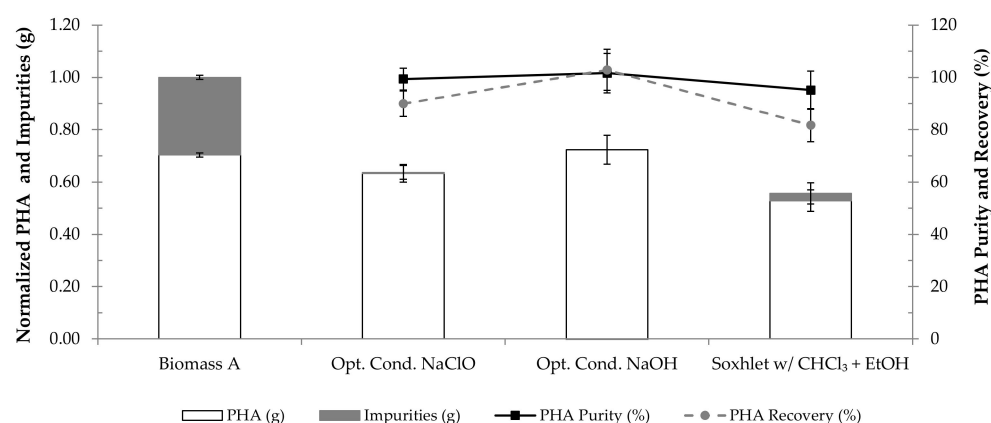
Considering the developed models, the conditions that should maximize both the PHA purity and the PHA recovery of the final product obtained by PHA extraction with NaOH were estimated at 0.3 M for concentration and 4.8 h for digestion time.

Figure 3a shows that according to the predictive models, PHA content and PHA recovery tend to rise with the increase in NaClO concentration, the increase in PHA purity being greater than the one observed for PHA recovery. In terms of digestion time, both the PHA purity and the PHA recovery are expected to improve as the digestion time increases.

Figure 3b shows that when applying digestion with NaClO, the PHA content of the final product is maximized when NaClO is at a concentration between 8% and 11% and when digestion lasts between approximately 2.7 h and 3 h. Regarding PHA recovery, this parameter should be greatest when the biomass is treated with NaClO at a concentration between 8% and 11% for about 2.8–3 h.

Considering the developed models, the conditions that maximize the PHA content and the PHA recovery of the final product obtained by PHA extraction with NaClO were estimated to be a concentration of 9.0% and a digestion time of 3.4 h.

Figure 4 shows the results of PHA extraction using the found optimal conditions for NaOH and NaClO digestions, as well as using the benchmark protocol (soxhlet extraction with chloroform followed by precipitation in cold ethanol) for comparison purposes. Digestion with NaClO resulted in a product with a PHA purity of  $99.4 \pm 4.2\%$ , having recovered  $89.9 \pm 4.8\%$  of the existing polymer. Treatment with NaOH, under the optimal conditions, recovered  $102.9 \pm 7.9\%$  of the existing polymer, and the extracted product presented a PHA purity of  $101.7 \pm 7.6\%$ . On the other hand, soxhlet extraction with chloroform followed by precipitation in ethanol recovered  $81.7 \pm 6.3\%$  of the polymer and originated a product with  $95.1 \pm 7.3\%$  of PHA. These results show that treatment with NaClO may have caused some polymer degradation, as it resulted in a lower PHA recovery than digestion with NaOH.

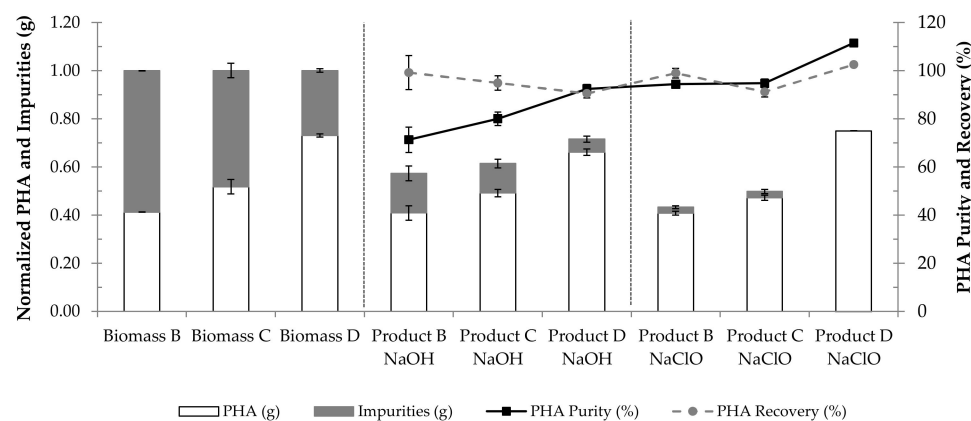


**Figure 4.** Results of PHA extraction using the optimal conditions for digestion with NaClO (9.0%, 3.4 h) or with NaOH (0.3 M, 4.8 h). The results are expressed in PHA purity (%), PHA recovery (%), normalized mass of PHA (g) and normalized mass of impurities (g). Biomass A corresponds to the starting biomass with intracellular PHA prior to extraction. The results of the conventional PHA extraction with chloroform (extraction with chloroform in soxhlet, followed by purification in ethanol (EtOH)) are also displayed as “Soxhlet w/CHCl<sub>3</sub> + EtOH”.

The PHA extraction results presented in Figure 4 suggest that NaOH treatment using the optimal conditions, 0.3 M for 4.8 h, can efficiently extract the polymer from the PHA-enriched biomass used in the present study.

### 3.3. Effect of the Initial Intracellular PHA Content on the PHA Extraction Performance

Studies have shown that the initial PHA content of biomass yields a great influence on the performance of the PHA extraction process [5,24]. It has been estimated that for a PHA extraction process to be cost efficient, the biomass should present a PHA content of over 60%, since when it is under this value, serious complications in the separation process could potentially occur [5,25,26]. To assess the influence of the biomass intracellular PHA content on the performance of the developed PHA extraction methods, three biomass samples produced at pilot scale with the same substrate (fruit pulp waste) but with varying intracellular PHA contents, namely 41%, 52% and 73%, i.e., biomasses B, C and D (see Section 2.1), were subjected to the previously determined optimal conditions for NPCM digestion with NaOH (0.3 M and 4.8 h) and NaClO (9.0% and 3.4 h). The results of these PHA extraction tests are presented in Figure 5.



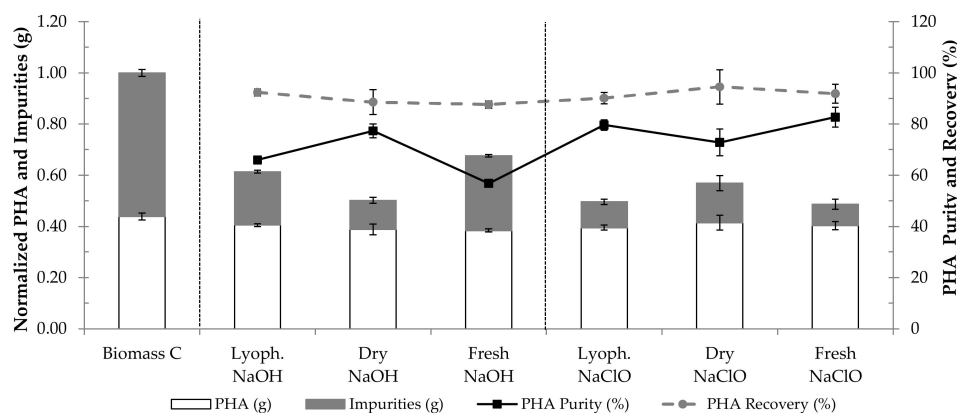
**Figure 5.** Results of PHA extraction from MMC biomass samples with intracellular PHA contents of 41%, 52% and 73% using the optimal conditions for digestion with either NaOH (0.3 M for 4.8 h) or NaClO (9.0% for 3.4 h). Biomass B, biomass C and biomass D correspond to the starting biomasses with intracellular PHA prior to extraction. Product B, product C and product D correspond to the products extracted from biomasses B, C and D, respectively. The results are expressed in PHA purity (%), PHA recovery (%), normalized mass of PHA (g) and normalized mass of impurities (g).

The results in Figure 5 are in accordance with the literature, as they present a clear influence of the initial intracellular PHA content on the polymer extraction performance. Figure 5 shows that the PHA purity of the extraction products increases with the increase in the initial intracellular PHA content of the biomass, irrespective of the digestion agent applied. Yet, an extraction product without impurities was only obtained when applying the optimal NaClO digestion conditions to the sample with the highest intracellular PHA content tested (73%; biomass D). These results confirm previous findings and allow us to conclude that the more enriched in PHA the biomass is, the purer the extracted polymer will be, translating into greater process efficiency.

### 3.4. Effect of Biomass Pre-Treatment on PHA Extraction Performance

To study the effect of biomass pre-treatment on PHA extraction by NPCM digestion with either NaOH or NaClO, extraction trials were performed with fresh, dried and lyophilized biomass. Biomass C (PHA content of ca. 44%, see Section 2.1) was used in these tests. After having been collected, biomass C was subjected to acidification, centrifugation and storage at 4 °C. This fresh biomass C was subjected to PHA extraction. The dry biomass C was obtained by subjecting the fresh biomass to drying at 60 °C for 3.5 days. The lyophilized biomass C was obtained after lyophilization of the fresh biomass.

Figure 6 displays the PHA extraction results of the application of the optimal conditions for either NaOH or NaClO digestion (determined in Section 3.2) to lyophilized, dry and fresh biomass C.



**Figure 6.** Results of PHA extraction from lyophilized, dry (at 60 °C) and fresh biomass, containing ca. 44% of PHA, using the optimal conditions for digestion with either NaOH (0.3 M for 4.8 h) or NaClO (9.0% for 3.4 h). Biomass C corresponds to the starting biomass with intracellular PHA prior to extraction. The results are expressed in PHA content (%), PHA recovery (%), normalized mass of PHA (g) and normalized mass of impurities (g).

The results of digestion with NaOH in Figure 6 suggest that this method was more efficient when used to process dry biomass rather than lyophilized or fresh biomass, as it resulted in a higher removal of impurities without compromising PHA recovery. While PHA recovery values were similar for all extraction trials with NaOH, ranging between 88 and 92%, the use of dry biomass resulted in a product with a PHA purity of 77%, while NaOH digestion of lyophilized and fresh biomass originated products with PHA purities of 66% and 57%, respectively.

The use of NaClO for PHA extraction from lyophilized, dry and fresh biomass resulted in products with PHA purities of 80%, 73% and 83%, respectively, and similar PHA recovery values, between 90 and 95% (Figure 6). Hence, contrary to PHA extraction by NaOH treatment, digestion with NaClO resulted in products with similar PHA purity and recovery, regardless of the pre-treatment applied to the biomass, though it was slightly less efficient when processing dry biomass.

### 3.5. Effect of Biomass Concentration on PHA Extraction Performance

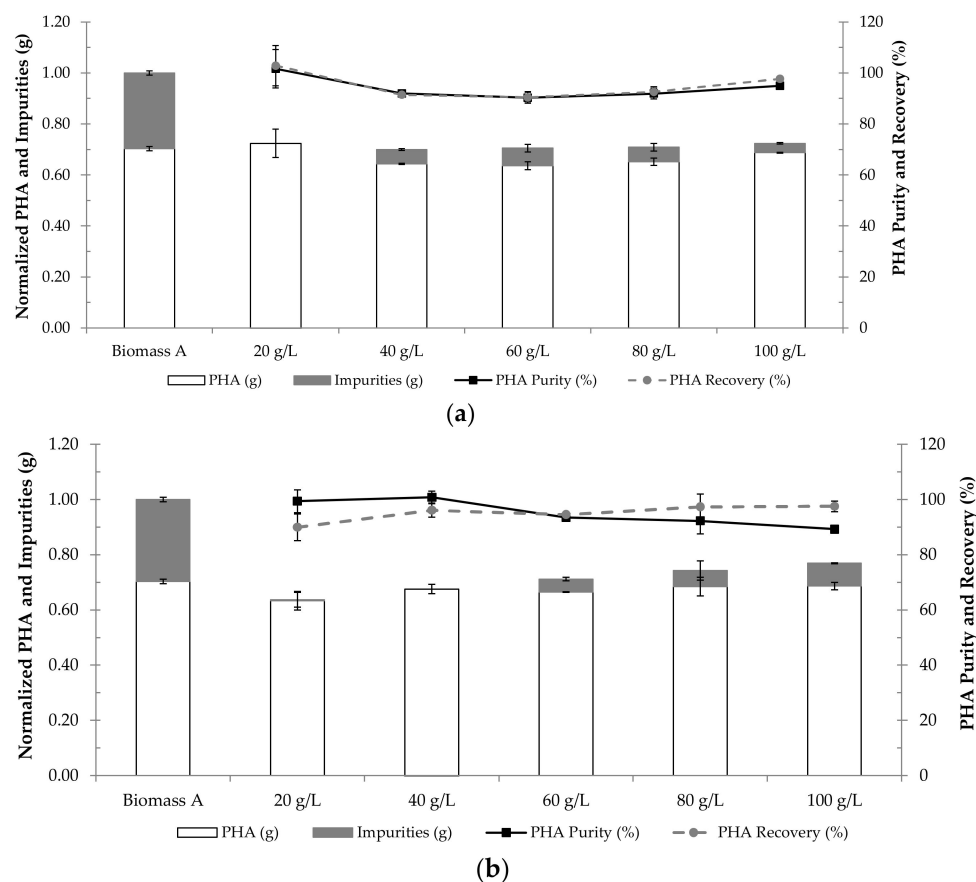
The effect of biomass concentration on PHA extraction by NaOH or NaClO digestion was also studied. For this purpose, biomass A (lyophilized biomass with ca. 70% PHA, see Section 2.1) at the concentrations of 20 g/L, 40 g/L, 60 g/L, 80 g/L and 100 g/L was subjected to the optimal conditions for digestion with NaOH (0.3 M, 4.8 h) or NaClO (9.0%, 3.4 h). The results concerning the effect of biomass concentration on PHA extraction by digestion with either NaOH or NaClO are presented in Figure 7a,b.

Figure 7 shows that at a biomass concentration of 20 g/L, NPCM digestion with either NaOH or NaClO originated products with PHA contents of ca. 100%. When biomass concentration was increased to 40 g/L, the product derived from NaOH digestion presented about 8% of impurities, while the one obtained from NaClO digestion still presented a PHA content of ca. 100%. This suggests that, at their respective optimal conditions, NaClO was able to digest more NPCM than NaOH.

After increasing biomass concentration to 60, 80 and 100 g/L, the PHA purity gradually decreased in the products extracted by NaClO digestion and remained approximately constant in the products extracted by NaOH digestion. Thus, it is possible to conclude that as the biomass concentration increased in the extraction trials using either digestion



agent, the PHA purity of the extracted samples tended to decrease, the higher amount of impurities being a consequence of a higher biomass concentration.



**Figure 7.** Results of PHA extraction from biomass at the concentrations of 20 g/L, 40 g/L, 60 g/L, 80 g/L and 100 g/L using the optimal conditions for digestion with either (a) NaOH (0.3 M for 4.8 h) or (b) NaClO (9.0% for 3.4 h). Biomass A corresponds to the starting biomass with intracellular PHA prior to extraction. The results are expressed in PHA purity (%), PHA recovery (%), normalized mass of PHA (g) and normalized mass of impurities (g).

### 3.6. Characterization of Extracted Polymers

Selected samples from the PHA extraction tests previously presented were analyzed in terms of Mw, DSC and FTIR spectroscopy. The analyzed samples and the extraction treatments they were obtained from are described in Table 6. The physical-chemical properties of the polymers extracted using the different treatments are presented in Table 7. In terms of physical-chemical properties, sample V will be considered the standard for comparison between samples obtained from the same biomass (lyophilized biomass A with ca. 70% PHA content; samples I, II and V) due to having been obtained using the benchmark protocol for PHA extraction, which, reportedly, causes negligible PHA degradation [27].

**Table 6.** Samples selected for analysis of molecular weight (Mw), differential scanning calorimetry (DSC) and Fourier transform infrared (FTIR) spectroscopy and the PHA extraction methods from which these samples were obtained.

Sample	Type of Biomass	PHA Content (%)	Extraction Method
I	lyophilized biomass A	70	NaOH (0.3 M, 4.8 h) + washing with water
II	lyophilized biomass A	70	NaClO (9.0%, 3.4 h) + washing with water
III	fresh biomass C	44	NaOH (0.3 M, 4.8 h) + washing with water
IV	dried biomass C (60 °C, 3.5 days)	44	NaOH (0.3 M, 4.8 h) + washing with water
V	lyophilized biomass A	70	Soxhlet extraction with chloroform + precipitation in absolute EtOH (benchmark protocol)

**Table 7.** Physical-chemical properties of the polymers extracted in selected PHA extraction trials, produced by MMC using fermented fruit waste as feedstock (3HB, 3-hydroxybutyrate; 3HV, 3-hydroxyvalerate; Mw, Mean molecular weight in weight; Mn, Mean molecular weight in number; PDI, Polydispersity index; T<sub>g</sub>, Glass transition temperature; T<sub>c</sub>, Crystallization temperature; ΔH<sub>c</sub>, Crystallization enthalpy; T<sub>m</sub>, Melting temperature; ΔH<sub>m</sub>, Melting enthalpy).

Sample	PHA Purity (%)	3HB in PHA (%wt)	3HV in PHA (%wt)	Mw (×10 <sup>5</sup> Da)	Mn (×10 <sup>5</sup> Da)	PDI	T <sub>g</sub> (°C)	T <sub>c</sub> (°C)	ΔH <sub>c</sub> (J/g)	T <sub>m</sub> (°C)	ΔH <sub>m</sub> (J/g)
I	101.7 ± 7.6	69.0	31.0	2.45	1.33	1.84	−1.57	57.1	6.7	109.6	20.8
II	99.4 ± 4.2	69.1	30.9	2.45	1.11	2.20	−1.19	-	-	111.1	27.5
III	56.8 ± 0.8	81.7	18.3	2.81	1.26	2.23	−4.92	-	-	138.1	2.5
IV	77.3 ± 2.7	81.7	18.3	0.87	0.12	7.12	−0.14	-	-	132.9	33.9
V	95.1 ± 7.3	68.8	31.2	2.63	1.31	2.00	0.51	62.1	11.3	109.1	18.5

### 3.6.1. Molecular Weight

When comparing the Mw (Table 7) of sample V with that of samples I and II, it is possible to infer that treating lyophilized biomass A with NaOH or NaClO, respectively, resulted in a slight decrease in Mw. This suggests that some polymer degradation occurred during these PHA extraction processes. Nevertheless, samples I and II presented high Mw and values of polydispersity index (PDI) similar to the ones for sample V, around 2, indicating the homogeneity of these polymers.

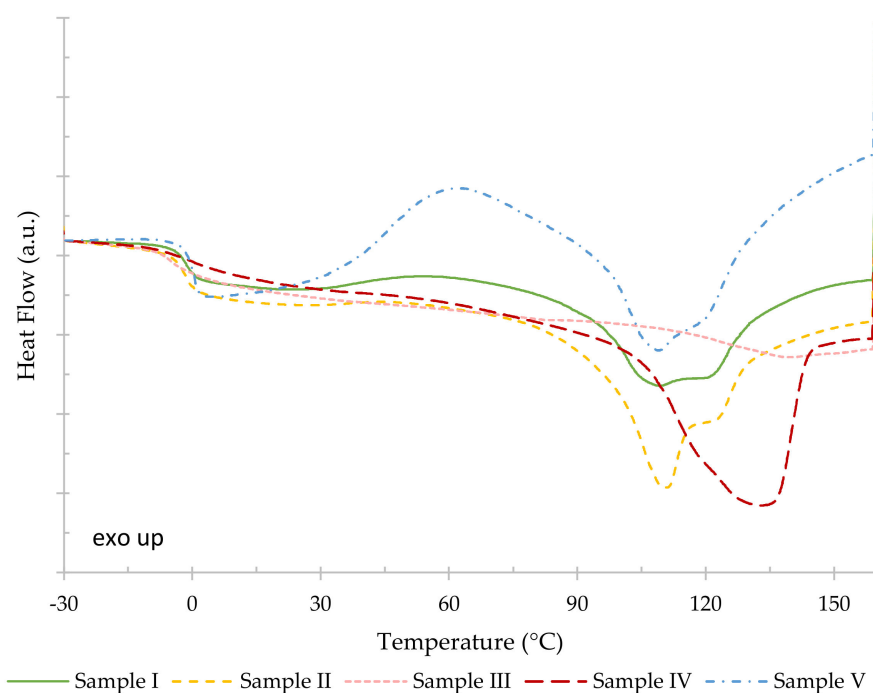
On the other hand, comparing the Mw and PDI values of samples III and IV suggests that drying biomass C at 60 °C for 3.5 days before extraction resulted in significant changes in the macromolecular features of the polymer, the Mw for sample IV being markedly lower than that for sample III ( $0.87 \times 10^5$  Da and  $2.81 \times 10^5$ , respectively). Furthermore, while sample III presented a PDI of 2.23, sample IV displayed a PDI of 7.12, indicative of a broad molecular weight distribution in the latter.

### 3.6.2. Thermal Properties

The thermal properties of each sample, namely glass transition temperature (T<sub>g</sub>), crystallization temperature (T<sub>c</sub>) and respective crystallization enthalpy (ΔH<sub>c</sub>), melting temperature (T<sub>m</sub>) and respective melting enthalpy (ΔH<sub>m</sub>), were determined using the second heating run of the respective thermogram (Figure 8). As moisture/solvent removal occurred during the first heating run, considering the second heating allowed a more accurate comparison between the samples. It should be noted, however, that crystallinity decreased for all samples after the first heating/cooling cycle, as samples recrystallized to a lesser extent. Furthermore, sample III presented a distinctive behavior on the first heating run, being the sample that lost the most mass, attributed to dehydration, the respective water removal endotherm masking the melting.

The second heating run of the thermograms of the considered samples (Figure 8) displays broad melting endotherms, likely due to a wide distribution of crystal thickness and/or size, which influenced their melting temperatures [28]. Furthermore, the thermograms in Figure 8 show that samples I and V undergo cold crystallization above glass transition, revealed by the emergence of a broad exotherm, which could be a consequence of a higher mobility of the polymer chains [29] enabling their ordered arrangement while crossing the glass transition temperature upon heating.

In Table 7, it is possible to observe that the samples with the highest melting temperatures were samples III (138.1 °C) and IV (132.9 °C). This may be due to their lower 3HV content when compared to the other samples, since a melting point decrease in PHBV has been associated with a 3HV content increase [30].



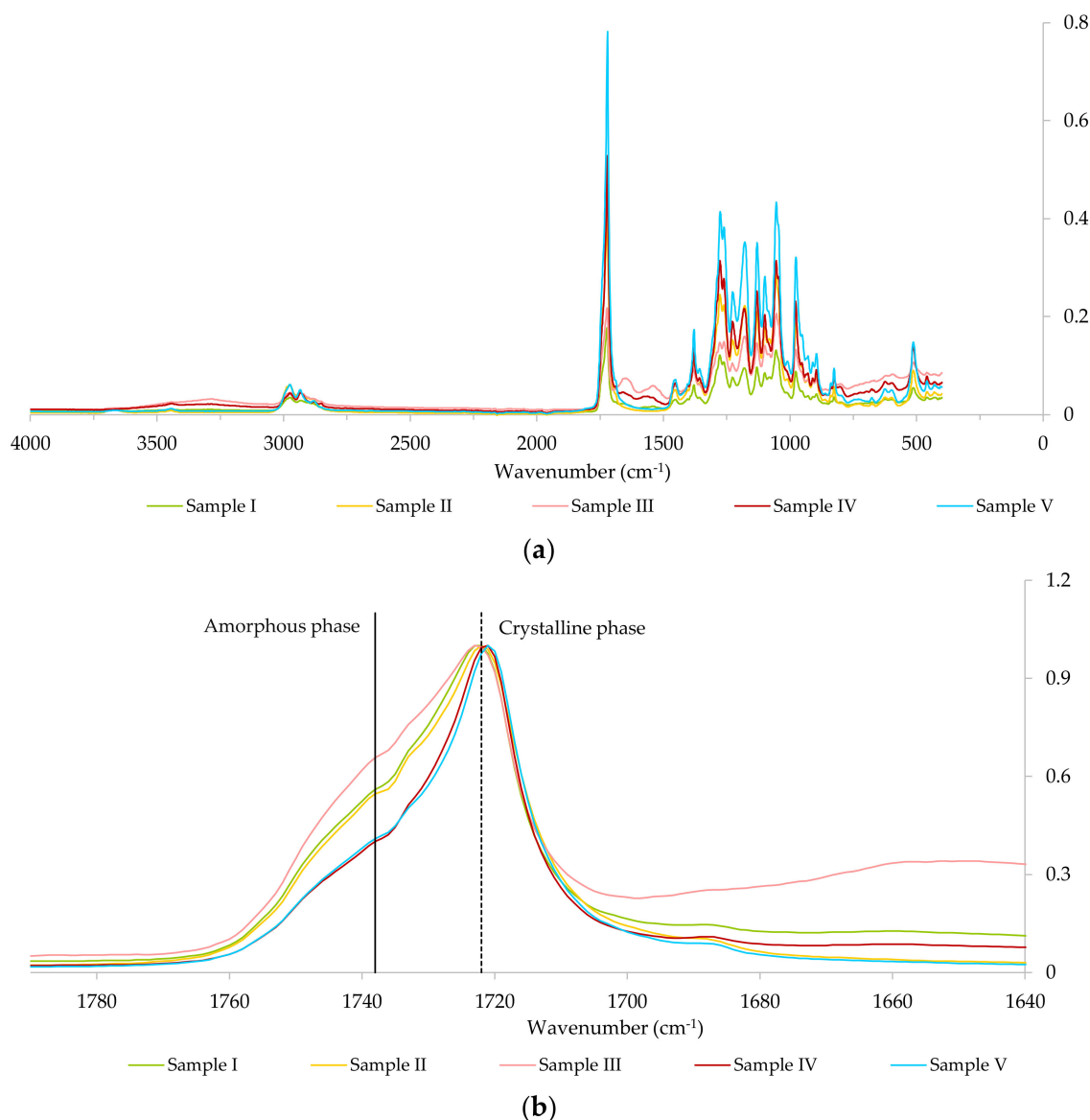
**Figure 8.** Second heating runs of the DSC thermograms of samples I (green, solid line), II (yellow, dash line), III (pink, short dash line), IV (red, long dash line), V (blue, dash dot line). The thermograms were vertically displaced in order to coincide in the low temperature region.

### 3.6.3. Attenuated Total Reflectance—Fourier Transform Infrared (ATR-FTIR) Spectra

ATR-FTIR spectroscopy was used to analyze the selected polymers extracted by NaOH- and NaClO-based methods and also by chloroform extraction followed by EtOH purification (Table 6). The FTIR spectra obtained are presented in Figure 9.

Figure 9a shows that all the samples present the typical PHA bands in FTIR, namely the ester carbonyl band (C=O), stretching in the  $1740\text{--}1700\text{ cm}^{-1}$  region, and the  $\text{-CH}_3$  and  $\text{-CH}_2$  bands, stretching at  $3000\text{--}2800\text{ cm}^{-1}$  [31]. In Figure 9b, all FTIR spectra were normalized by their maximum absorbance, at ca.  $1722\text{ cm}^{-1}$ , to allow a more accurate comparison between the samples in the ester carbonyl band (C=O) region.

Structurally, in the crystalline phase, oxygen atoms of the carbonyl group are located closer to hydrogen atoms, forming hydrogen-bond interactions and leading to a decrease in the carbonyl bond order and to absorbance at lower wavenumbers. On the other hand, the absence of an ordered structure in the amorphous phase leads to reduced hydrogen-bonding effects, resulting in increased carbonyl bond order and absorbance at higher wavenumbers [32], closer to the free C=O stretching mode. Hence, the carbonyl band presents two distinct regions: a relatively broad band at ca.  $1738\text{ cm}^{-1}$ , which corresponds to the amorphous phase of the polymer, and a sharper band at ca.  $1722\text{ cm}^{-1}$ , which corresponds to the crystalline phase [33]. Considering this information and Figure 9b, it is possible to infer that sample III exhibits the most amorphous character of all the samples, while the highest crystallinity was found for samples IV and V. The comparison between samples III and IV allows us to conclude that drying the biomass at  $60\text{ }^\circ\text{C}$  for 3.5 days, prior to the PHA extraction process, influenced the polymer crystallinity in sample IV, since this was the only difference between the pre-treatments of both samples (Table 6). Likewise, as samples I, II and V, which resulted from different extraction methods applied to the same lyophilized biomass, present distinct dynamics between the respective amorphous and crystalline phases, one might assess that the PHA extraction process influences the polymer crystallinity.



**Figure 9.** FTIR spectra of the polymer samples obtained using different PHA extraction methods considering: (a) the entire wavenumber range (400–4000 cm<sup>-1</sup>); (b) a close-up of the carbonyl (C=O) region, 1740–1700 cm<sup>-1</sup>, which includes a broad band at ca. 1738 cm<sup>-1</sup> and a sharp band at ca. 1722 cm<sup>-1</sup>, assigned to the amorphous and crystalline phases of the polymers, respectively; in (b) each FTIR spectra were normalized by the respective maximum absorbance, at ca. 1722 cm<sup>-1</sup>.

#### 4. Discussion

In the present study, when the optimal conditions for digestion with NaOH (0.3 M, 4.8 h) were applied to lyophilized biomass (biomass A, PHA content of ca. 70%) produced at pilot scale using fermented fruit pulp as substrate, a PHA purity of  $101.7 \pm 7.6\%$  and a PHA recovery of  $102.9 \pm 7.9\%$  were obtained. These values are similar to the ones reported by Jiang et al. (2015) [3], where lyophilized biomass with an intracellular PHA content of ca. 70%, produced with acetate as substrate, was digested using NaOH at 0.2 M for 1 h, resulting in the recovery of  $95.5 \pm 0.6\%$  of the polymer with a purity of  $95.9 \pm 3.7\%$ . However, in the current study, a higher NaOH concentration and a longer digestion time were necessary to obtain PHA purity and PHA recovery values similar to the ones reported by Jiang et al. (2015) [3], possibly due to the fact that a real substrate with a more complex matrix was used for biomass production in the case at study. Furthermore, the results of the aforementioned authors suggest that sole NaOH treatment was unable to remove all

NPCM from fresh biomass, the remaining impurities requiring the combined action of NaOH and sodium dodecyl sulfate (SDS) to be efficiently removed. In the present study, when testing the effect of different biomass pre-treatments on PHA extraction performance (Figure 6), using biomass with a lower intracellular PHA content (ca. 44%, biomass C), it was also observed that NaOH digestion was less efficient when processing fresh biomass when compared to lyophilized and dry biomass. Hence, one possible approach for future work might be the addition of SDS to NaOH digestion for the extraction of PHA from fresh biomass.

In the present study, the application of the found optimal conditions for NaOH digestion (0.3 M, 4.8 h) to lyophilized biomass with an intracellular PHA content of ca. 41% (biomass B) (Figure 5) resulted in an extraction product with a PHA purity of about 71% and a PHA recovery of ca. 99%. Mohammadi et al. (2012) [8] performed experiments of PHA (PHBHHx) extraction from lyophilized recombinant *C. necator* with a PHA content of ca. 38.3% at 4 °C and 30 °C. At 30 °C, the temperature used in the present study, the highest values of PHA purity and PHA recovery were ca. 95% and ca. 97%, respectively, obtained when biomass was subjected to digestion with NaOH at 0.1 M for 5 h. The lower PHA purity of the final product in the current study may be associated with the fact that MMC are reportedly more resistant to cell hydrolysis than pure cultures [34].

In this study, using the optimal NaOH digestion conditions for the extraction of PHA from fresh biomass C with a PHA content of ca. 44% (Figure 6) resulted in a PHA recovery and a PHA purity of around 88% and 57%, respectively. Villano et al. (2014) [11] performed PHA extraction trials at room temperature using fresh biomass with an average PHA (PHBV) content of 46%, produced with a synthetic mixture of acetic and propionic acids. When subjecting the fresh biomass to NaOH at 1 M (the ratio between the volume of biomass and the chemical solution being 6:1) for 3 h, these authors reported a PHA recovery and a PHA purity of around 87% and 54%, respectively. Using a digestion time of 24 h, a PHA recovery and a PHA purity of about 80% and 56%, respectively, were obtained. These values are similar to the ones obtained in the present study. Regarding digestion with NaClO at 5% Cl<sub>2</sub> (5.25% NaClO; the ratio between the volume of biomass and the chemical solution being 6:1), the aforementioned authors reported complete recovery of PHA after 3 h and 24 h of digestion. Furthermore, PHA purities of ca. 90% and ca. 98% were obtained after 3 h and 24 h of digestion, respectively. In the present study, subjecting fresh biomass with a PHA content of ca. 44% (biomass C) to the optimal conditions for NaClO digestion (9.0% NaClO, 3.4 h) resulted in a PHA recovery of around 92% and a final product with a PHA purity of ca. 83% (Figure 6). These values are lower than the ones obtained by Villano et al. (2014) [11], which may be due to the fact that the biomass in the current study was produced using real waste as substrate, namely fermented fruit pulp with a complex matrix, while in the former, a synthetic mixture of acetic and propionic acids was used. The use of real waste as substrate may result in the presence of impurities that are harder to remove. On the other hand, the conditions used for PHA extraction from fresh biomass C (PHA content of ca. 44%) with NaClO in the present study were determined using lyophilized biomass with a PHA content of ca. 70%, biomass A (Section 3.2). Thus, it is possible that applying the CCRD methodology to NaClO digestion for PHA extraction from fresh biomass C would determine a different set of optimal conditions that would result in increased PHA purity and PHA recovery. The same possibility can be posed for PHA extraction by NaOH digestion.

Considering Mw results, the polymer obtained from NaClO digestion (9.0%, 3.4 h) of lyophilized biomass with an intracellular PHA content of ca. 70% (sample II in Table 7) presented an average Mw of  $2.45 \times 10^5$  Da and PDI of 2.20. In the study by Villano et al. (2014) [11], digestion using NaClO, in the conditions mentioned above resulted in a polymer with a Mw range between  $3.4 \times 10^5$  and  $5.4 \times 10^5$  Da, and a PDI between 4 and 10. It is possible that the considerable difference between the PDI values of the two studies is due to the process conditions, since in the present study, the polymer was extracted from lyophilized biomass with an intracellular PHA content of ca. 70%, while

in the study by Villano et al. (2014) [11], the polymer was extracted from fresh biomass containing ca. 46% of PHA.

Digestion of lyophilized MMC (biomass A, PHA content of ca. 70%) with NaClO, using the optimal conditions (9.0% NaClO, 3.4 h), resulted in a PHA recovery of ca. 90% and a PHA purity of around 99% (Figure 4). Heinrich et al. (2012) [9] extracted PHA (PHB) from lyophilized *R. eutropha* H16 (intracellular PHA content of ca. 65.2%) by subjecting it to digestion with NaClO at 13% (v/v) for 1 h at room temperature. In that study, PHA extraction was performed at 0.1 L and 50 L scales. At the scale of 0.1 L, a PHA purity of ca. 95.7% and a PHA recovery of about 91.3% were obtained, whereas at the scale of 50 L, an average of about 87% of the existing polymer was recovered, the final product presenting an average PHA purity of ca. 93%. The reported PHA purity and PHA recovery values using a pure culture are similar to the ones obtained in the current study with an MMC. Nevertheless, in the case at study, PHA extraction by NaClO resulted in a Mw reduction of about 7% when compared to the polymer recovered by chloroform (Table 7), a value notably lower than the one observed by Heinrich et al. (2012) [9], which ranged between 50% and 70%, similarly to previous studies [18,19].

Regarding the effect of biomass concentration on PHA extraction, the results in Figure 7 are in accordance with those obtained by Berger et al. (1989) [19] and Choi and Lee (1999) [6], who observed a decrease in polymer purity when cell concentration was increased in PHA extraction by NaClO and NaOH digestions, respectively. Additionally, Heinrich et al. (2012) [9] also observed that in PHA extraction by digestion with NaClO at 13% (v/v), a biomass concentration higher than 30 g/L led to the saturation of the NaClO solution.

Regarding the effect of biomass pre-treatment on PHA extraction, Figure 6 shows that a higher PHA purity was obtained when NaOH digestion was applied to extract PHA from biomass C (intracellular PHA content of ca. 44%) that had been previously dried at 60 °C for 3.5 days, rather than fresh biomass C (ca. 77% of PHA purity in the former vs. ca. 57% in the latter). However, Mw results in Table 7 show that drying biomass C prior to NaOH digestion (sample IV in Table 7) resulted in a major decrease in Mw and increase in PDI when compared to the application of the same process to fresh biomass C (sample III in Table 7). Sample III presented a Mw of  $2.81 \times 10^5$  Da and a PDI of 2.23, whereas sample IV displayed a Mw of  $0.87 \times 10^5$  Da and a PDI of 7.12. Lorini et al. (2021) [35] also compared the Mw of polymers extracted from dried and fresh biomass and reported a 3-fold lower Mw for the one extracted from dried biomass. In the present study, it is possible that the drying process resulted in the physical association of the polymer in sample IV with low reversibility upon dissolution. This would justify the higher crystallinity of this sample when compared to sample III, as displayed in Figure 9b, and would explain the decrease in Mw. Considering these results, it is possible to conclude that higher PHA extraction performance does not guarantee superior polymer quality.

DSC and FTIR results presented in Figures 8 and 9b, respectively, suggest that the PHA extraction process influences the polymers' crystallinity. These results are in agreement with the results obtained by Jiang et al. (2015) [3], which show that chemical treatment and biomass pre-treatment have an impact on the polymer's crystallinity.

## 5. Conclusions

PHA extraction conditions should be adjusted to the properties of each biomass that is to be processed. In the current study, NaOH and NaClO were tested as green alternatives to organic solvents for the extraction of PHA from MMC biomass produced at pilot scale with fruit pulp waste, and the optimal chemical digestion conditions were determined by a design of experiments methodology. This methodology can be transposed to determine the optimal conditions for PHA recovery from other types of biomasses, subjected to different or no pre-treatments, and with different intracellular PHA contents.

High PHA extraction performances were obtained using the optimal digestion conditions for either NaOH (0.3 M, 4.8 h) or NaClO (9.0%, 3.4 h). However, treatments using

NaClO present the risk of formation of toxic halogenated compounds, hindering their application at a large scale. On the other hand, sole digestion with NaOH proved to be an efficient green alternative to chlorinated compounds.

NaClO was similarly efficient for PHA extraction from dry, lyophilized and fresh biomass, though displaying a slightly lower performance for dry biomass, while for NaOH, the greatest efficiency was attained for dry biomass and the lowest for fresh biomass. Digestion of lyophilized biomass with either NaOH or NaClO resulted in negligible loss of polymer molecular weight. However, biomass drying at 60 °C before PHA extraction resulted in a polymer with a broad molecular weight distribution and a decreased mean molecular weight. Furthermore, polymer characterization by DSC and FTIR suggested that its crystallinity is influenced by the applied extraction method.

Intracellular PHA content and biomass concentration were found to strongly influence the PHA extraction performance, irrespective of the digestion agent used. The higher the intracellular PHA content, the higher the PHA purity in the extraction products. On the other hand, when biomass concentration was increased above 20 g/L, the PHA purity of the extraction products tended to decrease. Thus, a compromise between the efficiency of polymer recovery/purity and the process productivity (related to the volume of biomass to be processed) should be considered according to the final polymer application.

**Author Contributions:** Conceptualization, M.A.M.R. and N.D.L.; Data curation, A.M.R., R.D.G.F., M.D. and C.S.; Formal analysis, A.M.R., R.D.G.F., M.D., C.S. and C.G.; Funding acquisition, M.A.M.R.; Investigation, A.M.R. and R.D.G.F.; Methodology, A.M.R., R.D.G.F., M.D., C.S. and C.G.; Project administration, M.A.M.R. and N.D.L.; Resources, M.D., C.G. and M.A.M.R.; Supervision, M.A.M.R. and N.D.L.; Validation, M.A.M.R. and N.D.L.; Visualization, A.M.R.; Writing—original draft, A.M.R. and N.D.L.; Writing—review and editing, M.A.M.R. and N.D.L. All authors have read and agreed to the published version of the manuscript.

**Funding:** This work was funded by the INGREEN project that has received funding from the Bio-based Industries Joint Undertaking (JU) under the European Union’s Horizon 2020 research and innovation programme under grant agreement No 838120. The JU receives support from the European Union’s Horizon 2020 research and innovation programme and the Bio-based Industries Consortium. This work was financed by national funds from FCT—Fundação para a Ciência e a Tecnologia, I.P., in the scope of the project UIDP/04378/2020 and UIDB/04378/2020 of the Research Unit on Applied Molecular Biosciences—UCIBIO and the project LA/P/0140/2020 of the Associate Laboratory Institute for Health and Bioeconomy—i4HB. A.M. Rodrigues acknowledges the financial support of FCT through the PhD grant 2020.08574.BD.

**Institutional Review Board Statement:** Not applicable.

**Informed Consent Statement:** Not applicable.

**Data Availability Statement:** Not applicable.

**Acknowledgments:** The authors acknowledge Cristiana Torres for her support in the CCRD.

**Conflicts of Interest:** The authors have no conflicts of interest to declare.

## References

1. Pagliano, G.; Galletti, P.; Samorì, C.; Zaghini, A.; Torri, C. Recovery of Polyhydroxyalkanoates From Single and Mixed Microbial Cultures: A Review. *Front. Bioeng. Biotechnol.* **2021**, *9*, 624021. [[CrossRef](#)]
2. Mannina, G.; Presti, D.; Montiel-Jarillo, G.; Carrera, J.; Suárez-Ojeda, M.E. Recovery of Polyhydroxyalkanoates (PHAs) from Wastewater: A Review. *Bioresour. Technol.* **2020**, *297*, 122478. [[CrossRef](#)] [[PubMed](#)]
3. Jiang, Y.; Mikova, G.; Kleerebezem, R.; van der Wielen, L.A.M.; Cuellar, M.C. Feasibility Study of an Alkaline-Based Chemical Treatment for the Purification of Polyhydroxybutyrate Produced by a Mixed Enriched Culture. *AMB Express* **2015**, *5*, 5. [[CrossRef](#)] [[PubMed](#)]
4. Koller, M. Established and Advanced Approaches for Recovery of Microbial Polyhydroxyalkanoate (PHA) Biopolyesters from Surrounding Microbial Biomass. *EuroBiotech J.* **2020**, *4*, 113–126. [[CrossRef](#)]
5. Koller, M.; Niebelschütz, H.; Brauneegg, G. Strategies for Recovery and Purification of Poly[(R)-3-Hydroxyalkanoates] (PHA) Biopolyesters from Surrounding Biomass. *Eng. Life Sci.* **2013**, *13*, 549–562. [[CrossRef](#)]

6. Choi, J.-I.; Lee, S.Y. Efficient and Economical Recovery of Poly(3-Hydroxybutyrate) from Recombinant *Escherichia Coli* by Simple Digestion with Chemicals. *Biotechnol. Bioeng.* **1999**, *62*, 546–553. [[CrossRef](#)]
7. Anis, S.N.S.; Nurhezreen, M.I.; Sudesh, K.; Amirul, A.A. Enhanced Recovery and Purification of P(3HB-Co-3HHx) from Recombinant *Cupriavidus Necator* Using Alkaline Digestion Method. *Appl. Biochem. Biotechnol.* **2012**, *167*, 524–535. [[CrossRef](#)]
8. Mohammadi, M.; Hassan, M.A.; Phang, L.Y.; Shirai, Y.; Che Man, H.; Ariffin, H.; Amirul, A.A.; Syairah, S.N. Efficient Polyhydroxyalkanoate Recovery from Recombinant *Cupriavidus Necator* by Using Low Concentration of NaOH. *Environ. Eng. Sci.* **2012**, *29*, 783–789. [[CrossRef](#)]
9. Heinrich, D.; Madkour, M.H.; Al-Ghamdi, M.A.; Shabbaj, I.I.; Steinbüchel, A. Large Scale Extraction of Poly(3-Hydroxybutyrate) from *Ralstonia Eutropha* H16 Using Sodium Hypochlorite. *AMB Express* **2012**, *2*, 59. [[CrossRef](#)]
10. Pérez-Rivero, C.; López-Gómez, J.P.; Roy, I. A Sustainable Approach for the Downstream Processing of Bacterial Polyhydroxyalkanoates: State-of-the-Art and Latest Developments. *Biochem. Eng. J.* **2019**, *150*, 107283. [[CrossRef](#)]
11. Villano, M.; Valentino, F.; Barbetta, A.; Martino, L.; Scandola, M.; Majone, M. Polyhydroxyalkanoates Production with Mixed Microbial Cultures: From Culture Selection to Polymer Recovery in a High-Rate Continuous Process. *New Biotechnol.* **2014**, *31*, 289–296. [[CrossRef](#)] [[PubMed](#)]
12. López-Abelairas, M.; García-Torreiro, M.; Lú-Chau, T.; Lema, J.M.; Steinbüchel, A. Comparison of Several Methods for the Separation of Poly(3-Hydroxybutyrate) from *Cupriavidus Necator* H16 Cultures. *Biochem. Eng. J.* **2015**, *93*, 250–259. [[CrossRef](#)]
13. Ratnam, B.V.V.; Narasimha Rao, M.; Damodar Rao, M.; Subba Rao, S.; Ayyanna, C. Optimization of Fermentation Conditions for the Production of Ethanol from Sago Starch Using Response Surface Methodology. *World J. Microbiol. Biotechnol.* **2003**, *19*, 523–526. [[CrossRef](#)]
14. Kumar, P.; Vincent, T.; Khanna, A. Application of Response Surface Methodology with Central Composite Design to Evaluate the Extraction of U(VI) into Ionic Liquids. *Mater. Today Proc.* **2022**, *57*, 1738–1744. [[CrossRef](#)]
15. Pereira, J.R.; Araújo, D.; Marques, A.C.; Neves, L.A.; Grandfils, C.; Sevrin, C.; Alves, V.D.; Fortunato, E.; Reis, M.A.M.; Freitas, F. Demonstration of the Adhesive Properties of the Medium-Chain-Length Polyhydroxyalkanoate Produced by *Pseudomonas Chlororaphis* Subsp. *Aurantiaca* from Glycerol. *Int. J. Biol. Macromol.* **2019**, *122*, 1144–1151. [[CrossRef](#)]
16. Cruz, M.V.; Araújo, D.; Alves, V.D.; Freitas, F.; Reis, M.A.M. Characterization of Medium Chain Length Polyhydroxyalkanoate Produced from Olive Oil Deodorizer Distillate. *Int. J. Biol. Macromol.* **2016**, *82*, 243–248. [[CrossRef](#)]
17. Mohammadi, M.; Hassan, M.A.; Shirai, Y.; Man, H.C.; Ariffin, H.; Yee, L.N.; Mumtaz, T.; Chong, M.L.; Phang, L.Y. Separation and Purification of Polyhydroxyalkanoates from Newly Isolated *Comamonas* Sp. EB172 by Simple Digestion with Sodium Hydroxide. *Sep. Sci. Technol.* **2012**, *47*, 534–541. [[CrossRef](#)]
18. Kwang Hahn, S.; Chang, Y.K.; Lee, S.Y. Recovery and Characterization of Poly(3-Hydroxybutyric Acid) Synthesized in *Alcaligenes Eutrophus* and Recombinant *Escherichia Coli*. *Appl. Environ. Microbiol.* **1995**, *61*, 34–39. [[CrossRef](#)]
19. Berger, E.; Ramsay, B.A.; Ramsay, J.A.; Chavarie, C.; Brauneegg, G. PHB Recovery by Hypochlorite Digestion of Non-PHB Biomass. *Biotechnol. Tech.* **1989**, *3*, 227–232. [[CrossRef](#)]
20. Yup Lee, S.; Choi, J.; Han, K.; Yong Song, J. Removal of Endotoxin during Purification of Poly(3-Hydroxybutyrate) from Gram-Negative Bacteria. *Appl. Environ. Microbiol.* **1999**, *65*, 2762–2764. [[CrossRef](#)]
21. Rawte, T.; Mav, S. A Rapid Hypochlorite Method for Extraction of Polyhydroxyalkanoates from Bacterial Cells. *Indian J. Exp. Biol.* **2002**, *40*, 924–929. [[PubMed](#)]
22. Lundstedt, T.; Seifert, E.; Abramo, L.; Thelin, B.; Nyström, Å.; Pettersen, J.; Bergman, R. Experimental Design and Optimization. *Chemom. Intell. Lab. Syst.* **1998**, *42*, 3–40. [[CrossRef](#)]
23. Torres, C.A.V.; Antunes, S.; Ricardo, A.R.; Grandfils, C.; Alves, V.D.; Freitas, F.; Reis, M.A.M. Study of the Interactive Effect of Temperature and PH on Exopolysaccharide Production by *Enterobacter* A47 Using Multivariate Statistical Analysis. *Bioresour. Technol.* **2012**, *119*, 148–156. [[CrossRef](#)] [[PubMed](#)]
24. Yang, Y.H.; Brigham, C.; Willis, L.; Rha, C.K.; Sinskey, A. Improved Detergent-Based Recovery of Polyhydroxyalkanoates (PHAs). *Biotechnol. Lett.* **2011**, *33*, 937–942. [[CrossRef](#)] [[PubMed](#)]
25. Luzier, W.D. Materials Derived from Biomass/Biodegradable Materials. *Proc. Natl. Acad. Sci. USA* **1992**, *89*, 839–842. [[CrossRef](#)]
26. Choi, J.; Lee, S.Y. Factors Affecting the Economics of Polyhydroxyalkanoate Production by Bacterial Fermentation. *Appl. Microb. Biotechnol.* **1999**, *51*, 13–21. [[CrossRef](#)]
27. Chen, Y.; Chen, J.; Yu, C.; Du, G.; Lun, S. Recovery of Poly-3-Hydroxybutyrate from *Alcaligenes Eutrophus* by Surfactant-Chelate Aqueous System. *Process Biochem.* **1999**, *34*, 153–157. [[CrossRef](#)]
28. Teixeira, S.S.; Gama, N.; Cordeiro, T.; Barros-Timmons, A.; Dionísio, M.; Graça, M.P.F.; Costa, L.C. Poly(L-Lactic Acid)/Lithium Ferrite Composites: Electrical Properties. *Polymer* **2021**, *230*, 124100. [[CrossRef](#)]
29. Yu, L.; Liu, H.; Dean, K.; Chen, L. Cold Crystallization and Postmelting Crystallization of PLA Plasticized by Compressed Carbon Dioxide. *J. Polym. Sci. Part B Polym. Phys.* **2008**, *46*, 2630–2636. [[CrossRef](#)]
30. Wang, Y.; Chen, R.; Cai, J.Y.; Liu, Z.; Zheng, Y.; Wang, H.; Li, Q.; He, N. Biosynthesis and Thermal Properties of PHBV Produced from Levulinic Acid by *Ralstonia Eutropha*. *PLoS ONE* **2013**, *8*, e60318. [[CrossRef](#)]
31. Colombo, B.; Pereira, J.; Martins, M.; Torres-Acosta, M.A.; Dias, A.C.R.V.; Lemos, P.C.; Ventura, S.P.M.; Eisele, G.; Alekseeva, A.; Adani, F.; et al. Recovering PHA from Mixed Microbial Biomass: Using Non-Ionic Surfactants as a Pretreatment Step. *Sep. Purif. Technol.* **2020**, *253*, 117521. [[CrossRef](#)]



32. Xu, J.; Guo, B.-H.; Yang, R.; Wu, Q.; Chen, G.-Q.; Zhang, Z.-M. In Situ FTIR Study on Melting and Crystallization of Polyhydroxyalkanoates. *Polymer* **2002**, *43*, 6893–6899. [[CrossRef](#)]
33. Kansiz, M.; Domínguez-Vidal, A.; McNaughton, D.; Lendl, B. Fourier-Transform Infrared (FTIR) Spectroscopy for Monitoring and Determining the Degree of Crystallisation of Polyhydroxyalkanoates (PHAs). *Anal. Bioanal. Chem.* **2007**, *388*, 1207–1213. [[CrossRef](#)] [[PubMed](#)]
34. Samori, C.; Abbondanzi, F.; Galletti, P.; Giorgini, L.; Mazzocchetti, L.; Torri, C.; Tagliavini, E. Extraction of Polyhydroxyalkanoates from Mixed Microbial Cultures: Impact on Polymer Quality and Recovery. *Bioresour. Technol.* **2015**, *189*, 195–202. [[CrossRef](#)] [[PubMed](#)]
35. Lorini, L.; Martinelli, A.; Pavan, P.; Majone, M.; Valentino, F. Downstream Processing and Characterization of Polyhydroxyalkanoates (PHAs) Produced by Mixed Microbial Culture (MMC) and Organic Urban Waste as Substrate. *Biomass Convers. Biorefinery* **2021**, *11*, 693–703. [[CrossRef](#)]

## Article

# Synthesis and Enzymatic Degradation of Sustainable Levoglucosenone-Derived Copolyesters with Renewable Citronellol Side Chains

Sami Fadlallah \*, Quentin Carboué \*, Louis M. M. Mouterde, Aihemaiti Kayishaer, Yasmine Werghi, Aurélien A. M. Peru, Michel Lopez and Florent Allais \*

URD Agro-Biotechnologies Industrielles (ABI), CEBB, AgroParisTech, 3 Rue des Rouges-Terres, 51110 Pomacle, France; louis.mouterde@agroparistech.fr (L.M.M.M.); aihemaiti.kayishaer@gmail.com (A.K.); yasmine.werghi1@gmail.com (Y.W.); aurelien.peru@agroparistech.fr (A.A.M.P.); michel.lopez@agroparistech.fr (M.L.)

\* Correspondence: sami.fadlallah@agroparistech.fr (S.F.); quentin.carboue@agroparistech.fr (Q.C.); florent.allais@agroparistech.fr (F.A.)

**Abstract:** Recently, a renewable five-membered lactone containing citronellol (HBO-citro) was synthesized from levoglucosenone (LGO). A one-pot two-step pathway was then developed to produce a mixture of 5- and 6-membered Lactol-citro molecules (5ML and 6ML, respectively) from HBO-citro. Proton nuclear magnetic resonance ( $^1\text{H}$  NMR) of a mixture of 5ML and 6ML at varying temperatures showed that the chemical shifts of the hydroxyls, as well as the 5ML:6ML ratio, are temperature-dependent. Indeed, a high temperature, such as 65 °C, led to an up-field shielding of the hydroxyl protons as well as a drop in the 5ML:6ML ratio. The monomers 5ML and 6ML were then engaged in polycondensation reactions involving diacyl chlorides. Renewable copolyesters with low glass transition temperatures (as low as  $-67$  °C) and cross-linked citronellol chains were prepared. The polymers were then hydrolyzed using a commercial lipase from *Thermomyces lanuginosus* (Lipopan<sup>®</sup> 50 BG). A higher degradation rate was found for the polymers prepared using Lactol-citro molecules, compared to those obtained by the polycondensation reactions of diacyl chlorides with Triol-citro—a monomer recently obtained by the selective reduction of HBO-citro.

**Keywords:** sustainability; levoglucosenone; oxa-Michael addition; cross-linkable polymers; renewable polyesters; biodegradation

**Citation:** Fadlallah, S.; Carboué, Q.; Mouterde, L.M.M.; Kayishaer, A.; Werghi, Y.; Peru, A.A.M.; Lopez, M.; Allais, F. Synthesis and Enzymatic Degradation of Sustainable Levoglucosenone-Derived Copolyesters with Renewable Citronellol Side Chains. *Polymers* **2022**, *14*, 2082. <https://doi.org/10.3390/polym14102082>

Academic Editors: José Miguel Ferri, Vicent Fombuena Borràs and Miguel Fernando Aldás Carrasco

Received: 21 April 2022

Accepted: 16 May 2022

Published: 20 May 2022

**Publisher's Note:** MDPI stays neutral with regard to jurisdictional claims in published maps and institutional affiliations.



**Copyright:** © 2022 by the authors. Licensee MDPI, Basel, Switzerland. This article is an open access article distributed under the terms and conditions of the Creative Commons Attribution (CC BY) license (<https://creativecommons.org/licenses/by/4.0/>).

## 1. Introduction

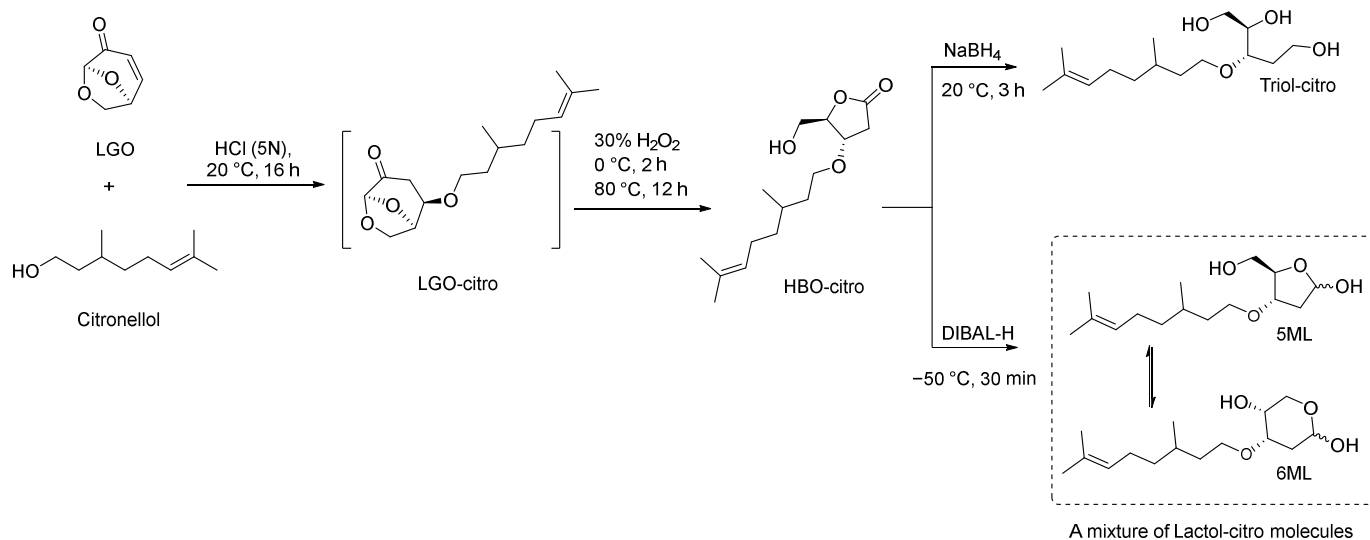
While converting biomass waste into high-performance renewable materials reduces fossil fuel use and greenhouse gas emissions [1,2], it does not solve the environmental problems caused by the accumulation of bioplastic waste [3]. Indeed, the prefix “bio” is likely to be misunderstood by producers/consumers. Bio-based polymers are products that are partially or fully derived from biomass. However, bio-based polymers can be either biodegradable or not [4,5]. Biodegradation is the decomposition of a specific material into final metabolic compounds, such as  $\text{CO}_2$ , through an in vivo or in vitro enzyme-initiated/mediated mechanism [6]. Thus, not all bio-based polymers are biodegradable. For these reasons, it is of utmost importance to consider the biodegradation of polymers obtained from biomass as a primary criterion in the evaluation of the sustainability of the corresponding materials. Pellis et al. have recently highlighted the synergy between chemistry and biotechnology to produce new generations of bio-based polymers with environmental and social benefits [7]. Indeed, the biodegradation of synthesized renewable polymers is barely described in the literature. From a general point of view, the (bio)degradation of a macromolecule/polymer is mainly affected by the following characteristics: optical purity [8], crystallinity [9], molecular weight [10] or chemical structure [11].

Polyesters constitute a highly versatile class of polymers that meet the market requirements in terms of production cost and desirable qualities [12]. For example, polyesters are widely used for making textiles, such as dress materials [13]. On the other hand, polyesters are polymers of repeating units containing ester groups that can undergo hydrolysis under certain circumstances. This facilitates their enzymatic degradation if they are susceptible to it [14]. The presence of aliphatic moieties in polyesters allows their biodegradability. Aromatic-containing polymers, such as bio-polyethylene terephthalate (PET) [15], the leading bioplastic in the market, suffer from their resistance to degradation when accumulated in the environment. In general, biodegradable aromatic/aliphatic polyesters typically contain a large fraction of aliphatic ester groups. Above a threshold, which depends on the properties of each polymer, the presence of aromatic groups decreases, or even suppresses, the biodegradability [16].

On the other hand, one of the key challenges in the field of sustainable polymers is to produce renewable materials that can compete with their fossil fuel-based counterparts [17–19]. A discussion was recently held to identify the most important topics that should be addressed over the next 100 years in polymer science [20]. Three major topics were identified: (i) new properties and applications, (ii) new synthetic methods, and (iii) sustainability. In this context, functional polymers offer great potential to be used in widespread applications [21,22]. Allcock et al. took advantage of citronellol, a natural acyclic monoterpene found in citronella oil [23], to synthesize polyphosphazenes containing citronellol side groups, as potential candidates for ligament and tendon tissue engineering [24]. Hydrolysis experiments in deionized water at 37 °C showed a mass loss of 8–16% and a decrease in molecular weight in the range of 28–88% over 12 weeks. The same authors prepared polyphosphazenes with pendant amino acid citronellol ester for biomedical applications [25]. Nevertheless, the synthesis of these functional polymers requires non-renewable backbone chains (polyphosphazenes) to hold the citronellol chains. In addition, a chlorine-based hexachlorophosphazene is needed to synthesize polyphosphazenes [26]. Citronellyl, geranyl and neryl methacrylate monomers were also prepared by Worzakowska [27]. Branched polymers were obtained through the UV-photoinitiated polymerization of these functional methacrylated monomers at room temperature. Interestingly, among the polymers obtained, poly(citronellyl methacrylate) was the most thermally stable material [27].

Given our strong expertise in levoglucosenone (LGO), a wood-based functional molecule produced at the scale of several tons per year [28–30], we have recently become interested in developing not only renewable functional monomers and polymers from LGO [31–36] but also biodegradation protocols to evaluate the end-of-life of our in-house corresponding materials. In this context, we recently reported the first fully renewable citronellol-containing monomers from LGO [34,35]. More precisely, we took advantage of the  $\alpha,\beta$ -conjugated double bond of LGO to perform the acid-catalyzed [37] oxa-Michael addition of citronellol (Scheme 1). This step was followed by the in situ organic solvent-free  $H_2O_2$ -mediated Baeyer-Villiger oxidation to access HBO-citro. From the latter, fully renewable monomers (Triol-citro and Lactols-citro) were prepared through the selective reduction of the HBO lactone moiety. Notably, when  $NaBH_4$  was used as a reducing agent, it led to the formation of the tris-hydroxy monomer, Triol-citro. However, when diisobutylaluminum hydride (DIBAL-H) was adopted, a mixture of 5- and 6-membered cyclic forms of Lactol-citro (5ML and 6ML) were obtained (Scheme 1) [34]. Indeed, the ring-chain tautomerism of furanoses (5-membered rings) and pyranoses (6-membered rings) is very common in sugars [38]. These furanose-pyranose interconversions exist in equilibrium which led, in our case, to a mixture of Lactol-citro molecules. In our previous work [34], Triol-citro was selected to prepare renewable polyesters (P1–P4) via its polycondensation reaction with diacyl chlorides having different chain lengths ( $m = 1-4$ , respectively). When P1–P4 were exposed to Lipopan<sup>®</sup> 50 BG, a commercial lipase from *Thermomyces lanuginosus*, an 80% degradation of P2–P4 was observed after 80 h [34]. Inspired by this work, we decided herein not only to prepare new fully renewable polyesters (P5–P8) that contain

two types of lactol rings (5-membered and 6-membered) but also to study and compare the biodegradation of the newly synthesized lactol-based copolyesters (P5–P8) to that of the previously reported triol-based polymers (P1–P4). Furthermore, the equilibrium of 5ML and 6ML was studied by  $^1\text{H}$  NMR at three temperatures: 25 °C, 50 °C and 65 °C.



**Scheme 1.** Recently reported syntheses of Triol-citro and Lactol-citro from LGO.

## 2. Materials and Methods

**Chemicals and reagents.** Levoglucosenone was graciously provided by Circa group. Citronellol (Sigma Aldrich, Saint-Louis, MO, USA), diisobutylaluminum hydride (DIBAL-H) (Acros, Geel, Belgium), malonyl chloride 97% (Sigma Aldrich), succinyl chloride 95% (Sigma Aldrich), adipoyl chloride 98% (Sigma Aldrich), glutaryl chloride 97% (Sigma Aldrich), Lipopan<sup>®</sup> 50 BG (Novozymes, Bagsværd, Denmark) a purified lipase from *Thermomyces lanuginosus* expressed in *Aspergillus oryzae*, were used as received. NMR solvents, including CDCl<sub>3</sub> and DMSO-*d*<sub>6</sub>, were purchased from Cambridge Isotopes Laboratories. HPLC grade solvents were purchased from Thermofisher Scientific, Waltham, MA, USA, and used as received. Ultra-pure laboratory-grade water was obtained from MilliQ, 18.2 megaOhms. TLC analyses were performed on an aluminum strip coated with Silica Gel 60 F254 from Merck, revealed under UV-light (254 nm), then in the presence of potassium permanganate staining solution. All manipulations with air-sensitive chemicals and reagents were performed using standard Schlenk techniques on a dual-manifold line, on a high-vacuum line.

### 2.1. Characterization

**Nuclear Magnetic Resonance (NMR) spectroscopy.**  $^1\text{H}$  NMR spectra were recorded on a Bruker Fourier 300 MHz (CDCl<sub>3</sub> residual signal at 7.26 ppm and DMSO-*d*<sub>6</sub> residual signal at 2.5 ppm).  $^{13}\text{C}$  NMR spectra were recorded on a Bruker Fourier 300 (75 MHz) (CDCl<sub>3</sub> residual signal at 77.16 ppm and DMSO-*d*<sub>6</sub> residual signal at 39.52 ppm). Data are reported as follows: chemical shift ( $\delta$  ppm), multiplicity, coupling constant (*J* Hz), integral, assignment. All NMR assignments were also made using  $^1\text{H}$ - $^1\text{H}$  COSY,  $^1\text{H}$ - $^{13}\text{C}$  HMBC and  $^1\text{H}$ - $^{13}\text{C}$  HSQC spectra.

Size exclusion chromatography (SEC) was performed at 50 °C using an Agilent Technologies (Santa Clara, CA, USA) 1260 Infinity Series liquid chromatography system with an internal differential refractive index detector, a viscometer detector, a laser and two PLgel columns (5  $\mu\text{m}$  MIXED-D 300  $\times$  7.5 mm), using 10 mM Lithium Bromide in HPLC grade dimethylformamide as the mobile phase at a flow rate of 1.0 mL/min. Calibration was performed with poly (methyl methacrylate) standards from Agilent Technologies. Typically, ~3 mg of each sample was dissolved in 1 mL of DMF (10 mM LiBr) prior to analysis.

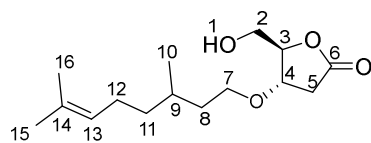
Thermogravimetric Analysis (TGA) was measured with a TGA Q500 (TA Instruments, New Castle, DE, USA). Typically, ~2 mg of each sample was equilibrated at 50 °C for 30 min and was flushed with highly pure nitrogen gas. All the experiments were performed with a heating rate of 10 °C/min up to 500 °C. The reported values  $T_{d5\%}$  and  $T_{d50\%}$  represent the temperature at which 5% and 50% of the mass is lost, respectively.

Differential Scanning Calorimetry (DSC) was performed with a DSC Q20 (TA Instruments). Typically, ~8 mg sample was placed in a sealed pan, flushed with highly pure nitrogen gas and passed through a heat-cool-heat cycle at 10 °C/min in a temperature range of –80 °C to 100 °C. Three heat/cool cycles were done for each sample where the last two cycles were dedicated to analyzing the heat flow of the sample after being cooled in controlled conditions. The  $T_g$  values recorded in this work are those obtained from the third cycle.

Fourier-transform infrared spectroscopy (FTIR) was recorded on a Cary 630 FTIR Spectrometer by Agilent (Wilmington, DE, USA).

## 2.2. Synthesis of Monomers

HBO-citro (Scheme 2). A biphasic mixture of LGO (50 g, 0.4 mol), citronellol (512 mL, 1.8 mol) and HCl (5 N, 0.6 mol) was stirred at room temperature for 16 h. The resulting mixture was cooled down with an ice bath followed by the dropwise addition of a 30% solution of H<sub>2</sub>O<sub>2</sub> (2 mL) for 2 h. After completion of the addition, the reaction was heated up to 80 °C and stirred for 12 h. The presence of H<sub>2</sub>O<sub>2</sub> was evaluated with peroxide strips and any residual H<sub>2</sub>O<sub>2</sub> was quenched using sodium sulfite. The reaction was extracted with ethyl acetate (two times). Organic layers were washed with brine, dried over anhydrous MgSO<sub>4</sub>, filtered and evaporated to dryness. This step was followed by distillation to remove excess citronellol. The crude product after distillation was purified by flash chromatography (gradient 90/10 to 20/80, cyclohexane/ethyl acetate as eluant) to give 62 g of HBO-citro as a pale-yellow oil (58%).

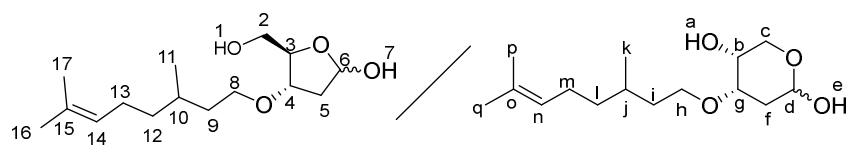


**Scheme 2.** Structure of HBO-citro.

<sup>1</sup>H NMR (CDCl<sub>3</sub>),  $\delta_H$ : 5.01 (broad t,  $J = 5.19$  Hz, 1H, H<sub>13</sub>), 4.43 (s, 1H, H<sub>3</sub>), 4.11 (d,  $J = 7.0$  Hz, 1H, OH), 3.84 (dd,  $J = 3.3$  and 12.4 Hz, 1H, H<sub>4</sub>), 3.65 (dd,  $J = 3.3$  and 12.4 Hz, 2H, H<sub>2</sub>), 3.39 (m, 2H, H<sub>7</sub>), 2.81 (dd,  $J = 7.0$  and 18.1 Hz, 1H, H<sub>5a</sub>), 2.44 (dd,  $J = 3.3$  and 18.1 Hz, 1H, H<sub>5s</sub>), 1.90 (m, 2H, H<sub>12</sub>), 1.61 (s, 3H, H<sub>15</sub>), 1.53 (s, 3H, H<sub>16</sub>), 1.27–1.07 (m, 4H, H<sub>11</sub>, H<sub>8</sub>), 0.82 (d,  $J = 6.4$  Hz, 3H, H<sub>10</sub>).

<sup>13</sup>C NMR (CDCl<sub>3</sub>),  $\delta_C$ : 176.7 (C<sub>6</sub>), 131.2 (C<sub>14</sub>), 124.6 (C<sub>13</sub>), 85.9 (C<sub>3</sub>), 76.1 (C<sub>4</sub>), 67.6 (C<sub>7</sub>), 62.1 (C<sub>2</sub>), 37.1 (C<sub>11</sub>), 36.5 (C<sub>8</sub>), 35.9 (C<sub>5</sub>), 29.3 (C<sub>9</sub>), 25.7 (C<sub>15</sub>), 25.3 (C<sub>12</sub>), 19.4 (C<sub>10</sub>), 17.6 (C<sub>16</sub>).

Lactol-citro (Scheme 3). A 1.2 M solution of DIBAL-H (27.5 mL of DCM, 33 mmol) was added dropwise to a solution of HBO-citro (4.5 g, 15 mmol) in DCM (68 mL) at –50 °C. The reaction mixture was stirred for 30 min at –50 °C then quenched with a 20% aqueous solution of citric acid (30 mL). The reaction was warmed to room temperature then stirred until the aluminum salt disappeared. Layers were separated and the organic layer was washed with brine, dried over anhydrous magnesium sulfate, filtered and evaporated to dryness. The crude product was purified by flash chromatography (gradient 90/10 to 20/80, cyclohexane/ethyl acetate as eluant) to give 3.63 g of Lactol-citro molecules as a colorless oil (89%).

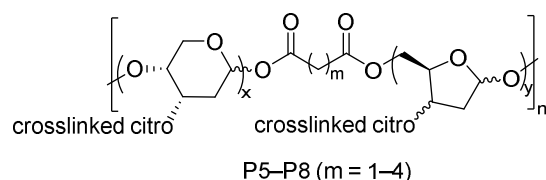


**Scheme 3.** Structures of 5ML (left) and 6ML (right).

The full interpretation of  $^1\text{H}$  and  $^{13}\text{C}$  NMR ( $\text{DMSO-}d_6$ ) is provided in Figures S1–S5 in the Supporting Information (SI).

### 2.3. Synthesis of Polymers

P5–P8 (Scheme 4). A typical two-step melt polycondensation experiment (run 1, Table 1) was performed as follows. Under  $\text{N}_2$  atmosphere, Lactol-citro (500 mg) was charged into a 10 mL round bottom flask connected to a vacuum line, equipped with a condensate trap. The flask was cooled down with an ice bath, then 1 equiv. of malonyl chloride (0.18 mL) was added. The mixture was stirred at room temperature for 19 h. The temperature was then increased gradually up to  $50\text{ }^\circ\text{C}$ . A high vacuum ( $10^{-3}$  bar) was then applied for 3 h. Additional polyesters were prepared with this protocol, employing other diacyl chlorides (succinyl chloride, adipoyl chloride and glutaryl chloride).



**Scheme 4.** Structure of P5–P8 obtained from the polycondensation of 5ML, 6ML and diacyl chlorides.

$^1\text{H}$  and  $^{13}\text{C}$  NMR ( $\text{DMSO-}d_6$ ) of P5–P8 are provided in Figures S6–S13 in the Supporting Information (SI).

### 2.4. Enzymatic Degradation

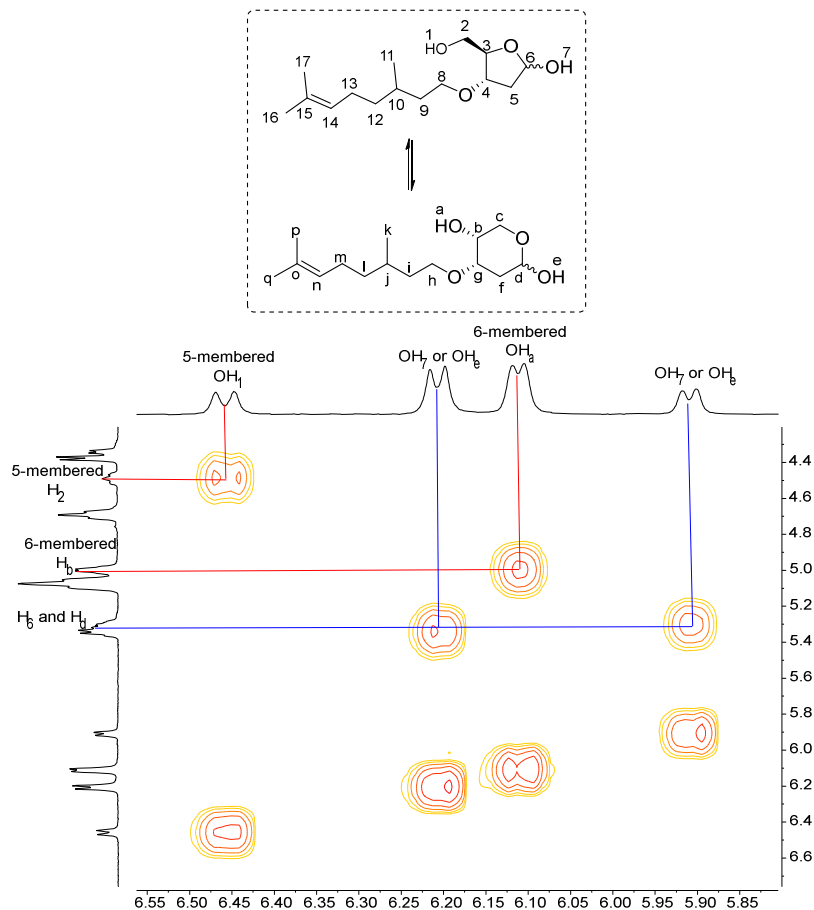
Before its use, the activity of the enzyme was assessed using the *p*-nitrophenyl butyrate colorimetric assay. Absorbance was monitored at 400 nm and the results were compared with a *p*-nitrophenol calibration curve. P5–P8 were ground using a spatula to yield powdered polyester samples. 50 mg of the ground samples were placed in 4 sealed vials containing phosphate buffer (3 mL, 0.05 M) and 10 mg/mL of Lipopan<sup>®</sup> 50 BG (50 KLU/g). Lipopan<sup>®</sup> 50 BG contains lipases from *Thermomyces lanuginosus* expressed in *Aspergillus oryzae* commercially used in bakery. The enzyme concentration was adapted from Alejandra et al. [39] The mixtures were then incubated at the pH and temperature optima for the enzyme ( $37\text{ }^\circ\text{C}$ , pH 7) and stirred gently at 50 rpm for 48 h. The reactions were then stopped by immersing the tubes in an ice bath. To remove the enzyme, the hydrolyzed polymers were washed three times with 10 mL of water followed by centrifugation for 10 min at  $10\text{ }^\circ\text{C}$  and 4750 rpm. The resulting products were freeze-dried to remove all traces of water before being subjected to mass loss measurement and characterization of polyester enzymatic degradation. All isolated powders were analyzed by  $^1\text{H}$  NMR, SEC, DSC and FTIR. Controls were realized for each polymer in phosphate buffer solution without enzyme and showed no degradation.

## 3. Results and Discussion

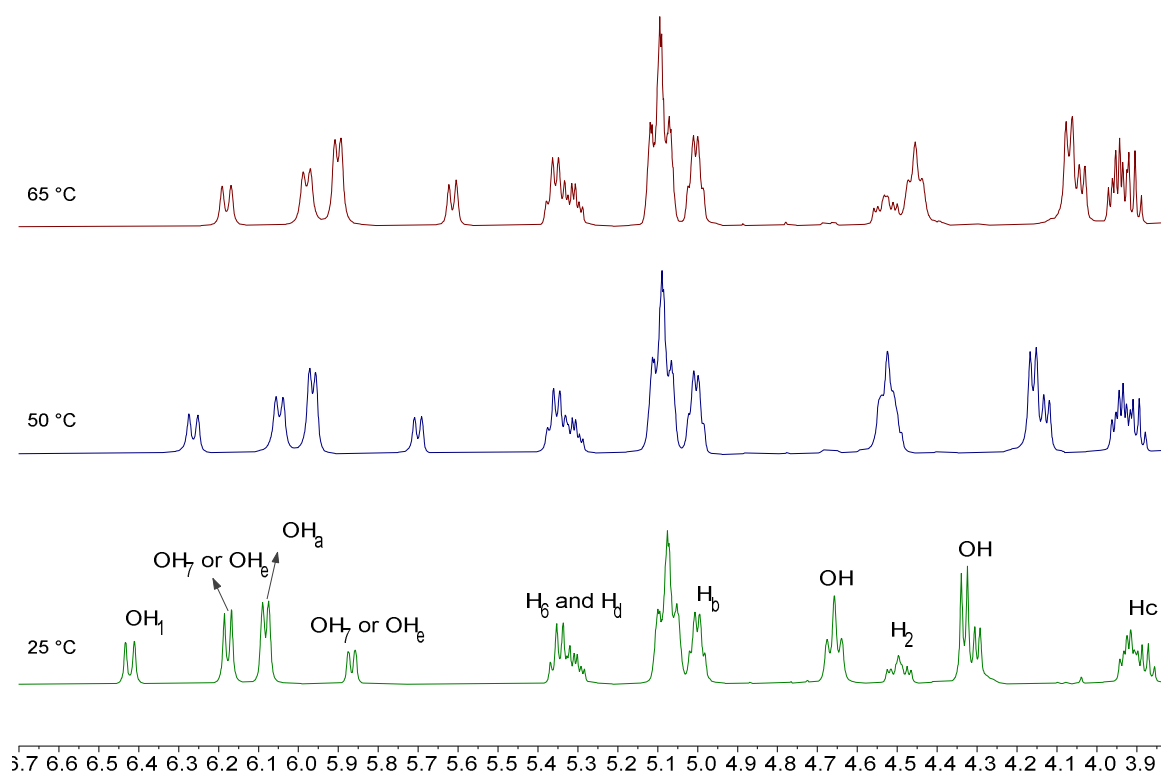
### 3.1. Lactol-Citro

The synthesis of 5- and 6-membered Lactol-citro (5ML and 6ML, respectively) was performed from HBO-citro according to a recently reported procedure [34]. It is worth mentioning that although the reduction of HBO-citro is easy to perform, reaction conditions must be strictly controlled to avoid the formation of Triol-citro (Scheme 1). Anhydrous

solvents, a nitrogen atmosphere and a short time period (30 min) are all necessary to promote the complete conversion of HBO-citro to Lactol-citro. Otherwise, in the presence of a trace amount of water, and for durations longer than 30 min, Triol-citro was observed. Although the separation of the two products was not possible, two cyclic structures of Lactol-citro were easily distinguishable by  $^1\text{H}$ - $^1\text{H}$  COSY NMR (Figure 1). The major occurrence (65%) of the more stable 6-membered derivative was observed at 6.11 ppm, corresponding to  $\text{OH}_a$  group of 6ML. On the other hand, the proton resonance of  $\text{OH}_1$  at 6.46 ppm identified the percentage of the less stable 5-membered lactol cycle, which was interestingly found to be 35%. Since the polycondensation using these molecules was performed in two steps (room temperature under  $\text{N}_2$  and  $50\text{ }^\circ\text{C}$  under vacuum, vide infra), we decided to study equilibrium of  $5\text{ML} \rightleftharpoons 6\text{ML}$  interconversions at different temperatures ( $25\text{ }^\circ\text{C}$ ,  $50\text{ }^\circ\text{C}$  and  $65\text{ }^\circ\text{C}$ ) using  $^1\text{H}$  NMR. The percentages of each of the 5ML and 6ML were monitored using the hydroxyl resonances  $\text{OH}_1$  and  $\text{H}_2$ , and  $\text{OH}_a$  and  $\text{H}_c$ , respectively. Figure 2 shows that temperature has an impact on the chemical shifts of the aforementioned protons; mainly on the hydroxyl peaks that showed an up-field shifting (to the right) when the temperature was increased from  $25\text{ }^\circ\text{C}$  to  $50\text{ }^\circ\text{C}$  and  $65\text{ }^\circ\text{C}$ . For example, at  $25\text{ }^\circ\text{C}$ , the chemical shifts of  $\text{OH}_1$  and  $\text{OH}_a$  are 6.42 ppm and 6.09 ppm, respectively. However, when the NMR measurement was performed at  $65\text{ }^\circ\text{C}$ , a shift of these two signals to 6.18 ppm and 5.90 ppm was recorded. Interestingly, when integrating the peaks of  $\text{H}_2$  and  $\text{H}_c$  we found a 3% and 9% increase of 6ML at  $50\text{ }^\circ\text{C}$  and  $65\text{ }^\circ\text{C}$ , respectively. Indeed, the variation of the 5ML:6ML ratio must be finely monitored during the two polymerization steps (vide infra)—especially in the presence of highly reactive co-monomers, such as acyl chloride—to allow the controlled incorporation of the Lactol-citro along the polyester chain. For these reasons, it is more convenient to carry out the polymerization step at  $50\text{ }^\circ\text{C}$  where only 3%, towards the formation of the more stable pyranose-like derivative, was obtained.



**Figure 1.**  $^1\text{H}$ - $^1\text{H}$  COSY (DMSO- $d_6$ ) spectrum of 5ML and 6ML mixture.



**Figure 2.** Effect of temperature on the  $^1\text{H}$  NMR ( $\text{DMSO-d}_6$ ) of 5ML  $\rightleftharpoons$  6ML interconversion.

### 3.2. Polycondensation

The potential of Lactol-citro (5ML–6ML) was then investigated in the synthesis of new renewable functional polyesters. Solvent-free polycondensations were first performed using aliphatic diacyl chlorides as co-monomers with different chain lengths ( $m = 1\text{--}4$ ) (Table 1). The first step of the polycondensation was started at room temperature for 19 h. The temperature was then increased to 50 °C to allow the polymerization of the oligomers formed in the 1st step while also controlling the interconversion of 5ML–6ML. The products isolated in both steps were found to be insoluble in all classical solvents (e.g., tetrahydrofuran, dioxane, chloroform), except in dimethylformamide (DMF) and dimethyl sulfoxide (DMSO), where partial solubility was observed. All our attempts to enhance the solubility of the prepared polyesters were unsuccessful. For example, we tried to use polymerization methods with solvents (e.g., THF) and base (e.g., pyridine) to control the condensation reactions of the first step or after oligomer formation. Furthermore, different times and temperatures were tested; however, only partially or non-soluble polymers could be isolated. Nevertheless, such descent solubility was sufficient to characterize the polymers (*vide infra*).

The NMR spectra assignment was consistent with the formation of cross-linked copolyesters. First, after the incorporation of acyl chloride co-monomer, the signals of the free hydroxyl groups of 5ML and 6ML in the range of 6.47–5.90 ppm and at 4.96 and 4.38 ppm disappeared (SI, Figures S6–S13). Also, the carbonyl groups of the polyesters formed were clearly detected by  $^{13}\text{C}$  NMR in the region of 175.0–169.0 ppm (SI, Figures S7, S9, S11 and S13 for P5, P6, P7 and P8 respectively). On the other hand, no presence of  $\text{H}_{14}$  and  $\text{H}_m$  of the citronellol double bond at 5.07 ppm was observed, demonstrating that the pendent citronellol moieties were possibly cross-linked at a relatively elevated temperature (50 °C) or/and in the presence of diacyl chloride. The crosslinking was more obvious when analyzing the  $^{13}\text{C}$  NMR spectra that showed the complete disappearance of  $\text{C}_{15}$ ,  $\text{C}_o$  and  $\text{C}_{14}$ ,  $\text{C}_n$  signals at 130.9 and 125.0 ppm, respectively. Indeed, this thermally-induced and/or acid-catalyzed complete crosslinking was observed regardless of the co-monomer chain length (acyl chlorides,  $m = 1\text{--}4$ ). FTIR analysis of P5–P8



was performed and showed the disappearance of the OH band of the lactol monomers at  $3400\text{ cm}^{-1}$  as well as the appearance of a carboxyl group band at  $1730\text{ cm}^{-1}$ , which corresponds to the newly formed esters (SI, Figure S15).

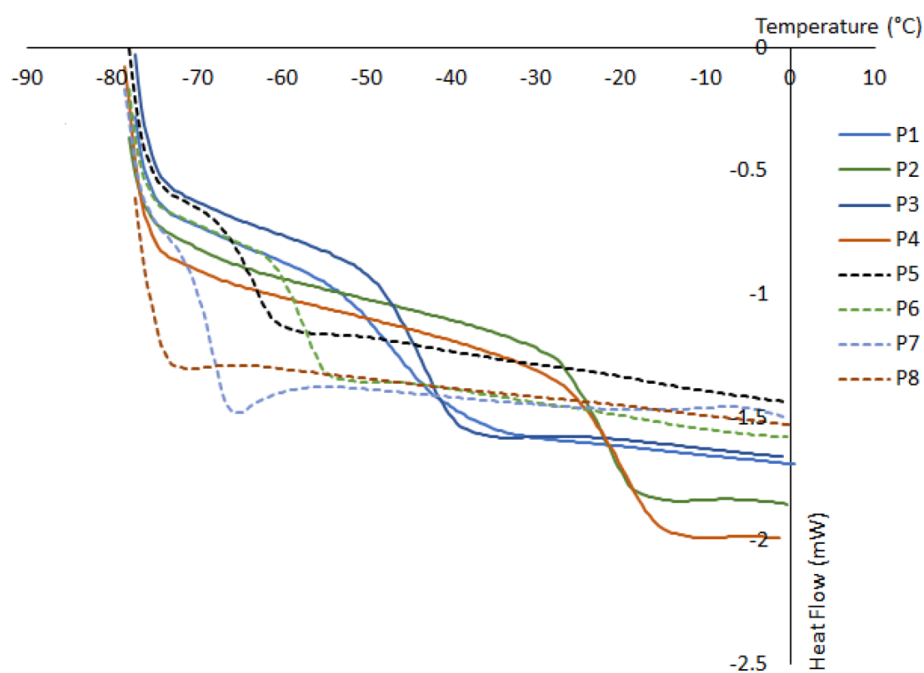
**Table 1.** Two-step polycondensation of 5ML and 6ML with acyl chloride derivatives.

Run	Polymer	$M_n$ (kDa) <sup>1</sup>	$\mathcal{D}$ <sup>1</sup>	$T_g$ (°C) <sup>2</sup>	$T_{d50\%}$ (°C) <sup>3</sup>
1	P5	- <sup>4</sup>	-	-62	198
2	P6	- <sup>4</sup>	-	-57	205
3	P7	12.5	1.3	-67	243
4	P8	25.8	1.8	-	210

<sup>1</sup> Determined in DMF (10 mM LiBr) at 50 °C, only showed the soluble parts of the polymers. <sup>2</sup> Glass transition determined by DSC. <sup>3</sup> TGA degradation temperature at which 50% ( $T_{d50\%}$ ) mass loss was observed under nitrogen. <sup>4</sup> Completely insoluble in DMF.

Size exclusion chromatography (SEC) was used to measure the number-average molecular weight ( $M_n$ ) as well as the dispersity ( $\mathcal{D}$ ). The polymers were partially soluble, or not soluble, in DMF prior to SEC analysis; thus, the results obtained by SEC represent only the soluble portions of the polymers. The copolyesters obtained from the lactol derivatives showed a higher  $M_n$  than the recently reported Triol-citro-based branched polyesters (P1–P4), e.g., 25.8 kDa for P8 (run 4, Table 1) vs. 1.6 kDa for the polyester of Triol-citro and glutaryl chloride (P4). Indeed, this is due to the formation of more complex and less soluble cross-linked/branched structures when Triol-citro, which contains three hydroxy groups with different reactivity, was employed.

The thermal analyses of P5–P8 were examined using differential scanning calorimetry (DSC) and thermogravimetric analysis (TGA) (SI, Figures S20–S22 and S27–S30, respectively). DSC showed negative glass transition ( $T_g$ ) values for all polymers. Nevertheless, it is worth mentioning that P5–P8 showed higher  $T_g$  ( $-57\text{ °C}$  to  $-67\text{ °C}$ ) than polyesters prepared using Triol-citro [34] (Figure 3). This confirms the higher mobility/flexibility of the chains contained within the Lactol-citro based structures. Having  $T_g$  values in this negative range is attractive for applications that require a  $T_g$  below body temperature, such as in the biomedical field. No melting temperature ( $T_m$ ) was observed for any of the polymers reported in this study. Moreover, no effect of the chain length of the acyl chloride was detected. This is probably due to the effect of the citronellol moiety which outweighs that of the number of carbons in the aliphatic co-monomer unit. This is in agreement with the formation of a more stable branched structure when the Triol-citro was engaged [34]. TGA showed that P5–P8 have lower thermal resistance than P1–P4. For example, P8 exhibited a  $T_{d5\%}$  of 127 °C and a  $T_{d50\%}$  of 210 °C, while those of Triol-citro polymer (P4) were 170 and 386 °C, respectively.



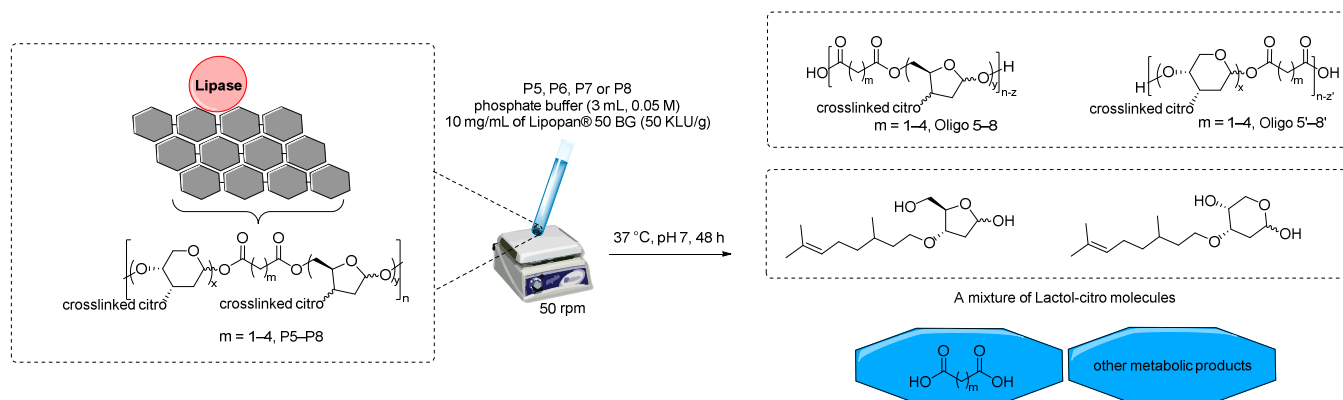
**Figure 3.** DSC thermograms of P1–P8.

### 3.3. Enzymatic Degradation

Given the promising degradation behavior that we have recently seen for the Triol-based polyesters (P2–P4) [34], we decided to investigate the enzymatic degradation of P5–P8 following the same procedure in the presence of a commercial lipase enzyme from *Thermomyces lanuginosus* (Lipopan<sup>®</sup> 50 BG, Novozymes<sup>®</sup>, Bagsværd, Denmark). Indeed, a lipase-mediated degradation occurs first by a surface erosion process triggered by the adsorption of the large-sized enzyme on the polymer surface. This step is followed by the hydrolysis of the ester bonds to form the corresponding oligomers with terminal hydroxyl and carboxylic acid. In this study, we were able to monitor the hydrolysis of the polymers that occurred during the second stage of the degradation process. Specifically, the hydrolysis of the ester bonds led to the formation of shorter oligomers and/or constituting monomers (Figure 4), the existence of which can be easily monitored by <sup>1</sup>H NMR and FTIR, as well as by SEC and DSC. Comparison of the initial analyses of the P5–P8 polymers in Table 1 with the results obtained after treatment with Lipopan<sup>®</sup> 50 BG (Table 2), demonstrates the effective enzymatic degradation of the copolymers. It is worth mentioning that purification of the degraded cross-linked oligomers and (co-)monomers by simple methods, such as precipitation, was not possible. Nevertheless, due to the presence of hydroxy and carboxylic acid groups in the products after enzymatic degradation (vide infra), they can be engaged as a whole in polycondensation reactions; however, this would lead to the formation of several cross-linked oligomers/polymers with no control of molecular weight or dispersity.

Due to the low solubility of P5–P8, all our attempts to make films by solvent casting failed. Thus, we studied the biodegradation using their powder form, which was collected by grinding at the end of the polymerization reactions. Notably, P5–P8 were degraded at a significantly higher rate (~80% mass loss in 48 h) compared to Triol-citro based polyesters P2–P4 (~80% mass loss in 96 h). Indeed, a highly cross-linked/branched structure as in P1–P4, can induce a globular polymer conformation that hinders the accessibility of the enzyme to the inner surface of the chains and delays/prevents the hydrolysis rate of the ester bonds. Therefore, in contrast to the polyester of Triol-citro and malonyl chloride (P1), a successful degradation was observed in the case of P5, as evidenced by the appearance of hydroxyl vibration band by FTIR. Indeed, the hydrolytic step of enzymatic degradation is determined by the hydrolysis time for polymers to form into shorter chains and the

diffusion of water through the material, which can be slowed down in the case of a short aliphatic co-monomer chain, such as that of malonyl chloride ( $m = 1$ ) accompanied by more complex cross-linked structures, as in the case of P1.



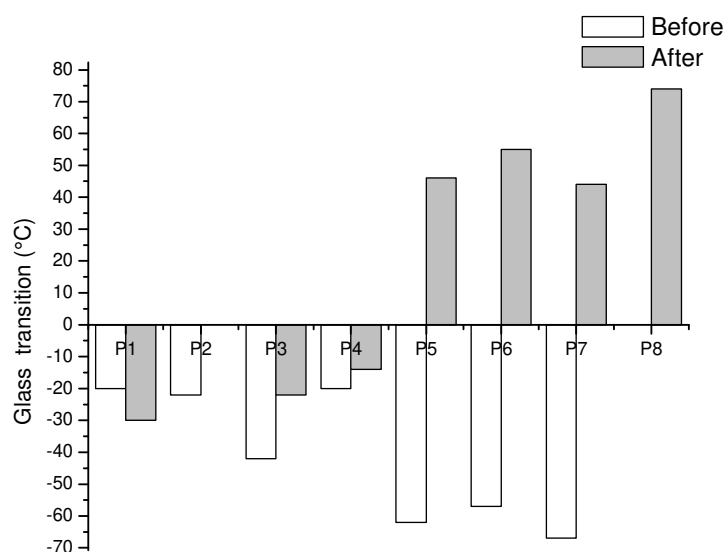
**Figure 4.** Illustration of the enzymatic degradation of P5–P8 and the corresponding hydrolyzed products.

**Table 2.** Characterization of P5–P8 after enzymatic degradation using Lipopan® 50 BG.

Run <sup>1</sup>	Polymer	$M_n$ (kDa) <sup>2</sup>	$T_g$ (°C) <sup>3</sup>	$\Delta T_g$ (°C) <sup>4</sup>	<sup>1</sup> H NMR <sup>5</sup>	FTIR <sup>6</sup>
1	P5	0.7	46	108	✓	✓
2	P6	0.8	55	112	✓	✓
3	P7	0.8	44	111	✓	✓
4	P8	0.8	74	- <sup>7</sup>	✓	✓

<sup>1</sup> Runs 1–4 are listed, following the same order as Table 1. <sup>2</sup> Determined in DMF (10 mM LiBr) at 50 °C. <sup>3</sup> Glass transition determined by DSC, temperature ramp 10 °C/min. <sup>4</sup>  $\Delta T_g = T_g$  (after degradation) –  $T_g$  (before degradation). <sup>5</sup> <sup>1</sup>H NMR of the hydrolyzed product in DMSO- $d_6$ , ✓: presence of hydroxyl signals. <sup>6</sup> Infra-red of the hydrolyzed product, ✓: presence of hydroxyl band. <sup>7</sup> No  $T_g$  was observed for P8 before degradation.

Examination of the <sup>1</sup>H NMR spectra showed the appearance of new peaks in the region of 5.53–4.59 ppm, which correspond to the hydroxyl protons of the hydrolyzed products (SI, Figure S14). In agreement with the <sup>1</sup>H NMR of P5–P8, FTIR showed the appearance of a large hydroxyl vibration band at around 3350  $\text{cm}^{-1}$  after enzymatic degradation (SI, Figure S16). The enzymatic degradation was also checked using SEC to determine the reduction in  $M_n$  (SI, Figures S31–S34). Notably, SEC and DSC also showed a considerable degradation of P5–P8. For example, a significant decrease in  $M_n$  of P7 from 12.5 kDa (run 7, Table 1) to 0.8 kDa (run 3, Table 2) was observed. The thermal properties of the resulting hydrolyzed products were also analyzed by DSC (SI, Figures S23–S26). A great variation of  $T_g$  from –67 °C to 44 °C ( $\Delta T_g = 111$  °C) was registered. Notably,  $\Delta T_g$  of P5–P8 was found to be much larger than those recorded for P1–P4 (see Figure 5 for more information). Such an increase in  $T_g$  can be due to a greater number of polymer chain cleavages that lead to lesser chain entanglement, and in turn a higher degree of crystallinity. The increase of crystalline portions within the oligomer chains can reduce molecular mobility, which causes an increase in  $T_g$  and, in turn,  $\Delta T_g$ .



**Figure 5.** Glass transition temperature ( $T_g$ ) of P1–P8 before and after enzymatic degradation (No  $T_g$  was observed for P8 and P2 before and after degradation, respectively).

#### 4. Conclusions

Ring-chain tautomerism of furanoses (5-membered rings) and pyranoses (6-membered rings) is very common in sugar chemistry. LGO was used as a starting material to produce new renewable 5- and 6-membered Lactol-citro molecules (5ML and 6ML) with citronellol side chains. The interconversion of both molecules was studied at a temperature ranging from 25 °C to 65 °C and showed the expected higher occurrence of the more stable cycle (6ML) at higher temperatures.

The polycondensation of the Lactol-citro mixture and aliphatic diacyl chlorides was then performed in solvent- and catalyst-free conditions. New LGO-derived copolyesters, with low  $T_g$  ranging from  $-57$  °C to  $-67$  °C, were formed. Furthermore, the analyses showed that the citronellol chains were unexpectedly cross-linked during polymerization. The enzymatic degradation of the polyesters, P5–P8, was then investigated in the presence of Lipopan<sup>®</sup> 50 BG under the same conditions recently reported for P1–P4 polymers obtained with Triol-citro and diacyl chlorides ( $m = 1-4$ ).  $^1\text{H}$  NMR, FTIR, SEC and DSC analyses showed a greater tendency to hydrolyze P5–P8 than P1–P4 when a lipase is used. This was probably due to the formation of a less strained structure when 5ML and 6ML were engaged, rather than Triol-citro monomer.

**Supplementary Materials:** The following supporting information can be downloaded at: <https://www.mdpi.com/article/10.3390/polym14102082/s1>, NMR (Figures S1–S14), FTIR (Figures S15–S19), DSC (Figures S20–S26), TGA (Figures S27–S30) and SEC (Figures S31–S34).

**Author Contributions:** Conceptualization, S.F., Q.C., L.M.M.M. and F.A.; Data curation, S.F. and Q.C.; Formal analysis, S.F.; Funding acquisition, F.A.; Investigation, S.F., A.K., Y.W. and A.A.M.P.; Methodology, S.F. and Q.C.; Supervision, S.F. and Q.C.; Visualization, S.F.; Writing—original draft, S.F.; Writing—review & editing, Q.C., L.M.M.M., M.L. and F.A. All authors have read and agreed to the published version of the manuscript.

**Funding:** This research received no external funding.

**Institutional Review Board Statement:** Not applicable.

**Informed Consent Statement:** Not applicable.

**Data Availability Statement:** Not applicable.

**Acknowledgments:** The authors are grateful to the Circa group for its generous gift of LGO, and to Grand Reims, Département de la Marne and Grand Est region for financial support.

**Conflicts of Interest:** The authors declare no conflict of interest.

## References

- Mecking, S. Nature or Petrochemistry?—Biologically Degradable Materials. *Angew. Chem. Int. Ed.* **2004**, *43*, 1078–1085. [[CrossRef](#)] [[PubMed](#)]
- Zhu, Y.; Romain, C.; Williams, C.K. Sustainable Polymers from Renewable Resources. *Nature* **2016**, *540*, 354–362. [[CrossRef](#)] [[PubMed](#)]
- Sidorov, O.F.; Shishov, M.G.; Deryugin, A.A.; Sidelnikov, A.Y. Environmental Impact of Polymer-Waste Disposal. *Coke Chem.* **2016**, *59*, 117–121. [[CrossRef](#)]
- Sivan, A. New Perspectives in Plastic Biodegradation. *Curr. Opin. Biotechnol.* **2011**, *22*, 422–426. [[CrossRef](#)]
- Nakajima, H.; Dijkstra, P.; Loos, K. The Recent Developments in Biobased Polymers toward General and Engineering Applications: Polymers That Are Upgraded from Biodegradable Polymers, Analogous to Petroleum-Derived Polymers, and Newly Developed. *Polymers* **2017**, *9*, 523. [[CrossRef](#)]
- Bahl, S.; Dolma, J.; Jyot Singh, J.; Sehgal, S. Biodegradation of Plastics: A State of the Art Review. *Mater. Today Proc.* **2021**, *39*, 31–34. [[CrossRef](#)]
- Pellis, A.; Malinconico, M.; Guarneri, A.; Gardossi, L. Renewable Polymers and Plastics: Performance beyond the Green. *New Biotechnol.* **2021**, *60*, 146–158. [[CrossRef](#)]
- Höglund, A.; Odelius, K.; Albertsson, A.-C. Crucial Differences in the Hydrolytic Degradation between Industrial Polylactide and Laboratory-Scale Poly(L-Lactide). *ACS Appl. Mater. Interfaces* **2012**, *4*, 2788–2793. [[CrossRef](#)]
- Huang, Y.; Chen, F.; Pan, Y.; Chen, C.; Jiang, L.; Dan, Y. Effect of Hydrophobic Fluoropolymer and Crystallinity on the Hydrolytic Degradation of Poly(Lactic Acid). *Eur. Polym. J.* **2017**, *97*, 308–318. [[CrossRef](#)]
- Sevim, K.; Pan, J. A Model for Hydrolytic Degradation and Erosion of Biodegradable Polymers. *Acta Biomater.* **2018**, *66*, 192–199. [[CrossRef](#)]
- Kijchavengkul, T.; Auras, R.; Rubino, M.; Selke, S.; Ngouajio, M.; Fernandez, R.T. Biodegradation and Hydrolysis Rate of Aliphatic Aromatic Polyester. *Polym. Degrad. Stab.* **2010**, *95*, 2641–2647. [[CrossRef](#)]
- Brown, A.E.; Reinhart, K.A. Polyester Fiber: From Its Invention to Its Present Position. *Science* **1971**, *173*, 287–293. [[CrossRef](#)] [[PubMed](#)]
- Deopura, B.L.; Padaki, N.V. Chapter 5—Synthetic Textile Fibres: Polyamide, Polyester and Aramid Fibres. In *Textiles and Fashion*; Sinclair, R., Ed.; Woodhead Publishing Series in Textiles; Woodhead Publishing: Sawston, UK, 2015; pp. 97–114. ISBN 978-1-84569-931-4.
- Rivard, C.; Moens, L.; Roberts, K.; Brigham, J.; Kelley, S. Starch Esters as Biodegradable Plastics: Effects of Ester Group Chain Length and Degree of Substitution on Anaerobic Biodegradation. *Enzym. Microb. Technol.* **1995**, *17*, 848–852. [[CrossRef](#)]
- Siracusa, V.; Blanco, I. Bio-Polyethylene (Bio-PE), Bio-Polypropylene (Bio-PP) and Bio-Poly(Ethylene Terephthalate) (Bio-PET): Recent Developments in Bio-Based Polymers Analogous to Petroleum-Derived Ones for Packaging and Engineering Applications. *Polymers* **2020**, *12*, 1641. [[CrossRef](#)]
- Larrañaga, A.; Lizundia, E. A Review on the Thermomechanical Properties and Biodegradation Behaviour of Polyesters. *Eur. Polym. J.* **2019**, *121*, 109296. [[CrossRef](#)]
- Miller, S.A. Sustainable Polymers: Opportunities for the Next Decade. *ACS Macro Lett.* **2013**, *2*, 550–554. [[CrossRef](#)]
- Fadlallah, S.; Sinha Roy, P.; Garnier, G.; Saito, K.; Allais, F. Are Lignin-Derived Monomers and Polymers Truly Sustainable? An in-Depth Green Metrics Calculations Approach. *Green Chem.* **2021**, *23*, 1495–1535. [[CrossRef](#)]
- Itawi, H.E.; Fadlallah, S.; Allais, F.; Perre, P. Green Assessment of Polymer Microparticles Production Processes: A Critical Review. *Green Chem.* **2022**. [[CrossRef](#)]
- Abd-El-Aziz, A.S.; Antonietti, M.; Barner-Kowollik, C.; Binder, W.H.; Böker, A.; Boyer, C.; Buchmeiser, M.R.; Cheng, S.Z.D.; D’Agosto, F.; Floudas, G.; et al. The Next 100 Years of Polymer Science. *Macromol. Chem. Phys.* **2020**, *221*, 2000216. [[CrossRef](#)]
- Gauthier, M.A.; Gibson, M.I.; Klok, H.-A. Synthesis of Functional Polymers by Post-Polymerization Modification. *Angew. Chem. Int. Ed.* **2009**, *48*, 48–58. [[CrossRef](#)]
- Seppälä, J.; van Bochove, B.; Lendlein, A. Developing Advanced Functional Polymers for Biomedical Applications. *Biomacromolecules* **2020**, *21*, 273–275. [[CrossRef](#)] [[PubMed](#)]
- Santos, P.L.; Matos, J.P.S.C.F.; Picot, L.; Almeida, J.R.G.S.; Quintans, J.S.S.; Quintans-Júnior, L.J. Citronellol, a Monoterpene Alcohol with Promising Pharmacological Activities—A Systematic Review. *Food Chem. Toxicol.* **2019**, *123*, 459–469. [[CrossRef](#)] [[PubMed](#)]
- Nichol, J.L.; Morozowich, N.L.; Decker, T.E.; Allcock, H.R. Crosslinkable Citronellol Containing Polyphosphazenes and Their Biomedical Potential. *J. Polym. Sci. Part A Polym. Chem.* **2014**, *52*, 2258–2265. [[CrossRef](#)]
- Nichol, J.L.; Allcock, H.R. Polyphosphazenes with Amino Acid Citronellol Ester Side Groups for Biomedical Applications. *Eur. Polym. J.* **2015**, *62*, 214–221. [[CrossRef](#)]
- Singler, R.E.; Schneider, N.S.; Hagnauer, G.L. Polyphosphazenes: Synthesis—Properties—Applications. *Polym. Eng. Sci.* **1975**, *15*, 321–338. [[CrossRef](#)]
- Worzakowska, M. High Chemical and Solvent Resistant, Branched Terpene Methacrylate Polymers—Preparation, Thermal Properties, and Decomposition Mechanism. *Polym. Adv. Technol.* **2018**, *29*, 1414–1425. [[CrossRef](#)]
- Ariel, M.S.; Maria, M.Z.; Rolando, A.S. Recent Applications of Levoglucosenone as Chiral Synthone. *Curr. Org. Synth.* **2012**, *9*, 439–459.

29. Clark, J.H.; Bruyn, M.D.; Budarin, V.L. Method for Producing Levoglucosenone. U.S. Patent 10,774,089, 15 September 2016.
30. Comba, M.B.; Tsai, Y.; Sarotti, A.M.; Mangione, M.I.; Suárez, A.G.; Spanevello, R.A. Levoglucosenone and Its New Applications: Valorization of Cellulose Residues. *Eur. J. Org. Chem.* **2018**, *2018*, 590–604. [[CrossRef](#)]
31. Fadlallah, S.; Mouterde, L.M.M.; Garnier, G.; Saito, K.; Allais, F. Cellulose-Derived Levoglucosenone, a Great Versatile Chemical Platform for the Production of Renewable Monomers and Polymers. In *Sustainability & Green Polymer Chemistry Volume 2: Biocatalysis and Biobased Polymers*; ACS Symposium Series; American Chemical Society: Washington, DC, USA, 2020; Volume 1373, pp. 77–97. ISBN 978-0-8412-9852-1.
32. Fadlallah, S.; Peru, A.A.M.; Longé, L.; Allais, F. Chemo-Enzymatic Synthesis of a Levoglucosenone-Derived Bi-Functional Monomer and Its Ring-Opening Metathesis Polymerization in the Green Solvent Cyrene™. *Polym. Chem.* **2020**, *11*, 7471–7475. [[CrossRef](#)]
33. Fadlallah, S.; Peru, A.A.M.; Flourat, A.L.; Allais, F. A Straightforward Access to Functionalizable Polymers through Ring-Opening Metathesis Polymerization of Levoglucosenone-Derived Monomers. *Eur. Polym. J.* **2020**, *138*, 109980. [[CrossRef](#)]
34. Kayishaer, A.; Fadlallah, S.; Mouterde, L.M.M.; Peru, A.A.M.; Werghi, Y.; Brunois, F.; Carboué, Q.; Lopez, M.; Allais, F. Unprecedented Biodegradable Cellulose-Derived Polyesters with Pendant Citronellol Moieties: From Monomer Synthesis to Enzymatic Degradation. *Molecules* **2021**, *26*, 7672. [[CrossRef](#)] [[PubMed](#)]
35. Fadlallah, S.; Kayishaer, A.; Annatelli, M.; Mouterde, L.M.M.; Peru, A.A.M.; Aricò, F.; Allais, F. Fully Renewable Photocrosslinkable Polycarbonates from Cellulose-Derived Monomers. *Green Chem.* **2022**, *24*, 2871–2881. [[CrossRef](#)]
36. Diot-Néant, F.; Mouterde, L.; Fadlallah, S.; Miller, S.A.; Allais, F. Sustainable Synthesis and Polycondensation of Levoglucosenone-Cyrene-Based Bicyclic Diol Monomer: Access to Renewable Polyesters. *ChemSusChem* **2020**, *13*, 2613–2620. [[CrossRef](#)]
37. Tsai, Y.; Borini Etichetti, C.M.; Cicetti, S.; Girardini, J.E.; Spanevello, R.A.; Suárez, A.G.; Sarotti, A.M. Design, Synthesis and Evaluation of Novel Levoglucosenone Derivatives as Promising Anticancer Agents. *Bioorganic Med. Chem. Lett.* **2020**, *30*, 127247. [[CrossRef](#)] [[PubMed](#)]
38. Mackie, W.; Perlin, A.S. Pyranose–Furanose and Anomeric Equilibria: Influence of Solvent and of Partial Methylation. *Can. J. Chem.* **1966**, *44*, 2039–2049. [[CrossRef](#)]
39. Alejandra, R.-C.; Margarita, C.-M.; María Soledad, M.-C. Enzymatic Degradation of Poly(3-Hydroxybutyrate) by a Commercial Lipase. *Polym. Degrad. Stab.* **2012**, *97*, 2473–2476. [[CrossRef](#)]



## Article

# Characterization of the Thermostable Biosurfactant Produced by *Burkholderia thailandensis* DSM 13276

Cátia V. Gil <sup>1,2</sup>, Ana Teresa Rebocho <sup>1,2</sup>, Asiyah Esmail <sup>1,2</sup>, Chantal Sevrin <sup>3</sup>, Christian Grandfils <sup>3</sup>,  
Cristiana A. V. Torres <sup>1,2,\*</sup>, Maria A. M. Reis <sup>1,2</sup> and Filomena Freitas <sup>1,2</sup>

<sup>1</sup> Laboratory i4HB—Institute for Health and Bioeconomy, School of Science and Technology, NOVA University Lisbon, 1099-085 Caparica, Portugal; cv.gil@campus.fct.unl.pt (C.V.G.); at.rebocho@campus.fct.unl.pt (A.T.R.); a.esmail@campus.fct.unl.pt (A.E.); amr@fct.unl.pt (M.A.M.R.); a4406@fct.unl.pt (F.F.)

<sup>2</sup> UCIBIO—Applied Molecular Biosciences Unit, Department of Chemistry, School of Science and Technology, NOVA University Lisbon, 2829–516 Caparica, Portugal

<sup>3</sup> Interfaculty Research Centre of Biomaterials (CEIB), University of Liège, B-4000 Liège, Belgium; csevrin@uliege.be (C.S.); c.grandfils@uliege.be (C.G.)

\* Correspondence: c.torres@fct.unl.pt; Tel.: +351-212948300

**Abstract:** Biosurfactants synthesized by microorganisms represent safe and sustainable alternatives to the use of synthetic surfactants, due to their lower toxicity, better biodegradability and biocompatibility, and their production from low-cost feedstocks. In line with this, the present study describes the physical, chemical, and functional characterization of the biopolymer secreted by the bacterium *Burkholderia thailandensis* DSM 13276, envisaging its validation as a biosurfactant. The biopolymer was found to be a glycolipopeptide with carbohydrate and protein contents of  $33.1 \pm 6.4\%$  and  $23.0 \pm 3.2\%$ , respectively. Galactose, glucose, rhamnose, mannose, and glucuronic acid were detected in the carbohydrate moiety at a relative molar ratio of 4:3:2:2:1. It is a high-molecular-weight biopolymer ( $1.0 \times 10^7$  Da) with low polydispersity (1.66), and forms aqueous solutions with shear-thinning behavior, which remained after autoclaving. The biopolymer has demonstrated a good emulsion-stabilizing capacity towards different hydrophobic compounds, namely, benzene, almond oil, and sunflower oil. The emulsions prepared with the biosurfactant, as well as with its autoclaved solution, displayed high emulsification activity (>90% and ~50%, respectively). Moreover, the almond and sunflower oil emulsions stabilized with the biosurfactant were stable for up to 4 weeks, which further supports the potential of this novel biopolymer for utilization as a natural bioemulsifier.

**Keywords:** biosurfactants; thermostability; emulsion stability; rheology

**Citation:** Gil, C.V.; Rebocho, A.T.; Esmail, A.; Sevrin, C.; Grandfils, C.; Torres, C.A.V.; Reis, M.A.M.; Freitas, F. Characterization of the Thermostable Biosurfactant Produced by *Burkholderia thailandensis* DSM 13276. *Polymers* **2022**, *14*, 2088. <https://doi.org/10.3390/polym14102088>

Academic Editors: José Miguel Ferri, Vicent Fombuena Borràs and Miguel Fernando Aldás Carrasco

Received: 30 April 2022

Accepted: 16 May 2022

Published: 20 May 2022

**Publisher's Note:** MDPI stays neutral with regard to jurisdictional claims in published maps and institutional affiliations.



**Copyright:** © 2022 by the authors. Licensee MDPI, Basel, Switzerland. This article is an open access article distributed under the terms and conditions of the Creative Commons Attribution (CC BY) license (<https://creativecommons.org/licenses/by/4.0/>).

## 1. Introduction

Surfactants are surface-active compounds comprising a structurally diverse group of chemical compounds that include amino acids, carbohydrates, or proteins (the hydrophilic functional head group) linked to a hydrophobic fatty acid carbon chain [1]. Due to their amphiphilic nature, surfactants can accumulate at the interface of fluid phases of different polarity degrees and reduce their surface tension. This particular feature of simultaneously displaying a high affinity for polar and nonpolar compounds [2] supports the exploitation of surfactants in a wide range of applications, including the bioremediation of chemical contaminants, such as oil [3], organic compounds, and heavy metals [4], their utilization as emulsion-stabilizing agents in food, biomedical, and cosmetic products [5,6], as well as their use as antibiofilm and antifungal agents [7,8].

Despite the proven efficacy of synthetic surfactants (e.g., sodium dodecyl sulphate (SDS), sodium lauryl sulphate (SLS), cetyltrimethylammonium chloride (CTAB), and Triton-X 100) [9], biosurfactants synthesized by microorganisms have gained significant attention over the last decade, due to the growing environmental concerns associated with the negative impact of synthetic tensides on ecosystems. Biosurfactants are niche and



present improved features, such as lower toxicity and better biodegradability and biocompatibility than their synthetic counterparts. According to several studies, biosurfactants are biocompatible with human cells and might find use as fibroblast growth factors [10]. Moreover, they can be produced using low-cost agro-industrial feedstocks, which makes the processes cost effective and environmentally sustainable [11,12].

Several microorganisms, including bacteria, yeast, and fungi, have been reported to produce such surface-active molecules, which are secreted by cells, being either extracellular compounds or remaining attached to microbial cell surfaces [13]. They are classified, according to their chemical composition, into several classes, including lipoproteins, glycolipids, phospholipids, neutral lipids or fatty acids, lipid–polysaccharide complexes, and other polymeric microbial biosurfactants [14]. They can be further subdivided according to their molecular weight (Mw). Low-Mw biosurfactants are able to reduce the surface tension between different phases at low critical micelle concentrations (CMCs), while high-Mw biosurfactants are better emulsion-stabilizing agents, but are less effective at reducing surface tension [15]. This last group comprises polymeric biosurfactants, including polysaccharides, lipopolysaccharides, glycoproteins, or mixtures of such macromolecules [16]. Several microbial genera, including *Pseudomonas* [17], *Acinetobacter* [18], *Candida* [19] and *Meyerozyma* [20], have been reported to produce polymeric biosurfactants of different chemical composition; the most studied are emulsan [18] and liposan [19].

Some biosurfactants were found to be highly stable over a wide range of physicochemical conditions, such as temperature, pH, and/or salinity [21,22]. Many of the surfactants' applications in the food, pharmaceutical, and cosmetic industries require the formulations to be processed at temperatures above room temperature, with their sterilization or pasteurization also being performed at high temperatures (150–121 °C) [23]. Therefore, the relevance of thermostable surfactants is of paramount importance. Examples of thermostable polymeric biosurfactants include biodispersan, which is secreted by *Acinetobacter calcoaceticus* A2 [18], and Liposan produced by *Candida lipolytica* [19], which sustain processing at temperatures up to 70 °C, without significant impacts on their emulsion-forming and -stabilizing capacities.

In the last decade, a number of *Burkholderia* species have been exploited as biosurfactant producers, including *B. glumae* [24], *B. thailandensis* [12], and *B. plantarii* [25], that synthesize glycolipids with long alkyl chains. To the best of our knowledge, the ability of *B. thailandensis* to produce polymeric biosurfactants has not been reported previously, but some *Burkholderia* species secrete exopolysaccharides (EPSs) [26], capsular polysaccharides [27], and lipopolysaccharides [28].

This study describes the physical, chemical, and functional properties of a novel polymeric biosurfactant secreted by the bacterium *Burkholderia thailandensis* DSM 13276, namely, its composition, structure, thermal and rheological properties, as well as its surface-active properties and emulsion-forming and -stabilizing capacities. Furthermore, the biopolymer's stability over time and after autoclaving was also assessed.

## 2. Materials and Methods

### 2.1. Biosurfactant Production and Recovery

The biosurfactant was produced by cultivation of *Burkholderia thailandensis* DSM 13276 in Medium E\* [29] supplemented with glucose (Scharlau, Barcelona, Spain) (10 g/L) and terephthalic acid (synthesis grade, Merck) (20 g/L). Cultivation was performed in a 2 L bioreactor (Jupiter 3, Solaris, Porto Mantovano, Italy) under controlled conditions of pH (7.0), temperature (30 °C), and dissolved oxygen concentration (30% of the air saturation). After 7 days of cultivation, the broth was collected and centrifuged (13,131 × *g*, 20 min) for cell removal. The biosurfactant was recovered from the cell-free supernatant (1700 mL) by diafiltration/ultrafiltration in a crossflow module (Sartocon Slide Holder, Sartorius, Göttingen, Germany), using a 30 kDa molecular weight cut-off membrane (Hydrosart, Sartorius, Göttingen, Germany), with a surface area of 0.1 m<sup>2</sup>. The module was operated in diafiltration mode by continuously adding fresh deionized water to the supernatant vessel,

thus maintaining the retentate volume constant (~1700 mL) for the removal of low-Mw compounds, until the conductivity reached a value below 10  $\mu\text{S}/\text{cm}$ . Subsequently, the module was operated in ultrafiltration mode (water addition to the retentate vessel was stopped) and the retentate was concentrated to a final volume of 500 mL. The concentrated retentate was freeze-dried (ScanVac CoolSafe™, LaboGene, Lillerød, Denmark) and  $3.07 \pm 0.69$  g of biosurfactant was recovered and stored in a closed vessel.

## 2.2. Biosurfactant Characterization

### 2.2.1. Composition

Freeze-dried samples (~5 mg) were dissolved in deionized water (~5 mL) and hydrolyzed with trifluoroacetic acid (100  $\mu\text{L}$ , Sigma-Aldrich, St. Louis, MO, USA) at 120 °C for 5 h [30]. The filtered hydrolysate was used to identify and quantify the constituent sugar monomers by liquid chromatography (HPLC), using a Thermo CarboPac PA10 250  $\times$  4 mm + Aminotrap column (DIONEX ICS3000, equipped with a PAD detector). The analysis was performed at 25 °C, with NaOH (4 mM) as the eluent, at a flow rate of 1 mL/min. D-(+)-galactose (Fluka), L-rhamnose monohydrate (Fluka), D-glucuronic acid (Alfa Aesar, Haverhill, MA, USA), mannose (Sigma-Aldrich), and glucose (Scharlau, Barcelona, Spain) were used as the standards at concentrations between 0.005 and 0.1 g/L. The anthrone assay [31] was used to estimate the total carbohydrate content of the biosurfactant. Briefly, about 0.125 mg of anthrone (Sigma-Aldrich) was dissolved in a 97% (*v/v*) sulfuric acid (Sigma-Aldrich, HPLC grade) solution in a water and ice bath. The anthrone solution (2.5 mL) was mixed with 0.5 mL of the biosurfactant solution at a concentration of 1.0 g/L. The samples were hydrolyzed at 100 °C for 14 min, and, after cooling to room temperature, their optical density was measured at 625 nm. Glucose solutions (0.005–0.5 g/L) (Scharlau) were used as the standards.

For total protein content determination, 5.5 mL of the biosurfactant solution (0.9 g/L) was mixed with 1 mL of 20% (*w/v*) NaOH (eka, São Domingos de Rana, Portugal) and placed at 100 °C for 5 min. After cooling on ice, 170  $\mu\text{L}$  of  $\text{CuSO}_4 \cdot 5\text{H}_2\text{O}$  (25%, *w/v*) was added, and the solution was agitated. The samples were centrifuged ( $3500 \times g$ , 5 min) and the optical density was measured at 560 nm [32]. Albumin (Sigma-Aldrich) solutions (0.05–1.75 g/L) were used as the protein standards. For assessing the presence of lipids in the biosurfactant, 1 mL of the biosurfactant solution (10 g/L) was mixed with 25  $\mu\text{L}$  of the cationic dye Nile blue A (Sigma-Aldrich). The solution was visualized by fluorescence microscopy (BX51, Olympus, Tokyo, Japan). Distilled water was used as a negative control. The samples' water content was evaluated by subjecting 50 mg of the biosurfactant to a temperature of 100 °C until constant weight was reached. The total inorganic content was evaluated by subjecting the oven-dried biosurfactant sample to pyrolysis at a temperature of 550 °C for 24 h [30].

For all analyses, the results were representative of 3–4 independent experiments and are presented as the mean value  $\pm$  standard deviation.

### 2.2.2. Fourier Transform Infrared Spectroscopy

Fourier transform infrared (FTIR) spectroscopy with diamond ATR (attenuated total reflectance) was used to collect the spectrum of the samples with a Perkin Elmer Spectrum Two FT-IR spectrometer (Perkin Elmer Inc., Waltham, MA, USA), equipped with a lithium tantalate ( $\text{LiTaO}_3$ ) detector with an SNR (signal-to-noise ratio) of 14,500:1. The resolution was 0.5  $\text{cm}^{-1}$  and the number of scans was 8. The samples were placed in the absorbance chamber and corrected by applying the ATR correction function of the Perkin Elmer Spectrum software in the region of 4500–500  $\text{cm}^{-1}$ .

### 2.2.3. Molecular Mass Distribution

The molecular number ( $M_n$ ), average molecular weights ( $M_w$ ), and polydispersity index ( $\text{PDI} = M_w/M_n$ ) of the biosurfactant were obtained by size-exclusion chromatography, coupled with multi-angle light scattering (SEC-MALS). The biosurfactant was dissolved in

0.1 M Tris-HCl + 0.2 M NaCl (which was also the SEC mobile phase), pH 8.09 buffer, at a concentration of 2 mg/mL. The SEC columns (PL Aquagel-OH mixed 8  $\mu\text{m}$ ; 300  $\times$  7.5 mm), protected by a guard column (Polymer Laboratory; 50  $\times$  7.5 mm, part no. 1149-1840), were equilibrated overnight before running the analysis at a flow rate of 1 mL/min at room temperature. Each analysis was conducted in duplicate. The purity and molecular mass distribution of the polysaccharide were monitored with MALS and RI detectors. These data were analyzed with Astra software (V 4.73.04). A  $dn/dc$  of 0.190 mL/g was adopted to calculate the  $M_w$ .

#### 2.2.4. Thermal Properties

A thermogravimetric analysis (TGA) was performed using a Thermogravimetric Analyzer Labsys EVO (Setaram, Lyon, France). The samples were placed in aluminum crucibles and heated from room temperature to 550  $^{\circ}\text{C}$ , with a heating rate of 10  $^{\circ}\text{C}/\text{min}$ , in air. The thermal degradation temperature ( $T_{\text{deg}}$ ,  $^{\circ}\text{C}$ ) corresponds to the temperature value obtained for the maximum decreasing peak of the sample mass. A differential scanning calorimetry (DSC) analysis was carried out in a DSC 131 (Setaram, France). The samples were placed in an aluminum pan and analyzed at temperatures ranging between 25 and 3000  $^{\circ}\text{C}$ , and heating and cooling rates of 10  $^{\circ}\text{C}/\text{min}$  were imposed.

#### 2.2.5. Rheological Behavior

The apparent viscosity of the samples (biosurfactant aqueous solution, 10 g/L; autoclaved biosurfactant solution, 10 g/L; biosurfactant emulsions) was studied using a controlled-stress rheometer (Anton Paar MCR92, Madrid, Spain) coupled with a plate and parallel cone geometry. Each sample, 500  $\mu\text{L}$ , was loaded onto the plate and the flow curves were obtained for a shear rate range from 0.01 to 1000  $\text{s}^{-1}$ , at 25  $^{\circ}\text{C}$ , with a 5 mm gap setting. The experimental data in the linear region of the flow curves were fitted using the power law model [33].

$$\eta = K \times \dot{\gamma}^{(n-1)} \quad (1)$$

where  $n$  is the flow behavior index,  $\dot{\gamma}$  is the shear rate,  $\eta$  is the viscosity of the solution, and  $K$  is the consistency index.

#### 2.3. Surface-Active Properties

The biosurfactant was dissolved in MilliQ water at concentrations ranging from 0.1 to 5.0 g/L, and the surface tension of the solutions was determined by the pendant drop method [34] using a tensiometer (Kruss, Advance), at room temperature. The critical micelle concentration (CMC) was determined by plotting the surface tension as a function of the polymer concentration, and it was taken as the point where the slope of the curve abruptly changed. The results were expressed as the mean of three solution drops  $\pm$  standard deviation.

#### 2.4. Emulsion-Forming and -Stabilizing Capacities

The emulsification activity (EA) of the biosurfactant was evaluated against three hydrophobic compounds, namely, benzene (Sigma Aldrich), as well as almond and sunflower oils (purchased from a local market). Two milliliters of the biosurfactant solution (10 g/L) and 2 mL of each hydrophobic compound were mixed in the test flasks. The mixtures were vigorously vortexed for 1 min and allowed to stand for 24 h at room temperature. The EA (%) was calculated as follows [30]:

$$\text{EA} = \frac{h_e}{h_T} \times 100 \quad (2)$$

where  $h_e$  (mm) is the height of the emulsion layer and  $h_T$  (mm) is the overall height of the mixture. Distilled water was used as a negative control, for which no emulsion was observed, and the chemical surfactant Triton X-100 (10 g/L) was used as a positive control.

The results were representative of three independent experiments and are presented as the mean value  $\pm$  standard deviation.

The emulsions were left at room temperature for 4 weeks to study their stability over time. The autoclaved biosurfactant solution was used to prepare emulsions against benzene, as described above, and the EA was determined at 24 h and at 2 weeks. The rheological properties and the surface tension of the autoclaved biosurfactant solution, as well as the viscosity of the resulting emulsions, were determined as described above.

### 3. Results and Discussion

#### 3.1. Biochemical and Structural Characterization of the Biosurfactant

The biosurfactant produced by *B. thailandensis* had total protein and carbohydrate contents of  $23.0 \pm 3.2\%$  and  $33.1 \pm 6.4\%$ , respectively. Furthermore, the fluorescence examination after Nile blue staining demonstrated a positive reaction to the presence of lipidic groups (Figure S1), thus revealing the biosurfactant's glycolipopeptide nature. The carbohydrate fraction of the biosurfactant was composed of galactose, glucose, rhamnose, mannose, and glucuronic acid, in a relative molar ratio of 4:3:2:2:1 (refer to Figure S2 for supporting information on the compositional analysis of the carbohydrate fraction of the biosurfactant). The same sugar monomers were identified in the composition of the glycolipopeptide biosurfactants produced by an alkaliphilic bacterium *Klebsiella* sp. strain RJ-03, but with different relative sugar monomer contents [35]. Similar macromolecule profiles were also reported for the glycolipoproteins produced by *Lactobacillus plantarum* ATCC 8014 [36], *Lactobacillus pentosus* CECT-4023T [37], and *Stenotrophomonas maltophilia* UCP 1601 [38], which were composed of 14–28% carbohydrate and 12.6–28.2% protein. To the best of our knowledge, the ability of *B. thailandensis* to produce glycolipopeptide biosurfactants has not been documented in the literature.

The freeze-dried biosurfactant had a moisture content of  $7.8 \pm 0.0\%$  and no ashes were detected upon incineration of the biosurfactant at  $550\text{ }^{\circ}\text{C}$ , thus demonstrating that the extraction procedure was effective in eliminating salts from the sample.

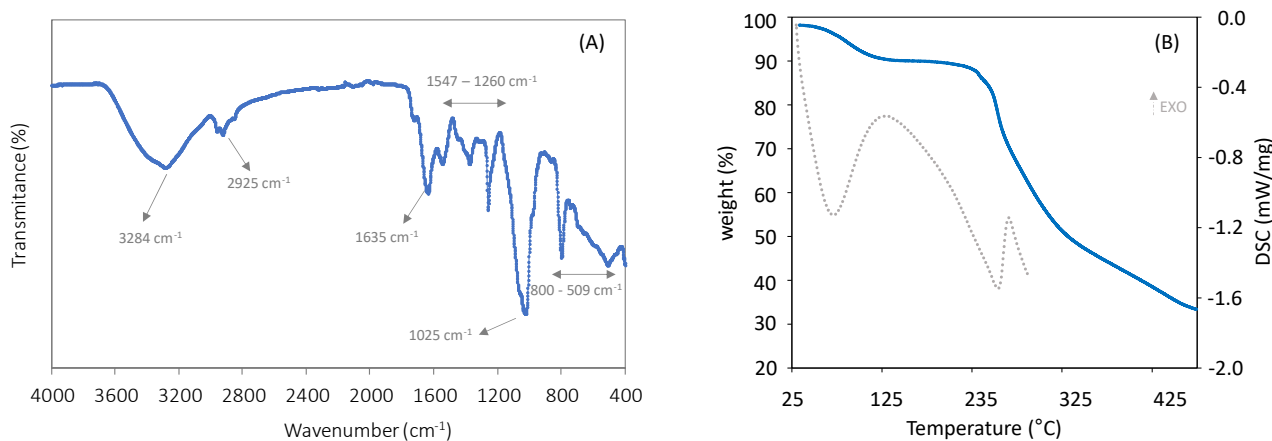
The FTIR spectrum of the biosurfactant (Figure 1A) confirmed the presence of carbohydrates, lipids, and proteins. The presence of aliphatic chains ( $-\text{CH}_2$  and  $-\text{CH}_3$  groups) is suggested by the peaks that appeared at around  $2925\text{ cm}^{-1}$ , which can be attributed to the  $-\text{CH}$  stretching vibrations [35]. The peak at  $3284\text{ cm}^{-1}$  suggests the presence of stretching vibrations from the  $-\text{NH}$  of the peptide portion [39]. Furthermore, the spectrum points to the presence of stretching vibrations in the transmittance region of  $1635\text{ cm}^{-1}$  (amide I bond) and  $1547\text{ cm}^{-1}$  (amide II bond), thus confirming the presence of proteins [40]. The peaks located in the region between  $1260$  and  $1025\text{ cm}^{-1}$  can be assigned to the ether bond (C–O) [41], a stretching vibration in sugars, and the glycosidic bonds present in polysaccharides (C–O–C) [41], respectively. Similar FTIR spectra were reported for the biosurfactants synthesized by other nonpathogenic species, such as *Lactococcus lactis* CECT-4434 [41], *Lactobacillus pentosus* [42], and *Corynebacterium kutscheri* [43].

The *B. thailandensis* biosurfactant had an Mw of  $1.0 \times 10^7$  Da (refer to Figure S3 for supporting information on the SEC-MALS analysis of the biosurfactant), a value that is within those reported for other polymeric biosurfactants of microbial origin (from  $5.0 \times 10^4$  Da to above  $1.0 \times 10^7$  Da) [44], but higher than the values reported for the glycolipopeptides produced by the *Klebsiella* sp. strain RJ-03 ( $2.2 \times 10^6$ – $2.7 \times 10^6$  Da) [35] and the proteoglycan-based bioemulsifier produced by the oleaginous yeast *Meyerozyma caribbica* ( $3.0 \times 10^6$  Da) [20]. The low PDI value of the biosurfactant (1.66) shows the homogeneity of the macromolecule's chain length.

#### 3.2. Thermal Properties

The thermal degradation curve of the *B. thailandensis* biosurfactant (Figure 1B) displayed three mass loss regions. The first degradation step, with a weight loss of around 7%, occurred between  $50$  and  $140\text{ }^{\circ}\text{C}$ , and can be attributed to water evaporation [30]. This shows the biosurfactant's ability to absorb moisture, which is in agreement with the

sample's moisture content ( $7.8 \pm 0.0\%$ ). The largest mass loss, around 40%, occurred between 180 and 340 °C, and is probably associated with the decomposition of proteins and polysaccharide side chains [45,46]. At higher temperatures, gradual weight loss was observed, associated with the third step of thermal degradation, wherein polymer main-chain scission occurred [47], resulting in a char yield of 33%. A similar profile was reported for biosurfactants composed of protein and carbohydrate moieties linked to lipids [35].



**Figure 1.** (A) FTIR spectrum of the freeze-dried biosurfactant; (B) TGA thermogram (full blue line) and DSC curves (dotted grey line) of *B. thailandensis* freeze-dried biosurfactant.

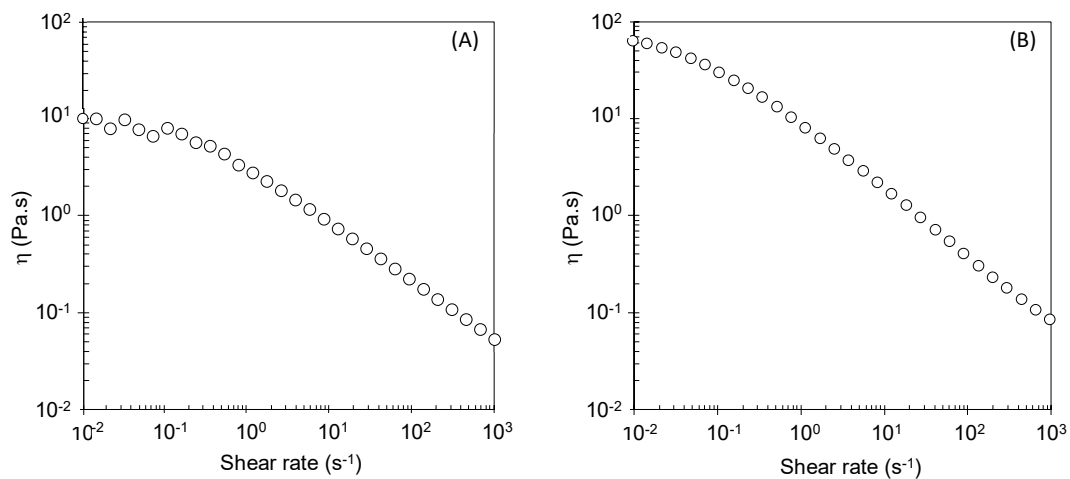
The DSC spectra of the biosurfactant displayed an exothermic peak at 139 °C, which corresponds to the first degradation step observed in the polymer's TGA analysis (Figure 1B), attributed to water evaporation. The spectrum also displays an endothermic peak at 255 °C (Figure 1B), which corresponds to the thermal degradation of the proteins and polysaccharide side chains of the polymer, as shown by the TGA thermogram.

### 3.3. Rheological Behavior

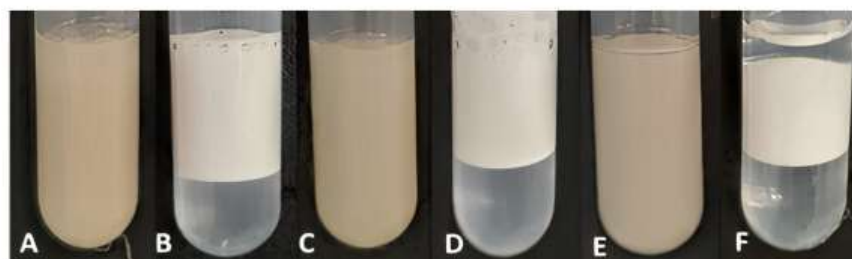
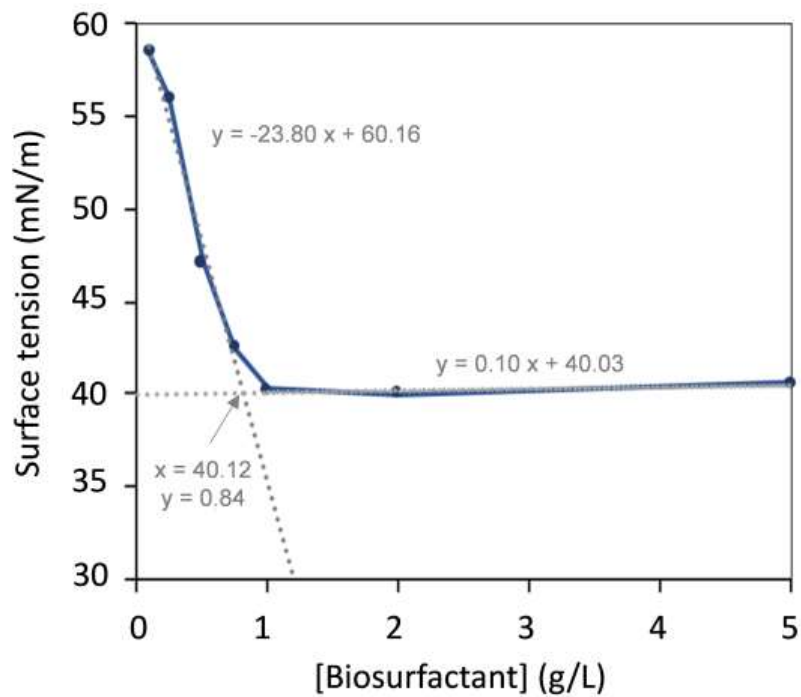
The *B. thailandensis* biosurfactant aqueous solution (10 g/L) displayed non-Newtonian fluid behavior with shear-thinning properties (Figure 2A), with the viscosity decreasing for increasing shear rates. This behavior is typical of high-molecular-weight polymers, and is frequently reported for biosurfactant solutions [48–50]. It occurs due to the reduction in intermolecular interactions between polymer chains, as a consequence of their alignment in the flow direction [51]. The solution presented apparent viscosity of 7.12 Pa.s, at a shear rate of  $0.01 \text{ s}^{-1}$ , with a flow behavior index ( $n$ ) of 0.44, which is in agreement with its shear-thinning behavior ( $0 < n < 1$ ) [52], and a consistency index of 1.97, according to the power law model (refer to Figure S4 for supporting information on fitting the power law model).

### 3.4. Surface-Active Properties

As shown in Figure 3, the surface tension decreased as the biosurfactant's concentration increased from 0.1 to 1.0 g/L, remaining unchanged for higher concentrations. The corresponding CMC was roughly 0.84 g/L, which is within the values reported for other biosurfactants (1.0 mg/L–2.0 g/L) [53]. The *B. thailandensis* biosurfactant outperforms synthetic surfactants such as SDS [40] and SLS [54], which display CMC values of 2.0–2.9 g/L, as well as the biosurfactant glycolipoprotein produced by a *Bacillus* sp. isolated from corn steep water, with a reported CMC value of around  $1.81 \pm 0.21 \text{ g/L}$  [10].



**Figure 2.** Flow curves of (A) *B. thailandensis* biosurfactant aqueous solution at a concentration of 10 g/L (at 25 °C) and (B) the sunflower oil emulsion stabilized with *B. thailandensis* biosurfactant (at 25 °C).



**Figure 3.** Surface tension of *B. thailandensis* biosurfactant solutions at concentrations ranging from 0.1 to 5.0 g/L and images of the biosurfactant's emulsions with almond oil (A), sunflower oil (C), and benzene (E), after standing for 24 h. The chemical surfactant Triton X-100, at the same concentration, was used to prepare emulsions with the same hydrophobic compounds (B,D,F, respectively) for comparison.

At the CMC, the *B. thailandensis* biosurfactant lowered the water's surface tension to  $40.31 \pm 0.26$  mN/m. This value, which corresponds to the surfactant effectiveness, is higher than those defined for good surfactants (25–30 mN/m) [55,56], but it is similar to those reported for a number of microbial biosurfactants, including the long-chain fatty acid anionic biosurfactants produced by the bacterium M87 *Microbacterium* sp. (around 40 mN/m) [57], the glycolipids produced by *Arthrobacter* sp. DSM2567 (40 mN/m) [58], the lipopeptides produced by *Bacillus* sp. isolates ( $39.3 \pm 0.6$  and  $37.7 \pm 0.6$  mN/m) [10], and the glycolipopeptide produced by *Klebsiella* sp. (40.36–69.09 mN/m) [35]. On the other hand, polymeric biosurfactants, such as glycolipoproteins, despite not significantly lowering the water's surface tension, are generally more effective in the formation and stabilization of emulsions [15].

### 3.5. Emulsion-Forming and -Stabilizing Capacities

The emulsion-forming and -stabilizing capacities of the *B. thailandensis* biosurfactant were evaluated against three organic phases, namely, benzene, almond oil, and sunflower oil (Figure 3). For comparison, emulsions were also prepared with the chemical surfactant Triton X-100. As shown in Figure 3A,C,E, the *B. thailandensis* biosurfactant was able to strongly emulsify all the tested hydrophobic compounds, with high EA values, as follows:  $92.0 \pm 4.1\%$  and  $93.3 \pm 0.2\%$  for the almond and sunflower oils, respectively, and  $100.0 \pm 0.0\%$  for benzene. These results show that the biopolymer is a good emulsifier ( $EA \geq 50\%$ ) [59]. Moreover, for all the tested compounds, the biosurfactant outperformed Triton X-100 (Figure 3B,D,F), as shown by the lower EA values observed for the Triton X-100 stabilized emulsions, as follows:  $60.4 \pm 2.0\%$ ,  $55.4 \pm 0.2\%$ , and  $43.9 \pm 0.2\%$  for almond oil, sunflower oil, and benzene, respectively. Similar results were reported by [60] for emulsions with oleic acid stabilized by jatropha oil-derived sophorolipids, which performed better than Triton X-100. Considering the fact that a stable emulsifier is able to maintain 50% emulsion of its original emulsion volume 24 h after its formation, the *B. thailandensis* biosurfactant has demonstrated good potential for advantageously replacing Triton X-100 in its applications as a surface-active agent, such as, for example, in the bioremediation of contaminated soils [3], or as an emulsifier for food and cosmetic products [5,6].

The sunflower emulsions stabilized with the *B. thailandensis* biosurfactant exhibited non Newtonian fluid behavior (Figure 2B), similar to that of the biopolymer's aqueous solution (Figure 2A), but with a significantly higher apparent viscosity (62.84 Pa.s, measured at a shear rate of  $0.01 \text{ s}^{-1}$ ) than the biosurfactant's solution (7.12 Pa.s). Concomitantly, the emulsion's consistency index was also significantly higher (8.55) than that of the biosurfactant's solution (1.97). Furthermore, the emulsion was more shear thinning, as shown by its flow behavior index (0.33, compared to 0.44 for the biosurfactant's solution) (refer to Figure S4 for supporting information on fitting the power law model).

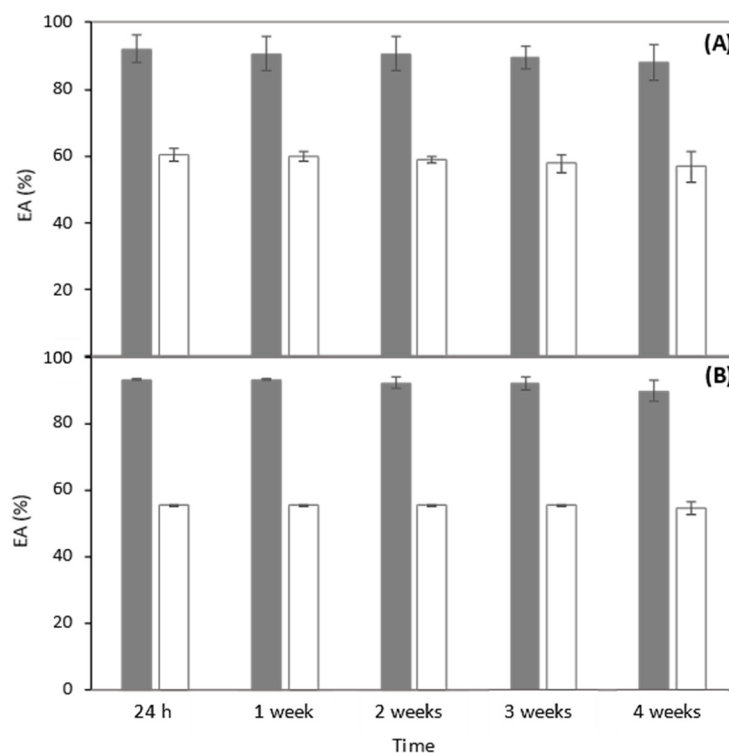
The emulsions prepared with the almond and sunflower oils were stable for 4 weeks, with their EA being practically unchanged (Figure 4). This stability could be due to the uronic acid and proteinaceous components of the *B. thailandensis* biosurfactant, since they have the capacity to adsorb at the oil/water interface and, consequently, develop a viscoelastic layer surrounding the lipid droplets, preventing coalescence and flocculation of the droplets in the dispersant phase [35,61]. Similar results were obtained by [62,63], which suggested that emulsions formed between lipopeptide biosurfactants and long-chain hydrocarbons (e.g., diesel) possess higher stability.

### 3.6. Thermal Stability

The thermal stability of the *B. thailandensis* biosurfactant was evaluated by exposing the biopolymer in an aqueous solution to a temperature of  $121 \text{ }^\circ\text{C}$  in an autoclave (0.98 bar) for 20 min. Interestingly, the treated solution maintained its shear-thinning behavior, with a slight increase in the flow behavior index value (0.46) compared to the untreated biosurfactant solution (0.44) (refer to Figure S4 for supporting information on fitting the power law model). The thermally treated biosurfactant also maintained a surface

tension value of  $40.36 \pm 0.5$  mN/m, which was identical to that of the untreated solution ( $40.31 \pm 0.26$  mN/m), thus confirming its thermal stability.

The emulsifying ability of the treated biosurfactant, on the other hand, was negatively affected, with a reduction in the EA to  $50.5 \pm 0.9\%$ , which is around half of the value observed for the non-treated biosurfactant ( $100.0 \pm 0.0\%$ ). Different biosurfactants (e.g., glycolipids) also showed a slight decrease in the emulsifying capacity after heat treatment at similar temperatures [64]. Nevertheless, the value is still within the range reported for good EA ( $\geq 50\%$ ) [59]. Moreover, Triton X-100 also suffered a similar reduction in its emulsification ability, as the EA of the emulsions stabilized with the autoclaved compound also reduced from  $43.9 \pm 2.1\%$  to  $33.4 \pm 5.2\%$ . These results underline the potential of the *B. thailandensis* biosurfactant for use, for example, in the food industry, in which the temperatures are elevated during processing or the final product is consumed.



**Figure 4.** EA of the biosurfactant produced by *B. thailandensis*, at a concentration of 10 g/L, emulsified with almond oil (A) and sunflower oil (B) for 4 weeks (gray bars). The chemical surfactant Triton X-100 (white bars) was used for comparison, at the same concentration.

#### 4. Conclusions

The glycolipopeptide biosurfactant secreted by *Burkholderia thailandensis* DSM 13276 was demonstrated to possess valuable surface-active properties, namely, a low CMC and high EA for almond and sunflower oils, and for benzene. Moreover, the biosurfactant showed good thermostability, with a thermal degradation temperature above 200 °C, and the ability to maintain stable rheological and surface-active properties, as well as good EA after exposure to elevated temperatures and pressure. These findings support the utilization of the *B. thailandensis* biosurfactant as an emulsion-forming and -stabilizing agent in food and/or cosmetic products/processing, and for bioremediation.

**Supplementary Materials:** The following supporting information can be downloaded at <https://www.mdpi.com/article/10.3390/polym14102088/s1>.

**Author Contributions:** Conceptualization, C.V.G., F.F. and C.A.V.T.; methodology, C.V.G., A.T.R., A.E. and C.S.; investigation, C.V.G., A.T.R., A.E. and C.S.; writing—original draft preparation, C.V.G.;



writing—review and editing, C.A.V.T., F.F., M.A.M.R. and C.G.; supervision and funding, M.A.M.R., F.F. and C.A.V.T. All authors have read and agreed to the published version of the manuscript.

**Funding:** This work was financed by national funds from FCT—Fundação para a Ciência e a Tecnologia, I.P., in the scope of the projects UIDP/04378/2020 and UIDB/04378/2020 of the Research Unit on Applied Molecular Biosciences—UCIBIO and the project LA/P/0140/2020 of the Associate Laboratory Institute for Health and Bioeconomy—i4HB, and by the European Union’s Horizon 2020 research and innovation program through Project Bio Innovation of a Circular Economy for Plastics (BioICEP), under grant agreement No. 870292, supported by the National Natural Science Foundation of China (grant numbers: Institute of Microbiology, Chinese Academy of Sciences: 31961133016; Beijing Institute of Technology: 31961133015; Shandong University: 31961133014). C.V.G., A.E. and A.T.R. acknowledge FCT I.P. for the Ph.D. grants 2021.05798.BD, 2021.05014.BD and 2020.06470.BD, respectively.

**Institutional Review Board Statement:** Not applicable.

**Informed Consent Statement:** Not applicable.

**Data Availability Statement:** Data will be available upon request.

**Conflicts of Interest:** The authors declare no conflict of interest.

## References

- Adetunji, A.I.; Olaniran, A.O. Production and potential biotechnological applications of microbial surfactants: An overview. *Saudi J. Biol. Sci.* **2021**, *28*, 669–679. [[CrossRef](#)] [[PubMed](#)]
- Varjani, S.J.; Upasani, V.N. Critical review on biosurfactant analysis, purification and characterization using rhamnolipid as a model biosurfactant. *Bioresour. Technol.* **2017**, *232*, 389–397. [[CrossRef](#)] [[PubMed](#)]
- Meena, K.R.; Dhiman, R.; Singh, K.; Kumar, S.; Sharma, A.; Kanwar, S.S.; Mondal, R.; Das, S.; Franco, O.L.; Mandal, A.K. Purification and characterization of a surfactin-like biosurfactant produced by *Bacillus velezensis* klp2016 and its application towards engine oil degradation. *Microb. Cell Fact.* **2021**, *20*, 26. [[CrossRef](#)] [[PubMed](#)]
- Mulligan, C.N. Environmental applications for biosurfactants. *Environ. Pollut.* **2005**, *133*, 183–198. [[CrossRef](#)] [[PubMed](#)]
- Campos, J.M.; Stamford, T.L.M.; Sarubbo, L.A. Characterization and application of a biosurfactant isolated from *Candida utilis* in salad dressings. *Biodegradation* **2019**, *30*, 313–324. [[CrossRef](#)] [[PubMed](#)]
- Vecino, X.; Cruz, J.M.; Moldes, A.B.; Rodrigues, L.R. Biosurfactants in cosmetic formulations: Trends and challenges. *Crit. Rev. Biotechnol.* **2017**, *37*, 911–923. [[CrossRef](#)] [[PubMed](#)]
- Paraszkiewicz, K.; Moryl, M.; Płaza, G.; Bhagat, D.K.; Satpute, S.; Bernat, P. Surfactants of microbial origin as antibiofilm agents. *Int. J. Environ. Health Res.* **2021**, *31*, 401–420. [[CrossRef](#)]
- Fait, M.E.; Bakas, L.; Garrote, G.L.; Morcelle, S.R.; Saparrat, M.C.N. Cationic surfactants as antifungal agents. *Appl. Microbiol. Biotechnol.* **2019**, *103*, 97–112. [[CrossRef](#)]
- Alwadani, N.; Fatehi, P. Synthetic and lignin-based surfactants: Challenges and opportunities. *Carbon Resour. Convers.* **2018**, *1*, 126–138. [[CrossRef](#)]
- Rodríguez-López, L.; López-Prieto, A.; Lopez-Álvarez, M.; Pérez-Davila, S.; Serra, J.; González, P.; Cruz, J.M.; Moldes, A.B. Characterization and cytotoxic effect of biosurfactants obtained from different sources. *ACS Omega* **2020**, *5*, 31381–31390. [[CrossRef](#)]
- Roberto, A.L.; Rosileide, F.S.A.; Dayana, M.R.; Helvia, W.C.A.; Vanessa, P.S.; Galba, M.C.-T. Production and characterization of biosurfactant isolated from *Candida glabrata* using renewable substrates. *Afr. J. Microbiol. Res.* **2017**, *11*, 237–244. [[CrossRef](#)]
- Kourmentza, C.; Costa, J.; Azevedo, Z.; Servin, C.; Grandfils, C.; De Freitas, V.; Reis, M.A.M. *Burkholderia thailandensis* as a microbial cell factory for the bioconversion of used cooking oil to polyhydroxyalkanoates and rhamnolipids. *Bioresour. Technol.* **2018**, *247*, 829–837. [[CrossRef](#)] [[PubMed](#)]
- Costa, J.A.V.; Treichel, H.; Santos, L.O.; Martins, V.G. Solid-State Fermentation for the Production of Biosurfactants and Their Applications. In *Current Developments in Biotechnology and Bioengineering*; Elsevier: Amsterdam, The Netherlands, 2018; pp. 357–372; ISBN 9780444639905.
- Fenibo, E.O.; Douglas, S.I.; Stanley, H.O. A Review on Microbial Surfactants: Production, Classifications, Properties and Characterization. *J. Adv. Microbiol.* **2019**, *18*, 1–22. [[CrossRef](#)]
- Banat, I.M.; Franzetti, A.; Gandolfi, I.; Bestetti, G.; Martinotti, M.G.; Fracchia, L.; Smyth, T.J.; Marchant, R. Microbial biosurfactants production, applications and future potential. *Appl. Microbiol. Biotechnol.* **2010**, *87*, 427–444. [[CrossRef](#)]
- Campos, J.M.; Montenegro Stamford, T.L.; Sarubbo, L.A.; de Luna, J.M.; Rufino, R.D.; Banat, I.M. Microbial biosurfactants as additives for food industries. *Biotechnol. Prog.* **2013**, *29*, 1097–1108. [[CrossRef](#)]
- Husain, D.R.; Goutx, M.; Acquaviva, M.; Gilewicz, M.; Bertrand, J.C. The effect of temperature on eicosane substrate uptake modes by a marine bacterium *Pseudomonas nautica* strain 617: Relationship with the biochemical content of cells and supernatants. *World J. Microbiol. Biotechnol.* **1997**, *13*, 587–590. [[CrossRef](#)]

18. Rosenberg, E.; Rubinovitz, C.; Legmann, R.; Ron, E.Z. Purification and Chemical Properties of *Acinetobacter calcoaceticus* A2 Biodispersan. *Appl. Environ. Microbiol.* **1988**, *54*, 323–326. [[CrossRef](#)]
19. Cirigliano, M.C.; Carman, G.M. Isolation of a bioemulsifier from candida lipolytica. *Appl. Environ. Microbiol.* **1984**, *48*, 747–750. [[CrossRef](#)]
20. Bhaumik, M.; Dhanarajan, G.; Chopra, J.; Kumar, R.; Hazra, C.; Sen, R. Production, partial purification and characterization of a proteoglycan bioemulsifier from an oleaginous yeast. *Bioprocess Biosyst. Eng.* **2020**, *43*, 1747–1759. [[CrossRef](#)]
21. Singh, S.; Kumar, V.; Singh, S.; Dhanjal, D.S.; Datta, S.; Sharma, D.; Singh, N.K.; Singh, J. Biosurfactant-based bioremediation. In *Bioremediation of Pollutants*; Elsevier: Amsterdam, The Netherlands, 2020; pp. 333–358; ISBN 9780128190258.
22. Irfan-Maqsood, M.; Seddiq-Shams, M. Rhamnolipids: Well-Characterized Glycolipids with Potential Broad Applicability as Biosurfactants. *Ind. Biotechnol.* **2014**, *10*, 285–291. [[CrossRef](#)]
23. Takeda, Y.; Shimada, M.; Ushida, Y.; Saito, H.; Iwamoto, H.; Okawa, T. Effects of sterilization process on the physicochemical and nutritional properties of liquid enteral formula. *Food Sci. Technol. Res.* **2015**, *21*, 573–581. [[CrossRef](#)]
24. Costa, S.G.V.A.O.; Déziel, E.; Lépine, F. Characterization of rhamnolipid production by *Burkholderia glumae*. *Letts. Appl. Microbiol.* **2011**, *53*, 620–627. [[CrossRef](#)] [[PubMed](#)]
25. Hörmann, B.; Müller, M.M.; Sylđatk, C.; Hausmann, R. Rhamnolipid production by *Burkholderia plantarii* DSM 9509 T. *Eur. J. Lipid Sci. Technol.* **2010**, *112*, 674–680. [[CrossRef](#)]
26. Ferreira, A.S.; Leitão, J.H.; Silva, I.N.; Pinheiro, P.F.; Sousa, S.A.; Ramos, C.G.; Moreira, L.M. Distribution of Cepacian Biosynthesis Genes among Environmental and Clinical *Burkholderia* Strains and Role of Cepacian Exopolysaccharide in Resistance to Stress Conditions. *Appl. Environ. Microbiol.* **2010**, *76*, 441–450. [[CrossRef](#)] [[PubMed](#)]
27. Reckseidler-Zenteno, S.L.; Viteri, D.-F.; Moore, R.; Wong, E.; Tuanyok, A.; Woods, D.E. Characterization of the type III capsular polysaccharide produced by *Burkholderia pseudomallei*. *J. Med. Microbiol.* **2010**, *59*, 1403–1414. [[CrossRef](#)]
28. Webb, J.R.; Sarovich, D.S.; Price, E.P.; Ward, L.M.; Mayo, M.; Currie, B.J. *Burkholderia pseudomallei* Lipopolysaccharide Genotype Does Not Correlate with Severity or Outcome in Melioidosis: Host Risk Factors Remain the Critical Determinant. *Open Forum Infect. Dis.* **2019**, *6*, ofz091. [[CrossRef](#)]
29. Freitas, F.; Alves, V.D.; Pais, J.; Costa, N.; Oliveira, C.; Mafra, L.; Hilliou, L.; Oliveira, R.; Reis, M.A.M. Characterization of an extracellular polysaccharide produced by a *Pseudomonas* strain grown on glycerol. *Bioresour. Technol.* **2009**, *100*, 859–865. [[CrossRef](#)]
30. Baptista, S.; Torres, C.A.V.; Sevrin, C.; Grandfils, C.; Reis, M.A.M.; Freitas, F. Extraction of the Bacterial Extracellular Polysaccharide FucoPol by Membrane-Based Methods: Efficiency and Impact on Biopolymer Properties. *Polymers* **2022**, *14*, 390. [[CrossRef](#)]
31. Smyth, T.J.P.; Rudden, M.; Tsaousi, K.; Marchant, R.; Banat, I.M. Protocols for the Detection and Chemical Characterisation of Microbial Glycolipids. In *Springer Protocols Handbooks, Switzerland*; Springer: Berlin/Heidelberg, Germany, 2014; pp. 29–60; ISBN 978-3-662-49135-5.
32. Hilliou, L.; Freitas, F.; Oliveira, R.; Reis, M.A.M.; Lespineux, D.; Grandfils, C.; Alves, V.D. Solution properties of an exopolysaccharide from a *Pseudomonas* strain obtained using glycerol as sole carbon source. *Carbohydr. Polym.* **2009**, *78*, 526–532. [[CrossRef](#)]
33. Delben, F.; Stefancich, S. Interaction of Food Proteins with Polysaccharides, I. Properties upon Mixing. *J. Food Eng.* **1997**, *31*, 325–346. [[CrossRef](#)]
34. Pansiripat, S.; Pornsunthorntawe, O.; Rujiravanit, R.; Kitiyanan, B.; Somboonthanate, P.; Chavadej, S. Biosurfactant production by *Pseudomonas aeruginosa* SP4 using sequencing batch reactors: Effect of oil-to-glucose ratio. *Biochem. Eng. J.* **2010**, *49*, 185–191. [[CrossRef](#)]
35. Jain, R.M.; Mody, K.; Joshi, N.; Mishra, A.; Jha, B. Production and structural characterization of biosurfactant produced by an alkaliphilic bacterium, *Klebsiella* sp.: Evaluation of different carbon sources. *Colloids Surf. B Biointerfaces* **2013**, *108*, 199–204. [[CrossRef](#)] [[PubMed](#)]
36. Behzadnia, A.; Moosavi-Nasab, M.; Tiwari, B.K.; Setoodeh, P. *Lactobacillus plantarum*-derived biosurfactant: Ultrasound-induced production and characterization. *Ultrason. Sonochem.* **2020**, *65*, 105037. [[CrossRef](#)]
37. Vecino, X.; Rodríguez-López, L.; Ferreira, D.; Cruz, J.M.; Moldes, A.B.; Rodrigues, L.R. Bioactivity of glycolipopeptide cell-bound biosurfactants against skin pathogens. *Int. J. Biol. Macromol.* **2018**, *109*, 971–979. [[CrossRef](#)] [[PubMed](#)]
38. Nogueira, I.B.; Rodríguez, D.M.; da Silva Andrade, R.F.; Lins, A.B.; Bione, A.P.; da Silva, I.G.S.; Franco, L.D.O.; de Campos-Takaki, G.M. Bioconversion of Agroindustrial Waste in the Production of Bioemulsifier by *Stenotrophomonas maltophilia* UCP 1601 and Application in Bioremediation Process. *Int. J. Chem. Eng.* **2020**, *2020*, 9434059. [[CrossRef](#)]
39. Solanki, J.; Patel, D.; Ingale, S.; Nataraj, M. Screening and Optimization of Agro-industrial wastes for glycoprotein biosurfactant production from *Sphingobacterium thalpophilum* DP9. *Res. Sq.* **2020**, 1–25. [[CrossRef](#)]
40. Velraeds, M.M.C.; van der Mei, H.C.; Reid, G.; Busscher, H.J. Physicochemical and biochemical characterization of biosurfactants released by *Lactobacillus* strains. *Colloids Surf. B Biointerfaces* **1996**, *8*, 51–61. [[CrossRef](#)]
41. Vera, E.C.S.; Azevedo, P.O.D.S.D.; Domínguez, J.M.; Oliveira, R. Optimization of biosurfactant and bacteriocin-like inhibitory substance (blis) production by lactococcus lactis cect-4434 from agroindustrial waste. *Biochem. Eng. J.* **2018**, *133*, 168–178. [[CrossRef](#)]
42. Vecino, X.; Barbosa-Pereira, L.; Devesa-Rey, R.; Cruz, J.M.; Moldes, A.B. Optimization of Extraction Conditions and Fatty Acid Characterization of *Lactobacillus pentosus* Cell-Bound Biosurfactant/Bioemulsifier. *J. Sci. Food Agric.* **2015**, *95*, 313–320. [[CrossRef](#)]

43. Thavasi, R.; Jayalakshmi, S.; Balasubramanian, T.; Banat, I.M. Biosurfactant production by *Corynebacterium kutscheri* from waste motor lubricant oil and peanut oil cake. *Lett. Appl. Microbiol.* **2007**, *45*, 686–691. [[CrossRef](#)]
44. Maier, R.M. Biosurfactants: Evolution and Diversity in Bacteria. In *Applied Microbiology*; Springer: New Delhi, India, 2003; pp. 101–121; ISBN 9780080490199.
45. Matsuura, Y.; Takehira, M.; Joti, Y.; Ogasahara, K.; Tanaka, T.; Ono, N.; Kunishima, N.; Yutani, K. Thermodynamics of protein denaturation at temperatures over 100 °C: CutA1 mutant proteins substituted with hydrophobic and charged residues. *Sci. Rep.* **2015**, *5*, 15545. [[CrossRef](#)] [[PubMed](#)]
46. Weiss, I.M.; Muth, C.; Drumm, R.; Kirchner, H.O.K. Thermal decomposition of the amino acids glycine, cysteine, aspartic acid, asparagine, glutamic acid, glutamine, arginine and histidine. *BMC Biophys.* **2018**, *11*, 2. [[CrossRef](#)] [[PubMed](#)]
47. Concórdio-Reis, P.; Pereira, C.V.; Batista, M.P.; Sevrin, C.; Grandfils, C.; Marques, A.C.; Fortunato, E.; Gaspar, F.B.; Matias, A.A.; Freitas, F.; et al. Silver nanocomposites based on the bacterial fucose-rich polysaccharide secreted by *Enterobacter* A47 for wound dressing applications: Synthesis, characterization and in vitro bioactivity. *Int. J. Biol. Macromol.* **2020**, *163*, 959–969. [[CrossRef](#)] [[PubMed](#)]
48. Jain, R.M.; Mody, K.; Mishra, A.; Jha, B. Isolation and structural characterization of biosurfactant produced by an alkaliphilic bacterium *Cronobacter sakazakii* isolated from oil contaminated wastewater. *Carbohydr. Polym.* **2012**, *87*, 2320–2326. [[CrossRef](#)]
49. Abbasi, H.; Hamed, M.M.; Lotfabad, T.B.; Zahiri, H.S.; Sharafi, H.; Masoomi, F.; Moosavi-Movahedi, A.A.; Ortiz, A.; Amanlou, M.; Noghabi, K.A. Biosurfactant-producing bacterium, *Pseudomonas aeruginosa* MA01 isolated from spoiled apples: Physicochemical and structural characteristics of isolated biosurfactant. *J. Biosci. Bioeng.* **2012**, *113*, 211–219. [[CrossRef](#)] [[PubMed](#)]
50. Trujillo-Cayado, L.A.; Alfaro, M.C.; Muñoz, J.; Raymundo, A.; Sousa, I. Development and rheological properties of ecological emulsions formulated with a biosolvent and two microbial polysaccharides. *Colloids Surf. B Biointerfaces* **2016**, *141*, 53–58. [[CrossRef](#)]
51. Machale, J.; Majumder, S.K.; Ghosh, P.; Sen, T.K. Development of a novel biosurfactant for enhanced oil recovery and its influence on the rheological properties of polymer. *Fuel* **2019**, *257*, 116067. [[CrossRef](#)]
52. Walter, R.H. *Polysaccharide Dispersions*; Elsevier: Geneva, Switzerland; New York, NY, USA, 1998; ISBN 9780127338651.
53. Shakeri, F.; Babavalian, H.; Amoozegar, M.A.; Ahmadzadeh, Z.; Zuhuriyanizadi, S.; Afsharian, M.P. Production and Application of Biosurfactants in Biotechnology. *Biointerface Res. Appl. Chem.* **2020**, *11*, 10446–10460. [[CrossRef](#)]
54. Bognolo, G. Biosurfactants as emulsifying agents for hydrocarbons. *Colloids Surf. A Physicochem. Eng. Asp.* **1999**, *152*, 41–52. [[CrossRef](#)]
55. Joshi, S.; Bharucha, C.; Desai, A.J. Production of biosurfactant and antifungal compound by fermented food isolate *Bacillus subtilis* 20B. *Bioresour. Technol.* **2008**, *99*, 4603–4608. [[CrossRef](#)]
56. Liu, J.; Chen, Y.; Xu, R.; Jia, Y. Screening and Evaluation of Biosurfactant-Producing Strains Isolated from Oilfield Wastewater. *Indian J. Microbiol.* **2013**, *53*, 168–174. [[CrossRef](#)] [[PubMed](#)]
57. Lima, J.M.S.; Pereira, J.O.; Batista, I.H.; Junior, R.C.P.; Barroso, H.D.S.; Neto, P.D.Q.C.; Matsuura, A.B.J.; França, S.D.C.; Azevedo, J.L. Biosurfactants produced by *Microbacterium* sp., isolated from aquatic macrophytes in hydrocarbon-contaminated area in the Rio Negro, Manaus, Amazonas. *Acta Sci. Biol. Sci.* **2017**, *39*, 13. [[CrossRef](#)]
58. Li, Z.-Y.; Lang, S.; Wagner, F.; Witte, L.; Wray, V. Formation and Identification of Interfacial-Active Glycolipids from Resting Microbial Cells. *Appl. Environ. Microbiol.* **1984**, *48*, 610–617. [[CrossRef](#)] [[PubMed](#)]
59. Willumsen, P.A.; Karlson, U. Screening of bacteria, isolated from PAH-contaminated soils, for production of biosurfactants and bioemulsifiers. *Biodegradation* **1997**, *7*, 415–423. [[CrossRef](#)]
60. Joshi-Navare, K.; Khanvilkar, P.; Prabhune, A. Jatropha Oil Derived Sophorolipids: Production and Characterization as Laundry Detergent Additive. *Biochem. Res. Int.* **2013**, *2013*, 169797. [[CrossRef](#)] [[PubMed](#)]
61. Kalaydzhev, H.; Gandova, V.D.; Ivanova, P.; Brandão, T.R.S.; Dessev, T.T.; Silva, C.L.M.; Chalova, V.I. Stability of sunflower and rapeseed oil-in-water emulsions supplemented with ethanol-treated rapeseed meal protein isolate. *J. Food Sci. Technol.* **2019**, *56*, 3090–3098. [[CrossRef](#)]
62. Barros, F.F.C.; de Quadros, C.P.; Pastore, G.M. Propriedades Emulsificantes e Estabilidade Do Biossurfactante Produzido Por *Bacillus Subtilis* Em Manipueira. *Ciência E Tecnol. Aliment.* **2008**, *28*, 979–985. [[CrossRef](#)]
63. Felix, A.K.N.; Martins, J.J.; Almeida, J.G.L.; Giro, M.E.A.; Cavalcante, K.F.; Melo, V.M.M.; Pessoa, O.D.L.; Rocha, M.V.P.; Gonçalves, L.R.B.; Aguiar, R. Purification and characterization of a biosurfactant produced by *Bacillus subtilis* in cashew apple juice and its application in the remediation of oil-contaminated soil. *Colloids Surf. B Biointerfaces* **2019**, *175*, 256–263. [[CrossRef](#)]
64. Correa, H.T.; Vieira, W.F.; Pinheiro, T.M.A.; Cardoso, V.L.; Silveira, E.; Sette, L.D.; Pessoa, A.; Filho, U.C. L-Asparaginase and Biosurfactants Produced by Extremophile Yeasts from Antarctic Environments. *Ind. Biotechnol.* **2020**, *16*, 107–116. [[CrossRef](#)]

## Article

# Development of a Highly Efficient Environmentally Friendly Plasticizer

Irina N. Vikhareva \*, Guliya K. Aminova and Aliya K. Mazitova

Applied and Natural Sciences Department, Ufa State Petroleum Technological University, Mendeleeva St. 195, 450080 Ufa, Russia; aminovagk@inbox.ru (G.K.A.); elenaasf@yandex.ru (A.K.M.)

\* Correspondence: irina.vikhareva2009@yandex.ru; Tel.: +7-(347)2420370

**Abstract:** The purpose of this work is the synthesis of adipic acid ester and the study of the possibility of its use as a PVC plasticizer. The resulting butyl phenoxyethyl adipate was characterized by Fourier-transform infrared spectrometry, thermogravimetric analysis (TGA) and differential scanning calorimetry (DSC). The compatibility, effectiveness and plasticizing effect of butyl phenoxyethyl adipate in comparison with dioctylphthalate (DOP) were determined. The new environmentally friendly plasticizer has good compatibility with PVC and high thermal stability. The effectiveness of the plasticizing action of adipate based on the glass-transition temperature was 132.2 °C in relation to pure PVC and 7.7 °C in comparison to compounds based on DOP. An increase in the fluidity of the melt of polyvinyl chloride (PVC) compounds in the temperature range of 160–205 °C by 19–50% confirms a decrease in the energy intensity of the processes of manufacturing and the processing of polymer materials containing a new additive.

**Keywords:** adipate; effective plasticizer; environmentally friendly; esterification; polyvinyl chloride; technological

**Citation:** Vikhareva, I.N.; Aminova, G.K.; Mazitova, A.K. Development of a Highly Efficient Environmentally Friendly Plasticizer. *Polymers* **2022**, *14*, 1888. <https://doi.org/10.3390/polym14091888>

Academic Editors: José Miguel Ferri, Vicent Fombuena Borràs and Miguel Fernando Aldás Carrasco

Received: 3 April 2022

Accepted: 2 May 2022

Published: 5 May 2022

**Publisher's Note:** MDPI stays neutral with regard to jurisdictional claims in published maps and institutional affiliations.



**Copyright:** © 2022 by the authors. Licensee MDPI, Basel, Switzerland. This article is an open access article distributed under the terms and conditions of the Creative Commons Attribution (CC BY) license (<https://creativecommons.org/licenses/by/4.0/>).

## 1. Introduction

Modern polymeric materials are high-quality substitutes for natural raw materials with valuable qualities, many of which are not inherent in natural materials. For this reason, polymeric materials are widely used and are reliably and effectively used in almost every sector of the world economy. The cumulative global production of polymer materials since the 1950s is 8.3 billion tons [1]. Plastic production over the past 13 years has totaled more than 300 million tons annually [2].

It is also important that the use of polymers contributes to the low-carbon development of the economy [3,4]. For example, plastic wrap films are lighter and more packable, which means less energy consumption and a smaller carbon footprint [5]. The amount of carbon dioxide emissions during the production (kg of CO<sub>2</sub> per 1 kg of products) of an aluminum can is 11.4 and that of PVC is 4.4 [6,7]. Plastic is an element of a circular economy, and its use allows the spending of resources more economically [8–14].

However, despite the enormous economic effect that is achieved when polymer materials are introduced into industry and everyday life, the environmental safety of their use is of great importance [15,16].

Currently, the composition of polymer materials includes various chemical additives that are systematically released during the manufacture, processing and operation of products, polluting the environment and possibly penetrating into the human body [17–19].

To reduce their negative impact, it is necessary to ensure the environmental safety of polymeric materials when creating plastics and when developing technological regulations using non-toxic additives [20,21].

Today, polyvinyl chloride in terms of consumption takes third place after polyethylene and polypropylene; therefore, the development and use of environmentally friendly

biodegradable additives for these polymers is relevant, which contributes to solving the urgent problem of environmental pollution with plastic waste [22].

Renewable sources based on plant materials or their production waste to be utilized as fillers for regulating the biodegradability of polymer composite materials are an alternative for the development of economically and environmentally attractive technologies [23]. However, such polymer composite materials are inferior in physical, mechanical, technological and operational characteristics to traditional polymers. For this reason, it is advisable to modify polymer compositions using plasticizers capable of serving as a source of organic substances for microorganism-destroyers under ambient conditions [24,25].

The expansion of applications for plasticizers since the 1960s has contributed to the search for new competitive additives [26]. In market conditions, phthalate plasticizers turned out to be the most economical and in demand [27]. According to expert data, in 2019, the capacity of the global market of plasticizers is about 8 million tons [28]. Of these, the phthalate-free market constitutes 35% of the total [29]. Among diester plasticizers, phthalates occupy more than 80% of the market [30].

DOP takes first place in terms of production and consumption [31]. DOP has optimal plasticizing properties at a low cost and is the main standard by which other plasticizers are compared.

However, due to the migration of DOP from polymer products and its identified toxicity, the share of consumption of this plasticizer tends to gradually decrease.

The demand for phthalate-free plasticizers around the world is gradually increasing. Among phthalate-free plasticizers, adipic acid esters are in the lead in terms of consumption [32].

For this purpose, it is possible to use biodegradable plasticizers in the formulations of PVC compositions, for example, esters of adipic acid [33,34]. In numerous works, the biotoxicity and the period of biodegradation of the industrial adipate plasticizer DOA were investigated, and it was shown that this additive for PVC is non-toxic to various types of living microorganisms and that the period of its biodegradation is 6 months [35].

The relevance of the transition to green technologies contributes to the expansion of research on the production of adipic acid from raw materials on a biological basis using chemical and/or biological processes [36–39]. The industry of end users of adipic acid is increasingly inclined towards the use of bioadipic acid [40].

Plasticizers based on other acids are known and used [41], for example, citrates [42], but the cost of their production is much higher [43].

Esters of succinic acid are a renewable resource, which makes them an attractive promising starting material for industrial production [44]. For this reason, succinates are increasingly replacing terephthalic acid esters [45]. Test results have shown that the plasticizing properties of succinates improve with an increase in the length of the hydrocarbon chain, while the biodegrading properties deteriorate [46,47].

Trimellitates are somewhat inferior to phthalate plasticizers in terms of frost resistance of plastic compounds [48].

The consumption of epoxy plasticizers has increased in recent years due to the availability of vegetable oils [49]. Three oils are mainly used as raw materials for production: soybean, linseed and tall oil [50]. These plasticizers are not fluid, increase resistance to heat and ultraviolet light, have low migration and low toxicity and increase the frost resistance of the material, and, with increases in the content reduce the stability of film properties in a humid atmosphere and sweat with increasing temperature. As a rule, they are used in conjunction with small amounts of low-molecular-weight plasticizer.

Known plasticizer based on castor oil, which is gradually hydrogenated, esterified and acetylated to obtain triacetylated monoglyceride ester. The disadvantage of using castor oil as a feedstock is that products based on it are more expensive than phthalates, and the world supply of castor oil is limited [51].

Another type of natural-product-based plasticizer is acetylated soybean oil [43]. Technology converts epoxy groups in epoxidized oil into esters of vicinally diacetylated fatty

acids. The technology can potentially be expanded to produce a variety of similar epoxy plasticizers [52].

Another example of the use of natural raw materials is the creation of bioplasticizers based on sucrose esters, which are also a renewable resource. Their content in molasses, a waste product of sugar beet production, is approximately 45%. In addition to the plasticizing effect, esters of sucrose and fructooligosaccharides have an antimicrobial effect [53]. Sucrose palmitate and glucose hexanoate were studied as bioplasticizers [54]. The esters showed good miscibility with PVC and good plasticization efficiency, as well as good mechanical properties in the form of higher strain at break and a lower modulus of elasticity.

Methods for processing polymer composite materials are characterized by high manufacturability, productivity, a high degree of automation, minimum energy consumption and the ability to manufacture several products of complex shape in one molding cycle [55]. The achievement of the desired characteristics of polymer composite materials is primarily determined by the type, quantity and ratio of components.

Taking into account the above factors, the development of environmentally friendly additives that contribute to the high manufacturability, productivity and minimal energy consumption of the processing and manufacturing of polymer composite materials is relevant.

In addition, it is important that the resulting additives contribute to solving the environmental problem of plastic pollution and render polymers biodegradable.

The introduction of plasticizers into the PVC composition formulation promotes a targeted change in the structure and properties of the polymer, which definitely leads to an improvement in the rheological and physicomechanical characteristics of the resulting compound: strength, frost resistance and brittleness, hardness, melt flow rate, impact strength and manufacturability, as well as thermal, electrophysical and other properties of polymers [56,57]. According to the studies, the manufacturability of PVC composite processing is evaluated according to the rheology of the melts. A fairly reliable and widespread method in practice is to determine the processability of polymers by the value of the melt flow rate (MFR). This indicator allows the establishment of a temperature range for the processing of the polymer composition and provides the necessary conditions for its implementation.

In this regard, when developing new environmentally friendly plasticizers, it is important to determine their effect on the processing of polymer composite materials. In order to create resource- and energy-saving technologies, additives are needed to ensure these characteristics. Therefore, in this work, technologically important characteristics of the developed plasticizers were studied: thermal stability, compatibility and rheology.

## 2. Materials and Methods

### 2.1. Starting Materials

Adipic acid was purchased from Radici Group, Selbitz-Hochfranken, Bavaria, Germany. Butanol and phenol were purchased from The Company «Rearus», Moscow, Russia. Ethylene oxide was purchased from ECOTECH Chemical Components Plant, Moscow, Russia. Sodium hydroxide was purchased from Joint Stock Company “Caustic”, Sterlitamak, Russia, it is a white solid with a main substance content of 98.2%. P-Toluenesulfonic acid was purchased from Component-Reagent, Moscow, Russia, it is a white solid with a main substance content of 95%. Toluene was purchased from Public Joint-Stock Company “Joint-Stock Oil Company Bashneft”, Ufa, Russia. It is a colorless liquid with a characteristic smell and a main substance content of 99%. Suspension polyvinyl chloride (PVC) (Joint Stock Company “Caustic”, Russia, Sterlitamak): industrial samples of PVC 7059M.

### 2.2. Synthesis Methods

#### 2.2.1. Synthesis of Phenoxyethol

A calculated amount of phenol and sodium hydroxide catalyst was loaded into a round-bottomed chemical reactor equipped with a thermometer, magnetic stirrer, reflux

condenser and a special device for introducing ethylene oxide into the prepared reaction mass.

The reaction mixture was heated to 130 °C and then purged with nitrogen to remove air. Further, with a working magnetic stirrer, the prepared ethylene oxide was gradually introduced. The required ethylene oxide feed rate was adjusted accordingly, so that the unreacted oxide condensed in the reflux condenser and was returned to the chemical reactor without flooding. After feeding all of the required amount of ethylene oxide, the temperature of the reaction mixture was maintained in the specified range for another 1–1.5 h and then gradually cooled to room temperature.

The catalyst was neutralized with a calculated amount of sulfuric acid, and the resulting mass was filtered. Then a fraction was distilled from the reaction mixture, boiling at 50 °C at 10 mm Hg.

### 2.2.2. The Synthesis of Butyl Phenoxyethyl Adipate

Butyl phenoxyethyl adipate was obtained by the sequential esterification of adipic acid. Initially, solvent (150 mL), adipic acid (146 g, 1 mol) and alcohol (1 mol) were loaded into the reactor in a 1:1 ratio. The heating was turned on. The required amount of catalyst was added (1% by weight). The reaction mass was bubbled with an inert gas. The heating of the reaction mixture continued for 1 h. Phenoxyethanol (1.2 mol) was then added, and heating continued for another 2 h. The reaction was monitored by the acid number of the esterificate and the amount of released water. The reaction mixture was cooled, and the target ester was isolated.

## 2.3. Methods of Analysis

### 2.3.1. Analysis of Physicochemical Parameters of Butyl Phenoxyethyl Adipate

An analysis of physicochemical characteristics was carried out in accordance with the regulatory requirements for plasticizers [58,59]. For this, the following indicators were determined: acid number, ester number and density.

### 2.3.2. Characterization of Butyl Phenoxyethyl Adipate

An analysis was performed by FTIR spectroscopy on an FTIR-8400S FTIR spectrometer (Shimadzu, Kyoto, Japan). For this, KBr tablets were prepared according to the standard procedure. The IR absorption spectra of the target product were recorded in the range 3700–450  $\text{cm}^{-1}$  at room temperature. The resolution was 4  $\text{cm}^{-1}$ , and the number of scans was 20.

### 2.3.3. High-Performance Liquid Chromatography

The study of the resulting product was carried out using HPLC (LC-10 from SHIMADZU, Kyoto, Japan) in reverse phase mode. A model refractometric detector (RIDK 101, Prague, Czech Republic) was used as a detector. To separate the components, columns (150 × 4.6 mm) filled with Separon-C18 sorbent (particle size 5  $\mu\text{m}$ ) were taken. Separation was carried out in an acetonitrile-water eluent system taken in a 67/33 volumetric ratio. The flow rate of the eluent was 0.5 mL/min. The volume of injected samples was 10  $\mu\text{L}$ . Quantitative analysis was performed using the absolute calibration method. Calibration solutions contained adipic acid, alcohols and esters.

### 2.3.4. Determination of PVC Compatibility with Plasticizer

This indicator was evaluated by the critical temperature of the dissolution of the synthesized ether in polyvinyl chloride. For this, 0.5 g of polymer was mixed with 5 g of plasticizer, and the mixture was gradually heated at a rate of 2 °C per minute, and the change in the appearance of the contents of the test tube was visually determined. The critical dissolution temperature was taken as the temperature at which PVC was completely dissolved in the studied plasticizer and the solution became transparent. The indicator was calculated as the average value of at least three measurements.

### 2.3.5. Thermogravimetric Analysis of Butyl Phenoxyethyl Adipate

Thermoanalytical studies were carried out on a TGA/DSC-1 thermal analysis device (Mettler Toledo, Uster, Switzerland).

The thermal stability of the product was investigated in a dynamic mode at a constant heating rate of 5 deg/min in the temperature range from 25 to 500 °C in air. For the experiment, the weight of the weighed portion of the sample was 5–10 mg. Crucibles with a volume of 100 µL were made of aluminum oxide. The results were processed using a computer.

### 2.3.6. Differential Scanning Calorimetry of Butyl Phenoxyethyl Adipate

DSC analysis of the product was performed on a DSC-1 instrument (Mettler Toledo, Uster, Switzerland).

The analysis was carried out in the temperature range from –50 to 150 °C in air in a dynamic mode with a constant heating/cooling rate of the sample—10 deg/min. To carry out the analysis, crucibles made of aluminum with a volume of 40 µL were used, which with a sample weighing 4–8 mg was sealed with a lid using a press. The results were processed using a computer. The final cooling temperature of the sample was –100 °C.

### 2.3.7. Determination of Glass Transition Temperature

The glass transition temperatures of PVC composites containing the developed plasticizers were determined by differential scanning calorimetry on a device DSC-1 (Mettler Toledo, Uster, Switzerland).

The glass-transition temperature was determined by DSC on a DSC-1 instrument (Mettler Toledo) in dynamic mode at a constant heating rate of 2 K/min. The analysis was carried out in the temperature range from –100 to 100 °C in air. The mass of the sample taken for measurements was 4–8 mg. For the analysis, aluminum crucibles with a volume of 40 µL were used. A weighed portion of the sample was placed in a crucible and sealed with a lid using a press. After quenching at 90 °C for 5 min, the sample was heated to 100 °C at a rate of 2 °C/min. The first heating cycle was used to remove any heat history. The glass-transition temperature of the polymer was determined from the DSC curve obtained in the second heating cycle of the sample using the supplied software. Using the tangent method, the middle of the bend (step) on the curve was determined, which was taken as the glass-transition temperature.

To assess the effect of the synthesized ether on the glass-transition temperature, PVC composition were made: 50 parts by weight of plasticizer per 100 parts by weight of PVC. The composition of the plasticizer was, in ppm, DOP: 83.3 and adipate plasticizer: 16.7.

### 2.3.8. Determination of the Melt Flow Rate

The melt flow rate (MFR) was estimated by capillary viscometry using an IIRT-AM plastometer (International Standard 1133-1:2011(E)). The MFR value corresponds to the mass of the polymer in grams flowing out of the capillary (capillary 8 mm long, 2.09 mm in diameter) of the device in 10 min at a certain temperature and pressure. The MFR of PVC composites was measured in the temperature range 160–205 °C at a load of 49N. A total of 4–5 g of the investigated PVC composition was introduced into the device heated to a predetermined temperature and kept under pressure for 5 min, then the capillary was opened, carrying out the outflow of the composition melt.

To measure the MFR parameter, at least five extruded segments of the composite were used, cut off at certain equal time intervals. The mass of the obtained extruded sections with an error of not more than 0.0001 g was measured after they were cooled. The value of the MFR parameter was calculated by the Equation (1):

$$MFR = (m * 600) / t \quad (1)$$



where  $m$ —average mass of extruded segments, g;  $t$ —time interval between two consecutive cutoffs of segments, sec.

### 3. Results

#### 3.1. Synthesis of Ethoxylated Alcohols

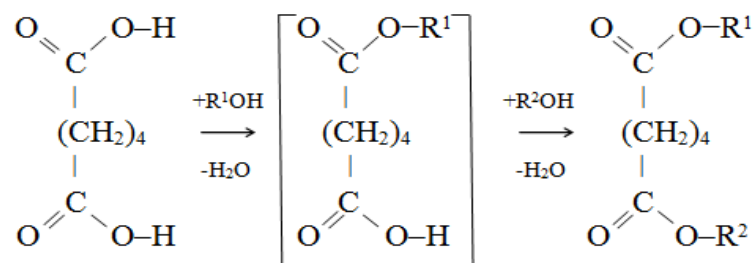
Phenoxyethanol was obtained by the reaction of ethylene oxide with phenol at an equimolar ratio.

In appearance, ethoxylated phenol of the composition  $C_6H_5O(CH_2CH_2O)H$  is a transparent liquid. Subsequently, phenoxyethanol was used to synthesize the target ester. Phenoxyethanol is a colorless oily liquid. The yield was 89% of the theoretical maximum.

The phenoxyethanol had a degree of ethoxylation  $n = 1$ : density—1.1007, refractive index—1.5314, molecular weight (calculated)—138, reaction time—1.3 h.

#### 3.2. The Synthesis of Phenoxyethyladipate

The synthesis was carried out according to Scheme 1.



**Scheme 1.** Synthesis of butyl phenoxyethyl adipate. Where  $R^1 = [CH_2-CH_2-O]-C_6H_5$ ,  $R^2 = \text{Butyl}$ .

The resulting ether is the light clear liquid.

The yield of butyl phenoxyethyl adipate was 279.2 g (86.7% of the theoretical maximum).

The physicochemical properties of butyl phenoxyethyl adipate are presented in Table 1.

**Table 1.** Physicochemical properties of butyl phenoxyethyl adipate.

Ester	Indicators			
	Molecular Weight	Acid Number, mg KOH/g	Ester Number, mg KOH/g	$d^{20}_4$
Butyl phenoxyethyl adipate (BPEA)	322	0.1	345	1.0510

#### 3.3. IR Spectra

In the synthesized compound, the stretching vibrations of the carbonyl group are shifted to the high-frequency region and are reflected in the spectrum as a strong characteristic band in the region of  $1735\text{ cm}^{-1}$  (Figure 1). There are absorption bands characteristic of the vibrations of the C–O–C ester fragment in the region of  $1156\text{ cm}^{-1}$ .

The spectrum of butyl phenoxyethyl adipate lacks an absorption band in the range of  $1685\text{--}1687\text{ cm}^{-1}$ , which is characteristic of the stretching vibrations of the carbonyl group in associates of aliphatic carboxylic acids.

#### 3.4. Determination of the Compatibility of Butyl Phenoxyethyl Adipate with PVC

For the plasticizer butyl phenoxyethyl adipate, which is a free-flowing solid product, the studies were carried out using a mixture as a plasticizer in the following ratio: DOP at 5 parts by weight and adipate ester at 1 part by weight. When determining the critical dissolution temperature, 0.05 g of PVC was dissolved in 5 mL of the mixture. The research results are shown in Table 2.

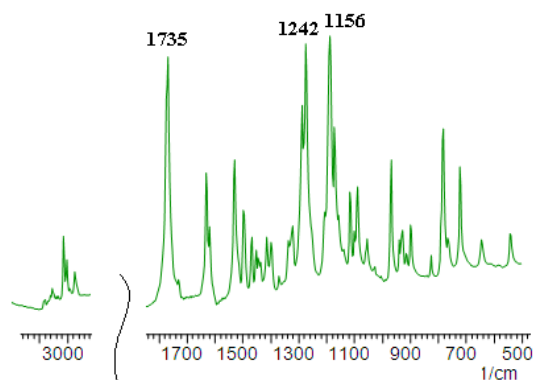


Figure 1. IR spectrum of butyl phenoxyethyl adipate.

Table 2. The results of determining the critical temperature of dissolution of PVC resin in the plasticizer.

Name	Indicators	
	$T_{cr}, ^\circ\text{C}$	$A, \%$
DOP	112.5	-
DOP + BPEA	101	111.4

The compatibility of the plasticizer with PVC resin was determined by the formula:

$$A = TDOP / Tcr \cdot 100\%, \tag{2}$$

where  $TDOP$  is the critical temperature of dissolution of the plasticizer in DOP, and  $Tcr$  is the critical temperature of the dissolution of PVC resin in a mixture of the investigated plasticizer with DOP.

### 3.5. TGA of Butyl Phenoxyethyl Adipate

In the course of thermal analysis, a sample of an industrial plasticizer, dioctyl phthalate, was used as a comparison.

To assess the thermal stability of the synthesized adipate according to the TGA thermogram, the following parameters were determined (Figure 2, Table 3):

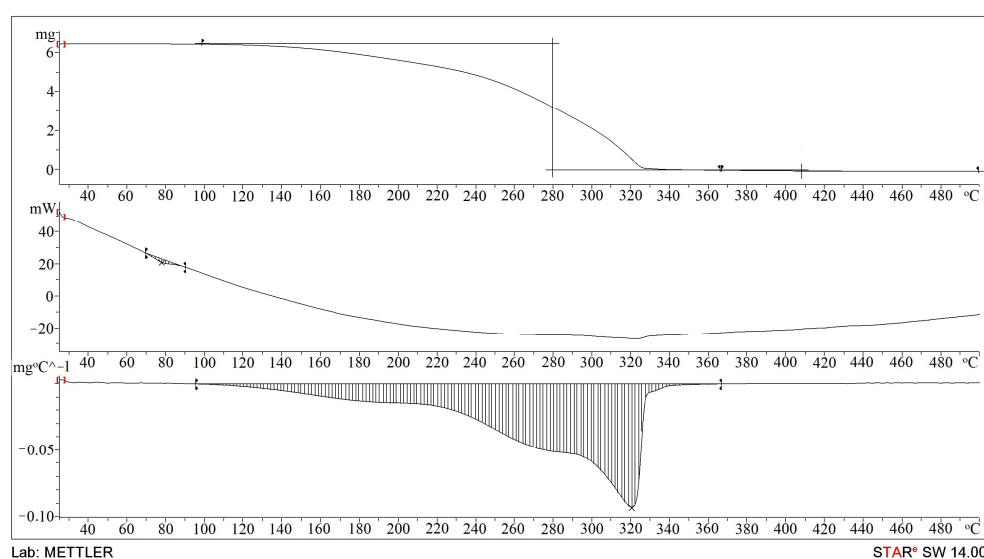


Figure 2. TGA curve of the analysis of the BPEA.

**Table 3.** Results of thermogravimetric analysis of plasticizer.

Name	$T_b$ , °C	$T_{melt}$ , °C	$T_{max}$ , °C	$\Delta m_{180}$ , %	$T_d$ , °C
DOP	132	-	285	1,0	467
BPEA	99	87	321	0.9	499

$T_b$ —temperature corresponding to the beginning of the decrease in the mass of the sample upon heating;

$\Delta m_{180}$ —reduction of the sample weight when heated to a temperature of 180 °C, corresponding to the temperature range of processing PVC compositions;

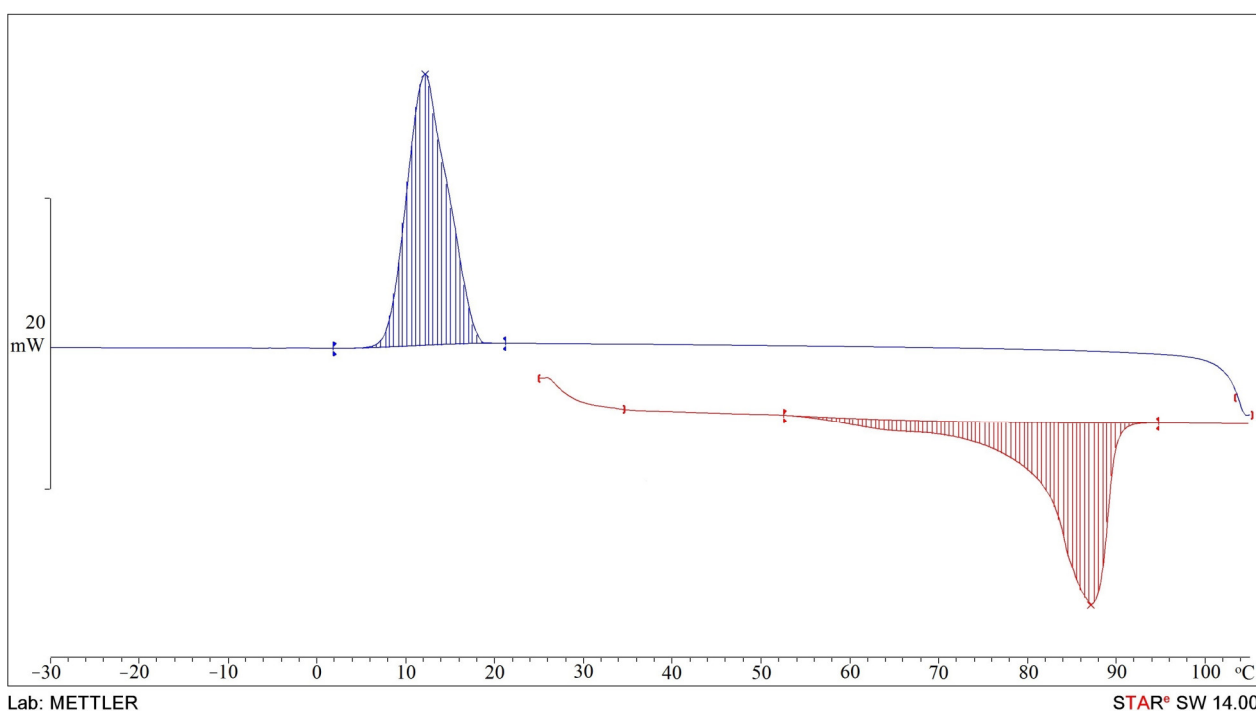
$T_{max}$ —temperature of the maximum decomposition rate of the sample;

$T_d$ —decomposition temperature.

### 3.6. DSC Analysis of Butyl Phenoxyethyl Adipate

In the course of thermal analysis, a sample of an industrial plasticizer dioctyl phthalate was used as a comparison.

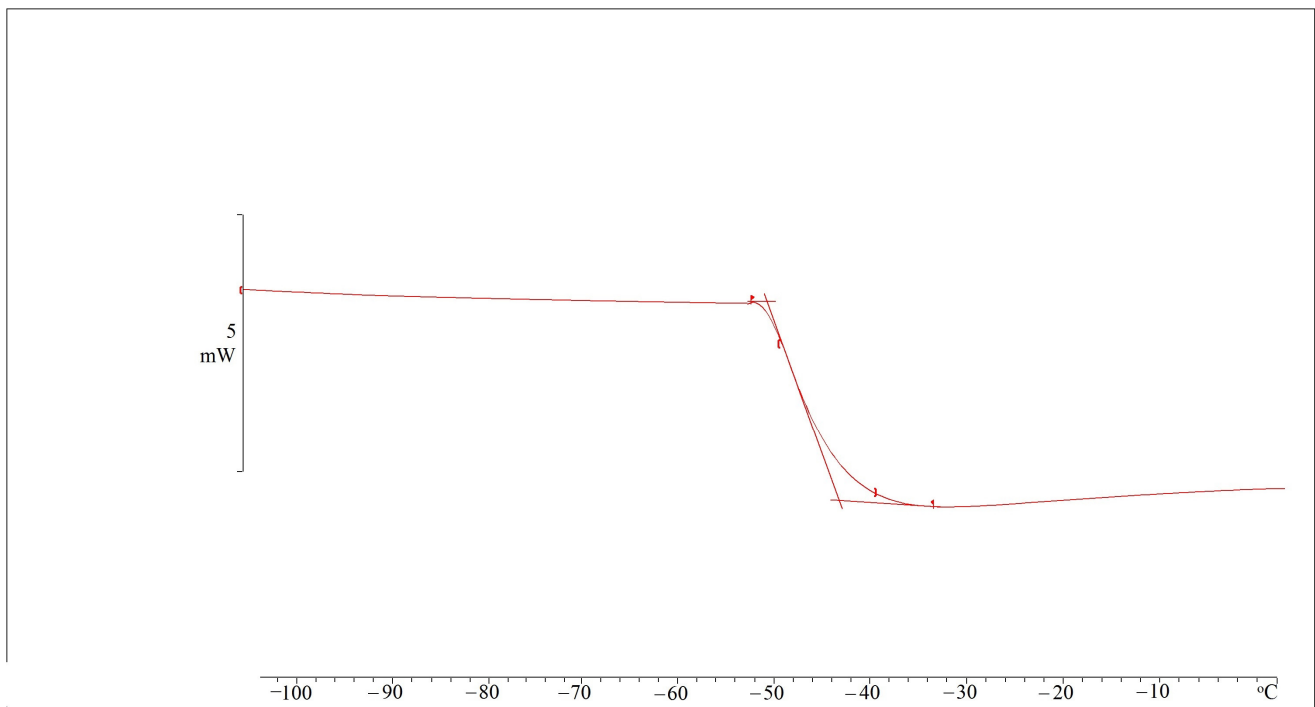
Melting and crystallization temperatures were determined for butyl phenoxyethyl adipate, which is a solid product, from the DSC curves shown in the thermograms (Figure 3, Table 4).

**Figure 3.** DSC thermogram of the BPEA.**Table 4.** DSC results of adipate ester.

Name	$T_{melt}$ , °C	$\Delta H_{melt}$ , J/g	$T_{cryst}$ , °C	$\Delta H_{cryst}$ , J/g
BPEA	87	-113	12	112

### 3.7. Determination of the Glass-Transition Temperatures of PVC Compositions

The transition of a polymer from a glassy to a highly elastic state is accompanied by an increase in the heat capacity of the polymer, which is reflected in the form of a characteristic break (step) on the DSC curve (Figure 4). The glass-transition temperature was found by the tangent method along the middle of the step corresponding to this transition.



**Figure 4.** DSC thermogram of a PVC composition containing BPEA.

Table 5 shows the results of a study of the effect of plasticizers on the glass-transition temperature of PVC compositions.

**Table 5.** Influence of plasticizers on the glass-transition temperature of PVC.

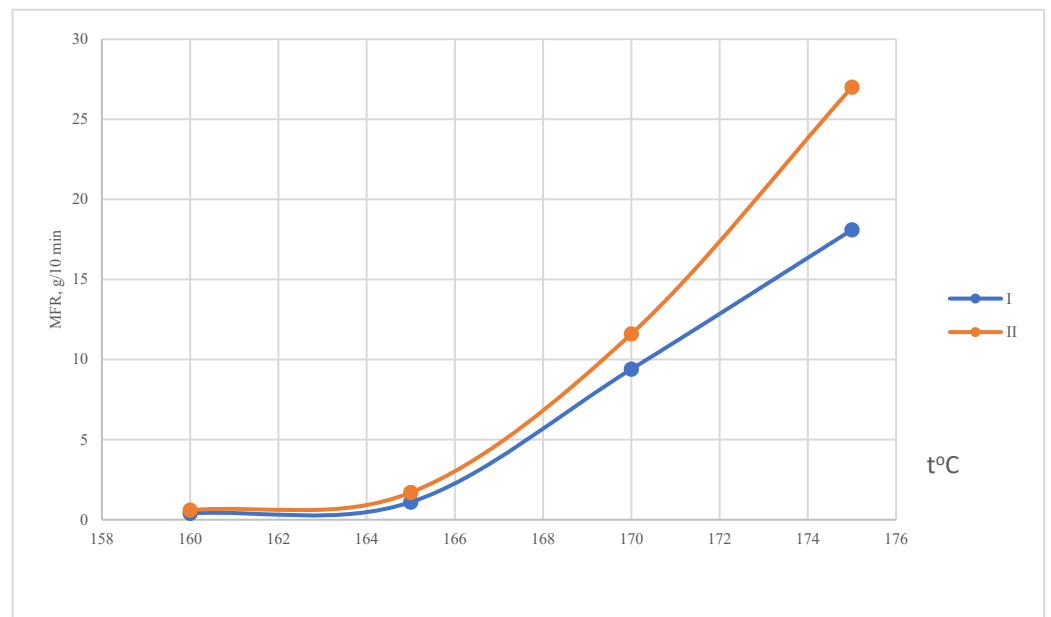
Composition	Glass-Transition Temperature, °C	$\Delta T_{gr}$ , °C
PVC	87	-
PVC + DOP (I)	-37	125
PVC + DOP + BPEA (II)	-45	132

### 3.8. Determination of the Rheological Characteristics of PVC Composition with BPEA

To assess the rheological properties of plasticized PVC composites, we used the melt flow rate (MFR) of the polymer, which is widely used in practice to characterize the processability of polymer materials and select a processing method. The studies were carried out on an IIRT-AM device in the temperature range of 160 to 205 °C.

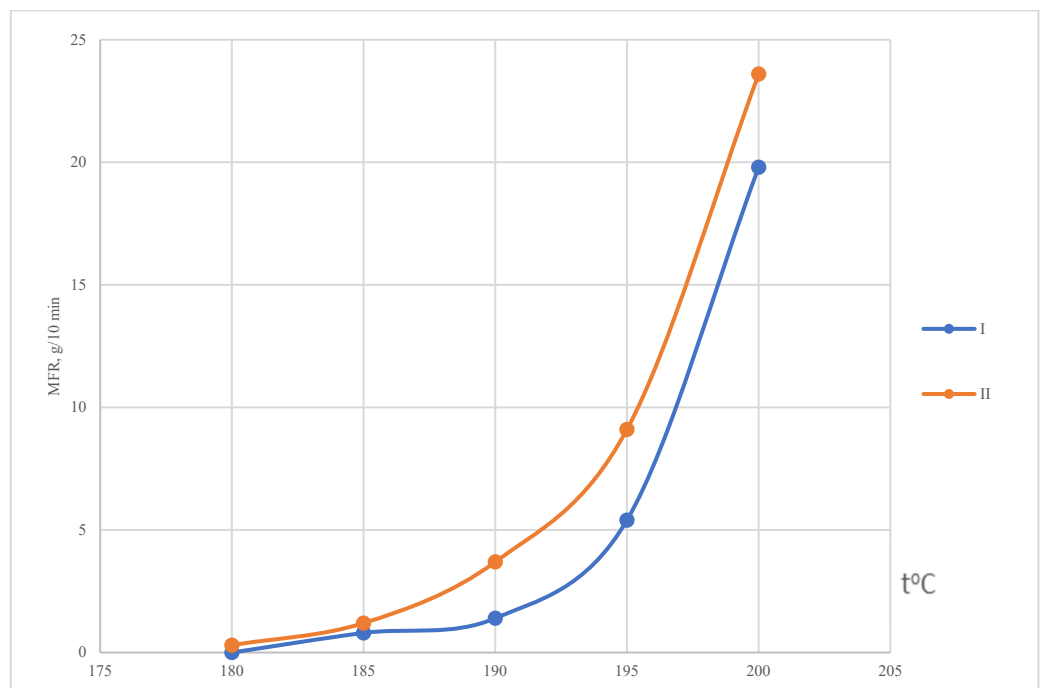
The rheological properties of PVC-compositions containing mixtures of the DOP plasticizer with the developed adipate of various compositions were studied. When preparing the PVC composition, a mixture of plasticizer was used in the ratio of DOP:adipate 5:1 (wt.).

Initially, the effect of temperature on the MFR of PVC compositions of the following composition (ppm) was investigated: PVC: 100, plasticizer: 100 and tribasic lead sulphate: 1. The composition of the plasticizer was, in ppm: DOP of 83.3 and adipate plasticizer of 16.7. The used load was 49N (Figure 5).



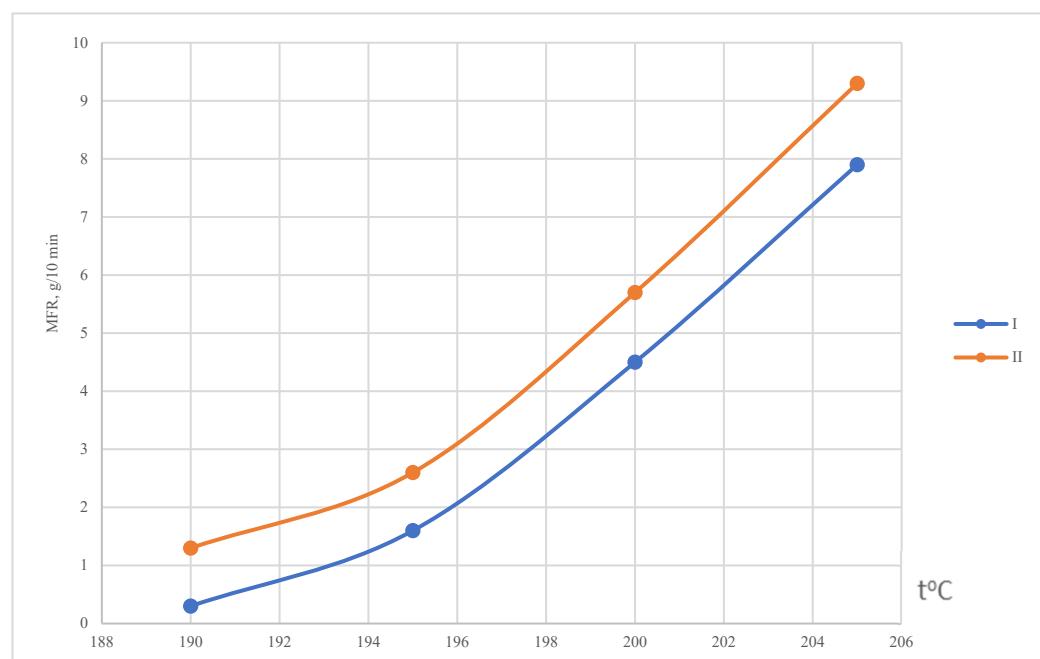
**Figure 5.** Dependence of the MFR of PVC composition on temperature. I, II—Symbols of plasticizers (Table 5).

Then the rheological characteristics of the PVC composition were studied (ppm): PVC: 100, plasticizer: 50 and tribasic lead sulphate: 1. The composition of the plasticizer, in ppm, was DOP of 83.3 and adipate plasticizer of 16.7. The used load was 49 N (Figure 6).



**Figure 6.** Dependence of the MFR of PVC composition on temperature. I, II—Symbols of plasticizers (Table 5).

We also studied the rheological characteristics of the PVC composition of the composition, in ppm: PVC of 100, plasticizer of 39 and tribasic lead sulphate of 1. The composition of the plasticizer was, in ppm: DOP of 83.3 and adipate plasticizer of 16.7. The used load was 49N (Figure 7).



**Figure 7.** Dependence of the MFR of PVC composition on temperature. I, II—Symbols of plasticizers (Table 5).

It has been experimentally established that, with an increase in temperature and plasticizer content, the melt fluidity of PVC composites, regardless of their composition, increases, and this dependence is close to exponential (Figures 5–7).

## 4. Discussions

### 4.1. Synthesis of Ethoxylated Alcohols

The literature describes the use of phenol derivatives for the plasticization of polyamides and cellulose acetate, but there are very few data on the possibility of using them as raw materials in the production of polyvinyl chloride plasticizers [60].

The synthesis of ethoxylated alcohols, including phenoxyethanol, is well studied and carried out on an industrial scale [61]. The ethoxylation of phenol was carried out according to well-known methods by the interaction of alcohol with ethylene oxide at a temperature of 120 °C in the presence of a sodium hydroxide catalyst.

The reaction proceeds according to the  $S_N^2$  mechanism and is a series-parallel addition of ethylene oxide to phenol.

The composition of the products of the ethoxylation reaction depends on the molar ratio of alcohol and ethylene oxide in the reaction mass. With an increase in the content of ethylene oxide, the degree of ethoxylation of the resulting alcohols increases.

Then the resulting phenoxyethanol was used for the synthesis of butyl phenoxyethyl adipate.

### 4.2. The Synthesis of Butyl Phenoxyethyl Adipate

Initially, the reaction flask was charged with adipic acid, solvent and alcohol butanol. The reflux of the reaction mixture was maintained until the required amount of water was released in the Dean–Stark trap. Then the alcohol phenoxyethanol was added with a slight excess relative to the acid.

### 4.3. High-Performance Liquid Chromatography

Undoubtedly, at the time of the addition of the second alcohol, the reaction mass contained monoester, dibutyl adipate and a small amount of unreacted adipic acid. When phenoxyethanol was added, transesterification of the previously formed diester was unambiguously observed, which is known from the literature on organic synthesis. Thus, the sym-

metric adipate was converted into the target unsymmetrical ester. The chromatograms obtained by HPLC have two peaks: one peak corresponds to symmetric, and the other to asymmetric.

#### 4.4. Analysis of Physicochemical Parameters of Butyl Phenoxyethyl Adipate

Butyl phenoxyethyl adipate was not separated from the symmetrical one. The obtained product was used for testing, and physicochemical analyses showed the compliance of the product with regulatory requirements for use as a plasticizer for polyvinyl chloride.

#### 4.5. Determination of the Compatibility of Butyl Phenoxyethyl Adipate with PVC

The compatibility of PVC resin with a plasticizer is one of the most important factors determining the possibility of its use in the development of a plasticized material formulation.

The plasticizer can be gradually released from the composite material by extraction, migration or evaporation. Over time, even a very low vapor pressure of the introduced plasticizer appears [62]. Therefore, the migration rate of the plasticizer from the polymer composition doubles with an increase in temperature by 7 °C [63]. The vapor pressure of the plasticizer used is for guidance only.

The migration of a plasticizer from a place with a higher concentration to a place with a lower concentration is determined by the nature of the polymer [63]. In this case, the less the interaction of the plasticizer with PVC, the lower the limit of compatibility of the plasticizer with PVC and the higher the migration value [64]. At plasticizer concentrations in PVC compositions up to 10%, the plasticizer is completely solvated by the polymer, which leads to a decrease in the detachment of the plasticizer molecules from the polymer [65].

With an increase in the amount of introduced plasticizer from 0 to 10%, migration increases insignificantly [66]. A further increase in the content of the plasticizer in the PVC composite from 15 to 35% leads to an almost linear dependence of the amount of migration on the amount of plasticizer [67]. Thus, with an increase in the content of the plasticizer, the number of fragile bonds in the polymer–plasticizer system increases, which contributes to an increase in migration [68]. The determination of the compatibility of the plasticizer with the polymer makes it possible to purposefully regulate its structure and the operational properties of the resulting material, in order to importantly prevent high volatility and the likelihood of migration to the surface of products, which negatively affects operational characteristics [69].

The determination of the compatibility of the new ethoxylated alcohol adipate with PVC was carried out according to the critical dissolution temperature of PVC resin and compatibility parameter A (%) [70]. For well-compatible plasticizers, this parameter should be greater than 100%.

The results obtained showed that the developed plasticizer butyl phenoxyethyl adipate is characterized by a high ability to dissolve polyvinyl chloride.

#### 4.6. Thermal Analysis of Butyl Phenoxyethyl Adipate

To study the possibility of the practical application of the plasticizer in the composition of PVC composites, the following indicators are important: thermal stability, melting and crystallization temperatures, enthalpy of melting and crystallization.

Thermoanalytical studies have shown that the developed adipate has a higher thermal stability in comparison with DOP. The introduction of the developed additive into the PVC composition provides a higher thermal stability during processing, which improves the manufacturability of the compounds.

#### 4.7. Determination of Glass-Transition Temperatures of PVC Compositions

At the next stage, the efficiency of the plasticizing action of the new plasticizer was assessed.

The chemical structure of polymer chains and their mutual arrangement determine the physical properties of polymers. These properties of polymers, in particular the glass-

transition temperature, are changed by introducing special substances—plasticizers—into the polymer composition during processing. The shift of the glass-transition temperature to the region of lower temperatures is commonly called plasticization. The introduction of a plasticizer into a polymer composition is important from a practical and theoretical point of view. Lowering the glass-transition temperature of the polymer with the introduction of a plasticizer makes it possible to expand the temperature range of its highly elastic state, that is, to increase its frost resistance. In addition, as a result, a decrease in the viscosity of polymer melts makes it possible to significantly facilitate their processing. It is especially important to lower the glass-transition temperature and pour point during the processing of polymers, in which these characteristics are close to or even higher than their decomposition temperature.

A decrease in the glass-transition temperature with the introduction of a plasticizer is an important criterion for assessing the effectiveness of its plasticizing action.

The results shown in Table 2 show that the sample of unplasticized polyvinyl chloride corresponds to  $T_{gt} = 87.5$  °C. The introduction of polyvinyl chloride 50 ppm plasticizer DOP led to a decrease in the glass-transition temperature of the polymer to  $-37$  °C, that is, by 124.5 °C. A significant decrease in the  $T_{gt}$  parameter was observed when 50 ppm is introduced into the polymer. The synthesized adipate totaled 133.2 °C.

#### 4.8. Determination of the Rheological Characteristics of PVC Composition with BPEA

Previously, the chemical nature of the plasticizer was not given due attention in the development of composites. It has now been proven that the plasticizing effect of the developed additive depends on the chemical structure (the nature of the atoms included in the molecule, the polarity of the bonds and the size and shape of the plasticizer molecules) and the ability of the molecule to undergo conformational changes, as well as on the thermodynamic affinity of the plasticizer for the polymer.

A comparison of the rheological characteristics of PVC compositions based on the developed BPEA plasticizer with similar compounds containing DOP showed an increase in melt flow in the temperature range (Figures 5–7), which indicates the high efficiency of the plasticizing action of the developed plasticizer, which is superior to the commercial DOP plasticizer. In this regard, this ester contributes to resource and energy efficiency when used as a PVC plasticizer.

## 5. Conclusions

The article describes the successful production of a new promising plasticizer for polyvinyl chloride, butyl phenoxyethyl adipate, by a method of sequential azeotropic esterification in one reaction vessel. The structure of the obtained compound was confirmed by FT-IR spectroscopy. Studies of the compatibility of the obtained compound with PVC showed the possibility of using it as a plasticizer: the critical temperature of polymer dissolution in ether is 101 °C compared to that for DOP, which is 112.5 °C. Thermal analysis by the TGA and DSC methods confirmed the higher thermal-oxidative stability of BPEA in comparison with DOP; the temperature of the maximum decomposition rate is 321 °C and 285 °C, respectively. The test results showed that the use of butyl phenoxyethyl adipate in the composition of the PVC composition provides a significant decrease in the glass-transition temperature of the polymer, by 132.2 °C compared to pure PVC and by 7.7 °C compared to DOP-based compounds. The study of the rheological characteristics of PVC compounds containing butyl phenoxyethyl adipate showed that the developed plasticizer has a pronounced plasticizing effect in relation to PVC, which consists of a significant increase in the melt flow of PVC compounds in the temperature range of 160–205 °C. So, for example, when the content of BPEA in the amount of 16.7 ppm per 100 ppm including PVC, the melt flow rate of the composition at 175 °C increases by 50%; when the content of BPEA in the amount of 8.35 ppm at 200 °C, it increase by 20%; when the content of BPEA in the amount of 6.5 ppm at 205 °C, it increases by 19%.



Thus, studies have shown that the new plasticizer is characterized by high technological indicators—the thermal stability and efficiency of the plasticizing action—and also contributes to an increase in the fluidity of the melt of polymer compositions and the expansion of the temperature range for processing compounds based on it. This paper also shows that the use of a new environmentally friendly plasticizer contributes to the resource and energy efficiency of PVC compound processing technologies with its content.

**Author Contributions:** Conceptualization, A.K.M.; methodology, A.K.M.; formal analysis, G.K.A.; investigation, I.N.V.; writing—original draft preparation, I.N.V.; writing—review and editing, I.N.V.; project administration, A.K.M. All authors have read and agreed to the published version of the manuscript.

**Funding:** This research received no external funding.

**Institutional Review Board Statement:** Not applicable.

**Informed Consent Statement:** Not applicable.

**Data Availability Statement:** The data presented in this study are available on request from the corresponding author.

**Conflicts of Interest:** The authors declare no conflict of interest.

## References

- Walker, T.R.; McGuinty, E. Plastics. In *The Palgrave Handbook of Global Sustainability*; Palgrave Macmillan Cham: London, UK, 2020; pp. 1–12.
- Chen, Y.; Awasthi, A.K.; Wei, F.; Tan, Q.; Li, J. Single-use plastics: Production, usage, disposal, and adverse impacts. *Sci. Total Environ.* **2021**, *752*, 141772. [[CrossRef](#)] [[PubMed](#)]
- Amulya, K.; Katakajwala, R.; Ramakrishna, S.; Mohan, S.V. Low carbon biodegradable polymer matrices for sustainable future. *Compos. Part C Open Access* **2021**, *4*, 100111. [[CrossRef](#)]
- Vinod, A.; Siengchin, B.; Parameswaranpillai, J. Renewable and sustainable biobased materials: An assessment on biofibres, biofilms, biopolymers and biocomposites. *J. Cleaner. Prod.* **2020**, *258*, 120978. [[CrossRef](#)]
- Reichert, C.L.; Bugnicourt, E.; Coltelli, M.-B.; Cinelli, P.; Lazzeri, A.; Canesi, I.; Braca, F.; Martínez, B.M.; Alonso, R.; Agostinis, L.; et al. Bio-Based Packaging: Materials, Modifications, Industrial Applications and Sustainability. *Polymers* **2020**, *12*, 1558. [[CrossRef](#)] [[PubMed](#)]
- Atmaca, N.; Atmaca, A.; Özçetin, A.I. The impacts of restoration and reconstruction of a heritage building on life cycle energy consumption and related carbon dioxide emissions. *Energy Build.* **2021**, *253*, 111507. [[CrossRef](#)]
- Rankin, W.J. *Minerals, Metals and Sustainability: Meeting Future Material Needs*; CSIRO Publishing: Boca Raton, FL, USA, 2011. [[CrossRef](#)]
- Dahiya, S.; Katakajwala, R.; Ramakrishna, S.; Venkata Mohan, S. Biobased products and life cycle assessment in the context of circular economy and sustainability. *Mat. Circ. Econ.* **2020**, *2*, 7. [[CrossRef](#)]
- Sohn, Y.J.; Kim, H.T.; Baritugo, K.A.; Jo, S.Y.; Song, H.M.; Park, S.Y.; Park, S.K.; Pyo, J.; Cha, H.G.; Kim, H.; et al. Recent advances in sustainable plastic upcycling and biopolymers. *Biotechnology* **2020**, *15*, 1900489. [[CrossRef](#)]
- Essity; IKEA; Royal DSM; Tetra Pak. *Renewable Materials for a Low-Carbon and Circular Future*; Ellen MacArthur Foundation: Isle of Wight, UK, April 2018.
- UNEP. *Single-Use Plastics: A Roadmap for Sustainability*; UNEP: Nairobi, Kenya, 2018.
- Ramakrishna, S. Circular economy and sustainability pathways to build a new-modern society. *Dry. Technol.* **2020**, *39*, 711–712. [[CrossRef](#)]
- Bucknall, D.G. Plastics as a materials system in a circular economy. *Philos. Trans. R. Soc. A.* **2020**, *378*, 20190268. [[CrossRef](#)]
- Sarkar, O.; Katakajwala, R.; Mohan, S.V. Low carbon hydrogen production from a waste-based biorefinery system and environmental sustainability assessment. *Green Chem.* **2020**, *23*, 561–574. [[CrossRef](#)]
- Ferreira-Filipe, D.A.; Paço, A.; Duarte, A.C.; Rocha-Santos, T.; Patrício Silva, A.L. Are biobased plastics green alternatives?—A critical review. *Int. J. Environ. Res. Public Health* **2021**, *18*, 7729. [[CrossRef](#)]
- Bahl, S.; Dolma, J.; Singh, J.J.; Sehgal, S. Biodegradation of plastics: A state of the art review. *Mater. Today Proc.* **2020**, *39*, 31–34. [[CrossRef](#)]
- Ali, H.; Khan, E.; Ilahi, I. Environmental Chemistry and Ecotoxicology of Hazardous Heavy Metals: Environmental Persistence, Toxicity, and Bioaccumulation. *J. Chem.* **2019**, *2019*, 6730305. [[CrossRef](#)]
- ISO 14044:2006; Environmental Management: Life Cycle Assessment. Requirements and Guidelines. International Organization for Standardization: Geneva, Switzerland, 2006.
- Evode, N.; Qamar, S.A.; Bilal, M.; Barceló, D.; Iqbal, H.M. Plastic waste and its management strategies for environmental sustainability. *Case Stud. Chem. Environ. Eng.* **2021**, *4*, 100142. [[CrossRef](#)]

20. Spierling, S.; Knüpffer, E.; Behnsen, H.; Mudersbach, M.; Krieg, H.; Springer, S.; Albrecht, S.; Herrmann, C.; Endres, H.J. Bio-based plastics—a review of environmental, social and economic impact assessments. *J. Clean. Prod.* **2018**, *185*, 476–491. [[CrossRef](#)]
21. Ramesh, M.; Deepa, C.; Kumar, L.R.; Sanjay, M.R.; Siengchin, S. Life-cycle and environmental impact assessments on processing of plant fibres and its bio-composites: A critical review. *J. Ind. Tex.* **2020**. [[CrossRef](#)]
22. Moshood, T.D.; Nawansir, G.; Mahmud, F. Sustainability of biodegradable plastics: A review on social, economic, and environmental factors. *Crit. Rev. Biotechnol.* **2021**, 1–21. [[CrossRef](#)]
23. Motaung, T.E.; Linganiso, L.Z. Critical review on agrowaste cellulose applications for biopolymers. *Int. J. Plast. Technol.* **2018**, *22*, 185–216. [[CrossRef](#)]
24. Vikhareva, I.; Aminova, G.; Mazitova, A. Ecotoxicity of the Adipate Plasticizers: Influence of the Structure of the Alcohol Substituent. *Molecules* **2021**, *26*, 4833. [[CrossRef](#)]
25. Crawford, R.J.; Martin, P. *Plastics Engineering*; Butterworth-Heinemann: Oxford, UK, 2020. [[CrossRef](#)]
26. Millican, J.M.; Agarwal, S. Plastic Pollution: A Material Problem? *Macromolecules* **2021**, *54*, 4455–4469. [[CrossRef](#)]
27. Wagner, S.; Schlummer, M. Legacy additives in a circular economy of plastics: Current dilemma, policy analysis, and emerging countermeasures. *Resour. Conserv. Recycl.* **2020**, *158*, 104800. [[CrossRef](#)]
28. White, S.R.; Moore, J.S.; Sottos, N.R.; Krull, B.P.; Santa Cruz, W.A.; Gergely, C.R. Restoration of Large Dam-age Volumes in Polymers. *Science* **2014**, *344*, 620–623. [[CrossRef](#)] [[PubMed](#)]
29. Alhanish, A.; Abu Ghaliya, M. Developments of biobased plasticizers for compostable polymers in the green packaging applications: A review. *Biotechnol. Prog.* **2021**, *37*, e3210. [[CrossRef](#)] [[PubMed](#)]
30. Maffini, M.V.; Geueke, B.; Groh, K.; Almroth, B.C.; Muncke, J. Role of epidemiology in risk assessment: A case study of five ortho-phthalates. *Environ. Heal.* **2021**, *20*, 1–14. [[CrossRef](#)]
31. Lioy, P.J.; Hauser, R.; Gennings, C.; Koch, H.M.; Mirkes, P.E.; Schwetz, B.A.; Kortenkamp, A. Assessment of phthalates/phthalate alternatives in children’s toys and childcare articles: Review of the report including conclusions and recommendation of the Chronic Hazard Advisory Panel of the Consumer Product Safety Commission. *J. Expo. Sci. Environ. Epidemiol.* **2015**, *25*, 343–353. [[CrossRef](#)]
32. Özeren, H.D.; Balçık, M.; Ahunbay, M.G.; Elliott, J.R. In silico screening of green plasticizers for poly (vinyl chloride). *Macromolecules* **2019**, *52*, 2421–2430. [[CrossRef](#)]
33. Zou, J.; Su, L.; You, F.; Chen, G.; Guo, S. Dynamic rheological behavior and microcrystalline structure of di-octyl phthalate plasticized poly (vinyl chloride). *J. Appl. Polym. Sci.* **2011**, *121*, 1725–1733. [[CrossRef](#)]
34. Jadaun, J.S.; Bansal, S.; Sonthalia, A.; Rai, A.K.; Singh, S.P. Biodegradation of Plastics for Sustainable Environment. *Bioresour. Technol.* **2022**, 126697. [[CrossRef](#)]
35. Acciaretto, F.; Pasquale, A. Di (2-ethylhexyl) adipate (DEHA), A NEW HOPE! A sustainable and promising process for the plasticisers industry. *bioRxiv.* **2020**. [[CrossRef](#)]
36. Rios, J.; Lebeau, J.; Yang, T.; Li, S.; Lynch, M.D. A critical review on the progress and challenges to a more sustainable, cost competitive synthesis of adipic acid. *Green Chem.* **2021**, *23*, 3172–3190. [[CrossRef](#)]
37. Bretschneider, L.; Heuschkel, I.; Bühler, K.; Karande, R.; Bühler, B. Rational orthologous pathway and bio-chemical process engineering for adipic acid production using *Pseudomonas taiwanensis* VLB120. *Metab. Eng.* **2022**, *70*, 206–217. [[CrossRef](#)]
38. Lang, M.; Li, H. Sustainable Routes for the Synthesis of Renewable Adipic Acid from Biomass Derivatives. *ChemSusChem* **2021**. [[CrossRef](#)]
39. Jin, X.; Liu, M.; Zhang, G.; Wang, J.; Xia, Q.; Sun, Y.; Zhou, Z.; Zhang, W.; Wang, S.; Lam, C.H.; et al. Chemical Synthesis of Adipic Acid from Glucose and Derivatives: Challenges for Nanocatalyst Design. *ACS Sustain. Chem. Eng.* **2020**, *8*, 18732–18754. [[CrossRef](#)]
40. Market Summary of Adipic Acid. Available online: <https://www.reportsanddata.com/report-detail/adipic-acid-market> (accessed on 1 November 2021).
41. Rahman, M.; Brazel, C.S. The plasticizer market: An assessment of traditional plasticizers and research trends to meet new challenges. *Prog. Polym. Sci.* **2004**, *29*, 1223–1248. [[CrossRef](#)]
42. Najafi, V.; Abdollahi, H. Internally plasticized PVC by four different green plasticizer compounds. *Eur. Polym. J.* **2020**, *128*, 109620. [[CrossRef](#)]
43. Bocqué, M.; Voirin, C.; Lapinte, V.; Caillol, S.; Robin, J.-J. Petro-based and bio-based plasticizers: Chemical structures to plasticizing properties. *J. Polym. Sci. Part A Polym. Chem.* **2015**, *54*, 11–33. [[CrossRef](#)]
44. Marcilla, A.; Garcia, S.; Garcia-Quesada, J.C. Study of the migration of PVC plasticizers. *J. Anal. Appl. Pyrolysis* **2004**, *71*, 457–463. [[CrossRef](#)]
45. Stuart, A.; McCallum, M.M.; Fan, D.; LeCaptain, D.J.; Lee, C.Y.; Mohanty, D.K. Poly(vinyl chloride) plasticized with succinate esters: Synthesis and characterization. *Polym. Bull.* **2010**, *65*, 589–598. [[CrossRef](#)]
46. Erythropel, H.C.; Dodd, P.; Leask, R.; Maric, M.; Cooper, D.G. Designing green plasticizers: Influence of alkyl chain length on biodegradation and plasticization properties of succinate based plasticizers. *Chemosphere* **2013**, *91*, 358–365. [[CrossRef](#)]
47. Erythropel, H.C.; Maric, M.; Cooper, D.G. Designing green plasticizers: Influence of molecular geometry on biodegradation and plasticization properties. *Chemosphere* **2011**, *86*, 759–766. [[CrossRef](#)]
48. de Lourdes, C.M.; Ringard, C.; Boissonnade, M.M.; Baszkin, A. Contact angles on polymer reference materials. In *The Reference Materials of the European Communities*; Springer: Dordrecht, The Netherlands, 1992; pp. 37–47.

49. Rudnick, L.R. *Synthetics, Mineral Oils, and Bio-Based Lubricants: Chemistry and Technology*, 2nd ed.; Rudnick, L.R., Ed.; CRC Press: Boca Raton, FL, USA, 2013; p. 1008. [[CrossRef](#)]
50. Jia, P.; Zhang, M.; Hu, L.; Zhou, Y. Green plasticizers derived from soybean oil for poly(vinyl chloride) as a renewable resource material. *Korean J. Chem. Eng.* **2016**, *33*, 1080–1087. [[CrossRef](#)]
51. Jia, P.; Ma, Y.; Zhang, M.; Hu, L.; Li, Q.; Yang, X.; Zhou, Y. Flexible PVC materials grafted with castor oil derivative containing synergistic flame retardant groups of nitrogen and phosphorus. *Sci. Rep.* **2019**, *9*, 1–8. [[CrossRef](#)]
52. Song, F.; Huang, C.; Zhu, X.; Liu, C.; Zhou, Y.; Jia, P. Synthesis and application of an environmental epoxy plasticizer with phthalate-like structure based on tung oil and cardanol for poly(vinyl chloride). *J. Appl. Polym. Sci.* **2021**, *138*, 50809. [[CrossRef](#)]
53. Teng, Y.; Stewart, S.G.; Hai, Y.-W.; Li, X.; Banwell, M.G.; Lan, P. Sucrose fatty acid esters: Synthesis, emulsifying capacities, biological activities and structure-property profiles. *Crit. Rev. Food Sci. Nutr.* **2020**, *61*, 3297–3317. [[CrossRef](#)]
54. Vassilev, D.; Petkova, N.; Koleva, M.; Denev, P. Optimization of ultrasound synthesis of sucrose esters by selection of a suitable catalyst and reaction conditions. *J. Chem. Technol. Metall.* **2021**, *56*, 268–274.
55. Vikhareva, I.N.; Aminova, G.K.; Abdrakhmanova, L.K.; Mazitova, A.K. Biodegradation chemistry of new adipate plasticizers. *J. Physics Conf. Ser.* **2021**, 2094. [[CrossRef](#)]
56. Sun, Z.; Mi, X.; Yu, Y.; Shi, W.; Feng, A.; Moad, G.; Thang, S.H. “All-PVC” Flexible Poly (vinyl Chloride): Nonmigratory Star-Poly (vinyl Chloride) as Plasticizers for PVC by RAFT Polymerization. *Macromolecules.* **2021**, *54*, 5022–5032. [[CrossRef](#)]
57. Aydin, I.; Kalaycioglu, I. Evaluation of Rheological Properties during Extrusion Compounding of Soft PVC Powder Blends. *Int. J. Emerg. Technol. Adv. Eng.* **2016**, *6*, 210–214.
58. *Interstate Standard 8728-88; Plasticizers. Specifications.* IPK Publishing House’s Standards of Quality: Moscow, Russia, 2003; p. 11.
59. *ISO 1675:1985; Liquid Resins and Plasticizers. Methods for Determination of Density.* FSA STANDARTIN-FORM: Moscow, Russia, 2015; p. 8.
60. Vikhareva, I.N.; Aminova, G.K.; Buylova, E.A.; Mazitova, A.K. Synthesis and investigation of properties of a plasticizer based on petrochemical raw materials. *Oil Gas Business.* **2020**, *4*, 57–73. [[CrossRef](#)]
61. Miller, S.A.; Bann, B.; Throver, R.D. The reaction between phenol and ethylene oxide. *J. Chem. Soc.* **1950**, 3623–3628. [[CrossRef](#)]
62. Semchikov, Y.D. *High-Molecular Compounds*; Publishing Center “Academy”: Moscow, Russia, 2003; p. 368.
63. Grossman, R.F. *Handbook of Vinyl Formulating*, 2nd ed.; Grossman, R.F., Ed.; Scientific Foundations and Technologies: St. Petersburg, Russia, 2009; p. 608.
64. Daniels, P.H.; Cabrera, A. Plasticizer compatibility testing: Dynamic mechanical analysis and glass transition temperatures. *J. Vinyl. Addit. Technol.* **2015**, *21*, 7–11. [[CrossRef](#)]
65. Zou, D.; Nunes, S.P.; Vankelecom, I.F.; Figoli, A.; Lee, Y.M. Recent advances in polymer membranes employing non-toxic solvents and materials. *Green Chem.* **2021**, *23*, 9815–9843. [[CrossRef](#)]
66. Navarro, R.; Perez, P.M.; Gomez, T.M.; Reinecke, H. Phthalate plasticizers covalently bound to PVC: Plasticizers with suppressed migration. *Macromolecules* **2010**, *43*, 2377–2381. [[CrossRef](#)]
67. Daniels, P.H. A brief overview of theories of PVC plasticization and methods used to evaluate PVC-plasticizer interaction. *J. Vinyl Addit. Technol.* **2009**, *15*, 219–223. [[CrossRef](#)]
68. Czogała, J.; Pankalla, E.; Turczyn, R. Recent attempts in the design of efficient PVC plasticizers with reduced migration. *Materials.* **2021**, *14*, 844. [[CrossRef](#)]
69. Krauskopf, L.G. Prediction of plasticizer solvency using hansen solubility parameters. *J. Vinyl Addit. Technol.* **1999**, *5*, 101–106. [[CrossRef](#)]
70. Halloran, M.W.; Nicell, J.A.; Leask, R.L.; Marić, M. Small molecule plasticizers for improved migration resistance: Investigation of branching and leaching behaviour in PVC blends. *Mater. Today Commun.* **2021**, *29*, 102874. [[CrossRef](#)]

Review

# Monomer Release from Dental Resins: The Current Status on Study Setup, Detection and Quantification for In Vitro Testing

Tristan Hampe<sup>1,\*</sup>, Andreas Wiessner<sup>1</sup>, Holm Frauendorf<sup>2</sup>, Mohammad Alhussein<sup>3</sup>, Petr Karlovsky<sup>3</sup>, Ralf Bürgers<sup>1</sup> and Sebastian Krohn<sup>1</sup>

<sup>1</sup> Department of Prosthodontics, University Medical Center Göttingen, 37075 Göttingen, Germany; andreas.wiessner@med.uni-goettingen.de (A.W.); ralf.buergers@med.uni-goettingen.de (R.B.); sebastian.krohn@med.uni-goettingen.de (S.K.)

<sup>2</sup> Institute for Organic and Biomolecular Chemistry, University of Göttingen, 37077 Göttingen, Germany; holm.frauendorf@chemie.uni-goettingen.de

<sup>3</sup> Molecular Phytopathology and Mycotoxin Research, University of Göttingen, 37077 Göttingen, Germany; mohammad.alhussein@uni-goettingen.de (M.A.); pkarlov@gwdg.de (P.K.)

\* Correspondence: tristan.hampe@med.uni-goettingen.de

**Abstract:** Improvements in mechanical properties and a shift of focus towards esthetic dentistry led to the application of dental resins in various areas of dentistry. However, dental resins are not inert in the oral environment and may release monomers and other substances such as Bisphenol-A (BPA) due to incomplete polymerization and intraoral degradation. Current research shows that various monomers present cytotoxic, genotoxic, proinflammatory, and even mutagenic effects. Of these eluting substances, the elution of BPA in the oral environment is of particular interest due to its role as an endocrine disruptor. For this reason, the release of residual monomers and especially BPA from dental resins has been a cause for public concern. The assessment of patient exposure and potential health risks of dental monomers require a reliable experimental and analytical setup. However, the heterogeneous study design applied in current research hinders biocompatibility testing by impeding comparative analysis of different studies and transfer to the clinical situation. Therefore, this review aims to provide information on each step of a robust experimental and analytical in vitro setup that allows the collection of clinically relevant data and future meta-analytical evaluations.

**Keywords:** materials testing; resin based dental materials; biocompatibility; monomer; bisphenol A; elution; leaching

**Citation:** Hampe, T.; Wiessner, A.; Frauendorf, H.; Alhussein, M.; Karlovsky, P.; Bürgers, R.; Krohn, S. Monomer Release from Dental Resins: The Current Status on Study Setup, Detection and Quantification for In Vitro Testing. *Polymers* **2022**, *14*, 1790. <https://doi.org/10.3390/polym14091790>

Academic Editors: José Miguel Ferri, Vicent Fombuena Borràs and Miguel Fernando Aldàs Carrasco

Received: 6 April 2022

Accepted: 25 April 2022

Published: 27 April 2022

**Publisher's Note:** MDPI stays neutral with regard to jurisdictional claims in published maps and institutional affiliations.



**Copyright:** © 2022 by the authors. Licensee MDPI, Basel, Switzerland. This article is an open access article distributed under the terms and conditions of the Creative Commons Attribution (CC BY) license (<https://creativecommons.org/licenses/by/4.0/>).

## 1. Introduction

Direct dental restorations of posterior teeth have been carried out with various materials, such as dental amalgam or composite resin [1]. Despite the successful application due to the high functional durability of dental amalgam for more than 150 years with a small number of reports on adverse effects [2,3], amalgam is being phased out due to the rise of safety concerns and the restriction of amalgam in some regions of the world [4–6]. Improvements in mechanical properties and a shift of focus towards esthetic dentistry led to the application of dental resins in various areas of dentistry [7,8], e.g., as restorative composites, bonding agents, resin-based cements, fissure, and root canal sealers as well as temporary crowns and bridges [9–12]. The specific monomer composition of dental resins is tailored to the particular area of application [13] and generally consists of one or more monomers, mostly bisphenol A diglycidyl methacrylate (Bis-GMA) and/or urethane dimethacrylate (UDMA) in addition to co-monomers, which are predominantly triethylene glycol dimethacrylate (TEGDMA) and 2-hydroxyethyl methacrylate (HEMA) [14]. Typical Bis-GMA/TEGDMA mixtures have a ratio between 60 and 80 wt.% Bis-GMA and 20 and 40 wt.% TEGDMA [15–17]. In combination with UDMA, less TEGDMA is required and most ratios between UDMA and Bis-GMA are possible, even complete replacement [15,17].

Bis-GMA is either the reaction product of bisphenol A (BPA) and glycidyl methacrylate or methacrylic acid and diglycidyl ether of bisphenol A (BADGE or DGEBA) [18]. Due to its low shrinkage, good mechanical properties, and excellent adhesion to enamel [19], Bis-GMA is the base monomer of most dental resins [20]. The central core of Bis-GMA is formed by a phenyl ring and two pendant hydroxyl groups, which are responsible for its extremely high viscosity and low mobility [21].

UDMA is the reaction product of 2-hydroxyethyl methacrylate and 2, 4, 4- trimethyl-hexamethylenediisocyanate and was developed by Foster and Walter in 1974 [22]. Instead of a phenol ring UDMA has an aliphatic urethane chain, which leads to higher flexibility and lower viscosity and results in higher mobility and a greater degree of conversion [23,24]. Due to these advantageous properties and health concerns regarding the release of bisphenol A (BPA) and its derivatives, more and more manufacturers substitute Bis-GMA with UDMA and introduced BPA-free composites to avoid the release of BPA and its derivatives [25–27].

Bis-GMA and UDMA are combined with a low-viscosity monomer such as TEGDMA, which improves the degree of conversion, filler loadings, and clinical handling [28]. TEGDMA is the reaction product of two molecules of methacrylic acid and triethylene glycol [18]. Its weaker polar hydrogen bonds lead to greater flexibility and its small size and its high number of double bonds increase conversion [29,30]. TEGDMA is only used as a co-monomer because its hydrophilicity amplifies undesirable properties like water sorption and polymerization shrinkage [31].

HEMA is a common co-monomer in dental adhesives and is characterized by its small dimensions and polar properties [28]. The major advantage of HEMA, especially in dental adhesives, is its ability to improve the miscibility between hydrophilic and hydrophobic monomers and thus dentine adhesion [32].

However, as of today, studies on the short-term release of compounds from the polymer network of composite resins are poorly comparable, studies on the long-term release are still rare, and degradation products are often not measured [33–36]. Due to its role as an endocrine disrupter of different metabolic pathways even in low concentrations [37], the release of bisphenol A (BPA) is of great interest in recent literature [38]. BPA interacts with the estrogen receptor and mimics the behavior of the natural hormone estradiol [39–41]. Furthermore, it is known that BPA exhibits potential cancerogenic, embryotoxic, and metabolic effects [40,42,43]. However, pure BPA is not being used as a monomer in dentistry, but rather as a reagent for the synthesis of derivatives like Bis-GMA, and thus only small amounts are leachable due to possible contaminations from the use of BPA derivatives [38,44]. Even though BPA is at the center of current research, cytotoxic, genotoxic, proinflammatory, and even mutagenic effects have been shown for various compounds used in dental resins [45–52]. Considering the advancements and changes in the composition of resin composites [53], monomers, as well as further compounds, e.g., additives eluting from dental resins, should be investigated. The biocompatibility of dental materials may be evaluated by using various *in vivo* or *in vitro* techniques [54] and the collection of reliable data depends on the application of adequate detection and quantification methods [55]. As a result of varying clinical situations occurring *in vivo*, these studies show a large spread width of released monomer concentrations [56–59]. Therefore, it has been established in biocompatibility testing to verify the results of standardized *in vitro* studies by *in vivo* trials [60]. The general setup of *in vitro* studies on the leachability of monomers from dental resins consists of an experimental part to produce an eluate by incubating resin samples in an extraction medium, and an analytical part to identify and quantify monomers within the eluate. However, as of today, comparative analysis of current *in vitro* studies is limited due to heterogeneous sample design as well as the diverse application of analytical methods with various extraction media and not standardized observation periods [34]. However, without a systematic meta-analysis, the impact of monomer release from dental resins on patient health remains unclear. The present review aims to provide information on each step of the experimental and analytical setup regarding the *in vitro* identification and quantification of eluting compounds from dental resins to develop a basis for future meta-analytical evaluations.

## 2. Sample Design

In current literature, samples are commonly disc-shaped and of various sizes, while the removal of the oxygen inhibition layer is either not performed or not mentioned [17,61–65]. However, the surface area and the oxygen inhibition layer influence the amount of eluting monomers heavily, and therefore sample design is a limiting factor in current research. ISO 4049 specifies the requirements for dental polymer-based restorative materials, and many authors recommend complying with ISO 10993-12 for the sample design [62,66–69]. ISO 10993-12 regulates sample preparation and reference materials for the biological evaluation of medical devices and recommends regular-shaped samples with a defined surface area [70]. Additionally, ISO 10993-12 specifies in dependency of the surface area the corresponding solvent volume and as a consequence the extraction ratio (Table 1) [70]. To our knowledge, there are no studies on the effects of different extraction ratios on the release of specific monomers, but it is known that the extraction ratio affects the amount of released monomers from the polymer matrix strongly [34,71,72]. The lack of studies with a uniform extraction ratio hinders meta-analytical analysis and limits the comparison to common restoration sizes [34]. Therefore, future studies should comply with ISO 10993-12.

**Table 1.** Recommended extraction ratios according to ISO 10993-12.

Thickness (mm)	Extraction Ratio $\pm$ 10%
$\leq 0.5$	6 cm <sup>2</sup> /mL
$> 0.5$	3 cm <sup>2</sup> /mL
Irregular shaped sample	0.1–0.2 g/mL, 6 cm <sup>2</sup> /mL

Besides the extraction ratio, the oxygen inhibition layer needs to be considered when evaluating the release of monomers from the polymer network. The oxygen inhibition layer contains unpolymerized monomers [73,74], which can be eluted, and especially TEGDMA concentrations seem to be elevated [71]. Therefore, the removal of the oxygen inhibition layer leads to fewer eluted monomers as well as reduced cytotoxicity, and thus the removal of the oxygen inhibition layer or prevention of its formation is recommended in clinical practice [75,76]. However, in many studies on the leachability from dental resins, the oxygen inhibition layer was either not or ineffectively removed [61–65]. Recent literature shows that water-spray or ethanol treatments are ineffective methods to remove the oxygen inhibition layer [77]. For research purposes, nitrogen [78–80], argon [81,82], or carbon dioxide [83] atmospheres have been used to produce samples without an oxygen inhibition layer. Even though these methods are effective, they are costly and not applicable in clinical practice. Effective methods that are applicable in vitro and in vivo include methods that prevent oxygen contact, e.g., glycerin gel or mylar strips, and mechanical methods, e.g., specimen polishing with a defined removal of 0.2 mm [84–86]. Recent studies show that these methods are well suited for the in vitro investigation of the release of monomers from dental resins [35,66,87–89]. Consequently, the removal or prevention of the oxygen inhibition layer should be included in the sample preparation process and based on the clinical workflow. Besides the oxygen inhibition layer, the surface roughness may influence monomer and BPA elution, but to our knowledge, there are no studies on the effect of surface roughness on the monomer release. Therefore, we recommend polishing procedures corresponding to the standard clinical workflow.

## 3. Selection of the Extraction Medium

Various solvents, such as water, ethanol-water mixtures, methanol, acetonitrile, tetrahydrofuran, cell culture media, artificial saliva, and collected saliva, have been used as extraction media in studies investigating the in vitro release of monomers from the polymer matrix [9,17,61,64,90–93]. However, interactions with the extraction medium due to substance-specific properties, such as molecular size and other chemical characteristics, significantly alter elution [94]. Literature assumes that in vivo conditions are somewhere

between the less aggressive water solvent and the more potent ethanol solvent [65]. Hence, the US Food and Drug Administration (FDA) recommends a 75 vol. % ethanol/water solution which is supposed to be a good food simulator (alcoholic beverages, fruits, and syrup) and therefore clinically relevant [9]. Due to this recommendation, many studies investigating the leachability of monomers from dental resins used a 75% vol. ethanol/water solution [9,33,95–98]. However, the solubility parameter of ethanol and Bis-GMA is almost equal, which leads to the softening of resins, with maximum softening reached at 75% vol. ethanol/water [99–101]. Ethanol/water solutions penetrate the polymer matrix, especially of Bis-GMA-based resins, and degenerate it irreversibly by expanding the space around the polymers and creating soluble units [94,101]. Considering these findings, it is questionable whether using a 75 vol. % ethanol/water solution results in clinically relevant data [71]. Supporting this hypothesis, many studies found significantly elevated Bis-GMA, TEGDMA, and UDMA levels in 75% vol. ethanol/water solutions compared to artificial saliva [36,72,102,103]. BPA was only detected in samples immersed in a 75% vol. ethanol/water solution [72,102,103]. In addition to elevated monomer concentrations, monomer elution is prolonged in 75 vol. % ethanol/water solutions [35]. Considering these findings, 75 vol. % ethanol/water solutions cannot be recommended to simulate the intraoral environment for the investigation of the leachability of dental monomers. Similarly, immersion in methanol leads to an increased monomer release compared to water or artificial saliva and should be therefore also avoided [92]. Besides alcohol-based solutions, cell culture media were used as extraction solvents, but it was shown that they may lead to false-negative results especially regarding TEGDMA detection due to the binding of albumin to it [17]. Instead, water, artificial saliva, or human saliva should be favored as extraction media. Literature shows similar concentrations of released compounds when comparing distilled water to artificial saliva [17,103,104]. In aqueous environments, mainly hydrophilic molecules of small sizes, such as TEGDMA, elute, while long-chain hydrophobic molecules, such as BisGMA, are hardly released [105,106]. Comparing the eluates from samples incubated in distilled water, artificial saliva, and collected saliva, the latter contains lower monomer levels, as proteins contained in collected saliva bind eluting monomers [104]. When using collected human saliva, the probands must not have restorations [107] and blank samples for the analytical procedure are needed to avoid false positives [91]. In conclusion, the most comparable results can be achieved with collected saliva, but blank samples and a robust analytical procedure are required. Moreover, water and artificial saliva are an option, but in contrast to former assumptions, they may even present slightly increased concentrations of eluted monomers. Further studies on the impact of the composition of human saliva on the elution from dental resins and the effect of protein-bound monomers on the metabolism are necessary.

#### 4. Incubation Parameters

The amount of eluted compounds highly depends on incubation parameters, such as the incubation time, buffering systems, solvent, monomer saturation, and pH value [71,108–110]. Under extreme temperature (100 °C) and an alkaline (pH 13) or acid (pH 1) environment, BPA is released due to hydrolytic degradation of Bis-GMA or bisphenol A diglycidylether (BADGE) [111]. Particularly very alkaline conditions seem to promote BPA elution [25]. A long-term study on the leakage of composite resins found that the effect of pH varied among monomers: more BPA was eluted at pH 8 than at pH 4 and 6, while the elution of TEGDMA followed the opposite trend [112]. Considering these findings, future studies on the elution from dental resins should report incubation parameters, especially the pH and temperature of incubation, whereas incubation at 37 °C is recommended to simulate *in vivo* conditions [34].

In some studies, samples are incubated after a post-irradiation cure, usually 24 h in the dark [61,113–115]. Incubation after the post-irradiation cure leads to lower concentrations of released substances [105]. Since direct incubation corresponds to the clinical workflow, it is recommended [114,116].

Studies on the long-term release from dental resins need to take salivation of the oral environment into account and must refresh the extraction medium to avoid saturation, which might lead to the underrepresentation of *in vivo* conditions [97,117]. This solvent refresh is usually performed once per week [33,35,94]. Furthermore, the stability of dental monomers in water, artificial saliva, or collected saliva must be considered, especially in long-term studies. Presumably, passive hydrolysis reactions lead to the degradation of monomers in water [118]. As a consequence, many studies showed decreasing monomer concentrations when successive incubation periods were analyzed [17,61,103,119,120]. This was not observed or observed to a lesser extent in other extraction media, such as ethanol/water mixtures or lactic acid [103,119]. Passive and/or enzyme-catalyzed hydrolysis, such as in collected saliva, cleaves the ester bonds of the methacrylate groups of BisGMA, TEGDMA, and UDMA [52,121–123]. Initial decreases in concentrations were observed after only six hours of incubation [103]. Due to the incomplete hydrolysis of dental monomers, molecules with different numbers of cleaved methacrylate groups may be present simultaneously [122,124]. These hydrolysis products each have different chemical properties as well as molecular masses, and thus detection requires adjustments to the analytical method [124,125]. In conclusion, the analysis of long incubation intervals could lead to the underrepresentation of the *in vivo* monomer release. Therefore, degradation products should be measured additionally [124,126,127]. Regular refreshment of the extraction medium and the cumulative determination of monomer concentrations are recommended. Cumulative analysis has already been performed in several studies [35,102,128].

In summary, the objective of *in vitro* incubation is the simulation of *in vivo* conditions. Therefore, incubation parameters should be based on the intraoral environment, the extraction medium should be refreshed regularly, and samples should be incubated directly. For future meta-analytical evaluation and comparability between studies, a 24-h incubation period should be included in every study on the elution from dental resins [34].

## 5. Analytical Setup

A wide range of techniques has been used to detect and quantify substances eluting from dental resins [118]. Many older methods such as infrared spectroscopy are nowadays regarded as outdated since the signals are not molecule-specific, the interpretation of spectra is difficult, and quantification unreliable [34]. Nowadays, the analytical setup consists of the separation of the eluate by chromatography followed by subsequent detection of the eluted compounds by optical methods or mass spectrometry. The FDA and recent literature recommend high-performance liquid chromatography (HPLC) and gas chromatography (GC) as separation methods [34,66,129]. Despite the recommendation of GC [66,129] and its application in various studies [107,109,112,130], recent literature showed that the high operating temperatures of GC lead to the overestimation of the leakage of BPA due to thermal degradation of Bis-GMA [64]. Bannach et al. [131] investigated the thermal stability of Bis-GMA, ethoxylated bisphenol A dimethacrylate (Bis-EMA), UDMA, and TEGDMA and found that thermal decomposition starts between 178 and 297 °C, which corresponds to the temperatures between 280 and 400 °C occurring during GC [109,130]. Consequently, GC is not capable of detecting Bis-GMA, Bis-EMA, or UDMA, but only corresponding thermal degradation products [56,132–134]. Due to the thermal degradation of BPA derivatives, BPA was found by GC in all samples regardless of the solvent, but HPLC-MS detected BPA only in samples immersed in methanol [64]. HEMA is a potential degradation product of UDMA, and therefore detection and differentiation between them are hindered [109]. Additionally, GC analysis of analytes from aqueous samples requires time-consuming sample preparation [135]. In conclusion, GC should be avoided for the separation of monomers with a high molecular weight in eluates from dental resins due to their thermal instability [136]. Instead, HPLC is the recommended separation method for the analysis of eluting monomers from dental resins. However, GC can be applied for low molecular weight, volatile, and thermally stable substances, e.g., additives contained in dental resins [133,136],

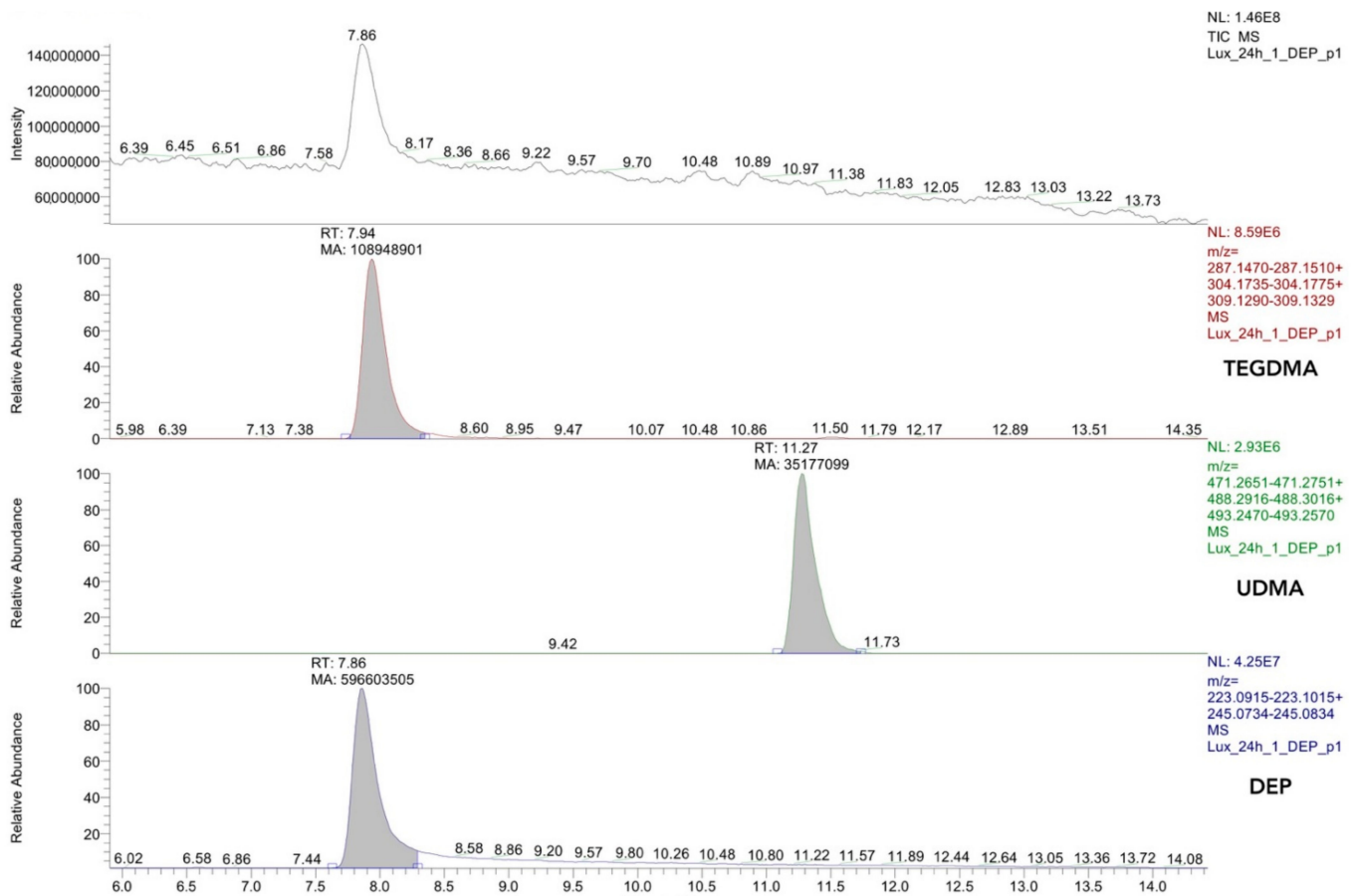


as it allows accurate quantitative determination within complex mixtures, including trace amounts of compounds down to parts per trillion in some cases [137].

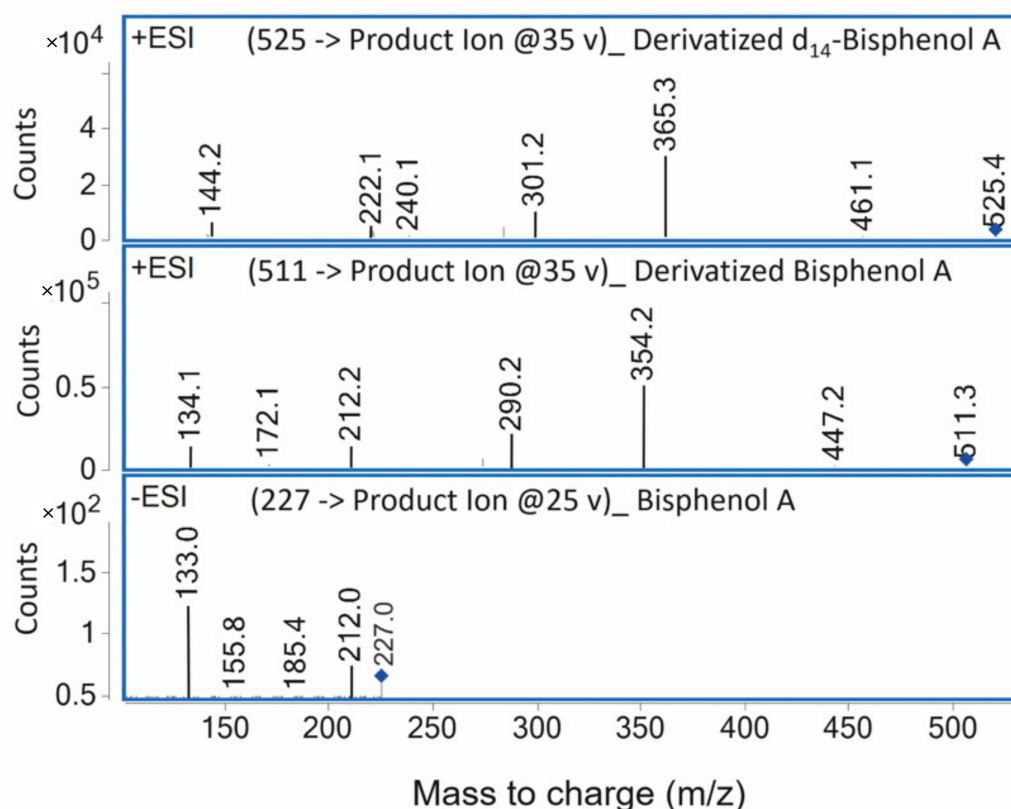
Most light absorption spectroscopy (UV/Vis) and mass spectrometry (MS) detectors coupled with HPLC are suitable for the identification and quantification of compounds in the eluate [138]. UV/Vis detectors are available in many analytical laboratories due to their easy use, low cost, and near-universal field of application [138]. It is known from other scientific fields that the sole use of UV/Vis can lead to the overestimation of analyte concentrations due to the presence of coeluting substances [139–141]. Hope et al. found that the wrong identification of a coeluting substance, probably a photoinitiator, in eluates from an experimental dental resin led to the overestimation of BPA levels by 30-fold when comparing UV/Vis to MS detection [66]. This discrepancy between UV/Vis and MS detection was also found in a recent study on the monomer elution from temporary crown and bridge materials [120]. Therefore, the sole identification and quantification by UV/Vis are not recommended and more sensitive and specific methods like MS should be used. MS is a very sensitive and selective method for the detection of unknown substances and degradation products in eluates from cured as well as uncured resins [67]. In this context, electrospray ionization (ESI), atmospheric pressure chemical ionization (APCI), and atmospheric pressure photoionization (APPI) are available for the ionization of nonvolatile and thermally unstable analytes [142]. Advanced MS detectors coupled with HPLC (HPLC-MS) allow tandem mass spectrometric analysis (HPLC-MS/MS), which increases the specificity of the analysis by the fragmentation of a pre-selected ion and specific detection of selected fragmentation products [143]. In recent years, high-resolution mass spectrometry (HRMS) following HPLC separation has proven to be a viable alternative due to high mass accuracy and sensitivity even in full-scan mode [144]. Even more information about the molecular structure can be obtained by the combination of HRMS and MS fragmentation [145]. Accordingly, HPLC coupled with MS, preferably HRMS and/or tandem MS, is the recommended analytical method for the analysis of monomers eluting from dental resins.

## 6. Detection/Qualitative Analysis

An essential part of a reliable study design for the detection of monomers is a clear definition of the analyte and the estimation of the limit of detection (LOD), which should be as low as technically achievable. In a typical HPLC-MS analysis with electrospray ionization, the retention time together with the mass of the molecular ion and in tandem MS as well as the fragmentation spectrum of the molecular ion are used to identify the analyte (Figures 1 and 2).



**Figure 1.** HPLC-MS Chromatogram of a Luxatemp Automix Plus (DMG Chemisch-Pharmazeutische Fabrik, Hamburg, Germany) sample immersed in HPLC grade water with diethyl phthalate (DEP) as an internal standard. At the top, the chromatogram and then, from top to bottom, the extracted ion chromatograms of TEGDMA, UDMA, and the internal standard DEP, respectively. Definitive peak identification is accomplished by the relative abundance of the corresponding molecular mass. This chromatogram was prepared for a study on the monomer elution from resin-based temporary crown and bridge materials [120].



**Figure 2.** Tandem mass spectrometry fragmentation spectra of derivatized isotope-labeled BPA (**top**), derivatized unlabeled BPA (**middle**), and underivatized BPA (**bottom**). The spectra were obtained by HPLC-MS/MS with negative ionization for native BPA and positive ionization for BPA derivatized with pyridine-3-sulfonyl chloride. The unique and most abundant product ion is highlighted by a blue square. This mass spectrum was prepared for a study on the monomer elution from resin-based temporary crown and bridge materials [120].

The fragmentation spectrum of a tandem MS analysis contains fragmentation ions, each of which has a separate peak in the mass spectrum [146]. The most abundant, unique fragmentation ion of an analyte is used for quantification (quantifier ion), and less abundant, unique ions are used for detection (qualifier ions) [147–149]. By analyzing more than one qualifier ion, confidence in detection can be increased [150]. For the analysis of unknown compounds, mass spectrometry allows the use of libraries with mass spectra collected from literature, like the NIST mass spectral library (National Institute of Science and Technology, Gaithersburg, MD, USA), which contains among other substances dental compounds [56,151,152]. Commercially available and open-source libraries help to identify unknown substances [153]. However, these libraries mostly contain spectra from GC-MS obtained after ionization with “hard” ionization techniques [154]. Due to the lower reproducibility of retention properties in HPLC instruments, the availability of libraries with spectra obtained by HPLC-MS with soft ionization techniques is limited [154–156]. Therefore, older studies on the release of dental monomers using libraries, e.g., the NIST applied GC-MS analysis [56,151,152]. However, the identification of an unknown compound should not solely rely on the comparison between a library and an experimental mass spectrum because co-eluting compounds may compromise the fragmentation spectra of the analyte, and library spectra do not reflect experimental conditions [144]. Therefore, the regulation 2002/657/EC issued by the European Union recommends the use of calibration solutions and an internal standard to validate the qualitative analysis [157]. For a clear definition of the reference substances, it is best practice to report their molecular masses and unique Chemical Abstract Service Registry Numbers (CAS Registry Number). This

is especially important in dental research, as recent research shows that the trivial name UDMA is used for a variety of molecules, and Bis-EMA is used for molecules of different degrees of ethoxylation [55,130].

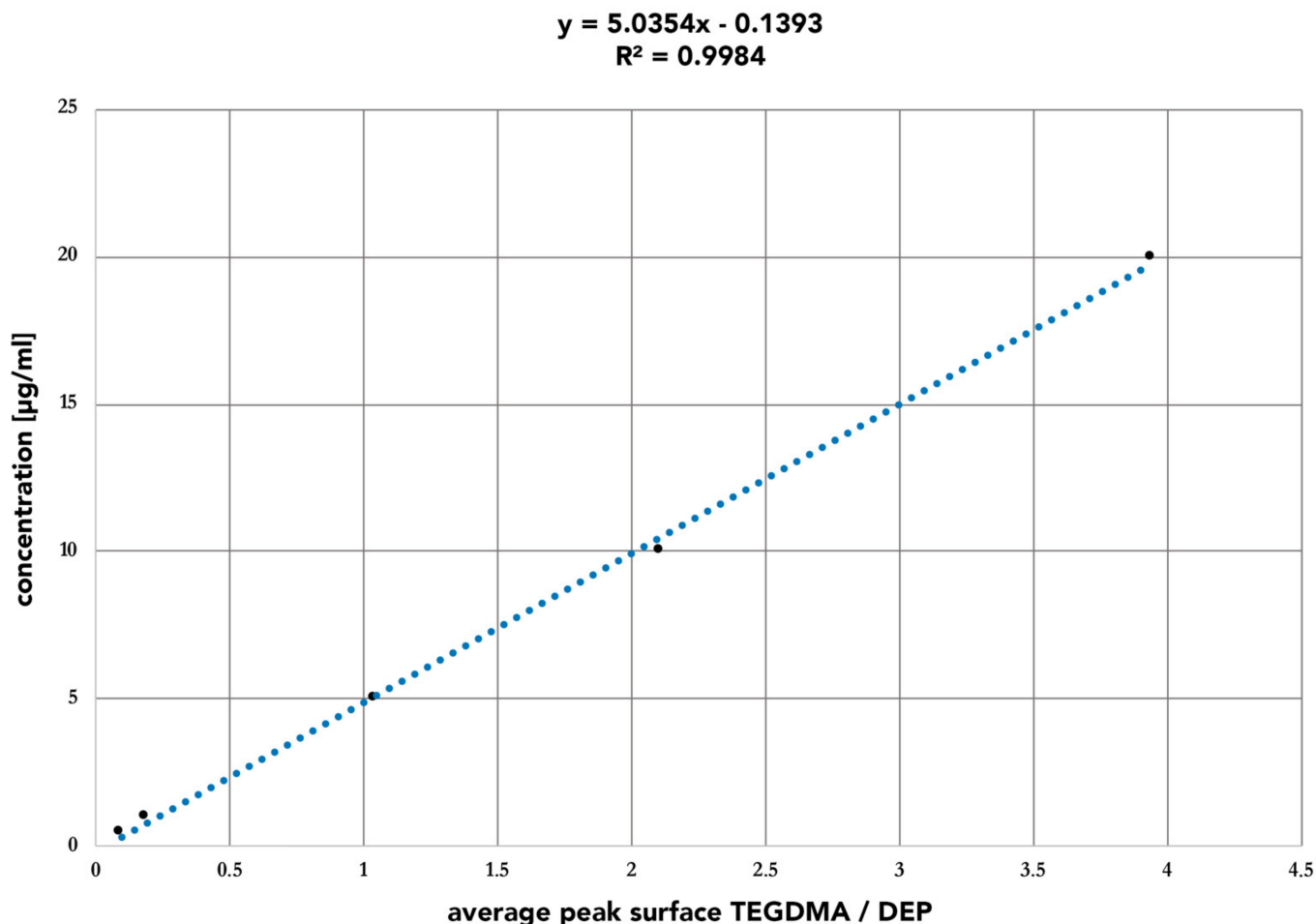
Furthermore, the LOD is essential for the assessment of the reliability of detection because compounds present at concentrations below the LOD cannot be detected though may be released and have a toxicological impact [158]. According to the International Union of the Pure and Applied Chemistry (IUPAC), LOD is defined as the lowest reliably detectable concentration of an analyte [159]. Various methods for determining the LOD can be found in the literature. The most common approach is the calculation based on the signal-to-noise ratio, but an experimental determination by a dilution series is also possible [160]. If the analyte is available, the Joint Research Centre of the European Commission recommends using 3.9 times the quotient of the standard deviation of the blank (pseudo-blank) signals and the slope of the calibration curve for the determination of a reliable LOD [161]. Therefore, LOD can be improved either by the reduction of noise or by the increase of signal strength [162]. Common ways to reduce noise are sample clean-up, temperature control of the column, and purity of the reagents and solvents [162]. Consequently, lower LODs are achievable with HPLC grade extraction media than with other media such as collected saliva. The signal strength can be increased by the injection of larger quantities of the sample, a more sensitive detector, and the choice of the mobile phase and column to change peak width [162]. Another way to improve the LOD might be derivatization. Recently, it was shown that the derivatization of BPA in composite eluates allows mass spectrometric detection in the more sensitive positive ESI mode and therefore leads to lower LODs [120,163].

As most studies on the leachability from dental resins do not report the LOD, only the positive and not the negative results can be interpreted [34]. The LODs in the current literature for Bis-GMA range from 0.07  $\mu\text{g}/\text{mL}$  to 1.18  $\mu\text{g}/\text{mL}$  [86,89,164,165] and for BPA from 0.003  $\mu\text{g}/\text{mL}$  to 0.075  $\mu\text{g}/\text{mL}$  [66,165,166]. The LODs for UDMA are reported between 0.075  $\mu\text{g}/\text{mL}$  and 0.63  $\mu\text{g}/\text{mL}$  [86,89,164,165]. Respective values for TEGDMA vary between 0.022  $\mu\text{g}/\text{mL}$  and 0.808  $\mu\text{g}/\text{mL}$  [86,89,164,165,167] and for HEMA between 0.022  $\mu\text{g}/\text{mL}$  and 2.43  $\mu\text{g}/\text{mL}$  [86,87,164,165,167].

## 7. Quantitative Analysis

For reliable quantitative analysis, precise calibration is vital. Calibration methods reconstruct the dependence between the analytical signal and the concentration of internal and/or external standards, which correspond to the relationship between the signal and the concentration of the analyte in the sample [168,169]. This relation is used to prepare a calibration curve and the data are fitted by a mathematical function, which usually is linear regression [170]. Calibration can be performed using single-point, double-point, or multi-point calibration, whereas today only multi-point calibration is considered acceptable [169]. For multi-point calibration, 5–10 concentrations of each standard in the range of 0–150% or 50–150% of the concentration likely to be encountered are analyzed in duplicates or triplicates [171–173]. Depending on the expected eluted concentrations, most studies analyzed a series of uniformly distributed standard solutions with concentrations between 0.005  $\text{ng}/\text{mL}$  and 1000  $\mu\text{g}/\text{mL}$  [64,89,107,120,164,171–176]. When linear regression is used, the linearity of the calibration curve is often assessed by the correlation coefficient  $r$  or the determination coefficient  $r^2$  [177]. The latest guideline by the clinical and laboratory standards institute (CLSI) considers a correlation coefficient  $r \geq 0.975$  or  $r^2 \geq 0.95$  as sufficient evidence for linearity [178]. However, it was shown that even in some cases with  $r > 0.99$  linearity is not always fulfilled and thereby a plot of residuals and possibly a lack of fit or Mandel's fitting test can be performed to verify a normal distribution of calibration points around the line, which is expected in cases of a true linear fit [172,179,180]. Any curvature of this plot is an indication of a lack of fit and therefore suggests the need for a non-linear regression model [179]. However, linear calibration is preferred over non-linear calibration models because of easy calculation and statistical assessment [180]. The lowest

calibration standard used is considered the limit of quantification (LOQ) and the signal corresponding to this calibration standard should be at least five times higher than the blank signal [181]. In order to evaluate the strength of the study, both the LOQ and the calibration curve, including its plot of residuals, the correlation or determination coefficient, and the slope of the curve, should be reported (Figure 3).



**Figure 3.** Calibration curve of TEGDMA in relation to the internal standard diethyl phthalate (DEP) including the plot of residuals. The data are fitted by a linear regression model and assessed by the determination coefficient  $r^2$ . This calibration curve was prepared for a study on the monomer elution from resin-based temporary crown and bridge materials [120].

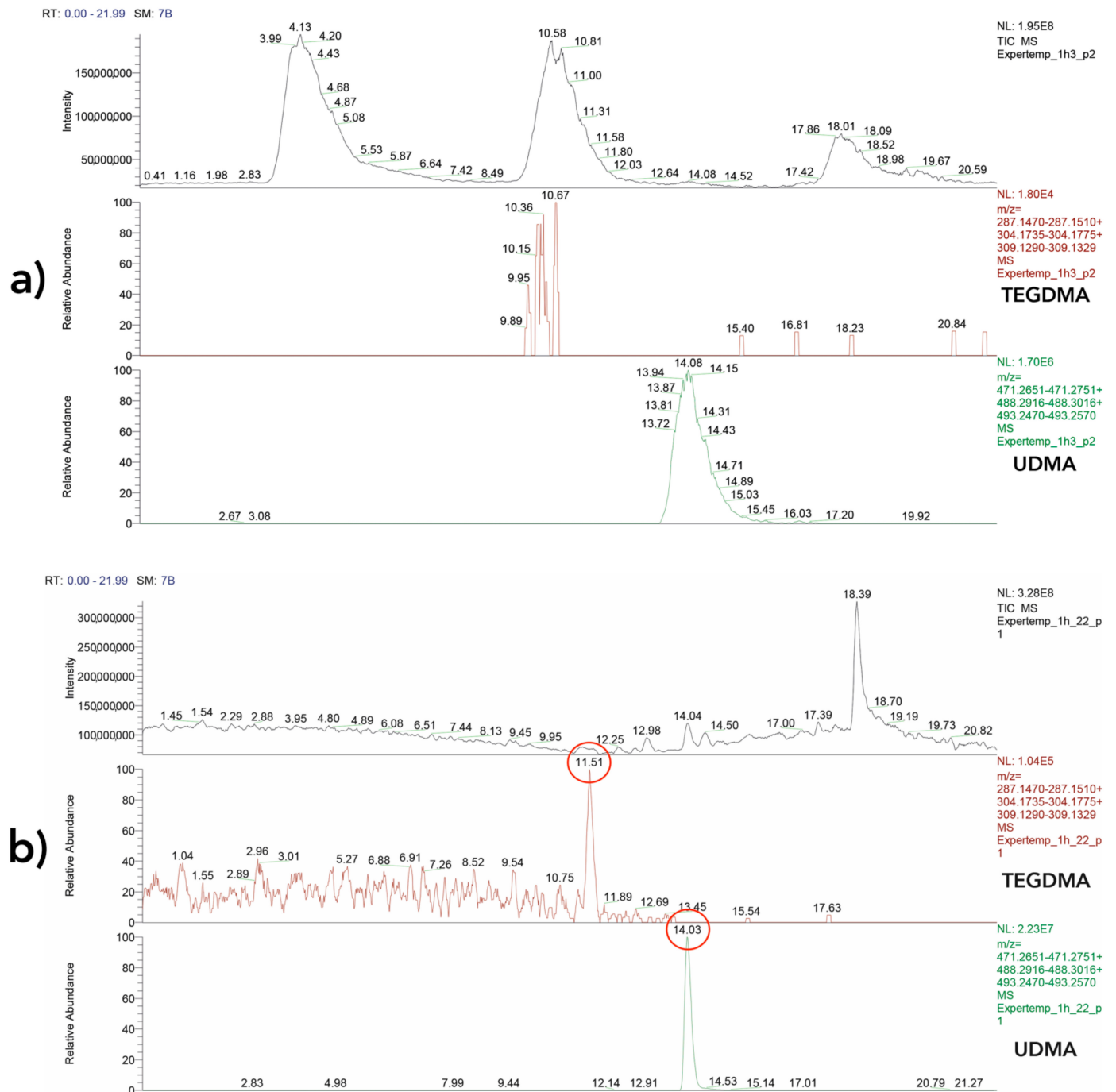
The LOQs in the current literature for Bis-GMA range from 0.01 µg/mL to 3.51 µg/mL [35,86,89,164] and for BPA from 0.00003 µg/mL to 0.2 µg/mL [64,120,182–184]. The LOQs for UDMA are reported between 0.005 µg/mL and 1.90 µg/mL [35,86,89,164]. Respective values for TEGDMA vary between 0.005 µg/mL and 2.424 µg/mL [35,86,89,164,167] and for HEMA between 0.2 µg/mL and 7.36 µg/mL [35,86,164,167].

## 8. Calibration Techniques

The most common calibration technique is known as external calibration and consists of the separate preparation and analysis of standards and samples [185]. External calibration is prone to matrix effects and does not consider losses in sample preparation or analysis [185,186]. Therefore, ISO Guide 33:2015 recommends using this technique only for matrix-free samples [187]. This source of error is reduced by calibration methods that use standards present in the sample during preparation and analysis [188]. These methods are known as internal calibration and standard addition calibration [186]. For internal calibra-

tion, a constant amount of an internal standard similar to the analyte of interest is added to the samples and calibration standards to obtain a calibration factor that is applied to the analyte signal (Figure 1) [185,186]. Most commonly, a set of standards containing the range of expected concentrations of analyte and a single concentration of internal standard is analyzed to obtain the corresponding calibration curve (Figure 3) [189]. Internal calibration requires substances with similar retention times—ideally, isotope-labeled standards of the analyte—and multiple standards may be required when analyzing multiple analytes [190]. Using standard addition, the signal change by adding increasing amounts of a standard to aliquots of the sample is measured and thereby the original concentration is calculated by applying a linear function fitting all experimental points [191]. Consequently, standard addition leads to long-lasting calibration procedures because the individual calibration of each sample is required [168]. However, in contrast to other methods, this is the only technique not affected by systematic matrix errors and is recommended for complex matrices [185].

Most studies on the release of residual monomers from dental resins are limited by the inaccuracy of external calibration [107]. However, the use of internal standards, especially in complex matrices, such as urine and artificial or collected saliva, is recommended [190]. In the literature, caffeine [64,134,192], diethyl phthalate [109,193,194], or standards labeled with stable isotopes [57,62,66,163] have been used as internal standards. Due to its omnipresence, caffeine should not be used in studies using collected human saliva as the solvent [107]. Special caution is required when using diethyl phthalate, as diethyl phthalate is used in dental materials and has already been detected in different composites [192,195]. However, the internal standard must not be present in the sample. Otherwise, quantification will be falsified [196]. In order to avoid this, deuterated diethyl phthalate has been used in more recent studies [197,198]. When adding internal standards or other compounds to the sample, it is important to rule out the introduction of matrix effects by coeluting substances because they may lead to decreased accuracy and sensitivity [199]. Recent studies added an antibiotic–antimycotic mixture to the solvent to avoid microbial colonialization [61,63], but a recent trial for a study of our working group showed that the peaks corresponding to the mixture overlapped the peaks of relevant dental monomers heavily and may have introduced matrix effects to the analytical procedure (Figure 4).



**Figure 4.** (a) HPLC-MS Chromatogram of an ExperTemp sample (Ultradent, South Jordan, UT, USA) immersed in HPLC grade water and Gibco Antibiotic-Antimycotic solution. Due to the overlapping peaks of the antibiotic-antimycotic solution, the peaks corresponding to the masses of TEGDMA and UDMA are not identifiable. (b) Chromatogram of an ExperTemp sample (Ultradent, South Jordan, USA) immersed in pure HPLC grade water. The peaks corresponding to TEGDMA and UDMA are highlighted. This figure was taken from preliminary tests made by our working group for a study on the elution of monomers from resin-based temporary crown and bridge materials [120].

For this reason, every added compound needs to be evaluated for the introduction of matrix effects. Because of similar properties to the analyte and close elution to the analyte, while being well separable, analytical standards labeled with stable isotopes, such

as deuterium or  $^{13}\text{C}$ , are the most appropriate internal standards [190]. Future studies should use internal standards, preferably labeled with stable isotopes, for calibration.

## 9. Method Validation

Method validation is mandatory before routine analysis for all analytical methods. International guidelines, by the FDA [177], European Medicines Agency (EMA) [181], and the International Union of the Pure and Applied Chemistry (IUPAC) [200] provide information on the validation of analytical methods. According to these guidelines, the main parameters which need to be validated are linearity, accuracy, precision, specificity, selectivity, matrix effects, and stability [201]. Key parameters of validation, especially the limits of detection (LOD) and quantification (LOQ) [34,66] as well as the slope of the calibration curve [201], should be stated in the method validation section, so readers can evaluate the strength of the study. Very few studies on the elution from dental resins reported these validation parameters [107,163,174].

## 10. Conclusions

Due to the diverse application of dental resins in various areas of dentistry, it is necessary to develop reliable, evidence-based analytical methods for the detection and quantification of eluting compounds. Analytical and experimental methods used in recent literature vary widely and validation parameters are reported rarely. We propose a consistent study design to collect reliable data that allows consistent meta-analytical evaluation. When researching the *in vitro* elution from dental resins, the following criteria should be met:

1. The surface area of the sample and the corresponding solvent volume should be standardized according to ISO 10993-12 and following the clinical workflow, the oxygen inhibition layer of the samples should be removed.
2. In order to achieve results comparable to *in vivo* conditions, solvents, such as water, artificial saliva, or preferably collected saliva, should be used.
3. Incubation parameters should mimic *in vivo* conditions. Therefore, immediate incubation at 37 °C and a frequent solvent refresh is recommended. For later meta-analysis, a 24-h incubation period should be included in all studies.
4. HPLC-MS, preferably with HRMS and/or tandem mass spectrometry, calibrated by internal standards is the recommended analytical method for detection and quantification.
5. CAS Registry numbers and molecular weights of standards and detected substances must be reported.
6. The analytical method should be validated properly. Key validation parameters, e.g., the LOD, LOQ, and the calibration curve, including its interception, slope, and the plot of residuals, need to be reported for interpretation of study results.

**Author Contributions:** Conceptualization: T.H., S.K., R.B.; Methodology: T.H., A.W., R.B., S.K.; Investigation: T.H., S.K., R.B., A.W., H.F., M.A., P.K.; Writing—review and editing: T.H., A.W., R.B., S.K., H.F., M.A., P.K.; Visualization: T.H., M.A., P.K.; H.F. Supervision: T.H., S.K.; Project administration: S.K., R.B. All authors have read and agreed to the published version of the manuscript.

**Funding:** We acknowledge support by the Open Access Publication Funds of the Göttingen University.

**Institutional Review Board Statement:** Not applicable.

**Informed Consent Statement:** Not applicable.

**Data Availability Statement:** Not applicable.

**Acknowledgments:** The authors would like to thank Ultradent, South Jordan, USA and DMG Chemisch-Pharmazeutische Fabrik, Hamburg, Germany for supplying the materials which have been analyzed for the figures.

**Conflicts of Interest:** The authors would like to thank Ultradent, South Jordan, USA and DMG Chemisch-Pharmazeutische Fabrik, Hamburg, Germany for supplying the materials which have been analyzed for the figures. Besides this the authors of this manuscript certify that they have no



proprietary, financial, or other interest of any nature or kind in any product, service, and/or company that is presented in this article.

### Abbreviations

Many different abbreviations are used in the scientific literature on the leachability of compounds from the polymer matrix of dental resins. This section provides an overview of the most commonly used abbreviations:

APCI	Atmospheric pressure chemical ionization
APPI	Atmospheric Pressure Photoionisation
BADGE	Bisphenol A diglycidyl ether
Bis-EMA	Ethoxylated bisphenol A dimethacrylate
Bis-GMA	Bisphenol A diglycidyl methacrylate
Bis-HPPP	Bis-hydroxy-propoxy-phenyl-propane
BPA	Bisphenol A
CAS	Chemical Abstracts Service
ESI	Electrospray ionization
GC	Gas chromatography
HEMA	2-hydroxyethyl methacrylate
HPLC	High-performance liquid chromatography
HRMS	High-resolution mass spectrometry
LC	Liquid chromatography
LOD	Limit of detection
LOQ	Limit of quantification
MS	Mass spectrometry
PDA	Photodiode array,
TEGDMA	Triethylene glycol dimethacrylate
UDMA	Urethane dimethacrylate
UV/Vis	Ultraviolet/visible

### References

- Schwendicke, F.; Göstemeyer, G.; Blunck, U.; Paris, S.; Hsu, L.Y.; Tu, Y.K. Directly Placed Restorative Materials: Review and Network Meta-analysis. *J. Dent. Res.* **2016**, *95*, 613–622. [[CrossRef](#)] [[PubMed](#)]
- ADA Council on Scientific Affairs. Dental amalgam: Update on safety concerns. *J. Am. Dent. Assoc.* **1998**, *129*, 494–503. [[CrossRef](#)] [[PubMed](#)]
- Sjögren, P.; Halling, A. Survival time of Class II molar restorations in relation to patient and dental health insurance costs for treatment. *Swed. Dent. J.* **2002**, *26*, 59–66. [[PubMed](#)]
- Jones, D.W. Has Dental Amalgam Been Torpedoed and Sunk? *J. Dent. Res.* **2008**, *87*, 101–102. [[CrossRef](#)] [[PubMed](#)]
- Mutter, J. Is dental amalgam safe for humans? The opinion of the scientific committee of the European Commission. *J. Occup. Med. Toxicol.* **2011**, *6*, 2. [[CrossRef](#)]
- Clarkson, T.W.; Magos, L. The Toxicology of Mercury and Its Chemical Compounds. *Crit. Rev. Toxicol.* **2006**, *36*, 609–662. [[CrossRef](#)]
- Cramer, N.; Stansbury, J.; Bowman, C. Recent advances and developments in composite dental restorative materials. *J. Dent. Res.* **2011**, *90*, 402–416. [[CrossRef](#)]
- Pegoraro, T.A.; da Silva, N.R.F.A.; Carvalho, R.M. Cements for use in esthetic dentistry. *Dent. Clin. N. Am.* **2007**, *51*, 453–471. [[CrossRef](#)]
- Sideridou, I.D.; Achilias, D.S.; Karabela, M.M. Sorption kinetics of ethanol/water solution by dimethacrylate-based dental resins and resin composites. *J. Biomed. Mater. Res. B Appl. Biomater.* **2007**, *81*, 207–218. [[CrossRef](#)]
- Nakamura, T.; Wakabayashi, K.; Kinuta, S.; Nishida, H.; Miyamae, M.; Yatani, H. Mechanical properties of new self-adhesive resin-based cement. *J. Prosthodont. Res.* **2010**, *54*, 59–64. [[CrossRef](#)]
- Leonardo, M.R.; Da Silva, L.; Almeida, W.; Utrilla, L.S. Tissue response to an epoxy resin-based root canal sealer. *Dent. Traumatol.* **1999**, *15*, 28–32. [[CrossRef](#)]
- Kim, S.H.; Watts, D.C. Polymerization shrinkage-strain kinetics of temporary crown and bridge materials. *Dent. Mater.* **2004**, *20*, 88–95. [[CrossRef](#)]
- Tiu, J.; Belli, R.; Lohbauer, U. Characterization of Heat-Polymerized Monomer Formulations for Dental Infiltrated Ceramic Networks. *Appl. Sci.* **2021**, *11*, 7370. [[CrossRef](#)]
- Dressano, D.; Salvador, M.V.; Oliveira, M.T.; Marchi, G.M.; Fronza, B.M.; Hadis, M.; Palin, W.M.; Lima, A.F. Chemistry of novel and contemporary resin-based dental adhesives. *J. Mech. Behav. Biomed. Mater.* **2020**, *110*, 103875. [[CrossRef](#)]

15. Szczesio-Wlodarczyk, A.; Domarecka, M.; Kopacz, K.; Sokolowski, J.; Bociong, K. An Evaluation of the Properties of Urethane Dimethacrylate-Based Dental Resins. *Materials* **2021**, *14*, 2727. [[CrossRef](#)]
16. Barszczewska-Rybarek, I.M.; Chrószcz, M.W.; Chladek, G. Physicochemical and Mechanical Properties of Bis-GMA/TEGDMA Dental Composite Resins Enriched with Quaternary Ammonium Polyethylenimine Nanoparticles. *Materials* **2021**, *14*, 2037. [[CrossRef](#)]
17. Moharamzadeh, K.; Van Noort, R.; Brook, I.M.; Scutt, A.M. HPLC analysis of components released from dental composites with different resin compositions using different extraction media. *J. Mater. Sci. Mater. Med.* **2007**, *18*, 133–137. [[CrossRef](#)]
18. Pratap, B.; Gupta, R.K.; Bhardwaj, B.; Nag, M. Resin based restorative dental materials: Characteristics and future perspectives. *Jpn. Dent. Sci. Rev.* **2019**, *55*, 126–138. [[CrossRef](#)]
19. Barszczewska-Rybarek, I.M.; Chrószcz, M.W.; Chladek, G. Novel Urethane-Dimethacrylate Monomers and Compositions for Use as Matrices in Dental Restorative Materials. *Int. J. Mol. Sci.* **2020**, *21*, 2644. [[CrossRef](#)]
20. De Nys, S.; Duca, R.C.; Vervliet, P.; Covaci, A.; Boonen, I.; Elskens, M.; Vanoirbeek, J.; Godderis, L.; Van Meerbeek, B.; Van Landuyt, K.L. Bisphenol A as degradation product of monomers used in resin-based dental materials. *Dent. Mater.* **2021**, *37*, 1020–1029. [[CrossRef](#)]
21. Catalán, A.; Martínez, A.; Muñoz, C.; Medina, C.; Marzalletti, T.; Montañó, M.; Jaramillo, A.F.; Meléndrez, M.F. The effect of preheating of nano-filler composite resins on their degree of conversion and microfiltration in dental fillings. *Polym. Bull.* **2022**. [[CrossRef](#)]
22. Canceill, T.; Pages, P.; Garnier, S.; Dandurand, J.; Joniot, S. Thermogravimetric study of the behaviour of organic and inorganic polymers contained in four dental resin-based composites. *Polym. Polym. Compos.* **2021**, *29*, 1251–1258. [[CrossRef](#)]
23. Fonseca, A.S.; Labruna Moreira, A.D.; de Albuquerque, P.P.; de Menezes, L.R.; Pfeifer, C.S.; Schneider, L.F. Effect of monomer type on the CC degree of conversion, water sorption and solubility, and color stability of model dental composites. *Dent. Mater.* **2017**, *33*, 394–401. [[CrossRef](#)]
24. Par, M.; Spanovic, N.; Tauböck, T.T.; Attin, T.; Tarle, Z. Degree of conversion of experimental resin composites containing bioactive glass 45S5: The effect of post-cure heating. *Sci. Rep.* **2019**, *9*, 17245. [[CrossRef](#)]
25. Pulgar, R.; Olea-Serrano, M.F.; Novillo-Fertrell, A.; Rivas, A.; Pazos, P.; Pedraza, V.; Navajas, J.M.; Olea, N. Determination of bisphenol A and related aromatic compounds released from bis-GMA-based composites and sealants by high performance liquid chromatography. *Environ. Health Perspect.* **2000**, *108*, 21–27. [[CrossRef](#)] [[PubMed](#)]
26. Luo, S.; Zhu, W.; Liu, F.; He, J. Preparation of a Bis-GMA-free dental resin system with synthesized fluorinated dimethacrylate monomers. *Int. J. Mol. Sci.* **2016**, *17*, 2014. [[CrossRef](#)] [[PubMed](#)]
27. Mourouzis, P.; Andreasidou, E.; Samanidou, V.; Tolidis, K. Short-term and long-term release of monomers from newly developed resin-modified ceramics and composite resin CAD-CAM blocks. *J. Prosthet. Dent.* **2020**, *123*, 339–348. [[CrossRef](#)] [[PubMed](#)]
28. Szczesio-Wlodarczyk, A.; Polikowski, A.; Krasowski, M.; Fronczek, M.; Sokolowski, J.; Bociong, K. The Influence of Low-Molecular-Weight Monomers (TEGDMA, HDDMA, HEMA) on the Properties of Selected Matrices and Composites Based on Bis-GMA and UDMA. *Materials* **2022**, *15*, 2649. [[CrossRef](#)] [[PubMed](#)]
29. Barszczewska-Rybarek, I.M. Structure-property relationships in dimethacrylate networks based on Bis-GMA, UDMA and TEGDMA. *Dent. Mater.* **2009**, *25*, 1082–1089. [[CrossRef](#)] [[PubMed](#)]
30. Araújo, G.S.; Sfalcin, R.A.; Araújo, T.G.; Alonso, R.C.; Puppini-Rontani, R.M. Evaluation of polymerization characteristics and penetration into enamel caries lesions of experimental infiltrants. *J. Dent.* **2013**, *41*, 1014–1019. [[CrossRef](#)]
31. Alrahlah, A.; Al-Odayni, A.B.; Al-Mutairi, H.F.; Almousa, B.M.; Alsubaie, F.S.; Khan, R.; Saeed, W.S. A Low-Viscosity BisGMA Derivative for Resin Composites: Synthesis, Characterization, and Evaluation of Its Rheological Properties. *Materials* **2021**, *14*, 338. [[CrossRef](#)]
32. Tauscher, S.; Angermann, J.; Catel, Y.; Moszner, N. Evaluation of alternative monomers to HEMA for dental applications. *Dent. Mater.* **2017**, *33*, 857–865. [[CrossRef](#)]
33. Polydorou, O.; König, A.; Hellwig, E.; Kümmerer, K. Long-term release of monomers from modern dental-composite materials. *Eur. J. Oral Sci.* **2009**, *117*, 68–75. [[CrossRef](#)]
34. Van Landuyt, K.L.; Nawrot, T.; Geebelen, B.; De Munck, J.; Snauwaert, J.; Yoshihara, K.; Scheers, H.; Godderis, L.; Hoet, P.; Van Meerbeek, B. How much do resin-based dental materials release? A meta-analytical approach. *Dent. Mater.* **2011**, *27*, 723–747. [[CrossRef](#)]
35. Putzeys, E.; Nys, S.D.; Cokic, S.M.; Duca, R.C.; Vanoirbeek, J.; Godderis, L.; Meerbeek, B.V.; Van Landuyt, K.L. Long-term elution of monomers from resin-based dental composites. *Dent. Mater.* **2019**, *35*, 477–485. [[CrossRef](#)]
36. De Nys, S.; Putzeys, E.; Duca, R.C.; Vervliet, P.; Covaci, A.; Boonen, I.; Elskens, M.; Vanoirbeek, J.; Godderis, L.; Van Meerbeek, B.; et al. Long-term elution of bisphenol A from dental composites. *Dent. Mater.* **2021**, *37*, 1561–1568. [[CrossRef](#)]
37. Colborn, T.; vom Saal, F.S.; Soto, A.M. Developmental effects of endocrine-disrupting chemicals in wildlife and humans. *Environ. Health Perspect.* **1993**, *101*, 378–384. [[CrossRef](#)]
38. Fleisch, A.F.; Sheffield, P.E.; Chinn, C.; Edelstein, B.L.; Landrigan, P.J. Bisphenol A and related compounds in dental materials. *Pediatrics* **2010**, *126*, 760–768. [[CrossRef](#)]
39. Gould, J.C.; Leonard, L.S.; Maness, S.C.; Wagner, B.L.; Conner, K.; Zacharewski, T.; Safe, S.; McDonnell, D.P.; Gaido, K.W. Bisphenol A interacts with the estrogen receptor alpha in a distinct manner from estradiol. *Mol. Cell. Endocrinol.* **1998**, *142*, 203–214. [[CrossRef](#)]

40. Li, L.; Wang, Q.; Zhang, Y.; Niu, Y.; Yao, X.; Liu, H. The molecular mechanism of bisphenol A (BPA) as an endocrine disruptor by interacting with nuclear receptors: Insights from molecular dynamics (MD) simulations. *PLoS ONE* **2015**, *10*, e012033. [[CrossRef](#)]
41. Takayanagi, S.; Tokunaga, T.; Liu, X.; Okada, H.; Matsushima, A.; Shimohigashi, Y. Endocrine disruptor bisphenol A strongly binds to human estrogen-related receptor gamma (ERRgamma) with high constitutive activity. *Toxicol. Lett.* **2006**, *167*, 95–105. [[CrossRef](#)]
42. Alonso-Magdalena, P.; Laribi, O.; Roperio, A.B.; Fuentes, E.; Ripoll, C.; Soria, B.; Nadal, A. Low doses of bisphenol A and diethylstilbestrol impair Ca<sup>2+</sup> signals in pancreatic alpha-cells through a nonclassical membrane estrogen receptor within intact islets of Langerhans. *Environ. Health Perspect.* **2005**, *113*, 969–977. [[CrossRef](#)]
43. Xing, L.; Xu, Y.; Xiao, Y.; Shang, L.; Liu, R.; Wei, X.; Jiang, J.; Hao, W. Embryotoxic and teratogenic effects of the combination of bisphenol A and genistein on in vitro cultured postimplantation rat embryos. *Toxicol. Sci.* **2010**, *115*, 577–588. [[CrossRef](#)]
44. Söderholm, K.J.; Mariotti, A. BIS-GMA—Based resins in dentistry: Are they safe? *J. Am. Dent. Assoc.* **1999**, *130*, 201–209. [[CrossRef](#)] [[PubMed](#)]
45. Geurtsen, W.; Lehmann, F.; Spahl, W.; Leyhausen, G. Cytotoxicity of 35 dental resin composite monomers/additives in permanent 3T3 and three human primary fibroblast cultures. *J. Biomed. Mater. Res.* **1998**, *41*, 474–480. [[CrossRef](#)]
46. Kuan, Y.H.; Li, Y.C.; Huang, F.M.; Chang, Y.C. The upregulation of tumour necrosis factor- $\alpha$  and surface antigens expression on macrophages by bisphenol A-glycidyl-methacrylate. *Int. Endod. J.* **2012**, *45*, 619–626. [[CrossRef](#)]
47. Styllou, M.; Reichl, F.X.; Styllou, P.; Urcan, E.; Rothmund, L.; Hickel, R.; Högg, C.; Scherthan, H. Dental composite components induce DNA-damage and altered nuclear morphology in gingiva fibroblasts. *Dent. Mater.* **2015**, *31*, 1335–1344. [[CrossRef](#)]
48. Arossi, G.A.; Lehmann, M.; Dihl, R.R.; Reguly, M.L.; De Andrade, H.H.R. Induced DNA damage by dental resin monomers in somatic cells. *Basic Clin. Pharmacol. Toxicol.* **2010**, *106*, 124–129. [[CrossRef](#)]
49. Kleinsasser, N.H.; Schmid, K.; Sassen, A.W.; Harréus, U.A.; Staudenmaier, R.; Folwaczny, M.; Glas, J.; Reichl, F.X. Cytotoxic and genotoxic effects of resin monomers in human salivary gland tissue and lymphocytes as assessed by the single cell microgel electrophoresis (Comet) assay. *Biomaterials* **2006**, *27*, 1762–1770. [[CrossRef](#)]
50. Kurt, A.; Altintas, S.H.; Kiziltas, M.V.; Tekkeli, S.E.; Guler, E.M.; Kocyigit, A.; Usumez, A. Evaluation of residual monomer release and toxicity of self-adhesive resin cements. *Dent. Mater. J.* **2018**, *37*, 40–48. [[CrossRef](#)] [[PubMed](#)]
51. Reichl, F.X.; Esters, M.; Simon, S.; Seiss, M.; Kehe, K.; Kleinsasser, N.; Folwaczny, M.; Glas, J.; Hickel, R. Cell death effects of resin-based dental material compounds and mercurials in human gingival fibroblasts. *Arch. Toxicol.* **2006**, *80*, 370–377. [[CrossRef](#)] [[PubMed](#)]
52. Emmeler, J.; Seiss, M.; Kreppel, H.; Reichl, F.X.; Hickel, R.; Kehe, K. Cytotoxicity of the dental composite component TEGDMA and selected metabolic by-products in human pulmonary cells. *Dent. Mater.* **2008**, *24*, 1670–1675. [[CrossRef](#)] [[PubMed](#)]
53. Ferracane, J.L. Resin composite—State of the art. *Dent. Mater.* **2011**, *27*, 29–38. [[CrossRef](#)] [[PubMed](#)]
54. Goldberg, M.; Lasfargues, J.J.; Legrand, J.M. Clinical testing of dental Materials—Histological considerations. *J. Dent.* **1994**, *22*, 25–28. [[CrossRef](#)]
55. Polydorou, O.; König, A.; Hellwig, E.; Kümmerer, K. Urethane dimethacrylate: A molecule that may cause confusion in dental research. *J. Biomed. Mater. Res. B Appl. Biomater.* **2009**, *91*, 1–4. [[CrossRef](#)]
56. Michelsen, V.B.; Kopperud, H.B.M.; Lygre, G.B.; Björkman, L.; Jensen, E.; Kleven, I.S.; Svahn, J.; Lygre, H. Detection and quantification of monomers in unstimulated whole saliva after treatment with resin-based composite fillings in vivo. *Eur. J. Oral Sci.* **2012**, *120*, 89–95. [[CrossRef](#)]
57. Berge, T.L.L.; Lygre, G.B.; Lie, S.A.; Lindh, C.H.; Björkman, L. Bisphenol A in human saliva and urine before and after treatment with dental polymer-based restorative materials. *Eur. J. Oral Sci.* **2019**, *127*, 435–444. [[CrossRef](#)]
58. Sasaki, N.; Okuda, K.; Kato, T.; Kakishima, H.; Okuma, H.; Abe, K.; Tachino, H.; Tuchida, K.; Kubono, K. Salivary bisphenol-A levels detected by ELISA after restoration with composite resin. *J. Mater. Sci. Mater. Med.* **2005**, *16*, 297–300. [[CrossRef](#)]
59. Moreira, M.R.; Matos, L.G.; de Souza, I.D.; Brigante, T.A.; Queiroz, M.E.; Romano, F.L.; Nelson-Filho, P.; Matsumoto, M.A. Bisphenol A release from orthodontic adhesives measured in vitro and in vivo with gas chromatography. *Am. J. Orthod. Dentofac. Orthop.* **2017**, *151*, 477–483. [[CrossRef](#)]
60. Anderson, J.M. Future challenges in the in vitro and in vivo evaluation of biomaterial biocompatibility. *Regen. Biomater.* **2016**, *3*, 73–77. [[CrossRef](#)]
61. Małkiewicz, K.; Owoc, A.; Kluska, M.; Grzech-Leśniak, K.; Turło, J. HPLC analysis of potentially harmful substances released from dental filing materials available on the EU market. *Ann. Agric. Environ. Med.* **2014**, *21*, 86–90.
62. Becher, R.; Wellendorf, H.; Sakhi, A.K.; Samuelson, J.T.; Thomsen, C.; Bølling, A.K.; Kopperud, H.M. Presence and leaching of bisphenol a (BPA) from dental materials. *Acta Biomater. Odontol. Scand.* **2018**, *4*, 56–62. [[CrossRef](#)]
63. Małkiewicz, K.; Turło, J.; Marciniuk-Kluska, A.; Grzech-Leśniak, K.; Gašior, M.; Kluska, M. Release of bisphenol A and its derivatives from orthodontic adhesive systems available on the European market as a potential health risk factor. *Ann. Agric. Environ. Med.* **2015**, *22*, 172–177. [[CrossRef](#)]
64. Deviot, M.; Lachaise, I.; Högg, C.; Durner, J.; Reichl, F.X.; Attal, J.-P.; Dursun, E. Bisphenol A release from an orthodontic resin composite: A GC/MS and LC/MS study. *Dent. Mater.* **2018**, *34*, 341–354. [[CrossRef](#)]
65. Ferracane, J.L. Elution of leachable components from composites. *J. Oral Rehabil.* **1994**, *21*, 441–452. [[CrossRef](#)]
66. Hope, E.; Reed, D.R.; Moilanen, L.H. Potential confounders of bisphenol-a analysis in dental materials. *Dent. Mater.* **2016**, *32*, 961–967. [[CrossRef](#)]

67. Alshali, R.Z.; Salim, N.A.; Sung, R.; Satterthwaite, J.D.; Silikas, N. Qualitative and quantitative characterization of monomers of uncured bulk-fill and conventional resin-composites using liquid chromatography/mass spectrometry. *Dent. Mater.* **2015**, *31*, 711–720. [[CrossRef](#)]
68. Schmalz, G. Concepts in biocompatibility testing of dental restorative materials. *Clin. Oral Investig.* **1998**, *1*, 154–162. [[CrossRef](#)]
69. *ISO 4049:2019; Dentistry—Polymer-Based Restorative Materials*. International Organization for Standardization (ISO): Geneva, Switzerland, 2019.
70. *ISO 10993-12:2012; Biological Evaluation of Medical Devices—Part 12: Sample Preparation and Reference Materials*. International Organization for Standardization (ISO): Geneva, Switzerland, 2012.
71. Pelka, M.; Distler, W.; Petschelt, A. Elution parameters and HPLC-detection of single components from resin composite. *Clin. Oral Investig.* **1999**, *3*, 194–200. [[CrossRef](#)]
72. Polydorou, O.; Huberty, C.; Wolkewitz, M.; Bolek, R.; Hellwig, E.; Kümmerer, K. The effect of storage medium on the elution of monomers from composite materials. *J. Biomed. Mater. Res. B Appl. Biomater.* **2012**, *100*, 68–74. [[CrossRef](#)]
73. Ruyter, I.E. Unpolymerized surface layers on sealants. *Acta Odontol. Scand.* **1981**, *39*, 27–32. [[CrossRef](#)] [[PubMed](#)]
74. Kim, J.S.; Choi, Y.H.; Cho, B.H.; Son, H.H.; Lee, I.B.; Um, C.M.; Kim, C.K. Effect of light-cure time of adhesive resin on the thickness of the oxygen-inhibited layer and the microtensile bond strength to dentin. *J. Biomed. Mater. Res. B Appl. Biomater.* **2006**, *78*, 115–123. [[CrossRef](#)] [[PubMed](#)]
75. Komurcuoglu, E.; Olmez, S.; Vural, N. Evaluation of residual monomer elimination methods in three different fissure sealants in vitro. *J. Oral Rehabil.* **2005**, *32*, 116–121. [[CrossRef](#)] [[PubMed](#)]
76. Tang, A.T.H.; Li, J.; Ekstrand, J.; Liu, Y. Cytotoxicity tests of in situ polymerized resins: Methodological comparisons and introduction of a tissue culture insert as a testing device. *J. Biomed. Mater. Res.* **1999**, *45*, 214–222. [[CrossRef](#)]
77. Bijelic-Donova, J.; Garoushi, S.; Lassila, L.V.J.; Vallittu, P.K. Oxygen inhibition layer of composite resins: Effects of layer thickness and surface layer treatment on the interlayer bond strength. *Eur. J. Oral Sci.* **2015**, *123*, 53–60. [[CrossRef](#)]
78. Shawkat, E.S.; Shortall, A.C.; Addison, O.; Palin, W.M. Oxygen inhibition and incremental layer bond strengths of resin composites. *Dent. Mater.* **2009**, *25*, 1338–1346. [[CrossRef](#)]
79. Dall’Oca, S.; Papacchini, F.; Goracci, C.; Cury, A.H.; Suh, B.I.; Tay, F.R.; Polimeni, A.; Ferrari, M. Effect of oxygen inhibition on composite repair strength over time. *J. Biomed. Mater. Res. B Appl. Biomater.* **2007**, *81*, 493–498. [[CrossRef](#)]
80. Mayinger, F.; Reymus, M.; Liebermann, A.; Richter, M.; Kubryk, P.; Großekappenberg, H.; Stawarczyk, B. Impact of polymerization and storage on the degree of conversion and mechanical properties of veneering resin composites. *Dent. Mater. J.* **2021**, *40*, 487–497. [[CrossRef](#)]
81. Sehgal, A.; Rao, Y.M.; Joshua, M.; Narayanan, L.L. Evaluation of the effects of the oxygen-inhibited layer on shear bond strength of two resin composites. *J. Conserv. Dent.* **2008**, *11*, 159–161. [[CrossRef](#)]
82. Rueggeberg, F.A.; Margeson, D.H. The effect of oxygen inhibition on an unfilled/filled composite system. *J. Dent. Res.* **1990**, *69*, 1652–1658. [[CrossRef](#)]
83. Studer, K.; Decker, C.; Beck, E.; Schwalm, R. Overcoming oxygen inhibition in UV-curing of acrylate coatings by carbon dioxide inerting, Part I. *Prog. Org. Coat.* **2003**, *48*, 92–100. [[CrossRef](#)]
84. Bergmann, P.; Noack, M.J.; Roulet, J.F. Marginal adaptation with glass-ceramic inlays adhesively luted with glycerine gel. *Quintessence Int.* **1991**, *22*, 739–744.
85. Park, H.-H.; Lee, I.-B. Effect of glycerin on the surface hardness of composites after curing. *J. Korean Acad. Conserv. Dent.* **2011**, *36*, 483–489. [[CrossRef](#)]
86. Bezgin, T.; Cimen, C.; Ozalp, N. Evaluation of Residual Monomers Eluted from Pediatric Dental Restorative Materials. *Biomed. Res. Int.* **2021**, *2021*, 6316171. [[CrossRef](#)]
87. Manojlovic, D.; Radisic, M.; Vasiljevic, T.; Zivkovic, S.; Lausevic, M.; Miletic, V. Monomer elution from nanohybrid and ormocer-based composites cured with different light sources. *Dent. Mater.* **2011**, *27*, 371–378. [[CrossRef](#)]
88. Meyer-Lückel, H.; Hartwig, C.; Börner, H.G.; Lausch, J. Elution of Monomers from an Infiltrant Compared with Different Resin-Based Dental Materials. *Oral Health Prev. Dent.* **2020**, *18*, 337–341.
89. Saleem, M.; Zahid, S.; Ghafoor, S.; Khalid, H.; Iqbal, H.; Zeeshan, R.; Ahmad, S.; Asif, A.; Khan, A.S. Physical, mechanical, and in vitro biological analysis of bioactive fibers-based dental composite. *J. Appl. Polym. Sci.* **2021**, *138*, 50336. [[CrossRef](#)]
90. Inoue, K.; Hayashi, I. Residual monomer (Bis-GMA) of composite resins. *J. Oral Rehabil.* **1982**, *9*, 493–497. [[CrossRef](#)]
91. Yang, S.H.; Morgan, A.A.; Nguyen, H.P.; Moore, H.; Figard, B.J.; Schug, K.A. Quantitative determination of Bisphenol A from human saliva using bulk derivatization and trap-and-elute liquid chromatography coupled to electrospray ionization mass spectrometry. *Environ. Toxicol. Chem.* **2011**, *30*, 1243–1251. [[CrossRef](#)]
92. Reichl, F.X.; Löhle, J.; Seiss, M.; Furche, S.; Shehata, M.M.; Hickel, R.; Müller, M.; Dränert, M.; Durner, J. Elution of TEGDMA and HEMA from polymerized resin-based bonding systems. *Dent. Mater.* **2012**, *28*, 1120–1125. [[CrossRef](#)]
93. Kessler, A.; Reichl, F.X.; Folwaczny, M.; Högg, C. Monomer release from surgical guide resins manufactured with different 3D printing devices. *Dent. Mater.* **2020**, *36*, 1486–1492. [[CrossRef](#)]
94. Polydorou, O.; Trittler, R.; Hellwig, E.; Kümmerer, K. Elution of monomers from two conventional dental composite materials. *Dent. Mater.* **2007**, *23*, 1535–1541. [[CrossRef](#)]
95. Cebe, M.A.; Cebe, F.; Cengiz, M.F.; Cetin, A.R.; Arpag, O.F.; Ozturk, B. Elution of monomer from different bulk fill dental composite resins. *Dent. Mater.* **2015**, *31*, 141–149. [[CrossRef](#)]

96. Altintas, S.H.; Usumez, A. Evaluation of TEGDMA leaching from four resin cements by HPLC. *Eur. J. Dent.* **2012**, *6*, 255–262. [[CrossRef](#)]
97. Shahabi, S.; Sayyari, M.; Sadrai, S.; Valizadeh, S.; Hajizamani, H.; Sadr, A. Effect of Volume and Renewal of the Storage Media on the Release of Monomer from Dental Composites. *Int. J. Dent.* **2021**, *2021*, 9769947. [[CrossRef](#)]
98. Durner, J.; Schrickel, K.; Watts, D.C.; Becker, M.; Draenert, M.E. Direct and indirect eluates from bulk fill resin-based-composites. *Dent. Mater.* **2022**, *38*, 489–507. [[CrossRef](#)]
99. McKinney, J.E.; Wu, W. Chemical softening and wear of dental composites. *J. Dent. Res.* **1985**, *64*, 1326–1331. [[CrossRef](#)]
100. Wu, W.; McKinney, J.E. Influence of chemicals on wear of dental composites. *J. Dent. Res.* **1982**, *61*, 1180–1183. [[CrossRef](#)]
101. Szczesio-Wlodarczyk, A.; Sokolowski, J.; Kleczewska, J.; Bociong, K. Ageing of Dental Composites Based on Methacrylate Resins—A Critical Review of the Causes and Method of Assessment. *Polymers* **2020**, *12*, 882. [[CrossRef](#)]
102. Tsitrou, E.; Kelogrigoris, S.; Koulaouzidou, E.; Antoniadis-Halvatjoglou, M.; Koliniotou-Koumpia, E.; van Noort, R. Effect of extraction media and storage time on the elution of monomers from four contemporary resin composite materials. *Toxicol. Int.* **2014**, *21*, 89–95. [[CrossRef](#)] [[PubMed](#)]
103. Zhang, Y.; Xu, J. Effect of immersion in various media on the sorption, solubility, elution of unreacted monomers, and flexural properties of two model dental composite compositions. *J. Mater. Sci. Mater. Med.* **2008**, *19*, 2477–2483. [[CrossRef](#)] [[PubMed](#)]
104. Rothmund, L.; Shehata, M.; Van Landuyt, K.L.; Schweikl, H.; Carell, T.; Geurtsen, W.; Hellwig, E.; Hickel, R.; Reichl, F.X.; Högg, C. Release and protein binding of components from resin based composites in native saliva and other extraction media. *Dent. Mater.* **2015**, *31*, 496–504. [[CrossRef](#)] [[PubMed](#)]
105. Tanaka, K.; Taira, M.; Shintani, H.; Wakasa, K.; Yamaki, M. Residual monomers (TEGDMA and Bis-GMA) of a set visible-light-cured dental composite resin when immersed in water. *J. Oral Rehabil.* **1991**, *18*, 353–362. [[CrossRef](#)] [[PubMed](#)]
106. Floyd, C.J.; Dickens, S.H. Network structure of Bis-GMA- and UDMA-based resin systems. *Dent. Mater.* **2006**, *22*, 1143–1149. [[CrossRef](#)]
107. Michelsen, V.B.; Moe, G.; Strøm, M.B.; Jensen, E.; Lygre, H. Quantitative analysis of TEGDMA and HEMA eluted into saliva from two dental composites by use of GC/MS and tailor-made internal standards. *Dent. Mater.* **2008**, *24*, 724–731. [[CrossRef](#)]
108. Gregson, K.; Beiswanger, A.; Platt, J. The impact of sorption, buffering, and proteins on leaching of organic and inorganic substances from dental resin core material. *J. Biomed. Mater. Res. A* **2008**, *84*, 256–264. [[CrossRef](#)]
109. Michelsen, V.B.; Moe, G.; Skålevik, R.; Jensen, E.; Lygre, H. Quantification of organic eluates from polymerized resin-based dental restorative materials by use of GC/MS. *J. Chromatogr. B* **2007**, *850*, 83–91. [[CrossRef](#)]
110. De Nys, S.; Duca, R.C.; Vervliet, P.; Covaci, A.; Boonen, I.; Elskens, M.; Vanoirbeek, J.; Godderis, L.; Van Meerbeek, B.; Van Landuyt, K.L. Bisphenol A release from short-term degraded resin-based dental materials. *J. Dent.* **2022**, *116*, 103894. [[CrossRef](#)]
111. Olea, N.; Pulgar, R.; Pérez, P.; Olea-Serrano, F.; Rivas, A.; Novillo-Fertrell, A.; Pedraza, V.; Soto, A.M.; Sonnenschein, C. Estrogenicity of resin-based composites and sealants used in dentistry. *Environ. Health Perspect.* **1996**, *104*, 298–305. [[CrossRef](#)]
112. Örtengren, U.; Langer, S.; Göransson, A.; Lundgren, T. Influence of pH and time on organic substance release from a model dental composite: A fluorescence spectrophotometry and gas chromatography/mass spectrometry analysis. *Eur. J. Oral Sci.* **2004**, *112*, 530–537. [[CrossRef](#)]
113. Al-Hiyasat, A.S.; Darmani, H.; Milhem, M.M. Cytotoxicity evaluation of dental resin composites and their flowable derivatives. *Clin. Oral Investig.* **2005**, *9*, 21–25. [[CrossRef](#)]
114. Hofmann, N.; Renner, J.; Hugo, B.; Klaiber, B. Elution of leachable components from resin composites after plasma arc vs. standard or soft-start halogen light irradiation. *J. Dent.* **2002**, *30*, 223–232. [[CrossRef](#)]
115. Yap, A.; Han, V.; Soh, M.; Siow, K. Elution of leachable components from composites after LED and halogen light irradiation. *Oper. Dent.* **2004**, *29*, 448–453.
116. Ferracane, J.L.; Condon, J.R. Rate of elution of leachable components from composite. *Dent. Mater.* **1990**, *6*, 282–287. [[CrossRef](#)]
117. Cokic, S.M.; Duca, R.C.; De Munck, J.; Hoet, P.; Van Meerbeek, B.; Smet, M.; Godderis, L.; Van Landuyt, K.L. Saturation reduces in-vitro leakage of monomers from composites. *Dent. Mater.* **2018**, *34*, 579–586. [[CrossRef](#)]
118. Ferracane, J.L. Hygroscopic and hydrolytic effects in dental polymer networks. *Dent. Mater.* **2006**, *22*, 211–222. [[CrossRef](#)]
119. Tabatabaei, M.H.; Sadrai, S.; Bassir, S.H.; Veisy, N.; Dehghan, S. Effect of food stimulated liquids and thermocycling on the monomer elution from a nanofilled composite. *Open Dent. J.* **2013**, *7*, 62–67. [[CrossRef](#)]
120. Hampe, T.; Wiessner, A.; Frauendorf, H.; Alhussain, M.; Karlovsky, P.; Bürgers, R.; Krohn, S. A comparative in vitro study on monomer release from bisphenol A-free and conventional temporary crown and bridge materials. *Eur. J. Oral Sci.* **2021**, *6*, e12826. [[CrossRef](#)]
121. Sanglar, C.; Defay, M.; Waton, H.; Bonhomme, A.; Alamercery, S.; Baudot, R.; Pâisse, O.; Grenier-Loustalot, M.F. Commercial dental composite: Determination of reaction advancement and study of the migration of organic compounds. *Polym. Polym. Compos.* **2005**, *13*, 223–234. [[CrossRef](#)]
122. Koin, P.J.; Kilislioglu, A.; Zhou, M.; Drummond, J.L.; Hanley, L. Analysis of the degradation of a model dental composite. *J. Dent. Res.* **2008**, *87*, 661–665. [[CrossRef](#)]
123. de Brito, O.; de Oliveira, I.; Monteiro, G. Hydrolytic and biological degradation of bulk-fill and self-adhering resin composites. *Oper. Dent.* **2019**, *44*, 223–233. [[CrossRef](#)]

124. Vervliet, P.; Den Plas, J.V.; De Nys, S.; Duca, R.C.; Boonen, I.; Elskens, M.; Van Landuyt, K.L.; Covaci, A. Investigating the in vitro metabolism of the dental resin monomers BisGMA, BisPMA, TCD-DI-HEA and UDMA using human liver microsomes and quadrupole time of flight mass spectrometry. *Toxicology* **2019**, *420*, 1–10. [[CrossRef](#)] [[PubMed](#)]
125. Hsu, W.Y.; Wang, V.S.; Lai, C.C.; Tsai, F.J. Simultaneous determination of components released from dental composite resins in human saliva by liquid chromatography/multiple-stage ion trap mass spectrometry. *Electrophoresis* **2012**, *33*, 719–725. [[CrossRef](#)]
126. Finer, Y.; Jaffer, F.; Santerre, J.P. Mutual influence of cholesterol esterase and pseudocholinesterase on the biodegradation of dental composites. *Biomaterials* **2004**, *25*, 1787–1793. [[CrossRef](#)] [[PubMed](#)]
127. Finer, Y.; Santerre, J.P. Salivary esterase activity and its association with the biodegradation of dental composites. *J. Dent. Res.* **2004**, *83*, 22–26. [[CrossRef](#)] [[PubMed](#)]
128. Alshali, R.Z.; Salim, N.A.; Sung, R.; Satterthwaite, J.D.; Silikas, N. Analysis of long-term monomer elution from bulk-fill and conventional resin-composites using high performance liquid chromatography. *Dent. Mater.* **2015**, *31*, 1587–1598. [[CrossRef](#)] [[PubMed](#)]
129. Shelby, M.D. NTP-CERHR monograph on the potential human reproductive and developmental effects of bisphenol A. *NTP CERHR MON* **2008**, *22*, v–vii, 1–64 passim.
130. Durner, J.; Schrickel, K.; Watts, D.C.; Ilie, N. Determination of homologous distributions of bisEMA dimethacrylates in bulk-fill resin-composites by GC–MS. *Dent. Mater.* **2015**, *31*, 473–480. [[CrossRef](#)] [[PubMed](#)]
131. Bannach, G.; Cavalheiro, C.C.; Calixto, L.; Cavalheiro, É.T.G. Thermoanalytical study of monomers: BisGMA, BisEMA, TEGDMA, UDMA and their mixture. *Braz. J. Therm. Anal.* **2015**, *4*, 28–34.
132. Rogalewicz, R.; Batko, K.; Voelkel, A. Identification of organic extractables from commercial resin-modified glass-ionomers using HPLC-MS. *J. Environ. Monit.* **2006**, *8*, 750–758. [[CrossRef](#)]
133. Spahl, W.; Budzikiewicz, H. Qualitative analysis of dental resin composites by gas and liquid chromatography/mass spectrometry. *Fresenius' J. Anal. Chem.* **1994**, *350*, 684–691. [[CrossRef](#)]
134. Geurtsen, W.; Spahl, W.; Leyhausen, G. Variability of cytotoxicity and leaching of substances from four light-curing pit and fissure sealants. *J. Biomed. Mater. Res.* **1999**, *44*, 73–77. [[CrossRef](#)]
135. Ternes, T.A. Analytical methods for the determination of pharmaceuticals in aqueous environmental samples. *Trends Anal. Chem.* **2001**, *20*, 419–434. [[CrossRef](#)]
136. Gul, P.; Senol, O.; Yaman, M.E.; Kadioglu, Y. Quantification and identification of components released from dental composites using different chromatographic techniques. *J. Liq. Chromatogr. Relat. Technol.* **2016**, *39*, 581–586. [[CrossRef](#)]
137. Siddiqui, M.R.; Alothman, Z.A.; Rahman, N. Analytical techniques in pharmaceutical analysis: A review. *Arab. J. Chem.* **2017**, *10*, S1409–S1421. [[CrossRef](#)]
138. Swartz, M. HPLC detectors: A brief review. *J. Liq. Chromatogr. Relat. Technol.* **2010**, *33*, 1130–1150. [[CrossRef](#)]
139. Mariappan, T.T.; Jindal, K.C.; Singh, S. Overestimation of rifampicin during colorimetric analysis of anti-tuberculosis products containing isoniazid due to formation of isonicotinyl hydrazone. *J. Pharm. Biomed. Anal.* **2004**, *36*, 905–908. [[CrossRef](#)]
140. Barba, A.I.O.; Hurtado, M.C.; Mata, M.C.S.; Ruiz, V.F.; Tejada, M.L.S.d. Application of a UV–vis detection-HPLC method for a rapid determination of lycopene and  $\beta$ -carotene in vegetables. *Food Chem.* **2006**, *95*, 328–336. [[CrossRef](#)]
141. Babic, N.; Larson, T.S.; Grebe, S.K.; Turner, S.T.; Kumar, R.; Singh, R.J. Application of liquid chromatography-mass spectrometry technology for early detection of microalbuminuria in patients with kidney disease. *Clin. Chem.* **2006**, *52*, 2155–2157. [[CrossRef](#)]
142. Fagiola, M. Current and future directions of high resolution and tandem mass spectrometry in postmortem and human performance toxicology. *Leg. Med.* **2019**, *37*, 86–94. [[CrossRef](#)]
143. Picó, Y.; Blasco, C.; Font, G. Environmental and food applications of LC–tandem mass spectrometry in pesticide-residue analysis: An overview. *Mass Spectrom. Rev.* **2004**, *23*, 45–85. [[CrossRef](#)]
144. Hernández, F.; Sancho, J.V.; Ibáñez, M.; Abad, E.; Portolés, T.; Mattioli, L. Current use of high-resolution mass spectrometry in the environmental sciences. *Anal. Bioanal. Chem.* **2012**, *403*, 1251–1264. [[CrossRef](#)]
145. Schollée, J.E.; Schymanski, E.L.; Stravs, M.A.; Gulde, R.; Thomaidis, N.S.; Hollender, J. Similarity of High-Resolution Tandem Mass Spectrometry Spectra of Structurally Related Micropollutants and Transformation Products. *J. Am. Soc. Mass Spectrom.* **2017**, *28*, 2692–2704. [[CrossRef](#)]
146. De Vijlder, T.; Valkenburg, D.; Lemièrre, F.; Romijn, E.P.; Laukens, K.; Cuyckens, F. A tutorial in small molecule identification via electrospray ionization-mass spectrometry: The practical art of structural elucidation. *Mass Spectrom. Rev.* **2018**, *37*, 607–629. [[CrossRef](#)] [[PubMed](#)]
147. Zhang, S.; Zhang, Q.; Darisaw, S.; Ehie, O.; Wang, G. Simultaneous quantification of polycyclic aromatic hydrocarbons (PAHs), polychlorinated biphenyls (PCBs), and pharmaceuticals and personal care products (PPCPs) in Mississippi river water, in New Orleans, Louisiana, USA. *Chemosphere* **2007**, *66*, 1057–1069. [[CrossRef](#)] [[PubMed](#)]
148. Devosa, C.; Vliegen, M.; Willaert, B.; David, F.; Moens, L.; Sandra, P. Automated headspace-solid-phase micro extraction-retention time locked-isotope dilution gas chromatography-mass spectrometry for the analysis of organotin compounds in water and sediment samples. *J. Chromatogr. A* **2005**, *1079*, 408–414. [[CrossRef](#)] [[PubMed](#)]
149. Schütze, A.; Pälme, C.; Angerer, J.; Weiss, T.; Brüning, T.; Koch, H.M. Quantification of biomarkers of environmental exposure to di(isononyl)cyclohexane-1,2-dicarboxylate (DINCH) in urine via HPLC-MS/MS. *J. Chromatogr. B Analyt. Technol. Biomed. Life Sci.* **2012**, *895–896*, 123–130. [[CrossRef](#)]

150. Kushnir, M.M.; Rockwood, A.L.; Nelson, G.J.; Yue, B.; Urry, F.M. Assessing analytical specificity in quantitative analysis using tandem mass spectrometry. *Clin. Biochem.* **2005**, *38*, 319–327. [[CrossRef](#)]
151. Michelsen, V.B.; Lygre, H.; Skålevik, R.; Tveit, A.B.; Solheim, E. Identification of organic eluates from four polymer-based dental filling materials. *Eur. J. Clin. Investig.* **2003**, *111*, 263–271. [[CrossRef](#)]
152. Lygre, H.; Høl, P.J.; Solheim, E.; Moe, G. Organic leachables from polymer-based dental filling materials. *Eur. J. Clin. Investig.* **1999**, *107*, 378–383. [[CrossRef](#)]
153. Rivier, L. Criteria for the identification of compounds by liquid chromatography–mass spectrometry and liquid chromatography–multiple mass spectrometry in forensic toxicology and doping analysis. *Anal. Chim. Acta* **2003**, *492*, 69–82. [[CrossRef](#)]
154. Mesihää, S.; Ketola, R.A.; Pelander, A.; Rasanen, I.; Ojanperä, I. Development of a GC-APCI-QTOFMS library for new psychoactive substances and comparison to a commercial ESI library. *Anal. Bioanal. Chem.* **2017**, *409*, 2007–2013. [[CrossRef](#)]
155. Reinstadler, V.; Lierheimer, S.; Boettcher, M.; Oberacher, H. A validated workflow for drug detection in oral fluid by non-targeted liquid chromatography-tandem mass spectrometry. *Anal. Bioanal. Chem.* **2019**, *411*, 867–876. [[CrossRef](#)]
156. Stein, S. Mass spectral reference libraries: An ever-expanding resource for chemical identification. *Anal. Chem.* **2012**, *84*, 7274–7282. [[CrossRef](#)]
157. European Commission. 2002/657/EC: Commission Decision of 12 August 2002 Implementing Council Directive 96/23/EC Concerning the Performance of Analytical Methods and the Interpretation of Results (Text with EEA Relevance) (Notified under Document Number C(2002) 3044); European Commission: Maastricht, The Netherlands, 2002.
158. Wataha, J.; Rueggeberg, F.; Lapp, C.; Lewis, J.; Lockwood, P.; Ergle, J.; Mettenburg, D.J. In vitro cytotoxicity of resin-containing restorative materials after aging in artificial saliva. *Clin. Oral Investig.* **1999**, *3*, 144–149. [[CrossRef](#)]
159. Mocak, J.; Bond, A.M.; Mitchell, S.; Scollary, G. A statistical overview of standard (IUPAC and ACS) and new procedures for determining the limits of detection and quantification: Application to voltammetric and stripping techniques (Technical Report). *Pure Appl. Chem.* **1997**, *69*, 297–328. [[CrossRef](#)]
160. Krueve, A.; Rebane, R.; Kipper, K.; Oldekop, M.L.; Evard, H.; Herodes, K.; Ravio, P.; Leito, I. Tutorial review on validation of liquid chromatography-mass spectrometry methods: Part I. *Anal. Chim. Acta* **2015**, *870*, 29–44. [[CrossRef](#)]
161. Wenzl, T.; Haedrich, J.; Schaechtele, A.; Robouch, P.; Stroka, J. *Guidance Document on the Estimation of LOD and LOQ for Measurements in the Field of Contaminants in Food and Feed*; Publications Office of the European Union: Luxembourg, 2016.
162. Dolan, J.W. The Role of the Signal-to-Noise Ratio in Precision and Accuracy. *LCGC Eur.* **2006**, *19*, 12–16.
163. De Nys, S.; Putzeys, E.; Vervliet, P.; Covaci, A.; Boonen, I.; Elskens, M.; Vanoirbeek, J.; Godderis, L.; Van Meerbeek, B.; Van Landuyt, K.L.; et al. A novel high sensitivity UPLC-MS/MS method for the evaluation of bisphenol A leaching from dental materials. *Sci. Rep.* **2018**, *8*, 6981. [[CrossRef](#)]
164. Barutçigil, K.; Dündar, A.; Batmaz, S.G.; Yıldırım, K.; Barutçugil, Ç. Do resin-based composite CAD/CAM blocks release monomers? *Clin. Oral Investig.* **2021**, *25*, 329–336. [[CrossRef](#)]
165. Kakonyi, G.; Mulligan, S.; Fairburn, A.W.; Moharamzadeh, K.; Thornton, S.F.; Walker, H.J.; Burrell, M.M.; Martin, N. Simultaneous detection of monomers associated with resin-based dental composites using SPME and HPLC. *Dent. Mater. J.* **2021**, *40*, 1007–1013. [[CrossRef](#)] [[PubMed](#)]
166. Kang, Y.-G.; Kim, J.-Y.; Kim, J.; Won, P.-J.; Nam, J.-H. Release of bisphenol A from resin composite used to bond orthodontic lingual retainers. *Am. J. Orthod. Dentofac. Orthop.* **2011**, *140*, 779–789. [[CrossRef](#)] [[PubMed](#)]
167. Bielicka-Daszkievicz, K.; Poniedziałek, K. Extraction of organic compounds released from dental materials. *Microchem. J.* **2021**, *169*, 106594. [[CrossRef](#)]
168. Kościelniak, P.; Kozak, J. Review of univariate standard addition calibration procedures in flow analysis. *Crit. Rev. Anal. Chem.* **2006**, *36*, 27–40. [[CrossRef](#)]
169. Cuadros-Rodríguez, L.; Gámiz-Gracia, L.; Almansa-López, E.M.; Bosque-Sendra, J.M. Calibration in chemical measurement processes. II. A methodological approach. *Trends Anal. Chem.* **2001**, *20*, 620–636. [[CrossRef](#)]
170. Zhao, Y.; Liu, G.; Shen, J.X.; Aubry, A.F. Reasons for calibration standard curve slope variation in LC-MS assays and how to address it. *Bioanalysis* **2014**, *6*, 1439–1443. [[CrossRef](#)]
171. Bisphenol A Analytical Research Task Group. *Analytical Method Criteria for the Determination of Bisphenol A in Various Matrices*; American Plastics Council (APC), the Association of Plastics Manufacturers in Europe (APME), and the Japan Chemical Industry Association (JCIA): Arlington, VA, USA, 2002.
172. Thompson, M.; Ellison Stephen, L.R.; Wood, R. Harmonized guidelines for single-laboratory validation of methods of analysis (IUPAC Technical Report). *Pure Appl. Chem.* **2002**, *74*, 835–855. [[CrossRef](#)]
173. *ISO 11095:1996*; Linear Calibration Using Reference Materials. International Organization for Standardization (ISO): Geneva, Switzerland, 1996.
174. Samanidou, V.; Hadjicharalampous, M.; Palaghias, G.; Papadoyannis, I. Development and validation of an isocratic HPLC method for the simultaneous determination of residual monomers released from dental polymeric materials in artificial saliva. *J. Liq. Chromatogr. Relat. Technol.* **2012**, *35*, 511–523. [[CrossRef](#)]
175. Aldhafyan, M.; Silikas, N.; Watts, D.C. Influence of curing modes on monomer elution, sorption and solubility of dual-cure resin-cements. *Dent. Mater.* **2022**. *Epub ahead of print.* [[CrossRef](#)]

176. Sarosi, C.; Moldovan, M.; Soanca, A.; Roman, A.; Gherman, T.; Trifoi, A.; Chisnoiu, A.M.; Cuc, S.; Filip, M.; Gheorghe, G.F.; et al. Effects of Monomer Composition of Urethane Methacrylate Based Resins on the C=C Degree of Conversion, Residual Monomer Content and Mechanical Properties. *Polymers* **2021**, *13*, 4415. [CrossRef]
177. Food and Drug Administration. *Analytical Procedures and Methods Validation for Drugs and Biologics*; Food and Drug Administration: Silver Spring, MD, USA, 2015.
178. Clinical and Laboratory Standards Institute. *Measurement Procedure Comparison and Bias Estimation Using Patient Samples*; Approved Guideline—Third Edition; Clinical and Laboratory Standards Institute: Malvern, PA, USA, 2013.
179. González, A.G.; Herrador, M.Á. A practical guide to analytical method validation, including measurement uncertainty and accuracy profiles. *Trends Anal. Chem.* **2007**, *26*, 227–238. [CrossRef]
180. Van Looco, J.; Elskens, M.; Croux, C.; Beernaert, H. Linearity of calibration curves: Use and misuse of the correlation coefficient. *Accredit. Qual. Assur.* **2002**, *7*, 281–285. [CrossRef]
181. European Medicines Agency. *Guideline on Bioanalytical Method Validation*; European Medicines Agency: Amsterdam, The Netherlands, 2011.
182. Šimková, M.; Tichý, A.; Dušková, M.; Bradna, P. Dental composites—A low-dose source of bisphenol A? *Physiol. Res.* **2020**, *69*, S295–S304. [CrossRef]
183. Bationo, R.; Rouamba, A.; Diarra, A.; Beugré-Kouassi, M.L.A.; Beugré, J.B.; Jordana, F. Cytotoxicity evaluation of dental and orthodontic light-cured composite resins. *Clin. Exp. Dent. Res.* **2021**, *7*, 40–48. [CrossRef]
184. Diamantopoulou, E.I.; Plastiras, O.E.; Mourouzis, P.; Samanidou, V. Validation of a Simple HPLC-UV Method for the Determination of Monomers Released from Dental Resin Composites in Artificial Saliva. *Methods Protoc.* **2020**, *3*, 35. [CrossRef]
185. Cuadros-Rodríguez, L.; Bagur-González, M.G.; Sánchez-Vinas, M.; González-Casado, A.; Gómez-Sáez, A.M. Principles of analytical calibration/quantification for the separation sciences. *J. Chromatogr. A* **2007**, *1158*, 33–46. [CrossRef]
186. Oliveira, E.D.C.; Muller, E.I.; Abad, F.; Dallarosa, J.; Adriano, C. Internal standard versus external standard calibration: An uncertainty case study of a liquid chromatography analysis. *Química Nova* **2010**, *33*, 984–987. [CrossRef]
187. *ISO Guide 33:2015*; Reference Materials—Good Practice in Using Reference Materials. International Organization for Standardization (ISO): Geneva, Switzerland, 2015.
188. Hajslova, J.; Zrostlikova, J. Matrix effects in (ultra)trace analysis of pesticide residues in food and biotic matrices. *J. Chromatogr. A* **2003**, *1000*, 181–197. [CrossRef]
189. Hewavitharana, A.K. Internal Standard—Friend or Foe? *Crit. Rev. Anal. Chem.* **2009**, *39*, 272–275. [CrossRef]
190. Hu, Y.L.; Chen, Z.P.; Chen, Y.; Shi, C.X.; Yu, R.Q. Generalized multiple internal standard method for quantitative liquid chromatography mass spectrometry. *J. Chromatogr. A* **2016**, *1445*, 112–117. [CrossRef]
191. Bader, M. A systematic approach to standard addition methods in instrumental analysis. *J. Chem. Educ.* **1980**, *57*, 703–706. [CrossRef]
192. Durner, J.; Spahl, W.; Zaspel, J.; Schweikl, H.; Hickel, R.; Reichl, F.X. Eluted substances from unpolymerized and polymerized dental restorative materials and their Nernst partition coefficient. *Dent. Mater.* **2010**, *26*, 91–99. [CrossRef]
193. Pongprueksa, P.; De Munck, J.; Duca, R.C.; Poels, K.; Covaci, A.; Hoet, P.; Godderis, L.; Van Meerbeek, B.; Van Landuyt, K.L. Monomer elution in relation to degree of conversion for different types of composite. *J. Dent.* **2015**, *43*, 1448–1455. [CrossRef]
194. Nilsen, B.W.; Jensen, E.; Örtengren, U.; Bang, B.; Michelsen, V.B. Airborne exposure to gaseous and particle-associated organic substances in resin-based dental materials during restorative procedures. *Eur. J. Oral Sci.* **2019**, *127*, 425–434. [CrossRef]
195. Bationo, R.; Jordana, F.; Boileau, M.J.; Colat-Parros, J. Release of monomers from orthodontic adhesives. *Am. J. Orthod. Dentofac. Orthop.* **2016**, *150*, 491–498. [CrossRef]
196. Finley-Jones, H.J.; Holcombe, J.A. Evaluation of internal standard predictions across instrumental platforms in inductively coupled plasma mass spectrometry. *J. Anal. At. Spectrom.* **2009**, *24*, 837–841. [CrossRef]
197. Putzeys, E.; Duca, R.C.; Coppens, L.; Vanoirbeek, J.; Godderis, L.; Van Meerbeek, B.; Van Landuyt, K.L. In-Vitro transdental diffusion of monomers from adhesives. *J. Dent.* **2018**, *75*, 91–97. [CrossRef]
198. Putzeys, E.; Vercruyssen, C.; Duca, R.C.; Saha, P.S.; Godderis, L.; Vanoirbeek, J.; Peumans, M.; Van Meerbeek, B.; Van Landuyt, K.L. Monomer release from direct and indirect adhesive restorations: A comparative in vitro study. *Dent. Mater.* **2020**, *36*, 1275–1281. [CrossRef] [PubMed]
199. Taylor, P.J. Matrix effects: The Achilles heel of quantitative high-performance liquid chromatography–electrospray–tandem mass spectrometry. *Clin. Biochem.* **2005**, *38*, 328–334. [CrossRef] [PubMed]
200. Danzer, K.; Currie, L.A. Guidelines for calibration in analytical chemistry. Part I. Fundamentals and single component calibration (IUPAC Recommendations 1998). *Pure Appl. Chem.* **1998**, *70*, 993–1014. [CrossRef]
201. Moosavi, S.M.; Ghassabian, S. Linearity of Calibration Curves for Analytical Methods: A Review of Criteria for Assessment of Method Reliability. In *Calibration and Validation of Analytical Methods: A Sampling of Current Approaches*; InTech: London, UK, 2018; pp. 109–128.





## Article

# Impact of Bis-*O*-dihydroferuloyl-1,4-butanediol Content on the Chemical, Enzymatic and Fungal Degradation Processes of Poly(3-hydroxybutyrate)

Quentin Carboué \*, Sami Fadlallah \*, Yasmine Werghi, Lionel Longé, Antoine Gallos, Florent Allais and Michel Lopez

URD Agro-Biotechnologies Industrielles (ABI), CEBB, AgroParisTech, 3 Rue des Rouges-Terres, 51110 Pomacle, France; yasmine.werghi1@gmail.com (Y.W.); lionel.longe@agroparistech.fr (L.L.); antoine.gallos@agroparistech.fr (A.G.); florent.allais@agroparistech.fr (F.A.); michel.lopez@agroparistech.fr (M.L.)  
\* Correspondence: quentin.carboue@agroparistech.fr (Q.C.); sami.fadlallah@agroparistech.fr (S.F.)

**Abstract:** Poly- $\beta$ -hydroxybutyrate (PHB) is a very common bio-based and biocompatible polymer obtained from the fermentation of soil bacteria. Due to its important crystallinity, PHB is extremely brittle in nature, which results in poor mechanical properties with low extension at the break. To overcome these issues, the crystallinity of PHB can be reduced by blending with plasticizers such as ferulic acid derivatives, e.g., bis-*O*-dihydroferuloyl-1,4-butanediol (BDF). The degradation potential of polymer blends of PHB containing various percentages (0, 5, 10, 20, and 40 w%) of BDF was investigated through chemical, enzymatic and fungal pathways. Chemical degradation revealed that, in 0.25 M NaOH solution, the presence of BDF in the blend was necessary to carry out the degradation, which increased as the BDF percentage increased. Whereas no enzymatic degradation could be achieved in the tested conditions. Fungal degradation was achieved with a strain isolated from the soil and monitored through imagery processing. Similar to the chemical degradation, higher BDF content resulted in higher degradation by the fungus.

**Keywords:** poly- $\beta$ -hydroxybutyrate; plasticizer; biodegradation; imagery analysis; *Actinomucor elegans*

**Citation:** Carboué, Q.; Fadlallah, S.; Werghi, Y.; Longé, L.; Gallos, A.; Allais, F.; Lopez, M. Impact of Bis-*O*-dihydroferuloyl-1,4-butanediol Content on the Chemical, Enzymatic and Fungal Degradation Processes of Poly(3-hydroxybutyrate). *Polymers* **2022**, *14*, 1564. <https://doi.org/10.3390/polym14081564>

Academic Editors: José Miguel Ferri, Vicent Fombuena Borràs and Miguel Fernando Aldás Carrasco

Received: 16 March 2022

Accepted: 7 April 2022

Published: 11 April 2022

**Publisher's Note:** MDPI stays neutral with regard to jurisdictional claims in published maps and institutional affiliations.



**Copyright:** © 2022 by the authors. Licensee MDPI, Basel, Switzerland. This article is an open access article distributed under the terms and conditions of the Creative Commons Attribution (CC BY) license (<https://creativecommons.org/licenses/by/4.0/>).

## 1. Introduction

The global environmental impact and the growing social concerns regarding conventional plastics, accompanied by the high rate of depletion of petroleum resources and the evolution of legislation, have led to the development of bio-based polymers [1]. However, the mere nature and renewable origin of bio-based polymers obtained from biomass are not sufficient to qualify a material as “green”. Indeed, many other criteria have to be considered, especially regarding its synthesis conditions and (bio)degradation [2]. Further, bio-based polymers are mostly used in packaging applications because of their higher costs of production and their significantly lower performances in comparison with petroleum-based materials [3]. In addition, confusion may exist regarding the bio-based and biodegradable aspects: not all bio-based polymers are biodegradable as some synthetic bio-based polymers exhibit very low biodegradation potentials. Some critical factors involved in the degradation of polymers are molecular weight, crystallinity, wettability, porosity, and material thickness [4–8]. On the other hand, all natural polymers are biodegradable [9].

Polyhydroxyalkanoates (PHA), such as poly(3-hydroxybutyrate) (PHB), are intracellular carbon and energy storage compounds (carbonosomes) found in some soil bacteria such as *Cupriavidus necator* [10]. It is a thermoplastic with similar properties to petroleum-based polypropylene with a melting point ( $T_m$ ) of 180 °C [11]. It can be produced through fermentation using renewable and low-cost biomass feedstocks such as wastewater from the sugar industry, permeate from the dairy industry, and lignocellulosic byproducts as culture media [12,13]. Further, PHB is a biocompatible polymer whose biocompatibility can

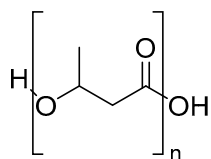
be increased through rapid lipase- or sodium hydroxide-based treatments [14]. However, PHB, because of its high crystallinity, is a brittle material due to a low glass transition temperature ( $T_g$ ) (i.e.,  $T_g$  of pure PHB is between 2 and 15 °C) and a secondary crystallization of the amorphous phase that occurs at room temperature [15,16]. The focus has been made to find compounds that improve the mechanical and chemical properties of PHB (e.g., notably improving the flexural strength, impact strength, heat deflection, long-term stability) while maintaining its biodegradability and biocompatibility levels. PHB copolymers involving 4-hydroxybutyrate, agave fibers, or lignin, have been developed and exhibited higher mechanical properties than neat PHB [17–19]. Another more economical way to improve the mechanical properties of PHB is through the formation of blends using plasticizers such as the PHB-glycerol blend, which shows a reduction in crystallinity when compared with PHB homopolymer [15]. It has been previously demonstrated that bio-based bis-*O*-dihydroferuloyl-1,4-butanediol (BDF)—obtained from the highly selective lipase-catalyzed enzymatic reaction of two ferulic acids with 1,4-butanediol—blended with PHA significantly improved the mechanical properties when compared with the polymer alone [20,21].

The current article aims to study the degradation processes and patterns of a blend of PHB with various incorporation levels of BDF (5, 10, 20, 30, and 40 w%) through various modalities: chemical, enzymatic and fungal to study the impact of BDF contents on the (bio)degradation processes. Indeed, as new polymeric compounds are produced, it is important to evaluate their (bio)degradation following different strategies and conditions to understand the underlying mechanisms and evaluate the most effective management strategy regarding environmental, economic, and societal considerations. In the case of fungal biodegradation, the monitoring of the evolution of the polymeric particles was carried out through image analysis of the binary images obtained after the treatment of pictures. This is an original approach as image analysis is usually used to evaluate the structural properties of various polymeric materials [22–24].

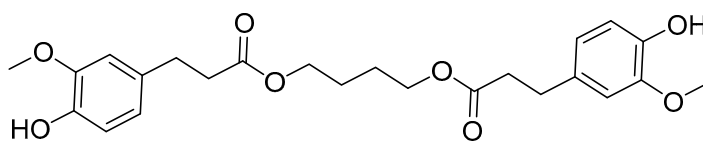
## 2. Materials and Methods

### 2.1. Polymers

Plasticizer-free PHB powder (Batch T19) was supplied by BIOMER<sup>®</sup> (Schwalbach am Taunus, Germany). Ferulic acid was acquired from Biosynth-Carbosynth<sup>®</sup> (Thal, Switzerland). BDF was synthesized following the protocol of Pion et al. (2013) [20]. The structures are presented in Figure 1.



poly- $\beta$ -hydroxybutyrate



bis-*O*-dihydroferuloyl-1,4-butanediol

**Figure 1.** Structures of PHB and BDF.

### 2.1.1. Preparation of PHB/BDF Specimens

Extrusion of PHB/BDF blends was performed on a compounding extruder HAAKE MiniLab II (Thermo Fisher Scientific<sup>®</sup>, Waltham, MA, USA) twin screw, screw diameter 16 mm, 24 mm. Screws were set in co-rotation, at 60 rpm at an extrusion temperature of 170 °C. HAAKE MiniJet Pro Piston Injection Molding System was used for the injection molding of samples specimen. A DMA test bar mold was used, with dimensions of 60 mm × 10 mm × 1 mm. The mold was maintained at 45 °C during the injection.

### 2.1.2. Preparation of PHB/BDF Films

The PHB films were formed using solvent casting: specimens of PHB/BDF blends were dissolved in chloroform (VWR Chemicals BDH<sup>®</sup>, Radnor, PA, USA) and the solution was then poured into stainless steel rectangular molds (11 × 6 cm). The solvent was then slowly evaporated under the fume hood at room temperature to obtain uniform films of around 0.1 μm thickness as measured by an electronic digital caliper.

### 2.1.3. Preparation of PHB/BDF Powders

Around 5 g of the specimen of PHB/BDF blend were ground using stainless steel marble agitated at a frequency of 20 Hz at −196 °C for 2 min using a Cryomill (Retsch GmbH<sup>®</sup>, Haan, Germany).

### 2.1.4. Characterization of the Material

#### Differential Scanning Calorimetry

Differential Scanning Calorimetry (DSC) was performed with a DSC Q20 (TA Instruments<sup>®</sup>, New Castle, DE, USA). Around 8 mg sample was placed in a sealed pan and flushed with highly pure nitrogen gas. The first heating ran from −80 °C to 200 °C with a heating rate of 10 °C·min<sup>−1</sup> was performed to determine the melting temperature ( $T_m$ ) and the fusion enthalpy ( $\Delta H_f$ ). This is followed by a cooling run to −80 °C with a cooling ramp of 200 °C·min<sup>−1</sup>. The glass transition temperature ( $T_g$ ) was obtained in the second heating run from −80 °C to 200 °C at 10 °C·min<sup>−1</sup>. Indeed, PHB tends to crystallize during the cooling step. The rate of the cooling was thus increased to quench the material and avoid its recrystallization easing this way the measurement of the  $T_g$ .

#### Fourier-Transform Infrared Spectroscopy

Fourier-transform infrared (FT-IR) spectra were recorded from film samples in the middle infrared (4000–650 cm<sup>−1</sup>) using a Cary 630 FTIR Spectrometer (Agilent Technologies<sup>®</sup>, Santa Clara, CA, USA) working in passing mode.

## 2.2. Enzymatic and Chemical Degradation

### 2.2.1. Chemical Degradation

Specimens of PHB/BDF blends (with BDF content of 0, 5, 10, 20, 30, and 40 w%) weighting 100 mg were put in a 4 mL of 0.25 M NaOH solution. The mixture was stirred at 100 rpm at room temperature for 32 h. HCl (3 M) was then added until reaching an acidic pH to stop the reaction. The obtained precipitate was washed with distilled water and the polymer was then dry-frozen prior to analysis. In order to confirm the results, the experiment was also carried out with commercial non-extruded PHB (Sigma-Aldrich<sup>®</sup>, Saint-Louis, MO, USA) powder. A reaction kinetic was also carried out for the PHB/BDF blend with (40 w% of BDF) with a sampling every 30 min during the first 9.5 h of alkali degradation reaction.

### 2.2.2. Enzymatic Degradation

The evaluation of the enzymatic biodegradation potential of the various PHB/BDF blends was carried out following the protocol used by Rodríguez-Contreras et al. (2012) [25]. Briefly, a suspension of 17 mg·mL<sup>−1</sup> of powder blend (with BDF content of 0, 5, 10, 20, 30, and 40 w%) was put to react with 17.5 mg of Lipopan<sup>®</sup> 50 BG (1,3 specific lipase

from *Thermomyces lanuginosus*; Novozymes<sup>®</sup>, Bagsværd, Denmark) into hemolytic tubes containing 3 mL of phosphate buffer (0.05 M, pH = 7.4) at 37 °C, agitated at 50 rpm for a week. The same protocol was repeated for films of PHB blends and with commercial PHB (Sigma-Aldrich<sup>®</sup>) powder. Some additional reaction parameters were also investigated, a pH of 9, a temperature of 45 °C, an absence of stirring, and a two-fold and ten-fold concentration of enzyme. Another industrial lipase was also tested: Eversa<sup>®</sup> (free liquid lipase from genetically modified *Aspergillus oryzae*; Novozymes<sup>®</sup>), following the previous protocol but at a temperature of 40 °C. The tube was then put at 0 °C to stop the reaction, and centrifuged at 4750 rpm for 10 min. The obtained precipitate was washed with distilled water, resuspended, and centrifuged again to remove the enzyme. The polymer was then lyophilized prior to analysis. Enzyme activities were checked using the p-nitrophenyl butyrate colorimetric assay. Absorbance was monitored at 400 nm and the results were compared with a p-nitrophenol calibration curve.

### 2.2.3. Evaluation of the Degradation Potential through Nuclear Magnetic Resonance (NMR) Spectroscopy

Degradation of both chemical and enzymatic ways was investigated using NMR. <sup>1</sup>H NMR spectra were recorded on a Bruker Fourier 300 MHz (CDCl<sub>3</sub> residual signal at 7.26 ppm). Data are reported in Figures S1 and S2 in the Supplementary Materials.

All NMR assignments were also carried out using <sup>1</sup>H-<sup>1</sup>H COSY (Figure S3, Supplementary Materials). The following peaks were followed: 4.20 ppm corresponding to β-hydroxybutyric acid (the constituting monomer of PHB) and 5.20 ppm corresponding to the PHB chain. Polymer degradation at a certain time *t* is then expressed as the ratio of the appearance of the integrated monomer peak to the disappearance of the integrated polymer peak.

$$\text{Degree of degradation}(t)(\%) = \frac{[\text{monomer peak}]_t}{[\text{monomer peak}]_t + [\text{polymer peak}]_t} \times 100 \quad (1)$$

With  $[\text{monomer peak}]_t$  and  $[\text{polymer peak}]_t$  corresponding to the integrated <sup>1</sup>H NMR of the monomer and polymer peaks at time *t*, respectively.

## 2.3. Fungal Degradation

### 2.3.1. Sample Collection

Two soil samples were collected in sterilized 1 L plastic bottles from two sites. One on the banks of the brook Le Petit Ru (Bazancourt, France) and one from the embankment of the highway (E420, Pomacle, France). Bigger fractions involving plastic pieces, wood, rocks, and leaves were removed and the soil samples were then kept at room temperature in the dark.

### 2.3.2. Isolation of PHB-Degrading Fungi

Five films were buried vertically at a depth of 5 cm in each soil sample complemented with 200 mL of a solution containing 2 g of glucose and incubated in a lab oven at 30 °C. After 4 weeks, films were recovered from the soil and placed on Petri dishes containing Sabouraud (SAB) agar medium (Sigma-Aldrich<sup>®</sup>). The Petri dishes were incubated at 30 °C for 4 days. The different fungal strains were then isolated on different SAB Petri dishes. To evaluate the PHB degradation potential of the various isolated fungi, each strain was cultivated on a medium containing PHB as the sole carbon source. The composition of the selective medium was: 11.28 g·L<sup>-1</sup> of M9 Minimal Salts 5× medium (Sigma-Aldrich<sup>®</sup>), 0.011 g·L<sup>-1</sup> of calcium chloride, 0.24 g·L<sup>-1</sup> of magnesium sulfate, 0.02 g·L<sup>-1</sup> of yeast extract and 15 g·L<sup>-1</sup> of agar and 1 g·L<sup>-1</sup> of PHB powder. One strain was able to grow on the selective medium with PHB as a sole carbon source and was identified as *Actinomucor elegans* at the Muséum National d'Histoire Naturelle de Paris (France). The purity of a 3-days' culture was tested with a DNEasy Plant mini Kit (Qiagen<sup>®</sup>, Venlo, The Netherlands). Internal transcribed spacer region amplification was carried out through polymerase chain

reaction using ITS5 and ITS4 primers. After sequencing, taxonomic affiliation was made using BLAST and GenBank (National Center for Biotechnology Information, Bethesda, MD, USA).

### 2.3.3. Evaluation of the Degradation Potential of PHB

The strain of *A. elegans* was grown on a SAB plate containing a PHB film of 2 cm in length. After 3 weeks, the mycelium was gently removed using a scalpel. The film was rinsed with distilled water and dried at 60 °C for 24 h before being analyzed through FT-IR and DSC.

### 2.3.4. Evaluation of the Degradation Potentials of the PHB Blends through Image Analysis

The PHB degradation ability of the isolated fungal strains able to grow on the PHB-containing selective medium was then investigated through image processing and analysis. Selective medium containing PHB powder with various percentages of BDF (0, 5, 10, 20, and 40 w%) were inoculated with 4 strains using 6-well plates. For 14 days, photos were taken using an Ebox CX5.TS (Vilber Lourmat<sup>®</sup>, Marne-la-Vallée, France). For the same kinetic series, the obtained pictures were then converted into binary images with the same threshold value in order to only visualize the PHB/BDF grains as white pixels. The evolution of the blend grains was then analyzed by observing the total white pixels in the matrixes of the binary pictures during the time. The pictures were treated using Illustrator (Adobe<sup>®</sup>, San José, CA, USA) and the image processing was carried out using the thresholding application in MATLAB (MathWorks<sup>®</sup>, Natick, MA, USA) [26]. Polymer degradation at a certain time *t* is then expressed as the percentage of the initial total white pixels (WP) of the binary matrix.

$$\text{Degree of degradation}(t)(\%) = \frac{WP_t}{WP_{t_0}} \times 100 \quad (2)$$

With  $WP_t$  the white pixels of the binary image at *t* and  $WP_{t_0}$  the white pixels of the photo at  $t_0$ .

To compare the degradation kinetics of the various PHB/BDF blends, the results for each sample were also expressed as  $t_{50}$ , which is the duration necessary to reach 50% of the degradation of the initial polymer. The  $t_{50}$  values were determined using polynomial regression with the highest significance (the selected polynomial degree for the model was significant when tested with an F-test and maximized both the coefficient of determination  $R^2$  and the adjusted coefficient of determination  $\text{adj-}R^2$ ).

### 2.3.5. Statistical Analysis

Experiments were carried out in triplicate. The results were tested by one-way ANOVA and the comparison of the means was done using Tukey post hoc range tests ( $\alpha = 0.05$ ). Statistical analyses were carried out using MATLAB (MathWorks<sup>®</sup>).

## 3. Results and Discussion

Along with the article, the polymer materials are tested under different forms—specimen, film, and powder—because certain forms are more suitable than others to carry out the tests. The thermal properties of the tested materials under the different forms are given in Table 1.

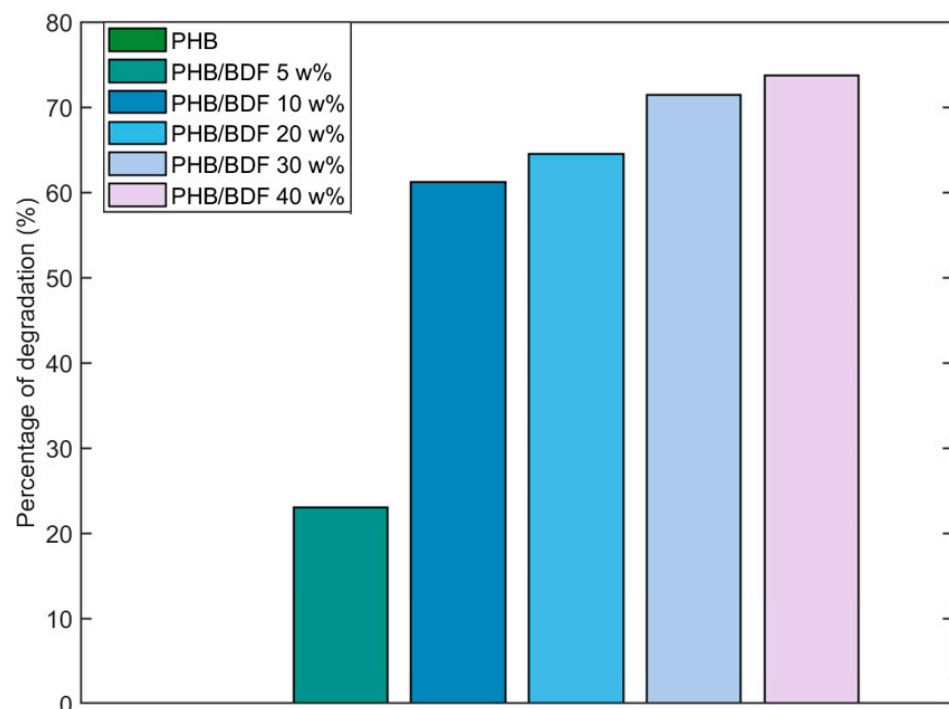
### 3.1. Chemical Degradation

The study of the degradation of the polymer blends through the use of a chemical agent was carried out to serve as a model to study the degradation processes with the other methods. Sodium hydroxide was chosen because it is a strong stress cracking agent to PHB. Indeed, it has been shown that a solution of 3 M NaOH dramatically damaged the surface and favored the surface cracking of PHB-HV (96/6%) during tensile testing [27]. However, at lower concentrations of 0.1 to 1 M, alkali treatments of 24 h increase the

hydrophilicity of PHB film surface through breaking of ester bonds and subsequent increase in densities of hydrophilic terminal carboxyl and hydroxyl groups without changing the overall mechanical properties as suggested by the weight loss values that were 0.3 and 3.7 w% for the 0.1 to 1 M treatments, respectively [28]. Following this idea, Yang et al. (2002) have shown that PHB films treated with 1 N NaOH solution at 60 °C for 1 h reduced the pore sizes of the films, although the authors did not observe any macroscopic morphological change on the surfaces. This modification of the texture of the film, coupled with the increase in the hydrophilicity improved the biocompatibility of the films as the mammal cells were more likely to attach on the surface to grow [14,29]. In the present case, alkali treatments (0.25 M NaOH solution) were carried out on the specimen. After 32 h, degradation was only observed for the samples that contained BDF. Furthermore, the results showed that as BDF increases, the percentage of degradation increases as well—23.0% and 73.7% for the PHB/BDF blends 5 w% and 40 w%, respectively—suggesting an important role of the plasticizer in the hydrolysis reaction (Figure 2).

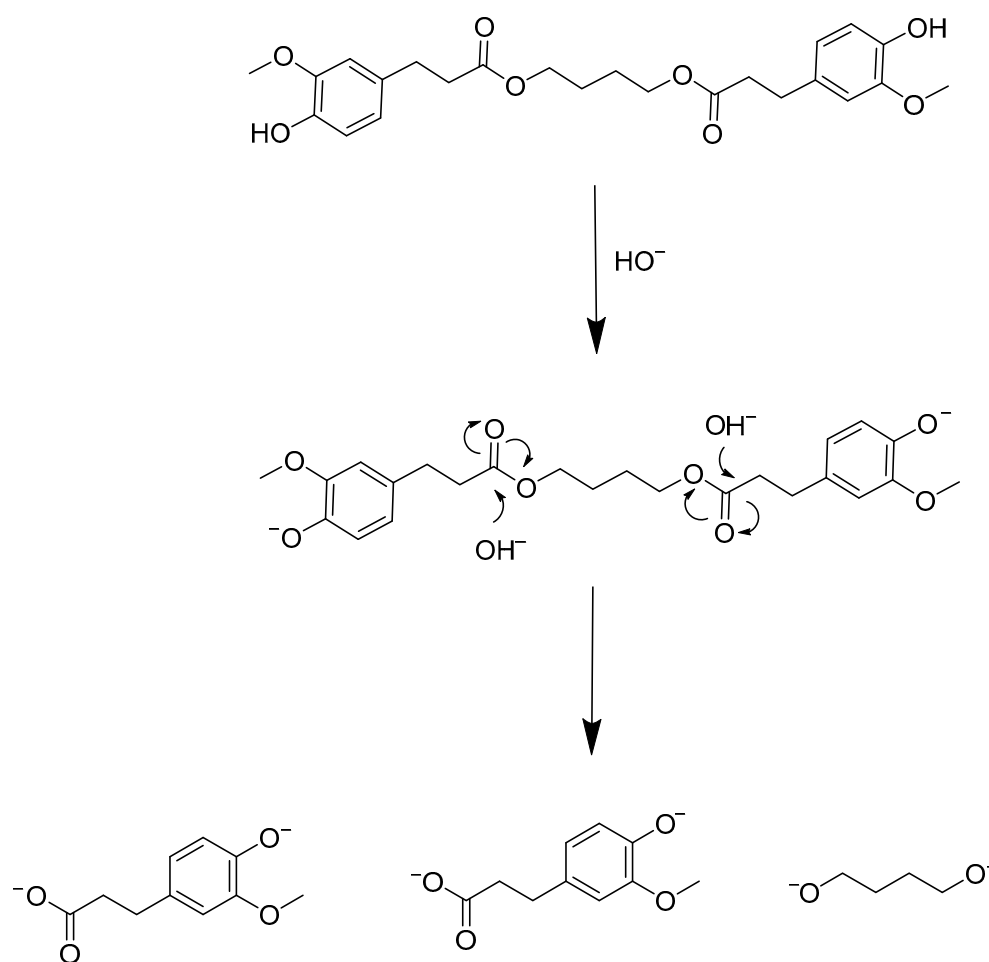
**Table 1.** DSC Analysis of the PHB/BDF Blends.

Type	Specimen				Film				Powder			
	$T_g$ (°C)	$T_m$ (°C)	$T_c$ (°C)	$T_{cc}$ (°C)	$T_g$ (°C)	$T_m$ (°C)	$T_c$ (°C)	$T_{cc}$ (°C)	$T_g$ (°C)	$T_m$ (°C)	$T_c$ (°C)	$T_{cc}$ (°C)
PHB	0.7	162.9	90.4	35.8	0.1	159.8	-	36.5	-	170.0	92.2	-
PHB/BDF 5 w%	0.0	162.0	64.1	36.2	-4.7	157.7	-	32.5	0.75	160.7	66.6	31.7
PHB/BDF 10 w%	-1.5	156.7	-	37.2	0.8	160.1	-	39.5	0.7	158.5	58.7	34.5
PHB/BDF 20 w%	-5.8	151.4	-	38.0	-2.5	152.7	-	39.8	-4.9	150.6	-	35.4
PHB/BDF 30 w%	-8.6	146.7	-	44.3	-11.7	140.0	-	42.4	-8.4	143.3	-	35.9
PHB/BDF 40 w%	-9.4	144.0	-	45.7	-10.3	145.5	-	37.4	-9.1	142.2	-	38.0



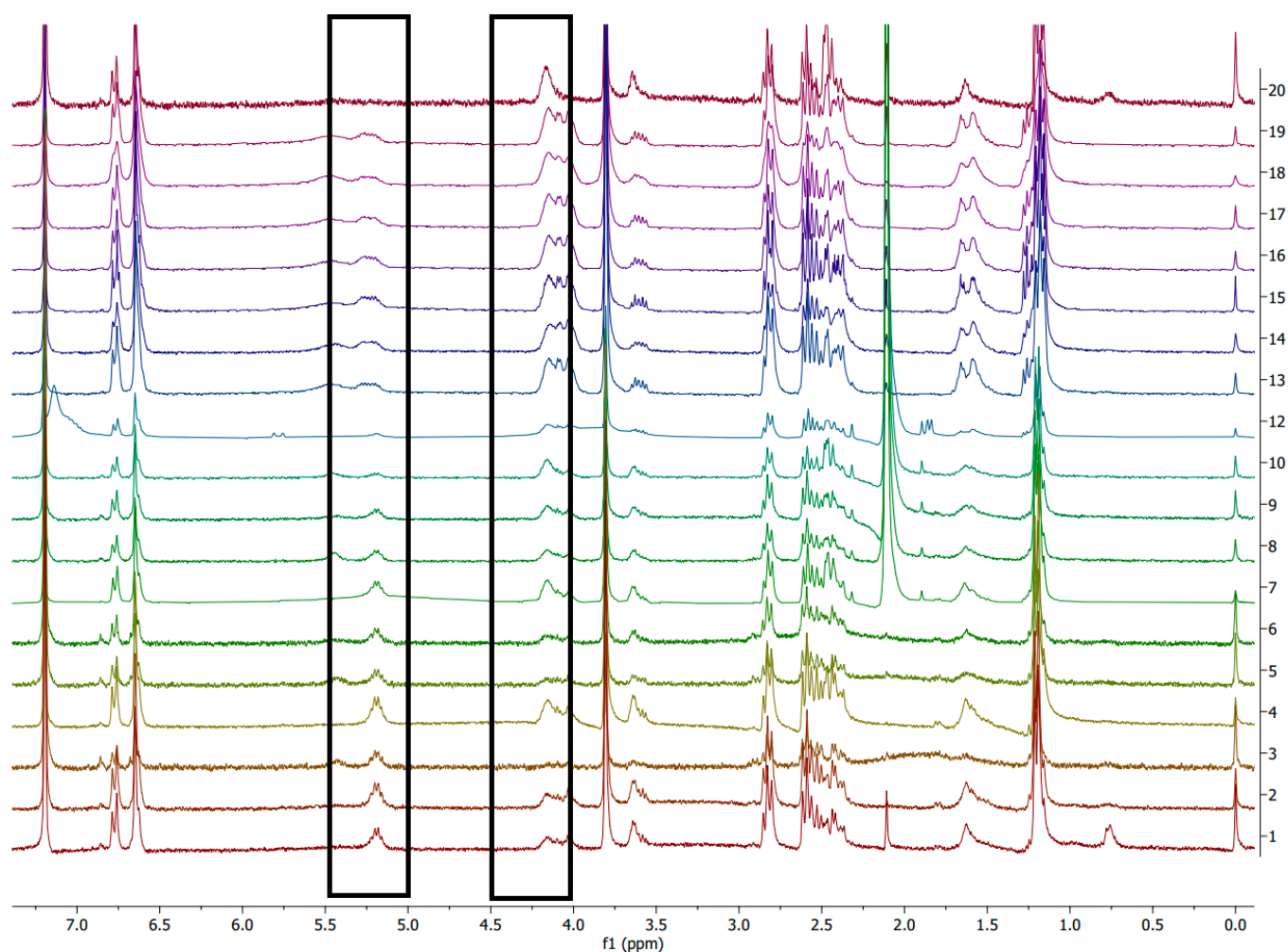
**Figure 2.** Degradation of specimens of PHB/BDF blends in a NaOH solution (0.25 M) during 32 h.

This aspect may be due to the altered properties of the blends in the presence of BDF. This renders the polymer chains of PHB more susceptible to NaOH hydrolytic action (Table 1). A possible mechanism is related to the saponification of BDF itself that liberates oxyanions and carboxylates that may participate in the PHB chains scissions in a bulk degradation process (Figure 3). On the contrary, no degradation was observed for the sample with 100 w% PHB. This result was confirmed by the fact that, in the case of the commercial PHB powder, no alkaline degradation could be observed either, suggesting that extrusion had no influence on the degradation process. Interpretations of the spectra were also made by comparison with the monomer ( $\beta$ -hydroxybutyric acid) spectrum (Figure S2, Supplementary Materials). Confirmation of the presence of monomers in the spectra was carried out with homonuclear correlation spectroscopy ( $^1\text{H}$ - $^1\text{H}$  COSY) (Figure S3 in the Supplementary Materials). The kinetics of the spectra during the alkali degradation showed a progressive appearance of the monomer—peak at 4.2 ppm—and disappearance of the polymer—peak at 5.2 ppm—(Figure 4).



**Figure 3.** Saponification reaction with BDF.





**Figure 4.**  $^1\text{H}$  NMR ( $\text{CDCl}_3$ ) spectrum of specimen PHB/BDF 40 w% during alkali degradation with NaOH solution (0.25 M), spectrum 1 corresponds to  $t_0$ ; up to spectrum 19, samples were taken every 30 min of reaction; spectrum 20 corresponds to 32 h reaction.

### 3.2. Enzymatic Degradation

The specific enzymes involved in PHB degradation are the PHB-depolymerase. There are two types of such enzymes: intracellular PHB-depolymerases for which the PHB represents the endogenous carbon reservoir and the hydrolysis is carried out by an accumulation of bacteria, and extracellular PHB-depolymerases for which PHB is an exogenous carbon source and is not limited to the producing bacteria but is also largely found in fungi [16]. In comparison, the occurrence of extracellular depolymerases is more widely reported amongst microorganisms as compared to that of intracellular depolymerases [30]. However, the number of commercially available PHB-depolymerases is still scarce as are the reports of commercial hydrolases that efficiently degrade PHB. Indeed, commercial lipases, esterases, and proteinases from various sources have shown no degradation effects on PHB [31]. In the present case, and unlike the study carried out by Alejandra et al. (2012), no degradation has been observed on any PHB film regardless of the BDF content during our enzymatic reactions carried out with Lipopan<sup>®</sup> 50 BG and Everva<sup>®</sup> [25] (Figure S4, Supplementary Materials). This absence of enzymatic degradation was observed regardless of the nature of the blends—powder or film. The extrusion also had no effect as the commercial PHB was not degraded either. Moreover, the tested pH (7.4 and 9), the tested temperatures of reaction (37 °C and 45 °C), the stirring (50 rpm) or the static conditions and the tested enzyme concentrations (17.5, 35, and 175  $\text{mg}\cdot\text{mL}^{-1}$ ) had no effect on the process.

### 3.3. Fungal Degradation

To carry out an isolation of PHB-degrading microorganisms, the film was chosen over the specimen because it maximizes the surface available for the microorganisms for colonization and, unlike powder, it can be recovered for further isolation. Soil samples were chosen as the source of inoculum because it is the natural environment of PHB-producing bacteria. This way, a study involving the isolation of PHB-degrading microorganisms from various habitats such as compost, soil, air, and horse dung has shown a prevalence of soil fungi over bacteria, protozoa, and lichens as potential degraders [32]. This is not surprising since fungi are primary decomposers of polymeric compounds in many ecosystems. Identified PHB-degrading fungi involve fungi of the genera *Paecilomyces*, *Aspergillus*, *Penicillium*, *Fusarium*, *Alternaria*, and *Trichoderma* [32–35]. After 4 weeks in the soils, the samples of PHB films were highly degraded, fragmented on the edges, and with variable thickness. The cultivation of these fragments of PHB film led to the isolation of 45 different strains. From this collection, further isolation using a selective medium containing PHB as the sole carbon source allowed us to isolate a strain of zygomycete belonging to the order of the Mucorales: a strain of *A. elegans* (Figure S5, Supplementary Materials). This species has previously been reported as a member of the fungal community colonizing PLA/PHB blend mulches in the soil [36]. The ability of the fungus was confirmed through FT-IR analysis of a PHB film after the *A. elegans* was grown on it for 3 weeks (Figure 5). After the cultivation of the fungus, there is the appearance of a large band between 3000 and 3600  $\text{cm}^{-1}$ , corresponding to the hydroxide and carboxylic acid functions carried by the oligomers after the cleavage of PHB chains. Moreover, bands located at 1634  $\text{cm}^{-1}$  also appeared after degradation, suggesting the formation of carbon–carbon double bonds in the backbone of the molecules, and the band at 1716  $\text{cm}^{-1}$  corresponding to the carbonyl ester group was reduced greatly. The conversion of carboxylic acid groups into alkenes has already been highlighted during fungal degradation [37].

After having selected the strain and confirmed its potential in the degradation of PHB, the effect of BDF composition in the blends was investigated using imagery analysis of the pictures that were taken during the fungal growth. Indeed, in the media containing the different PHB/BDF blends as the sole source of carbon, the PHB/BDF particles are visible as white grains and this form is thus convenient to measure their evolutions during the time, as the fungus grows (Figure 6).

In order to quantify the polymer degradation, the pictures were treated. Binarization is the conversion process of a multi-tone image into a bi-tonal image in which a threshold range is set; associating pixels to white (or 1) if its tone value is within the threshold boundaries, or to black (0) if it is outside the range. The generated binary matrixes ease the mathematical treatments, notably decreasing the computational load [38] (Figure 7). The selection of the threshold range is a delicate step as many factors may affect the final binary image beforehand, that is why it is important to standardize the shot of films with the same illumination, exposure time, and focal distance. Moreover, the mycelium being white may also interfere with the final calculation of the WP in the binary image. For that matter, the thresholding function is useful as it allows the user to set the threshold interval in order to find the right compromise in the grey tones acceptance to only consider PHB/BDF particles and reject mycelium from the binary image. In the present case, the image treatment had to involve the same threshold range on the complete photo series constituted by a degradation kinetic to obtain relative values regarding this degradation.

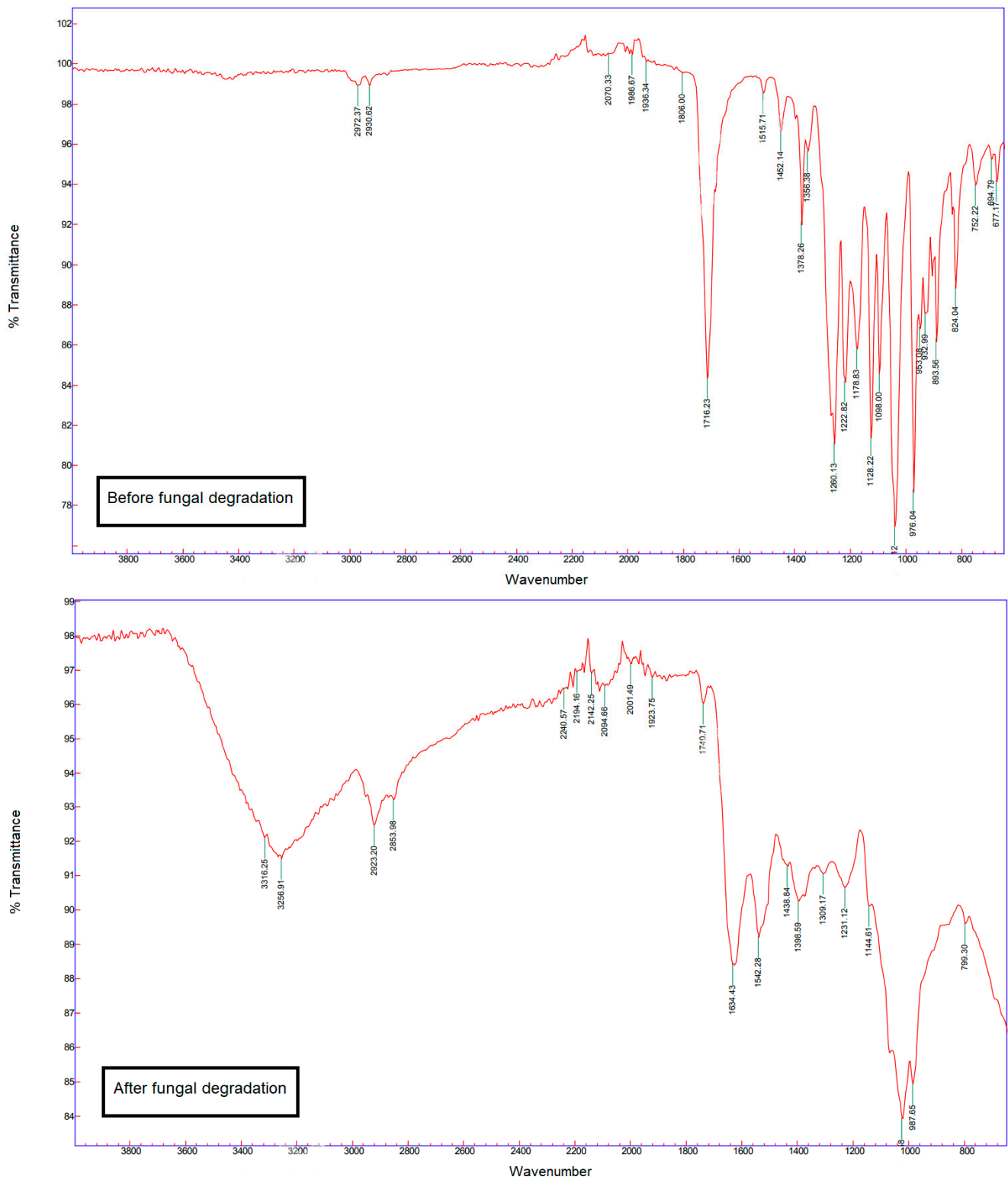
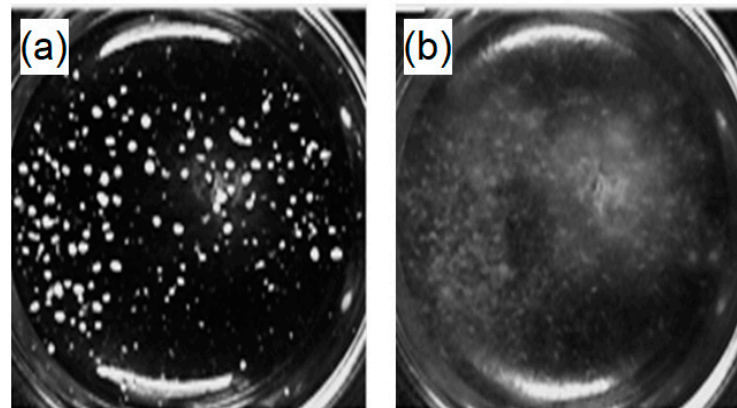
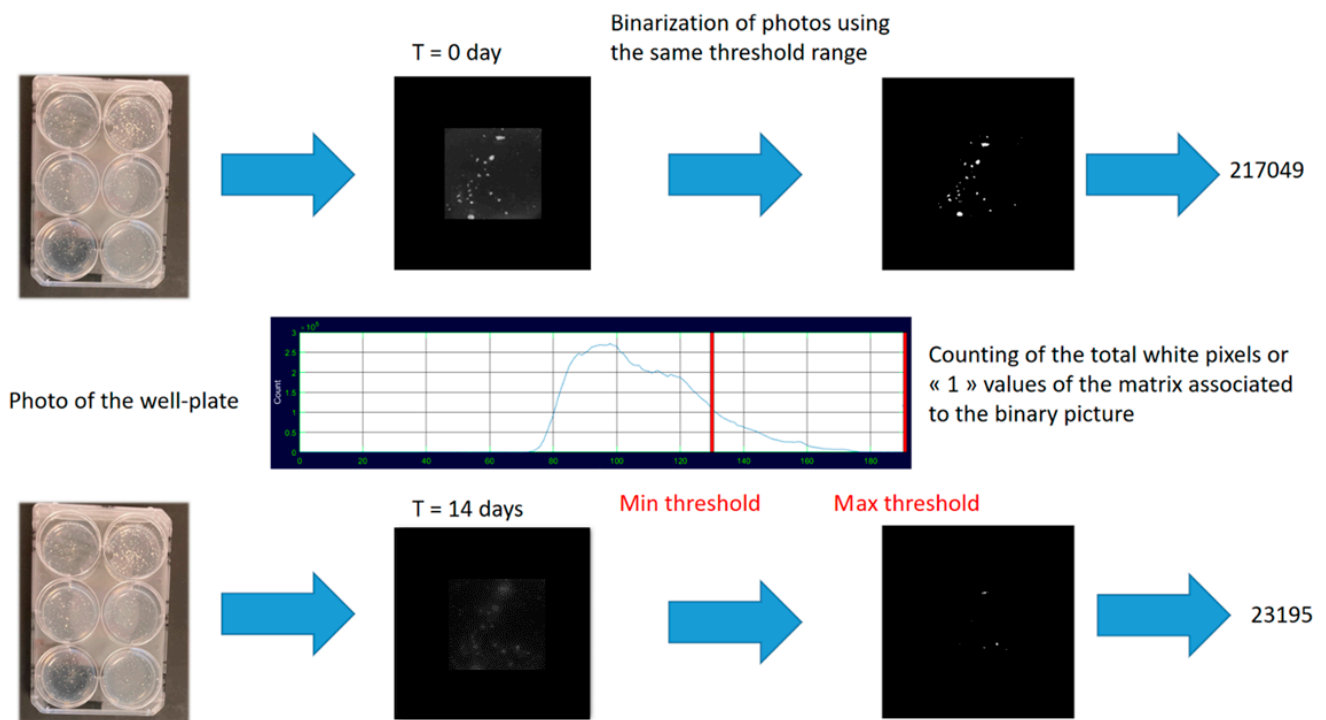


Figure 5. FT-IR spectra of the film before and after 21 days of colonization by the *A. elegans* strain.

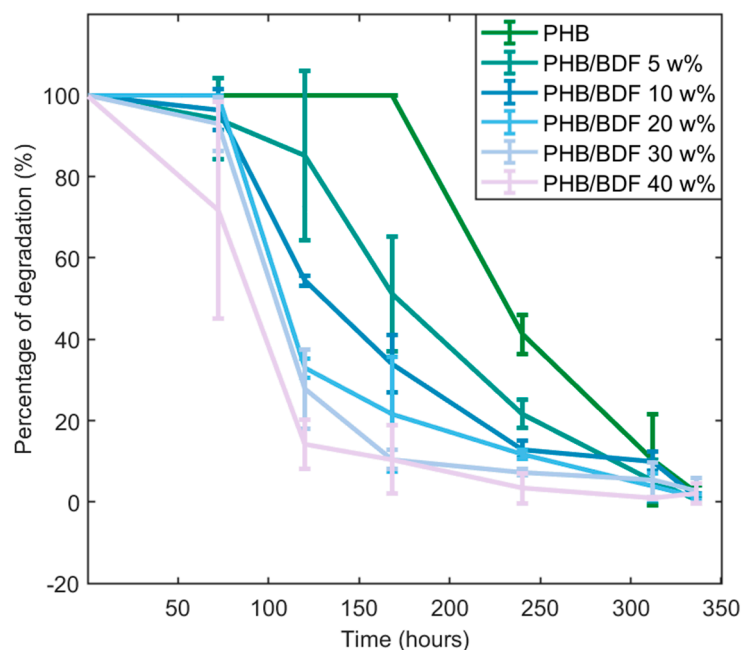


**Figure 6.** Pictures of a well containing the selective medium with powder of PHB/BDF blend as a sole carbon source: (a) medium at  $t_0$  and (b) after 240 h of fungal growth.

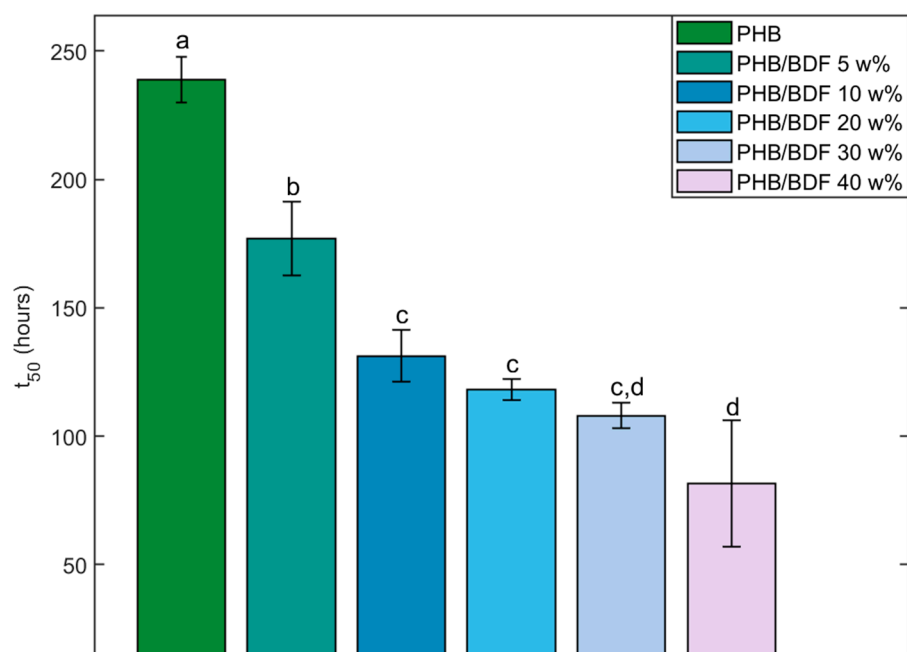


**Figure 7.** Image treatment and analysis process.

The results obtained from the image treatment and analysis revealed an influence of the BDF percentage on the degradation of the blend by the fungus (Figure 8). This was statistically verified by comparing the  $t_{50}$  that decreases as the BDF percentage increases (Figure 9). Pure PHB was slower to be degraded by *A. elegans* as it required more than 300 h to be fully degraded. On the other hand, the presence of more than 20 w% of BDF in the blend showed more rapid degradation of the material by the fungus as 50% of degradation was reached at around 100 h. It is worth mentioning that many fungi with plant-degrading activities are able to degrade and metabolize p-hydroxycinnamic acid derivatives such as ferulic acid, which is a structural compound in the lignocellulosic matrix [39,40]. In the present case, it seems that *A. elegans* preferentially degraded the PHB blends with higher BDF content. By contrast, blends of lignin and PHB obtained by melt extrusion were more resistant to microbial degradation after being buried in the soil. This phenomenon has been explained by the fact that lignin formed strong hydrogen bonds with the PHB, thus reducing its bioavailability for microbes [41].



**Figure 8.** Degradation kinetics of each powder of PHB/BDF blends obtained from image analysis.



**Figure 9.**  $t_{50}$  associated to each powder of PHB/BDF blend. Different letters mean a significant difference as determined with a one-way ANOVA and Tukey post hoc range tests ( $\alpha = 0.05$ ).

#### 4. Conclusions

Whatever the tested conditions, no enzymatic biodegradation of the PHB/BDF blends has been achieved in this work using industrial lipases. The chemical and fungal (bio)degradation processes of the PHB blends, on the other hand, were enhanced as higher contents of the plasticizer BDF were used. In the chemical degradation experiments in NaOH solution (0.25 M), it was shown that BDF was essential for the degradation to occur. In the case of fungal biodegradation, a new strain was isolated from soil samples and the evaluation of the fungus-mediated biodegradation was carried out through an image processing approach, which allows an indirect, non-destructive online monitoring of the

biodegradation. Nevertheless, other monitoring techniques can be used to evaluate the metabolic activity during fungal growth, such as respirometric measurements of the consumed O<sub>2</sub> or the produced CO<sub>2</sub>. This approach holds an interesting perspective since the experiments were carried out in well plates with the potential development of automated procedures, to use this approach in high-throughput screening studies. Regarding the *A. elegans* strain, evaluation of its metabolic potential could eventually result in the production of interesting high-value molecules from PHB residues and further evaluations should include proteomic studies to determine which enzymes are involved in the PHB degradation.

**Supplementary Materials:** The following supporting information can be downloaded at: <https://www.mdpi.com/article/10.3390/polym14081564/s1>; Figure S1: <sup>1</sup>H NMR (CDCl<sub>3</sub>) spectra of PHB/BDF 40 w% and PHB; Figure S2: <sup>1</sup>H NMR (CDCl<sub>3</sub>) spectrum of β-hydroxybutyric acid; Figure S3: <sup>1</sup>H-<sup>1</sup>H COSY (CDCl<sub>3</sub>) of PHB/BDF (40 w%) after 32 h of degradation with NaOH solution (0.25 M); Figure S4: <sup>1</sup>H NMR (CDCl<sub>3</sub>) spectra of powders of PHB blends after 7 days of reaction with 5.8 mg·mL<sup>-1</sup> of Lipopan<sup>®</sup> 50 BG at pH = 7.4, 37 °C and stirred at 50 rpm; Figure S5: Pictures of the PHB film a./ at t0 and b./ after 4 weeks in the soil samples c./ microscopic observation of *A. elegans*, the aseptate hyphae and sporangia are visible.

**Author Contributions:** Conceptualization, Q.C., S.F. and M.L.; Data curation, Y.W.; Formal analysis, Q.C., S.F. and Y.W.; Funding acquisition, F.A.; Investigation, Q.C., S.F. and Y.W.; Methodology, Q.C. and S.F.; Resources, L.L. and A.G.; Software, Q.C.; Supervision, F.A.; Validation, Q.C., S.F. and Y.W.; Visualization, Q.C.; Writing—original draft, Q.C.; Writing—review and editing, S.F., A.G. and F.A. All authors have read and agreed to the published version of the manuscript.

**Funding:** This research received no external funding.

**Institutional Review Board Statement:** Not applicable.

**Informed Consent Statement:** Not applicable.

**Data Availability Statement:** Data sharing not applicable.

**Acknowledgments:** Enzymes Lipopan<sup>®</sup> 50 BG and Eversa<sup>®</sup> were kindly provided by Novozymes (Denmark). The authors are grateful to Grand Reims, Département de la Marne and Grand Est region for financial support.

**Conflicts of Interest:** The authors declare no conflict of interest.

## References

1. Avella, M.; Buzarovska, A.; Errico, M.; Gentile, G.; Grozdanov, A. Eco-Challenges of Bio-Based Polymer Composites. *Materials* **2009**, *2*, 911–925. [[CrossRef](#)]
2. Fadlallah, S.; Sinha Roy, P.; Garnier, G.; Saito, K.; Allais, F. Are Lignin-Derived Monomers and Polymers Truly Sustainable? An in-Depth Green Metrics Calculations Approach. *Green Chem.* **2021**, *23*, 1495–1535. [[CrossRef](#)]
3. Koncar, V. Composites and Hybrid Structures. In *Smart Textiles for In Situ Monitoring of Composites*; Koncar, V., Ed.; Elsevier: Amsterdam, The Netherlands, 2019; pp. 153–215, ISBN 978-0-08-102308-2.
4. Sevim, K.; Pan, J. A Model for Hydrolytic Degradation and Erosion of Biodegradable Polymers. *Acta Biomater.* **2018**, *66*, 192–199. [[CrossRef](#)]
5. Huang, Y.; Chen, F.; Pan, Y.; Chen, C.; Jiang, L.; Dan, Y. Effect of Hydrophobic Fluoropolymer and Crystallinity on the Hydrolytic Degradation of Poly(Lactic Acid). *Eur. Polym. J.* **2017**, *97*, 308–318. [[CrossRef](#)]
6. Khakbaz, M.; Hejazi, I.; Seyfi, J.; Jafari, S.-H.; Khonakdar, H.A.; Davachi, S.M. A Novel Method to Control Hydrolytic Degradation of Nanocomposite Biocompatible Materials via Imparting Superhydrophobicity. *Appl. Surf. Sci.* **2015**, *357*, 880–886. [[CrossRef](#)]
7. Lizundia, E.; Sáenz-Pérez, M.; Patrocínio, D.; Aurrekoetxea, I.; dM Vivanco, M.; Vilas, J.L. Nanopatterned Polystyrene-b-Poly(Acrylic Acid) Surfaces to Modulate Cell-Material Interaction. *Mater. Sci. Eng. C* **2017**, *75*, 229–236. [[CrossRef](#)]
8. Siparsky, G.L.; Voorhees, K.J.; Miao, F. Hydrolysis of Polylactic Acid (PLA) and Polycaprolactone (PCL) in Aqueous Acetonitrile Solutions: Autocatalysis. *J. Polym. Environ.* **1998**, *6*, 31–41. [[CrossRef](#)]
9. Garrison, T.; Murawski, A.; Quirino, R. Bio-Based Polymers with Potential for Biodegradability. *Polymers* **2016**, *8*, 262. [[CrossRef](#)]
10. Jendrossek, D. Polyhydroxyalkanoate Granules Are Complex Subcellular Organelles (Carbonosomes). *J. Bacteriol.* **2009**, *191*, 3195–3202. [[CrossRef](#)]
11. McAdam, B.; Brennan Fournet, M.; McDonald, P.; Mojicevic, M. Production of Polyhydroxybutyrate (PHB) and Factors Impacting Its Chemical and Mechanical Characteristics. *Polymers* **2020**, *12*, 2908. [[CrossRef](#)]

12. Sen, K.Y.; Baidurah, S. Renewable Biomass Feedstocks for Production of Sustainable Biodegradable Polymer. *Curr. Opin. Green Sustain. Chem.* **2021**, *27*, 100412. [CrossRef]
13. Saratale, R.G.; Cho, S.K.; Saratale, G.D.; Ghodake, G.S.; Bharagava, R.N.; Kim, D.S.; Nair, S.; Shin, H.S. Efficient Bioconversion of Sugarcane Bagasse into Polyhydroxybutyrate (PHB) by *Lysinibacillus* sp. and Its Characterization. *Bioresour. Technol.* **2021**, *324*, 124673. [CrossRef]
14. Yang, X.; Zhao, K.; Chen, G.-Q. Effect of Surface Treatment on the Biocompatibility of Microbial Polyhydroxyalkanoates. *Biomaterials* **2002**, *23*, 1391–1397. [CrossRef]
15. El-Hadi, A.; Schnabel, R.; Straube, E.; Müller, G.; Henning, S. Correlation between Degree of Crystallinity, Morphology, Glass Temperature, Mechanical Properties and Biodegradation of Poly (3-Hydroxyalkanoate) PHAs and Their Blends. *Polym. Test.* **2002**, *21*, 665–674. [CrossRef]
16. Roohi; Zaheer, M.R.; Kuddus, M. PHB (Poly- $\beta$ -Hydroxybutyrate) and Its Enzymatic Degradation. *Polym. Adv. Technol.* **2018**, *29*, 30–40. [CrossRef]
17. Smith, M.K.M.; Paleri, D.M.; Abdelwahab, M.; Mielewski, D.F.; Misra, M.; Mohanty, A.K. Sustainable Composites from Poly(3-Hydroxybutyrate) (PHB) Bioplastic and Agave Natural Fibre. *Green Chem.* **2020**, *22*, 3906–3916. [CrossRef]
18. Omura, T.; Goto, T.; Maehara, A.; Kimura, S.; Abe, H.; Iwata, T. Thermal Degradation Behavior of Poly[(R)-3-Hydroxybutyrate-Co-4-Hydroxybutyrate]. *Polym. Degrad. Stab.* **2021**, *183*, 109460. [CrossRef]
19. Kai, D.; Zhang, K.; Liow, S.S.; Loh, X.J. New Dual Functional PHB-Grafted Lignin Copolymer: Synthesis, Mechanical Properties, and Biocompatibility Studies. *ACS Appl. Bio Mater.* **2019**, *2*, 127–134. [CrossRef]
20. Pion, F.; Reano, A.F.; Ducrot, P.-H.; Allais, F. Chemo-Enzymatic Preparation of New Bio-Based Bis- and Trisphenols: New Versatile Building Blocks for Polymer Chemistry. *RSC Adv.* **2013**, *3*, 8988. [CrossRef]
21. Gallos, A.; Allais, F. Shape Memory Polymer Based on Poly(Hydroxyalkanoates). French Patent WO2020165075A1, 20 August 2020.
22. Michalska-Požoga, I.; Tomkowski, R.; Rydzkowski, T.; Thakur, V.K. Towards the Usage of Image Analysis Technique to Measure Particles Size and Composition in Wood-Polymer Composites. *Ind. Crops Prod.* **2016**, *92*, 149–156. [CrossRef]
23. Ley, A.; Altschuh, P.; Thom, V.; Selzer, M.; Nestler, B.; Vana, P. Characterization of a Macro Porous Polymer Membrane at Micron-Scale by Confocal-Laser-Scanning Microscopy and 3D Image Analysis. *J. Membr. Sci.* **2018**, *564*, 543–551. [CrossRef]
24. Jelcic, Z.; Holjevac-Grguric, T.; Rek, V. Mechanical Properties and Fractal Morphology of High-Impact Polystyrene/Poly(Styrene-*b*-Butadiene-*b*-Styrene) Blends. *Polym. Degrad. Stab.* **2005**, *90*, 295–302. [CrossRef]
25. Rodríguez-Conterras, A.; Calafell-Monfort, M.; Marqués-Calvo, M.S. Enzymatic Degradation of Poly(3-Hydroxybutyrate) by a Commercial Lipase. *Polym. Degrad. Stab.* **2012**, *97*, 2473–2476. [CrossRef]
26. Image Analyst. Thresholding an Image. 2021. Available online: <https://fr.mathworks.com/matlabcentral/fileexchange/29372-thresholding-an-image> (accessed on 6 April 2022).
27. Farias, R.F.; Canedo, E.L.; Wellen, R.M.R.; Rabello, M.S. Environmental Stress Cracking of Poly(3-Hydroxybutyrate) Under Contact with Sodium Hydroxide. *Mater. Res.* **2015**, *18*, 258–266. [CrossRef]
28. Tsuji, H.; Suzuyoshi, K.; Tezuka, Y.; Ishida, T. Environmental Degradation of Biodegradable Polyesters: 3. Effects of Alkali Treatment on Biodegradation of Poly( $\epsilon$ -Caprolactone) and Poly[(R)-3-Hydroxybutyrate] Films in Controlled Soil. *J. Polym. Environ.* **2003**, *11*, 57–65. [CrossRef]
29. Zhao, K.; Yang, X.; Chen, G.-Q.; Chen, J.-C. Effect of Lipase Treatment on the Biocompatibility of Microbial Polyhydroxyalkanoates. *J. Mater. Sci. Mater. Med.* **2002**, *13*, 849–854. [CrossRef]
30. Gowda U.S., V.; Shivakumar, S. Poly(- $\beta$ -Hydroxybutyrate) (PHB) Depolymerase PHAZ Pen from *Penicillium Expansum*: Purification, Characterization and Kinetic Studies. *3 Biotech* **2015**, *5*, 901–909. [CrossRef]
31. Tarazona, N.A.; Machatschek, R.; Lendlein, A. Influence of Depolymerases and Lipases on the Degradation of Polyhydroxyalkanoates Determined in Langmuir Degradation Studies. *Adv. Mater. Interfaces* **2020**, *7*, 2000872. [CrossRef]
32. Lee, K.-M.; Gimore, D.F.; Huss, M.J. Fungal Degradation of the Bioplastic PHB (Poly-3-Hydroxy- Butyric Acid). *J. Polym. Environ.* **2005**, *13*, 213–219. [CrossRef]
33. Oda, Y.; Asari, H.; Urakami, T.; Tonomura, K. Microbial Degradation of Poly(3-Hydroxybutyrate) and Polycaprolactone by Filamentous Fungi. *J. Ferment. Bioeng.* **1995**, *80*, 265–269. [CrossRef]
34. Aburas, M.M.A. Degradation of Poly (3-Hydroxybutyrate) Using *Aspergillus oryzae* Obtained from Uncultivated Soil. *Life Sci. J.* **2016**, *13*, 51–56. [CrossRef]
35. Satti, S.M.; Shah, Z.; Luqman, A.; Hasan, F.; Osman, M.; Shah, A.A. Biodegradation of Poly(3-Hydroxybutyrate) and Poly(3-Hydroxybutyrate-Co-3-Hydroxyvalerate) by Newly Isolated *Penicillium Oxalicum* SS2 in Soil Microcosms and Partial Characterization of Extracellular Depolymerase. *Curr. Microbiol.* **2020**, *77*, 1622–1636. [CrossRef] [PubMed]
36. Jeszeová, L.; Puškárová, A.; Bučková, M.; Kraková, L.; Grivalský, T.; Danko, M.; Mosnáčková, K.; Chmela, Š.; Pangallo, D. Microbial Communities Responsible for the Degradation of Poly(Lactic Acid)/Poly(3-Hydroxybutyrate) Blend Mulches in Soil Burial Respirometric Tests. *World J. Microbiol. Biotechnol.* **2018**, *34*, 101. [CrossRef] [PubMed]
37. Arunprasath, T.; Sudalai, S.; Meenatchi, R.; Jeyavishnu, K.; Arumugam, A. Biodegradation of Triphenylmethane Dye Malachite Green by a Newly Isolated Fungus Strain. *Biocatal. Agric. Biotechnol.* **2019**, *17*, 672–679. [CrossRef]
38. Sauvola, J.; Pietikäinen, M. Adaptive Document Image Binarization. *Pattern Recognit.* **2000**, *33*, 225–236. [CrossRef]

39. Ghosh, S.; Sachan, A.; Mitra, A. Degradation of Ferulic Acid by a White Rot Fungus *Schizophyllum commune*. *World J. Microbiol. Biotechnol.* **2005**, *21*, 385–388. [[CrossRef](#)]
40. Carboué, Q.; Rébufa, C.; Hamrouni, R.; Roussos, S.; Bombarda, I. Statistical Approach to Evaluate Effect of Temperature and Moisture Content on the Production of Antioxidant Naphtho-Gamma-Pyrones and Hydroxycinnamic Acids by *Aspergillus Tubingensis* in Solid-State Fermentation. *Bioprocess Biosyst. Eng.* **2020**, *43*, 2283–2294. [[CrossRef](#)]
41. Mousavioun, P.; George, G.A.; Doherty, W.O.S. Environmental Degradation of Lignin/Poly(Hydroxybutyrate) Blends. *Polym. Degrad. Stab.* **2012**, *97*, 1114–1122. [[CrossRef](#)]





## Article

# Kraft Lignin/Tannin as a Potential Accelerator of Antioxidant and Antibacterial Properties in an Active Thermoplastic Polyester-Based Multifunctional Material

Klementina Pušnik Črešnar <sup>1</sup>, Alexandra Zamboulis <sup>2</sup>, Dimitrios N. Bikiaris <sup>2,\*</sup>, Alexandra Aulova <sup>3,4</sup> and Lidija Fras Zemljič <sup>1,\*</sup>

<sup>1</sup> Faculty of Mechanical Engineering, University of Maribor, SI-2000 Maribor, Slovenia; klementina.pusnik@um.si

<sup>2</sup> Laboratory of Polymer Chemistry and Technology, Department of Chemistry, Aristotle University of Thessaloniki, GR-541 24 Thessaloniki, Greece; azamboulis@gmail.com

<sup>3</sup> Faculty of Mechanical Engineering, University of Ljubljana, Aškerčeva 6, SI-1000 Ljubljana, Slovenia; aulova@chalmers.se

<sup>4</sup> Department of Industrial and Material Science, Chalmers Technical University, SE-41296 Gothenburg, Sweden

\* Correspondence: dbic@chem.auth.gr (D.N.B.); lidija.fras@um.si (L.F.Z.)

**Citation:** Črešnar, K.P.; Zamboulis, A.; Bikiaris, D.N.; Aulova, A.; Zemljič, L.F. Kraft Lignin/Tannin as a Potential Accelerator of Antioxidant and Antibacterial Properties in an Active Thermoplastic Polyester-Based Multifunctional Material. *Polymers* **2022**, *14*, 1532. <https://doi.org/10.3390/polym14081532>

Academic Editors: Miguel Fernando Aldás Carrasco, José Miguel Ferri and Vicent Fombuena Borràs

Received: 3 March 2022

Accepted: 31 March 2022

Published: 9 April 2022

**Publisher's Note:** MDPI stays neutral with regard to jurisdictional claims in published maps and institutional affiliations.



**Copyright:** © 2022 by the authors. Licensee MDPI, Basel, Switzerland. This article is an open access article distributed under the terms and conditions of the Creative Commons Attribution (CC BY) license (<https://creativecommons.org/licenses/by/4.0/>).

**Abstract:** This research focuses on key priorities in the field of sustainable plastic composites that will lead to a reduction in CO<sub>2</sub> pollution and support the EU's goal of becoming carbon neutral by 2050. The main challenge is to develop high-performance polyphenol-reinforced thermoplastic composites, where the use of natural fillers replaces the usual chemical additives with non-toxic ones, not only to improve the final performance but also to increase the desired multifunctionalities (structural, antioxidant, and antibacterial). Therefore, poly (lactic acid) (PLA) composites based on Kraft lignin (KL) and tannin (TANN) were investigated. Two series of PLA composites, PLA-KL and PLA-TANN, which contained natural fillers (0.5%, 1.0%, and 2.5% (*w/w*)) were prepared by hot melt extrusion. The effects of KL and TANN on the PLA matrices were investigated, especially the surface physicochemical properties, mechanical properties, and antioxidant/antimicrobial activity. The surface physicochemical properties were evaluated by measuring the contact angle (CA), roughness, zeta potential, and nanoindentation. The results of the water contact angle showed that neither KL nor TANN caused a significant change in the wettability, but only a slight increase in the hydrophilicity of the PLA composites. The filler loading, the size of the particles with their available functional groups on the surfaces of the PLA composites, and the interaction between the filler and the PLA polymer depend on the roughness and zeta potential behavior of the PLA-KL and PLA-TANN composites and ultimately improve the surface mechanical properties. The antioxidant properties of the PLA-KL and PLA-TANN composites were determined using the DPPH (2,2'-diphenyl-1-picrylhydrazyl) test. The results show an efficient antioxidant behavior of all PLA-KL and PLA-TANN composites, which increases with the filler content. Finally, the KL- and PLA-based TANN have shown resistance to the Gram-negative bacteria, *E. coli*, but without a correlation trend between polyphenol filler content and structure.

**Keywords:** poly (lactic acid); Kraft lignin; tannin; multifunctionality of PLA composites; surface mechanical properties; antioxidant/antibacterial activity

## 1. Introduction

Sustainable and environmentally friendly production of polymer-based composites is increasingly promoted due to the accumulation of the most commonly used non-biodegradable highly durable conventional plastics from the petrochemical industry, leading to uncontrolled environmental pollution. According to the new vision for plastics in Europe under the European Strategy for a Circular Economy, polymer composites derived

from natural resources are highly desirable to reduce CO<sub>2</sub> emissions and the environmental footprint [1–3].

In this context, biodegradable poly (lactic acid) PLA, a thermoplastic polyester produced from renewable resources such as starch or sugarcane, has emerged as the frontrunner among the numerous polymer-based material composites that have been used for industrial applications as packaging materials or as a leading functional material in biotechnology and medicine (drug delivery, tissue engineering, 3D-printed devices) [4–7]. Compared to other conventional biopolymers, PLA has the following advantages: (i) environmental friendliness, (ii) biocompatibility, and (iii) processability and energy saving (20–25% less energy is consumed during PLA production compared to petrol-based polymers) [8–10].

However, some disadvantages limit its applicability: (i) low toughness, (ii) slow degradation rate, (iii) hydrophobicity, and (iv) chemical inertness due to the absence of reactive side chain groups. Therefore, with the incorporation of reinforcing agents into PLA in the field of nanomaterials or bulk material leading to a synergistic effect, the new technological development has overcome the limitations of PLA and in this way also improved the properties of PLA composites and introduced functionality [11–16]. Functional materials are designed to perform one or more necessary functions. Self-cleaning, conductive, magnetic, optical, and bioactive properties are of great interest for plastic composites, offering advantages over conventional plastics. In the packaging sector in particular, bioactivity in the form of antioxidant, antimicrobial, and barrier-forming properties is critical to extending the shelf life of food and ensuring its safety [17–26].

Considering the natural renewable reinforcements based on polyphenolic material, Kraft lignin (KL) and tannin (TANN) have great potential for the preparation of PLA composites to enhance functionality, especially toward bioactivity, whilst both phenolics act as free radical scavengers and thus as natural antioxidants that are UV resistant and bioactive [27,28]. In general, the incorporation of KL/TANN in polymer matrix exhibits several positive impacts as a compatibilizer, plasticizer, water repellent, flame retardant, and stabilizer; it also generates interest in the development of thermoplastic composites as adhesives and resins [29–35].

It is accepted that the antioxidant properties of KL/TANN correlate with the structural characteristics of polyphenols (*Mw*, molecular weight, polydispersity, functional groups) and their purity and depend on the size of the filler particles, the type of KL/TANN (grape tannin, pine bark tannin, mimosa tannin), and the loading mass [27,33,35–37]. In general, non-esterified hydroxyl groups cause high heterogeneity and polydispersity, resulting in lower antioxidant activity. In contrast, aromatic hydroxyl groups and high *Mw* exhibit high antioxidant activity. When a nanoscale filler is used, the enhanced antioxidant activity is attributed to the higher specific surface area. Grape tannins in 1% content in the polymer confer antioxidant properties and the effect increases steadily with TANN loading. In addition to grape TANN, pine bark and mimosa also play a role as effective short-term stabilizers [27,31].

In addition, it is hypothesized that the incorporation of KL/TANN in PLA could induce structural changes in PLA-KL/TANN composites on the one hand and modification of PLA surfaces on the other, which could not only improve the mechanical properties of PLA composites but also enhance hydrophilicity and roughness and further on confer antibacterial/antioxidant properties, which is a key strategy for packaging and functional bioengineering materials. A recent publication also elaborated that the crystalline morphology, structure, and interaction between the reinforcing agent and PLA affected the mechanical properties of the surface [37]. The amphiphilic behavior of KL improves filler-polymer compatibility, reduces polarity, and improves dispersion. At low or moderate wt% of the addition of KL, the mechanical performance is improved yet it depends on the chain length of the KL filler. On the other hand, several reports have found that the reinforcement of KL in PLA, Poly (butylene succinate) (PBS) and Poly (caprolactone) (PCL), and most aliphatic polyesters deteriorates the mechanical properties of lignin-based thermoplastic composites due to insufficient bonding between lignin and polymer [38–40]. To over-

come this problem, chemical modifications have been carried out using coupling agents (e.g., esterification, acylation, and alkylation) and by organic solvent fractionation [39–44]. By incorporating TANN into PLA, the final properties also related to surface mechanical properties are associated with several problems: (i) the problem of incompatibility of hydrophilic TANN and polymer, leading to low adhesion of PLA-TANN composites, (ii) particle size control, and (iii) the mass fraction of TANN loading. The poor adhesion between hydrophilic TANN and hydrophobic polymer must be addressed, which leads to a severe decrease in mechanical properties. However, the addition of compatibilizers improves the interaction between TANN and polymer but poses some environmental and economic problems [27].

Although many studies have focused on the properties of polymer-based KL or TANN composites, no study has been published in the literature comparing the impact of KL/TANN natural additives on PLA-KL and PLA-TANN composite materials, without the addition of environmentally problematic toxic additives according to the sustainable attractive material from the point of view of safety and economy. In addition, there is the question of how admixture might affect the final synergistic end performance, including surface properties and mechanical and antibacterial/antioxidant activity. Surface properties are particularly important, because most plastics, especially those intended for packaging and biomaterials, work on the surface with contact media (food, tissue, etc.). Therefore, taking into consideration the multifunctionality of PLA-KL and TANN composites, the objective of this work is primarily focused on comparing the overall performance of PLA composites processed by the hot melt extrusion method, improving the surface mechanical properties, and providing the antioxidant/antimicrobial activity. The dependence on two different polyphenols, KL and TANN, on the functional surface properties was investigated, whilst those PLA-based renewable thermoplastic composites filled with KL and TANN were already studied in terms of crystallization phenomena, interfacial interactions between PLA and KL, TANN, molecular mobility, and thermal degradation in our previous work [45,46].

In general, the surface mechanical properties of PLA-KL and PLA-TANN composite films were correlated to roughness as well as the contact angle measurement using goniometry, surpass zeta potential, and nanoindentation. Finally, the antioxidant/antimicrobial activity of the developed composites was also estimated using standard methods (DPPH• (2,2'-diphenyl-1-picrylhydrazyl), DSM 1576) [34,47]. Reinforcement with two different polyphenols, KL and TANN, resulted in promising multifunctionality of the material, allowing it to be used for both packaging and biomedical applications. However, the antioxidant reinforcing agents not only endow the composites with antioxidant activity but also improve their stability and prolong their shelf life. On the other hand, the additional antimicrobial activity of PLA composites provides a high quality microbial inhibiting material required for many advanced applications.

## 2. Materials and Methods

### 2.1. Materials

The polymer used in this study as the matrix was neat PLA, poly (L-lactic acid, with 96% of L and 4% of D isomer) and was provided by Plastika Kritis S.A. (Iraklion, Greece) with molecular weight  $M_w \sim 75$  kg/mol and intrinsic viscosity  $\eta = 1.24$  dL/g. Kraft lignin (KL) and tannin (TANN) samples were acquired from Sigma-Aldrich. The physiochemical properties of KL and TANN were described in our previously published work [45,46].

### PLA Composites Processing

KL and TANN were incorporated in different percentages (0.5, 1.0 and 2.5 wt%) into the PLA matrix. To remove moisture, PLA granulates, KL, and TANN were left in a vacuum oven overnight at 110 °C. PLA-based KL and TANN composites (PLA-KL, PLA-TANN) were prepared by melt mixing. The dried materials were prepared in a corotating twin screw melt mixer with 30 rpm at 195 °C for 10 min. The thin films (330–500  $\mu$ m) of PLA-KL and PLA-TANN were obtained with thermal pressing at 180 °C with a Paul-Otto

Weber (Paul-Otto Weber GmbH, Remshalden, Germany) thermal press and followed by a sudden cooling.

A complete overview of the prepared PLA-KL and PLA-TANN composites is presented in Table 1 with names for each composite mixture.

**Table 1.** Prepared PLA-KL and PLA-TANN composites.

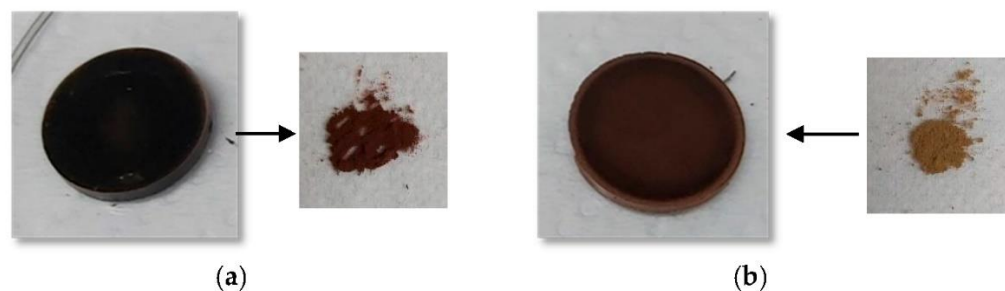
Material Description/Polyphenolic Filler Loading [wt. %]	0.5	1.0	2.5
PLA-based Kraft lignin	PLA-0.5KL	PLA-1.0KL	PLA-2.5KL
PLA-based tannin	PLA-0.5TANN	PLA-1.0TANN	PLA-2.5TANN

## 2.2. Methods

### 2.2.1. PLA Composites Based on KL/TANN Characterization

#### Surface Mechanical Properties of PLA-KL and PLA-TANN Composites

To study the surface mechanical properties of PLA-KL and PLA-TANN composites, the contact angle measurements of water was followed. In total, the contact angle of all seven PLA composites (neat PLA and PLA-KL and PLA-TANN) with three different KL and TANN contents were measured using a goniometer from DataPhysics (Filderstadt, Germany). For this purpose, 3  $\mu\text{L}$  of water was dropped onto the composite surfaces and an average of at least three liquid droplets per surface were calculated. In this way, the static contact angles (SCA) were measured at room temperature. The water contact angle determination of KL and TANN was also measured in the form of a pellet (Figure 1). The KL and TANN was dried overnight at 100 °C in a vacuum oven. The dried KL and TANN was ground into fine powder and a small amount of the KL and TANN powder was added to the collar of a Perkin Elmer Hydraulische Presse. The KL and TANN powder was pressed for 2 min to form a pellet. Contact angle measurements were performed using ultrapure water (Millipore, Burlington, MA, USA).



**Figure 1.** Images of the pellet sample of (a) Kraft lignin and (b) tannin.

For the *surface zeta potential as charge indication* analysis with SurPASS-3 (Anton Paar GmbH, Graz, Austria), two sample pieces of approximately 10 mm  $\times$  10 mm were cut for the streaming potential measurement. The sample pieces were fixed on the sample holders of the Adjustable Gap Cell (with a cross-section of 20 mm  $\times$  10 mm) using double-sided adhesive tape. The sample pieces were aligned opposite each other such that the maximum surface area of the samples overlapped. The permeability index of the sample, by rotating the micrometer, was set to around 100. A 1 mM KCl electrolyte solution was used and the pH was automatically adjusted with 0.05 M NaOH and 0.05 M HCl. The pH dependence of the zeta potential was determined in the range of pH 2–10. A pressure gradient of 200–600 mbar was applied to generate the streaming potential. The distance between the sample pieces was adjusted to  $105 \pm 5 \mu\text{m}$ . Streaming potential measurements were performed using an aqueous 0.001 mol/L KCl solution as the background electrolyte. The pH dependence of the surface zeta potential was determined by adjusting an initial pH 10, using 0.05 mol/L KOH as reported elsewhere [48].

The *surface roughness* of PLA, PLA-KL, and PLA-TANN composites was measured using scratch testing with topographical compensation available for G200 Nanoindenter (Agilent, Santa Clara, CA, USA) that was already described in the literature [37]. Roughness values in nanometers have been extracted from the 500  $\mu\text{m}$  long surface scan with an applied small force of 20  $\mu\text{N}$ . Profiling velocity was set to 10  $\mu\text{m/s}$  for every 10 scratches per material, which were located at 200  $\mu\text{m}$  from each other.

*Continuous Stiffness Measurement* is a nanoindentation characterization method developed by Oliver and Pharr [49], which utilizes the dynamic loading of the sample material. CSM tests were performed using Nanoindenter G200 equipped with XP head according to protocol established in [37] and testing parameters are presented in Table 2.

**Table 2.** Testing parameters of Nanoindenter G200.

Tip Geometry	Depth [nm]	Distance between Indents [ $\mu\text{m}$ ]	Poisson's Ratio	Number of Indents
Berkovich	2500	100	0.35	36

#### Antioxidant Properties of PLA-KL and PLA-TANN

The radical scavenging activity of neat PLA, PLA-KL, and PLA-TANN composites was evaluated using DPPH• (2,2'-diphenyl-1-picrylhydrazyl) (Sigma-Aldrich, France). The method of antiradical activities is based on the reduction of the DPPH• radical, which is analyzed spectrophotometrically at a wavelength of 517 nm (Spectrophotometer (UV-VIS) UV-1800 Shimadzu) as it was clearly introduced in our previously published paper [48]. The antioxidant capacity can be determined by the decrease of absorption at wavelength 517 nm. DPPH• radical can be reduced in the antioxidant (AO) presence, with the consequent decolorization from purple to yellow. DPPH solution was prepared in methanol ( $8.1 \times 10^{-5}$  mol/L) at ambient temperature [27,50].

Briefly, all the samples neat PLA, PLA-KL, and PLA-TANN composite samples disks (1 cm  $\times$  1 cm) were directly immersed into 3 mL of the methanol DPPH• solution. The antiradical activities of the neat PLA, PLA-KL, and PLA-TANN films were determined straightaway after 1 h, 6 h, 12 h, and 24 h. The radical scavenging activity was calculated as per the following expression:

$$\text{Inhibition} = (A_{\text{control}} - A_{\text{sample}}) / A_{\text{control}} \times 100\%,$$

where  $A_{\text{Control}}$  is the absorbance measured at the starting concentration of DPPH• and  $A_{\text{Sample}}$  is the absorbance of the remaining concentration of DPPH• in the presence of PLA-KL and PLA-TANN composite polymers. The reference neat PLA material was also tested.

#### Antibacterial Properties of PLA-KL/PLA-TANN Composites

The microbiological analysis of neat PLA, PLA-KL, and PLA-TANN composites against the bacteria *Escherichia coli* (DSM 1576) as standard Gram-negative bacteria was performed according to the internal protocols standardized for plastic surfaces by the Department of Microbiological Research, Center for Medical Microbiology of the National Laboratory for Health, Environment and Food in Maribor, d.i.e., No. P96 Biofilm production on various materials P90 (ISO22196) reported elsewhere [51,52]. In brief, the neat PLA, PLA-KL, and PLA-TANN composite films of size 10 mm  $\times$  10 mm (approximately, 0.12 g of PLA composite material) were exposed to the standardized medium inoculated with *Escherichia coli* and set at 0.5 on the McFarland scale at three different incubation times: 1 h, 12 h, and 24 h. Then, after inoculation of the neat PLA, PLA-KL, and PLA-TANN film composites, the viable bacteria were evaluated by the pour plate method (plate counting agar was used). The effect of incorporation of polyphenolic filler loading into the PLA matrix composites was calculated as a reduction of bacterial growth and counting of bacterial

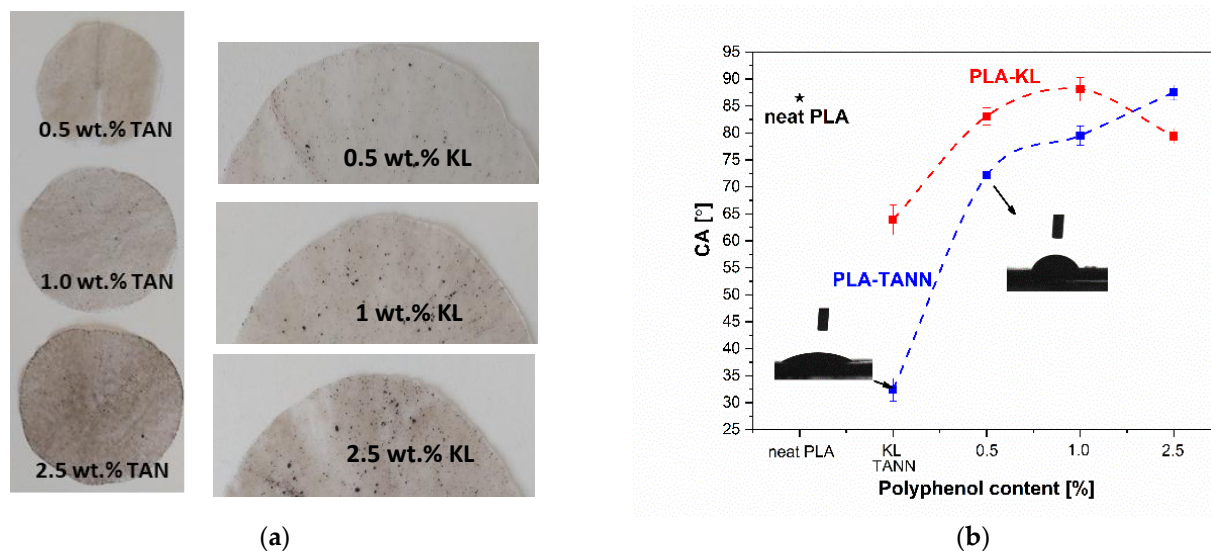
number after incubation of neat PLA polymer compared with PLA-KL and PLA-TANN composite films.

### 3. Results and Discussion

#### 3.1. Surface Mechanical Properties of PLA-KL and PLA-TANN Composites

The addition of polyphenolic fillers in PLA polymer such as KL and TANN leads on the one hand to changes, especially for packaging/biomedical applications, such as thermal behavior and degradation, semi-crystalline morphology, interfacial phenomena, and molecular mobility as published by our team [45,46], and on the other hand to improved functional properties with enhanced mechanical properties and antibacterial and antioxidant behavior of PLA-KL and PLA-TANN composites as shown here. To explore the distribution of KL and TANN in PLA polymer that causes the changes in PLA-KL and PLA-TANN surface behavior, the contact angle measurements, roughness measurements, zeta potential, and nanoindentation were investigated in more detail.

Figure 2a,b first shows the images of PLA-KL and PLA-TANN films with a homogeneous distribution of KL and TANN in the polymer material. Due to the native darker color of KL and TANN, the PLA composite material is darker, which could be explained by a suitable mixture between polyphenolic filler and PLA.



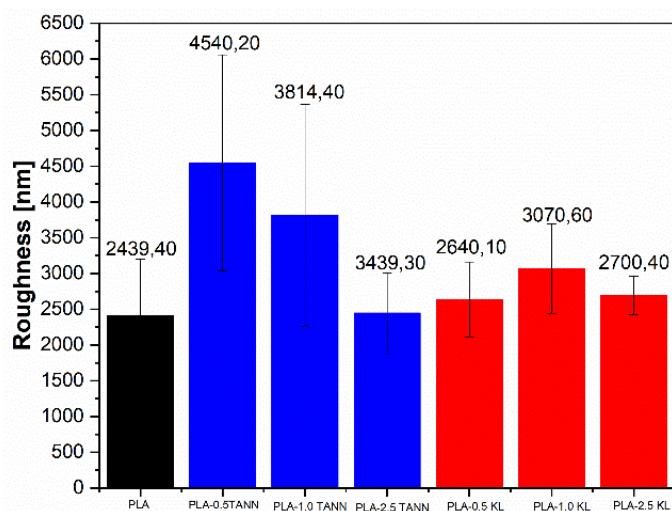
**Figure 2.** Images samples of (a) PLA-TANN and PLA-KL composite films using different KL and TANN concentrations. The wettability of (b) neat PLA, KL, TANN, PLA-KL, and PLA-TANN composites as a function of wt. % of KL and TANN loading. Star marker represents neat PLA material.

The water contact angle measurement was applied to investigate the hydrophilicity/hydrophobicity of PLA-KL and PLA-TANN composites. Due to the low hydrophilicity of neat PLA (neat PLA showed contact angle values of  $86.5 \pm 2.5^\circ$ ), the incorporation of KL and TANN with predominant hydrophilic character into PLA could accelerate it [53–56]. The wettability of water with the surface of PLA-KL and PLA-TANN composite material is shown in Figure 2c. Neither KL nor TANN cause a significant trend in wettability. KL with the main phenolic and non-polar reactive groups (phenolic derivatives and aromatic hydrocarbons were identified) analyzed by Pyrolysis–gas chromatography/mass spectrometry (Py–GC/MS) and published in the previous study could enhance either the hydrophilic or the hydrophobic character of PLA-KL composites [45]. However, in our case the hydrophilic character was determined (CA of PLA-0.5KL =  $83.2^\circ$ , PLA-1.0KL =  $87.8^\circ$ , PLA-2.5KL =  $79.2^\circ$ ). In contrast, TANN with polar phenolic groups was found to exhibit enhanced hydrophilicity. In general, all PLA composites with polyphenolic filler showed a change in contact angle compared with neat PLA, with a slight increase in hydrophilicity at

the lowest KL and TANN concentration. The 0.5 wt.% addition of KL and TANN decreased the contact angle of PLA-KL by 5%. On the other side, the contact angle of PLA-0.5TANN composites was 17% lower than neat PLA, resulting in a higher hydrophilic nature of PLA composites. By increasing the KL concentration (1.0 wt.%) the water contact angle does not significantly change compared with neat PLA, but the 1% of TANN in PLA leads to an improved contact angle at 10%. Finally, further addition of TANN (i.e., 2.5%) increases the contact angle of PLA-TANN composites by 5%; in contrast, the PLA-KL composites CA decreased.

The wettability of PLA-KL and PLA-TANN composites may be caused by the incorporation of KL and TANN and the interaction between neat PLA and KL/TANN filler and their available functional groups on the surfaces of PLA composites, which has already been explained in the literature [46]. Moreover, in the case of PLA-TANN, the hydrophilicity of TANN is more pronounced compared with KL (Figure 2c), which could be explained by the greater preferential interaction between the polar polyphenolic fillers of TANN than KL that exceeded an amphiphilic structure. Secondly, the wettability could be related to the differences in particle size of TANN and KL that provide available functional groups needed for interaction with PLA and a better distribution in PLA. Previous results of scanning electron microscopy (SEM) analysis determined the size of KL particles (600 nm) in comparison with TANN (450 nm). Thus, the results are consistent with those previously published [46] for PLA-polyphenol composites, but also differ from ours in terms of the origin and properties of KL and TANN and the processing of the final composite, which resulted in more hydrophilic composites (lower contact angle) compared with neat PLA [33,35,40,50,57].

The measurement of water contact angle has further been related to **surface roughness**, polymer, and filler chemistry. The average roughness of PLA, PLA-KL, and PLA-TANN composites is represented in Figure 3. Apparently, all samples, PLA, PLA-KL, and PLA-TANN, have a rough surface; however, the difference of material properties is still statistically significant according to ANOVA analysis. With the incorporation of KL and TANN, the roughness of the PLA composites changed and decreased with increasing polyphenol addition; more specifically, the PLA-TANN composites showed higher roughness than neat PLA and with increasing TANN loading the roughness of PLA-TANN decreased. In contrast, the roughness of PLA-KL showed approximately the same trend and did not change significantly. The smaller particles size of TANN and available functional groups at 0.5 wt.% of content of addition in PLA led to an increased interaction with PLA and, eventually, a more visible effect on the surface of the PLA-TANN composites. On the other hand, non-prominent interaction between KL and PLA neither in the small nor in the high concentration leading to agglomeration of KL in PLA does not much affect the roughness of PLA-KL film.

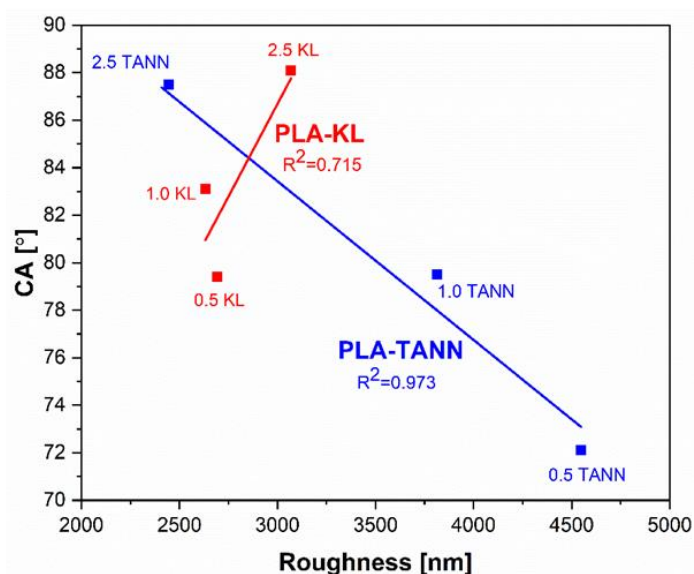


**Figure 3.** An average roughness value of neat PLA, PLA-TANN, and PLA-KL composites.



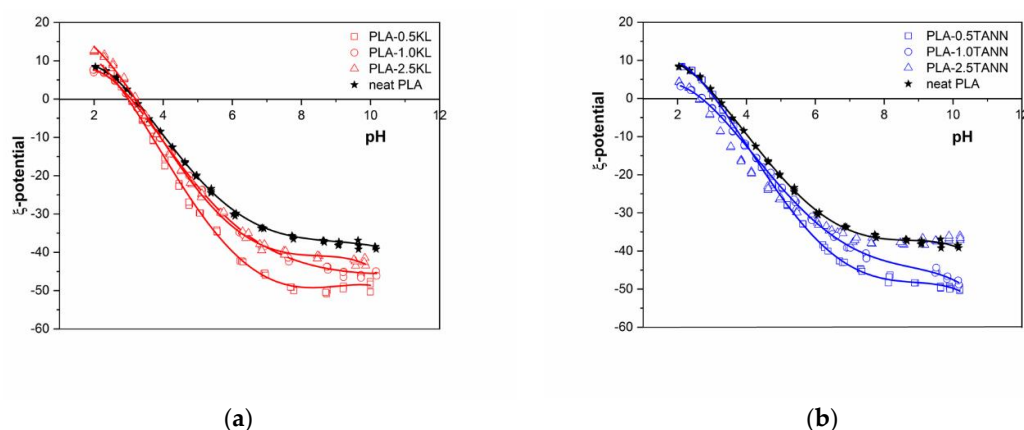
The roughness measurements of PLA-KL and PLA-TANN composites explain approximately the same trend of distribution of the polyphenolic filler in PLA polymer composites of metal oxide-based PLA composites in the PLA surface region and its roughness behavior [37]. This could be due to the incorporation and interaction of KL and TANN, which are stronger or more pronounced with decreasing loading of polyphenolic filler and lead to a higher availability in the inner region of PLA-KL and PLA-TANN composites, causing the changes in the surface region.

In general, the trend of change in the water contact angle of PLA-KL and PLA-TANN composites agrees well with that of surface roughness, indicating the distribution of KL and TANN in PLA composites and varies in different deep layers of PLA-KL and PLA-TANN composites (Figure 4). From the correlation plot between CA and roughness (Figure 4), the correlation coefficient for PLA-TANN is high (0.973), indicating higher linear strength, while the lowest correlation coefficient is calculated for PLA-KL (0.715), which is still considered strong.



**Figure 4.** Correlation between CA and roughness of PLA-KL and PLA-TANN composites.

Surface charge expresses the interaction between PLA composites in aqueous solution and solid surfaces and is a key factor in explaining the differences between PLA composites before and after incorporation of the polyphenolic fillers. Therefore, the surface properties of PLA-based polyphenolic filler as varying the filler types and filler content were followed by zeta potential measurements. Figure 5a,b presents the zeta potential values of the neat PLA, PLA-KL, and PLA-TANN composites with addition of polyphenolic filler as a function of pH ranging from 2 to 12. The isoelectric point and the value of zeta potential are indicators of the functional groups present on the surface of the PLA composites. The decrease of the isoelectric point indicates the addition of acidic groups, while the increase indicates the addition of basic groups. The isoelectric point (IEP) (Figure 5a,b) was observed at pH = 3 for neat PLA; it is in accordance with the literature and it remains almost the same with KL and TANN incorporation in PLA (PLA-0.5KL = 2.90, PLA-1.0KL = 3.05, PLA-2.5KL = 3.21, PLA-0.5TANN = 3.11, PLA-1.0TANN = 2.75, PLA-2.5KL = 2.82) [58,59]. The negligible change in the IEP value of PLA-KL and PLA-TANN composites could be related to the PLA polymer and polyphenolic structure. Both PLA and the KL and TANN structures consist of COOH and OH groups. The interfacial interaction of PLA with KL and TANN, namely by the carbonyl group reported in our previous work, does not affect the charges and consequently yields a constant IEP value [48].

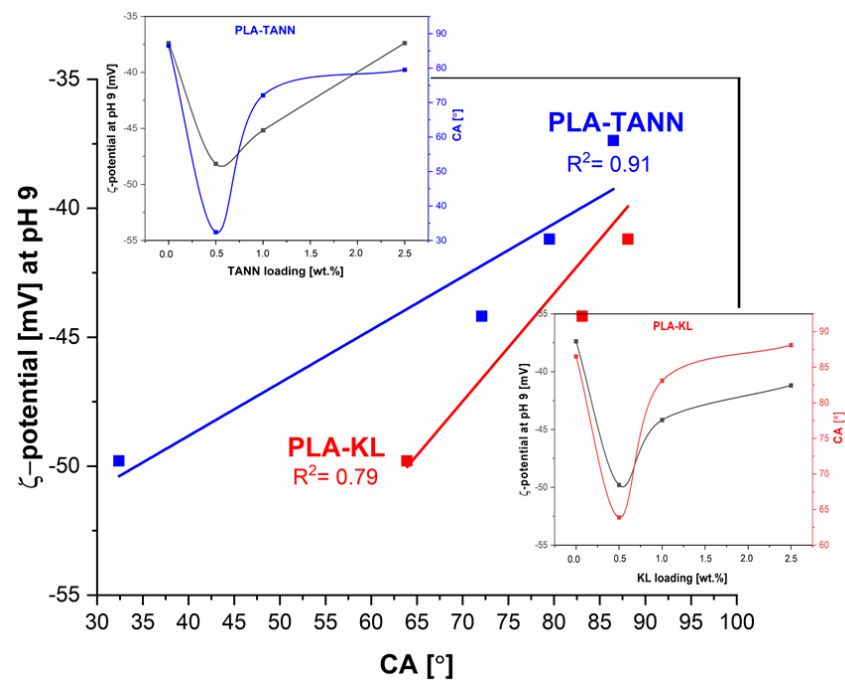


**Figure 5.** Zeta potential of (a) PLA-KL composites and (b) PLA-TANN composites in the range of pH 2–12.

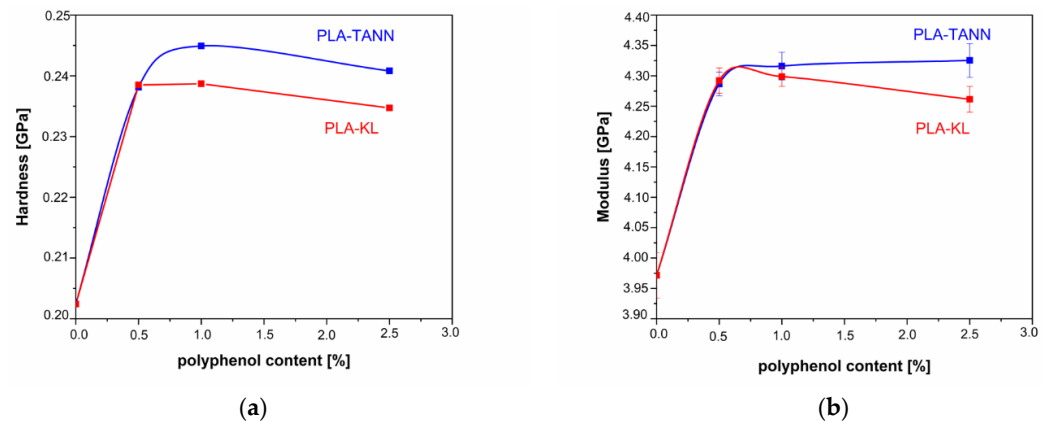
The total zeta potential of PLA-KL and PLA-TANN composites with high negative zeta potential at high pH towards more positive values was also determined in Figure 5. All PLA-KL and PLA-TANN above pH = 3 composites accelerate the negative zeta potential. The effects of the addition of KL and TANN in PLA on the surface and interfacial charge of PLA-KL and PLA-TANN are described by the negative zeta potential at pH = 9 (Figure 5a,b). It is clear that the zeta potential at pH = 9 plateau level follows a continuous trend related to the KL and TANN loading and distribution in the PLA matrix.

Due to the incorporation of KL and TANN into PLA, more charges are induced on the surface of PLA-KL and PLA-TANN, resulting in increased charge density, as shown by the increase of negative zeta potential plateau, but with decreasing KL and TANN loading. With increasing KL and TANN addition, the zeta potential at pH = 9 becomes more negative than neat PLA. The polar groups are introduced onto the surfaces of the composite, leading to an increase in PLA-KL and PLA-TANN surface hydrophilicity; also evidenced by the contact angle measurements. The zeta potential method correlates well with the measurement of the contact angle, which was shown in Figure 6 (the correlation coefficient for PLA-TANN is 0.91; for PLA-KL it was calculated at 0.79). In conclusion, the zeta potential measurements of all PLA-KL and PLA-TANN express anionic charge in almost the entire pH range, indicating a high affinity for adhesion/adsorption of cationic substances and repulsion of anionic substances, which may ultimately contribute to the antibacterial properties of PLA-KL and PLA-TANN composites.

Nanoindentation was applied to investigate the effect of KL and TANN on the surface mechanical properties of PLA-KL and PLA-TANN composites. Figure 7 shows the values of nanoindentation modulus and hardness as a function of concentration of added polyphenols. The values were analyzed in a depth range from 1000 to 1500 nm, where the substrate has no influence. The values at zero concentration correspond to the neat PLA material and are therefore the same for all added fillers. The addition of fillers increases the nanoindentation modulus and hardness by a maximum of 8.9% and 20.9%, respectively, but the effect of concentration is not significantly pronounced. The lowest concentration (0.5%) for both polyphenols gives similar values for modulus and hardness, with a further increase of filler content the values of the mechanical properties start to deviate. KL shows significantly lower values compared to TANN. Moreover, the maximum investigated concentration of additives leads to hardness values that are lower compared to the lower concentrations for both TANN and KL, but the modulus still slightly increases for TANN and decreases for KL. However, it can be seen that with increasing KL addition (from 0.5% to 2.5%) the modulus and hardness decrease slightly, which could be due to the distribution of the KL near the surface or in deeper layers of the film. This decrease correlates well with the decrease in the contact angle and the measurement of zeta potential at the maximum KL concentration.



**Figure 6.** The correlation between the plateau zeta potential at pH 9 and polyphenolic filler loading in PLA-KL and PLA-TANN composites. The insets show the dependence on CA, zeta potential at pH 9, and polyphenol loading.



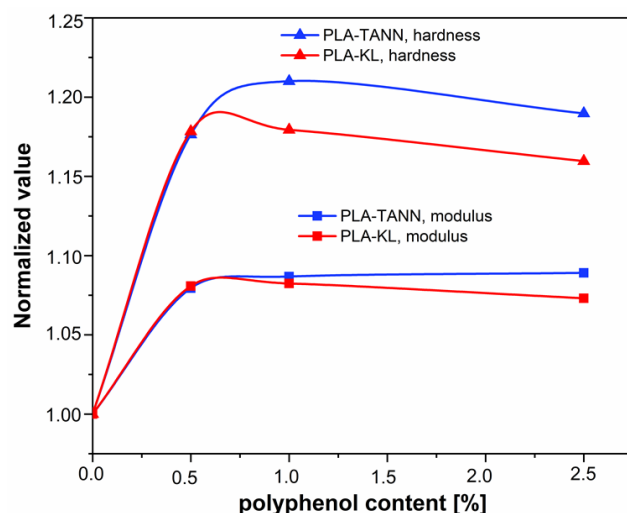
**Figure 7.** Nanoindentation hardness (a) and modulus (b) in respect to concentration of added polyphenols.

Analysis of the values normalized to neat PLA material properties shows a higher effect of the TANN additive compared to KL.

Figure 8 demonstrates normalized values of both measured properties, nanoindentation modulus and hardness, compared to the properties of neat PLA. Normalization has been done by the modulus and hardness value of neat PLA for all materials. It is visible that the addition of polyphenols affects hardness more than modulus measured by nanoindentation. While at low concentration of 0.5% the effect of KL and TANN are the same, for higher concentration TANN causes more pronounced increase of both mechanical properties.

The differences between KL and TANN in PLA composites could be related to the size of filler particles, interfacial interaction, and crystallization. First, the hydrodynamic diameter of the filler particles measured by scanning electron microscopy (SEM) was measured to be about 600 nm for the particles of KL in the previous work [46], while the average size of the TANN particles was about 450 nm. Indeed, larger aggregates formed in the PLA-KL composites than in the PLA-TANN composites. The results also show that the dispersion and interfacial interaction between TANN and PLA are better than those between KL and PLA, leading to improved adhesion and final surface mechanical

properties of the PLA-TANN films compared to the PLA-KL composite films. In general, incorporation of KL and TANN into PLA improved the final surface mechanical properties, while the effect is slightly less pronounced with KL and TANN loading.



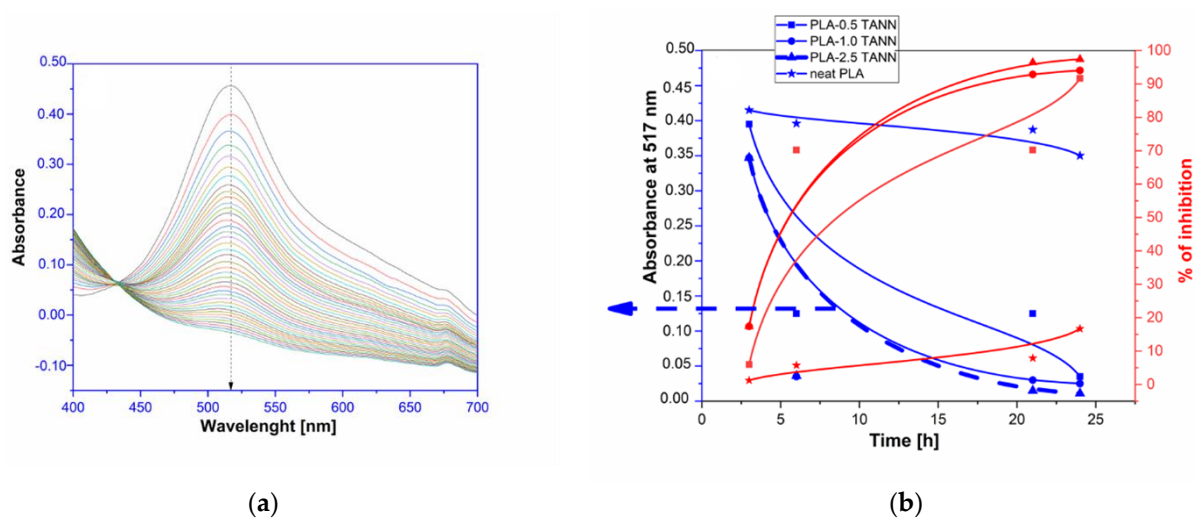
**Figure 8.** Normalized properties of neat material values of nanoindentation modulus and hardness are plotted in dependence on concentration of added polyphenols.

### 3.2. Antioxidant Properties of the PLA-KL and PLA-TANN Composites

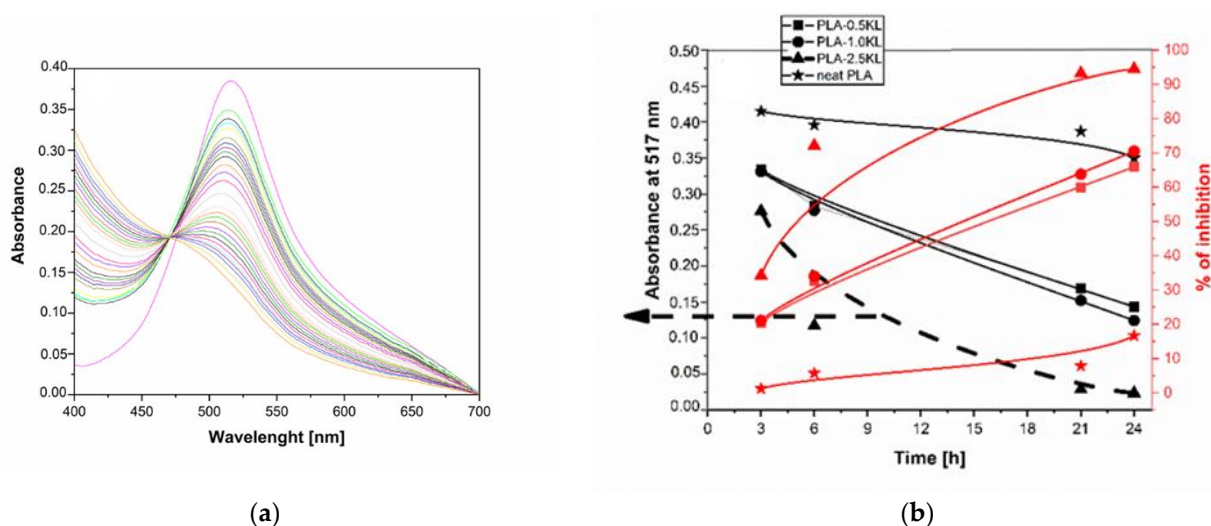
Natural antioxidant agents such as KL and TANN enhance the oxidation process and indeed improve the stability of thermoplastic composites. They reduce the concentration of reactive oxygen species and free radicals. Accordingly, antioxidant composites material accelerates the important preventing process in packaging as well as in biomedical applications.

Figures 9 and 10 show the dependence of UV-vis spectra of PLA-KL and TANN composites immersed directly in DPPH•-solution and measured at 517 nm, evaluated after 24 h (1, 12, 24 h). The results of antioxidant activity of PLA-TANN composites are shown in Figure 9. It can be clearly seen that neat PLA did not exhibit any antioxidant activity. The absorbance of neat PLA after 24 h slightly decreases and therefore provides around 17% of inhibition. With the incorporation of TANN into PLA, the antioxidant activity of the PLA-TANN composites increased and reached the max value after 24 h. Small differences between the PLA-TANN composites were measured, but the antioxidant activity is approximately independent of TANN loading. In general, the PLA-0.5 TANN composites after 24 h reach 91% of AO inhibition, the same value of AO inhibition 94% is measured for PLA-1.0 TANN composites. Furthermore, Figure 9 also shows that PLA-TANN composites containing 0.5 wt.% of TANN could reduce 50% of DPPH concentration after 10 h. Moreover, PLA-1.0 TANN and PLA-2.5 TANN composite films showed almost the same antioxidant activity up to about 17.5 h. The time-dependence study of the absorbance of PLA-2.5TANN composites measured every 3 min is also represented in Figure 9a.

Not only TANN but also KL is recognized as an efficient antioxidant accelerator in the polymer matrix. Figure 10 clearly shows the difference between the antioxidant activity of the PLA-KL composites with 0.5, 1.0., and 2.5% KL. As expected, the results represented that higher concentration of KL yielded PLA-KL composites with higher antioxidant activity during 12 h. With an increasing incorporation of KL in PLA, the antioxidant activity of the PLA-KL composites was enhanced and after 24 h only the PLA-KL composites with 2.5 wt.% reached the maximum value of inhibition. The other two PLA-KL composites with 0.5 and 1.0% of added KL provide 70% antioxidant activity after 24 h, with no significant differences between the composite activity.



**Figure 9.** (a) The absorbance of PLA-2.5 TANN composites as a function of Wavelength (blue) and (b) reaction kinetics and % of inhibition of the PLA based TANN composites film evaluated with DPPH radical scavenging in the methanol solution indicated during 24 h (red).



**Figure 10.** (a) The absorbance of PLA-KL composites as a function of Wavelength and time, (b) reaction kinetics of the PLA based KL composites film evaluated with DPPH radical scavenging in the methanol solution indicated during 24 h.

The results of the antioxidant activities of PLA-TANN and PLA-KL composites shown in Figures 9 and 10 followed with the same behavior of KL and TANN as an antioxidant accelerator, but with some differences; the PLA-TANN composites containing 0.5 wt.% of TANN were able to reduce 50% DPPH concentration after 10 h and on the other side the PLA-KL composites with 0.5 wt.% of KL after 15 h.

In all samples from PLA-TANN and PLA-KL, antioxidant activity is time-dependent and increases in the period from 1 h to 24 h. Only 0.5% of KL and TANN resulted in a halving of DPPH concentration, while the plateau is observed only in the samples with a higher value of KL and TANN; therefore, it is expected that the antioxidant activity of PLA-KL and PLA-TANN with 0.5 and 1.0% also increases when the 24 h is exceeded. The results indicate that the oxidative capacity of PLA-TANN and PLA-KL composites increases with increasing content of KL and TANN. Although our antioxidant evaluation of PLA-KL and PLA-TANN composites measured by DPPH assay showed the superior antioxidant properties of PLA-KL and PLA-TANN films, especially at a high loading of 2.5% of KL

and TANN, the PLA-TANN composites enhanced the antioxidant activity more than the PLA-KL composites at low levels of added polyphenols.

These results are consistent with a previous work that investigated the antioxidant properties of PLA-polyphenol composites. This showed that the antioxidant properties were improved as they were more efficient in reducing DPPH over time and increased with increasing polyphenol content compared with the neat PLA polymer [50,60–67]. However, our research provides some crucial differences between the measured antioxidant activities of PLA-KL and PLA-TANN composites that could be related to the properties explained below. In general, the antioxidant properties of polyphenolic fillers depend on the structural properties of KL and TANN (Mw, functional groups, polydispersity, and purity). The aliphatic hydroxyl groups in the side chains, non-esterified hydroxyl groups, polydispersity, and low purity decrease the radical scavenging activity of KL. Additionally, KL with less aliphatic hydroxyl groups and more phenolic hydroxyl groups, lower and narrower Mw distribution increased the antioxidant activity. Another reason for the altered antioxidant properties of KL could also be the length of the alkyl side chain in the phenylpropane units and in the carboxyl and alcohol groups, which increased the antioxidant activity [27,50].

In conclusion, in our study, the lower antioxidant activity of PLA-KL compared to PLA-TANN is probably related to the changes in polydispersity, low purity, and the presence of fewer phenolic groups compared with TANN, which accelerate the antioxidant behavior already measured in the study reported here [45,46]. The differences between the KL and TANN polydispersity were found: 0.64 for KL and 0.44 for TANN. Indeed, the bigger particles for KL (612 nm) in comparison with 454 nm of TANN contribute to more efficient surface available OH and COOH group with PLA that enhanced the interaction with polymer (measured in the study [45]). Moreover, the low purity of KL containing many residual carbohydrates that can generate hydrogen bonds with phenolic hydroxy groups of lignin and, therefore, interferes with the antioxidant activities of KL as was also studied in the literature [27,31,32,60,62,64,68,69].

### 3.3. Antibacterial Behavior of PLA, PLA-KL, and PLA-TANN Composites

The last aspect of multifunctional properties refers to the antibacterial properties of PLA-based KL and TANN composites. Regarding the charge of the polymer surfaces, typically positive charges in the polymers were found to be precursors for the antimicrobial activity and roughness of plastic surfaces altering the surface properties.

The antimicrobial assay of the neat PLA as a reference sample and the PLA composite samples containing KL and TANN filler (in the three different concentrations 0.5%, 1.0%, and 2.5%) was investigated against a model pathogen, namely *E. coli*, after 1 h, 6 h, and 24 h and is shown in Table 3. Accordingly, it can be seen that the antibacterial activity of the PLA composites in the presence of KL and TANN was much more evident than that of the neat PLA control, which showed resistance to the adhesion of *E. coli*, while neat PLA showed no antimicrobial activity, as expected.

**Table 3.** Antibacterial assay of Neat PLA, PLA-KL, and PLA-TANN composites.

Composites Name/% of Inhibition in Time	t <sub>1</sub> [1 h]	t <sub>2</sub> [12 h]	t <sub>3</sub> [24 h]
neat PLA	−14.11	−14.11	−14.11
PLA-0.5 TANN	1.78	20.87	20.87
PLA-1.0 TANN	13.02	58.1	58.1
PLA-2.5 TANN	14.2	88.11	87.21
PLA-0.5 KL	7.4	67.86	82.96
PLA-1.0 KL	3.25	54.27	36.52
PLA-2.5 KL	6.07	−4.85	−145.82

The antibacterial activity of the PLA-TANN (Table 3) composites monitored after 24 h showed that only the composite with 2.5% TANN achieved an antimicrobial activity of 88.5%. The composites with lower TANN content in PLA, i.e., 1.0% and 0.5%, achieved lower values of bacterial activities, namely 58% and 20%, respectively. It seems that the efficiency of antimicrobial activity of PLA-TANN composites increases with increasing filler content. In contrast, composites with KL, which were incorporated into the PLA composites, did not show the same trend against *E. coli* as PLA-TANN. The results of the antimicrobial activities of PLA-KL with a high content of added KL (2.5%) exhibited a lower antibacterial activity than neat PLA and thus showed no antimicrobial activities, but the PLA-KL composites with only 0.5% showed an antibacterial activity of almost 82% after 24 h.

The results also represent that the composites containing TANN and KL exhibited bacterial resistance to *E. coli* regardless of filler loading. A clear dependence on antibacterial activity is not evident. On the other hand, the antibacterial activity of PLA-KL is related to its origin, the polyphenol content, the presence of the phenolic compound and, in particular, the different functional groups containing carbonyl and hydroxyl groups considering the published research [70]. In our study, the effect of the incorporation of KL and TANN into PLA not only depends on the polyphenolic content and the carbonyl and hydroxyl groups, but the effect was also attenuated by the roughness of the PLA-KL and TANN composites and the presence of an active polyphenolic filler near the PLA surface. As noted in the study of metal-based nanoadditives into the PLA matrix [37], the presence of an active metal oxide filler on the surface of PLA altered the antibacterial properties of PLA composites against *E. coli*. Moreover, the rough surfaces with larger surface area inhibited the bacteria more.

Our results also indicate that bioactivity in the form of antioxidant and antimicrobial properties is not diminished by surface parameters. It has been shown that most of the monitored surface properties change more significantly when the amount of added TANN and KL is decreased. Conversely, antioxidant activity is higher when the added amount of polyphenols is higher, while for antimicrobial activity neither the added mass of polyphenols nor a change in surface parameters has a clear influence.

#### 4. Conclusions

In the present work, the preparation of sustainable and renewable PLA-based KL and TANN composites by hot melt extrusion was investigated. The synergistic effect of the incorporation of KL and TANN on the final surface mechanical properties as well as antioxidant and antimicrobial activity of these composites was monitored. Moreover, the incorporation of KL and TANN into PLA with three different contents proved to be an effective method to enhance the surface mechanical properties of neat PLA, resulting in a larger surface effect depending on the polyphenol loading, the size of the particles with available functional carbonyl and carboxyl groups on the surface, and the interaction between the polyphenol filler and PLA.

The results showed that the increased contact angle, roughness, and zeta potential of the PLA-based KL and TANN could be related to the differences in the distribution of polyphenols near the surface of the PLA composites. In addition, all PLA composites showed hydrophilic character, which was more pronounced in PLA-TANN than in PLA-KL. The zeta potential of the PLA-KL and PLA-TANN composites exhibited an anionic charge throughout the pH range and correlated well with the hydrophilic nature of the PLA-KL and TANN composites. The highest surface concentration of polyphenolic filler resulting in a higher surface charge at the lowest content compared with neat PLA was evaluated, confirming the preferential distribution of polyphenolic filler near the surface, and decreased with filler loading as well as in the depth of the PLA polymer composites themselves. Moreover, the nanoindentation measurements confirmed the performance of both nanoindentation modulus and hardness for PLA-KL and PLA-TANN by a maximum of 8.9% and 20.9%, respectively, with a higher effect of the TANN additive compared to KL.

Finally, the synergistic and multifunctional effect of PLA-KL and PLA-TANN composites was also followed/supported by antioxidant and antibacterial activity. In addition, the incorporation of KL and TANN into PLA resulted in the migration of radical scavengers, which was monitored by DPPH assay; the kinetic study showed increased antioxidant activity, which increased with polyphenol loading. The integration of KL and TANN into PLA was sufficient for the preparation of antimicrobially active PLA-based KL and TANN composites against *E. coli*, but the dependence of the polyphenol filler content on the final antibacterial properties has not yet been clearly elucidated.

**Author Contributions:** Conceptualization, K.P.Č., L.F.Z., and D.N.B.; methodology, K.P.Č.; software, K.P.Č.; validation, K.P.Č., L.F.Z., D.N.B., and A.Z.; formal analysis, K.P.Č., A.A., and A.Z.; investigation, K.P.Č., L.F.Z., and D.N.B.; resources, K.P.Č., L.F.Z., and D.N.B.; data curation, K.P.Č.; writing—original draft preparation, K.P.Č.; writing—review and editing, K.P.Č., and L.F.Z.; visualization, K.P.Č.; supervision, K.P.Č., L.F.Z., D.N.B., A.A., and A.Z.; project administration, K.P.Č.; funding acquisition, K.P.Č., L.F.Z., and D.N.B. All authors have read and agreed to the published version of the manuscript.

**Funding:** This research received no external funding.

**Institutional Review Board Statement:** Not applicable.

**Informed Consent Statement:** Not applicable.

**Data Availability Statement:** Not applicable.

**Acknowledgments:** This work was supported financially by the postdoctoral Research Core Funding of the Ministry of Education, Science and Sport, No. OP20.04343 and the funding through the Research Program P2-0118 Textile Chemistry (Slovenian Research Agency) and by the Slovenian Research Agency in the frame of Research Core Funding No. P2-0264 in a frame of project J2-9443 related within the framework of the Research Program is also gratefully acknowledged. Authors also would like to acknowledge SIO-Grafen, a joint investment of VINNOVA, Formas, and Energimyndigheten, Grant no. 2020-00792 for financial support.

**Conflicts of Interest:** The authors declare no conflict of interest.

## References

1. European Commission. A Plastics Strategy to Protect Europe's Citizens and the Environment. Available online: [https://ec.europa.eu/environment/strategy/plastics-strategy\\_en](https://ec.europa.eu/environment/strategy/plastics-strategy_en) (accessed on 28 February 2022).
2. European Commission. *Commission Staff Working Document. Report on Critical Raw Materials and the Circular Economy*; SWD(2018) 36 final. 16.1.2018 (PART 1/3); European Commission: Brussels, Belgium, 2018; pp. 1–15.
3. European Commission DG ENV. Plastic Waste in the Environment—Final Report. Available online: [https://ec.europa.eu/environment/system/files/2020-12/2011\\_CDW\\_Report\\_0.pdf](https://ec.europa.eu/environment/system/files/2020-12/2011_CDW_Report_0.pdf) (accessed on 16 February 2022).
4. Sha, L.; Chen, Z.; Chen, Z.; Zhang, A.; Yang, Z. Polylactic acid based nanocomposites: Promising safe and biodegradable materials in biomedical field. *Int. J. Polym. Sci.* **2016**, *2016*. [CrossRef]
5. Zhang, H.; Hortal, M.; Jordá-Beneyto, M.; Rosa, E.; Lara-Lledo, M.; Lorente, I. ZnO-PLA nanocomposite coated paper for antimicrobial packaging application. *LWT* **2017**, *78*, 250–257. [CrossRef]
6. Chinaglia, S.; Tosin, M.; Degli-innocenti, F. Biodegradation rate of biodegradable plastics at molecular level. *Polym. Degrad. Stab.* **2018**, *147*, 237–244. [CrossRef]
7. Murariu, M.; Dubois, P. PLA composites: From production to properties. *Adv. Drug Deliv. Rev.* **2016**, *107*, 17–46. [CrossRef]
8. Raquez, J.M.; Habibi, Y.; Murariu, M.; Dubois, P. Polylactide (PLA)-based nanocomposites. *Prog. Polym. Sci.* **2013**, *38*, 1504–1542. [CrossRef]
9. Nair, S.S.; Chen, H.; Peng, Y.; Huang, Y.; Yan, N. Polylactic Acid Biocomposites Reinforced with Nanocellulose Fibrils with High Lignin Content for Improved Mechanical, Thermal, and Barrier Properties. *ACS Sustain. Chem. Eng.* **2018**, *6*, 10058–10068. [CrossRef]
10. Madhavan Nampoothiri, K.; Nair, N.R.; John, R.P. An overview of the recent developments in polylactide (PLA) research. *Bioresour. Technol.* **2010**, *101*, 8493–8501. [CrossRef]
11. Yeo, S.Y.; Lee, H.J.; Jeong, S.H. Preparation of nanocomposite fibers for permanent antibacterial effect. *J. Mater. Sci.* **2003**, *38*, 2143–2147. [CrossRef]
12. Nakayama, N.; Hayashi, T. Preparation and characterization of poly(l-lactic acid)/TiO<sub>2</sub> nanoparticle nanocomposite films with high transparency and efficient photodegradability. *Polym. Degrad. Stab.* **2007**, *92*, 1255–1264. [CrossRef]
13. Meng, B.; Tao, J.; Deng, J.; Wu, Z.; Yang, M. Toughening of polylactide with higher loading of nano-titania particles coated by poly( $\epsilon$ -caprolactone). *Mater. Lett.* **2011**, *65*, 729–732. [CrossRef]



14. Araki, J.; Wada, M.; Kuga, S.; Okano, T. Flow properties of microcrystalline cellulose suspension prepared by acid treatment of native cellulose. *Colloids Surf. A Physicochem. Eng. Asp.* **1998**, *142*, 75–82. [[CrossRef](#)]
15. Oksman, K.; Mathew, A.P.; Bondeson, D.; Kvien, I. Manufacturing process of cellulose whiskers/poly(lactic acid) nanocomposites. *Compos. Sci. Technol.* **2006**, *66*, 2776–2784. [[CrossRef](#)]
16. Fortunati, E.; Armentano, I.; Zhou, Q.; Iannoni, A.; Saino, E.; Visai, L.; Berglund, L.A.; Kenny, J.M. Multifunctional bionanocomposite films of poly(lactic acid), cellulose nanocrystals and silver nanoparticles. *Carbohydr. Polym.* **2012**, *87*, 1596–1605. [[CrossRef](#)]
17. Raquez, J.M.; Murena, Y.; Goffin, A.L.; Habibi, Y.; Ruelle, B.; DeBuyl, F.; Dubois, P. Surface-modification of cellulose nanowhiskers and their use as nanoreinforcers into poly(lactide): A sustainably-integrated approach. *Compos. Sci. Technol.* **2012**, *72*, 544–549. [[CrossRef](#)]
18. Pouloupoulou, N.; Kasmi, N.; Bikiaris, D.N.; Papageorgiou, D.G.; Floudas, G.; Papageorgiou, G.Z. Sustainable Polymers from Renewable Resources: Polymer Blends of Furan-Based Polyesters. *Macromol. Mater. Eng.* **2018**, *303*, 1800153. [[CrossRef](#)]
19. Bordes, P.; Pollet, E.; Avérous, L. Nano-biocomposites: Biodegradable polyester/nanoclay systems. *Prog. Polym. Sci.* **2009**, *34*, 125–155. [[CrossRef](#)]
20. Pavlidou, S.; Papaspyrides, C.D. A review on polymer-layered silicate nanocomposites. *Prog. Polym. Sci.* **2008**, *33*, 1119–1198. [[CrossRef](#)]
21. Sinha Ray, S.; Yamada, K.; Okamoto, M.; Ueda, K. New poly(lactide)-layered silicate nanocomposites. 2. Concurrent improvements of material properties, biodegradability and melt rheology. *Polymer* **2002**, *44*, 857–866. [[CrossRef](#)]
22. Bocchini, S.; Fukushima, K.; Di Blasio, A.; Fina, A.; Frache, A.; Geobaldo, F. Poly(lactic acid) and poly(lactide)-based nanocomposite photooxidation. *Biomacromolecules* **2010**, *11*, 2919–2926. [[CrossRef](#)]
23. Robles, E.; Urruzola, I.; Labidi, J.; Serrano, L. Surface-modified nano-cellulose as reinforcement in poly(lactic acid) to conform new composites. *Ind. Crops Prod.* **2015**, *71*, 44–53. [[CrossRef](#)]
24. Nerantzaki, M.; Kehagias, N.; Francone, A.; Fernández, A.; Sotomayor Torres, C.M.; Papi, R.; Choli-Papadopoulou, T.; Bikiaris, D.N. Design of a Multifunctional Nanoengineered PLLA Surface by Maximizing the Synergies between Biochemical and Surface Design Bactericidal Effects. *ACS Omega* **2018**, *3*, 1509–1521. [[CrossRef](#)] [[PubMed](#)]
25. Farah, S.; Anderson, D.G.; Langer, R. Physical and mechanical properties of PLA, and their functions in widespread applications—A comprehensive review. *Adv. Drug Deliv. Rev.* **2016**, *107*, 367–392. [[CrossRef](#)] [[PubMed](#)]
26. Stefanescu, E.A.; Daranga, C.; Stefanescu, C. Insight into the broad field of polymer nanocomposites: From carbon nanotubes to clay nanoplatelets, via metal nanoparticles. *Materials* **2009**, *2*, 2095–2153. [[CrossRef](#)]
27. Hanková, L.; Holub, L.; Jeřábek, K. Relation between functionalization degree and activity of strongly acidic polymer supported catalysts. *React. Funct. Polym.* **2006**, *66*, 592–598. [[CrossRef](#)]
28. Liao, J. Preparation and Modification of Thermoplastic/Tannins Composites via Reactive Extrusion. Ph.D. Theses, Université de Lorraine, Metz, France, 2019.
29. Arbenz, A.; Avérous, L. Chemical modification of tannins to elaborate aromatic biobased macromolecular architectures. *Green Chem.* **2015**, *17*, 2626–2646. [[CrossRef](#)]
30. Zidanes, U.L.; Dias, M.C.; Lorenço, M.S.; da Silva Araujo, E.; e Silva, M.J.F.; Sousa, T.B.; Ferreira, S.R.; Ugucioni, J.C.; Tonoli, G.H.D.; Bianchi, M.L.; et al. Preparation and characterization of tannin-based adhesives reinforced with cellulose nanofibrils for wood bonding. *Holzforschung* **2021**, *75*, 159–167. [[CrossRef](#)]
31. Grigsby, W.J.; Bridson, J.H.; Lomas, C.; Elliot, J.A. Esterification of condensed tannins and their impact on the properties of poly(lactic acid). *Polymers* **2013**, *5*, 344–360. [[CrossRef](#)]
32. García, D.E.; Salazar, J.P.; Riquelme, S.; Delgado, N.; Paczkowski, S. Condensed Tannin-Based Polyurethane as Functional Modifier of PLA-Composites. *Polym. Plast. Technol. Eng.* **2018**, *57*, 709–726. [[CrossRef](#)]
33. Pan, T. A first-principles based chemophysical environment for studying lignins as an asphalt antioxidant. *Constr. Build. Mater.* **2012**, *36*, 654–664. [[CrossRef](#)]
34. André, C.; Castanheira, I.; Cruz, J.M.; Paseiro, P.; Sanches-Silva, A. Analytical strategies to evaluate antioxidants in food: A review. *Trends Food Sci. Technol.* **2010**, *21*, 229–246. [[CrossRef](#)]
35. Chiappero, L.R.; Bartolomei, S.S.; Estenoz, D.A.; Moura, E.A.B.; Nicolau, V.V. Lignin-Based Polyethylene Films with Enhanced Thermal, Opacity and Biodegradability Properties for Agricultural Mulch Applications. *J. Polym. Environ.* **2021**, *29*, 450–459. [[CrossRef](#)]
36. Cruz, J.M.; Domínguez, J.M.; Domínguez, H.; Parajó, J.C. Antioxidant and antimicrobial effects of extracts from hydrolysates of lignocellulosic materials. *J. Agric. Food Chem.* **2001**, *49*, 2459–2464. [[CrossRef](#)] [[PubMed](#)]
37. Črešnar, K.P.; Aulova, A.; Bikiaris, D.N.; Lambropoulou, D.; Kuzmič, K.; Zemljčič, L.F. Incorporation of metal-based nanoadditives into the PLA matrix: Effect of surface properties on antibacterial activity and mechanical performance of PLA nanoadditive films. *Molecules* **2021**, *26*, 4161. [[CrossRef](#)] [[PubMed](#)]
38. Sahoo, S.; Misra, M.; Mohanty, A.K. Enhanced properties of lignin-based biodegradable polymer composites using injection moulding process. *Compos. Part. A Appl. Sci. Manuf.* **2011**, *42*, 1710–1718. [[CrossRef](#)]
39. Park, C.W.; Youe, W.J.; Nangung, H.W.; Han, S.Y.; Seo, P.N.; Chae, H.M.; Lee, S.H. Effect of lignocellulose nanofibril and polymeric methylene diphenyl diisocyanate addition on plasticized lignin/polycaprolactone composites. *BioResources* **2019**, *13*, 6802–6817. [[CrossRef](#)]
40. Spiridon, I.; Leluk, K.; Resmerita, A.M.; Darie, R.N. Evaluation of PLA-lignin bioplastics properties before and after accelerated weathering. *Compos. Part. B Eng.* **2015**, *69*, 342–349. [[CrossRef](#)]

41. Anderson, S.; Zhang, J.; Wolcott, M.P. Effect of Interfacial Modifiers on Mechanical and Physical Properties of the PHB Composite with High Wood Flour Content. *J. Polym. Environ.* **2013**, *21*, 631–639. [CrossRef]
42. Sahoo, S.; Misra, M.; Mohanty, A.K. Biocomposites from switchgrass and lignin hybrid and poly(butylene succinate) bioplastic: Studies on reactive compatibilization and performance evaluation. *Macromol. Mater. Eng.* **2014**, *299*, 178–189. [CrossRef]
43. Park, C.W.; Youe, W.J.; Han, S.Y.; Park, J.S.; Lee, E.A.; Park, J.Y.; Kwon, G.J.; Kim, S.J.; Lee, S.H. Influence of lignin and polymeric diphenylmethane diisocyanate addition on the properties of poly(butylene succinate)/wood flour composite. *Polymers* **2019**, *11*, 1161. [CrossRef]
44. Sahoo, S.; Misra, M.; Mohanty, A.K. Effect of compatibilizer and fillers on the properties of injection molded lignin-based hybrid green composites. *J. Appl. Polym. Sci.* **2013**, *127*, 4110–4121. [CrossRef]
45. Ainali, N.M.; Tarani, E.; Zamboulis, A.; Črešnar, K.P.; Zemljč, L.F.; Chrissafis, K.; Lambropoulou, D.A.; Bikiaris, D.N. Thermal Stability and Decomposition Mechanism of PLA Nanocomposites with Kraft Lignin and Tannin. *Polymers* **2021**, *13*, 2818. [CrossRef] [PubMed]
46. Črešnar, K.P.; Klonos, P.A.; Zamboulis, A.; Terzopoulou, Z.; Xanthopoulou, E.; Papadopoulos, L.; Kyritsis, A.; Kuzmič, K.; Zemljč, L.F.; Bikiaris, D.N. Structure-Properties relationships in renewable composites based on polylactide filled with Tannin and Kraft Lignin—Crystallization and molecular mobility. *Thermochim. Acta.* **2021**, *703*, 178998. [CrossRef]
47. Sharma, O.P.; Bhat, T.K. DPPH antioxidant assay revisited. *Food Chem.* **2009**, *113*, 1202–1205. [CrossRef]
48. Črešnar, K.P.; Bek, M.; Luxbacher, T.; Brunčko, M.; Zemljč, L.F. Insight into the surface properties of wood fiber-polymer composites. *Polymers* **2021**, *13*, 1535. [CrossRef]
49. Oliver, W.C.; Pharr, G.M. Measurement of hardness and elastic modulus by instrumented indentation: Advances in understanding and refinements to methodology. *J. Mater. Res.* **2004**, *19*, 3–20. [CrossRef]
50. Domenek, S.; Louaifi, A.; Guinault, A.; Baumberger, S. Potential of Lignins as Antioxidant Additive in Active Biodegradable Packaging Materials. *J. Polym. Environ.* **2013**, *21*, 692–701. [CrossRef]
51. Zemljč, L.F.; Plohl, O.; Vesel, A.; Luxbacher, T.; Potrč, S. Physicochemical characterization of packaging foils coated by chitosan and polyphenols colloidal formulations. *Int. J. Mol. Sci.* **2020**, *21*, 495. [CrossRef]
52. Potrč, S.; Zemljč, L.F.; Sterniša, M.; Plohl, O. Development of Biodegradable Whey-Based Laminate Functionalised by Chitosan—Natural Extract Formulations. *Int. J. Biol. Macromol.* **2000**, *136*, 661–667. [CrossRef]
53. Maximova, N.; Österberg, M.; Laine, J.; Stenius, P. The wetting properties and morphology of lignin adsorbed on cellulose fibres and mica. *Colloids Surf. A Physicochem. Eng. Asp.* **2004**, *239*, 65–75. [CrossRef]
54. Alwadani, N. Lignin Modification to Produce Hydrophobic Products. 2017. Available online: <https://lurepository.lakeheadu.ca/bitstream/handle/2453/4099/AlwadaniN2017m-1b.pdf?sequence=1&isAllowed=y> (accessed on 26 February 2022).
55. Hubbe, M.A.; Gardner, D.J.; Shen, W. Contact Angles and Wettability of Cellulosic Surfaces: A Review of Proposed Mechanisms and Test Strategies. *BioResources* **2015**, *10*, 8657–8749. [CrossRef]
56. Senusi, F.; Shahadat, M.; Ismail, S. Treatment of emulsion oil using tannic acid/tetraethylenepentamine-supported polymeric membrane. *Int. J. Environ. Sci. Technol.* **2019**, *16*, 8255–8266. [CrossRef]
57. Gordobil, O.; Delucis, R.; Egüés, I.; Labidi, J. Kraft lignin as filler in PLA to improve ductility and thermal properties. *Ind. Crops Prod.* **2015**, *72*, 46–53. [CrossRef]
58. Heidemann, H.M.; Dotto, M.E.R.; Laurindo, J.B.; Carciofi, B.A.M.; Costa, C. Cold plasma treatment to improve the adhesion of cassava starch films onto PCL and PLA surface. *Colloids Surf. A Physicochem. Eng. Asp.* **2019**, *580*, 123739. [CrossRef]
59. Ivanova, R.; Kotsilkova, R.; Ivanov, E.; Donato, R.K.; Fehine, G.J.; Andrade, R.J.; di Maio, R.; Silvestre, C. Composition dependence in surface properties of poly(lactic acid)/graphene/carbon nanotube composites. *Mater. Chem. Phys.* **2020**, *249*, 122702. [CrossRef]
60. Dizhbite, T.; Telysheva, G.; Jurkane, V.; Viesturs, U. Characterization of the radical scavenging activity of lignins—Natural antioxidants. *Bioresour. Technol.* **2004**, *95*, 309–317. [CrossRef]
61. Yang, W.; Weng, Y.; Puglia, D.; Qi, G.; Dong, W.; Kenny, J.M.; Ma, P. Poly(lactic acid)/lignin films with enhanced toughness and anti-oxidation performance for active food packaging. *Int. J. Biol. Macromol.* **2020**, *144*, 102–110. [CrossRef]
62. Pan, X.; Kadla, J.F.; Ehara, K.; Gilkes, N.; Saddler, J.N. Organosolv ethanol lignin from hybrid poplar as a radical scavenger: Relationship between lignin structure, extraction conditions, and antioxidant activity. *J. Agric. Food Chem.* **2006**, *54*, 5806–5813. [CrossRef]
63. Tang, X.H.; Tang, Y.; Wang, Y.; Weng, Y.X.; Wang, M. Interfacial metallization in segregated poly(lactic acid)/poly( $\epsilon$ -caprolactone)/multi-walled carbon nanotubes composites for enhancing electromagnetic interference shielding. *Compos. Part. A Appl. Sci. Manuf.* **2020**, *139*, 106116. [CrossRef]
64. Domínguez-Robles, J.; Martín, N.K.; Fong, M.L.; Stewart, S.A.; Irwin, N.J.; Rial-Hermida, M.I.; Donnelly, R.F.; Larrañeta, E. Antioxidant PLA composites containing lignin for 3D printing applications: A potential material for healthcare applications. *Pharmaceutics* **2019**, *11*, 165. [CrossRef]
65. Domínguez-Robles, J.; Larrañeta, E.; Fong, M.L.; Martín, N.K.; Irwin, N.J.; Mutjé, P.; Tarrés, Q.; Delgado-Aguilar, M. Lignin/poly(butylene succinate) composites with antioxidant and antibacterial properties for potential biomedical applications. *Int. J. Biol. Macromol.* **2020**, *145*, 92–99. [CrossRef]
66. Anwer, M.A.S.; Naguib, H.E.; Celzard, A.; Fierro, V. Comparison of the thermal, dynamic mechanical and morphological properties of PLA-Lignin & PLA-Tannin particulate green composites. *Compos. Part. B Eng.* **2015**, *82*, 92–99. [CrossRef]

67. Tribot, A.; Amer, G.; Alio, M.A.; de Baynast, H.; Delattre, C.; Pons, A.; Mathias, J.D.; Callois, J.M.; Vial, C.; Michaud, P.; et al. Wood-lignin: Supply, extraction processes and use as bio-based material. *Eur. Polym. J.* **2019**, *112*, 228–240. [[CrossRef](#)]
68. Quideau, S.; Deffieux, D.; Douat-Casassus, C.; Pouységu, L. Plant polyphenols: Chemical properties, biological activities, and synthesis. *Angew. Chemie Int. Ed.* **2011**, *50*, 586–621. [[CrossRef](#)] [[PubMed](#)]
69. Liao, J.; Brosse, N.; Hoppe, S.; Du, G.; Zhou, X.; Pizzi, A. One-step compatibilization of poly(lactic acid) and tannin via reactive extrusion. *Mater. Des.* **2020**, *191*, 108603. [[CrossRef](#)]
70. Yang, W.; Fortunati, E.; Dominici, F.; Giovanale, G.; Mazzaglia, A.; Balestra, G.M.; Kenny, J.M.; Puglia, D. Synergic effect of cellulose and lignin nanostructures in PLA based systems for food antibacterial packaging. *Eur. Polym. J.* **2016**, *79*, 1–12. [[CrossRef](#)]

## Article

# Improvement in Thermochromic Offset Print UV Stability by Applying PCL Nanocomposite Coatings

Marina Vukoje \*, Rahela Kulčar \*, Katarina Itrić Ivanda, Josip Bota and Tomislav Cigula

University of Zagreb Faculty of Graphic Arts, Getaldićeva 2, 10000 Zagreb, Croatia;

katarina.itric.ivanda@grf.unizg.hr (K.I.I.); josip.bota@grf.unizg.hr (J.B.); tomislav.cigula@grf.unizg.hr (T.C.)

\* Correspondence: marina.vukoje@grf.unizg.hr (M.V.); rahela.kulcar@grf.unizg.hr (R.K.)

**Abstract:** Thermochromic (TC) printing inks change their colouration as a response to a change in temperature. This ability renders them attractive for various applications such as smart packaging, security printing, and marketing, but their application is limited due to their low UV stability, i.e., loss of their thermochromic effect when exposed to UV radiation. In order to improve the UV stability of TC prints, one offset TC printing ink was printed and coated with nanomodified polycaprolactone (PCL) coating. The coating was prepared with the incorporation of 1%, 2%, and 3% mass ratios of ZnO and TiO<sub>2</sub> nanoparticles in the PCL matrix. The prepared nanocomposite coatings were applied onto the TC print and exposed to UV radiation; afterwards, they were characterized by the colour properties of prints, SEM microscopy, FTIR, and fluorescence spectroscopy. SEM microscopy, FTIR, and fluorescence spectroscopy showed higher rates of polymer degradation, and the results of colour stability indicated that 3% TiO<sub>2</sub> in PCL matrix gave the best UV stability and protection of TC prints.

**Keywords:** thermochromic printing inks; UV stability; polycaprolactone; nanoparticles; TiO<sub>2</sub>; ZnO

**Citation:** Vukoje, M.; Kulčar, R.; Itrić Ivanda, K.; Bota, J.; Cigula, T. Improvement in Thermochromic Offset Print UV Stability by Applying PCL Nanocomposite Coatings. *Polymers* **2022**, *14*, 1484. <https://doi.org/10.3390/polym14071484>

Academic Editors: José Miguel Ferri, Vicent Fombuena Borràs and Miguel Fernando Aldás Carrasco

Received: 18 March 2022

Accepted: 3 April 2022

Published: 6 April 2022

**Publisher's Note:** MDPI stays neutral with regard to jurisdictional claims in published maps and institutional affiliations.



**Copyright:** © 2022 by the authors. Licensee MDPI, Basel, Switzerland. This article is an open access article distributed under the terms and conditions of the Creative Commons Attribution (CC BY) license (<https://creativecommons.org/licenses/by/4.0/>).

## 1. Introduction

Printing inks are used on a range of different products from packaging, commercial printing, protected documents, and ceramics to textiles, as a tool for communication, or as a specific design feature. In order to fulfil consumers' expectations, graphic products should be functional and attractive; in this sense, printing inks can play an important role. Thermochromic (TC) printing inks are just one example of how a graphic product can dynamically interact with consumers. Thermochromic printing inks change because of the influence of temperature, and due to that behaviour, they can convey a message to the consumer on the basis of the ink colour they perceive. Thermochromic (TC) materials are available in two forms: TC materials based on leuco dyes and on liquid crystals. In addition, TC materials may be reversible or irreversible. Reversible leuco-dye-based TC materials consist of at least three components, namely, colourant, colour developer, and solvent, which mutually participate in two competitive reactions causing the thermochemical effect. The first reaction occurs between colourant and developer when the coloured complex is formed (at lower temperatures, when the solvent is in solid state), while the other reaction occurs between solvent and developer (at higher temperatures, when organic solvent with the increase in temperature becomes liquid, consequently causing the breakdown of the colourant–developer complex). These reactions allow for the thermochemical complex with a cooling process to return to its original state [1]. Thermochemical printing inks are a mixture of TC pigments and binders. TC pigments are microencapsulated leuco-dye–developer systems responsible for the creation of the TC effect, and they are usually about 10 times larger than the particle size of conventional ink pigments [2]. Ink binders may be different depending on the printing processes for which they are intended or the preferred application.

In addition to their functionality and attractiveness, these inks also have some drawbacks that are mainly related to their poor stability to various chemicals and light [3,4].

Their poor stability when exposed to UV radiation limits the time of exposure of products to external conditions and limits their applications [4–6]. The polymer envelope is much more stable than the mere polymer binder of thermochromic ink [1]. Colour formers used in thermochromic systems have poor light fastness properties [7]. UV absorbers play a very important role in improving the light fastness of colourants, while zinc and nickel 2,4-dihydroxybenzophenone-3-carboxylates were proposed as effective stabilizers against the fading of colour formers [7–9]. Moreover, due to the very complex system of TC inks, the photo-oxidation stability of thermochromic prints is affected by the chemical composition of the binder and the TC microcapsules, interactions between printing ink binder and microcapsules, and the ink binder drying mechanism [10]. The increase in the stability of thermochromic inks to UV radiation was the subject matter of an increasing number of studies. Friškovec et al. showed that a UV protective layer can help in preserving the dynamic colour properties of TC prints [4]. Rožić et al. showed that small proportions (up to 20%) of zeolite tuff in the paper used as a filler act favourably on the UV stability of TC prints, while higher proportions reduce stability as an effect of photocatalytic oxidation features due to the presence of Fe oxides in the sample of natural zeolite tuff [5]. The stability of TC printing inks may also be influenced by the ink composition [11], i.e., mineral-oil-based TC inks have a lower degree of photostability than that of TC printing inks based on vegetable oil. Rožić and Vukoje showed that microcapsules in UV screen printing ink show higher stability to photo-oxidation compared to microcapsules present in offset print due to the different interactions of TC microcapsules with the ink binder from their chemical composition [10]. Despite the fact that TC printing inks have low UV stability, the overprint UV protection of TC prints was not intensively studied.

As overprint coatings, different materials and techniques can be used, such as lamination and varnishes, but these materials generally have some drawbacks due to environmental concerns. Thus, in the last decade, the use of biodegradable materials has been the subject of numerous studies. Even though they are environmentally friendlier, their lower stability to environmental factors, such as lower stability to photo-oxidation, limits their applications. In order to improve the photostabilisation of polymers, different stabilisation systems can be used as additives; on the basis of stabiliser action, they can be light screeners, UV absorbers, excited-state quenchers, peroxide decomposers, and radical scavengers [12]. Organic materials are used in the manufacture of UV absorbers, but their limited lifetime due to photodegradation, phototoxicity, and photoallergenic effects limits their practical applications. Therefore, considerable efforts were undertaken for the development and use of inorganic materials, such as metal oxides (e.g., ZnO, TiO<sub>2</sub> and SiO<sub>2</sub>, in the formulation of UV absorbers [13–15]. Inorganic UV absorbers (nano-metal oxides) attract much attention in the field of smart packaging materials due to their excellent biocompatibility and functional properties [16,17]. In addition, they are usually less toxic, environmentally friendly, thermally or chemically stable, with better resistance, and a wider range of UV blocking capability. Among them, nano-TiO<sub>2</sub> is widely used because of its reasonable price, nontoxicity, and light stability, in addition to its good UV blocking function, and the ability to reduce light transmission in UV-A and UV-B light, which plays an important role in the prevention of photo-oxidation [18]. Zinc oxide (ZnO) with high-efficiency UV absorption resulting from a wide band is currently listed as a generally safe (GRAS) material by the U.S. Food and Drug Administration [19].

With that in mind, this study investigates the possibility of creating nanocomposite coating from polycaprolactone and metal oxides at the nanoscale, which in other studies showed good behaviour and resistance to different environmental factors when it comes to conventional printing inks [20–23]. Poly( $\epsilon$ -caprolactone) or polycaprolactone (PCL) is biodegradable synthetic polyester. Recent studies showed the potential of using PCL nanocomposite coating to enhance the surface and mechanical properties, and UV stability of conventional offset prints [20,21,24,25]. Delgado Lima and Botelho found that TiO<sub>2</sub> nanoparticles enhance polymer chain scission during the UV exposure of PCL/TiO<sub>2</sub> nanocomposites, while the increased amount of inorganic nanoparticle nanocomposites

exhibited lower thermal stability [26]. In addition, França et al., and Tsuji et al. stated that PCL photodegradation takes place through the bulk erosion mechanism [27,28].

Although overprint varnishes are often used to protect prints from mechanical damage, this paper proposes nano-modified PCL coating for the improvement of thermochromic offset print UV stability while preserving its effect. Due to the different formulation and size of colourants, thermochromic offset inks differ from conventional offset inks, which in the end affects their UV stability. In general, conventional offset prints are far more stable in comparison to thermochromic offset prints. Hence, the objective of this study was to investigate the possibility of improving TC print UV stability. So far, there are no data on TC print UV stability protection through coating application. For this research, a typical commercially available TC offset ink based on leuco dyes was used. The used ink can be printed on different printing substrates, but in all cases, the same behaviour can be expected, i.e., the same thermochromic colour effect. In the PCL solution, two nano-metal oxides ( $\text{TiO}_2$  and  $\text{ZnO}$ ) were mixed in 1%, 2%, and 3% mass ratios. In addition to UV protection, this study examines the influence of different weight concentrations of nanoparticles (NPs) in a PCL matrix on the thermochromic colour change effect.

## 2. Materials and Methods

### 2.1. Printing Ink

One commercially available thermochromic offset ink based on leuco dye was printed on commercially available uncoated paper for the purpose of preparing samples for further testing. The activation temperature of thermochromic ink is 45 °C. Below its activation temperature, the print was coloured in green, and above its activation temperature, the print was coloured in yellow. The printing process was carried out using a Prüfbau Multipurpose Printability Tester (Prüfbau Peissenberg, Germany). A quantity of 1.5 cm<sup>3</sup> ink was applied on the distribution rollers, while printing was carried out with printing force of 600 N. All samples were printed in the full tone (marked as P) under the same conditions.

### 2.2. Coating Preparation

The coating was prepared by the dissolution of PCL polymer granulates (Sigma Aldrich, St. Louis, MO, USA) in ethyl-acetate solvent (Kemika, Zagreb, Croatia). Using a heated magnetic stirrer, the solution was heated to 40 °C and stirred for about 30 min to obtain a homogenic solution. The coatings on the printed samples were prepared from a PCL polymer solution by varying the concentrations of  $\text{TiO}_2$  and  $\text{ZnO}$  nanoparticles (NPs) (Table 1). Seven different coatings were prepared: without nanoparticles or neat PCL (P/PCL); by adding 1 mass % (P/PCL/1Ti), 2 mass % (P/PCL/2Ti), and 3 mass % (P/PCL/3Ti) of titanium dioxide ( $\text{TiO}_2$ , Aerioxide P25, Evonik industries AG, Essen, Germany); and 1 mass % (P/PCL/1Zn), 2 mass % (P/PCL/2Zn), and 3 mass % (P/PCL/3Zn) of zinc oxide ( $\text{ZnO}$ , Lach-Ner, Neratovice, Czech Republic), and dispersing them with an IKA T 25 digital Ultra-Disperser (IKA-Werke, Staufen, Germany) for 8 min at 15,000 rpm. Unwanted solvent evaporation was controlled by sealing the container using paraffin strips, and the mass of the solution was compared before and after the procedure.

**Table 1.** Composition of PCL nanocomposites (wt %) and designation.

Sample	Ethyl-acetate, %	PCL, %	$\text{TiO}_2$ , %	$\text{ZnO}$ , %
P/PCL	90	10	-	-
P/PCL/1Ti	89	10	1	-
P/PCL/2Ti	88	10	2	-
P/PCL/3Ti	87	10	3	-
P/PCL/1Zn	89	10	-	1
P/PCL/2Zn	88	10	-	2
P/PCL/3Zn	87	10	-	3

### 2.3. Coating Application

The coatings were applied using a K202 Control Coater (RK Print, Litlington, UK) in controlled conditions defined by the ISO 187:1990 standard. Wet coating thickness was

defined with the standard coating bar to 24  $\mu\text{m}$  (dry coating  $\sim 6 \mu\text{m}$ ). All coatings were applied on the printed side of the paper and designated according to Table 1.

#### 2.4. Exposure of Samples to UV Radiation

For the evaluation of UV stability of coated thermochromic prints, samples were exposed to UV radiation in a Solarbox 1500e device (CO.FO.ME.GRA, Milano, Italy), with controlled temperature and UV radiation. All samples were exposed to filtered xenon light for a period of 6, 12, and 18 h at a BST temperature of 40  $^{\circ}\text{C}$  and irradiation of 550  $\text{W}/\text{m}^2$ . The indoor UV filter was used to eliminate the UVB spectral range from the xenon spectral distribution curve. The used filter in that form allows for simulating sun rays filtered through a windowpane, i.e., it simulates the conditions of internal exposure.

#### 2.5. Determination of UV–Vis Absorption Spectra of $\text{TiO}_2$ and $\text{ZnO}$ Nanoparticles

For the measurement of the  $\text{TiO}_2$  and  $\text{ZnO}$  nanoparticles' UV absorption property, prior to measurement, a small amount of nanoparticle powder was placed between a quartz glass microscope slide and a quartz glass cover slip in order to prevent the powder material from penetrating the spectrophotometer's sphere aperture. An Ocean Optics USB 2000+ spectrometer (Ocean Optics, Orlando, FL, USA) with a 30 mm wide integrating sphere under (8:di) measuring geometry (diffuse geometry, specular component included) and the addition of deuterium–tungsten halogen UV light source DH-2000 (Ocean insight, Orlando, FL, USA) was placed on the upper side of the quartz glass cover slip; measurements were performed in steps of 1 nm for the spectral region from 200 to 800 nm.

#### 2.6. Colorimetric Measurement

Spectral reflectance was measured by using an Ocean Optics USB2000+ spectrometer (Ocean Optics, Orlando, FL, USA) with 30 mm wide integrating sphere under (8:di) measuring geometry (diffuse geometry, specular component included). Printed samples (uncoated and coated) were heated–cooled on a full-cover water block (EK Water Blocks, EKWB d.o.o., Komenda, Slovenia) whose temperature was varied with a thermostatically controlled water block. Reflectance spectra were measured in one heating–cooling cycle by heating samples from 25 to 55  $^{\circ}\text{C}$  and then cooling them back to 25  $^{\circ}\text{C}$ . Measurements were performed in steps of 1 nm for the spectral region from 400 to 800 nm. Ocean Optics SpectraSuite software (version 2.0.8) was used for the calculation of the CIELAB values from the measured reflectance. D50 illuminant and 2 $^{\circ}$  standard observer were applied in these calculations. Colour differences were calculated using the CIEDE2000 total colour difference formula [29].

#### 2.7. SEM Microscopy

Uncoated and coated thermochromic (TC) prints before and after exposure to UV radiation were monitored using a Tescan Vega III Easyprobe (Tescan, Brno, Czech Republic) field-emission scanning electron microscope. Micrographs were taken under magnification of 5000 $\times$ .

#### 2.8. FTIR Spectroscopy

ATR spectra of the samples before and after UV exposure were measured using a Shimadzu FTIR IRAffinity-21 spectrometer (Shimadzu, Kyoto, Japan) with Specac Silver Gate Evolution as a single-reflection ATR sampling accessory with a  $\text{ZnSe}$  flat crystal plate (index of refraction, 2.4). IR spectra were recorded in the spectral range between 4000 and 400  $\text{cm}^{-1}$  at 4  $\text{cm}^{-1}$  resolution and averaged over 15 scans.

#### 2.9. Fluorescence Spectroscopy

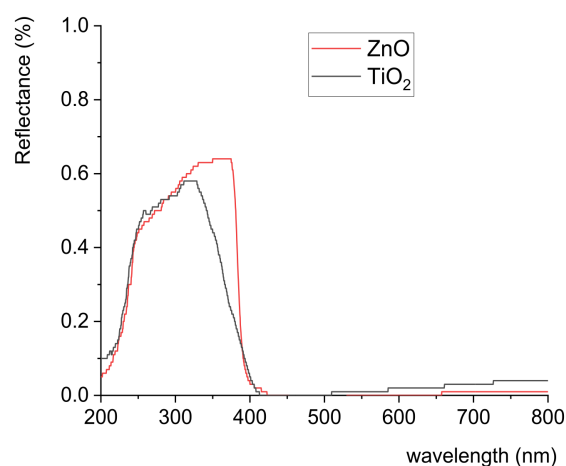
Fluorescence intensity was measured using an Ocean Optics USB4000+ spectrometer 2000 (Ocean Optics, Orlando, FL, USA) in combination with a 30 mm wide integrating sphere under (8:di) measuring geometry (diffuse geometry, specular component included)

with the addition of an LSM Series LED 2000 (Ocean insight, Orlando, FL, USA) light source at 365 nm as the fluorescence excitation wavelength. The use of an integrating sphere in fluorescence measurements were previously discussed and applied in different areas [30–33]. The excitation light source was kept stable at a constant current of 0.140 A. Fluorescence intensity was measured in the spectral range between 330 and 630 nm.

### 3. Results and Discussion

#### 3.1. UV–Vis Absorption Spectra of TiO<sub>2</sub> and ZnO Nanoparticles

UV–vis absorption spectra of the used nanoparticles (ZnO and TiO<sub>2</sub>) are presented in Figure 1. The band gap of ZnO is similar to that of TiO<sub>2</sub>, but the ZnO band gap is somewhat larger. Figure 1 shows that ZnO nanoparticles absorbed radiation in a UV range up to 374 nm, and almost all visible spectral radiation was scattered by the ZnO nanoparticles, while TiO<sub>2</sub> nanoparticles absorbed UV irradiation up to 329 nm. Obtained results are similar to those observed in another study [34]. UV absorption edges of the used nanoparticles differed in the case of TiO<sub>2</sub> being shifted towards lower wavelengths. The UV absorption edge can be influenced by the size of the nanoparticles [34].



**Figure 1.** UV–vis absorption spectra of ZnO and TiO<sub>2</sub> nanoparticles.

#### 3.2. Colorimetric Properties of Uncoated and Coated TC Prints

To determine the influence of coating application and UV radiation on the thermochromic effect (the dynamic colour change) of TC prints, prepared samples were analysed through the colour hysteresis, spectral reflectance curves, and total colour difference (TCD) of a sample measured between heating and cooling at a temperature well below the final chromic temperature (Figures 2 and S1). Colour hysteresis (Figures 2 and S1) describes the temperature dependence of prints for the  $L^*$  component of colour. Colour hysteresis is commonly called thermochromic memory [1]. The process is illustrated by the change in lightness  $L^*$  as a function of temperature. The CIELAB values of thermochromic print samples were calculated by applying measured reflectance spectra during heating from 25 to 55 °C and cooling down to 25 °C. At a temperature lower than the activation temperature (45 °C), microcapsules are blue, while they become yellow above that temperature.

The application of PCL nanocomposite coating caused notable differences in colour hysteresis, for example, for samples coated with nanomodified PCL coating, the lightness value at lower temperatures became smaller, i.e., the initial colouration of the samples appeared to be darker (Figure 2 and Figure S1). Dailliez et al. showed that, in the case of halftone prints, the application of a smooth transparent layer darkens the print and saturates its colour due to the lateral propagation of light within the coating during the multiple-reflection process that occurs between the printed diffusing substrate and the coating–air interface [35]. In this case, changes in colour can also be related to the presence of nanoparticles. With the increase in NP ratio in the PCL matrix, samples became darker at lower temperatures. This behaviour was observed for all samples containing ZnO and TiO<sub>2</sub>



nanoparticles, with somewhat greater changes (lower  $L^*$ ) for ZnO nanomodified coating. This behaviour can be explained by the increase in the number of NPs in the coating, i.e., the increase in the amount of absorbed light and consequent lower reflection. In the case of ZnO NPs, the higher band gap (Figure 1) caused a higher amount of absorbed light resulting in the darker appearance of samples in comparison to TiO<sub>2</sub>, which had a smaller band gap and absorbed less light, resulting in greater light reflection.

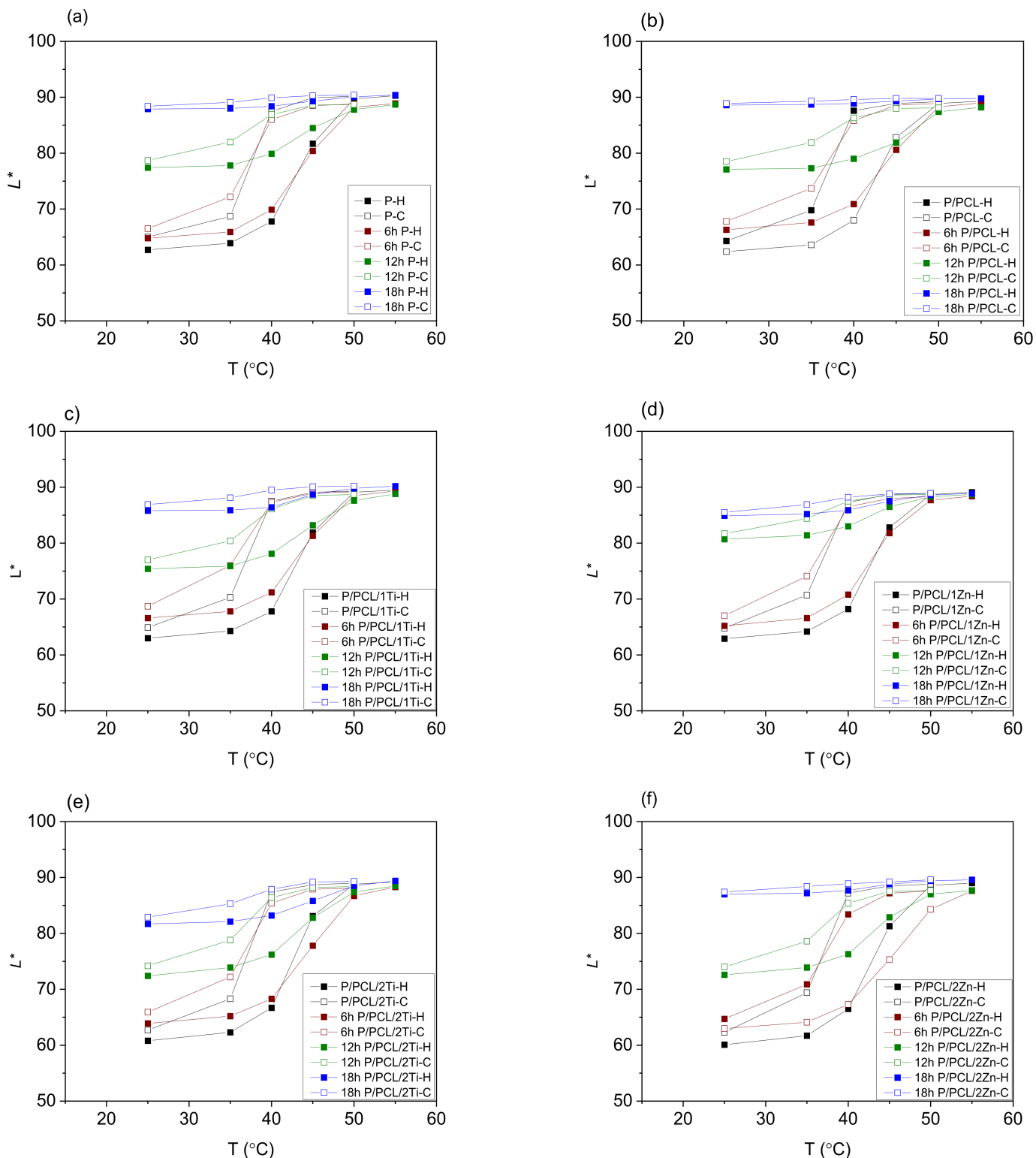
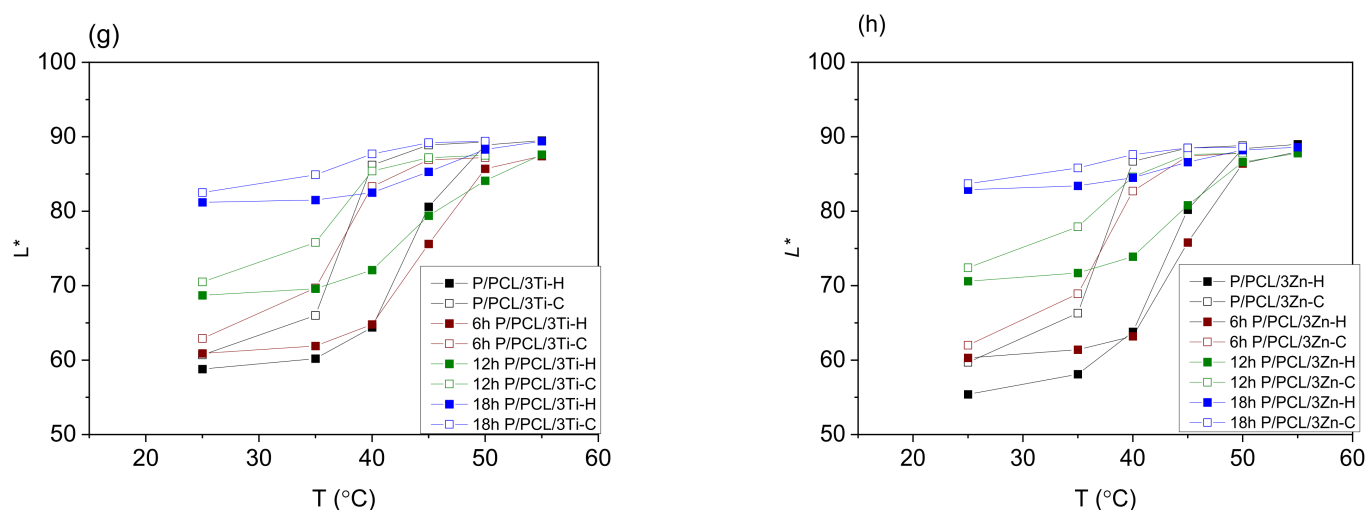


Figure 2. Cont.



**Figure 2.** Colour hysteresis of (a) uncoated TC print, (b) PCL coated TC print, (c) PCL/1%Ti coated TC print, (d) PCL/1% Zn coated TC print, (e) PCL/2% Ti coated TC print, (f) PCL/2% Zn coated TC print, (g) PCL/3% Ti coated TC print, (h) PCL/1% Zn coated TC print; before and after exposure to UV radiation for 6, 12, and 18 h.

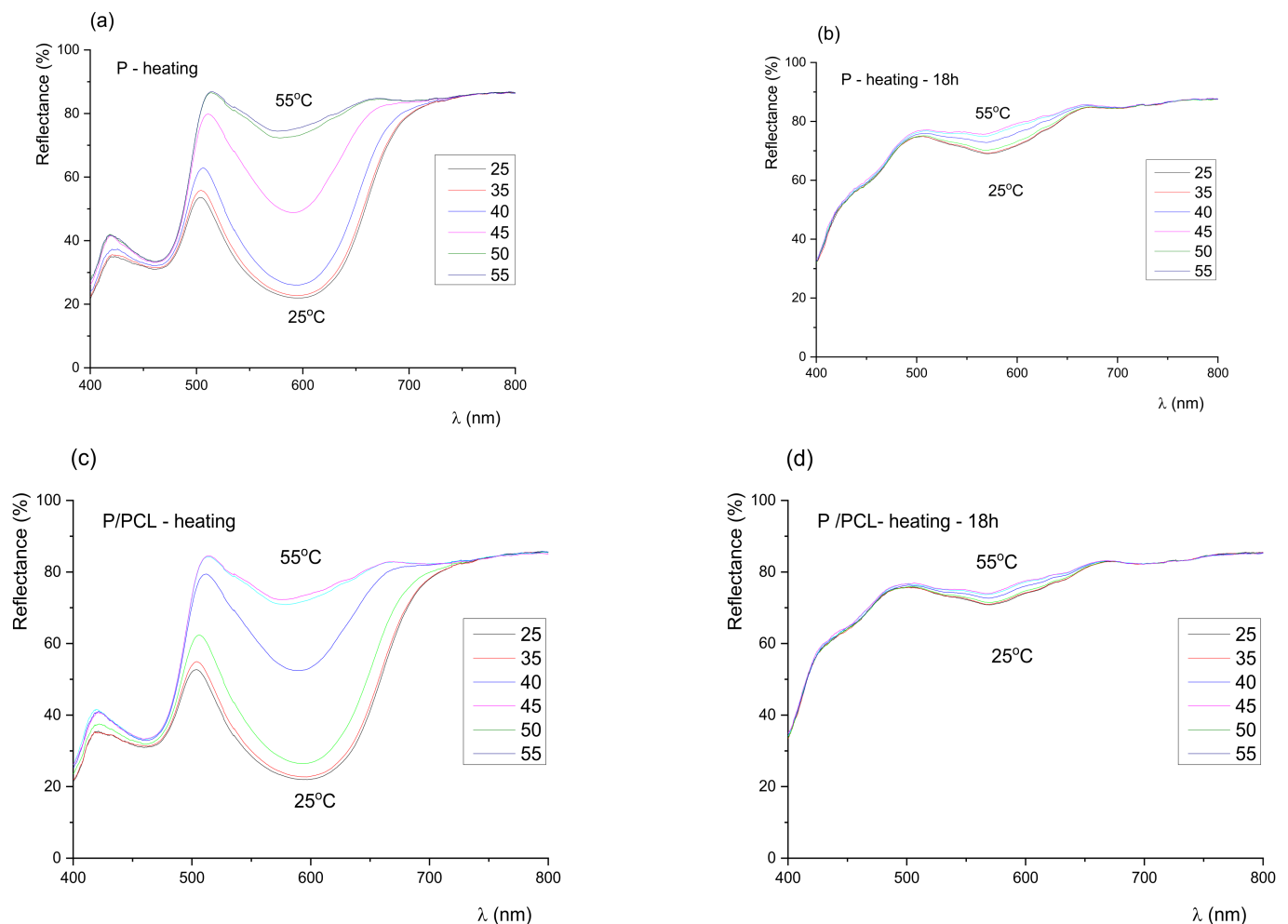
Figure 2 shows the influence of UV radiation on the TC prints' colour hysteresis loops. TC memory gradually degrades with the increase in exposure time to UV radiation. Their height becomes smaller (the result of reduced TCD), and slopes decrease a little more when cooled (denoted as -C) and less when heated (denoted as -H). After 6 h of exposure to UV radiation, all hysteresis loops were modified. Moreover, 18 h of UV exposure produced remarkable changes in the TC effect, which was completely destroyed for the uncoated TC print (Figure 2a) and the print coated with neat PCL (Figure 2b); therefore, there were no dynamic colour properties, whereas the resulting loop remained very small on TC prints coated with nanomodified PCL with 1% TiO<sub>2</sub> (Figure 2c), 1% ZnO (Figure 2d), and 2% ZnO (Figure 2f). Higher nanoparticle concentrations resulted in better protection, but the 3% TiO<sub>2</sub> content (Figure 2g) stood out on TC samples, as it offered better protection than that of 3% ZnO (Figure 2h). Best results were obtained for TiO<sub>2</sub>-coated samples, where these loops were wider, resulting in a more visible colour change effect.

The thermochromic effect increasingly decreased with the exposure of samples to UV radiation, and the reversible colour change was increasingly less present. The range and dynamics of colour through the heating and cooling cycle were reduced, which was especially evident in samples exposed to 18 h of UV radiation. On PCL-treated samples, the TC effect completely disappeared after 18 h of exposure to UV radiation, while the highest colour change dynamics was visible on TC prints coated with PCL modified with 3% TiO<sub>2</sub> coating.

Results of spectral reflection curves (Figures 3 and 4) show that the colour of the samples before exposure to UV radiation remained green until the activation temperature (45 °C), after which it slowly turned yellow. No sudden changes were observed, and the colour of the prints continuously changed with the increase in temperature. With exposure of the samples to UV radiation, the dynamics of colour change on the sample rapidly changed. Results of the spectral reflection curves show that with exposure of the samples to UV radiation after 18 h, part of the 400–450 nm spectrum was gradually lost, which indicated the degradation of the blue TC pigment, i.e., the degradation of the microcapsules. In the green (500–570 nm) and yellow–orange spectral range (570–630 nm), even after 18 h of exposure to UV radiation, a change was visible. Changes in the green area indicated that not all blue microcapsules were damaged by UV radiation, unlike the uncoated print and print coated with neat PCL coating, where the thermochromic effect had almost disappeared.

A TC sample is considered to work properly if the total colour difference between the two states below and above the activation temperature is well-visible. The total colour difference (TCD) between the two states for samples unexposed and exposed to UV radiation is shown in Figure 5, which indicates that the application of PCL coating over the TC print increased the total colour difference of the original samples with the increase in NP share in the formulation of PCL coating. This behaviour was also visible on the obtained hysteresis (Figure S1). TCD gradually decreased with the increased time of UV exposure.

Reversible colour change was present in all samples, implying that the thermochromic effect had not been lost during UV degradation, but it was significantly reduced after 18 h of UV irradiation. After 18 h of UV exposure, the colour change effect completely disappeared in the PCL sample and fell below 3 CIED2000 units, even more than that for the untreated sample. Figure 5 shows that nanoparticle deposition is effective, as the difference in TC effect between treated and untreated samples was quite obvious. Best results were obtained for the 3% TiO<sub>2</sub> nanomodified PCL coating.



**Figure 3.** Reflectance spectra during heating process of (a) uncoated TC print (untreated), (b) uncoated TC print exposed to UV radiation for 18 h, (c) PCL coated TC print (untreated), (d) PCL coated TC print exposed to UV radiation for 18 h.

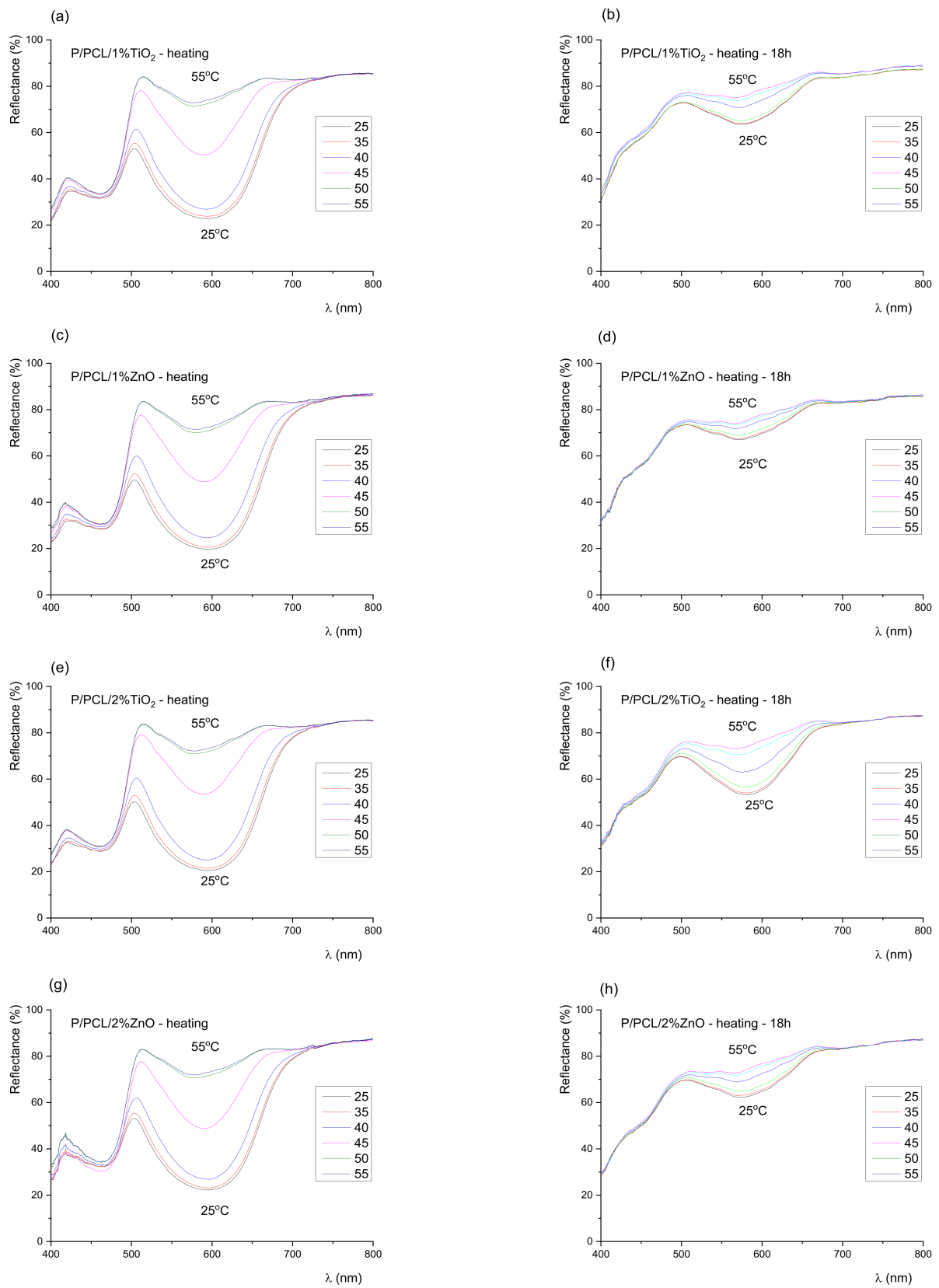
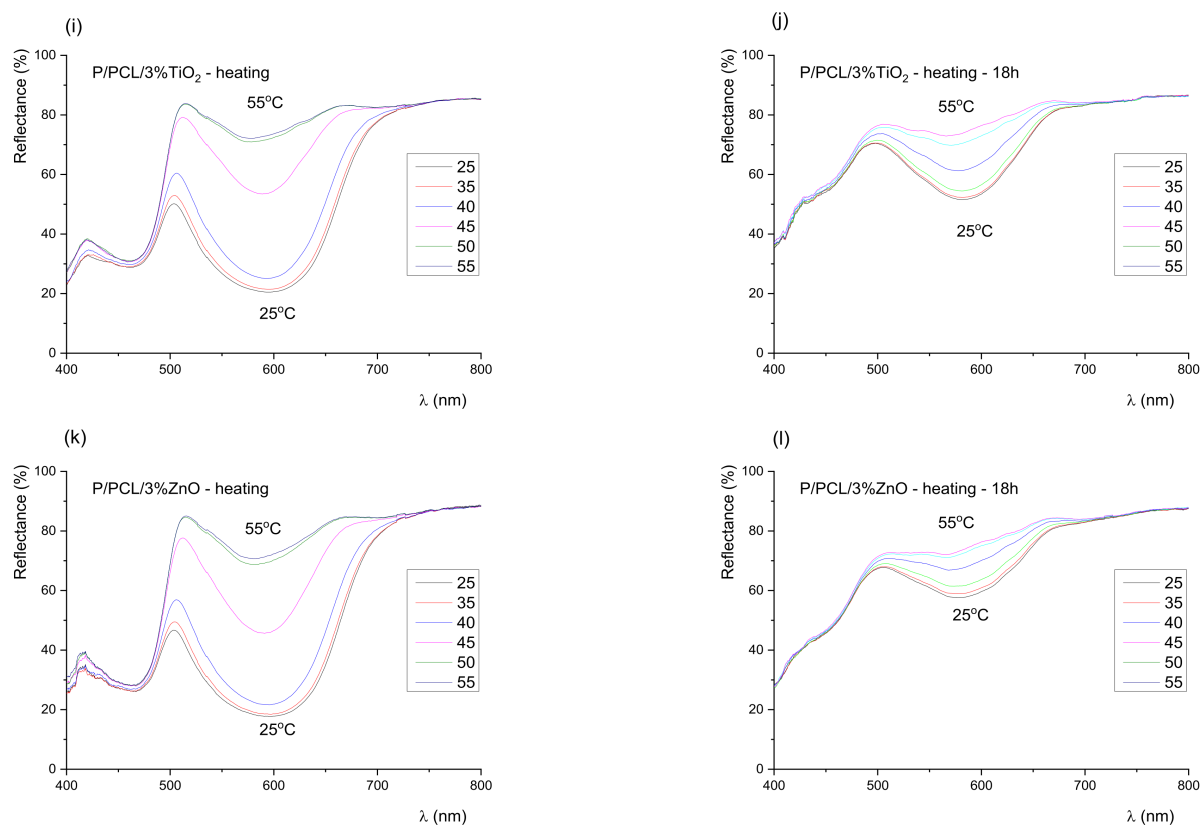
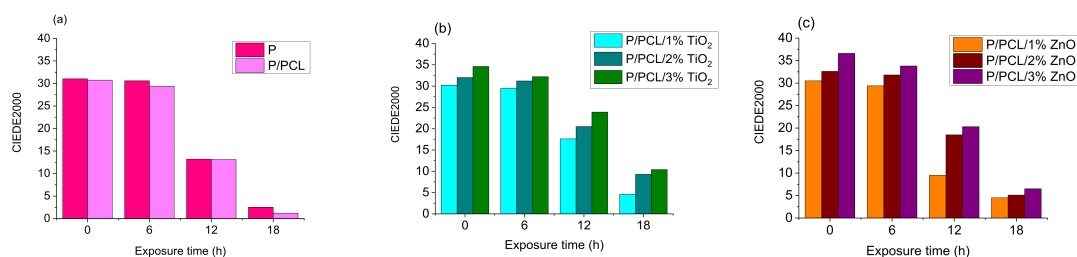


Figure 4. Cont.



**Figure 4.** Reflectance spectra of TC prints measured during heating, coated with (a) PCL/1% Ti (untreated), (b) PCL/1% Ti after 18 h of exposure to UV radiation, (c) PCL/1% Zn (untreated), (d) PCL/1% Zn after 18 h of exposure to UV radiation, (e) PCL/2% Ti (untreated), (f) PCL/2% Ti after 18 h of exposure to UV radiation, (g) PCL/2% Zn (untreated), (h) PCL/2% Zn after 18 h of exposure to UV radiation, (i) PCL/3% Ti (untreated), (j) PCL/3% Ti after 18 h of exposure to UV radiation, (k) PCL/3% Zn (untreated), (l) PCL/3% Zn after 18 h of exposure to UV radiation.



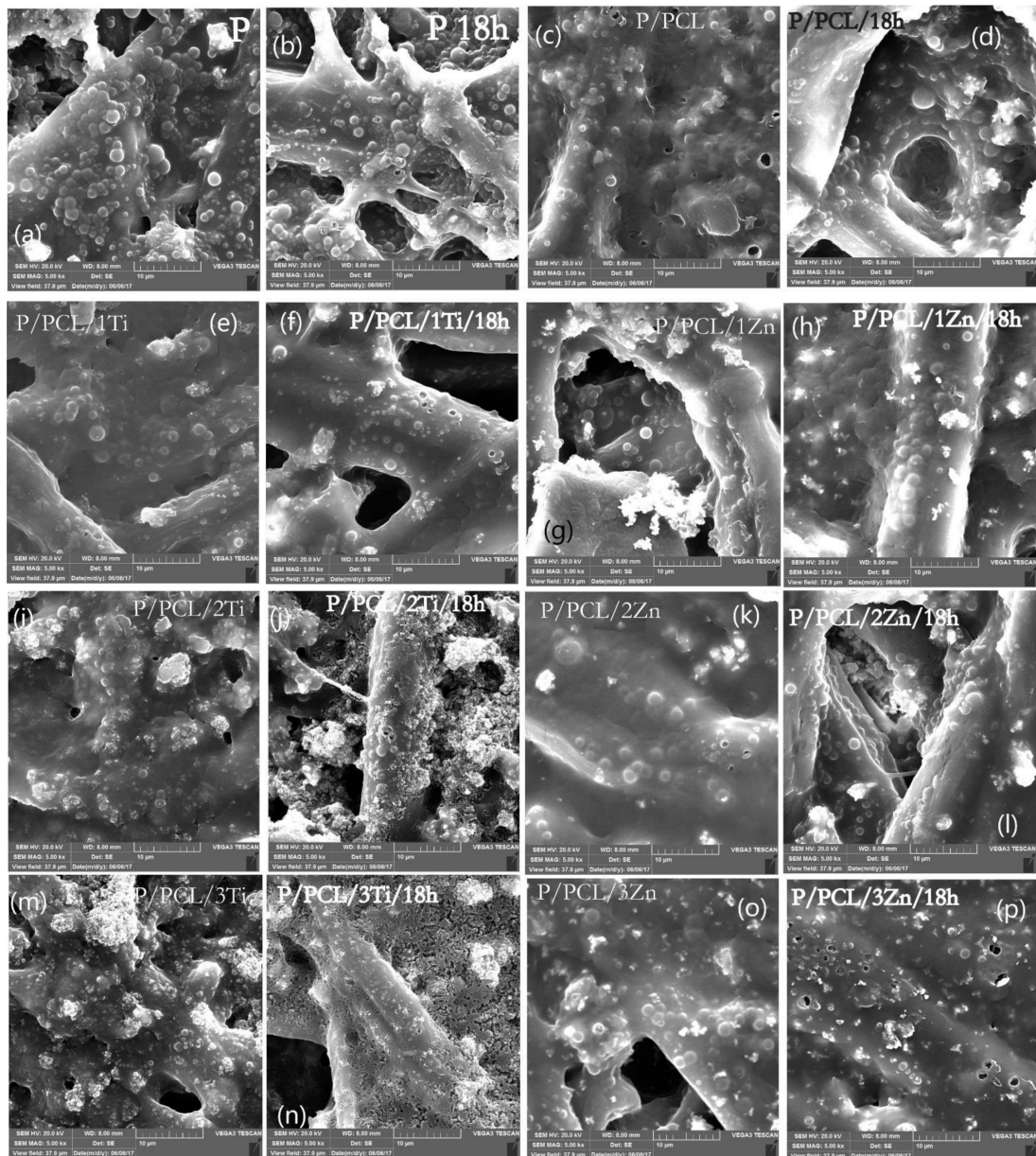
**Figure 5.** Total colour difference (TCD) between two states (measured at 25 and 50 °C) for (a) unprinted TC print and TC print coated with neat PCL, (b) TC print coated with 1, 2, 3% TiO<sub>2</sub> nanomodified PCL, (c) TC print coated with 1, 2, 3% ZnO nanomodified PCL, before and after 6, 12, and 18 h exposure to UV radiation.

Colorimetric results show that the incorporation of the greatest investigated amount (3%) of TiO<sub>2</sub> nanoparticles in PCL matrix significantly impacted the UV stability of TC prints. The UV stability of the uncoated TC print and the print coated with neat PCL was lower than that on prints coated with 3% TiO<sub>2</sub> nanomodified PCL coating, probably because the print under the PCL polymer layer absorbed UV radiation with TiO<sub>2</sub> nanoparticles, thus preventing UV radiation from penetrating into the print.

### 3.3. SEM Microscopy

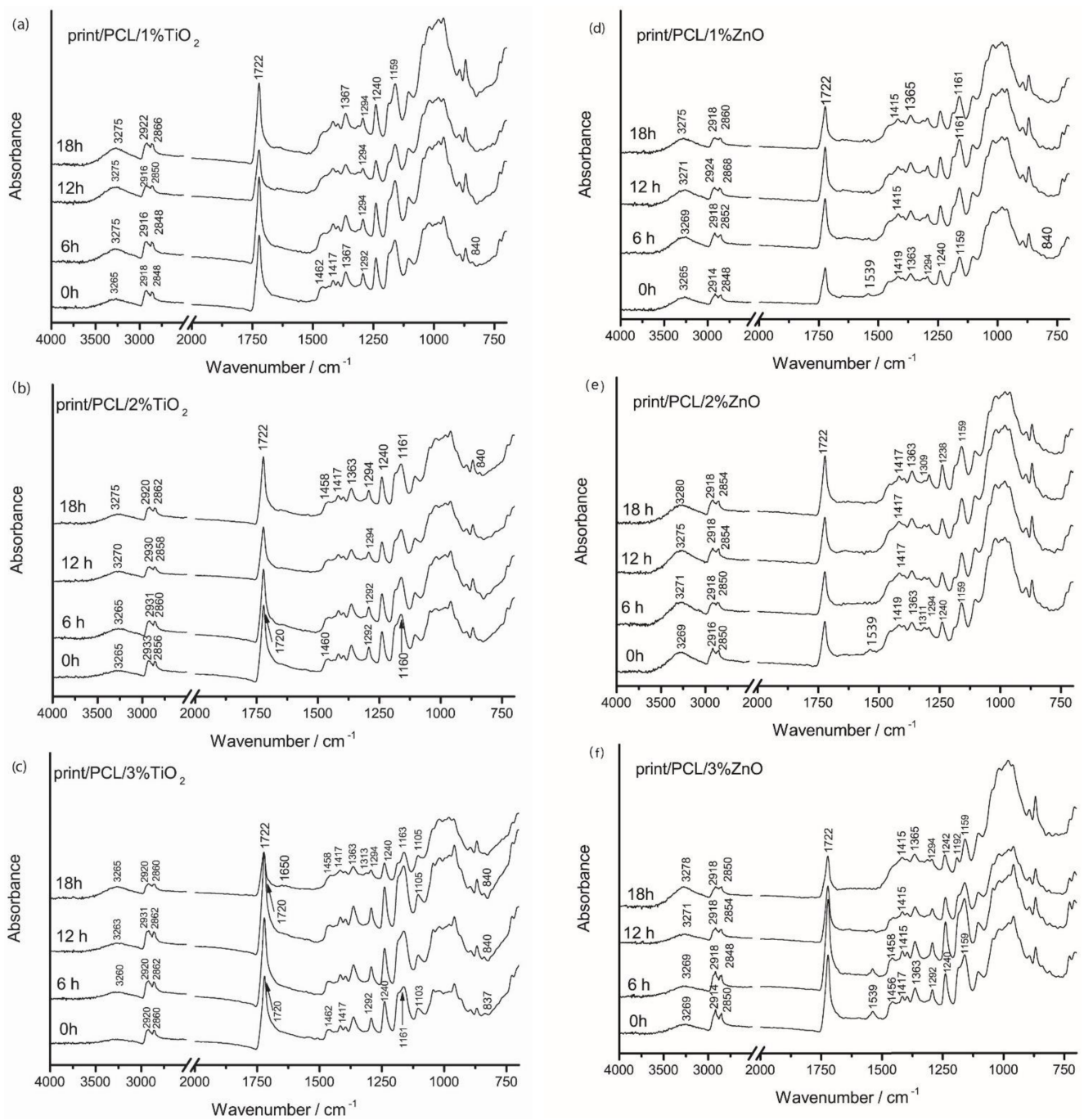
Figure 6 shows the SEM micrographs of samples before and after exposure to UV radiation for 18 h. SEM micrographs show that the surface of TC print before exposure to UV

radiation was heterogeneous, with the presence of significant number of TC microcapsules in regular circular forms with around 1–3  $\mu\text{m}$  diameter and covered with a thin layer of ink binder. In addition, the penetration of microcapsules in the paper structure between the cellulose fibres was visible. SEM micrographs do not show the significant degradation of TC microcapsules after the print had been exposed to UV radiation since only several holes in TC microcapsules are visible. The masking of degraded TC microcapsules probably occurred by the ink binder and their penetration between the cellulose fibres. The formation of craters probably occurred due to degradation of ink binder.



**Figure 6.** SEM micrographs of (a) uncoated TC print, (b) uncoated TC print after exposure to UV radiation for 18 h, (c) TC print coated with neat PCL, (d) TC print coated with neat PCL after exposure to UV radiation for 18 h, and coated TC prints with nanomodified PCL (e) PCL/1% Ti (untreated), (f) PCL/1% Ti after exposure to UV radiation for 18 h, (g) PCL/1% Zn (untreated), (h) PCL/1% Zn after exposure to UV radiation for 18 h, (i) PCL/2% Ti (untreated), (j) PCL/2% Ti after exposure to UV radiation for 18 h, (k) PCL/2% Zn (untreated), (l) PCL/2% Zn after exposure to UV radiation for 18 h, (m) PCL/3% Ti (untreated), (n) PCL/3% Ti after exposure to UV radiation for 18 h, (o) PCL/3% Zn (untreated), (p) PCL/3% Zn after exposure to UV radiation for 18 h.





**Figure 8.** FTIR spectra of TC print coated with nanomodified PCL coatings (a) PCL/1% Ti, (b) PCL/2% Ti, (c) PCL/3% Ti, (d) PCL/1% Zn, (e) PCL/2% Zn, (f) PCL/3% Zn before and after 6, 12, and 18 h exposure to UV radiation.

In the case of the FTIR spectra of the neat uncoated TC print, vibrational bands of used thermochromic printing ink most likely originated from the thermochromic ink binder, mainly vegetable oils as the common component of the ink binder. Thus, vibrational bands could not have been the result of the vibrational modes of the thermochromic composites within the microcapsules or the TC microcapsules' polymer shell since they were covered with the ink binder [38,39]. Due to the coverage of microcapsules with the ink binder, the vibrational bands of the microcapsules' wall material were probably covered and overlapped with the vibrational bands of the ink binder that was present in higher amounts. Regarding the FTIR spectra of thermochromic print, a significant contribution of



the cellulose bands could be noticed due to the penetration of the TC printing ink into the paper structure, especially in the 1500–800  $\text{cm}^{-1}$  spectral range. The carbonyl stretching band of the thermochromic ink at 1728  $\text{cm}^{-1}$  was present in the FTIR spectrum of the TC print, as opposed to the FTIR spectrum of unprinted paper. Bands at 2920 and 2850  $\text{cm}^{-1}$  in the spectrum of thermochromic print were assigned to the  $-\text{CH}_2$  and  $-\text{CH}_3$  stretching bonding vibration of aliphatic chains, respectively, and implied the presence of oils in the printing ink binder [40].

With the exposure of paper to UV radiation, changes in the FTIR spectra could be observed in the spectral range of 1500–1850  $\text{cm}^{-1}$ , where carbonyl groups appeared but only if the bending vibrations of the bound water molecules at 1640  $\text{cm}^{-1}$  were not present since they could mask the products of cellulose oxidation [41]. In our case, adsorbed water molecules were present and probably masking the vibrational bands of paper degradation products. No additional changes in the IR spectra of unprinted paper during 18 h of UV irradiation were observed, indicating that this relatively short radiation time (18 h) slightly affects paper stability and its properties.

Characteristic vibrational bands of the PCL polymer were obtained at 2918 and 2848  $\text{cm}^{-1}$ , attributed to the stretching of aliphatic C–H groups, the ester carbonyl (C=O) stretching absorption band at 1722  $\text{cm}^{-1}$ , and the asymmetric stretching of C–O–C bonds at 1240  $\text{cm}^{-1}$ , while their symmetric stretching corresponded to the peak at 1162  $\text{cm}^{-1}$  [24,41,42]. With the application of PCL coating over the TC print, the carbonyl peak was shifted to smaller wavelengths at around 1722  $\text{cm}^{-1}$ , unlike the TC print, where it was located at 1728  $\text{cm}^{-1}$ . This may indicate overlapping carbonyl groups vibrational bands.

By the exposure of the uncoated print to UV irradiation, changes in the spectral range of 2920–2850  $\text{cm}^{-1}$  occurred. These changes are related to the  $-\text{CH}_2$  and  $-\text{CH}_3$  stretching bonding vibrations of aliphatic chains, which imply the presence of oils in the printing ink binder, which indicates binder degradation. By the exposure of prints coated with PCL to UV irradiation, a decrease in vibrational bands in the spectral range of 2920–2850  $\text{cm}^{-1}$ , and a shift towards greater wavenumbers occurred. In addition, a decrease in vibrational bands intensities at 1417, 1367, 1294, and 1240  $\text{cm}^{-1}$  occurred. The band at 1294  $\text{cm}^{-1}$  gradually disappeared after 18 h of exposure to UV radiation.

The application of PCL–TiO<sub>2</sub> nanomodified coating (Figures 8a–c and S2) resulted in the partial masking of cellulose vibrational bands that were present in the FTIR spectra of the TC print and PCL-coated thermochromic print (Figure 7b,c). The addition of TiO<sub>2</sub> and ZnO nanoparticles to the PCL matrix lead to changes in the IR spectrum of PCL, i.e., functional groups, their displacement, and the formation of new bands and their shoulders, which indicated a change in the crystal structure of PCL (Figure S2). By the incorporation of TiO<sub>2</sub> and ZnO nanoparticles into the PCL matrix (Figure S2), the vibrational bond at 1160  $\text{cm}^{-1}$  was broadened, and the shoulders at 1186  $\text{cm}^{-1}$  in the case of TiO<sub>2</sub> particles and at 1190  $\text{cm}^{-1}$  in the case of ZnO particles were formed. In that spectral range (from 1167 to 1191  $\text{cm}^{-1}$ ), a symmetrical vibration describes C–O bonds. The vibration at 1191  $\text{cm}^{-1}$  was attributed to O–C–O bond stretching, while the vibrational bond at 1166  $\text{cm}^{-1}$  corresponded to CH<sub>2</sub> deformation [24,42]. Furthermore, the addition of 1%, 2%, and 3% TiO<sub>2</sub> nanoparticles (Figure 8a–c) lead to the formation of vibrations bands at 1462 and 1363  $\text{cm}^{-1}$ , which corresponded to the C–H bond stretching of alkanes, while absorbance at 729  $\text{cm}^{-1}$  represents the vibration of  $-\text{CH}_2$  bonds. In addition, through the incorporation of TiO<sub>2</sub> nanoparticles, the vibrational band at 1293  $\text{cm}^{-1}$  was formed that is related to the crystalline phase of PCL (C–C and C–O) [42,43]. The formation of the crystalline band at 1293  $\text{cm}^{-1}$  was also noticed in the case of addition 3% TiO<sub>2</sub> nanoparticles. The vibrational band at 1462  $\text{cm}^{-1}$  was attributed to the axial symmetric deformation of CH, while the band at 1292  $\text{cm}^{-1}$  could be assigned to backbone C–C (=O)–O, the stretching vibration of the crystalline phase of PCL.

In the case of the nanomodified ZnO PCL coating, differences could be seen in the FTIR spectra (Figure 8d–f and Figure S2). IR spectra indicated a lower degree of PCL

crystallinity in comparison to that of TiO<sub>2</sub> nanomodified coating. Only the addition of 3% ZnO NPs into the PCL matrix resulted in somewhat similar IR spectra to those of the TiO<sub>2</sub> nanomodified coatings (Figure 8f). Moreover, the addition of ZnO NPs into the PCL matrix caused the formation of the vibrational band at 1539 cm<sup>-1</sup>, which increased with the increase in ZnO NPs amount, which could be attributed to the main ZnO characteristic vibrational bands [44]. For the 1% and 2% ZnO nanomodified coating, IR spectra in the spectral range of 1125–750 cm<sup>-1</sup> looked like the IR spectra of paper, while the characteristic PCL vibrational bands in the spectral range of 1500–1125 cm<sup>-1</sup> were slightly pronounced, indicating a lower degree of polymerization and higher penetration within the paper structure (Figure 8d,e).

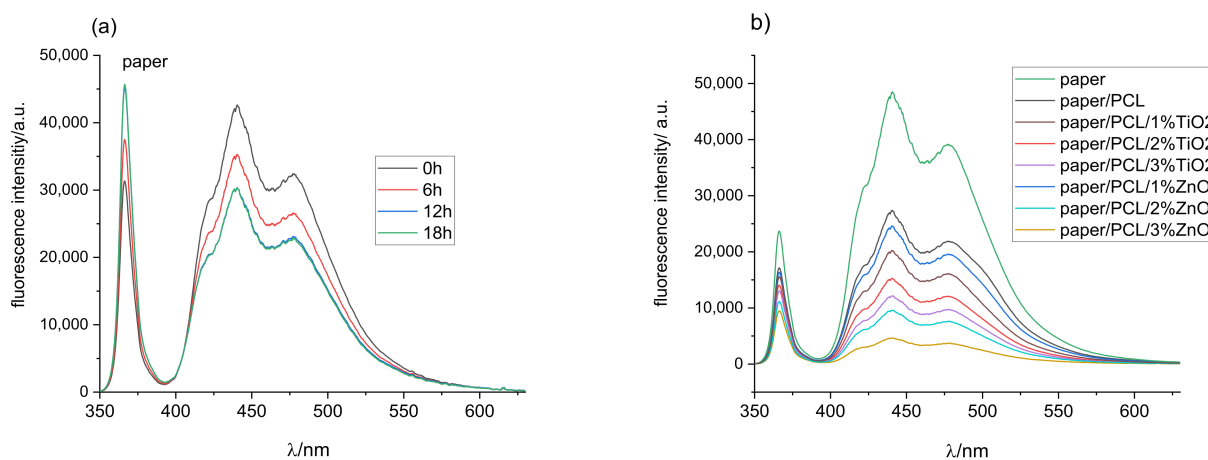
The photodegradation mechanism of PCL occurred due to the presence of light absorbing species and chromophore functional groups, i.e., carbonyl, resulting in the absorption of UV radiation by carbonyl groups present on the polymer backbone and proceeding via Norrish II-type reaction, which explains the chain scission (decrease in molecular weight), and the formation of C=C double bonds and hydroperoxide O–H at newly formed chain terminals [45]. The exposure of prints coated with 1% TiO<sub>2</sub> PCL to UV radiation (Figure 8a) caused the increase in vibrational band intensities at 3265 cm<sup>-1</sup> (O–H vibrational bands), and broadening and movement towards higher wavenumbers. For the prints coated with 2% TiO<sub>2</sub>/PCL (Figure 8b) after UV exposure, the carbonyl band was shifted from 1720 to 1722 cm<sup>-1</sup>. This vibrational band broadened with the increase in time to UV exposure, probably due to the formation of new radicals (C=O) and the overlap with those vibrational bands. The broadening of this band could be attributed to the formation of photodegradation products (C=C) and their mutual overlapping. In addition, the formation of new bands around 1650 cm<sup>-1</sup> after 18 h of UV exposure indicated the formation of C=C bonds and confirmed the photodegradation mechanism of PCL. The formation of this band was visible for the 3% TiO<sub>2</sub> nanomodified coating after 18 h of UV exposure (Figure 8c), while in other samples, this could be explained as the broadening of the carbonyl peak and not as the formation of a new band. In addition, with UV exposure, the band at 1462 cm<sup>-1</sup> was shifted towards 1458 cm<sup>-1</sup>. The vibrational band at 1292 cm<sup>-1</sup> was shifted to 1294 cm<sup>-1</sup> and slightly decreased by the influence of UV radiation. All these changes could be attributed to a change in polymer crystallinity resulting from photodegradation, the changes in PCL characteristic functional groups, and the absence of intermolecular interactions. For samples coated with nanomodified PCL/ZnO NPs, UV radiation caused significant changes in the IR spectra (Figure 8d,f). The absorption peak at 1539 cm<sup>-1</sup> gradually disappeared with the increase in exposure time to UV radiation. The greatest changes occurred in the spectral range of 1250–1125 cm<sup>-1</sup>, where vibrational bands disappeared.

### 3.5. Fluorescence Spectroscopy

Fluorescence occurs when fluorescent molecules absorb the light of the corresponding wavelength to move from the ground to the excited state, followed by the re-emission of energy in the form of visible light when returning to the ground state [46]. One of the advantages of fluorescence spectroscopy measurement is its high sensitivity, and even small concentrations of fluorescent material can be detected. Before examining print fluorescence, it was necessary to address the influence of coating on paper fluorescence and the fluorescence stability of paper substrate exposed to UV radiation for 6, 12, and 18 h (Figure 9a,b).

As expected, the measurements of printing substrate (Figure 9a) showed the highest amount of fluorescence intensity in the blue part of the spectrum (400–490 nm) due to the use of optical brighteners (OBAs) [33,47]. OBAs were added in the paper during the production process to increase paper whiteness [48]. After the exposure of unprinted paper to UV radiation for 6 h, fluorescence intensity decreased. A similar drop in fluorescence intensity could be seen after 12 h of UV exposure, after which paper fluorescence was not further reduced by prolonged exposure to UV radiation. This was confirmed by the high amount

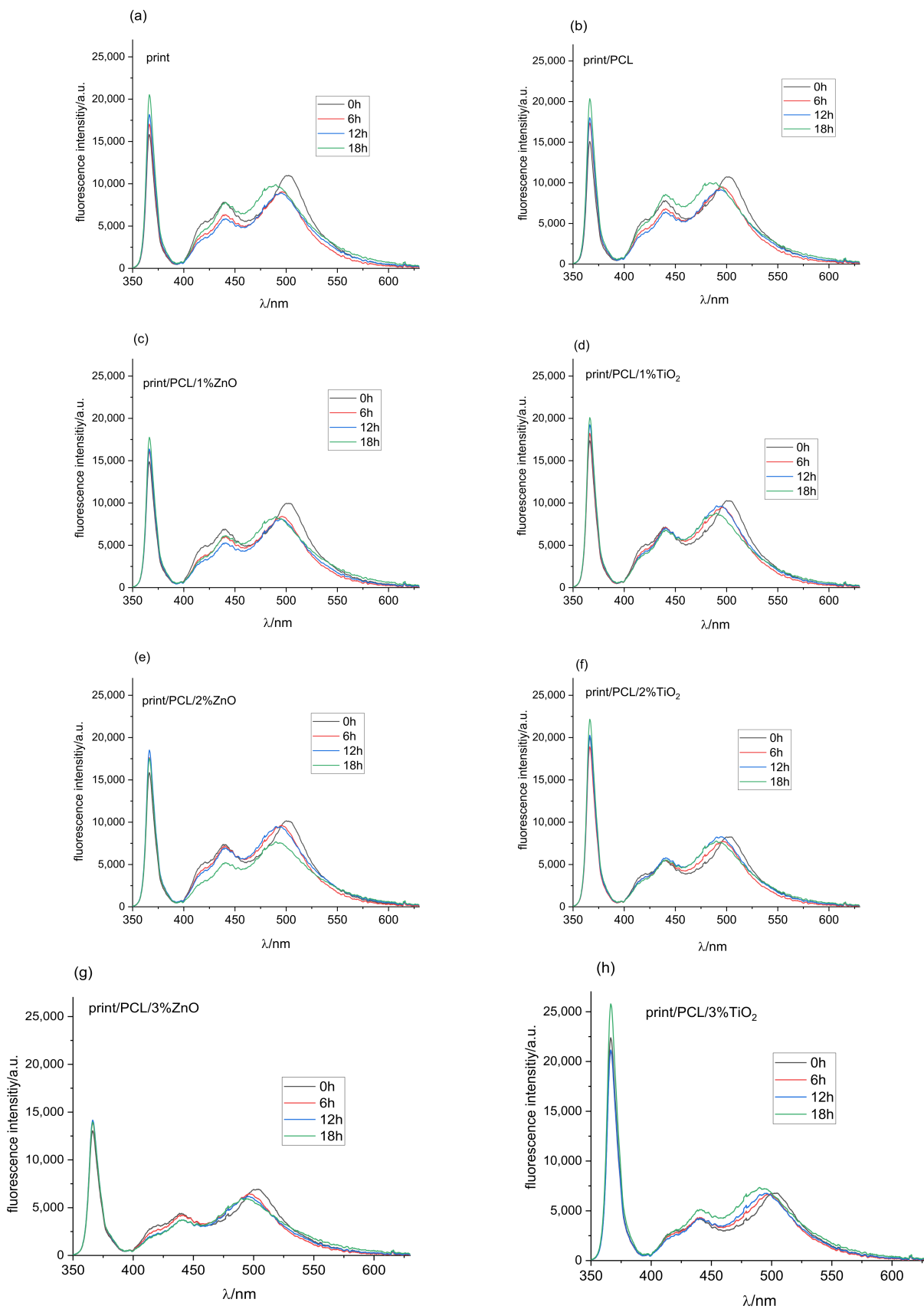
of absorbed excitation light at 365 nm for the unprinted paper, which decreased after its exposure to UV radiation, indicating the degradation of the optical whiteners.



**Figure 9.** Fluorescence intensity spectra of (a) unprinted paper before and after exposure to UV radiation, and (b) unprinted paper coated with neat PCL and nanomodified PCL coatings.

It is important to determine how the coverage of the substrate with different coatings affects the paper's fluorescence ability, i.e., a smaller amount of excitation light is available, causing less activation of the optical brighteners incorporated into the paper itself. The coating absorbs a certain amount of incident UV light, decreasing the amount of light accessible for activating optical brighteners in the paper itself. As a result, the fluorescence intensity of paper coated with PCL decreased by 55% compared to the untreated substrate (Figure 9b). The addition of different concentrations of  $\text{TiO}_2$  and  $\text{ZnO}$  nanoparticles into the PCL matrix further decreased the fluorescence intensity of the paper sample. Increasing the concentration of nanoparticles that strongly absorb in the spectral area in the wavelength of the exciting light affects the reduction in paper fluorescence. Since  $\text{ZnO}$  NPs used in the study strongly absorbed in the UV part of the spectrum from 200 to 374 nm (Figure 1), increasing its concentration in the PCL coating reduced the amount of incident excitation light, which reached the substrate to generate a fluorescent response. Accordingly, fluorescence intensity was the lowest for the paper coated with PCL coating modified with 3%  $\text{ZnO}$  (Figure 9b). This also confirmed that the initial colouration of the samples appeared to be darker when samples were coated with  $\text{ZnO}$  NPs due to the higher absorption rate and consequent lower reflection rate (Figures 1 and S1).

Once the characteristic fluorescence peaks of the substrate had been determined, the fluorescence spectroscopy of the prints could be measured and discussed. Fluorescence intensity spectra of all samples before their exposure to UV radiation followed by 6, 12, and 18 h exposure to UV radiation are shown in Figure 10a. The absorption range at the excitation wavelength of printed samples (Figure 10a) showed that the ratio of absorbed light was much lower than the absorbed intensity of the clear paper substrate (Figure 9a). Due to the absorption, scattering, and re-emission of components within the thermochromic ink, fluorescence intensity spectra were shifted towards higher wavelengths around 510 nm, while the peak at 440 nm corresponded to measurements obtained on the unprinted paper substrates.



**Figure 10.** Fluorescence intensity spectra of (a) uncoated TC print, (b) TC print coated with neat PCL, and nanomodified PCL coatings; (c) PCL/1% Zn, (d) PCL/1%Ti, (e) PCL/2% Zn, (f) PCL/2% Ti, (g) PCL/3% Zn, (h) PCL/3% Ti, before and after 6, 12, and 18 h exposure to UV radiation.

As the thermochromic inks used in the study were vegetable-oil-based, their fluorescent response was expected due to their composition of mainly chlorophylls, parinaric acid, and vitamin E [49]. Different oils show different exhibition peaks; sunflower oil exhibits fluorescence peaks in the 430 to 520 nm region [50], extra virgin olive oil between 500 and 720 nm [51,52], rapeseed oil with characteristic spectra from 300 to 500 and from 630 to 730 nm [49].

Exposure of the samples to UV radiation for 6 and 12 h (Figure 10a) resulted in a drop in fluorescence intensity and a shift of the peak from 510 to 500 nm. Further exposure degraded the ink, mostly the binder, of which vegetable oil is an integral part, leaving a higher ratio of the paper substrate available for the absorption of UV light, which was confirmed with the increase in fluorescence intensity corresponding the fluorescence spectra of paper substrates (Figure 9a).

Fluorescence intensity spectra of the print coated with PCL (Figure 10b) corresponded to the fluorescence intensity spectra of the print for unaged samples, and samples exposed to UV radiation for 6 and 12 h. After 18 h of exposure, fluorescence intensity increased in the area from 425 to 450 nm, indicating that PCL to some infinitesimal extent protected the paper even though it was not successful in protecting the print itself.

Increasing TiO<sub>2</sub> NPs in the PCL solution decreased the absorption of the fluorescence excitation light at 365 nm (Figure 10d,f,h). On the other hand, ZnO particles in the 1% and 2% concentrations did not influence absorption at the given wavelength (Figure 10c,e). The 3% of ZnO particles in the PCL polymer matrix increased absorption in the UV part of the spectrum (Figure 10g). The exposure of samples to UV radiation slightly reduced the absorption of light in the UV part of the spectrum for all examined samples. Comparing the results for ZnO and TiO<sub>2</sub> nanomodified coatings after 18 h hours of exposure to UV radiation showed that samples coated with 3% TiO<sub>2</sub> had a 43% higher level of fluorescence intensity in the excitation part of the spectrum.

The fluorescence response in the visible part of the spectrum showed that the 1% ZnO coatings show similar characteristics as those of the untreated samples after 6 and 12 h of exposure to UV radiation, while fluorescence peaks after 18 h showed much lower intensities (Figure 10c), and the main peaks were not completely shifted towards lower wavelengths, indicating the retention of binder fluorescence. This could similarly be confirmed for 2% ZnO nanomodified coatings, where a decrease in fluorescence intensity and a shift of peaks towards lower wavelengths were observed. Further UV radiation exposure only decreased intensity.

As expected, the 3% ZnO coating showed the lowest fluorescence intensity in the visible part of the spectrum (Figure 10g) since the amount of light absorption increased with the increasing concentration of ZnO nanoparticles. Exposure to UV radiation did not cause any major changes in the intensity and position of the fluorescent peaks.

The visible spectrum of samples coated with the PCL modified with 1% TiO<sub>2</sub> nanoparticles (Figure 10d) showed higher degradation of the peak around 500 nm, which had been moved towards the fluorescence peaks of OBAs in the paper after 6 h of exposure of the sample to UV radiation. After 12 and 18 h of exposure, fluorescence intensity spectra were almost identical, with an infinitesimal increase in fluorescence intensity in the region between 450 and 475 nm.

The 2% TiO<sub>2</sub> nanoparticle coating (Figure 10f) showed an identical fluorescence curve response in the visible part of the spectra as that of the 1% TiO<sub>2</sub> nanomodified coating, with the exception of a difference in fluorescence intensity, namely, it was equal in this case regardless of the exposure of samples to UV radiation.

The last of the examined samples, the TC print coated with 3% TiO<sub>2</sub>, showed an identical fluorescence response in the 400 to 450 nm region of the spectra as that of the untreated and exposed samples for the duration periods of 6 and 12 h, while a clear shift of the broad peak from 500 to 490 nm could be seen (Figure 10h). The sample exposed to 18 h of UV radiation showed slightly greater fluorescence intensity, indicating a further shift towards wavelengths corresponding to the OBAs in the paper.

Taking into account all the presented results, it could be concluded that the overall degradation of coated TC prints was the result of a combined effect due to the presented degradation mechanisms of paper, TC ink binder, neat PCL, and nanoparticles. The degradation of TC prints coated with nanomodified PCL coating by the action of UV radiation could be attributed to photochemical reactions arising from the absorption of UV radiation by light-absorbing groups present on the PCL backbone, and could mainly be expressed by Norrish reactions: photoionization (Norrish I) and chain scission (Norrish II) [45]. This mechanism was clearly presented by the FTIR spectroscopy, with the most notable changes occurring after 18 h of exposure to UV radiation. The main light-absorbing groups present on the PCL backbone and TC printing ink responsible for the initiation of photochemical reactions were carbonyl groups. SEM microscopy (Figure 6) indicated the photo-oxidation of the sample surface, while FTIR spectroscopy indicated changes in the amorphous part of the PCL structure, and changes occurring during cross-linking and chain scission (Figure 8). Fluorescence spectroscopy (Figure 10) confirmed the results of FTIR spectroscopy, the degradation of the carbonyl groups present in vegetable oil (ink binder), and the consequent degradation of the TC ink binder. The degradation of the TC microcapsules' polymer shell envelope probably occurred due to ink binder degradation, which in the end caused the degradation of a leuco-dye-developer complex inside the TC microcapsules, and the consequent degradation of colour. The degradation of the thermochromic effect by UV radiation was the greatest when the prints had been exposed for 18 h, with total destruction of the TC effect for the uncoated and TC print coated with neat PCL. The addition of NPs in the PCL solution improved the UV stability of the coated TC prints due to the absorption of a certain amount of incident UV radiation, which was clearly confirmed by fluorescence spectroscopy.

#### 4. Conclusions

Thermochromic printing inks in the function of smart materials have many application possibilities due to their simple communication with users and their attractiveness, which ultimately add value to the products. However, their limiting circumstance is poor stability against UV radiation, which limits their application. Despite this very well known fact, there is a lack of research related to the development of UV-protective coatings for TC prints. Therefore, the aim of this paper was to investigate the applicability of PCL nanocomposite coating to protect TC prints from UV degradation. Obtained results showed that, despite the higher band gap in comparison to that of TiO<sub>2</sub>, ZnO nanoparticles in a PCL matrix did not improve the UV stability of TC prints in higher proportion than that of TiO<sub>2</sub>. In addition, those results and results from NP UV absorbance determination indicated that all changes within the TC microcapsules and consequent influenced changes in TC print coloration were the result of UV radiation in wavelengths below 329 nm. Additionally, in this research, SEM micrographs showed that UV degradation caused the formation of voids, craters of nanomodified PCL coatings. Moreover, the addition of TiO<sub>2</sub> nanoparticles into the PCL matrix more effectively promoted the UV degradation of nanomodified PCL coating compared to in ZnO nanoparticles. UV irradiation caused changes in the IR spectrum of the PCL coating, which could be attributed to photodegradation, changes in PCL characteristic functional groups, and the absence of intermolecular interactions.

This paper proves that the use of fluorescence spectroscopy in the evaluation of UV absorption potential and of the degradation mechanisms of biodegradable polymer paper coatings is a promising tool. In addition, results of fluorescence spectroscopy indicate that the nanomodified PCL coating absorbed a certain amount of incident UV radiation and indicated the degradation of vegetable oil in the printing ink binder. Results indicate that changes occurring in the colouration of the prints could be described by colorimetric measurements and fluorescence spectroscopy, while FTIR spectroscopy only indicated the degradation mechanisms of the TC ink binder and nanomodified coating, but it could not indicate any degradation of the TC microcapsules. However, fluorescence spectroscopy could be used as an auxiliary tool to confirm FTIR spectroscopy results.

This research showed the possibility of using environmentally friendly nanomodified PCL coating to preserve the thermochromic effect of TC offset prints from the effects of UV radiation, and opens up the possibility of new research in this area. Future research will be focused on the optimization of TiO<sub>2</sub> weight concentrations in a PCL solution. Moreover, research shows the possibility of expanding applications of TC prints that were limited due to their poor resistance to UV light. For example, TC ink can be used in the development of smart packaging, but this application is limited due to its fast colour degradation when exposed to UV radiation. Nanomodified PCL coatings are a promising material in development and as mechanical protection of different paper-based packaging products. Thus, the combination of TC prints and PCL nanomodified coating is a promising structure in the development of smart packaging with extended applications.

**Supplementary Materials:** The following supporting information can be downloaded at <https://www.mdpi.com/article/10.3390/polym14071484/s1>. Figure S1: CIELAB lightness L\* of prepared samples before UV exposure in dependence on temperature at heating (-H) and cooling (-C); Figure S2: FTIR spectra of paper, TC print, and TC print coated with neat PCL coating, and nanomodified PCL coating.

**Author Contributions:** Conceptualization, M.V. and J.B.; methodology, M.V., R.K. and K.I.I.; software, J.B.; validation, J.B. and T.C.; formal analysis, J.B. and T.C.; investigation, M.V., R.K. and K.I.I.; resources, M.V. and K.I.I.; data curation, M.V., R.K. and K.I.I.; writing—original draft preparation, M.V., R.K. and K.I.I.; writing—review and editing, J.B. and T.C.; visualization, M.V., R.K., K.I.I., J.B. and T.C.; supervision, M.V.; project administration, M.V., R.K. and K.I.I.; funding acquisition, M.V. and K.I.I. All authors have read and agreed to the published version of the manuscript.

**Funding:** This research received no external funding.

**Institutional Review Board Statement:** Not applicable.

**Informed Consent Statement:** Not applicable.

**Data Availability Statement:** Not applicable.

**Conflicts of Interest:** The authors declare no conflict of interest.

## References

- Kulčar, R.; Friskovec, M.; Hauptman, N.; Vesel, A.; Klanjšek Gunde, M. Colorimetric properties of reversible thermochromic printing inks. *Dye. Pigment.* **2010**, *86*, 271–277. [[CrossRef](#)]
- Seeboth, A.; Lotzsch, D. *Thermochromic and Thermotropic Materials*; CRC Press by Taylor & Francis Group: Boca Raton, FL, USA, 2013.
- Rožić, M.; Vukoje, M.; Kapović, D.; Marošević, L. Solvents interactions with thermochromic print. *J. Graph. Eng. Des.* **2017**, *8*, 19–25. [[CrossRef](#)]
- Friškovec, M.; Kulčar, R.; Klanjšek Gunde, M. Light fastness and high-temperature stability of thermochromic printing inks. *Color. Technol.* **2013**, *129*, 214–222. [[CrossRef](#)]
- Rožić, M.; Kulčar, R.; Jamnicki, S.; Lozo, B.; Gregor-Svetec, D. UV stability of thermochromic ink on paper containing clinoptilolite tuff as a filler. *Cellul. Chem. Technol.* **2015**, *49*, 693–699.
- Stržičić Jakovljević, M.; Kulčar, R.; Friškovec, M.; Lozo, B.; Klanjšek Gunde, M. Light fastness of liquid crystal-based thermochromic printing inks. *Dye. Pigment.* **2020**, *180*, 108482. [[CrossRef](#)]
- Oda, H. New developments in the stabilization of leuco dyes: Effect of UV absorbers containing an amphoteric counter-ion moiety on the light fastness of color formers. *Dye. Pigment.* **2005**, *66*, 103–108. [[CrossRef](#)]
- Oda, H. Photostabilization of organic thermochromic pigments: Action of benzotriazole type UV absorbers bearing an amphoteric counter-ion moiety on the light fastness of color formers. *Dye. Pigment.* **2008**, *76*, 270–276. [[CrossRef](#)]
- Oda, H. Photostabilization of organic thermochromic pigments. Part 2: Effect of hydroxyarylbenzotriazoles containing an amphoteric counter-ion moiety on the light fastness of color formers. *Dye. Pigment.* **2008**, *76*, 400–405. [[CrossRef](#)]
- Rožić, M.; Vukoje, M. Photo-oxidation stability of microcapsules in thermochromic prints. *ACTA Graph. J. Print. Sci. Graph. Commun.* **2018**, *28*, 109. [[CrossRef](#)]
- Kulčar, R.; Vukoje, M.; Krajnović, I.; Rožić, M. Influence of recycled fibres in paper on the UV stability of thermochromic prints. In *Proceedings of the 10th International Symposium GRID 2020, Novi Sad, Serbia, 12–14 November 2020*; Dedijer, S., Ed.; University of Novi Sad Faculty of Technical Sciences Department of Graphic Engineering and Design: Novi Sad, Serbia; pp. 161–168. 2020.

12. Yousif, E.; Haddad, R. Photodegradation and photostabilization of polymers, especially polystyrene: Review. *Springerplus* **2013**, *2*, 398. [[CrossRef](#)]
13. Calvo, M.E.; Castro Smirnov, J.R.; Míguez, H. Novel approaches to flexible visible transparent hybrid films for ultraviolet protection. *J. Polym. Sci. Part B Polym. Phys.* **2012**, *50*, 945–956. [[CrossRef](#)]
14. Rabani, I.; Lee, S.H.; Kim, H.S.; Yoo, J.; Hussain, S.; Maqbool, T.; Seo, Y.S. Engineering-safer-by design ZnO nanoparticles incorporated cellulose nanofiber hybrid for high UV protection and low photocatalytic activity with mechanism. *J. Environ. Chem. Eng.* **2021**, *9*, 105845. [[CrossRef](#)]
15. Wang, H.; Wang, Y.; Fu, F.; Qian, Y.; Xiao, Y.; Yang, D.; Qiu, X. Controlled preparation of lignin/titanium dioxide hybrid composite particles with excellent UV aging resistance and its high value application. *Int. J. Biol. Macromol.* **2020**, *150*, 371–379. [[CrossRef](#)] [[PubMed](#)]
16. Yang, Z.; Zhai, X.; Zou, X.; Shi, J.; Huang, X.; Li, Z.; Gong, Y.; Holmes, M.; Povey, M.; Xiao, J. Bilayer pH-sensitive colorimetric films with light-blocking ability and electrochemical writing property: Application in monitoring crucial spoilage in smart packaging. *Food Chem.* **2021**, *336*, 127634. [[CrossRef](#)]
17. Grüneberger, F.; Künniger, T.; Huch, A.; Zimmermann, T.; Arnold, M. Nanofibrillated cellulose in wood coatings: Dispersion and stabilization of ZnO as UV absorber. *Prog. Org. Coatings* **2015**, *87*, 112–121. [[CrossRef](#)]
18. Li, Y.; Jiang, Y.; Liu, F.; Ren, F.; Zhao, G.; Leng, X. Fabrication and characterization of TiO<sub>2</sub>/whey protein isolate nanocomposite film. *Food Hydrocoll.* **2011**, *25*, 1098–1104. [[CrossRef](#)]
19. Shao, J.; Shen, H.; Gao, K.; Huo, X.; Saddique, J.; Wang, X.; Meng, W. UV- and NIR-blocking properties of ZnO/ATO bilayer films prepared by RF magnetron sputtering. *Opt. Mater.* **2021**, *118*, 111287. [[CrossRef](#)]
20. Hudika, T.; Cigula, T.; Žličarić, M.; Stričić Jakovljević, M. PCL-TiO<sub>2</sub> nanocomposite to improve ageing of offset prints. In *Proceedings of the 10th International Symposium GRID 2020, Novi Sad, Serbia, 12–14 November 2020*; Dedijer, S., Ed.; University of Novi Sad Faculty of Technical Sciences Department of Graphic Engineering and Design: Novi Sad, Serbia, 2020; pp. 119–129.
21. Cigula, T.; Hudika, T.; Katana, M.; Golik Krizmanić, M.; Tomašegović, T. The influence of PCL-ZnO coating composition on coated offset cardboard prints. In *Proceedings of the 10th International Symposium GRID 2020, Novi Sad, Serbia, 12–14 November 2020*; Dedijer, S., Ed.; University of Novi Sad Faculty of Technical Sciences Department of Graphic Engineering and Design: Novi Sad, Serbia, 2020; pp. 101–108.
22. Bota, J.; Brozović, M.; Hrnjak-Murčić, Z. Influence of silica nanoparticles in PCL overprint coating on the color change of offset print. In *Proceedings of the 7th International Symposium on Graphic Engineering and Design GRID, Novi Sad, Serbia, 13–14 November 2020*; Novaković, D., Ed.; Faculty of Technical Sciences, Department of Graphic Engineering and Design: Novi Sad, Serbia, 2020; pp. 225–232.
23. Bota, J.; Brozović, M.; Hrnjak Murčić, Z. The effect of film thickness and concentration of SiO<sub>2</sub> nanoparticles in PCL coatings on color change of tonal value increase. *Acta Graph.* **2016**, *27*, 15–22.
24. Bota, J.; Kratofil Krehula, L.; Katančić, Z.; Brozović, M.; Hrnjak-Murčić, Z. Surface characteristics and enhancement of water vapour properties of paperboard coated with polycaprolactone nanocomposites. *J. Adhes. Sci. Technol.* **2017**, *31*, 466–486. [[CrossRef](#)]
25. Cigula, T.; Hudika, T.; Tomasegovic, T. Lightfastness, surface and interfacial properties of colour-printed paper substrates coated with PCL/ZnO and PCL/TiO<sub>2</sub> nanocomposites. *Surf. Interfaces* **2021**, *27*, 101522. [[CrossRef](#)]
26. Delgado-Lima, A.; Botelho, G.; Silva, M.M.; Machado, A.V. Durability of PCL Nanocomposites Under Different Environments. *J. Polym. Environ.* **2013**, *21*, 710–717. [[CrossRef](#)]
27. França, D.C.; Morais, D.D.; Bezerra, E.B.; Araújo, E.M.; Wellen, R.M.R. Photodegradation Mechanisms on Poly( $\epsilon$ -caprolactone) (PCL). *Mater. Res.* **2018**, *21*, 1–8. [[CrossRef](#)]
28. Tsuji, H.; Echizen, Y.; Nishimura, Y. Photodegradation of biodegradable polyesters: A comprehensive study on poly(L-lactide) and poly( $\epsilon$ -caprolactone). *Polym. Degrad. Stab.* **2006**, *91*, 1128–1137. [[CrossRef](#)]
29. CIE Central Bureau. *Colorimetry*, 3rd ed.; CIE Central Bureau: Vienna, Austria, 2004.
30. Shaw, P.S.; Li, Z. On the fluorescence from integrating spheres. *Appl. Opt.* **2008**, *47*, 3962–3967. [[CrossRef](#)]
31. Zwinkels, J.C. Errors and accuracies in integrating sphere measurements of diffuse reflectance and transmittance. In *Proceedings of the Non-Nuclear Energies Workshop on Optical Property Measurement Techniques, Ispra, Italy, 27–29 October 1988*.
32. Zwinkels, J.C.; DeRose, P.C.; Leland, J.E. *Spectral Fluorescence Measurements*; Elsevier Inc.: Amsterdam, The Netherlands, 2014.
33. Vukoje, M.; Itrić Ivanda, K.; Kulčar, R.; Marošević Dolovski, A. Spectroscopic Stability Studies of Pressure Sensitive Labels Facestock Made from Recycled Post-Consumer Waste and Agro-Industrial By-Products. *Forests* **2021**, *12*, 1703. [[CrossRef](#)]
34. Reinosa, J.J.; Leret, P.; Álvarez-Docio, C.M.; Del Campo, A.; Fernández, J.F. Enhancement of UV absorption behavior in ZnO-TiO<sub>2</sub> composites. *Bol. la Soc. Esp. Ceram. y Vidr.* **2016**, *55*, 55–62. [[CrossRef](#)]
35. Dailliez, F.; Hébert, M.; Blayo, A.; Chagas, L.; Fournel, T. Impact of a Transparent Coating on the Reflectance of a Line Halftone Pattern. *Coatings* **2021**, *11*, 1465. [[CrossRef](#)]
36. Proniewicz, L.M.; Paluszkiwicz, C.; Weselucha-Birczyńska, A.; Barański, A.; Dutka, D. FT-IR and FT-Raman study of hydrothermally degraded groundwood containing paper. *J. Mol. Struct.* **2002**, *614*, 345–353. [[CrossRef](#)]
37. Itrić, K.; Džimbeg-malčić, V.; Modrić, D. Optical deterioration of coated wrapping paper. *Acta Graph. J. Print. Sci. Graph. Commun.* **2015**, *26*, 5–10.



38. Vukoje, M.; Miljanić, S.; Hrenović, J.; Rožić, M. Thermochromic ink–paper interactions and their role in biodegradation of UV curable prints. *Cellulose* **2018**, *25*, 6121–6138. [[CrossRef](#)]
39. Vukoje, M.; Rožić, M.; Miljanić, S.; Pasanec Preprotić, S. Biodegradation of thermochromic offset prints. *Nord. Pulp Pap. Res. J.* **2017**, *32*, 289–298. [[CrossRef](#)]
40. Gómez, N.; Molleda, C.; Quintana, E.; Carbajo, J.M.; Rodríguez, A.; Villar, J.C. Attenuated Total Reflection Fourier Transform Infrared Spectroscopy (ATR FT-IR) Applied to Study the Distribution of Ink Components in Printed Newspapers. *Appl. Spectrosc.* **2016**, *70*, 1537–1545. [[CrossRef](#)] [[PubMed](#)]
41. Lojewski, T.; Zieba, K.; Knapik, A.; Bagniuk, J.; Lubanska, A.; Lojewska, J. Evaluating paper degradation progress. Cross-linking between chromatographic, spectroscopic and chemical results. *Appl. Phys. A Mater. Sci. Process.* **2010**, *100*, 809–821. [[CrossRef](#)]
42. Bajsić, E.G.; Mijović, B.; Penava, N.V.; Grgurić, T.H.; Slouf, M.; Zdraveva, E. The effect of UV irradiation on the electrospun PCL/TiO<sub>2</sub> composites fibers. *J. Appl. Polym. Sci.* **2016**, *133*, 1–9. [[CrossRef](#)]
43. Elzein, T.; Nasser-Eddine, M.; Delaite, C.; Bistac, S.; Dumas, P. FTIR study of polycaprolactone chain organization at interfaces. *J. Colloid Interface Sci.* **2004**, *273*, 381–387. [[CrossRef](#)]
44. Bashal, A.H.; Riyadh, S.M.; Alharbi, W.; Alharbi, K.H.; Farghaly, T.A.; Khalil, K.D. Bio-Based (Chitosan-ZnO) Nanocomposite: Synthesis, Characterization, and Its Use as Recyclable, Ecofriendly Biocatalyst for Synthesis of Thiazoles Tethered Azo Groups. *Polymers* **2022**, *14*, 386. [[CrossRef](#)]
45. Niaounakis, M. *Biopolymers: Applications and Trends*; Elsevier: Amsterdam, The Netherlands, 2015.
46. Itagaki, H. *Fluorescence Spectroscopy*; Academic Press: Cambridge, MA, USA, 2012.
47. Coppel, L.G.; Andersson, M.; Edstrom, P.; Kinnunen, J. Limitations in the efficiency of fluorescent whitening agents in uncoated paper. *Nord. Pulp Pap. Res. J.* **2011**, *26*, 319–328. [[CrossRef](#)]
48. Pauler, N. *Paper Optics*; AB Lorentzen & Wettre: Mohista, Sweden, 2012.
49. Wolfbeis, O.S.; Leiner, M. Charakterisierung von Speiseölen mit Hilfe der Fluoreszenztopographie-(Fluorimetrische analyse, X)1. *Mikrochim. Acta* **1984**, *82*, 221–233. [[CrossRef](#)]
50. Nikolova, K.; Zlatanov, M.; Eftimov, T.; Brabant, D.; Yosifova, S.; Halil, E.; Antova, G.; Angelova, M. Fluorescence spectra from vegetable oils using violet and blue Ld/Led excitation and an optical fiber spectrometer. *Int. J. Food Prop.* **2014**, *17*, 1211–1223. [[CrossRef](#)]
51. Zandomenighi, M.; Carbonaro, L.; Caffarata, C. Fluorescence of vegetable oils: Olive oils. *J. Agric. Food Chem.* **2005**, *53*, 759–766. [[CrossRef](#)]
52. Guimet, F.; Ferré, J.; Boqué, R. Rapid detection of olive-pomace oil adulteration in extra virgin olive oils from the protected denomination of origin “Siurana” using excitation-emission fluorescence spectroscopy and three-way methods of analysis. *Anal. Chim. Acta* **2005**, *544*, 143–152. [[CrossRef](#)]

## Article

# Evaluation of Biodegradabilities of Biosynthetic Polyhydroxyalkanoates in Thailand Seawater and Toxicity Assessment of Environmental Safety Levels

Nuttapol Tanadchangsang<sup>1,\*</sup> and Anchana Pattanasupong<sup>2</sup>

<sup>1</sup> College of Biomedical Engineering, Rangsit University, 52/347 Phahonyothin Road, Lak-Hok, Pathumthani 12000, Thailand

<sup>2</sup> Material Biodegradation Testing Laboratory, Material Properties Analysis and Development Centre, Thailand Institute of Scientific and Technological Research (TISTR), 35 Technopolis, Tambon Khlong Ha, Amphoe Khlong Luang, Pathumthani 12120, Thailand; anchana@tistr.or.th

\* Correspondence: nuttapol.t@rsu.ac.th; Tel.: +66-(0)2-997-2200 (ext. 1428); Fax: +66-(0)2-997-2200 (ext. 1408)

**Abstract:** Every year, thousands of tons of non-biodegradable plastic products are dumped into marine environments in Thailand's territorial seawater, impacting various marine animals. Recently, there has been a surge in interest in biodegradable plastics as a solution for aquatic environments. However, in Thailand's coastal waters, no suitable biodegradable plastic has been used as ocean-biodegradable packaging. Among them, polyhydroxyalkanoates (PHAs) have excellent biodegradability even in seawater, which is the desired property for packaging applications in tourist places such as plastic bags and bottles. In this report, we assess the environment's safety and study the biodegradation in Thailand seawater of polyhydroxybutyrate (PHB) and PHA copolymer (PHBVV) that were successfully synthesized by bacteria with similar molecular weight. The two types of extracted PHA samples were preliminary biodegradability tested in the marine environment compared with cellulose and polyethylene. Within 28 days, PHB and PHBVV could be biodegraded in both natural and synthetic seawater with 61.2 and 96.5%, respectively. Furthermore, we assessed residual toxicity after biodegradation for environmental safety using seawater samples containing residual digested compounds and the standard guide for acute toxicity tests. It was discovered that marine water mites (*Artemia franciscana*) have 100 percent viability, indicating that they are non-toxic to the marine environment.

**Citation:** Tanadchangsang, N.; Pattanasupong, A. Evaluation of Biodegradabilities of Biosynthetic Polyhydroxyalkanoates in Thailand Seawater and Toxicity Assessment of Environmental Safety Levels. *Polymers* **2022**, *14*, 428. <https://doi.org/10.3390/polym14030428>

Academic Editors: José Miguel Ferri, Vicent Fombuena Borràs and Miguel Fernando Aldás Carrasco

Received: 26 November 2021

Accepted: 17 January 2022

Published: 21 January 2022

**Publisher's Note:** MDPI stays neutral with regard to jurisdictional claims in published maps and institutional affiliations.



**Copyright:** © 2022 by the authors. Licensee MDPI, Basel, Switzerland. This article is an open access article distributed under the terms and conditions of the Creative Commons Attribution (CC BY) license (<https://creativecommons.org/licenses/by/4.0/>).

**Keywords:** biodegradation; biosynthesized polyesters; polyhydroxyalkanoates; seawater; residual toxicity assessment

## 1. Introduction

According to the data of the garbage situation in Thailand, Thai people have created 1.15 kg/person/day, equivalent to 76,164 tons/day, giving rise to the amount of plastic waste contaminated into the sea up to 32,600 tons/year [1]. Most of the marine waste, up to 80%, comes from land-based activities such as communities, dumpsites on the harbor side, and beach tourism. The remaining 20 percent comes from marine activities such as sea transportation, fishery, and marine tourism. Plastic waste in the sea directly affects marine ecosystems, such as coral reefs, seagrass, and mangrove forests. The animals are killed either by choking on floating plastic items or becoming entangled in plastic debris. Moreover, it also affects tourism from deteriorated scenery and causes health problems by the contaminated microplastics from which plastics can be broken down into smaller sizes by sunlight (photodegradation). These give rise to some toxic chemicals dissolving into the seawater, while some plastics can still absorb toxic substances in seawater into the food chain. When aquatic animals eat, they can pass it on to the consumers in a higher order. As a result of this problem, biodegradable or compostable bioplastics are

an important alternative to Thailand's marine ecosystem development. Nowadays, many kinds of bioplastics are extensively studied and employed, such as polyhydroxyalkanoates (PHAs) [2], which we investigated in this research. Polyhydroxybutyrate (PHB) is a polymer short-chain aliphatic polyester belonging to the group of PHAs and can be produced by accumulating carbon compounds in microbial cells that synthesize the biopolyesters such as *Ralstonia eutropha* [3,4]. Under some situations, such as a scarcity of nitrogen, phosphorus, sulfur, potassium, or oxygen, the bacteria produce more PHB [5]. Besides, PHB can also be produced by microalgae (cyanobacteria) [6] and transgenic plants [7]. PHB has received much attention in the plastic industry due to the chemical and physical properties that are similar to those of synthetic polymers, especially polypropylene [8,9]. It can be used to generate various products in the form of packaging and medical equipment [10,11]. In the initial research, glucose, fructose, and sucrose are used as a source of carbon for microbes to produce PHB, which has a higher production cost than the production of polymers from petrochemicals [12]. Currently, there has been developed technology using carbon sources from waste-stream glycerol or co-substrates of glycerol and levulinic acid (LA), which are inexpensive for PHA production by bacteria [13]. Furthermore, microorganisms can use LA to create PHA terpolyester consisting of 3-hydroxybutyrate (3HB), 3-hydroxyvalerate (3HV) and 4-hydroxyvalerate (4HV) monomers that are P(3HB-co-3HV-co-4HV) or PHBVV [14].

This report evaluated the preliminary biodegradation and toxicity of PHB and PHBVV bioplastics in Thailand seawater samples using different methods to prepare both types of polymer samples in similar molecular sizes. Previous studies measured weight loss, oxygen consumption as biological oxygen demand (BOD), or CO<sub>2</sub> evolution to assess the biodegradability of possibly biodegradable polymers in seawater [15,16]. The samples in this study were tested in natural and synthetic seawater modified from standard methods by analyzing evolved carbon dioxide from biodegradable activity in seawater and determining aerobic biodegradation of plastic materials in the marine environment. Additionally, an initial assessment of residual toxicity levels of the seawater after PHAs biodegradation test using the marine crustacean *Artemia franciscana* was also conducted to investigate the possibility of using PHAs as packaging items and marine equipment that do not become harmful to the marine and coastal environments.

## 2. Materials and Methods

### 2.1. Biosynthesis of Microbial PHB and PHBVV Polyesters

A laboratory mutant strain of *Ralstonia eutropha* (ATCC 17699) was used in this study. PHB and PHBVV were produced in a glycerol-rich and/or levulinic acid (LA) environment, respectively. Initial culture media for PHB and PHBVV synthesis is a mineral solution (MS) that combines glycerol 20 g/L, NaH<sub>2</sub>PO<sub>4</sub> 1.2 g/L, (NH<sub>4</sub>)<sub>2</sub>SO<sub>4</sub> 2 g/L, MgSO<sub>4</sub>·7H<sub>2</sub>O 0.5 g/L, K<sub>2</sub>HPO<sub>4</sub> 7.34 g/L, and trace element 1 mL/l (consisting of 700 μM Fe(NH<sub>4</sub>)SO<sub>4</sub>, 17 μM ZnSO<sub>4</sub>·7H<sub>2</sub>O, 25 μM MnCl<sub>2</sub>·4H<sub>2</sub>O, 8 μM CuSO<sub>4</sub>·5H<sub>2</sub>O, 7.2 μM NaB<sub>4</sub>O<sub>7</sub>·10H<sub>2</sub>O, and 8.3 μM NaMoO<sub>4</sub>·2H<sub>2</sub>O). The *Ralstonia eutropha* was stimulated to produce PHB and PHBVV polyesters by enrichment techniques in subculture five times to find an adaptable PHA-producing cell. Pre-cultivation of *Ralstonia eutropha* cells was performed in 5 mL nutrient broth and 50% glucose 0.05 mL with 50% glycerol 0.05 mL for 24 h. Then the cells were transferred into 50 mL MS containing 20 g/L of glycerol and incubate at 30 °C for 48 h with a 200-rpm rotary incubating shaker.

A 200 mL seed flask culture was inoculated into a bioreactor. Fermentation is carried out in a 5 L Bioreactor (MDFT-N-5L/B.E.Marubishi/Thailand) containing the 2.5 L mineral solution described above, with a culture period of 62 hours. The temperature, pH, and dissolved oxygen probes monitored and controlled the fermentation. The initial OD of the wavelength of 620 nm is approximately 1.4–1.6 with culture conditions at a temperature of 30 °C, pH 6.8, which is controlled by the pH-stat system with a pH and DO controller (Mettler Toledo/Switzerland). Agitation speeds were 200 rpm or above to control the dissolved oxygen at 10% of air saturation.

For PHB biosynthesis as described previously [17], the fermentation is continuous beginning with 2.5 L of MS medium and 20 g/L of glycerol at a C/N ratio of 5. After the cell dry weight reaches the desired level (approximately 5 g/L), a glycerol solution is added using a peristaltic pump at a speed of 0.1 mL/min to allow the system to enter the growth phase. The initial pH is controlled by adding 15% ammonia solution. When the cell dry weight reaches the desired state (the value of 80 at OD<sub>600</sub>), it is adjusted to the PHA accumulation phase, which the pH control from ammonia will be replaced by a 5N NaOH solution. Then, the feed rate of the glycerol carbon solution was adjusted to 0.2 mL/min to start the nitrogen limiting and PHB accumulation conditions.

For PHBVV biosynthesis as previously described [14], the fed-batch fermentation began with 2.5 L of the mineral solution containing 20 g/L of glycerol and an initial C/N ratio of 5. After the cell dry weight reached the desired level (5 g/L), a 750 g/L glycerol solution was added via a pump to keep the residual glycerol concentration above 10 g/L. To maintain a C/N ratio of about 5, a solution of 15% ammonia water was added to the culture for initial pH control and nitrogen feeding. When the cell dry weight reached the desired level (80 at OD<sub>600</sub>) and no additional nitrogen was required, the ammonia nitrogen solution and the glycerol solution were replaced with a NaOH/KOH (5M/5M) solution and a glycerol:levulinate solution (7:3 ratio) to initiate the nitrogen limitation condition for PHBVV copolymer accumulation.

Aliquots of 10–15 mL culture medium were collected for analysis of OD<sub>600</sub> and cell dry weight. The fermentation was stopped when the OD<sub>600</sub> started to decrease. At 62 h of cultivation, the cells were harvested, centrifuged, lyophilized, and used to determine the dry cell weight and PHA content.

## 2.2. Extraction and Characterization of PHAs

For PHBVV extraction, the polymer that accumulated in cells was extracted with chloroform (10 mL chloroform/1 g dry cells) for at least 48 h at 60 °C and purified by two rounds of precipitation with cold methanol. The extracted PHBVV sample was further aged in a vacuum at 50 °C for at least one week to reach equilibrium crystallinity prior to further analysis. Whereas, for PHB purification, the accumulated PHB polymer in bacteria was extracted by selective dissolution of cell mass as previously reported [18]. A predetermined amount of PHB-containing cell slurry was acidified with a sulfuric acid solution (2M) and sealed in glass tubes for 1–2 h, and the solution pH was adjusted to 10 with 5N NaOH. After centrifugation at 5000 g for 15 min, the pellets were washed with an equal volume of water. The washed pellets were then re-suspended in a bleaching solution for 1–2 h. White wet PHB pellets were collected by centrifugation at 5000 g for 20 minutes, rinsed with an equal volume of water, and oven dried.

For gas chromatography quantification of PHAs, 50 mg of lyophilized cells were mixed with 2 mL chloroform and 2 mL of 3 percent H<sub>2</sub>SO<sub>4</sub> (*v/v*) in methanol, supplemented with 10 mg/mL benzoic acid as the internal standard, and then heated at 100 °C for 4 hours with mixing every 30 minutes. After that, the tube containing the mixture was placed at room temperature and allowed to cool overnight. The tube was then filled with 2 mL of distilled water, vortexed vigorously for 4 minutes, and left to stand overnight. The chloroform layer was used to determine PHA in milligrams by comparing it to the standard curve obtained from gas chromatography data analysis, which was performed on a gas chromatography instrument (Agilent technologies 7890A). In addition, the percentage of PHA content per dry cell weight (% *w/w*) was calculated as previously described [19].

To measure the molecular weight of PHAs, gel permeation chromatography (GPC) analyses were carried out on Waters 2414 refractive index (RI) detector, equipped with Styragel HR5E 7.8 × 300 mm column (molecular weight resolving range = 2000 – 4,000,000). Samples dissolved in hot chloroform were eluted with chloroform at a flow rate of 1.0 mL/min at 40 °C and calibrated with polystyrene standards.

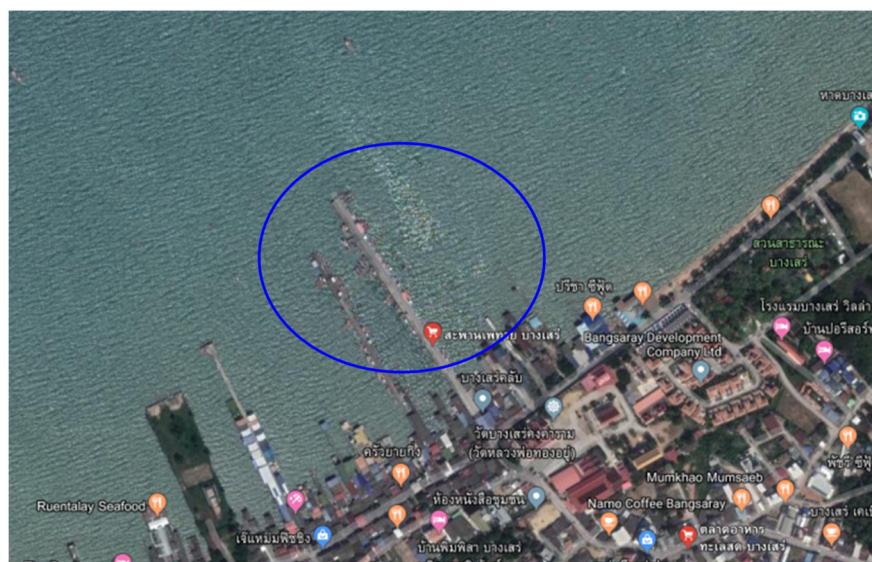
The PHA polymer was further characterized by using nuclear magnetic resonance (NMR). PHA samples were dissolved in CDCl<sub>3</sub> (25 mg/mL) via gentle mixing and heating,

and analyzed with  $^1\text{H}$  spectroscopy (Varian Unity Inova 500 MHz) to find the monomer composition and chemical structure information.

### 2.3. Preliminary Biodegradation Test

The preliminary biodegradation method is performed for biodegradability screening of materials compared with reference material by measurement carbon dioxide ( $\text{CO}_2$ ) accumulation from the microbial degradation activities in both natural and synthetic seawater with sediment under laboratory scale test. The result is designed to percentage of biodegradation that calculated from conversion of carbon in the reference or test materials to amount of cumulative carbon dioxide. As a result, this method was carried out using modified versions of ISO 19679:2016 [20], which specified a test method for determining the degree and rate of aerobic biodegradation of plastic materials when settled on sandy marine sediment, and ASTM D6691-17 [21], which was used to measure the degree and rate of aerobic biodegradation of plastic materials exposed to a pre-grown population of at least ten aerobic marine microorganisms of recognized genera or the indigenous population found in natural seawater.

The preliminary biodegradation of PHB and PHBVV bioplastic samples was estimated in both natural and synthetic seawater with sediment by measuring the amount of accumulated carbon dioxide generated by the degradation activity of the samples within a group of effective bacteria isolated from the coast of Thailand. The bacterial consortium is composed of *Bacillus marisflavi* (TISTR 2158), *Bacillus safensis* (TISTR 2163), *Bacillus subtilis* (TISTR 2173), *Bacillus methylotrophicus* (TISTR 2193), *Pseudomonas* spp., and *Enterobacter* spp. The natural seawater sample was collected at the Phethai Bridge, Bang-Sare Subdistrict, Sattahip District, Chonburi Province, Thailand as shown in Figure 1, and the characteristics of the collected natural seawater are listed in Table 1. In parallel, the reference material that is known to biodegrade (as chromatography-grade cellulose) must be included in each test run to check the activity of the bacterial consortium. Synthetic seawater was made according to ASTM D6691 (2017) standard [22] by dissolving the following substances in 1000 mL of distilled water: 2 g  $\text{NH}_4\text{Cl}$ , 17.5 g synthetic sea salt, 2 g  $\text{MgSO}_4 \cdot 7\text{H}_2\text{O}$ , 0.5 g  $\text{KNO}_3$  and 0.1 g  $\text{K}_2\text{HPO}_4 \cdot 3\text{H}_2\text{O}$ , and subsequently autoclaved for sterilization.





**Figure 1.** Map showing the coordinate of the seawater sampling point at Phethai bridge, Bang-Sare subdistrict, Sattahip district, Chonburi province, Thailand.

**Table 1.** Physical and chemical properties of natural seawater.

Parameters	Analysis Results
1. Temperature, °C	30.9
2. Salinity, ppt	34.0
3. pH	8.13
4. Dissolved oxygen, mg/L	6.51

For the preparation of the biodegradation test, the PHA test samples, or positive or negative references as shown in Table 2, the test size not over 1 mm, were mixed in the amount of 1% *w/v* with natural or synthetic seawater with a total bacterial count of 5–6 log CFU per ml. The samples were incubated in a closed condition at a temperature of  $30 \pm 2$  °C. The amount of carbon dioxide (CO<sub>2</sub>) that occurs in the system from the activity of microbes was measured throughout the 28 test days in 3 repetitions per sample test. The samples were tested against positive reference and negative reference samples in closed conditions under temperature control conditions of  $30 \pm 2$  °C at the laboratory, as shown in Table 2.

**Table 2.** Sample details employed for the biodegradation test in natural and synthetic seawater.

No.	Sample Test	Sample Code	Sample Details
1	ControlSample	Control	Natural seawater or Synthetic seawater
2	Positive reference sample	R+	Chromatography-grade cellulose
3	Negative reference sample	R–	Polyethylene
4	Sample 1	PHB	
5	Sample 2	PHBVV	

The biodegradability (% Biodegradation) of PHA polyester samples was calculated by subtracting the cumulative amount of carbon dioxide of the control blank from that of the test sample and by dividing the value by the theoretical amount of carbon dioxide (ThCO<sub>2</sub>) of the test sample as shown in the following equation:

$$\% \text{ Biodegradation} = \frac{\text{CO}_2 (\text{test}) - \text{CO}_2 (\text{Control})}{\text{ThCO}_2} \times 100 \quad (1)$$

It is noted that the total organic carbon (TOC) values of the PHB and PHBVV samples are 54.26 and 53.91 g/g, respectively.

#### 2.4. Acute Toxicity Tests Using Rotifers

The seawater solution samples of PHB and PHBVV biopolymers that have examined initial biodegradation tests in natural and synthetic seawater were subsequently assessed for the environmental safety levels by the ARTOXKIT M test set following the standard guide for acute toxicity test with the *Rotifer Brachionus* (ASTM E1440-91) by seawater mites (*Artemia franciscana*) as shown in Figure 2. The procedural details of the test are described in Snell et al. (1991), and the standardized ASTM protocol [23]. The rotifer 24-h acute toxicity test was performed as a convenient monitor for screening the most effective material according to the standard method.



**Figure 2.** Optical micrographs of seawater mites (*Artemia franciscana*) used in this study.

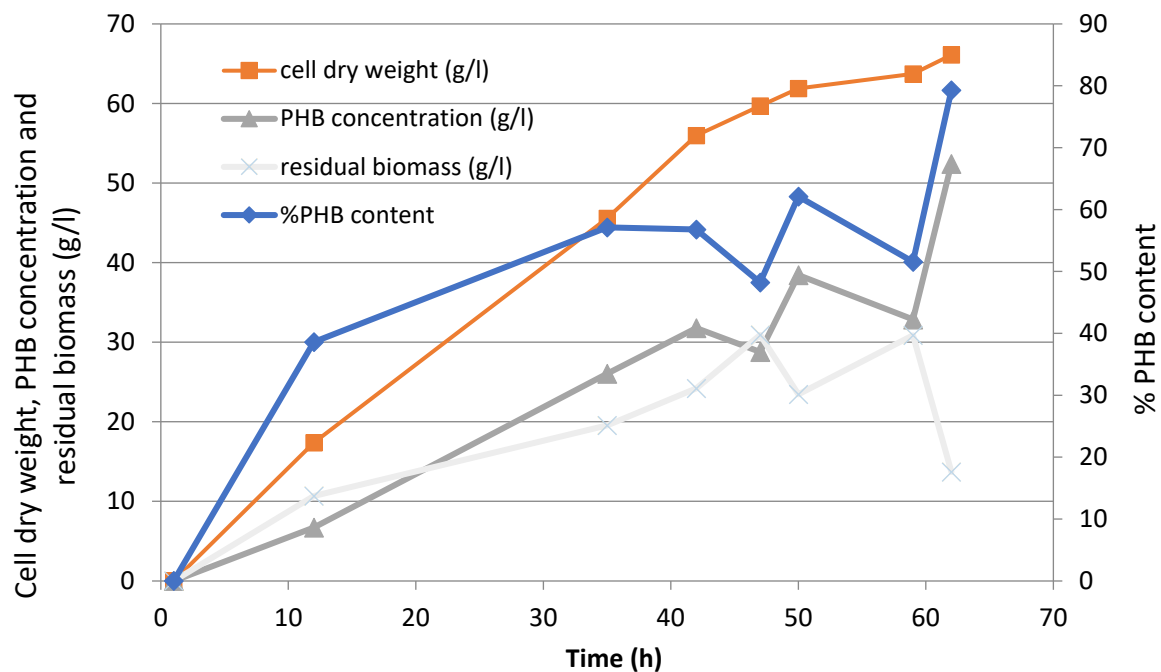
#### 2.5. Statistical Analysis

The SPSS Statistics program version 25.0 (IBM, Armonk, NJ, USA) and Microsoft Excel 2019 were used to analyze the data (Microsoft, Redmond, WA, USA). A paired t-test was employed to compare two sets of data. The differences in averages were judged statistically significant at the 95 percent confidence level ( $p \leq 0.05$ ).

### 3. Results and Discussion

#### 3.1. Biosynthesis of Bacterial PHB and PHBVV Polyesters

The cultivation of *Ralstonia eutropha* ATCC 17,699 with glycerol as a sole carbon source in order to obtain a PHB polymer yielded the following results as shown in Figure 3. Inoculated at 2.5 L for a period of 62 h under fed-batch cultivation, the cell dry weight increased up to 68 g/L. During the feasting period of 35 h onwards, it was found that PHB was rapidly accumulated within the cells, whereas the PHB concentration was higher and residual biomass tended to be lower. PHB content increased up to 82% at the end of fermentation. Table 3 summarized the fermentation results corresponding to the PHB production rate, and the PHB productivity can be calculated at 0.8 g/L/h.



**Figure 3.** Time courses of PHB homopolyester formation: cell dry weight, PHB content, and PHA concentration cultured by fed-batch fermentation in 5 L bioreactor using glycerol as a single substrate.

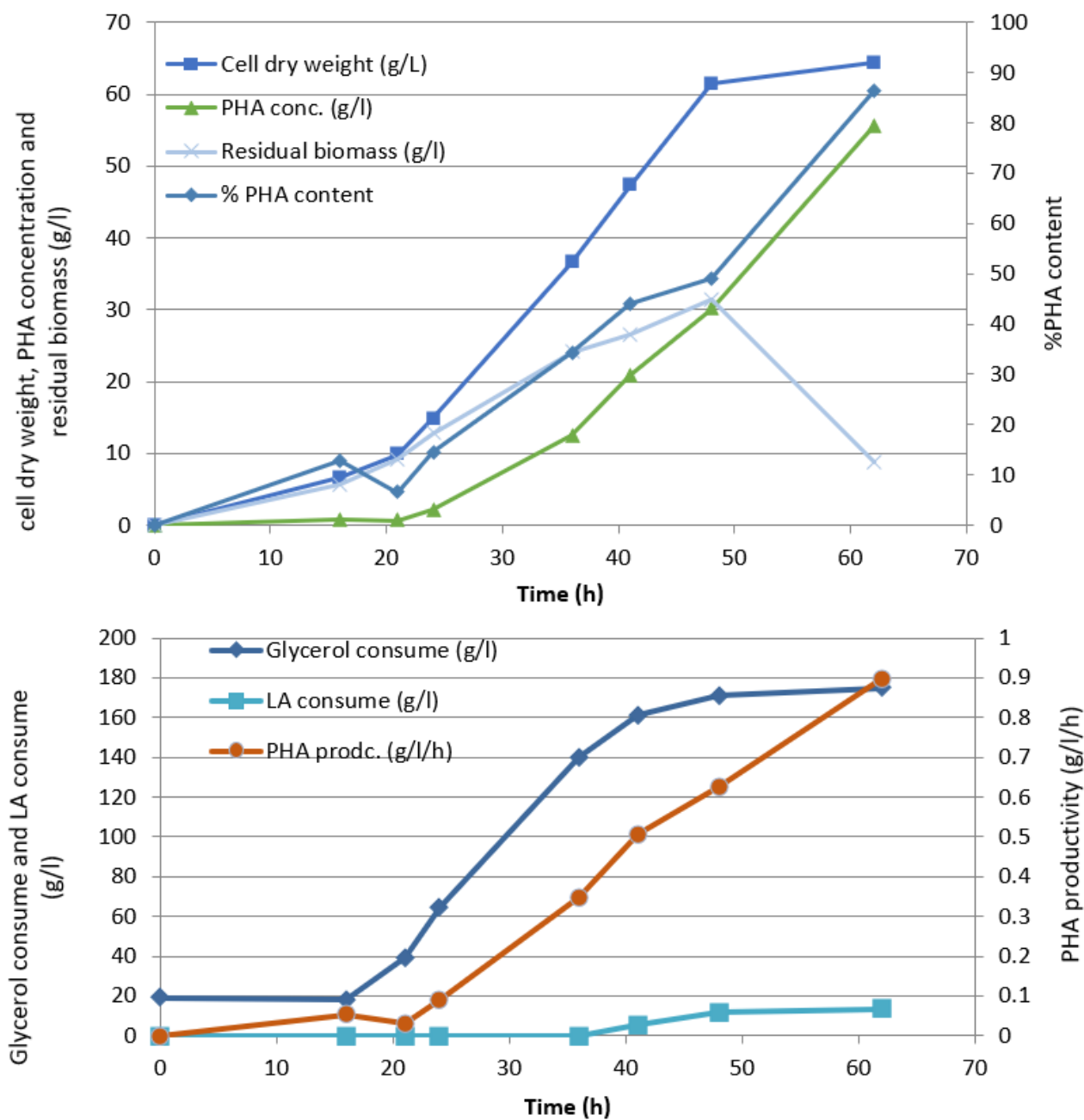
**Table 3.** Biosynthesis of harvested PHA samples after fed-batch cultivation of *Ralstonia eutropha* for 62 h.

PHA Type Sample	Cell Dry Weight (g/L)	PHA Content per Dry Cell <sup>a</sup> (%)	PHA Productivity (g/L/h)	PHA Monomer Composition <sup>b</sup>			M <sub>w</sub> <sup>c</sup> (kDa)	PDI <sup>c</sup>
				3HB (%)	3HV (%)	4HV (%)		
PHB	68	82	0.8	100	0	0	195	1.71
PHBVV	64	83	0.9	87	12	1	163	1.98

<sup>a</sup> PHA content incorporated in cells was determined by gas chromatography (GC). <sup>b</sup> PHA monomer composition was determined by 500 MHz <sup>1</sup>H NMR. <sup>c</sup> Molecular weight of PHA was determined by gel permeation chromatography (GPC). (M<sub>w</sub>: weight average molecular weight, PDI: polydispersity index).

On the other hand, fed-batch fermentation of *Ralstonia eutropha* ATCC 17,699 was performed in a 5 L bioreactor containing 2.5 L mineral solution supplemented with a carbon source of glycerol:levulinic acid cosubstrates at a ratio of 7:3 as precursors of 3HB, 3HV and 4HV monomer unit. The cultivation of PHBVV copolyester was obtained as shown in Figure 4, providing that at the period of 20–35 and 42–62 h the cell growth rate and the PHA concentration increased dramatically to 64 g/L and 55 g/L, respectively. During the 40-h cultivation period onwards, there was a rapid accumulation of PHA within the cells giving rise to the concentration of PHA being higher and the residual biomass tended to be lower. The PHA content increased as high as 83% at the end of fermentation harvested at 62 h. We found that the rate of cell production in the bioreactor tended to increase over time relating to PHBVV biosynthesis. In addition, the graph shows that levulinic acid was applied at approximately 40 h, which is the PHA accumulation period resulting in the PHA productivity increased up to 0.9 g/L/h.





**Figure 4.** Time courses of PHBVV copolyester biosynthesis: cell dry weight, PHA content, cell-PHA productivity, and substrate consumption cultured by fed-batch fermentation in 5 L bioreactor using glycerol/levulinate co-substrates.

Table 3 listed PHA copolymer accumulation observed in the PHBVV terpolymer consisting of 3HB 87 mol%, 3HV 12 mol% and 4HV 1 mol%, which affect the mechanical property of PHA polymer by making it more flexible. The molecular weight and polydispersity of PHB homopolymer were at 95 kDa and 1.71 and of PHBVV biopolymer, which was at 163 kDa and 1.98 (similar to commercial PHA), appropriate for further polymer processing for packaging application [24,25].

It should be mentioned that PHB and PHBVV biosynthesis from glycerol and levulinic acid is capable of meeting the requisite yields of cell mass and PHA production with acceptable molecular size and chemical composition. Normally, bacterially synthesized PHB homopolymer has a higher amount of  $M_w$  than that of PHA copolymer. However, in this study, we performed different extraction and purification methods on PHA and PHBVV. The PHB sample was dissolved by dissolution of non-PHB cell mass while the PHBVV sample was extracted using the chloroform/methanol precipitation method. As a result, the values of molecular weight and PDI of both PHB and PHBVV are very similar giving rise to the suitable specimen for biodegradation tests as initial characteristics of the samples ideally should be the same.

The NMR measurement confirmed the purified PHB and PHBVV samples to determine the chemical structure using the proton-NMR technique. The spectra were shown in Figure 5, and the results PHB homopolymer and PHBVV copolymer have been intrinsically produced and extracted from *Ralstonia eutropha* cells.

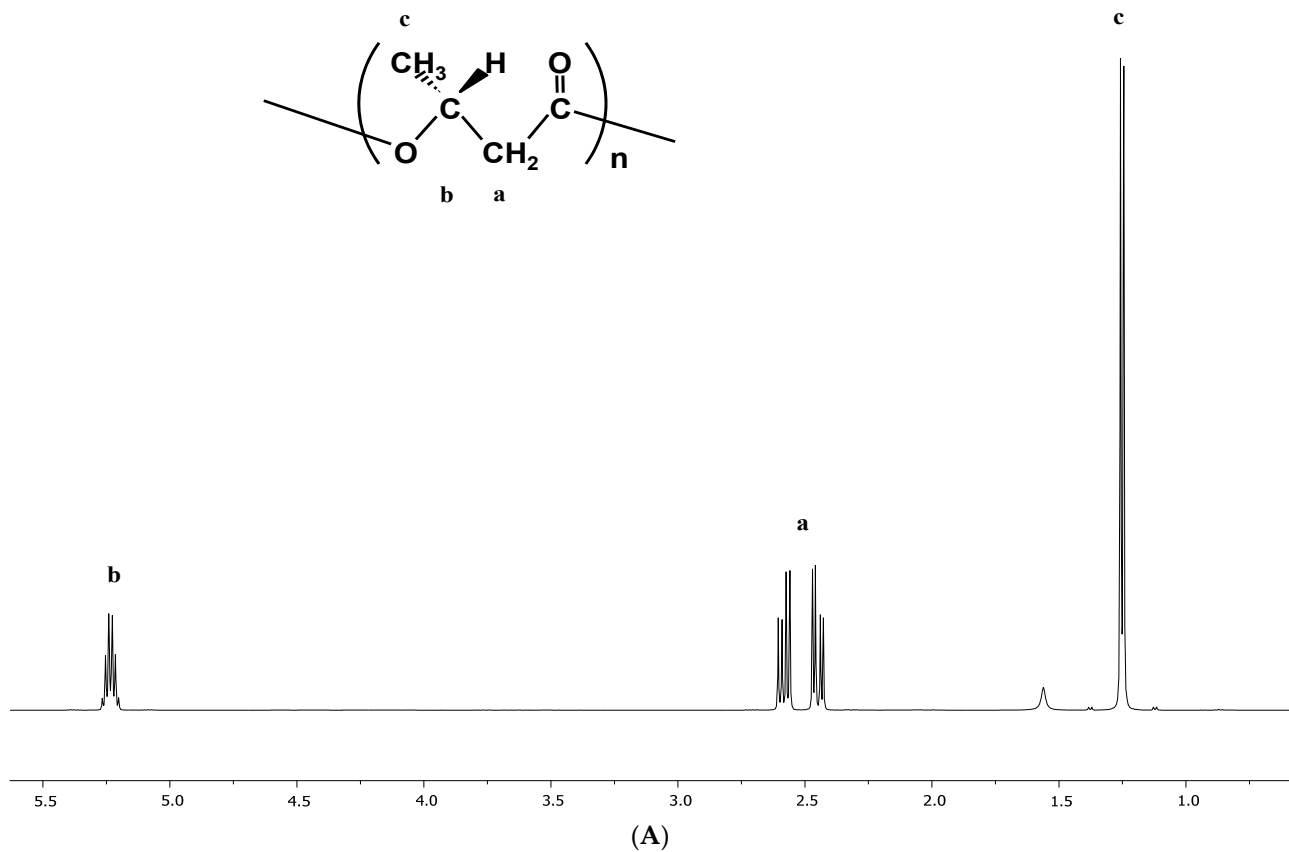
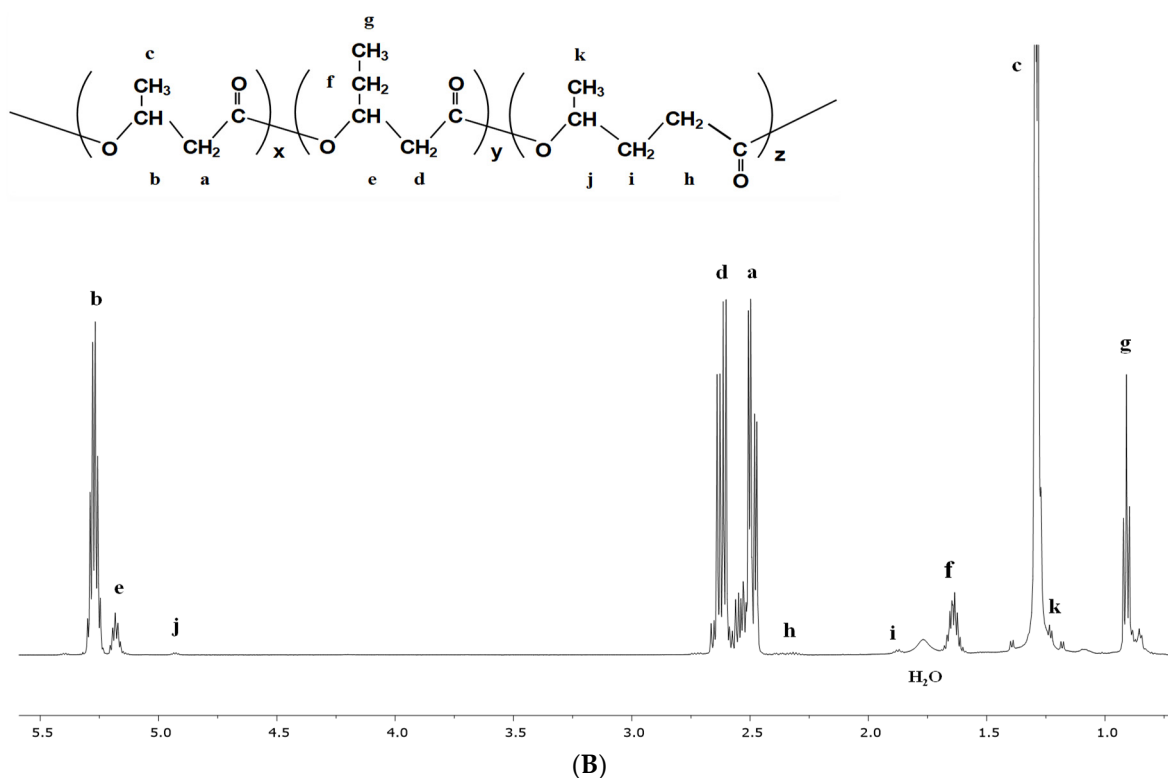


Figure 5. Cont.



**Figure 5.**  $^1\text{H-NMR}$  spectra of the extracted PHA samples used in biodegradation test in seawater: (A) PHB, (B) PHBVV.

### 3.2. Biodegradation in Seawater of PHB and PHBVV

In this Thailand seawater degradation study, we used two biosynthetic PHA samples of PHB and PHBVV, both of which had a similar amount of molecular weight approximately 160–200 kDa with closed PDI as shown in Table 3.

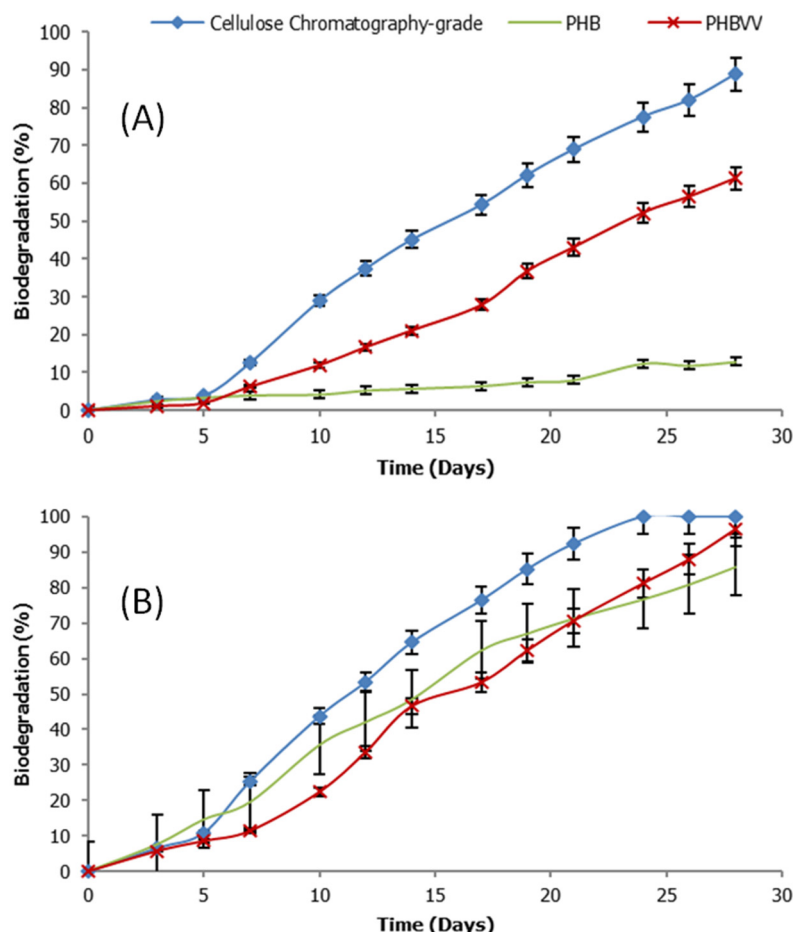
Table 4 shows the percentage of biodegradation generated from the cumulative amount of carbon dioxide resulting from degradation activities in natural or synthetic seawater for 28 days by the modified methods of ISO 19679:2016 and ASTM D6691-17. PHB and PHBVV samples that were tested, compared to cellulose (R+) and polyethylene (R−) references. The results show that PHBVV had a higher biodegradability than PHB in both natural (61.2%:12.8%) and synthetic (96.5%:86%) seawaters correlated to the control and reference samples. It was noted that PHB and PHBVV copolyesters can be almost completely biodegraded in synthetic seawater within 28 days, whereas PHBVV has the ability to mineralize to  $\text{CO}_2$  to over half the amount of biodegradation in Thailand natural seawater.

Figure 6 shows biodegradation curves of PHB and PHBVV samples compared to cellulose reference samples in natural seawater and synthetic seawater. In synthetic seawater, the degree of biodegradation of both the PHB and PHBVV increased with time at a rapid rate after 5 days and could be completely converted to carbon dioxide for 28 days, correlating to cellulose reference. Whereas the degree of biodegradation in Thailand's natural seawater of PHB was almost stable with time, but that of PHBVV still increased with time up to around 60% biodegradation, suggesting that PHA microorganisms are present in natural seawater in Thailand. This indicated that PHBVV copolyester had a higher ability to be biodegraded than PHB homopolyester. Typically, copolymer composition affects a decrease of the degree of crystallinity ( $X_c$ ) of PHA copolymer giving rise to the lower PHBVV crystallinity than PHB [14]. In this case, from the enzymatic biodegradation report [12], PHA copolymer with low  $X_c$  has more easily biodegraded than PHB homopolymer with high  $X_c$ , which tends to have a relationship with the biodegradation in seawater.

**Table 4.** Biodegradability of PHB and PHBVV samples in Thailand natural and synthetic seawaters compared with control, positive and negative references.

Sample Code	% Biodegradation at 28 Days			
	Natural Seawater		Synthetic Seawater	
	Average	SD	Average	SD
Control <sup>1/</sup>	-	-	-	-
R+ <sup>2/</sup>	88.8	6.5	100.0	0.8
R- <sup>3/</sup>	0.8	1.2	5.5	8.5
PHB <sup>4/</sup>	12.8	5.3	86.0	5.2
PHBVV <sup>4/</sup>	61.2	3.4	96.5	7.2

Note: The percentage of biodegradation is calculated from <sup>1</sup> The amount of accumulated carbon dioxide generated by microbial activity in natural or synthetic seawater. (Not including the amount of carbon dioxide in the test container); <sup>2</sup> The cumulative amount of carbon dioxide resulting from degradation activities. Chromatography-grade cellulose by a group of microbes from the coastal sea. (Cellulose chromatography-grade easily decomposed in natural conditions: according to ASTM D6691: 2017 [21]); <sup>3</sup> The cumulative amount of carbon dioxide from polyethylene degradation activities by a group of coastal microbes. (Polyethylene is difficult to decompose in natural conditions: according to ASTM D5338-98: 2003 [26]); <sup>4</sup> The cumulative amount of carbon dioxide from the decomposition activities tested by microbial communities from the coast of Thailand.

**Figure 6.** Biodegradation of PHB and PHBVV samples compared to cellulose reference sample in natural seawater (A) and synthetic seawater (B).

### 3.3. Initial Assessment of Residual Toxicity Levels of Biodegraded PHAs Seawater

The degraded PHAs seawater samples were subsequently assessed to investigate the residual toxicity of environmental safety level by using ARTOXKIT M, a 24-h assay based on the mortality of the test organisms with a calculation of the 24-h LC<sub>50</sub> of *Artemia franciscana* in test solutions containing 25% and 50% of natural or synthetic seawater samples. Table 5

shows the percentage viability of *Artemia franciscana* in natural seawater samples. The survivability of all of the samples is nearly 100 percent, demonstrating that the degraded seawater of PHB and PHBVV biodegradation had no residual toxicity. Moreover, as seen in Table 6, the percentage viability of *Artemia franciscana* in synthetic seawater in the solution of ARTOXKIT M shows slightly decreased for PHBVV degraded solution, which does not impact the environmental safety level [27].

**Table 5.** Percent viability of *Artemia franciscana* in natural seawater samples.

Percentage of Natural Seawater Samples in the Solution of ARTOXKIT M Test	% Viability at 24 h				
	Control	R+	R−	PHB	PHBVV
25%	100	100	100	100	100
50%	100	100	100	93	100

**Table 6.** Percent viability of *Artemia franciscana* in synthetic seawater.

Percentage of Synthetic Seawater Samples in the Solution of ARTOXKIT M Test	% Viability at 24 h				
	Control	R+	R−	PHB	PHBVV
25%	97	100	100	100	97
50%	67	100	97	100	87

This finding indicates that Thai seawater can decompose PHA in the presence of local microorganism consortia, allowing for the usage of bioplastic PHA in coastal areas or islands. Moreover, even when degraded, it does not produce microplastic. The compounds that have been digested are also non-toxic to the marine environment. In the near future, the application of PHA to manufacture bags or marine supplies is quite likely to be used in Thailand and other countries in Southeast Asia.

#### 4. Conclusions

In this research, we successfully synthesized PHB and PHBVV polyesters in fed-batch fermentation of *Ralsonia eutropha* bacterium grown on glycerol-based substrates. PHB and PHBVV samples were prepared with similar molecular weight by different extraction and recovery processes. We initiated a method for measuring the quantity of carbon dioxide accumulated from breakdown processes, which was evaluated using bacteria isolated from Thailand's coast. Biodegradation of biosynthetic PHB and PHBVV in synthetic seawater can be over 60 and 95 percent, respectively, while natural seawater in Thailand can be over 12 and 85 percent, respectively, in 28 days. Residual toxicity levels after biodegradation using seawater mites (*Artemia franciscana*) can confirm that the percent viability of PHB and PHBV degraded solutions is nearly 100 percent viability at 24 h when compared to all control groups that have no impact on the marine environment.

**Author Contributions:** Conceptualization, N.T. and A.P.; Formal analysis, N.T. and A.P.; Funding acquisition, N.T.; Investigation, N.T. and A.P.; Methodology, N.T. and A.P.; Project administration, N.T. and A.P.; Resources, N.T. and A.P.; Validation, N.T. and A.P.; Visualization, A.P.; Writing—original draft, N.T.; Writing—review & editing, N.T. and A.P. All authors have read and agreed to the published version of the manuscript.

**Funding:** This research was funded by Biodiversity-Based Economy Development Office (BEDO) and National Research Council of Thailand (NRCT), grant number 9/2559, 67/2560 and 47/2561.

**Institutional Review Board Statement:** Not applicable.

**Informed Consent Statement:** Not applicable.

**Data Availability Statement:** The data presented in this study are available on request from the corresponding author.

**Acknowledgments:** The authors would like to thank Nakornrat Ongpimai, Anuchan Panaksri, and Wimol Chobchuenchom for the sample preparation and valuable discussion.

**Conflicts of Interest:** The authors declare no conflict of interest.

## References

1. Division of Waste and Hazardous Substances. *Report on the Situation of Community Solid Waste Disposal Sites in Thailand*; KP. 04-205; Department of Pollution Control, Government of Thailand: Phaya Thai, Bangkok, Thailand, 2018.
2. Jambunathan, P.; Zhang, K. Engineered biosynthesis of biodegradable polymers. *J. Ind. Microbiol. Biotechnol.* **2016**, *43*, 1037–1058. [[CrossRef](#)]
3. Luengo, J.; García, B.; Sandoval, A.; Carrasco, G.; Olivera, E. Bioplastics from microorganisms. *Curr. Opin. Microbiol.* **2003**, *6*, 251–260. [[CrossRef](#)]
4. Tan, G.-Y.A.; Chen, C.-L.; Li, L.; Ge, L.; Wang, L.; Razaad, I.M.N.; Li, Y.; Zhao, L.; Mo, Y.; Wang, J.-Y. Start a research on biopolymer polyhydroxyalkanoate (PHA): A review. *Polymers* **2014**, *6*, 706–754. [[CrossRef](#)]
5. Sabapathy, P.C.; Devaraj, S.; Meixner, K.; Anburajan, P.; Kathirvel, P.; Ravikumar, Y.; Zaved, H.M.; Qi, X. Recent developments in Polyhydroxyalkanoates (PHAs) production—A review. *Bioresour. Technol.* **2020**, *306*, 123132. [[CrossRef](#)] [[PubMed](#)]
6. García, G.; Sosa-Hernández, J.E.; Rodas-Zuluaga, L.I.; Castillo-Zacarias, C.; Iqbal, H.; Parra-Saldivar, R. Accumulation of PHA in the Microalgae *Scenedesmus* sp. under Nutrient-Deficient Conditions. *Polymers* **2021**, *13*, 131. [[CrossRef](#)] [[PubMed](#)]
7. Dobrogojski, J.; Szychalski, M.; Luciński, R.; Borek, S. Transgenic plants as a source of polyhydroxyalkanoates. *Acta Physiol. Plant.* **2018**, *40*, 162. [[CrossRef](#)]
8. Zinn, M.; Witholt, B.; Egli, T. Occurrence, synthesis and medical application of bacterial polyhydroxyalkanoate. *Adv. Drug Deliv. Rev.* **2001**, *53*, 5–21. [[CrossRef](#)]
9. Koller, M.; Maršálek, L.; de Sousa Dias, M.M.; Braunegg, G. Producing microbial polyhydroxyalkanoate (PHA) biopolyesters in a sustainable manner. *New Biotechnol.* **2017**, *37*, 24–38. [[CrossRef](#)]
10. Chen, G.-Q.; Wu, Q. The application of polyhydroxyalkanoates as tissue engineering materials. *Biomaterials* **2005**, *26*, 6565–6578. [[CrossRef](#)]
11. Papanephytou, C.; Katsipis, G.; Halevas, E.; Pantazaki, A. Polyhydroxyalkanoates Applications in Drug Carriers. In *Biotechnological Applications of Polyhydroxyalkanoates*; Springer: Singapore, 2019; pp. 77–124. [[CrossRef](#)]
12. Sudesh, K.; Abe, H.; Doi, Y. Synthesis, structure and properties of polyhydroxyalkanoates: Biological polyesters. *Prog. Polym. Sci.* **2000**, *25*, 1503–1555. [[CrossRef](#)]
13. Yu, J.; Chen, L.X.L.; Sato, S. Biopolyester Synthesis and Protein Regulations in *Ralstonia eutropha* on Levulinic Acid and Its Derivatives from Biomass Refining. *J. Biobased Mater. Bioenergy* **2009**, *3*, 113–122. [[CrossRef](#)]
14. Tanadchangsang, N.; Yu, J. Miscibility of natural polyhydroxyalkanoate blend with controllable material properties. *J. Appl. Polym. Sci.* **2013**, *129*, 2004–2016. [[CrossRef](#)]
15. Tosin, M.; Weber, M.; Siotto, M.; Lott, C.; Degli-Innocenti, F. Laboratory Test Methods to Determine the Degradation of Plastics in Marine Environmental Conditions. *Front. Microbiol.* **2012**, *3*, 225. [[CrossRef](#)] [[PubMed](#)]
16. Tachibana, K.; Urano, Y.; Numata, K. Biodegradability of nylon 4 film in a marine environment. *Polym. Degrad. Stab.* **2013**, *98*, 1847–1851. [[CrossRef](#)]
17. Tanadchangsang, N.; Yu, J. Microbial synthesis of polyhydroxybutyrate from glycerol: Gluconeogenesis, molecular weight and material properties of biopolyester. *Biotechnol. Bioeng.* **2012**, *109*, 2808–2818. [[CrossRef](#)]
18. Yu, J.; Chen, L.X. Cost-effective recovery and purification of polyhydroxyalkanoates by selective dissolution of cell mass. *Biotechnol. Prog.* **2006**, *22*, 547–553. [[CrossRef](#)]
19. Braunegg, G.; Sonnleitner, B.; Lafferty, R.M. A rapid gas chromatographic method for the determination of poly- $\beta$ -hydroxybutyric acid in microbial biomass. *Eur. J. Appl. Microbiol. Biotechnol.* **1978**, *6*, 29–37. [[CrossRef](#)]
20. ISO 19679:2016. *Plastics—Determination of Aerobic Biodegradation of Non-Floating Plastic Materials in a Seawater/Sediment Interface—Method by Analysis of Evolved Carbon Dioxide*; ASTM International: West Conshohocken, PA, USA, 2016.
21. ASTM D6691-17. *Standard Test Method for Determining Aerobic Biodegradation of Plastic Materials in the Marine Environment by a Defined Microbial Consortium or Natural Sea Water Inoculum*; ASTM International: West Conshohocken, PA, USA, 2001.
22. ASTM D1141-98. *Standard Practice for the Preparation of Substitute Ocean Water*; ASTM International: West Conshohocken, PA, USA, 2013.
23. Snell, T.W. A Standard Practice for Performing Acute Toxicity Tests Using Rotifers in the Genus *Brachionus*. *Am. Soc. Test. Mater* **1991**, *11*, 1210–1216.
24. Tanadchangsang, N.; Yu, J. Thermal stability and degradation of biological terpolyesters over a broad temperature range. *J. Appl. Polym. Sci.* **2015**, *132*. [[CrossRef](#)]
25. Cavalheiro, J.M.B.T.; de Almeida, M.C.M.D.; Grandfils, C.; da Fonseca, M.M.R. Poly(3-hydroxybutyrate) production by *Cupriavidus necator* using waste glycerol. *Process Biochem.* **2009**, *44*, 509–515. [[CrossRef](#)]

26. ASTM D5338-98. *Standard Test Method for Determining Aerobic Biodegradation of Plastic Materials Under Controlled Composting Conditions*; ASTM International: West Conshohocken, PA, USA, 2003.
27. Alonso-López, O.; López-Ibáñez, S.; Beiras, R. Assessment of Toxicity and Biodegradability of Poly(vinyl alcohol)-Based Materials in Marine Water. *Polymers* **2021**, *13*, 3742. [[CrossRef](#)] [[PubMed](#)]

## Article

# Characterization and Parametric Study on Mechanical Properties Enhancement in Biodegradable Chitosan-Reinforced Starch-Based Bioplastic Film

Shiou Xuan Tan <sup>1</sup>, Hwai Chyuan Ong <sup>2,\*</sup>, Andri Andriyana <sup>1</sup>, Steven Lim <sup>3,4,\*</sup>, Yean Ling Pang <sup>3,4</sup>, Fitranto Kusumo <sup>5</sup> and Gek Cheng Ngoh <sup>6,\*</sup>

<sup>1</sup> Department of Mechanical Engineering, Faculty of Engineering, Universiti Malaya, Kuala Lumpur 50603, Malaysia; kva190014@siswa.um.edu.my (S.X.T.); andri.andriyana@um.edu.my (A.A.)

<sup>2</sup> Future Technology Research Center, National Yunlin University of Science and Technology, Douliou 64002, Taiwan

<sup>3</sup> Department of Chemical Engineering, Lee Kong Chian Faculty of Engineering and Science, Universiti Tunku Abdul Rahman, Kajang 43000, Malaysia; pangyl@utar.edu.my

<sup>4</sup> Centre of Photonics and Advanced Materials Research, Universiti Tunku Abdul Rahman, Kajang 43000, Malaysia

<sup>5</sup> Centre for Green Technology, School of Civil and Environmental Engineering, University of Technology, Sydney, NSW 2007, Australia; Fitranto.Kusumo@student.uts.edu.au

<sup>6</sup> Department of Chemical Engineering, Faculty of Engineering, Universiti Malaya, Kuala Lumpur 50603, Malaysia

\* Correspondence: onghc@yuntech.edu.tw (H.C.O.); stevenlim@utar.edu.my (S.L.); ngoh@um.edu.my (G.C.N.)

**Citation:** Tan, S.X.; Ong, H.C.; Andriyana, A.; Lim, S.; Pang, Y.L.; Kusumo, F.; Ngoh, G.C.

Characterization and Parametric Study on Mechanical Properties Enhancement in Biodegradable Chitosan-Reinforced Starch-Based Bioplastic Film. *Polymers* **2022**, *14*, 278. <https://doi.org/10.3390/polym14020278>

Academic Editors: José Miguel Ferri, Vicent Fombuena Borràs and Miguel Fernando Aldás Carrasco

Received: 24 November 2021

Accepted: 24 December 2021

Published: 11 January 2022

**Publisher's Note:** MDPI stays neutral with regard to jurisdictional claims in published maps and institutional affiliations.



**Copyright:** © 2022 by the authors. Licensee MDPI, Basel, Switzerland. This article is an open access article distributed under the terms and conditions of the Creative Commons Attribution (CC BY) license (<https://creativecommons.org/licenses/by/4.0/>).

**Abstract:** Bioplastic has been perceived as a promising candidate to replace petroleum-based plastics due to its environment-friendly and biodegradable characteristics. This study presents the chitosan reinforced starch-based bioplastic film prepared by the solution casting and evaporation method. The effects of processing parameters, i.e., starch concentration, glycerol loading, process temperature and chitosan loading on mechanical properties were examined. Optimum tensile strength of 5.19 MPa and elongation at break of 44.6% were obtained under the combined reaction conditions of 5 wt.% starch concentration, 40 wt.% glycerol loading, 20 wt.% chitosan loading and at a process temperature of 70 °C. From the artificial neural network (ANN) modeling, the coefficient of determination ( $R^2$ ) for tensile strength and elongation at break were found to be 0.9955 and 0.9859, respectively, which proved the model had good fit with the experimental data. Interaction and miscibility between starch and chitosan were proven through the peaks shifting to a lower wavenumber in FTIR and a reduction of crystallinity in XRD. TGA results suggested the chitosan-reinforced starch-based bioplastic possessed reasonable thermal stability under 290 °C. Enhancement in water resistance of chitosan-incorporated starch-based bioplastic film was evidenced with a water uptake of 251% as compared to a 302% registered by the pure starch-based bioplastic film. In addition, the fact that the chitosan-reinforced starch-based bioplastic film degraded to 52.1% of its initial weight after 28 days suggests it is a more sustainable alternative than the petroleum-based plastics.

**Keywords:** starch-based bioplastic; chitosan; co-polymer; reinforcement; biodegradation

## 1. Introduction

Petroleum-based plastics have constituted major parts of our daily life, ranging from bottled drinks, household appliances and toys to food packaging. The reasons for plastics having such popular usage are due to their high strength, low cost and light-weight as well as their thermal and chemical insulating properties [1,2]. However, petroleum-based plastics are resistant to chemical, solar and microbial degradation [1,3]. This leads to a build-up of plastic waste in the environment along with increasing utilization of plastic products [4,5]. The shortcomings can be addressed by the emergence of bioplastics.



Bioplastics' renewable nature is associated with constituents that are derived from plants such as starch, cellulose and lignin or from animal-derived casein, protein and lipid [6]. Bioplastics have an edge over petroleum-based plastics due to their biodegradability, instead of the combustion of plastic wastes adopted by the latter [7,8]. Among the diverse feedstocks for synthesizing of bioplastic, starch is preferred, as it can be easily degraded into environment-friendly compounds [9]. In addition, its affordability, abundance and availability in various starch-producing plants such as sago, cassava, corn and potato have also added to its superior advantages. However, pure starch-based bioplastic film is hydrophilic and highly sensitive to water, which would negatively affect its mechanical and barrier properties, and thereby greatly limit its utilization [10–12].

In starch-based bioplastic film fabrication, plasticizer can be used to overcome film brittleness caused by the high intermolecular forces [13,14]. The commonly used plasticizers for starch-based bioplastic film are water, sorbitol and glycerol [15]. Nevertheless, it is not recommended for water to be used directly as plasticizer in view of the high volatility of its molecules, which would lead to brittleness in film [16,17]. Glycerol, conversely, possesses hydroxyl groups that are responsible for inter- and intra-molecular interactions (hydrogen bonds) in polymeric chains. Thus, it is regarded as the best plasticizer for water-soluble polymers in providing a more flexible structure for bioplastic films [5,13,18].

The properties of pure starch-based bioplastic film could also be enhanced by blending it with other polymers such as chitosan with its hydrophobic nature [19,20]. Chitosan is obtained from the de-acetylation of chitin, which could be abundantly found in natural sources such as shells and heads of crabs, lobsters or shrimps [21,22]. The non-toxic and low-cost nature of chitosan has made it a suitable choice as a co-polymer in bioplastic film fabrication for improving mechanical properties, while reducing the hydrophilic characteristic of starch-based bioplastic film [19]. In addition, the bioplastic film produced from blending of starch with chitosan would be very attractive as a food-packaging application due to the intrinsic antimicrobial property of chitosan. Starch-based bioplastic films have been synthesized by many researchers from various sources, such as potato [23], corn [24,25], mango seed [26], jackfruit seed [27], sago [21], avocado seed [28] and cassava peel [29]. Despite bioplastic fabrication being conducted by many researchers, the parametric studies on plasticizer and filler/co-polymer loadings using solution and casting techniques are rarely being conducted. Possibly, this has been due to the restrictions of smaller scale (laboratory scale), which was less developed in its present status. Moreover, the results obtained had not been proven for industrial scale compared to other matured techniques such as extrusion, blow molding and compression molding. The effects of starch concentration and process temperature on the mechanical properties of bioplastic film are also seldom being investigated and their relationships are still unclear. Hence, this paper aims to provide more insights into the effects of operating parameters, including starch concentration, glycerol loading, process temperature and chitosan loading on the mechanical properties of the synthesized bioplastic film, based on the solution casting and evaporation technique. The present work employs corn starch as matrix, chitosan as co-polymer and glycerol as plasticizer in the fabrication of a sustainable bioplastic film. The results of this parametric study on the mechanical properties of the starch-based bioplastic film will develop a fundamental framework for more in-depth studies in the future. Artificial neural network (ANN) was adopted in this study in order to compare the experimental and predicted tensile strength and elongation at break. In addition, pure starch-based and chitosan-reinforced starch-based bioplastic films were compared in terms of their water uptake capability and actual biodegradability in soil to address the future of applicability of bioplastics.

## 2. Materials and Methods

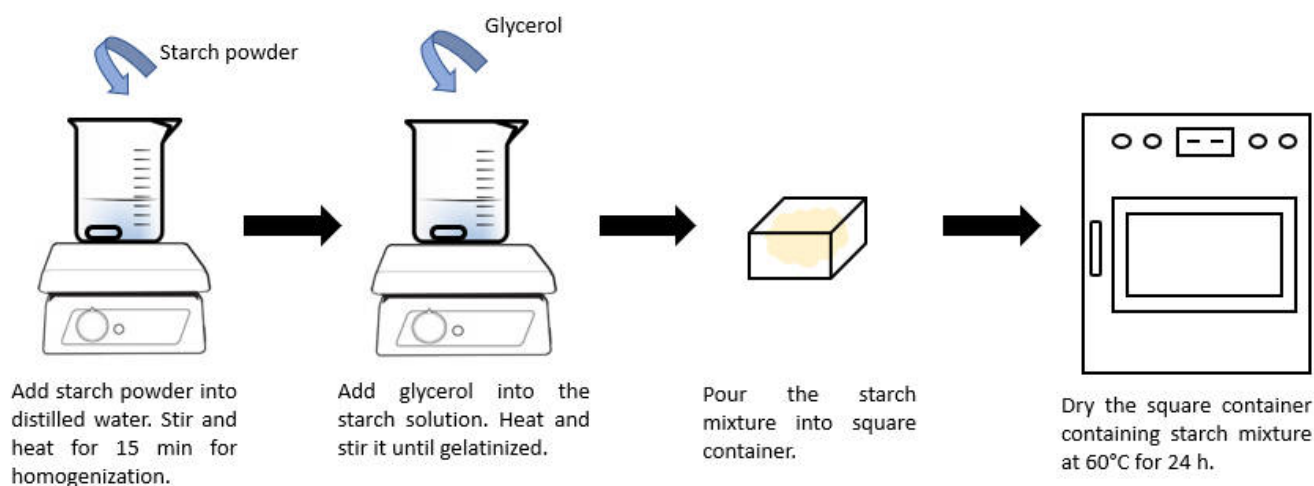
### 2.1. Materials

Corn starch powder was procured from Thye Huat Chan Sdn. Bhd., Malaysia. Glycerol (99.5% purity) was procured from Friendemann Schmidt. Acetic acid (glacial, 100% purity)

and chitosan (from shrimp shells, medium molecular weight) were purchased from Merck and Sigma-Aldrich, respectively. Laboratory-formulated distilled water was used throughout the experiments. All the chemicals were used as received, without further purification.

## 2.2. Preparation of Corn Starch Bioplastic Film

The solution casting and evaporation method was adopted for bioplastic film preparation in this study. The formulation was modified from the work of Salehudin et al. [30]. A schematic diagram of the experimental setup is shown in Figure 1. First, a varying amount of corn starch (2.5 wt.%–10 wt.% of distilled water), which corresponded to starch: glycerol ratio ( $w/w$ ) of 10:8–40:8 was added into a 250 mL beaker containing 100 mL distilled water in a form of suspension to avoid agglomeration. The starch solution was homogenized at 250 rpm and heated at 60 °C for 15 min. Glycerol of varying weight percentages (40 wt.%–80 wt.% based on weight of starch only) was added into the starch solution and subjected to different process temperatures (65 °C–90 °C) until it was gelatinized. For the addition of varying chitosan loading (0 wt.%–20 wt.% of starch), chitosan was dispersed in aqueous solution of 1  $v/v\%$  acetic acid. Upon completion of the reaction, 15 g of starch mixture or starch-chitosan mixture was poured into a square container with dimension of 10 cm  $\times$  10 cm. The mixture was then dried in a heating oven at 60 °C for 24 h. The film was peeled off and stored in a desiccator with a sealed plastic bag prior to thickness measurement and further testing. The final thickness of each film was measured and was in the range of  $0.11 \pm 0.02$  mm. The effects of fabrication parameters, including starch concentration, glycerol loading, process temperature and chitosan loading towards the mechanical properties of corn starch bioplastic film were investigated using the one factor at a time method. Each experiment was conducted in triplicates to ensure the data reproducibility. The reported values were the average of the individual runs, with errors within an acceptable range of 5%. The pure starch-based and chitosan-reinforced starch-based bioplastic films with the optimum tensile strength were then subjected to water uptake and biodegradation tests to further characterize the bioplastic properties.



**Figure 1.** Experimental setup for bioplastic film fabrication.

## 2.3. ANN Modeling

The ANN model was developed using MATLAB Version 7.10 R2010a software (The MathWorks Inc., Natick, MA, USA). In this study, the hyperbolic tangent sigmoid transfer function (*tansig*) was used for the input layer to the hidden layer and the linear transfer function (*purelin*) was used from the hidden layer to the output layer. Once the mean squared error (MSE) reached the minimum value and the average correlation coefficient (*R*) was close or equal to 1, the training of ANN model was terminated.

#### 2.4. Data Verification

The performance of the ANN model was measured statistically based on the coefficient of determination ( $R^2$ ) according to Equation (1) [31]. Generally, a higher  $R^2$  value indicated higher accuracy for the developed model.

$$R^2 = 1 - \sum_{i=1}^n \left( \frac{(y_{bi} - y_{pi})^2}{(y_m - y_{pi})^2} \right) \quad (1)$$

where  $n$  is the number of experimental data, while  $y_{bi}$  is the experimental tensile strength/elongation at break,  $y_{pi}$  is the predicted tensile strength/elongation at break and  $y_m$  is the average value of the tensile strength/elongation at break obtained from the experiments.

#### 2.5. Characterization of Bioplastic Film

##### 2.5.1. Mechanical Properties

The mechanical properties of bioplastic film such as tensile strength and elongation at break were determined using Universal Testing Machine (Autograph AG-X, Shimadzu, Japan) interfaced with computer operating Trapezium software. Measurements were performed with load cell of 500 N, crosshead speed of 5 mm/min and grip separation of 30 mm. Three readings were taken from three random places of each film, measuring 7 cm × 1 cm. The average values from three measurements were reported.

##### 2.5.2. Fourier-Transform Infrared (FTIR) Analysis

FTIR spectra of pure starch-based and chitosan-reinforced starch-based bioplastic films were recorded using FTIR spectrometer operating in attenuated total reflectance (ATR) mode by positioning the measuring probe directly on the film surface (Perkin Elmer, model Spectrum 400) to compare the functional groups and chemical bonds between the films. FTIR spectra of corn starch and chitosan powders were also acquired by placing the samples on the test area. All the samples were scanned at a frequency range of 4000–450  $\text{cm}^{-1}$  with 32 scans at a resolution of 4  $\text{cm}^{-1}$ .

##### 2.5.3. X-ray Diffraction (XRD)

XRD patterns were recorded using an X-ray diffractometer (Rigaku, model MiniFlex 300/600) equipped with  $\text{CuK}\alpha$  radiation, operating at 40 kV and 14 mA. All the samples were measured at room temperature over the angular range 3–90° ( $2\theta$ ) at a step size of 0.02° in continuous mode.

##### 2.5.4. Thermal Analysis

Thermal behaviors of pure starch-based and chitosan-reinforced starch-based bioplastic films were characterized by thermal gravimetric analysis (TGA). This thermal decomposition analysis was performed by using a thermogravimetric analyzer (Perkin Elmer, model TGA Pyris 1). A bioplastic film of around 5 mg was placed in a platinum pan and heated from ambient temperature to a final temperature of 900 °C at a heating rate of 20 °C/min with nitrogen flow rate of 50 mL/min [19,32].

##### 2.5.5. Water Uptake Test

The water uptake test was modified from the study of Maulida and Tarigan [29] and Wu [33]. Bioplastic film was cut into a uniform size of 2 cm × 2 cm with its mass being weighed. The film was then immersed in a container filled with distilled water for 90 min. During the period, the film was removed from the water at 10-min intervals. Immediately after it was blotted dried with tissue paper, the film was weighed before returning to the

water. The water uptake by the film was calculated according to Equation (2) [4]. The average values from three measurements were reported.

$$\text{Water uptake} = \frac{W - W_0}{W_0} \times 100\% \quad (2)$$

where  $W_0$  is the weight of dry sample (g),  $W$  is the weight of sample after immersion in distilled water (g)

#### 2.5.6. Biodegradation Test

Bioplastic samples with the dimension 2 cm × 2 cm were buried in compost soil purchased from a local plant nursery at ±3 cm depth and left for 28 days with weekly sampling being performed. The buried samples were cleaned of soil and weighed. The biodegradation test was conducted at room temperature with relative humidity of 40–50%. The weight loss of the bioplastics was calculated using Equation (3) [9]. Three replicates of each sample were subjected to the biodegradation test and the average values were reported.

$$\text{Weight loss} = \frac{W_0 - W_f}{W_0} \times 100\% \quad (3)$$

where  $W_0$  is the initial bioplastic weight (g),  $W_f$  is the final bioplastic weight (g).

#### 2.6. Statistical Analysis

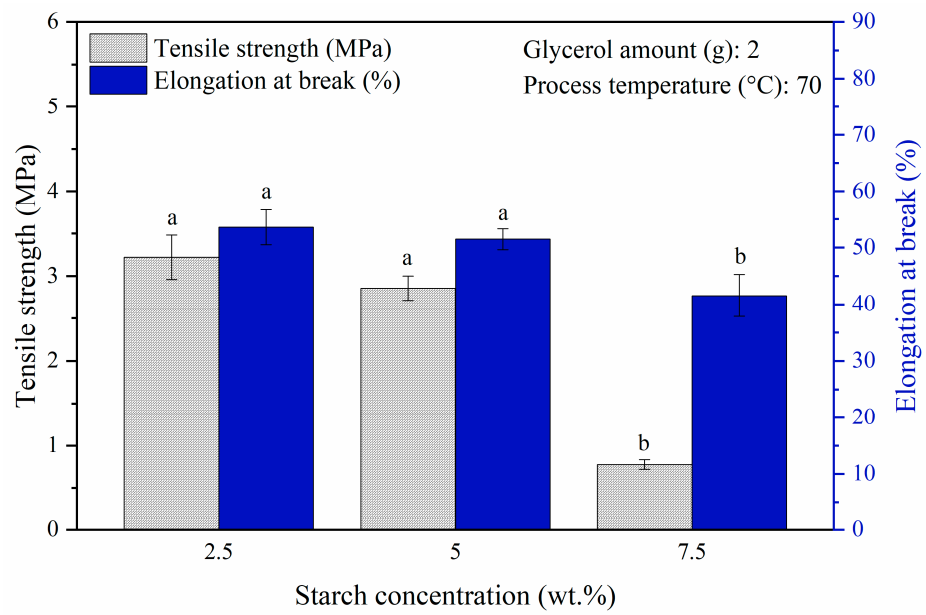
Statistical analysis was performed on OriginPro 2018 software (OriginLab, USA). One-way analysis of variance (ANOVA) with Tukey test was performed to compare the mean values at the significance level of 5% ( $p < 0.05$ ).

### 3. Results and Discussion

#### 3.1. Mechanical Properties

##### 3.1.1. Effect of Starch Concentration

The effects of starch concentration on the mechanical properties that were evaluated by fixing a glycerol amount of 2 g and a process temperature of 70 °C without incorporation of chitosan are presented in Figure 2. The tensile strength of bioplastic film decreased significantly from 3.22 MPa to 0.78 MPa ( $p < 0.05$ ) and so did the elongation at break, indicating a substantial drop from 53.6% to 41.6% ( $p < 0.05$ ) with the addition of starch concentration from 2.5 wt.% to 7.5 wt.%. The significant decrement of 75.8% in tensile strength could be explained by the increase in amylopectin content as the starch concentration increased. The branched structure of amylopectin created a distance between the polymer chains resulting in weaker hydrogen bonds between them [21,34]. These research findings were in accord with the work of Sapei et al. [34] on the effects of different banana starch concentrations (10 to 30 vol.%) on the mechanical properties of chitosan-starch bioplastic film. It was worth noting that a very brittle bioplastic film was formed at 10 wt.% starch concentration. The brittleness incapacitated the tensile test, which can be evidenced from Table 1 exhibiting the cracked film with small broken pieces. This finding revealed that a 10 wt.% starch solution was too saturated to produce a smooth and uniform film whereas glycerol at 40 wt.% was insufficient to facilitate the formation of a film. The decrease in the elongation at break could be explained through the saturation phenomenon, whereby the bondings between the starch molecules increased as the starch concentration was increased to a saturation amount that would prevent glycerol molecules to fit into the molecular chains [35].



**Figure 2.** Tensile strength and elongation at break of pure starch-based biplastic films at different starch concentrations. Different letters indicate the values are significantly different ( $p < 0.05$ ).

**Table 1.** Gelatinized duration required and film appearance at different starch concentrations.

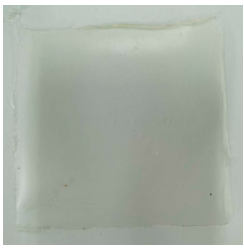

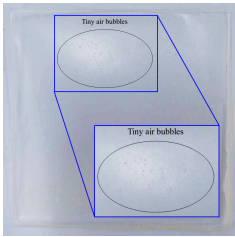
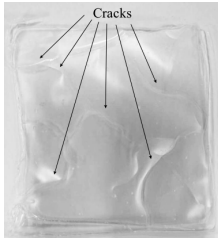
Starch Concentration (wt.%)	Gelatinized Duration (h)	Film Appearance
2.5	5.5	Film free of air bubbles. 
5	2	Film free of air bubbles. 
7.5	1.5	Film with tiny air bubbles. 

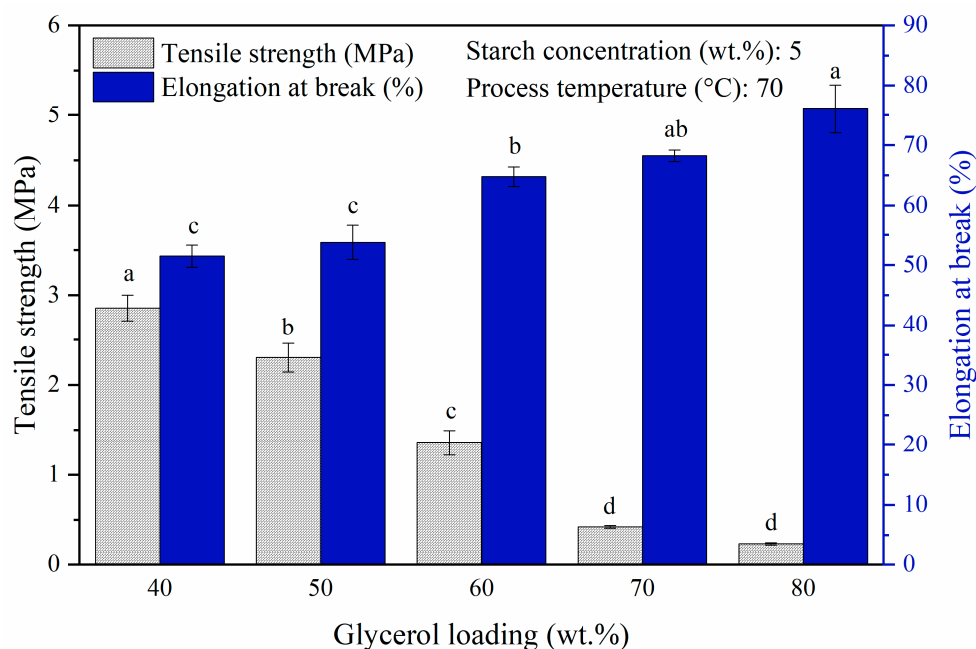
Table 1. Cont.

Starch Concentration (wt.%)	Gelatinized Duration (h)	Film Appearance
10	1	Brittle film. 

To gain an insightful overview of the starch synthesized bioplastic film and the effects on its mechanical properties, gelatinized duration required and appearance of film at diverse starch concentrations are presented in Table 1. In general, the surface of bioplastic film in contact with the container was shiny and glossy; meanwhile, the surface exposed to air during drying was dull looking. Starch is responsible for the cohesion of bioplastic during heating; a lower starch concentration required a longer heating process and would consume a greater energy consumption to evaporate the water content in achieving cohesion of bioplastic [36]. Despite that at 2.5 wt.% starch concentration, the bioplastic film possessed tensile strength that was 11.2% higher than that of 5 wt.% starch concentration, the gelatinization duration was 3.5 h longer. This implied 2.5 wt.% was not feasible to be considered as the optimum starch concentration from an economic perspective. Therefore, a 5 wt.% starch concentration was used to optimize the subsequent parameter investigated.

### 3.1.2. Effect of Glycerol Loading

Glycerol was used as a plasticizer to synthesize bioplastic in the present study to reduce the film brittleness by reducing the intermolecular forces between polymer chains, while increasing their mobility to produce a more elastic and flexible film [37]. From the findings of varying glycerol loadings (40 wt.% to 80 wt.% at 10 wt.% increments, which corresponded to starch: glycerol ratio ( $w/w$ ) of 20:8 to 20:16) on the mechanical properties of the synthesized bioplastic film, the results in Figure 3 show that tensile strength exhibited a decreasing trend, in which it dropped from 2.86 MPa to 0.24 MPa when the glycerol loading was increased from 40 wt.% to 80 wt.%, and in contrast the elasticity of the film showed an opposite trend ( $p < 0.05$ ). This could be reflected from the significant increase of 24.6% (from 51.5% to 76.1%) in the elongation at break value within the investigated range of glycerol loading. Higher glycerol loading provides greater free-movement space for the glycerol molecules to slip between the amylose-amylopectin chains. This weakens the interaction between the polymer in preventing the formation of rigid structures, while softening the polymer matrix, simultaneously [38]. The same behavioral plasticizing effect of glycerol on starch-based bioplastic film was observed by Ginting et al. [38] and Santana et al. [39] in the fabrication of durian seed starch-chitosan-sorbitol and cassava starch-glycerol films, respectively. Glycerol of 40 wt.% was used to optimize the subsequent parameters investigated, as the film obtained at lower amount of 30 wt.% glycerol was too brittle to be subjected for tensile test.



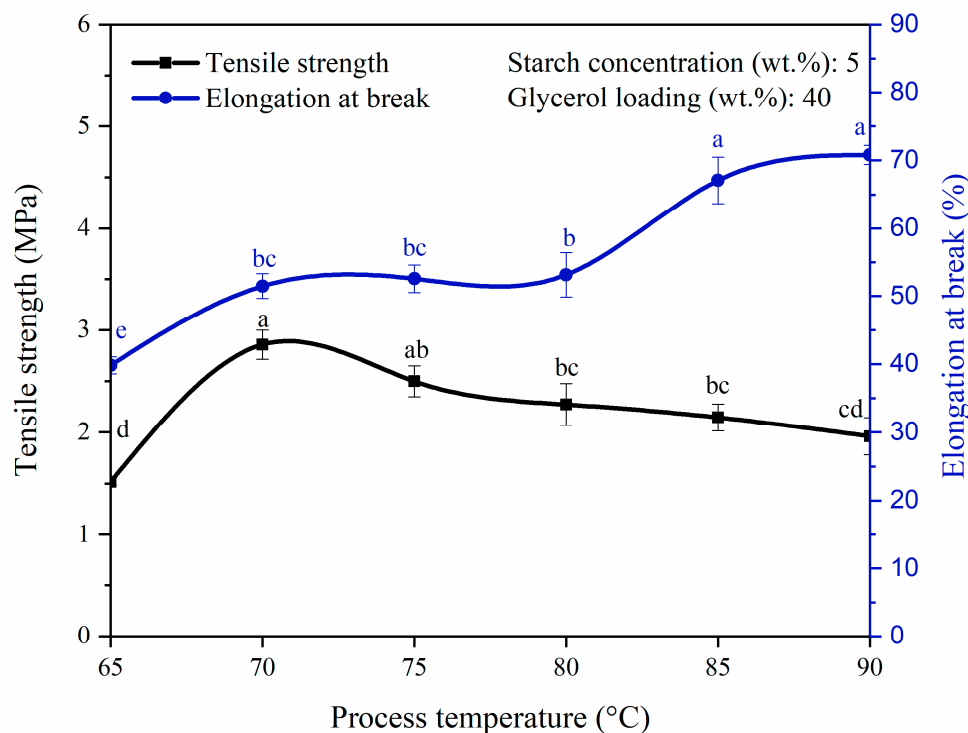
**Figure 3.** Tensile strength and elongation at break of pure starch-based bioplastic films with varying glycerol loadings. Different letters indicate the values are significantly different ( $p < 0.05$ ).

### 3.1.3. Effect of Process Temperature

Temperature always exerts an effect on reaction. Preliminary study indicated that process temperature below 65 °C did not successfully produce a film. To elucidate the temperature effect on the fabrication of bioplastic, temperatures ranging from 65 °C to 90 °C were applied to the bioplastic solution and their effects on the mechanical properties of the bioplastic film are shown in Figure 4. When the process temperature increased from 65 °C to 70 °C, the tensile strength of the bioplastic film increased from 1.52 MPa to an optimum value of 2.86 MPa within the range of the investigated temperature ( $p < 0.05$ ). The temperature increased from 65 °C to 70 °C had induced gelatinization by producing a film that is free of air bubbles, which can be observed from Table 1. However, tensile strength had then dropped to 1.96 MPa as the process temperature further increased to 90 °C ( $p < 0.05$ ). The declining of tensile strength at higher process temperature might be caused by the weakening of intermolecular bonds in starch as excessive heating breaks the glycosidic bonds (bonds between monomers) in amylose [38]. Amylose plays an important role in the gel formation and the production of compact thin film. The excessive heat provided at 90 °C resulted in the depolymerization of long chain amylose into short chain amylose. This has subsequently decreased the amylose content [40,41]. A reduction in amylose content lowers the cohesiveness of bioplastics formation and, thus, its tensile strength is decreased [38].

Moreover, elongation at break increased with increasing process temperature. The highest investigation temperature of 90 °C gave rise to the longest elongation at break of 71.0%. At lower process temperature, the molecules in the polymer matrix are closely packed with lower kinetic energy. Thus, small free volume is present within the polymer matrix and the movement of the molecules are somewhat restricted. As the process temperature increases, the higher kinetic and thermal energies imparted to the polymer molecules could trigger more intense vibrations and generate more free volumes available for larger molecular chain rotation in the solution [42]. This suggests that besides the addition of glycerol, increase in the free volume between the polymer chains can also be achieved with increase in temperature. Eventually, the increasing mobility of starch molecules and the softening of film matrix would synergistically increase the flexibility of the synthesized film. This could be observed from the increase of 31.2% (39.8% to 71.0%) in the elongation at break percentage of bioplastic film as the process temperature was elevated

from 65 °C to 90 °C ( $p < 0.05$ ) [42,43]. Furthermore, Ginting et al. [38] also reported similar trends of tensile strength and elongation at break with respect to the process temperature. Both the optimum tensile strength and elongation at break, respectively, of 19 MPa and 2.6% were obtained at 70 °C when durian seed starch was used as matrix, sorbitol as plasticizer and chitosan as co-polymer.



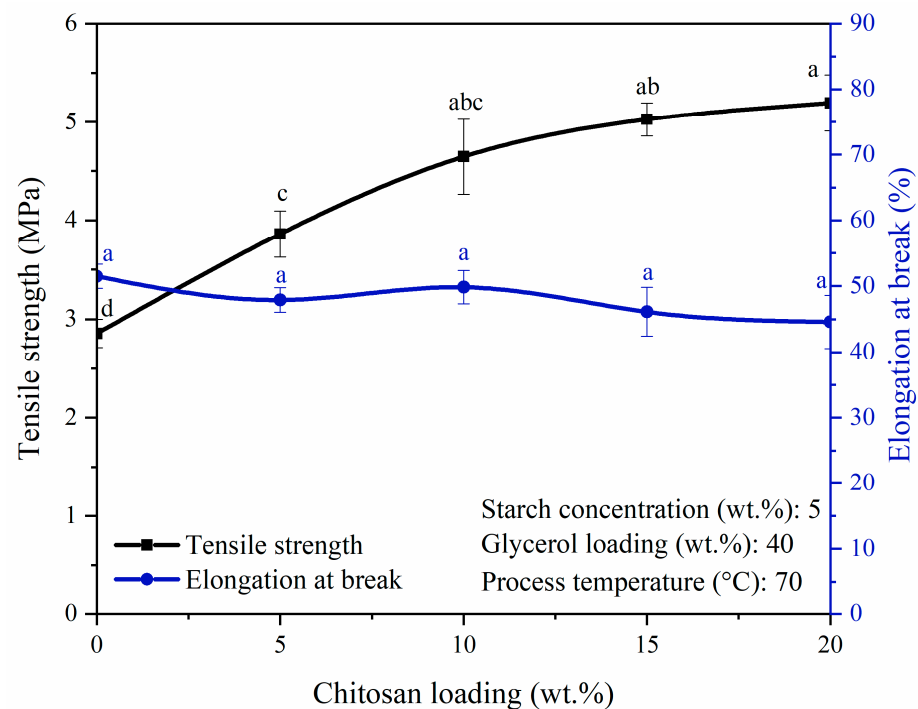
**Figure 4.** Tensile strength and elongation at break of pure starch-based bioplastic films at different process temperatures. Different letters indicate the values are significantly different ( $p < 0.05$ ).

#### 3.1.4. Effect of Chitosan Loading

The effects of chitosan loading (0 wt.% to 20 wt.%, which corresponded to starch: glycerol: chitosan ratio ( $w/w$ ) of 20:8:0 to 20:8:1) on the mechanical properties of bioplastic film are shown in Figure 5. With the addition of 5 wt.% chitosan loading, the tensile strength was improved to 3.86 MPa, which was 1.35 times greater than that of the pure starch-based bioplastic film at 2.86 MPa ( $p < 0.05$ ). Further increase in the chitosan loading to 20 wt.% resulted in the tensile strength increasing to 5.19 MPa ( $p < 0.05$ ). The reinforcement in the tensile strength could be attributed to the presence of more hydrogen bonds between  $\text{NH}_3^+$  of the chitosan and  $\text{OH}^-$  of the corn starch. The amino groups ( $\text{NH}_2$ ) from chitosan were protonated to  $\text{NH}_3^+$  in the acetic acid solution, while the orderly arranged crystalline structure of starch molecules was disrupted during the gelatinization process, resulting in the  $\text{OH}^-$  groups being exposed to form hydrogen bonds with  $\text{NH}_3^+$  of the chitosan. Hence, chemical bonds of the bioplastic film were stronger and harder to be broken [27,38,44]. In contrast to the trend in tensile strength, elongation at break showed a decreasing trend with higher chitosan loading, although the perceived difference was not very significant ( $p > 0.05$ ). Pure starch-based bioplastic film had elongation at break of 51.5%, whereas the chitosan-incorporated starch-based bioplastic film had elongation at break of 47.9% with 5 wt.% chitosan loading. When the chitosan loading was increased to 20 wt.%, the lowest elongation at break of 44.6% was obtained and similar results were reported by Hasan and Rahmayani [4] on the negative effect exerted by the increase in chitosan loading on the film flexibility. Another study published in the literature also demonstrated the improvement of tensile strength but lower elongation of break by 25 wt.% of chitosan loading in starch-based bioplastic film [27]. The tensile strength demonstrated in the



published study [27] was higher than that of the present study (13.52 MPa vs. 5.19 MPa). In addition to the higher chitosan loading demonstrated in the published study (25 wt.% vs. 20 wt.%), this observation could be due to different plasticizers employed in both studies, in which sorbitol was employed. Sorbitol has six hydroxyl groups, which is double the number of hydroxyl groups compared to the glycerol. Sorbitol could bind more hydroxyl groups to the starch via hydrogen bonding, thereby achieving higher tensile strength than the present study [45].



**Figure 5.** Tensile strength and elongation at break of bioplastic films at various chitosan loadings. Different letters indicate the values are significantly different ( $p < 0.05$ ).

In the present study, optimum tensile strength was determined at 20 wt.% chitosan loading. It is apparent that when the additional 5 wt.% chitosan loading was added, chitosan could not be dissolved completely in the starch solution leading to chitosan aggregation and the formation of numerous big lumps.

### 3.2. ANN Modeling Results

A total of 16 experimental runs were conducted using four input variables, i.e., starch concentration, glycerol loading, process temperature and chitosan loading and two output variables, i.e., average tensile strength and average elongation at break. The experimental data were randomly divided into 60% for the training, 20% for testing and 20% for validation. Based on the heuristic procedure, the optimum numbers of hidden neurons that fulfilled the requirements of minimum MSE and maximum R were 4 for tensile strength and 3 for elongation at break. Thus, the best topology was found to be 4-4-1 for tensile strength (Figure 6) and 4-3-1 for elongation at break (Figure 7) prediction. The values of R for training, validation, test and all, for tensile strength were 1, 0.97975, 0.99123 and 0.99552, respectively, (Figure 8). For elongation at break, the values of R for training, validation, test and all, were 0.99149, 0.99897, 0.99781 and 0.98593, respectively, (Figure 9). It could be observed from Tables 2 and 3 that the values of  $R^2$  for tensile strength and elongation at break were 0.9955 and 0.9859, respectively, which were very close to unity. Therefore, it could be concluded that the model had good fit with the experimental data [46].

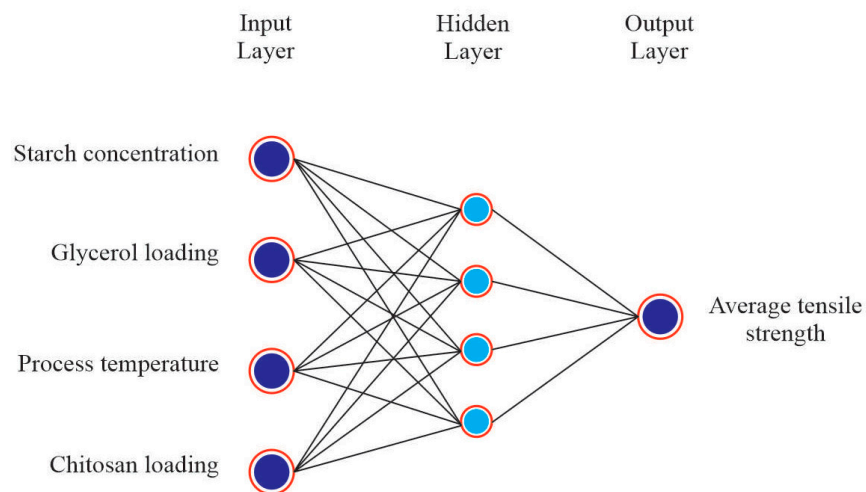


Figure 6. Architecture of ANN model for tensile strength.

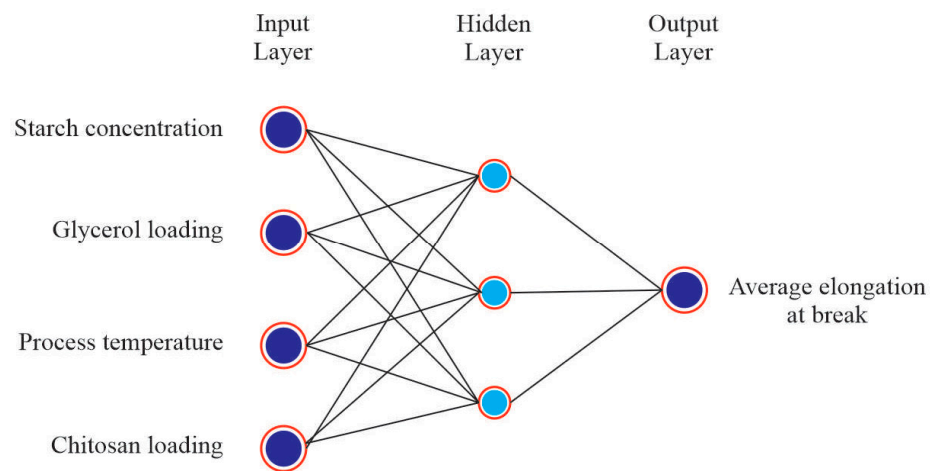


Figure 7. Architecture of ANN model for elongation at break.

Table 2. Comparison of the experimental tensile strength and predicted tensile strength by ANN model.

Experimental Run	Starch Concentration (wt.%)	Glycerol Loading (wt.%)	Process Temperature (°C)	Chitosan Loading (wt.%)	Experimental Tensile Strength (MPa)	Predicted Tensile Strength (MPa)
1	2.5	40	70	0	3.22	3.22
2	5	40	70	0	2.86	2.85
3	7.5	40	70	0	0.78	0.78
4	5	50	70	0	2.30	2.29
5	5	60	70	0	1.36	1.30
6	5	70	70	0	0.42	0.51
7	5	80	70	0	0.24	0.23
8	5	40	65	0	1.52	1.52
9	5	40	75	0	2.50	2.94
10	5	40	80	0	2.27	2.20
11	5	40	85	0	2.15	2.14
12	5	40	90	0	1.96	2.34
13	5	40	70	5	3.86	3.86
14	5	40	70	10	4.65	4.68
15	5	40	70	15	5.03	5.02
16	5	40	70	20	5.19	5.18
R <sup>2</sup>	0.9955					

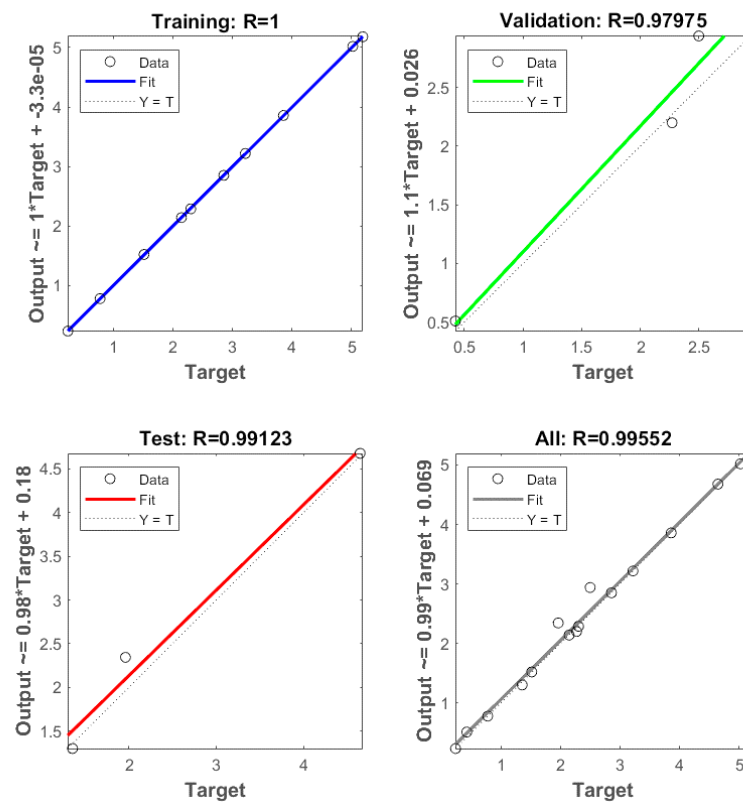


Figure 8. Coefficient of correlation (R) values of training, validation testing and overall datasets, for tensile strength.

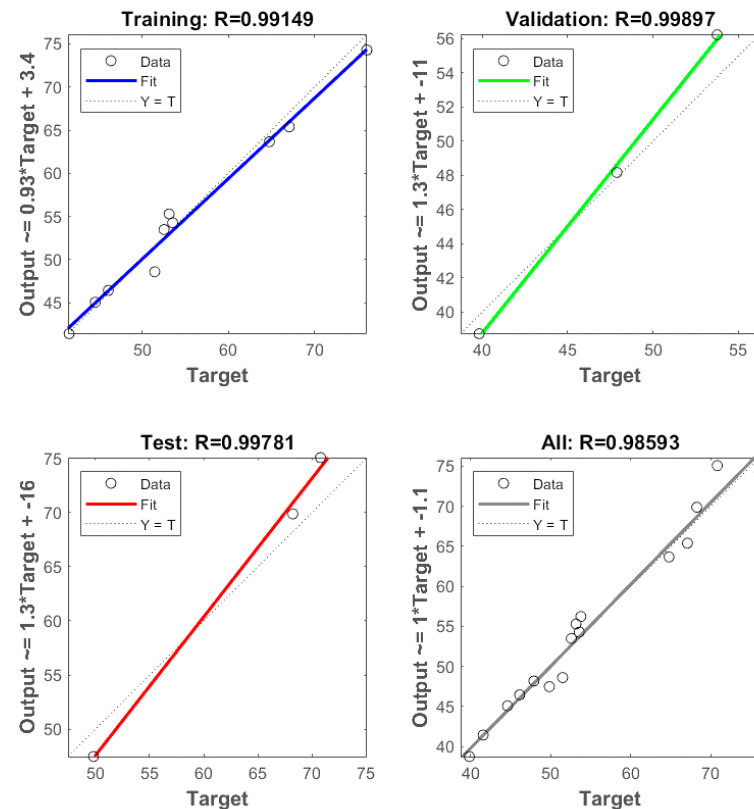


Figure 9. Coefficient of correlation (R) values of training, validation, testing and overall datasets, for elongation at break.

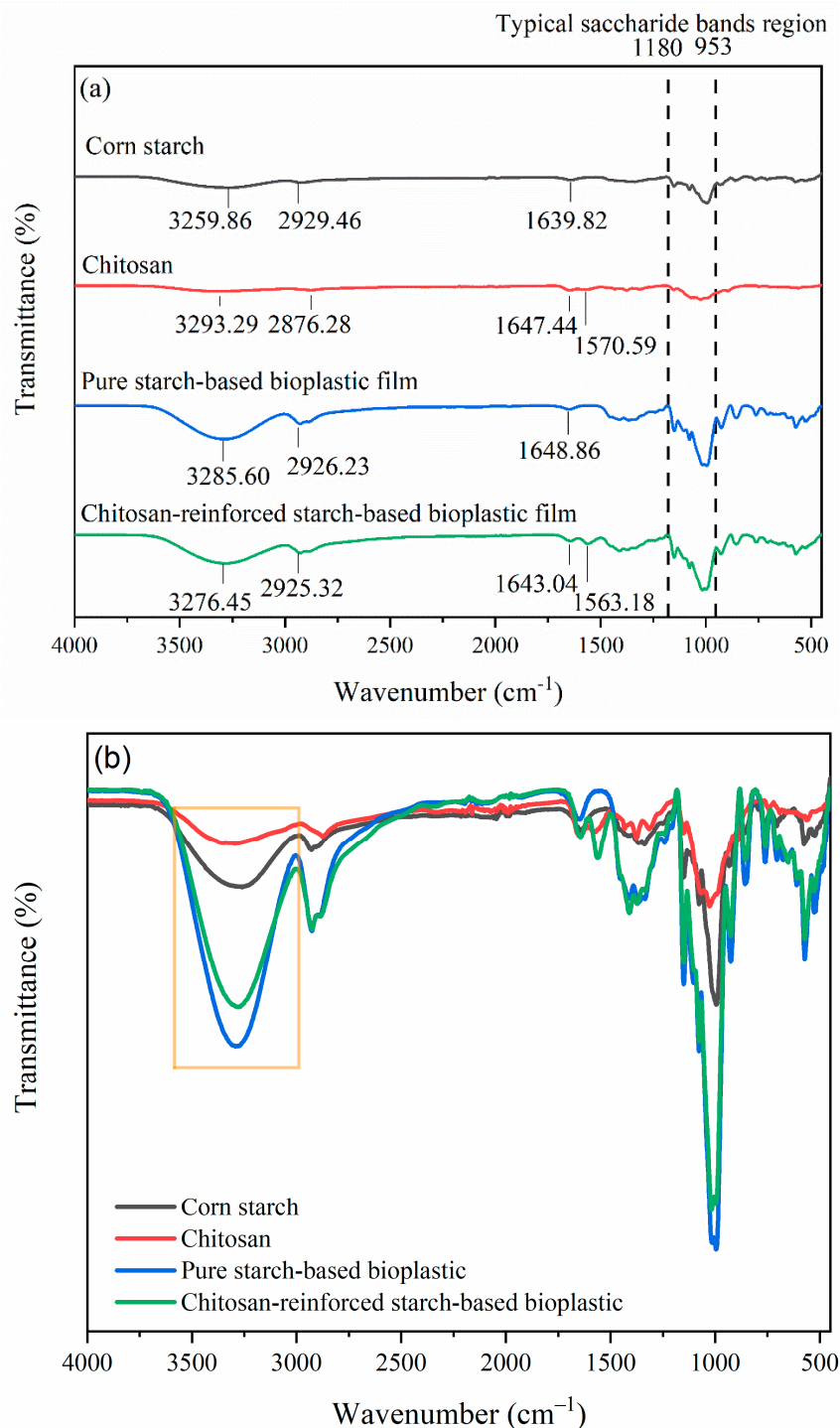
**Table 3.** Comparison of the experimental elongation at break and predicted elongation at break by ANN model.

Experimental Run	Starch Concentration (wt.%)	Glycerol Loading (wt.%)	Process Temperature (°C)	Chitosan Loading (wt.%)	Experimental Elongation at Break (%)	Predicted Elongation at Break (%)
1	2.5	40	70	0	53.6	54.3
2	5	40	70	0	51.5	48.6
3	7.5	40	70	0	41.6	41.4
4	5	50	70	0	53.8	56.2
5	5	60	70	0	64.8	63.7
6	5	70	70	0	68.2	69.9
7	5	80	70	0	76.1	74.3
8	5	40	65	0	39.8	38.7
9	5	40	75	0	52.6	53.5
10	5	40	80	0	53.2	55.3
11	5	40	85	0	67.1	65.4
12	5	40	90	0	70.8	75.1
13	5	40	70	5	47.9	48.2
14	5	40	70	10	49.8	47.5
15	5	40	70	15	46.1	46.4
16	5	40	70	20	44.6	45.1
R <sup>2</sup>	0.9859					

### 3.3. FTIR

FTIR spectra of pure starch-based bioplastic film and chitosan-reinforced starch-based bioplastic films are compared with the spectra of corn starch and chitosan powders as shown in Figure 10a. The following bands observed in the corn starch powder at  $3259.86\text{ cm}^{-1}$ ,  $2929.46\text{ cm}^{-1}$  and  $1639.82\text{ cm}^{-1}$  corresponded to O–H stretching,  $-\text{CH}_2$  stretching vibrations and O–H bending of water, respectively, [47]. Chitosan powder showed characteristic peaks at  $3293.29\text{ cm}^{-1}$ , which were attributed to N–H and O–H stretching,  $1647.44\text{ cm}^{-1}$ , which was assigned to amide I (C=O stretching) and  $1570.59\text{ cm}^{-1}$ , which was assigned to amide II (C–N stretching and C–N–H bending vibrations) [48]. In the spectra of pure starch-based bioplastic film, the peaks observed at  $3285.60\text{ cm}^{-1}$  and  $2926.23\text{ cm}^{-1}$  were associated with O–H and  $-\text{CH}_2$  stretching vibrations, respectively, [49]. The bands at  $1648.46\text{ cm}^{-1}$  and  $1411.63\text{ cm}^{-1}$  were, respectively, assigned to the O–H bending of water and  $\text{CH}_2$  groups [50]. The typical region of saccharide bands covered  $1180\text{--}953\text{ cm}^{-1}$  in which the peaks at  $1150.46\text{ cm}^{-1}$  and  $1077.95\text{ cm}^{-1}$  were associated to stretching vibration of C–O in C–O–H groups, while the bands at  $1015.68\text{ cm}^{-1}$  and  $995.09\text{ cm}^{-1}$  were attributed to C–O in C–O–C groups [51,52].

Changes in FTIR spectrum were observed after chitosan was added to the starch-based bioplastic film. As compared with the chitosan powder, the amide I and amide II characteristic peaks of chitosan in the spectra of chitosan-reinforced starch-based bioplastic film were shifted from  $1647.44\text{ cm}^{-1}$  to  $1643.04\text{ cm}^{-1}$  and  $1570.59\text{ cm}^{-1}$  to  $1563.18\text{ cm}^{-1}$ , respectively. The findings illustrated the interactions between hydroxyl groups of starch and amino groups of chitosan, which had promoted the compatibility of starch and chitosan [44,53]. Furthermore, the characteristic peak of inter- and intra-molecular hydrogen bonds in starch ( $3259.86\text{ cm}^{-1}$ ) and chitosan ( $3293.29\text{ cm}^{-1}$ ) were shifted to  $3276.45\text{ cm}^{-1}$ . This shift revealed the formation of inter- and intra-molecular hydrogen bonding between starch and chitosan [53]. Increase in the intensities of absorption peaks were noted in both pure starch-based and chitosan-reinforced starch-based bioplastic films relative to that of the corn starch and the chitosan powders as illustrated in the inset of Figure 10b. This was resulted from the overlapping of chemical bonds, indicating the presence of strong interaction between the molecules of different material components such as starch, chitosan and glycerol [54].

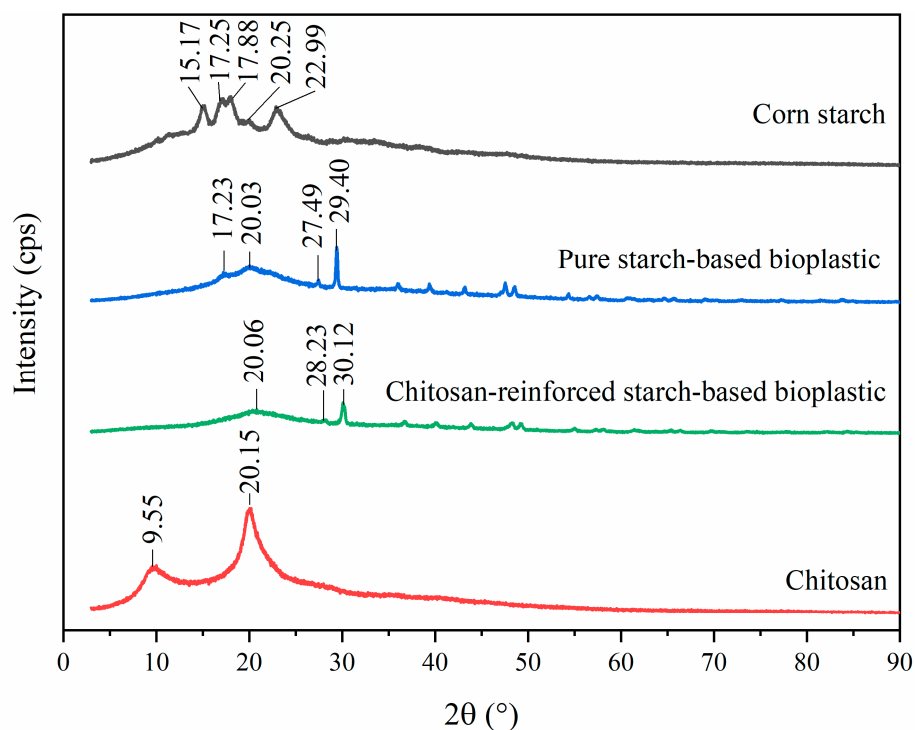


**Figure 10.** (a) FTIR spectra and (b) overlapping FTIR spectra of corn starch, chitosan powders, pure starch-based and chitosan-reinforced starch-based bioplastic films.

### 3.4. XRD

Figure 11 presents the XRD profiles of corn starch powder, pure starch-based bioplastic film, chitosan-reinforced starch-based bioplastic film and chitosan powder. The corn starch powder had diffraction peaks at 15.17°, 17.25°, 17.88°, 20.25° and 22.99°, which corresponded to A-type crystalline structure [12,55,56]. Unlike that of the corn starch powder, the pure starch-based bioplastic film exhibited a different XRD pattern with peaks at 17.23°, 20.03°, 27.49° and 29.40°. This probably could be explained by the glycerol molecules that replaced the inter- and intramolecular hydrogen bonds, which had disrupted

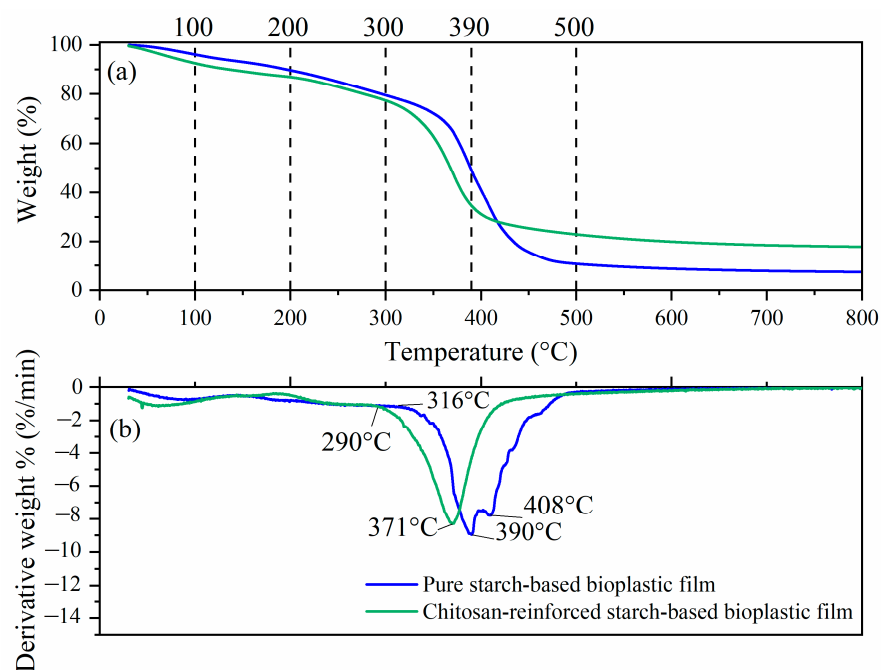
the crystallinity of starch during the bioplastic film fabrication [52]. The chitosan powder was in a crystalline state as two main diffraction peaks ( $2\theta = 9.55^\circ$  and  $20.15^\circ$ ) were manifested in the XRD profile [44]. When chitosan was added into the pure starch-based bioplastic film, the crystallinity of the blend film (chitosan-reinforced starch-based bioplastic film) was decreased as reflected in the lower diffraction peaks at  $20.06^\circ$ ,  $28.23^\circ$  and  $30.12^\circ$ . A similar finding was also discovered by other researchers [50,53,57]. The disappearance of peak at  $17.23^\circ$  in chitosan-reinforced starch-based bioplastic film could be considered as further evidence of the interaction between starch and chitosan [53]. In addition, the characteristic peak of chitosan ( $9.55^\circ$ ) did not appear in the chitosan reinforced starch-based bioplastic film. This could be due to the formation of intermolecular hydrogen bonding between starch and chitosan, which did not favor the crystallization of starch but had altered the chitosan structure [53]. These results further corroborated the FTIR results in which there was miscibility between corn starch and chitosan owing to their intermolecular interaction.



**Figure 11.** XRD profiles of corn starch, pure starch-based bioplastic film, chitosan-reinforced starch-based bioplastic film and chitosan.

### 3.5. Thermal Analysis

The TGA and derivative thermogravimetric (DTG) profiles of pure starch-based and chitosan-reinforced starch-based bioplastic films are shown in Figure 12a,b, respectively. There are five weight losses in both films. The first weight loss occurred between  $\sim 30^\circ\text{C}$  and  $\sim 100^\circ\text{C}$  was associated with the evaporation of free water [18]. The second weight loss took place between  $\sim 100^\circ\text{C}$  and  $\sim 200^\circ\text{C}$  was related to the evaporation of moisture from the bioplastic films [58]. The third weight loss range of  $\sim 200^\circ\text{C}$  to  $\sim 300^\circ\text{C}$  corresponded to the thermal decomposition of starch in bioplastic films and degradation of glycerol (boiling point of  $290^\circ\text{C}$ ) [18]. Starch contained amylose particles, which could form carbon, hydrogen and oxygen in its volatile state [59]. Around  $300^\circ\text{C}$  to  $\sim 500^\circ\text{C}$ , compounds with lower molecular weight such as plasticizer (glycerol) and additive (chitosan) were released as well as the degradation of starch which took place at  $408^\circ\text{C}$ , as shown in Figure 12b. Beyond  $500^\circ\text{C}$ , pyrolysis of carbonated compounds took place resulted in inorganic materials in the remaining residue samples [60].



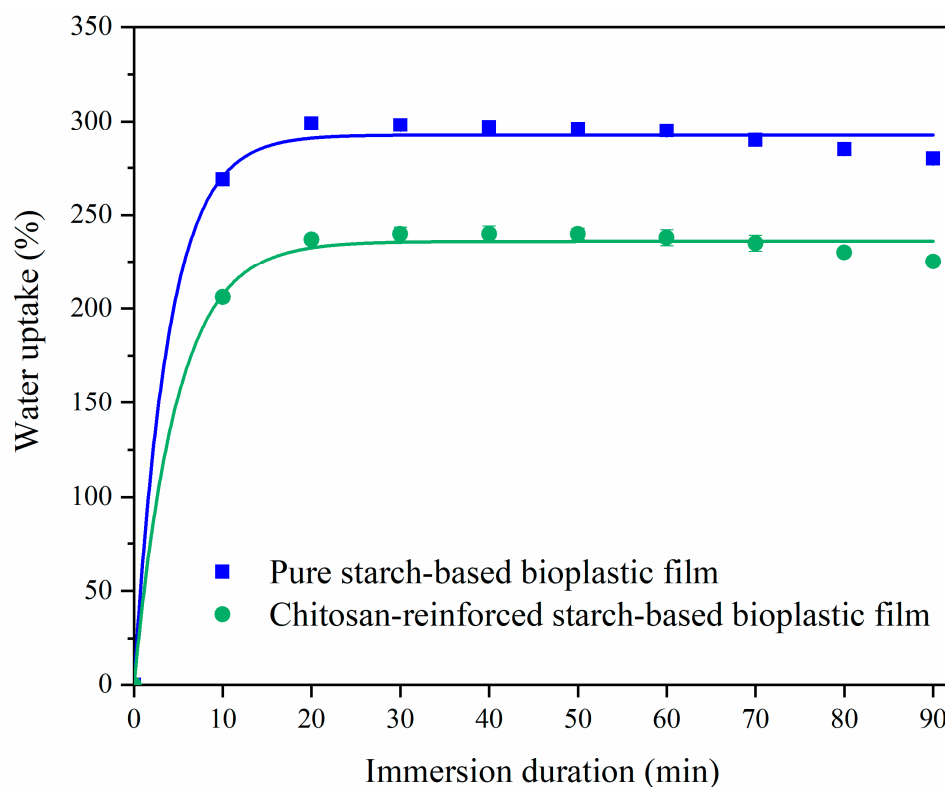
**Figure 12.** (a) TGA and (b) DTG curves of pure starch-based and chitosan-reinforced starch-based bioplastic films.

From the DTG curve as shown in Figure 12b, the decomposition temperatures of pure starch-based and chitosan reinforced starch-based bioplastic films were recorded at 390 °C and 371 °C, respectively. The latter film had a much lower decomposition temperature, which might be attributed to the presence of acetic acid that disrupted the inter- and intra-molecular hydrogen bonds to induce thermal degradation [61,62]. Another reason could be ascribed to the decreased crystallinity in the chitosan-reinforced starch-based bioplastic film, as previously discussed in the XRD results. Film with lower crystallinity would have more molecular movement in the polymer chains and thereby lower the degradation temperature [63,64]. As approaching 900 °C, the chitosan-reinforced starch-based bioplastic film was found to have 17% residue, which was 10% higher than pure starch-based bioplastic film with 7% residue. From the DTG curves, as shown in Figure 12b, the results suggested that pure starch-based and chitosan-reinforced starch-based bioplastic films should be subjected to applications below 316 °C and 290 °C, respectively, without degradation or loss of their characteristics. Most of the applications associated with this type of bioplastic, such as packaging and containers, are usually operated from room temperature to slightly higher than 100 °C. These operating temperatures are well below the thermal stability of the bioplastic films.

### 3.6. Water Uptake Test

Water uptake capability of bioplastic film is directly related to its hydrophilic nature [37]. The water uptake trends of pure starch-based and chitosan-reinforced starch-based bioplastic films of the study are depicted in Figure 13. Comparatively, chitosan-reinforced starch-based bioplastic film had a lower water uptake capability. Both types of bioplastic films absorbed water rapidly within the first 10 min of water immersion, indicating their strong hydrophilic nature. This was due to the abundance of free hydroxyl groups available in starch and chitosan, which would allow large amount of water to penetrate into the film within minutes [10]. After 10 min of immersion time, starch-based bioplastic film absorbed 270% water and chitosan-reinforced starch-based bioplastic film absorbed 206% water. Beyond 40 min immersion period, pure starch-based bioplastic film reached its maximum water uptake of 302%, whereas the chitosan-reinforced starch-based bioplastic film only achieved a maximum water uptake of 251% after 50 min immersion.

Once exceeded their respective optimum uptake threshold, both the pure starch-based and chitosan-reinforced starch-based bioplastic films showed a gradual decrease in water uptake and mass losses. The pure starch bioplastic film can be dissolved in water faster than chitosan-reinforced starch-based bioplastic film, indicating that the latter film possesses better stability in water. When the water immersion time was prolonged to 90 min, both pure starch and chitosan-reinforced starch-based bioplastic films showed a decrease in water uptakes at 281% and 217%, respectively. Comparing the maximum water uptake capability between pure starch-based bioplastic film (302%) and chitosan-reinforced starch-based bioplastic film (251%), the larger water uptake capability demonstrated by the latter suggesting that chitosan could be used to improve the water resistance of pure starch-based bioplastic film attributing to the hydrophilic nature of amylose. Water molecules were easily absorbed by the pure starch-based bioplastic film during immersion [4]. With the incorporation of chitosan into the starch-based bioplastic film, the interlink network formed between starch and chitosan could prevent water molecules penetrating through the film [10]. Additionally, from another perspective, water resistance of bioplastic film was enhanced by the hydrophobic nature of chitosan, which has mitigated the hydrophilic nature of starch, diminishing their interactions with water molecules [4,65]. The observation is in agreement with the work of Anggraini et al. [21] on sago starch-chitosan-sorbitol bioplastic film reporting a water uptake of 204.97% for bioplastic film without chitosan, and a much reduced water uptake of 130.31% in 20 wt.% chitosan-loaded bioplastic film.



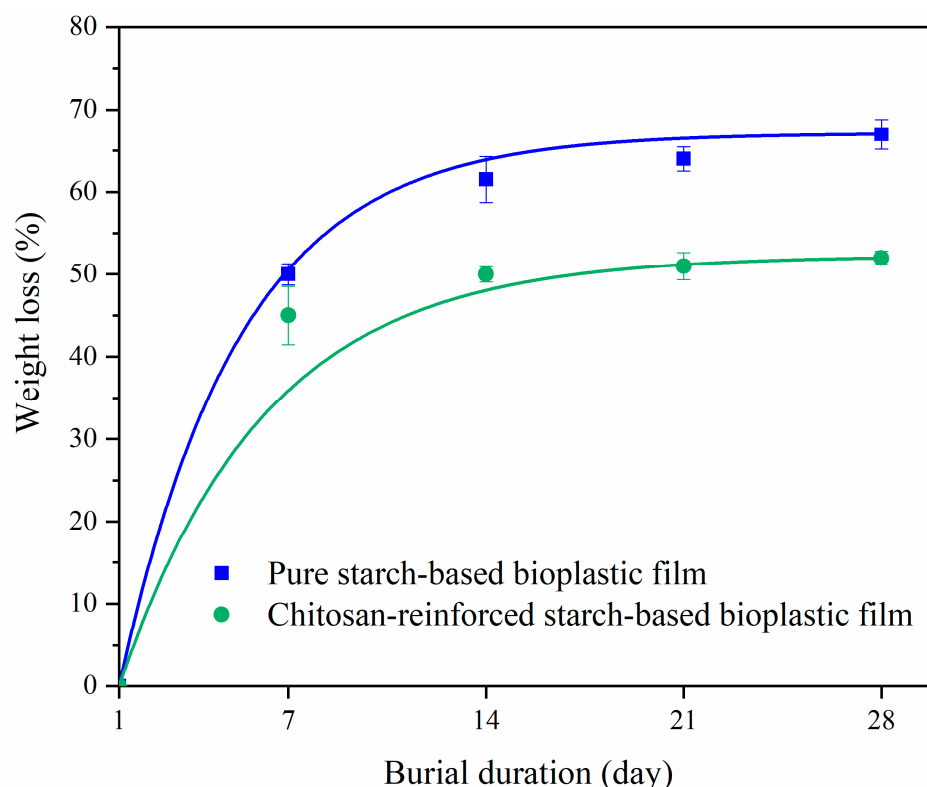
**Figure 13.** Water uptake percentages of pure starch-based and chitosan-reinforced starch-based bioplastic films at various immersion durations.

### 3.7. Biodegradation Test

The percentage weight losses of pure starch-based and chitosan-reinforced starch-based bioplastic films are displayed in Figure 14. The weight losses of both bioplastic films increased with the burial time, suggesting the degradation of bioplastic films. On day 7, both films were found to have degraded by more than 40% of their initial weight. Pure starch-based bioplastic film degraded by 53.6% and chitosan-reinforced starch-based bioplastic film degraded by 47.5%. There was no significant weight loss for both bioplastic



films on the 2nd and the 3rd week. On day 28, the weight losses of pure starch-based and chitosan-reinforced starch-based bioplastic films, respectively, reached 67.7% and 52.1%. Pure starch-based bioplastic film showed more weight loss than the chitosan-reinforced starch-based bioplastic film throughout the burial period, which could be due to higher hydrophilicity of the starch matrix [66]. The chitosan-reinforced starch-based bioplastic film had slower degradation, which might be due to the antimicrobial properties of chitosan as well as the interaction between starch and chitosan via hydrogen bonding, which possibly reduced the hydrophilicity of the starch matrix and thus slowing down the biodegradation rate [34,67].



**Figure 14.** Weight loss percentages of pure starch and chitosan-reinforced starch-based bioplastic films during burial period.

#### 4. Conclusions

Chitosan-reinforced starch-based bioplastic film was successfully prepared through the solution casting and evaporation method. This study described the effects of various parameters in attaining the optimum tensile strength of bioplastic film, and also confirmed the relationship between starch concentration and process temperature with the gelatinized duration. Higher starch concentration and process temperature would shorten the gelatinized duration and negatively affect the tensile strength. Using the hydrophobic nature of chitosan as a reinforcement agent not only could help to enhance the tensile strength, but also could improve the water resistance of starch-based bioplastic film. Although chitosan-reinforced starch-based bioplastic film could only be subjected to application below 290 °C, which was lower than pure starch-based bioplastic film (316 °C), it exhibited more than 50% faster biodegradability property, which will be greener for the environment.

This study has also laid the foundation in developing similar types of biodegradable chitosan-reinforced starch-based bioplastic film, which could be used to replace petroleum-based plastics. The formulation of composition based on corn starch as a matrix would also be beneficial in designing a more complete experimental study using starch derived from other agricultural waste. Although the present study demonstrated that the mechanical properties of bioplastic film were affected by the starch concentration, the relationship

between the starch concentration and the mechanical properties of the bioplastic films is still not conclusive. Therefore, more empirical studies are required to refine and improve the reported findings.

**Author Contributions:** Conceptualization, S.X.T., H.C.O. and S.L.; methodology, S.X.T.; software, S.X.T. and F.K.; validation, S.X.T. and F.K.; formal analysis, S.X.T. and F.K.; investigation, S.X.T.; data curation, S.X.T. and F.K.; writing—original draft preparation, S.X.T.; writing—review and editing, A.A., G.C.N., H.C.O., S.L. and Y.L.P.; visualization, H.C.O. and Y.L.P.; supervision, A.A., G.C.N. and S.L.; project administration, S.L. and G.C.N.; funding acquisition, S.L. and G.C.N. All authors have read and agreed to the published version of the manuscript.

**Funding:** The research was funded under Fundamental Research Grant Scheme (FRGS/1/2018/TK10/UTAR/02/1) from Ministry of Education, Malaysia, Universiti Malaya, Kuala Lumpur under RU Grant (GPF059A-2020) and Universiti Tunku Abdul Rahman Research Grant (UTARRF/6200-W83).

**Data Availability Statement:** The data presented in this study are available on request from the corresponding author.

**Conflicts of Interest:** The authors declare no conflict of interest.

## References

1. Pathak, S.; Sneha, C.; Mathew, B.B. Bioplastics: Its timeline based scenario & challenges. *J. Polym. Biopolym. Phys. Chem.* **2014**, *2*, 84–90. [[CrossRef](#)]
2. Zeller, M.A.; Hunt, R.; Jones, A.; Sharma, S. Bioplastics and their thermoplastic blends from Spirulina and Chlorella microalgae. *J. Appl. Polym. Sci.* **2013**, *130*, 3263–3275. [[CrossRef](#)]
3. Thiruchelvi, R.; Das, A.; Sikdar, E. Bioplastics as better alternative to petro plastic. *Mater. Today Proc.* **2021**, *37*, 1634–1639. [[CrossRef](#)]
4. Hasan, M.; Rahmayani, R. Bioplastic from Chitosan and Yellow Pumpkin Starch with Castor Oil as Plasticizer. *Proc. IOP Conf. Ser. Mater. Sci. Eng.* **2018**, *333*, 012087. [[CrossRef](#)]
5. Jiménez-Rosado, M.; Bouroudian, E.; Perez-Puyana, V.; Guerrero, A.; Romero, A. Evaluation of different strengthening methods in the mechanical and functional properties of soy protein-based bioplastics. *J. Clean. Prod.* **2020**, *262*, 121517. [[CrossRef](#)]
6. Ginting, M.H.S.; Hasibuan, R.; Lubis, M.; Tanjung, D.; Iqbal, N. Effect of Hydrochloric Acid Concentration as Chitosan Solvent on Mechanical Properties of Bioplastics from Durian Seed Starch (*Durio Zibethinus*) with Filler Chitosan and Plasticizer Sorbitol. *Proc. IOP Conf. Ser. Mater. Sci. Eng.* **2017**, *180*, 012126. [[CrossRef](#)]
7. Ginting, M.H.S.; Tarigan, F.R.; Singgih, A.M. Effect of gelatinization temperature and chitosan on mechanical properties of bioplastics from avocado seed starch (*Persea Americana* mill) with plasticizer glycerol. *Int. J. Eng. Sci.* **2015**, *4*, 36–43.
8. de Azévedo, L.C.; Rovani, S.; Santos, J.J.; Dias, D.B.; Nascimento, S.S.; Oliveira, F.F.; Silva, L.G.; Fungaro, D.A. Study of Renewable Silica Powder Influence in the Preparation of Bioplastics from Corn and Potato Starch. *J. Polym. Environ.* **2021**, *29*, 707–720. [[CrossRef](#)]
9. Nissa, R.; Fikriyyah, A.; Abdullah, A.; Pudjiraharti, S. Preliminary study of biodegradability of starch-based bioplastics using ASTM G21-70, dip-hanging, and Soil Burial Test methods. *Proc. IOP Conf. Ser. Earth Environ. Sci.* **2019**, *277*, 012007. [[CrossRef](#)]
10. Akter, N.; Khan, R.A.; Tuhin, M.O.; Haque, M.E.; Nurnabi, M.; Parvin, F.; Islam, R. Thermomechanical, barrier, and morphological properties of chitosan-reinforced starch-based biodegradable composite films. *J. Thermoplast. Compos. Mater.* **2014**, *27*, 933–948. [[CrossRef](#)]
11. Talón, E.; Trifkovic, K.T.; Nedovic, V.A.; Bugarski, B.M.; Vargas, M.; Chiralt, A.; González-Martínez, C. Antioxidant edible films based on chitosan and starch containing polyphenols from thyme extracts. *Carbohydr. Polym.* **2017**, *157*, 1153–1161. [[CrossRef](#)] [[PubMed](#)]
12. Dome, K.; Podgorbunskikh, E.; Bychkov, A.; Lomovsky, O. Changes in the Crystallinity Degree of Starch Having Different Types of Crystal Structure after Mechanical Pretreatment. *Polymers* **2020**, *12*, 641. [[CrossRef](#)] [[PubMed](#)]
13. Souza, A.; Benze, R.; Ferrão, E.; Ditchfield, C.; Coelho, A.; Tadini, C. Cassava starch biodegradable films: Influence of glycerol and clay nanoparticles content on tensile and barrier properties and glass transition temperature. *LWT-Food Sci. Technol.* **2012**, *46*, 110–117. [[CrossRef](#)]
14. Jakubowska, E.; Gierszewska, M.; Nowaczyk, J.; Olewnik-Kruszkowska, E. Physicochemical and storage properties of chitosan-based films plasticized with deep eutectic solvent. *Food Hydrocoll.* **2020**, *108*, 106007. [[CrossRef](#)]
15. Zdanowicz, M.; Jędrzejewski, R.; Pilawka, R. Deep eutectic solvents as simultaneous plasticizing and crosslinking agents for starch. *Int. J. Biol. Macromol.* **2019**, *129*, 1040–1046. [[CrossRef](#)]
16. Chan, Y.; Phang, S.; Tee, T.; Lee, T.; Soo, T. Preliminary Study of Mechanical Properties in Thermoplastic Starch (TPS)/Coffee-Waste-Derived Fillers Composites. In Proceedings of the Engineering Undergraduate Research Catalyst Conference (EURECA), Selangor, Malaysia, 1–2 July 2015; pp. 1–14.

17. Mallakpour, S. Fructose functionalized MWCNT as a filler for starch nanocomposites: Fabrication and characterizations. *Prog. Org. Coat.* **2018**, *114*, 244–249. [[CrossRef](#)]
18. de Azevedo, L.C.; Rovani, S.; Santos, J.J.; Dias, D.B.; Nascimento, S.S.; Oliveira, F.F.; Silva, L.G.; Fungaro, D.A. Biodegradable films derived from corn and potato starch and study of the effect of silicate extracted from sugarcane waste ash. *ACS Appl. Polym. Mater.* **2020**, *2*, 2160–2169. [[CrossRef](#)]
19. Agustin, M.B.; Ahmmad, B.; Alonzo, S.M.M.; Patriana, F.M. Bioplastic based on starch and cellulose nanocrystals from rice straw. *J. Reinf. Plast. Compos.* **2014**, *33*, 2205–2213. [[CrossRef](#)]
20. Méité, N.; Konan, L.K.; Tognonvi, M.T.; Doubi, B.I.H.G.; Gomina, M.; Oyetola, S. Properties of hydric and biodegradability of cassava starch-based bioplastics reinforced with thermally modified kaolin. *Carbohydr. Polym.* **2020**, *254*, 117322. [[CrossRef](#)]
21. Anggraini, T.; Ulfimarjan, A.F.; Yenrina, R. The effect of chitosan concentration on the characteristics of sago (metroxylyon sp) starch bioplastics. *Res. J. Pharm. Biol. Chem. Sci.* **2017**, *8*, 1339–1351. [[CrossRef](#)]
22. Lopez, O.; Garcia, M.A.; Villar, M.A.; Gentili, A.; Rodriguez, M.; Albertengo, L. Thermo-compression of biodegradable thermo-plastic corn starch films containing chitin and chitosan. *LWT-Food Sci. Technol.* **2014**, *57*, 106–115. [[CrossRef](#)]
23. Zakaria, N.; Muhammad, N.; Sandu, A.; Abdullah, M. Effect of Mixing Temperature on Characteristics of Thermoplastic Potato Starch Film. *Drug Deliv. Syst.* **2018**, *5*, 7. [[CrossRef](#)]
24. Yusof, Y.; Shukur, M.; Illias, H.; Kadir, M. Conductivity and electrical properties of corn starch–chitosan blend biopolymer electrolyte incorporated with ammonium iodide. *Phys. Scr.* **2014**, *89*, 035701. [[CrossRef](#)]
25. Fakhouri, F.M.; Costa, D.; Yamashita, F.; Martelli, S.M.; Jesus, R.C.; Alganer, K.; Collares-Queiroz, F.P.; Innocentini-Mei, L.H. Comparative study of processing methods for starch/gelatin films. *Carbohydr. Polym.* **2013**, *95*, 681–689. [[CrossRef](#)]
26. Kartika, T.; Harahap, M.B.; Ginting, M.H.S. Utilization of mango seed starch in manufacture of bioplastic reinforced with microparticle clay using glycerol as plasticizer. *Proc. IOP Conf. Ser. Mater. Sci. Eng.* **2018**, *309*, 012068.
27. Lubis, M.; Harahap, M.; Manullang, A.; Ginting, M.; Sartika, M. Utilization starch of jackfruit seed (*Artocarpus heterophyllus*) as raw material for bioplastics manufacturing using sorbitol as plasticizer and chitosan as filler. *Proc. J. Phys. Conf. Ser.* **2017**, *801*, 012014. [[CrossRef](#)]
28. Lubis, M.; Harahap, M.B.; Ginting, M.H.S.; Sartika, M.; Azmi, H. Production of bioplastic from avocado seed starch reinforced with microcrystalline cellulose from sugar palm fibers. *J. Eng. Sci. Technol.* **2018**, *13*, 381–393.
29. Maulida, S.M.; Tarigan, P. Production of starch based bioplastic from cassava peel reinforced with microcrystalline cellulose avicel PH101 using sorbitol as plasticizer. *Proc. J. Phys. Conf. Ser.* **2016**, *710*, 012012. [[CrossRef](#)]
30. Salehudin, M.H.; Salleh, E.; Mamat, S.N.H.; Muhamad, I.I. Starch based active packaging film reinforced with empty fruit bunch (EFB) cellulose nanofiber. *Procedia Chem.* **2014**, *9*, 23–33. [[CrossRef](#)]
31. Maran, J.P.; Sivakumar, V.; Thirugnanasambandham, K.; Sridhar, R. Artificial neural network and response surface methodology modeling in mass transfer parameters predictions during osmotic dehydration of *Carica papaya* L. *Alex. Eng. J.* **2013**, *52*, 507–516. [[CrossRef](#)]
32. Abrial, H.; Basri, A.; Muhammad, F.; Fernando, Y.; Hafizulhaq, F.; Mahardika, M.; Sugiarti, E.; Sapuan, S.; Ilyas, R.; Stephane, I. A simple method for improving the properties of the sago starch films prepared by using ultrasonication treatment. *Food Hydrocoll.* **2019**, *93*, 276–283. [[CrossRef](#)]
33. Wu, C.-S. Renewable resource-based green composites of surface-treated spent coffee grounds and polylactide: Characterisation and biodegradability. *Polym. Degrad. Stab.* **2015**, *121*, 51–59. [[CrossRef](#)]
34. Sapei, L.; Padmawijaya, K.S.; Sijayanti, O.; Wardhana, P.J. The effect of banana starch concentration on the properties of chitosan-starch bioplastics. *J. Chem. Pharm. Res.* **2015**, *7*, 101–105.
35. Sultan, N.F.K.; Johari, W.L.W. The development of banana peel/corn starch bioplastic film: A preliminary study. *Bioremediation Sci. Technol. Res.* **2017**, *5*, 12–17.
36. Samer, M.; Khalefa, Z.; Abdelall, T.; Moawya, W.; Farouk, A.; Abdelaziz, S.; Soliman, N.; Salah, A.; Gomaa, M.; Mohamed, M. Bioplastics production from agricultural crop residues. *Agric. Eng. Int. CIGR J.* **2019**, *21*, 190–194.
37. Almeida, C.M.; Magalhães, J.M.; Souza, H.K.; Gonçalves, M.P. The role of choline chloride-based deep eutectic solvent and curcumin on chitosan films properties. *Food Hydrocoll.* **2018**, *81*, 456–466. [[CrossRef](#)]
38. Ginting, M.H.S.; Kristiani, M.; Amelia, Y.; Hasibuan, R. The effect of chitosan, sorbitol, and heating temperature bioplastic solution on mechanical properties of bioplastic from durian seed starch (*Durio zibehinus*). *Int. J. Eng. Res. Appl.* **2015**, *6*, 33–38.
39. Santana, R.F.; Bonomo, R.C.F.; Gandolfi, O.R.R.; Rodrigues, L.B.; Santos, L.S.; dos Santos Pires, A.C.; de Oliveira, C.P.; Fontan, R.d.C.I.; Veloso, C.M. Characterization of starch-based bioplastics from jackfruit seed plasticized with glycerol. *J. Food Sci. Technol.* **2018**, *55*, 278–286. [[CrossRef](#)]
40. Haryanti, P.; Setyawati, R.; Wicaksono, R. Pengaruh Suhu dan Lama Pemanasan Suspensi Pati serta Konsentrasi Butanol terhadap Karakteristik Fisikokimia Pati Tinggi Amilosa dari Tapioka. *Agritech* **2014**, *34*, 308–315. [[CrossRef](#)]
41. Zhao, Y.; Saldaña, M.D. Hydrolysis of cassava starch, chitosan and their mixtures in pressurized hot water media. *J. Supercrit. Fluids* **2019**, *147*, 293–301. [[CrossRef](#)]
42. Wojciechowska, P. The effect of concentration and type of plasticizer on the mechanical properties of cellulose acetate butyrate organic-inorganic hybrids. In *Recent Advances in Plasticizers*; IntechOpen: London, UK, 2012; pp. 141–164.
43. Shi, A.-M.; Wang, L.-J.; Li, D.; Adhikari, B. Characterization of starch films containing starch nanoparticles: Part 1: Physical and mechanical properties. *Carbohydr. Polym.* **2013**, *96*, 593–601. [[CrossRef](#)]

44. Bourtoom, T.; Chinnan, M.S. Preparation and properties of rice starch–chitosan blend biodegradable film. *LWT-Food Sci. Technol.* **2008**, *41*, 1633–1641. [[CrossRef](#)]
45. Zdanowicz, M.; Johansson, C. Mechanical and barrier properties of starch-based films plasticized with two-or three component deep eutectic solvents. *Carbohydr. Polym.* **2016**, *151*, 103–112. [[CrossRef](#)]
46. Silitonga, A.; Masjuki, H.; Ong, H.C.; Yusaf, T.; Kusumo, F.; Mahlia, T. Synthesis and optimization of Hevea brasiliensis and Ricinus communis as feedstock for biodiesel production: A comparative study. *Ind. Crops Prod.* **2016**, *85*, 274–286. [[CrossRef](#)]
47. Minakawa, A.F.; Faria-Tischer, P.C.; Mali, S. Simple ultrasound method to obtain starch micro-and nanoparticles from cassava, corn and yam starches. *Food Chem.* **2019**, *283*, 11–18. [[CrossRef](#)] [[PubMed](#)]
48. Pereira, P.F.; Andrade, C.T. Optimized pH-responsive film based on a eutectic mixture-plasticized chitosan. *Carbohydr. Polym.* **2017**, *165*, 238–246. [[CrossRef](#)] [[PubMed](#)]
49. Valodkar, M.; Thakore, S. Isocyanate crosslinked reactive starch nanoparticles for thermo-responsive conducting applications. *Carbohydr. Res.* **2010**, *345*, 2354–2360. [[CrossRef](#)] [[PubMed](#)]
50. Xu, Y.; Kim, K.; Hanna, M.; Nag, D. Chitosan-starch composite film: Preparation and characterization. *Ind. Crops Prod.* **2005**, *2*, 185–192. [[CrossRef](#)]
51. Namazi, H.; Dadkhah, A. Convenient method for preparation of hydrophobically modified starch nanocrystals with using fatty acids. *Carbohydr. Polym.* **2010**, *79*, 731–737. [[CrossRef](#)]
52. Jiugao, Y.; Ning, W.; Xiaofei, M. The effects of citric acid on the properties of thermoplastic starch plasticized by glycerol. *J. Starch-Stärke* **2005**, *57*, 494–504. [[CrossRef](#)]
53. Liu, H.; Adhikari, R.; Guo, Q.; Adhikari, B. Preparation and characterization of glycerol plasticized (high-amylose) starch–chitosan films. *J. Food Eng.* **2013**, *116*, 588–597. [[CrossRef](#)]
54. Souza, V.G.L.; Pires, J.R.A.; Rodrigues, C.; Rodrigues, P.F.; Lopes, A.; Silva, R.J.; Caldeira, J.; Duarte, M.P.; Fernandes, F.B.; Coelho, I.M.J.C. Physical and morphological characterization of chitosan/montmorillonite films incorporated with ginger essential oil. *Coatings* **2019**, *9*, 700. [[CrossRef](#)]
55. Singh, V.; Ali, S.; Somashekar, R.; Mukherjee, P. Nature of crystallinity in native and acid modified starches. *Int. J. Food Prop.* **2006**, *9*, 845–854. [[CrossRef](#)]
56. Muñoz, L.A.; Pedreschi, F.; Leiva, A.; Aguilera, J.M. Loss of birefringence and swelling behavior in native starch granules: Microstructural and thermal properties. *J. Food Eng.* **2015**, *152*, 65–71. [[CrossRef](#)]
57. Ren, L.; Yan, X.; Zhou, J.; Tong, J.; Su, X. Influence of chitosan concentration on mechanical and barrier properties of corn starch/chitosan films. *Int. J. Biol. Macromol.* **2017**, *105*, 1636–1643. [[CrossRef](#)] [[PubMed](#)]
58. Syafri, E.; Kasim, A.; Abral, H.; Sulungbudi, G.T.; Sanjay, M.; Sari, N.H. Synthesis and characterization of cellulose nanofibers (CNF) ramie reinforced cassava starch hybrid composites. *Int. J. Biol. Macromol.* **2018**, *120*, 578–586. [[CrossRef](#)] [[PubMed](#)]
59. Wahyuningtyas, N.E.; Suryanto, H.; Rudianto, E.; Sukarni, S.; Puspitasari, P. Thermogravimetric and Kinetic Analysis of Cassava Starch Based Bioplastic. *J. Mech. Eng. Sci.* **2017**, *1*, 69–77. [[CrossRef](#)]
60. Krishnamurthy, A.; Amritkumar, P.J.S.A.S. Synthesis and characterization of eco-friendly bioplastic from low-cost plant resources. *SN Appl. Sci.* **2019**, *1*, 1432. [[CrossRef](#)]
61. Mathew, S.; Brahmakumar, M.; Abraham, T.E. Microstructural imaging and characterization of the mechanical, chemical, thermal, and swelling properties of starch–chitosan blend films. *Biopolym. Orig. Res. Biomol.* **2006**, *82*, 176–187. [[CrossRef](#)]
62. Zuraida, A.; Anuar, H.; Yusof, Y. The study of biodegradable thermoplastics sago starch. *Proc. Key Eng. Mater.* **2011**, *471*, 397–402. [[CrossRef](#)]
63. McKeen, L. Introduction to the physical, mechanical, and thermal properties of plastics and elastomers. In *The Effect of Sterilization Methods on Plastics and Elastomers*; Elsevier: Amsterdam, The Netherlands, 2012; pp. 57–84.
64. Klinmalai, P.; Srisa, A.; Laorenza, Y.; Katekhong, W.; Harnkarnsujarit, N. Antifungal and plasticization effects of carvacrol in biodegradable poly (lactic acid) and poly (butylene adipate terephthalate) blend films for bakery packaging. *LWT* **2021**, *152*, 112356. [[CrossRef](#)]
65. Luchese, C.L.; Pavoni, J.M.F.; dos Santos, N.Z.; Quines, L.K.; Pollo, L.D.; Spada, J.C.; Tessaro, I.C. Effect of chitosan addition on the properties of films prepared with corn and cassava starches. *J. Food Sci. Technol.* **2018**, *55*, 2963–2973. [[CrossRef](#)] [[PubMed](#)]
66. Wadaugsorn, K.; Panrong, T.; Wongphan, P.; Harnkarnsujarit, N. Plasticized hydroxypropyl cassava starch blended PBAT for improved clarity blown films: Morphology and properties. *Ind. Crops Prod.* **2022**, *176*, 114311. [[CrossRef](#)]
67. Raspo, M.A.; Gomez, C.G.; Andreatta, A.E. Optimization of antioxidant, mechanical and chemical physical properties of chitosan-sorbitol-gallic acid films by response surface methodology. *Polym. Test.* **2018**, *70*, 180–187. [[CrossRef](#)]



## Article

# Material Extrusion-Based Additive Manufacturing of Poly(Lactic Acid) Antibacterial Filaments—A Case Study of Antimicrobial Properties

Piotr Gruber<sup>1,2</sup>, Viktoria Hoppe<sup>1,2,\*</sup>, Emilia Grochowska<sup>1,2</sup>, Justyna Paleczny<sup>3</sup>, Adam Junka<sup>3</sup>, Irina Smolina<sup>1,2</sup> and Tomasz Kurzynowski<sup>1,2</sup>

<sup>1</sup> Center for Advanced Manufacturing Technologies (CAMT-FPC), Faculty of Mechanical Engineering, Wrocław University of Science and Technology, 50-371 Wrocław, Poland; piotr.gruber@pwr.edu.pl (P.G.); emilia.grochowska@pwr.edu.pl (E.G.); iryna.smolina@pwr.edu.pl (I.S.); tomasz.kurzynowski@pwr.edu.pl (T.K.)

<sup>2</sup> Faculty of Mechanical Engineering, Wrocław University of Science and Technology, 50-371 Wrocław, Poland

<sup>3</sup> Department of Pharmaceutical Microbiology and Parasitology, Wrocław Medical University, 50-556 Wrocław, Poland; justyna.paleczny@student.umw.edu.pl (J.P.); adam.junka@umw.edu.pl (A.J.)

\* Correspondence: Viktoria.hoppe@pwr.edu.pl; Tel.: +48-713-204-446

**Citation:** Gruber, P.; Hoppe, V.; Grochowska, E.; Paleczny, J.; Junka, A.; Smolina, I.; Kurzynowski, T. Material Extrusion-Based Additive Manufacturing of Poly(Lactic Acid) Antibacterial Filaments—A Case Study of Antimicrobial Properties. *Polymers* **2021**, *13*, 4337. <https://doi.org/10.3390/polym13244337>

Academic Editors: José Miguel Ferri, Vicent Fombuena Borràs, Miguel Fernando Aldás Carrasco and Dimitrios Bikiaris

Received: 4 November 2021

Accepted: 7 December 2021

Published: 11 December 2021

**Publisher's Note:** MDPI stays neutral with regard to jurisdictional claims in published maps and institutional affiliations.



**Copyright:** © 2021 by the authors. Licensee MDPI, Basel, Switzerland. This article is an open access article distributed under the terms and conditions of the Creative Commons Attribution (CC BY) license (<https://creativecommons.org/licenses/by/4.0/>).

**Abstract:** In the era of the coronavirus pandemic, one of the most demanding areas was the supply of healthcare systems in essential Personal Protection Equipment (PPE), including face-shields and hands-free door openers. This need, impossible to fill by traditional manufacturing methods, was met by implementing of such emerging technologies as additive manufacturing (AM/3D printing). In this article, Poly(lactic acid) (PLA) filaments for Fused filament fabrication (FFF) technology in the context of the antibacterial properties of finished products were analyzed. The methodology included 2D radiography and scanning electron microscopy (SEM) analysis to determine the presence of antimicrobial additives in the material and their impact on such hospital pathogens as *Staphylococcus aureus*, *Pseudomonas aeruginosa*, and *Clostridium difficile*. The results show that not all tested materials displayed the expected antimicrobial properties after processing in FFF technology. The results showed that in the case of specific species of bacteria, the FFF samples, produced using the declared antibacterial materials, may even stimulate the microbial growth. The novelty of the results relies on methodological approach exceeding scope of ISO 22196 standard and is based on tests with three different species of bacteria in two types of media simulating common body fluids that can be found on frequently touched, nosocomial surfaces. The data presented in this article is of pivotal meaning taking under consideration the increasing interest in application of such products in the clinical setting.

**Keywords:** biomaterials; filaments; antimicrobial; fused filament fabrication (FFF); fused deposition modelling (FDM); Poly(lactic acid) (PLA)

## 1. Introduction

The Food and Drug Administration (FDA) reporting activities indicated that the COVID-19 epidemic would affect the supply chain of medical products and supply disruptions or shortages of critical medical products [1–3]. In the context of the COVID-19 pandemic, the choice of fillers in polymers is, to a significant extent, dictated by copper's strong antiviral and antibacterial effect [4]. In addition, also due to the increased production of personal protective equipment (PPE) and other critical medical materials and devices, the demand for additive technologies has increased [5]. All surfaces should be considered at risk of contamination by microorganisms transmitted from the patients, visitors, and medical personnel in the clinical setting. Microbes (viruses, bacteria, and fungi) can also be dispersed by aerosols or body fluids on medical surfaces. Therefore, biocidal surfaces

are essential in preventing so-called nosocomial (hospital) infections and epidemic outbreaks [6]. Palza [7] suggests that the addition of copper nanoparticles to polymers, thanks to their antimicrobial properties, is a promising application for the development of medical devices protected from microbial contamination. In the polymer–Cu composites, there is a similar tendency, dependent on the number of particles in the polymer, directly related to the release of the metal ions responsible for the antimicrobial effect [8].

Poly(lactic acid) (PLA) is a low-crystalline, biodegradable polymer widely used numerous of industry fields [9]. PLA due to its innate characteristics is also commonly used in 3D printing technology, especially considering its ease of production and source material availability [10]. As an additive manufacturing method, Fused Filament Fabrication (FFF), also known as Fused Deposition Modelling (FDM), enables rapid prototyping and on-demand production [11]. Thanks to the properties mentioned above, PLA is used to produce medical equipment, such as PPE, needed to keep healthcare personnel, patients, and public service employees safe during the COVID-19 pandemic [10]. The combination of the production capabilities of FFF devices, along with the availability of materials and open-source digital models, allowed for a quick response during a pandemic crisis and immediate production of the necessary products [12].

Applications such as medical and biomedical as well as food packaging would benefit from antibacterial properties acquisition [9,13,14]. There are two strategies for the design of antimicrobial materials. The basic approach is to change the chemical properties by adding active agents to the polymer matrix, which are usually added on mesoporous silica nanoparticles carriers [15]. Typical antimicrobial additives or fillers reported in literature are Ag, Cu, Zn, ZnO, TiO<sub>2</sub>, MgO, or SiO<sub>2</sub> [16,17] as well as blends consisting of ceramics—Al<sub>2</sub>O<sub>3</sub> or SiO<sub>2</sub> in combination with active nanoparticles [18,19]. Another way is to modify the surface by adding geometric patterns on it that reduce bacterial colonization of the surface. Due to the limitations of the developed surface topography, the contact area of bacteria is narrower compared to the condition of the smooth surface. And it is possible to use the synergistic effect of both methods, which may lead to even better antimicrobial properties [20]. Research on a commercial product for FFF technology applications showed that PLA with a 1% addition of copper nanoparticles was up to 99.99% effective against *S. aureus* and *E. coli* after a 24-h incubation period [21]. PLA, as an additively manufactured material, is one of the most widely used polymers in medicine applications [22].

Therefore, the subject of this article is the verification of commercially available filaments, whose manufacturers claim antimicrobial properties of their product. The lack of antibacterial properties may lead to the inappropriate use of these materials or mislead a potential customer. The verification was done on two levels: (1) analysis of the additives' presence in filaments using 2D digital radiography and SEM and (2) biological tests to analyze the antimicrobial properties of filaments. The biological tests were carried out using three different bacterial species (*S. aureus*, *P. aeruginosa*, and *C. difficile*), considered to be the prevalent etiological factors of hospital infections.

The novelty of the results consists of considering the potential antibacterial properties declared by the manufacturer, represented by details produced using FFF technology, and verifying them to our own research, using other than provided in the standard bacterial species, concerning potential medical applications.

## 2. Materials and Methods

### 2.1. Materials

Nine antibacterial filaments with a diameter of 1.75 mm from commercial producers were evaluated (Table 1). The base material of filament is PLA. The antibacterial additives are copper (Cu) or silver (Ag) in different forms, such as nano- or micro-particles. Each manufacturer used a different type of additive (Table 1). According to manufacturers' claims, all materials displayed strong antibacterial properties.

**Table 1.** The list of filaments with additions.

Name in the Manuscript	Trade Name	Manufacturer	Chemical Composition	LOT; S/N; Batch No.
A	AbFil PLA 850	3D Fils (Elche, Spain)	PLA with silver additives	20042908DIJ
B	Mega 3D Antibacterial PLA	FiberForce (Treviso, Italy)	Based on PLA, manufacturer doesn't specify additives	FX-100-30
C	NanoCICLA	Cicla3D (Bío, Argentina)	PLA with copper nanoparticles	0000000503
D	PLA Antibacterial	Philament/Filaticum (Miskolc, Hungary)	PLA with metal additives	N/S *
E	PLActive AN <sup>1</sup>	Copper3D (Santiago, Chile)	PLA with Nano-Copper additive	16708001
F	PrimaSelect PLA AntiBac	PrimaCreator (Malmö, Sweden)	Based on PLA, manufacturer doesn't specify additives	FB0195
G	Smartfil	SMART MATERIALS 3D (Alcalá la Real (Jaén), Spain)	PLA with silver nanoparticles	129417002085
H	Tarfuse <sup>®</sup> PLA AM	Grupa Azoty S.A. (Tarnów, Polska)	Based on PLA, manufacturer doesn't specify additives	N/S *
I	Antibacterial PLA	XYZ Printing Inc. (New Taipei City, Taiwan)	PLA with silver additives	RFPLK-FPE-B6W-TH-92K-0364

\* manufacturer does not specify identification number.

## 2.2. Sample Manufacturing

The samples were manufactured with Fused Filament Fabrication technology. Prusa i3 MK3S+ (Prusa Research a.s, Prague, Czech Republic) device with a 0.4-mm nozzle diameter was used. The manufacturing process was prepared in PrusaSlicer 2.3.0 (Prusa Research a.s, Prague, Czech Republic) consisting of 30 cylindrical biosamples ( $\varnothing 10 \text{ mm} \times 2 \text{ mm}$ ) and a single specimen dedicated for 2D digital radiography analysis ( $2 \text{ mm} \times 10 \text{ mm} \times 2 \text{ mm}$ ). Each material was processed separately using temperature experimentally selected from the range given by the materials' manufacturer. The process parameters, along with temperature settings, are presented in Table 2.

**Table 2.** Non-variable manufacturing process parameters and material specific parameters.

Process Parameters				
Layer Thickness (mm)	Infill (%)	Cooling Fan Speed (%)	Perimeter Speed (mm/s)	Infill Speed (mm/s)
0.2	100	100	45	80
Material Specific Process Parameters				
Material Name	Printhead Temperature (°C)		Bed Temperature (°C)	
A	210		50	
B	210		55	
C	200		60	
D	210		60	
E	200		60	
F	210		50	
G	220		60	
H	220		60	
I	205		50	

The process parameters were selected based on typical values for PLA material and the recommendations of the manufacturers of individual materials.

## 2.3. 2D Digital Radiography

The test samples, a piece of filament ( $\varnothing 1.75 \text{ mm} \times 35 \text{ mm}$ ) and 3D printed (FFF) specimen ( $2 \text{ mm} \times 10 \text{ mm} \times 2 \text{ mm}$ ) were analyzed using the digital radiography technique, which allows for a non-destructive qualitative assessment of the internal features of the tested objects. Furthermore, it is a tool for quick and therefore cost and time-efficient



verification of samples [23,24]. For this purpose, a 300-kV microfocus X-ray tube and a high-contrast digital flat panel detector GE DXR250 (GE Sensing & Inspection Technologies GmbH, Wunstorf, Germany) was used. X-rays were taken using constant and repeatable parameters for all analyzed filaments: voltage of 70 kV, current of 90  $\mu$ A, the integration time of 1000 ms, and a magnification of 130 $\times$ . Additionally, the detector was calibrated before each measurement to avoid image distortion caused by constant pattern noise caused by differences in detector components and electronics.

#### 2.4. Scanning Electron Microscopy (SEM) Analysis

In order to determine the presence of additives in the filament, the cross-sections of all filaments were performed. The samples ( $\phi$ 1.75 mm  $\times$  35 mm) obtained in this way were sputtered with a gold layer to obtain a conductive layer enabling better imaging. Then, they were examined using a scanning electron microscopy (SEM) Sigma VP 500 microscope (Zeiss, Oberkochen, Germany) in HDBSD imaging mode. Point analysis was performed using the Octane Elect EDS System detector (Ametek, Mahwah, NJ, USA), with the acceleration voltage 20 keV and working distance WD = 8.5 mm.

#### 2.5. Antimicrobial Properties

The assessment of the ability to colonize the surface by microorganism/potential antimicrobial activity was carried out in the standard Tryptoc Soya Broth (Biocorp, Warsaw, Poland) medium (System I) or in artificial saliva (AS) (System II) with the following composition: an aqueous solution containing 2.5 g of mucin, 0.25 g of sodium chloride in 1 L, 0.2 g of calcium chloride; 2 g of yeast extract, 5 g of peptone, and 1.35 mL of 40% urea [25]. After introducing the ingredients and mixing, the artificial saliva was adjusted to a pH of 6. The microbiological tests against the Gram-positive *S. aureus* ATCC 6538, non-toxicogenic strain *C. difficile* BAA 1801 and Gram-negative *P. aeruginosa* ATCC 15442 bacteria, were performed using:

- (1) a standard method to assess the level of biofilm formation using the non-specific ability of crystal violet to bind to bacterial biomass [26];
- (2) a method using the reduction of colorless tetrazolium chloride to red formazan crystals in the presence of the living, metabolically active microorganisms [27];
- (3) quantitative cultures in an anaerobic atmosphere [28].

Research using techniques (1) and (2) was carried out for *S. aureus* and *P. aeruginosa*; technique (3) was used towards *C. difficile*. As a control surface, polypropylene (PP) specimens with a diameter of 10 mm and a height of 1 mm were used for cell culture tests; (1) and (2) were performed in 6 replications; tests (2) were performed in triplicate. The reduction of bacterial cells grown on the test surfaces compared to the cells grown on the control surfaces was calculated using the following Equation (1):

$$100\% - \left( \frac{\text{absorbance defined for analysed samples}}{\text{absorbance defined for control samples}} \right) \times 100 \quad (1)$$

Or, in case of quantitative culturing, according the following Equation (2):

$$100\% - \left( \frac{\text{number of colony - forming units defined for analysed samples}}{\text{number of colony - forming units defined for control samples}} \right) \times 100 \quad (2)$$

### 3. Results and Discussion

#### 3.1. 2D Digital Radiography

Images obtained with the radiographic method for filaments and additively produced samples are compiled in Table 3. Images obtained in the radiography technique are in grayscale, corresponding to the density of the scanned material. Therefore, the background and voids are seen as relatively bright areas, while the higher density areas are seen as darker in the grayscale. It can be observed that the filaments do not show visible

internal voids. The inclusions of materials of higher density than polymer matrix are recorded instead. These fillers are expected to improve the antimicrobial properties of tested materials. In addition, most of the materials show a characteristic content of additives with an even distribution over the verified height. The exceptions are A and D filaments, which, as revealed by image analysis, did not show the content of an additive with a higher density than the base material. This may suggest using a dispersion filling that does not allow registering the footprint of antibacterial additives at a given resolution or suggesting an uneven additive distribution over the entire mass of the filament spool. The samples produced in the FFF technology from the tested filaments show similar results. In addition to additives and their unequal distribution, the produced samples show defects and discontinuities due to the disconnection of the layers during the FFF process. Despite the use of the same process parameters, the dedicated printhead temperatures and bed temperatures of the sample differ from each other. This behavior can be explained by differences in melt flow rate for a given material in a selected processing temperature. The worst filling effect was obtained for A, B, and I.

**Table 3.** Results of 2D digital radiography of filaments and samples manufactured additively.

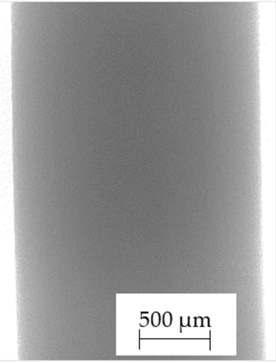
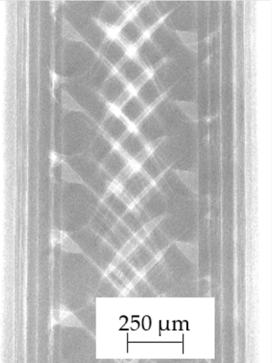
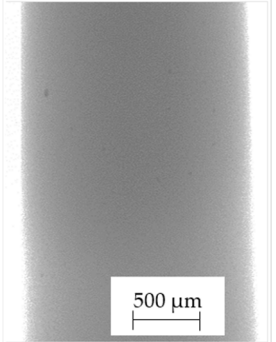
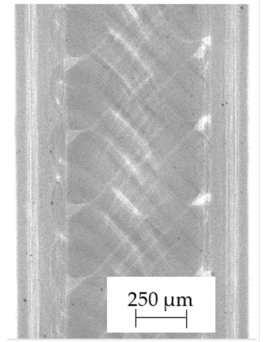
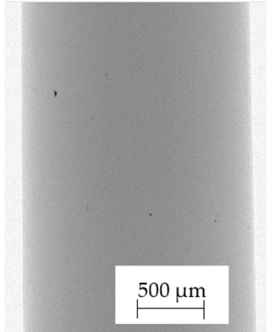
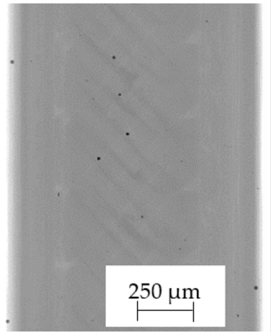
Material Name	RTG of Filament	RTG of FFF Sample
A		
B		
C		

Table 3. Cont.

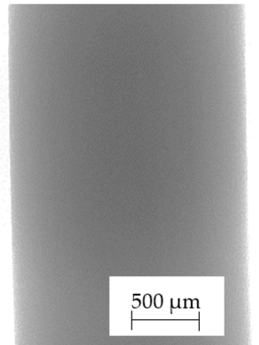
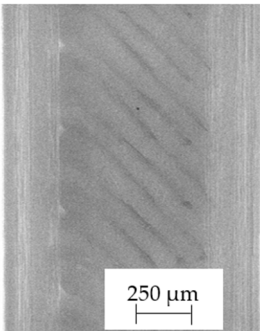
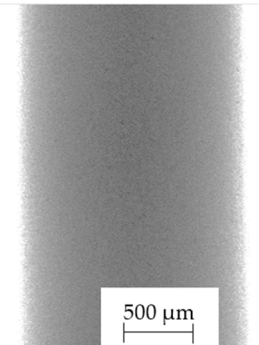
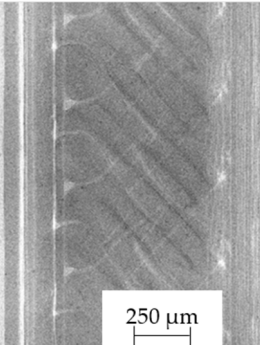
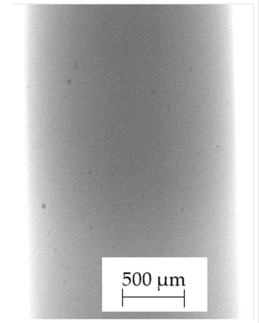
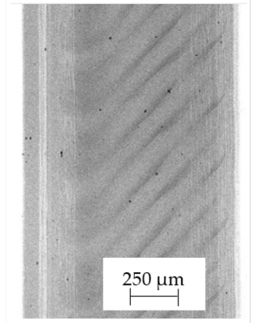
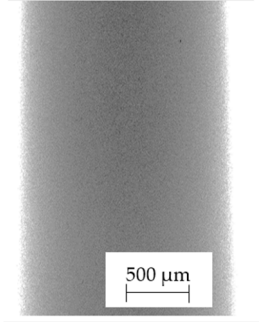
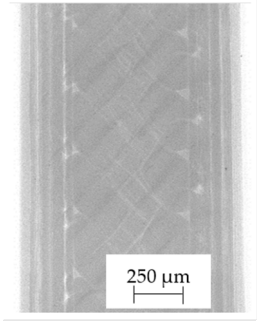
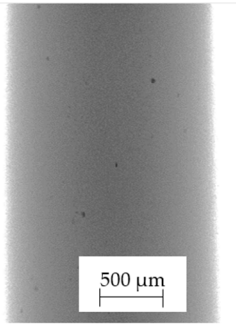
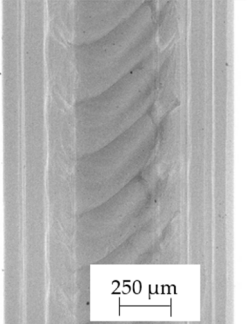
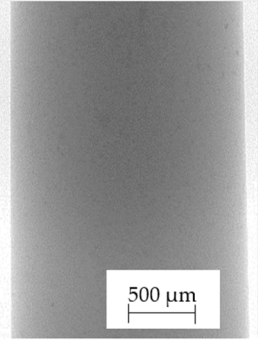
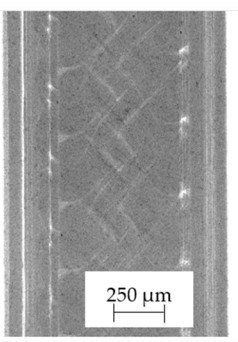
Material Name	RTG of Filament	RTG of FFF Sample
D	 <p>500 <math>\mu\text{m}</math></p>	 <p>250 <math>\mu\text{m}</math></p>
E	 <p>500 <math>\mu\text{m}</math></p>	 <p>250 <math>\mu\text{m}</math></p>
F	 <p>500 <math>\mu\text{m}</math></p>	 <p>250 <math>\mu\text{m}</math></p>
G	 <p>500 <math>\mu\text{m}</math></p>	 <p>250 <math>\mu\text{m}</math></p>

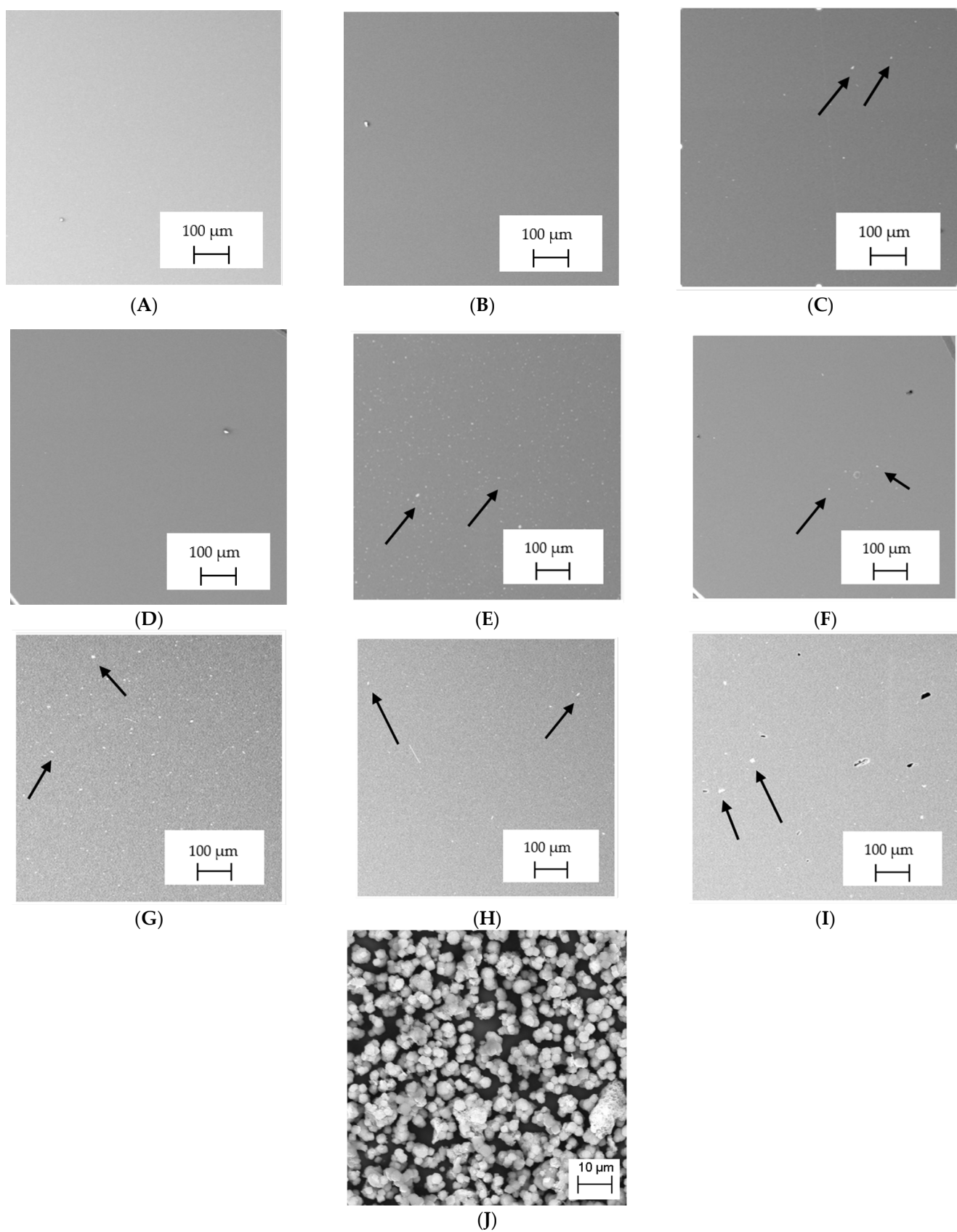
Table 3. Cont.

Material Name	RTG of Filament	RTG of FFF Sample
H	 A grayscale image of a filament for material H, showing a smooth, uniform surface. A scale bar at the bottom indicates 500 μm.	 A grayscale image of an FFF sample for material H, showing a layered structure with some surface irregularities. A scale bar at the bottom indicates 250 μm.
I	 A grayscale image of a filament for material I, showing a smooth, uniform surface. A scale bar at the bottom indicates 500 μm.	 A grayscale image of an FFF sample for material I, showing a porous structure with many small dark spots. A scale bar at the bottom indicates 250 μm.

### 3.2. SEM–EDS Analysis

The backscattered electrons (BSE) imaging mode enabled contrast imaging of the difference in material density. Results are presented in Figure 1. No additions were observed in the SEM images on the cross-section of samples of A, B, and D. Areas with a different density than the matrix were observed in the highest manner in samples E and G. Material I was characterized by high porosity (black areas) and the presence of metallic additives. On the other hand, a small concentration of the metallic additives was observed for materials C, F, and H.

It should be emphasized that in the case of SEM–BSE, the bright particles corresponded to the material of a higher density ( $\rho_{\text{PLA}} = 1.25 \text{ g/cm}^3$ ,  $\rho_{\text{Ag}} = 10.49 \text{ g/cm}^3$ , and  $\rho_{\text{Cu}} = 8.96 \text{ g/cm}^3$ ). Only 5 out of 11 tested filaments had a specific metallic additive—copper or silver. In the remaining six cases, the manufacturers did not specify what material the antibacterial additives are. Therefore, it was decided to carry out a point analysis of the places indicated by the arrows. Due to the availability of additive (J) used in E-material used by the manufacturer, it was decided to present the SEM–EDS analysis of this additive.



**Figure 1.** Results of SEM–BSE cross-area observations. Black arrows indicate exemplary particles of additives. (A–I): specific type of material analyzed. (J)—additive used in material E.

Literature indicates that such nano additives as Ag, Cu, ZnO, TiO<sub>2</sub>, MgO, or SiO<sub>2</sub> are successfully used as antimicrobial components against popular species of bacteria, in particular *S. aureus* and *E. coli* [16]. Moreover, it is popular to use mixtures consisting of ceramics—Al<sub>2</sub>O<sub>3</sub> or SiO<sub>2</sub> in combination e.g., with silver nanoparticles [18,19]. According to the manufacturer's declaration, the SEM–EDS analyses confirmed that the G-material contains Ag, and the material C and E, respectively, contains Cu. The detailed results of the point analysis of micro-areas with different phase contrast presented in Figure 1 are presented below (Table 4).

**Table 4.** Results of SEM–EDS analysis—the presence of specific elements in analyzed micro-areas of filaments.

Material Name	Elements											
	C	O	Al	Si	Ag	Ca	Cu	P	Mg	Na	Ti	Cl
A	66.55 ± 16.25	19.3 ± 9.8	0.45 ± 0.05	6.35 ± 5.55	-	6.70 ± 0.01	-	-	0.50 ± 0.01	1.10 ± 0.01	6.50 ± 0.01	-
B	88.37 ± 5.76	5.40 ± 1.49	0.30 ± 0.20	0.70 ± 0.16	-	-	-	-	0.10 ± 0.01	0.15 ± 0.05	1.10 ± 0.20	13.20 ± 0.10
C	90.50 ± 0.92	7.73 ± 0.75	-	0.60 ± 0.01	-	1.50 ± 0.01	0.10 ± 0.01	1.10 ± 0.01	0.40 ± 0.01	-	-	-
D	91.50 ± 1.28	7.37 ± 1.22	0.30 ± 0.08	0.67 ± 0.24	-	-	-	-	0.25 ± 0.05	0.20 ± 0.01	-	-
E	90.03 ± 1.27	7.97 ± 0.73	0.90 ± 0.22	0.83 ± 0.17	-	-	0.50 ± 0.10	-	-	-	-	-
F	91.43 ± 1.47	6.73 ± 0.90	0.43 ± 0.05	0.40 ± 0.08	-	-	-	-	0.30 ± 0.10	0.40 ± 0.01	2.10 ± 0.01	-
G	76.17 ± 9.38	9.10 ± 0.21	1.16 ± 0.24	4.36 ± 2.64	0.03 ± 0.05	9.13 ± 10.9	-	-	-	-	-	-
H	88.17 ± 6.41	6.70 ± 0.22	2.60 ± 3.18	2.53 ± 2.95	-	-	0.10 ± 0.01	-	-	-	-	-
I	86.64 ± 4.52	10.60 ± 3.29	0.40 ± 0.22	0.80 ± 0.36	-	-	-	-	1.20 ± 0.54	1.20 ± 0.01	-	-
J	3.52 ± 0.68	29.17 ± 3.50	3.74 ± 0.23	2.56 ± 0.11	-	-	57.65 ± 1.58	-	-	-	-	4.33 ± 0.23

All analyzed materials, due to the declared presence of nano additives or other metallic additives, which are usually dispersed in the ceramic support, contain Al, Si, and O, which leads to the reflection that these elements form silica or alumina compounds. Moreover, in the case of materials B, D, and F, the presence of Mg was found, which can form the MgO compound of antibacterial properties according to the relevant literature data [29]. The attention should be paid to the Ti present in the A, B, D, F, and I materials. Apart from the antibacterial properties of the TiO<sub>2</sub> compound [30], its presence may also be dictated by the role of the dye in these filaments. Among the analyzed materials, the filament from E and H manufacturers is characterized by the highest purity, i.e., the absence of any other chemical elements than Cu.

### 3.3. Microbiological Properties of Tested Materials

The biological tests had shown that when standard microbial TSB medium (which conditioned the surface of analyzed materials) was applied, in specific cases, the higher colonization of bacteria was observed on analyzed than on control samples, devoid of antimicrobial additive (Figure 2). Especially in the case when *P. aeruginosa* was scrutinized, there was no significant decrease in bacterial colonization on the surfaces, particularly when the XYZ Printing material was applied. In turn, the bacterial survival rate ranged between 90 and 95% indicated that such materials as G, B, D, A, or E do not show significant antimicrobial activity within the experimental setting used. The most significant reduction of bacterial cells was observed for *S. aureus* regardless type of surface applied. The level of bacterial survival ranged from about 40% for G material to 63% for F material. In the case of *C. difficile*, the survival rate of bacterial cells for most materials was ca. 60 to 80%. When the second system (based on artificial saliva) was used (Figure 3), a similar trend in the behavior of bacterial cells was observed.

Number of cells [%] compared to the number of cells in the control setting system I [TSB]

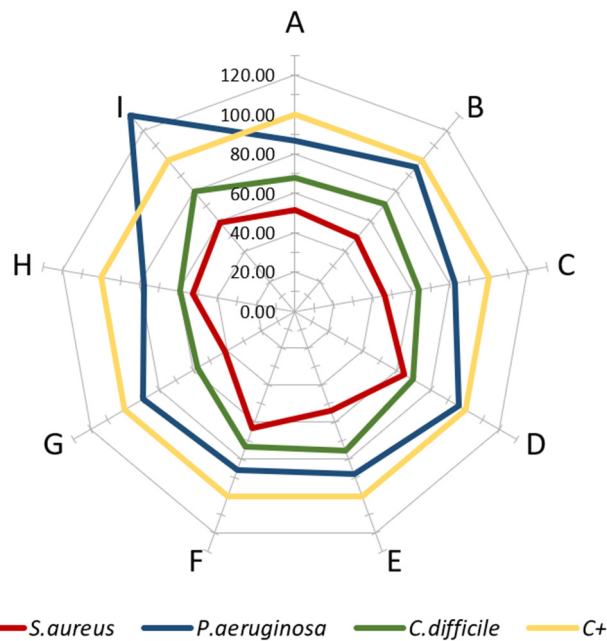


Figure 2. Plot of number of viable cells (%) on the surface of the test samples compared to the number of cells grown on the control surfaces in test setup I. Letters A–I: specific type of material applied.

Number of cells [%] compared to the control system II [AS]

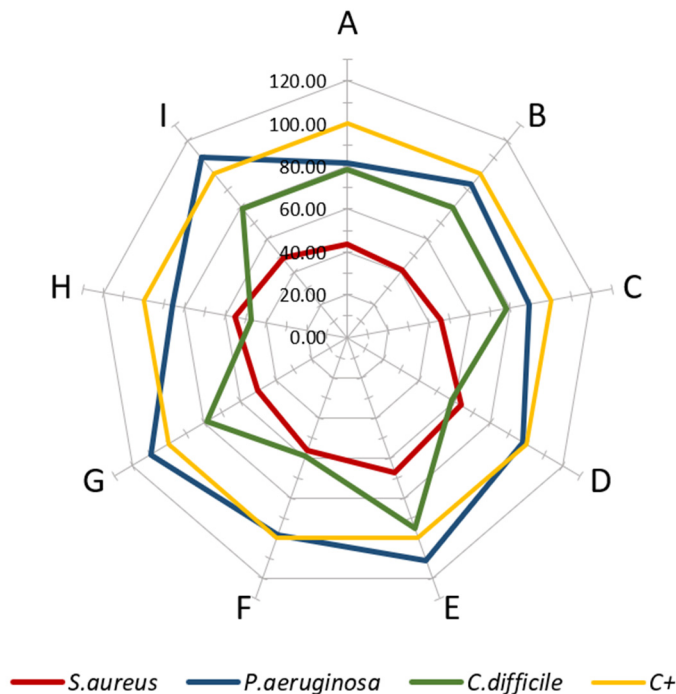


Figure 3. Plot of number of cells (%) compared to the control system II [AS]. Letters A–I: specific type of material applied.

In the case of *P. aeruginosa*, incubated in the medium-I, the growth of bacterial cells was higher than in the control setting. The most extraordinary stimulation was observed for G, E, and I material, where the number of bacteria compared to the control was over 100%. An insignificant decrease of cell number (5–20%) for F, A, D or C, and H was observed. A

higher decrease of *S. aureus* cell number (in comparison with *P. aeruginosa*) was detected (30–60%) for the aforementioned materials. In turn, *C. difficile* displayed differentiated susceptibility to applied materials (5–60% reduction rate, dependent on surface, Figure 3). The highest reduction for species above was recorded towards A-material (60%).

Thus, the obtained results (Figures 2 and 3) show that not all tested materials after processing in FFF technology display the expected antimicrobial properties declared by the materials' manufacturers.

Confronting the obtained results with the data provided by the manufacturers, it can be observed that the producers mainly rely on the ISO 22196 method for testing the antimicrobial activity of plastics. According to the mentioned standard, research is conducted against *E. coli* and *S. aureus* usually in a long, 24-h contact time (Table 5).

**Table 5.** A study based on the manufacturers' report on the antimicrobial activity of filaments. Letters A–I: specific type of material analyzed.

Material Name	Producer Report According to Antimicrobial Activity
A	N/A
B	N/A
C	Method based on ISO 22196. Effectiveness on <i>E. coli</i> ATCC 8739 after 8 h—99.97181% Effectiveness on <i>E. coli</i> ATCC 8739 after 24 h—99.98909%
D	N/A
E	Effectiveness on <i>S. aureus</i> MRSA after 8 h >98%; after 24 h > 99.99% Effectiveness on <i>E. coli</i> DH5 after 8 h > 98% after 24 h > 99.99%.
F	Method based on ISO 22196. Effectiveness on <i>S. aureus</i> after 24 h 99.59% Effectiveness on <i>E. coli</i> DH5 after 24 h 88.43%
G	Method based on JIS Z 2801 (ISO 22196). Effectiveness on <i>S. aureus</i> CECT 240, ATCC 6538 P after 24 h—99.99% Effectiveness on <i>E. coli</i> CECT 516, ATCC 8739 after 24 h—99.99%
H	The antibacterial additives used in the H filament are approved for marketing in the European Union—they comply with the European Regulation on biocidal products (BPR, Regulation (EU) 528/2012 and with the requirements of the American Environmental Protection Agency—Antimicrobial Division of the Environmental Protection Agency (EPA).The antibacterial additives used are included in the list of chemical compounds approved by OEKO-TEX.
I	N/A

These tests, however, do not reflect the real conditions faced by PLA materials, which are exposed to the recurring heavy burden of plethora of various nosocomial pathogens to which *P. aeruginosa* and *C. difficile* also belong. Moreover, there are important etiological factors of a wide spectrum of disease entities, including infections of respiratory, alimentary, urinary tract and skin, soft tissue, bones, and gut [31–34]. It is noteworthy that the 24-h contact time (period of exposure of microbes to additives included to surface of material) seems to be rather irrelevant concerning the potential application (face masks, door openers) of PLA materials in a hospital setting due to the frequency of real use of the PLA-finished products is decisively higher. Rather than searching for implementation in shared space equipment and public areas, emphasis should be put on parts used during the provision of hospital care or by a single patient. The approach represented in this manuscript, which is not only based on the guidance given by the standard, has also been implemented by Thavomyutikarn et al. [35]. These studies are based only on Gram-positive bacteria—*S. aureus*, *S. epidermidis*, and *B. subtilis*.



Interestingly, Maróti et al. [36] dealt with the problem of PLA processing and the analysis of the antibacterial effect on these materials, using the following bacterial species: *Micrococcus luteus*—*Sarcina*, *Bacillus subtilis*, *Staphylococcus aureus*, *Escherichia coli*, and *Pseudomonas aeruginosa*. This approach confirms that it is also worth analyzing other bacterial species that constitute the skin bacterial microbiota and those that cause severe respiratory and urinary tract infections. The approach is consistent with the standard for the analysis of PLA material and was represented by other research groups, Mania et al. [37] and León-Cabezas et al. [38], which, following the guidelines, analyzed the antimicrobial response using bacterial *E. coli* and *S. aureus* species. FFF technology can also influence the filler distribution in terms of antimicrobial properties, which may affect its final properties. Unfortunately, materials' manufacturers do not always provide complete information about the conducted microbial test. Thus, there is no certainty if tests were performed on raw feedstock material (filament) or manufactured samples.

The other common issue is not providing the chemical composition of materials by manufacturers. It is understandable from the "know-how" perspective; however, it also significantly decreases the possibility of deducing how the given materials may work or be applied in the specific, actual clinical situation. We are convinced that in the pandemic period, the basic chemical composition should be revealed for the sake of customers. Another issue is a lack of a common standard for the antimicrobial tests of polymer samples. For example, certain manufacturers in materials datasheets present results of such testing after 8 h. The others show datasets and changes for measurements for 6, 8, and 24 h. The lack of clearly defined rules makes assessing the antibacterial effectiveness between individual filament samples impossible or significantly challenging. Particular attention should be paid to the time intervals between subsequent disinfection due to the use of such materials in the hospital practice. For example, as dedicated material for door openers, during the coronavirus pandemic, hospitals point out the problem of the disinfection of basically all places that can be touched by hospital staff, patients, or visitors. Therefore, the question that should be addressed and answered is how effectively the antimicrobial additives act within shorter times; the results of our case study indicate that their activity within such contact time is rather scanty. We are aware that extrapolation of data shown in this study in actual clinical settings should be taken with precaution. Further experiments (shorter contact times, higher number of strains scrutinized) should be performed to verify our discovery's importance. Nevertheless, we are convinced that our article may be considered an essential step in applying PLA products of high antibacterial activity.

#### 4. Conclusions

The approach includes tests that exceeded the test scope dictated by the standards and significantly expanded state of the art regarding antimicrobial commercial polymer materials used in FFF printing. Due to the COVID-19 pandemic, the demand on antimicrobial surfaces is needed. Not all commercially available surfaces declared as "antibacterial" in our study meet the actual clinical requirements concerning their antimicrobial activity. Higher availability of data on materials' composition and testing details should be provided during a pandemic crisis. 3D printing technologies enable the use of antibacterial materials and a quick response to immediate prototyping of elements for hospitals and other public utilities in the crisis caused by COVID-19. Activities should focus on the development of antibacterial materials used in FFFs, which can be successfully used in low-volume and specialized production. Commercial research performed by laboratories focuses on ad hoc material analysis. However, an essential factor is the process of additive processing itself, which is often overlooked in such analyses.

The development of commercially available antimicrobial polymers for additive manufacturing has enabled the prototyping of a wide variety of critical medical devices by many printers worldwide. Although the materials used were to be antibacterial, in most cases, these polymers do not meet the expectations and criteria that should be set for hospital use. Therefore, for commercial use in the specific hospital environments and

other peri-medical applications, these materials should undergo a series of other tests on dedicated demonstrators.

**Author Contributions:** Conceptualization, P.G., V.H. and I.S.; methodology, P.G., I.S., E.G. and A.J.; software, P.G. and E.G.; validation, E.G.; formal analysis, P.G. and A.J.; investigation, V.H., E.G., J.P. and A.J.; resources, V.H. and I.S.; data curation, P.G., E.G., V.H. and J.P.; writing—original draft preparation, P.G., V.H. and E.G.; writing—review and editing, I.S.; visualization, E.G. and V.H.; supervision, T.K.; project administration, T.K.; funding acquisition, T.K. All authors have read and agreed to the published version of the manuscript.

**Funding:** This research was funded by Polish National Centre for Research and Development (NCBR Poland), grant number SZPITALEJEDNOIMIENNE/6/2020. Title of the project “Implementation of comprehensive technological solutions for the production of spare parts of medical equipment and personal protective equipment (PPE), produced in a dispersed environment in crisis situations—Virtual AM Storage Covid-19”.

**Institutional Review Board Statement:** Not applicable.

**Informed Consent Statement:** Not applicable.

**Conflicts of Interest:** The authors declare no conflict of interest.

## References

- COVID-19 Supply Chain Update: Importation of Vital Food and Medical Products | FDA. Available online: <https://www.fda.gov/news-events/fda-voices/covid-19-supply-chain-update-importation-vital-food-and-medical-products> (accessed on 23 November 2021).
- Konda, A.; Prakash, A.; Moss, G.A.; Schmoldt, M.; Grant, G.D.; Guha, S. Aerosol Filtration Efficiency of Common Fabrics Used in Respiratory Cloth Masks. *ACS Nano* **2020**, *14*, 6339–6347. [[CrossRef](#)] [[PubMed](#)]
- Mostaghimi, A.; Antonini, M.J.; Plana, D.; Anderson, P.D.; Beller, B.; Boyer, E.W.; Fannin, A.; Freake, J.; Oakley, R.; Sinha, M.S.; et al. Regulatory and Safety Considerations in Deploying a Locally Fabricated, Reusable Face Shield in a Hospital Responding to the COVID-19 Pandemic. *Med* **2020**, *1*, 139–151.e4. [[CrossRef](#)] [[PubMed](#)]
- Borkow, G.; Gabbay, J. Copper as a biocidal tool. *Curr. Med. Chem.* **2005**, *12*, 2163–2175. [[CrossRef](#)] [[PubMed](#)]
- Budinoff, H.D.; Bushra, J.; Shafae, M. Community-driven PPE production using additive manufacturing during the COVID-19 pandemic: Survey and lessons learned. *J. Manuf. Syst.* **2021**, *60*, 799–810. [[CrossRef](#)]
- Maillard, J.Y. Testing the Effectiveness of Disinfectants and Sanitizers. *Handb. Hyg. Control Food Ind. Second Ed.* **2016**, 569–586. [[CrossRef](#)]
- Palza, H. Antimicrobial polymers with metal nanoparticles. *Int. J. Mol. Sci.* **2015**, *16*, 2099–2116. [[CrossRef](#)] [[PubMed](#)]
- Palza, H.; Quijada, R.; Delgado, K. Antimicrobial polymer composites with copper micro- and nanoparticles: Effect of particle size and polymer matrix. *J. Bioact. Compat. Polym.* **2015**, *30*, 366–380. [[CrossRef](#)]
- Balla, E.; Daniilidis, V.; Karlioti, G.; Kalamas, T.; Stefanidou, M.; Bikiaris, N.D.; Vlachopoulos, A.; Koumentakou, I.; Bikiaris, D.N. Poly(lactic acid): A versatile biobased polymer for the future with multifunctional properties—from monomer synthesis, polymerization techniques and molecular weight increase to PLA applications. *Polymers* **2021**, *13*, 1822. [[CrossRef](#)] [[PubMed](#)]
- DeStefano, V.; Khan, S.; Tabada, A. Applications of PLA in modern medicine. *Eng. Regen.* **2020**, *1*, 76–87. [[CrossRef](#)]
- Cano-Vicent, A.; Tambuwala, M.M.; Hassan, S.S.; Barh, D.; Aljabali, A.A.A.; Birkett, M.; Arjunan, A.; Serrano-Aroca, Á. Fused deposition modelling: Current status, methodology, applications and future prospects. *Addit. Manuf.* **2021**, *47*, 102378. [[CrossRef](#)]
- Armijo, P.R.; Markin, N.W.; Nguyen, S.; Ho, D.H.; Horseman, T.S.; Lisco, S.J.; Schiller, A.M. 3D printing of face shields to meet the immediate need for PPE in an anesthesiology department during the COVID-19 pandemic. *Am. J. Infect. Control* **2021**, *49*, 302–308. [[CrossRef](#)]
- Gomaa, S.F.; Madkour, T.M.; Moghannem, S.; El-Sherbiny, I.M. New polylactic acid/cellulose acetate-based antimicrobial interactive single dose nanofibrous wound dressing mats. *Int. J. Biol. Macromol.* **2017**, *105*, 1148–1160. [[CrossRef](#)]
- Ghozali, M.; Fahmiati, S.; Triwulandari, E.; Restu, W.K.; Farhan, D.; Wulansari, M.; Fatriasari, W. PLA/metal oxide biocomposites for antimicrobial packaging application. *Polym. Technol. Mater.* **2020**, *59*, 1332–1342. [[CrossRef](#)]
- Psochia, E.; Papadopoulos, L.; Gkiliopoulos, D.J.; Francone, A.; Grigora, M.-E.; Tzetzis, D.; de Castro, J.V.; Neves, N.M.; Triantafyllidis, K.S.; Torres, C.M.S.; et al. Bottom-Up Development of Nanoimprinted PLLA Composite Films with Enhanced Antibacterial Properties for Smart Packaging Applications. *Macromolecules* **2021**, *1*, 5. [[CrossRef](#)]
- Omerović, N.; Djisalov, M.; Živojević, K.; Mladenović, M.; Vunduk, J.; Milenković, I.; Knežević, N.; Gadjanski, I.; Vidić, J. Antimicrobial nanoparticles and biodegradable polymer composites for active food packaging applications. *Compr. Rev. Food Sci. Food Saf.* **2021**, *20*, 2428–2454. [[CrossRef](#)]
- Zou, L.; Zhang, Y.; Liu, X.; Chen, J.; Zhang, Q. Biomimetic mineralization on natural and synthetic polymers to prepare hybrid scaffolds for bone tissue engineering. *Colloids Surf. B Biointerfaces* **2019**, *178*, 222–229. [[CrossRef](#)] [[PubMed](#)]

18. Rezanova, V.G.; Rezanova, N.M.; Plavan, V.P.; Viltsaniuk, O.O. The influence of nano-additives on the formation of matrix-fibrillar structure in the polymer mixture melts and on the properties of complex threads. *Fibres Text.* **2017**, *24*, 37–42.
19. Álvarez-Paino, M.; Muñoz-Bonilla, A.; Fernández-García, M. Antimicrobial Polymers in the Nano-World. *Nanomaterials* **2017**, *7*, 48. [[CrossRef](#)]
20. Nerantzaki, M.; Kehagias, N.; Francone, A.; Fernández, A.; Sotomayor Torres, C.M.; Papi, R.; Choli-Papadopoulou, T.; Bikiaris, D.N. Design of a Multifunctional Nanoengineered PLLA Surface by Maximizing the Synergies between Biochemical and Surface Design Bactericidal Effects. *ACS Omega* **2018**, *3*, 1509–1521. [[CrossRef](#)] [[PubMed](#)]
21. Zuniga, J.M. 3D Printed Antibacterial Prostheses. *Appl. Sci.* **2018**, *8*, 1651. [[CrossRef](#)]
22. Brounstein, Z.; Yeager, C.M.; Labouriau, A. Development of Antimicrobial PLA Composites for Fused Filament Fabrication. *Polymer* **2021**, *13*, 580. [[CrossRef](#)] [[PubMed](#)]
23. Patel, R.J. Digital Applications of Radiography. In Proceedings of the 3rd MENDT—East Nondestructive Testing Conference & Exhibition, Manama, Bahrain, 13–16 September 2005. Available online: [www.ndt.net](http://www.ndt.net) (accessed on 23 November 2021).
24. Ewert, U. Current Developments in Digital Radiography and Computed Tomography from nm to macro scale. In Proceedings of the 12th European Conference on Non-Destructive Testing (ECNDT 2018), Gothenburg, Sweden, 11–15 June 2018.
25. Junka, A.; Szymczyk, P.; Ziolkowski, G.; Karuga-Kuzniewska, E.; Smutnicka, D.; Bil-Lula, I.; Bartoszewicz, M.; Mahabady, S.; Sedghizadeh, P.P. Bad to the Bone: On In Vitro and Ex Vivo Microbial Biofilm Ability to Directly Destroy Colonized Bone Surfaces without Participation of Host Immunity or Osteoclastogenesis. *PLoS ONE* **2017**, *12*, e0169565. [[CrossRef](#)] [[PubMed](#)]
26. Coffey, B.M.; Anderson, G.G. Biofilm formation in the 96-well microtiter plate. *Methods Mol. Biol.* **2014**, *1149*, 631–641. [[CrossRef](#)] [[PubMed](#)]
27. Grela, E.; Kozłowska, J.; Grabowiecka, A. Current methodology of MTT assay in bacteria—A review. *Acta Histochem.* **2018**, *120*, 303–311. [[CrossRef](#)]
28. Naaber, P.; Štšepetova, J.; Smidt, I.; Rätsep, M.; Kõljalg, S.; Lõivukene, K.; Jaanimäe, L.; Löhr, I.H.; Natås, O.B.; Truusalu, K.; et al. Quantification of *Clostridium difficile* in antibiotic-associated-diarrhea patients. *J. Clin. Microbiol.* **2011**, *49*, 3656–3658. [[CrossRef](#)] [[PubMed](#)]
29. Nguyen, N.Y.T.; Grelling, N.; Wetteland, C.L.; Rosario, R.; Liu, H. Antimicrobial Activities and Mechanisms of Magnesium Oxide Nanoparticles (nmMgO) against Pathogenic Bacteria, Yeasts, and Biofilms. *Sci. Rep.* **2018**, *8*, 16260. [[CrossRef](#)] [[PubMed](#)]
30. Huppmann, T.; Yatsenko, S.; Leonhardt, S.; Krampe, E.; Radovanovic, I.; Bastian, M.; Wintermantel, E. Antimicrobial polymers—The antibacterial effect of photoactivated nano titanium dioxide polymer composites. *AIP Conf. Proc.* **2015**, *1593*, 440. [[CrossRef](#)]
31. Lister, P.D.; Wolter, D.J.; Hanson, N.D. Antibacterial-resistant *Pseudomonas aeruginosa*: Clinical impact and complex regulation of chromosomally encoded resistance mechanisms. *Clin. Microbiol. Rev.* **2009**, *22*, 582–610. [[CrossRef](#)] [[PubMed](#)]
32. Moradali, M.F.; Ghods, S.; Rehm, B.H.A. *Pseudomonas aeruginosa* Lifestyle: A Paradigm for Adaptation, Survival, and Persistence. *Front. Cell. Infect. Microbiol.* **2017**, *7*, 39. [[CrossRef](#)]
33. Czepiel, J.; Drózdź, M.; Pituch, H.; Kuijper, E.J.; Perucki, W.; Mielimonka, A.; Goldman, S.; Wultańska, D.; Garlicki, A.; Biesiada, G. *Clostridium difficile* infection: Review. *Eur. J. Clin. Microbiol. Infect. Dis.* **2019**, *38*, 1211–1221. [[CrossRef](#)]
34. Jarmo, O.; Veli-Jukka, A.; Eero, M. Treatment of *Clostridioides (Clostridium) difficile* infection. *Ann. Med.* **2019**, *52*, 12–20. [[CrossRef](#)] [[PubMed](#)]
35. Thavornnyutikarn, B.; Lertwimol, T.; Kosorn, W.; Hankamolsiri, W.; Nampichai, N.; Janvikul, W. 3D-printing antibacterial composite filaments containing synergistic antibacterial activity of green tea and tannic acid. *Polym. Adv. Technol.* **2021**, *32*, 4733–4744. [[CrossRef](#)]
36. Maróti, P.; Kocsis, B.; Ferencz, A.; Nyitrai, M.; Lőrinczy, D. Differential thermal analysis of the antibacterial effect of PLA-based materials planned for 3D printing. *J. Therm. Anal. Calorim.* **2020**, *139*, 367–374. [[CrossRef](#)]
37. Mania, S.; Ryl, J.; Jinn, J.R.; Wang, Y.J.; Michałowska, A.; Tylingo, R. The Production Possibility of the Antimicrobial Filaments by Co-Extrusion of the PLA Pellet with Chitosan Powder for FDM 3D Printing Technology. *Polymer* **2019**, *11*, 1893. [[CrossRef](#)] [[PubMed](#)]
38. León-Cabezas, M.A.; Martínez-García, A.; Varela-Gandía, F.J. Innovative functionalized monofilaments for 3D printing using fused deposition modeling for the toy industry. *Procedia Manuf.* **2017**, *13*, 738–745. [[CrossRef](#)]

## Article

# Modeling of the Influence of Input AM Parameters on Dimensional Error and Form Errors in PLA Parts Printed with FFF Technology

Carmelo J. Luis-Pérez <sup>1</sup>, Irene Buj-Corral <sup>2,\*</sup> and Xavier Sánchez-Casas <sup>2</sup>

<sup>1</sup> Engineering Department, Arrosadia Campus, Public University of Navarre (UPNA), 31006 Pamplona, Spain; cluis.perez@unavarra.es

<sup>2</sup> Department of Mechanical Engineering, Barcelona School of Engineering (ETSEIB), Universitat Politècnica de Catalunya-Barcelona Tech (UPC), 08028 Barcelona, Spain; xasc95@gmail.com

\* Correspondence: irene.buj@upc.edu; Tel.: +34-93-4054015

**Citation:** Luis-Pérez, C.J.; Buj-Corral, I.; Sánchez-Casas, X. Modeling of the Influence of Input AM Parameters on Dimensional Error and Form Errors in PLA Parts Printed with FFF Technology. *Polymers* **2021**, *13*, 4152. <https://doi.org/10.3390/polym13234152>

Academic Editors: José Miguel Ferri, Vicent Fombuena Borràs and Miguel Fernando Aldás Carrasco

Received: 15 October 2021

Accepted: 24 November 2021

Published: 27 November 2021

**Publisher's Note:** MDPI stays neutral with regard to jurisdictional claims in published maps and institutional affiliations.



**Copyright:** © 2021 by the authors. Licensee MDPI, Basel, Switzerland. This article is an open access article distributed under the terms and conditions of the Creative Commons Attribution (CC BY) license (<https://creativecommons.org/licenses/by/4.0/>).

**Abstract:** As is widely known, additive manufacturing (AM) allows very complex parts to be manufactured with porous structures at a relatively low cost and in relatively low manufacturing times. However, it is necessary to determine in a precise way the input values that allow better results to be obtained in terms of microgeometry, form errors, and dimensional error. In an earlier work, the influence of the process parameters on surface roughness obtained in fused filament fabrication (FFF) processes was analyzed. This present study focuses on form errors as well as on dimensional error of hemispherical cups, with a similar shape to that of the acetabular cup of hip prostheses. The specimens were 3D printed in polylactic acid (PLA). Process variables are nozzle diameter, temperature, layer height, print speed, and extrusion multiplier. Their influence on roundness, concentricity, and dimensional error is considered. To do this, adaptive neuro-fuzzy inference systems (ANFIS) models were used. It was observed that dimensional error, roundness, and concentricity depend mainly on the nozzle diameter and on layer height. Moreover, high nozzle diameter of 0.6 mm and high layer height of 0.3 mm are not recommended. A desirability function was employed along with the ANFIS models in order to determine the optimal manufacturing conditions. The main aim of the multi-objective optimization study was to minimize average surface roughness (Ra) and roundness, while dimensional error was kept within the interval  $|Dimensional\ Error| \leq 0.01$ . When the simultaneous optimization of both the internal and the external surface of the parts is performed, it is recommended that a nozzle diameter of 0.4 mm be used, to have a temperature of 197 °C, a layer height of 0.1 mm, a print speed of 42 mm/s, and extrusion multiplier of 94.8%. This study will help to determine the influence of the process parameters on the quality of the manufactured parts.

**Keywords:** additive manufacturing; surface roughness; FFF; ANFIS; modeling; desirability

## 1. Introduction

Extrusion printing processes such as fused filament fabrication (FFF) allow printing parts with complex shapes without high costs if low-cost machines are employed. However, surface finish, form error, and dimensional quality of the printed parts are not excellent [1,2]. Additive manufacturing (AM) processes have been widely used in different sectors such as the automotive, electronics, and medical sectors. In the latter case, AM has been used to manufacture, among others, surgical guides, phantoms, implants, etc. [3]. Specifically, prostheses require a smooth surface in those areas which will be in contact with sliding elements. They also require low form errors, so that they are as similar as possible to the original bone. For example, it is important to have a low concentricity error in order to ensure a good fit between the different elements and good operation of the prosthesis. As for dimensional error, in the specific case of hip arthroplasty, in order to reduce costs, standardized prostheses of different sizes are currently used that suppliers offer on the

basis of anthropomorphic data and market needs. However, in those patients who exceed the standard ranges, between two sizes or with special requirements due to diseases or genetic problems, the surgical process becomes much more complex and expensive [4].

The effect of FFF printing parameters on dimensional error and on form errors of printed parts has been previously studied in the literature. For example, Rahman et al. [5] studied the dimensional deviations in X, Y, and Z of acrylonitrile–butadiene–styrene (ABS) printed parts. They recommend low bed temperature, low nozzle temperature, high print speed, medium infill, low layer thickness, and a low number of shells in order to reduce dimensional error. Ceretti et al. [6] 3D printed polycaprolactone (PCL) parts with rectilinear grid structure. They observed that the nominal size of pores was the most influential parameter on the extruded diameter of the filament, while the head type greatly influenced the resulting height of the pores. Nancharaiah et al. [7] found that small thickness layer and large bead width improve part accuracy. Raster angle showed a slight effect on part accuracy. In ABS parts, Pennington et al. [8] found that the most influential factors on dimensional accuracy were part size, the location of the part in the work envelope, and the envelope temperature. Garg et al. [1] showed that the dimensional accuracy of ABS parts did not vary significantly when they were submitted to cold vapor treatment. Akbaş et al. [9] observed higher dimensional accuracy in polylactic acid (PLA) than in acrylonitrile butadiene styrene (ABS) printed parts. As a general trend, for PLA, the strip width increased with increasing temperature and decreased with increased feed rate.

Regarding form errors of 3D printed parts, Maurya et al. [10] studied the effect of infill pattern, layer thickness, build orientation, and infill density on flatness and cylindricity of 3D printed components. The most appropriate printing conditions were found to be layer thickness 100  $\mu\text{m}$ , linear infill pattern, 45° orientation, and 20% infill density. Knoop et al. [11] investigated the cylindricity of inner and outer cylinders, with different diameters between 3 and 80 mm. They observed better roundness in the XY-plane than in the Z direction. Highest mean roundness values up to 0.27 mm were reported for holes and up to 0.32 mm for cylinders, corresponding to highest diameter of 80 mm. Saqib and Urbanic [12] evaluated flatness, perpendicularity, and cylindricity of cope and drag casting elements. They observed that the shape of the parts had a greater influence on their form errors than the printing parameters. Ollison and Beriso [13] studied the effect of build orientation, diameter, and printhead life on cylindricity of 3D printed parts. Build orientation was the most influential parameter, a 90° angle having the highest cylindricity error (part rotated 90° about the X axis). Paul and Anand [14] proposed a voxel-based approach to optimize the flatness and cylindricity of parts, while reducing the utilization of support materials. Spindola Filho et al. [15] found cylindricity values up to 0.140 mm being higher on the external surface than on the internal surface of cylindrical shapes.

As for concentricity, Boejang et al. reported different values in FDM processes, depending on the machine employed, ranging between 0.1622 and 0.5784 mm [16]. Concentricity values up to 0.2229 mm were obtained by Abdelrhman [17]. Spindola Filho et al. [15] found concentricity values up to 0.090 mm, being print speed the most influential factor.

In addition, dealing with the application of artificial neural networks (ANN) and adaptive neuro-fuzzy inference systems (ANFIS) for modelling manufacturing processes, several studies can be found in the literature. However, the application of these soft computing techniques for modelling input parameters in additive manufacturing process has been employed to a lesser extent. Among the recent published studies, it is worth mentioning that of Deswal et al. [18] where response surface methods and ANNs are employed for optimization of input process parameter in order to improve the precision of FFF 3D printed parts. Likewise, Noriega et al. [19] employed an ANN for improving the accuracy of FDM parts. The ANN was used to determine the optimal dimensional values for the CAD model. In another study Padhi et al. [20] employed a Mamdani Fuzzy Inference Systems (FIS) along with the Taguchi method to optimize the extrusion process for the manufacturing of acrylonitrile-butadiene-styrene (ABSP 400) parts. In the study from Peng et al. [21] the authors employed response surface method combined with FIS

and genetic algorithm (GA) in order to predict dimensional errors, warp deformation, and build time in FFF.

Some other properties dealing with FFF additive manufacturing technique, have also been studied in recent years. For example, it is worth mentioning the study of Nasiri et al. [22] where a review of applications of machine learning to predict mechanical behavior of 3D printed parts is presented or that of Trivedi et al. [23], where tensile strength is predicted by using Taguchi design of experiments and fuzzy logic. On the other hand, in the study of Rajpurohit et al. [24], an ANFIS is used to predict the tensile strength of FFF printed parts. An ANFIS model is also employed to predict surface roughness, build time, and compressive strength with respect to changes in FFF in Sai et al. [25].

Further examples of the application of fuzzy logic can be found in the study from Xia et al. [26] where surface roughness obtained in wire arc additive manufacturing is predicted by using an ANFIS, that of Sahu et al. [27] where a Mamdani FIS combined with Taguchi method is employed to improve the dimensional accuracy of FFF ABSP 400 parts, and that of Saleh et al. [28] where building orientation, layer thickness, and slurry impact angle are used as input variables in an ANFIS for modelling the effect of slurry impacts on polylactic acid processed by fused deposition modeling or that of or that of Mensah et al. [29] where an ANFIS is employed for flammability parameter modeling among many others.

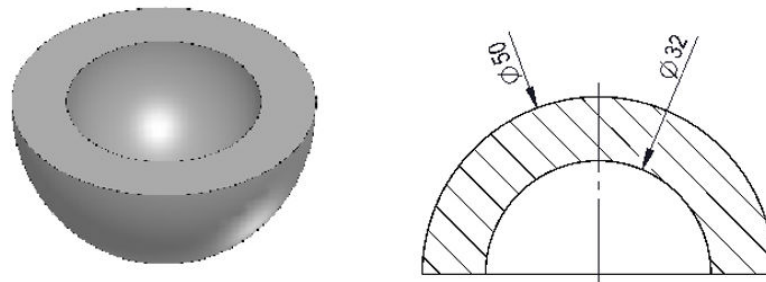
In a previous work, hemispherical cups were 3D printed in polylactic acid (PLA), with different printing conditions, according to a fractional factorial design. ANFIS models were obtained for different surface roughness parameters measured on hemispherical surfaces that are similar to those of the acetabular part of hip prostheses [30]. In this present work, dimensional error and form errors of FFF 3D printed spherical parts are addressed. Unlike flat surfaces, 3D printed curved surfaces have hardly been studied in the literature regarding dimensional and form errors. When manufacturing a customized prosthesis (for example, to replace the acetabulum), it is important to ensure dimensional accuracy. In addition, form errors such as roundness or concentricity should be reduced in order to ensure the correct performance of the hip joint. ANFIS models are applied to dimensional error and roundness error (measured both on the internal and on the external surface of the parts), as well as to concentricity between both spherical surfaces. Moreover, the methodology and the desirability function proposed by Luis-Pérez [31] is used in this present study to obtain the optimal values of the manufacturing conditions in order to simultaneously minimize the roundness and the average surface roughness and at the same time keeping the dimensional error within a specified tolerance. The results of this work will help to select appropriate 3D printing conditions when obtaining curved surfaces.

## 2. Materials and Methods

In this section, the process that was used to manufacture the parts is explained, as well as the measurement and analysis methodology that were employed.

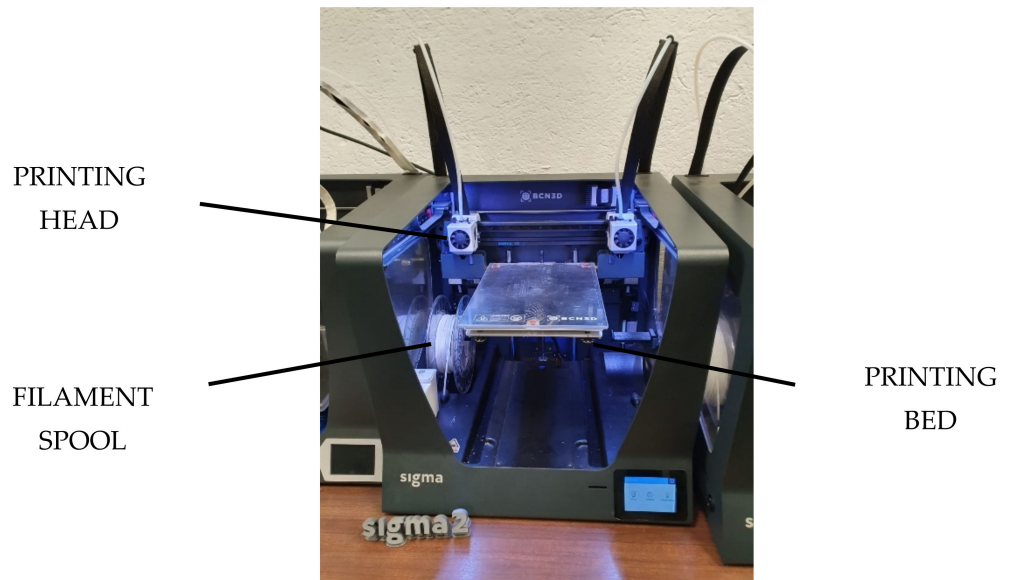
### 2.1. Printing Process

The samples were printed with a Sigma R19 printer from BCN3D Technologies (Gavà, Spain), with white polylactic acid (PLA) filament of 2.85 mm diameter, from BCN3D Technologies. The samples have the shape of hemispherical cups, which are similar to the prostheses that are used to replace the acetabula in hip prostheses. Internal diameter of 32 mm and external diameter of 50 mm were selected, which are common dimensions of prostheses [32] (Figure 1 shows).



**Figure 1.** Shape and dimensions of the specimens.

The hemispherical cups were printed in a Sigma R19 machine from BCN3D as shown in Figure 2, with infill value of 20% and shell thickness of 1.2 mm. Printing bed temperature was 65 °C. Printing supports were required, in PLA material. Further details of the printing process are provided in a previous work [30].



**Figure 2.** Sigma R19 from BCN3D.

The experiments were defined according to a fractional factorial design  $2^{5-1}$ , with 5 variables and 2 levels. Selected variables are as follows [30]: Nozzle diameter (ND) between 0.4 and 0.6 mm, temperature (T) between 195 and 205 °C, layer height (LH) between 0.1 and 0.3 mm, print speed (PS) between 30 and 50 mm/s, and extrusion multiplier between 93 and 97%.

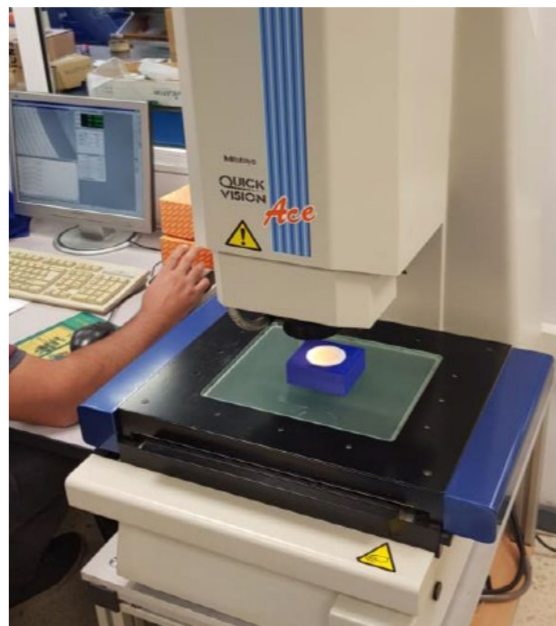
The selected responses are shown in Table 1. Both roundness and concentricity are defined in the UNE-EN-ISO 1101:2017 standard [33].

**Table 1.** Outputs.

Outputs (Int/Ext)		
Dimensional error (Dim Err, mm)	Roundness (Rnd, mm)	Concentricity (Con, mm)

### 2.2. Determination of the Dimensional Error

Dimensional error was measured with a Mitutoyo Quick Vision Ace Equipment. Both the external and the internal diameter of the hemispherical cups were measured, on the base of the hemispherical cups as shown in Figure 3. The specimens were placed on a 3D printed support.



**Figure 3.** Measurement process of dimensional error.

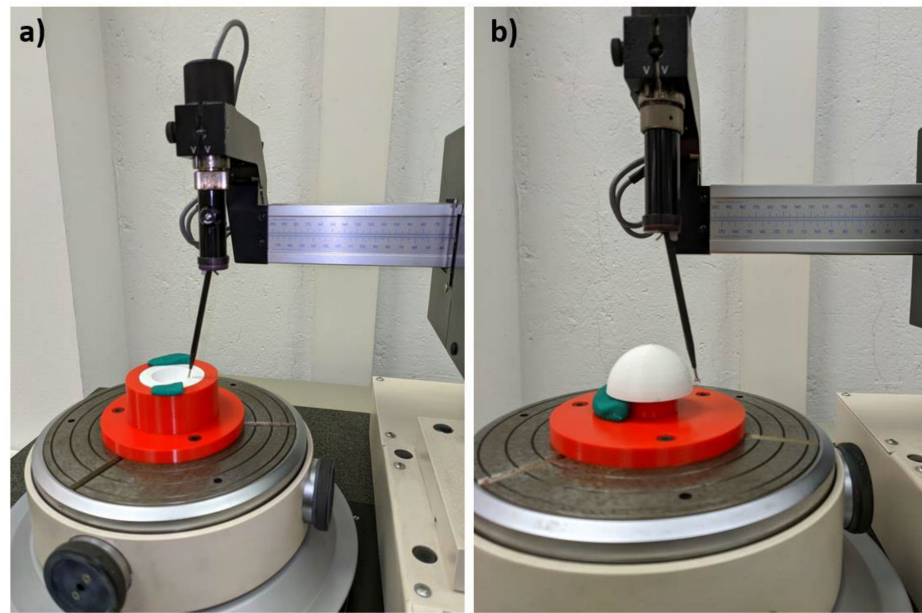
The equipment shown in Figure 3 has a platform on which the support and the part are placed, as well as a head with a lens with 2X magnification. The software allows a digitally magnified and focused image of the part's surface to be obtained. The platform moves along the XY plane, and its displacement is measured. In order to determine the dimensional error, first the platform is moved so that by clicking on the image six points are obtained along each circumference (external or internal). Then, the software uses these six points to calculate the diameter and the location of the center point of the measured circumference.

Dimensional error is then calculated as the difference between the measured value and the theoretical nominal value of a certain dimension. For this reason, in this case dimensional error takes positive values when the measured diameter is higher than the nominal diameter (and it takes negative values when the measured diameter is lower than the nominal diameter).

### 2.3. Determinación of Roundness

Roundness tolerance measures how far a measured circumference is from an ideal circumference and, according to ISO 1101 standard [33], it is defined as the distance between two ideal circumferences (inscribed and circumscribed of the measured circumference) which are defined on a perpendicular plane to the measured circumference. Roundness was determined with a Taylor Hobson Talyrond 252 measuring machine (as shown in Figure 4). This machine has a spherical point with 16 nm resolution, which can measure roundness errors below 1  $\mu\text{m}$ . It only moves along the Z axis, with high precision, while the part, which is located on a circular platform, rotates. It was necessary to design two different 3D print supports, to fix the parts to the platform of the machine, in order to measure roundness of the internal and of the external surface of the parts, respectively.





**Figure 4.** Measurement process of roundness on: (a) the internal surface, (b) the external surface.

#### 2.4. Determination of the Concentricity

According to ISO 1101 standard [33], concentricity is defined as the difference between the measured center of a certain measured circumference and a theoretical reference center. In this case, the center of a circumference measured on the internal surface of the hemispherical cups is taken as the reference center, from which concentricity is defined. Concentricity was determined from the data of the position of the circumferences' centers that were measured with the Mitutoyo Quick Vision Equipment in order to obtain the dimensional error (see Section 2.2).

#### 2.5. ANFIS Modelling

A zero-order Sugeno FIS is employed by using the Fuzzy Logic Toolbox™ of Matlab™2020a (Natick, MA, USA) [34] where Gaussian membership functions were employed for fuzzification of the independent variables. Likewise, Equation (1) shows the product implication method and Equation (2) shows the output of the Sugeno system [34–36].

$$\lambda_j(x) = \text{AndMethod}\{\mu_1(x_1), \dots, \mu_n(x_n)\} \quad (1)$$

$$\{\text{Output}\} = \frac{\sum_{j=1}^{\text{Number of rules}} \lambda_j \times z_j}{\sum_{j=1}^{\text{Number of rules}} \lambda_j} \quad (2)$$

where the parameters analyzed in this present study are the dimensional error, the roundness error, and the concentricity, which have been defined in the previous section.

### 3. Results and Discussion

This section shows the results obtained when applying the ANFIS for modelling the above-mentioned dimensional parameters. As previously mentioned, the form errors of the manufactured parts were measured inside and outside of the hemispherical cups made of PLA material that were printed using FFF technology. Table 2 presents the form error results for both the internal and the external surfaces of the specimens.

**Table 2.** Form errors (dimensional error, roundness) and concentricity.

Exp	ND	T	LH	PS	EM	External		Internal		Concentricity
						Dim Err	Rnd	Dim Err	Rnd	Con
						(mm)	(mm)	(mm)	(mm)	(mm)
1	0.4	195	0.1	30	97	0.084	0.137	−0.161	0.086	0.098
2	0.6	195	0.1	30	93	0.135	0.153	−0.384	0.201	0.125
3	0.4	205	0.1	30	93	−0.018	0.143	−0.090	0.089	0.093
4	0.6	205	0.1	30	97	0.243	0.137	−0.229	0.165	0.051
5	0.4	195	0.3	30	93	0.153	0.153	−0.112	0.190	0.120
6	0.6	195	0.3	30	97	0.198	0.229	−0.137	0.297	0.272
7	0.4	205	0.3	30	97	0.044	0.222	0.156	0.162	0.176
8	0.6	205	0.3	30	93	0.146	0.164	−0.178	0.235	0.182
9	0.4	195	0.1	50	93	−0.210	0.141	0.217	0.137	0.083
10	0.6	195	0.1	50	97	0.057	0.149	−0.057	0.167	0.127
11	0.4	205	0.1	50	97	0.361	0.147	−0.26	0.129	0.100
12	0.6	205	0.1	50	93	0.290	0.209	−0.184	0.270	0.202
13	0.4	195	0.3	50	97	0.188	0.195	−0.187	0.163	0.158
14	0.6	195	0.3	50	93	−0.025	0.206	−0.053	0.194	0.175
15	0.4	205	0.3	50	93	0.314	0.161	−0.200	0.129	0.140
16	0.6	205	0.3	50	97	0.190	0.262	−0.153	0.214	0.190
17-1	0.5	200	0.2	40	95	0.145	0.180	−0.074	0.110	0.053
17-2	0.5	200	0.2	40	95	0.234	0.175	−0.042	0.101	0.066
17-3	0.5	200	0.2	40	95	0.113	0.155	−0.115	0.099	0.026

Most experiments show positive dimensional error on the external wall of the parts, showing that the diameter of the printed parts is higher than the theoretical one. Conversely, dimensional error is mainly negative in the internal wall of the parts, indicating that diameters are smaller than expected. This suggests an excess of material in the printed parts with respect to the original geometry of the hemispherical cups. The highest dimensional error value of 0.314 mm was obtained on the external wall of experiment 15, corresponding to low nozzle diameter, high temperature, high layer height, high speed and low extrusion multiplier. Lowest dimensional error was found in experiment three, obtained with low nozzle diameter, high temperature, low layer height, low print speed and low extrusion multiplier. In an earlier paper, higher relative dimensional errors between 0.82% and 2.60% were reported in prismatic porous samples [37]. In this present work, lower relative dimensional errors were obtained, ranging between 0.036% and 0.625%. This can be attributed to the fact that, in this work, dimensional errors have been measured at the base of the printed samples, corresponding to the first layer of the parts, which is directly deposited on the printing bed. Thus, it is less likely to suffer deformation than other layers. Equbal et al. [38] obtained relative error values of up to 0.300% in length, 0.628% in width, and 3.143% in thickness in the ABS material. Spindola Filho et al. [15] found cylindricity values up to 0.140 mm in ABS parts.

Roundness values range between 0.089 mm for experiment 3 and 0.297 mm for experiment 6. Similar values of 0.292 mm were reported by Maurya et al. in PLA parts [39]. Sajan et al. [40] studied circularity of parts that were printed on different planes. For the plane XY, on which the parts of the present study were printed, a maximum circularity value of 0.401 mm is reported.

Concentricity ranges between 0.048 mm (average value for experiment 17, central point) and 0.272 mm for experiment 6. Rupal et al. [41] obtained similar average concentricity values of 0.300 mm in ABS, PLA, and magnetic-PLA parts.

### 3.1. Models for Dimensional Error

Figure 5 corresponds to an image of the vision machine showing the base (flat surface) of a hemispherical sample, where both the diameter of the external and of the internal circumference are measured, as well as the location of their center points. From the position of the center points the concentricity error was measured.

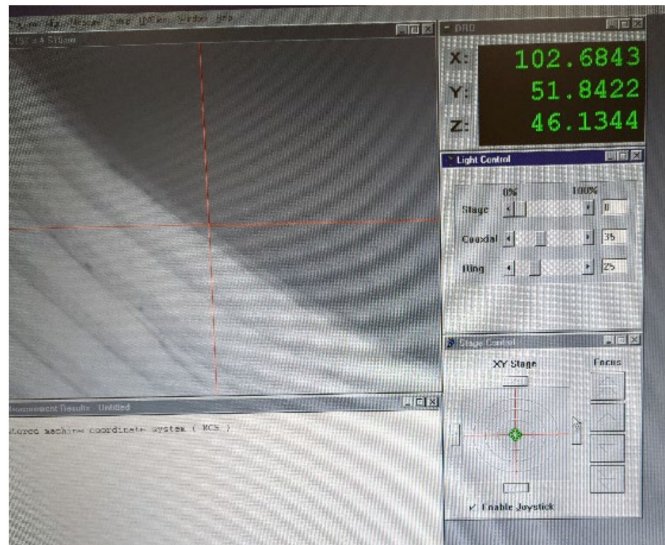


Figure 5. Example of an image obtained with the vision machine.

Figure 6 shows the response surfaces by using the ANFIS models for the case of the dimensional error in the outer surface of the manufactured parts and Figure 7 shows those obtained for the internal part of the prototypes.

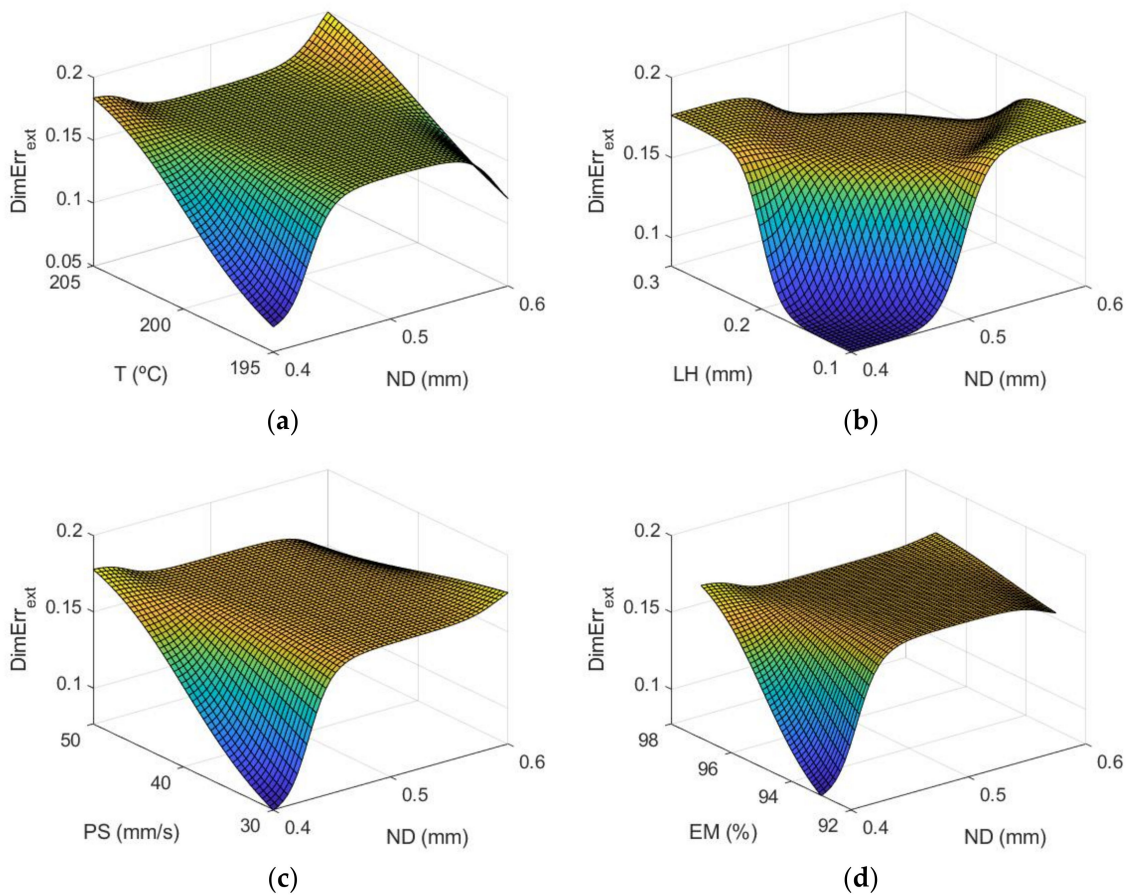
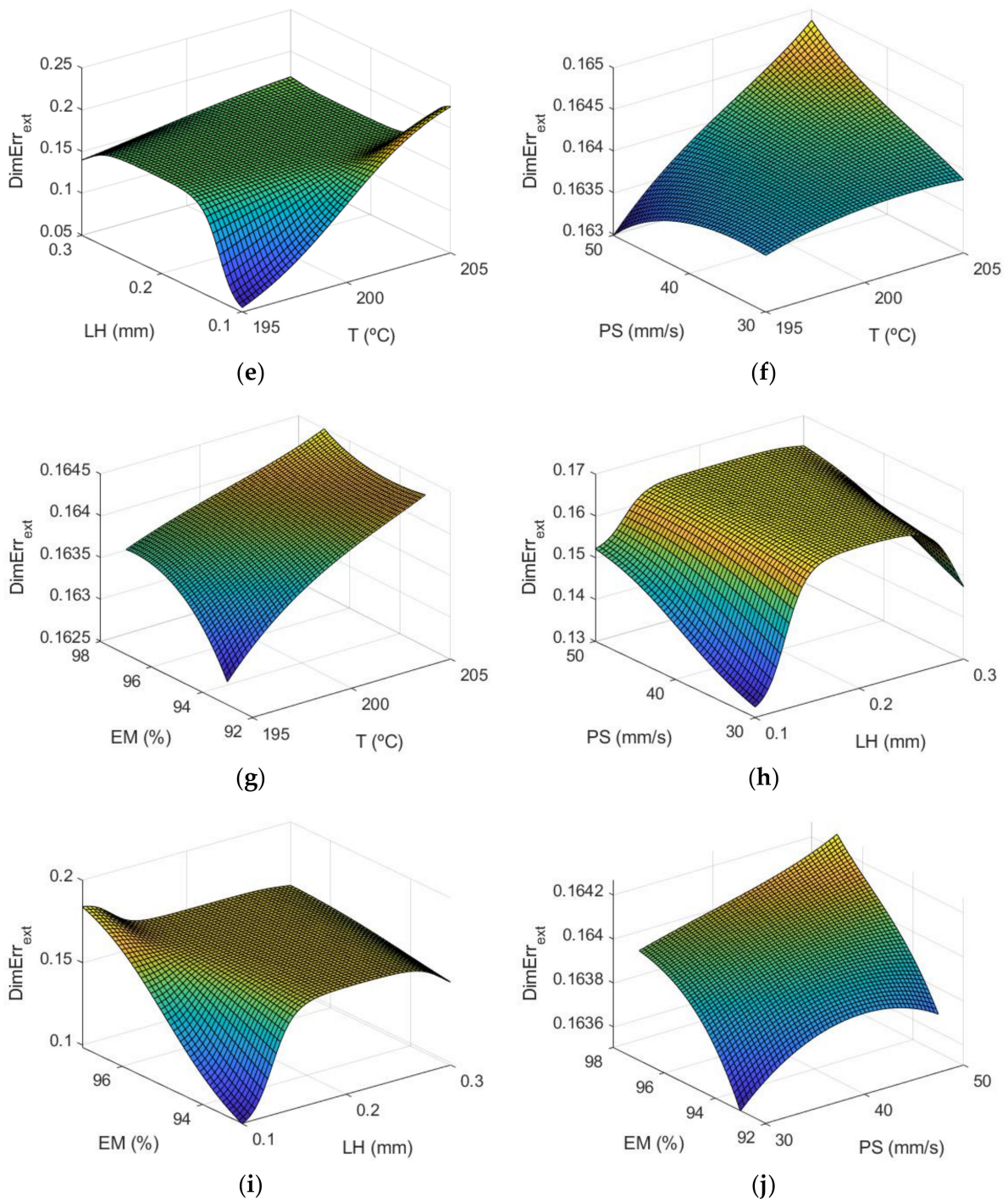


Figure 6. Cont.



**Figure 6.** Response surfaces of dimensional error (mm) using the ANFIS for the case of the outer layer of the manufactured prototypes: (a) ND and T; (b) ND and LH; (c) ND and PS; (d) ND and EM; (e) T and LH; (f) T and PS; (g) T and EM; (h) LH and PS; (i) LH and EM; and (j) PS and EM.

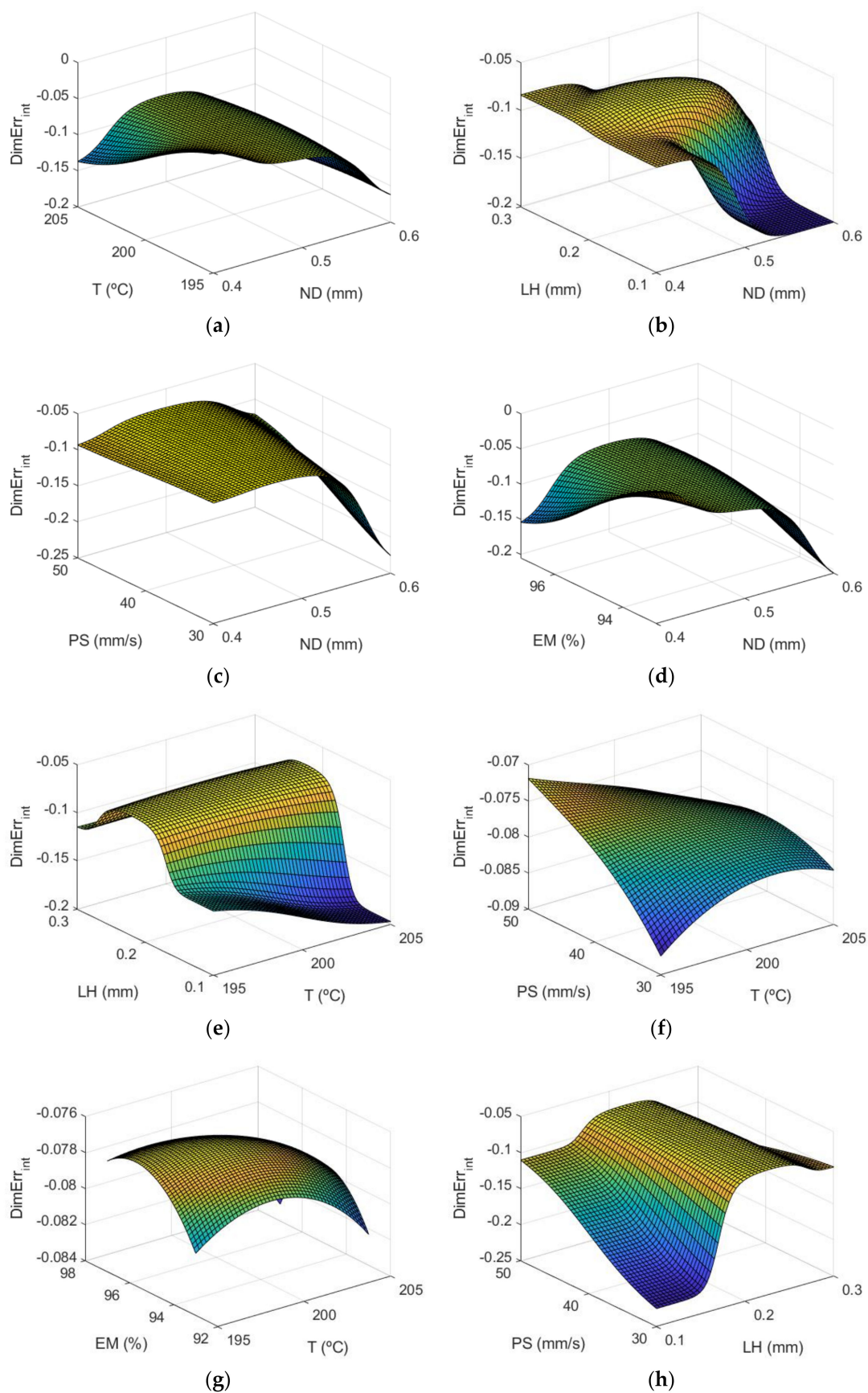
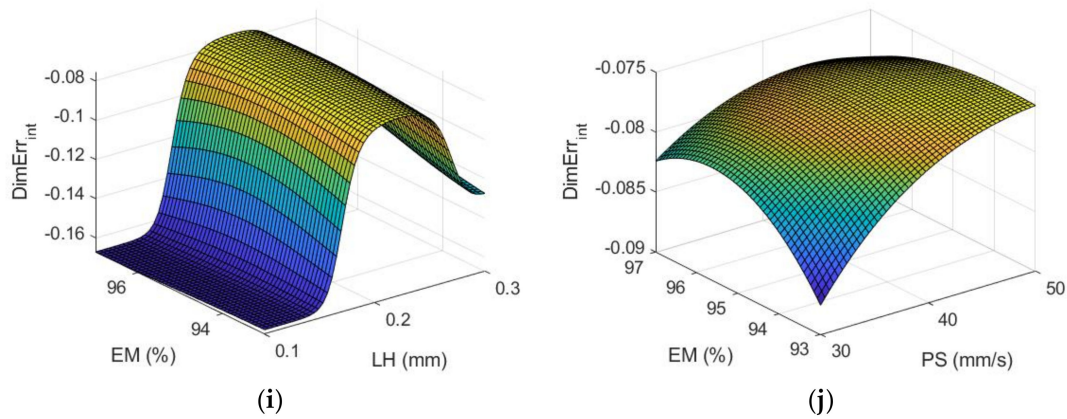


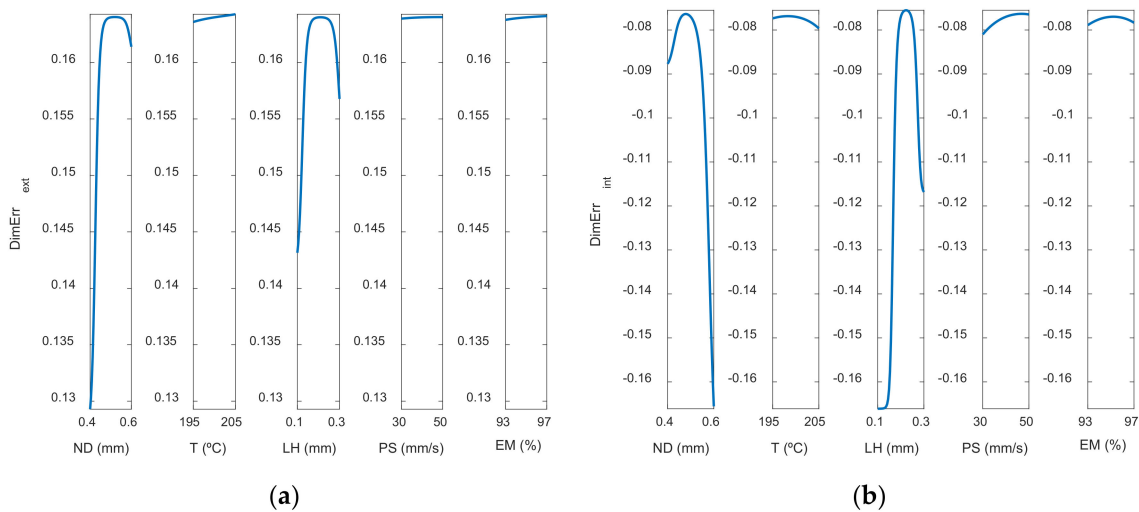
Figure 7. Cont.



**Figure 7.** Response surfaces of dimensional error (mm) using the ANFIS for the case of the inner layer of the manufactured prototypes: (a) ND and T; (b) ND and LH; (c) ND and PS; (d) ND and EM; (e) T and LH; (f) T and PS; (g) T and EM; (h) LH and PS; (i) LH and EM; and (j) PS and EM.

Figure 7 corresponds to the response surfaces for dimensional error of the inner surfaces of the parts.

The most influential parameters on dimensional error are nozzle diameter and layer height. This is also observed in Figure 8 (main effects plots), and in Figure 9 (interaction effects plots).

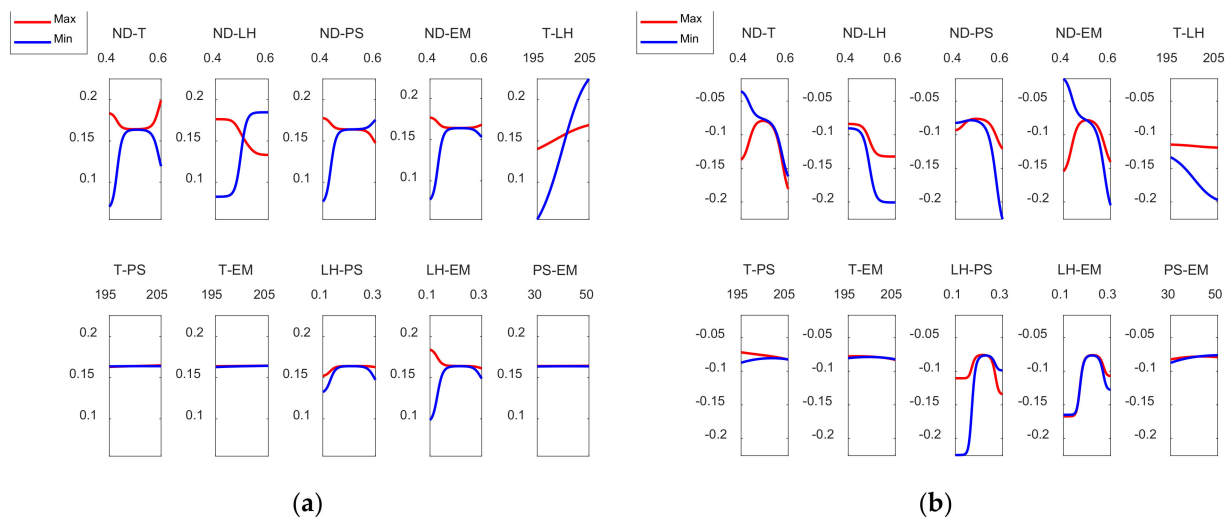


**Figure 8.** Main effects plots for (a) Dimensional Error<sub>ext</sub> (mm) and (b) Dimensional Error<sub>int</sub> (mm).

Figure 8 depicts the main effect plots for both (a) the outer and (b) the inner zones of the manufactured prototypes. In these plots is shown the variation of each variable between its maximum and minimum levels, when all of the other factors are held at their average level.

As can be observed, the main parameters that affect the dimensional error are ND and LH, where the rest of the input variables have less influence on the dimensional error. An increase in nozzle diameter leads to an increase in dimensional error. In the outer surface of the parts, high nozzle diameter of 0.6 mm leads to high dimensional error. The measured diameter is higher than the theoretical one. In the inner surface of the parts, high nozzle diameter of 0.6 mm produces high dimensional error. In this case, since dimensional error values are negative, the measured diameter is lower than the theoretical one. This suggests that, when high nozzle diameter is employed, there is an excess of material. Dimensional error increases noticeably when layer height increases from 0.1 mm to 0.2 mm, but then

decreases slightly if layer height of 0.3 mm is selected. Thus, low layer height of 0.1 mm is recommended in order to obtain low dimensional error. These results are in accordance with Nancharaiah et al. [7] regarding layer height. However, they recommended large bead width in order to reduce dimensional error. Spindola Filho et al. [15] found that print speed followed by layer height and the interaction between fill density and printing temperature (confounded with the interaction between print speed and layer height) were the most influential terms on dimensional error in ABS parts.



**Figure 9.** Inter action effects plots for (a) *Dimensional Error<sub>ext</sub>* (mm) and (b) *Dimensional Error<sub>int</sub>* (mm).

Figure 9 shows the interaction effects plot for the case of the dimensional error in both the outer and the inner zones of the prototypes.

As Figure 9a shows, in order to reduce the dimensional error, on the external surface, ND should be kept at its lowest level and at the same time T, LH, PS and EM should be kept at their minimum levels. On the other hand, the interaction between T and LH suggests that for low temperature values, LH should be at its minimum value to minimize the dimensional error. With regard to LH and EM, LH should be kept at its minimum level and the same is applicable to EM. In the case of Figure 9b, dimensional errors inside are mostly negative, since the measured diameter is lower than the nominal (theoretical) diameter. In this case, it is still interesting to keep ND at its lowest value and for T and EM to be at the minimum values. It does not matter that LH or PS are at minimum or maximum values while ND remains at its lowest level. In the case of the T-LH interaction, T should be kept at its minimum value. The effect of LH while ND is kept at the minimum value is not significant. However, if ND rises, LH should be at the maximum level, in order to minimize the dimensional error inside the manufactured parts. In the case of the interaction between LH and PS, for low LH values, it is interesting to keep PS at high values. On the other hand, for high LH values PS should be kept at low values. The rest of the interactions has less influence.

### 3.2. Models for Concentricity

Figure 10 shows the response surface for the case of the concentricity.

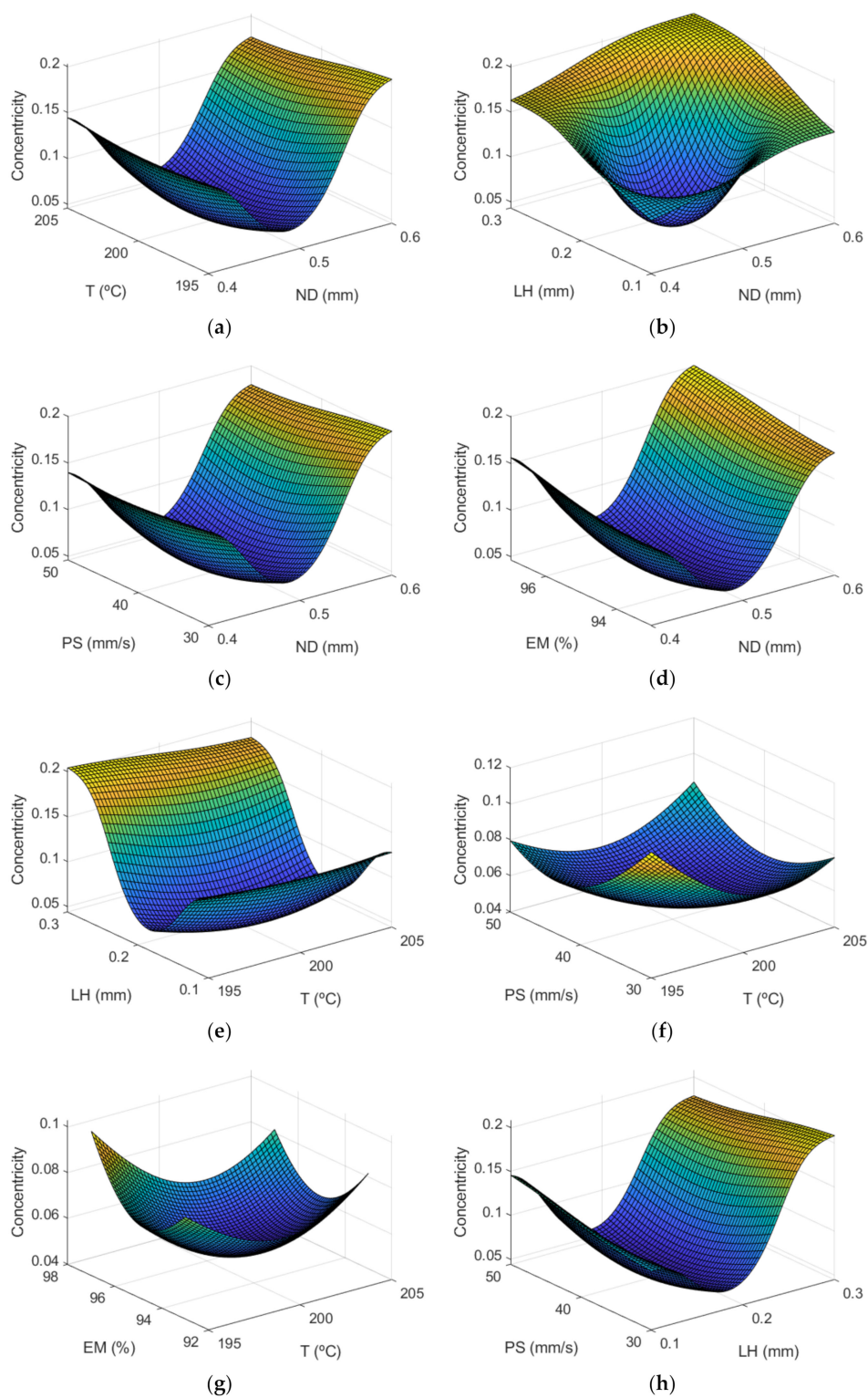
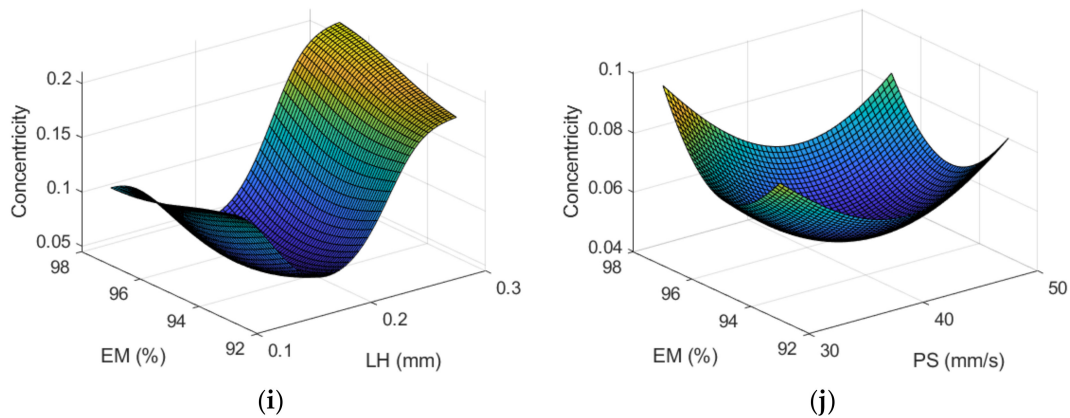


Figure 10. Cont.

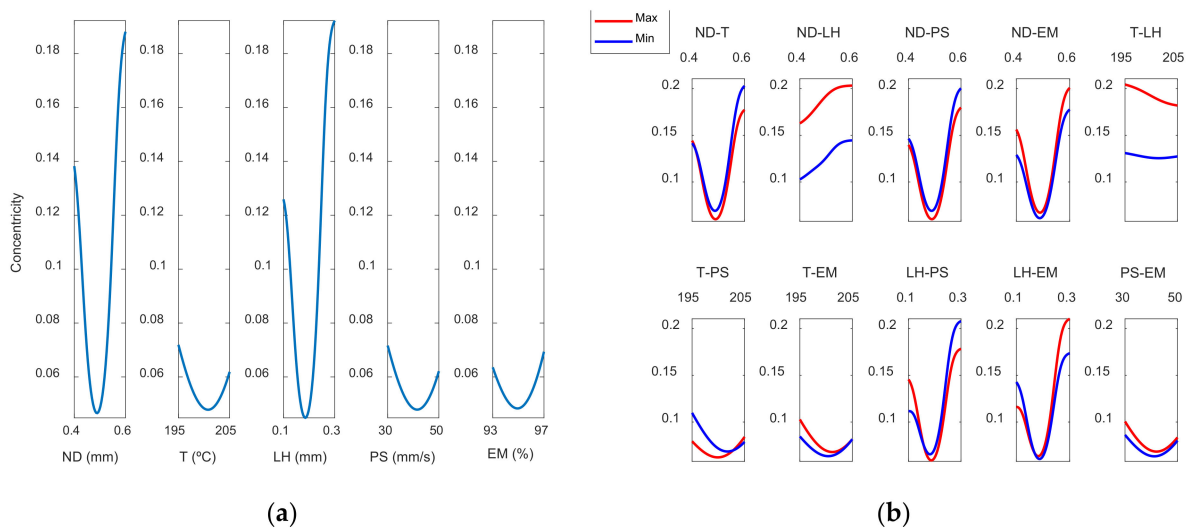




**Figure 10.** Surface response of concentricity (mm) using the ANFIS for the case of the manufactured prototypes: (a) ND and T; (b) ND and LH; (c) ND and PS; (d) ND and EM; (e) T and LH; (f) T and PS; (g) T and EM; (h) LH and PS; (i) LH and EM; and (j) PS and EM.

As can be observed, the parameters that have the most effect are LH and ND. Conversely, Spindola Filho et al. [15] found that most influential parameter on concentricity was print speed. However, they did not vary the nozzle diameter and they employed higher layer height values between 0.2 and 0.4 mm.

Finally, Figure 11 shows both the main and the interaction effects plot for the input variables under study.



**Figure 11.** (a) Main effects plots and (b) interaction effects plots for Concentricity.

Lowest concentricity error is obtained when medium nozzle diameter of 0.5 mm and medium layer height of 0.2 mm are selected. However, those conditions provide highest dimensional error (see Figure 8).

It may be noted that the interaction between variables is less than that obtained in the case of the dimensional error.

### 3.3. Models for Roundness Errors

Figures 12 and 13 show the response surfaces for the case of the roundness by using the ANFIS models, in the outer and inner areas, respectively.

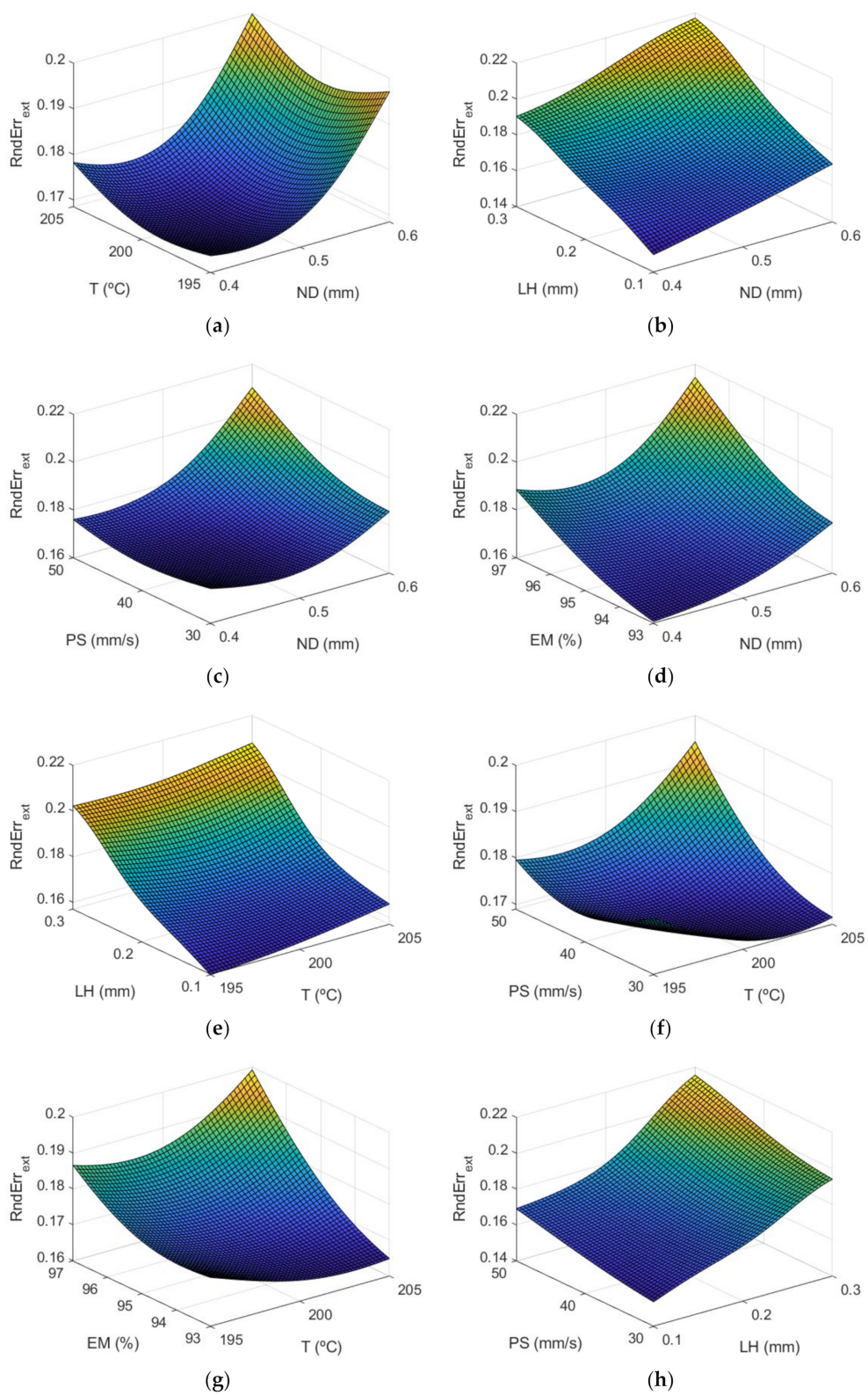
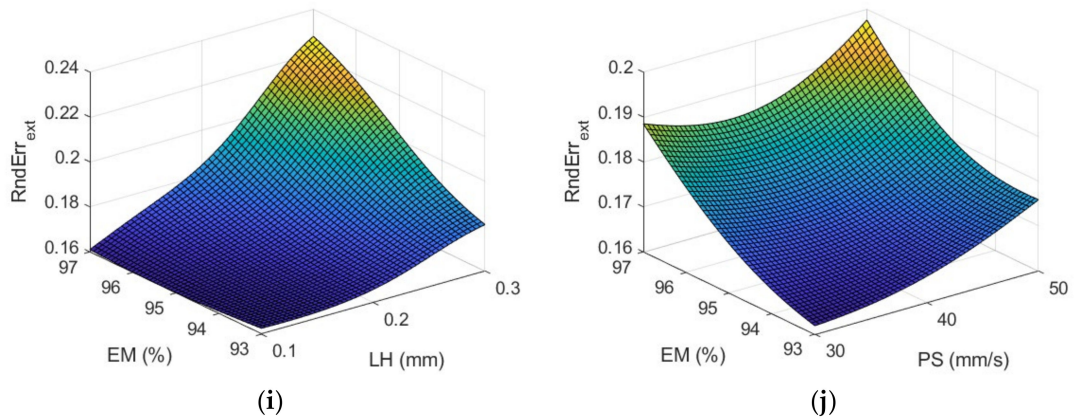
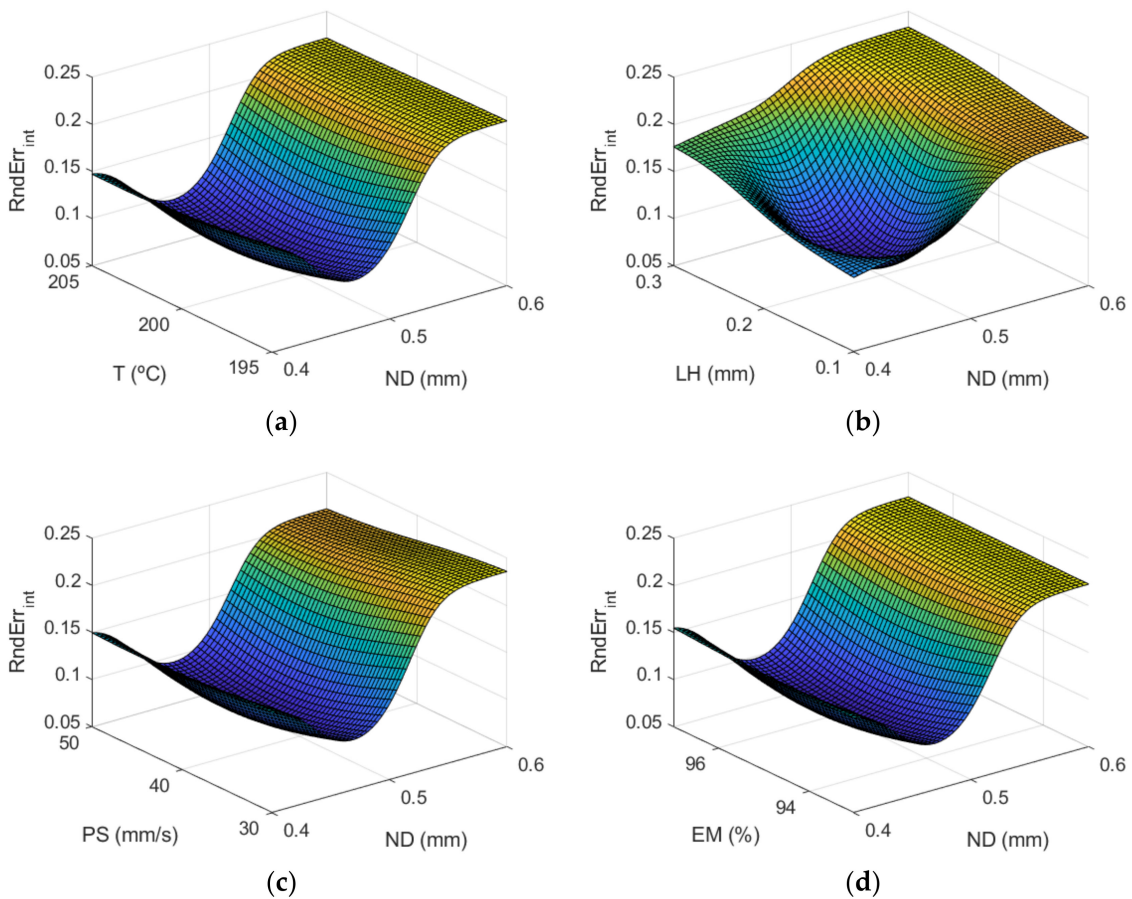


Figure 12. Cont.

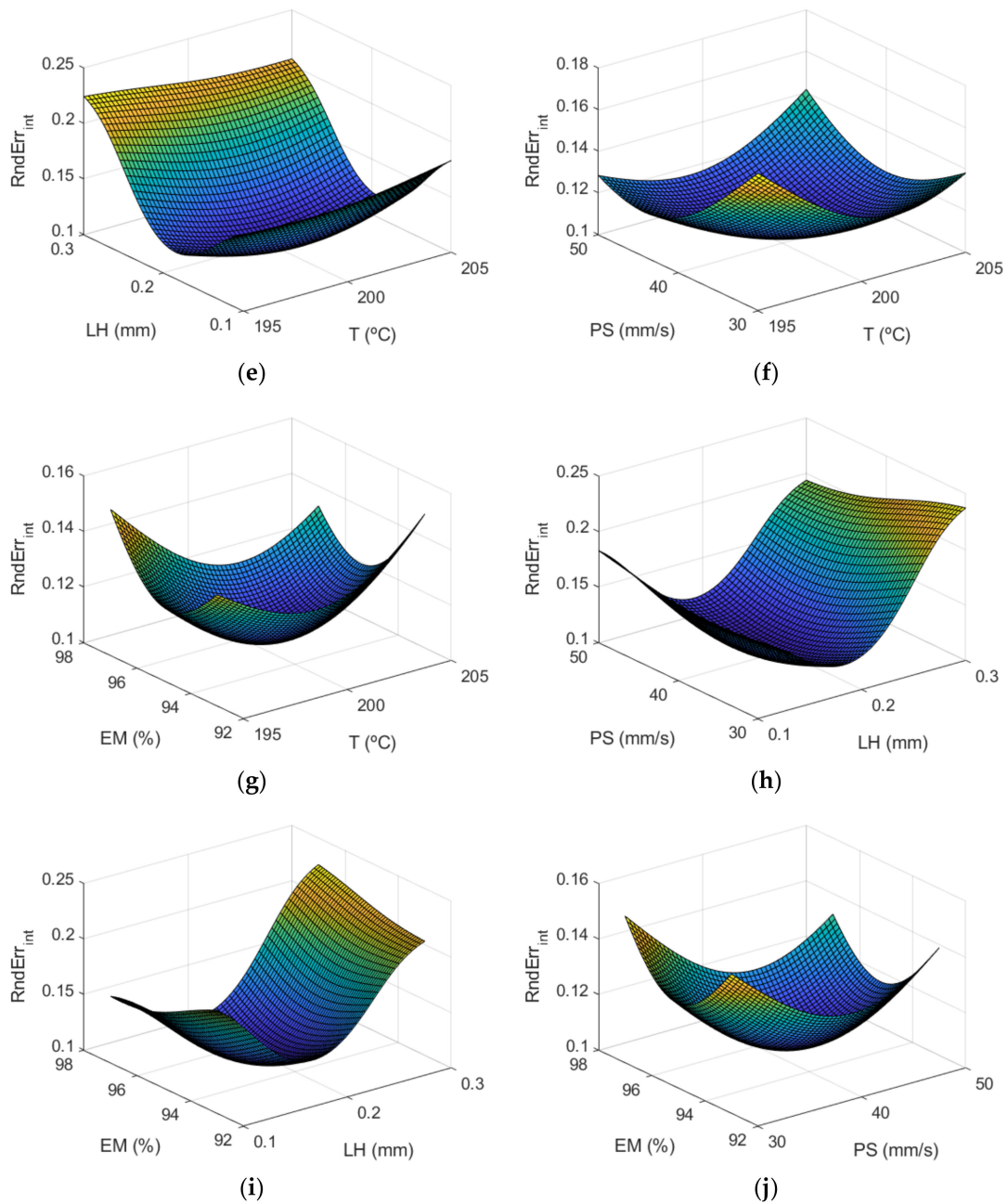


**Figure 12.** Response surfaces of roundness (mm) using the ANFIS for the case of the outer layer of the manufactured prototypes: (a) ND and T; (b) ND and LH; (c) ND and PS; (d) ND and EM; (e) T and LH; (f) T and PS; (g) T and EM; (h) LH and PS; (i) LH and EM; and (j) PS and EM.

The information included in Figures 12 and 13 is explained in more detail in Figures 14 and 15. Figure 14 shows the main effect plots for the case of the roundness on both surfaces.



**Figure 13.** Cont.



**Figure 13.** Surface response of roundness (mm) using the ANFIS for the case of the inner layer of the manufactured prototypes: (a) ND and T; (b) ND and LH; (c) ND and PS; (d) ND and EM; (e) T and LH; (f) T and PS; (g) T and EM; (h) LH and PS; (i) LH and EM; and (j) PS and EM.

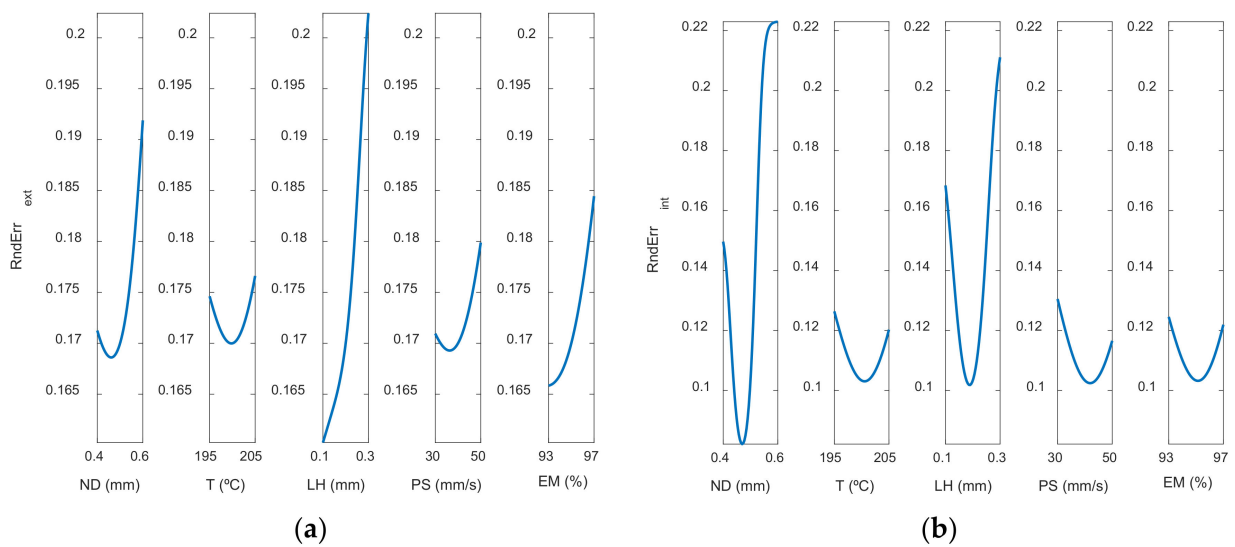


Figure 14. Main effects plots for (a) Roundness<sub>ext</sub> (mm) and (b) Roundness<sub>int</sub> (mm).

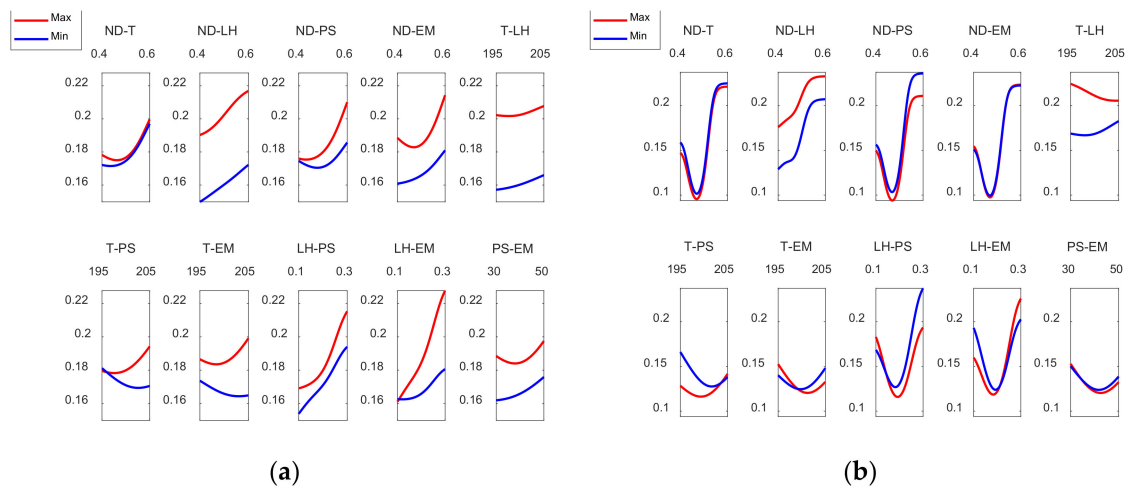


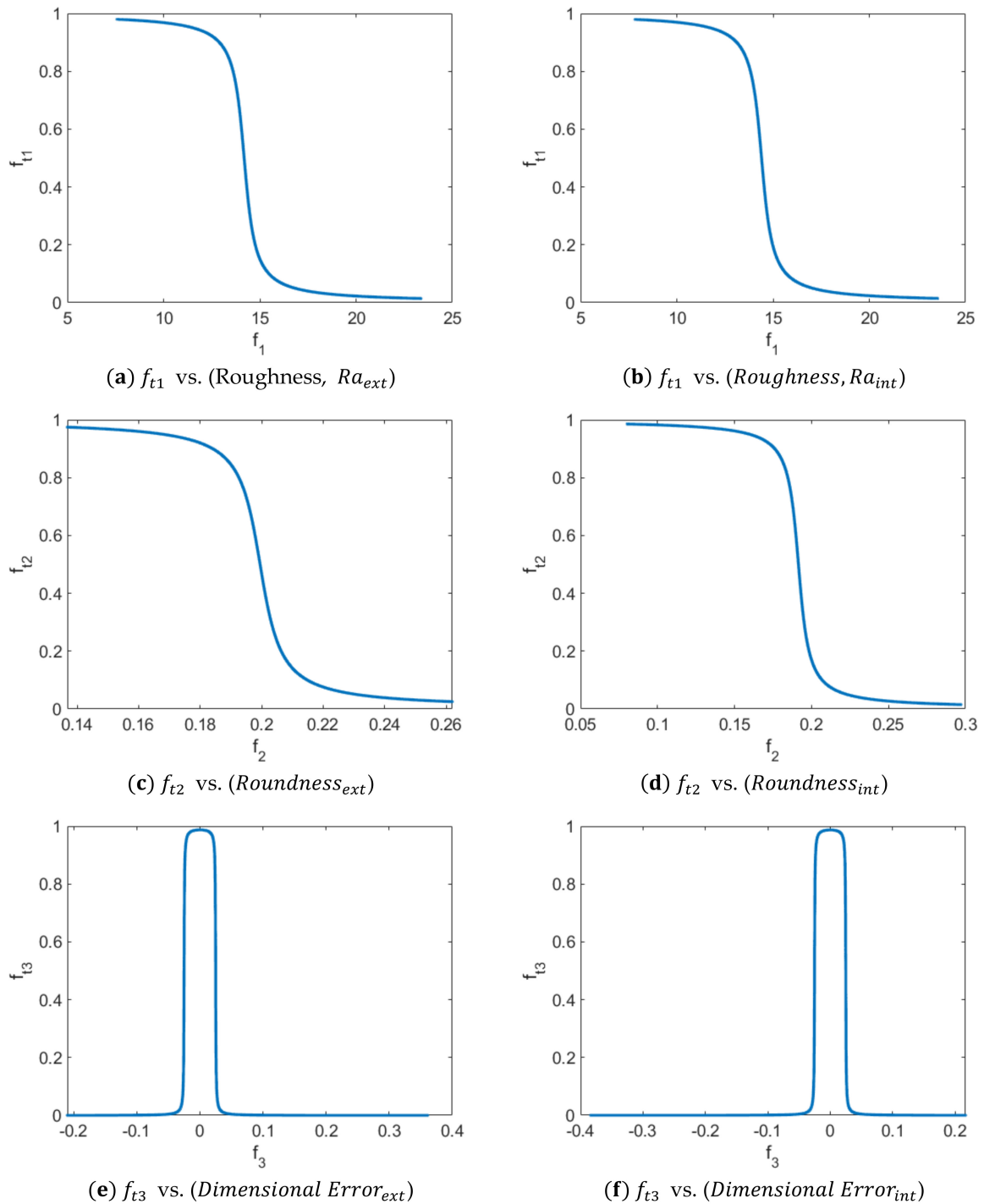
Figure 15. Interaction effects plots for (a) Roundness<sub>ext</sub> (mm) and (b) Roundness<sub>int</sub> (mm).

It may be seen that the parameters that most affect roundness are LH and ND. Roundness error decreases slightly when nozzle diameter increases from 0.4 to 0.5 mm but increases noticeably when nozzle diameter of 0.6 mm is selected. Highest roundness error is found when layer height of 0.3 mm is selected. To sum up, high layer height of 0.3 mm and high nozzle diameter of 0.6 mm are not recommended, since they provide high roughness error, high concentricity error and high dimensional error. Accordingly, as for the reduction of cylindricity of the printed parts, Maurya et al. [10] recommended low layer thickness of 100  $\mu\text{m}$ . Conversely, Spindola Filho et al. [15] observed that print speed was the most influential factor on the cylindricity of ABS printed parts.

Finally, Figure 15 shows the interaction effects plot for roundness for the case of the outer and inner zones, respectively.

Figure 16a shows that ND should be kept at its lowest value to minimize external roundness and that the preferred variation for T, LH, and EM is the minimum value. Likewise, the interaction between T and LH, suggests that both the temperature and the layer height are kept at their minimum values. A contrary behavior is observed in the T-PS and T-EM interactions where the temperature should be at the highest level and PS and EM should be kept at their lowest levels. Dealing with the interaction LH-PS, it can be pointed out that LH should be at its lowest level and the same is applicable to PS. Moreover, in the interaction between LH and EM, if LH is set to its minimum, the level of EM does not

matter. However, if LH rises EM should remain at its lowest level. On the other hand, Figure 16b shows that, in order to minimize internal roundness, ND should be close to its minimum value, in this case it does not matter if T, PS and EM are at the maximum or minimum values. In the case of the interaction between ND and LH, it can be observed that both ND and LH should be kept at their lowest values. Similarly, in the T-LH interaction it can be observed that both the temperature and LH should be kept at their lowest values.



**Figure 16.** Transformation of the values of the response functions obtained by using the ANFIS and the desirability function proposed by Luis-Pérez [31] for the case of the outer surface (a–c) and for the case of the inner surface (d–e): (a)  $f_{t1}$  vs. (Roughness,  $Ra_{ext}$ ), (b)  $f_{t2}$  vs. (Roundness $_{ext}$ ), (c)  $f_{t3}$  vs. (Dimensional Error $_{ext}$ ), (d)  $f_{t2}$  vs. (Roundness $_{int}$ ), (e)  $f_{t2}$  vs. (Roundness $_{int}$ ), and (f)  $f_{t3}$  vs. (Dimensional Error $_{int}$ ).

### 3.4. Multiobjective Optimization

In order to determine a set of values that simultaneously optimize roughness, roundness and dimensional error, a multi-objective optimization has been carried out following the methodology shown in the research work by Luis-Pérez [31]. For this purpose, the modeling obtained with the ANFIS for the response variables under study along with the desirability function proposed by [31] is used for optimization. The variables to be optimized have been selected as the surface roughness, characterized by the arithmetic mean roughness (Ra), which was already studied in a previous work carried out by the authors of this manuscript. Therefore, the ANFIS models developed in this present study for roundness and dimensional error are employed, as well as the ANFIS developed for Ra in [30].

The multi-objective optimization study has been carried out for the five input variables and three cases have been considered as output variables to be optimized: (a) Minimize (Ra and Roundness) and at the same time keep  $|Dimensional\ Error| \leq 0.01$ , in the outer zone; (b) Minimize (Ra and Roundness) and at the same time keep  $|Dimensional\ Error| \leq 0.01$  in the inner zone and (c) simultaneously optimize the outer and inner zone. That is, minimize (Ra and Roundness) (for both zones) and at the same time keep  $|Dimensional\ Error| \leq 0.01$ , for both the outer zone and the inner zone.

Figure 16 shows the transformation of the values of the response functions obtained by using the ANFIS (for Ra, Roundness and Dimensional Error) and the desirability function proposed by Luis-Pérez [31] for the case of the outer surface (a–c) and for the case of the inner surface (e–f).

The values used to represent the functions shown in Figure 16 are those obtained after observing convergence in the values provided by the desirability function for both the outer zone and the inner zone. Table 3 shows the results of the multi-objective optimization for case a) in which minimize (Ra and Roundness) and  $|Dimensional\ Error| \leq 0.01$ , for the outer surface of the manufactured parts. On the other hand, Table 4 shows the results of the multi-objective optimization: Minimize (Ra & Roundness) and  $|Dimensional\ Error| \leq 0.01$  for the inner surface of the manufactured parts and finally Table 5 shows the results obtained for the case of the simultaneous optimization of the outer and inner surface.

**Table 3.** Multi-objective optimization results: minimize (Ra & Roundness) and  $|Dimensional\ Error| \leq 0.01$ , for the outer surface of the manufactured parts using the desirability function and the methodology proposed by Luis-Pérez [31].

Desirability Value	ND	T	LH	PS	EM	Ra ( $\mu\text{m}$ )	Roundness (mm)	Dimensional Error (mm)
0.9780	0.4000	205.0000	0.1000	31.0526	93.6316	8.3972	0.1460	−0.0054

**Table 4.** Multi-objective optimization results: minimize (Ra & Roundness) and  $|Dimensional\ Error| \leq 0.01$ , for the inner surface of the manufactured parts using the desirability function and the methodology proposed by Luis-Pérez [31].

Desirability Value	ND	T	LH	PS	EM	Ra ( $\mu\text{m}$ )	Roundness (mm)	Dimensional Error (mm)
0.9764	0.4000	195.5882	0.1000	39.4118	94.8824	10.4376	0.1267	−0.0010

**Table 5.** Multi-objective optimization results: minimize (Ra and Roundness) and  $|Dimensional\ Error| \leq 0.01$ , simultaneously for the inner and the outer surfaces of the manufactured parts using the desirability function and the methodology proposed by Luis-Pérez [31].

Desirability Value	ND	T	LH	PS	EM		Ra ( $\mu\text{m}$ )	Roundness (mm)	Dimensional Error (mm)
0.9759	0.4000	197.6667	0.1000	42.0000	94.8667	Ext.	9.2643	0.1476	−0.0048
						Int.	10.4977	0.1320	−0.0022

As can be observed in Table 3, it is shown that the preferred values to simultaneously optimize roughness and roundness as well as dimensional error are those in which ND and LH are kept at their lower levels and PS and EM are also close to the lower values of the input variables, within the range of the values studied. On the other hand, the working temperature should be increased to the highest level. Other solutions were found with slightly lower desirability values, for example 0.9771, in which a low temperature of 195 °C is recommended, with the rest of the variables in their low values or similar, except for the extrusion multiplier which should be around 95%. Low temperature is recommended for the inner surface (Table 4) and for the simultaneous optimization of both surfaces (Table 5).

On the other hand, Table 4 shows that, similarly to results obtained in Table 3, ND and LH should be kept at their minimum values and PS and EM should be slightly increased in relation to the previous case. On the other hand, the temperature value, in the case of the interior zone, should be selected close to the minimum value selected for experimentation.

Finally, Table 5 shows the simultaneous optimization of roughness, roundness, and dimensional error for the case of both inner and outer surfaces (that is, six response variables). In this case, ND and LH should be kept at their minimum value, T should be close to its low value, while PS and EM should be close to their medium value. As was previously observed (Figures 8, 11 and 14), high nozzle diameter and high layer height are not recommended if dimensional and form errors are to be minimized.

#### 4. Conclusions

In this present research study, the main factors that affect the dimensional accuracy and form error of hemispherical cups 3D printed in PLA using the FFF technology have been examined. Different experimental tests were carried out according to a fractional factorial design of experiments (DOE).

Modeling has been carried out using ANFIS to obtain response models for dimensional error, roundness and concentricity of the hemispherical cups. It was observed that all of the responses, namely dimensional error, roundness error, and concentricity depend mainly on nozzle diameter and layer height (considering both the outer and the inner surfaces of the parts). High nozzle diameter of 0.6 mm and high layer height of 0.3 mm are not recommended due to the fact that they increase dimensional and form errors.

The models were used together with a desirability function to obtain the input parameters that simultaneously optimize surface finish, roundness and dimensional error. This has been carried out both independently, for the outer surface and the inner surface of the manufactured parts, as well as for simultaneous optimization (that is, with the results obtained for the outer and the inner zones of the prototypes).

In the range of values and parts analyzed in this study, it has been found that in the first and second cases (outer and inner surface, respectively) layer height and nozzle diameter should be kept at their lower values (0.1 mm and 0.4 mm, respectively) and also print speed and extrusion multiplier should be kept, in both cases, at values close to the lowest ones (30 mm/s and 93%). Regarding the first case, which is related to the outer surface of the parts, unlike the other two cases, temperature should be kept at the maximum value, 205 °C. However, other solutions were found for the outer surface with slightly lower desirability values, in which a low temperature of 195 °C is recommended, with the rest of the variables are in their low values or similar (except for the extrusion multiplier, which should be around 95%).

Regarding the third case, simultaneous optimization (inner-outer), nozzle diameter and layer height, as well as temperature, should be kept at the lowest value of the DOE (0.4 mm, 0.1 mm and 195 °C respectively). Meanwhile, print speed and extrusion multiplier should be approximately at their central value (40 mm/s and 95%).



**Author Contributions:** Conceptualization, I.B.-C. and C.J.L.-P.; methodology, I.B.-C. and X.S.-C.; software, C.J.L.-P. and X.S.-C.; validation, I.B.-C.; formal analysis, I.B.-C.; investigation, I.B.-C. and C.J.L.-P.; resources, I.B.-C.; data curation, X.S.-C.; writing—original draft preparation, I.B.-C. and C.J.L.-P.; writing—review and editing, I.B.-C. and C.J.L.-P.; visualization, I.B.-C., C.J.L.-P., and X.S.-C.; supervision, C.J.L.-P.; project administration, I.B.-C.; funding acquisition, I.B.-C. All authors have read and agreed to the published version of the manuscript.

**Funding:** This research was financed by the Spanish Ministry of Industry, Economy and Competitiveness, grant number PID2020-115647RB-C21.

**Institutional Review Board Statement:** Not applicable.

**Informed Consent Statement:** Not applicable.

**Data Availability Statement:** Not applicable.

**Acknowledgments:** The authors thank Alejandro Domínguez-Fernández and Ramón Casado-López for their help with the experimental tests.

**Conflicts of Interest:** The authors declare no conflict of interest.

## References

- Garg, A.; Bhattacharya, A.; Batish, A. On Surface Finish and Dimensional Accuracy of FDM Parts after Cold Vapor Treatment. *Mater. Manuf. Process.* **2016**, *31*, 522–529. [\[CrossRef\]](#)
- Peng, T.; Yan, F. Dual-objective Analysis for Desktop FDM Printers: Energy Consumption and Surface Roughness. *Procedia CIRP* **2018**, *69*, 106–111. [\[CrossRef\]](#)
- Buj-Corral, I.; Tejo-Otero, A.; Fenollosa-Artés, F. Development of AM Technologies for Metals in the Sector of Medical Implants. *Metals* **2020**, *10*, 686. [\[CrossRef\]](#)
- Chua, C.K.; Leong, K.F. *3D Printing and Additive Manufacturing: Principles and Applications: The 5th Edition of Rapid Prototyping: Principles and Applications*; World Scientific Publishing Co: Singapore, 2016; pp. 1–456. ISBN 9789813149274.
- Rahman, H.; John, T.; Sivadasan, M.; Singh, N. Investigation on the Scale Factor applicable to ABS based FDM Additive Manufacturing. *Mater. Today Proc.* **2018**, *5*, 1640–1648. [\[CrossRef\]](#)
- Ceretti, E.; Ginestra, P.; Neto, P.; Fiorentino, A.; da Silva, J.V.L. Multi-layered Scaffolds Production via Fused Deposition Modeling (FDM) Using an Open Source 3D Printer: Process Parameters Optimization for Dimensional Accuracy and Design Reproducibility. *Procedia CIRP* **2017**, *65*, 13–18. [\[CrossRef\]](#)
- Nancharaiyah, T.; Raju, D.R.; Raju, V.R. An experimental investigation on surface quality and dimensional accuracy of FDM components. *Int. J. Emerg. Technol.* **2010**, *1*, 106–111.
- Pennington, R.C.; Hoekstra, N.L.; Newcomer, J.L. Significant factors in the dimensional accuracy of fused deposition modelling. *Proc. Inst. Mech. Eng. Part E J. Process. Mech. Eng.* **2005**, *219*, 89–92. [\[CrossRef\]](#)
- Akbaş, O.E.; Hira, O.; Hervan, S.Z.; Samankan, S.; Altunkaynak, A. Dimensional accuracy of FDM-printed polymer parts. *Rapid Prototyp. J.* **2019**, *26*, 288–298. [\[CrossRef\]](#)
- Maurya, N.K.; Rastogi, V.; Singh, P. Fabrication of prototype connecting rod of PLA plastic material using FDM prototype technology. *Indian J. Eng. Mater. Sci.* **2020**, *27*, 333–343.
- Knoop, F.; Schoeppner, V. Geometrical accuracy of holes and cylinders manufactured with fused deposition modeling. In Proceedings of the 2017 International Solid Freeform Fabrication Symposium, Austin, TX, USA, 7–9 August 2017; pp. 2757–2776.
- Saqib, S.; Urbanic, J. An Experimental Study to Determine Geometric and Dimensional Accuracy Impact Factors for Fused Deposition Modelled Parts. In *Enabling Manufacturing Competitiveness and Economic Sustainability*; Springer: Berlin/Heidelberg, Germany, 2012. [\[CrossRef\]](#)
- Ollison, T.; Berisso, K. Three-dimensional printing build variables that impact cylindricity. *J. Ind. Technol.* **2010**, *26*, 1–10.
- Paul, R.; Anand, S. Optimization of layered manufacturing process for reducing form errors with minimal support structures. *J. Manuf. Syst.* **2015**, *36*, 231–243. [\[CrossRef\]](#)
- Spindola-Filho, J.; Piratelli-Filho, A.; Arencibia, R. Application of Reference Part and Design of Experiments for Metrological Evaluation of AM Manufacturing Machine with FDM Technology. In Proceedings of the CAD'20, Barcelona, Spain, 6–8 July 2020; pp. 61–65.
- Boejang, H.; Ramli, F.R.; Alkahari, M.R.; Juzaila, M.; Latif, A. Performance Assessment of Rapid Prototyping Technologies. In Proceedings of the International Conference on Mechanical and Manufacturing Engineering 2008, Johor Baharu, Malaysia, 1–8 May 2008.
- Abdelrhman, A.M. Assessment of Geometrical Dimension and Tolerance of FDM Part. Ph.D. Thesis, Universiti Teknologi Malaysia, Johor Bahru, Malaysia, 2008.
- Deswal, S.; Narang, R.; Chhabra, D. Modeling and parametric optimization of FDM 3D printing process using hybrid techniques for enhancing dimensional preciseness. *Int. J. Interact. Des. Manuf.* **2019**, *13*, 1197–1214. [\[CrossRef\]](#)

19. Noriega, A.; Blanco, D.; Alvarez, B.J.; Garcia, A. Dimensional accuracy improvement of FDM square cross-section parts using artificial neural networks and an optimization algorithm. *Int. J. Adv. Manuf. Technol.* **2013**, *69*, 2301–2313. [[CrossRef](#)]
20. Padhi, S.K.; Sahu, R.K.; Mahapatra, S.S.; Das, H.C.; Sood, A.K.; Patro, B.; Mondal, A.K. Optimization of fused deposition modeling process parameters using a fuzzy inference system coupled with Taguchi philosophy. *Adv. Manuf.* **2017**, *5*, 231–242. [[CrossRef](#)]
21. Peng, A.; Xiao, X.; Yue, R. Process parameter optimization for fused deposition modeling using response surface methodology combined with fuzzy inference system. *Int. J. Adv. Manuf. Technol.* **2014**, *73*, 87–100. [[CrossRef](#)]
22. Nasiri, S.; Khosravani, M.R. Machine learning in predicting mechanical behavior of additively manufactured parts. *J. Mater. Res. Technol.* **2021**, *14*, 1137–1153. [[CrossRef](#)]
23. Trivedi, A.; Gurrula, P.K. Fuzzy logic based expert system for prediction of tensile strength in Fused Filament Fabrication (FFF) process. *Mater. Today Proc.* **2021**, *44*, 1344–1349. [[CrossRef](#)]
24. Rajpurohit, S.R.; Dave, H.K. Prediction and Optimization of Tensile Strength in FDM Based 3D Printing Using ANFIS. In *Optimization of Manufacturing Processes*; Gupta, K., Gupta, M., Eds.; Springer Series in Advanced Manufacturing; Springer Nature: Cham, Switzerland, 2020; pp. 111–128.
25. Sai, T.; Pathak, V.K.; Srivastava, A.K. Modeling and optimization of fused deposition modeling (FDM) process through printing PLA implants using adaptive neuro-fuzzy inference system (ANFIS) model and whale optimization algorithm. *J. Braz. Soc. Mech. Sci. Eng.* **2020**, *42*, 1–19. [[CrossRef](#)]
26. Xia, C.; Pan, Z.; Polden, J.; Li, H.; Xu, Y.; Chen, S. Modelling and prediction of surface roughness in wire arc additive manufacturing using machine learning. *J. Intell. Manuf.* **2021**, 1–16. [[CrossRef](#)]
27. Sahu, R.K.; Mahapatra, S.; Sood, A.K. A Study on Dimensional Accuracy of Fused Deposition Modeling (FDM) Processed Parts using Fuzzy Logic. *J. Manuf. Sci. Prod.* **2013**, *13*, 183–197. [[CrossRef](#)]
28. Saleh, B.; Maher, I.; Abdelrhman, Y.; Heshmat, M.; Abdelaal, O. Adaptive Neuro-Fuzzy Inference System for Modelling the Effect of Slurry Impacts on PLA Material Processed by FDM. *Polymers* **2020**, *13*, 118. [[CrossRef](#)]
29. Mensah, R.A.; Xiao, J.; Das, O.; Jiang, L.; Xu, Q.; Alhassan, M.O. Application of Adaptive Neuro-Fuzzy Inference System in Flammability Parameter Prediction. *Polymers* **2020**, *12*, 122. [[CrossRef](#)] [[PubMed](#)]
30. Buj-Corral, I.; Sánchez-Casas, X.; Luis-Pérez, C. Analysis of AM Parameters on Surface Roughness Obtained in PLA Parts Printed with FFF Technology. *Polymers* **2021**, *13*, 2384. [[CrossRef](#)] [[PubMed](#)]
31. Pérez, C.L. On the Application of a Design of Experiments along with an ANFIS and a Desirability Function to Model Response Variables. *Symmetry* **2021**, *13*, 897. [[CrossRef](#)]
32. Meftah, M.; Ebrahimpour, P.B.; He, C.; Ranawat, A.S.; Ranawat, C.S. Preliminary Clinical and Radiographic Results of Large Ceramic Heads on Highly Cross-Linked Polyethylene. *Orthopedics* **2011**, *34*, e133–e137. [[CrossRef](#)] [[PubMed](#)]
33. International Organization for Standardization. *Geometrical Product Specifications (GPS)—Geometrical Tolerancing—Tolerances of Form, Orientation, Location and Run-Out*; ISO 1101:2017; International Organization for Standardization: Geneva, Switzerland, 2017.
34. *The MathWorks Inc. Fuzzy Logic Toolbox™ User's Guide* © Copyright 1995–2020 by The MathWorks; Math Works Inc.: Natick, MA, USA, 2020.
35. Pérez, C.J.L. A Proposal of an Adaptive Neuro-Fuzzy Inference System for Modeling Experimental Data in Manufacturing Engineering. *Mathematics* **2020**, *8*, 1390. [[CrossRef](#)]
36. Burrascano, P.; Callegari, S.; Montisci, A.; Ricci, M.; Versaci, M. Chapter 6: Standard Soft Computing Techniques for Characterization of Defects in Nondestructive Evaluation. In *Ultrasonic Nondestructive Evaluation Systems, Industrial Application Issues*; Burrascano, P., Callegari, S., Montisci, A., Ricci, M., Versaci, M., Eds.; Springer International Publishing: Cham, Switzerland, 2015; pp. 175–199.
37. Buj-Corral, I.; Bagheri, A.; Sivatte-Adroer, M. Effect of Printing Parameters on Dimensional Error, Surface Roughness and Porosity of FFF Printed Parts with Grid Structure. *Polymers* **2021**, *13*, 1213. [[CrossRef](#)]
38. Eqbal, A.; Sood, A.K.; Ansari, A.R.; Eqbal, M.A. Optimization of process parameters of FDM part for minimizing its dimensional inaccuracy. *Int. J. Mech. Prod. Eng. Res. Dev.* **2017**, *7*, 57–66.
39. Maurya, N.K.; Rastogi, V.; Singh, P. Comparative Study and Measurement of Form Errors for the Component Printed by FDM and PolyJet Process. *J. Homepage Http://ieta.org/journals/ijm* **2019**, *18*, 353–359. [[CrossRef](#)]
40. Sajjan, N.; John, T.; Sivadasan, M.; Singh, N. An investigation on circularity error of components processed on Fused Deposition Modeling (FDM). *Mater. Today Proc.* **2018**, *5*, 1327–1334. [[CrossRef](#)]
41. Rupal, B.S.; Ramadass, K.; Qureshi, A.J. Investigating the effect of motor micro-stepping on the geometric tolerances of Fused Filament Fabrication printed parts. *Procedia CIRP* **2020**, *92*, 9–14. [[CrossRef](#)]



## Article

# Biostable Shape Memory Polymer Foams for Smart Biomaterial Applications

Anand Utpal Vakil, Natalie Marie Petryk, Ellen Shepherd and Mary Beth B. Monroe \*

Department of Biomedical and Chemical Engineering, Syracuse Biomaterials Institute, and BioInspired Syracuse: Institute for Material and Living Systems, Syracuse University, Syracuse, NY 13244, USA; [aувakil@syr.edu](mailto:aувakil@syr.edu) (A.U.V.); [nmpetryk@syr.edu](mailto:nmpetryk@syr.edu) (N.M.P.); [eshepher@syr.edu](mailto:eshepher@syr.edu) (E.S.)

\* Correspondence: [mbmonroe@syr.edu](mailto:mbmonroe@syr.edu); Tel.: +1-315-443-3323

**Abstract:** Polyurethane foams provide a wide range of applications as a biomaterial system due to the ability to tune their physical, chemical, and biological properties to meet the requirements of the intended applications. Another key parameter that determines the usability of this biomaterial is its degradability under body conditions. Several current approaches focus on slowing the degradation rate for applications that require the implant to be present for a longer time frame (over 100 days). Here, biostable shape memory polymer (SMP) foams were synthesized with added ether-containing monomers to tune the degradation rates. The physical, thermal and shape memory properties of these foams were characterized along with their cytocompatibility and blood interactions. Degradation profiles were assessed in vitro in oxidative (3% H<sub>2</sub>O<sub>2</sub>; real-time) and hydrolytic media (0.1 M NaOH; accelerated) at 37 °C. The resulting foams had tunable degradation rates, with up to 15% mass remaining after 108 days, and controlled erosion profiles. These easy-to-use, shape-filling SMP foams have the potential for various biomaterial applications where longer-term stability without the need for implant removal is desired.

**Keywords:** shape memory polymers; polyurethanes; oxidation; degradation; biostable; foams

**Citation:** Vakil, A.U.; Petryk, N.M.; Shepherd, E.; Monroe, M.B.B. Biostable Shape Memory Polymer Foams for Smart Biomaterial Applications. *Polymers* **2021**, *13*, 4084. <https://doi.org/10.3390/polym13234084>

Academic Editors: José Miguel Ferri, Vicent Fombuena Borràs and Miguel Fernando Aldás Carrasco

Received: 28 October 2021  
Accepted: 17 November 2021  
Published: 24 November 2021

**Publisher's Note:** MDPI stays neutral with regard to jurisdictional claims in published maps and institutional affiliations.



**Copyright:** © 2021 by the authors. Licensee MDPI, Basel, Switzerland. This article is an open access article distributed under the terms and conditions of the Creative Commons Attribution (CC BY) license (<https://creativecommons.org/licenses/by/4.0/>).

## 1. Introduction

Shape memory polymers (SMPs) are smart materials with many potential biomedical applications. SMPs can be prepared in a primary/original shape, deformed into a temporary shape upon exposure to an external stimulus, and stored in this temporary shape once the stimulus is removed. The external stimulus can be temperature, light, pH, electrical stimulus, or a magnetic field. Upon re-exposure to the stimulus, the shape memory effect can be triggered to recover the material back to its original shape.

Based on the application, biomaterials require varying degrees of biodegradability, tissue integration, cell and blood interactions, nutrient transfer, space-filling ability, and clinical functionality. Polyurethane SMPs have been extensively employed as biomaterial scaffolds in vascular applications, [1] drug delivery, [2] and tissue engineering due to their excellent tunable mechanical properties, [3] high cytocompatibility and biocompatibility, [4,5] and the ability to tune degradation rates to match application requirements [6,7].

Biodegradation affects cell infiltration, vascular in-growth, and neo-tissue formation to allow successful integration of host tissue with biomaterials at the implant location. Biodegradation can occur via three major mechanisms: oxidation, hydrolysis, and enzymatic degradation [8]. Some applications, such as degradable sutures, require a fast degradation rate, while others require biostable scaffolds that remain in the body over long time frames. Polyurethane SMPs present an ideal system for controlling degradation rates by selectively incorporating oxidatively, hydrolytically, and/or enzymatically responsive groups. The ability to control architecture changes with shape memory properties while tuning degradation profiles presents several potential benefits for healing, and previous research in this area is rich [9–11].

Within the large field of polyurethane SMPs, a crosslinked, amorphous polyurethane SMP foam system has been used for vascular occlusion applications, such as aneurysm filling [12,13], peripheral vascular disease [14], and hemorrhage control [15]. These materials are highly tunable, with prior work focusing on altering shape memory profiles, [16] pore structure [17], and/or toughness [18] and on incorporation of functional motifs to enable in vivo imaging [19,20] or infection control [21]. In vitro degradation characterization of SMP foams showed that they are hydrolytically stable, but that they degrade via oxidation [7]. Degradation was attributed to tertiary amines in the polyol crosslinkers that are used to form the polyurethane network. In a rabbit elastase aneurysm model, Herting et al. found that the materials underwent ~97% mass loss by 90 days using cross-sectional histological images [22].

Based on these findings, several subsequent studies have focused on improving the biostability of this valuable biomaterial system. Hasan et al. replaced the tertiary amine-containing monomers in the SMP foams with glycerol and hexanetriol. These foams were highly stable, with <10% mass loss over 45 days in accelerated hydrolytic and oxidation medias (0.1 M NaOH and 50% H<sub>2</sub>O<sub>2</sub>, respectively) [23]. However, their shape recovery profiles were significantly slower than the original SMP foams, with 100% volume recovery achieved after ~40 min in 50 °C water vs. full recovery in <10 min in 37 °C water in the control foams. This property would limit their ability to be actuated upon implantation at body temperature in future applications.

Weems et al. focused on improving the biostability of shape memory polyurethanes by incorporating isocyanurate-containing alcohols [24]. This approach resulted in increased biostability and delayed degradation. While tested in an accelerated oxidative degradation media (20% H<sub>2</sub>O<sub>2</sub> catalyzed by 0.1 M CoCl<sub>2</sub>), SMP films had more than 80% mass remaining after 100 days and porous SMP foams had close to 75% mass remaining after 40 days. This is a promising approach to significantly increasing biostability; however, the eventual degradation byproduct of these polymers may contain small molecules like cyclic isocyanurates, whose cytocompatibility has not been determined. Additionally, materials with intermediate degradation rates may be required.

In a separate approach, Weems et al. achieved a reduced degradation rate by incorporating small molecule antioxidants into the foams to form an SMP composite [25]. The microparticles were physically mixed within the polymer solution; thus, this approach could result in the antioxidant-loaded microparticles leaching out of the polymer system to alter the scaffold biostability over time. In most of the composite formulations, the antioxidant payloads were released during the initial cleaning procedure. The composite that did have a well-retained antioxidant content after washing underwent complete release of the antioxidant during the first three days of the degradation study, and thus did not significantly alter the long-term degradation profile.

While these SMP foams have been widely employed in embolic applications, none of the prior studies characterized blood interactions following modifications, which are highly dependent on material chemistry. Additionally, there may be benefits to more moderate increases in biostability or in altering the physical erosion profiles of SMP foams, such as in load-bearing applications where bulk device failure may be detrimental to healing. To that end, we synthesized polyurethane SMP foams that were modified with ether linkages using diethylene glycol (DEG) or triethylene glycol (TEG) to extend their biostability relative to control foams. We characterized the ability to tune the rate of degradation while maintaining other properties, such as pore size and volume recovery rates, the physical erosion profiles, and cell and blood interactions in the resulting ether-containing foams. In the long-term, these foams could provide an option for biomaterial implants with controlled degradation after implantation to maintain scaffold properties over longer time frames and to eliminate the need for implant removal.

## 2. Materials and Methods

Materials: Hexamethylene diisocyanate (HDI), diethylene glycol (DEG), triethylene glycol (TEG), N,N,N',N'-tetrakis-(2-hydroxypropyl)-ethylene diamine (HPED), triethanol amine (TEA), hydrogen peroxide (H<sub>2</sub>O<sub>2</sub>, Certified ACS, 30%), sodium hydroxide (NaOH), and ethanol (reagent alcohol) were purchased as used as received from Fisher Scientific (Waltham, MA, USA). All chemicals were purchased at reagent grade unless specified. Catalysts (T-131 and BL-22) and surfactant (EP-H-190) were used as received from Evonik Corporation (Essen, Germany).

Foam Synthesis: Polyurethane foams were synthesized in a two-part process by first preparing an isocyanate (NCO) pre-mix that contained 35 equivalents of hydroxyl groups provided by varying ratios of HPED, TEA, DEG, and TEG, and 100 equivalents of isocyanates. The pre-polymer was formed by crosslinking the NCO pre-mix at 50 °C for 48 h. Surfactant (EP-H-190) was added to the pre-mix after 48 h. The NCO pre-mix was allowed to cool down to room temperature while the hydroxyl pre-mix was made. The hydroxyl (OH) mix contained the remaining hydroxyls to balance the NCO groups, deionized (DI) water as a chemical blowing agent, and catalysts (T-131-tin based gelling catalyst) and BL-22-amine based blowing catalyst). The hydroxyl components were mixed at 3500 rpm for 30 s. The required amount of catalysts were added to the hydroxyl contents and mixed at 3500 rpm for 30 s. The final hydroxyl mix was added to the isocyanate pre-mix and mixed at 1800 rpm for 5 s and poured into a large mold to form a gas-blown foam in an isothermal oven maintained at 50 °C. All mixing was carried out in a high-speed mixer (Flacktek, Landrum, SC, USA). The overall hydroxyl to isocyanate ratio in the foam was maintained at 1.04 to ensure the complete reaction of isocyanates during the synthesis. Synthesized foam compositions are shown in Table 1.

**Table 1.** Synthesized foam compositions.

Sample ID	HDI (wt%)	HPED (wt%)	TEA (wt%)	DEG (wt%)	TEG (wt%)	EPH 190 (wt%)	T-131 (wt%)	BL-22 (wt%)	Water (wt%)
Control	54.03	27.61	8.05	-	-	6.44	0.46	1.01	2.37
15% DEG	52.36	29.21	-	4.24	-	6.26	0.56	1.2	2.9
15% TEG	51.2	32.28	-	-	5.83	6.28	0.56	1.2	2.73
30% DEG	53.16	27.15	-	8.69	-	6.19	0.60	1.18	2.91
30% TEG	51.34	26.25	-	-	11.52	6.33	0.53	1.2	2.80

Foam Pore Analysis: Foam slices (n = 3, ~1 cm<sup>2</sup>) were cut parallel and perpendicular to the foam rise direction. Each piece was coated with gold using a high vacuum sputter coater (Denton, Moorestown, NJ, USA) at 100 mTorr for 45 s to form a consistent and a stable coating. Pore structures were characterized via a JEOL JSM 5600 scanning electron microscope (SEM; JEOL USA, Peabody, MA, USA) at 35× magnification under 10 kV high vacuum. The micrographs were analyzed via ImageJ (National Institutes of Health, Bethesda, MD, USA) to quantify pore diameters.

Density: Cube samples (n = 3, ~1 cm<sup>3</sup>) were cut via a hot wire cutter, (Proxxon Thermocut 115/E, Hickory, NC, USA). Dimensions and weights were measured to obtain foam densities.

Mechanical Testing: Dogbone punches were cut from each foam (n = 3) according to the ASTM D638 (scaled down by a factor of 4; length: 6.25 mm, width: ~1.5 mm). The thickness of each piece was measured prior to testing. Samples were tested in both dry and wet conditions. To test the samples in wet conditions, they were placed in DI water at 50 °C for 5 min and patted dry prior to analysis. Based on thermal and swelling analysis, this time frame/temperature provided equilibrium water absorption to ensure sample wetting. Samples (n = 3) were stretched in a tensile tester via a 24 N load cell at a rate

of 2 mm/min until failure to measure elastic modulus, elongation at break, and ultimate tensile strength.

**Thermal analysis:** Glass transition temperature ( $T_g$ ) was measured for each sample ( $n = 3$ , 3–5 mg) using a Q200 differential scanning calorimeter (DSC, TA instruments, New Castle, DE, USA) in both dry and wet (plasticized) conditions. Samples were placed in t-zero aluminum pans, equilibrated at  $-40\text{ }^\circ\text{C}$ , heated to  $120\text{ }^\circ\text{C}$  at  $10\text{ }^\circ\text{C}/\text{min}$ , kept isothermally for 2 min, cooled to  $-40\text{ }^\circ\text{C}$  at  $10\text{ }^\circ\text{C}/\text{min}$ , and heated back to  $120\text{ }^\circ\text{C}$  at  $10\text{ }^\circ\text{C}/\text{min}$ . Dry  $T_g$  was measured as the half-height transition temperature during the second heating cycle. To measure wet  $T_g$ , samples were plasticized by placing in DI water at  $50\text{ }^\circ\text{C}$  for 10 min, pressed dry, and placed in t-zero aluminum pans with hermetic lids. A pin hole was pierced on the hermetic lid to allow water to escape during the heating cycle. Samples were equilibrated at  $-60\text{ }^\circ\text{C}$  and heated to  $80\text{ }^\circ\text{C}$  at  $10\text{ }^\circ\text{C}/\text{min}$ . Wet  $T_g$  was measured as the half-height transition temperature during the single heating cycle.

**Shape Memory Behavior:** Volume expansion was used to quantify shape memory behavior. Cylindrical foam samples (1 cm long, 8 mm diameter) were cut, cleaned in DI water and 70% ethanol, and dried under vacuum for 24 h prior to testing. Each sample was heated to  $100\text{ }^\circ\text{C}$  for 10 min to allow softening, and the diameter was recorded using digital calipers prior to manual crimping in a radial compression crimper (Blockwise Engineering, Tempe, AZ, USA). After cooling to room temperature, the final crimped sample diameter and length were recorded, samples were placed in scintillation vial in a desiccator for 24 h and fixed on a  $300\text{ }\mu\text{m}$  Nitinol wire to allow for complete shape setting and relaxation to occur. After 24 h, the foam's initial diameter and length were measured, and samples were placed in a DI water bath set at  $37\text{ }^\circ\text{C}$  and allowed to expand for 5 min. Images were captured every 3 s to observe changes in diameter over time ( $t$ ) and generate a volume recovery profile. Images were analyzed using ImageJ and volume recovery was measured as:

$$\% \text{ Volume Recovery} = \frac{\text{Sample Diameter}(t) \times \text{Sample Length}(t)}{\text{Initial Diameter} (d1) \times \text{Initial Length} (l1)} \times 100 \quad (1)$$

Change in volume vs. time was plotted over the expansion time frame.

**Spectroscopic Analysis:** Surface chemistry was characterized on thin slices of cleaned foam pieces using a Nicolet i70 Attenuate total reflectance (ATR)-Fourier transform infrared (FTIR) Spectrometer (Fisher Scientific, Waltham, MA, USA) at  $0.8\text{ cm}^{-1}$  resolution using OMNIC software (Fisher Scientific, Waltham, MA, USA). Incorporation of ethers into polyurethane foams was confirmed by the presence of peaks corresponding to the C-O of the ether group at  $\sim 1090$  and  $\sim 1050\text{ cm}^{-1}$  and the carbonyl of urethane at  $\sim 1688\text{ cm}^{-1}$ .

**Degradation Analysis:** Cylindrical foams ( $n = 8$ , 8 mm diameter, 1 cm height) were washed and dried, and initial masses were obtained using a gravimetric scale. Samples were placed in 3%  $\text{H}_2\text{O}_2$  (real-time oxidative degradation media) or in 0.1 M NaOH (accelerated hydrolytic degradation media) at  $37\text{ }^\circ\text{C}$  with regular media changes. At selected time points, samples were washed with ethanol and dried under vacuum for 24 h. After drying, samples were imaged using a camera, and masses were measured ( $n = 5$ ). A thin slice was cut from a sacrificial set of foams ( $n = 3$ ) and used to measure pore morphology (SEM),  $T_g$  (DSC), and surface chemistry (FTIR) as described above.

**Cytocompatibility:** Sample cytocompatibility was tested using 3T3 Swiss mouse fibroblasts (ATCC-CCL92; ATCC, Manassas, VA, USA). Cells were cultured with Dulbecco's modified Eagle's medium (DMEM, high glucose GlutaMAX), supplemented with 10% heat-inactivated fetal bovine serum (FBS) and 1% penicillin-streptomycin (P/S, Gibco) at  $37\text{ }^\circ\text{C}/5\%\text{ CO}_2$ . Cells from passage 11 were used after three days of culture. Cells were seeded onto a 24-well tissue culture polystyrene plate at 10,000 cells/well and incubated for 24 h at  $37\text{ }^\circ\text{C}/5\%\text{ CO}_2$  for 24 h. Samples were cleaned using water, 20% Contrad solution, and isopropyl alcohol, and then soaked in  $1\times$  PBS overnight prior to testing to leach out any alcohol. Samples ( $n = 3$ ) were placed in each well along with positive controls (media-only with cells,  $n = 3$ ), and negative controls (media-only with no cells).

Samples were incubated with cells, and viability was assessed after 24 h using a Live/Dead assay (ThermoFisher Scientific, Waltham, MA, USA). Briefly, cells were stained with green fluorescent calcein-AM (live cells) and red-fluorescent ethidium homodimer-1 (dead cells) for 15 min at room temperature while protecting from light. Cells were imaged using an inverted microscope (Leica, DMI6000) at 10× magnification to determine the number of live (green) and dead (red) cells. Three images were captured for each sample. Cell viability of each sample (x) was measured as:

$$\text{Cell Viability (x)} = \frac{\text{Live Cells}}{\text{Total number of cells}} \times 100\% \quad (2)$$

Blood Interactions: Porcine blood (Lampire Biological Laboratories, Pipersville, PA, USA) anticoagulated with Na-Citrate upon collection was stored at 4 °C for up to 3 weeks from the bleed date, according to supplier guidelines. Control, 30% DEG, and 30% TEG foams were washed and dried prior to characterization in all studies. QuikClot Combat Gauze was included as a clinical control. Blood absorption was analyzed by weighing dry samples (n = 3; ~50 mg) and incubating them in blood at 37 °C. Samples were weighed at 24 h, and blood absorption was calculated as:

$$\% \text{ Absorbed} = \frac{W_b - W_d}{W_d} \times 100\% \quad (3)$$

where  $W_b$  is the mass of the sample in blood and  $W_d$  is the dry mass.

Platelet attachment was measured via LDH cytotoxicity assay kit (Cayman Chemical, Ann Arbor, MI, USA). Platelet-rich plasma (PRP) was collected by centrifuging whole blood at 3000 rpm for 15 min to obtain a standard curve. PRP was diluted with PBS to obtain multiple concentrations (100, 50, 25, 12.5, and 6%) to generate a standard. Hemocytometer counts were acquired at each PRP concentration (n = 4) to quantify the standard values. SMP foams (n = 4) were cut to equal surface area and placed in individual wells in a 24-well plate. Gauze was used as a clinical control. One milliliter of blood was added to each well and the soaked samples were incubated at 37 °C for 30 min. PBS was used to wash out any unattached platelets. Samples were then added to wells on a separate plate containing 1 mL PBS and 100 µL of 10% Triton X-100 to lyse unattached platelets. Supernatant (100 µL) from each well was added to wells on a separate 96 well plate along with 100 µL of LDH reaction solution. The mixture was incubated at 37 °C for 30 min on an orbital shaker. Microplate reader was then used to obtain absorbance values from each sample at 490 nm.

Samples that were washed with PBS to remove unattached platelets were then imaged via SEM to observe activity states and platelet activation. Prior to imaging, samples were soaked in 2% glutaraldehyde solution (Electron Microscopy Sciences, Hartfield, PA, USA) to fix them and later dehydrated. To achieve complete dehydration, samples were soaked in a series of ethanol concentrations: (1) 30 min in 50% ethanol, (2) 30 min in 70% ethanol, (3) 30 min in 95% ethanol and finally (4) 30 min in 95% ethanol. Post dehydration samples were dried overnight in a vacuum oven at 50 °C and –30 inches Hg. SEM analysis was performed using JEOL NeoScope JSM-5600 (JEOL USA, Peabody, MA, USA) operated at 10 kV. Images were captured at regions of interest at 1000× and 5000× magnification. These images were later analyzed via ImageJ assess platelet aggregations and activation (morphology change).

The time required for coagulation was measured for each sample (n = 4) by placing them in 1.5 mL microcentrifuge tubes and exposing them to blood. One tube was maintained as a negative control with no sample. Samples were weighed and cut to have the same surface area throughout. Blood was brought to room temperature and the Na-citrate anticoagulant was reversed by adding 1 M CaCl<sub>2</sub> solution to obtain a net 0.01 M CaCl<sub>2</sub> solution. Then, 50 µL of this blood was added to each sample tube. The clotting process was stopped at each time point (every 6 min over 30 min) by adding 1 mL DI water to each tube to lyse the free red blood cells. These tubes were centrifuged at 2300 rpm for 15 min, inverted, and images were captured using a digital camera (AKASO V50 Pro



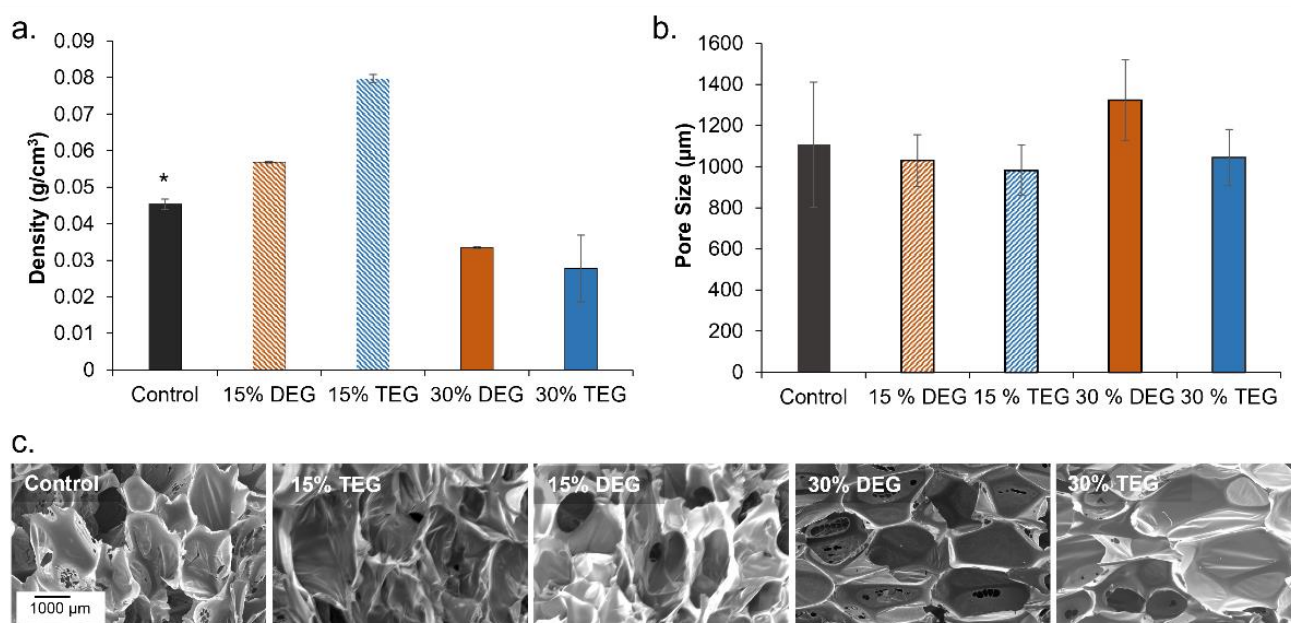
Native, AKASO, Frederick, MD, USA). The relative amount of hemoglobin released at each time point was determined by adding 200  $\mu\text{L}$  of the lysate from each tube to a 96-well plate and measuring the absorbance at 540 nm using a BioTek Synergy 2 Multimode Microplate Reader (Winooski, VT, USA).

Statistical Analysis: Measurements are presented as mean  $\pm$  standard deviations. Student's *t*-tests were performed to determine differences between ether foams and controls. Statistical significance was taken as  $p < 0.05$ .

### 3. Results

#### 3.1. Structural Properties

Low density polyurethane foams were synthesized with a target density below  $0.08 \text{ g/cm}^3$ , Figure 1a. General increases in density were observed with the introduction of lower amounts (15%) of ether-containing monomers, while general decreases in density were observed in higher ether content foams (30%). Pore sizes for each foam were targeted to be between 1000 and 1400  $\mu\text{m}$  to ensure comparable properties to the control. 30% DEG foams have the largest pore size of 1323  $\mu\text{m}$  (vs. control foams: 1151  $\mu\text{m}$ ), Figure 1b. In the SEM images, Figure 1c, 15% DEG and TEG foams appear to have thicker walls, which corresponds with their increased density. In addition to the higher pore size in 30% DEG foams, evidence of pore opening (pinholes in pore walls) can be observed in the 30% DEG and TEG foam SEM images, which resulted in lower density relative to the control foam.

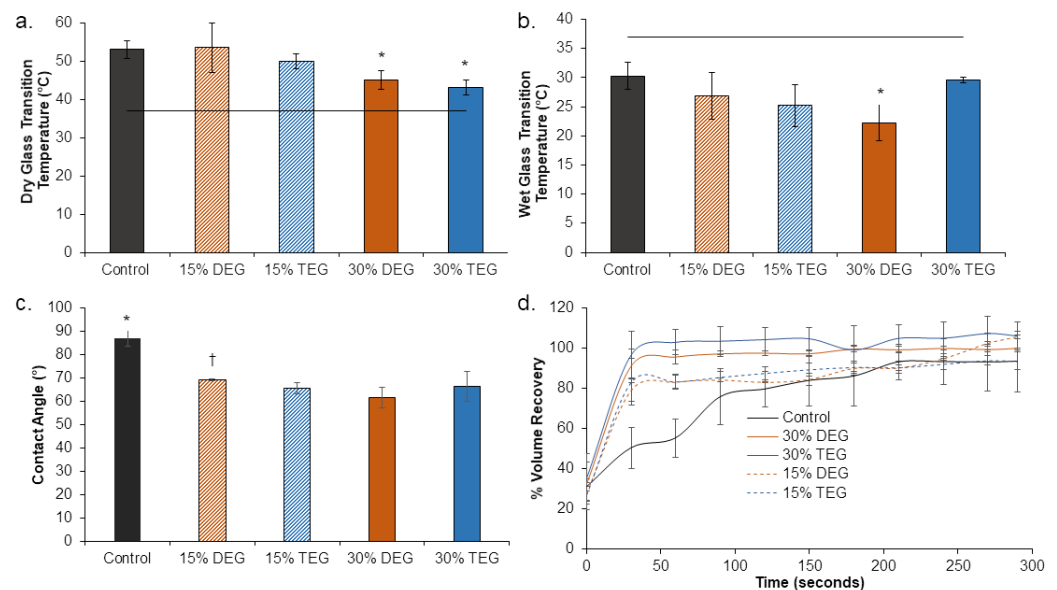


**Figure 1.** Structural properties of shape memory polymer foams. (a) The density of foams ( $n = 3$ ), (b) average pore size of foams ( $n = 6$ ) measured using SEM images on samples cut parallel and perpendicular to foam rise, and (c) representative micrographs of pore morphology. Scale bar of 1000  $\mu\text{m}$  applies to all images. Mean  $\pm$  standard deviation displayed in all panels. \*  $p < 0.05$  relative to all other foams.

#### 3.2. Thermal Properties

Highly crosslinked amorphous networks were formed using polyol crosslinkers with three (TEA) and four (HPED) hydroxyl groups, along with short-chain diol monomers (DEG and TEG), which was indicated by the absence of melting peaks in the DSC traces (Figure S1 in Supplementary Materials). As seen in Figure 2a, all foams had dry  $T_g$ 's above  $40^\circ\text{C}$ , which enables stable storage of foams at room temperature ( $\sim 22^\circ\text{C}$ ) without premature shape memory actuation. The target wet glass transition temperature below  $37^\circ\text{C}$  was also obtained in all foams, Figure 2b, which enables actuation of shape memory

behavior upon implantation and exposure to water present in the body via water-induced plasticization of the SMPs.



**Figure 2.** Thermal, shape memory, and hydrophilicity properties of SMP foams. (a) Dry glass transition temperature ( $n = 3$ ,  $* p < 0.05$  relative to control), (b) wet glass transition temperature ( $n = 3$ ,  $* p < 0.05$  relative to control), horizontal line is provided as a reference for body temperature ( $37\text{ }^{\circ}\text{C}$ ) in (a,b). (c) contact angle ( $n = 5$ ,  $* p < 0.05$  relative to all other samples,  $\dagger p < 0.05$  relative to 15% TEG and 30% DEG samples), and (d) volume recovery of samples ( $n = 3$ ) in deionized water at  $37\text{ }^{\circ}\text{C}$ . Mean  $\pm$  standard deviation displayed in all panels.

### 3.3. Hydrophilicity and Shape Memory

The contact angle was measured on each formulation in bulk film form to compare the difference in water interactions between the foams. Control films had the highest contact angle ( $87^{\circ}$ ) and the inclusion of DEG and TEG increased hydrophilicity, as evidenced by decreased contact angles (down to  $63^{\circ}$  for TEG and  $70^{\circ}$  for DEG), as shown in Figure 2c. Shape recovery profiles of samples were evaluated to indicate their capability to return from their secondary, compressed shape to their original, expanded shape after implantation and exposure to water in the body, Figure 2d. All foams expanded back to 100% of their original volume within  $\sim 200$  s. In general, volume expansion profiles were similar, but the 15% DEG and TEG foams had faster expansion in the first 30 s, and the 30% DEG and TEG foams had slower expansion in the first 60 s relative to the control.

### 3.4. Tensile Testing

The addition of ether-containing diol monomers resulted in an overall reduction of elastic modulus and an increase in maximum elongation in the wet and dry states compared to controls, Table 2. The highest reduction in modulus relative to the control ( $22\times$ ) was observed in 30% TEG foams, which corresponds with the highest increase ( $8\times$ ) in elongation at break. All foams had a reduction in modulus and the corresponding increase in elongation after undergoing water-induced plasticization in DI water at  $50\text{ }^{\circ}\text{C}$  for 5 min. The wet foam mechanical properties were overall more similar between formulations.

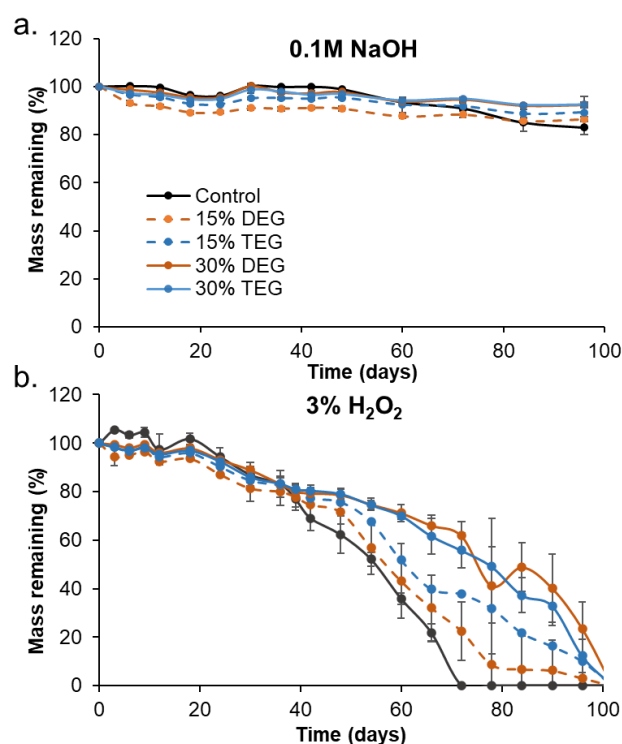
**Table 2.** Tensile properties of shape memory polymer foams in dry and wet conditions.  $n = 3$ , mean  $\pm$  standard deviation displayed.

Sample ID	Elastic Modulus (kPa)		Maximum Elongation $\epsilon$ (mm/mm)	
	Dry	Wet	Dry	Wet
Control	3200 $\pm$ 1700	150 $\pm$ 20	0.17 $\pm$ 0.04	0.4 $\pm$ 0.2
15% DEG	840 $\pm$ 140	41 $\pm$ 5	0.25 $\pm$ 0.01	0.9 $\pm$ 0.5
15% TEG	140 $\pm$ 40	32 $\pm$ 6	0.46 $\pm$ 0.17	3.0 $\pm$ 1.2
30% DEG	790 $\pm$ 270	45 $\pm$ 13	0.28 $\pm$ 0.14	1.2 $\pm$ 0.2
30% TEG	170 $\pm$ 110	12 $\pm$ 3	1.25 $\pm$ 0.45	1.0 $\pm$ 0.1

### 3.5. Degradation Analysis

#### 3.5.1. Mass Loss and Physical Erosion

All foams remained stable in accelerated hydrolytic media (0.1 M NaOH), with less than 10% mass loss over 98 days, Figure 3a. In the oxidative media (3% H<sub>2</sub>O<sub>2</sub>) foams had comparable, approximately linear mass loss rates over the first 40 days, Figure 3b. After that, control foams began to degrade more quickly, and they underwent bulk erosion and started breaking into smaller pieces by ~56 days, Figure 4. Amongst the ether-containing foams, 30% DEG foams had the slowest degradation rate and had 5% mass remaining after 105 days, followed by 30% TEG foams, which fully degraded in 98 days. The ether-containing foams appeared to undergo surface erosion, maintaining their bulk geometries over >80 days, Figures 4 and 5.

**Figure 3.** Mass loss profiles of samples as a function of time in (a) accelerated hydrolytic degradation media, 0.1 M NaOH, and (b) oxidative degradation media, 3% H<sub>2</sub>O<sub>2</sub>.  $n = 5$ , mean  $\pm$  standard deviation displayed. Legend provided in (a) applies to both charts.

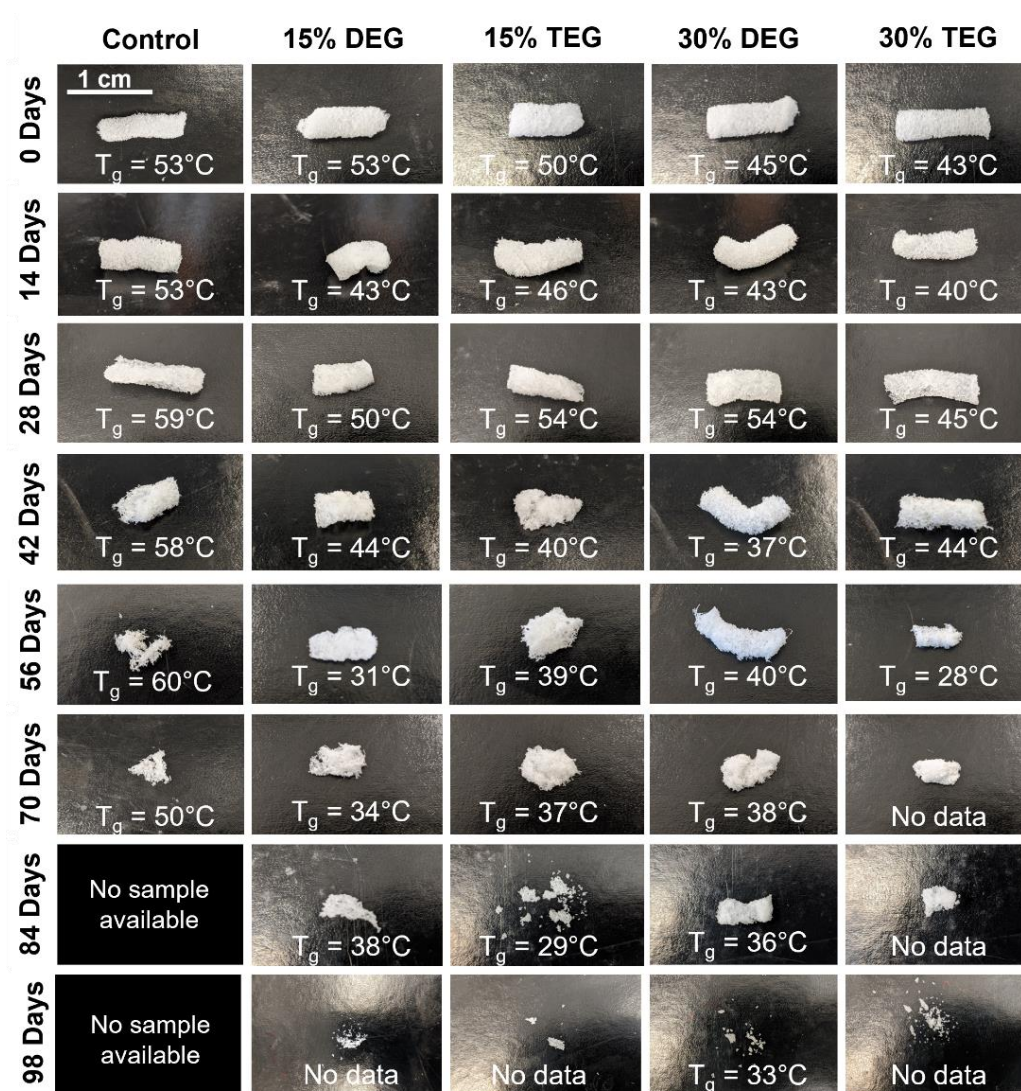
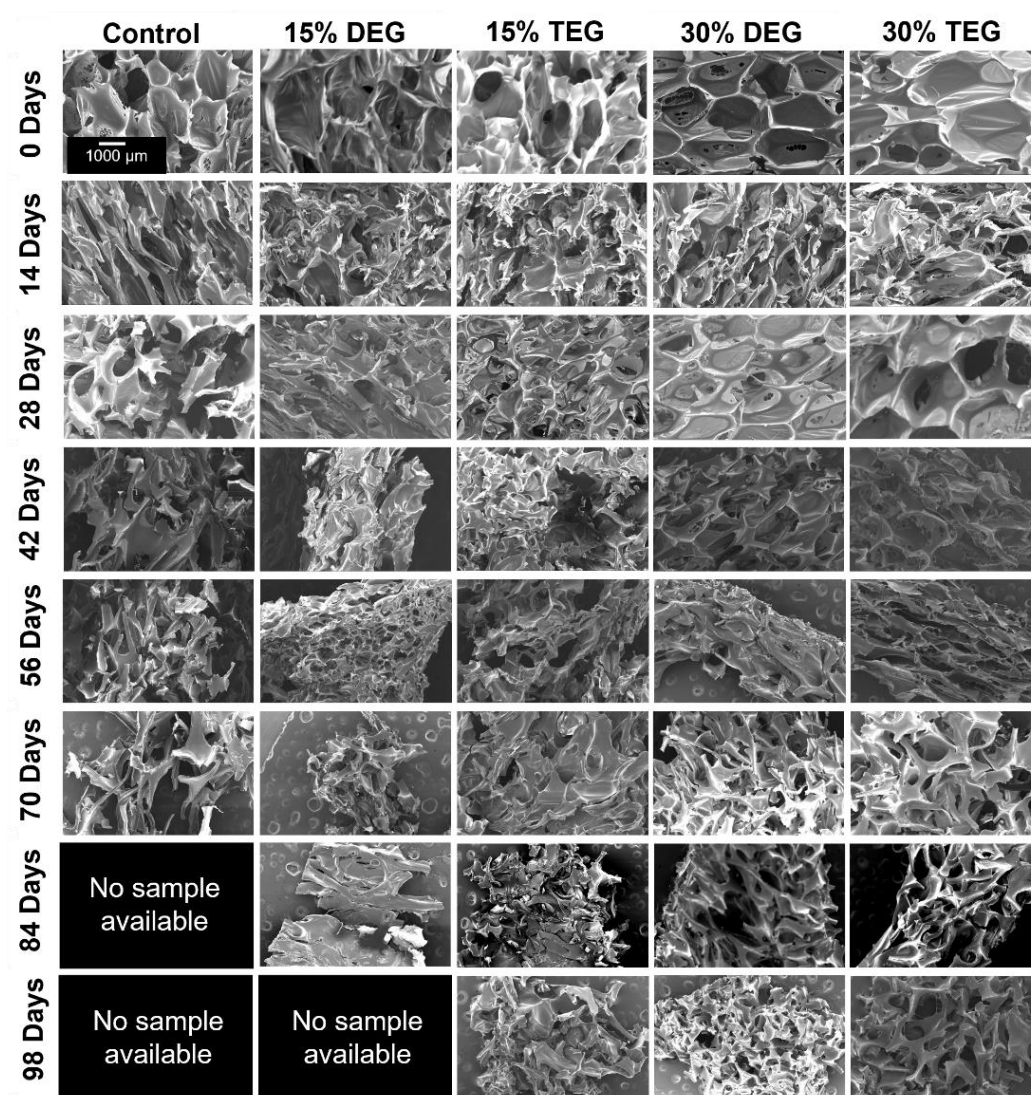


Figure 4. Physical erosion profile of samples degrading in oxidative degradation media, 3%  $\text{H}_2\text{O}_2$  along with respective  $T_g$ 's measured at each time point. Scale bar applies to all images.

### 3.5.2. Thermal Analysis

As degradation proceeded, thermal analysis was performed to measure  $T_g$  as an indication of network crosslink density over time, Figure 4. This data can be used as an indication of whether the foams underwent surface or bulk degradation, where surface degradation would indicate that the polymer network and crosslink density remain intact during material breakdown. Interestingly, despite their observed physical bulk erosion, Figure 4, control foams retained their  $T_g$  (~50–60 °C) throughout the entire degradation process. Due to complete sample degradation, no images could be obtained of control foams past 70 days. All ether-containing foams retained their  $T_g$ 's until ~56 days, after which there was an observed decrease in  $T_g$ . Thus, surface degradation likely occurred throughout most of the degradation process, as is expected for oxidative degradation, due to the high reactivity of reactive oxygen species.



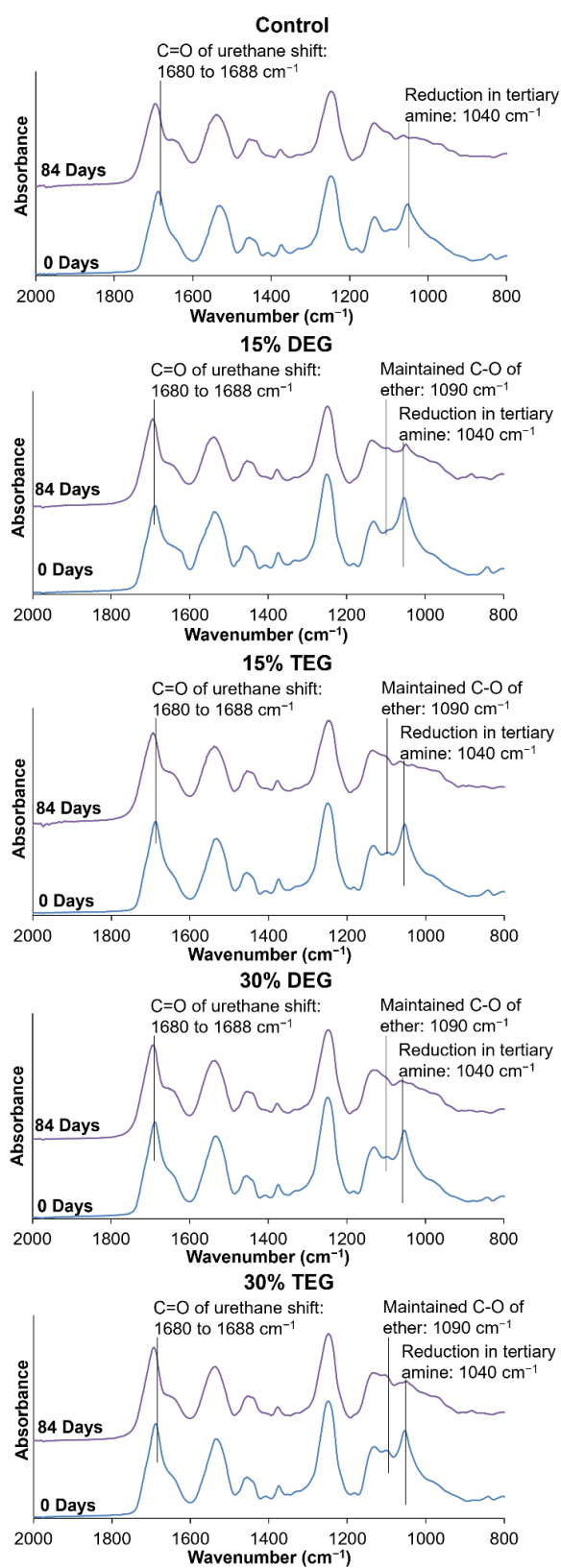
**Figure 5.** SEM micrographs depicting the overall pore morphology observed during degradation in oxidative media, 3%  $\text{H}_2\text{O}_2$ , over 98 days. Scale bar of 1000  $\mu\text{m}$  applies to all images.

### 3.5.3. Pore Morphology

SEM was used to analyze pore morphology every two weeks, as shown in Figure 5. Control foams began losing their porous structure by 14 days and underwent significant strut breaking by 28 days. Total pore collapse was observed in control foams by 42 days. Among the ether-containing foams, 30% DEG and 30% TEG generally maintained their pore morphology while shrinking over time, with some strut breakage at ~70 days and collapse at ~98 days. Material shrinkage can also be seen in 15% DEG and TEG foams, with maintained visible pores over ~70 days. Due to complete sample degradation, no images could be obtained of control foams past 70 days or of 15% DEG foams past 84 days.

### 3.5.4. Spectroscopic Analysis

FTIR spectra during degradation in 3%  $\text{H}_2\text{O}_2$  revealed a shift in the urethane peak from  $1680\text{ cm}^{-1}$  to  $1688\text{ cm}^{-1}$  and a reduction in tertiary amine peaks of HPED and TEA at  $1050\text{ cm}^{-1}$ , which has been previously observed, Figure 6 [7]. As the tertiary amine peak in the ether-containing foams is reduced, the ether peak at  $\sim 1090\text{ cm}^{-1}$  become more apparent, indicating that the ether groups remain stable during degradation. There is no visible evidence of ether crosslinking (branched ether peak at  $\sim 1174\text{ cm}^{-1}$ ) during degradation in the FTIR spectra [26].



**Figure 6.** FTIR spectroscopic analysis of samples during degradation in oxidative media, 3% H<sub>2</sub>O<sub>2</sub> at 0 days (blue lines) and 84 days (purple lines).

### 3.6. Cell and Blood Interactions

Since 15% DEG and 15% TEG had a faster degradation rate compared to 30% DEG and 30% TEG samples, cell and blood interactions were studied exclusively for the foams containing 30% ether linkages along with control foams and a clinical control (QuickClot gauze). Cell viability was confirmed to be ~100% for all samples after 24 h of incubation, Figure 7a. Images of live/dead cells can be seen in Figure 7b. Live cells are stained green and dead cells are stained red. As seen in Figure 8a control foams absorbed the highest amount of blood among the tested samples, and all materials absorbed between 100 and 200% of their dry weight in blood. In the coagulation study, the amount of free RBCs was higher in SMP foams relative to gauze at 0 min. However, comparable coagulation profiles were observed by 6 min Figure 8b. At 18 min and beyond, 30% DEG had the lowest number of free RBCs amongst all test samples, indicating a higher clotting capability. Images of lysates can be seen in Supplementary Materials Figure S2. Platelet attachment was quantified after incubation of samples in platelet-rich plasma. As shown in Figure 8c, maximum platelet attachment was observed on 30% DEG, followed by gauze and 30% TEG with comparable platelet numbers that were approximately half that of 30% DEG. Control foams had the lowest number of attached platelets. These results correlate the platelet aggregation and activation visualized using SEM micrographs, Figure 8d. The gauze clinical control had aggregated platelets with evidence of thrombus formation. All three SMP foams showed evidence of platelet activation (small protrusions on platelet surfaces) and aggregation, and imaged platelet densities correspond with the numbers quantified using the LDH assay.

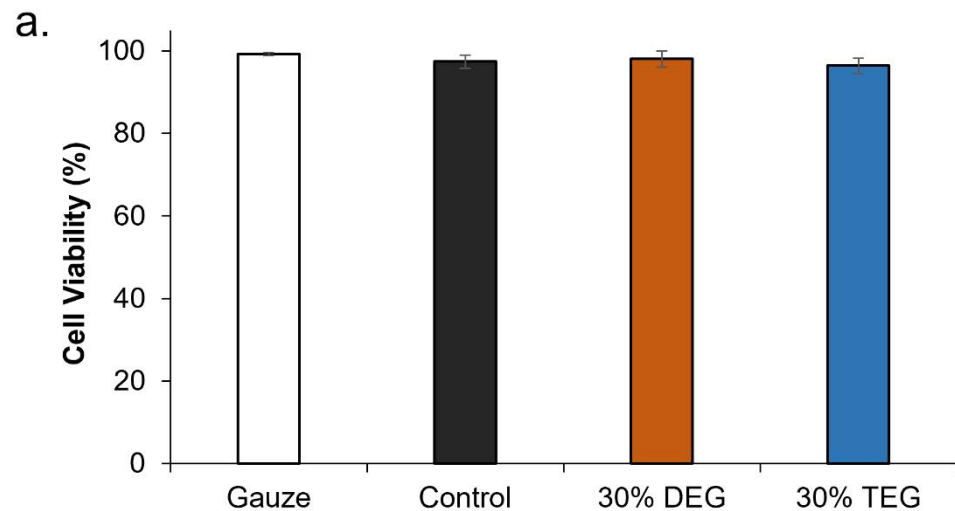
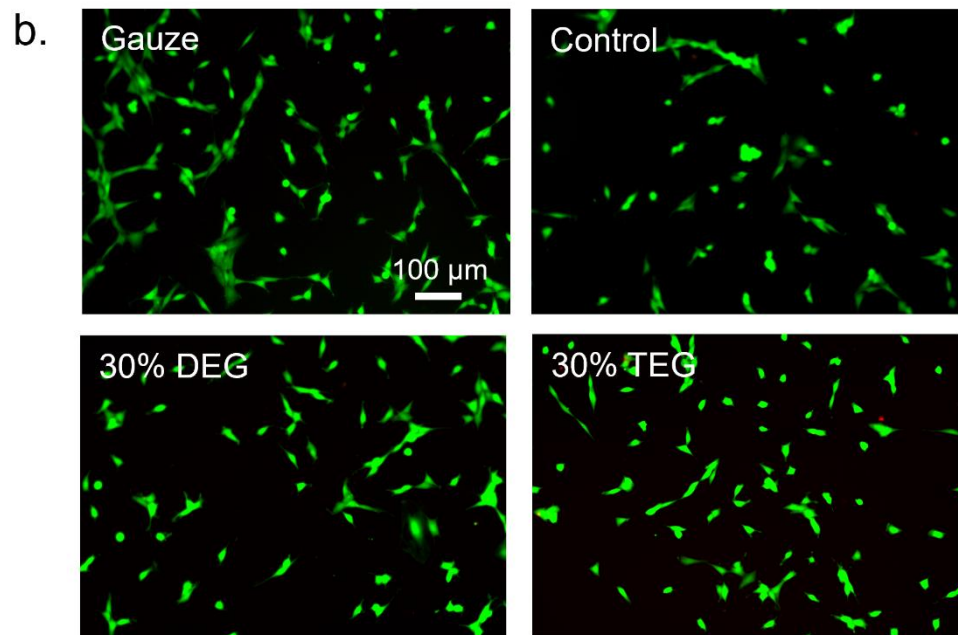
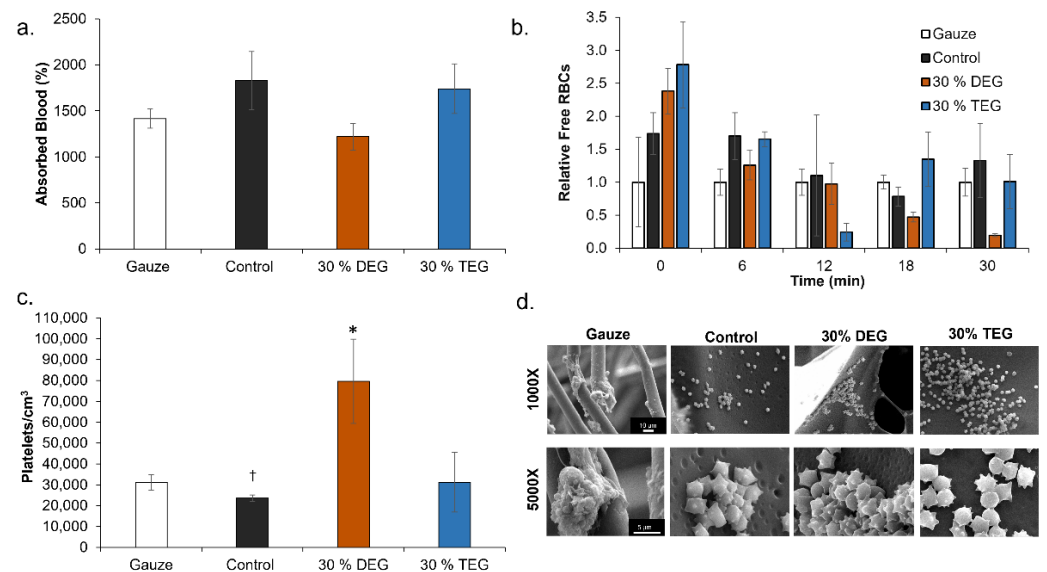


Figure 7. Cont.



**Figure 7.** Cytocompatibility of SMP foams. (a) 3T3 mouse fibroblast viability over 24 h (n = 3). (b) Representative live/dead cell images were used to calculate viability. Live cells were stained green and dead cells were stained red. Scale bar applies to all images.



**Figure 8.** Cell and blood interactions with SMP foams. (a) Whole porcine blood absorption after 24 h of incubation (n = 3). (b) Average blood coagulation profiles represented free RBCs relative to clinical control (gauze) over 30 min (n = 4). \*  $p < 0.05$  relative to gauze. (c) Platelet attachment to sample surfaces (n = 3, \*  $p < 0.05$  relative to all samples, †  $p < 0.05$  relative to gauze). Mean  $\pm$  standard deviation displayed in all panels. (d) SEM micrographs of attached platelets. Scale bars are shown in Gauze column apply to all other images in each row.

#### 4. Discussion

Overall, it was observed that adding ether-containing monomers, DEG and TEG, resulted in increased pore interconnectivity and reduction in  $T_g$  compared to control foams. We hypothesize that the increased hydrophilicity of DEG and TEG enabled increased interactions between the monomers in the pre-polymer and the chemical blowing agent (water) and/or the surfactant, which resulted in pore opening in the 30% DEG and TEG



foams. This phenomenon could be advantageous in applications that require increased interconnectivity without relying on physical or mechanical modifications like mechanical reticulation, [17] plasma treatment, [27], and/or the addition of physical blowing agents.

TEG-containing foams had slightly lower  $T_g$ 's compared to corollary DEG-containing foams and increasing TEG and DEG content induced further decreases in  $T_g$ . Reduction in foam  $T_g$  is attributed to increased hydrophilicity and flexibility of DEG and TEG, which corresponds with the contact angle measurements. Additionally, replacing the tri-functional TEA with difunctional DEG or TEG theoretically reduces foam crosslink density, which would result in lower  $T_g$ . However, all foams had dry  $T_g$  well above room temperature, which would enable their stable storage in the secondary shape. Exposure to water at 37 °C results in a reduction in  $T_g$  due to plasticization by water molecules penetrating the inner structure of the foams. This reduced  $T_g$  aids in rapid volume recovery once implanted in the body and exposed to water in body temperature blood.

The factors that determine the volume recovery of foams are wet  $T_g$ , pore size, and hydrophilicity. Higher hydrophilicity (lower contact angle) allows for easier water absorption that corresponds to faster plasticization of foams, which is also indicated by a lower wet  $T_g$ . Larger pore size can also increase water penetration speed into foams, further accelerating volume recovery. Compared to control foams, DEG and TEG foams have a higher hydrophilicity (lower contact angle) due to the addition of hydrophilic ether linkages. Among the ether-containing foams, 30% DEG and 30% TEG foams have increased hydrophilicity compared to 15% DEG and 15% TEG foams and have a correspondingly faster volume recovery expected. This increased volume recovery may be valuable in rapidly filling wounds during implantation.

The increased elongation at break and decreased stiffness of the ether-containing foams were expected due to the overall decreases in crosslink density and increased chain flexibility of ether linkages. The penetration of water molecules into the polymer network and interruption of hydrogen bonds allows the polymer chains to move more freely, as indicated by the overall decreased modulus and increased elongation at break of all samples in the wet conditions compared to foams tested in dry conditions. The dry measurements are important for considering material handling prior to implantation, and all materials are mechanically robust and easy to handle in the dry state. The wet measurements provide information about the material properties after implantation, which is important for matching native tissue properties. Again, all materials are mechanically within the range of soft tissues, and the differences between the ether foams and controls are reduced in the wet state [28]. In future work, the ether foams could be modified with stiffer diisocyanate species to increase the modulus if needed [16].

When incubated in an accelerated hydrolytic degradation medium containing 0.1 M NaOH, all samples remained stable, with no significant mass loss due to the lack of hydrolytically labile linkages. This result agrees with previous work on this material system that consistently shows high hydrolytic stability. [7,29] In oxidative degradation medium containing 3%  $H_2O_2$ , control foams physically broke apart after ~42 days, while the other formulations maintained their geometry for longer times throughout the degradation time frame. These physical changes were accompanied by an increase in the mass-loss rate in control foams. The breaking apart of control foams may be attributed to their relatively high brittleness, evidenced by the lowest elongation at break ( $0.17 \pm 0.04$  mm/mm), compared to the other formulations. During the degradation study, foams are repeatedly subjected to minor mechanical forces during the weekly washing and drying steps. Since the control foams are more brittle, they may break apart more easily and be more susceptible to bulk erosion, despite maintaining  $T_g$  values throughout degradation. The ether-containing foams were more flexible and less susceptible to these stresses, as demonstrated by their increased overall physical integrity throughout degradation, which translates to slower and more consistent degradation rates. The ether linkages appear to remain intact during the degradation process, as evidenced in FTIR spectra. This stability of the ether linkages

could potentially contribute to their increased stability and more consistent degradation profiles.

While the overall changes in degradation rates were not hugely different, the introduction of ether linkages increased the oxidative stability by ~40% (an increase from 72 days for control to 100+ days for ether foams). Additionally, the observed surface erosion and maintenance of pore structure over longer time frames may be beneficial for graded load transfer during new tissue formation as the SMP foams degrade. Finally, the ability to tune degradation independently of thermal and shape memory properties enables easy transition to ether-containing foams to increase degradation rates without altering storage or implantation considerations.

While future studies will require more in-depth analysis of biocompatibility after implantation and cytocompatibility of degradation byproducts, the addition of TEG and DEG does not affect the cytocompatibility of SMP foams. In terms of blood absorption, the increased absorption by TEG foams compared to DEG foams is attributed to increased hydrophilicity, which increases fluid uptake. The increased absorption by control foams may be attributed to their closed pore structure, which increases blood retention compared to open pore ether foams.

Various surface characteristics, like surface charge, relative hydrophilicity, and surface roughness, can impact protein absorption and subsequent blood and/or cell interactions with biomaterials. Thus, blood interactions must be considered when making chemical changes in any biomaterial system, particularly for embolic applications. All samples had complete clotting within 12 min as seen by a reduction in free RBCs. The highest clotting at later time points (>18 min) was observed on 30% DEG foams, which corresponds with the higher platelet attachment observed on these foams, both in the quantified LDH assay and the qualitative SEM imaging. The 30% TEG foams had similar platelet attachment values to clinical gauze control, and control foams showed the lowest number of attached platelets. When visualized using SEM, gauze promoted thrombus formation within the testing time frame, while all SMP foams had aggregated and activated platelets with similar trends observed in relative platelet numbers on each surface. This result shows that incorporating ether linkages into the SMP foams enhanced platelet attachment and activation, which may translate to increased efficacy of these materials in embolic applications and provides a new tool for increasing clotting in SMP foams. These results are analyzed in a static model. Going further, we will focus on analyzing clotting capabilities using a dynamic *in vitro* hemorrhage model where blood is allowed to flow through the foams [30].

These smart biomaterials with increased biostability and excellent biocompatibility have a wide application in multiple tissue engineering applications. One such application involves the use as a temporary embolic device in minimally invasive medical applications that may require removal after a certain time point. The removal process can be avoided using these biomaterials.

## 5. Conclusions

A reduction in SMP foam degradation rate was achieved by incorporating ether linkages. The resulting foams maintain desired thermal properties, which allows stable storage in the secondary shape at room temperature prior to use and rapid volume recovery upon implantation. The modified foams have rapid volume recovery and increased flexibility, allowing easy implantation without premature breaks or tears. The addition of ether linkages to the foams enabled uniform surface erosion that improves retainment of scaffold integrity, which can be vital in slowly-degrading biomaterials applications. Increased clotting capabilities were seen in the 30% DEG foams that also have the slowest degradation rates. Overall, these materials could be employed in hemostatic applications and then left in place to slowly degrade during healing, eliminating risks associated with implant removal after its intended application.

**Supplementary Materials:** The following are available online at <https://www.mdpi.com/article/10.3390/polym13234084/s1>, Figure S1: Representative differential scanning calorimetry traces for synthesized materials in the dry state. Glass transition temperatures were taken as the half-height transition of the endothermic shift in the data. Figure S2: Representative images of lysates from coagulation time assay. Negative control contains empty tube with no samples.

**Author Contributions:** Conceptualization, A.U.V. and M.B.B.M.; methodology, A.U.V., N.M.P., E.S. and M.B.B.M.; validation, A.U.V., N.M.P., E.S. and M.B.B.M.; formal analysis, A.U.V., N.M.P., E.S. and M.B.B.M.; investigation, A.U.V., N.M.P., E.S. and M.B.B.M.; resources, M.B.B.M.; data curation, A.U.V., N.M.P., E.S. and M.B.B.M.; writing—original draft preparation, A.U.V.; writing—review and editing, M.B.B.M.; visualization, all; supervision, M.B.B.M.; project administration, M.B.B.M.; funding acquisition, M.B.B.M. All authors have read and agreed to the published version of the manuscript.

**Funding:** This material is based on research sponsored by U.S. Air Force under agreement number FA8650-18-2-6978. The U.S. Government is authorized to reproduce and distribute reprints for Governmental purposes, notwithstanding any copyright notation thereon. The views and conclusions contained herein are those of the authors. They should not be interpreted as necessarily representing the official policies or endorsements, either expressed or implied, of U.S. Air Force or the U.S. Government.

**Institutional Review Board Statement:** Not applicable.

**Informed Consent Statement:** Not applicable.

**Data Availability Statement:** The data presented in this study are available on request from the corresponding author.

**Conflicts of Interest:** The authors declare no conflict of interest. The funders had no role in the design of the study; in the collection, analyses, or interpretation of data; in the writing of the manuscript, or in the decision to publish the results.

## References

- Laschke, M.; Strohe, A.; Scheuer, C.; Eglin, D.; Verrier, S.; Alini, M.; Pohlemann, T.; Menger, M. In vivo biocompatibility and vascularization of biodegradable porous polyurethane scaffolds for tissue engineering. *Acta Biomater.* **2009**, *5*, 1991–2001. [[CrossRef](#)]
- Wache, H.M.; Tartakowska, D.J.; Hentrich, A.; Wagner, M.H. Development of a polymer stent with shape memory effect as a drug delivery system. *J. Mater. Sci. Mater. Med.* **2003**, *14*, 109–112. [[CrossRef](#)]
- Sormana, J.-L.; Carson, M.J. High-Throughput Discovery of Structure–Mechanical Property Relationships for Segmented Poly(urethane–urea)s. *Macromolecules* **2004**, *37*, 2186–2195. [[CrossRef](#)]
- Guan, J.; Wagner, W.R. Synthesis, Characterization and Cytocompatibility of Polyurethaneurea Elastomers with Designed Elastase Sensitivity. *Biomacromolecules* **2005**, *6*, 2833–2842. [[CrossRef](#)]
- Singhal, P.; Small, W.; Cosgriff-Hernandez, E.; Maitland, D.J.; Wilson, T.S. Low density biodegradable shape memory polyurethane foams for embolic biomedical applications. *Acta Biomater.* **2014**, *10*, 67–76. [[CrossRef](#)]
- Jang, L.K.; Fletcher, G.K.; Monroe, M.B.B.; Maitland, D.J. Biodegradable shape memory polymer foams with appropriate thermal properties for hemostatic applications. *J. Biomed. Mater. Res. Part A* **2020**, *108*, 1281–1294. [[CrossRef](#)] [[PubMed](#)]
- Weems, A.C.; Wacker, K.T.; Carrow, J.K.; Boyle, A.J.; Maitland, D.J. Shape memory polyurethanes with oxidation-induced degradation: In vivo and in vitro correlations for endovascular material applications. *Acta Biomater.* **2017**, *59*, 33–44. [[CrossRef](#)] [[PubMed](#)]
- Lyu, S.; Untereker, D. Degradability of Polymers for Implantable Biomedical Devices. *Int. J. Mol. Sci.* **2009**, *10*, 4033–4065. [[CrossRef](#)]
- Huang, W.M.; Yang, B.; Zhao, Y.; Ding, Z. Thermo-moisture responsive polyurethane shape-memory polymer and composites: A review. *J. Mater. Chem.* **2010**, *20*, 3367–3381. [[CrossRef](#)]
- Lee, J.; Kang, S.-K. Principles for Controlling the Shape Recovery and Degradation Behavior of Biodegradable Shape-Memory Polymers in Biomedical Applications. *Micromachines* **2021**, *12*, 757. [[CrossRef](#)]
- Zare, M.; Davoodi, P.; Ramakrishna, S. Electrospun Shape Memory Polymer Micro-/Nanofibers and Tailoring Their Roles for Biomedical Applications. *Nanomaterials* **2021**, *11*, 933. [[CrossRef](#)]
- Boyle, A.J.; Landsman, T.L.; Wierzbicki, M.A.; Nash, L.D.; Hwang, W.; Miller, M.W.; Tuzun, E.; Hasan, S.M.; Maitland, D.J. In vitro and in vivo evaluation of a shape memory polymer foam-over-wire embolization device delivered in saccular aneurysm models. *J. Biomed. Mater. Res. Part B Appl. Biomater.* **2016**, *104*, 1407–1415. [[CrossRef](#)] [[PubMed](#)]
- Boyle, A.J.; Wierzbicki, M.A.; Herting, S.; Weems, A.C.; Nathan, A.; Hwang, W.; Maitland, D.J. In vitro performance of a shape memory polymer foam-coated coil embolization device. *Med. Eng. Phys.* **2017**, *49*, 56–62. [[CrossRef](#)]

14. Landsman, T.L.; Bush, R.L.; Glowczwski, A.; Horn, J.; Jessen, S.; Ungchusri, E.; Diguette, K.; Smith, H.R.; Hasan, S.M.; Nash, D.; et al. Design and verification of a shape memory polymer peripheral occlusion device. *J. Mech. Behav. Biomed. Mater.* **2016**, *63*, 195–206. [[CrossRef](#)] [[PubMed](#)]
15. Beaman, H.T.; Shepherd, E.; Satalin, J.; Blair, S.; Ramcharran, H.; Serinelli, S.; Gitto, L.; Dong, K.S.; Fikhman, D.; Nieman, G.; et al. Hemostatic shape memory polymer foams with improved survival in a lethal traumatic hemorrhage model. *Acta Biomater.* **2021**. Available online: <https://papers.ssrn.com/abstract=3864497> (accessed on 10 October 2021).
16. Singhal, P.; Boyle, A.; Brooks, M.L.; Infanger, S.; Letts, S.; Small, W.; Maitland, D.J.; Wilson, T.S. Controlling the Actuation Rate of Low-Density Shape-Memory Polymer Foams in Water. *Macromol. Chem. Phys.* **2012**, *214*, 1204–1214. [[CrossRef](#)] [[PubMed](#)]
17. Rodriguez, J.N.; Miller, M.W.; Boyle, A.; Horn, J.; Yang, C.-K.; Wilson, T.; Ortega, J.M.; Small, W.; Nash, L.; Skoog, H.; et al. Reticulation of low density shape memory polymer foam with an in vivo demonstration of vascular occlusion. *J. Mech. Behav. Biomed. Mater.* **2014**, *40*, 102–114. [[CrossRef](#)] [[PubMed](#)]
18. Easley, A.D.; Monroe, M.B.B.; Hasan, S.M.; Weems, A.C.; Frederick, J.; Maitland, D.J. Shape memory polyurethane-urea foams with improved toughness. *J. Appl. Polym. Sci.* **2018**, *136*, 47268. [[CrossRef](#)]
19. Weems, A.C.; Raymond, J.E.; Easley, A.D.; Wierzbicki, M.A.; Gustafson, T.; Monroe, M.B.B.; Maitland, D.J. Shape memory polymers with visible and near-infrared imaging modalities: Synthesis, characterization and in vitro analysis. *RSC Adv.* **2017**, *7*, 19742–19753. [[CrossRef](#)]
20. Hasan, S.M.; Harmon, G.; Zhou, F.; Raymond, J.E.; Gustafson, T.P.; Wilson, T.; Maitland, D.J. Tungsten-loaded SMP foam nanocomposites with inherent radiopacity and tunable thermo-mechanical properties. *Polym. Adv. Technol.* **2016**, *27*, 195–203. [[CrossRef](#)]
21. Monroe, M.B.B.; Easley, A.D.; Grant, K.; Fletcher, G.K.; Boyer, C.; Maitland, D.J. Multifunctional Shape-Memory Polymer Foams with Bio-inspired Antimicrobials. *ChemPhysChem* **2017**, *19*, 1999–2008. [[CrossRef](#)]
22. Herting, S.M.; Ding, Y.; Boyle, A.J.; Dai, D.; Nash, L.D.; Asnafi, S.; Jakaitis, D.R.; Johnson, C.R.; Graul, L.M.; Yeh, C.; et al. In vivo comparison of shape memory polymer foam-coated and bare metal coils for aneurysm occlusion in the rabbit elastase model. *J. Biomed. Mater. Res. Part B Appl. Biomater.* **2019**, *107*, 2466–2475. [[CrossRef](#)]
23. Hasan, S.M.; Fletcher, G.K.; Monroe, M.B.B.; Wierzbicki, M.A.; Nash, L.D.; Maitland, D.J. Shape Memory Polymer Foams Synthesized Using Glycerol and Hexanetriol for Enhanced Degradation Resistance. *Polymers* **2020**, *12*, 2290. [[CrossRef](#)]
24. Weems, A.C.; Carrow, J.K.; Gaharwar, A.K.; Maitland, D.J. Improving the Oxidative Stability of Shape Memory Polyurethanes Containing Tertiary Amines by the Presence of Isocyanurate Triols. *Macromolecules* **2018**, *51*, 9078–9087. [[CrossRef](#)]
25. Weems, A.; Li, W.; Maitland, D.J.; Calle, L.M. Polyurethane Microparticles for Stimuli Response and Reduced Oxidative Degradation in Highly Porous Shape Memory Polymers. *ACS Appl. Mater. Interfaces* **2018**, *10*, 32998–33009. [[CrossRef](#)]
26. Christenson, E.M.; Anderson, J.M.; Hiltner, A. Oxidative mechanisms of poly(carbonate urethane) and poly(ether urethane) biodegradation: In vivo and in vitro correlations. *J. Biomed. Mater. Res.* **2004**, *70*, 245–255. [[CrossRef](#)]
27. Nash, L.D.; Docherty, N.C.; Monroe, M.B.B.; Ezell, K.P.; Carrow, J.K.; Hasan, S.M.; Gaharwar, A.K.; Maitland, D.J. Cold Plasma Reticulation of Shape Memory Embolic Tissue Scaffolds. *Macromol. Rapid Commun.* **2016**, *37*, 1945–1951. [[CrossRef](#)]
28. Alekya, B.; Rao, S.; Pandya, H.J. Engineering approaches for characterizing soft tissue mechanical properties: A review. *Clin. Biomech.* **2019**, *69*, 127–140.
29. Vakil, A.U.; Petryk, N.M.; Shepherd, E.; Beaman, H.T.; Ganesh, P.S.; Dong, K.S.; Monroe, M.B.B. Shape Memory Polymer Foams with Tunable Degradation Profiles. *ACS Appl. Bio Mater.* **2021**, *4*, 6769–6779. [[CrossRef](#)]
30. Christmas, N.; Vakil, A.U.; Hatch, C.J.; Dong, S.; Fikhman, D.; Beaman, H.T.; Monroe, M.B.B. Characterization of shape memory polymer foam hemostats in in vitro hemorrhagic wound models. *J. Biomed. Mater. Res. Part. B Appl. Biomater.* **2021**, *109*, 681–692. [[CrossRef](#)] [[PubMed](#)]



## Article

# Kinetics of the Thermal Degradation of Poly(lactic acid) and Polyamide Bioblends

Félix Carrasco <sup>1,\*</sup>, Orlando Santana Pérez <sup>2</sup> and Maria Lluïsa Maspoch <sup>2</sup>

<sup>1</sup> Department of Chemical Engineering, Universitat de Girona (UdG), C/Maria Aurèlia Capmany 61, 17003 Girona, Spain

<sup>2</sup> Centre Català del Plàstic (CCP), Universitat Politècnica de Catalunya Barcelona Tech (UPC-EEBE), C/Colom 114, 08222 Terrassa, Spain; orlando.santana@upc.edu (O.S.P.); maria.lluisa.maspoch@upc.edu (M.L.M.)

\* Correspondence: felix.carrasco@udg.edu

**Abstract:** Poly(lactic acid) (PLA) and biosourced polyamide (PA) bioblends, with a variable PA weight content of 10–50%, were prepared by melt blending in order to overcome the high brittleness of PLA. During processing, the properties of the melt were stabilized and enhanced by the addition of a styrene-acrylic multi-functional-epoxide oligomeric reactive agent (SAMfE). The general analytical equation (GAE) was used to evaluate the kinetic parameters of the thermal degradation of PLA within bioblends. Various empirical and theoretical solid-state mechanisms were tested to find the best kinetic model. In order to study the effect of PA on the PLA matrix, only the first stage of the thermal degradation was taken into consideration in the kinetic analysis ( $\alpha < 0.4$ ). On the other hand, standardized conversion functions were evaluated. Given that it is not easy to visualize the best accordance between experimental and theoretical values of standardized conversion functions, an index, based on the integral mean error, was evaluated to quantitatively support our findings relative to the best reaction mechanism. It was demonstrated that the most probable mechanism for the thermal degradation of PLA is the random scission of macromolecular chains. Moreover,  $y(\alpha)$  master plots, which are independent of activation energy values, were used to confirm that the selected reaction mechanism was the most adequate. Activation energy values were calculated as a function of PA content. Moreover, the onset thermal stability of PLA was also determined.

**Keywords:** PLA; PA; bioblend; thermal stability; kinetic models; reaction mechanisms; random scission

**Citation:** Carrasco, F.; Santana Pérez, O.; Maspoch, M.L. Kinetics of the Thermal Degradation of Poly(lactic acid) and Polyamide Bioblends. *Polymers* **2021**, *13*, 3996. <https://doi.org/10.3390/polym13223996>

Academic Editors:

Sergio Torres-Giner and Maria Vargas

Received: 30 October 2021

Accepted: 16 November 2021

Published: 19 November 2021

**Publisher's Note:** MDPI stays neutral with regard to jurisdictional claims in published maps and institutional affiliations.



**Copyright:** © 2021 by the authors. Licensee MDPI, Basel, Switzerland. This article is an open access article distributed under the terms and conditions of the Creative Commons Attribution (CC BY) license (<https://creativecommons.org/licenses/by/4.0/>).

## 1. Introduction

The generation of polymers derived from renewable sources, also called bio-based polymers, is an important field of research due to the role that these ecofriendly polymers play in reducing plastic residues, which are a source of pollution, and carbon dioxide production, which leads to a decrease in the carbon footprint of its lifecycle [1,2]. Over the past decade, bio-based polymers, such as poly(lactic acid) (PLA), have gained interest as a substitute for conventional fossil-based polymers in biomedical and commodity applications. Its main features are its biodegradable nature, the decrease in the CO<sub>2</sub> footprint associated with the product, and the non-toxic residues released during processing [3–6].

Despite its great potential, PLA still has limitations, such as its brittleness, its reduced service temperature range, and its high instability during processing where good melt strength is required. There is a large amount of research dedicated to solving these drawbacks with the aim of expanding its application window to become a commodity or even an engineering thermoplastic [7–11].

Blending PLA with other engineering soft polymers represents an industrially relevant strategy for developing bio-based formulations with tailored performances [12]. Specifically, numerous works report the investigation of melt blending PLA with polyamides (PA) [13–18]. However, the inherent immiscibility of this binary polymer system results in

rather poor mechanical properties. To overcome the aforementioned issue, Pai et al. [14] and Patel et al. [18] reported the first attempts to compatibilize PLA/PA blends by adding titanium isopropoxide and a low molecular weight epoxy resin, respectively. Unfortunately, a high PA content ( $\geq 50\%$ ) is needed to change the blend morphology from a droplet-matrix to co-continuous in order to improve the mechanical properties [15,17,18]. Therefore, PLA/PA blends with a predominant PLA content still exhibit brittleness. Polymer blends exhibiting a fine-tuned morphology with a significantly reduced droplet size of the minor phase are promising due to their enhanced toughness in comparison to coarse sea-island morphologies. Indeed, the challenge is not only the compatibility of phases but also the control of the resulting morphology after processing, which contributes to determine the mechanical performance. Initially, a refined droplet morphology of the minor phase should be better, in terms of enhanced toughness in comparison to a coarse sea-island morphology. However, it has been demonstrated that the generation during processing of a suitably compatibilized and oriented fibril morphology of the dispersed phase could generate a mechanical reinforcing effect [19].

Among all available strategies that enable a processing-controlled morphology, the viscosity ratio of the parent polymers in blends is that which is considered in industrial practice. Indeed, using PLA as a matrix with enhanced melt viscosity and melt elasticity through reactive extrusion (using a styrene-acrylic multi-functional epoxide reactive agent) promotes a more homogeneous PA microstructure with improved interfacial adhesion, thus promoting a nucleant effect in the PLA phase [20]. Based on the work of Walha et al. [21], this enhanced feature could be attributed to the reaction between the unreacted epoxy groups present in modified PLA and the amine chain ends of PA.

Along with many types of aliphatic polyesters, PLA is subject to some thermal decomposition above its melting temperature, especially during processing. Radical and non-radical reactions have been proposed to explain the various complex mechanisms that could occur during processing that lead to a reduction in the molecular weight and viscosity. As a result, a general decrease in the material properties is expected. Yu et al. (2003) [22] argued that thermal and hydrolysis reactions for biocopolymers could be generated by random chain scission reactions of the ester groups. Coupled with this mechanism, intra- and inter-molecular transesterification reactions could also cause a drop in molecular weight at longer reaction times.

The ever-increasing commercial importance of polymeric materials has aroused continuous interest in their thermal stability. The kinetic modeling of the decomposition process plays a central role in many of these studies, as it is crucial for an accurate prediction of the material behavior under different working conditions [23–31]. A precise prediction requires knowledge of the so-called kinetic triplet: the activation energy, pre-exponential factor, and kinetic model. The latter parameter, also known as conversion function,  $f(\alpha)$ , is an algebraic expression that is associated with the mathematical model that describes the kinetics of solid-state reactions. Therefore, the kinetic analysis also provides some understanding of the mechanism of the reaction under study. Knowledge of the kinetic model and the mechanism of thermal degradation of macromolecules is very helpful in the study of the thermal stability of polymers [32–34].

The goal of this paper was to determine the thermal stability of PLA/PA bioblends containing between 50% and 90% rheologically modified PLA. Moreover, empirical (n-order and autocatalytic) and theoretical (R1, F1, D1, R2, F2, D2, R3, F3, D3, and random scission) kinetic models were tested in order to elucidate the best mechanism to describe the thermal degradation of PLA within these bioblends. The variation in activation energy values with PA content was also assessed.

## 2. Theoretical Background

Thermally stimulated solid-state reactions, such as thermal decompositions, are heterogeneous processes. The reaction rates of such processes can be kinetically described when they take place under conditions that are far from equilibrium, by the following expression:

$$\frac{d\alpha}{dt} = k f(\alpha) = A \exp\left(-\frac{E}{RT}\right) f(\alpha) \quad (1)$$

where  $d\alpha/dt$  is the reaction rate,  $k$  is the kinetic constant,  $A$  is the Arrhenius frequency factor,  $R$  is the gas constant,  $E$  is the activation energy,  $\alpha$  is the reacted fraction or conversion,  $T$  is the process temperature, and  $f(\alpha)$  accounts for the reaction rate dependence on  $\alpha$ . The conversion function,  $f(\alpha)$ , describes the dependence of the reaction rate with the process mechanism.

When integrating Equation (1) and truncating the infinite series to the second term, the linear integral equation is derived for experiments carried out at a constant heating rate ( $\beta = dT/dt$ ). This equation is called the general analytical equation (GAE), developed by Carrasco [35].

$$\ln \left[ \beta \frac{g(\alpha)}{T^2 \left(1 - \frac{2RT}{E}\right)} \right] = \ln \frac{AR}{E} - \frac{E}{R} \frac{1}{T} \quad (2)$$

where

$$g(\alpha) = \int_0^\alpha \frac{d\alpha}{f(\alpha)} \quad (3)$$

It must be considered that the activation energy calculation, through Equation (2), requires an iterative procedure given that  $E$  is needed to evaluate the first member of the equation. The  $E$  value determined from the slope was introduced in the first member. The new  $E$  value obtained from the slope was again introduced in the first member and so on, until reaching a constant  $E$  value.

Different conversion functions are reported in literature for describing the kinetic mechanism of solid-state reactions. These mechanisms are proposed to consider different geometrical assumptions for the shape of the material particles (spherical, cylindrical, and planar) and driving forces (interface growth, diffusion, nucleation, and growth of nuclei). Table 1 shows the equations used for the linear regression analysis of the most common solid-state theoretical mechanisms (R1, R2, R3, F1, F2, F3, D1, D2, D3, and random scission). The random scission mechanism is applied to  $L = 2$ , where  $L$  is the minimum length of the polymer that is not volatile. For  $L \geq 3$ , there is no symbolic solution and an iterative procedure is required. The conversion functions,  $f(\alpha)$ , assume idealized models, which may not be necessarily fulfilled in real systems. On the other hand, empirical kinetic models are also proposed:  $n$ -order and autocatalytic. The exponents  $n = 0.550$  (for  $n$ -order kinetics), and  $n = 0.771$  and  $m = 0.244$  (for autocatalytic kinetics) were previously optimized for the thermal degradation of PLA [36]. The activation energy and frequency factor values for each kinetic model were calculated using Equations (2) and (3).



**Table 1.** Integral kinetic equations for various solid-state mechanisms.

Mechanism	$f(\alpha)$	General Analytical Equation in Linear Form
n-order	$(1 - \alpha)^n$	$\ln \left[ \beta \frac{1 - (1 - \alpha)^{1-n}}{(1-n) T^2 (1 - \frac{2RT}{E})} \right] = \ln \frac{AR}{E} - \frac{E}{R} \frac{1}{T}$
Autocatalytic	$(1 - \alpha)^n \alpha^m$	$\ln \left[ \beta \frac{1 - (1 - \alpha)^{1-n} + \frac{\alpha^{1-m}}{1-m}}{T^2 (1 - \frac{2RT}{E})} \right] = \ln \frac{AR}{E} - \frac{E}{R} \frac{1}{T}$
Random scission	$2 (\alpha^{1/2} - \alpha)$	$\ln \left[ \beta \frac{-\ln(1 - \alpha^{1/2})}{T^2 (1 - \frac{2RT}{E})} \right] = \ln \frac{AR}{E} - \frac{E}{R} \frac{1}{T}$
R1	1	$\ln \left[ \beta \frac{\alpha}{T^2 (1 - \frac{2RT}{E})} \right] = \ln \frac{AR}{E} - \frac{E}{R} \frac{1}{T}$
R2	$2 (1 - \alpha)^{1/2}$	$\ln \left[ \beta \frac{1 - (1 - \alpha)^{1/2}}{T^2 (1 - \frac{2RT}{E})} \right] = \ln \frac{AR}{E} - \frac{E}{R} \frac{1}{T}$
R3	$3 (1 - \alpha)^{2/3}$	$\ln \left[ \beta \frac{1 - (1 - \alpha)^{1/3}}{T^2 (1 - \frac{2RT}{E})} \right] = \ln \frac{AR}{E} - \frac{E}{R} \frac{1}{T}$
F1	$(1 - \alpha)$	$\ln \left[ \beta \frac{-\ln(1 - \alpha)}{T^2 (1 - \frac{2RT}{E})} \right] = \ln \frac{AR}{E} - \frac{E}{R} \frac{1}{T}$
F2	$(1 - \alpha)^2$	$\ln \left[ \beta \frac{\left(\frac{\alpha}{1-\alpha}\right)}{T^2 (1 - \frac{2RT}{E})} \right] = \ln \frac{AR}{E} - \frac{E}{R} \frac{1}{T}$
F3	$(1 - \alpha)^3$	$\ln \left[ \beta \frac{(1 - \alpha)^{-2} - 1}{2 T^2 (1 - \frac{2RT}{E})} \right] = \ln \frac{AR}{E} - \frac{E}{R} \frac{1}{T}$
D1	$\frac{1}{2\alpha}$	$\ln \left[ \beta \frac{\alpha^2}{T^2 (1 - \frac{2RT}{E})} \right] = \ln \frac{AR}{E} - \frac{E}{R} \frac{1}{T}$
D2	$\frac{1}{-\ln(1 - \alpha)}$	$\ln \left[ \beta \frac{(1 - \alpha) \ln(1 - \alpha) + \alpha}{T^2 (1 - \frac{2RT}{E})} \right] = \ln \frac{AR}{E} - \frac{E}{R} \frac{1}{T}$
D3	$\frac{3 (1 - \alpha)^{2/3}}{2 [1 - (1 - \alpha)^{1/3}]}$	$\ln \left[ \beta \frac{1 + (1 - \alpha)^{2/3} - 2 (1 - \alpha)^{1/3}}{T^2 (1 - \frac{2RT}{E})} \right] = \ln \frac{AR}{E} - \frac{E}{R} \frac{1}{T}$

### 3. Materials and Methods

#### 3.1. Materials

A commercially extrusion-grade PLA (Ingeo 4032DR; D lactide content: 2%) was purchased from Natureworks (Arendonk, Belgium) and used as received.

SAMfE reactive agent, namely Joncryl ADR-4300FR, was kindly supplied by BASF (Ludwigshafen, Germany) with an epoxy equivalent weight of 433 Da and a functionality of about 12.

The predominantly bio-based PA10.10 was produced by Dupont (Midland, MI, USA) under the trade name Zytel RS LC1000 BK385.

#### 3.2. Reactive Extrusion and Bioblend Preparation

Bioblends were prepared by using a two-step process. Prior to processing, raw PLA was dried at 80 °C for 4 h in a Piovan (DSN506HE, Venice, Italy) hopper-dryer (dew point = −40 °C). SAMfE flakes were vacuum-dried overnight at RT over silica gel. The enhancement of the PLA melt properties was achieved through reactive extrusion using a corotating twin-screw extruder with a screw diameter of 25 mm (L/D = 36) (KNETER 25 × 24D, Collin GmbH, Ebersberg, Germany) and a nominal SAMfE weight content of 0.6%. The seven heating zones were set to 45, 165, 165, 170, 180, 190, 190 °C from feeding to die zones.

The screw speed was set to 35 rpm, leading to a residence time of 4.1 min. The extrudate was water-cooled and pelletized. Then, five PLA/PA blends, covering the 10–50% PA weight composition range, were prepared by melt mixing, using a Brabender batch mixer (Brabender Plastic-Corder W50EHT, Brabender GmbH & Co., Duisburg, Germany) operated at 210 °C and 50 rpm for 12 min. The obtained materials were further compression molded into 0.6 mm thick plates in an IQAP LAP PL-15 hot plate press (IQAP Master-

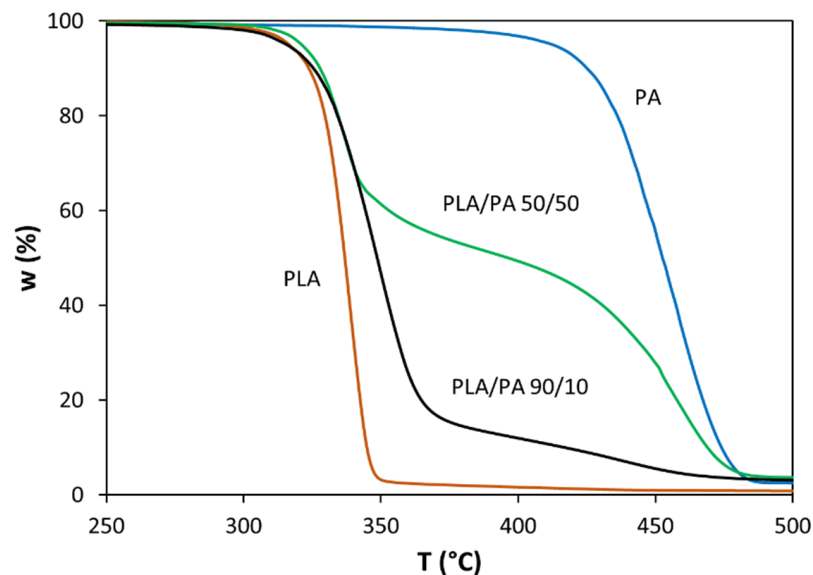
batch S.L., Barcelona, Spain) for 5 min at 210 °C and 4 MPa and then cooled at  $-50$  °C/min. Prior to processing, PLA and PA were vacuum dried overnight at 80 °C over silica gel.

### 3.3. Thermal Characterization

TGA data were processed on a Mettler Toledo thermogravimetric analyzer, model TGA-SDTA851. Samples of 20 mg were heated at various linear heating rates (2.5, 5, and 10 K/min) from room temperature to 600 °C, under a dry nitrogen gas flow rate of 40 cm<sup>3</sup>/min. Two replicates were scanned and errors were lower than 1.5%.

## 4. Results and Discussion

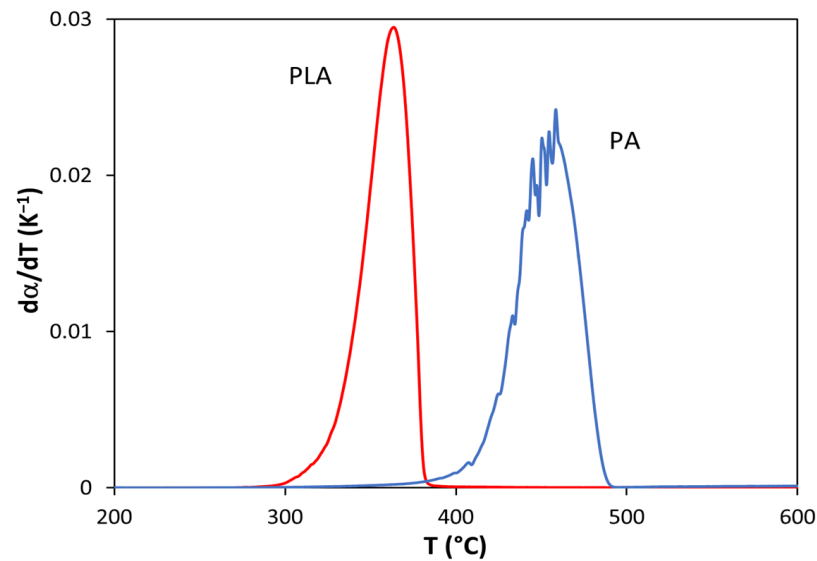
Figure 1 shows the experimental curves recorded for the thermal degradation of PLA (produced by reactive extrusion), PA, and two PLA/PA bioblends (with PLA weight contents of 50% and 90%), under a nominal linear heating rate of 10 K/min. It is clear that PA is significantly more resistant to thermal degradation compared to PLA. TG curves of PLA and PA are sigmoidal and they present a unique profile of decomposition. Therefore, the thermal degradation of these pure polymers presents a unique value of activation energy within the entire range of conversion. Contrarily, the TG curves of PLA/PA bioblends clearly exhibit three different zones of decomposition: a first step, where PLA degrades, a second step, where the decomposition of PLA and PA takes place simultaneously, and a third phase, where residual PA degrades until the total disappearance of the organic material. When comparing the first stages of the TG curves of the 90/10 and 50/50 bioblends, it can be concluded that the bioblend with a higher PA content is a more thermally resistant material. Therefore, the presence of PA in higher proportions clearly protects the matrix of PLA. From the TG data, it was possible to evaluate the conversion and the conversion derivative by taking into account the inorganic residual material at 600 °C, which was lower than 2%.



**Figure 1.** TG curves (i.e., variation in residual weight as a function of temperature) for PLA, PA, and bioblends containing 50% and 90% PLA (nominal heating rate = 10 K/min).

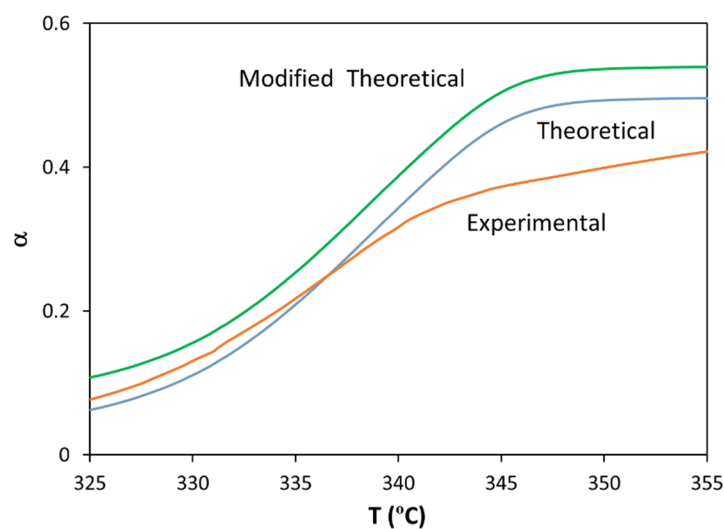
Figure 2 shows the conversion derivative values of PLA and PA as a function of temperature. This graphic clearly reveals that PLA and PA degrade in a completely different temperature range: 290–380 °C for PLA and 380–490 °C for PA. This finding is very important because it means that we were able to study the thermal degradation of PLA without any decomposition of PA. For this reason, it was possible to study the influence of PA on the thermal degradation of the PLA matrix. Given that the different materials contain 10–50% PA, the kinetic study of the degradation of PLA was considered for conversions of PLA lower than 0.4. Within this interval ( $\alpha = 0-0.4$ ), no degradation of

PA can occur, thus allowing for the specific study of the thermal stability of PLA in the presence of various proportions of PA.



**Figure 2.** Variation in the conversion derivative of PLA and PA as a function of temperature (nominal heating rate = 10 K/min).

Figure 3 shows the experimental conversion curve for the bioblend containing 50/50 PLA/PA (under a nominal linear heating rate of 10 K/min) and the theoretical conversion curve constructed by a linear combination of PLA and PA experimental curves. The difference between these curves was caused by the additional melting process needed to prepare the bioblend and the development of a new tridimensional structure, as a consequence of interactions between the molecular chains of PLA and PA. At  $\alpha < 0.25$ , the bioblend is less resistant to heat (due to the melting process), whereas at  $\alpha > 0.25$ , it is more resistant (due to interactions between PLA and PA). If we consider the degradation of single components equivalent to 5% of thermal degradation (in order to “take into account the bioblening process”), the “modified theoretical” curve clearly shows that thermal degradation is higher for the sum of single components compared to that of the bioblend, thus demonstrating the protective effect of PA on the PLA matrix.



**Figure 3.** Variation in conversion with temperature for the bioblend containing 50% PLA (nominal heating rate = 10 K/min).

From Figure 1, it was possible to obtain various decomposition temperatures, i.e., the onset decomposition ( $T_5$ ) and final decomposition ( $T_{95}$ ) temperatures, defined as the temperatures at which 5% and 95% of the mass was lost, respectively, as shown in Table 2. The values of  $T_5$  for the bioblends increased with PA content, from 315.8 °C to 321.2 °C when the PA content increased from 10% to 50%. On the other hand, the values of  $T_{95}$  ranged from 455 °C to 554 °C, with an erratic variation as a function of the PA content. Table 2 also shows other thermal parameters, i.e., conversion ( $\alpha_m$ ), conversion derivative ( $(d\alpha/dT)_m$ ), and temperature ( $T_m$ ) at the maximum decomposition rate of PLA.

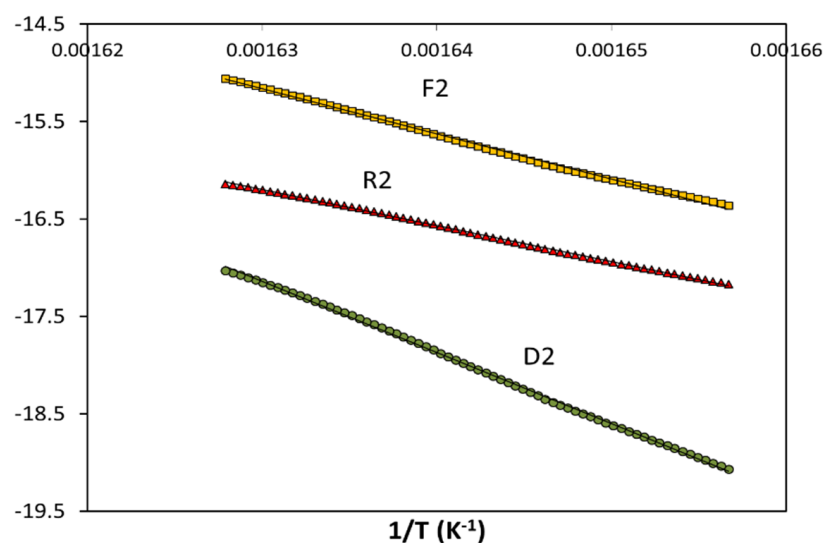
**Table 2.** Decomposition temperatures of the PLA/PA bioblends, at a nominal heating rate of 10 K/min.

	$T_5$ (°C)	$T_{95}$ (°C)	$\alpha_m$	$T_m$ (°C)	$(d\alpha/dT)_m$ (K <sup>-1</sup> )	$\alpha_r$	$T_r$ (°C)	$(d\alpha/dT)_r$ (K <sup>-1</sup> )
PLA/PA 90/10	315.8	455.0	0.54	349.8	$2.39 \cdot 10^{-2}$	0.45	346.1	$2.38 \cdot 10^{-2}$
PLA/PA 80/20	317.4	554.4	0.43	343.1	$2.49 \cdot 10^{-2}$	0.40	341.8	$2.46 \cdot 10^{-2}$
PLA/PA 70/30	318.8	540.2	0.35	339.2	$2.83 \cdot 10^{-2}$	0.35	339.3	$1.76 \cdot 10^{-2}$
PLA/PA 60/40	320.5	484.1	0.30	338.5	$2.69 \cdot 10^{-2}$	0.30	338.4	$0.49 \cdot 10^{-2}$
PLA/PA 50/50	321.2	479.2	0.27	337.6	$2.01 \cdot 10^{-2}$	0.25	336.6	$0.18 \cdot 10^{-2}$

It is clear that the presence of PA considerably modified the conversion values at the maximum rate from 45% to 27% when the PA content increased from 10% to 50%. This shift was essentially due to the variable content of PLA in the bioblends and also to the presence of interactions between the PLA matrix and PA.

Table 2 also contains the temperature ( $T_r$ ) and conversion derivative  $(d\alpha/dT)_r$  values at  $\alpha = \alpha_r$  (reference conversion). These values are necessary to construct standardized conversion functions, as is shown later. Usually, reference conversion is taken as being equal to 0.5. This is correct for pure polymers. In the case of mixed polymers, this value must not be considered. For example, for the 50/50 bioblend, a conversion of 0.5 means the total decomposition of PLA and this cannot be considered as a reference of the PLA thermal decomposition. For this reason, a new reference conversion was defined in this work:  $\alpha_r = 0.5 \times$ , where  $x$  is the mass fraction of PLA in bioblends. Therefore, the reference conversions are 0.45, 0.40, 0.35, 0.30, and 0.25 for bioblends containing 90%, 80%, 70%, 60%, and 50% PLA. Curiously, these reference conversion values are very near to the conversion values at the maximum decomposition rate.

Figure 4 shows the results of the general analytical equation (GAE) for three theoretical conventional mechanisms (F2, R2, and D2) for the thermal degradation of the bioblend containing 70% PLA, under a nominal linear heating rate of 10 K/min. The experimental data fit was excellent ( $r^2 > 0.99$ ) for the three kinetic models. The activation energy values evaluated are shown in Table 3 (mean value for the three heating rates  $\pm$  confidence interval). The activation energy values for the thermal degradation of PLA depend on the considered mechanism and the content of PA. These  $E$  values ranged, for the various bioblends, as a function of the reaction mechanism as follows: 236–311 kJ/mol (n-order), 192–254 kJ/mol (autocatalytic), 154–205 kJ/mol (random scission), 253–334 kJ/mol (F1), 216–284 kJ/mol (R1), 441–578 kJ/mol (D1), 294–389 kJ/mol (F2), 234–308 kJ/mol (R2), 464–610 kJ/mol (D2), 340–450 kJ/mol (F3), 240–317 kJ/mol (R3), and 490–643 kJ/mol (D3). Therefore, the activation energy values are highly influenced by the presence of PA for each mechanism. Diffusion (D1, D2, and D3) and the F2 mechanisms had the highest activation energies, whereas random scission, autocatalytic, and R1 had the lowest activation energies.

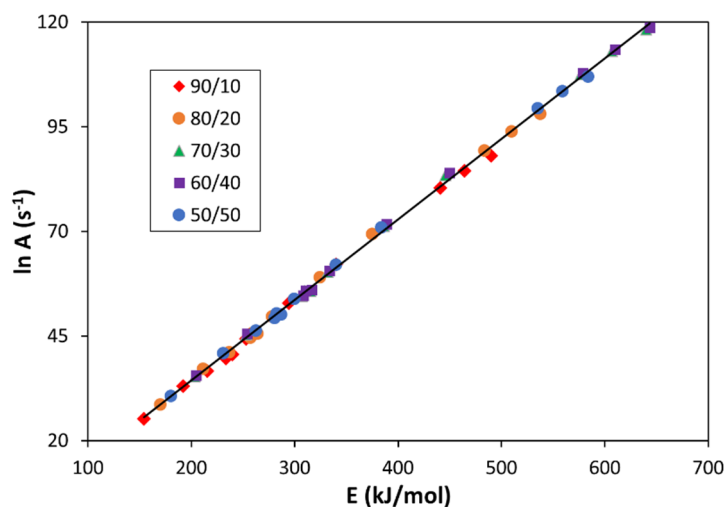


**Figure 4.** Integral kinetic analysis by means of the general analytical equation (GAE) for the thermal degradation of the bioblend containing 70% PLA using three theoretical conventional mechanisms (F2, R2, and D2) (nominal heating rate = 10 K/min).

**Table 3.** Mean activation energies of the thermal degradation of PLA, obtained using the general analytical equation at various heating rates, for PLA/PA bioblends containing from 50% to 90% PLA.

Mechanism	E (kJ/mol)				
	90/10	80/20	70/30	60/40	50/50
n-order	236 ± 4	259 ± 3	309 ± 3	311 ± 3	283 ± 3
Autocatalytic	192 ± 3	212 ± 3	253 ± 3	254 ± 3	231 ± 2
Random scission	154 ± 2	170 ± 2	204 ± 3	205 ± 3	180 ± 2
F1	253 ± 4	278 ± 4	332 ± 4	334 ± 5	300 ± 4
R1	216 ± 4	237 ± 3	283 ± 3	284 ± 3	263 ± 3
D1	441 ± 5	484 ± 5	576 ± 6	578 ± 6	536 ± 6
F2	294 ± 4	324 ± 5	386 ± 5	389 ± 5	340 ± 4
R2	234 ± 4	257 ± 3	307 ± 3	308 ± 4	281 ± 3
D2	464 ± 6	510 ± 6	607 ± 6	610 ± 5	559 ± 6
F3	340 ± 5	375 ± 5	446 ± 6	450 ± 6	384 ± 5
R3	240 ± 3	264 ± 3	315 ± 4	317 ± 4	287 ± 3
D3	490 ± 7	538 ± 7	640 ± 8	643 ± 8	584 ± 7

There was a compensation factor between the frequency factor and activation energy for all the empirical and theoretical kinetic models and for all the materials under study. Figure 5 shows an excellent linear relationship between  $\ln A$  and  $E$  (for TG experiments carried out at a nominal heating rate of 10 K/min). The equation relating these two kinetic parameters is  $\ln A \text{ (s}^{-1}\text{)} = -4.15 + 0.19 E \text{ (kJ/mol)}$ . This means that an increase in the activation energy (i.e., a higher energy barrier for the thermal degradation) leads to an increase in the frequency factor (i.e., a higher probability to be decomposed). This compensation factor was also observed for the other heating rates used in this work.



**Figure 5.** Compensation factor between the frequency factor and activation energy for all the empirical and theoretical kinetic models studied and for all the bioblends analyzed (nominal heating rate = 10 K/min).

When summarizing the results of the linear regressions, all the mechanisms led to regression coefficients higher than 0.99 for all the bioblends. This means that all the mechanisms are satisfactory, from a mathematical point-of view, to represent the kinetics of the thermal degradation of the samples considered in this study. Therefore, it was necessary to employ a method that is able to discern the best mechanism (and then it became possible to evaluate the activation energy responsible for splitting the macromolecules, which occurred during the thermal degradation). For this reason, an isoconversional kinetic analysis was carried out.

Following the ICTAC recommendations [37], the Kissinger–Akahira–Sunose method was employed:

$$\ln \left[ \frac{\beta_i}{T_{\alpha,i}^2} \right] = \text{Const} - \frac{E_\alpha}{R} \frac{1}{T_\alpha} \quad (4)$$

From this method, it was possible to evaluate the isoconversional values of the activation energy without assuming any particular form of reaction model. For this reason, isoconversional methods are frequently called “model-free” methods. The nominal heating rates used for this analysis were 2.5, 5, and 10 K/min. As reported by Vyazovkin et al. [37], determination of the reaction model requires that the variation in  $E_\alpha$  with  $\alpha$  to be negligible so that  $E_\alpha$  dependence can be replaced with a single average value,  $E_o$ . In our study, no sample exhibited a significant dependence of activation energy with conversion.

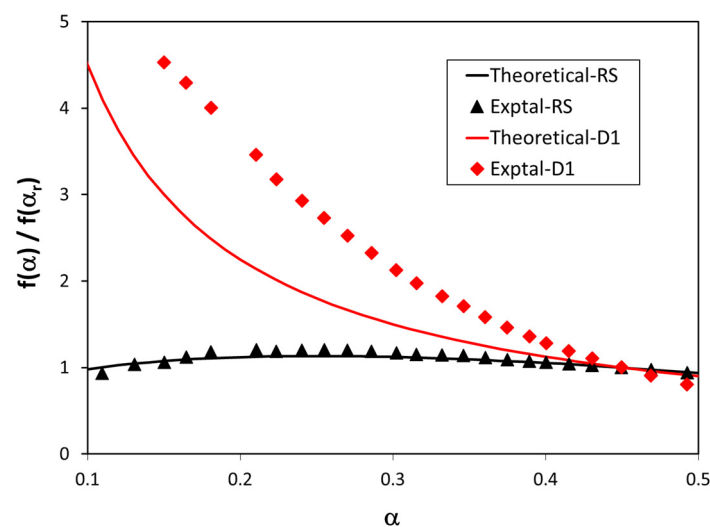
In order to elucidate the best reaction mechanism, standardized conversion functions were successfully used to compare the experimental and theoretical data relative to the reaction mechanisms. Theoretical values were determined using conversion functions, as shown in Table 1, and they depended only on the reaction mechanism. On the other hand, experimental values were calculated by means of the following equation:

$$\frac{f(\alpha)}{f(\alpha_r)} = \frac{(d\alpha/dT)}{(d\alpha/dT)_r} \exp \left[ \frac{E}{R} \left( \frac{1}{T} - \frac{1}{T_r} \right) \right] \quad (5)$$

where  $f(\alpha_r)$ ,  $(d\alpha/dT)_r$ , and  $T_r$  are the conversion function, conversion derivative, and temperature at  $\alpha = \alpha_r$  (reference conversion), respectively. These reference conversions are reported in Table 2. The conversion derivative and temperature at  $\alpha = \alpha_r$  are experimental values and  $E$  is the activation energy previously evaluated for each of the mechanisms considered, as shown in Table 3. Therefore, the experimental values depend on the activation energy values.

Figure 6 shows the variation in the standardized conversion functions with the conversion for two mechanisms: random scission and D1. The fitting between the experimental and theoretical values was excellent for the random scission mechanism, but this fitting was very poor when mechanism D1 was considered. These standardized conversion functions give valuable information about the most suitable mechanism. However, this information is only qualitative. In order to elucidate the most appropriate kinetic model, it was necessary to develop a quantitative procedure. For this reason, an index, the integral mean error (*IME*), was proposed in a previous work [38]. This index takes into consideration the mean area under the curve of absolute error of the standardized conversion function vs. conversion, and is defined as follows:

$$IME = \frac{\int_0^\alpha \left| \Delta_{f(\alpha)/f(\alpha_r)} \right| d\alpha}{\int_0^\alpha d\alpha} \cdot 100 \quad (6)$$



**Figure 6.** Variation in standardized conversion functions as a function of conversion for the thermal degradation of PLA in the bioblend containing 90% PLA, when considering two reaction mechanisms: random scission and D1.

Table 4 contains integral mean error (*IME*) values for all the mechanisms studied in this work. For each bioblend, the minimum *IME* values were found for the random scission mechanism (5.5–6.7%), which correspond with the lowest errors.

**Table 4.** Integral mean error (*IME*) between experimental and theoretical data of  $f(\alpha)/f(\alpha_r)$  for various mechanisms for the thermal degradation of PLA for bioblends containing from 50% to 90% PLA.

Mechanism	<i>IME</i> (%)				
	90/10	80/20	70/30	60/40	50/50
n-order	28.7 ± 0.7	22.9 ± 0.6	7.9 ± 0.2	7.8 ± 0.2	21.1 ± 0.5
Autocatalytic	20.3 ± 0.6	17.7 ± 0.4	7.1 ± 0.2	7.0 ± 0.2	40.1 ± 0.5
Random scission	5.5 ± 0.2	6.0 ± 0.2	6.2 ± 0.2	6.2 ± 0.2	6.7 ± 0.3
F1	20.3 ± 0.5	18.1 ± 0.4	7.2 ± 0.2	7.6 ± 0.3	25.7 ± 0.4
R1	37.2 ± 0.8	28.1 ± 0.6	11.1 ± 0.3	9.4 ± 0.3	19.5 ± 0.4
D1	87.8 ± 0.9	57.5 ± 0.8	14.5 ± 0.3	17.3 ± 0.4	27.3 ± 0.5
F2	5.8 ± 0.3	6.8 ± 0.2	8.9 ± 0.3	9.0 ± 0.3	25.7 ± 0.5

Table 4. Cont.

Mechanism	IME (%)				
	90/10	80/20	70/30	60/40	50/50
R2	29.5 ± 0.6	23.4 ± 0.5	8.9 ± 0.3	7.8 ± 0.2	20.9 ± 0.4
D2	81.3 ± 0.9	54.0 ± 0.7	11.0 ± 0.3	17.1 ± 0.4	28.7 ± 0.6
F3	40.3 ± 0.7	12.2 ± 0.4	15.7 ± 0.4	12.3 ± 0.3	28.0 ± 0.7
R3	26.7 ± 0.5	21.7 ± 0.4	8.6 ± 0.3	8.0 ± 0.3	21.4 ± 0.6
D3	71.1 ± 0.7	48.9 ± 0.8	10.8 ± 0.3	17.0 ± 0.4	30.0 ± 0.7

The activation energy values of the thermal decomposition of PLA, through a random scission mechanism, are those shown in Figure 7. These results indicate that the activation energy increases when the PA content increases because of the protecting effect of PA on the PLA matrix (especially for a PA content up to 30%). Indeed, the activation energy increased by 16 kJ/mol when the PA content increased from 10% to 20%, and it increased by 34 kJ/mol when the PA content increased from 20% to 30%. The activation energy remained almost constant when the PA content increased from 30% to 40%. Contrarily, an activation energy decrease of 25 kJ/mol was observed when the PA content increased from 40% to 50%; the latter was likely due to an inversion of phases caused by the high PA content.

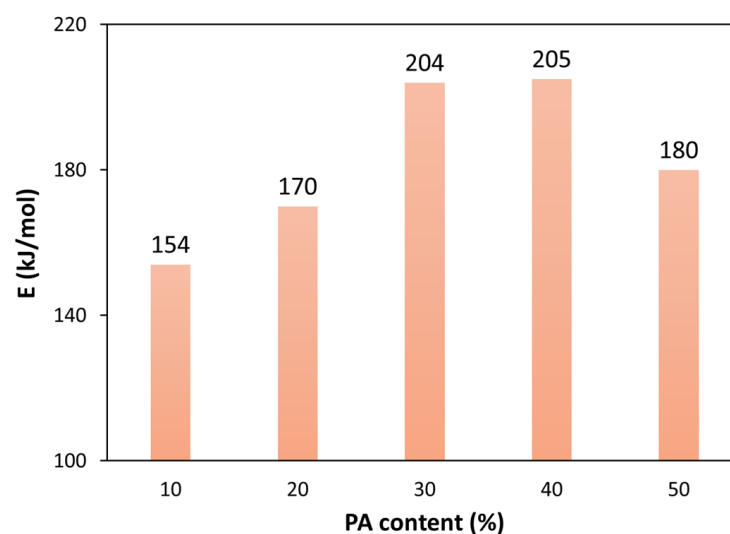


Figure 7. Activation energy values of the thermal decomposition of PLA through a random scission mechanism: the influence of PA content.

In a previous work dealing with the morphology of PLA/PA bioblends, Cailloux et al. [39] stated that both droplet and elongated PA domains coexisted when the PA content was 30%. The morphology transition to co-continuous was completed when the PA content was further increased to 40%. Therefore, the bioblend morphology clearly has a protective effect against the thermal decomposition of PLA within the bioblend. Moreover, a decrease in the stiffness and strength and an increase in the strain were reported with an increasing PA content. On the other hand, diffusion mechanisms led to the highest IME values (27–88%), which are unacceptable. This is later corroborated by means of standardized conversion function plots and  $y(\alpha)$  master plots.

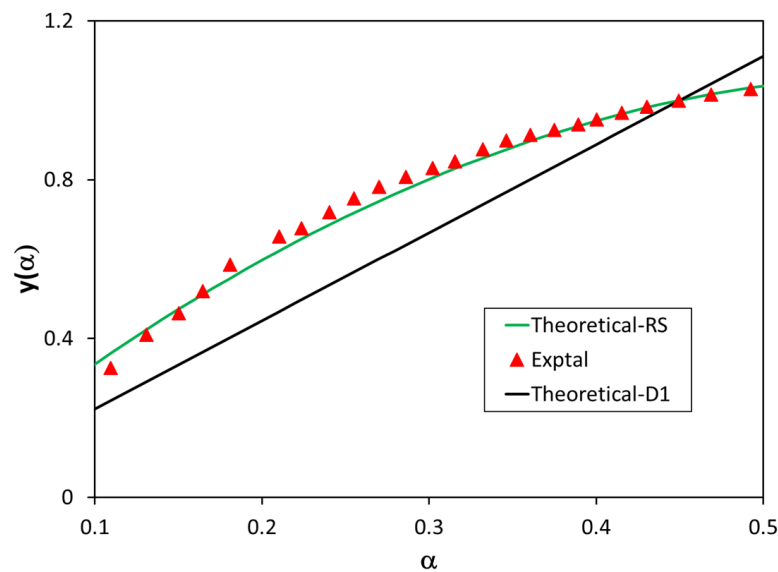
In order to check the validity of the activation energy values obtained for the thermal degradation of PLA,  $y(\alpha)$  master plots, as proposed by Criado et al. [40], were used:

$$y(\alpha)_{\text{exptal}} = \left( \frac{T}{T_r} \right)^2 \frac{(d\alpha/dT)}{(d\alpha/dT)_r} \quad (7)$$



$$y(\alpha)_{theor} = \frac{f(\alpha) g(\alpha)}{f(\alpha_r) g(\alpha_r)} \tag{8}$$

These master plots are very interesting because experimental data are not dependent on activation energy values. Figure 8 shows  $y(\alpha)$  master plots for the thermal degradation of PLA for the bioblend containing 90% PLA. These findings corroborate the previously reported results, i.e., the best reaction mechanism for the thermal degradation of PLA is random scission, whereas D1 and F2 mechanisms showed poor fitting between experimental and theoretical data. The rest of the mechanisms also provided poor fitting. In conclusion, the best mechanism is that of random scission of macromolecular chains, as confirmed through three different pieces of evidence: the standardized conversion functions, *IME* values, and  $y(\alpha)$  master plots.

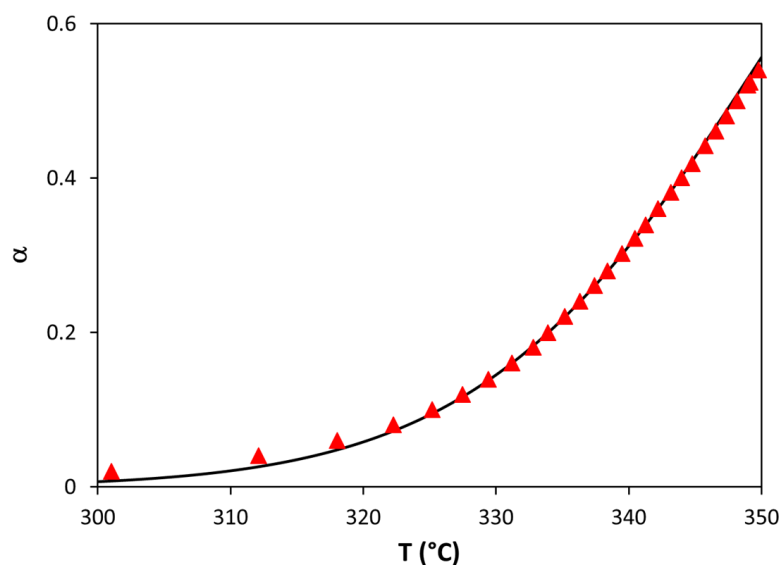


**Figure 8.** Comparison between experimental and theoretical values of  $y(\alpha)$  master plots for random scission (RS) and D1 mechanisms for the bioblend containing 90% PLA.

The variation in conversion with temperature for the thermal degradation of PLA, through a random scission mechanism, is evaluated as follows:

$$\alpha = \left[ 1 - \exp \left[ -\frac{A R T^2}{\beta E} \left( 1 - \frac{2RT}{E} \right) \exp \left( -\frac{E}{RT} \right) \right] \right]^2 \tag{9}$$

Figure 9 shows the variation in conversion with temperature when the random scission mechanism was considered for the bioblend containing 90% PLA. The fitting between the experimental and theoretical data was excellent, thus confirming that random scission is the best mechanism with which to explain the thermal degradation of PLA in PLA/PA bioblends.



**Figure 9.** Comparison between experimental and random scission theoretical values of conversion for the thermal degradation of PLA in the bioblend containing 90% PLA.

## 5. Conclusions

The thermal stability and potential degradation mechanisms of PLA in PLA/bio-based PA 10.10 were analyzed. In this case, a matrix of a rheologically modified PLA from reactive extrusion was employed, with the addition of 10–50% of bio-based PA as a second phase. PLA/PA bioblends (with a predominantly bio-sourced PA10.10) containing 10–50% PA were prepared by melt blending in order to overcome the extreme brittleness of PLA.

The temperature at which 5% of the mass was lost ( $T_5$ ) increased from 315 to 321 °C when the PA content increased from 10% to 50% (at a nominal heating rate of 10 K/min). On the other hand, the temperature at which 95% of the mass was lost ( $T_{95}$ ) varied erratically in the range 455–540 °C. Similar conclusions were obtained at the other heating rates employed in this study.

The general analytical equation (GAE) was used in order to evaluate the kinetic parameters of the thermal degradation of PLA (at conversions lower than 0.4). Various empirical and theoretical solid-state mechanisms were tested to elucidate the best kinetic model: n-order, autocatalytic, random scission, F1, F2, F3, R1, R2, R3, D1, D2, and D3. Three different methodologies were used for this: the standardized conversion functions, *IME* (integral mean error) indexes, and  $y(\alpha)$  master plots, which revealed that the most probable mechanism for the thermal degradation of PLA was random scission of the macromolecular chains. The activation energies obtained were 154, 170, 204, 205, and 180 kJ/mol for the bioblends containing 10%, 20%, 30%, 40%, and 50% PA. These results indicate that the activation energy increases when the PA content increases because of the protecting effect of PA on the PLA matrix (especially for PA contents up to 30%). Indeed, the activation energy increased by 16 kJ/mol when the PA content increased from 10% to 20%, and it increased by 34 kJ/mol when the PA content increased from 20% to 30%. The activation energy remained almost constant when the PA content increased from 30% to 40%. Contrarily, an activation energy decrease of 25 kJ/mol was observed when the PA content increased from 40% to 50%; the latter was likely due to an inversion of phases caused by the high PA content. Therefore, the bioblend containing 30% PLA exhibited an excellent thermal resistance against degradation. This result is in accordance with previous rheological and morphological analyses.

**Author Contributions:** Conceptualization, F.C.; methodology, F.C. and M.L.M.; formal analysis, F.C. and O.S.P.; investigation, F.C., O.S.P. and M.L.M.; writing—original draft preparation, F.C.; writing—reviewed editing, F.C.; project administration, M.L.M.; funding acquisition, M.L.M. and O.S.P. All authors have read and agreed to the published version of the manuscript.

**Funding:** This research was funded by the Ministry of Science and Innovation of the Spanish Government, grant number PID2019-106518RB-I00.

**Conflicts of Interest:** The authors declare no conflict of interest. The funders had no role in the design of the study; in the collection, analyses, or interpretation of data; in the writing of the manuscript, or in the decision to publish the results.

## Nomenclature

$A$	frequency factor ( $s^{-1}$ )
$E$	activation energy (J/mol)
$f(\alpha)$	conversion function (adimensional)
$k$	kinetic constant ( $s^{-1}$ )
$R$	gas constant (J/mol·K)
$t$	time (s)
$T$	temperature (K)
$w$	residual weight (%)
$y(\alpha)$	master plot as a function of conversion
Greek letters	
$\alpha$	conversion (adimensional)
$\beta$	linear heating rate (K/s)

## References

- Nakajima, H.; Dijkstra, P.; Loos, K. The recent developments in biobased polymers toward general and engineering applications: Polymers that are upgraded from biodegradable polymers, analogous to petroleum-derived polymers, and newly developed. *Polymers* **2017**, *9*, 523. [\[CrossRef\]](#)
- Vadori, R.; Misra, M.; Mohanty, A.K. Sustainable biobased blends from the reactive extrusion of polylactide and acrylonitrile butadiene styrene. *J. Appl. Polym. Sci.* **2016**, *133*, 4377. [\[CrossRef\]](#)
- Siracusa, V.; Rocculi, P.; Romani, S.; Rosa, M.D. Biodegradable polymers for food packaging: A review. *Trends Food Sci. Technol.* **2008**, *19*, 634–643. [\[CrossRef\]](#)
- Garlotta, D. A Literature Review of Poly(Lactic Acid). *J. Polym. Environ.* **2001**, *9*, 63–84. [\[CrossRef\]](#)
- Auras, R.; Harte, B.; Selke, S. An overview of polylactides as packaging materials. *Macromol. Biosci.* **2004**, *4*, 835–864. [\[CrossRef\]](#)
- Zeng, J.B.; Li, K.A.; Du, A.K. Compatibilization strategies in poly(lactic acid)-based blends. *RSC Adv.* **2015**, *5*, 32546–32565. [\[CrossRef\]](#)
- García-Masabet, V.; Santana Pérez, O.; Cailloux, J.; Abt, T.; Sánchez-Soto, M.; Carrasco, F.; MasPOCH, M.L. PLA/PA bio-blends: Induced morphology by extrusion. *Polymers* **2020**, *12*, 10. [\[CrossRef\]](#)
- Anderson, K.S.; Schreck, K.M.; Hillmyer, M.A. Toughening polylactide. *Polym. Rev.* **2008**, *48*, 85–108. [\[CrossRef\]](#)
- Babu, R.P.; O'Connor, K.; Seeram, R. Current progress on bio-based polymers and their future trends. *Prog. Biomater.* **2013**, *2*, 8. [\[CrossRef\]](#)
- Silva, A.P.B.; Montagna, L.S.; Passador, F.R.; Rezende, M.C.; Lemes, A.P. Biodegradable nanocomposites based on PLA/PHBV blend reinforced with carbon nanotubes with potential for electrical and electromagnetic applications. *Express Polym. Lett.* **2021**, *15*, 987–1003. [\[CrossRef\]](#)
- Hamad, K.; Kaseem, M.; Ayyoob, M.; Joo, J.; Deri, F. Polylactic acid blends: The future of green, light and tough. *Progr. Polym. Sci.* **2018**, *85*, 83–127. [\[CrossRef\]](#)
- Spinella, S.; Cai, J.; Samuel, C.; Zhu, J.; McCallum, S.A.; Habibi, Y.; Raquez, J.M.; Dubois, P.; Gross, R.A. Polylactide/poly( $\omega$ -hydroxytetradecanoic acid) reactive blending: A green renewable approach to improving polylactide properties. *Biomacromolecules* **2015**, *16*, 1818–1826. [\[CrossRef\]](#)
- Kakroodi, A.R.; Kazemi, Y.; Ding, W.; Ameli, A.; Park, C.B. Poly(lactic acid)-based in situ microfibrillar composites with enhanced crystallization kinetics, mechanical properties, rheological behavior, and foaming ability. *Biomacromolecules* **2015**, *16*, 3925–3935. [\[CrossRef\]](#)
- Pai, F.C.; Lai, S.M.; Chu, H.H. Characterization and properties of reactive poly(lactic acid)/polyamide 610 biomass blends. *J. Appl. Polym. Sci.* **2013**, *130*, 2563–2571. [\[CrossRef\]](#)
- Stoclet, G.; Seguela, R.; Lefebvre, J.M. Morphology, thermal behavior and mechanical properties of binary blends of compatible biosourced polymers: Polylactide/polyamide-11. *Polymer* **2011**, *52*, 1417–1425. [\[CrossRef\]](#)

16. Rashmi, B.J.; Prashantha, K.; Lacrampe, M.F.; Krawczak, P. Toughening of poly(lactic acid) without sacrificing stiffness and strength by melt-blending with polyamide-11 and selective localization of halloysite nanotubes. *Express Polym. Lett.* **2015**, *9*, 721–735. [[CrossRef](#)]
17. Nuzzo, A.; Coiai, S.; Carroccio, S.C.; Dintcheva, N.T.; Gambarotti, C.; Filippone, G. Heat-resistant fully biobased nanocomposite blends based on poly(lactic acid). *Macromol. Mater. Eng.* **2014**, *299*, 31–40. [[CrossRef](#)]
18. Patel, R.; Ruehle, D.A.; Dorgan, J.R.; Halley, P.; Martin, D. Biorenewable blends of polyamide-11 and polylactide. *Polym. Eng. Sci.* **2014**, *54*, 1523–1532. [[CrossRef](#)]
19. Palacios, J.K.; Sangroniz, A.; Eguiazabal, J.I.; Etxeberria, A.; Muller, A.J. Tailoring the properties of PP/PA6 nano-structured blends by the addition of nanosilica and compatibilizer agents. *Eur. Polym. J.* **2016**, *85*, 532–552. [[CrossRef](#)]
20. Keridou, I.; Cailloux, J.; Martínez, J.C.; Santana, O.; Maspoch, M.L.; Puiggali, J.; Franco, L. Biphasic polylactide/polyamide 6,10 blends: Influence of composition on polyamide structure and polyester crystallization. *Polymer* **2020**, *202*, 122676. [[CrossRef](#)]
21. Walha, F.; Lamnawar, K.; Maazouz, A.; Jaziri, M. Rheological, morphological and mechanical studies of sustainably sourced polymer blends based on poly(lactic acid) and polyamide 11. *Polymers* **2016**, *8*, 61. [[CrossRef](#)]
22. Yu, H.; Huang, N.; Wang, C.; Tang, Z. Modeling of poly(L-lactide) thermal degradation: Theoretical prediction of molecular weight and polydispersity index. *J. Appl. Polym. Sci.* **2003**, *11*, 2557–2562. [[CrossRef](#)]
23. Antunes, A.; Luyt, A.S.; Kasak, P.; Aljarod, O.; Hassan, M.K.; Popelka, A. Effect of plasma treatment on accelerated PLA degradation. *Express Polym. Lett.* **2021**, *15*, 725–743. [[CrossRef](#)]
24. Carrasco, F.; Pagès, P. Thermogravimetric analysis of polystyrene: Influence of sample weight and heating rate on thermal and kinetic parameters. *J. Appl. Polym. Sci.* **1996**, *61*, 187–197. [[CrossRef](#)]
25. Bianchi, O.; Martins, J.D.; Florio, R.; Oliveira, R.V.B. Changes in activation energy and kinetic mechanism during EVA crosslinking. *Polym. Test.* **2011**, *30*, 616–624. [[CrossRef](#)]
26. Paik, P.; Kar, K.K. Thermal degradation kinetics and estimation of lifetime of polyethylene particles: Effects of particle size. *Mater. Chem. Phys.* **2009**, *113*, 953–961. [[CrossRef](#)]
27. Carrasco, F.; Pagès, P. Thermal degradation and stability of epoxy nanocomposites: Influence of montmorillonite content and cure temperature. *Polym. Degrad. Stab.* **2008**, *93*, 1000–1007. [[CrossRef](#)]
28. Pérez-Maqueda, L.A.; Criado, J.M.; Sánchez-Jiménez, P.E. Combined kinetic analysis of solid-state reactions: A powerful tool for the simultaneous determination of kinetic parameters and the kinetic model without previous assumptions on the reaction mechanism. *J. Phys. Chem. A* **2006**, *110*, 12456–12462. [[CrossRef](#)]
29. Carrasco, F.; Pagès, P.; Gámez-Pérez, J.; Santana, O.O.; Maspoch, M.L. Processing of poly(lactic acid): Characterization of chemical structure, thermal stability and mechanical properties. *Polym. Degrad. Stab.* **2010**, *95*, 116–125. [[CrossRef](#)]
30. Velázquez-Infante, J.C.; Gámez-Pérez, J.; Franco-Urquiza, E.A.; Santana, O.O.; Carrasco, F.; Maspoch, M.L. Effect of the unidirectional drawing on the thermal and mechanical properties of PLA film with different L-isomer content. *J. Appl. Polym. Sci.* **2013**, *127*, 2661–2669. [[CrossRef](#)]
31. Vyazovkin, S.; Sbirrazzuoli, N. Isoconversional Kinetic Analysis of Thermally Stimulated Processes in Polymers. *Macromol. Rapid Commun.* **2006**, *27*, 1515–1532. [[CrossRef](#)]
32. Cañavate, J.; Pagès, P.; Saurina, J.; Colom, X.; Carrasco, F. Determination of small interactions in polymer composites by means of FTIR and DSC. *Polym. Bull.* **2000**, *44*, 293–300. [[CrossRef](#)]
33. Sánchez-Jiménez, P.E.; Pérez-Maqueda, L.A.; Perejón, A.; Criado, J.M. Combined kinetic analysis of thermal degradation of polymeric materials under any thermal pathway. *Polym. Degrad. Stab.* **2009**, *94*, 2079–2085. [[CrossRef](#)]
34. Pérez-Maqueda, L.A.; Sánchez-Jiménez, P.E.; Perejón, A.; García-Garrido, C.; Criado, J.M.; Benítez-Guerrero, M. Scission kinetic model for the prediction of polymer pyrolysis curves from chain structure. *Polym. Test.* **2014**, *37*, 1–5. [[CrossRef](#)]
35. Carrasco, F. The evaluation of kinetic parameters from thermogravimetric data: Comparison between established methods and the general analytical equation. *Thermochim. Acta* **1993**, *213*, 115–134. [[CrossRef](#)]
36. Carrasco, F.; Pérez-Maqueda, L.A.; Sánchez-Jiménez, P.E.; Perejón, A.; Santana, O.O.; Maspoch, M.L. Enhanced general analytical equation for the kinetics of the thermal degradation of poly(lactic acid) driven by random scission. *Polym. Test.* **2013**, *32*, 937–945. [[CrossRef](#)]
37. Vyazovkin, S.; Burnham, A.K.; Criado, J.M.; Pérez-Maqueda, L.A.; Popescu, C.; Sbirrazzuoli, N. ICTAC Kinetics Committee recommendations for performing kinetic computations on thermal analysis data. *Thermochim. Acta* **2011**, *520*, 1–19. [[CrossRef](#)]
38. Carrasco, F.; Santana, O.; Cailloux, J.; Maspoch, M.L. Kinetics of the thermal degradation of poly(lactic acid) obtained by reactive extrusion: Influence of the addition of montmorillonite nanoparticles. *Polym. Test.* **2015**, *48*, 69–81. [[CrossRef](#)]
39. Cailloux, J.; Abt, T.; García-Masabet, V.; Santana, O.; Sánchez-Soto, M.; Carrasco, F.; Maspoch, M.L. Effect of the viscosity ratio on the PLA/PA 10.10 bioblends morphology and mechanical properties. *Express Polym. Lett.* **2018**, *12*, 569–582. [[CrossRef](#)]
40. Criado, J.M.; Málek, J.; Ortega, A. Applicability of the master plots in kinetic analysis of non-isothermal data. *Thermochim. Acta* **1989**, *147*, 377–385. [[CrossRef](#)]



## Article

# Poly(L-lactic acid) Reinforced with Hydroxyapatite and Tungsten Disulfide Nanotubes

Ofek Golan <sup>1,2</sup>, Hila Shalom <sup>2</sup>, Ifat Kaplan-Ashiri <sup>3</sup>, Sidney R. Cohen <sup>3</sup>, Yishay Feldman <sup>3</sup>, Iddo Pinkas <sup>3</sup>, Rakefet Ofek Almog <sup>1</sup>, Alla Zak <sup>4</sup> and Reshef Tenne <sup>2,\*</sup>

<sup>1</sup> Department of Materials Engineering, Azrieli College of Engineering, Jerusalem 9103501, Israel; ofekgo1994@gmail.com (O.G.); rakefetof@jce.ac.il (R.O.A.)

<sup>2</sup> Department of Molecular Chemistry and Materials Science, Weizmann Institute, Rehovot 76100, Israel; hilasha4@gmail.com

<sup>3</sup> Chemical Research Support Department, Weizmann Institute, Rehovot 76100, Israel; ifat.kaplan-ashiri@weizmann.ac.il (I.K.-A.); Sidney.Cohen@weizmann.ac.il (S.R.C.); Isai.Feldman@weizmann.ac.il (Y.F.); iddo.pinkas@weizmann.ac.il (I.P.)

<sup>4</sup> Department of Sciences, Holon Institute of Technology, Holon 58102, Israel; alzak@hit.ac.il

\* Correspondence: reshef.tenne@weizmann.ac.il; Tel.: +972-8-9342394

**Abstract:** Poly(L-lactic acid) (PLLA) is a biocompatible, biodegradable, and semi-crystalline polymer with numerous applications including food packaging, medical implants, stents, tissue engineering scaffolds, etc. Hydroxyapatite (HA) is the major component of natural bone. Conceptually, combining PLLA and HA could produce a bioceramic suitable for implants and bone repair. However, this nanocomposite suffers from poor mechanical behavior under tensile strain. In this study, films of PLLA and HA were prepared with small amounts of nontoxic WS<sub>2</sub> nanotubes (INT-WS<sub>2</sub>). The structural aspects of the films were investigated via electron microscopy, X-ray diffraction, Raman microscopy, and infrared absorption spectroscopy. The mechanical properties were evaluated via tensile measurements, micro-hardness tests, and nanoindentation. The thermal properties were investigated via differential scanning calorimetry. The composite films exhibited improved mechanical and thermal properties compared to the films prepared from the PLLA and HA alone, which is advantageous for medical applications.

**Keywords:** PLLA; hydroxyapatite; WS<sub>2</sub> nanotubes; biodegradable polymers; mechanical properties

**Citation:** Golan, O.; Shalom, H.; Kaplan-Ashiri, I.; Cohen, S.R.; Feldman, Y.; Pinkas, I.; Ofek Almog, R.; Zak, A.; Tenne, R. Poly(L-lactic acid) Reinforced with Hydroxyapatite and Tungsten Disulfide Nanotubes. *Polymers* **2021**, *13*, 3851. <https://doi.org/10.3390/polym13213851>

Academic Editor: José Miguel Ferri

Received: 18 August 2021

Accepted: 4 November 2021

Published: 8 November 2021

**Publisher's Note:** MDPI stays neutral with regard to jurisdictional claims in published maps and institutional affiliations.



**Copyright:** © 2021 by the authors. Licensee MDPI, Basel, Switzerland. This article is an open access article distributed under the terms and conditions of the Creative Commons Attribution (CC BY) license (<https://creativecommons.org/licenses/by/4.0/>).

## 1. Introduction

Poly(L-lactic acid) (PLLA) is a biocompatible, degradable, and semi-crystalline polymer. It is one of the most investigated polymers for biodegradable/biocompatible applications including food packaging [1–3], medical implants [4–7], tissue engineering scaffolds [8,9], and many more [10]. PLLA can be processed by various techniques, including extrusion, solvent casting, 3D printing, electrospinning, etc. [11]. Hydroxyapatite (Ca<sub>10</sub>(PO<sub>4</sub>)<sub>6</sub>(OH))<sub>2</sub> is the major component of natural bone [12]. Hydroxyapatite (HA) has many stoichiometric phases, called calcium phosphate phases, with Ca/P ratios varying between 1.67 and 1.5 [13]. All the calcium phosphate nonstoichiometric phases are biocompatible, induce bone repair by osteoconductivity and osteoinductivity, and, furthermore, exhibit good mechanical properties. Despite these attributes, their major disadvantage for medical applications is their brittleness [14]. Incorporated hydroxyapatite in the PLLA matrix can improve the flexibility of the bioceramic HA and consequently, produce biodegradable ceramic-polymer composites, which can be an alternative to the traditional materials used for implants or bone repair and for tissue engineering. However, both PLLA and HA and their composites suffer from low toughness, which limits their application in the human body [15,16]. Reinforcing the PLLA/HA composite with nanotubes of WS<sub>2</sub> (INT-WS<sub>2</sub>) can remedy this disadvantage [6,17,18]. The INT-WS<sub>2</sub> are

multiwall nanostructures 1–20  $\mu\text{m}$  long with diameters of 30–150 nm (aspect ratios of 50–100 and even larger). They are nontoxic [19–22] with very good mechanical properties (Young's modulus 150–170 GPa, bending modulus of 217 GPa, tensile strength between 10 and 22 GPa, and strain  $\epsilon > 10\%$ ) [23]. Thus, by classical polymer reinforcement concepts, they would be expected to enhance the mechanical behavior of polymer composites under optimal conditions. However, the interface between polymer and filler is in fact a critical factor in determining the ultimate composite strength [24]. This is particularly relevant for nanocomposites. For carbon nanotubes, the effects of aspect ratio and interfacial strength have been thoroughly studied [25]. Such bonding is a mixed bag—strong bonding leads to strong, but brittle composites, while weak bonds can produce a weaker but tougher composite [17]. Nonetheless, it has been shown that structurally-modified fibers can enhance both strength and toughness [26].

Interfacial properties can be enhanced by appropriate chemical modifications: INT-WS<sub>2</sub> can also be readily functionalized [27,28] and dispersed in organic solvents, polymers, epoxy resins, etc. [29–32]. HA does not disperse well in the PLLA matrix and tends to agglomerate as secondary particles a few micrometers in size. This is because HA is hydrophilic, while the organic solvents used to dissolve the polymers are mostly hydrophobic [33]. However, oleic acid (OA) is an amphiphilic surfactant, used to mediate the interaction between the HA (hydrophilic ceramic) and a hydrophobic polymer, like PLLA [34]. Therefore, OA induces a homogeneous dispersion of the HA in the PLLA matrix. Previous studies conducted on PLLA/HA/INT-WS<sub>2</sub> nanocomposites indicated their potential for medical applications [35–38].

This report focuses on the preparation and characterization of PLLA/HA bioceramic films reinforced by small amounts of INT-WS<sub>2</sub>. The nanocomposite was prepared via solvent casting using OA as a dispersant. The nanocomposite morphology was investigated by high-resolution scanning electron microscopy (HR-SEM). The structural aspects were investigated by X-ray diffraction (XRD), micro-Raman spectroscopy, and Fourier transform infrared spectroscopy (FTIR). Their mechanical properties were determined by tensile testing, micro-hardness, nanomechanical testing, and their thermal properties by differential scanning calorimetry (DSC).

## 2. Materials and Methods

### 2.1. Materials

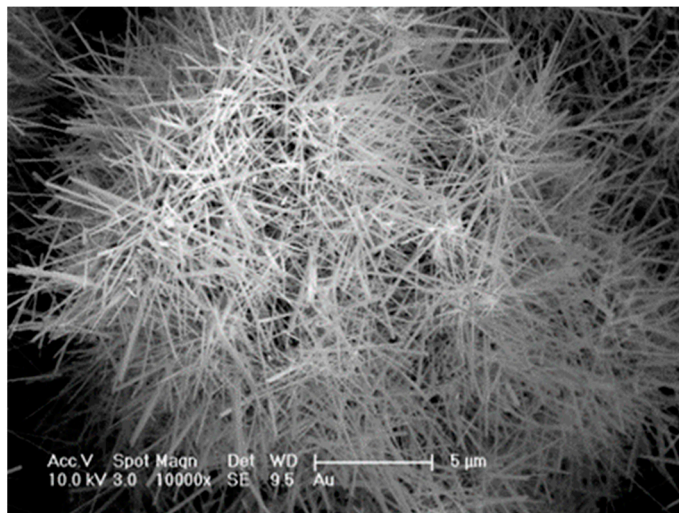
Poly L-lactic acid (PLLA) with an inherent viscosity midpoint of 2.4 dL/g was purchased from Corbion (Gorinchem, The Netherlands). Oleic acid (OA,  $\geq 99\%$ ) and Hydroxyapatite (HA, nanopowder,  $< 200$  nm particle size (BET),  $\geq 97\%$ , synthetic) were purchased from Sigma Aldrich Chemical Company (St. Louis, MO, USA).

INT-WS<sub>2</sub> with diameters between 30 and 150 nm and lengths between 1 and 20 micrometers were synthesized using a published procedure [39]. Briefly, the precursor nanoparticles of tungsten trioxide, grow into high aspect ratio tungsten suboxide nanowhiskers under a mild reducing atmosphere at 840 °C. Subsequent sulfurization of the nanowhiskers results in hollow WS<sub>2</sub> nanotubes. A representative SEM image of the typical INT-WS<sub>2</sub> is shown in Figure 1.

The PLLA/HA/INT films were prepared by the solvent casting method according to the following procedure.

- PLLA neat films: 0.75 g of PLLA powder was dissolved in 20 mL chloroform and mechanically mixed. Subsequently, the solution was poured onto a Teflon plate for drying in the hood with an aluminum foil cover punctuated with 10 holes.
- PLLA films with 40 wt% hydroxyapatite: 0.75 g of PLLA powder was dissolved in 15 mL chloroform; 300 mg of hydroxyapatite nanoparticles were mixed with 5 mL chloroform and 150  $\mu\text{L}$  oleic acid for 30 min. The two solutions were mixed together using a magnetic stirrer for 5 min before pouring onto a Teflon plate and were then dried in the hood using an aluminum foil cover punctuated with 10 holes.

- PLLA films with 0.5 wt% INT-WS<sub>2</sub>: first, 3.8 mg INT-WS<sub>2</sub> powder was dispersed in 5 mL ethanol for 3 min and vacuum annealed for 1.5 h at 80 °C. Next, 0.75 g of PLLA powder was dissolved in 15 mL chloroform and mechanically mixed for 5 h; then the annealed INT-WS<sub>2</sub> were dispersed in 5 mL chloroform for 3 min. Finally, the two solutions were mixed together using a magnetic stirrer for 5 min before pouring onto a Teflon plate for drying in the hood with an aluminum foil cover punctuated with 10 holes.
- PLLA films with 40 wt% hydroxyapatite and 0.25, 0.5, and 0.75 wt% INT-WS<sub>2</sub>: first, 1.9, 3.8, or 5.6 mg of INT-WS<sub>2</sub> powder were dispersed in 5 mL ethanol for 3 min and vacuum annealed for 1.5 h at 80 °C. Next, 0.75 g PLLA powder was dissolved in 10 mL chloroform, while 300 mg of hydroxyapatite nanoparticles were dispersed in 5 mL chloroform and 150 µL oleic acid for 30 min. Afterward, the annealed INT-WS<sub>2</sub> were dispersed in 5 mL chloroform for 3 min. Finally, the three solutions were mixed together using a magnetic stirrer for 5 min before pouring onto a Teflon plate for drying in the hood with an aluminum foil cover punctuated with 10 holes.



**Figure 1.** SEM view of an assortment of WS<sub>2</sub> nanotubes.

The dried samples were vacuum annealed for 5 days at 45 °C [36]. The thickness of the films was determined by caliper and was, on average, 80 µm for pure PLLA; 113 µm for PLLA+HA; 93 µm for PLLA+HA+INT. The densification of the films upon the addition of the nanotubes is attributed to the alignment of the polymer molecules along the nanotube surface. The texturing of the polymer molecules is indirect evidence of the non-specific but nevertheless strong nanotube–polymer interfacial interaction and explains the mechanical reinforcement of the PLLA by the INT (see below).

## 2.2. Characterization Techniques

### 2.2.1. X-ray Diffraction

X-ray diffraction (XRD) was performed for various nanocomposite films in reflection geometry using Rigaku (Tokyo, Japan) theta-theta diffractometers: an Ultima III equipped with a sealed cooper anode tube operating at 40 kV/40 mA and a TTRAX III equipped with a rotating copper anode X-ray tube operating at 50 kV/200 mA. A scintillation detector was aligned at the diffracted beam after a bent Graphite monochromator, which was used for X-ray cleaning, effectively removing K<sub>β</sub>. 2θ/θ scans were carried out at specular conditions in Bragg–Brentano mode with variable slits with a step size of 0.025° and a scan speed of 0.5 degrees per minute. Quantitative phase analysis, degree of crystallinity, and crystallite size (coherent scattering length) estimations were made using the Pawley-based [40] Whole Pattern Fitting (WPF) module in the Jade Pro software (Materials Data, Inc., Livermore, CA, USA) and PDF-4+ 2020 database (ICDD). According to the Pawley



method, the structural data for each component of the nanocomposite film is fitted to the measured XRD pattern by non-linear least-squares optimization at each diffraction point. The modeling parameters include instrumental zero error, the intensity of each reflection with indices ( $hkl$ ), profile parameters, and lattice constants. The crystallite sizes were also estimated according to the Scherrer formula.

#### 2.2.2. High-Resolution Scanning Electron Microscopy (HR-SEM)

For HR-SEM, cross-sections of the samples were prepared by breaking the film, which was first immersed in liquid nitrogen for ten minutes for hardening. The composite samples were mounted on aluminum stubs using two-sided carbon tape. Scanning electron microscope (SEM) images were acquired using the Ultra 55 (Zeiss, Oberkochen, Germany). at 8 kV and 30  $\mu\text{m}$  aperture, in both secondary electron (SE) and backscattering electron (BSE) modes. SEM imaging was followed by the acquisition of energy-dispersive X-ray spectroscopy (EDS) hypermaps with a four-quadrant retractable detector mounted above the sample (QUANTAX FlatQUAD EDS, Bruker, Billerica, MA, USA). The normalized X-ray intensity maps of the following element lines were produced from the EDS data: C-K $\alpha$ , O-K $\alpha$ , S-K $\alpha$ , P-K $\alpha$ , Ca-K $\alpha$ , and W-M. In order to avoid sample charging that could alter the effective potential on the sample surface and therefore influence the EDS measurements, the samples were coated with a conductive carbon film, 5 nm thick using the CCU-010 HV coater (Safematic, Zizers, Switzerland), prior to the EDS analysis. The EDS signals were acquired at 8 kV. This energy was set according to the highest-energy X-ray line that was measured, in this case, Ca-K $\alpha$  (3.69 keV). For successful EDS measurements, the acceleration voltage should be set to 1.5–3 times the highest measured-energy line.

#### 2.2.3. Tensile Testing

The mechanical properties of the films under tension were measured by performing tensile tests, using an Instron-5965 (Instron, Norwood, MA, USA) equipped with a 5 kN load cell at room temperature and a stretching speed of 1 mm/min. The samples were cut into strips 5 mm wide and 50 mm long. The gauge length of the tested strip was 30 mm. Three specimens were tested for each type of sample, and the results were given as average values and standard deviation. The load and displacement were recorded by dedicated software provided by the manufacturer (Bluehill3, Norwood, MA, USA). The significance of the differences between samples was evaluated using a 2-tailed *T*-test.

#### 2.2.4. Micro-Hardness Test

Micro Vickers hardness test was performed using HMV-G21 ST (Shimadzu, Tokyo, Japan). A load of HV 0.025 (0.2452 N) was applied to the sample and held for 10 s before release. Prior to the measurement, each sample was rubbed 5 times on a silicon-carbide (SiC) paper (1200 grit). Five indentation tests were performed for each type of sample, and the results were given as average values and standard deviation.

#### 2.2.5. Nanomechanical Testing

Nanoindentation was performed on a XP Nanoindenter (KLA-Tencor, Milpitas, CA, USA), using a 10  $\mu\text{m}$  diameter spherical diamond indenter tip. The area function of this probe was calibrated on a sample of poly (methyl methacrylate), with Young's modulus of 2.9 GPa. The samples (approximately 100 micrometers thick) were attached to the stub with a very thin layer of epoxy. Indentations were performed to a depth of 1200 nm at a constant strain rate of 0.1  $\text{s}^{-1}$ , using continuous stiffness measurement (CSM) [41]. In this method, a small (2 nm) oscillation is superimposed on the loading ramp, which allows continuous measurement of Oliver and Pharr modulus and hardness with depth [42]. The reported measurements represent average CSM values between 400 and 800 nm depth, over which the traces have levelled out to a constant value. Sets of 8 indentations were made at 2–3 different positions on the sample, and indentations for which the curve did not level out by 400 nm depth were discarded.

### 2.2.6. Differential Scanning Calorimeter (DSC)

DSC Q200 (TA Instruments, New Castle, DE, USA) was used for the analysis of the thermal properties of the samples and their degree of crystallinity. The samples were placed in an aluminum pan and heated from 30 °C to 200 °C; the temperature 200 °C was held for 3 min then lowered back to 30 °C at a rate of 10 °C/min and held for 3 min. This cycle was performed in order to erase the thermal history. In the second series of measurements, the temperature was raised to 200 °C, held for 3 min and lowered back to 30 °C. Here the temperature scan was performed at a rate of 10 °C/min and under a 50 mL/min nitrogen flow rate. From the midpoint of the (heating scan) thermograms, the glass transition ( $T_g$ ), cold crystallization ( $T_{cc}$ ), and melting ( $T_m$ ) temperatures were determined. The crystallization temperature ( $T_c$ ) was determined from the cooling scan. The degree of crystallinity was calculated from the DSC curves in two ways:

$$X_c = \frac{(\Delta H_m - \Delta H_{cc})}{\Delta H_m^{\circ}} \times 100\% \quad (1)$$

for heating [43,44], and

$$(1 - \lambda) = \frac{\Delta H_c}{\Delta H_m^{\circ}} \quad (2)$$

for cooling [45].

$\Delta H_m$ ,  $\Delta H_{cc}$  (heating), and  $\Delta H_c$  (cooling) are the melting enthalpy, cold crystallization enthalpy, and crystallization enthalpy (J/g), respectively;  $\Delta H_m^{\circ}$  is the heat of fusion for completely crystallized PLA (93 J/g).

### 2.2.7. Micro-Raman Spectroscopy

Raman spectroscopy was performed using a Horiba-Jobin Yvon (Lille, France) LabRAM HR Evolution micro-Raman set-up with a 532 nm wavelength, solid-state laser. Both spectral measurements of the samples and the Raman mapping of PLLA film with 40 wt% HA and 0.5 wt% INT-WS<sub>2</sub> were carried out using 600 grooves/mm grating, spectral range between 70 and 1700 cm<sup>-1</sup>, with 30 s for each spectrum. The reported spectra represent the average of two measurements. The Raman spectra were obtained over all composites of PLLA and HA and INT-WS<sub>2</sub> film, while the mapping was performed on an area of 10 × 10 μm<sup>2</sup> of the PLLA film with 40 wt% HA and 0.5 wt% INT-WS<sub>2</sub>.

### 2.2.8. Fourier Transform Infrared Spectroscopy (FTIR)

Attenuated total reflectance Fourier transform infrared spectroscopy (ATR-FTIR) was performed using Alpha-T (Bruker, Billerica, MA, USA) in the range of 375 cm<sup>-1</sup> to 4000 cm<sup>-1</sup>.

## 3. Results and Discussion

### 3.1. X-ray Diffraction

A comparison between the XRD patterns of the nano-composite films and HA powder is shown in Figure 2. The XRD pattern of the composite PLLA and HA and INT-WS<sub>2</sub> film contains peaks of the different components, which indicates that the composition and structure of PLLA and HA and nanotubes are not affected by the fabrication process of the film.

Using the Pawley-based WPF analysis, the degree of crystallinity of the samples was calculated by comparing the total area under all the crystal peaks and the area under the amorphous halo. The results are presented in Table 1. The degree of crystallinity of the PLLA film is calculated to be 32.8%. After adding 0.5 wt% of INT-WS<sub>2</sub> the degree of crystallinity is nearly unchanged at 33.2%. However, after adding HA nanoparticles to the PLLA film, the degree of crystallinity increased significantly to 37.1%, rising slightly more after the addition of INT-WS<sub>2</sub> at the different wt% values.

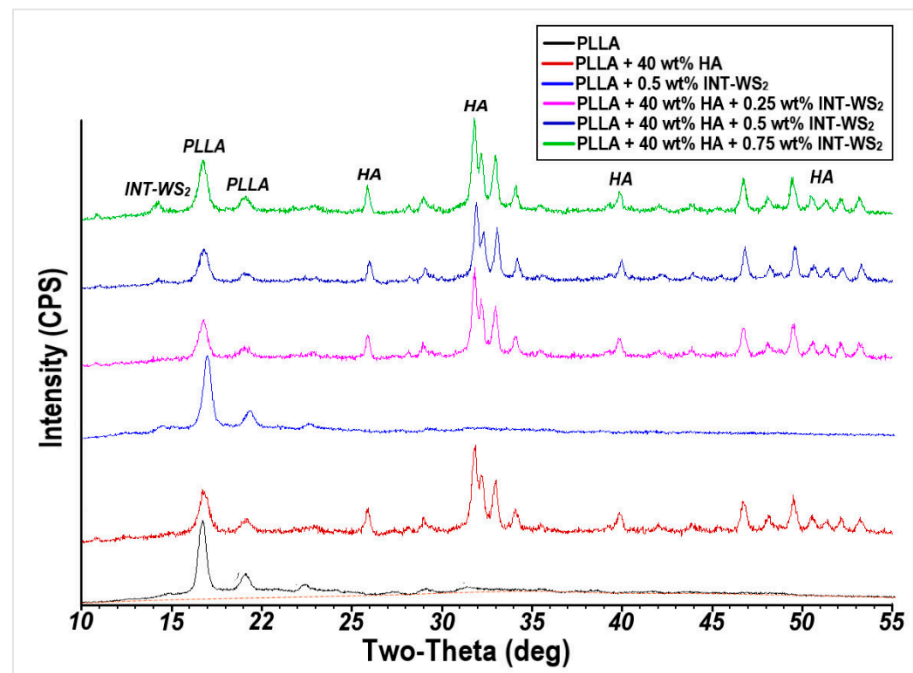


Figure 2. XRD patterns of PLLA film and HA/INT-WS<sub>2</sub>/PLLA nanocomposites.

Table 1. The degree of crystallinity of PLLA film and HA/INT-WS<sub>2</sub>/PLLA nanocomposites.

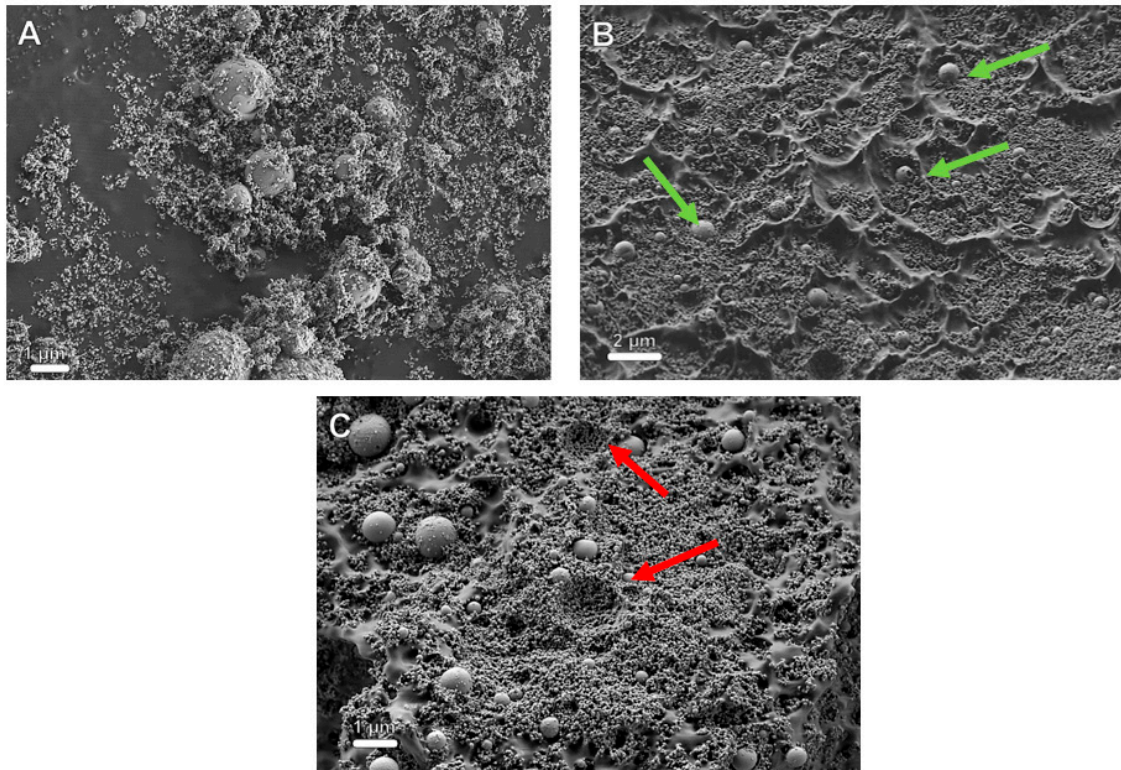
Sample Type	Degree of Crystallinity (%)		Average Crystallite Size (Å)		
	WPF	Scherrer	PLLA	WPF	HA
PLLA film	32.8 ± 0.9	170	171 ± 2	–	–
PLLA film with 40 wt% HA	37.1 ± 3.0	130	128 ± 5	–	291 ± 18
PLLA film with 0.5 wt% INT-WS <sub>2</sub>	33.2 ± 1.6	165	162 ± 2	–	–
PLLA film with 40 wt% HA and 0.25 wt% INT-WS <sub>2</sub>	38.2 ± 2.5	145	145 ± 5	–	331 ± 20
PLLA film with 40 wt% HA and 0.5 wt% INT-WS <sub>2</sub>	42.7 ± 2.7	140	144 ± 4	–	353 ± 19
PLLA film with 40 wt% HA and 0.75 wt% INT-WS <sub>2</sub>	42.1 ± 2.2	150	145 ± 4	–	342 ± 16

The average crystallite size of the different compositions was estimated using the Williamson–Hall approach from the XRD peak widths fitted in the Pawley-based WPF analysis and the Scherrer equation using the main peak of the PLLA at 16.5° and is also reported in Table 1. The largest crystallite size (171 Å) occurs for the neat PLLA film. As expected, the foreign ingredients (HA and INT) serve as crystallization nuclei for the PLLA and reduce its average crystallite size.

### 3.2. High-Resolution Scanning Electron Microscopy (HR-SEM)

Figure 3 shows the SEM images of HA powder (Figure 3A), and a cross-section of PLLA with 40 wt% HA film in secondary electron (SE) mode (Figure 3B,C). Visibly (Figure 3A), the HA particles constitute a bimodal size distribution made of micron-size agglomerates and a majority phase of well-dispersed HA nanoparticles (<50 nm). The surface of the large agglomerates is decorated with small HA NPs. However, the same agglomerates appear to have a smooth and uniform surface, i.e., free of the decorating HA NPs after being incorporated into the polymer (Figure 3B—marked with green arrows). To further understand this effect, the HA phase was washed in an ultrasonic bath with the polymer-free solvent (chloroform) containing OA. The surface of the large spherical HA agglomerates was smooth and free of the HA NP decoration after this washing procedure. Therefore, the solvent treatment appears to be responsible for the “cleaning” of the HA

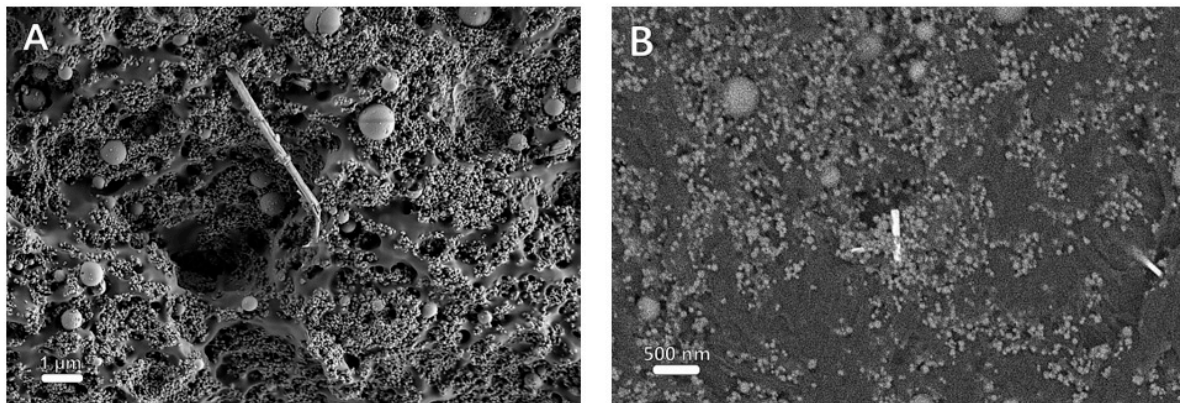
spherical agglomerates. These smooth spherical agglomerates of HA are likely to impair the mechanical properties of the film.



**Figure 3.** HR-SEM images (secondary electrons—SE mode) of pure HA powder (A) and PLLA film reinforced with 40 wt% HA observed in the SE mode at two magnifications, scale bars are 2  $\mu\text{m}$  (B) and 1  $\mu\text{m}$  (C). Green arrows point to the spherical agglomerates of HA nanoparticles. Red arrows point to pits formed by the pullout of the HA agglomerates during film breakage.

Figure 3B,C show that the HA nanoparticles (NPs) were well dispersed in the polymer matrix. i.e., no phase separation or excessive additional agglomeration was observed, which was not the case in the absence of OA. Furthermore, Figure 3C shows that the HA agglomerates ( $>0.5 \mu\text{m}$ ) were not damaged during the film breaking process, but were uprooted as a whole from the polymer matrix surface. Furthermore, the hemispherical depressions in Figure 3C (red arrows) appear to be remnants of entire HA agglomerates, which were uprooted from the polymer matrix during fracture, possibly being stuck to the other surface of the broken contact. Consequently, one can conclude that the strain was not well transferred to these agglomerates during fracture, and hence they adversely affected the mechanical strength of the film.

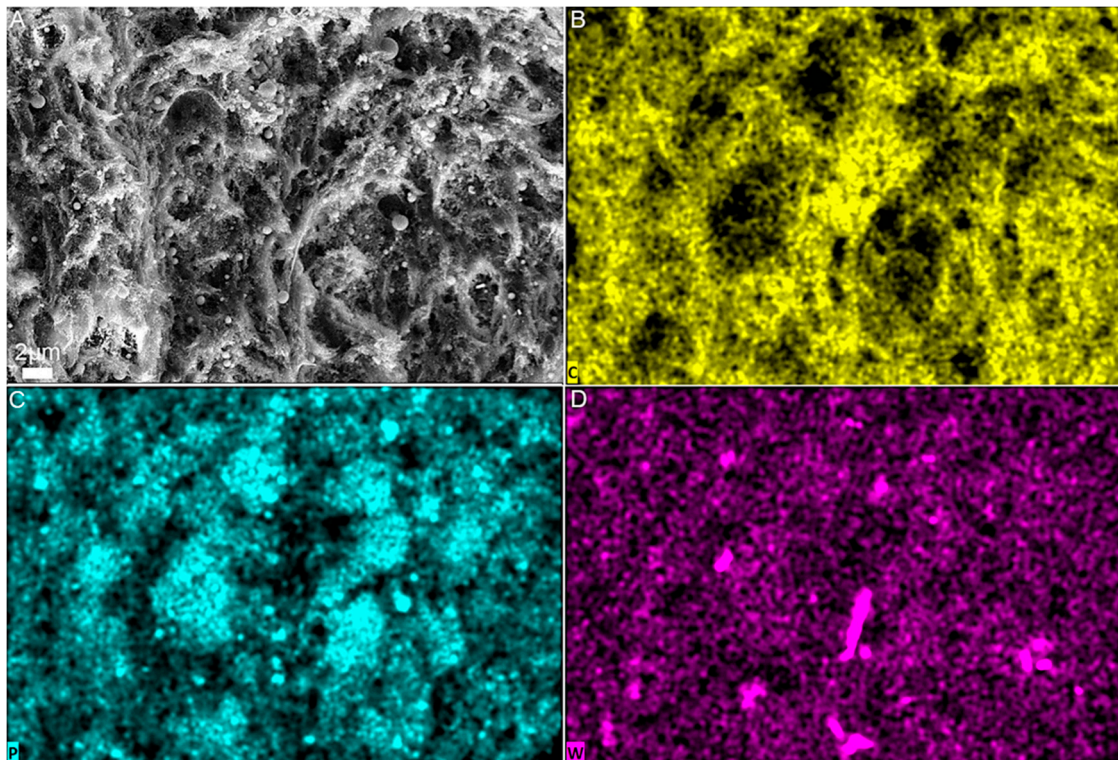
HR-SEM images of the cross-section of PLLA reinforced with 40 wt% HA and 0.75 wt% INT-WS<sub>2</sub> are presented in Figure 4. It can be seen in Figure 4A that there is no phase separation and consequently the nanotubes PLLA and the HA NPs are compatible and form a uniformly mixed matrix. The nanotubes protrude from the broken surface, which indicates that they carry some of the applied stress transferred to them from the matrix. In addition, BSE analysis shows that the INT-WS<sub>2</sub>, which are shown as bright stripes due to their relatively high atomic number, are fully dispersed in the PLLA matrix.



**Figure 4.** HR-SEM images of PLLA film reinforced with 40 wt% HA and 0.75 wt% INT-WS<sub>2</sub> film in SE mode (A), scale bar is 1 μm (B) BSE mode, scale bar is 500 nm.

Visibly, the nanotubes protrude from the PLLA matrix, suggesting that they reinforce the polymer via bridging and pullout mechanisms [46,47].

EDS elemental mappings of the PLLA film with 40 wt% HA and 0.75 wt% INT-WS<sub>2</sub> are presented in Figure 5. The carbon mapping displayed in Figure 5B shows that the strong carbon signal is evenly distributed throughout the film. This observation reflects the fact that the matrix of the material is PLLA whose chemical composition is mostly carbon. Figure 5C presents the phosphorus mapping, which is a major component of HA. It can be seen that the HA NPs are well dispersed throughout the film. The bimodal (size) distribution with distinct micron and submicron-sized spherical agglomerates and evenly distributed HA nanoparticles is clearly discernable. The INT-WS<sub>2</sub> distribution is represented by the tungsten mapping in Figure 5D, which shows that the nanotubes are well dispersed in the PLLA matrix.



**Figure 5.** HR-SEM image of PLLA film reinforced with 40 wt% HA and 0.75 wt% INT-WS<sub>2</sub> in SE mode (A) and EDS elemental mapping of the same area: carbon (B), phosphorus (C), and tungsten (D).

### 3.3. Tensile Test

The mechanical properties derived from the stress–strain curves of the films are displayed in Figure 6 and are also presented in Table 2.

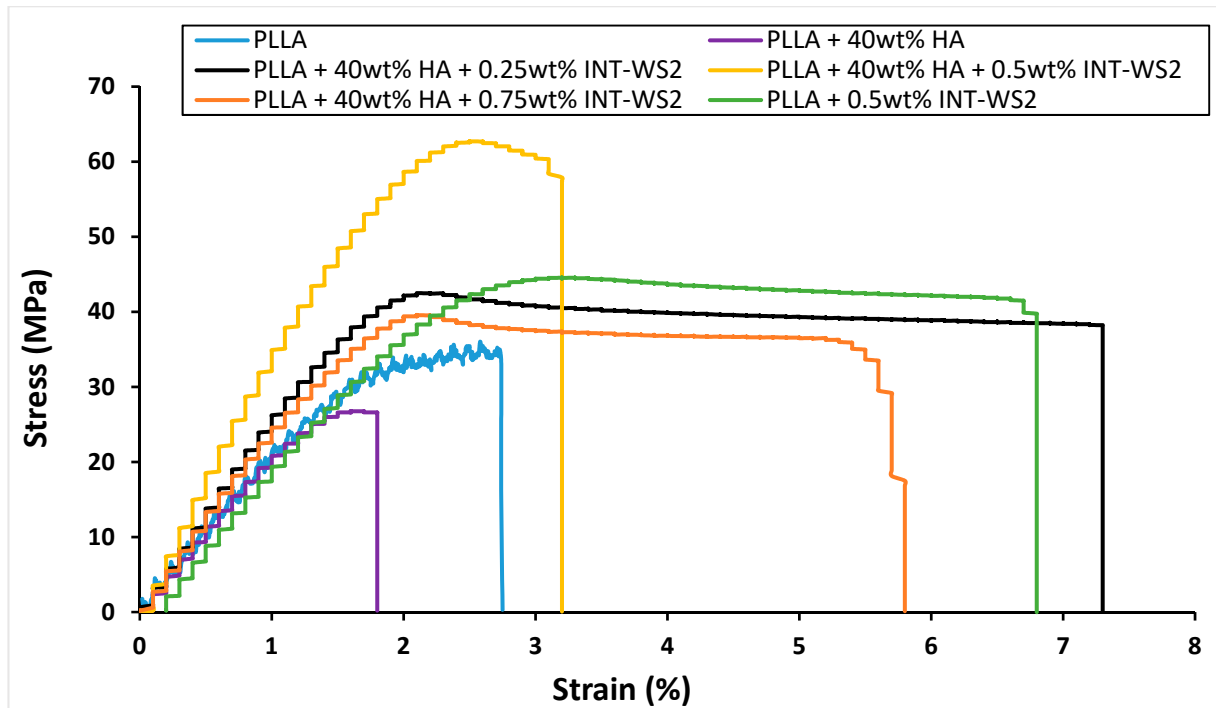


Figure 6. Stress–strain curves of PLLA film and its HA/INT-WS<sub>2</sub>/PLLA nanocomposites.

Table 2. The mechanical properties of PLLA film and HA/INT-WS<sub>2</sub>/PLLA nanocomposites from tensile testing.

Sample Type	Young's Modulus (GPa)	Yield Strength (MPa)	Strain at Failure (%)	Toughness (MPa)
PLLA film	1.55 ± 0.15	31.0 ± 2.4	2.7 ± 1.3	0.6 ± 0.2
PLLA film with 40 wt% HA	2.4 ± 0.1	26.7 ± 1.1	2.1 ± 0.1	0.3 ± 0.1
PLLA film with 0.5 wt% INT-WS <sub>2</sub>	2.25 ± 0.2	44.6 ± 4.65	6.8 ± 1.0	2.4 ± 0.5
PLLA film with 40 wt% HA and 0.25 wt% INT-WS <sub>2</sub>	2.7 ± 0.4	42.5 ± 5.8	7.3 ± 1.0	2.6 ± 0.3
PLLA film with 40 wt% HA and 0.5 wt% INT-WS <sub>2</sub>	3.8 ± 0.5	62.7 ± 1.2	3.2 ± 1.6	1.4 ± 0.7
PLLA film with 40 wt% HA and 0.75 wt% INT-WS <sub>2</sub>	2.7 ± 0.35	39.6 ± 4.9	5.8 ± 0.7	1.8 ± 0.25

The Young's modulus of PLLA film with 40 wt% HA (2.4 GPa) increased 1.5 times compared to the neat PLLA film (1.55 GPa), while the yield strength (26.7 MPa) and strain at failure (2.1%) of PLLA film with 40 wt% HA decreased to 0.85 and 0.75 of their values, respectively. Therefore, the toughness (area under the curve) of PLLA film with 40 wt% HA (0.3 MPa) was reduced by half compared to that of neat PLLA film (0.6 MPa). This is not surprising, since the HA is an oxide with a small strain to failure. Also, the binding of the HA to the PLLA is not chemical in nature and is rather weak (mostly van der Waals and polar interactions). These two factors adversely affect the fracture toughness of the composite. However, the indentation hardness and modulus of the PLLA+HA composite are appreciably higher than that of pure PLLA (see below). Obviously, the most rational way to mediate between the HA and the PLLA phases and increase the mechanical properties of the nanocomposite would be through surface functionalization [48]. The surface functionalization must have chemical versatility and biocompatibility in order to permit the three constituents (PLLA, HA, and INT-WS<sub>2</sub>) to optimally interact with each other and exhibit no biotoxicity effects.

The Young's modulus and yield strength of PLLA film with 0.5 wt% INT-WS<sub>2</sub> (2.25 GPa and 44.6 MPa, respectively) increased 1.45 times compared to the neat PLLA

film, while the strain at failure of the film with 0.5 wt% INT-WS<sub>2</sub> (6.8%) increased 2.5 times. Therefore, the toughness (area under the curve) of the PLLA film with 0.5 wt% INT-WS<sub>2</sub> (2.4 MPa) increased significantly by four times compared to the toughness of the neat PLLA film [36].

The Young's modulus of the PLLA film with 40 wt% HA and 0.5 wt% of INT-WS<sub>2</sub> (3.8 GPa) increased up to 1.7 times compared to the PLLA film with 40 wt% HA and the PLLA film with 0.5 wt% INT-WS<sub>2</sub>. The yield strength of the PLLA film with 40 wt% HA and 0.5 wt% of INT-WS<sub>2</sub> (62.7 MPa) increased by 2.35 and 1.4 times compared to the PLLA film with 40 wt% HA and the PLLA film with 0.5 wt% INT-WS<sub>2</sub>. The strain at failure of the PLLA film with 40 wt% HA and 0.5 wt% of INT-WS<sub>2</sub> (3.2%) increased 1.5 times compared to the PLLA film with 40 wt% HA. However, the PLLA film with HA and 0.5 wt% INT-WS<sub>2</sub> had strain at failure only half the value of the PLLA film and 0.5 wt% of INT-WS<sub>2</sub>. Therefore, the toughness of the PLLA film with 40 wt% HA and 0.5 wt% INT-WS<sub>2</sub> (1.4 MPa) increased significantly by 4.7 times compared to the PLLA film with 40 wt% HA and decreased to 0.6 times the value of the PLLA film with 0.5 wt% INT-WS<sub>2</sub>.

### 3.4. Micro-Hardness Test

Figure 7 shows the results of the micro-hardness test of PLLA film and the PLLA/HA/INT-WS<sub>2</sub> nanocomposites.

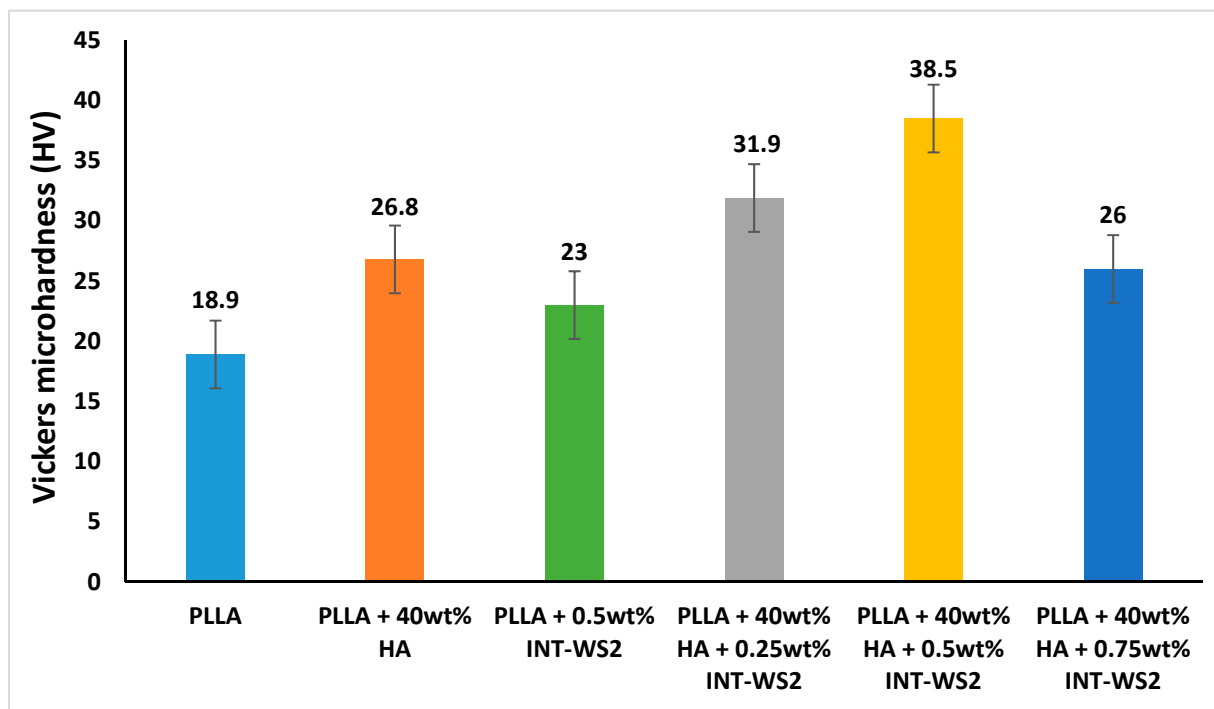


Figure 7. Vickers micro-hardness test of PLLA film and HA/INT-WS<sub>2</sub>/PLLA nanocomposites.

The addition of HA nanoparticles to the PLLA film increased the hardness value (26.8 HV) by 1.4 times compared to the hardness value of the neat PLLA film (18.9 HV). In addition, the hardness of the PLLA film with 0.5 wt% INT-WS<sub>2</sub> (23 HV) increased 1.2 times compared to the hardness of the neat PLLA film, with a significance level of  $p = 0.1$  for a two-tailed T-test.

A more significant increase in hardness was achieved with the combination of HA and INT-WS<sub>2</sub> in PLLA. The optimum hardness value was obtained for the films containing PLLA with 40 wt% HA NPs and 0.5 wt% INT-WS<sub>2</sub> with 38.5 HV, a value that is two times higher than the hardness of the pure PLLA film. It can be deduced that a small number of nanotubes added to the matrix can bridge the gap between the HA nanoparticles creating a uniform network of hardening material [49,50]. Beyond the optimal concentration of

0.5 wt%, the nanotubes have a deleterious effect on the hardness of the nanocomposite, likely due to agglomeration [51].

### 3.5. Nanomechanical Testing (Nanoindentation Tests)

While micro-hardness measurements provide an average hardness value, the small domain size in the present nanocomposite calls for a more local measurement, which serves to reveal inhomogeneities in the film. The results from the nanoindentation analysis are presented in Table 3 and are consistent with the Vickers micro-hardness tests reported above (Section 3.4).

**Table 3.** Parameters determined from the nanoindentation of PLLA film and HA/INT-WS<sub>2</sub>/PLLA nanocomposites.

Sample Type	Young's Modulus (GPa)	Hardness (GPa)
PLLA film	3.3 ± 0.4	0.16 ± 0.05
PLLA film with 40 wt% HA	4.9 ± 0.7	0.24 ± 0.06
PLLA film with 0.5 wt% INT-WS <sub>2</sub>	3.4 ± 0.7	0.18 ± 0.08
PLLA film with 40 wt% HA and 0.25 wt% INT-WS <sub>2</sub>	5.6 ± 1.2	0.36 ± 0.15
PLLA film with 40 wt% HA and 0.5 wt% INT-WS <sub>2</sub>	4.6 ± 0.8	0.25 ± 0.08
PLLA film with 40 wt% HA and 0.75 wt% INT-WS <sub>2</sub>	4.3 ± 0.6	0.22 ± 0.07

The addition of 0.5 wt% INT-WS<sub>2</sub> to the PLLA film caused almost no change in the Young's modulus (3.4 GPa) and hardness (0.18 GPa) values compared to the parameters of the neat PLLA film with Young's modulus of 3.3 GPa and hardness of 0.16 GPa. However, the Young's modulus and hardness of the PLLA film with 40 wt% HA (4.9 GPa, 0.24 GPa) each increased by 1.5 times compared to the Young's modulus and hardness of the neat PLLA film. The addition of a small number of nanotubes to the PLLA film with HA increased the Young's modulus and hardness significantly with the optimum being at the lowest concentration measured—0.25 wt% INT-WS<sub>2</sub>. The Young's modulus and hardness of the PLLA film with 40 wt% HA and 0.25 wt% INT-WS<sub>2</sub> (5.6 GPa, 0.36 GPa) were significantly larger than that of the neat PLLA film, increasing by 1.7 and 2.25 times, respectively. These values were also higher than those for the PLLA+HA. Notwithstanding the large fraction of HA in the film (40 wt%), the hardness values measured here are more than an order of magnitude lower than those reported for a pure HA single crystal [52]. We ascribe the relatively low hardness to the presence of HA NPs agglomerates, which degrade the mechanical properties of the material as suggested above (Section 3.2), as well as the weak links between the HA and the PLLA. Should the HA, PLLA, and the INT be intimately and strongly bound together via surface functionalization, the picture would probably be different and the overall mechanical properties of the nanocomposite would be much improved.

Larger statistical variations for some of the composite samples are consistent with local inhomogeneities in the nanoparticles' distribution, as is supported by the EDS measurements and mapping, and the Raman studies (below). Nanoindentation results show relative uncertainties an order of magnitude higher in comparison with the micro-hardness data. This can be attributed to the scale of the inhomogeneities within the sample: EDS mappings in Figure 5 show HA "pockets" of several μm extent, and WS<sub>2</sub> inhomogeneities on a smaller scale. The area of the microindentation imprint varies between 1000 and 2500 μm<sup>2</sup> (axial length of 30–50 μm) whereas for the nanoindentations the relevant indentation size is 4–5 μm, which is on the scale of the HA pockets, and INT length.

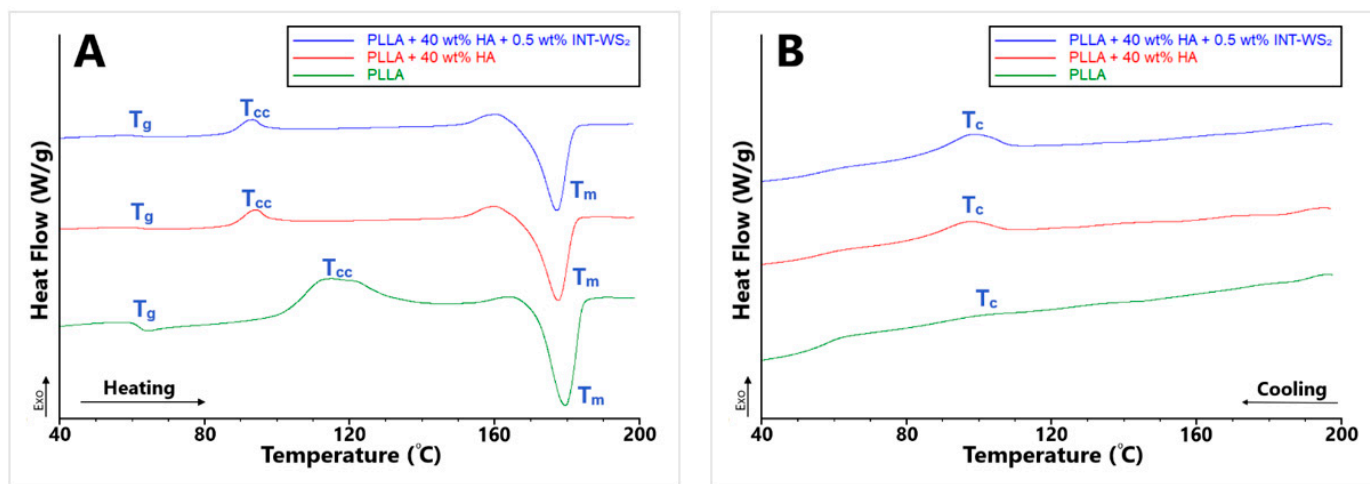
### 3.6. Thermal Properties of PLLA Film and HA/INT-WS<sub>2</sub>/PLLA Nanocomposites by DSC

The thermal behavior of the different PLLA films and PLLA/HA/INT-WS<sub>2</sub> nanocomposites films were measured using DSC. The results are summarized in Table 4, and the heating and cooling curves are presented in Figure 8.



**Table 4.** Thermal properties of PLLA film and HA/INT-WS<sub>2</sub>/PLLA nanocomposites.

Sample Type	$T_g$ (°C)	$T_{cc}$ (°C)	$\Delta H_{cc}$ (J/g)	$T_m$ (°C)	$\Delta H_m$ (J/g)	$T_c$ (°C)	$\Delta H_c$ (J/g)	$X_c$ (%)	$(1 - \lambda)_c$ (%)
PLLA film	61.5	114.1	32.1	179.6	39.1	101.6	2.0	7.5	2.2
PLLA film with 40 wt% HA	62.7	93.6	3.2	177.6	33.2	96.9	5.6	32.2	6.0
PLLA film with 0.5 wt% INT-WS <sub>2</sub>	66.7	107.9	3.1	181.7	34.3	116.9	34.2	33.5	36.7
PLLA film with 40 wt% HA and 0.25 wt% INT-WS <sub>2</sub>	62.9	93.5	4.8	177.3	31.1	97.2	8.5	28.3	9.2
PLLA film with 40 wt% HA and 0.5 wt% INT-WS <sub>2</sub>	62.9	92.6	2.5	177.2	32.6	98.3	5.5	32.3	5.9
PLLA film with 40 wt% HA and 0.75 wt% INT-WS <sub>2</sub>	62.6	95.2	2.4	177.0	32.3	99.3	5.0	32.1	5.4

**Figure 8.** DSC thermograms of heating (A) and cooling (B) of PLLA film and HA/INT-WS<sub>2</sub>/PLLA nanocomposites.

The addition of 40 wt% HA nanoparticles to the PLLA film increased the glass transition temperature ( $T_g$ ) (62.7 °C) by merely 1.9% compared to the neat PLLA film (61.5 °C). The addition of 0.5 wt% INT-WS<sub>2</sub> to the PLLA film increased  $T_g$  (66.7 °C) significantly by 8.5% compared to the  $T_g$  of the neat PLLA film. Therefore, the PLLA film with 0.5 wt% INT-WS<sub>2</sub> has the highest thermal deformation resistance of the films tested.

The cold crystallization temperature ( $T_{cc}$ ) of the PLLA film with 0.5 wt% INT-WS<sub>2</sub> (107.9 °C) is lower than the  $T_{cc}$  of the neat PLLA film (114.1 °C). In addition, the PLLA film with 40 wt% HA has lower  $T_{cc}$  (93.6 °C) than both the neat PLLA film and the PLLA film with 0.5 wt% INT-WS<sub>2</sub>, which indicates that the PLLA with 40 wt% HA NPs film consists of smaller crystallites, compared to the neat PLLA film. The lower  $\Delta H_{cc}$  of PLLA film with 40 wt% HA and PLLA film with 0.5 wt% INT-WS<sub>2</sub> compared to the neat PLLA film also indicates the presence of bigger PLLA crystallites in the neat PLLA film, which is consistent with the findings from XRD (see discussion of Table 1 data, above).

The addition of 40 wt% HA nanoparticles to the PLLA reduced  $T_m$  (177.6 °C) compared to the neat PLLA film (179.6 °C), while the addition of 0.5 wt% INT-WS<sub>2</sub> resulted in increased  $T_m$  (181.7 °C). Therefore, the PLLA film with 0.5 wt% INT-WS<sub>2</sub> has the highest thermal stability [36]. The  $\Delta H_m$  values of the PLLA films with 40 wt% HA (33.2 J/g) and PLLA film with 0.5 wt% INT-WS<sub>2</sub> (34.3 J/g) are lower compared to the PLLA film (39.1 J/g). Therefore, the HA nanoparticles and the INT-WS<sub>2</sub> each, independently lower the energy required for breaking the polymer chain-chain interactions. The lower  $T_c$  and higher  $\Delta H_c$  of PLLA film with 40 wt% HA (96.9 °C, 5.6 J/g) compared to the PLLA film (101.6 °C, 2.0 J/g), shows that the PLLA with 40 wt% HA film has a higher cooling rate [53–55] and smaller crystal nuclei. The higher  $T_c$  and higher  $\Delta H_c$  of PLLA film with 0.5 wt% INT-WS<sub>2</sub> (116.9 °C, 34.9 J/g) compared to the PLLA film, indicate that the PLLA film with 0.5 wt% INT-WS<sub>2</sub> has a lower cooling rate and even smaller crystal nuclei.

The degree of crystallinity ( $X_c$  and  $(1 - \lambda)_c$ ) of the PLLA film with 40 wt% HA (32.2%, 6.0%) is higher compared to the neat PLLA film (7.5%, 2.2%), which indicates that the PLLA film with 40 wt% HA is harder and denser than the neat PLLA film. However, the  $X_c$  and

$(1 - \lambda)_c$  of PLLA film with 0.5 wt% INT-WS<sub>2</sub> (33.5%, 36.7%) are even higher compared to the PLLA film with 40 wt% HA, therefore, the PLLA film with 0.5 wt% INT-WS<sub>2</sub> is the hardest, and the densest film among the three [56–58]. However, the results of the micro-hardness test and the nanoindentation tests, show that the hardest film among the three is not the PLLA film with 0.5 wt% INT-WS<sub>2</sub>, but the PLLA film with 40 wt% HA. The reason for the difference between the estimated hardness trend and the mechanical measurements could possibly be linked to the nuclei size. The crystallites of the PLLA film with 0.5 wt% INT-WS<sub>2</sub> are larger than the crystallites of the PLLA film with 40 wt% HA. Although this is a very different material, these results are consistent with the Hall–Petch effect, usually associated with polycrystalline metallic films. According to this law, as the size of the crystallites is reduced, the area of their grain boundaries increases; thereby increasing the hardness of the material [59,60].

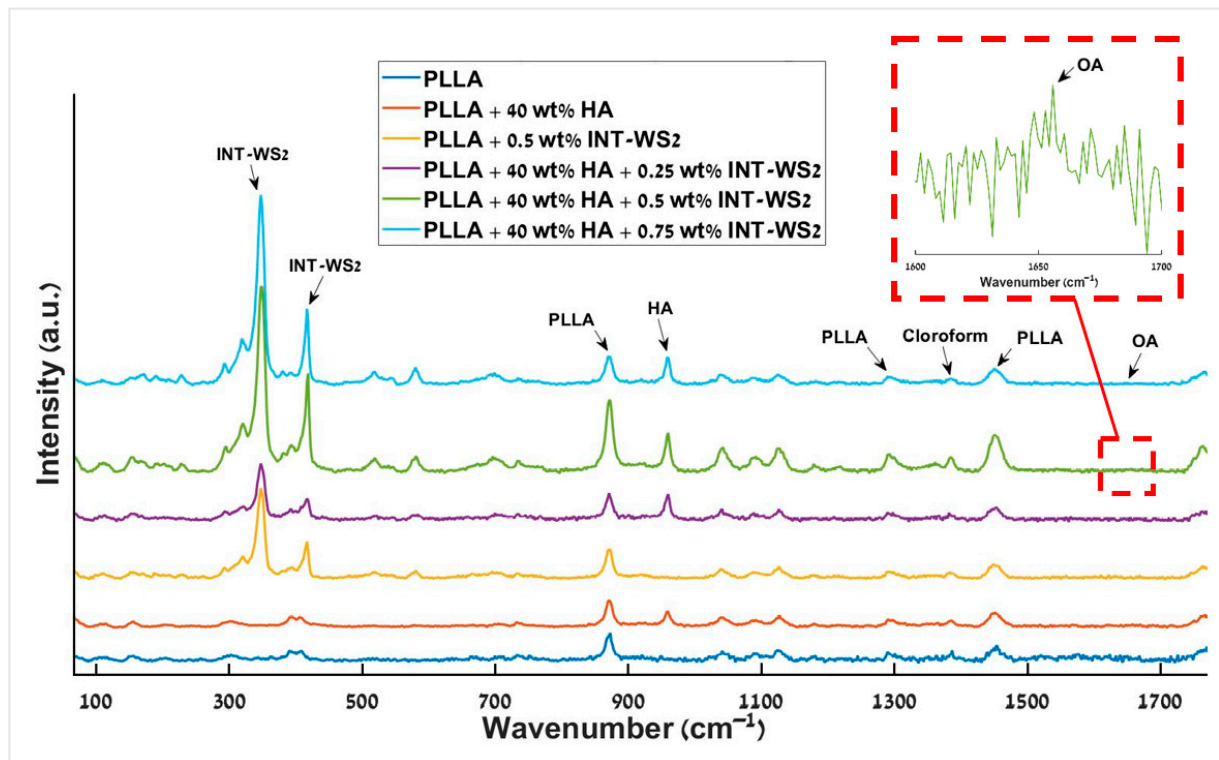
PLLA films with 40 wt% HA and 0.25–0.75 wt% INT-WS<sub>2</sub> have thermal properties ( $T_g$ ,  $T_{cc}$ ,  $T_m$ , and  $T_c$ ) similar to the PLLA film with 40 wt% HA. Consequently, the PLLA film with 40 wt% HA and 0.25–0.75 wt% INT-WS<sub>2</sub> have smaller thermal deformation resistance, crystallite size, thermal stability, and lower cooling rate compared with the PLLA film with 0.5 wt% INT-WS<sub>2</sub>. However, the PLLA film with 40 wt% HA and 0.25–0.75 wt% INT-WS<sub>2</sub> have better thermal deformation resistance, smaller crystallites, smaller thermal stability, and lower cooling rate compared to the neat PLLA film.

The  $\Delta H_{cc}$  of PLLA film with 40 wt% HA and 0.5–0.75 wt% INT-WS<sub>2</sub> (2.5–2.4 J/g) is lower compared to the other samples, which is attributed to the smaller crystallites in the nanocomposite films, due to the combined addition of HA nanoparticles and INT-WS<sub>2</sub> to the PLLA film. The PLLA film with 40 wt% HA and 0.25 wt% INT-WS<sub>2</sub> has lower  $\Delta H_{cc}$  (4.8 J/g) compared to the neat PLLA film and higher  $\Delta H_{cc}$  compared to the rest of the samples. This data demonstrates that the addition of a small amount of INT-WS<sub>2</sub> combined with 40 wt% HA produced smaller crystallites compared to the neat PLLA film. The  $\Delta H_m$  of the PLLA film with 40 wt% HA and 0.25–0.75 wt% INT-WS<sub>2</sub> is lower compared to the other samples, thus the combined addition of HA nanoparticles and INT-WS<sub>2</sub> to the PLLA film decreased the flexibility of the polymer chains and the energy required to break the interaction between the polymer chains.

PLLA films with 40 wt% HA and 0.25–0.75 wt% INT-WS<sub>2</sub> have similar  $X_c$  and  $(1 - \lambda)_c$  to the PLLA film with 40 wt% HA, but lower  $X_c$  and  $(1 - \lambda)_c$  compared to the PLLA film with 0.5 wt% INT-WS<sub>2</sub>. The  $X_c$  and  $(1 - \lambda)_c$  of PLLA films with 40 wt% HA and 0.5 wt% and 0.75% INT-WS<sub>2</sub> are very similar; thus they are equally hard. However, the PLLA film with 40 wt% HA and 0.25 wt% INT-WS<sub>2</sub> has lower  $X_c$  but higher  $(1 - \lambda)_c$  compared to the PLLA film with 40 wt% HA and 0.5–0.75 wt% INT-WS<sub>2</sub>. Therefore, the PLLA film with 40 wt% HA and 0.25 wt% INT-WS<sub>2</sub> is more elastic and but not as hard as the PLLA films with 40 wt% HA and 0.5–0.75 wt% INT-WS<sub>2</sub>. This is in agreement with the results of the mechanical properties (Section 3.3).

### 3.7. Micro-Raman Spectroscopy

The Raman spectra of the different PLLA films and PLLA/HA/INT-WS<sub>2</sub> nanocomposite films are presented in Figure 9. The PLLA film with 40 wt% HA and the neat PLLA film has exactly the same pattern of peaks as well as identical energies (873 cm<sup>-1</sup>, 1452 cm<sup>-1</sup>) [61,62], except for the peak of the HA at 960 cm<sup>-1</sup> [63]. In addition, comparing the PLLA film with 0.5 wt% INT-WS<sub>2</sub> to the neat PLLA film also shows the same pattern of peaks and intensity, except for the peaks of the INT-WS<sub>2</sub> at 350 cm<sup>-1</sup> and 418 cm<sup>-1</sup> [64]. The match between the different spectral patterns is excellent, indicating that no chemical reaction took place between the different ingredients of the nanocomposite, as all the identified peaks belong to the pure reagents, with no missing peaks. Hence the chemical composition of the PLLA was not affected by the addition of the HA NPs and INT-WS<sub>2</sub>, or from the preparation of the film as suggested above (Section 3.1).



**Figure 9.** Raman spectra of the different PLLA films and PLLA/HA/INT-WS<sub>2</sub> nanocomposites films. The Raman peak of the oleic acid is shown in the inset.

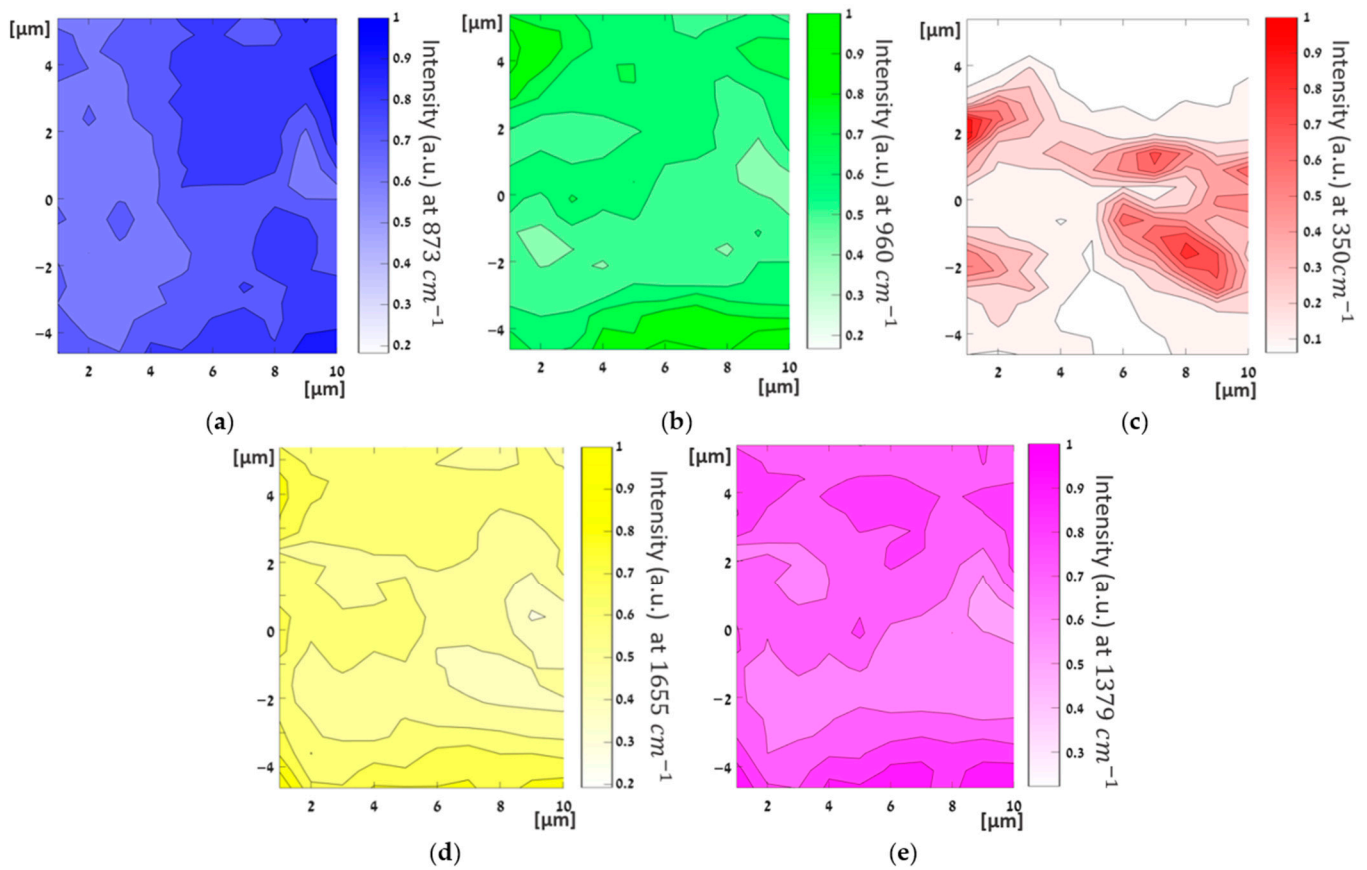
The band at  $1379\text{ cm}^{-1}$  is associated with chloroform [65]. That band can be seen in the spectra of all the different PLLA films and PLLA/HA/INT-WS<sub>2</sub> nanocomposites films. The existence of this peak indicates that residual amounts of the solvent remain in the films. The presence of solvent residues can significantly alter the mechanical properties of the nanocomposite film and its long-term behavior [66–68].

The film of PLLA with 0.5 wt% INT-WS<sub>2</sub> and the films of PLLA with 40 wt% HA and 0.25–0.75 wt% INT-WS<sub>2</sub> present peaks at  $350\text{ cm}^{-1}$  and  $418\text{ cm}^{-1}$ , which are associated with the E<sub>2g</sub> and A<sub>1g</sub> modes of the INT-WS<sub>2</sub> [69].

OA is a component that was incorporated only into the films of PLLA with 40 wt% HA and 0.25–0.75 wt% INT-WS<sub>2</sub> (see Section 2.1). However, the main peak associated with the OA at  $1655\text{ cm}^{-1}$  [70] is rather small and can be observed by focusing on the portion of the spectrum near this peak (red dashed square) and magnifying the scale. The low intensity of the peak reflects the fact that the OA concentration is very low in the films (150  $\mu\text{L}$ ).

Raman intensity mappings of the PLLA with 40 wt% HA and 0.5 wt% INT-WS<sub>2</sub> films were carried out and are displayed in Figure 10.

Intensity mapping of the PLLA peak at  $873\text{ cm}^{-1}$  (blue) shows a relatively uniform Raman light scattering intensity on the entire scanned area, with a minimum value of 60% with respect to the maximum (normalized) intensity. This indicates, as suggested above, that the PLLA film was uniform and that it was not affected by the addition of the solvent, HA, or and INT-WS<sub>2</sub>, nor from the fabrication process of the film. The result also shows that no chemical reactions occurred between the four main components during their mixing and processing of the film. Furthermore, the intensity mapping of HA NPs at  $960\text{ cm}^{-1}$  (green) shows a good dispersion of the HA nanoparticles in the film, which confirms the observation of a uniform HA distribution obtained via SEM imaging (Section 3.2).



**Figure 10.** Raman intensity mapping of PLLA film with 40 wt% HA and 0.5 wt% INT-WS<sub>2</sub> on an area of (10 × 10 μm<sup>2</sup>). Blue—PLLA at 873 cm<sup>-1</sup> (a), green—HA at 960 cm<sup>-1</sup> (b), red—INT-WS<sub>2</sub> at 350 cm<sup>-1</sup> (c), yellow—OA at 1655 cm<sup>-1</sup> (d), and purple—chloroform at 1379 cm<sup>-1</sup> (e).

Notwithstanding the limited resolution of the technique (>1 μm), the INT-WS<sub>2</sub> are clearly seen as elongated red shapes throughout the film in the Raman mapping (red features in Figure 10c). Obviously, the asymmetric shape of the nanotube does not reflect its genuine shape, since the coarse size of the focused laser beam (1–2 μm) is at least 10 times larger than the tube diameter (~100 nm). Moreover, it can be seen that the nanotubes are fully dispersed in the film. Their long axis seems to lie in the film plane with orientation roughly in the x-direction. The preferred directionality of the tubes could be related to the mode of evaporation of the solvent from the casted film. For example, a higher evaporation rate from the container wall could induce radial flow, which would orient the tubes accordingly with their long axis parallel to the (radial) flow direction.

Raman mapping of OA at 1655 cm<sup>-1</sup> (yellow) presents relatively strong and uniform intensity throughout the film area, with a minimum value of (normalized) intensity around 40%. Thus, it can be concluded that the OA was uniformly dispersed throughout the nanocomposite film during its preparation. Noticeably, the Raman mapping of the HA (green); OA (yellow), and chloroform (purple) exhibit some similarities. As for the OA, which is purposely used as the surfactant for the HA, the similar spatial distribution is not that astonishing. The analog spatial distribution of the chloroform and the HA indicates that the remnants of the solvent are adsorbed tightly to the HA surface and cannot be easily driven out, even after the long drying procedure used here.

The (normalized) intensity mapping of chloroform at 1379 cm<sup>-1</sup> (purple) shows that it is uniform throughout the film. This indicates that notwithstanding the efforts to remove it, non-negligible amounts of chloroform residues (ca. 1 wt%) remained in the film, which correlates well with the observed feature in the Raman spectra above. Given the lengthy drying process under vacuum and heating at 45 °C, it is most likely that the

residual chloroform was chemisorbed to one of the film ingredients and could not be easily removed from the film.

### 3.8. FTIR Spectroscopy

FTIR of the different PLLA/HA/INT-WS<sub>2</sub> nanocomposite films was conducted and the resulting spectra are displayed in Figure 11.

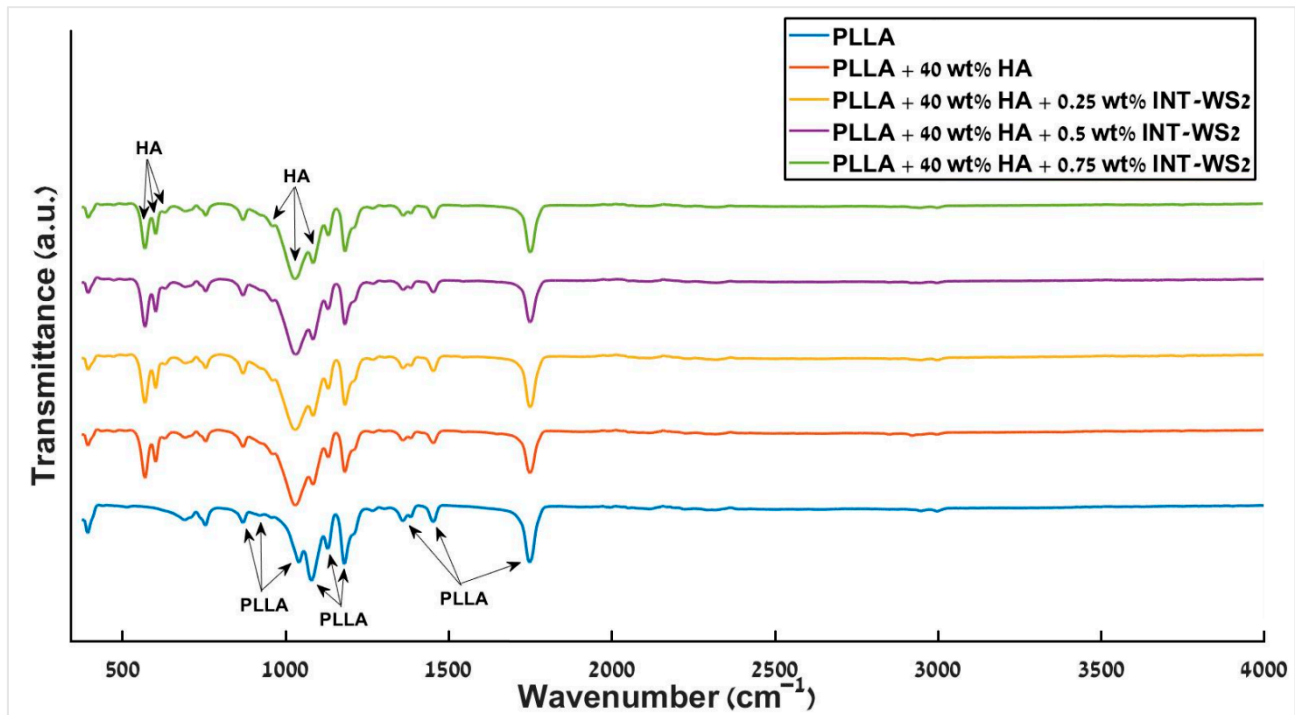


Figure 11. FTIR spectra of different PLLA/HA/INT-WS<sub>2</sub> nanocomposite films.

Visibly, PLLA peaks are observed for all different films at the same position, accounting for the fact that the peaks at 1044 cm<sup>-1</sup> and 1086 cm<sup>-1</sup> [71] overlap with those of HA at 1033 cm<sup>-1</sup> and 1093 cm<sup>-1</sup> [72]. No extra peaks occur due to the addition of HA and nanotubes to the PLLA.

The nanotube peaks (<500 cm<sup>-1</sup>) [73] are not visible due to the dominant PLLA peak in this region. Thus, in agreement with the previous measurements, the FTIR results indicate that the four components (PLLA, HA, OA, and INT) are mixed together uniformly and are compatible with each other.

## 4. Discussion

The current work builds upon a previous work [36], where a nanocomposite of PLLA with small amounts of WS<sub>2</sub> nanotubes dissolved in dichloromethane (DCM) was cast into a film. In this earlier work, the major obstacle was to fine-tune the drying procedure, which proved to be rather tricky. The PLLA-WS<sub>2</sub> nanotube composites were dried in a vacuum oven at 30 °C for one week while monitoring the weight loss. This temperature was adopted after many trials because it is lower than the DCM boiling temperature (39.6 °C) which is important to ensure uniformity of the film. As anticipated, films that were not properly dried exhibited poor mechanical properties. The present three-component nanocomposite drying process presented a more challenging task. HA could not be properly dispersed in DCM. Therefore, chloroform (boiling point 61.15 °C) was used as a solvent and oleic acid as a compatibilizer between the HA phase and the other two components (PLLA and INT-WS<sub>2</sub>). The chloroform is less volatile than DCM and hence a higher drying temperature (45 °C) was selected for the casting. The presence of minute amounts of solvent adversely

affected the nanotube-PLLA interaction and consequently the mechanical properties of the film. In the future, solvent-free processing of the film can be envisaged, like hot-pressing, or extrusion, and subsequent 3D printing [74].

The control of the interfacial interaction between the two majority phases, i.e., PLLA and HA and the minority phase—INT-WS<sub>2</sub> has major implications on the mechanical stability of the nanocomposite subject to different stress and environmental conditions. The oleic acid, which has been used in the past for compatibilizing HA in different polymer phases, was found to be indispensable here. First, both oleic acid [75] and HA nanoparticles [76] are nontoxic and biocompatible. The FTIR, XRD, and Raman measurements reported here do not reveal any specific chemical bonding between any of the four components (PLLA, HA, OA, and INT) used in this work or new phase formation during the preparation of the film. It remains to be seen if other specific functionalization processes of the nanotube surface could further improve their interfacial interaction with the matrix and influence the mechanical behavior of the nanocomposite without sacrificing its biocompatibility. In the absence of a specific interaction between the nanotubes and the polymer-HA, their large surface area and aspect ratio (50–100) as well as their mechanical strength (10–22 GPa), large strain (10%) [77], nontoxic nature [21], and their facile dispersion make them ideally suited for reinforcing biodegradable polymers, even if added in minute amounts (~0.2 at%, ~0.6 wt%) [36,78,79]. Beyond this limit the nanotubes start agglomerating and their effectiveness in the polymer matrix is gradually impaired. PLLA is only one of a class of biodegradable polymers being intensively studied in order to improve the quality of medical care and make life more sustainable [80,81]. Obviously, more work, including in vivo experiments, is needed to determine the usefulness and biocompatibility of the WS<sub>2</sub> nanotubes for potential future use in medical technologies.

## 5. Conclusions

PLLA films containing both hydroxyapatite and WS<sub>2</sub> nanotubes were prepared via solvent casting process. While hydroxyapatite increases the hardness of the composite film, its tensile properties are compromised. The addition of the nontoxic nanotubes partially mitigates the reduced tensile properties of the film, providing biocompatible films with high hardness and tensile properties. XRD analysis and thermal measurements indicate that this is due to a reduction in crystal nuclei size. The addition of the nanotubes also improves the thermal stability of the films. Such nanocomposites could find numerous applications in medical technologies.

**Author Contributions:** O.G., H.S., I.K.-A., S.R.C., Y.F. and I.P.—data curation and validation; R.O.A.—supervision; A.Z.—synthesis of the INT-WS<sub>2</sub> and investigation; R.T. and S.R.C.—writing, review and editing. All authors have read and agreed to the published version of the manuscript.

**Funding:** This research was supported by the Israel Science Foundation grant No. 339/18 (Internal grant No. 120924).

**Institutional Review Board Statement:** Not applicable.

**Informed Consent Statement:** Not applicable.

**Data Availability Statement:** Not applicable.

**Acknowledgments:** We thank Natali Yosef from Shenkar College for the help with the FTIR measurements. This work was supported by the Israel Science Foundation grant No. 339/18 (Internal grant No. 120924) (RT). The following foundations of the Weizmann Institute are acknowledged: Perlman Family Foundation; the Kimmel Center for Nanoscale Science Grant No. 43535000350000; the Irving and Cherna Moskowitz Center for Nano and Bio-Nano Imaging. IP is the incumbent of the Sharon Zuckerman research fellow chair.

**Conflicts of Interest:** The authors declare no conflict of interest.

## References

1. Genovese, L.; Soccio, M.; Lotti, N.; Gazzano, M.; Siracusa, V.; Salatelli, E.; Balestra, F.; Munari, A. Design of biobased PLLA triblock copolymers for sustainable food packaging: Thermo-mechanical properties, gas barrier ability and compostability. *Eur. Polym. J.* **2017**, *95*, 289–303. [[CrossRef](#)]
2. Wang, H.; Liu, H.; Chu, C.; She, Y.; Jiang, S.; Zhai, L.; Jiang, S.; Li, X. Diffusion and antibacterial properties of nisin-loaded chitosan/poly (l-lactic acid) towards development of active food packaging film. *Food Bioprocess Technol.* **2015**, *8*, 1657–1667. [[CrossRef](#)]
3. El-hadi, A.M. Increase the elongation at break of poly (lactic acid) composites for use in food packaging films. *Sci. Rep.* **2017**, *7*, 46767. [[CrossRef](#)]
4. Ramachandran, K.; Di Luccio, T.; Ailianou, A.; Kossuth, M.B.; Oberhauser, J.P.; Kornfield, J.A. Crimping-induced structural gradients explain the lasting strength of poly L-lactide bioresorbable vascular scaffolds during hydrolysis. *Proc. Natl. Acad. Sci. USA* **2018**, *115*, 10239–10244. [[CrossRef](#)]
5. Ailianou, A.; Ramachandran, K.; Kossuth, M.B.; Oberhauser, J.P.; Kornfield, J.A. Multiplicity of morphologies in poly (L-lactide) bioresorbable vascular scaffolds. *Proc. Natl. Acad. Sci. USA* **2016**, *113*, 11670–11675. [[CrossRef](#)] [[PubMed](#)]
6. Rocher, L.; Ylitalo, A.S.; Di Luccio, T.; Miscioscia, R.; De Filippo, G.; Pandolfi, G.; Villani, F.; Zak, A.; Menary, G.H.; Lennon, A.B.; et al. Interaction of Poly L-lactide and tungsten disulfide nanotubes studied by in Situ X-ray scattering during expansion of PLLA/WS<sub>2</sub> NT nanocomposite tubes. *Polymers* **2021**, *13*, 1764. [[CrossRef](#)]
7. Wan, P.; Yuan, C.; Tan, L.L.; Li, Q.; Yang, K. Fabrication and evaluation of bioresorbable PLLA/magnesium and PLLA/magnesium fluoride hybrid composites for orthopedic implants. *Compos. Sci. Technol.* **2014**, *98*, 36–43. [[CrossRef](#)]
8. Díaz, E.; Molpeceres, A.L.; Sandonis, I.; Puerto, I. PLLA/nHA composite films and scaffolds for medical Implants: In vitro degradation, thermal and mechanical properties. *J. Inorg. Organomet. Polym. Mater.* **2018**, *29*, 121–131. [[CrossRef](#)]
9. Davachi, S.M.; Kaffashi, B.; Torabinejad, B.; Zamanian, A. In-vitro investigation and hydrolytic degradation of antibacterial nanocomposites based on PLLA/triclosan/nano-hydroxyapatite. *Polymer* **2016**, *83*, 101–110. [[CrossRef](#)]
10. Xiao, L.; Wang, B.; Yang, G.; Gauthier, M. Poly(lactic acid)-based biomaterials: Synthesis, modification and applications. In *Biomedical Science, Engineering and Technology*; Ghista, D.N., Ed.; InTech: London, UK, 2012; Volume 11, pp. 247–282.
11. Farah, S.; Anderson, D.G.; Langer, R. Physical and mechanical properties of PLA, and their functions in widespread applications—A comprehensive review. *Adv. Drug Deliv. Rev.* **2016**, *107*, 367–392. [[CrossRef](#)] [[PubMed](#)]
12. Alvarez, K.; Nakajima, H. Metallic scaffolds for bone regeneration. *Materials* **2009**, *2*, 790–832. [[CrossRef](#)]
13. Tariq, U.; Haider, Z.; Chaudhary, K.; Hussain, R.; Ali, J. Calcium to phosphate ratio measurements in calcium phosphates using libs. *J. Phys. Conf. Ser.* **2018**, *1027*, 012015. [[CrossRef](#)]
14. Kong, Y.-M.; Kim, D.-H.; Kim, H.-E.; Heo, S.-J.; Koak, J.-Y. Hydroxyapatite-based composite for dental implants: An in vivo removal torque experiment. *J. Biomed. Mater. Res.* **2002**, *63*, 714–721. [[CrossRef](#)] [[PubMed](#)]
15. Shikinami, Y. Bioresorbable devices made of forged composites of hydroxyapatite (HA) particles and poly-L-lactide (PLLA): Part I. basic characteristics. *Biomaterials* **1999**, *20*, 859–877. [[CrossRef](#)]
16. Takayama, T.; Todo, M. Improvement of mechanical properties of hydroxyapatite particle-filled poly(L-lactide) biocomposites using lysine tri-isocyanate. *J. Mater. Sci.* **2009**, *44*, 5017–5020. [[CrossRef](#)]
17. Chua, P.S.; Piggott, M.R. The glass fibre—Polymer interface: I—Theoretical consideration for single fibre pull-out tests. *Compos. Sci. Technol.* **1985**, *22*, 33–42. [[CrossRef](#)]
18. Sedova, A.; Khodorov, S.; Ehre, D.; Achrai, B.; Wagner, H.D.; Tenne, R.; Dodiuk, H.; Kenig, S. Dielectric and electrical properties of WS<sub>2</sub> nanotubes/epoxy composites and their use for stress monitoring of structures. *J. Nanomater.* **2017**, *2017*, 4838095. [[CrossRef](#)]
19. Ke, S.; Lai, Y.; Zhou, T.; Li, L.; Wang, Y.; Ren, L.; Ye, S. Molybdenum disulfide nanoparticles resist oxidative stress-mediated impairment of autophagic flux and mitigate endothelial cell senescence and angiogenic dysfunctions. *ACS Biomater. Sci. Eng.* **2018**, *4*, 663–674. [[CrossRef](#)]
20. Rashkow, J.T.; Talukdar, Y.; Lalwani, G.; Sitharaman, B. Interactions of 1D- and 2D-layered inorganic nanoparticles with fibroblasts and human mesenchymal stem cells. *Nanomedicine* **2015**, *10*, 1693–1706. [[CrossRef](#)]
21. Pardo, M.; Shuster-Meiseles, T.; Levin-Zaidman, S.; Rudich, A.; Rudich, Y. Low cytotoxicity of inorganic nanotubes and fullerene-like nanostructures in human bronchial epithelial cells: Relation to inflammatory gene induction and antioxidant response. *Environ. Sci. Technol.* **2014**, *48*, 3457–3466. [[CrossRef](#)]
22. Fojtů, M.; Teo, W.Z.; Pumera, M. Environmental impact and potential health risks of 2D nanomaterials. *Environ. Sci. Nano* **2017**, *4*, 1617–1633. [[CrossRef](#)]
23. Kaplan-Ashiri, I.; Cohen, S.R.; Gartsman, K.; Ivanovskaya, V.; Heine, T.; Seifert, G.; Wiesel, I.; Wagner, H.D.; Tenne, R. On the mechanical behavior of WS<sub>2</sub> nanotubes under axial tension and compression. *Proc. Natl. Acad. Sci. USA* **2006**, *103*, 523–528. [[CrossRef](#)]
24. Jarzabek, D.M. The impact of weak interfacial bonding strength on mechanical properties of metal matrix–ceramic reinforced composites. *Compos. Struct.* **2018**, *201*, 352–362. [[CrossRef](#)]
25. Barber, A.H.; Cohen, S.R.; Kenig, S.; Wagner, H.D. Interfacial fracture energy measurements for multi-walled carbon nanotubes pulled from a polymer matrix. *Compos. Sci. Technol.* **2004**, *64*, 2283–2289. [[CrossRef](#)]
26. Rodricks, C.W.; Greenfeld, I.; Wagner, H.D. Polymer beads as interfacial obstacles in fibre composites. *Compos. Sci. Technol.* **2021**, *210*, 108793. [[CrossRef](#)]

27. Kumar, V.B.; Harel, Y.; Ben-Ishay, R.; Lellouche, J.P.; Gedanken, A. Functionalization of WS<sub>2</sub> nanotubes with fluorescent C-dots and conductive polythiophenes. *Macromol. Chem. Phys.* **2019**, *220*, 1800476. [[CrossRef](#)]
28. Palomar, Q.; Gondran, C.; Lellouche, J.-P.; Cosnier, S.; Holzinger, M. Functionalized tungsten disulfide nanotubes for dopamine and catechol detection in a tyrosinase-based amperometric biosensor design. *J. Mater. Chem. B* **2020**, *8*, 3566–3573. [[CrossRef](#)] [[PubMed](#)]
29. Naffakh, M.; Marco, C. Isothermal crystallization kinetics and melting behavior of Poly(L-lactic acid)/WS<sub>2</sub> inorganic nanotube nanocomposites. *J. Mater. Sci.* **2015**, *50*, 6066–6074. [[CrossRef](#)]
30. Naffakh, M.; Marco, C.; Ellis, G.; Cohen, S.R.; Laikhtman, A.; Rapoport, L.; Zak, A. Novel poly(3-hydroxybutyrate) nanocomposites containing WS<sub>2</sub> inorganic nanotubes with improved thermal, mechanical and tribological properties. *Mater. Chem. Phys.* **2014**, *147*, 273–284. [[CrossRef](#)]
31. Ghosh, S.; Otorgust, G.; Idelevich, A.; Regev, O.; Lapsker, I.; Lewitus, D.Y.; Zak, A. Reinforcement of poly (methyl methacrylate) by WS<sub>2</sub> nanotubes towards antiballistic applications. *Compos. Sci. Technol.* **2021**, *207*, 108736. [[CrossRef](#)]
32. Zohar, E.; Baruch, S.; Shneider, M.; Dodiuk, H.; Kenig, S.; Tenne, R.; Wagner, H.D. The effect of WS<sub>2</sub> nanotubes on the properties of epoxy-based nanocomposites. *J. Adhes. Sci. Technol.* **2011**, *25*, 1603–1617. [[CrossRef](#)]
33. Šupová, M. Problem of hydroxyapatite dispersion in polymer matrices: A review. *J. Mater. Sci. Mater. Med.* **2009**, *20*, 1201–1213. [[CrossRef](#)]
34. Kim, H.-W.; Kim, H.-E. Nanofiber generation of hydroxyapatite and fluor-hydroxyapatite bioceramics. *J. Biomed. Mater. Res. Part B Appl. Biomater.* **2006**, *77B*, 323–328. [[CrossRef](#)]
35. Naffakh, M.; Díez-Pascual, A.M. WS<sub>2</sub> inorganic nanotubes reinforced Poly(L-lactic acid)/hydroxyapatite hybrid composite biomaterials. *RSC Adv.* **2015**, *5*, 65514–65525. [[CrossRef](#)]
36. Shalom, H.; Sui, X.M.; Elianov, O.; Brumfeld, V.; Rosentsveig, R.; Pinkas, I.; Feldman, Y.; Kampf, N.; Wagner, H.D.; Lachman, N.; et al. Nanocomposite of Poly(L-lactic acid) with inorganic nanotubes of WS<sub>2</sub>. *Lubricants* **2019**, *7*, 28. [[CrossRef](#)]
37. Stares, S.L.; Fredel, M.C.; Aragones, A.; Gutmanas, E.Y.; Gotman, I.; Greil, P.; Travitzky, N. PLLA/HA composite laminates. *Adv. Eng. Mater.* **2013**, *15*, 1122–1124. [[CrossRef](#)]
38. Albano, C.; González, G.; Palacios, J.; Karam, A.; Covis, M. PLLA-HA vs. PLGA-HA characterization and comparative analysis. *Polym. Compos.* **2013**, *34*, 1433–1442. [[CrossRef](#)]
39. Chithaiah, P.; Ghosh, S.; Idelevich, A.; Rovinsky, L.; Livneh, T.; Zak, A. Solving the “MoS<sub>2</sub> nanotubes” synthetic enigma and elucidating the route for their catalyst-free and scalable production. *ACS Nano* **2020**, *14*, 3004–3016. [[CrossRef](#)]
40. Pawley, G.S. Unit-cell refinement from powder diffraction scans. *J. Appl. Crystallogr.* **1981**, *14*, 357–361. [[CrossRef](#)]
41. Li, X.; Bhushan, B. A review of nanoindentation continuous stiffness measurement technique and its applications. *Mater. Charact.* **2002**, *48*, 11–36. [[CrossRef](#)]
42. Oliver, W.C.; Pharr, G.M. An improved technique for determining hardness and elastic modulus using load and displacement sensing indentation experiments. *J. Mater. Res.* **1992**, *7*, 1564–1583. [[CrossRef](#)]
43. Carrasco, F.; Pagès, P.; Gámez-Pérez, J.; Santana, O.O.; Maspoch, M.L. Processing of Poly(lactic acid): Characterization of chemical structure, thermal stability and mechanical properties. *Polym. Degrad. Stab.* **2010**, *95*, 116–125. [[CrossRef](#)]
44. Ero-Phillips, O.; Jenkins, M.; Stamboulis, A. Tailoring crystallinity of electrospun PLLA fibers by control of electrospinning parameters. *Polymers* **2012**, *4*, 1331–1348. [[CrossRef](#)]
45. Naffakh, M.; Marco, C.; Ellis, G. Development of novel melt-processable biopolymer nanocomposites based on Poly(L-lactic acid) and WS<sub>2</sub> inorganic nanotubes. *CrystEngComm* **2014**, *16*, 5062. [[CrossRef](#)]
46. Wichmann, M.H.G.; Schulte, K.; Wagner, H.D. On nanocomposite toughness. *Compos. Sci. Technol.* **2008**, *68*, 329–331. [[CrossRef](#)]
47. Johnsen, B.B.; Kinloch, A.J.; Mohammed, R.D.; Taylor, A.C.; Sprenger, S. Toughening mechanisms of nanoparticle-modified epoxy polymers. *Polymer* **2007**, *48*, 530–541. [[CrossRef](#)]
48. Shi, X.; Wang, S.; Wen, S.; Shen, M.; Guo, R.; Cao, X.; Wang, J. Aminopropyltriethoxysilane-mediated surface functionalization of hydroxyapatite nanoparticles: Synthesis, characterization, and in vitro toxicity assay. *Int. J. Nanomed.* **2011**, *6*, 3449–3459. [[CrossRef](#)]
49. Yang, Z.; Dong, B.; Huang, Y.; Liu, L.; Yan, F.-Y.; Li, H.-L. A study on carbon nanotubes reinforced Poly(methyl methacrylate) nanocomposites. *Mater. Lett.* **2005**, *59*, 2128–2132. [[CrossRef](#)]
50. Nyanor, P.; El-Kady, O.; Yehia, H.M.; Hamada, A.S.; Nakamura, K.; Hassan, M.A. Effect of carbon nanotube (CNT) content on the hardness, wear resistance and thermal expansion of in-situ reduced graphene oxide (rGO)-Reinforced aluminum matrix composites. *Met. Mater. Int.* **2019**, *27*, 1315–1326. [[CrossRef](#)]
51. Shneider, M.; Dodiuk, H.; Tenne, R.; Kenig, S. Nanoinduced morphology and enhanced properties of epoxy containing tungsten disulfide nanoparticles. *Polym. Eng. Sci.* **2013**, *53*, 2624–2632. [[CrossRef](#)]
52. Zamiri, A.; De, S. Mechanical properties of hydroxyapatite single crystals from nanoindentation data. *J. Mech. Behav. Biomed. Mater.* **2011**, *4*, 146–152. [[CrossRef](#)]
53. George, W. Effect of nucleating agents on physical-mechanical properties. In *Handbook of Nucleating Agents*; Elsevier: Amsterdam, The Netherlands, 2016; pp. 205–215. ISBN 978-1-895198-93-5.
54. Zia, Q.; Androsch, R.; Radusch, H.-J.; Piccarolo, S. Morphology, reorganization and stability of mesomorphic nanocrystals in isotactic polypropylene. *Polymer* **2006**, *47*, 8163–8172. [[CrossRef](#)]



55. Mollova, A.; Androsch, R.; Mileva, D.; Gahleitner, M.; Funari, S.S. Crystallization of isotactic polypropylene containing beta-phase nucleating agent at rapid cooling. *Eur. Polym. J.* **2013**, *49*, 1057–1065. [[CrossRef](#)]
56. Starkweather, H.W.; Moore, G.E.; Hansen, J.E.; Roder, T.M.; Brooks, R.E. Effect of crystallinity on the properties of nylons. *J. Polym. Sci.* **1956**, *21*, 189–204. [[CrossRef](#)]
57. Stuart, B.H.; Briscoe, B.J. The effect of crystallinity on the scratch hardness of Poly(ether ether ketone). *Polymer* **1996**, *37*, 3819–3824. [[CrossRef](#)]
58. Dos Santos, B.B.; Pita, V.J.; da Costa, M.F. Characterization of properties of Poly(vinylidene fluoride) using instrumented microindentation test. *Macromol. Symp.* **2020**, *394*, 2000136. [[CrossRef](#)]
59. Naik, S.N.; Walley, S.M. The Hall–Petch and inverse Hall–Petch relations and the hardness of nanocrystalline metals. *J. Mater. Sci.* **2019**, *55*, 2661–2681. [[CrossRef](#)]
60. Gupta, S.; Dixit, M.; Baboo, M.; Sharma, K.; Saxena, N.S. Thickness-dependent mechanical behaviour of aluminium-coated polyethylene terephthalate (pet) films. *Polym.-Plast. Technol. Eng.* **2009**, *48*, 1333–1337. [[CrossRef](#)]
61. Suzuki, T.; Ei, A.; Takada, Y.; Uehara, H.; Yamanobe, T.; Takahashi, K. Modification of physical properties of poly(L-lactic acid) by addition of methyl- $\beta$ -cyclodextrin. *Beilstein J. Org. Chem.* **2014**, *10*, 2997–3006. [[CrossRef](#)]
62. Furukawa, T.; Sato, H.; Murakami, R.; Zhang, J.; Noda, I.; Ochiai, S.; Ozaki, Y. Raman microspectroscopy study of structure, dispersibility, and crystallinity of poly(hydroxybutyrate)/Poly(L-lactic Acid) blends. *Polymer* **2006**, *47*, 3132–3140. [[CrossRef](#)]
63. Ciobanu, C.S.; Iconaru, S.L.; Massuyeau, F.; Constantin, L.V.; Costescu, A.; Predoi, D. Synthesis, structure, and luminescent properties of europium-doped hydroxyapatite nanocrystalline powders. *J. Nanomater.* **2012**, *2012*, 61. [[CrossRef](#)]
64. Viršek, M.; Jesih, A.; Milošević, I.; Damnjanović, M.; Remškar, M. Raman scattering of the MoS<sub>2</sub> and WS<sub>2</sub> single nanotubes. *Surf. Sci.* **2007**, *601*, 2868–2872. [[CrossRef](#)]
65. Masanari, O. Hyper-Raman spectroscopy of polar liquids excited at 1064 nm: Acetone, acetonitrile, chloroform, and dimethyl sulfoxide. *J. Chem. Phys.* **2020**, *152*, 174202.
66. Gonçalves, C.; Gonçalves, I.; Magalhães, F.; Pinto, A. Poly(lactic acid) composites containing carbon-based nanomaterials: A review. *Polymers* **2017**, *9*, 269. [[CrossRef](#)] [[PubMed](#)]
67. Sun, J.; Li, H.; Wang, C.; Yuan, D.; Stubbs, L.P.; He, C. The effect of residual solvent N,N'-Dimethylformamide on the curing reaction and mechanical properties of epoxy and lignin epoxy composites. *Macromol. Chem. Phys.* **2016**, *217*, 1065–1073. [[CrossRef](#)]
68. Fugolin, A.P.; Dobson, A.; Ferracane, J.L.; Pfeifer, C.S. Effect of residual solvent on performance of acrylamide-containing dental materials. *Dent. Mater.* **2019**, *35*, 1378–1387. [[CrossRef](#)]
69. Grinberg, O.; Deng, S.; Zussman, E.; Livneh, T.; Zak, A. Raman scattering from single WS<sub>2</sub> nanotubes in stretched PVDF electrospun fibers. *Phys. Chem. Chem. Phys.* **2017**, *19*, 18443–18451. [[CrossRef](#)] [[PubMed](#)]
70. De Gelder, J.; De Gussem, K.; Vandenabeele, P.; Moens, L. Reference database of Raman spectra of biological molecules. *J. Raman Spectrosc.* **2007**, *38*, 1133–1147. [[CrossRef](#)]
71. Thangaraju, E.; Srinivasan, N.T.; Kumar, R.; Sehgal, P.K.; Rajiv, S. Fabrication of electrospun poly L-lactide and curcumin loaded poly L-lactide nanofibers for drug delivery. *Fibers Polym.* **2012**, *13*, 823–830. [[CrossRef](#)]
72. Murugesan, M.; Krishnamurthy, V.; Hebalkar, N.; Devanesan, M.; Nagamony, P.; Palaniappan, M.; Krishnaswamy, S.; Yuan, A. Nano-hydroxyapatite (HAp) and hydroxyapatite/platinum (HAp/Pt) core shell nanorods: Development, structural study, and their catalytic activity. *Can. J. Chem. Eng.* **2020**, *99*, 268–280. [[CrossRef](#)]
73. O'Neal, K.R.; Cherian, J.G.; Zak, A.; Tenne, R.; Liu, Z.; Musfeldt, J.L. High pressure vibrational properties of WS<sub>2</sub> nanotubes. *Nano Lett.* **2016**, *16*, 993–999. [[CrossRef](#)]
74. Shalom, H.; Kapishnikov, S.; Brumfeld, V.; Naveh, N.; Tenne, R.; Lachman, N. Strong, Tough and bio-degradable polymer-based 3D-ink for fused filament fabrication (FFF) using WS<sub>2</sub> nanotubes. *Sci. Rep.* **2020**, *10*, 8892. [[CrossRef](#)]
75. Kalhapure, R.S.; Akamanchi, K.G. A novel biocompatible bicephalous dianionic surfactant from oleic acid for solid lipid nanoparticles. *Colloids Surf. B Biointerfaces* **2013**, *105*, 215–222. [[CrossRef](#)] [[PubMed](#)]
76. Venkatesan, J.; Kim, S.-K. Nano-hydroxyapatite composite biomaterials for bone tissue engineering—A review. *J. Biomed. Nanotechnol.* **2014**, *10*, 3124–3140. [[CrossRef](#)]
77. Tang, D.-M.; Wei, X.; Wang, M.-S.; Kawamoto, N.; Bando, Y.; Zhi, C.; Mitome, M.; Zak, A.; Tenne, R.; Golberg, D. Revealing the anomalous tensile properties of WS<sub>2</sub> nanotubes by in situ transmission electron microscopy. *Nano Lett.* **2013**, *13*, 1034–1040. [[CrossRef](#)] [[PubMed](#)]
78. Loffredo, F.; Tammaro, L.; Di Luccio, T.; Borriello, C.; Villani, F.; De Vito, S.; Ramachandran, K.; Kornfield, J.A. Effect of tungsten disulfide nanotubes on crystallization of polylactide under uniaxial deformation and annealing. *Funct. Compos. Mater.* **2021**, *2*, 3. [[CrossRef](#)]
79. Tammaro, L.; Di Luccio, T.; Borriello, C.; Loffredo, F.; Ramachandran, K.; Villani, F.; Di Benedetto, F.; Schiller, T.; Minarini, C.; Kornfield, J.A. Effect of tungsten disulfide (WS<sub>2</sub>) nanotubes on structural, morphological and mechanical properties of poly(L-lactide) (PLLA) films. In *AIP Conference Proceedings*; AIP Publishing LLC: Melville, NY, USA, 2018; Volume 1981, p. 020073.
80. Samantaray, P.K.; Little, A.; Haddleton, D.M.; McNally, T.; Tan, B.; Sun, Z.; Huang, W.; Ji, Y.; Wan, C. Poly(glycolic acid) (PGA): A versatile building block expanding high performance and sustainable bioplastic applications. *Green Chem.* **2020**, *22*, 4055–4081. [[CrossRef](#)]
81. Naffakh, M. Biopolymer nanocomposite materials based on Poly(L-lactic acid) and inorganic fullerene-like WS<sub>2</sub> nanoparticles. *Polymers* **2021**, *13*, 2947. [[CrossRef](#)] [[PubMed](#)]

## Article

# Multifunctional, Robust, and Porous PHBV—GO/MXene Composite Membranes with Good Hydrophilicity, Antibacterial Activity, and Platelet Adsorption Performance

Yuandong Wu<sup>1,2</sup>, Weishuang Zheng<sup>1,2</sup>, Yinan Xiao<sup>1,2</sup>, Beining Du<sup>1,2</sup>, Xingru Zhang<sup>1,2</sup>, Min Wen<sup>1,2</sup>, Chen Lai<sup>1,2</sup>, Yi Huang<sup>1,2,3</sup> and Liyuan Sheng<sup>1,2,\*</sup>

<sup>1</sup> Shenzhen Institute, Peking University, Shenzhen 518057, China; wuyd@ier.org.cn (Y.W.); zhengws@ier.org.cn (W.Z.); xiaoyin@ier.org.cn (Y.X.); bndu10s@alum.imr.ac.cn (B.D.); zhangxr@ier.org.cn (X.Z.); min.wen@siat.ac.cn (M.W.); laic@ier.org.cn (C.L.); yhuang@pku.edu.cn (Y.H.)

<sup>2</sup> PKU-HKUST Shenzhen-Hong Kong Institution, Shenzhen 518057, China

<sup>3</sup> School of Environmental Science and Engineering, Peking University, Beijing 100871, China

\* Correspondence: lysheng@yeah.net

**Citation:** Wu, Y.; Zheng, W.; Xiao, Y.; Du, B.; Zhang, X.; Wen, M.; Lai, C.; Huang, Y.; Sheng, L. Multifunctional, Robust, and Porous PHBV—GO/MXene Composite Membranes with Good Hydrophilicity, Antibacterial Activity, and Platelet Adsorption Performance. *Polymers* **2021**, *13*, 3748. <https://doi.org/10.3390/polym13213748>

Academic Editors: José Miguel Ferri, Vicent Fombuena Borràs and Miguel Fernando Aldás Carrasco

Received: 23 September 2021

Accepted: 26 October 2021

Published: 29 October 2021

**Publisher's Note:** MDPI stays neutral with regard to jurisdictional claims in published maps and institutional affiliations.



**Copyright:** © 2021 by the authors. Licensee MDPI, Basel, Switzerland. This article is an open access article distributed under the terms and conditions of the Creative Commons Attribution (CC BY) license (<https://creativecommons.org/licenses/by/4.0/>).

**Abstract:** The limitations of hydrophilicity, strength, antibacterial activity adsorption performance of the biobased and biocompatible polymer materials, such as polyhydroxyalkanoates (PHAs), significantly restrict their wider applications especially in medical areas. In this paper, a novel composite membrane with high antibacterial activity and platelet adsorption performance was prepared based on graphene oxide (GO), MXene and 3-hydroxybutyrate-co-hydroxyvalerate (PHBV), which are medium-chain-length-copolymers of PHA. The GO/MXene nanosheets can uniformly inset on the surface of PHBV fibre and give the PHBV—GO/MXene composite membranes superior hydrophilicity due to the presence of hydroxyl groups and terminal oxygen on the surface of nanosheets, which further provides the functional site for the free radical polymerization of ester bonds between GO/MXene and PHBV. As a result, the tensile strength, platelet adsorption, and blood coagulation time of the PHBV—GO/MXene composite membranes were remarkably increased compared with those of the pure PHBV membranes. The antibacterial rate of the PHBV—GO/MXene composite membranes against gram-positive and gram-negative bacteria can reach 97% due to the antibacterial nature of MXene. The improved strength, hydrophilicity, antibacterial activity and platelet adsorption performance suggest that PHBV—GO/MXene composite membranes might be ideal candidates for multifunctional materials for haemostatic applications.

**Keywords:** MXene; PHBV; composite membrane; hydrophilicity; antibacterial properties; coagulation

## 1. Introduction

All countries are aware of the serious environmental problems caused by white pollution with the rapid development of the national economy, especially the petrochemical industry [1–4]. Every year, the amount of plastic waste that is difficult to recycle reaches tens of millions of tons [5,6]. China has already committed to achieving peak emissions of carbon dioxide before 2030 and carbon neutrality before 2060 [7,8]. The government urged quicker steps to take actions that enabled the peak of emissions [9]. It is necessary that the government accelerates bolstering the development of the green industry [10,11]. Hence, the widespread use of biodegradable materials is expected.

At present, biodegradable materials such as (1) natural polymer materials derived from chitosan, cellulose, and starch [12–14]; (2) synthetic materials such as poly (glycolic acid) (PGA), poly (lactic acid) (PLA), poly (butylene succinate) (PBS), copolymer of aliphatic polyester, and polyamide (CPAE) [15–17]; and (3) microbial synthetic materials such as polyhydroxyalkanoate (PHAs) [18–20] have attracted widespread attention. Due to its good biocompatible and biodegradable properties [21,22], polyhydroxyalkanoate (PHAs)

generated by bacteria growing under oligotrophic conditions is considered a promising haemostatic material and has attracted extensive attention from medical biomaterial researchers [21–23].

PHA is a kind of thermoplastic polyester synthesized by prokaryotes as a carbon source and energy storage under the carbon and nitrogen imbalance condition [24,25]. Poly(3-hydroxybutyrate) (PHB), discovered by M. Lemoigne in 1925, was the first-generation product in the PHAs family [26,27]. At least 150 different monomer structures of PHA have been discovered to date [28–32]. The medium-chain-length-copolymers poly(3-hydroxybutyrate-co-hydroxyvalerate) (PHBV) and poly(3-hydroxybutyrate-co-hydroxyhexanoate) (PHBHHx) are the latest generation products in the PHAs family, with improved toughness and processability. However, the tensile strength and adsorption performance of PHBV and PHBHHx still need to be further improved to achieve the application requirements of haemostatic materials [21]. Moreover, fewer functional features, such as poor antibacterial and hydrophilic capacity, further limit PHAs applications, especially in biomedical materials [4,21]. PHAs-based materials have been widely applied in the fields of biomedicine, such as biodegradable sutures, bone tissue engineering and drug-loaded applications [21,33–35]. However, few investigators studied PHAs-based materials to simultaneously solve the problems of surgical wound haemostasis. Vigneswari et al. prepared nanofibrous P(3HB-Co-4HB)/collagen peptide constructs using an electrospinning system and the results indicate that these PHAs-based composites may be a potential leave-on wound dressing but have insufficient antimicrobial activity and hydrophilic capacity [36].

In recent years, these problems have led to a new breakthrough with the rapid development of nanotechnology. Graphene oxide (GO) is a novel two-dimensional material with high hydrophilicity and excellent mechanical performance and has considerable good potential for preparing high-performance polymer nanocomposites [4,37,38]. Abundance of oxygenic groups of GO can provide binding sites with organic polymer matrices, such as PHAs [4]. The poor dispersibility makes the GO sheets agglomerate and results in poor adhesion between GO and PVAs, which gives polyvinyl acetate and GO (PVA—GO) composites good tensile strength but low breaking elongation [39]. Some investigators further improved the dispersion of GO in polymers through chemical and physical modifications [4,40]. Niyogl et al. found that GO modified via alkylamine can give GO good dispersion in organic solutions [41]. The ball milling of GO can improve the dispersibility in PHBV and develop PHBV—graphene nanocomposites with good tensile properties [42]. Xu et al. fabricated PHA films with good tensile and antibacterial activity by grafting them with functionalized GO [4]. These studies confirmed that GO could be loaded in as a polymer as nanofiller to improve the mechanical performance of organic polymers, which is critical to improving the performance of polymers and GO composites. However, few investigations have discussed the prospects of GO as a multifunctional nanofiller to simultaneously enhance the tensile, hydrophilic, and antimicrobial properties of PHAs for haemostatic materials.

Mxenes, first discovered by Naguib et al. in 2011 [43], are a developing novel material family of two-dimensional (2D) materials with a formula of  $M_{n+1}X_nT_x$ , which are composed of transition metals (M), carbides/nitrides (X), and functional groups such as hydroxyl, oxygen or fluorine (X) [44–46]. The presence of hydroxyl groups or terminal oxygen on the surface gives MXene materials more application prospects, such as high hydrophilicity and processability [47]. The laminar structure and hydrophilicity give MXene materials rapid and selective delivery of water molecules. Many investigations also revealed that MXene materials obtain high permeable flux. In addition, some investigators have confirmed that MXene nanosheets have antibacterial properties and that the sharp edges of MXene nanosheets lead to the release of bacterial DNA [48].

This study attempts to describe the development and detection of a novel PHBV—GO/MXene composite membrane with improved mechanical properties, antibacterial abilities, high hydrophilicity, and adsorption capacity. These characteristics make the PHBV—GO/MXene composite membrane an ideal material for biodegradable haemostatic

applications. Various contents of GO and MXene have been blended with PHBV to prepare PHBV—GO/MXene composite membranes by electrostatic spinning techniques. The mechanical properties, microscopic morphology, physical properties, antibacterial properties, and adsorption properties of the composites were analysed. Therefore, the investigation aimed to provide a biodegradable haemostatic material with good mechanical properties, excellent antibacterial abilities, high hydrophilicity, and adsorption capacity.

## 2. Materials and Methods

### 2.1. Materials

PHBV containing 92.3 mol% 3-hydroxybutyrate and 7.7 mol% hydroxyvalerate was bacterially synthesized.  $Ti_3AlC_2$  MAX powders, graphite, methylene chloride (DCM), sulfuric acid ( $H_2SO_4$ ), hydrochloric acid (HCl), potassium permanganate ( $KMnO_4$ ), 40% HF, hydrogen peroxide ( $H_2O_2$ ), and lithium fluoride (LiF) were obtained from Shanghai Aladdin Bio-Chem Corporation (Shanghai, China). Deionized (DI) water was produced by a Milli-Q HX 7040 water system (Burlington, MA, USA). All reagents without special instructions were of analytical grade.

### 2.2. Synthesis of Graphene Oxide (GO) and MXene ( $Ti_3C_2T_x$ )

The preparation method of GO used the Hummers' method [49].

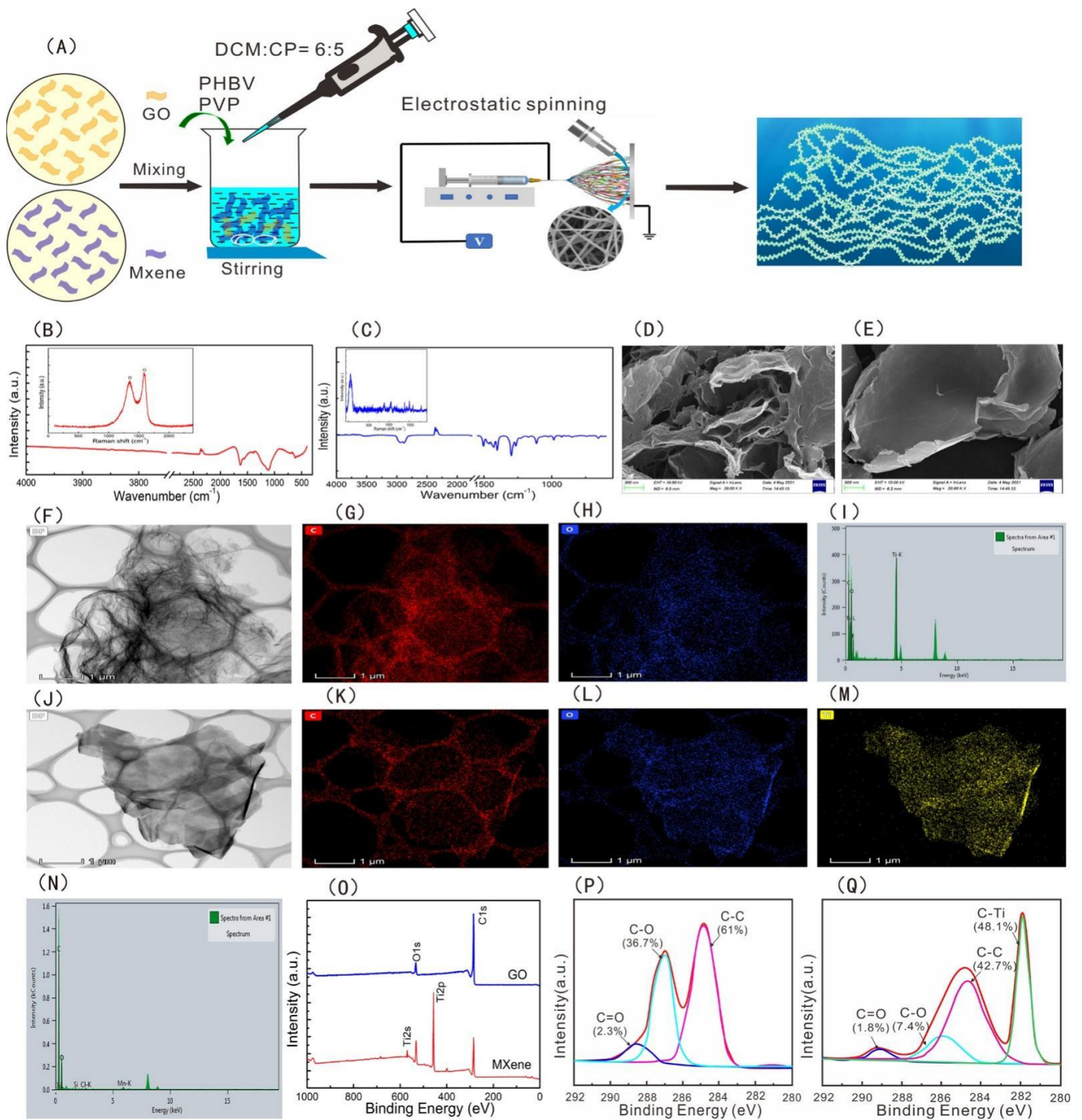
MXenes are mainly synthesized from MAX precursors. Two grams of  $Ti_3AlC_2$  MAX phase powder was slowly added to 2 g LiF, and 20 mL 9 M HCl [37] and stirred by magnetic stirrers for 24 h at 35 °C. The products were washed until the pH values of the solutions reached 6, using DI water with centrifugation at 3500 rpm for 5 min per cycle. The sediment was  $Ti_3CT_x$  and needed to be shaken vigorously for approximately 10 min. Finally, the unexfoliated sheets were removed via centrifugation at 3500 rpm for 1 h. Then, the concentration of MXene solution reached 1 mg/mL.

### 2.3. Electrospinning of Composite Membranes

PVP, a water-soluble polymer, was added before electrospinning to promote pore formation to avoid the swathing of GO and MXene nanoparticles in PHBV fibre mats. PHBV and PVP were dissolved in solvents containing DCM and acetone (6:5 *v:v*) along with 0.5% and 1% nanoparticles with a GO/MXene mass ratio of a 1/4 to prepare porous electrospun fibres. Some investigations suggested that the composite membrane with a 1/4 GO/MXene ratio had good water flux [37], which may help improve the hydrophilicity and adsorption capacity of PHBV—GO/MXene composite membranes. The weight percentage of PHBV and PVP was 5:1. The mixed solution was magnetically stirred for 18 h and then a 6 mL syringe filled with homogenous polymer solutions was connected to a needle. The electrospinning conditions were 25 kV voltage, 0.1 mL/h speed and 15 cm width between two parallel plates. The electrospinning process continued for 10 h at 25 °C and 60% relative humidity. After electrospinning, PVP was removed by washing it with water at 70 °C and ultrasonic treatment. Finally, the washed fibre mats were dried in a vacuum (Figure 1A).

### 2.4. Characterization Methods

The surface morphologies of the fibre mats were examined by field emission scanning electron microscopy (FE-SEM, Merlin, Berlin, Germany). Transmission electron microscopy (TEM, JEOL Ltd., Tokyo, Japan), Alpha 300M Raman spectrometry (WITec, Berlin, Germany), energy spectroscopy (EDS, Oxford, London, UK), BRUKER D8 Advance (Berlin, Germany), Frontier FT-IR Spectrometer (Berlin, Germany), Thermo Fisher Scientific K-Alpha (Waltham, MA, USA), and DSA100 (Berlin, Germany) were used to obtain insight into the microstructure and composition of PHBV—GO/MXene composite membranes.



**Figure 1.** Schematic diagram of preparation of the PHBV—GO/MXene composite membranes (A), FT-IR and Raman spectra of GO (B), and MXene (C); SEM images of GO (D) and MXene (E). TEM analysis of GO (F) and MXene (J). Distribution of elements: C for GO (G), O for GO (H), C for MXene (K), O for MXene (L), and C for MXene (M). The element composition of GO (N) and MXene (I). XPS spectra of GO and MXene (O). C1s XPS spectra of GO (P) and MXene (Q).

### 2.5. Platelet Adsorption Experiments

The haemostatic performance of the PHBV and PHBV—GO/MXene composite membranes was evaluated by platelet adsorption and blood coagulation. The blood of healthy rabbit with 3.8% anticoagulant sodium citrate (2:8) was used to make platelet-rich plasma (PRP). A Thermo Scientific centrifuge was used to centrifuge with 1500 rpm at 4 °C and hold 10 min. 5 cm<sup>2</sup> PHBV and PHBV—GO/MXene composite membranes were dropped

in 5 mL of PRP at 37 °C. Platelets were detected before and after adsorption using platelet analyzer. Three parallel experiments were carried out. Blood coagulation time was detected using the method of Wu et al. (2013) [50].

### 2.6. Method of the Antibacterial Activity Test

The antibacterial experiment of PHBV—MXene composite membranes were divided into PHBV, PHBV—GO/MXene 0.1%, PHBV—GO/MXene 0.5%, PHBV—GO/MXene 1%, and the blank group against *E. coli* and *S. aureus*. The composition of luria broth (LB) solid medium is: 10 g/L peptone, 10 g/L NaCl, 5.0 g/L beef extract, and 20% agar powder. The dosages of PHBV, PHBV—GO/MXene 0.1%, PHBV—GO/MXene 0.5%, and PHBV—GO/MXene 1% composite membranes were 10 mg. The bacteria used here were *E. coli* (ATCC 25922) and *S. aureus* (ATCC 6538). The liquid LB medium was used for cultures *E. coli* and *S. aureus* at 37 °C and 200 rpm. Bacteria growth kinetics was measured using the optical density (OD) of bacteria suspensions at 600 nm. Bacteria with 0.1 OD<sub>600</sub> (10<sup>8</sup>CFU/mL), which indicate the *E. coli* and *S. aureus* were in an exponential phase, were used to perform thentibacterial activity test. A measured 10 mg composite membranes and 10μL bacterial solution were evenly smeared on the surface of solid LB medium. Then culture dishes with bacteria and composite membranes were cultivated for 24 h at 37 °C in a microbiological incubator. The camera took pictures of the culture dishes after culture and identified the number of bacteria colony.

The antibacterial activity against *E. coli* ( $\alpha$ ) and *S. aureus* ( $\beta$ ) of PHBV and PHBV—GO/MXene composite membranes were calculated using Equations (1) and (2), respectively.

$$\alpha = \frac{C_t}{C_0} \times 100\% \quad (1)$$

$$\beta = \frac{D_t}{D_0} \times 100\% \quad (2)$$

where  $C_0$  and  $C_t$  are the colony numbers of *E. coli* in the blank group and experimental groups, respectively.  $D_t$  represents the colony numbers of *S. aureus* in experimental groups, and  $D_0$  represents the colony numbers of *S. aureus* in the blank group.

## 3. Results and Discussion

### 3.1. Characterization of GO and MXene Nanosheets

To observe the microscopic morphology characteristics of GO and MXene nanosheets, SEM and TEM were used. The microscopic morphology characteristics of the GO and MXene nanosheets are illustrated in Figure 1. The FT-IR spectral bands of GO showed characteristic peaks of C=O, and C–O–C stretching vibrations, which occur at 1715 cm<sup>-1</sup> and 1045 cm<sup>-1</sup>. (Figure 1B). The FT-IR spectra of MXene nanosheets appeared at 3423 cm<sup>-1</sup>, 2923 cm<sup>-1</sup>, 2848 cm<sup>-1</sup>, 1715 cm<sup>-1</sup>, and 1045 cm<sup>-1</sup>, which correspond to the –OH, C-H in benzene rings and alkane carbon chains, C=O, and C–O–C stretching vibration, respectively [37], mainly owing to the oxygenic groups on GO and MXene. GO had Raman characteristic peaks at 1365 cm<sup>-1</sup> and 1610 cm<sup>-1</sup>, belonging to the D peak and G peaks of carbon atomic crystals. The significance of the D peaks confirms the effective introduction of oxygenic groups into GO; the G peak is the stretching vibration of the graphene lattice [37]. Raman spectral bands appeared at 201 cm<sup>-1</sup> and 720 cm<sup>-1</sup>, which are the characteristic Raman peaks of MXene nanosheets [51].

The SEM images showed that the morphologies of the GO and MXene nanosheets are lamellar textures (Figure 1C,D), and the TEM images also indicated that the textures of GO and MXene nanosheets are lamellar (Figure 1F,J). X-ray photoelectron spectroscopy (XPS) and energy dispersive spectrometry (EDS) mapping illustrated that GO nanosheets are mainly composed of C and O elements, and MXene nanosheets contain C, O, and Ti elements (Figure 1K,L,N,O). The C1s XPS spectra further showed that GO was fitted into three peaks (C=O, C-O, and C-C) and that MXene had four peaks (C=O, C-O, C-C, and C-Ti) (Figure 1P,Q). The results suggested that there are plenty of hydrophilic groups,

for example, hydroxyl and carboxyl groups, located on nanosheets of GO and MXene surfaces. These factors may be helpful for improving the hydrophilic performance of PHBV.

### 3.2. Characterization of Composite Membranes

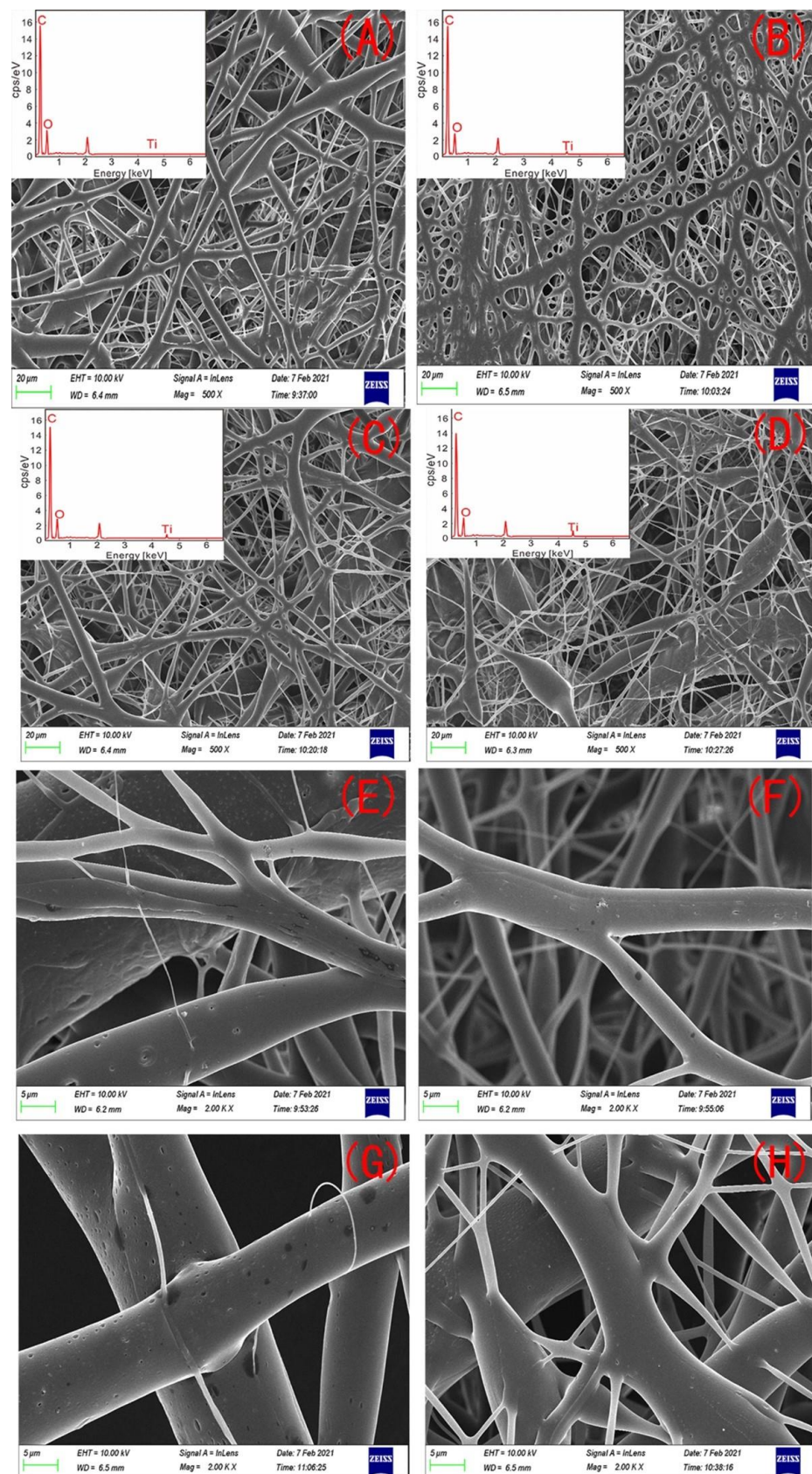
The microscopic morphology characteristics of the PHBV and PHBV—GO/MXene composite membranes were remarkably affected by the different GO/MXene dosages (Figure 1). The PHBV fibre had a smooth surface with many nanopores (Figure 1A,E). Elements of C and O are the main components (Figure 1A). So many three-dimensional (3D) nano-round pores may indicate that the PHBV—GO/MXene 0.1% composite membranes have good mechanical properties, because round holes can avoid stress concentrations (Figure 1B). The main elements of the PHBV—GO/MXene 0.1% composite membranes were still C and O, but the energy dispersive X-ray spectrometry (EDS) results showed that a certain amount of Ti was introduced by MXene (Figure 1B). PHBV—GO/MXene 0.5% composite membrane morphology is similar to that of PHBV (Figure 1A, C), but the elemental compositions of the PHBV—GO/MXene 0.5% composite membranes were C, O, and Ti (Figure 1C), similar to PHBV—GO/MXene 0.1% composite membranes (Figure 1B). A large number of fusiform structures and nanofibres with small diameters appearing simultaneously may indicate that the mechanical properties of PHBV—GO/MXene 1% composite membranes were poor (Figure 1D). The fusiform structures may be caused by abnormal turbulence during electrospinning due to the increase in solution viscosity [52]. Many Ti elements are contained in the PHBV—GO/MXene 1% composite membranes (Figure 1D). The dark patches on the surface of the fibres with 0.1% and 0.5% GO/MXene content likely indicate GO/MXene aggregation (Figure 1F,G). However, no dark patches on the surface of the fibres further suggested that the fusiform structures are the aggregate of GO/MXene in the PHBV—GO/MXene 1% composite membranes (Figure 1H).

The PHBV fibres had a diameter of  $4.32 \pm 1.93 \mu\text{m}$  (Figure 2A,E). Adding GO/MXene resulted in feature surface morphology (Figure 2B–D,F–H). PHBV—GO/MXene 0.1%, PHBV—GO/MXene 0.5%, and PHBV—GO/MXene 1% had diameters of  $3.23 \pm 2.06 \mu\text{m}$ ,  $3.16 \pm 2.43 \mu\text{m}$ , and  $1.36 \pm 2.06 \mu\text{m}$ , respectively (Table 1). The combined weight percentages of Ti in the PHBV—GO/MXene 0.1%, PHBV—GO/MXene 0.5%, and PHBV—GO/MXene 1% fibre mats were 0.07%, 0.28%, and 0.75%, respectively (Table 1). These weight percentages detected were lower than that of Ti addition. This may be due to the loss of mass in the fabrication process of the fibre mats and/or instrumental error.

**Table 1.** The element composition and properties of PHBV and PHBV—GO/MXene composite membranes.

	PHBV	PHBV—GO/MXene 0.1%	PHBV—GO/MXene 0.5%	PHBV—GO/MXene 1%
Element components% (C/O/Ti) <sup>a</sup>	79.03/20.97	77.26/21.82/0.07	75.22/23.05/0.28	75.63/23.38/0.75
Fibre diameter (FD) ( $\mu\text{m}$ ) <sup>b</sup>	$4.32 \pm 1.93$	$3.23 \pm 2.06$	$3.16 \pm 2.43$	$1.36 \pm 2.06$
Superficial area (SA) ( $\text{m}^2 \text{g}^{-1}$ ) <sup>c</sup>	16.75	/	45.51	24.46
Pore volume ( $\text{ml g}^{-1}$ ) <sup>d</sup>	0.023	/	0.051	0.035
Dimension (D) <sup>e</sup>	2.371	/	2.489	2.563
Isoelectric point (IEP)	4.23	/	4.02	3.74
Water contact angle ( $^\circ$ ) <sup>f</sup>	$130.0 \pm 2.3$	$54.2 \pm 3.1$	$62.2 \pm 1.8$	$55.9 \pm 2.8$

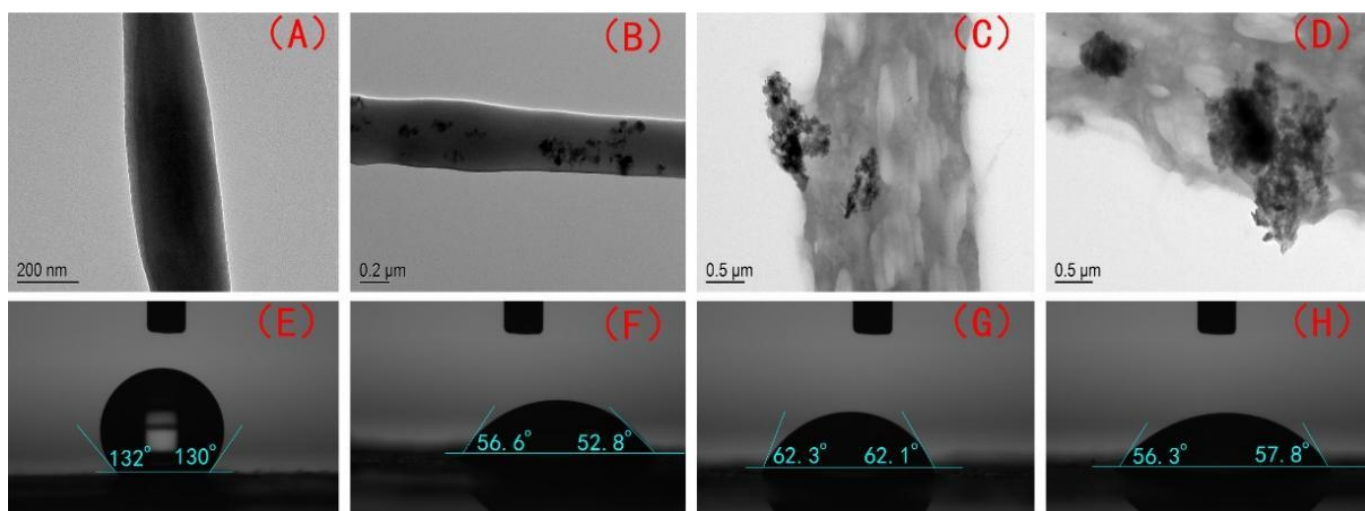
<sup>a</sup> detected by EDS. <sup>b</sup> based on tape measure in SEM images (Mean  $\pm$  SD). <sup>c</sup> based on BET. <sup>d</sup> NLDFT. <sup>e</sup> based on BET. <sup>f</sup> Angle (Mean  $\pm$  SD).



**Figure 2.** SEM images of PHBV (A,E), PHBV—GO/MXene 0.1% (B,F), PHBV—GO/MXene 0.5% (C,G), and PHBV—GO/MXene 1% (D,H) composite membranes. Inset figures show the EDS spectrum.



The morphologies of the PHBV and PHBV—GO/MXene composite membranes were also detected by TEM. Figure 3A–D shows the microscopic morphology characteristics of single PHBV and PHBV—GO/MXene fibres. Figure 3A presents the smooth surface of the PHBV fibre, while the surface of the PHBV—GO/MXene fibre has many dark patches (Figure 3B–D). The smooth surfaces of the PHBV and PHBV—GO/MXene fibres are consistent with the SEM observations (Figure 2F,G). These nano-GO/MXene embedded in the surface of the fibre nanosheets may act as active hydrophilic sites. The surface of PHBV fibres may help absorb platelets and accelerate blood coagulation for the hydrophobicity of PHBV [53–55].



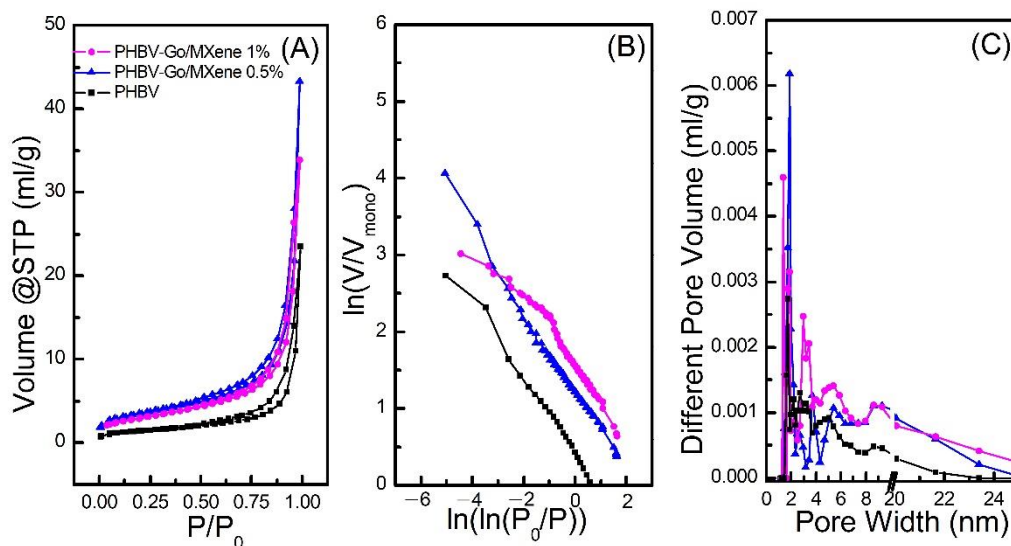
**Figure 3.** TEM images and water contact angle of PHBV (A,E), PHBV—GO/MXene 0.1% (B,F), PHBV—GO/MXene 0.5% (C,G), and PHBV—GO/MXene 1% (D,H) composite membranes.

The water contact angles ( $130.0 \pm 2.3^\circ$ , Table 1) of the PHBV composite membranes were similar to those reported for EPF mats [56] and PVDF membranes [52]. They were also lower than those of hydrophobic ZnO-containing fibre mats ( $152 \pm 3.0^\circ$ ) [57] and SiO<sub>2</sub>-containing fibre mats ( $160.5 \pm 2.3^\circ$ ) [58,59] but higher than those of PHBV—GO/MXene membranes (Table 1). The water contact angles of the PHBV—GO/MXene 0.1%, PHBV—GO/MXene 0.5%, and PHBV—GO/MXene 1% composite membranes were  $54.2 \pm 3.1^\circ$ ,  $62.2 \pm 1.8^\circ$ ,  $55.9 \pm 2.8^\circ$ , respectively (Table 1; Figure 3E–H). The water contact angles of the PHBV—GO/MXene composite membranes were not significantly different in present investigation. Many investigators also found similar results, where nanoparticles dosage did not dramatically change the water contact angle [56,60,61].

The better hydrophilicity of PHBV—GO/MXene composite membranes is due to the high amount of hydrophilic functional groups, as hydroxyl and carboxyl groups [37,62]. Moreover, the laminar flow structure of MXene nanosheets can rapidly and selectively transport water molecules [37,45], which further improves the hydrophilicity of PHBV—GO/MXene composite membranes. In addition, some investigations have also reported that increasing the interlayer spacing and introducing nanoparticles into MXene can further improve the water flux and antifouling properties [63,64]. Therefore, the interlayer spacing of MXene and the doping effect of GO and MXene are other reasons to enhance the hydrophilicity of PHBV—GO/MXene composite membranes.

BET-SA and PSD analyses were carried out to investigate the adsorption and pore characteristics of PHBV and PHBV—GO/MXene composite membranes. The results are illustrated in Figure 4. The isotherms of PHBV and PHBV—GO/MXene composite membranes showed hysteresis loops formed by the separation of adsorption—desorption curves (Figure 4A). Generally, a hysteresis loop occurs in the mesoporous materials [65,66]. Based on the thermodynamics principle, the formation of a hysteresis loop is related to the

difference in heat released and absorbed during the adsorption—desorption process [67,68]. According to the IUPAC classification criteria, the isotherms of the PHBV and PHBV—GO/MXene composite membranes were type I (Figure 4A), indicating a highly uniform pore size, good pore connectivity, rapid coagulation, and monolayer adsorption. Figure 4 also shows that the adsorbed  $N_2$  increased after the  $P/P_0$  rate increased from 0 to 0.9. Moreover, the highest separation of adsorption—desorption curves appeared at  $P/P_0 = 0.9$ , which confirms that many micropores consist of PHBV and PHBV—GO/MXene composite membranes. In addition, the more remarkable hysteresis loop further suggests that the proportion of micropores is higher in the PHBV—GO/MXene composite membrane than that in the PHBV composite membrane.



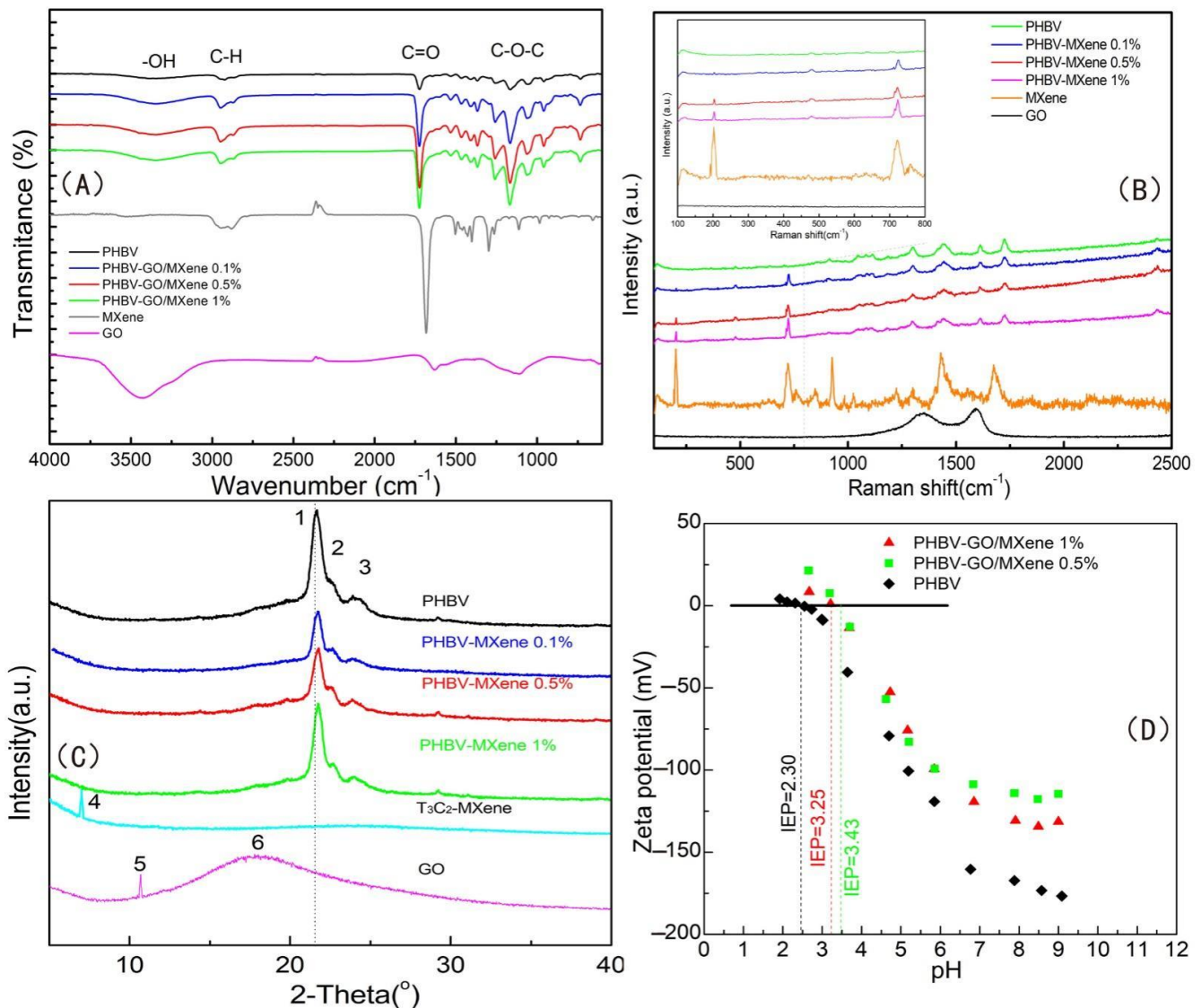
**Figure 4.** Plots of  $N_2$  adsorption—desorption (A),  $\ln(V/V_{mono})$  vs.  $\ln(P/P_0)$  (B) and pore diameter (C) distributions of PHBV, PHBV—GO/MXene 0.5%, and PHBV—GO/MXene 1% composite membranes.

The pure PHBV membranes had a  $16.75 \text{ m}^2 \text{ g}^{-1}$  surface area (SA) and  $0.023 \text{ cm}^{-3} \text{ g}^{-1}$  pore volume (PV) (Table 1; Figure 4A) and the peak  $N_2$  adsorption value was  $23.52 \text{ cm}^{-3} \text{ g}^{-1}$  at  $P/P_0 = 0.99$ . Notably,  $45.51 \text{ m}^2 \text{ g}^{-1}$  of SA,  $0.051 \text{ cm}^{-3} \text{ g}^{-1}$  of PV and  $43.23 \text{ cm}^{-3} \text{ g}^{-1}$  of the maximum  $N_2$  adsorption capacity indicate that the adsorption capacity of PHBV—GO/MXene 0.5% composite membranes was higher than that of PHBV—GO/MXene 1% composite membrane, which had  $24.46 \text{ m}^2 \text{ g}^{-1}$  of SA,  $0.035 \text{ cm}^{-3} \text{ g}^{-1}$  of PV and  $33.89 \text{ cm}^{-3} \text{ g}^{-1}$  of the maximum  $N_2$  adsorption capacity (Table 1; Figure 4A).

Furthermore, fractal dimension (D) was calculated to investigate the characteristics of pore structure in PHBV and PHBV—GO/MXene composite membrane, based on the Frenkel—Halsey—Hill (FHH) theory and the isotherms of the PHBV and PHBV—GO/MXene composite membrane (Figure 4B). The D value of the PHBV—GO/MXene 0.5% composite membrane was the maximum observed for the plots of  $\ln(V/V_{mono})$  vs.  $\ln(\ln(P_0/P))$ , however, the low plot range of  $\ln(V/V_{mono})$  vs.  $\ln(\ln(P_0/P))$  indicate that the pure PHBV composite membrane had the lowest D value. The D values of the PHBV—GO/MXene 0.5% composite membrane were similar to those of the pure PHBV composite membrane. The calculated D values of the PHBV, PHBV—GO/MXene 0.5%, and PHBV—GO/MXene 1% composite membranes were 2.371, 2.489, and 2.563, respectively, which further confirmed that the PHBV—GO/MXene composite membranes were structurally different and mainly contained mesopores and micropores. Figure 4C shows that most mesopores on the surface of the PHBV, PHBV—GO/MXene 0.5%, and PHBV—GO/MXene 1% composite membranes are 1–6 nm in diameter. The lowest amounts of pores with diameters larger than 6 nm confirm the higher proportion of micropores in the PHBV composite membrane. In addition, the 3D hierarchical architectures of the PHBV

and PHBV—GO/MXene composite membranes can provide active sites and may act as transmission paths that can accelerate the adsorption process.

Fourier transform infrared spectroscopy (Waltham, MA, USA), Raman spectroscopy (Berlin, Germany), X-ray diffraction (XRD) spectra (Waltham, MA, USA) and zeta potential ( $\xi$ ) (Waltham, MA, USA) values of the PHBV and PHBV—GO/MXene composite membranes were also obtained to investigate the surface chemistry of the composite membrane. Moreover, FT-IR, Raman, and XRD analyses of GO and MXene were performed as references. The results are illustrated in Figure 5.



**Figure 5.** FT-IR (A), Raman (B), and XRD (C) spectra of PHBV, GO, MXene, PHBV—GO/MXene 0.1%, PHBV—GO/MXene 0.5%, and PHBV—GO/MXene 1% composite membranes. Zeta potential (D) of PHBV, PHBV—GO/MXene 0.5%, and PHBV—GO/MXene 1% composite membranes.

The peak at  $\sim 3390 \text{ cm}^{-1}$  in the FT-IR spectrum of PHBV can be assigned to the stretching vibration of the hydroxyl (-OH) group (Figure 5A). The peaks appearing at 2921 and 2857  $\text{cm}^{-1}$  corresponded to the C-H stretching vibrations. The peaks at 1723 and 1050  $\text{cm}^{-1}$  can be assigned to the C=O stretching vibration and the C-O-C stretching vibration, respectively [4]. For pure GO, the broad band at  $\sim 3423 \text{ cm}^{-1}$  corresponded to the stretching vibration of hydroxyl -OH. The peaks at 2923 and 2848  $\text{cm}^{-1}$  corresponded to the C-H stretching vibrations (Figure 5A). The peaks at 1715 and 1045  $\text{cm}^{-1}$  corresponded

to the C=O stretching vibration and the C–O–C stretching vibration, respectively [37]. MXene nanosheets had strong C=O stretching vibrations in the carboxyl group, while the C–O–C stretching vibrations were weak (Figure 5A). The stretching vibration of –OH, C=O, and C–O–C increased with the mixing of GO/MXene into the PHBV–GO/MXene composite membrane, due to the oxygenic groups on the surface of GO and MXene.

Usually, the Raman spectral bands of GO showed two broad peaks between 1000 and 1800  $\text{cm}^{-1}$ . The peak appearing at high wavenumbers was the G-band, which usually appeared between 1500 and 1600  $\text{cm}^{-1}$ . The peak appearing at low wavenumbers was the D-band, which was generally located between 1300 and 1400  $\text{cm}^{-1}$ . The G-band is induced by crystalline graphitic/ $sp^2$  carbon atoms and involves out-of-phase intra-layer displacement in the graphene structure; the latter originates from  $sp^3$  hybridization and relates to polycrystalline imperfect graphite [66,69]. The peaks at 201 and 720  $\text{cm}^{-1}$  are the characteristic peaks of MXene [37,51]. Among them, the 201  $\text{cm}^{-1}$  peak was the symmetric out-of-plane vibration (A<sub>1g</sub>) of Ti and the 720  $\text{cm}^{-1}$  peak was the out-of-plane vibration (A<sub>1g</sub>) of C [51]. The peak range from 230 to 470  $\text{cm}^{-1}$  corresponded to the in-plane (E<sub>g</sub>) vibration of the surface groups around titanium atoms [51]. The peaks at 201 and 720  $\text{cm}^{-1}$  identifying MXene were more evident with increasing GO/MXene dosage in PHBV–GO/MXene composite membrane (Figure 5B). These results indicate that GO/MXene is effectively mixed into PHBV, which is consistent with the SEM and TEM results (Figures 3 and 4).

The XRD pattern of GO shows a broad band at 18.2° and a sharp peak at 10.7°, which are the characteristic peaks of GO [37]. The small peak at 7° is the characteristic peak of MXene [37]. In addition, the 7° peak also indicates that the sample has not been oxidized by air and is well preserved [70]. The peaks of 2 $\theta$  appearing at 21°, 22°, and 26° suggest that there were helical lamellae in the pure PHBV membrane. The crystal planes were (101), (111), and (121). The lower diffraction peaks of PHBV–GO/MXene may indicate that PHBV has a smaller crystal size (Figure 5C), which further suggests that GO/MXene modification may increase the molecular structure of the polymer and reduce the crystal forming ability of the PHBV molecule. The lower diffraction peaks also indicate that the grain size of PHBV in the PHBV–GO/MXene membrane is smaller than that in PHBV (Figure 5C). Therefore, the decrease in the crystallization index (CI) may suggest a significant improvement in the toughness of the PHBV–GO/MXene membrane due to the GO/MXene hybrid effect. In addition, the XRD peaks of the PHBV–GO/MXene membrane are shifted at high angles, which may indicate that GO/MXene enters the PHBV crystal. The higher diffraction peak of the PHBV–GO/MXene 1% composite membrane may be due to the agglomeration effect, resulting in a small amount of GO/MXene in the PHBV crystal, which has a high angle deflection and a strong diffraction peak.

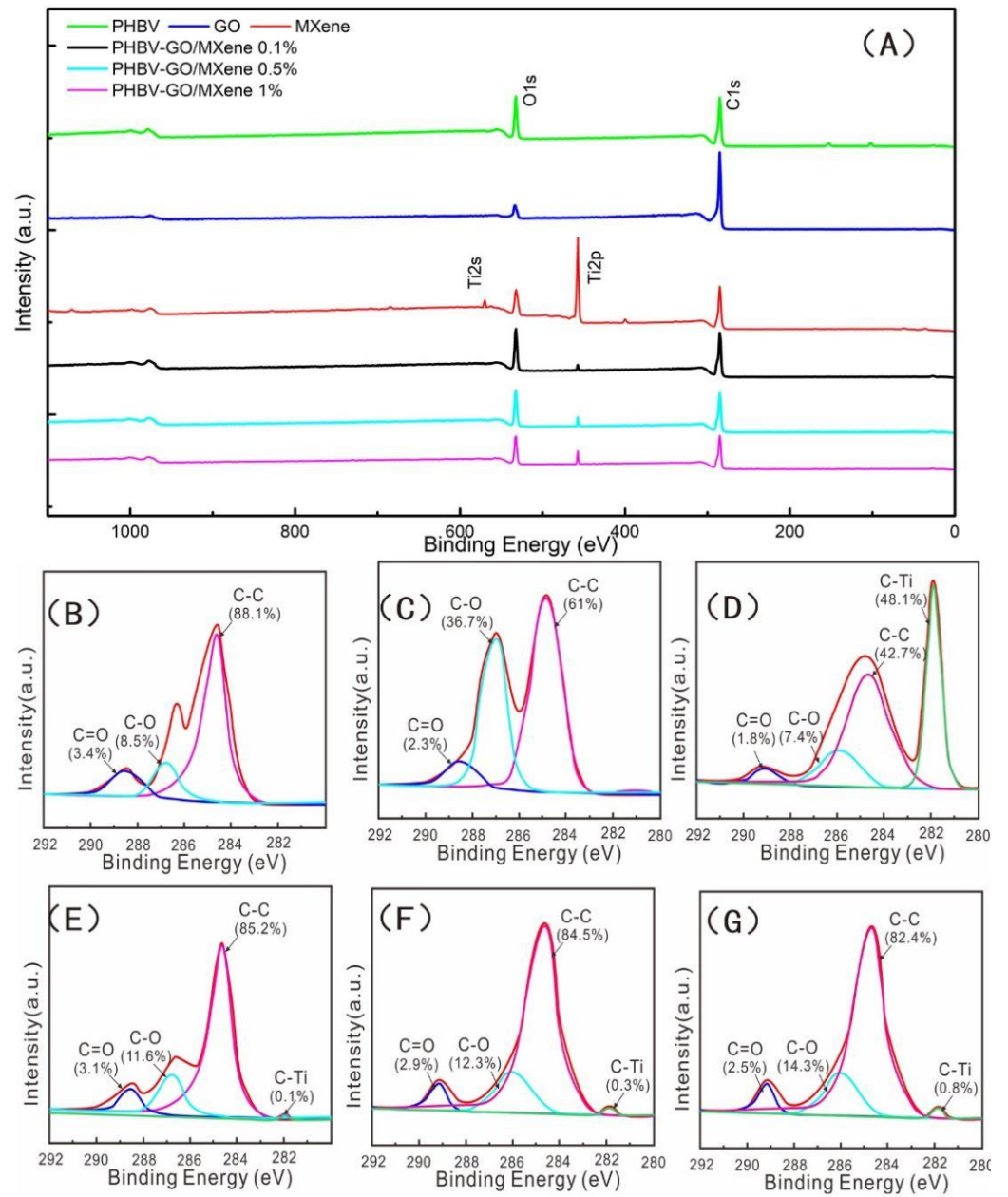
The zeta potential ( $\xi$ ) values of the PHBV and PHBV–GO/MXene composite membranes were detected within a pH range from 2 to 11 (Figure 5D). The  $\zeta$  values of the PHBV and PHBV–GO/MXene composite membranes decreased with increasing pH. The pure PHBV membranes were more negative than the PHBV–GO/MXene composite membranes (Figure 5D). The GO/MXene-functionalized PHBV membranes had remarkably different surface charge features and became less negative owing to the decreasing of carboxyl groups. Most of the carboxyl groups in GO/MXene reacted with oxhydroxyl groups in PHBV, forming C–O–C bonds, which was confirmed by the FT-IR analysis results (Figure 5A). Due to progressive deprotonation, the  $\zeta$  values of the PHBV and PHBV–GO/MXene composite membranes were less than zero. The isoelectric point (pI) values of PHBV appeared at 2.30. Moreover, the pI values of PHBV–GO/MXene 0.5% and PHBV–GO/MXene 1% composite membranes were 3.25 and 3.43, respectively. The remarkably different surface charge features of PHBV–GO/MXene composite membranes indicate that the incorporation of GO/MXene significantly enhanced the surface charge properties of PHBV. Some investigations have revealed that platelets are negatively charged [71,72]. GO/MXene addition reduces the electronegativity of PHBV (Figure 5D). Hence, the results of zeta potential analysis indicate that GO/MXene can enhance the adsorption capacity of the PHBV–

GO/MXene composite membrane towards platelets. These results may suggest that this kind of composite material has good application prospects for haemostatic materials.

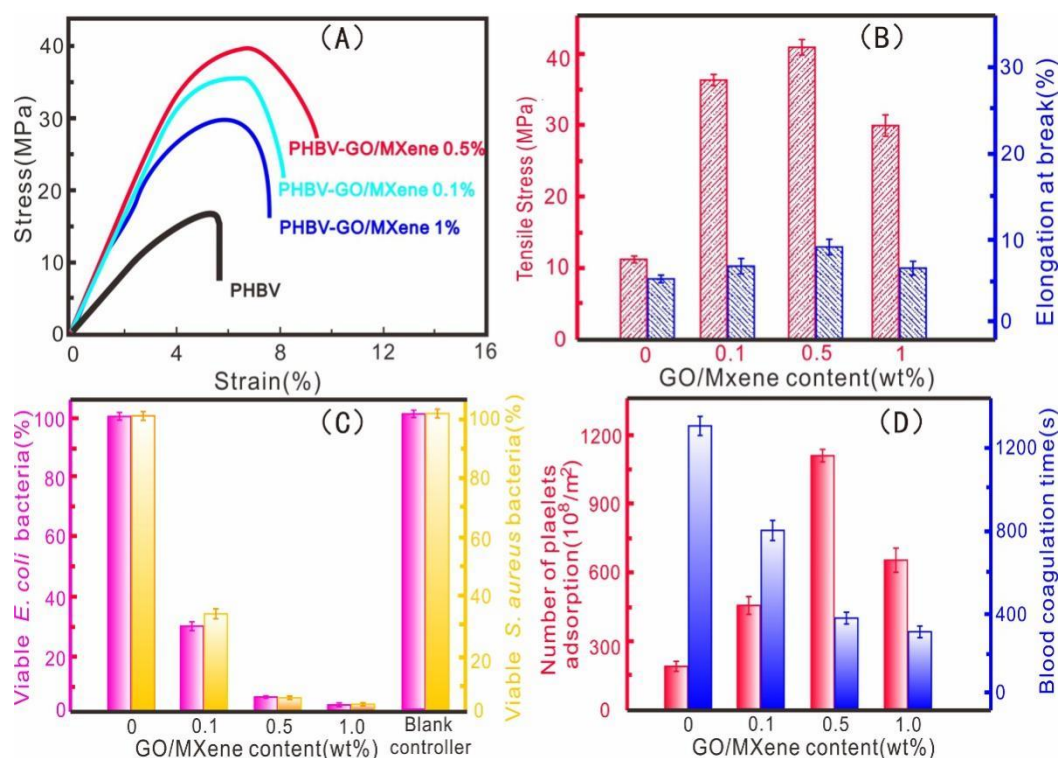
To quantify the binding forms of oxygen, carbon, nitrogen, and titanium in the PHBV and PHBV—GO/MXene composite membranes, high resolution XPS spectra of O1s, C1s, Ti2p and Ti2s were deconvoluted using Gaussian-Lorentzian peaks [37,73,74]. The XPS results of the PHBV and PHBV—GO/MXene composite membranes are illustrated in Figure 6. The wide-scan XPS spectra showed sharp peaks of O1s and C1s (Figure 6A), which indicate that the pure PHBV membrane mainly contained elements of C and O. These results are consistent with the SEM-EDS results (Figure 2A and Figure S1). Further investigation illustrated that the intensities of the C=O, C-O, and C-C bonds were 3.4%, 8.5%, and 88.1%, respectively (Figure 6B). The C1s peak for GO was fitted to C=O, C-O, and C-C peaks (Figure 6C), which were similar to the PHBV results. However, the intensity of C-O in GO was higher than that in PHBV. Figure 6D shows that the C1s peak for MXene can be fitted to C=O, C-O, C-C, and C-Ti peaks (Figure 6D). The significant intensity of C=O and C-O confirmed the existence of hydrophilic oxygen-containing functional groups. The wide-scan XPS spectra showed that the PHBV—GO/MXene composite membrane contained elements of Ti introduced by MXene (Figure 6A). These results were also consistent with the results of SEM-EDS (Figure 2A and Figures S2–S4). The intensity of the C-O and C-Ti bonds increased with the increasing GO/MXene addition (Figure 6E–G), indicating that some GO and MXene were grafted onto the surface of the PHBV—GO/MXene composite membranes. In addition, the increase in C-O bonds was significantly higher than the summation of PHBV and GO/MXene, for the low GO/MXene addition amounts. Combining the high C-O peak in PHBV—GO/MXene and the low C-O peak in PHBV, GO, and MXene in FT-IR, the high intensity of C-O may suggest that GO was esterified with PHBV and the graft reaction occurred. These factors may be beneficial to toughen the PHBV—GO/MXene composite membranes.

### 3.3. Mechanical Property, Antibacterial Activity, and Platelet Adsorption

The mechanical properties of the PHBV and PHBV—GO/MXene composite membranes were tested. The tensile strength and elongation at break were obtained, as shown in Figure 7A,B. The pure PHBV composite membranes exhibited low tensile stress (16 MPa) and low strain at break (4.6%) (Figure 7A,B). The tensile stress and strain at break are similar to those of commercial PHAs [75,76]. The tensile strengths of the PHBV—GO/MXene 0.1% and PHBV—GO/MXene 0.5% composite membranes were 36 MPa and 42 MPa, respectively, which are comparable to those of PHA/GO-g-LAQ 5 wt% films with 39.8 MPa tensile strength [4], higher than that of the PHA/ZnO 4 wt% nanocomposites, with 29.5 MPa tensile strength and PHA/nanofibrillated cellulose (NFC) nanocomposites 5 wt%, with a tensile strength of 34.4 MPa [75,76]. However, the tensile strength of the PHBV—GO/MXene composite membranes decreased from 42 MPa to 29 MPa as GO/MXene content increased from 0.5% to 1.0% (Figure 7A). This change may be triggered by the poor interfacial reaction between PHBV and GO/MXene (Figure 5A) and the aggregation effect of GO/MXene forming the fusiform structure, which also led to a decrease in elongation at break of the PHBV—GO/MXene 1.0% composite membranes. Good dispersion and esterification reactions may correspond to the increasing elongation at break of the PHBV—GO/MXene 0.1% and PHBV—GO/MXene 0.5% composite membranes (Figure 5B). These results confirmed that GO/MXene can greatly improve the tensile strength and elongation at break of PHBV.



**Figure 6.** XPS spectrum (A) of PHBV, GO, MXene, PHBV—GO/MXene 0.1%, PHBV—GO/MXene 0.5%, and PHBV—GO/MXene 1% composite membranes. C1s XPS spectra of PHBV (B), GO (C), MXene (D), PHBV—GO/MXene 0.1% (E), PHBV—GO/MXene 0.5% (F), and PHBV—GO/MXene 1% (G) composite membranes.



**Figure 7.** Stress-strain curves (A), elongation at break (B), antibacterial activity at 24 h and (C) platelet adsorption and blood coagulation time (D) of PHBV of PHBV, PHBV—GO/MXene 0.1%, PHBV—GO/MXene 0.5% and PHBV—GO/MXene 1% composite membranes.

*E. coli* and *S. aureus* bacteria are generally used to detect antibacterial activity against gram-negative and gram-positive bacteria [4,75,77,78]. The antimicrobial activity against *E. coli* and *S. aureus* bacteria of the PHBV and PHBV—GO/MXene composite membranes was detected. The results are shown in Figure 7C and Figure S4. After 24 h of incubation, the *E. coli* and *S. aureus* bacteria aggregated on the film surface and formed larger colonies on the PHBV composite membranes, which indicates that PHBV has a poor bactericidal ability (Figure 7C and Figure S5). Compared to the PHBV composite membranes, PHBV—GO/MXene 0.1% composite membranes showed good bacterial reduction in *E. coli* and *S. aureus* bacteria. The antibacterial activity of PHBV—GO/MXene 0.5% composite membranes reached 95% (Figure 7C and Figure S5). The antibacterial activity of PHBV—GO/MXene composite membranes increased from 95% to over 99% and the GO/MXene content increased from 0.5% to 1.0% (Figure 7C and Figure S5). These results suggest that PHBV—GO/MXene had a good antibacterial performance for the addition of GO/MXene. Although some studies reported that GO has no antibacterial activity [4,77], GO/MXene still showed excellent antibacterial properties in this investigation. These results may be due to the excellent antibacterial properties of MXene [48].

Generally, haemostatic capacity can be characterized by the number of platelets, adsorption and blood coagulation time [55]. The adsorption capacity towards platelet and blood coagulation of PHBV and PHBV—GO/MXene composite membranes are presented in Figure 7D. The pure PHBV composite membranes had a low adsorption capacity towards platelets and long blood coagulation times (Figure 7D). Compared to pure PHBV, PHBV—GO/MXene composite membranes had good platelet adsorption capacity. Among them, the PHBV—GO/MXene 0.5% composite membranes adsorbed  $1143 \pm 43 \times 10^8/m^2$ , almost five times that of the PHBV composite membranes (Figure 7D). The good platelet-adsorption performance were consistent with the conclusions of BET and zeta potential, which indicate that PHBV—GO/MXene 0.5% composite membranes have good application prospects for haemostatic materials (Figures 4 and 5D). Moreover, the blood coagulation

time of the PHBV—GO/MXene 0.5% composite membranes was also short, at  $379 \pm 34$  s, which was three times shorter than that of the PHBV composite membranes (Figure 7D). The blood coagulation time of the PHBV—GO/MXene 1.0% composite membranes was the fastest at  $341 \pm 28$  s (Figure 7D). Therefore, the PHBV—GO/MXene 0.5% composite membranes showed the best procoagulant properties. These results also indicate that GO/MXene can significantly enhance the haemostatic properties of PHBV and PHBV—GO/MXene composite membranes, which may be valuable in wound healing applications.

Previous investigations have reported that platelet adsorption can be affected by many factors, such as surface properties [55]. Among them, hydrophobic surfaces can absorb more platelets compared to hydrophilic surfaces [50,79]. For the PHBV—GO/MXene composite membranes, the hydrophobic and rough surface may act as the active site for platelet adsorption, while the GO and MXene embedded in the fibres may act as hydrophilic active sites. Moreover, the GO and MXene may also react with PHBV and form more ester bond groups, which can further improve the tensile strength. Furthermore, due to the antibacterial properties of MXene, PHBV—GO/MXene composite membranes have good antibacterial properties. Therefore, we believe that the good properties of GO and MXene nanoparticles improve the mechanical properties, antimicrobial performance and platelet adsorption of PHBV. There are also some limitations of this study, due to the differences between rabbit and human platelets [80–82]. The 95–99% antibacterial activity of PHBV—GO/MXene composite membranes is also not a remarkable antibacterial performance. It is also necessary to improve the antibacterial ability of PHBV—GO/MXene composite membranes.

#### 4. Conclusions

In this investigation, GO/MXene nanosheets were successfully prepared and grafted onto PHBV to obtain multifunctional, robust, and porous PHBV—GO/MXene composite membranes, with PVP acting as a pore-forming agent. The laminar structure and hydrophilicity of GO and MXene nanosheets gave PHBV—GO/MXene composite membranes superior hydrophilicity due to the presence of hydroxyl groups and terminal oxygen, which also provided functional site for the free radical polymerization of ester bonds between GO/MXene and PHBV. The interfacial embeddedness of GO/MXene nanosheets in the PHBV matrix significantly induced the crystallization behaviours of PHBV. Therefore, the mechanical properties, antimicrobial performance, and platelet adsorption were remarkably improved, which indicates that GO/MXene nanosheets contribute to enhancing the properties of PHBV. The tensile strength, platelet adsorption, and blood coagulation time of PHBV composite membranes were improved from 16 MPa,  $213 \pm 28 \times 10^8/\text{m}^2$ , and  $1312 \pm 116$  s to 42 MPa,  $1143 \pm 43 \times 10^8/\text{m}^2$ , and  $379 \pm 34$  s after incorporation of 0.5 wt% GO/MXene nanosheets. The antimicrobial performance also reached 95% for the PHBV—GO/MXene 0.5% composite membranes. These data supported that our investigation may provide a promising method for preparing facile and high-performance PHBV nanocomposites that could offer prosperous applications for multifunctional haemostatic materials.

**Supplementary Materials:** The following are available online at <https://www.mdpi.com/article/10.3390/polym13213748/s1>, Figure S1: The SEM-EDS mapping of PHBV composite membranes, Figure S2: The SEM-EDS mapping of PHBV—GO/MXene 0.1% composite membranes, Figure S3: The SEM-EDS mapping of PHBV—GO/MXene 0.5% composite membranes, Figure S4: The SEM-EDS mapping of PHBV—GO/MXene 1.0% composite membranes; Figure S5: Formation of bacteria colonies: antibacterial activity of PHBV, PHBV—GO/MXene 0.1%, PHBV—GO/MXene 0.5%, PHBV—GO/MXene 1%, and blank group composite membranes for *E. coli* and *S. aureus*, method of the antibacterial activity test and detail platelet adsorption experiments

**Author Contributions:** Conceptualization, Y.W. and W.Z.; methodology, Y.W.; software, Y.X.; validation, B.D., M.W. and X.Z.; formal analysis, C.L.; investigation, Y.W.; resources, X.Z.; data curation, W.Z.; writing—original draft preparation, Y.W.; writing—review and editing, B.D.; visualization, M.W.; supervision, L.S.; project administration, Y.W.; funding acquisition, Y.H. All authors have read and agreed to the published version of the manuscript.



**Funding:** This work is supported by the National Key Research and Development Program of China (Nos. 2018YFC1106702), the Key Program of Marine Economy Development (Six Marine Industries) Special Foundation of Department of Natural Resources of Guangdong Province (GDNRC [2020]034), Guangdong Basic and Applied Basic Research Foundation (2020A1515010694, 2020A1515011301, and 2018A030313950), the Shenzhen Fund in Special Foundation for Guiding Local Science and Technology Development of the Central Government (2021Szvup001), the Shenzhen Basic Research Project (JCYJ20170815153143221, JCYJ20200109144608205, and JCYJ202000109144604020), the China Postdoctoral Science Foundation (2021M690247), and the IER Innovation Foundation (HT-JD-CXY-201902 and HT-JD-CXY-201907).

**Institutional Review Board Statement:** Not applicable.

**Informed Consent Statement:** Not applicable.

**Data Availability Statement:** Not applicable.

**Conflicts of Interest:** The authors declare no conflict of interest.

## References

- Gross, R.A.; Kalra, B. Biodegradable polymers for the environment. *Science* **2002**, *297*, 803–807.
- Rochman, C.M.; Browne, M.A.; Halpern, B.S.; Hentschel, B.T.; Hoh, E.; Karapanagioti, H.K.; Rios-Mendoza, L.M.; Takada, H.; Teh, S.; Thompson, R.C. Classify plastic waste as hazardous. *Nature* **2013**, *494*, 169–171. [[CrossRef](#)]
- Rochman, C.M.; Hoh, E.; Hentschel, B.T.; Kaye, S. Long-term field measurement of sorption of organic contaminants to five types of plastic pellets: Implications for plastic marine debris. *Environ. Sci. Technol.* **2013**, *47*, 1646–1654. [[PubMed](#)]
- Xu, P.; Yang, W.; Niu, D.; Yu, M.; Du, M.; Dong, W.; Chen, M.; Lemstra, P.J.; Ma, P. Multifunctional and robust polyhydroxyalkanoate nanocomposites with superior gas barrier, heat resistant and inherent antibacterial performances. *Chem. Eng. J.* **2020**, *382*, 122864. [[CrossRef](#)]
- Ignatyev, I.A.; Thielemans, W.; Vander, B. Recycling of polymers: A review. *ChemSusChem* **2014**, *7*, 1579–1593. [[CrossRef](#)] [[PubMed](#)]
- Porta, R. Anthropocene, the plastic age and future perspectives. *FEBS Open Bio.* **2021**, *11*, 948–953.
- Shi, X.; Zheng, Y.; Lei, Y.; Xue, W.; Yan, G.; Liu, X.; Cai, B.; Tong, D.; Wang, J. Air quality benefits of achieving carbon neutrality in China. *Sci. Total Environ.* **2021**, *795*, 148784. [[CrossRef](#)]
- Chen, J.; Cui, H.; Xu, Y.; Ge, Q. Long-term temperature and sea-level rise stabilization before and beyond 2100: Estimating the additional climate mitigation contribution from China’s recent 2060 carbon neutrality pledge. *Environ Res. Lett.* **2021**, *16*, 074032. [[CrossRef](#)]
- Heggelund, G.M. China’s climate and energy policy: At a turning point? International Environmental Agreements: Politics. *Law Econ.* **2021**, *21*, 9–23.
- Li, Y.; Yang, X.; Ran, Q.; Wu, H.; Irfan, M.; Ahmad, M. Energy structure, digital economy, and carbon emissions: Evidence from China. *Environ. Sci. Pollut. Res.* **2021**, *7*, 1–24.
- Tan, H.; Thurbon, E.; Kim, S.Y.; Mathews, J.A. Overcoming incumbent resistance to the clean energy shift: How local governments act as change agents in coal power station closures in China. *Energy Policy* **2021**, *149*, 112058. [[CrossRef](#)]
- Lai, C.; Zhang, S.; Sheng, L.; Xi, T. Comparative evaluation of the biocompatible and physical–chemical properties of poly (lactide-co-glycolide) and polydopamine as coating materials for bacterial cellulose. *J. Mater. Chem. B* **2019**, *7*, 630–639.
- Lai, C.; Zhang, S.; Chen, X.; Sheng, L. Nanocomposite films based on TEMPO-mediated oxidized bacterial cellulose and chitosan. *Cellulose* **2014**, *21*, 2757–2772. [[CrossRef](#)]
- Jangong, O.S.; Heryanto, H.; Rahmat, R.; Mutmainna, I.; Gareso, P.L.; Tahir, D. Effect of Sugar Palm Fiber (SPF) to the Structural and Optical Properties of Bioplastics (SPF/Starch/Chitosan/Polypropylene) in supporting Mechanical Properties and Degradation Performance. *J. Polym. Environ.* **2021**, *29*, 1694–1705. [[CrossRef](#)]
- Nakayama, Y.; Yagumo, W.; Tanaka, R.; Shiono, T.; Inumaru, K.; Tsutsumi, C.; Kawasaki, N.; Ymano, N.; Nakayama, A. Synthesis, properties and biodegradation of periodic copolyesters composed of hydroxy acids, ethylene glycol, and terephthalic acid. *Polym. Degrad. Stabil.* **2020**, *174*, 109095. [[CrossRef](#)]
- Hu, H.; Li, J.; Tian, Y.; Chen, C.; Li, F.; Ying, W.; Zhang, R.; Zhu, J. Experimental and Theoretical Study on Glycolic Acid Provided Fast Bio/Seawater-Degradable Poly (Butylene Succinate-co-Glycolate). *ACS Sustain. Chem. Eng.* **2021**, *9*, 3850–3859. [[CrossRef](#)]
- Shen, J.; Wang, K.; Ma, Z.; Xu, N.; Pang, S.; Pan, L. Biodegradable blends of poly (butylene adipate-co-terephthalate) and polyglycolic acid with enhanced mechanical, rheological and barrier performances. *J. Appl. Polym. Sci.* **2021**, *138*, 51285. [[CrossRef](#)]
- Rayasam, V.; Chavan, P.; Kumar, T. Polyhydroxyalkanoate synthesis by bacteria isolated from landfill and ETP with pomegranate peels as carbon source. *Arch. Microbiol.* **2020**, *202*, 2799–2808. [[CrossRef](#)] [[PubMed](#)]
- Muneer, F.; Rasul, I.; Azeem, F.; Siddique, M.H.; Zubair, M.; Nadeem, H. Microbial polyhydroxyalkanoates (PHAs): Efficient replacement of synthetic polymers. *J. Polym. Environ.* **2020**, *28*, 2301–2323. [[CrossRef](#)]

20. Anitha, N.N.N.; Srivastava, R.K. Microbial Synthesis of Polyhydroxyalkanoates (PHAs) and Their Applications. In *Environmental and Agricultural Microbiology: Applications for Sustainability*; Scrivener Publishing LLC: Beverly, MA, USA, 2021; pp. 151–181.
21. Luo, Z.; Wu, Y.L.; Li, Z.; Loh, X. Recent Progress in Polyhydroxyalkanoates-Based Copolymers for Biomedical Applications. *Biotechnol. J.* **2019**, *14*, 1900283. [[CrossRef](#)]
22. Zhao, X.H.; Niu, Y.N.; Mi, C.H.; Gong, H.; Yang, X.; Cheng, J.; Zhou, Z.; Liu, J.; Peng, X.; Wei, D. Electrospinning nanofibers of microbial polyhydroxyalkanoates for applications in medical tissue engineering. *J. Polym. Sci.* **2021**, *59*, 1994–2013. [[CrossRef](#)]
23. Vigneswari, S.; Murugaiyah, V.; Kaur, G.; Khail, A.H.P.S.; Amirul, A.A. Simultaneous Dual Syringe Electrospinning System Using Benign Solvent to Fabricate Nanofibrous P(3HB-Co-4HB)/Collagen Peptides Construct as Potential Leave-on Wound Dressing. *Mat. Sci. Engin.* **2016**, *66*, 147–155. [[CrossRef](#)]
24. Greco, P.; Martuscelli, E. Crystallization and thermal behaviour of poly ( $\beta$ -3-hydroxybutyrate)-based blends. *Polymer* **1989**, *30*, 1475–1483. [[CrossRef](#)]
25. Chen, G.Q. Plastics completely synthesized by bacteria: Polyhydroxyalkanoates. In *Plastics from Bacteria*; Springer: Berlin/Heidelberg, Germany, 2010; pp. 17–37.
26. Chiellini, E.; Corti, A.; D'Antone, S.; Solaro, R. Biodegradation of poly (vinyl alcohol) based materials. *Prog. Polym. Sci.* **2003**, *28*, 963–1014. [[CrossRef](#)]
27. Chen, G.Q.; Wu, Q. The application of polyhydroxyalkanoates as tissue engineering materials. *Biomaterials* **2005**, *26*, 6565–6578. [[CrossRef](#)] [[PubMed](#)]
28. Reddy, C.S.K.; Ghai, R.; Kalia, V.C. Polyhydroxyalkanoates: An overview. *Bioresour. Techn.* **2003**, *87*, 137–146. [[CrossRef](#)]
29. Sudesh, K.; Abe, H.; Doi, Y. Synthesis, structure and properties of polyhydroxyalkanoates: Biological polyesters. *Prog. Polym. Sci.* **2000**, *25*, 1503–1555. [[CrossRef](#)]
30. Valappil, S.P.; Misra, S.K.; Boccaccini, A.R.; Roy, I. Biomedical applications of polyhydroxyalkanoates, an overview of animal testing and in vivo responses. *Expert Rev. Med. Devic.* **2006**, *3*, 853–868. [[CrossRef](#)]
31. Chen, G.Q.; Patel, M.K. Plastics derived from biological sources: Present and future: A technical and environmental review. *Chem. Rev.* **2012**, *112*, 2082–2099. [[CrossRef](#)]
32. Volova, T.; Kiselev, E.; Nemtsev, I.; Lukyanenko, A.; Sukovatyi, A.; Kuzmin, A.; Ryltseva, G.; Shishatskaya, E. Properties of degradable polyhydroxyalkanoates with different monomer compositions. *Int. J. Biol. Macromol.* **2021**, *182*, 98–114. [[CrossRef](#)]
33. Sharma, S.; Sudhakara, P.; Singh, J.; Ilyas, R.A.; Asyraf, M.R.M.; Razman, M.R. Critical Review of Biodegradable and Bioactive Polymer Composites for Bone Tissue Engineering and Drug Delivery Applications. *Polymers* **2021**, *13*, 2623. [[CrossRef](#)]
34. Kalia, V.C.; Patel, S.K.S.; Kang, Y.C.; Lee, J. Quorum sensing inhibitors as antipathogens: Biotechnological applications. *Biotechnol. Adv.* **2019**, *37*, 68–90. [[CrossRef](#)] [[PubMed](#)]
35. Elmowafy, E.; Abdal-Hay, A.; Skouras, A.; Tiboni, M.; Casettari, L.; Guarino, V. Polyhydroxyalkanoate (PHA): Applications in drug delivery and tissue engineering. *Expert Rev. Med. Devic.* **2019**, *16*, 467–482. [[CrossRef](#)] [[PubMed](#)]
36. Vigneswari, S.; Chai, J.M.; Kamarudin, K.H.; Amirul, A.A.; Focarete, M.L.; Ramakrishna, S. Elucidating the surface functionality of biomimetic rgd peptides immobilized on nano-p (3hb-co-4hb) for h9c2 myoblast cell proliferation. *Front. Bioeng. Biotech.* **2020**, *8*, 1253. [[CrossRef](#)] [[PubMed](#)]
37. Huang, Q.; Cai, Y.; Zhang, X.; Liu, J.; Liu, Z.; Li, B.; Wong, H.; Xu, F.; Sheng, L.; Sun, D.; et al. Aligned Graphene Mesh-Supported Double Network Natural Hydrogel Conduit Loaded with Netrin-1 for Peripheral Nerve Regeneration. *ACS Appl. Mater. Inter.* **2021**, *13*, 122.
38. Zhou, W.; Rao, Y.; Zhuang, W.; Ge, L.; Lin, R.; Tang, T.; Wu, J.; Li, M.; Yang, P.; Zhu, C.; et al. Improved enzymatic activity by oriented immobilization on graphene oxide with tunable surface heterogeneity. *Compos. Part B-Eng.* **2021**, *216*, 108788. [[CrossRef](#)]
39. Zhao, X.; Zhang, Q.; Chen, D.; Lu, P. Enhanced mechanical properties of graphene-based poly (vinyl alcohol) composites. *Macromolecules* **2010**, *43*, 2357–2363. [[CrossRef](#)]
40. Lee, K.W.; Chung, J.W.; Kwak, S.Y. Flexible poly (vinyl chloride) nanocomposites reinforced with hyperbranched polyglycerol-functionalized graphene oxide for enhanced gas barrier performance. *ACS Appl. Mater. Inter.* **2017**, *9*, 33149–33158. [[CrossRef](#)] [[PubMed](#)]
41. Niyogi, S.; Bekyarova, E.; Itkis, M.E.; McWilliams, J.L.; Hamon, M.A.; Haddon, R.C. Solution properties of graphite and graphene. *J. Am. Chem. Soc.* **2006**, *128*, 7720–7721. [[CrossRef](#)]
42. Ambrosio-Martín, J.; Gorrasi, G.; Lopez-Rubio, A.; Fabra, M.J.; Mas, L.C.; López-Manchado, A.L.; Lagaron, J.M. On the use of ball milling to develop poly (3-hydroxybutyrate-co-3-hydroxyvalerate)-graphene nanocomposites (II)—Mechanical, barrier, and electrical properties. *J. Appl. Polym. Sci.* **2015**, *132*, 42217. [[CrossRef](#)]
43. Naguib, M.; Kurtoglu, M.; Presser, V.; Lu, J.; Niu, J.; Heon, M.; Hultman, L.; Gogotsi, Y.; Barsoun, M.W. Two-dimensional nanocrystals produced by exfoliation of  $\text{Ti}_3\text{AlC}_2$ . *Adv. Mater.* **2011**, *23*, 4248–4253. [[CrossRef](#)] [[PubMed](#)]
44. Bhimanapati, G.R.; Lin, Z.; Meunier, V.; Jung, Y.; Cha, J.; Das, S.; Xiao, D.; Son, Y.; Strano, M.S.; Cooper, V.R.; et al. Recent advances in two-dimensional materials beyond graphene. *ACS Nano* **2015**, *9*, 11509–11539. [[CrossRef](#)] [[PubMed](#)]
45. Gong, K.; Zhou, K.; Qian, X.; Shi, C.; Yu, B. MXene as emerging nanofillers for high-performance polymer composites: A review. *Compos. Part B Eng.* **2021**, *217*, 108867. [[CrossRef](#)]
46. Kumar, J.A.; Prakash, P.; Krithiga, T.; Amarnath, D.J.; Kumar, J.P.; Natarajan, R.; Yasser, V.; Panchamoorthy, S.; Manivasagan, R. Methods of synthesis, characteristics, and environmental applications of Mxene: A comprehensive review. *Chemosphere* **2021**, *286*, 131607. [[CrossRef](#)]

47. Han, Y.; Jiang, Y.; Gao, C. High-flux graphene oxide nanofiltration membrane intercalated by carbon nanotubes. *ACS Appl. Mat. Inter.* **2015**, *7*, 8147–8155. [[CrossRef](#)]
48. Shamsabadi, A.A.; Sharifian, G.M.; Anasori, B.; Soroush, M. Antimicrobial mode-of-action of colloidal  $Ti_3C_2T_x$  MXene nanosheets. *ACS Sustain. Chem. Eng.* **2018**, *6*, 16586–16596. [[CrossRef](#)]
49. Hummers, W.S., Jr.; Offeman, R.E. Preparation of graphitic oxide. *J. Am. Chem. Soc.* **1958**, *80*, 1339. [[CrossRef](#)]
50. Wu, L.P.; You, M.; Wang, D.; Peng, G.; Wang, Z.; Chen, G.Q. Fabrication of carbon nanotube (CNT)/poly (3-hydroxybutyrate-co-3-hydroxyhexanoate) (PHBHHx) nanocomposite films for human mesenchymal stem cell (hMSC) differentiation. *Polym. Chem.* **2013**, *4*, 4490–4498. [[CrossRef](#)]
51. Sarycheva, A.; Gogotsi, Y. Raman Spectroscopy Analysis of the Structure and Surface Chemistry of  $Ti_3C_2T_x$  MXene. *Chem. Mat.* **2020**, *32*, 3480–3488. [[CrossRef](#)]
52. Wu, Y.; Sun, Y.; Zhou, C.; Niu, J. Regeneration of porous electrospun membranes embedding alumina nanoparticles saturated with minocycline by UV radiation. *Chemosphere* **2019**, *237*, 124495. [[CrossRef](#)]
53. Qu, X.H.; Wu, Q.; Liang, J.; Qu, X.; Wang, S.; Chen, G. Enhanced vascular-related cellular affinity on surface modified copolyesters of 3-hydroxybutyrate and 3-hydroxyhexanoate (PHBHHx). *Biomaterials* **2005**, *26*, 6991–7001. [[CrossRef](#)]
54. Lomas, A.J.; Webb, W.R.; Han, J.F.; Chen, G.; Sun, X.; Zhang, Z.; Haj, A.J.E.; Forsyth, N.R. Poly (3-hydroxybutyrate-co-3-hydroxyhexanoate)/collagen hybrid scaffolds for tissue engineering applications. *Tissue Eng. Part C-Methods* **2013**, *19*, 577–585. [[CrossRef](#)]
55. Han, J.; Wu, L.P.; Hou, J.; Zhao, D.; Xiang, H. Biosynthesis, characterization, and hemostasis potential of tailor-made poly (3-hydroxybutyrate-co-3-hydroxyvalerate) produced by *Haloferax mediterranei*. *Biomacromolecules* **2015**, *16*, 578–588. [[CrossRef](#)]
56. Lee, C.G.; Javed, H.; Zhang, D.; Kim, J.H.; Westerhoff, P.; Li, Q.; Alvarez, P.J. Porous electrospun fibers embedding  $TiO_2$  for adsorption and photocatalytic degradation of water pollutants. *Environ. Sci. Technol.* **2018**, *52*, 4285–4293. [[CrossRef](#)] [[PubMed](#)]
57. Spasova, M.; Manolova, N.; Markova, N.; Rashkov, I. Superhydrophobic PVDF and PVDF-HFP nanofibrous mats with antibacterial and anti-biofouling properties. *Appl. Surf. Sci.* **2016**, *363*, 363–371. [[CrossRef](#)]
58. Moghadam, M.T.; Lesage, G.; Mohammadi, T.; Mericq, J.P.; Mendret, J.; Heran, M.; Faur, C.; Brosillon, S.; Hemmati, M.; Naeimpoor, F. Improved antifouling properties of  $TiO_2$ /PVDF nanocomposite membranes in UV-coupled ultrafiltration. *J. Appl. Polym. Sci.* **2015**, *132*, 132–153. [[CrossRef](#)]
59. Dong, Z.; Ma, X.; Xu, Z.; Gu, Z. Superhydrophobic modification of PVDF- $SiO_2$  electrospun nanofiber membranes for vacuum membrane distillation. *RSC Adv.* **2015**, *83*, 67962–67970. [[CrossRef](#)]
60. Vild, A.; Teixeira, S.; Kühn, K.; Cuniberti, G.; Sencadas, V. Orthogonal experimental design of titanium dioxide—Poly (methyl methacrylate) electrospun nanocomposite membranes for photocatalytic applications. *J. Environ. Chem. Eng.* **2016**, *4*, 3151–3158. [[CrossRef](#)]
61. Cossich, E.; Bergamasco, R.; Pessoa de Amorim, M.T.; Martins, P.M.; Marques, J.; Tavares, C.J.; Lanceros-Mendez, S.; Sencadas, V. Development of electrospun photocatalytic  $TiO_2$ -polyamide-12 nanocomposites. *Mater. Chem. Phys.* **2015**, *164*, 91–97. [[CrossRef](#)]
62. Feng, T.; Li, X.; Guo, P.; Zhang, Y.; Liu, J.; Zhang, H. MXene: Two dimensional inorganic compounds, for generation of bound state soliton pulses in nonlinear optical system. *Nanophotonics* **2020**, *9*, 2505–2513. [[CrossRef](#)]
63. Ding, L.; Wei, Y.; Wang, Y.; Chen, H.; Caro, J.; Wang, H. A two-dimensional lamellar membrane: MXene nanosheet stacks. *Angew. Chem. Int. Edit.* **2017**, *56*, 1825–1829. [[CrossRef](#)]
64. Pandey, R.P.; Rasool, K.; Madhavan, V.E.; Aissa, B.; Gogotsi, Y.; Mahnoud, K. Ultrahigh-flux and fouling-resistant membranes based on layered silver/MXene ( $Ti_3C_2T_x$ ) nanosheets. *J. Mat. Chem. A* **2018**, *6*, 3522–3533. [[CrossRef](#)]
65. Sun, L.; Tuo, J.; Zhang, M.; Wu, C.; Wang, Z.; Zheng, Y. Formation and development of the pore structure in Chang 7 member oil-shale from Ordos Basin during organic matter evolution induced by hydrous pyrolysis. *Fuel* **2015**, *158*, 549–557. [[CrossRef](#)]
66. Ghaffar, A.; Zhang, L.; Zhu, X.; Chen, B. Porous PVdF/GO nanofibrous membranes for selective separation and recycling of charged organic dyes from water. *Environ. Sci. Technol.* **2018**, *52*, 4265–4274. [[CrossRef](#)]
67. Sing, K.S.W.; Williams, R.T. Physisorption hysteresis loops and the characterization of nanoporous materials. *Adsorpt. Sci. Technol.* **2004**, *22*, 773–782. [[CrossRef](#)]
68. Kruk, M.; Jaroniec, M. Gas adsorption characterization of ordered organic–inorganic nanocomposite materials. *Chem. Mat.* **2001**, *13*, 3169–3183. [[CrossRef](#)]
69. Krishna, R.; Jones, A.N.; Marsden, B.J. Transmission electron microscopy, Raman and X-ray photoelectron spectroscopy studies on neutron irradiated polycrystalline graphite. *Radiat. Phys. Chem.* **2015**, *107*, 121–127. [[CrossRef](#)]
70. Yang, L.; Kan, D.; Dall’Agnese, C.; Dall’Agnese, Y.; Wang, B.; Jena, A.K.; Wei, Y.; Chen, G.; Wang, X.; Gogotsi, Y.; et al. Performance improvement of MXene-based perovskite solar cells upon property transition from metallic to semiconductive by oxidation of  $Ti_3C_2T_x$  in air. *J. Mat. Chem. A* **2021**, *9*, 5016–5025. [[CrossRef](#)]
71. Murata, M.; Ware, J.; Ruggeri, Z.M. Site-directed mutagenesis of a soluble recombinant fragment of platelet glycoprotein Ib alpha demonstrating negatively charged residues involved in von Willebrand factor binding. *J. Biol. Chem.* **1991**, *266*, 15474–15480. [[CrossRef](#)]
72. Milić, M.; Cvetic, Ž.; Bendelja, K.; Vuković, B.; Galić, E.; Ćurlin, M.; Dobroševića, B.; Begonja, A.J.; Vrček, I.V. Response of platelets to silver nanoparticles designed with different surface functionalization. *J. Inorg. Biochem.* **2021**, *224*, 111565. [[CrossRef](#)]
73. Kim, S.; Wang, H.; Lee, Y.M. 2D nanosheets and their composite membranes for water, gas, and ion separation. *Angew. Chem. Int. Edit.* **2019**, *131*, 17674–17689. [[CrossRef](#)]

74. Jing, Z.; Rodrigues, S.; Strounina, E.; Li, M.; Wood, B.; Underschultz, J.R.; Esterle, J.S.; Steel, K.M. Use of FTIR, XPS, NMR to characterize oxidative effects of NaClO on coal molecular structures. *Int. J. Coal Geol.* **2019**, *201*, 1–13. [[CrossRef](#)]
75. Díez-Pascual, A.M.; Díez-Vicente, A.L. ZnO-reinforced poly (3-hydroxybutyrate-co-3-hydroxyvalerate) bionanocomposites with antimicrobial function for food packaging. *ACS Appl. Mat. Inter.* **2014**, *6*, 9822–9834. [[CrossRef](#)]
76. Srithep, Y.; Ellingham, T.; Peng, J.; Sabo, R.; Clemons, C.; Turng, L.-S.; Pilla, S. Melt compounding of poly (3-hydroxybutyrate-co-3-hydroxyvalerate)/nanofibrillated cellulose nanocomposites. *Polym. Degrad. Stabil.* **2013**, *98*, 1439–1449. [[CrossRef](#)]
77. Ruiz, O.N.; Fernando, K.A.S.; Wang, B.; Brown, N.A.; Luo, P.G.; McNamara, N.D.; Vagsness, M.; Sun, Y.; Bunker, C.E. Graphene oxide: A nonspecific enhancer of cellular growth. *ACS Nano* **2011**, *5*, 8100–8107. [[CrossRef](#)]
78. Guo, J.; Xu, Q.; Shi, R.; Zheng, Z.; Mao, H.; Yan, F. Polyanionic antimicrobial membranes: An experimental and theoretical study. *Langmuir* **2017**, *33*, 4346–4355. [[CrossRef](#)] [[PubMed](#)]
79. Qu, X.H.; Wu, Q.; Chen, G.Q. In vitro study on hemocompatibility and cytocompatibility of poly (3-hydroxybutyrate-co-3-hydroxyhexanoate). *J. Biomater. Sci. Polym. Ed.* **2006**, *17*, 1107–1121. [[CrossRef](#)]
80. Manning, J.E.; Geyelin, A.J.; Ansmits, L.M.; Oakey, H.J.; Knox, K.W. A comparative study of the aggregation of human, rat and rabbit platelets by members of the *Streptococcus sanguis* group. *J. Med. Microbiol.* **1994**, *41*, 10–13. [[CrossRef](#)]
81. Tarandovskiy, I.D.; Shin, H.K.H.; Baek, J.H.; Karnaukhova, K.; Buehler, P.W. Interspecies comparison of simultaneous thrombin and plasmin generation. *Sci. Rep.* **2020**, *10*, 1–8. [[CrossRef](#)] [[PubMed](#)]
82. Packham, M.A.; Rand, M.L.; Kinlough-Rathbone, R.L. Similarities and differences between rabbit and human platelet characteristics and functions. *Comp. Biochem. Physiol. A* **1992**, *103*, 35–54. [[CrossRef](#)]



## Article

# Biodegradation of Polystyrene by *Tenebrio molitor*, *Galleria mellonella*, and *Zophobas atratus* Larvae and Comparison of Their Degradation Effects

Shan Jiang <sup>1</sup>, Tingting Su <sup>1</sup>, Jingjing Zhao <sup>1,\*</sup> and Zhanyong Wang <sup>2,\*</sup>

<sup>1</sup> School of Petrochemical Engineering, Liaoning Petrochemical University, Fushun 113001, China; js18341318089@163.com (S.J.); sutingting1978@126.com (T.S.)

<sup>2</sup> Department of Biotechnology, College of Bioscience and Biotechnology, Shenyang Agricultural University, Shenyang 110866, China

\* Correspondence: zhaojingjing@lnpu.edu.cn (J.Z.); wangzy125@syau.edu.cn (Z.W.)

**Abstract:** Plastic waste pollution and its difficult degradation process have aroused widespread concern. Research has demonstrated that the larvae of *Tenebrio molitor* (yellow mealworm), *Galleria mellonella* (greater wax moth), and *Zophobas atratus* (superworm) possess a biodegradation ability for polystyrene (PS) within the gut microbiota of these organisms. In this study, the difference in PS degradation and the changes of the gut microbiota were compared before and after feeding PS. The results showed that superworm had the strongest PS consumption capacity and the highest survival rate during the 30 d experiment period. They all could degrade PS to different degrees. Superworm showed the highest ability to degrade PS into low-molecular-weight substances, while yellow mealworm depolymerized PS strongly by destroying the benzene ring. The changes of the intestinal microbiome caused by feeding PS showed that after ingesting PS, there was a decrease in community diversity in superworm and yellow mealworm, but an increase in greater wax moth. Meanwhile, Enterococcus and Enterobacteriaceae, found in all three species' larvae upon 20 d of PS feeding, might play an important role in PS degradation. The results will provide more accurate PS degradation comparative data of the three species' larvae and theoretical guidance for further research on the efficient PS biodegradations.

**Keywords:** biodegradation; polystyrene; comparison; gut microbes; insect larvae

**Citation:** Jiang, S.; Su, T.; Zhao, J.; Wang, Z. Biodegradation of Polystyrene by *Tenebrio molitor*, *Galleria mellonella*, and *Zophobas atratus* Larvae and Comparison of Their Degradation Effects. *Polymers* **2021**, *13*, 3539. <https://doi.org/10.3390/polym13203539>

Academic Editors: José Miguel Ferri, Vicent Fombuena Borràs and Miguel Fernando Aldás Carrasco

Received: 29 September 2021

Accepted: 12 October 2021

Published: 14 October 2021

**Publisher's Note:** MDPI stays neutral with regard to jurisdictional claims in published maps and institutional affiliations.



**Copyright:** © 2021 by the authors. Licensee MDPI, Basel, Switzerland. This article is an open access article distributed under the terms and conditions of the Creative Commons Attribution (CC BY) license (<https://creativecommons.org/licenses/by/4.0/>).

## 1. Introduction

It is generally believed that petroleum-based plastics, including polyethylene (PE), polystyrene (PS), polyvinyl chloride (PVC), polypropylene (PP), etc., are widely used due to their light weight, high strength, waterproof capacity, corrosion resistance, and low cost [1]. The convenience of using plastics by humans has led to the release of a large amount of plastic waste into the environment. These waste plastics have stable chemical properties, thus making it extremely difficult to naturally degrade them in the environment [2,3]. Therefore, they lead to the pollution of the soil, atmosphere, and water to different degrees. These wastes breakdown into microplastics, which might enter an organism's body and accumulate there, seriously endangering the life and health of the organism [4].

Some of the traditional methods of disposing of waste plastic include incineration, landfill, or chemical recycling, which cannot fundamentally solve the problem of environmental pollution. Thus, biodegradation is an ideal way to solve this problem [5,6]. Previous studies have been conducted on the biodegradation of plastic, in which several bacteria and fungi were found to be capable of degrading plastic materials [7–9]. In recent years, more and more insect larvae have been found to possess the ability to feed on, degrade, and mineralize plastics, such as *Tenebrio molitor* L., *Galleria mellonella* L., *Zophobas atratus* Fab., *Tenebrio obscurus* Fab., *Plodia interpunctella* Htibner, *Tribolium castaneum* Herbst, *Lasioderma*

*serricornis* F., *Rhyzopertha dominica* F., and *Sitophilus oryzae* L. [10–18]. Meanwhile, the plastic consumption rate of insects is higher than that of bacteria and fungi, which are isolated from various sources, such as soil, garbage, and sewage sludge [19–21]. Among these insect larvae, three species have been studied further, including the yellow mealworm (larvae of *Tenebrio molitor* L.), the greater wax moth (larvae of *Galleria mellonella* L.), and the superworm (larvae of *Zophobas atratus* Fab.). The literature and our studies have shown that all three insects can eat and degrade PS [16,22,23].

PS, as one of traditional petroleum-based plastics, is made from the polymerization of styrene monomers. The annual production of PS reaches approximately 33 million t, accounting for about 7% of the total global plastic production [24]. It is widely used in various industries, agriculture, medical treatment, and all aspects of daily life. However, PS waste is generated proportionally to its production, and a large amount of PS waste is produced every year [25]. We hope to find effective PS degradation organisms and provide the theoretical foundation to control plastic pollution. Therefore, in this study, the larvae of yellow mealworm, greater wax moth, and superworm were chosen and prepared to carry out the following research: (1) the three species of insect larvae were fed PS as their sole diet to determine and compare their feeding abilities and their survival rates; (2) the changes in the product properties of the larvae after feeding on PS were analyzed; (3) the changes in intestinal microbiome of the larvae after feeding on PS were compared for all three species' larvae.

## 2. Materials and Methods

### 2.1. Test Materials

*G. mellonella* larvae (15–20 mm long) and beeswax were purchased from Huiyude Co. (Tianjin, China). The larvae of *T. molitor* (20–25 mm long) and *Z. atratus* (30–40 mm long) and wheat bran were purchased from Hongqiao Insect Breeding Plant (Tianjin, China). Prior to the tests, *G. mellonella* larvae were fed with beeswax, while the larvae of *T. molitor* and *Z. atratus* were fed with wheat bran. None of the larvae were fed with any kind of antibiotics or additives. The larvae were starved for 36 h before the experiment to avoid any effect of the previously eaten food.

Styrofoam (PS foam) was obtained from SINOPEC Beijing Yanshan Company (Beijing, China). No catalysts and additives were added as per the manufacturing standard in China (QB/T 4009-2010). The number-averaged molecular weight ( $M_n$ ) and weight-averaged molecular weight ( $M_w$ ) were measured by GPC, and the values were 64,400 Da and 144,400 Da, respectively.

### 2.2. Feeding Tests

Each species' larvae were divided into two groups (200 larvae per group). Each group was reared in a polypropylene plastic container (L × W × H = 14 cm × 14 cm × 7 cm), and the treated group was fed with Styrofoam blocks (3.0 g a group) as the sole diet. As a control, *G. mellonella* larvae were reared on beeswax (3.0 g), and the larvae of *T. molitor* and *Z. atratus* were reared on wheat bran (3.0 g), respectively. Additional Styrofoam blocks and bran were added for 3 d to maintain adequate diet within each container. Both the test group and the control group were prepared in triplicate (n = 3). The measurement of the survival rates and plastic mass loss caused by the larval activities was carried out every 5 d and ended on Day 30. During the testing time, dead larvae and molted exoskeletons were removed from the containers immediately to prevent them from being eaten by the remaining larvae, as cannibalism existed in the later period. Containers were stored in a controlled environment maintained at 25 ± 2 °C.

### 2.3. Collection and Characterization of Frass

The biodegradation assay was characterized by its weight loss and change in bonding upon transforming the PS foam to frass. To obtain enough frass for characterization, additional larvae (approximately 1000 for each group) were fed with Styrofoam blocks as

their sole diet for 21 d. After the period, larvae were transferred to a clean container for the collection of frass every 12 h. In this way, the carryover of uningested Styrofoam morsels and molted exoskeletons in the frass was avoided. The collected frass was immediately stored at  $-80\text{ }^{\circ}\text{C}$  for further analysis, and the stored frass was characterized by four methods as follows, with Styrofoam foam as the control sample.

The changes in molecular weight of Styrofoam or the degradation products in frass were analyzed by gel permeation chromatography (GPC, Waters, GPC1525, Milford, MA, USA). PS extraction from PS feedstock (1.0 g) and frass samples' (1.0 g) collection from the PS-feed larvae was performed by dissolving in tetrahydrofuran (THF) (Peng et al. 2019).

Fourier transform infrared spectroscopy (FTIR, Agilent, FTIR-660+610, Santa Clara, CA, USA) was conducted in the range from  $4000\text{--}500\text{ cm}^{-1}$  to characterize major functional groups of PS feedstock and frass samples. Prior to the analyses, dry samples were ground with KBr to prepare a homogeneous KBr pellet for scanning.

Thermal gravimetric analysis (TGA, TA, Q600, New Castle, DE, USA) was performed to characterize thermal changes during the conversion of PS to frass. Samples of PS (5 mg) and frass (5 mg) were analyzed within a temperature range of  $40\text{--}800\text{ }^{\circ}\text{C}$  at a rate of  $20\text{ }^{\circ}\text{C}/\text{min}$ . A high-purity nitrogen flow (99.999%) was used at a rate of  $20\text{ mL}/\text{min}$  for protection of the sample.

$^1\text{H}$  nuclear magnetic resonance ( $^1\text{H-NMR}$ , Bruker BioSpin, AVANCE III HD 400, Fällanden, Switzerland) was used to characterize changes in the end group of the egested polymer at the ambient temperature. Samples were dissolved in deuterated chloroform with 99.8% purity.  $^1\text{H-NMR}$  spectra were measured on a 400 MHz NMR spectrometer and with  $^1\text{H}$  sensitivity  $\geq 500:1$  (0.1% EB, noise range of 200 Hz).

#### 2.4. Analysis of Gut Microbial Community

Larvae of *G. mellonella*, *T. molitor*, and *Z. atratus* (200 per group) used for gut microbial community analysis were fed with PS as their sole diet and maintained under the same conditions as mentioned above. About 0.4 g of gut tissue was collected respectively on Day 0, Day 10, and Day 20 for further analysis. Prior to the dissection, larvae were immersed in 75% ethanol for 1 min and dipped into saline 3 times. Then, their guts were removed and put into a 1.5 mL centrifuge tube. The operation was performed in a sterile environment. The samples collected were stored at  $-80\text{ }^{\circ}\text{C}$  until further use. The V3–V4 region of the 16S rRNA gene of the sample was sequenced using Majorbio Bio-Pharm Technology Co., Ltd. (Shanghai, China). Microbial DNA was extracted using the E.Z.N.A.<sup>®</sup> Soil DNA Kit (Omega Bio-tek, Norcross, GA, USA) according to the manufacturer's protocol. The amplicons were extracted with 2% agarose gel and further purified using the AxyPrep DNA Gel Extraction Kit (Axygen Biosciences, Union City, CA, USA). The purified amplicons were pooled in equimolar and paired-end sequenced ( $2 \times 300$ ) on an Illumina MiSeq platform.

#### 2.5. Determination of Degradation Products

Gas chromatography–mass spectrometry (GC–MS, Agilent, Agilent 7890A/5975C, USA) was performed for further investigation of the intermediates and products generated from the biodegradation of plastic. The samples of frass and gut were collected using the process described above and pretreated based on the method mentioned by Lou et al. (2020) with modifications. The ground frass and gut from the PS-fed larvae were extracted with 10 mL of chloroform:methanol (2:1), then kept in a water bath at  $55\text{ }^{\circ}\text{C}$  for 3 h. The solvents were allowed to evaporate, and the residual polymers were redissolved in 100% hexane for the GC–MS analysis. The PS sample underwent the same pretreatment and was treated as the control group. The GC–MS used HP-5 ( $30\text{ m} \times 250\text{ }\mu\text{m} \times 0.25\text{ }\mu\text{m}$ ) column and helium as the carrier gas. The oven temperature programming started at  $40\text{ }^{\circ}\text{C}$  followed by a hold for 4 min, an increase to  $280\text{ }^{\circ}\text{C}$  at a rate of  $10\text{ }^{\circ}\text{C}/\text{min}$ , and a 5 min hold. The compounds were identified based on the NIST17 database.



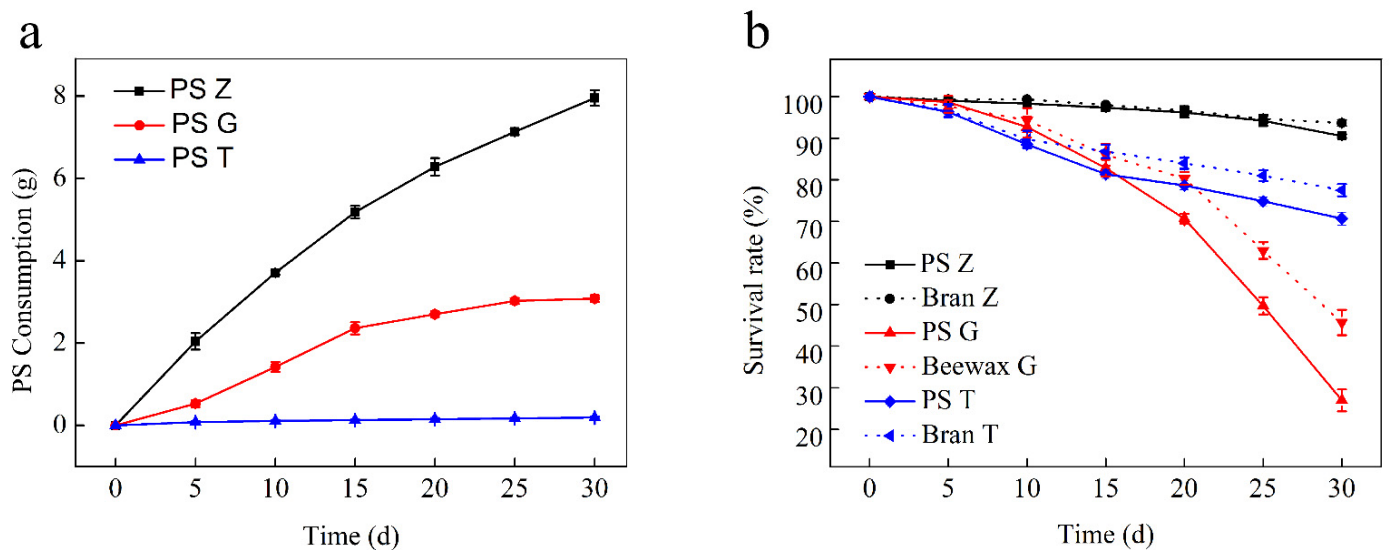
## 2.6. Statistical Analysis

Statistical ANOVAs were performed using SPSS 20.0 (SPSS Inc., Chicago, IL, USA). Pairwise comparisons were analyzed by Student's *t*-test, as all data were normally distributed. All error values are reported as the mean value  $\pm$  the standard deviation.

## 3. Results and Discussion

### 3.1. Changes in PS Consumption, Larvae Weight, and Survival Rates

When Styrofoam was placed in a container as the only diet, superworms, greater wax moths, and yellow mealworms began to feed on it and gradually produced etch loss. During the 30 d test, the PS mass consumption by superworms was 7.95 g, while that of the greater wax moths and yellow mealworms was 3.08 g and 0.19 g, respectively. There was a progressive increase in the PS consumption by all three species (Figure 1a). The average PS consumption rates were found to be  $2.78 \pm 0.060 \text{ mg larva}^{-1} \text{ d}^{-1}$ ,  $1.57 \pm 0.066 \text{ mg larva}^{-1} \text{ d}^{-1}$  and  $0.07 \pm 0.009 \text{ mg larva}^{-1} \text{ d}^{-1}$ , respectively (Table 1). During the 30 d experiment period, the survival rate of larvae in the PS group and the feed group showed a downward trend, and the survival rate of the three kinds of larvae showed a significant difference. The survival rate of superworms, greater wax moths, and yellow mealworms in the feed group was  $93.67 \pm 1.53\%$ ,  $45.67 \pm 3.06\%$ , and  $80.83 \pm 7.11\%$ , respectively, and that of the PS group was  $90.50 \pm 0.50\%$ ,  $27.00 \pm 2.65\%$ , and  $75.5 \pm 7.4\%$ , respectively (Figure 1b). The results showed that the survival rate of superworms was the highest, followed by the yellow mealworm and the greater wax moths. For the same kind of larvae, the survival rate of the PS group was lower than that of the feed group.



**Figure 1.** PS consumption by superworms, greater wax moths, and yellow mealworms (a), the survival rate for the three species' larvae that were fed with PS and bran/beeswax (b). Z: superworms, G: greater wax moths, T: yellow mealworms.

After the experiment, the weight changes of the PS group were  $-51.67 \pm 1.15\%$ ,  $-43.61 \pm 4.67\%$ , and  $-17.06 \pm 5.28\%$ , and the weight changes of feed group were  $+12.11 \pm 3.37\%$ ,  $+18.89 \pm 2.12\%$ , and  $+25.92 \pm 1.84\%$ , respectively. The results showed that all three kinds of larvae were able to feed on PS; however, there were significant differences in PS consumption among the larvae of each species (Table 1). Meanwhile, a marked decrease in the mass weight of the PS-feeding larvae was observed. According to the comparison data of the survival rate and the weight changes between the PS group and feed group, it can be noted that PS cannot meet the energy needed for their growth and development. The study also showed that the PS consumption rate and weight loss of the three kinds of larvae were found to be directly proportional to their body size. The superworm was the largest in size, so the PS consumption rates were recorded as high and its body weight changed the most; yellow mealworm was the

smallest, and the PS consumption rate was the lowest and its own body weight changed the least. This result is consistent with the analysis by Peng et al. [23], who stated that the greater consumption capability of superworms was likely associated with their larger size and intrinsically aggressive foraging habit.

**Table 1.** Summary of PS biodegradation by the three species' larvae.

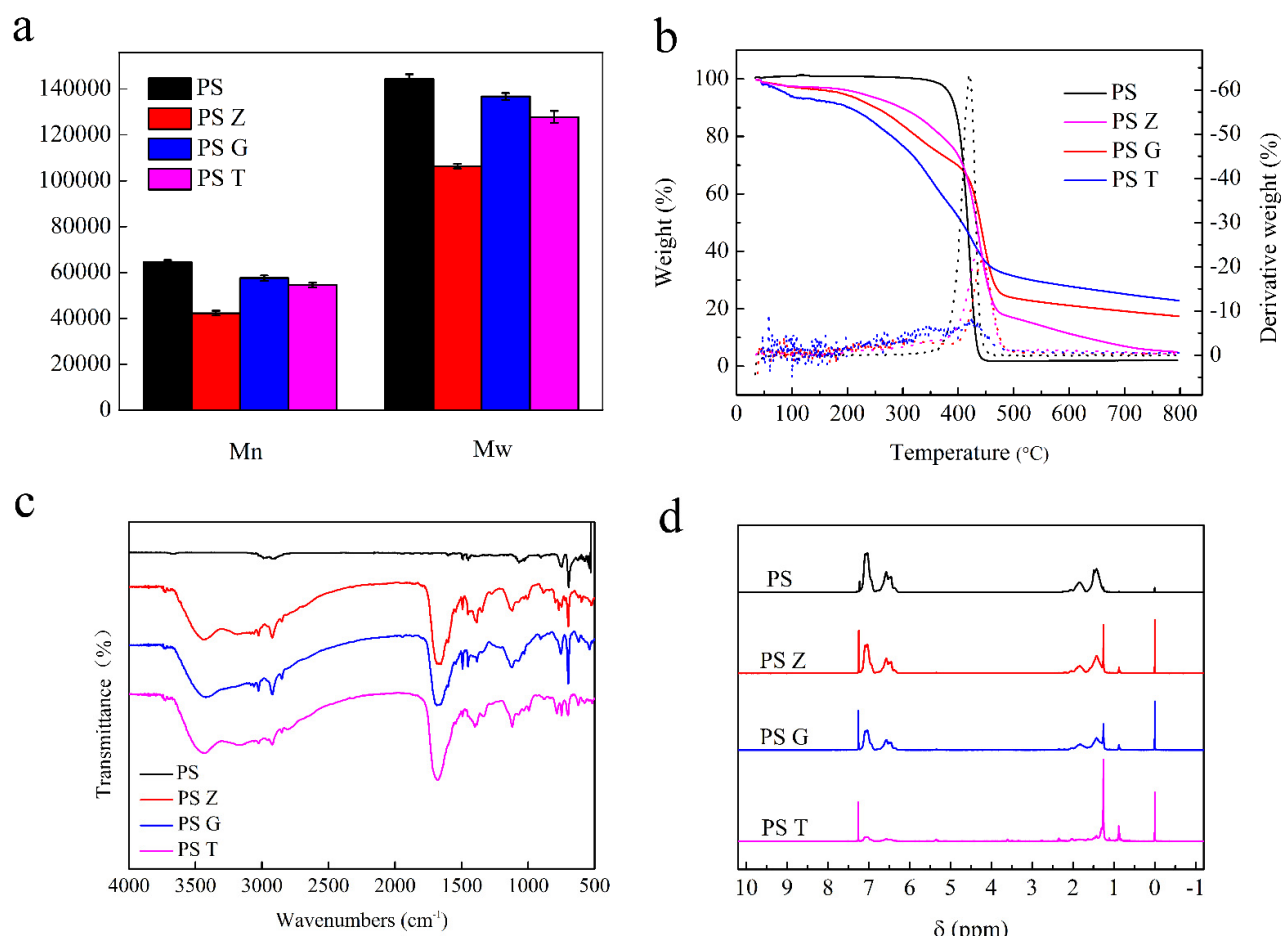
Larvae	Initial Weight/Larva (g)	Feed	Weight Change at the End of the Test (%)	Survival Rate (%)	mg PS/Larva/d
Superworm	0.86 ± 0.021	PS	−51.67 ± 1.15	90.5 ± 0.5	2.78 ± 0.060 a
		Bran	+12.11 ± 3.37	93.67 ± 1.53	
Greater wax moth	0.21 ± 0.015	PS	−43.61 ± 4.67	27 ± 2.65	1.57 ± 0.066 b
		Beeswax	+18.89 ± 2.12	45.67 ± 3.06	
Yellow mealworm	0.08 ± 0.015	PS	−17.06 ± 5.28	75.5 ± 7.4	0.07 ± 0.009 c
		Bran	+25.92 ± 1.84	80.83 ± 7.11	

Values followed by different small letters (a–c) within a column are significantly different ( $p < 0.05$ ).

### 3.2. Evidence and Differences of Biodegradation

The THF extract of frass and the THF-dissolved pristine Styrofoam were analyzed using GPC, respectively. The results showed that the number-averaged molecular weight ( $M_n$ ) and weight-averaged molecular weight ( $M_w$ ) of Styrofoam were 64,400 Da and 144,400 Da, respectively. The frass extractions from superworm, greater wax moth, and yellow mealworm were 42,304 Da and 106,381 Da, 57,458 Da and 136,735 Da, 54,472 Da and 127,793 Da, respectively. It was clearly shown that the  $M_n$  and  $M_w$  of the frass of the three species' larvae showed a decline compared to that of the Styrofoam (Figure 2a). Generally, the decline of  $M_n$  and  $M_w$  analyzed by GPC is considered as a major indication of polymer modification, depolymerization, and degradation [13,26]. These results suggested that the depolymerization of long chains of PS molecules and the lower molecular weight of the degraded products were formed in the insect larvae's guts. Meanwhile, the decrease in both  $M_n$  and  $M_w$  of PS gave evidence of chain scission by enzymatic depolymerization or microbial attack [27,28]. In this study, the molecular weight of the degradation products of superworm was minimum, followed by yellow mealworm and greater wax moth, which indicated that the intestinal microorganisms of superworm may have the highest ability to degrade PS into low-molecular-weight substances.

TGA was used to detect the thermal modification of larvae from pristine Styrofoam to frass at the end of the 30 d test. As shown in Figure 2b, the TGA curve of Styrofoam showed only one sharp mass loss where more than 95% of the loss occurred between 380 °C and 440 °C, and the maximum decomposition rate occurred at 420 °C. In contrast, there was no significant or sudden drop detected in the TGA curves for the frass of PS-fed larvae of the three species. There was a gradual decrease in the curves from the beginning to 800 °C. A sudden drop in the PS curve represented the degradation of PS at high temperatures. However, the frass curve did not show any kind of degradation range, thus illustrating that the PS content in frass was low or absent and the biodegradation of PS took place resulting in the formation of other compounds in the insect intestines. Compared to the curves of the superworm and greater wax moth, yellow mealworm frass presented the lowest derivative weight, which indicated that the PS content in the yellow mealworm frass was lower and the degradation efficiency of PS was higher. Interestingly, yellow mealworm frass was detected at one obvious mass loss stage at 50–100 °C; however, it was absent in the other two larvae, which is in line with the findings of Yang et al. [12]. This was believed to be related to the material source that was used for the experiment.



**Figure 2.** Depolymerization of PS by the three species' larvae. Comparison of the  $M_n$  and  $M_w$  of PS and polymers extracted from frass (a), the TGA spectra of the PS and frass of PS-fed larvae (b), the FTIR spectra of the PS and frass of PS-fed larvae (c), and the  $^1\text{H-NMR}$  spectra for the PS and frass of larvae fed with PS only (d). Z: superworms, G: greater wax moths, T: yellow mealworms.

The FTIR spectra were analyzed to study the oxidation and depolymerization of Styrofoam to frass in the gut of larvae. The results showed that PS-fed larvae's frass presented more undulate peaks and obvious peaks at around  $1075\text{ cm}^{-1}$ ,  $1700\text{ cm}^{-1}$ , and  $3450\text{ cm}^{-1}$ , thus representing C–O, C=O, and R–OH, respectively (Figure 2c). This finding suggested that the oxidation and depolymerization processes of PS occurred in the gut of the larvae [14]. Meanwhile, the frass of the three larvae produced similar FTIR spectra, except yellow mealworm at a  $650\text{ cm}^{-1}$  peak, which represented weak ring-bending vibrations. These characteristic peaks indicated that the gut microbes of all three species' larvae were able to degrade Styrofoam and that of yellow mealworm was found to destroy the benzene ring.

The  $^1\text{H-NMR}$  spectra for PS and frass Z revealed new peaks in the frass of larvae that fed on PS only. These peaks included  $\delta 0$ ,  $\delta 0.9$ ,  $\delta 1.3$ ,  $\delta 5.4$ , and  $\delta 7.2$  and were detected in the region of hydrogen bond changes. In addition, the frass of yellow mealworm presented some unique peaks, such as  $\delta 1.5\text{--}2.0$ ,  $\delta 3.5$ , and  $\delta 6\text{--}7$  (Figure 2d), which indicated that PS may be depolymerized strongly by the gut microbes of yellow mealworm. Meanwhile, this result was consistent with the FTIR conclusion that yellow mealworm could destroy the benzene ring.

### 3.3. Comparison of Gut Microbial Diversity

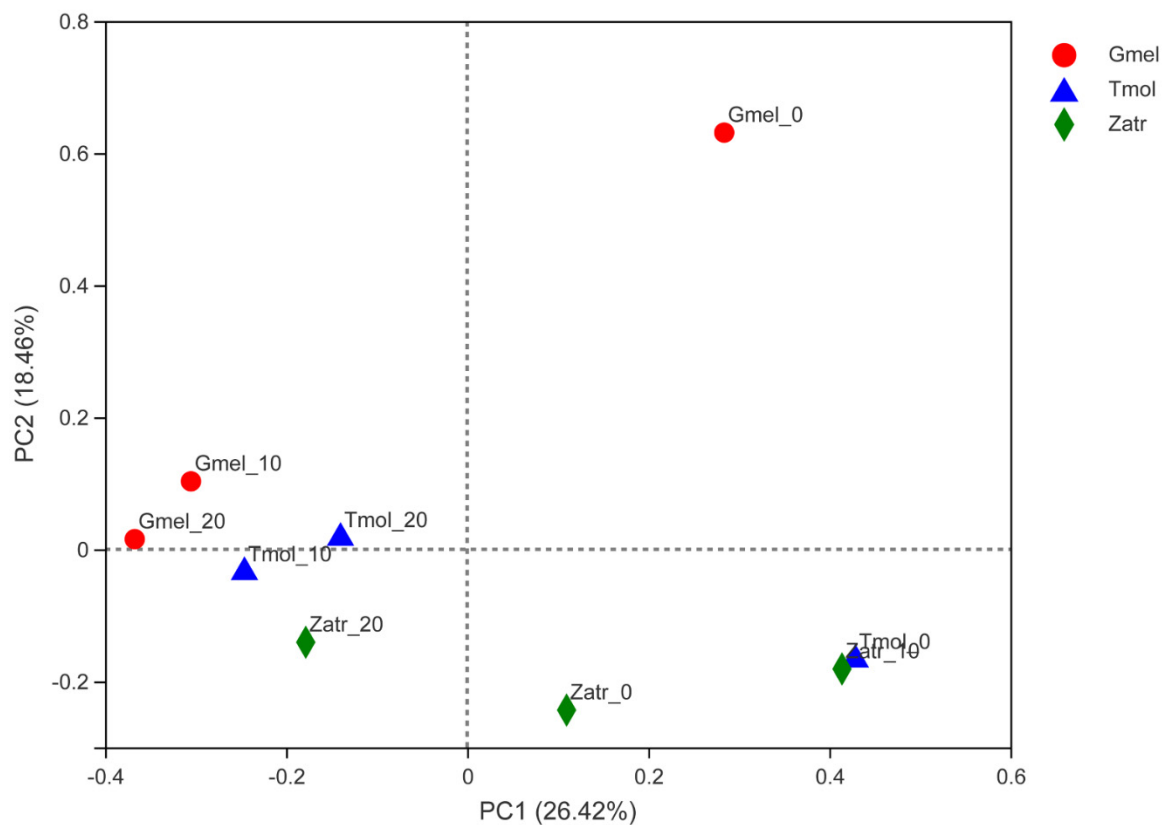
The gut microbiome of insects has an important role to play in their digestion process [29,30]. In order to determine and compare the changes of intestinal microbiome

caused by feeding on polystyrene, the gut bacterial community richness, diversity, and composition of three species' larvae were detected at three stages (0 d, 10 d, 20 d) using Illumina sequencing of 16S rRNA gene amplicons. A total of four-hundred and nine-thousand, six-hundred and sixty-four sequences of nine samples were obtained and listed in Table 2 with sampling coverage above 0.99, thus suggesting that Illumina sequencing was capable of detecting most of the reads. For greater wax moth and yellow mealworm, the OTU trends of the three stages showed a decrease in value, but the trend increased for superworm. The OTUs of the 0 d yellow mealworm gut bacterial community were relatively more than the other two groups. The Ace and Chao estimators were used to analyze the community richness. The results showed that Tmol\_0 had the highest taxonomic richness, Gmel\_0 and Gmel\_10 had a lower taxonomic richness, while the other samples showed similar richness. Meanwhile, the Shannon and Simpson indexes of the Alpha diversity estimators were used to indicate community diversity. The results showed that there was a change in the gut microbe species diversity with respect to the prolongation of PS feeding time. Furthermore, the three species' larvae showed different trends. The gut microbiome showed higher diversity in superworm and yellow mealworm before feeding them with PS. Upon PS feeding, a decrease in community diversity was observed in the case of superworm and yellow mealworm, but an increase was marked in the case of greater wax moth. The difference in diversity at 0 d might be due to their initial dietary differences; however, the difference on later days may be related to their gut ecophysiology [14]. Therefore, after feeding them the same food, i.e., polystyrene, the gut microbiome began to develop in a way that helped them digest it.

**Table 2.** Quality of the samples and bacterial diversity analyses based on Illumina sequencing of the 16S rRNA gene amplicons.

Sample	Size	OTUs	Shannon	Simpson	Ace	Chao	Coverage
Gmel_0	52,347	35	0.180129	0.931893	50.41519	43.75	0.999543
Gmel_10	44,132	43	0.224694	0.925592	72.07289	60.1	0.999421
Gmel_20	48,381	13	1.336777	0.319691	13.375	13	0.99997
Tmol_0	36,796	1268	5.892504	0.009599	1269.646	1268.35	0.999756
Tmol_10	47,699	37	1.964937	0.197299	60.83233	42.6	0.999756
Tmol_20	43,830	27	1.605712	0.267592	38.36263	30.75	0.999817
Zatr_0	41,939	148	2.399686	0.189472	179.5835	168.6667	0.999024
Zatr_10	49,021	157	1.570013	0.32704	186.085	190.4762	0.998842
Zatr_20	45,519	161	2.337035	0.176703	199.1793	191.4412	0.998598

Beta analysis through principal co-ordinates analysis (PCoA) based on the Bray–Curtis distance was carried out to reveal the differences of the sample community composition among different groups of the three species' larvae. According to Figure 3, feeding on PS had an obvious influence on the gut microbial composition. Gmel\_0, Tmol\_0, and Zatr\_0 presented long-distance comparisons with 10 d and 20 d PS-fed groups of each species' larvae, thus indicating a conspicuous difference before and after feeding PS. Meanwhile, Gmel\_10 and Gmel\_20 and Tmol\_10 and Tmol\_20 showed close distance comparisons with Gmel\_0 and Tmol\_0, which showed that the longer the PS feeding time was, the smaller the change in the gut microbial composition was for greater wax moth and yellow mealworm. The trend was also observed in *T. castaneum* larvae and *T. molitor* larvae before and after feeding with PS [14,17,28]. The distances of the Gmel\_10, Gmel\_20, Tmol\_10, Tmol\_20, and Zatr\_20 community were found to be relatively close, which showed a similarity of their community composition. The findings showed that the degradation by the bacterial community that was involved in PS degradation in the intestines of the three species' larvae was similar.



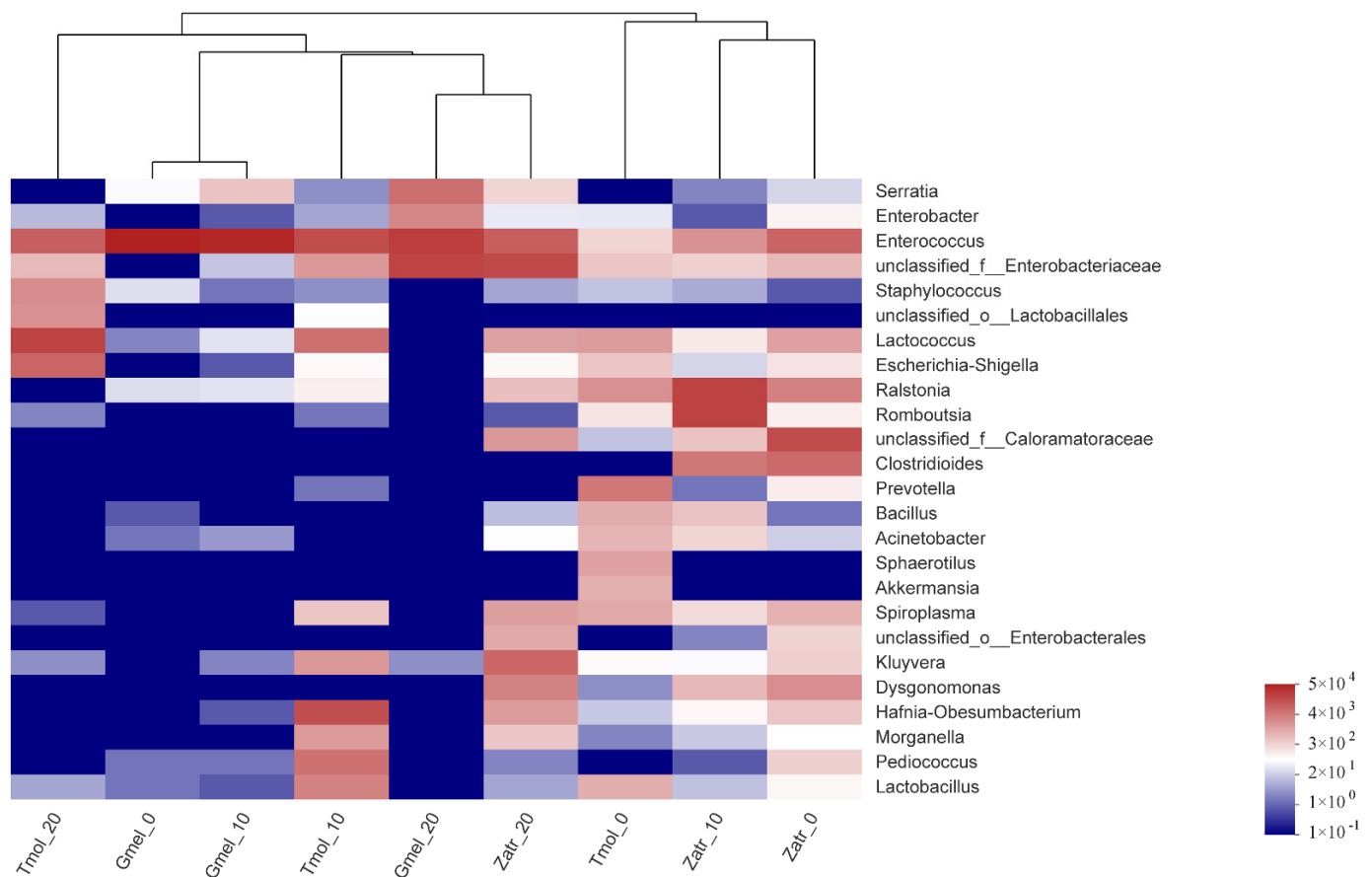
**Figure 3.** Principle co-ordinates analysis based on the Bray–Curtis distance among the nine groups of the three species' larvae. Tmol: yellow mealworm, Gmel: greater wax moth, Zatr: superworm.

The microbial community composition for the three species was analyzed by community bar plot analysis (Figure 4) based on the phylum and genus level and community heatmap analysis (Figure 5). The results showed that feeding on PS can induce the enrichment of some intestinal microorganisms, which may be the microorganisms responsible for PS digestion. For superworm, the core gut microbiome species were *Enterococcus*, *Enterobacteriaceae*, *Kluyvera*, and *Lactococcus*; for greater wax moth, they were *Enterococcus*, *Enterobacteriaceae*, *Serratia*, and *Enterobacter*; for yellow mealworm, they were *Enterococcus*, *Enterobacteriaceae*, *Escherichia-Shigella*, and *Lactococcus* (Figure 4a). The bacteria affiliated with *Enterococcus* and *Enterobacteriaceae* were found in all three species' larvae of 20 d of PS feeding (Figures 4a and 5), which indicated their crucial role in PS degradation. Figure 4b shows that *Firmicutes* and *Proteobacteria* were the predominant phyla in the guts of 20 d PS-fed groups. This result is consistent with the results of previous studies [16,28]. So far, many studies have successfully screened out the PS-degrading microbes from the insects' guts. A similar study was carried out by Wang et al. [17], who investigated the gut microbiome of plastic- and bran-fed *T. castaneum* larvae and found that *Acinetobacter* sp. was strongly associated with PS degradation. Later, they were successful in isolating *Acinetobacter* sp. AnTc-1, which is a PS-degrading bacteria. Yang et al. [31] isolated a PS degrading bacterial strain *Exiguobacterium* sp. YT2 from the guts of *T. molitor* larvae. Brandon et al. [22] identified eight unique gut microorganisms associated with PS biodegradation including *Citrobacter freundii*, *Serratia marcescens*, and *Klebsiella aerogenes*. Woo et al. [32] isolated a PS-degrading strain *Serratia* sp. WSW from the gut flora of *P. davidis* larvae. These isolated strains belong to *Firmicutes* or *Proteobacteria*. Heatmap analysis also showed that four clusters were generated from the nine groups: Cluster I (Tmol\_0, Zatr\_0, and Zatr\_10), Cluster II (Tmol\_10, Gmel\_20, and Zatr\_20), Cluster III (Gmel\_0 and Gmel\_10), and Cluster IV (Tmol\_20) (Figure 5), where each cluster implied a homology of microbial community structure. That is to say, the guts with a long PS feeding time tended

to cluster together, while those with a short PS feeding time tended to cluster into another group. This result is consistent with the result of the Beta analysis.



**Figure 4.** Community bar plot analysis of nine samples of the three species' larvae based on genus (a) and phylum levels (b). Tmol: yellow mealworm, Gmel: greater wax moth, Zatr: superworm.



**Figure 5.** Gut bacterial community heatmap analysis of nine samples of the three species' larvae. The analysis is on the basis of the top 25 abundant genera. The color intensity of the scale indicates the relative abundance. Tmol: yellow mealworm, Gmel: greater wax moth, Zatr: superworm.

### 3.4. Analysis of Degradation Products

In PS metabolism, the formation of intermediates represents the digestion of the PS by the larvae and its biodegradation [16]. Previous studies have reported that fatty acids and carboxylic esters represent the generated metabolic intermediates of plastics [33]. GC-MS analysis was conducted to determine the intermediates and products during PS metabolism in the gut and frass of larvae. The results revealed that a variety of acids and alcohols, such as 2-propenoic acid, benzenepropanoic acid, behenic alcohol, and phthalic acid, and long chain fatty acids, such as oleic acid, hexadecanoic acid, and octadecanoic acid (Table 3), were detected in the frass and gut of larvae fed on PS, thus representing the possible metabolism of the benzene structure and biodegradation of PS. In addition, 2-propenoic acid and behenic alcohol were detected in the frass of all three species' larvae. Hexadecanoic acid was detected in the gut of all three species' larvae. These results suggested that some of these gut microbes present in these three insect larvae were similar in their physiology and action of disrupting the bonding sites in the PS. Then, the microbes were found to be *Enterococcus* and *Enterobacteriaceae*, as mentioned above. Compounds with oxygen were detected in the PS samples, and some compounds appearing to be toxic and dangerous, such as phenol, heptane, and toluene, were also detected, which may be attributed to plasticizers, antioxidants, and other additives in the plastic foam [4]. However, these toxic and dangerous compounds were not detected in the gut and frass of larvae, suggesting that they may have been degraded by the larvae. Although the larvae degraded these compounds, which may also be harmful to them, this may also be a reason for the low survival rate of the treated group.

**Table 3.** Chemical compounds of PS and the frass, and gut of larvae analyzed by GC–MS.

Larvae	Sample	Chemical Compound
Greater wax moth	Frass	2-propenoic acid, behenic alcohol, benzenepropanoic acid, acetic acid, 6-tetradecanesulfonic acid
	Gut	Hexadecanoic acid, oxalic acid, phthalic acid, benzenepropanoic acid, benzoic acid
Yellow mealworm	Frass	2-propenoic acid, behenic alcohol, benzenepropanoic acid, silicic acid, [1,2,4]triazolo[1,5-a]pyrimidine-6-carboxylic acid
	Gut	Hexadecanoic acid, 9-octadecenoic acid, z-8-methyl-9-tetradecenoic acid
Superworm	Frass	2-propenoic acid, behenic alcohol, 9-octadecenoic acid, phthalic acid, hexadecanoic acid, methoxyacetic acid
	Gut	hexadecanoic acid, stearic acid, phthalic acid, 6-octadecenoic acid
	PS	phenol, heptane, toluene, o-xylene, 3-(benzylthio)acrylic acid

#### 4. Conclusions

The eating and degradation of plastics by insect larvae is a new way to solve white pollution. The biodegradation of PS and the changes of the intestinal microbial diversity occurred in the insect guts, which may be closely related to these changed intestinal microorganisms. Currently, scientists have screened out the PS-degrading bacteria from the gut of some insect larvae. However, insect larvae and intestinal microorganisms have a mutually beneficial symbiotic relationship. After eating plastic, not only the intestinal microorganisms of insect larvae play an important role in the biodegradation of plastic, but also their enzyme system plays a crucial part in the degradation process. Therefore, further study is needed to determine the interaction between these insects and their gut microorganisms to reveal the degradation mechanism of plastic by insect eating.

**Author Contributions:** Conceptualization, Z.W.; data curation, S.J.; formal analysis, S.J.; funding acquisition, J.Z. and Z.W.; investigation, S.J.; methodology, T.S., J.Z., and Z.W.; supervision, J.Z. and Z.W.; visualization, J.Z. and Z.W.; writing—review and editing, T.S. and J.Z. All authors have read and agreed to the published version of the manuscript.

**Funding:** This work was supported by the Education Department of Liaoning Province (Grant Number L2019040), the Natural Science Foundation of Liaoning Province (Grant Number 2020-BS-229), the Liaoning Revitalization Talents Program (Grant Number XLYC1807034), and the Talent Scientific Research Funds of Liaoning Petrochemical University (Grant Number 2019XJL-012).

**Institutional Review Board Statement:** Not applicable.

**Informed Consent Statement:** Not applicable.

**Data Availability Statement:** The data presented in this study are available upon request from the corresponding author.

**Conflicts of Interest:** The authors declare no conflict of interest.

#### References

- Mohan, N.; Montazer, Z.; Sharma, P.K.; Levin, D.B. Microbial and Enzymatic Degradation of Synthetic Plastics. *Front. Microbiol.* **2020**, *11*, 2837. [[CrossRef](#)]
- Veerasingam, S.; Vethamony, P.; Aboobacker, V.M.; Giraldez, A.E.; Al Khayat, J.A. Factors influencing the vertical distribution of microplastics in the beach sediments around the Ras Rakan Island, Qatar. *Environ. Sci. Pollut. Res.* **2021**, *28*, 34259–34268. [[CrossRef](#)]
- Chamas, A.; Moon, H.; Zheng, J.J.; Qiu, Y.; Tabassum, T.; Jang, J.H.; Abu-Omar, M.; Scott, S.L.; Suh, S. Degradation Rates of Plastics in the Environment. *ACS Sustain. Chem. Eng.* **2020**, *8*, 3494–3511. [[CrossRef](#)]
- Carmen, S. Microbial capability for the degradation of chemical additives present in petroleum-based plastic products: A review on current status and perspectives. *J. Hazard. Mater.* **2021**, *402*, 123534. [[CrossRef](#)] [[PubMed](#)]
- Gabriel, M.; Salazar Robles, G.; José, M.; Cunill, J. Aiding the Environment: Microorganisms for the Degradation of Plastic in Soil and Water. *Indian J. Appl. Microbiol.* **2019**, *22*, 19–37.
- Krueger, M.C.; Harms, H.; Schlosser, D. Prospects for microbiological solutions to environmental pollution with plastics. *Appl. Microbiol. Biotechnol.* **2015**, *99*, 8857–8874. [[CrossRef](#)] [[PubMed](#)]



7. Malachová, K.; Novotná, Č.; Adamus, G.; Lotti, N.; Fava, F. Ability of *Trichoderma hamatum* Isolated from Plastics-Polluted Environments to Attack Petroleum-Based, Synthetic Polymer Films. *Processes* **2020**, *8*, 467. [[CrossRef](#)]
8. Mor, R.; Sivan, A. Biofilm formation and partial biodegradation of polystyrene by the actinomycete *Rhodococcus ruber*: Biodegradation of polystyrene. *Biodegradation* **2008**, *19*, 851–858. [[CrossRef](#)]
9. Sekhar, V.C.; Nampoothiri, K.M.; Mohan, A.J.; Nair, N.R.; Bhaskar, T.; Pandey, A. Microbial degradation of high impact polystyrene (HIPS), an e-plastic with decabromodiphenyl oxide and antimony trioxide. *J. Hazard. Mater.* **2016**, *318*, 347–354. [[CrossRef](#)]
10. Riudavets, J.; Salas, I.; Pons, M.J. Damage characteristics produced by insect pests in packaging film. *J. Stored Prod. Res.* **2007**, *43*, 564–570. [[CrossRef](#)]
11. Yang, J.; Yang, Y.; Wu, W.M.; Zhao, J.; Jiang, L. Evidence of Polyethylene Biodegradation by Bacterial Strains from the Guts of Plastic-Eating Waxworms. *Environ. Sci. Technol.* **2014**, *48*, 13776–13784. [[CrossRef](#)] [[PubMed](#)]
12. Yang, Y.; Yang, J.; Wu, W.M.; Zhao, J.; Song, Y.L.; Gao, L.C.; Yang, R.F.; Jiang, L. Biodegradation and Mineralization of Polystyrene by Plastic-Eating Mealworms: Part 1. Chemical and Physical Characterization and Isotopic Tests. *Environ. Sci. Technol.* **2015**, *49*, 12080–12086. [[CrossRef](#)]
13. Yang, S.S.; Brandon, A.M.; Flanagan, J.C.A.; Yang, J.; Ning, D.; Cai, S.Y.; Fan, H.Q.; Wang, Z.Y.; Ren, J.; Benbow, E.; et al. Biodegradation of polystyrene wastes in yellow mealworms (larvae of *Tenebrio molitor* Linnaeus): Factors affecting biodegradation rates and the ability of polystyrene-fed larvae to complete their life cycle. *Chemosphere* **2018**, *191*, 979–989. [[CrossRef](#)]
14. Peng, B.Y.; Su, Y.M.; Chen, Z.B.; Chen, J.B.; Zhou, X.F.; Benbow, M.E.; Criddle, C.S.; Wu, W.M.; Zhang, Y.L. Biodegradation of Polystyrene by Dark (*Tenebrio obscurus*) and Yellow (*Tenebrio molitor*) Mealworms (Coleoptera: Tenebrionidae). *Environ. Sci. Technol.* **2019**, *53*, 5256–5265.
15. Bryan, J.C.; Grove, H.; Elebute, O.; Villanueva, S.; LeMoine, C. Role of the intestinal microbiome in low-density polyethylene degradation by caterpillar larvae of the greater wax moth, *Galleria mellonella*. *Proc. R. Soc. B* **2020**, *287*, 1–8.
16. Lou, Y.; Ekaterina, P.; Yang, S.S.; Lu, B.Y.; Liu, B.F.; Ren, N.; Corvini, P.; Xing, D.F. Bio-degradation of Polyethylene and Polystyrene by Greater Wax Moth Larvae (*Galleria mellonella* L.) and the Effect of Co-diet Supplementation on the Core Gut Microbiome. *Environ. Sci. Technol.* **2020**, *54*, 2821–2831. [[CrossRef](#)] [[PubMed](#)]
17. Wang, Z.; Xin, X.; Shi, X.; Zhang, Y. A polystyrene-degrading *Acinetobacter* bacterium isolated from the larvae of *Tribolium castaneum*. *Sci. Total Environ.* **2020**, *726*, 138564. [[CrossRef](#)] [[PubMed](#)]
18. Yang, Y.; Wang, J.; Xia, M. Biodegradation and mineralization of polystyrene by plastic-eating superworms *Zophobas atratus*. *Sci. Total Environ.* **2020**, *708*, 1352331–1352337.
19. Atiq, N.; Ahmed, S.; Ali, M.I.; Andleeb, S.; Ahmad, B.; Robson, G. Isolation and identification of polystyrene biodegrading bacteria from soil. *Afr. J. Microbiol. Res.* **2011**, *4*, 1537–1541.
20. Kaplan, D.L.; Hartenstein, R.; Sutter, J. Biodegradation of polystyrene, poly(methyl methacrylate), and phenol formaldehyde. *Appl. Environ. Microbiol.* **1979**, *38*, 551–553. [[CrossRef](#)]
21. Skariyachan, S.; Megha, M.; Kini, M.N.; Mukund, K.M.; Rizvi, A.; Vasist, K. Selection and screening of microbial consortia for efficient and ecofriendly degradation of plastic garbage collected from urban and rural areas of Bangalore, India. *Environ. Monit. Assess.* **2015**, *187*, 4174. [[CrossRef](#)] [[PubMed](#)]
22. Brandon, A.M.; Garcia, A.M.; Khlystov, N.A.; Wu, W.M.; Criddle, C.S. Enhanced Bioavailability and Microbial Biodegradation of Polystyrene in an Enrichment Derived from the Gut Microbiome of *Tenebrio molitor* (Mealworm Larvae). *Environ. Sci. Technol.* **2021**, *55*, 2027–2036. [[CrossRef](#)] [[PubMed](#)]
23. Peng, B.Y.; Li, Y.R.; Fan, R.; Chen, Z.B.; Wu, W.M. Biodegradation of low-density polyethylene and polystyrene in superworms, larvae of *Zophobas atratus* (Coleoptera: Tenebrionidae): Broad and limited extent depolymerization. *Environ. Pollut.* **2020**, *266*, 115206. [[CrossRef](#)]
24. Farrelly, T.A.; Shaw, I.C. Polystyrene as Hazardous Household Waste. In *Household Hazardous Waste Management*; Mmereki, D., Ed.; IntechOpen: London, UK, 2017; pp. 45–60.
25. Machado, N.C.; De Jesus, L.A.; Pinto, P.S.; De Paula, F.G.; Alves, M.O.; Mendes, K.H.; Mambrini, R.V.; Barrreda, D.; Rocha, V.; Santamaría, R.; et al. Waste-polystyrene foams-derived magnetic carbon material for adsorption and redox supercapacitor applications. *J. Clean. Prod.* **2021**, *313*, 127903. [[CrossRef](#)]
26. Albertsson, A.C.; Erlandsson, B.; Hakkarainen, M.; Karlsson, S. Molecular Weight Changes and Polymeric Matrix Changes Correlated with the Formation of Degradation Products in Biodegraded Polyethylene. *J. Environ. Polym. Degrad.* **1998**, *6*, 187–195. [[CrossRef](#)]
27. Ali, M.I.; Ahmed, S.; Robson, G.; Javed, I.; Hameed, A. Isolation and molecular characterization of polyvinyl chloride (PVC) plastic degrading fungal isolates. *J. Basic Microbiol.* **2014**, *54*, 18–27. [[CrossRef](#)]
28. Brandon, A.M.; Gao, S.H.; Tian, R.M.; Ning, D.L.; Yang, S.S.; Zhou, J.Z.; Wu, W.M.; Criddle, C.S. Biodegradation of Polyethylene and Plastic Mixtures in Mealworms (Larvae of *Tenebrio molitor*) and Effects on the Gut Microbiome. *Environ. Sci. Technol.* **2018**, *52*, 6526–6533. [[CrossRef](#)]
29. Tinker, K.A.; Ottesen, E.A. The Core Gut Microbiome of the American Cockroach, *Periplaneta americana*, Is Stable and Resilient to Dietary Shifts. *Appl. Environ. Microbiol.* **2016**, *82*, 6603–6610. [[CrossRef](#)]
30. Wang, Y.; Zhang, Y.L. Investigation of Gut-Associated Bacteria in *Tenebrio molitor* (Coleoptera: Tenebrionidae) Larvae Using Culture-Dependent and DGGE Methods. *Ann. Entomol. Soc. Am.* **2015**, *108*, 941–949. [[CrossRef](#)]

31. Yang, Y.; Yang, J.; Wu, W.M.; Zhao, J.; Song, Y.L.; Gao, L.C.; Yang, R.F.; Jiang, L. Biodegradation and Mineralization of Polystyrene by Plastic-Eating Mealworms: Part 2. Role of Gut Microorganisms. *Environ. Sci. Technol.* **2015**, *49*, 12087–12093.
32. Woo, S.; Song, I.; Cha, H.J. Fast and Facile Biodegradation of Polystyrene by the Gut Microbial Flora of *Plesiophthalmus davidis* Larvae. *Appl. Environ. Microbiol.* **2020**, *86*, e01361–e013620. [[CrossRef](#)] [[PubMed](#)]
33. Kong, H.G.; Kim, H.H.; Chung, J.-H.; Jun, J.H.; Soohyun, L.; Kim, H.-M.; Jeon, S.; Park, S.G.; Bhak, J.; Ryu, C.-M. The *Galleria mellonella* Hologenome Supports Microbiota-Independent Metabolism of Long-Chain Hydrocarbon Beeswax. *Cell Rep.* **2019**, *26*, 2451–2464. [[CrossRef](#)] [[PubMed](#)]



## Article

# Poly lactide, Processed by a Foaming Method Using Compressed Freon R134a, for Tissue Engineering

María Aguado <sup>1,2</sup>, Laura Saldaña <sup>2,3</sup>, Eduardo Pérez del Río <sup>1,2</sup>, Judith Guasch <sup>1,2,4</sup>, Marc Parera <sup>1,2</sup>, Alba Córdoba <sup>1,2</sup>, Joaquín Seras-Franzoso <sup>2,4,5</sup>, Olivia Cano-Garrido <sup>2,4,5,6</sup>, Esther Vázquez <sup>2,4,5</sup>, Antonio Villaverde <sup>2,4,5</sup>, Jaume Veciana <sup>1,2</sup>, Imma Ratera <sup>1,2,\*</sup>, Nuria Vilaboa <sup>2,3,\*</sup> and Nora Ventosa <sup>1,2,\*</sup>

- <sup>1</sup> Institut de Ciència de Materials de Barcelona, ICMAB-CSIC, Campus UAB, 08193 Bellaterra, Spain; m.aguado.olalla@gmail.com (M.A.); eperez2@icmab.es (E.P.d.R.); jguasch@icmab.es (J.G.); marc.parera@applus.com (M.P.); acordoba@nanomol-tech.com (A.C.); vecianaj@icmab.es (J.V.)
- <sup>2</sup> CIBER de Bioingeniería, Biomateriales y Nanomedicina (CIBER-BBN), 28029 Madrid, Spain; laura.saldana@salud.madrid.org (L.S.); joaquin.seras@gmail.com (J.S.-F.); olivia.cano.garrido@gmail.com (O.C.-G.); Esther.Vazquez@uab.cat (E.V.); antoni.villaverde@uab.cat (A.V.)
- <sup>3</sup> Hospital Universitario La Paz-IdiPAZ, Paseo de la Castellana 261, 28046 Madrid, Spain
- <sup>4</sup> Dynamic Biomimetics for Cancer Immunotherapy, Max Planck Partner Group, ICMAB-CSIC, Campus UAB, Bellaterra, 08193 Barcelona, Spain
- <sup>5</sup> Institut de Biotecnologia i Biomedicina, Universitat Autònoma de Barcelona, Bellaterra, 08193 Barcelona, Spain
- <sup>6</sup> Departament de Genètica i de Microbiologia, Universitat Autònoma de Barcelona, Bellaterra, 08193 Barcelona, Spain
- \* Correspondence: iratera@icmab.es (I.R.); nuria.vilaboa@salud.madrid.org (N.V.); ventosa@icmab.es (N.V.)

**Citation:** Aguado, M.; Saldaña, L.; Pérez del Río, E.; Guasch, J.; Parera, M.; Córdoba, A.; Seras-Franzoso, J.; Cano-Garrido, O.; Vázquez, E.; Villaverde, A.; et al. Poly lactide, Processed by a Foaming Method Using Compressed Freon R134a, for Tissue Engineering. *Polymers* **2021**, *13*, 3453. <https://doi.org/10.3390/polym13203453>

Academic Editors: José Miguel Ferri, Vicent Fombuena Borràs and Miguel Fernando Aldás Carrasco

Received: 2 September 2021

Accepted: 1 October 2021

Published: 9 October 2021

**Publisher's Note:** MDPI stays neutral with regard to jurisdictional claims in published maps and institutional affiliations.



**Copyright:** © 2021 by the authors. Licensee MDPI, Basel, Switzerland. This article is an open access article distributed under the terms and conditions of the Creative Commons Attribution (CC BY) license (<https://creativecommons.org/licenses/by/4.0/>).

**Abstract:** Fabricating polymeric scaffolds using cost-effective manufacturing processes is still challenging. Gas foaming techniques using supercritical carbon dioxide (scCO<sub>2</sub>) have attracted attention for producing synthetic polymer matrices; however, the high-pressure requirements are often a technological barrier for its widespread use. Compressed 1,1,1,2-tetrafluoroethane, known as Freon R134a, offers advantages over CO<sub>2</sub> in manufacturing processes in terms of lower pressure and temperature conditions and the use of low-cost equipment. Here, we report for the first time the use of Freon R134a for generating porous polymer matrices, specifically polylactide (PLA). PLA scaffolds processed with Freon R134a exhibited larger pore sizes, and total porosity, and appropriate mechanical properties compared with those achieved by scCO<sub>2</sub> processing. PLGA scaffolds processed with Freon R134a were highly porous and showed a relatively fragile structure. Human mesenchymal stem cells (MSCs) attached to PLA scaffolds processed with Freon R134a, and their metabolic activity increased during culturing. In addition, MSCs displayed spread morphology on the PLA scaffolds processed with Freon R134a, with a well-organized actin cytoskeleton and a dense matrix of fibronectin fibrils. Functionalization of Freon R134a-processed PLA scaffolds with protein nanoparticles, used as bioactive factors, enhanced the scaffolds' cytocompatibility. These findings indicate that gas foaming using compressed Freon R134a could represent a cost-effective and environmentally friendly fabrication technology to produce polymeric scaffolds for tissue engineering approaches.

**Keywords:** 3D scaffolds; biomaterial engineering; tissue engineering; mesenchymal stem cells; polymeric foams; surface functionalization; protein nanoparticles; cell growth; compressed fluids; Freon R134a

## 1. Introduction

Scaffolds for tissue engineering should be degradable and biocompatible and have an appropriate porous structure and mechanical properties to allow cell colonization and growth [1–5]. Indeed, the presence of pores is essential not only for allowing cell migration and growth but also for enabling the diffusion of nutrients, oxygen and metabolic waste, which are necessary for the tissue regeneration process. Although cell migration

and nutrient transport are ensured with the presence of intercommunicated pores of approximately 150  $\mu\text{m}$  in diameter, larger sizes ( $>300 \mu\text{m}$ ) are recommended to promote vascularization and enhance osteogenesis [2]. However, a high degree of porosity usually implies a reduction in the mechanical properties of scaffolds, which could compromise the structure's integrity [4–6]. Consequently, a compromise between the pores' structure and dimensions and the mechanical properties is required.

Developing cost-effective procedures to fabricate synthetic polymers with controlled porous structures is an ongoing challenge in the biomedical engineering field. A variety of methods are available, including conventional solvent casting/particulate leaching, thermally induced phase separation, freeze drying, compression molding, electrospinning, as well as more advanced processing and fabrication methods such as those based on 3D printing [2,7,8]. However, all such conventional methods entail the use of organic solvents and high temperatures during the fabrication process, which limit their use when loading bioactive molecules into the matrices. Indeed, growth factors and other proteins are prone to denaturation at high temperatures or in the presence of certain organic solvents. In addition, solvent residues can trigger undesired harmful side effects at the implantation site. Salt leaching with sodium chloride is a common strategy for obtaining porous scaffolds; however, pore size distributions are difficult to reproduce, and therefore the scale-up of this procedure is highly challenging. Moreover, additive manufacturing methods such as rapid prototyping, which enables the generation of patient-customized, precise, and complex architectures, face several scale-up and cost-related difficulties that limit their massive clinical application.

An attractive alternative for overcoming the limitations associated with conventional methods is the “gas foaming” technique, which uses supercritical carbon dioxide ( $\text{scCO}_2$ ) to obtain materials with a high degree of porosity (up to 80%) [9–11]. This organic solvent-free process can occur at physiological temperatures, allowing the incorporation of biological agents [12–16].  $\text{scCO}_2$  is an attractive solvent because it is non-toxic, non-flammable and relatively inert [5,17]. Foaming with  $\text{scCO}_2$  requires pressures above the critical value (around 10 MPa) to achieve the gas' supercritical state. To achieve these processing conditions ( $T_c$  of 304 K and  $P_c$  of 7.38 MPa), high-pressure equipment is required [18]. An alternative to  $\text{scCO}_2$  is 1,1,1,2-tetrafluoroethane, commercially known as Freon R134a or norflurane, which despite its higher price provides significant advantages over  $\text{CO}_2$  in supercritical processing, including a much lower pressure and temperature setting to become liquid ( $<2 \text{ MPa}$  at room temperature), resulting not only in a reduction of the risks associated with working at high pressures but also in the cost of the equipment, with less specialized units and fittings, thereby facilitating its industrial application [19]. Similar to  $\text{scCO}_2$ , Freon R134a is non-toxic and non-flammable, with insignificant ozone depletion potential compared with other freons, and it is currently used in numerous biomedical applications [20]. Freon R134a can be more easily compressed and recycled in a gas-foaming process than  $\text{CO}_2$  due to the lower  $P_c$  of Freon R134a. To our knowledge, however, its use for preparing polymeric scaffolds using the gas foaming technique has not been attempted to date.

The functionalization of scaffold surfaces with bioactive factors has been investigated as a strategy to enhance cell colonization and growth [3,21–23]. Inclusion bodies like protein nanoparticles (pNPs) are deposits formed in bacteria due to recombinant protein overexpression [24]. These pNPs (in the range of few hundreds of nanometers) are commonly found in the bacteria cytoplasm [25]. In the past, such pNPs have been described as an obstacle in recombinant processes and considered as non-desired products. However, recent studies have demonstrated their potential as bioactive factors for tissue engineering. These protein aggregates not only are non-cytotoxic but, when incorporated to surfaces, also generate mechanical and biochemical signals that stimulate cell adhesion and proliferation [26–32]. The addition of bioactive factors to scaffolds can be achieved by various strategies, with direct surface adsorption being the most frequently used [4,21].

Due to their biocompatibility and biodegradability, polylactide (PLA) and poly(lactide-co-glycolide) (PLGA) saturated aliphatic polyesters stand out among the synthetic polymers used for tissue engineering [33–38]. In this study, we explored the use of compressed Freon R134a for processing PLA matrices at low pressure and compared the results with the same polymeric matrices processed at higher pressure using the well-implemented scCO<sub>2</sub>. For comparative purposes, we also fabricated PLGA matrices using compressed Freon R134a. To enhance their bioactivity, pNPs derived from green fluorescence protein (GFP), a commonly used marker for live-cell imaging, were used to functionalize the surface of the resulting porous scaffolds by means of a filtration process. Lastly, to explore the suitability of scaffolds processed with compressed fluids and functionalized with pNPs for bone tissue engineering applications, we investigated their cytocompatibility using human mesenchymal stem cells (MSCs) as precursors of osteoblasts, the bone-forming cells.

## 2. Materials and Methods

### 2.1. Materials

We employed semicrystalline polylactide (PDL, LLA; abbreviated as PLA) and amorphous PLGA with different molecular weights and inherent viscosities. The PDL, LLA (70:30, with inherent viscosity between 5.7–6.5 dL/g), Resomer<sup>®</sup> LR 708 (molecular weight, 150,000 Da), and PLGA (50:50, with inherent viscosity between 0.32–0.44 dL/g), and RESOMER RG503 (molecular weight, 30,000 Da) were purchased from Evonik Röhm GmbH (Darmstadt, Germany). Carbon dioxide (purity 99.995%) and Freon R134a were supplied by Carbueros Metálicos-Air products S.A. (Barcelona, Spain).

### 2.2. Methods

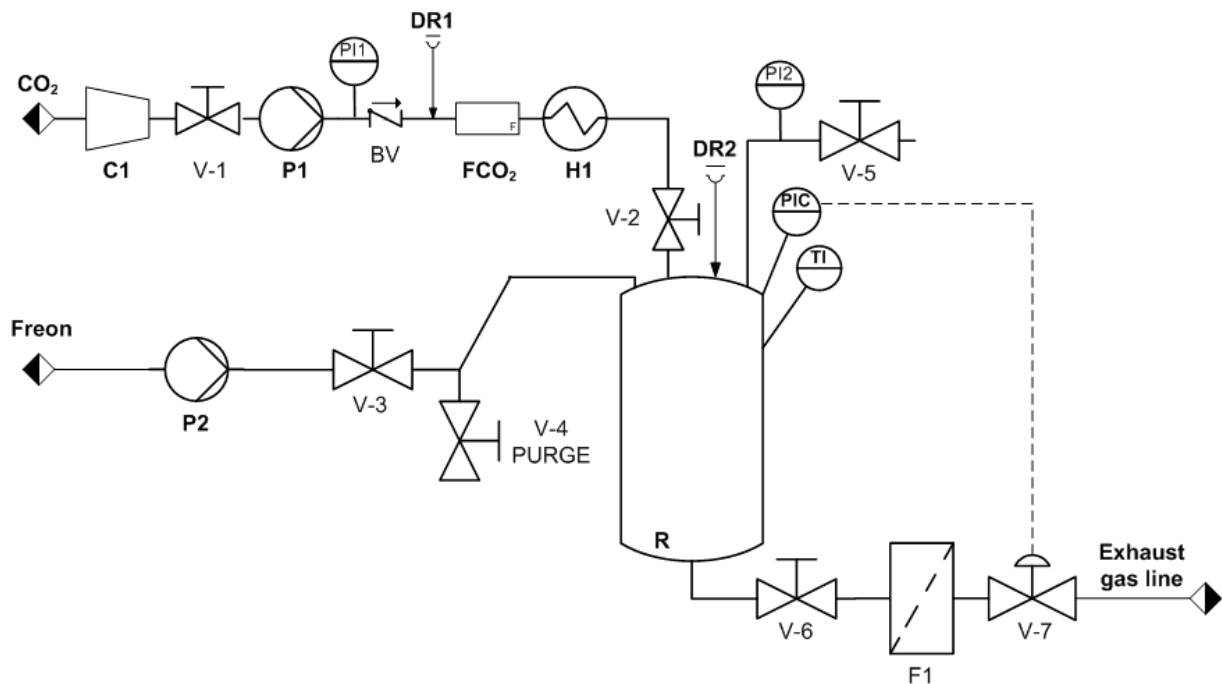
#### 2.2.1. Preparation of Polymer Disks

The desired mass of polymer was weighed and placed in a special polytetrafluoroethylene mold with a diameter of 13 mm and formed by two detachable parts, allowing for disk removal after preparation. The polymer pellets were then compressed with 3 tonnes for 20 s to form compressed non-porous polymer disks using a hydraulic press (Perkin Elmer, Waltham, MA, USA). Due to the lower diffusion of compressed fluids in semicrystalline polymers than in amorphous ones [9], an annealing pretreatment to amorphize the crystalline region of PLA was performed. As shown by the thermograms of the differential scanning calorimetry (DSC) (PerkinElmer DSC 8500 Lab System) (Supplementary Materials, Figures S1 and S2), the PLA crystalline phase was removed by thermal annealing of the disks in an oven at 150 °C. Fifteen minutes were sufficient for the complete amorphization of the PLA prior to its processing with compressed fluids. DSC analysis of the annealed PLA was performed from 20 °C to 250 °C at a heating rate of 10 °C/min. One mg of the sample was sealed into a 40- $\mu$ L aluminum pan and heated under a nitrogen purge of 50 mL/min. The temperature calibrations were performed using indium as the standard.

#### 2.2.2. 3D Porous Scaffold Fabrication Using Compressed Fluids

We prepared 3D porous scaffolds from the polymer disks using a foaming process with compressed fluids in a high-pressure plant at a laboratory scale (Figure 1). Several polymer disks were placed in a high-pressure vessel using a special stainless-steel basket divided into seven levels. The vessel, R (300 mL), was pre-heated to the working temperature ( $T_w$ ) and then pressurized to the desired pressure ( $P_w$ ) by adding the corresponding compressed fluid (scCO<sub>2</sub> or Freon R134a). A high-pressure pump (P1 or P2) was used to introduce the compressed fluid into the vessel up to the desired working pressure. The polymer/compressed-fluid mixture was maintained at  $P_w$  for a specific soaking time ( $t_s$ ). The vessel was then depressurized from  $P_w$  to ambient pressure at a constant flow rate by opening valve V-7 to 60% of its aperture. The foaming process occurs in three different steps. First, the polymer matrix is saturated with the corresponding compressed fluid at the working pressure and temperature. Second, once saturation is achieved, the diffusion of the compressed fluid forms a single phase of polymer/compressed fluid. Third, a decrease

in pressure causes phase segregation, and the compressed fluid evaporates, leading to the generation of pores or foaming of the polymer. The resulting foamed polymeric matrices were then cut with a diamond saw to eliminate the generated outer non-porous layer and to shape the specimens as cylinders with a radius of 15 mm and thickness of 3.5 mm. Non-complete foaming of the polymer disks was detected visually by the non-expansion of the disk and by the presence of non-foamed polymer at the center of the disk, once it was cut with the diamond saw (Supplementary Materials, Figure S3). The resulting porous specimens were stored for 1 week at room temperature until no loss of weight (due to gas release) was registered, the specimens were then kept at 4 °C until use.



**Figure 1.** Diagram of the equipment used for preparing 3D porous polymeric scaffolds with compressed CO<sub>2</sub> or Freon R134a. P1 and P2: pumps for compressing the fluids; DR1 and DR2: rupture disks; F1: mass flow meter; V-1/V-7: valves; H1: heater; R: high-pressure vessel; F1 and FCO<sub>2</sub>: filters; PI1 and PI2: pressure indicators; PIC: pressure controller; TI: temperature indicator.

### 2.2.3. Porous Scaffold Characterization Solid Density and Porosity

We calculated the density of the foamed (“apparent”) and unfoamed (“absolute”) scaffolds with a helium pycnometer (Ultrapycometer 1200e, Quantachrome Instruments, Boynton Beach, FL, USA). For the foamed disks, the pycnometer determined the volume occupied by the solid material plus the volume of the closed porosity, while for the unfoamed disks, the device determined the volume of solid material without pores.

The porosity, including the closed and open porosity, was estimated by correlating the porosity ( $P$ ) to the density ( $\rho$ ) of the foamed and unfoamed materials [39]. We calculated the total porosity ( $P_T$ ) of the prepared materials by dividing the geometric density ( $\rho_{\text{geometric}}$ ) by the unfoamed density ( $\rho_{\text{unfoamed}}$ ), using the formula  $P_T = [1 - (\rho_{\text{geometric}}/\rho_{\text{unfoamed}})] \times 100$ , where the geometric density ( $\rho_{\text{geometric}}$ ) refers to the density of the foamed disk, once the outer layer was removed, and using the foamed mass and geometric volume. We calculated this volume with the theoretical volume of a cylinder ( $v = \pi \cdot r^2 \cdot h$ , where  $r$  is the radius of the disk and  $h$  is the height). The diameter and height of each disk was measured using a standard caliper (Mitutoyo, Tokyo, Japan). Similarly, we calculated the closed porosity ( $P_{\text{closed}}$ ) by dividing the foamed density ( $\rho_{\text{pycnometry}}$ ) by the unfoamed density ( $\rho_{\text{unfoamed}}$ ), using the formula  $P_{\text{closed}} = (1 - \rho_{\text{pycnometry}}/\rho_{\text{unfoamed}}) \times 100$ . We then obtained the open porosity ( $P_O$ ) simply as the difference between the total and closed porosity (i.e.,  $P_O = P_T - P_{\text{closed}}$ ).

We calculated the mean porosity values and corresponding standard deviations from the experimental measurements performed on three samples of each type of scaffold.

#### Morphology by Scanning Electron Microscopy (SEM)

We analyzed the microscopic and nanoscopic morphologies of the porous polymeric matrices by scanning electron microscopy (Quanta 200 FEG-ESEM, FEI, Hillsboro, OR, USA). Prior to the analysis, the porous disks were coated with gold for 4 min at 20 mA in a sputter coater (K550X, Emitech, Surrey, UK) by modifying the inclination of the holder to achieve a homogeneous coverage of the scaffolds.

#### Micro X-ray Computed Tomography

All scaffolds were characterized using X-ray micro-computed tomography (SkyScan-1272; Bruker, Kontich, Belgium), a non-destructive analysis in which the pore size distribution and 3D visualization can be simultaneously obtained. Cylindrical scaffolds with a thickness 3.5 mm and diameter of 15 mm were mounted in the equipment. Analyses were performed with a charged-couple device camera at a pixel size of 9  $\mu\text{m}$ , using a source voltage of 50 kV and a current of 200  $\mu\text{A}$ . All generated images were saved in TIFF format with a pixel size of 12  $\mu\text{m}$ . We employed NRecon software (Micro Photonics, Allentown, PA, USA) to reconstruct cross-section images from the tomography projection images.

#### Rheological Properties

We measured the rheological properties of the porous scaffolds through the small-amplitude oscillatory shear technique, as previously shown [40–42], using a rheometer (HAAKE RheoStress RS600, Thermo Electron Corporation, Waltham, MA, USA) with a rotor diameter of 10 mm. This technique consists of applying a small-amplitude torsional oscillation that generates a shear flow on the sample. Strain and frequency sweeps were performed to determine the range of pressure and frequency where the scaffolds maintain their viscoelastic behavior and achieve the value of the shear modulus ( $G'$ ).

#### 2.2.4. pNPs Production and Purification

pNPs were produced in the *E. coli* strain MC4100, transformed with the expression vector pTV1GFP. *E. coli* was grown in LB-rich medium supplemented with 100  $\mu\text{g}/\text{mL}$  of ampicillin and 30  $\mu\text{g}/\text{mL}$  of streptomycin at 37 °C and 250 rpm. Production of pNPs was induced when reaching an optical density at 550 nm of 0.5 by adding 1 mM isopropyl Beta-D-1-thiogalactopyranoside. After 3 h, the cell cultures were harvested for pNPs purification with a combination of mechanical and enzymatic procedures, as previously described [43].

#### 2.2.5. Porous Scaffold Functionalization with pNPs

Surface functionalization of the porous scaffolds was performed using a filtration procedure in which an aqueous suspension of pNPs was forced through the porous material. We first resuspended 600  $\mu\text{g}$  of pNPs in 20 mL of phosphate-buffered saline (PBS) supplemented with a mixture of 1.6 mL of tetracycline, kanamycin and chloramphenicol to prevent microbial contamination of the scaffolds during their manipulation. The suspension was sonicated for 10 min, and 5 mL of the suspension was then filtered through the porous specimen to decorate the material. To increase the efficiency of the process, the procedure was repeated 3 times, each time using the same previously filtrated 5 mL. The pNPs-loaded scaffolds obtained were dried with compressed air and weighed before ( $m_0$ ) and after filtration and after the drying process ( $m_f$ ). The scaffolds were kept at  $-20$  °C until use. pNPs loading was calculated using the following equation:  $(m_f - m_0)/m_0$ .

We estimated the amount of pNPs retained on the surface of the functionalized scaffolds using a fluorescence spectrophotometer (Cary Eclipse Fluorescence Spectrometer, Santa Clara, CA, USA) by comparing the fluorescence intensities at 510 nm of the suspension before and after the decoration process. To study the penetrability of pNPs into PLA-based scaffolds, we cut a cross-section of the scaffold using a diamond wire saw and



mounted it on glass-bottom slides (Nunc, Wiesbaden, Germany). Images were taken using a TCS SPE confocal microscope (Leica, Wetzlar, Germany). The fluorescence from pNPs was excited with a 488-nm laser line and collected at the emission range of 495–590 nm.

#### 2.2.6. Cell Culture and Viability Assay

Purified human bone marrow-derived MSCs (CD105<sup>+</sup>, CD29<sup>+</sup>, CD44<sup>+</sup>, CD14<sup>-</sup>, CD34<sup>-</sup> and CD45<sup>-</sup>) were purchased from Lonza (Basel, Switzerland). The cells were cultured in a defined medium (Lonza) consisting of basal medium and SingleQuots growth supplements containing fetal bovine serum (FBS), L-glutamine, penicillin, and streptomycin. All experiments were performed below seven cell passages. The experiments were performed in duplicate using cells isolated from three different donors aged 20–31 years. Before cell seeding, scaffolds decorated or not with pNPs were incubated in DMEM containing 15% FBS and antibiotics (DMEM-15%FBS) for 24 h. We seeded  $2 \times 10^5$  MSCs on scaffolds placed in 24-well plates and cultured them in DMEM-15%FBS for 1–18 days. Cell viability was evaluated using the alamarBlue assay (Biosource, Nivelles, Belgium). Cells were incubated in DMEM containing 10% alamarBlue dye; 3 h later, the fluorescence emitted by the cell-reduced alamarBlue was quantified using a spectrofluorometer (Synergie4, Evry, France).

#### 2.2.7. Immunofluorescence Assays

The MSCs cultured for 8 days on the scaffolds were washed with PBS followed by fixation in 4% (*w/v*) paraformaldehyde in PBS and permeabilization with 0.1% Triton X-100 in PBS. For fibronectin immunostaining, the cells were blocked in 2% bovine serum albumin (BSA) in PBS containing 0.05% Tween 20 and then incubated with mouse anti-human fibronectin monoclonal antibody (Santa Cruz, Heidelberg, Germany) diluted 1:50 in 1% BSA in PBS. The cells were washed with 0.05% Tween 20 in PBS followed by incubation with goat anti-mouse Alexa-Fluor 488 (Molecular Probes, Leiden, The Netherlands) diluted 1:1000 in 1% BSA in PBS. To label actin cytoskeleton, the cells were stained with PBS containing  $4 \times 10^{-7}$  M phalloidin-TRITC (Sigma-Aldrich, Madrid, Spain). For nuclei staining, the cells were incubated in PBS containing  $3 \times 10^{-6}$  M 4,6-diamidino-2-phenylindole (DAPI; Sigma) before the confocal microscopy examination.

#### 2.2.8. Statistical Analysis

Experiments were conducted in duplicate, and the data are presented as mean values  $\pm$  SD of four independent experiments. The statistical analyses were performed using the Statistical Package for the Social Sciences, version 15.0 (SPSS Inc., Chicago, IL, USA). The quantitative data were tested using the Kruskal-Wallis test followed by Dunn's multiple comparison test, and the level of significance was set at  $p < 0.05$ .

### 3. Results and Discussion

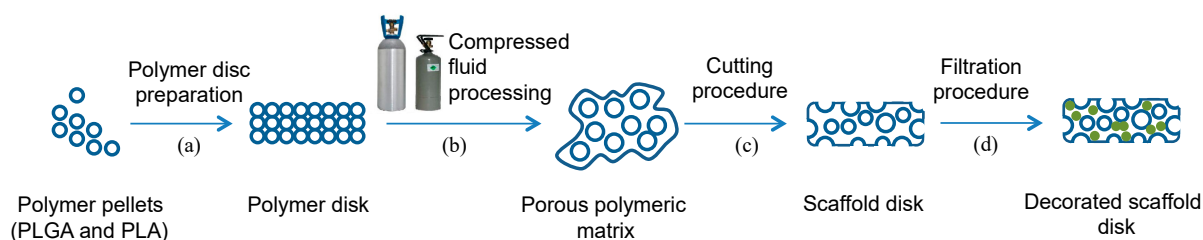
We studied the processing conditions of PLA with CO<sub>2</sub> and Freon R134a compressed fluids and their influence on the physicochemical and mechanical properties of the resulting porous matrices. We also functionalized the surface of the obtained 3D porous matrices with bioactive pNPs and evaluated their *in vitro* cytocompatibility by culturing MSCs on them. Given that the bioactivity of 3D porous scaffolds depends not only on the fabrication routes and processing media but also on the nature of the material, we processed PLGA (a polymer widely used in the biomedical field) with Freon R134a.

#### 3.1. Preparation of 3D Porous Scaffolds

The three most common options for polymer foaming with compressed fluids are batch foaming, foam extrusion and the injection foam molding [9]. The methodology used in this study for preparing 3D porous scaffolds was based on batch foaming process, which is extensively employed in research because it allows for a fine control of the processing variables and is relatively simple to perform. However, extrusion foaming is the industrially

preferred option for foaming due to its adaptability for continuous production and easier scaling-up potential [44].

The general experimental procedure employed in this study to prepare the various types of porous polymeric matrices consisted of several steps (Figure 2). In a high-pressure vessel, polymer disks were exposed to compressed fluids (either Freon R134a or scCO<sub>2</sub>) at a given working pressure ( $P_w$ ) and temperature ( $T_w$ ) to ensure the compressed fluid reached a supercritical state for a suitable soaking time ( $t$ ), depending on the polymer/compressed fluid mutual diffusivity, to allow sorption and fluid solubilization in the polymeric matrix. This was then followed by a depressurization step, which induced gas bubble nucleation and growth and the formation of the porous structure.



**Figure 2.** Scheme of the experimental procedure for preparing 3D porous scaffolds. (a) First, polymeric disks were prepared from PLA or PLGA polymer pellets. (b) The disks were then transformed into porous scaffolds using compressed fluid processing in a high-pressure plant. (c) The non-porous skin layer was cut out, obtaining a porous scaffold disk. (d) The disk was subsequently loaded with bioactive pNPs by a filtration procedure.

While scCO<sub>2</sub> requires working pressures >10 MPa, Freon R134a requires almost an order of magnitude lower pressure (2 MPa) [45]. Although all resulting 3D scaffolds showed a porous structure, they also presented an outer non-porous layer. Outer layer formation, previously reported for the CO<sub>2</sub> foaming process [16,46,47], has been attributed to rapid gas diffusivity as the gas escapes from the scaffold surface during depressurization and to the solubility of the CO<sub>2</sub> at the pressure employed, the effects of which have been previously described [48]. The same mechanism could explain the formation of the outer non-porous layer in the case of the dense Freon. When depressurizing, the solubility of the Freon decreases, and, consequently, the diffusivity increases, resulting in the formation of this undesirable layer, which acts as a barrier for deep cell colonization and for the delivery of inductive factors to the inner part of the scaffold. We therefore developed a cutting procedure to remove the outer layer of the scaffold using a diamond saw, obtaining porous disks with the desired thickness of 3.5 mm. Lastly, the resulting 3D porous scaffolds were internally functionalized with controlled amounts of GFP-based pNPs. The gas foaming processing conditions evaluated for PLA and PLGA are shown in Table 1, which lists the operational process values for the pressure, temperature and soaking times that yielded complete foaming of the polymer disks and appropriate scaffold characteristics, such as a high degree of porosity and mechanical strength, to behave as scaffolds for tissue engineering. Foaming with Freon R134a required a slightly higher temperature than foaming with scCO<sub>2</sub>, as well as a longer soaking time.

Given that the molecular weight and viscosity of PLGA is lower than that of PLA, the solubility of dense Freon inside the polymer increases. Consequently, a lower  $T_w$  is needed to produce the expansion of PLGA disks inside the vessel. Indeed, a smaller mass of PLGA was employed to prepare the polymer disk due to the higher expansion during processing. It is known that the diffusion of compressed fluids is much lower in semicrystalline polymers than in amorphous ones, due to the free volume effect [9]. Therefore, the annealing pretreatment causing an amorphous transformation of the crystalline region of PLA was essential for achieving a complete polymer expansion by gas foaming. This pre-treatment was not needed for PLGA due to its amorphous nature.

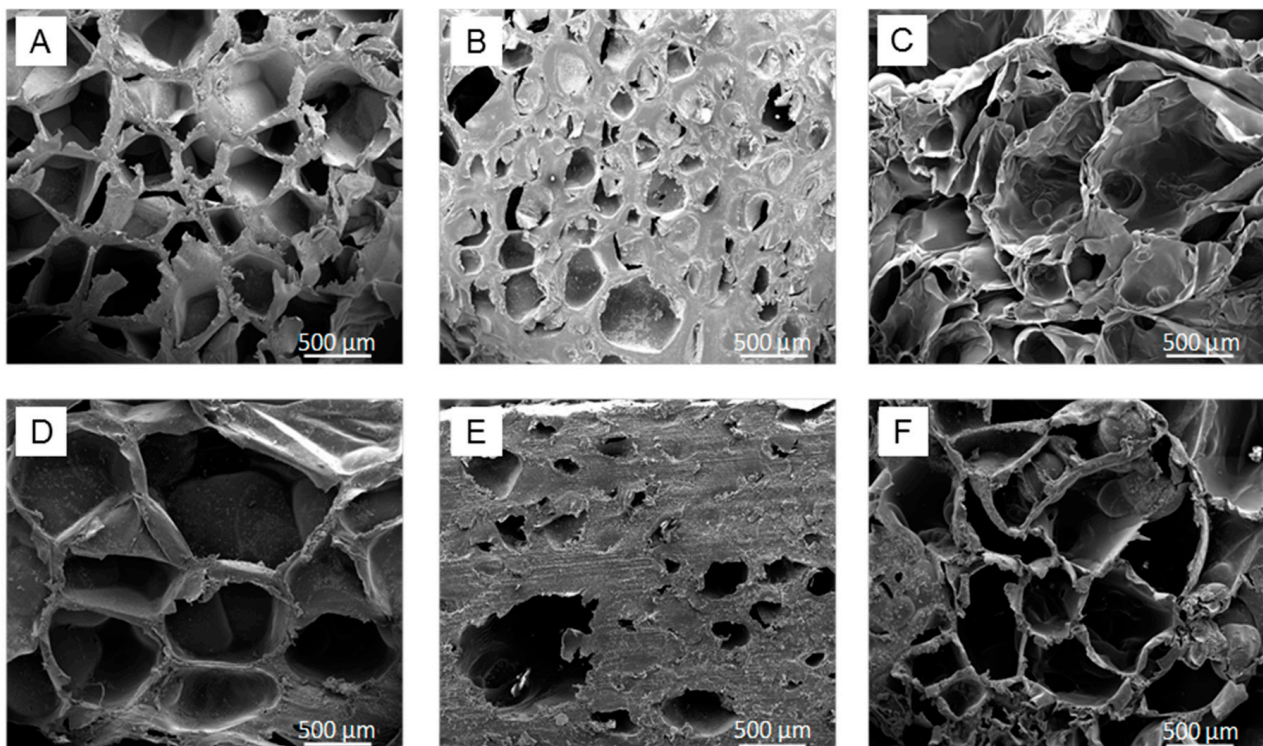
**Table 1.** Experimental conditions for preparing the porous polymeric matrices.

Stage	Processing Parameters	Material				
		PLA	PLA	PLA	PLA	PLGA
Polymer disk preparation	Thermal annealing	Yes	Yes	Yes	Yes	No
	m (g)	0.4	0.4	0.8	0.8	0.3
	T (°C)	150	150	150	150	-
	Applied pressure (Kg)	3000	3000	3000	3000	500
Porous scaffold fabrication	Compressed fluid	Freon R134a	Freon R134a	scCO <sub>2</sub>	scCO <sub>2</sub>	Freon R134a
	Tw (°C)	40	40	35	35	35
	Pw (MPa)	2	2	10.3	10.3	2
	Soaking time, t (h)	3	3	2	2	2
pNP Scaffold decoration	-	No	Yes	No	Yes	No

### 3.2. 3D Porous Scaffold Characterization

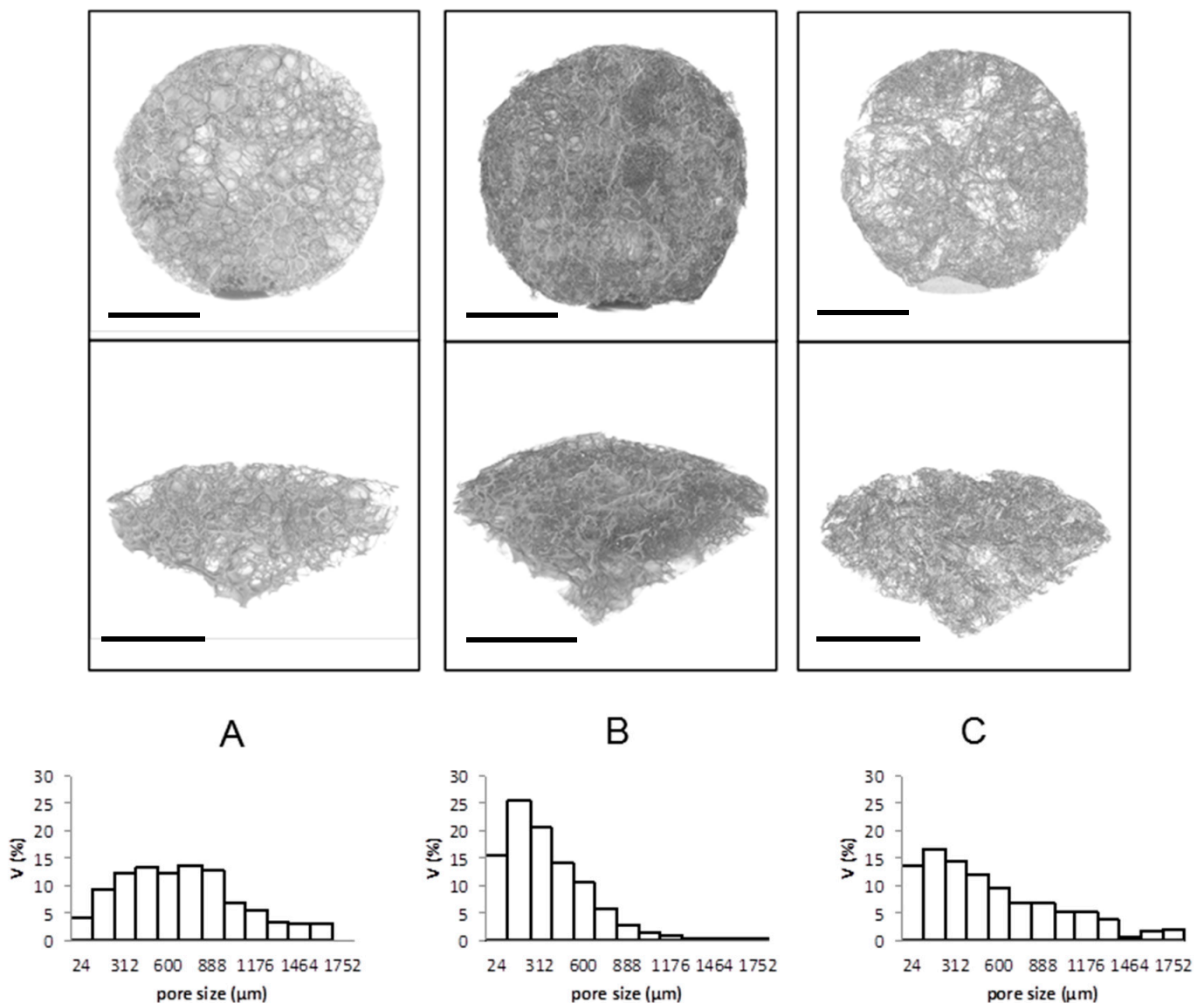
Using SEM and micro-computed tomography, we characterized the morphology and pore size distribution of PLA processed with Freon R134a or scCO<sub>2</sub> and of PLGA scaffolds processed with Freon R134a.

The SEM images of the longitudinal and cross-sections of the processed polymers revealed porous structures for the three materials (Figure 3), confirming that dense Freon can be used to successfully prepare 3D porous scaffolds of PLA and PLGA. Moreover, PLA-based scaffolds processed with Freon R134a showed larger pores with thinner walls than those processed with CO<sub>2</sub>.



**Figure 3.** SEM images corresponding to longitudinal (A–C) and cross-sections (D–F) of (A,D) PLA processed with Freon R134a; (B,E) PLA processed with scCO<sub>2</sub>; and (C,F) PLGA processed with Freon R134a.

The microtomography analysis confirmed the heterogeneous pore size distributions in the three fabricated 3D structures, which were especially wide when Freon R134a was employed as the processing media. Indeed, the PLA and PLGA scaffolds processed with Freon R134a showed a heterogeneous pore size distribution, with high proportions of pores larger than 500  $\mu\text{m}$  (Figure 4). Conversely, PLA processed with  $\text{scCO}_2$  exhibited a more homogeneous pore size distribution, with a high proportion of 50–500- $\mu\text{m}$  pores. The impact of pressure on the diffusivity is linked to the plasticization effect and hydrostatic pressure, which is a key factor at higher pressure because it decreases the available free volume in the polymer mixture leading to a reduced diffusion coefficient. However, the plasticizing effect of the foaming agent at lower pressure is the key factor because it increases the polymer chain mobility, which in turn results in a higher diffusion coefficient [49,50].



**Figure 4.** Top view and cross-section morphology (top) and pore size distribution (bottom) obtained by microtomography of cylindrical scaffolds with 3.5 mm of thickness and 15 mm of diameter. (A) PLA processed with Freon R134a; (B) PLA processed with  $\text{scCO}_2$  and (C) PLGA processed with Freon R134a. Scale bar 5 mm.

A valuable processing aid in any gas foaming process is the plasticization of the polymer brought about by the dissolved blowing agent, which could induce a significant reduction in the melting and glass transition temperatures. In the case of  $\text{CO}_2$ , this effect is well-reported [9]. Taking into account these considerations, the larger pore size and the

larger total porosity of PLA achieved with Freon R134a at low pressure, compared with that achieved by scCO<sub>2</sub> processing, is likely due to the larger T<sub>m</sub> reduction and larger plasticization of the PLA upon exposure to Freon R134a. This could also be linked to the hydrostatic pressure under high pressure scCO<sub>2</sub> processing, which might cause a decrease in gas diffusivity due to the reduction in the available free volume in the system.

Given that the minimum pore size that allows cell growth within scaffolds is approximately 150 μm [51–53] and that bone regeneration is enhanced with pore sizes of approximately 300 μm and higher [54], the pore structures obtained by the mild and environmentally friendly processing with Freon R143a seem to be adequate for tissue engineering applications.

To further characterize the scaffolds porosity and pore size, mercury intrusion may be considered. Due to the high pressures applied to the materials under study, however, mercury intrusion is not recommended when working with non-rigid materials, like those in this study, because of potential pore re-arrangement [55,56]. Thus, as detailed in the Methods section, the porosity of the three different materials was finally evaluated through the absolute density of unfoamed disks, the apparent density of foamed disks and the geometric densities as determined by helium pycnometry (Table 2 and Supplementary Materials (Figure S4)). Open porosity values were not directly measured. Instead, they were calculated by subtracting the closed porosity from the total porosity, which explains their relatively high errors compared with those of P<sub>closed</sub> and P<sub>T</sub>. As expected, the three tested materials were found to be highly porous, with values >80% in terms of total porosity. PLGA-based scaffolds presented the highest degree of total porosity, while the lowest corresponded to the PLA-based scaffolds processed with scCO<sub>2</sub>. However, large percentages of closed pores (>80%) were obtained in the PLA and PLGA scaffolds produced with Freon R134a, because of the gas foaming technique. In contrast, the PLA-based scaffolds processed with scCO<sub>2</sub> exhibited lower closed porosity values (56.9%) and, therefore, a higher volume of open pores. At the explored processing conditions, the pore size was larger in the Freon R134a-processed materials, although scCO<sub>2</sub> led to larger degrees of internal connectivity.

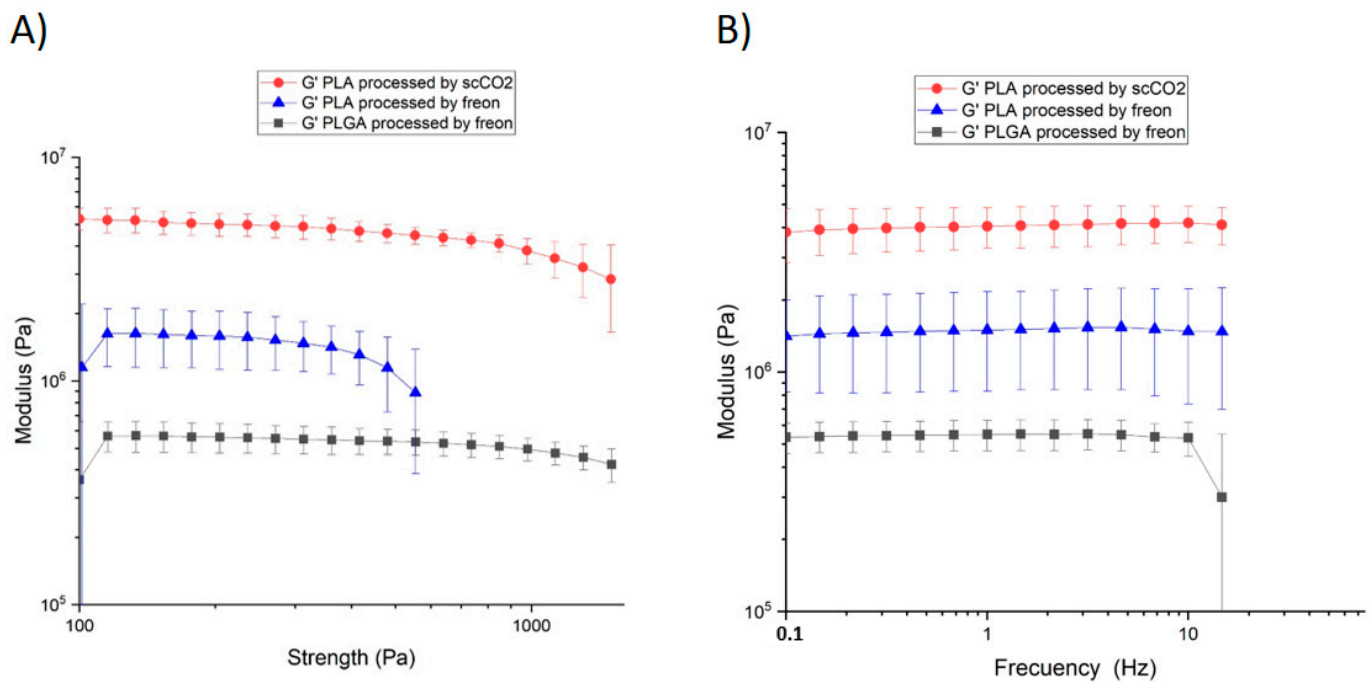
**Table 2.** Porosities of the studied 3D porous scaffolds.

Material	Total Porosity, P <sub>T</sub> (%)	Closed Porosity, P <sub>closed</sub> (%)	Open Porosity, P <sub>O</sub> (%)
PLA-Freon R134a	92.8 ± 2.0	83.2 ± 3.3	9.6 ± 1.3
PLA-scCO <sub>2</sub>	82.3 ± 0.9	56.9 ± 7.5	25.4 ± 6.6
PLGA-Freon R134a	96.7 ± 0.8	89.1 ± 3.3	7.6 ± 3.4

Mean porosity values and the corresponding standard deviations were calculated, as described in Methods section, from experimental measurements performed over 3 samples of each type of scaffold.

Although a high degree of porosity, as well as large and open pores, are generally desired to facilitate cell ingrowth and vascularization, these characteristics might result in the scaffolds' loss of mechanical properties due to the increased void volume, compromising their structural integrity. We performed a rheological analysis of the scaffolds to characterize their structural integrity by determining the dynamic ( $G'$ ) and loss modulus ( $G''$ ) in the linear-viscoelastic regime (Figures 5 and S5). Strain sweeps were performed at a constant frequency of 1.0 Hz, and the pressure was varied from 100 Pa to 2000 Pa to study the range in which the scaffolds show a constant  $G'$ . We then fixed a value of 500 Pa and performed frequency sweeps from 0.1 Hz to 100 Hz. All scaffolds showed a linear  $G'$  behavior from 100 Pa to 1500 Pa, except PLA processed with Freon R134a, whose linear range was 100–550 Pa (Figure 5A). The frequency varied from 0.1 Hz to 15 Hz for all samples (Figure 5B). The modulus achieved showed that the PLA processed with scCO<sub>2</sub> was the hardest and most compact scaffold, reaching stability at  $4.52 \pm 0.58$  MPa, followed by PLA processed with Freon R134a, which is also hard ( $G' = 1.08 \pm 0.49$  MPa) within a similar range. The morphology, degree of heterogeneity and orientation of the pores, as well as the pore size

distribution and open porosity, strongly influence the scaffold's mechanical behavior. In this regard, differences in the shear moduli of PLA processed with CO<sub>2</sub> and Freon134a can be related to their differences in porosity and pore size and distribution. As expected, the PLGA scaffold was the softest ( $G' = 0.52 \pm 0.08$  MPa), resulting in a relatively fragile structure (see Supplementary Materials, Figure S5). Bone shows a complex, anisotropic structure in which highly different types of non-homogeneously distributed organic and inorganic matter are present. In addition, changes related to anatomical location, shape and physiopathological conditions result in major variations of the measured mechanical parameters, with the shear modulus values of trabecular bone ranging from 8 to 40 MPa [57]. Although the  $G'$  values of the PLA scaffolds processed with scCO<sub>2</sub> and FreonR134 are close to those measured in bone, these scaffolds might not meet the mechanical requirements for repairing load-bearing defects. However, there might be a window of opportunity in the treatment of non-load-bearing defects (e.g., for repairing craniofacial defects). Reinforced porous matrices could be obtained by preparing composites of polymer and bioceramic fillers. In fact, supercritical CO<sub>2</sub> foaming allowed for the manufacture of porous composites of PLA and hydroxyapatite or  $\beta$ -TCP microparticles with superior viscoelastic properties [58].



**Figure 5.** (A) Strain and (B) frequency sweeps of PLA processed with Freon R134a (blue triangles) or scCO<sub>2</sub> (red dots), as well as PLGA processed with Freon R134a (grey squares).

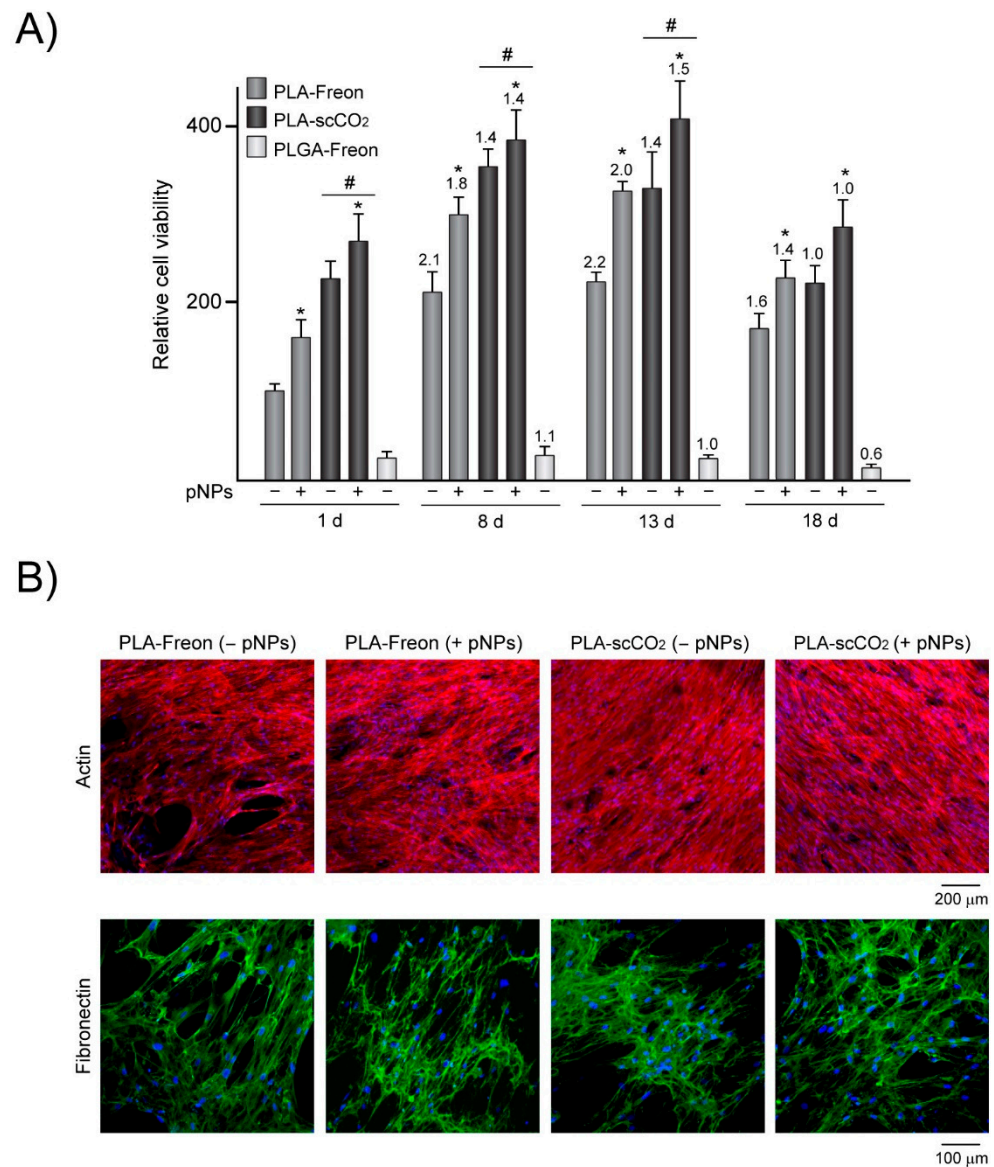
### 3.3. Surface Functionalization of 3D Porous Scaffolds with GFP-Based pNPs

We next attempted to decorate the PLA scaffolds processed with Freon R134a or scCO<sub>2</sub> with pNPs that promote cell growth [43]. GFP-based pNPs were adsorbed on the surface of the inner and external porous walls by means of a filtration step, and their localization was observed by confocal microscopy taking advantage of the pNP fluorescence, confirming that the internal connectivity of the pores created with Freon R134a or scCO<sub>2</sub> allowed pNPs to reach the inner pores of the scaffold (Supplementary Materials, Figure S6). However, we observed slightly higher loading of pNPs in the scaffolds generated with scCO<sub>2</sub> than with Freon R134a, both on the surface and inside the material. Quantification of retained pNPs in the functionalized scaffolds revealed that  $69.8 \pm 3.8\%$  and  $75.4 \pm 2.2\%$  of the loaded pNPs were adsorbed into the PLA scaffolds processed with Freon R134a and scCO<sub>2</sub>, respectively.

### 3.4. Cytocompatibility of 3D Porous Scaffolds

To evaluate the cytocompatibility of the PLA and PLGA scaffolds processed with Freon R134a, we cultured MSCs on these materials for 1–18 days (Figure 6). The metabolic activity data after culturing for one day showed that both polymeric matrices support MSC attachment, as observed in previous studies in which this cell type was cultured on polymeric scaffolds developed by conventional techniques [59,60]. The composition of the polymer has been shown to influence the scaffold's structure [61]. In fact, processing of PLA and PLGA polymers with Freon R134a led to the generation of scaffolds with different structures, which might affect MSC behavior. The MSCs' metabolic activity at day 1 was notably higher on the PLA scaffolds than on the PLGA scaffolds. The MSC viability on the PLGA scaffolds also did not increase over culture time (Figure 6A), suggesting that the physicochemical properties of PLGA scaffolds, including sharp edges (Figure 3C) and fragile microstructure (Figure S2), were inadequate for supporting MSC attachment and growth. In contrast to that observed for PLGA, the physicochemical properties of the PLA scaffolds processed with Freon R134a provided a more suitable environment for cell growth. A comparison between the PLA scaffolds processed with Freon R134a and with scCO<sub>2</sub> revealed that the metabolic activity of the MSCs cultured for 1 day was reduced on the matrices processed with Freon R134a, which could be attributed to lower cell adhesion. The morphological features of the porous interfaces and, in particular, the pore sizes have an important effect on the number of cells that can attach and adhere to the materials. Regardless of the biomaterial or adherent cells tested, seeding efficiency decreases as the pore size increases [62–64]. Increased pore size reduces the surface area within the structure, lowering the available space for cell adhesion and limiting the cell attachment sites. In our study, MSCs likely attached at a higher extent to the surface of the PLA scaffolds processed with scCO<sub>2</sub>, with a higher proportion of 50–500- $\mu$ m pores, than to scaffolds processed with Freon R134a, with a higher proportion of pores >500  $\mu$ m (Figure 4). In addition to increased pore size, the PLA scaffolds processed with Freon R134a exhibited topographical features consisting of curved surfaces limited by sharp ridges (Figure 3), which could hinder the formation of focal adhesions, structures providing cell anchoring to attachment sites in the substrate. MSC viability increased from day 1 to day 8 on the PLA scaffolds processed with Freon R134a, and the increase was more pronounced than that observed on the matrices processed with scCO<sub>2</sub>. The metabolic activity of the MSCs cultured on the PLA scaffolds remained constant at day 13 and decreased at day 18. The microscopic examination revealed that the MSCs cultured for 8 days reached confluence on the PLA scaffolds processed with Freon R134a or scCO<sub>2</sub> and displayed spread morphology with a similarly well-organized actin cytoskeleton and a dense matrix of fibronectin fibrils (Figure 6B). Lastly, we studied the impact of functionalized PLA scaffolds with pNPs [27,28,65]. There were no signs of toxicity promoted by pNPs in the cells cultured on the pNP-decorated scaffolds, as revealed by alamarBlue assay and DAPI staining. On the contrary, the functionalization of the PLA scaffolds processed with Freon R134a or scCO<sub>2</sub> improved MSC viability, an effect observed at all studied periods. High tunability regarding protein composition, as well as the architectural features of pNPs, provides a huge range of possibilities for combining mechanical, biochemical and temporal stimulation of selected cellular responses such as adhesion, proliferation and differentiation [43,66,67].

Although the pore interconnectivity and open porosity of the fabricated structures is low, open porosity is expected to increase as the scaffold degrades, facilitating cell migration to the inside. Scaffolds processed with Freon R134a show a high percentage of pores larger than 500  $\mu$ m (Figure 4) and with a wall width between pores much smaller than the pore size, as clearly observed in the SEM images of longitudinal and cross-sections of the processed polymers (Figure 3). The features of Freon R134a-processed PLA are ideal for the rapid formation of open porosity, which depends on the rate of polymer degradation and on the microscopic structural characteristics of the separation between the scaffold's pores.



**Figure 6.** (A) Cell viability of MSCs cultured for 1–18 days on PLA processed with Freon R134a (PLA-Freon) or scCO<sub>2</sub> (PLA-scCO<sub>2</sub>), decorated (+) or not (–) with pNPs, or on PLGA processed with Freon R134a (PLGA-Freon). The data were normalized relative to those measured in MSCs cultured for 1 day on PLA-Freon without pNPs, which were assigned an arbitrary value of 100. Fold-change values relative to cell viability at day 1 are shown above the graph bars. (B) Confocal maximum projections showing nuclei (blue), actin (red) or fibronectin (green) of MSCs cultured on the scaffolds for 8 days. \*  $p < 0.05$  compared with the scaffolds without pNPs. #  $p < 0.05$  compared with PLA-Freon.

#### 4. Conclusions

Scaffolds consisting of PLA can be successfully engineered by compressed fluid technology using dense Freon R134a as a solvent media, obtaining desirable structural characteristics such as a high degree of total porosity (>80%) with high proportions of pores larger than 500 μm and a  $G'$  of  $1.08 \pm 0.49$  MPa. This manufacturing method is performed at a working pressure of 2 MPa, nearly one order of magnitude lower than that employed in scaffold manufacturing with scCO<sub>2</sub> (>10 MPa). CO<sub>2</sub> is a gas at 2 MPa and above 25 °C; therefore, polymer foaming at such low pressures cannot be achieved with this compressible gas. This reduced operating pressure will have a positive impact in terms of reduced equipment and operational costs and increased safety and on process



scalability of industrially relevant foaming technologies, such as extrusion foaming and bead foaming, performed up to now with scCO<sub>2</sub> at higher pressures.

In this study, we produced for the first time polymeric porous materials for biomedical applications using dense Freon R134a as a solvent media and demonstrated its processing advantages, which could be further improved upon through technological development. Further research on optimizing the processing parameters such as the working pressure and depressurization flow, which have been shown to have a significant impact on CO<sub>2</sub>-processed polymeric scaffolds and could likely lead to enhanced results in terms of a higher percentage of open porosity with dense Freon R134a and even higher cytocompatibility. The presented method could also be employed for polymers in which the compressed gas can diffuse and plasticize. Freon R134a has been shown to be a good plasticizer, and it can solubilize in polyvinyl acetate, cellulosic polymers, and certain vinylidene fluoride polymers, in addition to saturated aliphatic polyesters, such as PLA and PLGA, thereby promising a wide applicability of the methodology reported herein [68]. In vitro studies using human MSCs have shown that PLA scaffolds processed with Freon R134a are cytocompatible. This study also demonstrates for the first time that pNP functionalization of PLA scaffolds processed with Freon R134a is an effective approach for increasing the viability of osteoprogenitor cells, taking into account its processing advantages.

**Supplementary Materials:** The following are available online at <https://www.mdpi.com/article/10.3390/polym13203453/s1>, Figure S1: DSC thermogram of raw PLA before annealing, Figure S2: DSC thermogram of PLA after annealing at 150 °C, Figure S3: Picture of a PLA scaffold with a non-complete foaming visually observed at the center of the disk., Figure S4: Absolute and apparent densities of the studied porous scaffolds, Figure S5: (A) Strain and (B) frequency sweeps of PLA processed with Freon R-134a (blue) and scCO<sub>2</sub> (red) as well as PLGA processed with Freon R-134a (grey squares), Figure S6: pNPs penetrability in PLA-based scaffolds.

**Author Contributions:** Conceptualization, A.C., E.V., A.V., J.V., I.R., N.V. (Nuria Vilaboa) and N.V. (Nora Ventosa); methodology, M.A., E.P.d.R., J.G., M.P., J.S.-F. and O.C.-G.; formal analysis, M.A., L.S., J.G., M.P., A.C., E.V., I.R., N.V. (Nuria Vilaboa), and N.V. (Nora Ventosa); investigation, M.A., L.S., E.P.d.R., J.G., A.C., J.S.-F. and O.C.-G.; writing—original draft preparation, M.A., L.S. and E.P.d.R., I.R., N.V. (Nuria Vilaboa) and N.V. (Nora Ventosa); writing—review and editing, L.S., J.G., M.P., A.C., J.S.-F., O.C.-G., E.V., A.V., J.V., I.R., N.V. (Nuria Vilaboa) and N.V. (Nora Ventosa); supervision, J.G., I.R., N.V. (Nuria Vilaboa) and N.V. (Nora Ventosa); project administration, I.R., N.V. (Nuria Vilaboa) and N.V. (Nora Ventosa); funding acquisition, L.S., J.G., A.V., J.V., I.R., N.V. (Nuria Vilaboa) and N.V. (Nora Ventosa). All authors have read and agreed to the published version of the manuscript.

**Funding:** This work was supported by the Spanish Ministry of Economy and Competitiveness (MOTHER MAT2016-80826-R and Mol4Bio PID2019-105622RBI00); Spanish Ministry of Science, Innovation and Universities (RTI2018-095159-B-100); *Instituto de Salud Carlos III* (ISCIII)- European Regional Development Fund (ERDF); MINECO-AES (PI15/00752, PI15/01118 and PI18/00643); the Networking Research Center on Bioengineering, Biomaterials and Nanomedicine (CIBER-BBN); CSIC through grant 2019AEP133; Comunidad Autónoma de Madrid (grant S2013/MIT-2862); Generalitat de Catalunya (grants 2017-SGR-918, 2017-SGR-229 and CERCA Programme); the Fundació Marató de TV3 (Nr. 201812); the COST Action CA15126 Between Atom and Cell; and the European Social Fund and EU to J.V., A.V. and I.R. (H2020-INFRAIA-2014-2015; NFFA-654360).

**Institutional Review Board Statement:** Not applicable.

**Informed Consent Statement:** Not applicable.

**Data Availability Statement:** The data presented in this study are available on request from the corresponding author.

**Acknowledgments:** pNPs were partially produced by the ICTS “NANBIOSIS”, more specifically by the Protein Production Platform. Unit #1 (<http://www.nanbiosis.es/unit/u1-protein-production-platform-ppp/>) and characterized by the Biomaterials Processing and Nanostructuring. Unit #6 (<http://www.nanbiosis.es/portfolio/u6-biomaterial-processing-and-nanostructuring-unit/>). J.G. acknowledges financial support from the Ramón y Cajal Program (RYC-2017-22614), CIBER-BBN (grants BBN18PI01 and BBN20PIV02) and the Max Planck Society through the Max Planck Partner

Group “Dynamic Biomimetics for Cancer Immunotherapy” in collaboration with the Max Planck Institute for Medical Research (Heidelberg, Germany). A.V. is grateful for an ICREA ACADEMIA award. ICMAB acknowledges support from the Spanish Ministry of Economy and Competitiveness through the “Severo Ochoa” Programme for Centres of Excellence in R&D (CEX2019-000917-S). L.S. is supported by a Miguel Servet contract from ISCIII-MINECO-AES-FEDER-FSE. N.V. is supported by Program I2 from CAM.

**Conflicts of Interest:** The authors declare no conflict of interest.

## References

- Dvir, T.; Timko, B.P.; Kohane, D.S.; Langer, R. Nanotechnological strategies for engineering complex tissues. *Nat. Nanotechnol.* **2011**, *6*, 13–22. [[CrossRef](#)] [[PubMed](#)]
- Ma, P.X. Scaffolds for tissue fabrication. *Mater. Today* **2004**, *7*, 31. [[CrossRef](#)]
- Kanczler, J.; Oreffo, R. Osteogenesis and angiogenesis: The potential for engineering bone. *Eur. Cells Mater.* **2008**, *15*, 100–114. [[CrossRef](#)]
- Wang, Z.; Wang, Z.; Lu, W.W.; Zhen, W.; Yang, D.; Peng, S. Novel biomaterial strategies for controlled growth factor delivery for biomedical applications. *NPG Asia Mater.* **2017**, *9*, e435. [[CrossRef](#)]
- Kanczler, J.; Ginty, P.J.; Barry, J.J.; Clarke, N.M.; Howdle, S.M.; Shakesheff, K.; Oreffo, R.O. The effect of mesenchymal populations and vascular endothelial growth factor delivered from biodegradable polymer scaffolds on bone formation. *Biomaterials* **2008**, *29*, 1892–1900. [[CrossRef](#)] [[PubMed](#)]
- Perez, R.A.; Mestres, G. Role of pore size and morphology in musculo-skeletal tissue regeneration. *Mater. Sci. Eng. C Mater. Biol. Appl.* **2016**, *61*, 922–939. [[CrossRef](#)]
- Guo, J.L.; Kim, Y.S.; Mikos, A.G. Biomacromolecules for Tissue Engineering: Emerging Biomimetic Strategies. *Biomacromolecules* **2019**, *20*, 2904–2912. [[CrossRef](#)] [[PubMed](#)]
- Porter, J.R.; Ruckh, T.T.; Popat, K.C. Bone tissue engineering: A review in bone biomimetics and drug delivery strategies. *Biotechnol. Prog.* **2009**, *25*, 1539–1560. [[CrossRef](#)] [[PubMed](#)]
- Di Maio, E.; Kiran, E. Foaming of polymers with supercritical fluids and perspectives on the current knowledge gaps and challenges. *J. Supercrit. Fluids* **2018**, *134*, 157–166. [[CrossRef](#)]
- Santos-Rosales, V.; Iglesias-Mejuto, A.; García-González, C. Solvent-Free Approaches for the Processing of Scaffolds in Regenerative Medicine. *Polymers* **2020**, *12*, 533. [[CrossRef](#)] [[PubMed](#)]
- White, L.J.; Hutter, V.; Tai, H.; Howdle, S.M.; Shakesheff, K.M. The effect of processing variables on morphological and mechanical properties of supercritical CO<sub>2</sub> foamed scaffolds for tissue engineering. *Acta Biomater.* **2012**, *8*, 61–71. [[CrossRef](#)]
- García-González, C.A.; Concheiro, A.; Alvarez-Lorenzo, C. Processing of Materials for Regenerative Medicine Using Supercritical Fluid Technology. *Bioconjugate Chem.* **2015**, *26*, 1159–1171. [[CrossRef](#)]
- Reverchon, E.; Cardea, S. Supercritical fluids in 3-D tissue engineering. *J. Supercrit. Fluids* **2012**, *69*, 97–107. [[CrossRef](#)]
- Duarte, A.; Mano, J.; Reis, R.L. Supercritical fluids in biomedical and tissue engineering applications: A review. *Int. Mater. Rev.* **2009**, *54*, 214–222. [[CrossRef](#)]
- Bhamidipati, M.; Scurto, A.M.; Detamore, M.S. The Future of Carbon Dioxide for Polymer Processing in Tissue Engineering. *Tissue Eng. Part B Rev.* **2013**, *19*, 221–232. [[CrossRef](#)] [[PubMed](#)]
- Davies, O.R.; Lewis, A.L.; Whitaker, M.J.; Tai, H.; Shakesheff, K.; Howdle, S.M. Applications of supercritical CO<sub>2</sub> in the fabrication of polymer systems for drug delivery and tissue engineering. *Adv. Drug Deliv. Rev.* **2008**, *60*, 373–387. [[CrossRef](#)] [[PubMed](#)]
- Kankala, R.K.; Zhang, Y.S.; Wang, S.-B.; Lee, C.-H.; Chen, A.-Z. Supercritical Fluid Technology: An Emphasis on Drug Delivery and Related Biomedical Applications. *Adv. Health Mater.* **2017**, *6*, 1700433. [[CrossRef](#)] [[PubMed](#)]
- Jacobs, L.; Danen, K.; Kemmere, M.; Keurentjes, J. A parametric study into the morphology of polystyrene-co-methyl methacrylate foams using supercritical carbon dioxide as a blowing agent. *Polymer* **2007**, *48*, 3771–3780. [[CrossRef](#)]
- Gimeno, M.; Ventosa, N.; Sala, S.; Veciana, J. Use of 1,1,1,2-Tetrafluoroethane (R-134a)-Expanded Liquids as Solvent Media for Ecoefficient Particle Design with the DELOS Crystallization Process. *Cryst. Growth Des.* **2006**, *6*, 23–25. [[CrossRef](#)]
- Huchon, G.; Hofbauer, P.; Cannizzaro, G.; Iacono, P.; Wald, F. Comparison of the safety of drug delivery via HFA- and CFC-metered dose inhalers in CAO. *Eur. Respir. J.* **2000**, *15*, 663–669. [[CrossRef](#)] [[PubMed](#)]
- Chen, F.-M.; Zhang, M.; Wu, Z.-F. Toward delivery of multiple growth factors in tissue engineering. *Biomaterials* **2010**, *31*, 6279–6308. [[CrossRef](#)]
- del Río, E.P.; Martínez-Miguel, M.; Veciana, J.; Ratera, I.; Guasch, J. Artificial 3D Culture Systems for T Cell Expansion. *ACS Omega* **2018**, *3*, 5273–5280. [[CrossRef](#)] [[PubMed](#)]
- del Río, E.P.; Santos, F.; Rodríguez, X.R.; Martínez-Miguel, M.; Roca-Pinilla, R.; Aris, A.; Garcia-Fruitos, E.; Veciana, J.; Spatz, J.P.; Ratera, I.; et al. CCL21-loaded 3D hydrogels for T cell expansion and differentiation. *Biomaterials* **2020**, *259*, 120313. [[CrossRef](#)] [[PubMed](#)]
- De Marco, A.; Ferrer-Mirallas, N.; Garcia-Fruitos, E.; Mitraki, A.; Peternel, S.; Rinas, U.; Trujillo-Roldán, M.A.; Valdez-Cruz, N.A.; Vazquez, E.; Villaverde, A. Bacterial inclusion bodies are industrially exploitable amyloids. *FEMS Microbiol. Rev.* **2019**, *43*, 53–72. [[CrossRef](#)] [[PubMed](#)]

25. Rinas, U.; Garcia-Fruitos, E.; Corchero, J.L.; Vazquez, E.; Seras-Franzoso, J.; Villaverde, A. Bacterial Inclusion Bodies: Discovering Their Better Half. *Trends Biochem. Sci.* **2017**, *42*, 726–737. [[CrossRef](#)]
26. Seras-Franzoso, J.; Steurer, C.; Roldán, M.; Vendrell, M.; Vidaurre-Agut, C.; Tarruella, A.; Saldaña, L.; Vilaboa, N.; Parera, M.; Elizondo, E.; et al. Functionalization of 3D scaffolds with protein-releasing biomaterials for intracellular delivery. *J. Control. Release* **2013**, *171*, 63–72. [[CrossRef](#)] [[PubMed](#)]
27. Tatkiewicz, W.I.; Seras-Franzoso, J.; Fruitos, E.G.; Vazquez, E.; Kyvik, A.R.; Guasch, J.; Villaverde, A.; Veciana, J.; Ratera, I. Surface-Bound Gradient Deposition of Protein Nanoparticles for Cell Motility Studies. *ACS Appl. Mater. Interfaces* **2018**, *10*, 25779–25786. [[CrossRef](#)]
28. Tatkiewicz, W.I.; Seras-Franzoso, J.; Garcia-Fruitos, E.; Vazquez, E.; Ventosa, N.; Peebo, K.; Ratera, I.; Villaverde, A.; Veciana, J. Two-Dimensional Microscale Engineering of Protein-Based Nanoparticles for Cell Guidance. *ACS Nano* **2013**, *7*, 4774–4784. [[CrossRef](#)]
29. Seras-Franzoso, J.; Díez-Gil, C.; Vazquez, E.; García-Fruitós, E.; Cubarsi, R.; Ratera, I.; Veciana, J.; Villaverde, A. Bioadhesiveness and efficient mechanotransduction stimuli synergistically provided by bacterial inclusion bodies as scaffolds for tissue engineering. *Nanomedicine* **2012**, *7*, 79–93. [[CrossRef](#)]
30. Pesarrodonna, M.; Ferrer-Miralles, N.; Unzueta, U.; Gener, P.; Tatkiewicz, W.; Abasolo, I.; Ratera, I.; Veciana, S.J.; Schwartz, A.; Villaverde, A. Intracellular targeting of CD44+ cells with self-assembling, protein only nanoparticles. *Int. J. Pharm.* **2014**, *473*, 286–295. [[CrossRef](#)]
31. Seras-Franzoso, J.; Tsimbouri, P.M.; Burgess, K.V.; Unzueta, U.; Garcia-Fruitos, E.; Vazquez, E.; Villaverde, A.; Dalby, M.J. Topographically targeted osteogenesis of mesenchymal stem cells stimulated by inclusion bodies attached to polycaprolactone surfaces. *Nanomedicine* **2014**, *9*, 207–220. [[CrossRef](#)] [[PubMed](#)]
32. Tatkiewicz, W.I.; Seras-Franzoso, J.; García-Fruitós, E.; Vazquez, E.; Kyvik, A.R.; Ventosa, N.; Guasch, J.; Villaverde, A.; Veciana, J.; Ratera, I. High-Throughput Cell Motility Studies on Surface-Bound Protein Nanoparticles with Diverse Structural and Compositional Characteristics. *ACS Biomater. Sci. Eng.* **2019**, *5*, 5470–5480. [[CrossRef](#)] [[PubMed](#)]
33. Roseti, L.; Parisi, V.; Petretta, M.; Cavallo, C.; Desando, G.; Bartolotti, I.; Grigolo, B. Scaffolds for Bone Tissue Engineering: State of the art and new perspectives. *Mater. Sci. Eng. C Mater. Biol. Appl.* **2017**, *78*, 1246–1262. [[CrossRef](#)] [[PubMed](#)]
34. Rezwan, K.; Chen, Q.Z.; Blaker, J.J.; Boccaccini, A.R. Biodegradable and bioactive porous polymer/inorganic composite scaffolds for bone tissue engineering. *Biomaterials* **2006**, *27*, 3413–3431. [[CrossRef](#)]
35. Okamoto, M.; John, B. Synthetic biopolymer nanocomposites for tissue engineering scaffolds. *Prog. Polym. Sci.* **2013**, *38*, 1487–1503. [[CrossRef](#)]
36. Tang, Y.X.; Thankappan, S.K.; Lee, P.; Fard, S.E.; Harmon, M.D.; Tran, K.; Yu, X. Polymeric Biomaterials in Tissue Engineering and Regenerative Medicine. *Nat. Synth. Biomed. Polym. Elsevier Sci.* **2014**, 351–371. [[CrossRef](#)]
37. Gentile, P.; Chiono, V.; Carmagnola, I.; Hatton, P.V. An Overview of Poly(lactic-co-glycolic) Acid (PLGA)-Based Biomaterials for Bone Tissue Engineering. *Int. J. Mol. Sci.* **2014**, *15*, 3640–3659. [[CrossRef](#)]
38. James, R.; Manoukian, O.S.; Kumbar, S.G. Poly(lactic acid) for delivery of bioactive macromolecules. *Adv. Drug Deliv. Rev.* **2016**, *107*, 277–288. [[CrossRef](#)]
39. Barry, J.; Gidda, H.; Scotchford, C.; Howdle, S. Porous methacrylate scaffolds: Supercritical fluid fabrication and in vitro chondrocyte responses. *Biomaterials* **2004**, *25*, 3559–3568. [[CrossRef](#)]
40. Zuidema, J.M.; Rivet, C.J.; Gilbert, R.J.; Morrison, F.A. A protocol for rheological characterization of hydrogels for tissue engineering strategies. *J. Biomed. Mater. Res. Part B Appl. Biomater.* **2014**, *102*, 1063–1073. [[CrossRef](#)]
41. Zhong, T.; Deng, C.; Gao, Y.; Chen, M.; Zuo, B. Studies of in situ-forming hydrogels by blending PLA-PEG-PLA copolymer with silk fibroin solution. *J. Biomed. Mater. Res. Part A* **2012**, *100*, 1983–1989. [[CrossRef](#)]
42. Mi, H.-Y.; Salick, M.R.; Jing, X.; Jacques, B.R.; Crone, W.C.; Peng, X.-F.; Turng, L.-S. Characterization of thermoplastic polyurethane/poly(lactic acid) (TPU/PLA) tissue engineering scaffolds fabricated by microcellular injection molding. *Mater. Sci. Eng. C* **2013**, *33*, 4767–4776. [[CrossRef](#)]
43. Unzueta, U.; Cespedes, M.V.; Sala, R.; Alamo, P.; Sánchez-Chardi, A.; Pesarrodonna, M.; Sánchez-García, L.; Cano-Garrido, O.; Villaverde, A.; Vázquez, E.; et al. Release of targeted protein nanoparticles from functional bacterial amyloids: A death star-like approach. *J. Control. Release* **2018**, *279*, 29–39. [[CrossRef](#)]
44. Chauvet, M.; Sauceau, M.; Fages, J. Extrusion assisted by supercritical CO<sub>2</sub>: A review on its application to biopolymers. *J. Supercrit. Fluids* **2017**, *120*, 408–420. [[CrossRef](#)]
45. Ventosa, N.; Sala, A.S.; Veciana, J.; Torres, J.; Llibre, J. Depressurization of an Expanded Liquid Organic Solution (DELOS): A New Procedure for Obtaining Submicron- or Micron-Sized Crystalline Particles. *Cryst. Growth Des.* **2001**, *1*, 299–303. [[CrossRef](#)]
46. Mooney, D.; Baldwin, D.F.; Suh, N.P.; Vacanti, J.P.; Langer, R. Novel approach to fabricate porous sponges of poly(D,L-lactic-co-glycolic acid) without the use of organic solvents. *Biomaterials* **1996**, *17*, 1417–1422. [[CrossRef](#)]
47. Quirk, R.A.; France, R.M.; Shakesheff, K.M.; Howdle, S.M. Supercritical fluid technologies and tissue engineering scaffolds. *Curr. Opin. Solid State Mater. Sci.* **2004**, *8*, 313–321. [[CrossRef](#)]
48. Hatami, T.; Johnner, J.C.F.; de Castro, K.C.; Mei, L.H.I.; Vieira, M.G.A.; Meireles, M.A.A. New Insight into a Step-by-Step Modeling of Supercritical CO<sub>2</sub> Foaming to Fabricate Poly(ε-caprolactone) Scaffold. *Ind. Eng. Chem. Res.* **2020**, *59*, 20033–20044. [[CrossRef](#)]
49. Markočič, E.; Škerget, M.; Knez, Ž. Effect of Temperature and Pressure on the Behavior of Poly(ε-caprolactone) in the Presence of Supercritical Carbon Dioxide. *Ind. Eng. Chem. Res.* **2013**, *52*, 15594–15601. [[CrossRef](#)]

50. Hatami, T.; Mei, L.H.I.; Shabanian, S.R. Modeling of Two-Step Supercritical CO<sub>2</sub> Foaming to Fabricate Poly( $\epsilon$ -caprolactone) Scaffolds. *Chem. Eng. Technol.* **2021**, *44*, 1233–1240. [[CrossRef](#)]
51. Kuboki, Y.; Jin, Q.; Takita, H. Geometry of Carriers Controlling Phenotypic Expression in BMP-Induced Osteogenesis and Chondrogenesis. *J. Bone Jt. Surg.-Am. Vol.* **2001**, *83*, S105–S115. [[CrossRef](#)]
52. Tsuruga, E.; Takita, H.; Itoh, H.; Wakisaka, Y.; Kuboki, Y. Pore Size of Porous Hydroxyapatite as the Cell-Substratum Controls BMP-Induced Osteogenesis. *J. Biochem.* **1997**, *121*, 317–324. [[CrossRef](#)]
53. Götz, H.; Müller, M.; Emmel, A.; Holzwarth, U.; Erben, R.; Stangl, R. Effect of surface finish on the osseointegration of laser-treated titanium alloy implants. *Biomaterials* **2004**, *25*, 4057–4064. [[CrossRef](#)]
54. Murphy, C.M.; O'Brien, F.J.; Little, D.G.; Schindeler, A. Cell-scaffold interactions in the bone tissue engineering triad. *Eur. Cells Mater.* **2013**, *26*, 120–132. [[CrossRef](#)] [[PubMed](#)]
55. Sarazin, P.; Roy, X.; Favis, B.D. Controlled preparation and properties of porous poly(l-lactide) obtained from a co-continuous blend of two biodegradable polymers. *Biomaterials* **2004**, *25*, 5965–5978. [[CrossRef](#)] [[PubMed](#)]
56. Oh, S.H.; Kang, S.G.; Kim, E.S.; Cho, S.H.; Lee, J.H. Fabrication and characterization of hydrophilic poly(lactic-co-glycolic acid)/poly(vinyl alcohol) blend cell scaffolds by melt-molding particulate-leaching method. *Biomaterials* **2003**, *24*, 4011–4021. [[CrossRef](#)]
57. Wirtz, D.C.; Schiffers, N.; Pandorf, T.; Radermacher, K.; Weichert, D.; Forst, R. Critical evaluation of known bone material properties to realize anisotropic FE-simulation of the proximal femur. *J. Biomech.* **2000**, *33*, 1325–1330. [[CrossRef](#)]
58. Mathieu, L.M.; Mueller, T.L.; Bourban, P.-E.; Pioletti, D.; Müller, R.; Månson, J.-A.E. Architecture and properties of anisotropic polymer composite scaffolds for bone tissue engineering. *Biomaterials* **2006**, *27*, 905–916. [[CrossRef](#)]
59. Chastain, S.R.; Kundu, A.K.; Dhar, S.; Calvert, J.W.; Putnam, A.J. Adhesion of mesenchymal stem cells to polymer scaffolds occurs via distinct ECM ligands and controls their osteogenic differentiation. *J. Biomed. Mater. Res. A* **2006**, *78*, 73–85. [[CrossRef](#)] [[PubMed](#)]
60. Marei, N.H.; El-Sherbiny, I.M.; Lotfy, A.; El-Badawy, A.; El-Badri, N. Mesenchymal stem cells growth and proliferation enhancement using PLA vs PCL based nanofibrous scaffolds. *Int. J. Biol. Macromol.* **2016**, *93*, 9–19. [[CrossRef](#)]
61. Milovanovic, S.; Markovic, D.; Mrakovic, A.; Kuska, R.; Zizovic, I.; Frerich, S.; Ivanovic, J. Supercritical CO<sub>2</sub>-assisted production of PLA and PLGA foams for controlled thymol release. *Mater. Sci. Eng. C Mater. Biol. Appl.* **2019**, *99*, 394–404. [[CrossRef](#)]
62. Murphy, C.M.; Haugh, M.G.; O'Brien, F.J. The effect of mean pore size on cell attachment, proliferation and migration in collagen—Glycosaminoglycan scaffolds for bone tissue engineering. *Biomaterials* **2010**, *31*, 461–466. [[CrossRef](#)] [[PubMed](#)]
63. Amini, A.R.; Adams, U.J.; Laurencin, C.T.; Nukavarapu, S.P. Optimally Porous and Biomechanically Compatible Scaffolds for Large-Area Bone Regeneration. *Tissue Eng. Part A* **2012**, *18*, 1376–1388. [[CrossRef](#)] [[PubMed](#)]
64. Bobbert, F.S.L.; Zadpoor, A.A. Effects of bone substitute architecture and surface properties on cell response, angiogenesis, and structure of new bone. *J. Mater. Chem. B* **2017**, *5*, 6175–6192. [[CrossRef](#)]
65. Seras-Franzoso, J.; Tatkiwicz, W.I.; Vazquez, E.; García-Fruitós, E.; Ratera, I.; Veciana, J.; Villaverde, A. Integrating mechanical and biological control of cell proliferation through bioinspired multieffector materials. *Nanomedicine* **2015**, *10*, 873–891. [[CrossRef](#)] [[PubMed](#)]
66. Seras-Franzoso, J.; Peebo, K.; García-Fruitós, E.; Vázquez, E.; Rinas, U.; Villaverde, A. Improving protein delivery of fibroblast growth factor-2 from bacterial inclusion bodies used as cell culture substrates. *Acta Biomater.* **2014**, *10*, 1354–1359. [[CrossRef](#)]
67. Vázquez, E.; Corchero, J.L.; Burgueño, J.F.; Seras-Franzoso, J.; Kosoy, A.; Bosser, R.; Mendoza, R.; Martínez-Láinez, J.M.; Rinas, U.; Fernández, E.; et al. Functional Inclusion Bodies Produced in Bacteria as Naturally Occurring Nanopills for Advanced Cell Therapies. *Adv. Mater.* **2012**, *24*, 1742–1747. [[CrossRef](#)] [[PubMed](#)]
68. Wood, C.D.; Cooper, A.I. Synthesis of Polystyrene by Dispersion Polymerization in 1,1,1,2-Tetrafluoroethane (R134a) Using Inexpensive Hydrocarbon Macromonomer Stabilizers. *Macromolecules* **2003**, *36*, 7534–7542. [[CrossRef](#)]



Review

# Application of Non-Viral Vectors in Drug Delivery and Gene Therapy

Shuaikai Ren, Mengjie Wang, Chunxin Wang, Yan Wang, Changjiao Sun, Zhanghua Zeng, Haixin Cui and Xiang Zhao \*

Institute of Environment and Sustainable Development in Agriculture, Chinese Academy of Agricultural Sciences, Beijing 100081, China; ren19801266562@163.com (S.R.); wangmengjie@caas.cn (M.W.); wangchunxin@caas.cn (C.W.); wangyan03@caas.cn (Y.W.); sunchangjiao@caas.cn (C.S.); zengzhanghua@caas.cn (Z.Z.); cuihaixin@caas.cn (H.C.)

\* Correspondence: zhaoxiang@caas.cn

**Abstract:** Vectors and carriers play an indispensable role in gene therapy and drug delivery. Non-viral vectors are widely developed and applied in clinical practice due to their low immunogenicity, good biocompatibility, easy synthesis and modification, and low cost of production. This review summarized a variety of non-viral vectors and carriers including polymers, liposomes, gold nanoparticles, mesoporous silica nanoparticles and carbon nanotubes from the aspects of physicochemical characteristics, synthesis methods, functional modifications, and research applications. Notably, non-viral vectors can enhance the absorption of cargos, prolong the circulation time, improve therapeutic effects, and provide targeted delivery. Additional studies focused on recent innovation of novel synthesis techniques for vector materials. We also elaborated on the problems and future research directions in the development of non-viral vectors, which provided a theoretical basis for their broad applications.

**Keywords:** non-viral vectors; polymers; liposomes; gold nanoparticles; mesoporous silica nanoparticles; carbon nanotubes

**Citation:** Ren, S.; Wang, M.; Wang, C.; Wang, Y.; Sun, C.; Zeng, Z.; Cui, H.; Zhao, X. Application of Non-Viral Vectors in Drug Delivery and Gene Therapy. *Polymers* **2021**, *13*, 3307. <https://doi.org/10.3390/polym13193307>

Academic Editors: José Miguel Ferri, Vicent Fombuena Borràs and Miguel Fernando Aldás Carrasco

Received: 23 August 2021  
Accepted: 18 September 2021  
Published: 28 September 2021

**Publisher's Note:** MDPI stays neutral with regard to jurisdictional claims in published maps and institutional affiliations.



**Copyright:** © 2021 by the authors. Licensee MDPI, Basel, Switzerland. This article is an open access article distributed under the terms and conditions of the Creative Commons Attribution (CC BY) license (<https://creativecommons.org/licenses/by/4.0/>).

## 1. Introduction

With the development of biotechnology, drug delivery and gene therapy play an important role in the treatment of many diseases such as hereditary diseases, malignant tumors, cardiovascular diseases, infectious diseases, and neurodegenerative diseases [1–6]. However, there are some drawbacks containing rapid degradation [7–9], nontargeted delivery [10,11], unsatisfactory efficacy [12], multiple side effects [13,14] after nucleic acids, proteins, peptides, and other substances entering the body circulation. Therefore, suitable vectors, effective transport route, or chemical modification are necessary to improve the pharmacokinetic properties [15–18]. A growing number of vectors for gene therapy or vaccines and carriers for drug delivery have been extensively researched owing to their facile use, targeting ability, high bioavailability, and good biocompatibility [19–21].

Viruses, such as adenovirus, vesicular stomatitis virus, cytomegalovirus, lentivirus, and retrovirus, are commonly used vectors because of highly infectious, effective delivery, and efficient expression [22–25]. However, viral vectors have several limitations including toxicity, immunogenicity, carcinogenicity, high cost, and difficulty of large-scale production in clinical practice [26–28]. Consequently, more and more scientists have turned their attention to the development of non-viral vectors and carriers [29–31]. Recent studies have shown that non-viral vectors have the following advantages: low immunogenicity, biodegradability, easy synthesis, low cost of production, and no restriction on the size of the molecules to be introduced [32–36]. The most extensively researched non-viral vectors are mainly polymers, liposomes, and nanoparticles [37–42]. This review introduces several non-viral vectors that have been extensively studied in the past few decades and summarizes

their biomedical applications, providing a theoretical basis for the development of new non-viral vectors in the future (Figure 1). Table 1 shows the characteristics and commonly used preparation methods of several non-viral vectors. Table 2 shows the patent reports related to non-viral vectors in recent years.

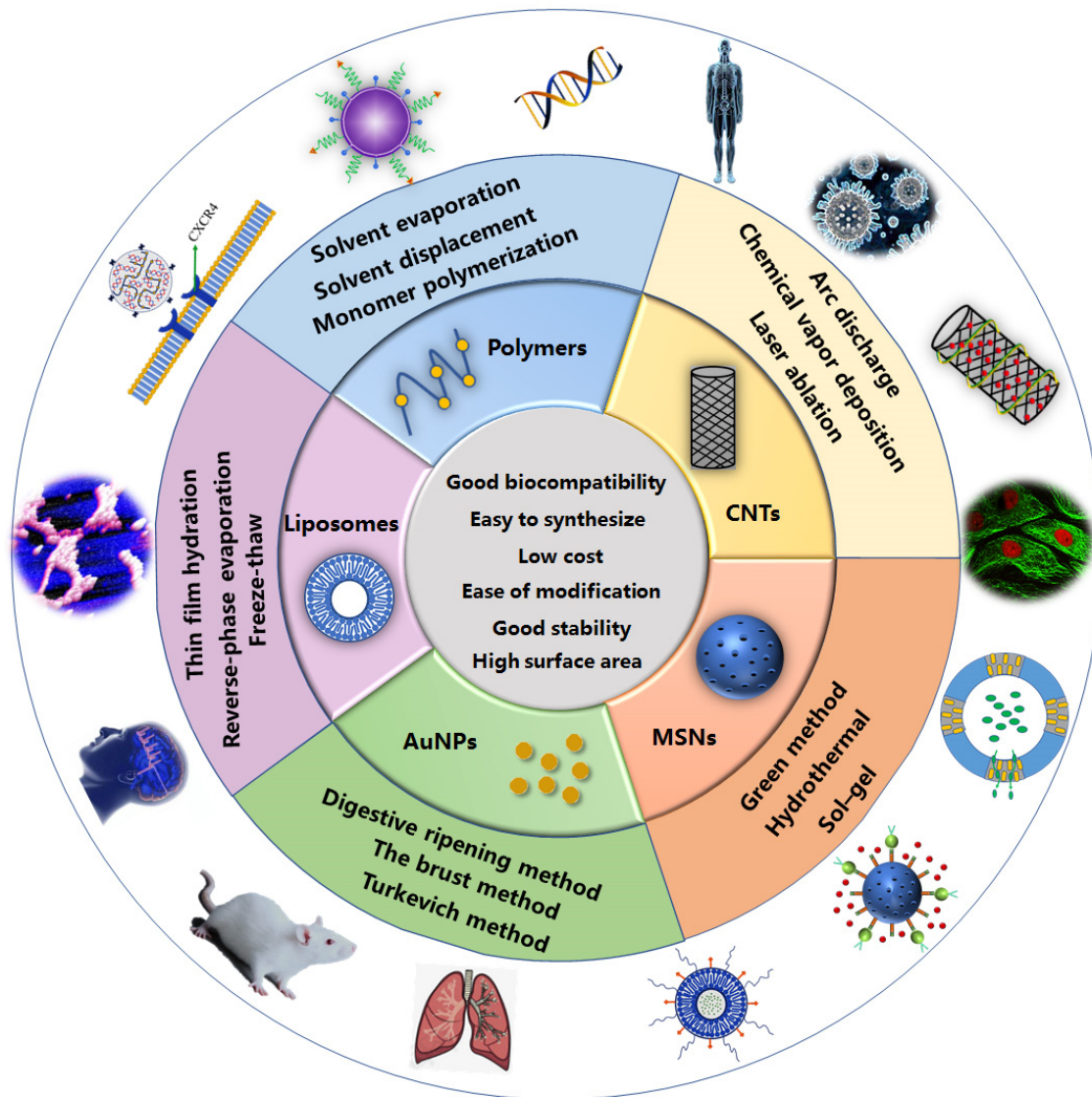


Figure 1. The characteristics, preparation methods, and biomedical applications of several non-viral vectors.

Table 1. The characteristics and preparation methods of several non-viral vectors.

Vector	Characteristics	Preparation Methods
Polymers	Easy to synthesize Low cost Biodegradable No immunogenicity Allow to be extensively modified	Solvent evaporation Emulsification–solvent diffusion Solvent displacement Monomer polymerization Double emulsion solvent evaporation
Liposomes	Low toxicity Good biocompatibility Improved pharmacokinetics Ease of synthesis	Thin film hydration Reverse-phase evaporation Injection Dehydration-rehydration Freeze-thaw

Table 1. Cont.

Vector	Characteristics	Preparation Methods
Gold nanoparticles	Good stability and biocompatibility High surface area-to-volume ratio Easy to modify	Turkevich method The brust method Digestive ripening method Green method
Mesoporous silica nanoparticles	Substantial surface area Large pore size Low density Adsorption capacity Tunable pore size Ease of modification High biocompatibility	Sol-gel Hydrothermal Green method
Carbon nanotubes	Good adsorption ability Excellent chemical stability High tensile strength Significant electrical Thermal conductivity	Arc discharge Chemical vapor deposition (CVD) Laser ablation

Table 2. The patent reports related to non-viral vectors in recent years.

Vector	Summary	References
Polymer	Gene transfer composition using a tri-block polymer electrolyte being polyethyleneimine-poly(lactic acid)-poly(ethylene glycol)	[43]
Polymer	A methoxypolyethylene glycol-poly(lactic acid) block copolymer was prepared to improve the drug encapsulation rate	[44]
Polymer	The chitosan modified with a carboxymethyl group and a hexanoyl group can be used as a material for a drug carrier	[45]
Polymer	Chitosan microspheres capable of precisely controlling the release of the drug	[46]
Polymer	Alginate extraction method	[47]
Polymer	Injectable hybrid alginate hydrogels	[48]
Liposomes	A method for preparing a Decoy nucleic acid cationic liposome carrier	[49]
Liposomes	An efficient, stable human lung tissues-active targeting immune nanoliposome, with specific active lung targeting	[50]
Liposomes	A liposome preparation, a preparation method and an application thereof in treatment for related diseases caused by abnormal expression of gene	[51]
Gold nanoparticles	A method for producing confetto-like gold nanoparticles using hydroxyl peroxide in an aqueous alkaline condition in the presence of a biocompatible protecting agent	[52]
Gold nanoparticles	Method for the size controlled preparation of these monodisperse carboxylate functionalized gold nanoparticles	[53]
Silica nanoparticles	Mesoporous silica nanoparticles and supported lipid bi-layer nanoparticles for biomedical applications	[54]
Silica nanoparticles	Mesoporous silica nanoparticles with lipid bilayer coating for cargo delivery	[55]
Carbon nanotubes	Payload molecule delivery using functionalized discrete carbon nanotubes	[56]
Carbon nanotubes	Carbon nanotubes for imaging and drug delivery	[57]

## 2. Polymers

Recent trends in biodegradable polymers, especially aliphatic polymers, indicate significant developments in terms of novel design strategies and clinical biomedicine applications [58]. Polymer as a non-viral vector has the following advantages: (1) easy



to synthesize and low cost [59]; (2) multiple polymers are biodegradable [60]; (3) no immunogenicity [61]; (4) allow being extensively modified [62]; (5) ability to protect the nucleic acid drugs from various enzymes by forming polyelectrolyte complexes [63]. There are four main types of production methods: solvent evaporation, emulsification–solvent diffusion, solvent displacement and monomer polymerization [59]. Various polymers such as dendrimers, polylactic acid (PLA), polyethylenimine (PEI), and chitosan (CS) have been widely used in delivery systems [51,64–68]. Table 3 summarizes the structural characteristics, synthesis methods and properties of several polymer materials.

**Table 3.** The information of several polymer materials.

Polymer	Structure	Synthesis Methods	Characteristics	Limitations
Dendrimers	Linear polymers with dendron on each repeating unit	Divergent approaches, Convergent approaches	Uniform size, High degree of branching, Polyvalency, Water solubility, Available internal cavities	-
Polyethylenimine	Cationic polymer of ethylenediamine monomers	-	High transfection efficiency	High toxicity
Chitosan	Repeating $\beta$ -(1,4)-2-amino-D-glucose and $\beta$ -(1,4)-2-acetamido-D-glucose units	Chemical method, enzymatic	Good biocompatibility	Poor solubility in water, Low transfection efficiency
Polylactic acid	The polymerization of lactic acid	Direct condensation polymerization, Azeotropic dehydration condensation, Lactide ring-opening polymerization, Double emulsion solvent evaporation technique	Strong plasticity, Low price, Good versatility	Poor hydrophilicity
Amino acid derived biopolymers	Amino acid polymerization	Direct polycondensation, Solution or activated polycondensation, Ring-opening polymerization, Interfacial polymerization, Melt polycondensation, Chemoenzymatic synthesis	Wide-range of functional groups, Good biocompatibility	Production of by-products in the synthesis process
Alginate	Linear copolymer	Ionic crosslinking, Covalent crosslinking, Phase transition, Cell crosslinking, Free radical polymerization, Click chemistry	easy availability, hydrophilicity, biodegradability, versatility	Aggregation tendency with protein at high pHs

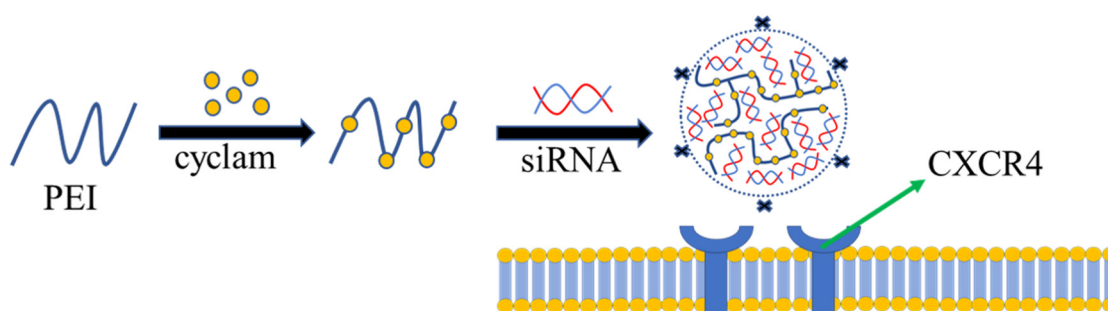
### 2.1. Dendrimers

Dendrimers are linear polymers with dendron on each repeating unit and have a hyper-branched 3D structure [61,69]. Their size, degree of branching and functionality can be controlled and adjusted through the synthetic procedures [70]. Meanwhile, dendrimers contain a variety of peripheral functional groups, which can be functionally modified using

surface engineering technology such as antibody, transferrin, biotin, folic acid, galactose, and peptide [71–73]. A variety of dendrimers such as poly (propylene imine) (PPI) dendrimers, polyamidoamine (PAMAM) dendrimers, and poly-L-lysine (PLL) dendrimers were synthesized by divergent and convergent approaches [74]. Guan et al. prepared fluorescent PAMAM dendrimer by conjugating PAMAM dendrimers to fluorescein. The vector has low cytotoxicity and high siRNA binding affinity which can improve the efficiency of Cy5-siRNA delivery in A549 cells [75]. Mastorakos et al. prepared the hydroxyl PAMAM dendrimer-based gene vectors which had high gene transfection efficiency and the stability of compound can be improved after polyethylene glycol treatment [76]. Liaw et al. prepared targeted novel hydroxyl dendrimer to deliver CSF-1R inhibitor BLZ945 (D-BLZ), these dendrimers penetrated into orthotopic brain tumors and localize specifically within TAMs. In vivo experiments on mice showed that the dendritic polymer could improve the therapeutic effect of D-BLZ on glioblastoma [77].

## 2.2. Polyethylenimine

Various molecular weights of PEI can be synthesized by linear and branched forms [78]. Because PEI has a large amount of positive charge on its surface, it can be adsorbed together with negatively charged nucleic acid drugs through electrostatic action to protect them from lysosomal degradation [79–83]. However, PEI cannot be degraded in vivo, and its high toxicity limits its application development [84,85]. Various polyethylenimine derivatives containing coordination groups have been developed to reduce toxicity [86,87]. Mattheolabakis et al. used polyethylenimine, hyaluronic acid, and polyethylene glycol to produce a polymer with a good ability to deliver siRNA to A549 cells [88]. Zhou et al. prepared a PEI derivative modified by a cyclic amine derivative. Compared with unmodified PEI, modification with cyclic amine derivatives can significantly reduce cytotoxicity. At the same time, the polymer has a good antagonistic effect on Chemokine receptor CXCR4, and has a good inhibitory ability on tumor cell invasion (Figure 2) [83]. Low molecular weight PEI has lower toxicity, but the transfection efficiency is correspondingly lower [89]. More and more studies have been conducted to modify low molecular weight PEI to improve transfection efficiency [90,91]. Zhang et al. modified PEI 600 Da with aromatic rings in order to improve DNA affinity. Cell uptake experiments showed that the polymer had higher transfection efficiency for DNA compared with PEI 25 kDa. Meanwhile, the toxicity of the polymer has low toxicity in both 7702 and HeLa cells by CCK-8 assay [92].



**Figure 2.** Cyclam modified PEI is used for the delivery of siRNA.

## 2.3. Chitosan

Chitosan (CS) is one of the most abundant biopolymers derived from natural chitin that commonly exists in the exoskeletons of arthropods, crustacean shells, insects, and fungal cell walls [93]. CS can be degraded by internal enzymes, which makes chitosan have good biocompatibility [94,95]. Like other cationic polymers, chitosan is linked to nucleic acids by electrostatic interaction [96,97]. However, the poor solubility in water and low transfection efficiency are the main factors limiting its application [98–100]. The presence of amino and hydroxyl groups makes chitosan easy to modify, modification of

chitosan with other substances such as PEI, gold nanoparticles, PLGA, and PEG have been widely reported [101]. Chen et al. incorporated hydrophobic deoxycholic acid (DCA) onto the chitosan backbone of poly (amidoamine) dendronized chitosan derivative (PAMAM-Cs) to obtain an amphiphilic derivative-PAMAM-Cs-DCA. Doxorubicin was wrapped inside the particle, and pDNA was electrostatically adsorbed on the surface of the particle. The system delivered both pDNA and drugs at the same time, and the transfection efficiency reached 74%. These results suggested that PAMAM-Cs-DCA NPs hold great promise to co-deliver chemotherapeutics and nucleic acid drugs [102]. Lee et al. prepared the triphenylphosphonium-glycol chitosan derivative (GME-TPP) with 36% substitution by Michael addition. GME-TPP microspheres successfully targeted DOX delivery to mitochondria in cells, which indicated the microsphere possess great potential as effective drug delivery carrier [103]. Babii et al. synthesized mannosyl chitosan with a degree of substitution of 15%. The particle has high encapsulation efficiency for CpG oligodeoxynucleotides (CpG ODN) and can target CpG ODN to immune cells, which indicated the particle may be used as an efficient carrier for intracellular CpG ODN delivery [104]. Masjedi et al. prepared targeted nanoparticles by modifying N, N, N-trimethyl chitosan with hyaluronic acid, which had low toxicity and high transfection efficiency for siRNA. The particle loaded with siRNA can block the proliferation of cancer cells by inhibiting the expression of IL-6/STAT3 [105].

#### 2.4. Polylactic Acid/Poly (Lactic-Co-Glycolic Acid)

PLA and PLGA are biodegradable functional polymer organic compounds with good biocompatibility and encapsulation properties which can be metabolized in the body [106,107]. The synthesis of polylactic acid by direct condensation is described in the following four ways: (1) direct condensation polymerization; (2) azeotropic dehydration condensation; (3) lactide ring-opening polymerization; (4) double emulsion (water/oil/water) solvent evaporation technique [108–110]. The characteristics of strong plasticity, low price and good versatility have enabled them to be developed for biomedical applications such as drug delivery [111–113]. Zabihi et al. prepared poly (lactide-co-glycerol) (PLG) particles by combining hyperbranched polyglycerol and PLA. The encapsulation efficiency of this particle on tacrolimus is 14.5%, which was able to improve the skin penetration and therapeutic efficiency of this therapeutic agent [114]. Ren et al. prepared a dextran modified PLGA microsphere that delivered IL-1 receptor antagonist (IL-1RA). The microsphere can prolong the half-life of IL-1RA, allowing it to be released continuously. The results showed that IL-1ra-loaded dextran/PLGA microsphere might be a useful tool to combat periodontal disease [115]. Bazylińska et al. prepared effective nanocarriers coated with PLGA, PLGA-PEG, or PLGA-FA by double emulsion evaporation process, which enabled co-encapsulation of cisplatin and verteporfin. The nanocarriers successfully delivered cargo to target cells and significantly enhanced the ability of drugs to kill cancer cells [116].

#### 2.5. Amino Acid Derived Biopolymers

Amino acids have become promising biomaterials for their abundant source and diverse functional groups. Various polymerization methods are used to synthesize different types of amino acid derived biopolymers such as polyamides(PA)s, polyesters(PE)s, poly(ester-amide)s(PEA)s, polyurethanes(PU)s, and poly (depsipeptide)s (PDP)s [117]. Commonly used synthesis pathways are as follows: Direct polycondensation [118]; solution or activated polycondensation [119]; ring-opening polymerization [120]; interfacial polymerization [121]; melt polycondensation [122]; chemoenzymatic synthesis [123]. Poly( $\alpha$ -amino acid)s have the capability of readily self-assemble into discrete, stable, structures in solution. The positive charge of poly(beta-amino ester)s can bind to nucleic acids and be internalized into cells. At the same time, they can escape from the endolysosomal compartment and release nucleic acids into the appropriate cell compartment for gene delivery through a variety of targeted degradation mechanisms [68]. In addition, abundant functional groups provide multiple modification sites for amino acid derived biopolymers.

Various ligand-modified amino acid derived biopolymers were extensively studied in drug delivery (Table 4).

**Table 4.** Various responsive Amino acid derived biopolymers are used to deliver cargos.

Type	Ligands	Stimulus	Cargo	References
ssPBAE	HA	PH/redox	DOX/CXB	[124]
LPAE	-	Light	DNA	[125]
PBAE	PEG	PH	VP	[126]
PBLG	PEG	PH/Temperature	DOX	[127]
PBAE	-	PH	ATRA	[128]
SCA-PAE	HA	PH	siRNA	[129]

### 2.6. Alginates

Alginate (ALG) is a linear copolymer compound which has (1, 4)-linked- $\beta$ -D- manuronic (M) and  $\alpha$ -L-guluronic (G) acid units [130]. The composition and length of the M and G units determine the molecular and physicochemical properties of ALG. ALG is a widely used anionic biopolymer due to its easy availability, hydrophilicity, biodegradability and versatility. The hydroxyl groups and carboxyl groups of ALG can be modified easily by oxidation, acetylation, and esterification reactions [131]. The wide particle size distribution of ALG enables it create complexes with various other biomaterials by electrostatic interactions, chemical modification, or crosslinking [132]. The most important property of alginates is their ability to form ionic gel in the presence of polyvalent cations. So-gel is the most commonly used form of carrier for ALG. In recent years, the methods of producing hydrogels included ionic crosslinking, covalent crosslinking, phase transition, cell crosslinking, free radical polymerization, and click chemistry [130]. Alginate hydrogels have outstanding properties such as high-water content, nontoxicity, soft consistency, and biodegradability [133]. Meanwhile, alginate hydrogels can regulate the release of the drug according to the pH of the surrounding medium [134]. In addition, ALG can also be developed into microspheres and nanoparticles for drug delivery. Table 5 illustrates several alginate-based drug delivery systems.

**Table 5.** Various alginate-based vehicles used in drug delivery.

Carriers	Type	Cargo	References
ALG/Keratin	Hydrogels	Doxorubicin	[135]
ALG/HA/Folate	Hydrogels	OXA	[136]
ALG/CS/BSA	Microcapsule	DOX	[137]
ALG/PEG	Microspheres	Polystyrene	[138]
ALG/CS	Nanoparticles	Cur	[139]
ALG/Laponite	Nanohybrids	DOX	[140]

### 3. Liposomes

Liposomes are spherical vesicles composed of one or more layers of phospholipids which belong to amphiphilic molecules, hydrophilic drugs are encapsulated in a water core, and hydrophobic drugs are embedded in the lipid bilayer of the vesicle [141–143]. Liposomes as carriers have many advantages, including low toxicity, good biocompatibility, improved pharmacokinetics, and ease of synthesis [144–146]. The commonly used preparation methods are thin film hydration, reverse-phase evaporation, injection, dehydration-rehydration, and freeze-thaw. Liposomes are widely used in cancer treatment, viral infection, infectious disease, vaccines, and other medical research [147–150]. However,

unmodified liposomes are unstable in structure, thus are easily eliminated in the body's circulation, making drugs unable to effectively reach target organs and target sites [151–153]. Therefore, various ligand-targeting liposomes and stimulus-responding liposomes have been developed to improve the delivery and targeting performance of liposomes [154–159]. Table 6 shows that liposomes modified with different ligands to deliver different cargos.

**Table 6.** Various ligands modified liposomes to deliver different cargos.

Ligands	Stimulus	Cargo	References
H16 peptide	-	Alpha-galactosidase A	[160]
Ferritin receptors	-	Resveratrol	[161]
Lactoferrin	-	Doxorubicin	[162]
PEG and anti-EphA10 antibody	-	siRNA	[163]
Anti-CD44 aptamer	-	siRNA	[164]
DSPE-PEG-2000	Temperature	Doxorubicin	[165]
Peptide H7K(R2)2	PH	dDoxorubicin	[166]
Superparamagnetic magnetite	Magnetic Field	5-fluorouracil	[167]
Hyaluronic acid	Redox	Doxorubicin	[168]
Enzymatically cleavable peptide linkers GFLG	enzyme	pDNA	[169]

### 3.1. Ligand-Targeting Liposomes

Peptides as ligands have the advantages of small size, easy production, and high stability [170]. Peptides can be combined with liposomes through various covalent and non-covalent bonds, and are mainly divided into cell-penetrating peptides (CPP) and cell-targeting peptides (CTP) [171–173]. RGD sequences are the most widely used class of liposomal binding peptides, especially in tumor therapy [174]. Kang et al. developed a cyclic peptide c(RGDyC) modified liposomal delivery system to deliver the integrins  $\alpha v \beta 3$ , which had a higher cellular uptake compared with liposomes without c(RGDyC) [175]. Belhadj et al. designed a Y-shaped multifunctional targeting material c(RGDyK)-pHA-PEG-DSPE to deliver DOX, which prolonged the survival time of mice [176]. The encapsulation rate of RGD-DXRL-PEG liposomes prepared by Chen et al. for doxorubicin was more than 98%, and the cellular doxorubicin uptake for RGD-DXRL-PEG was about 2.5-fold higher than that for DXRL-PEG (Figure 3) [177]. CPP typically contains 5 to 35 amino acid residues and is widely used in cancer treatment [178]. Ding et al. constructed CPP-modified pH-sensitive PEGylated liposomes (CPPL) which had high cell-penetrating and endosomal escape abilities [179]. Hayashi et al. developed H16 peptide-modified liposomes (H16-Lipo) which effectively delivered alpha-galactosidase A (GLA) to intracellular lysosomes and improved proliferation of GLA knockdown cells [160]. Some other types of peptides have also been used to modify liposomes. Chen et al. used peptide-20 modified liposome as a carrier for DOX delivery, and U87 cells had a high uptake rate of this liposome [177]. Jhaveri et al. used ferritin receptors modified liposomes to deliver resveratrol, which has a good effect on inhibiting tumor growth and improving the survival rate of mice [161]. Wei et al. developed a lactoferrin modified, polyethylene glycolated liposomes for doxorubicin delivery. The results of experiments in mice indicated that the liposome-loaded DOX has the potential to treat hepatocellular carcinoma [162].

Various immune liposomes can be obtained by attaching antibodies to the surface of liposomes using surface engineering techniques [180–182]. Gao et al. developed a liposome system modified with anti-EGFR Fab to deliver DOX and ribonucleotide reductase M2 siRNA, in vivo and in vitro experimental results showed that the vector system can improve the efficiency of gene therapy and had a certain therapeutic effect on hepatocellular carcinoma [183]. Saeed et al. prepared the immunoliposomes coupled to anti-MAGE A1

TCR-like single-chain antibody which can be specifically bound to and be internalized by positive melanoma cells [184]. Zang et al. prepared liposomes modified by PEG and anti-EphA10 antibody, the immunoliposome significantly improved the transfection efficiency of siRNA in MCF-7/ADR cells [163].

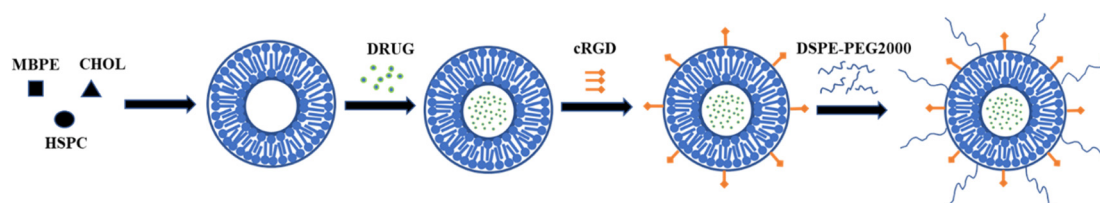


Figure 3. Schematic representation for preparation of RGD-DXRL-PEG.

An aptamer is a short synthetic single stranded DNA or RNA that can specifically bind to the target through hydrogen bonds, Van der Waals forces and electrostatic interactions [185,186]. Using aptamers as ligands has the characteristics of small volume, simple synthesis process, low toxicity, good stability, high affinity, and good targeting selectivity [187]. Alshaer et al. used anti-CD44 aptamer (APT1) modified liposome as a carrier system for siRNA delivery and achieved a good gene silencing effect in tumor cells [164]. Powell et al. used Aptamer A6 modified liposome as a vector to deliver siRNA to breast cancer cells which enhanced cytotoxicity and antitumor efficacy [188]. Li et al. combined Aptamer AS1411 with PEGylated liposome surface to prepare a targeted carrier for siRNA delivery. Cell uptake experiment results showed that the accumulation of siRNA in tumor cells was greater than that in normal cells. Meanwhile, the carrier system showed significant silencing activity in tumor xenograft mice and inhibited the melanoma growth which indicated that the targeted delivery system of liposomes may have potential in the treatment of melanoma [189].

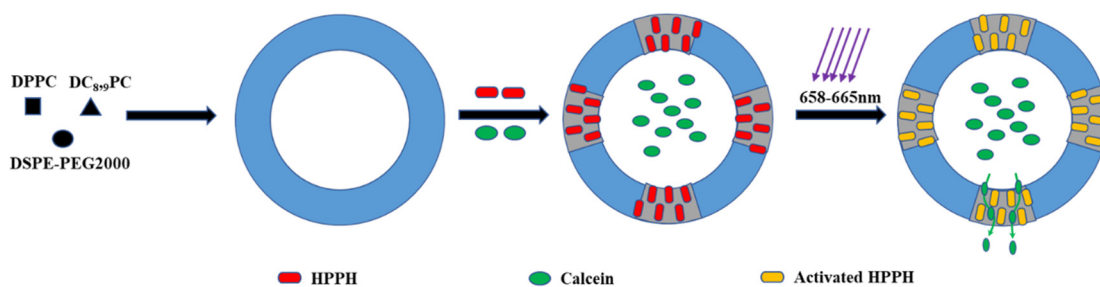
Molecules such as folate and sugars also serve as ligands for liposomes [190–192]. There are also studies devoted to the development of liposome carriers modified with various ligands, multivalent ligands have multiple binding groups and enhance the therapeutic efficacy of drugs [193]. Kang et al. prepared a dual ligand liposome drug delivery system modified with Pep-1 peptide and folate which showed higher cellular uptake and cytotoxicity in HeLa cells as compared to chimeric-ligand oriented liposomes [194]. Zong et al. prepared a dual ligand liposome drug delivery system modified with cell-penetrating peptide (TAT) and transferrin, which effectively delivered drugs to targeted tumor cells, the results of in vivo experiments also demonstrated that this drug delivery system could improve the survival time of brain tumor-bearing animals [195].

Abbreviations: HSPC, hydrogenated soybean phosphatidylcholine; CHOL, cholesterol; MBPE, maleimidobenzoylphosphatidylethanolamine; DSPE-PEG2000, N-(carbonylmethoxypolyethylene glycol 2000)-1, 2-distearoyl-sn-glycero-3-phosphoethanolamine sodium salt; DRUG, doxorubicin; DXRL-PEG, DXR-loaded PEGylated liposomes; RGD-DXRL-PEG, cRGD-modified DXRL-PEG.

### 3.2. Stimulus-Responding Liposomes

Internal physiological conditions and external stimuli were used to promote the release of drug delivery systems in specific locations and environments to alter pharmacokinetic characteristics [196,197]. Depending on the stimulus, scientists developed various liposome drug carrying systems such as temperature-responsive liposomes, pH-responsive liposomes, ultrasound responsive liposomes, magnetic-field responsive liposomes, redox-responsive liposomes, light-responsive liposomes, and enzyme-responsive liposomes. Needham et al. prepared a kind of temperature sensitive liposome using dipalmitoylphosphatidylcholine (DPPC), monopalmitoylphosphatidylcholine (MSPC), and distearoylphosphatidylethanolamine (DSPE)-PEG2000. The liposome is relatively stable at 37 °C. When the temperature reaches 41.5 °C, 31% of the drug can be released within one to two seconds

which was much higher than the unmodified liposome group [165]. Zhao et al. prepared a pH-responsive liposome drug delivery system using tumor-specific pH-responsive peptide H7K(R2)2 as a ligand. In vitro experiments proved that the drug delivery system effectively released drugs under acidic conditions, and in vivo experiments showed that the system had a good anti-tumor ability in C6 tumor-bearing mice [166]. Clares et al. used a reproducible thin film hiatus technique to prepare magnetic liposomes coated with 5-fluorouracil. Magnetic field caused the release of the drug and a good inhibition effect was observed in human colon cancer cells [167]. Sine et al. prepared a light-responsive liposome encapsulated with 2-(1-hexyloxyethyl)-2-devinyl pyropheophorbide-A and calcein, laser irradiation (660 nm, 90 mW) can promote drug release which showed enhanced antitumor efficacy (Figure 4) [198]. Chi et al. prepared redox-responsive liposomes using hyaluronic acid as a compound. The drug can be effectively released when the liposome is exposed to reduced conditions. All animals treated with liposomal formulations survived in contrast to those animals treated with free-DOX, indicating the liposomal formulation have an effective tumor suppressive effect [168]. Song et al. synthesized enzymatic-responsive liposomes using the enzymatically cleavable peptide linkers GFLG (Gly-Phe-Leu-Gly) as the ligand system. After GFLG was degraded by endo-lysosomal enzyme, the encapsulated pDNA was released and the transfection efficiency was 100 times higher than that of the control group without GFPG modification [169].



**Figure 4.** Design consideration of light-responsive liposomes.

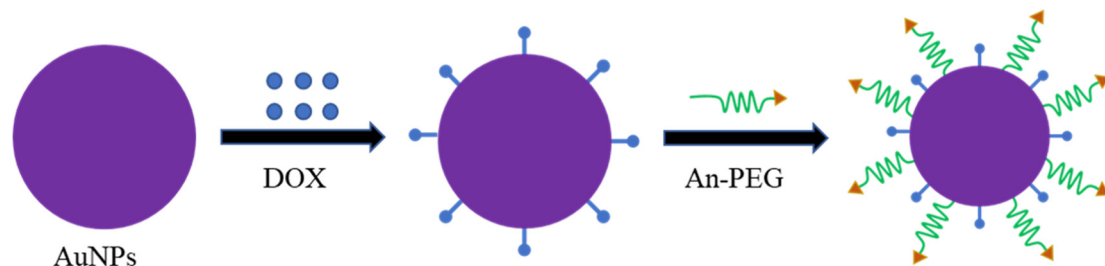
Abbreviations: DPPC, 1,2-dipalmitoyl-sn-glycero-3-phosphocholine; DC<sub>8,9</sub>PC, 1,2 bis(tricoso-10,12-diynoyl)-sn-glycero-3-phosphocholine; DSPE-PEG2000, 1,2-distearoyl -sn-Glycero-3-Phosphoethanolamine-N-[Methoxy(Polyethylene glycol)-2000].

#### 4. Gold Nanoparticles

Gold nanoparticles (AuNPs) have good stability and biocompatibility [199]. Quantum size effect and high surface area-to-volume ratio make AuNPs have high drug loading [200]. Meanwhile, gold nanoparticles are easy to modify and can improve the pharmacokinetics of many drugs which makes gold nanoparticles widely used in immune analysis, drug delivery, and detection of cancer cells and microorganisms [201–203]. For example, Ruan et al. synthesized the Angiopep-2-PEG modified AuNPs which could specifically deliver and release DOX in glioma and significantly expand the median survival time of glioma-bearing mice (Figure 5) [204]. The synthesis methods of gold nanoparticles include chemical synthesis and biological synthesis. The commonly used chemical methods include the turkevich method, the brust method, and digestive ripening method [205–207]. The chemosynthesis method has some limitations including low yield, difficulty in controlling particle shape, strict preparation conditions, and poor biocompatibility [208–211]. Therefore, more and more scientists are using friendly biosynthesis methods to synthesize gold nanoparticles.

Bacteria are important biological sources for the synthesis of AuNPs. The extracellular enzymes work as a reducing agent in the reduction of metals during the synthesis of microbial NPs and NADH-dependent reductase can carry out electron transfer from NADH, leading to reduction of metal ions [212,213]. Parastoo et al. prepared the gold nanoparticles with spherical, hexagonal, and octagonal shapes by reducing H<sub>2</sub>AuCl<sub>4</sub> in

supernatant microbial of bacillus cereus culture [214]. Sharma et al. screened a marine bacterium from different sea coast in India to produce gold nanoparticles. The prepared gold nanoparticles were mostly spherical with a particle size of 10 nm [215]. Fungi also can be used to synthesize gold nanoparticles. Sanghi et al. synthesized intracellular gold nanoparticles with Phanerochaete chrysosporium and demonstrated that ligninase played an important role [216]. Molnár et al. synthesized gold nanoparticles of different sizes (between 6 nm and 40 nm) under controlled experimental conditions [217].



**Figure 5.** An-PEG modified gold nanoparticles are used to deliver DOX. Abbreviations: DOX, doxorubicin; An, Angiopep-2.

As a cheap biological material, plants were used to synthesize gold nanoparticles in recent years. Different plant species, different parts of the same plant species such as leaves, roots, stems, and fruits can be used as raw materials for the synthesis of gold nanoparticles [218]. Gopinath et al. synthesized spherical gold nanoparticles with particle size of 20 nm to 50 nm by aqueous leaf extract of terminalia arjuna [219]. Yu et al. used Citrus Maxima (*C. Maxima*) fruit extract to synthesize gold nanoparticles with an average particle size of 25.7 nm [220]. In addition, some studies have shown that gold nanoparticles can be synthesized from seaweed [221,222]. Table 7 shows the various biomaterials that can be used to synthesize gold nanoparticles.

**Table 7.** Characteristics of gold nanoparticles synthesized from different raw materials.

Name of Organism	Size (nm)	Shape	References
<b>Bacteria</b>			
<i>Bacillus cereus</i>	20–50	Spherical, hexagonal, octagonal	[214]
<i>Brevibacterium casei</i>	10–50	Spherical	[223]
<i>Vibrio alginolyticus</i>	50–100	Irregular	[224]
<i>Paracoccus haeundaensis</i> BC74171(T)	20.93 ± 3.46	Spherical	[225]
<b>Fungi</b>			
<i>Macrophomina phaseolina</i>	14–16	Spherical	[226]
<i>Morchella esculenta</i>	16.51	Spherical and hexagonal	[227]
endophytic <i>Cladosporium</i> species	5–10	Spherical	[228]
<i>Ttichoderma</i> sp. WL-Go	1–24	Spherical and pseudo-spherical	[229]
<b>Plants</b>			
<i>Annona muricata</i>	25.5	Spherical	[230]
<i>Benincasa hispida</i>	22.18 ± 2	Spherical	[231]
<i>Capsicum annum</i>	19.97	Spherical	[232]
<i>Turnera diffusa</i>	24	Spherical	[233]



Table 7. Cont.

Name of Organism	Size (nm)	Shape	References
<b>Algae</b>			
Sargassum serratifolium	5.22	slightly spherical, triangles, pentagons, and narrow square	[234]
marine red alga Acanthophora spiciferaby	<20	Spherical	[235]
marine brown algae S. ilicifolium	20–25	Near-spherical	[236]
Chlorella sorokiniana Shihira & R.W	5–15	Spherical	[237]

The size and shape of gold nanoparticles can be tuned by controlling the synthesis conditions such as temperature, type of surfactant, and concentration of metal matrix in both chemical and biosynthetic methods [238]. The size and shape of gold nanoparticles strongly influence their toxicity, drug loading, and penetration properties, and then affect their biomedical applications. A study showed that 5 nm AuNPs in a concentration of more than 50  $\mu$ M were associated with cytotoxic effects, while 15 nm AuNPs presented good biocompatibility [239]. Karol et al. studied the relationship between toxicity and shape of gold nanoparticles (rods, stars, and spheres). The results showed that star shape gold nanoparticles has the highest anticancer potential but has the slowest cellular uptake due to their big size, while the sphere shape gold nanoparticles exhibited the most safety, the fastest cellular uptake and weak anticancer potential [240]. A study about the size dependence of the antiviral activity of AuNPs demonstrated that small particles (2 nm) had no inhibitory effect for influenza virus, while medium-sized AuNPs (14 nm) inhibited the virus binding and infection [241].

### 5. Mesoporous Silica Nanoparticles

In 1992, the first ordered mesoporous silica (MCM type) was synthesized by the Mobile Research and Development Corporation [242,243]. Subsequently, many other types of mesoporous silica nanomaterials (MSNs) such as BSA type, HMM type, KIT type, KCC type, FSM type, and TUD type were synthesized using a variety of improved methods. Table 8 shows the specific example of the synthesis of various MSNs. Various distinctive properties of MSNs including substantial surface area, large pore size, low density, good adsorption and encapsulation capacity, controllable superficial charge, ease of modification, and high biocompatibility showed great potential in drug delivery applications [244–249]. The synthesis techniques of MSNs can be classified into sol–gel, as well as hydrothermal and green method (Table 9) [250].

Table 8. Synthesis of different series of MSNs.

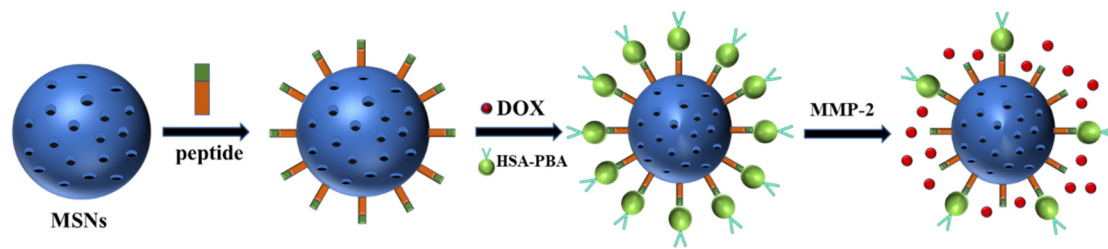
Type	Silica Sources	Surfactant	References
MCM	Sodium silicate, Tetramethylammonium silicate, Tetraethyl orthosilicate	Quaternary ammonium surfactant	[242]
BSA	Sodium silicate	C <sub>18</sub> TMACl	[251]
HMM	1,2-bis(trimethoxysilyl)ethane	C <sub>18</sub> H <sub>37</sub> N(CH <sub>3</sub> ) <sub>3</sub> Cl	[252]
KIT	Tetraethyl orthosilicate, Carboxyethylsilanetriol sodium salt	Pluronic F127	[253]
KCC	Tetraethyl orthosilicate	Cetylpyridinium bromide	[254]
FSM	Layered polysilicate kanemite	Quaternary ammonium surfactant	[255]
TUD	Tetraethyl orthosilicate	Tetraethyl ammonium hydroxide	[256]

**Table 9.** Three different synthesis methods of MSNs.

Method	Silica Sources	Surfactant	Catalyst	References
Sol-gel	Sodium silicate	Polyethylene glycol	Acetic acid	[257]
	Tetraethylorthosilicate	Cetyltrimethylammonium chloride	Triethanolamine	[258]
Hydrothermal	Tetraethylorthosilicate	Cetyltrimethylammonium bromide	Ammonia	[259]
	Tetraethylorthosilicate	Pluronic F-127	Chloride acid	[260]
Green	Banana Peel	Cetyltrimethylammonium bromide	NaOH	[261]
	Tetraethyl orthosilicate	C16-L-histidine, C16-L-poline and C16-L-tryptophan	HCl	[262]

Regardless of the synthesis method, studies have shown that selection of surfactant molecule, silica precursors, solvents, reaction temperature, stir speed, and pH of the media affect the shape, size, surface area, and pore size of MSNs [263,264], and these physical properties further affect the drug loading, toxicity, and uptake efficiency of the carriers [265–267]. Cho et al. found that compared with MSNs with a particle size of 100 nm or 200 nm, MSNs with a particle size of 50 nm had the fastest clearance rate in urine and bile [268]. Lu et al. prepared a series of MSNs with particle sizes of 30 nm, 50 nm, 110 nm, 170 nm, and 280 nm, the cellular uptake amount of 50 nm nanoparticles was much higher than other groups [269]. In addition, studies showed that rod-shaped MSNs internalize faster and higher on tumor cells than spherical MSNs [270]. Meanwhile, the pores of MSNs have a large surface area, and for different drugs, the release of drugs can be controlled by regulating the size of the pores [271]. Mellaerts et al. prepared four SBA-15 MSNs with pore size varying from 4.5 to 9.0 nm, and they found that the increase of the pore size from 4.5 to 6.4 nm significantly improved the release of itraconazole, while a further increase to 7.9 and 9.0 nm revealed a slight improvement in the release profile [272].

However, two challenges of MSNs may limit its broader application. The open pores of MSNs are ideal reservoirs for drugs, which adversely trigger a premature release of drugs before reach the target [266]. A simple way to minimize the leakage is the attachment of the drugs through a cleavable bond onto the inner surface of the particle [273]. Wong et al. connected doxorubicin (DOX) and zinc(II) phthalocyanine (ZnPc) to form a DOX-ZnPc complex using an acid cleavable hydrazone linker, and the resulted delivery system achieved drug release under acidic conditions [274]. Another method involved loading one drug inside the pores and attaching another drug at the outlet of the pores [273]. Willner et al. loaded the anticancer drug mitoxantrone into boric acid modified MSNs, the pores were capped with gossypol, then the capping units unlocked the pores and the drug is released under mild acidic conditions [275]. Another challenge is that unmodified MSNs lack the active targeting and slow-release ability; therefore, various responsive delivery systems were prepared through surface modification. Various ligands such as polyethylene glycol, folic acid, polyethylenimine, hyaluronic acid, phenyl, thiol, and sulfonate have been reported to modify MSNs [276–280]. After ligand modification, MSNs can realize the function of drug release under specific environment including pH, redox, enzyme, temperature, magnetic field, and light stimulation. Liu et al. designed and fabricated a biocompatible, enzyme-responsive drug delivery system based on MSNs for targeted drug delivery in vitro and in vivo. The system demonstrated sensitivity to MMP-2 for drug delivery, leading to cell apoptosis which displayed a good curative effect on the inhibition of tumor growth with minimal toxic side effects (Figure 6) [281]. Table 10 shows various stimulus-responsive-MSNs for controlled release.



**Figure 6.** Design consideration of enzyme-responsive MSNs. Abbreviations: DOX, doxorubicin; HAS, human serum albumin; PBA, phenylboronic acid; MMP-2, matrix metalloproteinase-2.

**Table 10.** Various responsive MSNs are used to deliver cargos.

Ligands	Stimulus	Cargo	References
FA-PEG-COOH	Redox	Doxorubicin and Bcl-2	[282]
Disulfide bonds modified polyethylene glycol	Redox	Rhodamine B	[283]
Galactose-modified trimethyl chitosan-cysteine	PH	Doxorubicin and vascular endothelial growth factor siRNA	[284]
Succinylated $\epsilon$ -polylysine	PH	Prednisolone	[285]
Peptide LVPRGSGGLVPRGSGGLVPRGSK-pentanoic acid (P)	Enzyme	Anticoagulant drug	[286]
Phenylboronic acid-human serum albumin	Enzyme	Doxorubicin	[281]
Superparamagnetic magnetite nanocrystal clusters	Magnetic Field	Small interfering RNA	[287]
PEI-Iron oxide	Magnetic Field	siRNA-PLK1	[288]
PEO-b-poly (N-isopropylacrylamide) based copolymeric micelles	Temperature	Ibuprofen	[289]
Poly(N-isopropylacrylamide)-co-(1-butyl-3-vinyl imidazolium bromide) (p-NIBIm)	Temperature	Cytochrome C	[290]
1-tetradecanol	Light	Doxorubicin	[291]
Ruthenium complex	Light	Safranin O	[292]

## 6. Carbon Nanotubes

The diameter of CNTs is in the order of nano and the length is in the order of micron, giving them a high aspect ratio and large surface area [293–296]. Due to their outstanding properties such as good adsorption ability, excellent chemical stability, high tensile strength, significant electrical, and thermal conductivity, CNTs have been used in a variety of biomedical fields, especially drug delivery and cancer treatment [297–299]. There are three main ways to manufacture CNTs, including arc discharge, chemical vapor deposition (CVD), and laser ablation [300]. Toxicity is often a concern in clinic applications. Several physical and chemical factors including purity of the material, morphology, and administration route are crucial for the toxicity of CNTs [301]. It has been reported that residual transition metal catalysts such as iron, cobalt or nickel contained in the pristine CNTs can catalyze the intracellular formation of free radicals and oxidative stress leading to cytotoxic effects [302]. Therefore, the purification of CNTs by exposing them to high temperatures or bathing sonication assisted acid oxidation reduced the remains of catalytic metals used in their synthesis, increasing their biocompatibility and decreasing the toxicity levels [303]. In addition, the modification of CNTs is also an effective method to reduce their toxicity [304].

CNTs tend to agglomerate uncontrollably due to Van der Waals forces among bundles and high surface energy, which hinders their dispersion in almost all organic and inorganic solvents [298]. Meanwhile, the morphology and chemical properties of CNTs are the main factors affecting their entry into target cells [305]. Chemical functionalization can modify CNTs' electronic properties, reduce agglomeration, and improve their solubility in different

solvents [306]. The main approaches for CNTs' functionalization can be divided into two main groups including covalent functionalization and non-covalent functionalization. The covalent functionalization mainly relies on covalent bond to connect carbon nanotubes to molecules. The non-covalent modification mainly relies on Van der Waals forces and electrostatic interaction to connect carbon nanotubes to molecules [307]. Antibodies, peptides, hyaluronic acid, oligonucleotides, polyethylene glycol, and other substances are often used to modify CNTs [308,309]. Mo et al. prepared a pH-responsive drug delivery system with SWCNTs as the core and CHI and HA as ligands (Figure 7) [310]. Table 11 provides detailed cases of various functionalized CNTs delivered to different cargoes.

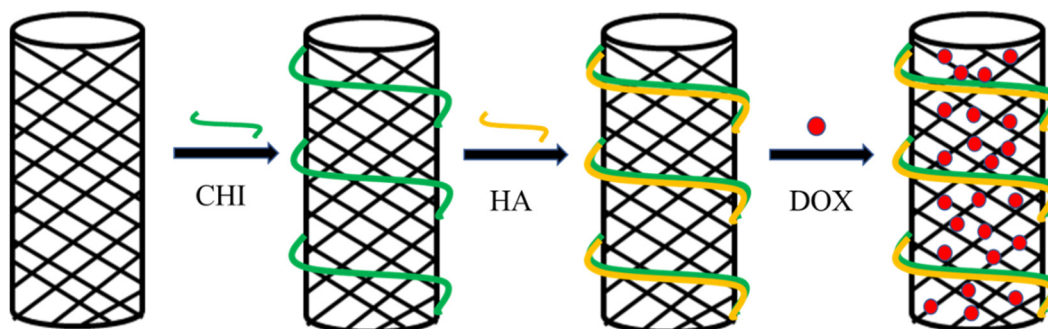


Figure 7. CHI- and HA-modified SWCNTs were used to deliver DOX. Abbreviations: CHI, chitosan; HA, hyaluronan; DOX, doxorubicin.

Table 11. Various ligand-modified SWNTs and WWNTs are used to deliver cargoes.

Type	Ligands	Cargo	Stimulus	References
SWCNTs	Polysaccharide chitosan-hyaluronic acid	Doxorubicin	pH	[310]
	Oligonucleotides	DNA/RNA	-	[311]
	Chitosan	Curcumin	pH	[312]
	Polyethylenimine with betaine	Survivin siRNA, Doxorubicin	pH	[313]
MWCNTs	Folic acid	Doxorubicin	Magnetic Field	[314]
	1-octadecanethiol-f-GNPs	Cisplatin	-	[315]
	Chitosan	Methotrexate	pH	[316]
	Distearyl phosphatidyl ethanolamine-PEG	-	Light	[317]

### 7. Conclusions and Perspectives

Viral vectors are the earliest and most widely used type of vectors. However, toxicity, immunogenicity, carcinogenicity, high cost, and other issues limit their broader application. The investigation of non-viral vectors such as liposomes, polymer, gold nanoparticles, mesoporous silica nanoparticles, and carbon nanotubes in medical research is growing rapidly. In this contribution, the application of non-viral vectors in drug delivery and gene therapy is summarized. Non-viral vectors can prevent the premature degradation of nucleic acids, proteins or drugs, prolong therapeutic effect, and reduce side effects. In addition, ligand modifications make the vectors better connect with the cargo or with the target site of action, increase the loading capacity and uptake rate, as well as improve the sustained release and targeting properties of the delivery system. Polyethylene glycol, folic acid, hyaluronic acid, peptides, oligonucleotide sequences, and other ligands have been reported to modify various materials. Further research will be necessary to introduce new ligands and develop novel smart delivery systems. Furthermore, biomedical applications have high requirements for the physicochemical properties of the vectors, thus synthesizing

and purifying vector materials with suitable particle size, uniform morphology, and good biocompatibility are essential. Meanwhile, the residual toxic effects of catalysts, solvents, and other substances in a synthesis process cannot be ignored. Consequently, non-viral vector materials are constantly improving new synthetic methods especially green synthesis methods, which is also a key direction of future research.

Although many studies have pointed out that non-viral vectors are biocompatible, most of the results focus on the short-term toxicity in vivo, and the protocols used in some toxicity tests are not standardized, posing an important safety concern in clinical application. Therefore, standardizing the toxicological tests and determining the safe exposure limits are crucial. Despite these challenges, with the development of novel materials and new synthetic strategies, non-viral vectors are expected to be widely applied to enhance the performance of drug delivery and gene therapy in the near future.

**Author Contributions:** Conceptualization, X.Z. and H.C.; formal analysis, S.R. and M.W.; investigation, S.R., M.W., C.W., Y.W. and C.S.; resources, M.W.; data curation, Y.W. and C.S.; writing—original draft preparation, S.R. and C.W.; writing—review and editing, S.R. and X.Z.; visualization, X.Z.; supervision, X.Z.; project administration, X.Z. and Z.Z.; funding acquisition, X.Z. and H.C. All authors have read and agreed to the published version of the manuscript.

**Funding:** This paper was supported by the Agricultural Science and Technology Innovation Program (CAAS-ZDRW202008), the National Key Research and Development Program (2017YFD0500900), the Basic Scientific Research Foundation of National non-Profit Scientific Institute of China (BSRF201907, BSRF202006).

**Institutional Review Board Statement:** Not applicable.

**Informed Consent Statement:** Not applicable.

**Data Availability Statement:** The data presented in this study are available on request from the corresponding author.

**Conflicts of Interest:** The authors declare no conflict of interest.

## References

- Choi, J.W.; Lee, J.S.; Kim, S.W.; Yun, C.O. Evolution of oncolytic adenovirus for cancer treatment. *Adv. Drug Deliv. Rev.* **2012**, *64*, 720–729. [\[CrossRef\]](#)
- Gao, X.; Tao, Y.; Lamas, V.; Huang, M.; Yeh, W.H.; Pan, B.; Hu, Y.J.; Hu, J.H.; Thompson, D.B.; Shu, Y.; et al. Treatment of autosomal dominant hearing loss by in vivo delivery of genome editing agents. *Nature* **2018**, *553*, 217–221. [\[CrossRef\]](#) [\[PubMed\]](#)
- Rossidis, A.C.; Stratigis, J.D.; Chadwick, A.C.; Hartman, H.A.; Ahn, N.J.; Li, H.; Singh, K.; Coons, B.E.; Li, L.; Lv, W.; et al. In utero CRISPR-mediated therapeutic editing of metabolic genes. *Nat. Med.* **2018**, *24*, 1513–1518. [\[CrossRef\]](#)
- Ryu, S.M.; Koo, T.; Kim, K.; Lim, K.; Baek, G.; Kim, S.T.; Kim, H.S.; Kim, D.E.; Lee, H.; Chung, E.; et al. Adenine base editing in mouse embryos and an adult mouse model of Duchenne muscular dystrophy. *Nat. Biotechnol.* **2018**, *36*, 536–539. [\[CrossRef\]](#)
- Erdoğan, N.; Akkin, S.; Bilensoy, E. Nanocapsules for Drug Delivery: An Updated Review of the Last Decade. *Recent Pat. Drug Deliv. Formul.* **2018**, *12*, 252–266. [\[CrossRef\]](#)
- Unsoy, G.; Gunduz, U. Smart Drug Delivery Systems in Cancer Therapy. *Curr. Drug Targets* **2018**, *19*, 202–212. [\[CrossRef\]](#)
- Bono, N.; Ponti, F.; Mantovani, D.; Candiani, G. Non-Viral in Vitro Gene Delivery: It is Now Time to Set the Bar! *Pharmaceutics* **2020**, *12*, 183. [\[CrossRef\]](#)
- Durymanov, M.; Reineke, J. Non-viral Delivery of Nucleic Acids: Insight into Mechanisms of Overcoming Intracellular Barriers. *Front. Pharmacol.* **2018**, *9*, 971. [\[CrossRef\]](#)
- Schoch, K.M.; Miller, T.M. Antisense oligonucleotides: Translation from mouse models to human neurodegenerative diseases. *Neuron* **2017**, *94*, 1056–1070. [\[CrossRef\]](#) [\[PubMed\]](#)
- Zhao, X.; Ye, Y.; Ge, S.; Sun, P.; Yu, P. Cellular and Molecular Targeted Drug Delivery in Central Nervous System Cancers: Advances in Targeting Strategies. *Curr. Top. Med. Chem.* **2020**, *20*, 2762–2776. [\[CrossRef\]](#)
- Durymanov, M.O.; Rosenkranz, A.A.; Sobolev, A.S. Current Approaches for Improving Intratumoral Accumulation and Distribution of Nanomedicines. *Theranostics* **2015**, *5*, 1007–1020. [\[CrossRef\]](#)
- Sun, B.; Hyun, H.; Li, L.T.; Wang, A.Z. Harnessing nanomedicine to overcome the immunosuppressive tumor microenvironment. *Acta Pharmacol. Sin.* **2020**, *41*, 970–985. [\[CrossRef\]](#)
- Meng, Q.Y.; Hu, H.; Zhou, L.P.; Zhang, Y.X.; Yu, B.; Shen, Y.Q.; Cong, H.L. Logical design and application of prodrug platforms. *Polym. Chem.* **2019**, *10*, 306–324. [\[CrossRef\]](#)

14. He, B.; Sui, X.; Yu, B.; Wang, S.; Shen, Y.; Cong, H. Recent advances in drug delivery systems for enhancing drug penetration into tumors. *Drug Deliv.* **2020**, *27*, 1474–1490. [[CrossRef](#)] [[PubMed](#)]
15. Pezzoli, D.; Chiesa, R.; De Nardo, L.; Candiani, G. We still have a long way to go to effectively deliver genes! *J. Appl. Biomater. Funct. Mater.* **2012**, *10*, 82–91. [[CrossRef](#)] [[PubMed](#)]
16. Pezzoli, D.; Candiani, G. Non-viral gene delivery strategies for gene therapy: A “ménage à trois” among nucleic acids, materials, and the biological environment: Stimuli-responsive gene delivery vectors. *J. Nanopart. Res.* **2013**, *15*, 1523. [[CrossRef](#)]
17. Bennett, C.F.; Swayze, E.E. RNA targeting therapeutics: Molecular mechanisms of antisense oligonucleotides as a therapeutic platform. *Annu. Rev. Pharmacol. Toxicol.* **2010**, *50*, 259–293. [[CrossRef](#)]
18. Cavazzana-Calvo, M.; Thrasher, A.; Mavilio, F. The future of gene therapy. *Nature* **2004**, *427*, 779–781. [[CrossRef](#)]
19. Ashfaq, U.A.; Riaz, M.; Yasmeen, E.; Yousaf, M.Z. Recent Advances in Nanoparticle-Based Targeted Drug-Delivery Systems Against Cancer and Role of Tumor Microenvironment. *Crit. Rev. Ther. Drug Carr. Syst.* **2017**, *34*, 317–353. [[CrossRef](#)]
20. Liyanage, P.Y.; Hettiarachchi, S.D.; Zhou, Y.; Ouhtit, A.; Seven, E.S.; Oztan, C.Y.; Celik, E.; Leblanc, R.M. Nanoparticle-mediated targeted drug delivery for breast cancer treatment. *Biochim. Biophys. Acta Rev. Cancer* **2019**, *1871*, 419–433. [[CrossRef](#)]
21. De Jong, W.H.; Borm, P.J. Drug delivery and nanoparticles: Applications and hazards. *Int. J. Nanomed.* **2008**, *3*, 133–149. [[CrossRef](#)]
22. Yu, W.; Mookherjee, S.; Chaitankar, V.; Hiriyanna, S.; Kim, J.W.; Brooks, M.; Ataeijannati, Y.; Sun, X.; Dong, L.; Li, T.; et al. Nrl knockdown by AAV-delivered CRISPR/Cas9 prevents retinal degeneration in mice. *Nat. Commun.* **2017**, *8*, 14716. [[CrossRef](#)]
23. Shalem, O.; Sanjana, N.E.; Hartenstein, E.; Shi, X.; Scott, D.A.; Mikkelsen, T.; Heckl, D.; Ebert, B.L.; Root, D.E.; Doench, J.G.; et al. Genome-scale CRISPR-Cas9 knockout screening in human cells. *Science* **2014**, *343*, 84–87. [[CrossRef](#)]
24. Humphreys, I.R.; Sebastian, S. Novel viral vectors in infectious diseases. *Immunology* **2018**, *153*, 1–9. [[CrossRef](#)] [[PubMed](#)]
25. Finer, M.; Glorioso, J. A brief account of viral vectors and their promise for gene therapy. *Gene Ther.* **2017**, *24*, 1–2. [[CrossRef](#)] [[PubMed](#)]
26. Lehrman, S. Virus treatment questioned after gene therapy death. *Nature* **1999**, *401*, 517–518. [[CrossRef](#)] [[PubMed](#)]
27. Thomas, C.E.; Ehrhardt, A.; Kay, M.A. Progress and problems with the use of viral vectors for gene therapy. *Nat. Rev. Genet.* **2003**, *4*, 346–358. [[CrossRef](#)]
28. Ahi, Y.S.; Bangari, D.S.; Mittal, S.K. Adenoviral vector immunity: Its implications and circumvention strategies. *Curr. Gene Ther.* **2011**, *11*, 307–320. [[CrossRef](#)]
29. Li, L.; Hu, S.; Chen, X. Non-viral delivery systems for CRISPR/Cas9-based genome editing: Challenges and opportunities. *Biomaterials* **2018**, *171*, 207–218. [[CrossRef](#)]
30. Zhang, Y.; Ren, T.; Gou, J.; Zhang, L.; Tao, X.; Tian, B.; Tian, P.; Yu, D.; Song, J.; Liu, X.; et al. Strategies for improving the payload of small molecular drugs in polymeric micelles. *J. Control. Release* **2017**, *261*, 352–366. [[CrossRef](#)]
31. Sung, Y.K.; Kim, S.W. Recent advances in the development of gene delivery systems. *Biomater. Res.* **2019**, *23*, 8. [[CrossRef](#)] [[PubMed](#)]
32. Li, L.; He, Z.Y.; Wei, X.W.; Gao, G.P.; Wei, Y.Q. Challenges in CRISPR/CAS9 Delivery: Potential Roles of Nonviral Vectors. *Hum. Gene Ther.* **2015**, *26*, 452–462. [[CrossRef](#)] [[PubMed](#)]
33. Wang, M.; Cheng, Y. The effect of fluorination on the transfection efficacy of surface-engineered dendrimers. *Biomaterials* **2014**, *35*, 6603–6613. [[CrossRef](#)] [[PubMed](#)]
34. Zinchenko, A. DNA conformational behavior and compaction in biomimetic systems, toward better understanding of DNA packaging in cell. *Adv. Colloid Interface Sci.* **2016**, *232*, 70–79. [[CrossRef](#)]
35. Jeong, G.W.; Nah, J.W. Evaluation of disulfide bond-conjugated LMWSC-g-bPEI as non-viral vector for low cytotoxicity and efficient gene delivery. *Carbohydr. Polym.* **2017**, *178*, 322–330. [[CrossRef](#)]
36. Vijayanathan, V.; Agostinelli, E.; Thomas, T.; Thomas, T.J. Innovative approaches to the use of polyamines for DNA nanoparticle preparation for gene therapy. *Amino Acids* **2014**, *46*, 499–509. [[CrossRef](#)]
37. Takahashi, Y.; Chen, Q.; Rajala, R.V.S.; Ma, J.X. MicroRNA-184 modulates canonical Wnt signaling through the regulation of frizzled-7 expression in the retina with ischemia-induced neovascularization. *FEBS Lett.* **2015**, *589*, 1143–1149. [[CrossRef](#)]
38. Sahay, G.; Querbes, W.; Alabi, C.; Eltoukhy, A.; Sarkar, S.; Zurenko, C.; Karagiannis, E.; Love, K.; Chen, D.; Zoncu, R.; et al. Efficiency of siRNA delivery by lipid nanoparticles is limited by endocytic recycling. *Nat. Biotechnol.* **2013**, *31*, 653–658. [[CrossRef](#)]
39. Zhi, D.; Bai, Y.; Yang, J.; Cui, S.; Zhao, Y.; Chen, H.; Zhang, S. A review on cationic lipids with different linkers for gene delivery. *Adv. Colloid Interface Sci.* **2018**, *253*, 117–140. [[CrossRef](#)]
40. Bazylińska, U. Rationally designed double emulsion process for co-encapsulation of hybrid cargo in stealth nanocarriers. *Colloids Surf. A Physicochem. Eng. Asp.* **2017**, *532*, 476–482. [[CrossRef](#)]
41. Hong, S.J.; Ahn, M.H.; Sangshetti, J.; Choung, P.H.; Arote, R.B. Sugar-based gene delivery systems, Current knowledge and new perspectives. *Carbohydr. Polym.* **2018**, *181*, 1180–1193. [[CrossRef](#)]
42. Wang, P.; Lin, L.; Guo, Z.; Chen, J.; Tian, H.; Chen, X.; Yang, H. Highly Fluorescent Gene Carrier Based on Ag-Au Alloy Nanoclusters. *Macromol. Biosci.* **2016**, *16*, 160–167. [[CrossRef](#)] [[PubMed](#)]
43. Chung Ang University Industry Academic Cooperation Foundation. *Composition for Gene Carrier Using a Triblock Co-Polyelectrolyte with Polyethylene Imine-Polylactic Acid-Polyethylene Glycol:KR20170025927[P]*; Chung Ang University Industry Academic Cooperation Foundation: Seoul, Korea, 5 September 2018.
44. Suzhou High-Tech Bioscience Co., Ltd. *Methoxypolyethylene Glycol-Polylactic Acid Block Copolymer and Preparation Method Thereof:US201414897504[P]*; Suzhou High-Tech Bioscience Co., Ltd.: Suzhou, China, 20 July 2017.

45. Dongguk University Industry-Academic Cooperation Foundation. *Amphiphilic Chitosan Derivative and Drug Carrier Containing the Same*:KR20160016553[P]; Dongguk University Industry-Academic Cooperation Foundation: Seoul, Korea, 22 August 2017.
46. Chung-Ang University Industry Academic Cooperation Foundation. *Method for Preparing Microspheres for Emboli, and Method for Preparing Microspheres to Which Drug-Containing Carrier Is Bound*:EP20130833842[P]; Chung-Ang University Industry Academic Cooperation Foundation: Seoul, Korea, 26 December 2018.
47. Haskoningdhv Nederland B.V. *Alginate Extraction Method*:US201716085880[P]; Haskoningdhv Nederland B.V.: Maastricht, The Netherlands, 28 March 2019.
48. Université de Strasbourg, Centre National de la Recherche Scientifique, ihu Strasbourg—Institut Hospitalo-Universitaire de Strasbourg. *Injectable Hybrid Alginate Hydrogels and Uses Thereof*:WO2018EP75097[P]; Institut Hospitalo-Universitaire de Strasbourg: Strasbourg, France, 21 March 2019.
49. Jiangsu Keygen Biotech Corp., Ltd.; Nanjing Core Tech Co., Ltd. *Decory Nucleic Acid Cationic Liposome Carrier and Preparation Method Thereof*:US201515572845[P]; Jiangsu Keygen Biotech Corp., Ltd.: Nanjing, China; Nanjing Core Tech Co., Ltd.: Nanjing, China, 17 May 2018.
50. Shanghai Pulmonary Hospital. *Human Lung Tissues—Active Targeting Immune Nanoliposome of Methylprednisolone and a Method for Producing the Same*:US201515026219[P]; Shanghai Pulmonary Hospital: Shanghai, China, 7 May 2019.
51. Biomics Biotechnologies CO., Ltd. *Liposome Preparation, Preparation Method and Application Thereof*:AU20130380825[P]; Biomics Biotechnologies CO., Ltd.: Nantong, China, 20 July 2017.
52. National Taiwan University of Science and Technology. *Biocompatible Confeito-Like Gold Nanoparticles, Method for Making the Same, and Their Biomedical Applications*:US201113333868[P]; National Taiwan University of Science and Technology: Taipei, Taiwan, 20 October 2015.
53. King Fahd University of Petroleum and Minerals. *Method for the Size Controlled Preparation of These Monodisperse Carboxylate Functionalized Gold Nanoparticles*:US201816222748[P]; King Fahd University of Petroleum and Minerals: Dhahran, Saudi Arabia, 18 April 2019.
54. Jeffrey, B.C.; Durfee, P.N.; Townson, J. *Mesoporous Silica Nanoparticles and Supported Lipid Bi-Layer Nanoparticles for Biomedical Applications*: US201615757269[P]; University of New Mexico: Albuquerque, NM, USA, 6 December 2018.
55. The Regents of The University of California. *Mesoporous Silica Nanoparticles with Lipid Bilayer Coating for Cargo Delivery*:US201715798287[P]; The University of California: Oakland, CA, USA, 4 December 2018.
56. Molecular Rebar Design, LLC. *Payload Molecule Delivery Using Functionalized Discrete Carbon Nanotubes*:AU20150218735[P]; Molecular Rebar Design, LLC.: Austin, TX, USA, 22 September 2016.
57. Smith, B.R.; Ghosn, E. *The Board of Trustees of The Leland Stanford Junior University. Carbon Nanotubes for Imaging and Drug Delivery*:US201314020794[P]; The Leland Stanford Junior University: Stanford, CA, USA, 20 March 2014.
58. Abed, O.S.A.; Chaw, C.; Williams, L.; Elkordy, A.A. Lysozyme and DNase I loaded poly (D, L lactide-co-caprolactone) nanocapsules as an oral delivery system. *Sci. Rep.* **2018**, *8*, 13158. [[CrossRef](#)]
59. Boca, S.; Gulei, D.; Zimta, A.A.; Onaciu, A.; Magdo, L.; Tigu, A.B.; Ionescu, C.; Irimie, A.; Buiga, R.; Berindan-Neagoe, I. Nanoscale delivery systems for microRNAs in cancer therapy. *Cell. Mol. Life Sci.* **2020**, *77*, 1059–1086. [[CrossRef](#)] [[PubMed](#)]
60. Bolhassani, A.; Javan zad, S.; Saleh, T.; Hashemi, M.; Aghasadeghi, M.R.; Sadat, S.M. Polymeric nanoparticles: Potent vectors for vaccine delivery targeting cancer and infectious diseases. *Hum. Vaccines Immunother.* **2014**, *10*, 321–332. [[CrossRef](#)]
61. Yang, J.; Zhang, Q.; Chang, H.; Cheng, Y. Surface-engineered dendrimers in gene delivery. *Chem. Rev.* **2015**, *115*, 5274–5300. [[CrossRef](#)]
62. Lostalé-Seijo, I.; Montenegro, J. Synthetic materials at the forefront of gene delivery. *Nat. Rev. Chem.* **2018**, *2*, 258–277. [[CrossRef](#)]
63. Teixeira, H.F.; Bruxel, F.; Fraga, M.; Schuh, R.S.; Zorzi, G.K.; Matte, U.; Fattal, E. Cationic nanoemulsions as nucleic acids delivery systems. *Int. J. Pharm.* **2017**, *534*, 356–367. [[CrossRef](#)] [[PubMed](#)]
64. Ding, X.; Wang, W.; Wang, Y.; Bao, X.; Wang, Y.; Wang, C.; Chen, J.; Zhang, F.; Zhou, J. Versatile reticular polyethylenimine derivative-mediated targeted drug and gene codelivery for tumor therapy. *Mol. Pharm.* **2014**, *11*, 3307–3321. [[CrossRef](#)]
65. Casettari, L.; Vllasaliu, D.; Lam, J.K.; Soliman, M.; Illum, L. Biomedical applications of amino acid-modified chitosans: A review. *Biomaterials* **2012**, *33*, 7565–7583. [[CrossRef](#)]
66. Tian, W.D.; Ma, Y.Q. Theoretical and computational studies of dendrimers as delivery vectors. *Chem. Soc. Rev.* **2013**, *42*, 705–727. [[CrossRef](#)]
67. Ghasemi, R.; Abdollahi, M.; Zadeh, E.E.; Khodabakhshi, K.; Badeli, A.; Bagheri, H.; Hosseinkhani, S. mPEG-PLA and PLA-PEG-PLA nanoparticles as new carriers for delivery of recombinant human Growth Hormone (rhGH). *Sci. Rep.* **2018**, *8*, 9854. [[CrossRef](#)] [[PubMed](#)]
68. Karlsson, J.; Rhodes, K.R.; Green, J.J.; Tzeng, S.Y. Poly(beta-amino ester)s as gene delivery vehicles: Challenges and opportunities. *Expert Opin. Drug Deliv.* **2020**, *17*, 1395–1410. [[CrossRef](#)] [[PubMed](#)]
69. Sherje, A.P.; Jadhav, M.; Dravyakar, B.R.; Kadam, D. Dendrimers: A versatile nanocarrier for drug delivery and targeting. *Int. J. Pharm.* **2018**, *548*, 707–720. [[CrossRef](#)] [[PubMed](#)]
70. Sung, Y.K.; Kim, S.W. Recent advances in polymeric drug delivery systems. *Biomater. Res.* **2020**, *24*, 12. [[CrossRef](#)]
71. Amreddy, N.; Babu, A.; Muralidharan, R.; Munshi, A.; Ramesh, R. Polymeric Nanoparticle-Mediated Gene Delivery for Lung Cancer Treatment. *Top. Curr. Chem.* **2017**, *375*, 35. [[CrossRef](#)]

72. Sharma, A.K.; Gothwal, A.; Kesharwani, P.; Alsaab, H.; Iyer, A.K.; Gupta, U. Dendrimer nanoarchitectures for cancer diagnosis and anticancer drug delivery. *Drug Discov. Today* **2017**, *22*, 314–326. [[CrossRef](#)] [[PubMed](#)]
73. Wang, X.; Shao, N.; Zhang, Q.; Cheng, Y. Mitochondrial targeting dendrimer allows efficient and safe gene delivery. *J. Mater. Chem. B* **2014**, *2*, 2546–2553. [[CrossRef](#)]
74. Mendes, L.P.; Pan, J.; Torchilin, V.P. Dendrimers as Nanocarriers for Nucleic Acid and Drug Delivery in Cancer Therapy. *Molecules* **2017**, *22*, 1401. [[CrossRef](#)]
75. Guan, L.; Huang, S.; Chen, Z.; Li, Y.; Liu, K.; Liu, Y.; Du, L. Low Cytotoxicity Fluorescent PAMAM Dendrimer as Gene Carriers for Monitoring the Delivery of siRNA. *J. Nanopart. Res.* **2015**, *17*, 385. [[CrossRef](#)]
76. Mastorakos, P.; Kambhampati, S.P.; Mishra, M.K.; Wu, T.; Song, E.; Hanes, J.; Kannan, R.M. Hydroxyl PAMAM dendrimer-based gene vectors for transgene delivery to human retinal pigment epithelial cells. *Nanoscale* **2015**, *7*, 3845–3856. [[CrossRef](#)]
77. Liaw, K.; Reddy, R.; Sharma, A.; Li, J.; Chang, M.; Sharma, R.; Salazar, S.; Kannan, S.; Kannan, R.M. Targeted systemic dendrimer delivery of CSF-1R inhibitor to tumor-associated macrophages improves outcomes in orthotopic glioblastoma. *Bioeng. Transl. Med.* **2020**, *6*, e10205.
78. Qadir, A.; Gao, Y.; Suryaji, P.; Tian, Y.; Lin, X.; Dang, K.; Jiang, S.; Li, Y.; Miao, Z.; Qian, A. Non-Viral Delivery System and Targeted Bone Disease Therapy. *Int. J. Mol. Sci.* **2019**, *20*, 565. [[CrossRef](#)]
79. Liu, S.; Huang, W.; Jin, M.J.; Fan, B.; Xia, G.M.; Gao, Z.G. Inhibition of murine breast cancer growth and metastasis by survivin-targeted siRNA using disulfide cross-linked linear PEI. *Eur. J. Pharm. Sci.* **2016**, *82*, 171–182. [[CrossRef](#)]
80. Thomas, T.J.; Tajmir-Riahi, H.A.; Pillai, C.K.S. Biodegradable Polymers for Gene Delivery. *Molecules* **2019**, *24*, 3744. [[CrossRef](#)]
81. Boussif, O.; Lezoualc'h, F.; Zanta, M.A.; Mergny, M.D.; Scherman, D.; Demeneix, B.; Behr, J.P. A versatile vector for gene and oligonucleotide transfer into cells in culture and in vivo: Polyethylenimine. *Proc. Natl. Acad. Sci. USA* **1995**, *92*, 7297–7301. [[CrossRef](#)]
82. Hall, A.; Lächelt, U.; Bartek, J.; Wagner, E.; Moghimi, S.M. Polyplex Evolution: Understanding Biology, Optimizing Performance. *Mol. Ther.* **2017**, *25*, 1476–1490. [[CrossRef](#)]
83. Zhou, Y.; Yu, F.; Zhang, F.; Chen, G.; Wang, K.; Sun, M.; Li, J.; Oupický, D. Cyclam-Modified PEI for Combined VEGF siRNA Silencing and CXCR4 Inhibition To Treat Metastatic Breast Cancer. *Biomacromolecules* **2018**, *19*, 392–401. [[CrossRef](#)] [[PubMed](#)]
84. Huang, Q.; Li, S.; Ding, Y.F.; Yin, H.; Wang, L.H.; Wang, R. Macrocyclic-wrapped polyethylenimine for gene delivery with reduced cytotoxicity. *Biomater. Sci.* **2018**, *6*, 1031–1039. [[CrossRef](#)] [[PubMed](#)]
85. Jiang, H.L.; Islam, M.A.; Xing, L.; Firdous, J.; Cao, W.; He, Y.J.; Zhu, Y.; Cho, K.H.; Li, H.S.; Cho, C.S. Degradable Polyethylenimine-Based Gene Carriers for Cancer Therapy. *Top. Curr. Chem.* **2017**, *375*, 34. [[CrossRef](#)] [[PubMed](#)]
86. Zakeri, A.; Kouhbanani, M.A.J.; Beheshtkhou, N.; Beigi, V.; Mousavi, S.M.; Hashemi, S.A.R.; Karimi Zade, A.; Amani, A.M.; Savardashtaki, A.; Mirzaei, E.; et al. Polyethylenimine-based nanocarriers in co-delivery of drug and gene: A developing horizon. *Nano Rev. Exp.* **2018**, *9*, 1488497. [[CrossRef](#)] [[PubMed](#)]
87. Patnaik, S.; Gupta, K.C. Novel polyethylenimine-derived nanoparticles for in vivo gene delivery. *Expert Opin. Drug Deliv.* **2013**, *10*, 215–228. [[CrossRef](#)]
88. Mattheolabakis, G.; Ling, D.; Ahmad, G.; Amiji, M. Enhanced Anti-Tumor Efficacy of Lipid-Modified Platinum Derivatives in Combination with Survivin Silencing siRNA in Resistant Non-Small Cell Lung Cancer. *Pharm. Res.* **2016**, *33*, 2943–2953. [[CrossRef](#)] [[PubMed](#)]
89. Liu, S.; Zhou, D.; Yang, J.; Zhou, H.; Chen, J.; Guo, T. Bioreducible Zinc(II)-Coordinative Polyethylenimine with Low Molecular Weight for Robust Gene Delivery of Primary and Stem Cells. *J. Am. Chem. Soc.* **2017**, *139*, 5102–5109. [[CrossRef](#)] [[PubMed](#)]
90. Taranejo, S.; Chandrasekaran, R.; Cheng, W.; Hourigan, K. Bioreducible PEI-functionalized glycol chitosan: A novel gene vector with reduced cytotoxicity and improved transfection efficiency. *Carbohydr. Polym.* **2016**, *153*, 160–168. [[CrossRef](#)] [[PubMed](#)]
91. Davoodi, P.; Srinivasan, M.P.; Wang, C.H. Synthesis of intracellular reduction-sensitive amphiphilic polyethylenimine and poly( $\epsilon$ -caprolactone) graft copolymer for on-demand release of doxorubicin and p53 plasmid DNA. *Acta Biomater.* **2016**, *39*, 79–93. [[CrossRef](#)] [[PubMed](#)]
92. Zhang, J.H.; Yang, H.Z.; Zhang, J.; Liu, Y.H.; He, X.; Xiao, Y.P.; Yu, X.Q. Biodegradable Gene Carriers Containing Rigid Aromatic Linkage with Enhanced DNA Binding and Cell Uptake. *Polymers* **2018**, *10*, 1080. [[CrossRef](#)]
93. Motiei, M.; Kashanian, S.; Lucia, L.A.; Khazaei, M. Intrinsic parameters for the synthesis and tuned properties of amphiphilic chitosan drug delivery nanocarriers. *J. Control. Release* **2017**, *260*, 213–225. [[CrossRef](#)] [[PubMed](#)]
94. Nicolle, L.; Casper, J.; Willmann, M.; Journot, C.M.A.; Detampel, P.; Einfalt, T.; Grisch-Chan, H.M.; Thöny, B.; Gerber-Lemaire, S.; Huwyler, J. Development of Covalent Chitosan-Polyethylenimine Derivatives as Gene Delivery Vehicle: Synthesis, Characterization, and Evaluation. *Int. J. Mol. Sci.* **2021**, *8*, 3828. [[CrossRef](#)]
95. Woraphatphadung, T.; Sajomsang, W.; Rojanarata, T.; Ngawhirunpat, T.; Tonglairoum, P.; Opanasopit, P. Development of Chitosan-Based pH-Sensitive Polymeric Micelles Containing Curcumin for Colon-Targeted Drug Delivery. *AAPS Pharm. Sci. Technol.* **2018**, *19*, 991–1000. [[CrossRef](#)]
96. Meng, Q.; Sun, Y.; Cong, H.; Hu, H.; Xu, F.J. An overview of chitosan and its application in infectious diseases. *Drug Deliv. Transl. Res.* **2021**, *11*, 1340–1351. [[CrossRef](#)] [[PubMed](#)]
97. Bravo-Anaya, L.M.; Soltero, J.F.; Rinaudo, M. DNA/chitosan electrostatic complex. *Int. J. Biol. Macromol.* **2016**, *88*, 345–353. [[CrossRef](#)] [[PubMed](#)]



98. Amaduzzi, F.; Bomboi, F.; Bonincontro, A.; Bordi, F.; Casciardi, S.; Chronopoulou, L.; Diociaiuti, M.; Mura, F.; Palocci, C.; Sennato, S. Chitosan-DNA complexes: Charge inversion and DNA condensation. *Colloids Surf. B Biointerfaces* **2014**, *114*, 1–10. [[CrossRef](#)] [[PubMed](#)]
99. Oliveira, A.V.; Marcelo, A.; da Costa, A.M.; Silva, G.A. Evaluation of cystamine-modified hyaluronic acid/chitosan polyplex as retinal gene vector. *Mater. Sci. Eng. C Mater. Biol. Appl.* **2016**, *58*, 264–272. [[CrossRef](#)] [[PubMed](#)]
100. Oliveira, A.V.; Silva, G.A.; Chung, D.C. Enhancement of chitosan-mediated gene delivery through combination with phiC31 integrase. *Acta Biomater.* **2015**, *17*, 89–97. [[CrossRef](#)] [[PubMed](#)]
101. Kamra, M.; Moitra, P.; Ponnalagu, D.; Karande, A.A.; Bhattacharya, S. New Water-Soluble Oxyamino Chitosans as Biocompatible Vectors for Efficacious Anticancer Therapy via Co-Delivery of Gene and Drug. *ACS Appl. Mater. Interfaces* **2019**, *11*, 37442–37460. [[CrossRef](#)]
102. Chen, S.; Deng, J.; Zhang, L.M. Cationic nanoparticles self-assembled from amphiphilic chitosan derivatives containing poly(amidoamine) dendrons and deoxycholic acid as a vector for co-delivery of doxorubicin and gene. *Carbohydr. Polym.* **2021**, *258*, 117706. [[CrossRef](#)]
103. Lee, Y.H.; Park, H.I.; Chang, W.S.; Choi, J.S. Triphenylphosphonium-conjugated glycol chitosan microspheres for mitochondria-targeted drug delivery. *Int. J. Biol. Macromol.* **2021**, *167*, 35–45. [[CrossRef](#)]
104. Babii, O.; Wang, Z.; Liu, G.; Martinez, E.C.; van Drunen, L.; van den Hurk, S.; Chen, L. Low molecular weight chitosan nanoparticles for CpG oligodeoxynucleotides delivery: Impact of molecular weight, degree of deacetylation, and mannosylation on intracellular uptake and cytokine induction. *Int. J. Biol. Macromol.* **2020**, *159*, 46–56. [[CrossRef](#)]
105. Masjedi, A.; Ahmadi, A.; Atyabi, F.; Farhadi, S.; Irandoust, M.; Khazaei-Poul, Y.; Chaleshtari, M.G.; Fathabad, M.E.; Baghaei, M.; Haghnavaz, N.; et al. Silencing of IL-6 and STAT3 by siRNA loaded hyaluronate-N,N,N-trimethyl chitosan nanoparticles potently reduces cancer cell progression. *Int. J. Biol. Macromol.* **2020**, *149*, 487–500. [[CrossRef](#)]
106. Singhvi, M.S.; Zinjarde, S.S.; Gokhale, D.V. Polylactic acid: Synthesis and biomedical applications. *J. Appl. Microbiol.* **2019**, *127*, 1612–1626. [[CrossRef](#)] [[PubMed](#)]
107. Zhou, M.; Lai, W.; Li, G.; Wang, F.; Liu, W.; Liao, J.; Yang, H.; Liu, Y.; Zhang, Q.; Tang, Q.; et al. Platelet Membrane-Coated and VAR2CSA Malaria Protein-Functionalized Nanoparticles for Targeted Treatment of Primary and Metastatic Cancer. *ACS Appl. Mater. Interfaces* **2021**, *13*, 25635–25648. [[CrossRef](#)] [[PubMed](#)]
108. Tyler, B.; Gullotti, D.; Mangraviti, A.; Utsuki, T.; Brem, H. Polylactic acid (PLA) controlled delivery carriers for biomedical applications. *Adv. Drug Deliv. Rev.* **2016**, *107*, 163–175. [[CrossRef](#)] [[PubMed](#)]
109. Li, G.; Zhao, M.; Xu, F.; Yang, B.; Li, X.; Meng, X.; Teng, L.; Sun, F.; Li, Y. Synthesis and Biological Application of Polylactic Acid. *Molecules* **2020**, *25*, 5023. [[CrossRef](#)]
110. Ali, M.; Walboomers, X.F.; Jansen, J.A.; Yang, F. Influence of formulation parameters on encapsulation of doxycycline in PLGA microspheres prepared by double emulsion technique for the treatment of periodontitis. *J. Drug Deliv. Sci. Technol.* **2019**, *52*, 263–271. [[CrossRef](#)]
111. Kamel, R.; Abbas, H.; Shaffie, N.M. Development and evaluation of PLA-coated co-micellar nanosystem of Resveratrol for the intra-articular treatment of arthritis. *Int. J. Pharm.* **2019**, *569*, 118560. [[CrossRef](#)]
112. Lai, X.; Geng, X.; Li, M.; Tang, M.; Liu, Q.; Yang, M.; Shen, L.; Zhu, Y.; Wang, S. Glutathione-responsive PLGA nanocomplex for dual delivery of doxorubicin and curcumin to overcome tumor multidrug resistance. *Nanomedicine* **2021**, *16*, 1411–1427. [[CrossRef](#)]
113. Zhou, J.; Zhai, Y.; Xu, J.; Zhou, T.; Cen, L. Microfluidic preparation of PLGA composite microspheres with mesoporous silica nanoparticles for finely manipulated drug release. *Int. J. Pharm.* **2021**, *593*, 120173. [[CrossRef](#)] [[PubMed](#)]
114. Zabihi, F.; Graff, P.; Schumacher, F.; Kleuser, B.; Hedtrich, S.; Haag, R. Synthesis of poly(lactide-co-glycerol) as a biodegradable and biocompatible polymer with high loading capacity for dermal drug delivery. *Nanoscale* **2018**, *10*, 16848–16856. [[CrossRef](#)] [[PubMed](#)]
115. Ren, B.; Lu, J.; Li, M.; Zou, X.; Liu, Y.; Wang, C.; Wang, L. Anti-inflammatory effect of IL-1ra-loaded dextran/PLGA microspheres on Porphyromonas gingivalis lipopolysaccharide-stimulated macrophages in vitro and in vivo in a rat model of periodontitis. *Biomed. Pharmacother.* **2021**, *134*, 111171. [[CrossRef](#)]
116. Bazylińska, U.; Kulbacka, J.; Chodaczek, G. Nanoemulsion Structural Design in Co-Encapsulation of Hybrid Multifunctional Agents: Influence of the Smart PLGA Polymers on the Nanosystem-Enhanced Delivery and Electro-Photodynamic Treatment. *Pharmaceutics* **2019**, *11*, 405. [[CrossRef](#)]
117. Gupta, S.S.; Mishra, V.; Mukherjee, M.D.; Saini, P.; Ranjan, K.R. Amino acid derived biopolymers: Recent advances and biomedical applications. *Int. J. Biol. Macromol.* **2021**, *188*, 542–567. [[CrossRef](#)]
118. Feng, J.H.; He, F.Y.; Yang, Z.Z.; Yao, J.S. Differential study of the biological degradation of polyamide-imides based on the amino acids. *Polym. Degrad. Stab.* **2016**, *129*, 231–238. [[CrossRef](#)]
119. Yamanouchi, D.; Wu, J.; Lazar, A.N.; Kent, K.C.; Chu, C.C.; Liu, B. Biodegradable arginine-based poly(ester-amide)s as non-viral gene delivery reagents. *Biomaterials* **2008**, *29*, 3269–3277. [[CrossRef](#)] [[PubMed](#)]
120. Pounder, R.J.; Dove, A.P. Towards poly(ester) nanoparticles: Recent advances in the synthesis of functional poly(ester)s by ring-opening polymerization. *Polym. Chem.* **2010**, *1*, 260–271. [[CrossRef](#)]
121. Karimi, P.; Rizkalla, A.S.; Mequanint, K. Versatile Biodegradable Poly(ester amide)s Derived from  $\alpha$ -Amino Acids for Vascular Tissue Engineering. *Materials* **2010**, *3*, 2346. [[CrossRef](#)]

122. Patrick, A.J.M.; Paul, P.K.C.; Khoshdel, E.; Wilson, P.; Kempe, K.; Haddleton, D.M. High Tg poly(ester amide)s by melt polycondensation of monomers from renewable resources; citric acid, D-glucono- $\delta$ -lactone and amino acids: A DSC study. *Eur. Polym. J.* **2017**, *94*, 11–19.
123. Nitta, S.; Komatsu, A.; Ishii, T.; Iwamoto, H.; Numata, K. Synthesis of peptides with narrow molecular weight distributions via exopeptidase-catalyzed aminolysis of hydrophobic amino-acid alkyl esters. *Polym. J.* **2016**, *48*, 955–961. [[CrossRef](#)]
124. Zhang, S.; Guo, N.; Wan, G.; Zhang, T.; Li, C.; Wang, Y.; Wang, Y.; Liu, Y. pH and redox dual-responsive nanoparticles based on disulfide-containing poly( $\beta$ -amino ester) for combining chemotherapy and COX-2 inhibitor to overcome drug resistance in breast cancer. *J. Nanobiotechnol.* **2019**, *17*, 109. [[CrossRef](#)]
125. Duan, S.; Cao, D.; Li, X.; Zhu, H.; Lan, M.; Tan, Z.; Song, Z.; Zhu, R.; Yin, L.; Chen, Y. Topology-assisted, photo-strengthened DNA/siRNA delivery mediated by branched poly( $\beta$ -amino ester)s via synchronized intracellular kinetics. *Biomater. Sci.* **2020**, *8*, 290–301. [[CrossRef](#)]
126. Shamul, J.G.; Shah, S.R.; Kim, J.; Schiapparelli, P.; Vazquez-Ramos, C.A.; Lee, B.J.; Patel, K.K.; Shin, A.; Quinones-Hinojosa, A.; Green, J.J. Verteporfin-Loaded Anisotropic Poly(Beta-Amino Ester)-Based Micelles Demonstrate Brain Cancer-Selective Cytotoxicity and Enhanced Pharmacokinetics. *Int. J. Nanomed.* **2019**, *14*, 10047–10060. [[CrossRef](#)]
127. Yu, H.; Ingram, N.; Rowley, J.V.; Green, D.C.; Thornton, P.D. Meticulous Doxorubicin Release from pH-Responsive Nanoparticles Entrapped within an Injectable Thermo responsive Depot. *Chemistry* **2020**, *26*, 13352–13358. [[CrossRef](#)]
128. Karimi, N.; Mansouri, K.; Soleiman-Beigi, M.; Fattahi, A. All-Trans Retinoic Acid Grafted Poly Beta-Amino Ester Nanoparticles: A Novel Anti-angiogenic Drug Delivery System. *Adv. Pharm. Bull.* **2020**, *10*, 221–232. [[CrossRef](#)] [[PubMed](#)]
129. Wang, M.Z.; Niu, J.; Ma, H.J.; Dad, H.A.; Shao, H.T.; Yuan, T.J.; Peng, L.H. Transdermal siRNA delivery by pH-switchable micelles with targeting effect suppress skin melanoma progression. *J. Control. Release* **2020**, *322*, 95–107. [[CrossRef](#)] [[PubMed](#)]
130. Wagle, S.R.; Kovacevic, B.; Walker, D.; Ionescu, C.M.; Shah, U.; Stojanovic, G.; Kojic, S.; Mooranian, A.; Al-Salami, H. Alginate-based drug oral targeting using bio-micro/nano encapsulation technologies. *Expert Opin. Drug Deliv.* **2020**, *17*, 1361–1376. [[CrossRef](#)] [[PubMed](#)]
131. Pawar, S.N.; Edgar, K.J. Alginate derivatization: A review of chemistry, properties and applications. *Biomaterials* **2012**, *33*, 3279–3305. [[CrossRef](#)]
132. Hariyadi, D.M.; Islam, N. Current Status of Alginate in Drug Delivery. *Adv. Pharmacol. Pharm. Sci.* **2020**, *2020*, 8886095. [[CrossRef](#)]
133. Abraham, E.; Weber, D.E.; Sharon, S.; Lapidot, S.; Shoseyov, O. Multifunctional Cellulosic Scaffolds from Modified Cellulose Nanocrystals. *ACS Appl. Mater. Interfaces* **2017**, *9*, 2010–2015. [[CrossRef](#)]
134. Danafar, H.; Davaran, S.; Rostamizadeh, K.; Valizadeh, H.; Hamidi, M. Biodegradable m-PEG/PCL Core-Shell Micelles: Preparation and Characterization as a Sustained Release Formulation for Curcumin. *Adv. Pharm. Bull.* **2014**, *4*, 501–510.
135. Hosseinfar, T.; Sheybani, S.; Abdouss, M.; Najafabadi, S.A.H.; Ardestani, M.S. Pressure responsive nanogel base on Alginate-Cyclodextrin with enhanced apoptosis mechanism for colon cancer delivery. *J. Biomed. Mater. Res. A* **2018**, *106*, 349–359. [[CrossRef](#)]
136. Shad, P.M.; Karizi, S.Z.; Javan, R.S.; Mirzaie, A.; Noorbazargan, H.; Akbarzadeh, I.; Rezaie, H. Folate conjugated hyaluronic acid coated alginate nanogels encapsulated oxaliplatin enhance antitumor and apoptosis efficacy on colorectal cancer cells (HT29 cell line). *Toxicol. In Vitro* **2020**, *65*, 104756. [[CrossRef](#)]
137. Shen, H.; Li, F.; Wang, D.; Yang, Z.; Yao, C.; Ye, Y.; Wang, X. Chitosan-alginate BSA-gel-capsules for local chemotherapy against drug-resistant breast cancer. *Drug Des. Dev. Ther.* **2018**, *12*, 921–934. [[CrossRef](#)]
138. Kang, S.M.; Lee, G.W.; Huh, Y.S. Centrifugal Force-Driven Modular Micronozzle System: Generation of Engineered Alginate Microspheres. *Sci. Rep.* **2019**, *9*, 12776. [[CrossRef](#)]
139. Song, W.; Su, X.; Gregory, D.A.; Li, W.; Cai, Z.; Zhao, X. Magnetic Alginate/Chitosan Nanoparticles for Targeted Delivery of Curcumin into Human Breast Cancer Cells. *Nanomaterials* **2018**, *8*, 907. [[CrossRef](#)]
140. Gonçalves, M.; Figueira, P.; Maciel, D.; Rodrigues, J.; Qu, X.; Liu, C.; Tomás, H.; Li, Y. pH-sensitive Laponite<sup>®</sup>/doxorubicin/alginate nanohybrids with improved anticancer efficacy. *Acta Biomater.* **2014**, *10*, 300–307. [[CrossRef](#)]
141. Nisini, R.; Poerio, N.; Mariotti, S.; De Santis, F.; Fraziano, M. The Multirole of Liposomes in Therapy and Prevention of Infectious Diseases. *Front. Immunol.* **2018**, *9*, 155. [[CrossRef](#)]
142. El-Hammadi, M.M.; Arias, J.L. An update on liposomes in drug delivery, a patent review (2014–2018). *Expert Opin. Ther. Pat.* **2019**, *29*, 891–907. [[CrossRef](#)]
143. Torchilin, V.P. Recent advances with liposomes as pharmaceutical carriers. *Nat. Rev. Drug Discov.* **2005**, *4*, 145–160. [[CrossRef](#)]
144. Bozzuto, G.; Molinari, A. Liposomes as nanomedical devices. *Int. J. Nanomed.* **2015**, *10*, 975–999. [[CrossRef](#)]
145. Yan, W.; Leung, S.S.; To, K.K. Updates on the use of liposomes for active tumor targeting in cancer therapy. *Nanomedicine* **2020**, *15*, 303–318. [[CrossRef](#)]
146. Torchilin, V. Multifunctional and stimuli-sensitive pharmaceutical nanocarriers. *Eur. J. Pharm. Biopharm.* **2009**, *71*, 431–444. [[CrossRef](#)]
147. Bangham, A.D.; Horne, R.W. Negative staining of phospholipids and their structural modification by surface-active agents as observed in the electron microscope. *J. Mol. Biol.* **1964**, *8*, 660–668. [[CrossRef](#)]
148. Mandpe, P.; Prabhakar, B.; Shende, P. Role of Liposomes-Based Stem Cell for Multimodal Cancer Therapy. *Stem Cell Rev. Rep.* **2020**, *16*, 103–117. [[CrossRef](#)]

149. Bulbake, U.; Doppalapudi, S.; Kommineni, N.; Khan, W. Liposomal Formulations in Clinical Use, An Updated Review. *Pharmaceutics* **2017**, *9*, 12. [[CrossRef](#)]
150. Xu, Y.; Yao, Y.; Wang, L.; Chen, H.; Tan, N. Hyaluronic Acid Coated Liposomes Co-Delivery of Natural Cyclic Peptide RA-XII and Mitochondrial Targeted Photosensitizer for Highly Selective Precise Combined Treatment of Colon Cancer. *Int. J. Nanomed.* **2021**, *16*, 4929–4942. [[CrossRef](#)]
151. Lorenzer, C.; Dirin, M.; Winkler, A.M.; Baumann, V.; Winkler, J. Going beyond the liver, progress and challenges of targeted delivery of siRNA therapeutics. *J. Control. Release* **2015**, *203*, 1–15. [[CrossRef](#)] [[PubMed](#)]
152. Akbarzadeh, A.; Rezaei-Sadabady, R.; Davaran, S.; Joo, S.W.; Zarghami, N.; Hanifehpour, Y.; Samiei, M.; Kouhi, M.; Nejati-Koshki, K. Liposome: Classification, preparation, and applications. *Nanoscale Res. Lett.* **2013**, *8*, 102. [[CrossRef](#)]
153. Perche, F.; Torchilin, V.P. Recent trends in multifunctional liposomal nanocarriers for enhanced tumor targeting. *J. Drug Deliv.* **2013**, *2013*, 705265. [[CrossRef](#)]
154. Eloy, J.O.; Petrilli, R.; Trevizan, L.N.F.; Chorilli, M. Immunoliposomes, A review on functionalization strategies and targets for drug delivery. *Colloids Surf. B Biointerfaces* **2017**, *159*, 454–467. [[CrossRef](#)] [[PubMed](#)]
155. Ta, T.; Porter, T.M. Thermosensitive liposomes for localized delivery and triggered release of chemotherapy. *J. Control. Release* **2013**, *169*, 112–125. [[CrossRef](#)] [[PubMed](#)]
156. Lee, Y.; Thompson, D.H. Stimuli-responsive liposomes for drug delivery. *Wiley Interdiscip. Rev. Nanomed. Nanobiotechnol.* **2017**, *9*, 1450. [[CrossRef](#)]
157. Riaz, M.K.; Riaz, M.A.; Zhang, X.; Lin, C.; Wong, K.H.; Chen, X.; Zhang, G.; Lu, A.; Yang, Z. Surface Functionalization and Targeting Strategies of Liposomes in Solid Tumor Therapy, A Review. *Int. J. Mol. Sci.* **2018**, *19*, 195. [[CrossRef](#)]
158. Yang, T.; Sui, X.; Yu, B.; Shen, Y.; Cong, H. Recent Advances in the Rational Drug Design Based on Multi-target Ligands. *Curr. Med. Chem.* **2020**, *27*, 4720–4740. [[CrossRef](#)]
159. Gao, Y.G.; Alam, U.; Ding, A.X.; Tang, Q.; Tan, Z.L.; Shi, Y.D.; Lu, Z.L.; Qian, A.R. AneN3-based lipid with naphthalimide moiety for enhanced gene transfection efficiency. *Bioorg. Chem.* **2018**, *79*, 334–340. [[CrossRef](#)]
160. Hayashi, T.; Shinagawa, M.; Kawano, T.; Iwasaki, T. Drug delivery using polyhistidine peptide-modified liposomes that target endogenous lysosome. *Biochem. Biophys. Res. Commun.* **2018**, *501*, 648–653. [[CrossRef](#)]
161. Jhaveri, A.; Deshpande, P.; Pattni, B.; Torchilin, V. Transferrin-targeted, resveratrol-loaded liposomes for the treatment of glioblastoma. *J. Control. Release* **2018**, *277*, 89–101. [[CrossRef](#)] [[PubMed](#)]
162. Wei, M.; Guo, X.; Tu, L.; Zou, Q.; Li, Q.; Tang, C.; Chen, B.; Xu, Y.; Wu, C. Lactoferrin-modified PEGylated liposomes loaded with doxorubicin for targeting delivery to hepatocellular carcinoma. *Int. J. Nanomed.* **2015**, *10*, 5123–5137.
163. Zang, X.; Ding, H.; Zhao, X.; Li, X.; Du, Z.; Hu, H.; Qiao, M.; Chen, D.; Deng, Y.; Zhao, X. Anti-EphA10 antibody-conjugated pH-sensitive liposomes for specific intracellular delivery of siRNA. *Int. J. Nanomed.* **2016**, *11*, 3951–3967. [[CrossRef](#)] [[PubMed](#)]
164. Alshaer, W.; Hillaireau, H.; Vergnaud, J.; Mura, S.; Deloménie, C.; Sauvage, F.; Ismail, S.; Fattal, E. Aptamer-guided siRNA-loaded nanomedicines for systemic gene silencing in CD-44 expressing murine triple-negative breast cancer model. *J. Control. Release* **2018**, *271*, 98–106. [[CrossRef](#)] [[PubMed](#)]
165. Needham, D.; Park, J.Y.; Wright, A.M.; Tong, J. Materials characterization of the low temperature sensitive liposome (LTSL): Effects of the lipid composition (lysolipid and DSPE-PEG2000) on the thermal transition and release of doxorubicin. *Faraday Discuss.* **2013**, *161*, 515–534, discussion 563–589. [[CrossRef](#)]
166. Zhao, Y.; Ren, W.; Zhong, T.; Zhang, S.; Huang, D.; Guo, Y.; Yao, X.; Wang, C.; Zhang, W.Q.; Zhang, X.; et al. Tumor-specific pH-responsive peptide-modified pH-sensitive liposomes containing doxorubicin for enhancing glioma targeting and anti-tumor activity. *J. Control. Release* **2016**, *222*, 56–66. [[CrossRef](#)]
167. Clares, B.; Biedma-Ortiz, R.A.; Sáez-Fernández, E.; Prados, J.C.; Melguizo, C.; Cabeza, L.; Ortiz, R.; Arias, J.L. Nano-engineering of 5-fluorouracil-loaded magnetoliposomes for combined hyperthermia and chemotherapy against colon cancer. *Eur. J. Pharm. Biopharm.* **2013**, *85*, 329–338. [[CrossRef](#)] [[PubMed](#)]
168. Chi, Y.; Yin, X.; Sun, K.; Feng, S.; Liu, J.; Chen, D.; Guo, C.; Wu, Z. Redox-sensitive and hyaluronic acid functionalized liposomes for cytoplasmic drug delivery to osteosarcoma in animal models. *J. Control. Release* **2017**, *261*, 113–125. [[CrossRef](#)] [[PubMed](#)]
169. Song, S.J.; Lee, S.; Lee, Y.; Choi, J.S. Enzyme-responsive destabilization of stabilized plasmid-lipid nanoparticles as an efficient gene delivery. *Eur. J. Pharm. Sci.* **2016**, *91*, 20–30. [[CrossRef](#)]
170. Zylberberg, C.; Gaskill, K.; Pasley, S.; Matosevic, S. Engineering liposomal nanoparticles for targeted gene therapy. *Gene Ther.* **2017**, *24*, 441–452. [[CrossRef](#)]
171. Koren, E.; Torchilin, V.P. Cell-penetrating peptides, breaking through to the other side. *Trends Mol. Med.* **2012**, *18*, 385–393. [[CrossRef](#)] [[PubMed](#)]
172. Munyendo, W.L.; Lv, H.; Benza-Ingoula, H.; Baraza, L.D.; Zhou, J. Cell penetrating peptides in the delivery of biopharmaceuticals. *Biomolecules* **2012**, *2*, 187–202. [[CrossRef](#)] [[PubMed](#)]
173. McClorey, G.; Banerjee, S. Cell-Penetrating Peptides to Enhance Delivery of Oligonucleotide-Based Therapeutics. *Biomedicines* **2018**, *6*, 51. [[CrossRef](#)] [[PubMed](#)]
174. Park, J.; Singha, K.; Son, S.; Kim, J.; Namgung, R.; Yun, C.O.; Kim, W.J. A review of RGD-functionalized nonviral gene delivery vectors for cancer therapy. *Cancer Gene Ther.* **2012**, *19*, 741–748. [[CrossRef](#)] [[PubMed](#)]

175. Kang, W.; Svirskis, D.; Sarojini, V.; McGregor, A.L.; Bevitt, J.; Wu, Z. Cyclic-RGDyC functionalized liposomes for dual-targeting of tumor vasculature and cancer cells in glioblastoma, An in vitro boron neutron capture therapy study. *Oncotarget* **2017**, *8*, 36614–36627. [[CrossRef](#)]
176. Belhadj, Z.; Ying, M.; Cao, X.; Hu, X.; Zhan, C.; Wei, X.; Gao, J.; Wang, X.; Yan, Z.; Lu, W. Design of Y-shaped targeting material for liposome-based multifunctional glioblastoma-targeted drug delivery. *J. Control. Release* **2017**, *255*, 132–141. [[CrossRef](#)]
177. Chen, Z.; Deng, J.; Zhao, Y.; Tao, T. Cyclic RGD peptide-modified liposomal drug delivery system, enhanced cellular uptake in vitro and improved pharmacokinetics in rats. *Int. J. Nanomed.* **2012**, *7*, 3803–3811. [[CrossRef](#)]
178. Nakase, I.; Akita, H.; Kogure, K.; Gräslund, A.; Langel, U.; Harashima, H.; Futaki, S. Efficient intracellular delivery of nucleic acid pharmaceuticals using cell-penetrating peptides. *Acc. Chem. Res.* **2012**, *45*, 1132–1139. [[CrossRef](#)]
179. Ding, Y.; Sun, D.; Wang, G.L.; Yang, H.G.; Xu, H.F.; Chen, J.H.; Xie, Y.; Wang, Z.Q. An efficient PEGylated liposomal nanocarrier containing cell-penetrating peptide and pH-sensitive hydrazone bond for enhancing tumor-targeted drug delivery. *Int. J. Nanomed.* **2015**, *10*, 6199–6214.
180. Al-Ahmady, Z.S.; Chaloin, O.; Kostarelos, K. Monoclonal antibody-targeted.; temperature-sensitive liposomes, in vivo tumor chemotherapeutics in combination with mild hyperthermia. *J. Control. Release* **2014**, *196*, 332–343. [[CrossRef](#)] [[PubMed](#)]
181. Petrilli, R.; Eloy, J.O.; Lee, R.J.; Lopez, R.F.V. Preparation of Immunoliposomes by Direct Coupling of Antibodies Based on a Thioether Bond. *Methods Mol. Biol.* **2018**, *1674*, 229–237.
182. Lu, L.; Ding, Y.; Zhang, Y.; Ho, R.J.; Zhao, Y.; Zhang, T.; Guo, C. Antibody-modified liposomes for tumor-targeting delivery of timosaponin AIII. *Int. J. Nanomed.* **2018**, *13*, 1927–1944. [[CrossRef](#)] [[PubMed](#)]
183. Gao, J.; Chen, H.; Yu, Y.; Song, J.; Song, H.; Su, X.; Li, W.; Tong, X.; Qian, W.; Wang, H.; et al. Inhibition of hepatocellular carcinoma growth using immunoliposomes for co-delivery of adriamycin and ribonucleotide reductase M2 siRNA. *Biomaterials* **2013**, *34*, 10084–10098. [[CrossRef](#)]
184. Saeed, M.; van Brakel, M.; Zalba, S.; Schooten, E.; Rens, J.A.; Koning, G.A.; Debets, R.; Hagen, T.L.T. Targeting melanoma with immunoliposomes coupled to anti-MAGE A1 TCR-like single-chain antibody. *Int. J. Nanomed.* **2016**, *11*, 955–975. [[CrossRef](#)] [[PubMed](#)]
185. Moosavian, S.A.; Sahebkar, A. Aptamer-functionalized liposomes for targeted cancer therapy. *Cancer Lett.* **2019**, *448*, 144–154. [[CrossRef](#)]
186. Prakash, J.S.; Rajamanickam, K. Aptamers and their significant role in cancer therapy and diagnosis. *Biomedicines* **2015**, *3*, 248–269. [[CrossRef](#)]
187. Torchilin, V.P. Passive and active drug targeting: Drug delivery to tumors as an example. *Drug Deliv.* **2010**, *197*, 3–53.
188. Powell, D.; Chandra, S.; Dodson, K.; Shaheen, F.; Wiltz, K.; Ireland, S.; Syed, M.; Dash, S.; Wiese, T.; Mandal, T.; et al. Aptamer-functionalized hybrid nanoparticle for the treatment of breast cancer. *Eur. J. Pharm. Biopharm.* **2017**, *114*, 108–118. [[CrossRef](#)]
189. Li, L.; Hou, J.; Liu, X.; Guo, Y.; Wu, Y.; Zhang, L.; Yang, Z. Nucleolin-targeting liposomes guided by aptamer AS1411 for the delivery of siRNA for the treatment of malignant melanomas. *Biomaterials* **2014**, *35*, 3840–3850. [[CrossRef](#)] [[PubMed](#)]
190. Palchetti, S.; Digiacomo, L.; Pozzi, D.; Chiozzi, R.Z.; Capriotti, A.L.; Laganà, A.; Coppola, R.; Caputo, D.; Sharifzadeh, M.; Mahmoudi, M.; et al. Effect of Glucose on Liposome-Plasma Protein Interactions, Relevance for the Physiological Response of Clinically Approved Liposomal Formulations. *Adv. Biosyst.* **2019**, *3*, e1800221. [[CrossRef](#)]
191. Soe, Z.C.; Thapa, R.K.; Ou, W.; Gautam, M.; Nguyen, H.T.; Jin, S.G.; Ku, S.K.; Oh, K.T.; Choi, H.G.; Yong, C.S.; et al. Folate receptor-mediated celastrol and irinotecan combination delivery using liposomes for effective chemotherapy. *Colloids Surf. B Biointerfaces* **2018**, *170*, 718–728. [[CrossRef](#)] [[PubMed](#)]
192. Sakashita, M.; Mochizuki, S.; Sakurai, K. Hepatocyte-targeting gene delivery using a lipoplex composed of galactose-modified aromatic lipid synthesized with click chemistry. *Bioorg. Med. Chem.* **2014**, *22*, 5212–5219. [[CrossRef](#)]
193. Kraft, J.C.; Freeling, J.P.; Wang, Z.; Ho, R.J. Emerging research and clinical development trends of liposome and lipid nanoparticle drug delivery systems. *J. Pharm. Sci.* **2014**, *103*, 29–52. [[CrossRef](#)] [[PubMed](#)]
194. Kang, M.H.; Yoo, H.J.; Kwon, Y.H.; Yoon, H.Y.; Lee, S.G.; Kim, S.R.; Yeom, D.W.; Kang, M.J.; Choi, Y.W. Design of Multifunctional Liposomal Nanocarriers for Folate Receptor-Specific Intracellular Drug Delivery. *Mol. Pharm.* **2015**, *12*, 4200–4213. [[CrossRef](#)]
195. Zong, T.; Mei, L.; Gao, H.; Cai, W.; Zhu, P.; Shi, K.; Chen, J.; Wang, Y.; Gao, F.; He, Q. Synergistic dual-ligand doxorubicin liposomes improve targeting and therapeutic efficacy of brain glioma in animals. *Mol. Pharm.* **2014**, *11*, 2346–2357. [[CrossRef](#)]
196. Lu, Y.; Sun, W.; Gu, Z. Stimuli-responsive nanomaterials for therapeutic protein delivery. *J. Control. Release* **2014**, *194*, 1–19. [[CrossRef](#)]
197. Lou, J.; Carr, A.J.; Watson, A.J.; Mattern-Schain, S.I.; Best, M.D. Calcium-Responsive Liposomes via a Synthetic Lipid Switch. *Chemistry* **2018**, *24*, 3599–3607. [[CrossRef](#)]
198. Sine, J.; Urban, C.; Thayer, D.; Charron, H.; Valim, N.; Tata, D.B.; Schiff, R.; Blumenthal, R.; Joshi, A.; Puri, A. Photo activation of HPPH encapsulated in “Pocket” liposomes triggers multiple drug release and tumor cell killing in mouse breast cancer xenografts. *Int. J. Nanomed.* **2014**, *10*, 125–145.
199. Rosarin, F.S.; Mirunalini, S. Nobel Metallic Nanoparticles with Novel Biomedical Properties. *J. Bioanal. Biomed.* **2011**, *3*, 85–91. [[CrossRef](#)]
200. Daniel, M.C.; Astruc, D. Gold nanoparticles: Assembly, supramolecular chemistry, quantum-size-related properties, and applications toward biology, catalysis, and nanotechnology. *Chem. Rev.* **2004**, *104*, 293–346. [[CrossRef](#)]

201. Singh, P.; Mijakovic, I. Advances in gold nanoparticle technology as a tool for diagnostics and treatment of cancer. *Expert Rev. Mol. Diagn.* **2021**, *21*, 627–630. [[CrossRef](#)]
202. Petrushev, B.; Boca, S.; Simon, T.; Berce, C.; Frinc, I.; Dima, D.; Selicean, S.; Gafencu, G.A.; Tanase, A.; Zdrengea, M.; et al. Gold nanoparticles enhance the effect of tyrosine kinase inhibitors in acute myeloid leukemia therapy. *Int. J. Nanomed.* **2016**, *11*, 641–660.
203. Hyeon-Ho, J.; Eunjin, C.; Elizabeth, E.; Tung-Chun, L. Recent advances in gold nanoparticles for biomedical applications: From hybrid structures to multi-functionality. *J. Mater. Chem. B* **2019**, *7*, 3480–3496.
204. Ruan, S.; Yuan, M.; Zhang, L.; Hu, G.; Chen, J.; Cun, X.; Zhang, Q.; Yang, Y.; He, Q.; Gao, H. Tumor microenvironment sensitive doxorubicin delivery and release to glioma using angiopep-2 decorated gold nanoparticles. *Biomaterials* **2015**, *37*, 425–435. [[CrossRef](#)]
205. Turkevich, J.; Cooper, P.H.J. A study of the nucleation and growth process in the synthesis of colloidal gold. *Discuss. Faraday Soc.* **1951**, *55*, 55–75. [[CrossRef](#)]
206. Brust, M.; Walker, M.; Bethell, D.; Schiffrin, D.J.; Whyman, R. Synthesis of thiol-derivatised gold nanoparticles in a two-phase liquid-liquid system. *J. Chem. Soc. Chem. Commun.* **1994**, *7*, 5–7. [[CrossRef](#)]
207. Sahu, P.; Prasad, B.L. Time and temperature effects on the digestive ripening of gold nanoparticles: Is there a crossover from digestive ripening to Ostwald ripening? *Langmuir* **2014**, *30*, 10143–10150. [[CrossRef](#)]
208. Dong, J.; Carpinone, P.L.; Pyrgiotakis, G.; Demokritou, P.; Moudgil, B.M. Synthesis of Precision Gold Nanoparticles Using Turkevich Method. *KONA Powder Part. J.* **2020**, *37*, 224–232. [[CrossRef](#)] [[PubMed](#)]
209. Shimpi, J.R.; Sidhaye, D.S.; Prasad, B.L.V. Digestive Ripening: A Fine Chemical Machining Process on the Nanoscale. *Langmuir* **2017**, *33*, 9491–9507. [[CrossRef](#)] [[PubMed](#)]
210. Herizchi, R.; Abbasi, E.; Milani, M.; Akbarzadeh, A. Current methods for synthesis of gold nanoparticles. *Artif. Cells Nanomed. Biotechnol.* **2016**, *44*, 596–602. [[CrossRef](#)] [[PubMed](#)]
211. Chen, Y.S.; Hung, Y.C.; Liao, I.; Huang, G.S. Assessment of the In Vivo Toxicity of Gold Nanoparticles. *Nanoscale Res. Lett.* **2009**, *4*, 858–864. [[CrossRef](#)]
212. Subbaiya, R.; Saravanan, M.; Priya, A.R.; Shankar, K.R.; Selvam, M.; Ovais, M.; Balajee, R.; Barabadi, H. Biomimetic synthesis of silver nanoparticles from *Streptomyces atrovirens* and their potential anticancer activity against human breast cancer cells. *IET Nanobiotechnol.* **2017**, *11*, 965–972. [[CrossRef](#)]
213. Bose, D.; Chatterjee, S. Biogenic synthesis of silver nanoparticles using guava (*Psidium guajava*) leaf extract and its antibacterial activity against *Pseudomonas aeruginosa*. *Appl. Nanosci.* **2016**, *6*, 895–901. [[CrossRef](#)]
214. Pourali, P.; Badiiee, S.H.; Manafi, S.; Noorani, T.; Rezaei, A.; Yahyaiee, B. Biosynthesis of gold nanoparticles by two bacterial and fungal strains, *Bacillus cereus* and *Fusarium oxysporum*, and assessment and comparison of their nanotoxicity in vitro by direct and indirect assays. *Electron. J. Biotechnol.* **2017**, *29*, 86–93. [[CrossRef](#)]
215. Sharma, N.; Pinnaka, A.K.; Raje, M.; Fnu, A.; Bhattacharyya, M.S.; Choudhury, A.R. Exploitation of marine bacteria for production of gold nanoparticles. *Microb. Cell Fact.* **2012**, *11*, 86. [[CrossRef](#)]
216. Sanghi, R.; Verma, P.; Puri, S. Enzymatic formation of gold nanoparticles using *phanerochaete chrysosporium*. *Adv. Chem. Eng. Sci.* **2011**, *1*, 154–162. [[CrossRef](#)]
217. Molnár, Z.; Bódai, V.; Szakacs, G.; Erdélyi, B.; Fogarassy, Z.; Sáfrán, G.; Varga, T.; Kónya, Z.; Tóth-Szeles, E.; Szűcs, R.; et al. Green synthesis of gold nanoparticles by thermophilic filamentous fungi. *Sci. Rep.* **2018**, *8*, 3943. [[CrossRef](#)]
218. Amina, S.J.; Guo, B. A Review on the Synthesis and Functionalization of Gold Nanoparticles as a Drug Delivery Vehicle. *Int. J. Nanomed.* **2020**, *15*, 9823–9857. [[CrossRef](#)]
219. Gopinath, K.; Venkatesh, K.S.; Ilangovan, R.; Sankaranarayanan, K.; Arumugam, A. Green synthesis of gold nanoparticles from leaf extract of *terminalia arjuna*, for the enhanced mitotic cell division and pollen germination activity. *Ind. Crops Prod.* **2013**, *50*, 737–742. [[CrossRef](#)]
220. Yu, J.; Xu, D.; Guan, H.N.; Wang, C.; Huang, L.K.; Chi, D.F. Facile one-step green synthesis of gold nanoparticles using *Citrus maxima* aqueous extracts and its catalytic activity. *Mater. Lett.* **2016**, *166*, 110–112. [[CrossRef](#)]
221. Naveena, B.E.; Prakash, S. Biological synthesis of gold nanoparticles using marine algae *gracilaria corticata* and its application as a potent antimicrobial and antioxidant agent. *Asian J. Pharm. Clin. Res.* **2013**, *6*, 179–182.
222. Swaminathan, S.; Subbiah, M.; Damodarkumar, S.; Dhamotharan, R.; Bhuvaneshwari, S. Synthesis and characterization of gold nanoparticles from alga *acanthophora specifera* (VAHL) boergesen. *Int. J. Nano Sci. Nanotechnol.* **2011**, *2*, 85–94.
223. Kalishwaralal, K.; Deepak, V.; Pandian, S.R.K.; Kottaisamy, M.; Kanth, S.B.; Kartikeyan, B.; Gurunathan, S. Biosynthesis of silver and gold nanoparticles using *Brevibacterium casei*. *Colloids Surf. B Biointerfaces* **2010**, *77*, 257–262. [[CrossRef](#)] [[PubMed](#)]
224. Rajeshkumar, S.; Sri, R.B.; Venkat, K.; Soumya, M.; Lakshmi, T.; Haribalan, P. Biosynthesis of gold nanoparticles using marine microbe (*Vibrio alginolyticus*) and its anticancer and antioxidant analysis. *J. King Saud Univ. Sci.* **2021**, *33*, 101260.
225. Patil, M.P.; Kang, M.J.; Niyonizigiye, I.; Singh, A.; Kim, J.O.; Seo, Y.B.; Kim, G.D. Extracellular synthesis of gold nanoparticles using the marine bacterium *Paracoccus haeundaensis* BC74171T and evaluation of their antioxidant activity and antiproliferative effect on normal and cancer cell lines. *Colloids Surf. B Biointerfaces* **2019**, *183*, 110455. [[CrossRef](#)]
226. Sreedharan, S.M.; Gupta, S.; Saxena, A.K.; Singh, R. Macrophomina phaseolina: Microbased biorefinery for gold nanoparticle production. *Ann. Microbiol.* **2019**, *69*, 435–445. [[CrossRef](#)]

227. Acay, H. Utilization of *Morchella esculenta*-mediated green synthesis golden nanoparticles in biomedicine applications. *Prep. Biochem. Biotechnol.* **2021**, *51*, 127–136. [[CrossRef](#)] [[PubMed](#)]
228. Munawer, U.; Raghavendra, V.B.; Ningaraju, S.; Krishna, K.L.; Ghosh, A.R.; Melappa, G.; Pugazhendhi, A. Biofabrication of gold nanoparticles mediated by the endophytic *Cladosporium* species: Photodegradation, in vitro anticancer activity and in vivo antitumor studies. *Int. J. Pharm.* **2020**, *588*, 119729. [[CrossRef](#)]
229. Qu, Y.; Li, X.; Lian, S.; Dai, C.; Jv, Z.; Zhao, B.; Zhou, H. Biosynthesis of gold nanoparticles using fungus *Trichoderma* sp. WL-Go and their catalysis in degradation of aromatic pollutants. *IET Nanobiotechnol.* **2019**, *13*, 12–17. [[CrossRef](#)] [[PubMed](#)]
230. Folorunso, A.; Akintelu, S.; Oyebamiji, A.K.; Ajayi, S.; Abiola, B.; Abdusalam, I.; Morakinyo, A. Biosynthesis, characterization and antimicrobial activity of gold nanoparticles from leaf extracts of *Annona muricata*. *J. Nanostruct. Chem.* **2019**, *9*, 111–117. [[CrossRef](#)]
231. Al Saqr, A.; Khafagy, E.S.; Alalaiwe, A.; Aldawsari, M.F.; Alshahrani, S.M.; Anwer, M.K.; Khan, S.; Lila, A.S.A.; Arab, H.H.; Hegazy, W.A.H. Synthesis of Gold Nanoparticles by Using Green Machinery: Characterization and In Vitro Toxicity. *Nanomaterials* **2021**, *11*, 808. [[CrossRef](#)]
232. Qais, F.A.; Ahmad, I.; Altaf, M.; Alotaibi, S.H. Biofabrication of Gold Nanoparticles Using Capsicum annum Extract and Its Antiquorum Sensing and Antibiofilm Activity against Bacterial Pathogens. *ACS Omega* **2021**, *6*, 16670–16682. [[CrossRef](#)]
233. Martha, R.B.; Fernando, R.; Veronica, S.; Mercedes, G.L.; Jorge, S.J.; Luis, H.A.; Carlos, A. Green synthesis of gold nanoparticles using *Turnera diffusa* Willd enhanced antimicrobial properties and immune response in Longfin yellowtail leukocytes. *Aquac. Res.* **2021**, *52*, 3391–3402.
234. Kim, B.; Song, W.C.; Park, S.Y.; Park, G. Green Synthesis of Silver and Gold Nanoparticles via *Sargassum serratifolium* Extract for Catalytic Reduction of Organic Dyes. *Catalysts* **2021**, *11*, 347. [[CrossRef](#)]
235. Babu, B.; Palanisamy, S.; Vinosha, M.; Anjali, R.; Kumar, P.; Pandi, B.; Tabarsa, M.; You, S.; Prabhu, N.M. Bioengineered gold nanoparticles from marine seaweed *Acanthophora spicifera* for pharmaceutical uses: Antioxidant, antibacterial, and anticancer activities. *Bioprocess Biosyst. Eng.* **2020**, *43*, 2231–2242. [[CrossRef](#)]
236. Xavier, H.F.M.; Nadar, V.M.; Patel, P.; Umopathy, D.; Joseph, A.V.; Manivannan, S.; Santhiyagu, P.; Pandi, B.; Muthusamy, G.; Rathinam, Y.; et al. Selective antibacterial and apoptosis-inducing effects of hybrid gold nanoparticles—A green approach. *J. Drug Deliv. Sci. Technol.* **2020**, *59*, 101890. [[CrossRef](#)]
237. Gürsoy, N.; Öztürk, B.Y.; Dağ, İ. Synthesis of intracellular and extracellular gold nanoparticles with a green machine and its antifungal activity. *Turk. J. Biol.* **2021**, *45*, 196–213. [[CrossRef](#)]
238. Singla, R.; Guliani, A.; Kumari, A.; Yadav, S. Toxicity issues and applications in medicine. *Met. Nanopart.* **2016**, 41–80. [[CrossRef](#)]
239. Coradeghini, R.; Gioria, S.; Garcia, C.P.; Nativo, P.; Franchini, F.; Gilliland, D.; Ponti, J.; Rossi, F. Size-dependent toxicity and cell interaction mechanisms of gold nanoparticles on mouse fibroblasts. *Toxicol. Lett.* **2013**, *217*, 205–216. [[CrossRef](#)] [[PubMed](#)]
240. Steckiewicz, K.P.; Barcinska, E.; Malankowska, A.; Zauszkiewicz-Pawlak, A.; Nowaczyk, G.; Zaleska-Medynska, A.; Inkielewicz-Stepniak, I. Impact of gold nanoparticles shape on their cytotoxicity against human osteoblast and osteosarcoma in in vitro model. Evaluation of the safety of use and anti-cancer potential. *J. Mater. Sci. Mater. Med.* **2019**, *30*, 22. [[CrossRef](#)]
241. Papp, I.; Sieben, C.; Ludwig, K.; Roskamp, M.; Böttcher, C.; Schlecht, S.; Herrmann, A.; Haag, R. Inhibition of influenza virus infection by multivalent sialic-acid-functionalized gold nanoparticles. *Small* **2010**, *6*, 2900–2906. [[CrossRef](#)] [[PubMed](#)]
242. Beck, J.S.; Vartuli, J.C.; Roth, W.J.; Leonowicz, M.E.; Kresge, C.T.; Schmitt, K.D.; Chu, C.T.W.; Olson, D.H.; Sheppard, E.W.; McCullen, S.B.; et al. A new family of mesoporous molecular sieves prepared with liquid crystal templates. *J. Am. Chem. Soc.* **1992**, *114*, 10834–10843. [[CrossRef](#)]
243. Kresge, C.T.; Leonowicz, M.E.; Roth, W.J.; Vartuli, J.C.; Beck, J.S. Ordered mesoporous molecular sieves synthesized by a liquid-crystal template mechanism. *Nature* **1992**, *359*, 710–712. [[CrossRef](#)]
244. Cheng, Y.J.; Luo, G.F.; Zhu, J.Y.; Xu, X.D.; Zeng, X.; Cheng, D.B.; Li, Y.M.; Wu, Y.; Zhang, X.Z.; Zhuo, R.X.; et al. Enzyme-induced and tumor-targeted drug delivery system based on multifunctional mesoporous silica nanoparticles. *ACS Appl. Mater. Interfaces* **2015**, *7*, 9078–9087. [[CrossRef](#)] [[PubMed](#)]
245. Bagheri, E.; Ansari, L.; Abnous, K.; Taghdisi, S.M.; Charbgo, F.; Ramezani, M.; Alibolandi, M. Silica based hybrid materials for drug delivery and bioimaging. *J. Control. Release* **2018**, *277*, 57–76. [[CrossRef](#)]
246. Bitar, A.; Ahmad, N.M.; Fessi, H.; Elaissari, A. Silica-based nanoparticles for biomedical applications. *Drug Discov. Today* **2012**, *17*, 1147–1154. [[CrossRef](#)] [[PubMed](#)]
247. Fijneman, A.J.; Höglblom, J.; Palmlöf, M.; With, G.; Persson, M.; Friedrich, H. Multiscale Colloidal Assembly of Silica Nanoparticles into Microspheres with Tunable Mesopores. *Adv. Funct. Mater.* **2020**, *30*, 2002725–2002732. [[CrossRef](#)]
248. Thi, T.T.H.; Cao, V.D.; Nguyen, T.N.Q.; Hoang, D.T.; Ngo, V.C.; Nguyen, D.H. Functionalized mesoporous silica nanoparticles and biomedical applications. *Mater. Sci. Eng. C Mater. Biol. Appl.* **2019**, *99*, 631–656.
249. Watermann, A.; Brieger, J. Mesoporous Silica Nanoparticles as Drug Delivery Vehicles in Cancer. *Nanomaterials* **2017**, *7*, 189. [[CrossRef](#)]
250. Mohamed Isa, E.D.; Ahmad, H.; Rahman, M.B.A.; Gill, M.R. Progress in Mesoporous Silica Nanoparticles as Drug Delivery Agents for Cancer Treatment. *Pharmaceutics* **2021**, *13*, 152. [[CrossRef](#)] [[PubMed](#)]
251. Chao, M.C.; Wang, D.S.; Lin, H.P.; Mou, C.Y. Control of single crystal morphology of SBA-1 mesoporous silica. *J. Mater. Chem.* **2003**, *13*, 2853–2854. [[CrossRef](#)]

252. Inagaki, S.; Guan, S.Y.; Fukushima, Y.; Ohsuna, T.; Terasaki, O. Novel Mesoporous Materials with a Uniform Distribution of Organic Groups and Inorganic Oxide in Their Frameworks. *J. Am. Chem. Soc.* **1999**, *121*, 9611–9614. [[CrossRef](#)]
253. Deka, J.R.; Lin, Y.H.; Kao, H.M. Ordered cubic mesoporous silica KIT-5 functionalized with carboxylic acid groups for dye removal. *RSC Adv.* **2014**, *4*, 49061–49069. [[CrossRef](#)]
254. Polshettiwar, V.; Cha, D.; Zhang, X.; Basset, J.M. High-surface-area silica nanospheres (KCC-1) with a fibrous morphology. *Angew. Chem. Int. Ed. Eng.* **2010**, *49*, 9652–9656. [[CrossRef](#)]
255. Tozuka, Y.; Wongmekiat, A.; Kimura, K.; Moribe, K.; Yamamura, S.; Yamamoto, K. Effect of pore size of FSM-16 on the entrapment of flurbiprofen in mesoporous structures. *Chem. Pharm. Bull.* **2005**, *53*, 974–977. [[CrossRef](#)]
256. Saleh, K.A.; Abdulmani, S.A.A.; Awwad, N.S.; Ibrahim, H.A.; Asiri, T.H.; Hamdy, M.S. Utilization of lithium incorporated mesoporous silica for preventing necrosis and increase apoptosis in different cancer cells. *BMC Chem.* **2019**, *13*, 8. [[CrossRef](#)] [[PubMed](#)]
257. Hwang, J.; Lee, J.H.; Chun, J. Facile approach for the synthesis of spherical mesoporous silica nanoparticles from sodium silicate. *Mater. Lett.* **2021**, *283*, 128765. [[CrossRef](#)]
258. Lv, X.; Zhang, L.; Xing, F.; Lin, H. Controlled synthesis of monodispersed mesoporous silica nanoparticles: Particle size tuning and formation mechanism investigation. *Microporous Mesoporous Mater.* **2016**, *225*, 238–244. [[CrossRef](#)]
259. Song, T.; Zhao, H.; Hu, Y.; Sun, N.; Zhang, H. Facile assembly of mesoporous silica nanoparticles with hierarchical pore structure for CO<sub>2</sub> capture. *Chin. Chem. Lett.* **2019**, *30*, 2347–2350. [[CrossRef](#)]
260. Soares, D.C.F.; Soares, L.M.; de Goes, A.M.; Melo, E.M.; de Barros, A.L.B.; Bicalho, T.C.A.S.; Leao, N.M.; Tebaldi, M.L. Mesoporous SBA-16 silica nanoparticles as a potential vaccine adjuvant against *Paracoccidioides brasiliensis*. *Microporous Mesoporous Mater.* **2020**, *291*, 109676. [[CrossRef](#)]
261. Mohamad, D.F.; Osman, N.S.; Nazri, M.K.H.M.; Mazlan, A.A.; Hanafi, M.F.; Esa, Y.A.M.; Rafi, M.I.I.M.; Zailani, M.N.; Rahman, N.N.; Rahman, A.H.A.; et al. Synthesis of Mesoporous Silica Nanoparticle from Banana Peel Ash for Removal of Phenol and Methyl Orange in Aqueous Solution. *Mater. Today Proc.* **2019**, *19*, 1119–1125. [[CrossRef](#)]
262. Li, H.; Wu, X.; Yang, B.; Li, J.; Xu, L.; Liu, H.; Li, S.; Xu, J.; Yang, M.; Wei, M. Evaluation of biomimetically synthesized mesoporous silica nanoparticles as drug carriers: Structure, wettability, degradation, biocompatibility and brain distribution. *Mater. Sci. Eng. C Mater. Biol. Appl.* **2019**, *94*, 453–464. [[CrossRef](#)] [[PubMed](#)]
263. Naik, S.P.; Elangovan, S.P.; Tatsuya, O.; Sokolov, I. Morphology control of mesoporous silica particles. *J. Phys. Chem. C* **2007**, *111*, 11168–11173. [[CrossRef](#)]
264. Frickenstein, A.N.; Hagood, J.M.; Britten, C.N.; Abbott, B.S.; McNally, M.W.; Vopat, C.A.; Patterson, E.G.; MacCuaig, W.M.; Jain, A.; Walters, K.B.; et al. Mesoporous Silica Nanoparticles: Properties and Strategies for Enhancing Clinical Effect. *Pharmaceutics* **2021**, *13*, 570. [[CrossRef](#)]
265. Tang, F.; Li, L.; Chen, D. Mesoporous silica nanoparticles: Synthesis, biocompatibility and drug delivery. *Adv. Mater.* **2012**, *24*, 1504–1534. [[CrossRef](#)]
266. Küçüktürkmen, B.; Rosenholm, J.M. Mesoporous Silica Nanoparticles as Carriers for Biomolecules in Cancer Therapy. *Adv. Exp. Med. Biol.* **2021**, *1295*, 99–120.
267. He, Q.; Zhang, Z.; Gao, Y.; Shi, J.; Li, Y. Intracellular localization and cytotoxicity of spherical mesoporous silica nano- and microparticles. *Small* **2009**, *5*, 2722–2729. [[CrossRef](#)] [[PubMed](#)]
268. Cho, M.; Cho, W.S.; Choi, M.; Kim, S.J.; Han, B.S.; Kim, S.H.; Kim, H.O.; Sheen, Y.Y.; Jeong, J. The impact of size on tissue distribution and elimination by single intravenous injection of silica nanoparticles. *Toxicol. Lett.* **2009**, *189*, 177–183. [[CrossRef](#)] [[PubMed](#)]
269. Lu, F.; Wu, S.H.; Hung, Y.; Mou, C.Y. Size effect on cell uptake in well-suspended, uniform mesoporous silica nanoparticles. *Small* **2009**, *5*, 1408–1413. [[CrossRef](#)] [[PubMed](#)]
270. Huang, X.; Li, L.; Liu, T.; Hao, N.; Liu, H.; Chen, D.; Tang, F. The shape effect of mesoporous silica nanoparticles on biodistribution, clearance, and biocompatibility in vivo. *ACS Nano* **2011**, *5*, 5390–5399. [[CrossRef](#)] [[PubMed](#)]
271. Lin, Y.S.; Haynes, C.L. Impacts of mesoporous silica nanoparticle size, pore ordering, and pore integrity on hemolytic activity. *J. Am. Chem. Soc.* **2010**, *132*, 4834–4842. [[CrossRef](#)] [[PubMed](#)]
272. Mellaerts, R.; Aerts, C.A.; Van Humbeeck, J.; Augustijns, P.; Van den Mooter, G.; Martens, J.A. Enhanced release of itraconazole from ordered mesoporous SBA-15 silica materials. *Chem. Commun.* **2007**, *13*, 1375–1377. [[CrossRef](#)]
273. Pontón, I.; Del Rio, A.M.; Gómez, M.G.; Sánchez-García, D. Preparation and Applications of Organo-Silica Hybrid Mesoporous Silica Nanoparticles for the Co-Delivery of Drugs and Nucleic Acids. *Nanomaterials* **2020**, *10*, 2466. [[CrossRef](#)]
274. Wong, R.C.H.; Ng, D.K.P.; Fong, W.P.; Lo, P.C. Encapsulating pH-responsive doxorubicin-phthalocyanine conjugates in mesoporous silica nanoparticles for combined photodynamic therapy and controlled chemotherapy. *Chem. Eur. J.* **2017**, *23*, 16505–16515. [[CrossRef](#)]
275. Heleg-Shabtai, V.; Aizen, R.; Sharon, E.; Sohn, Y.S.; Trifonov, A.; Enkin, N.; Freage, L.; Nechushtai, R.; Willner, I. Gossypol-Capped Mitoxantrone-Loaded Mesoporous SiO<sub>2</sub> NPs for the Cooperative Controlled Release of Two Anti-Cancer Drugs. *ACS Appl. Mater. Interfaces* **2016**, *8*, 14414–14422. [[CrossRef](#)]
276. Croissant, J.G.; Fatieiev, Y.; Khashab, N.M. Degradability and Clearance of Silicon, Organosilica, Silsesquioxane, Silica Mixed Oxide, and Mesoporous Silica Nanoparticles. *Adv. Mater.* **2017**, *29*, 1604634. [[CrossRef](#)] [[PubMed](#)]

277. Ma, X.; Zhao, Y.; Ng, K.W.; Zhao, Y. Integrated Hollow Mesoporous Silica Nanoparticles for Target Drug/siRNA Co-Delivery. *Chem. Eur. J.* **2013**, *19*, 15593–15603. [[CrossRef](#)] [[PubMed](#)]
278. Meng, H.; Liang, M.; Xia, T.; Li, Z.; Ji, Z.; Zink, J.I.; Nel, A.E. Engineered design of mesoporous silica nanoparticles to deliver doxorubicin and P-glycoprotein siRNA to overcome drug resistance in a cancer cell line. *ACS Nano* **2010**, *4*, 4539–4550. [[CrossRef](#)] [[PubMed](#)]
279. Shahin, S.A.; Wang, R.; Simargi, S.I.; Contreras, A.; Echavarria, L.P.; Qu, L.; Wen, W.; Dellinger, T.; Unternaehrer, J.; Tamanoi, F.; et al. Hyaluronic acid conjugated nanoparticle delivery of siRNA against TWIST reduces tumor burden and enhances sensitivity to cisplatin in ovarian cancer. *Nanomedicine* **2018**, *4*, 1381–1394. [[CrossRef](#)] [[PubMed](#)]
280. Deaconu, M.; Nicu, I.; Tincu, R.; Brezoiu, A.M.; Mitran, R.A.; Vasile, E.; Matei, C.; Berger, D. Tailored doxycycline delivery from MCM-41-type silica carriers. *Chem. Pap.* **2018**, *72*, 1869–1880. [[CrossRef](#)]
281. Liu, J.; Zhang, B.; Luo, Z.; Ding, X.; Li, J.; Dai, L.; Zhou, J.; Zhao, X.; Ye, J.; Cai, K. Enzyme responsive mesoporous silica nanoparticles for targeted tumor therapy in vitro and in vivo. *Nanoscale* **2015**, *7*, 3614–3626. [[CrossRef](#)]
282. Zhou, X.; Chen, L.; Nie, W.; Wang, W.; Qin, M.; Mo, X.; Wang, H.; He, C. Dual-Responsive Mesoporous Silica Nanoparticles Mediated Codelivery of Doxorubicin and Bcl-2 SiRNA for Targeted Treatment of Breast Cancer. *J. Phys. Chem. C* **2016**, *120*, 22375–22387. [[CrossRef](#)]
283. Wang, Y.; Han, N.; Zhao, Q.; Bai, L.; Li, J.; Jiang, T.; Wang, S. Redox-responsive mesoporous silica as carriers for controlled drug delivery: A comparative study based on silica and PEG gatekeepers. *Eur. J. Pharm. Sci.* **2015**, *72*, 12–20. [[CrossRef](#)]
284. Han, L.; Tang, C.; Yin, C. Dual-targeting and pH/redox-responsive multi-layered nanocomplexes for smart co-delivery of doxorubicin and siRNA. *Biomaterials* **2015**, *60*, 42–52. [[CrossRef](#)]
285. Nguyen, C.T.; Webb, R.I.; Lambert, L.K.; Strounina, E.; Lee, E.C.; Parat, M.O.; McGuckin, M.A.; Popat, A.; Cabot, P.J.; Ross, B.P. Bifunctional Succinylated  $\epsilon$ -Polylysine-Coated Mesoporous Silica Nanoparticles for pH-Responsive and Intracellular Drug Delivery Targeting the Colon. *ACS Appl. Mater. Interfaces* **2017**, *9*, 9470–9483. [[CrossRef](#)]
286. Bhat, R.; Ribes, À.; Mas, N.; Aznar, E.; Sancenón, F.; Marcos, M.D.; Murguía, J.R.; Venkataraman, A.; Martínez-Máñez, R. Thrombin-Responsive Gated Silica Mesoporous Nanoparticles As Coagulation Regulators. *Langmuir* **2016**, *32*, 1195–1200. [[CrossRef](#)] [[PubMed](#)]
287. Xiong, L.; Bi, J.; Tang, Y.; Qiao, S.Z. Magnetic Core-Shell Silica Nanoparticles with Large Radial Mesopores for siRNA Delivery. *Small* **2016**, *12*, 4735–4742. [[CrossRef](#)] [[PubMed](#)]
288. Hartono, S.B.; Yu, M.; Gu, W.; Yang, J.; Strounina, E.; Wang, X.; Qiao, S.; Yu, C. Synthesis of multi-functional large pore mesoporous silica nanoparticles as gene carriers. *Nanotechnology* **2014**, *25*, 055701. [[CrossRef](#)] [[PubMed](#)]
289. Bathfield, M.; Reboul, J.; Cacciaguerra, T.; Lacroix-Desmazes, P.; Gérardin, C. Thermosensitive and Drug-Loaded Ordered Mesoporous Silica: A Direct and Effective Synthesis Using PEO-b-PNIPAM Block Copolymers. *Chem. Mater.* **2016**, *28*, 3374–3384. [[CrossRef](#)]
290. Eltohamy, M.; Seo, J.W.; Hwang, J.Y.; Jang, W.C.; Kim, H.W.; Shin, U.S. Ionic and thermo-switchable polymer-masked mesoporous silica drug-nanocarrier: High drug loading capacity at 10 °C and fast drug release completion at 40 °C. *Colloids Surf. B BioInterfaces* **2016**, *144*, 229–237. [[CrossRef](#)] [[PubMed](#)]
291. Liu, J.; Detrembleur, C.; De Pauw-Gillet, M.C.; Mornet, S.; Jérôme, C.; Duguet, E. Gold nanorods coated with mesoporous silica shell as drug delivery system for remote near infrared light-activated release and potential phototherapy. *Small* **2015**, *11*, 2323–2332. [[CrossRef](#)]
292. Salinas, Y.; Brüggemann, O.; Monkowius, U.; Teasdale, I. Visible Light Photocleavable Ruthenium-Based Molecular Gates to Reversibly Control Release from Mesoporous Silica Nanoparticles. *Nanomaterials* **2020**, *10*, 1030. [[CrossRef](#)]
293. Iijima, S. Helical microtubules of graphitic carbon. *Nature* **1991**, *354*, 56. [[CrossRef](#)]
294. Baughman, R.H.; Zakhidov, A.A.; de Heer, W.A. Carbon nanotubes—the route toward applications. *Science* **2002**, *297*, 787–792. [[CrossRef](#)]
295. Lay, C.L.; Liu, H.Q.; Tan, H.R.; Liu, Y. Delivery of paclitaxel by physically loading onto poly(ethylene glycol) (PEG)-graft-carbon nanotubes for potent cancer therapeutics. *Nanotechnology* **2010**, *21*, 065101. [[CrossRef](#)]
296. Costa, P.M.; Bourgognon, M.; Wang, J.T.; Al-Jamal, K.T. Functionalised carbon nanotubes: From intracellular uptake and cell-related toxicity to systemic brain delivery. *J. Control. Release* **2016**, *241*, 200–219. [[CrossRef](#)]
297. Liu, X.; Tao, H.; Yang, K.; Zhang, S.; Lee, S.T.; Liu, Z. Optimization of surface chemistry on single-walled carbon nanotubes for in vivo photothermal ablation of tumors. *Biomaterials* **2011**, *32*, 144–151. [[CrossRef](#)]
298. Dizaji, B.F.; Khoshbakht, S.; Farboudi, A.; Azarbaijan, M.H.; Irani, M. Far-reaching advances in the role of carbon nanotubes in cancer therapy. *Life Sci.* **2020**, *257*, 118059. [[CrossRef](#)]
299. Saeednia, L.; Yao, L.; Cluff, K.; Asmatulu, R. Sustained Releasing of Methotrexate from Injectable and Thermosensitive Chitosan-Carbon Nanotube Hybrid Hydrogels Effectively Controls Tumor Cell Growth. *ACS Omega* **2019**, *4*, 4040–4048. [[CrossRef](#)]
300. Karimi, M.; Solati, N.; Amiri, M.; Mirshekari, H.; Mohamed, E.; Taheri, M.; Hashemkhani, M.; Saeidi, A.; Estiar, M.A.; Kiani, P.; et al. Carbon nanotubes part I: Preparation of a novel and versatile drug-delivery vehicle. *Expert Opin. Drug Deliv.* **2015**, *12*, 1071–1087. [[CrossRef](#)]
301. Salas-Trevino, D.; Saucedo-Cardenas, O.; de Jesus Loera-Arias, M.; De Casas-Ortiz, E.G.; Rodriguez-Rocha, H.; Garcia-Garcia, A.; Montes-de-Oca-Luna, R.; Soto-Dominguez, A. Carbon nanotubes: An alternative for platinum-based drugs delivery systems. *J. BU ON* **2018**, *23*, 541–549.



302. Hassan, H.A.F.M.; Diebold, S.S.; Smyth, L.A.; Walters, A.A.; Lombardi, G.; Al-Jamal, K.T. Application of carbon nanotubes in cancer vaccines: Achievements, challenges and chances. *J. Control. Release* **2019**, *297*, 79–90. [[CrossRef](#)]
303. Tsukahara, T.; Matsuda, Y.; Usui, Y.; Haniu, H. Highly purified, multi-wall carbon nanotubes induce light-chain3B expression in human lung cells. *Biochem. Biophys. Res. Commun.* **2013**, *440*, 348–453. [[CrossRef](#)]
304. Dumortier, H.; Lacotte, S.; Pastorin, G.; Marega, R.; Wu, W.; Bonifazi, D.; Briand, J.P.; Prato, M.; Muller, S.; Bianco, A. Functionalized carbon nanotubes are non-cytotoxic and preserve the functionality of primary immune cells. *Nano Lett.* **2006**, *6*, 1522–1528. [[CrossRef](#)]
305. Kang, B.; Chang, S.; Dai, Y.; Yu, D.; Chen, D. Cell response to carbon nanotubes: Size-dependent intracellular uptake mechanism and subcellular fate. *Small* **2010**, *6*, 2362–2366. [[CrossRef](#)]
306. Bekyarova, E.; Ni, Y.; Malarkey, E.B.; Montana, V.; McWilliams, J.L.; Haddon, R.C.; Parpura, V. Applications of Carbon Nanotubes in Biotechnology and Biomedicine. *J. Biomed. Nanotechnol.* **2005**, *1*, 3–17. [[CrossRef](#)]
307. Martincic, M.; Tobias, G. Filled carbon nanotubes in biomedical imaging and drug delivery. *Expert Opin. Drug Deliv.* **2014**, *12*, 563–581. [[CrossRef](#)]
308. Comparetti, E.J.; Pedrosa, V.A.; Kaneno, R. Carbon Nanotube as a Tool for Fighting Cancer. *Bioconjug. Chem.* **2018**, *29*, 709–718. [[CrossRef](#)] [[PubMed](#)]
309. Son, K.H.; Hong, J.H.; Lee, J.W. Carbon nanotubes as cancer therapeutic carriers and mediators. *Int. J. Nanomed.* **2016**, *11*, 5163–5185. [[CrossRef](#)]
310. Mo, Y.; Wang, H.; Liu, J.; Lan, Y.; Guo, R.; Zhang, Y.; Xue, W.; Zhang, Y. Controlled release and targeted delivery to cancer cells of doxorubicin from polysaccharide-functionalised single-walled carbon nanotubes. *J. Mater. Chem. B* **2015**, *3*, 1846–1855. [[CrossRef](#)]
311. Alidori, S.; Asqiriba, K.; Londero, P.; Bergkvist, M.; Leona, M.; Scheinberg, D.A.; McDevitt, M.R. Deploying RNA and DNA with Functionalized Carbon Nanotubes. *J. Phys. Chem. C Nanomater. Interfaces* **2013**, *117*, 5982–5992. [[CrossRef](#)]
312. Singh, N.; Sachdev, A.; Gopinath, P. Polysaccharide Functionalized Single Walled Carbon Nanotubes as Nanocarriers for Delivery of Curcumin in Lung Cancer Cells. *J. Nanosci. Nanotechnol.* **2018**, *18*, 1534–1541. [[CrossRef](#)]
313. Cao, Y.; Huang, H.Y.; Chen, L.Q.; Du, H.H.; Cui, J.H.; Zhang, L.W.; Lee, B.J.; Cao, Q.R. Enhanced Lysosomal Escape of pH-Responsive Polyethylenimine-Betaine Functionalized Carbon Nanotube for the Codelivery of Survivin Small Interfering RNA and Doxorubicin. *ACS Appl. Mater. Interfaces* **2019**, *11*, 9763–9776. [[CrossRef](#)] [[PubMed](#)]
314. Lu, Y.J.; Wei, K.C.; Ma, C.C.; Yang, S.Y.; Chen, J.P. Dual targeted delivery of doxorubicin to cancer cells using folate-conjugated magnetic multi-walled carbon nanotubes. *Colloids Surf. B Biointerfaces* **2012**, *89*, 1–9. [[CrossRef](#)] [[PubMed](#)]
315. Li, J.; Yap, S.Q.; Yoong, S.L.; Nayak, T.R.; Chandra, G.W.; Ang, W.H.; Panczyk, T.; Ramaprabhu, S.; Vashist, S.K.; Sheu, F.S.; et al. Carbon nanotube bottles for incorporation, release and enhanced cytotoxic effect of cisplatin. *Carbon* **2019**, *50*, 1625–1634. [[CrossRef](#)]
316. Cirillo, G.; Vittorio, O.; Kunhardt, D.; Valli, E.; Voli, F.; Farfalla, A.; Curcio, M.; Spizzirri, U.G.; Hampel, S. Combining Carbon Nanotubes and Chitosan for the Vectorization of Methotrexate to Lung Cancer Cells. *Materials* **2019**, *12*, 2889. [[CrossRef](#)]
317. Eldridge, B.N.; Bernish, B.W.; Fahrenholtz, C.D.; Singh, R. Photothermal therapy of glioblastoma multiforme using multiwalled carbon nanotubes optimized for diffusion in extracellular space. *ACS Biomater. Sci. Eng.* **2016**, *2*, 963–976. [[CrossRef](#)]

## Article

# Novel Poly(Methylenelactide-g-L-Lactide) Graft Copolymers Synthesized by a Combination of Vinyl Addition and Ring-Opening Polymerizations

Tanyaluck Mekpothi <sup>1,2</sup>, Puttinan Meepowpan <sup>1,2,3</sup>, Montira Sriyai <sup>3,4,5</sup>, Robert Molloy <sup>4,5</sup> and Winita Punyodom <sup>1,2,3,4,5,\*</sup>

<sup>1</sup> Department of Chemistry, Faculty of Science, Chiang Mai University, Chiang Mai 50200, Thailand; tanyaluck01@hotmail.com (T.M.); pmeepowpan@gmail.com (P.M.)

<sup>2</sup> Center of Excellence for Innovation in Chemistry (PERCH-CIC), Faculty of Science, Chiang Mai University, Chiang Mai 50200, Thailand

<sup>3</sup> Bioplastics Production Laboratory for Medical Applications, Faculty of Science, Chiang Mai University, Chiang Mai 50200, Thailand; msriyai@yahoo.com

<sup>4</sup> Center of Excellence in Materials Science and Technology, Chiang Mai University, Chiang Mai 50200, Thailand; bob.chiangmai@gmail.com

<sup>5</sup> Materials Science Research Center, Faculty of Science, Chiang Mai University, Chiang Mai 50200, Thailand

\* Correspondence: winitacmu@gmail.com

**Citation:** Mekpothi, T.; Meepowpan, P.; Sriyai, M.; Molloy, R.; Punyodom, W. Novel Poly(Methylenelactide-g-L-Lactide) Graft Copolymers Synthesized by a Combination of Vinyl Addition and Ring-Opening Polymerizations. *Polymers* **2021**, *13*, 3374. <https://doi.org/10.3390/polym13193374>

Academic Editors: José Miguel Ferri, Vicent Fombuena Borrás and Miguel Fernando Aldás Carrasco

Received: 27 August 2021

Accepted: 21 September 2021

Published: 30 September 2021

**Publisher's Note:** MDPI stays neutral with regard to jurisdictional claims in published maps and institutional affiliations.



**Copyright:** © 2021 by the authors. Licensee MDPI, Basel, Switzerland. This article is an open access article distributed under the terms and conditions of the Creative Commons Attribution (CC BY) license (<https://creativecommons.org/licenses/by/4.0/>).

**Abstract:** In this work, a novel poly (methylenelactide-g-L-lactide), P(MLA-g-LLA) graft copolymer was synthesized from poly(methylenelactide) (PMLA) and L-lactide (LLA) using 0.03 mol% liquid tin(II) *n*-butoxide (Sn(*On*Bu)<sub>2</sub>) as an initiator by a combination of vinyl addition and ring-opening polymerization (ROP) at 120 °C for 72 h. Proton and carbon-13 nuclear magnetic resonance spectroscopy (<sup>1</sup>H- and <sup>13</sup>C-NMR) and Fourier-transform infrared spectroscopy (FT-IR) confirmed the grafted structure of P(MLA-g-LLA). The P(MLA-g-LLA) melting temperatures (*T*<sub>m</sub>) range of 144–164 °C, which was lower than that of PLA (170–180 °C), while the thermal decomposition temperature (*T*<sub>d</sub>) of around 314–335 °C was higher than that of PLA (approx. 300 °C). These results indicated that the grafting reaction could widen the melt processing range of PLA and in doing so increase PLA's thermal stability during melt processing. The graft copolymers were obtained with weight-average molecular weights ( $\overline{M}_w$ ) = 4200–11,000 g mol<sup>-1</sup> and a narrow dispersity (*D* = 1.1–1.4).

**Keywords:** vinyl addition polymerization; ring-opening polymerization (ROP); bromolactide; methylenelactide; poly(methylenelactide); poly(methylenelactide-g-L-lactide); thermal stability

## 1. Introduction

Poly(lactic acid) or polylactide (PLA), an aliphatic polyester derived from renewable starch-containing resources such as corn; sugar beet; and cassava, is one of the most significant biodegradable polymers extensively used as a petroleum-based materials replacement due to its biodegradability and environmentally-friendly properties [1–11]. However, it has been commonly known that PLA shows brittleness with poor melt strength and thermal stability which limit its processability and performance in desired applications [12–20]. For instance, PLA has been reported to show a rather low heat deflection temperature (HDT) of approximately 55 °C because of the low degree of crystallinity of PLA materials resulting from the low crystallization rate while processing [21–25]. Since these drawbacks in toughness and heat resistance confine specific applications of PLA, thereby, many attempts for improving PLA inferior properties via various modification methods have been investigated over the past decades [26,27]. The strategies include annealing, nucleating agents, plasticization, chain extending, copolymerization, blending, polymer (nano)composites, stereocomplexes, crosslinking, and functionalization [27–33].

For the modification of PLA by copolymerization, most studies have been paying attention to the copolymerizing of the lactide with either lactide/lactone monomers or other monomers with functional groups such as amino and carboxylic groups, etc [34–36]. The copolymers such as poly(lactide-*co*-glycolide) (PLGA), poly(lactide-*co*- $\epsilon$ -caprolactone) (PLCL), poly(lactic acid)-poly(ethylene oxide) (PLA-PEO) and poly(lactic acid-glutamic acid) (PLGM) are generally synthesized via ring-opening polymerization (ROP) of cyclic ester monomers [37–39]. These copolymers could synergistically combine the advantages of both components showing greater properties, thus, overcome the limitations of the individual ones. Similar to the homopolymerization process, the copolymerization consists of three stages: (1) initiation, (2) propagation, and (3) termination [40]. The copolymer molecules contain two different repeating units in which different monomers can be arranged in various types such as random, alternating, block and graft copolymers [41]. As such, a graft copolymer is one of the most widely used methods for a modification of PLA to achieve improved properties such as processability and physicochemical properties since it can produce a large variety of polymers with different properties for widely used in many applications [42–45]. For the synthesis of a well-defined graft copolymer, there are substantial difficulties in achieving precise control over its specific end groups, microstructure, and composition [46]. Therefore, the experimental conditions must be optimized in order to obtain the suitable polymerization process for the designed system.

O-heterocyclic monomers such as lactide (LA) and methylenelactide (MLA) functionalities are of interest to be used as functional materials due to their potential to be selectively polymerized via either vinyl-addition or ring-opening pathways [47–49]. Since PLA does not bear any functional groups, many efforts for synthesizing new alkyl modified lactides have been made aiming to modulate the physicochemical properties such as glass transition temperature ( $T_g$ ), toughness, thermal stability, and processability [34,50–53]. However, certain endeavors for chemical modifications of lactide are scarce because of fast ester bonds hydrolysis [54–56].

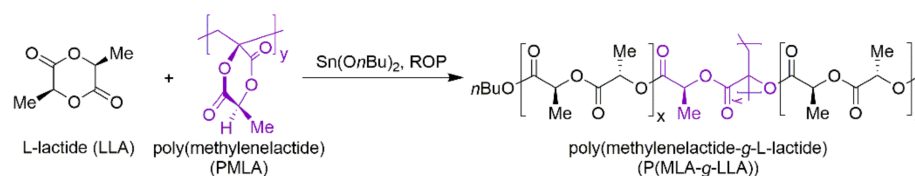
In contrast to lactide, methylenelactide (MLA, 3-methylene-6-methyl-1,4-dioxane-2,5-dione) represents a free radical polymerizable derivative of lactide. In 1969, the synthesis of a methylene-functional lactide from the monobromination of lactide using *N*-bromosuccinimide (NBS) followed by base-catalysed dehydrobromination (HBr elimination) was studied for the first time by Scheibelhoffer et al. [57]. Moreover, from the work of Miyake and coworkers [48], it was found that MLA could be polymerized by a radical vinyl-addition. ROP pathways, however, resulted in monomer decomposition to produce nonpolymerizable derivatives instead. Nonetheless, Jiang and Hillmyer [54] showed that further derivatization of MLA could provide functional monomers for ROP using MLA as a dienophile in a Diels–Alder reaction with cyclopentadiene. The resultant tricyclic product could be polymerized by either ROP of the lactide ring or via ring-opening metathesis polymerization (ROMP). Afterwards, Hillmyer and coworkers continued exploring other dienes to gather more data on functional lactide monomers, and further polymerization provided new polyesters with diverse thermal properties [55].

Recently, Britner and Ritter [58,59] reinvestigated Scheibelhoffer's first study of a radical polymerizable lactide derivative with respect to polymerization and polymer analogous aminolysis under mild conditions. In this work, the optically active MLA was polymerized by free radical polymerization in solution using AIBN as an initiator and resulted in isotactic-biased atactic optically active poly(methylenelactide) (PMLA) with molecular weights ranging between  $4 \times 10^4$ – $1 \times 10^5$  g mol<sup>-1</sup> with dispersity,  $D \sim 2.5$  and a  $T_g$  of 244 °C. Britner and Ritter also performed a further study on free-radical polymerization, copolymerization, and controlled radical polymerization of the cyclic monomer MLA in comparison to the non-cyclic monomer  $\alpha$ -acetoxyacrylate (AA). The results showed that MLA undergoes a self-initiated polymerization. Moreover, in this study, reversible addition fragmentation chain transfer (RAFT)-controlled homopolymerization of MLA and copolymerization with *N,N*-dimethylacrylamide (DMAA) was performed at 70 °C in

1,4-dioxane using AIBN and 2-(((ethylthio)carbonothioyl)thio)-2-methylpropanoic acid as an initiator and a transfer agent respectively.

Derivatization of MLA via the Diels–Alder cycloaddition with dienes leads to bifunctional monomers that can be polymerized into various functionalized PLA materials. The need for functionalized PLA materials with enhanced physical and mechanical properties has led to an effective strategy to derivatize PLA, which is synthesized through a bromination of L-lactide (LLA) with *N*-bromosuccinimide using benzoyl peroxide as an initiator and followed by a basic HBr elimination with Et<sub>3</sub>N in dichloromethane to produce a monomer MLA. After that, MLA was used as a substrate of PMLA synthesis which was then synthesized through a vinyl-addition polymerization with AIBN initiator via the free radical polymerization. According to previous works, PMLA has poor solubility, sluggish dissolution, and that it is challenging to handle the polymer as a melt for polymerization. As previously mentioned, Britner et al. [58,59] have found a way to overcome this challenge by PMLA functionalization. In the underlying study, Britner and Ritter focused on spatial effects with respect to interactions between neighboring lactide rings. Moreover, it was found that the PMLA attached lactide rings react like activated esters and thus readily undergo quantitative amidation reactions with aliphatic primary amines under mild conditions. However, up to present, no information on the copolymerization of MLA and LLA via the ROP has been reported [54–56,58–62].

Accordingly, the main objective of this study was to synthesize poly(methylenelactide-*g*-L-lactide), P(MLA-*g*-LLA), graft copolymers from L-lactide (LLA) and PMLA via ROP in solution using a novel soluble liquid tin(II) *n*-butoxide (Sn(*On*Bu)<sub>2</sub>) as an initiator [63–68]. These materials have not been previously reported in the literature. The synthesis reaction of a P(MLA-*g*-LLA) via ROP and its chemical structure are shown in Scheme 1. The intended application of these graft copolymers is as potentially reactive, network-bound (by transesterification) additives to improve the melt processability and thermal properties of commercial PLA.



**Scheme 1.** The synthesis of poly(methylenelactide-*g*-L-lactide), P(MLA-*g*-LLA), via ROP.

## 2. Materials and Methods

### 2.1. Materials

L-lactide (LLA) and liquid tin(II) *n*-butoxide (Sn(*On*Bu)<sub>2</sub>) were purchased from the Bioplastics Production Laboratory for Medical Applications (ISO 13485:2016 TÜV SÜD America Accredited Laboratory, Chiang Mai University, Chiang Mai, Thailand) and used as received [64]. Benzoyl peroxide (75%), triethylamine ( $\geq 99\%$ ), calcium hydride (90–95%), and azobisisobutyronitrile (AIBN) were purchased from Sigma-Aldrich (Saint Louis, MO, USA). *N*-bromosuccinimide (99%) was purchased from Acros (Geel, Belgium). Magnesium sulfate anhydrous (96%) was purchased from PanReac AppliChem (Barcelona, Spain). Sodium bisulfite (58.5–67.4%) was purchased from HiMedia (Mumbai, India). 1,2-Dichlorobenzene ( $\geq 98\%$ ) was purchased from Carlo Erba (Milano, Italy). Chloroform-*d*<sub>1</sub> (99.8% CDCl<sub>3</sub>) and dimethyl sulfoxide-*d*<sub>6</sub> (99.9% DMSO) were purchased from CIL (Kolkata, India). Chloroform (99.8%) and hydrochloric acid (37%) were purchased from RCI Labscan (Bangkok, Thailand). Methanol, dichloromethane, ethyl acetate, and *n*-hexane (RCI Labscan) were purified by distillation prior to use.

### 2.2. Methods

In this study, bromolactide (Br-LA) and methylenelactide (MLA) were synthesized according to literature procedures reported by Britner and Ritter [58] with minor modifications.

### 2.2.1. Synthesis of Bromolactide (Br-LA)

L-lactide (120.0 g, 832.6 mmol), *N*-bromosuccinimide (164.0 g, 921.4 mmol), and dichloromethane (600 mL) were added into a 1 L three-neck round-bottom flask equipped with a magnetic stirring bar, septum stoppers, and a reflux condenser. The reaction mixture was refluxed at 80 °C with continuous stirring, benzoyl peroxide (4.020 g, 16.60 mmol) in a 60 mL dichloromethane was then gradually added to the mixture solution. The mixture continued to be heated under reflux at 80 °C for 72 h and allowed to cool to room temperature. The precipitate was filtered off through the filter paper several times until a clear filtrate was obtained. The filtrate was then vacuum dried using a rotary evaporator (Heidolph, Hei-VAP Core, Schwabach, Germany) to yield a yellow solid residue. The yellow solid was dissolved in a 450 mL dichloromethane before pouring into a separatory funnel and washing with 0.2 M sodium bisulfite three times ( $3 \times 1000$  mL) and once (900 mL) with saturated sodium chloride. Subsequently, the organic layer was dried over  $\text{MgSO}_4$  and evaporated under reduced pressure to obtain a pale yellow needle-like crystal. The Br-LA product was then purified by recrystallization from the mixture of dichloromethane and *n*-hexane (1:1), filtered off, and vacuum dried at room temperature.

### 2.2.2. Synthesis of Methylene lactide (MLA)

For the preparation of methylene lactide (MLA), 10.00 g (44.84 mmol) of the synthesized Br-LA product from Section 2.2.1 and 20 mL of dichloromethane were added into a 250 mL three-neck round-bottom flask. The solution was stirred under an inert ( $\text{N}_2$ ) atmosphere and cooled to 0 °C using an ice bath. Triethylamine (2.0 mL, 14.33 mmol) was then added dropwise to a solution and the mixture was kept stirring at 0 °C for 2 h and at room temperature for 1 h. The reaction mixture was washed with 150 mL of 1 M HCl (three times) and saturated sodium chloride (once) successively, dried over  $\text{MgSO}_4$ , evaporated, and dried under vacuum to obtain the MLA product as a yellowish-brown solid.

### 2.2.3. Synthesis of Poly(methylene lactide) (PMLA)

In this work, the preparation of poly(methylene lactide) (PMLA) was followed the method as described by Miyake et al. [48]. Firstly, a 100 mL round-bottom flask equipped with a magnetic stirring, methylene lactide (4.000 g, 28.15 mmol) and 50 mL of 1,2-dichlorobenzene (*o*-DCB) was added and the reaction mixture was purged with  $\text{N}_2$  for 30 min. Then, various required amounts of AIBN (5, 10, 15, 20, and 25 mol%) was added and the flask was sealed with a rubber septum. The reaction flask was then immersed in a silicone oil bath at 75 °C for 1 h. The reaction solution was quench cooled and then poured into 800 mL of methanol to obtain the polymer precipitate. The PMLA polymer was isolated by filtration, washed extensively with methanol and dried to constant weight in a vacuum oven at 50 °C overnight to constant weight.

### 2.2.4. Synthesis of Poly(methylene lactide-*g*-L-lactide) (P(MLA-*g*-LLA)) via Solution Polymerization

Poly(methylene lactide-*g*-L-lactide) (P(MLA-*g*-LLA) with the composition ratio of PMLA to LLA = 1:30 and 1:50 *w/w* and the composition ratio of 1:300, 1:600 *w/w* for PMLA (20 mol% AIBN) was synthesized via ring-opening polymerization (ROP). Firstly, PMLA and LLA with 0.03 mol% liquid tin(II) *n*-butoxide ( $\text{Sn}(\text{OnBu})_2$ ) initiator, 2.0 mL of 1,2-dichlorobenzene (*o*-DCB), and a magnetic stirring bar were loaded into a round-bottom flask. The solution polymerization of P(MLA-*g*-LLA) was carried out at 120 °C for 72 h, after which, the graft copolymers were purified by methanol. The graft polymer was again isolated by filtration, washed with more methanol, and dried in a vacuum oven at 50 °C overnight to constant weight.

### 2.2.5. Synthesis of Poly(L-lactide) (PLA) via Solution Polymerization

L-lactide (10.00 g) with 0.03 mol% of liquid  $\text{Sn}(\text{OnBu})_2$  initiator, 5.0 mL of 1,2-dichlorobenzene (*o*-DCB), and a magnetic stirring bar were loaded into a round-bottom

flask. Solution polymerization of PLA was carried out at 120 °C for 72 h under vacuum. The crude PLA product was purified by precipitation in methanol, in filtration, washing with more methanol, and drying in a vacuum oven at 50 °C overnight to constant weight.

### 2.3. Instrumental Methods

IR spectra were recorded using an attenuated total reflectance (ATR-FTIR model Nicolet™ iS5 (Thermo Scientific™, Waltham, MA, USA) spectrometer and the wavenumbers of maximum absorption peaks are reported in  $\text{cm}^{-1}$ .  $^1\text{H-NMR}$  (400 MHz) and  $^{13}\text{C-NMR}$  (100 MHz) were recorded on a Bruker DRX-400 spectrometer (Billerica, MA, USA). Where necessary, 2D NMR experiments (HMBC and HBQC) were carried out to assist the structure elucidation and signal assignments. Chemical shifts ( $\delta$ ) were reported in ppm down-field from TMS as an internal reference or with the solvent resonance as the internal standard ( $\text{CHCl}_3$  impurity in  $\text{CHCl}_3\text{-}d_1$ ,  $\delta$  7.26 and 77.0 ppm; DMSO impurity in  $\text{DMSO-}d_6$ , 2.50 and 39.52 ppm); data are reported in the following order: chemical shift, multiplicity and coupling constants ( $J$ ) are given in hertz. Splitting patterns are indicated as *s*, singlet; *d*, doublet; *t*, triplet; *m*, multiplet; *q*, quartet for  $^1\text{H-NMR}$  data. Broad peaks are denoted by *br* before the chemical shift multiplicity. Gel permeation chromatograph (GPC) analyses were carried out on Waters 2414 refractive index (RI) detector, equipped with Styragel HR5E 7.8 × 300 mm column (molecular weight resolving range = 2000–4,000,000). The GPC columns were eluted using tetrahydrofuran (THF) with a flow rate of 1.0  $\text{mL min}^{-1}$  at 40 °C with an injection volume of 100  $\mu\text{L}$ , a 30 min run time, and a toluene flow marker. Number-average molecular weights ( $\bar{M}_n$ ) and dispersity ( $\bar{D}$ ) of the polymers were determined based on calibration with polystyrene (PS) standards using Empower 3 Software. DSC measurements were performed on a Mettler-Toledo DSC-1 Differential Scanning Calorimeter (Columbus, OH, USA) under a flowing nitrogen ( $\text{N}_2$ ) atmosphere (20  $\text{mL min}^{-1}$ ). Prior to measurement, the instrument was calibrated using high purity (>99.999%) indium and tin standards and the data obtained were analyzed by using STARe Software v12.10. For each experiment, 3–5 mg of the polymer sample was weighed into a 50 mL aluminium pan and hermetically sealed. Measurements were performed at a heating rate of 10 °C  $\text{min}^{-1}$  over the temperature range of 0 to 280 °C for two heating cycles. In the first scan, the polymer was heated from 0 to 280 °C at a heating rate of 10 °C  $\text{min}^{-1}$ , hold at 280 °C for 3 min, then cooled to 0 °C at 10 °C  $\text{min}^{-1}$ , hold at this temperature for another 3 min, and reheated to 280 °C at a ramp of 10 °C  $\text{min}^{-1}$ . All of the transition temperature (i.e.,  $T_g$ ,  $T_c$ , and  $T_m$ ) values were obtained from the second scan after eliminating thermal history in the first scan. Degradation temperature ( $T_d$ ) values of the polymers were measured by thermal gravimetric analysis (TGA) method on a Perkin-Elmer TGA7 Thermogravimetric Analyzer (Pyris 1 Software). The TGA temperature and weight calibrations were performed using magnetic transition temperature standards: alumel, nickel, and perkallo (  $T_{\text{onset}}$  = 154.20, 355.30, and 596.00 °C) with high purity of 99.999% and a stainless steel standard weight (100 mg) respectively. For all measurements, the temperature range of 50 to 550 °C was scanned at a heating rate of 20 °C/min under dry  $\text{N}_2$  purge gas.

## 3. Results and Discussion

### 3.1. Synthesis of Bromolactide (Br-LA)

The purified Br-LA product of >99.5% purity (DSC) was obtained as a white, needle-like crystals in a percentage yield of ~60%. DSC results showed a narrow melting peak ( $T_m$ ) range of 104–112 °C.  $^1\text{H-NMR}$  (400 MHz,  $\text{CDCl}_3$ ,  $\delta$ ): 7.26 (*q*,  $J$  = 5.50 Hz, 1H; CH), (*s*,  $J$  = 2.33 Hz, 3H;  $\text{CH}_3$ ), (*d*,  $J$  = 1.73 Hz, 3H;  $\text{CH}_3$ );  $^{13}\text{C-NMR}$  (100 MHz,  $\text{CDCl}_3$ ,  $\delta$ ): 164.95 (C=O), 162.13 (C=O), 81.52 (quaternary carbon C), 73.87 (CH), 29.82 ( $\text{CH}_3$ ), 16.60 ( $\text{CH}_3$ ).

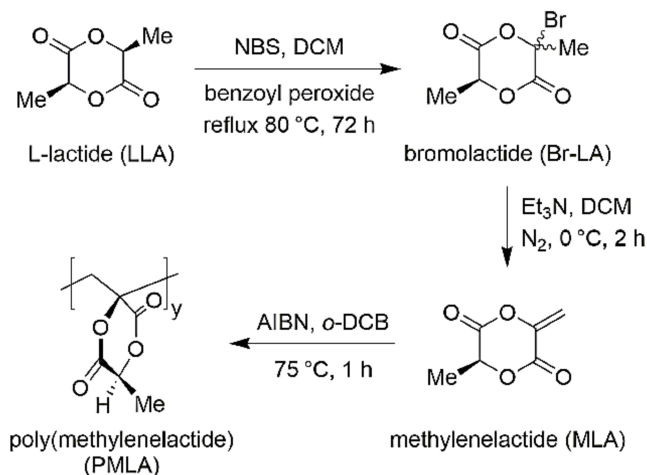
### 3.2. Synthesis of Methylene lactide (MLA)

The synthesized MLA product was obtained as a pale yellow solid (60% yield). However, a rather broad melting temperature range of 77–132 °C was observed indicating

the purity of < 95%.  $^1\text{H-NMR}$  (400 MHz,  $\text{CDCl}_3$ ,  $\delta$ ): 7.26 (d,  $J = 5.95$  Hz, 2H;  $\text{CH}_2$ ), (d,  $J = 5.55$  Hz, 2H;  $\text{CH}_2$ ), (q,  $J = 5.04$  Hz, 1H; CH), (m,  $J = 1.71$  Hz, 3H;  $\text{CH}_3$ );  $^{13}\text{C-NMR}$  (100 MHz,  $\text{CDCl}_3$ ,  $\delta$ ): 190.99 (C=O), 175.25 (C=O), 159.83 (quaternary carbon C), 110.68 ( $\text{CH}_2$ ), 69.86 (CH), 16.71 ( $\text{CH}_3$ ).

### 3.3. Synthesis of Poly(methylenelactide) (PMLA)

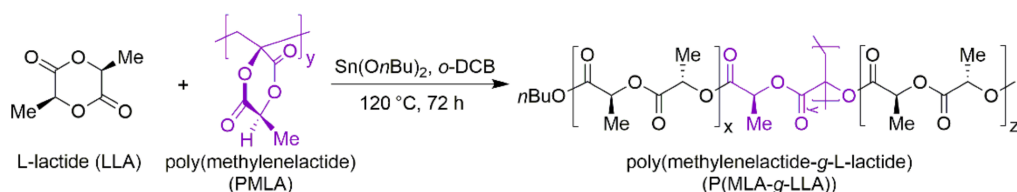
The synthetic pathway of PMLA is as shown in Scheme 2. From Scheme 2, it can be seen that, in the first step, Br-LA was synthesized via the bromination of LLA with *N*-bromosuccinimide using benzoyl peroxide as an initiator. The effect of the bromination reaction was the production of strong acids of hydrobromic acid (HBr) which was removed by using an excess of 0.2 M sodium bisulfite solution. Then, the MLA was synthesized via the elimination of Br-LA with triethylamine in dichloromethane. After that, the MLA was used as an initial substance in the synthesis of PMLA. It was found that PMLA was obtained as a white solid with a % yield of 60–65%.  $^1\text{H-NMR}$  (400 MHz,  $\text{DMSO-}d_6$ ,  $\delta$ ): 2.50 (broad q,  $J = 5.45$ – $5.46$  Hz, 1H; CH), (broad s,  $J = 3.35$ – $3.37$  Hz, 2H;  $\text{CH}_2$ ), (broad d,  $J = 1.41$ – $1.43$  Hz, 3H;  $\text{CH}_3$ );  $^{13}\text{C-NMR}$  (100 MHz,  $\text{DMSO-}d_6$ ,  $\delta$ ): 166.50 (C=O), 163.74 (C=O), 80.76 (CH), 72.77 (main-chain quaternary carbon C), 45.08 ( $\text{CH}_2$ ), 18.63 ( $\text{CH}_3$ ), which  $^1\text{H-}$  and  $^{13}\text{C-NMR}$  spectral data are identical to those previously published [48]; FT-IR ( $\text{cm}^{-1}$ ): 2449 and 1447 (w), 1747 (s), 1258 (s).



**Scheme 2.** Synthetic pathway of poly(methylenelactide) (PMLA).

### 3.4. Synthesis of Poly(methylenelactide-*g*-L-lactide) (P(MLA-*g*-LLA))

Scheme 3 shows the synthetic pathway of P(MLA-*g*-LLA). The physical appearances of the purified P(MLA-*g*-LLA) products from solution polymerization with the composition ratios of PMLA:LLA of 1:30 and 1:50 *w/w* were as white solids in ~90% yield. The copolymers were characterized in terms of their chemical structure by  $^1\text{H-NMR}$ .  $^1\text{H-NMR}$  (400 MHz,  $\text{CDCl}_3$ ,  $\delta$ ): 7.26 (q,  $J = 5.15$  Hz, 1H; CH), (q,  $J = 4.34$  Hz, 1H; CH), (broad m,  $J = 2.75$ – $4.25$  Hz, 2H;  $\text{CH}_2$ ), (m,  $J = 1.57$  Hz, 3H;  $\text{CH}_3$ );  $^{13}\text{C-NMR}$  (100 MHz,  $\text{CDCl}_3$ ,  $\delta$ ): 174.94 (C=O), 173.36 (C=O), 169.41 (C=O), 69.01 (CH), 68.77 ( $\text{CH}_2$ ), 68.18 (main-chain quaternary carbon C), 66.71 (CH), 20.30 ( $\text{CH}_3$ ), 16.45 ( $\text{CH}_3$ ); FT-IR ( $\text{cm}^{-1}$ ): 2997 and 1455 (w), 1755 (s), 1087 (s).



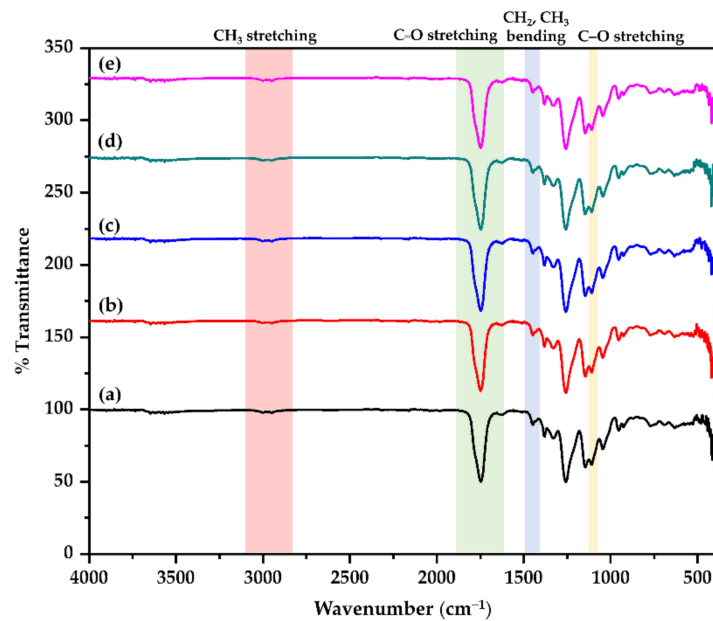
**Scheme 3.** Synthesis of poly(methylenelactide-*g*-L-lactide) (P(MLA-*g*-LLA)).

### 3.5. Synthesis of Poly(L-Lactide) (PLA)

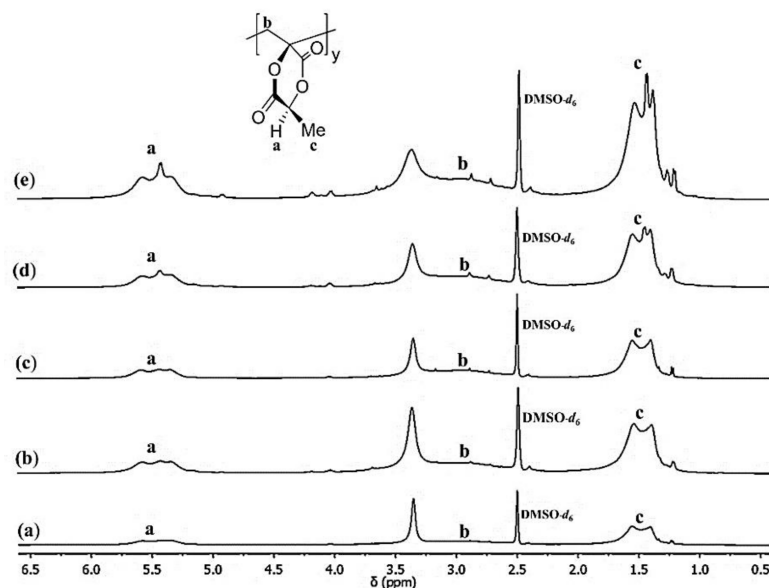
PLA was obtained as a white solid with a % yield of ~90%.  $^1\text{H-NMR}$  ( $\text{CDCl}_3$ , 400 MHz):  $\delta = 7.26$  (q,  $J = 5.16$  Hz, 1H; CH), (d,  $J = 1.58$  Hz, 3H;  $\text{CH}_3$ ) ppm;  $^{13}\text{C-NMR}$  ( $\text{CDCl}_3$ , 100 MHz  $\delta$ ): 169.73 (C=O), 69.14 (CH), 16.78 ( $\text{CH}_3$ ) ppm; FT-IR ( $\text{cm}^{-1}$ ): 2997 and 1455 (w;  $\nu$  (C-H)), 1754 (s;  $\nu$  (C=O)), 1085 (s;  $\nu$  (C-O)).

### 3.6. Characterization of PMLA, PLA, and P(MLA-g-LLA)

The chemical structure of PMLA, PLA, and P(MLA-g-LLA) were characterized by FT-IR and NMR. The FT-IR and NMR ( $^1\text{H}$ ,  $^{13}\text{C}$ ) spectra of homopolymers and graft copolymers are as shown in Figures 1–5. Some selected data for characterization of PMLA, PLA and P(MLA-g-LLA) are shown in Table 1.

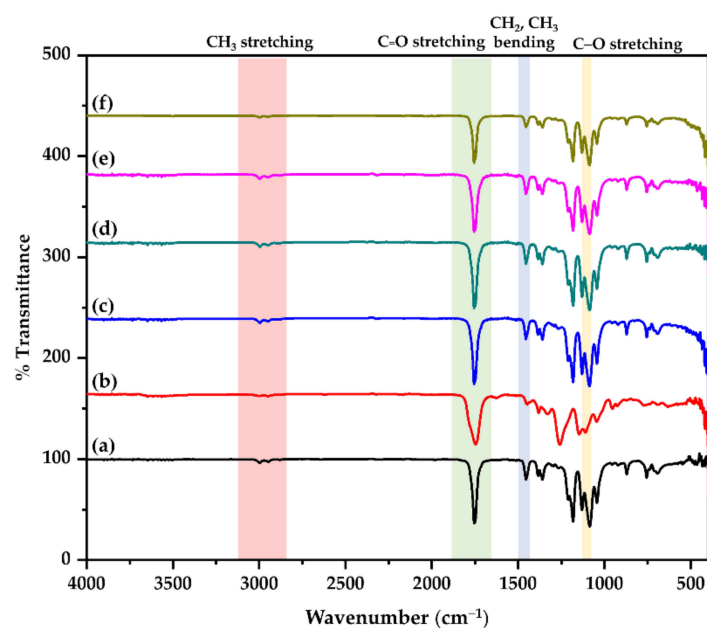


**Figure 1.** FT-IR spectra of poly(methylenelactide) with different amounts of AIBN (5, 10, 15, 20, and 25 mol%): (a) PMLA<sub>5</sub>; (b) PMLA<sub>10</sub>; (c) PMLA<sub>15</sub>; (d) PMLA<sub>20</sub>; and (e) PMLA<sub>25</sub>.

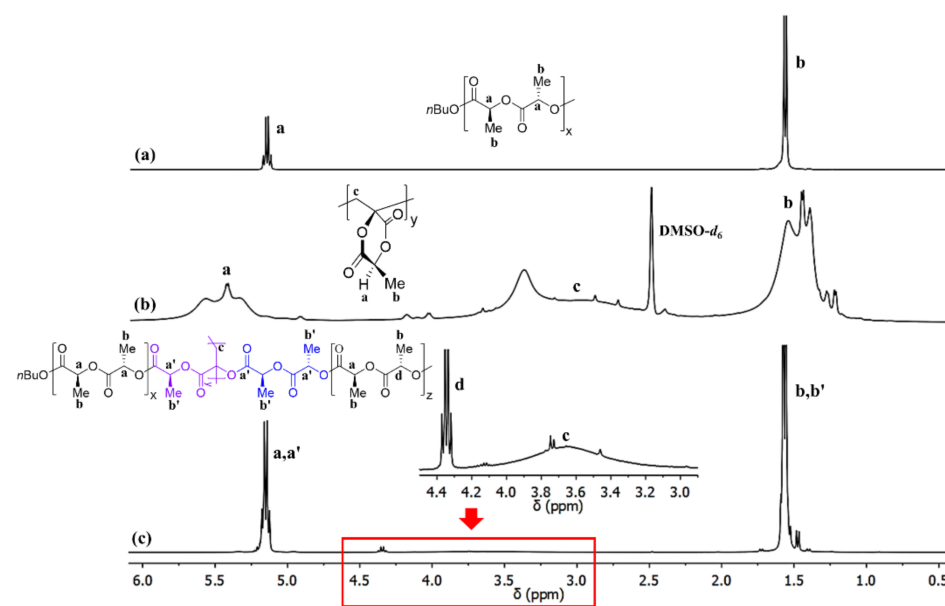


**Figure 2.**  $^1\text{H-NMR}$  (400 MHz,  $\text{DMSO-}d_6$ ) spectra of poly(methylenelactide) with different amounts of AIBN (5, 10, 15, 20, 25 mol%): (a) PMLA<sub>5</sub>; (b) PMLA<sub>10</sub>; (c) PMLA<sub>15</sub>; (d) PMLA<sub>20</sub>; and (e) PMLA<sub>25</sub>.





**Figure 3.** FT-IR spectra of homopolymers and graft copolymers with composition ratios of PMLA:LLA = 1:30, 1:50, 1:300, and 1:600 *w/w*: (a) PLA; (b) PMLA; (c) P(MLA20-*g*-LLA)<sub>1:30</sub>; (d) P(MLA20-*g*-LLA)<sub>1:50</sub>; (e) P(MLA20-*g*-LLA)<sub>1:300</sub>; and (f) P(MLA20-*g*-LLA)<sub>1:600</sub>.



**Figure 4.** <sup>1</sup>H-NMR spectra of homopolymers and graft copolymers: (a) PLA (400 MHz, CHCl<sub>3</sub>-*d*<sub>1</sub>); (b) PMLA (400 MHz, DMSO-*d*<sub>6</sub>); and (c) P(MLA-*g*-LLA) (400 MHz, CHCl<sub>3</sub>-*d*<sub>1</sub>).

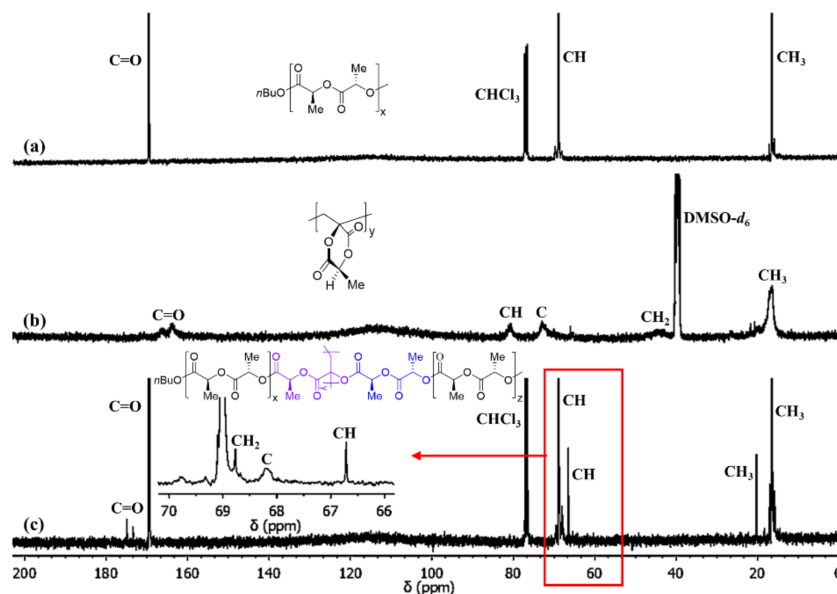
**Table 1.** Selected characterization data of PMLA, PLA, and P(MLA-*g*-LLA).

Sample	Initiator	Composition Ratio PMLA:LLA ( <i>w/w</i> )	<i>T<sub>g</sub></i> (°C) <sup>a</sup>	<i>T<sub>c</sub></i> (°C) <sup>a</sup>	<i>T<sub>m</sub></i> (°C) <sup>a</sup>	<i>T<sub>d</sub></i> (°C) <sup>b</sup>	$\bar{M}_w$ (g/mol) <sup>c</sup>	$\bar{M}_n$ (g/mol) <sup>c</sup>	Dispersity ( <i>D</i> ) $\bar{M}_w/\bar{M}_n$ <sup>c</sup>
PMLA-5	AIBN	-	244.0	-	-	368.0	-	-	-
PMLA-10	AIBN	-	225.7	-	-	360.1	-	-	-
PMLA-15	AIBN	-	223.7	-	-	361.1	-	-	-
PMLA-20	AIBN	-	221.4	-	-	356.9	-	-	-

Table 1. Cont.

Sample	Initiator	Composition Ratio PMLA:LLA ( <i>w/w</i> )	$T_g$ (°C) <sup>a</sup>	$T_c$ (°C) <sup>a</sup>	$T_m$ (°C) <sup>a</sup>	$T_d$ (°C) <sup>b</sup>	$\bar{M}_w$ (g/mol) <sup>c</sup>	$\bar{M}_n$ (g/mol) <sup>c</sup>	Dispersity ( $D$ ) $\bar{M}_w/\bar{M}_n$ <sup>c</sup>
PMLA-25	AIBN	-	220.3	-	-	356.4	-	-	-
PLA	Sn( <i>O</i> <i>n</i> Bu) <sub>2</sub>	-	71.5	110.8	168.3	301.1	$1.68 \times 10^4$	$1.11 \times 10^4$	1.5
P(MLA5- <i>g</i> -LLA)	Sn( <i>O</i> <i>n</i> Bu) <sub>2</sub>	1:30	70.1	-	159.8	318.5	$9.04 \times 10^4$	$6.78 \times 10^3$	1.3
P(MLA5- <i>g</i> -LLA)	Sn( <i>O</i> <i>n</i> Bu) <sub>2</sub>	1:50	73.3	-	164.2	328.8	$1.14 \times 10^4$	$8.24 \times 10^3$	1.4
P(MLA10- <i>g</i> -LLA)	Sn( <i>O</i> <i>n</i> Bu) <sub>2</sub>	1:30	70.6	-	155.5	318.5	$7.08 \times 10^3$	$5.66 \times 10^3$	1.2
P(MLA10- <i>g</i> -LLA)	Sn( <i>O</i> <i>n</i> Bu) <sub>2</sub>	1:50	74.8	-	159.7	325.3	$8.74 \times 10^3$	$6.63 \times 10^3$	1.3
P(MLA15- <i>g</i> -LLA)	Sn( <i>O</i> <i>n</i> Bu) <sub>2</sub>	1:30	73.4	-	155.8	321.4	$6.11 \times 10^3$	$5.15 \times 10^3$	1.2
P(MLA15- <i>g</i> -LLA)	Sn( <i>O</i> <i>n</i> Bu) <sub>2</sub>	1:50	66.8	-	160.3	326.8	$8.21 \times 10^3$	$6.34 \times 10^3$	1.3
P(MLA20- <i>g</i> -LLA)	Sn( <i>O</i> <i>n</i> Bu) <sub>2</sub>	1:30	72.3	-	144.0	314.4	$4.30 \times 10^3$	$3.76 \times 10^3$	1.1
P(MLA20- <i>g</i> -LLA)	Sn( <i>O</i> <i>n</i> Bu) <sub>2</sub>	1:50	73.0	-	161.0	324.1	$8.45 \times 10^3$	$6.48 \times 10^3$	1.3
P(MLA25- <i>g</i> -LLA)	Sn( <i>O</i> <i>n</i> Bu) <sub>2</sub>	1:30	73.6	-	163.3	328.1	$4.87 \times 10^3$	$4.08 \times 10^3$	1.2
P(MLA25- <i>g</i> -LLA)	Sn( <i>O</i> <i>n</i> Bu) <sub>2</sub>	1:50	73.5	-	163.8	386.7	$4.59 \times 10^3$	$3.81 \times 10^3$	1.2
P(MLA20- <i>g</i> -LLA)	Sn( <i>O</i> <i>n</i> Bu) <sub>2</sub>	1:300	68.8	-	164.3	335.4	$1.01 \times 10^4$	$7.86 \times 10^3$	1.4
P(MLA20- <i>g</i> -LLA)	Sn( <i>O</i> <i>n</i> Bu) <sub>2</sub>	1:600	68.4	-	162.8	328.9	$1.10 \times 10^4$	$7.88 \times 10^3$	1.3

<sup>a</sup> Determined by differential scanning calorimetry (DSC),  $T_g$ ;  $T_c$ ; and  $T_m$  values obtained from the 2nd scan; <sup>b</sup> Determined by thermal gravimetric analysis (TGA),  $T_d$  observed from peak maximum of the thermal decomposition, temperature; and <sup>c</sup> Weight-average molecular weight ( $\bar{M}_w$ ), number-average molecular weight ( $\bar{M}_n$ ), and dispersity ( $D$ ) determined by gel permeation chromatography (GPC) using a 2414 RI detector and PS standard (Empower 3 Software).



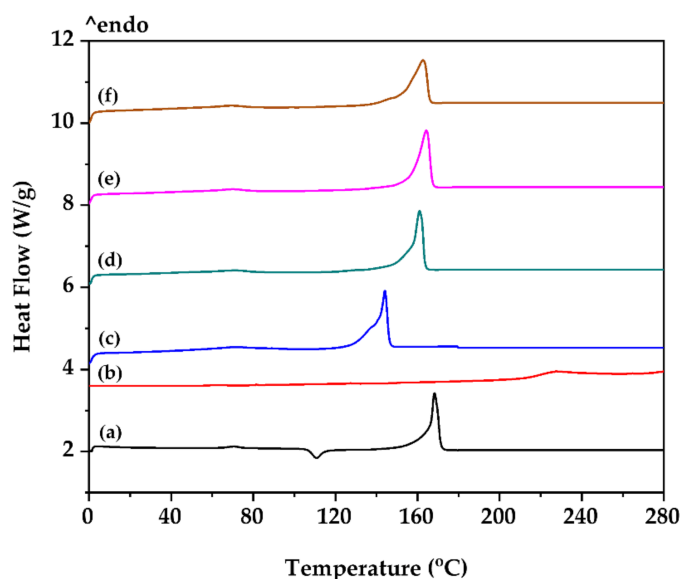
**Figure 5.**  $^{13}\text{C}$ -NMR spectra of homopolymers and graft copolymers: (a) PLA (100 MHz,  $\text{CHCl}_3\text{-}d_1$ ); (b) PMLA (100 MHz,  $\text{DMSO-}d_6$ ); and (c) P(MLA-*g*-LLA) (100 MHz,  $\text{CHCl}_3\text{-}d_1$ ).

FT-IR spectra of PMLA with different amounts of AIBN (5, 10, 15, 20, and 25 mol%) are shown in Figure 1. The spectrum of PMLA shows vibrational peaks of C=O and C–O stretching at around 1747 and 1110  $\text{cm}^{-1}$ , while the stretching and bending vibrations of C–H are seen at around 2949–2950 and 1447  $\text{cm}^{-1}$ . The PLA shows vibrational bands due to C–O stretching around 1085  $\text{cm}^{-1}$ , C=O stretching at 1754  $\text{cm}^{-1}$  and C–H bending and stretching at 1455 and 2997  $\text{cm}^{-1}$ , respectively. Figure 3 shows the FT-IR spectra of PMLA, PLA and P(MLA20-*g*-LLA) with various PMLA:LLA composition ratios respectively. In comparison, the P(MLA-*g*-LLA) spectrum shows the characteristic peaks of C–O stretching

around  $1087\text{ cm}^{-1}$ , C=O stretching around  $1754\text{ cm}^{-1}$  and C–H bending and stretching at  $1455$  and  $2997\text{ cm}^{-1}$ , similar to the data reported for PLA [4].

The MLA conversion with different amounts of AIBN (5, 10, 15, 20, 25 mol%) was determined via  $^1\text{H-NMR}$  spectroscopy (Figure 2). The intensity of the NMR peak of PMLA increased according to the amount of AIBN. The comparison  $^1\text{H-NMR}$  spectra of PLA, PMLA and P(MLA-g-LLA) are shown in Figure 4. As expected, the methine proton (-CH) at 5.45–5.46 ppm of PMLA and 5.15–5.16 ppm of P(MLA-g-LLA) and PLA, methyl proton (-CH<sub>3</sub>) at 1.41–1.43 ppm of PMLA, and 1.57–1.58 ppm of P(MLA-g-LLA) and PLA structure were observed accordingly. In Figure 4,  $^1\text{H-NMR}$  peak of P(MLA-g-LL) around 3.0–4.3 ppm are very similar to the methyl proton of PMLA. From  $^1\text{H-NMR}$  spectrum combined with  $^{13}\text{C-NMR}$  spectrum (Figures 4 and 5), the results confirmed the grafted structure of P(MLA-g-LLA). The black and blue units show PLA part on P(MLA-g-LLA) structure whereas the violet unit shows PMLA part on the backbone of the graft copolymer structure.  $^{13}\text{C-NMR}$  spectroscopy was further employed to provide a better view on the electron density of quaternary carbon and methylene carbon atom. From the results obtained (Figure 5), the quaternary carbon atoms of PMLA at 80.76 ppm and P(MLA-g-LLA) at 68.18 ppm were observed. This methylene carbon atom shows a relatively upfield in the case of PMLA at 45.08 ppm compared to the downfield in P(MLA-g-LLA) at 68.77 ppm. The electron-withdrawing of the ester group and oxygen atom influences preferentially the methylene carbon atom of P(MLA-g-LLA).

The DSC and TGA data of PMLA, PLA and P(MLA-g-LLA) are summarized in Table 1. From Figure 6, DSC thermograms of all PMLA obtained from using AIBN at different concentrations as an initiator show rather high glass transition temperature ( $T_g$ ) at about 221 to 225 °C.  $T_g$  of PMLA decreased as the amount of AIBN in PMLA increased from 5 to 25 mol%. No melting temperature ( $T_m$ ) was observed due to the amorphous structure of the PMLA which is in good agreement with the previously published work [48]. However, when it comes to the P(MLA-g-LLA) graft copolymers, the melting temperature of about 144–164 °C was detected. Figure 7 shows the heating-cooling-heating cycles of the DSC measurement of the P(MLA20-g-LLA) with a ratio of 1:30 *w/w*. For this P(MLA-g-LLA)<sub>1:30</sub>, in comparison to other P(MLA-g-LLA)s with different composition ratios, the lowest melting temperature of approximately 144 °C was observed. Also, it can be seen that for all cases, excluding P(MLA-g-LLA)<sub>1:600</sub>,  $T_m$  of the graft copolymer increased as the amount of LLA increased (Figure 6 and Table 1).



**Figure 6.** DSC thermograms (2nd scan) of PLA and P(MLA20-g-LLA) with composition ratio of PMLA:LLA of: (a) PLA; (b) PMLA<sub>20</sub>; (c) P(MLA20-g-LLA)<sub>1:30</sub>; (d) P(MLA20-g-LLA)<sub>1:50</sub>; (e) P(MLA20-g-LLA)<sub>1:300</sub>; and (f) P(MLA20-g-LLA)<sub>1:600</sub>.

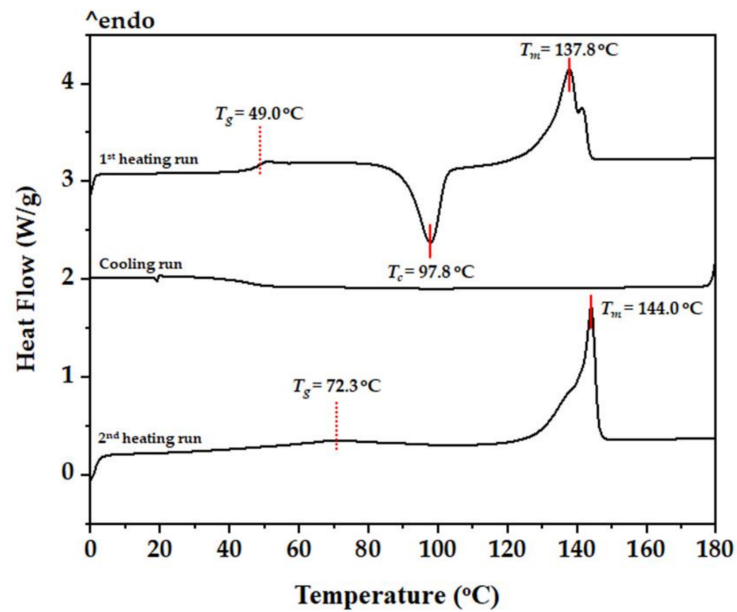


Figure 7. Representative DSC heating/cooling/heating thermograms of the P(MLA20-g-LLA)<sub>1:30</sub> showing its  $T_g$ ,  $T_c$ , and  $T_m$ .

As shown in Figure 8, the TGA thermogram of the PLA sample displays a decomposition onset temperature ( $T_{\text{onset}}$ ) of 210 °C and an end temperature ( $T_{\text{end}}$ ) of 315 °C with about 98% weight loss. In comparison, the P(MLA-g-LLA) graft copolymers with composition ratios of PMLA:LLA of 1:30, 1:50, 1:300, and 1:600  $w/w$  show onset temperatures of around 200–245 °C with degradation complete at ~344–400 °C and ~96–98% weight loss. The results show that the presence of PMLA in the P(MLA-g-LLA) structure increases the decomposition temperature, therefore, an improvement of thermal stability, comparing with the  $T_d$  value of PLA alone.

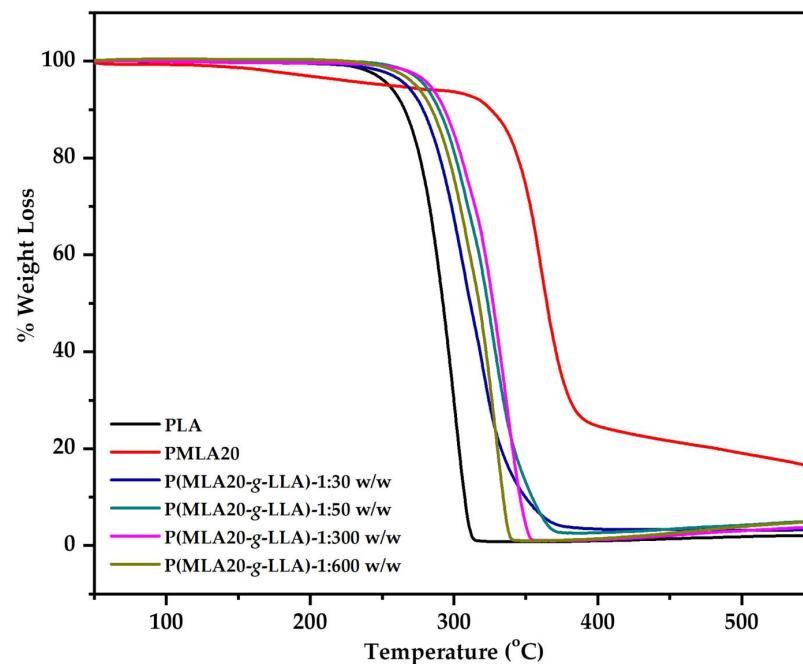
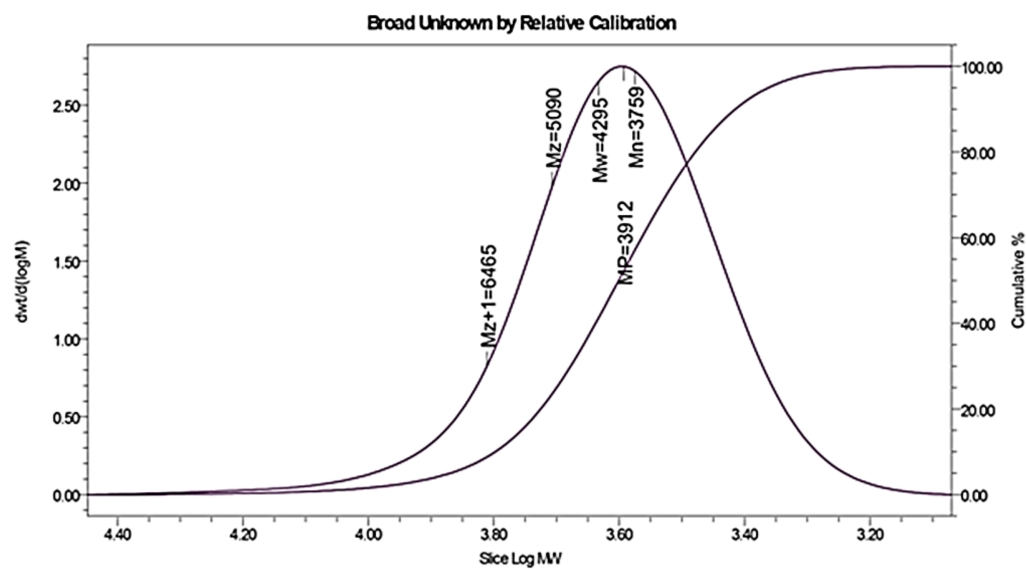


Figure 8. TG thermograms of PLA, PMLA<sub>20</sub>, and P(MLA20-g-LLA) with composition ratio of PMLA:LLA = 1:30, 1:50, 1:300, and 1:600  $w/w$ .

For the molar mass characterization, the number- and weight-average molecular weights ( $\overline{M}_n$  and  $\overline{M}_w$ ) and dispersity ( $D = \overline{M}_w / \overline{M}_n$ ) of the polymers were determined by gel permeation chromatography (GPC) using THF as a solvent at 40 °C (flow rate = 1 mL min<sup>-1</sup>) and calibrated with polystyrene (PS) standards using Empower Software. From the results obtained (see Table 1), the graft copolymers showed rather low molecular weights with  $\overline{M}_w \sim 4000$ – $10,000$  g mol<sup>-1</sup> and narrow dispersity ( $D \sim 1.1$ – $1.5$ ). Figure 9 shows the GPC chromatogram of P(MLA20-g-LLA)<sub>1:30</sub> graft copolymer which the  $\overline{M}_w$ ,  $\overline{M}_n$ , and  $D$  values of  $4.30 \times 10^3$ ,  $3.76 \times 10^3$ , and 1.1 were observed respectively.



**Figure 9.** GPC chromatogram of the P(MLA20-g-LLA)<sub>1:30</sub> showing the average molecular weight values of:  $\overline{M}_{Z+1}$ ,  $\overline{M}_Z$ ,  $\overline{M}_w$ , and  $\overline{M}_n$ , respectively.

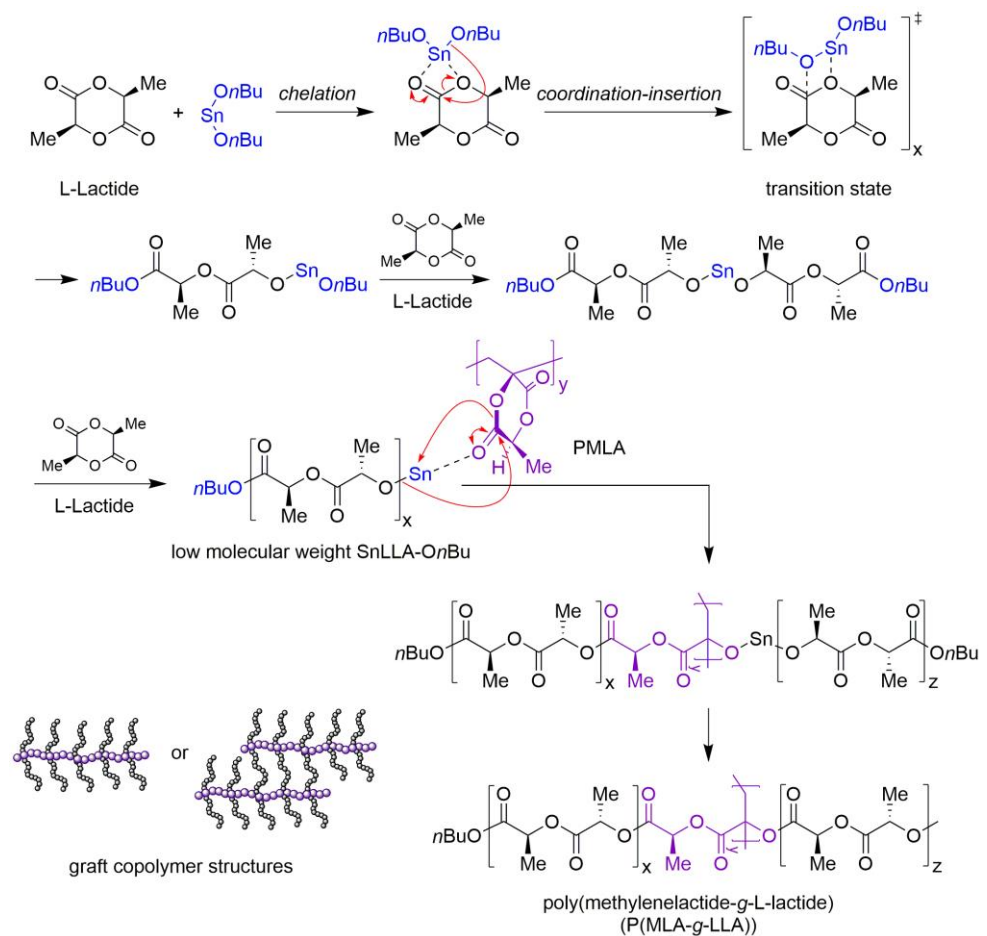
### 3.7. PMLA via Vinyl-Addition Polymerization

The homopolymerization reactions of PMLA were carried out in the presence of 5, 10, 15, 20 and 25 mol% of AIBN at 75 °C in 1,2-dichlorobenzene (*o*-DCB). PMLA was synthesized via vinyl addition polymerization using AIBN as an initiator using the free radical to yield predominantly isotactic polymer structures [59] and PMLA product was obtained as a white solid in a percentage yield of 60–65%. From the results obtained, it was found that as the amount of AIBN increased, the molecular weight of the polymer decreased.

### 3.8. P(MLA-g-LLA) and PLA via Ring-Opening Polymerization

P(MLA-g-LLA) and PLA were synthesized via ring-opening polymerization (ROP). The optimal condition for the synthesis of P(MLA-g-LLA) and PLA was 0.03 mol% of liquid tin(II) *n*-butoxide at 120 °C for 72 h. The physical appearance of the purified P(MLA-g-LLA) and PLA were obtained as a white solid with percentage yield of synthesis around 70–90% and 90% respectively. P(MLA-g-LLA) was found to have a relatively low molecular weight of  $\overline{M}_w \sim 4000$ – $11,000$  g mol<sup>-1</sup> and a narrow dispersity ( $D$ ) of  $\sim 1.1$ – $1.4$  compared to PLA as the data shown in Table 1. For P(MLA-g-LLA), it was synthesized via ROP by LLA initiated of ester group on PMLA chain with the proposed mechanisms as shown in Scheme 4.

From Scheme 4, the proposed mechanism of the synthesized poly(methylenelactide-g-L-lactide), P(MLA-g-LLA) starts with the O atoms of LLA have been activated by chelation with the Sn atom of Sn(*On*Bu)<sub>2</sub> initiator. Then, the reactive butoxy group of initiator attacks the carbonyl group of LLA through coordination-insertion to give *n*BuOSn–butyl lactate. Next, this intermediate was reacted with LLA in the propagation step to obtain the propagating species as low molecular weight SnLLA–*On*Bu. After that, the Sn atom of low molecular weight SnLLA–*On*Bu attacks the carbonyl carbon of PMLA chain and inserts into LLA ring of PMLA to form the P(MLA-g-LLA).



**Scheme 4.** Proposed mechanism for the synthesis of poly(methylenelactide-g-L-lactide), P(MLA-g-LLA).

#### 4. Conclusions

In this research work, the synthesis of P(MLA-g-LLA) graft copolymers were successfully performed by a combination of vinyl-addition and ring-opening polymerizations (ROP). The optimum condition for the synthesis of the graft copolymer was obtained from using 0.03 mol% of liquid  $\text{Sn}(\text{OnBu})_2$  at 120 °C for 72 h. The physical appearance of P(MLA-g-LLA) was obtained as a white solid with a percentage yield of approximately 90%. To investigate the polymerization behavior of P(MLA-g-LLA), different molar amounts of PMLA were used. The grafted structure of P(MLA-g-LLA) can be confirmed by a combination of  $^1\text{H}$ ,  $^{13}\text{C}$ -NMR, and FT-IR techniques.

Thermal properties were characterized by DSC and TGA. The melting temperature ( $T_m$ ) of P(MLA-g-LLA) with PMLA:LLA ratios of 1:30 and 1:50  $w/w$  in the range of about 144–164 °C was observed. From the DSC results, it can be seen that the  $T_m$  values of the copolymers decreased according to the amount of AIBN in PMLA from 5 to 25 mol%. The thermal decomposition temperature ( $T_d$ ) of around 328–386 °C from TGA was higher than that of the PLA homopolymer (~300 °C) indicating that the grafting reaction has increased their thermal stability due to the PMLA content of the graft copolymers.

These graft copolymers were obtained with the weight-average molecular weights ( $\overline{M}_w$ ) ~ 4000–11,000  $\text{g mol}^{-1}$  and narrow dispersities ( $D = 1.1$ – $1.4$ ). It is considered that they could be incorporated as additives in commercial PLA to improve both its melt processing characteristics and various thermo-mechanical properties. Such improvements would further broaden the range of applications of PLA as a bioplastic.

**Author Contributions:** P.M. developed the original idea and methodology; T.M. conducted the experiments, analyzed data, and wrote the original draft; M.S. wrote and edited the manuscript; R.M. edited manuscript; W.P. is responsible for project administration and funding acquisition. All authors have read and agreed to the published version of the manuscript.

**Funding:** This research was funded by the Program Management Unit for Human Resources & Institutional Development, Research and Innovation, Office of National Higher Education Science Research and Innovation Policy Council (NXPO), Grant Number B16F640001; the Center of Excellence for Innovation in Chemistry (PERCH-CIC); Center of Excellence in Materials Science and Technology, Chiang Mai University; the Graduate School, Chiang Mai University; and the CMU Presidential Scholarship (Post-Doctoral Fellowship) 2021.

**Institutional Review Board Statement:** Not applicable.

**Informed Consent Statement:** Not applicable.

**Acknowledgments:** This research was supported by the Program Management Unit for Human Resources & Institutional Development, Research and Innovation, Office of National Higher Education Science Research and Innovation Policy Council (NXPO) [Grant Number B16F640001]. In addition, we also would like to thank the Center of Excellence for Innovation in Chemistry (PERCH-CIC), Center of Excellence in Materials Science and Technology and Graduate School, Chiang Mai University for partially supports. Lastly, the authors also wish to thank the CMU Presidential Scholarship (Post-Doctoral Fellowship) 2021 for partially funding this research project.

**Conflicts of Interest:** The authors declare no conflict of interest.

## References

- Castillo Martinez, F.A.; Balciunas, E.M.; Salgado, J.M.; Domínguez González, J.M.; Converti, A.; Oliveira, R.P.d.S. Lactic acid Properties, Applications and Production: A review. *Trends Food Sci. Technol.* **2013**, *30*, 70–83. [\[CrossRef\]](#)
- Carothers, W.H.; Dorough, G.L.; van Natta, F.J. Studies of Polymerization and Ring Formation. X. The Reversible Polymerization of Six-Membered Cyclic Esters. *J. Am. Chem. Soc.* **1932**, *54*, 761–772. [\[CrossRef\]](#)
- Hartmann, M.H. High Molecular Weight Polylactic Acid Polymers. In *Biopolymers from Renewable Resources*, 1st ed.; Springer: Berlin/Heidelberg, Germany, 1998; pp. 367–411.
- Garlotta, D. A Literature Review of Poly(Lactic Acid). *J. Polym. Environ.* **2001**, *9*, 63–84. [\[CrossRef\]](#)
- Kricheldorf, H.R. Syntheses and Application of Poly lactides. *Chemosphere* **2001**, *43*, 49–54. [\[CrossRef\]](#)
- Gupta, A.P.; Kumar, V. New Emerging Trends in Synthetic Biodegradable Polymers-Polylactide: A Critique. *Eur. Polym. J.* **2007**, *43*, 4053–4074. [\[CrossRef\]](#)
- Groot, W.; van Krieken, J.; Sliemers, O.; de Vos, S. Production and Purification of Lactic acid and Lactide. In *Poly(lactic acid) Synthesis, Structures, Properties, Processing, and Applications*, 1st ed.; John Wiley & Sons, Inc.: Hoboken, NJ, USA, 2010; pp. 3–16.
- Dechy-Cabaret, O.; Martin-Vaca, B.; Bourissou, D. Polyesters from Dilactones. In *Handbook of Ring-Opening Polymerization*, 1st ed.; Wiley-VCH Verlag GmbH & Co. KGaA: Weinheim, Germany, 2009; pp. 255–280.
- Castro-Aguirre, E.; Iñiguez-Franco, F.; Samsudin, H.; Fang, X.; Auras, R. Poly(lactic acid)-Mass Production, Processing, Industrial Applications, and End of Life. *Adv. Drug. Deliv. Rev.* **2016**, *107*, 333–366. [\[CrossRef\]](#) [\[PubMed\]](#)
- Lee, C.; Hong, S. An Overview of the Synthesis and Synthetic Mechanism of Poly (Lactic acid). *Mod. Chem. Appl.* **2014**, *2*, 1–5.
- Nofar, M.; Sacligil, D.; Carreau, P.J.; Kamal, M.R.; Heuzey, M.-C. Poly (lactic acid) blends: Processing, Properties and Applications. *Int. J. Biol. Macromol.* **2019**, *125*, 307–360. [\[CrossRef\]](#) [\[PubMed\]](#)
- Zhou, Y.; Huang, Z.; Diao, X.; Weng, Y.; Wang, Y. Characterization of the Effect of REC on the Compatibility of PHBH and PLA. *Polym. Test.* **2015**, *42*, 17–25. [\[CrossRef\]](#)
- Hsu, Y.I.; Masutani, K.; Yamaoka, T.; Kimura, Y. Strengthening of Hydrogels made from Enantiomeric Block Copolymers of Polylactide (PLA) and Poly(ethylene glycol) (PEG) by the Chain Extending Diels-Alder Reaction at the Hydrophilic PEG Terminals. *Polymer* **2015**, *67*, 157–166. [\[CrossRef\]](#)
- Al-Itry, R.; Lamnawar, K.; Maazouz, A.; Billon, N.; Combeaud, C. Effect of the Simultaneous Biaxial Stretching on the Structural and Mechanical Properties of PLA, PBAT and their Blends at Rubbery State. *Eur. Polym. J.* **2015**, *68*, 288–301. [\[CrossRef\]](#)
- Zuo, H.; Liu, J.; Huang, D.; Bai, Y.; Cui, L.; Pan, L.; Zhang, K.; Wang, H. Sustainable and High-Performance Ternary Blends from Polylactide, CO<sub>2</sub>-Based Polyester and Microbial Polyesters with Different Chemical Structure. *J. Polym. Sci.* **2021**, *59*, 1578–1595. [\[CrossRef\]](#)
- Chen, J.; Zhang, T.-Y.; Jin, F.-L.; Park, S.-J. Fracture Toughness Improvement of Poly(lactic acid) Reinforced with Poly( $\epsilon$ -caprolactone) and Surface-Modified Silicon Carbide. *Adv. Mater. Sci. Eng.* **2018**, *2018*, 6537621. [\[CrossRef\]](#)
- Liu, X.; Yu, L.; Dean, K.; Toikka, G.; Bateman, S.; Nguyen, T.; Yuan, Q.; Filippou, C. Improving Melt Strength of Polylactic Acid. *Int. Polym. Process.* **2013**, *28*, 64–71. [\[CrossRef\]](#)

18. Quiles-Carrillo, L.; Duart, S.; Montanes, N.; Torres-Giner, S.; Balart, R. Enhancement of the Mechanical and Thermal Properties of Injection-Molded Polylactide Parts by the Addition of Acrylated Epoxidized Soybean Oil. *Mater. Des.* **2018**, *140*, 54–63. [[CrossRef](#)]
19. Herrera, N.; Roch, H.; Salaberria, A.M.; Pino-Orellana, M.A.; Labidi, J.; Fernandes, S.C.M.; Radic, D.; Leiva, A.; Oksman, K. Functionalized Blown Films of Plasticized Poly(lactic acid)/Chitin Nanocomposite: Preparation and Characterization. *Mater. Des.* **2016**, *92*, 846–852. [[CrossRef](#)]
20. Wojtczak, E.; Kubisa, P.; Bednarek, M. Thermal Stability of Polylactide with Different End-Groups Depending on the Catalyst used for the Polymerization. *Polym. Degrad. Stab.* **2018**, *151*, 100–104. [[CrossRef](#)]
21. Nagarajan, V.; Mohanty, A.K.; Misra, M. Perspective on Poly(lactic acid) (PLA) Based Sustainable Materials for Durable Applications: Focus on Toughness and Heat Resistance. *ACS Sustain. Chem. Eng.* **2016**, *4*, 2899–2916. [[CrossRef](#)]
22. Jin, F.-L.; Hu, R.-R.; Park, S.-J. Improvement of Thermal Behaviors of Biodegradable Poly(lactic acid) Polymer: A Review. *Composites Part B: Engineering*. *Compos. B Eng.* **2018**, *164*, 287–296. [[CrossRef](#)]
23. Wu, F.; Misra, M.; Mohanty, A.K. Studies on Why the Heat Deflection Temperature of Polylactide Bioplastic cannot be Improved by Overcrosslinking. *Polym. Cryst.* **2019**, *2*, e10088. [[CrossRef](#)]
24. Södergård, A.; Stolt, M. Properties of Lactic Acid Based Polymers and their Correlation with Composition. *Prog. Polym. Sci.* **2002**, *27*, 1123–1163. [[CrossRef](#)]
25. Zhang, Z.C.; Gao, X.R.; Hu, Z.J.; Yan, Z.; Xu, J.Z.; Xu, L.; Zhong, G.J.; Li, Z.M. Inducing Stereocomplex Crystals by Template Effect of Residual Stereocomplex Crystals during Thermal Annealing of Injection-Molded Polylactide. *Ind. Eng. Chem. Res.* **2016**, *55*, 10896–10905. [[CrossRef](#)]
26. Deng, L.; Xu, C.; Wang, X.; Wang, Z. Supertoughened Polylactide Binary Blend with High Heat Deflection Temperature Achieved by Thermal Annealing above the Glass Transition Temperature. *ACS Sustain. Chem. Eng.* **2017**, *6*, 480–490. [[CrossRef](#)]
27. Al-Itry, R.; Lamnawar, K.; Maazouz, A. Improvement of Thermal Stability, Rheological and Mechanical Properties of PLA, PBAT and their Blends by Reactive Extrusion with Functionalized Epoxy. *Polym. Degrad. Stab.* **2012**, *97*, 1898–1914. [[CrossRef](#)]
28. Barczewski, M.; Mysiukiewicz, O.; Matykiewicz, D.; Kloziński, A.; Andrzejewski, J.; Piasecki, A. Synergistic Effect of Different Basalt Fillers and Annealing on the Structure and Properties of Polylactide Composites. *Polym. Test.* **2020**, *89*, 106628. [[CrossRef](#)]
29. Purnama, P.; Samsuri, M.; Iswaldi, I. Properties Enhancement of High Molecular Weight Polylactide Using Stereocomplex Polylactide as a Nucleating Agent. *Polymers* **2021**, *13*, 1725. [[CrossRef](#)] [[PubMed](#)]
30. Zhang, B.; Sun, B.; Bian, X.; Li, G.; Chen, X. High Melt Strength and High Toughness PLLA/PBS Blends by Copolymerization and In Situ Reactive Compatibilization. *Ind. Eng. Chem. Res.* **2016**, *56*, 52–62. [[CrossRef](#)]
31. Safandowska, M.; Rozanski, A.; Galeski, A. Plasticization of Polylactide after Solidification: An Effectiveness and Utilization for Correct Interpretation of Thermal Properties. *Polymers* **2020**, *12*, 561. [[CrossRef](#)] [[PubMed](#)]
32. Purnama, P.; Kim, S.H. Bio-Based Composite of Stereocomplex Polylactide and Cellulose Nanowhiskers. *Polym. Degrad. Stab.* **2014**, *109*, 430–435. [[CrossRef](#)]
33. Yang, S.; Wu, Z.-H.; Yang, W.; Yang, M.-B. Thermal and Mechanical Properties of Chemical Crosslinked Polylactide (PLA). *Polym. Test.* **2008**, *27*, 957–963. [[CrossRef](#)]
34. Lou, X.; Detrembleur, C.; Jérôme, R. Novel Aliphatic Polyesters Based on Functional Cyclic(Di)Esters. *Macromol. Rapid Commun.* **2003**, *24*, 161–172. [[CrossRef](#)]
35. Cheng, Y.; Deng, S.; Chen, P.; Ruan, R. Poly(lactic acid) (PLA) Synthesis and Modifications: A Review. *Front. Chem. China* **2009**, *4*, 259–264. [[CrossRef](#)]
36. Agarwal, S.; Jin, Q.; Maji, A. Biobased Polymers from Plant-Derived Tulipalin A. *J. Am. Chem. Soc.* **2012**, *1105*, 197–212.
37. Castillejos, S.; Cerna, J.; Meléndez, F.; Castro, M.E.; Aguilar, R.; Beltrán, C.M.; González, M. Bulk Modification of Poly(lactide) (PLA) via Copolymerization with Poly(propylene glycol) Diglycidylether (PPGDGE). *Polymers* **2018**, *10*, 1184. [[CrossRef](#)] [[PubMed](#)]
38. Dechy-Cabaret, O.; Martin-Vaca, B.; Bourissou, D. Controlled Ring-Opening Polymerization of Lactide and Glycolide. *Chem. Rev.* **2004**, *104*, 6147–6176. [[CrossRef](#)]
39. Nuyken, O.; Pask, S.D. Ring-Opening Polymerization—An Introductory Review. *Polymers* **2013**, *5*, 361–403. [[CrossRef](#)]
40. Hagiopol, C. Binary Copolymerization. In *Copolymerization: Toward a Systematic Approach*, 1st ed.; Kluwer Academic/Plenum Publishers: New York, NY, USA, 1999; pp. 1–18.
41. Osswald, T.A.; Menges, G. Structure of Polymers. In *Materials Science of Polymers for Engineers*, 3rd ed.; Hanser Publishers: Munich, Germany, 2012; pp. 49–82.
42. Kaliva, M.; Georgopoulou, A.; Dragatogiannis, D.A.; Charitidis, C.A.; Chatzinikolaidou, M.; Vamvakaki, M. Biodegradable Chitosan-graft-Poly(L-lactide) Copolymers For Bone Tissue Engineering. *Polymers* **2020**, *12*, 316. [[CrossRef](#)]
43. Xia, L.; Zhang, Z.; Hong, C.Y.; You, Y.Z. Synthesis of Copolymer via Hybrid Polymerization: From Random to Well-Defined Sequence. *Eur. Polym. J.* **2019**, *122*, 109374. [[CrossRef](#)]
44. Stannett, V. Grafting. *Radiat. Phys. Chem.* **1981**, *18*, 215–222. [[CrossRef](#)]
45. Athawale, V.D.; Rathi, S.C. Graft Polymerization: Starch as a Model Substrate. *J. Macromol. Sci. Part C* **1999**, *C39*, 445–480. [[CrossRef](#)]
46. Deng, Y.; Zhang, S.; Lu, G.; Huang, X. Constructing Well-Defined Star Graft Copolymers. *Polym. Chem.* **2013**, *4*, 1289–1299. [[CrossRef](#)]



47. Gowda, R.R.; Chen, E.Y.-X. Sustainable Polymers from Biomass-Derived  $\alpha$ -Methylene- $\gamma$ -Butyrolactones. In *Encyclopedia of Polymer Science and Technology*; Wiley Online Library: Hoboken, NJ, USA, 2013; pp. 1–37.
48. Miyake, G.M.; Zhang, Y.; Chen, E.Y.-X. Polymerizability of Exo-Methylene-Lactide Toward Vinyl Addition and Ring Opening. *J. Polym. Sci. A Polym. Chem.* **2015**, *53*, 1523–1532. [[CrossRef](#)]
49. Stridberg, K.M.; Ryner, M.; Albertsson, A.C. Controlled Ring-Opening Polymerization: Polymers with Designed Macromolecular Architecture. *Adv. Polym. Sci.* **2002**, *157*, 41–65.
50. Yin, M.; Baker, G.L. Preparation and Characterization of Substituted Polylactides. *Macromolecules* **1999**, *32*, 7711–7718. [[CrossRef](#)]
51. Trimaille, T.; Möller, M.; Gurny, R. Synthesis and Ring-Opening Polymerization of New Monoalkyl-Substituted Lactides. *J. Polym. Sci. A Polym. Chem.* **2004**, *42*, 4379–4391. [[CrossRef](#)]
52. Marcincinova Benabdillah, K.; Boustta, M.; Coudane, J.; Vert, M. Novel Degradable Polymers Combining D-Gluconic Acid, a Sugar of Vegetal Origin, with Lactic and Glycolic Acids. *Biomacromolecules* **2001**, *2*, 1279–1284. [[CrossRef](#)]
53. Such, G.K.; Quinn, J.F.; Quinn, A.; Tjipto, E.; Caruso, F. Assembly of Ultrathin Polymer Multilayer Films by Click Chemistry. *J. Am. Chem. Soc.* **2006**, *128*, 9318–9319. [[CrossRef](#)]
54. Jing, F.; Hillmyer, M.A. A Bifunctional Monomer Derived from Lactide for Toughening Polylactide. *J. Am. Chem. Soc.* **2008**, *130*, 13826–13827. [[CrossRef](#)] [[PubMed](#)]
55. Fiore, G.L.; Jing, F.; Young, V.G., Jr.; Cramer, C.J.; Hillmyer, M.A. High  $T_g$  Aliphatic Polyesters by the Polymerization of Spirolactone Derivatives. *Polym. Chem.* **2010**, *1*, 870–877. [[CrossRef](#)]
56. Castillo, J.A.; Borchmann, D.E.; Cheng, A.Y.; Wang, Y.; Hu, C.; García, A.J.; Weck, M. Well-Defined Poly(lactic acid)s Containing Poly(ethylene glycol) Side Chains. *Macromolecules* **2012**, *45*, 62–69. [[CrossRef](#)]
57. Beuille, E.; Darcos, V.; Coudane, J.; Lacroix-Desmazes, P.; Nottelet, B. Regioselective Halogenation of Poly(lactide) by Free-Radical Process. *Macromol. React. Eng.* **2013**, *8*, 141–148. [[CrossRef](#)]
58. Britner, J.; Ritter, H. Self-Activation of Poly(methylenelactide) through Neighboring-Group Effects: A Sophisticated Type of Reactive Polymer. *Macromolecules* **2015**, *48*, 3516–3522. [[CrossRef](#)]
59. Britner, J.; Ritter, H. Methylenelactide: Vinyl polymerization and spatial reactivity effects. *Beilstein J. Org. Chem.* **2016**, *12*, 2378–2389. [[CrossRef](#)]
60. Zhu, J.B.; Tang, X.; Falivene, L.; Caporaso, L.; Cavallo, L.; Chen, E.Y.-X. Organocatalytic Coupling of Bromo-Lactide with Cyclic Ethers and Carbonates to Chiral Bromo-Diesters: NHC or Anion Catalysis? *ACS Catal.* **2017**, *7*, 3929–3933. [[CrossRef](#)]
61. Mauldin, T.C.; Wertz, J.T.; Boday, D.J. Acrylic Platform from Renewable Resources via a Paradigm Shift in Lactide Polymerization. *ACS Macro Lett.* **2016**, *5*, 544–546. [[CrossRef](#)]
62. Sinclair, F.; Shaver, M.P. Cross-Metathesis Functionalized Exo-Olefin Derivatives of Lactide. *J. Polym. Sci. A Polym. Chem.* **2018**, *56*, 741–748. [[CrossRef](#)]
63. Boday, D.J.; Garcia, J.M.; Hedrick, J.L.; Kobilka, B.M.; Wertz, J.T.; Wojtecki, R.J. Lactide-Derived Polymers with Improved Materials Properties via Polyhexahydrotriazines (PHT) Reaction. U.S. Patent 10,329,380 B2, 25 June 2019.
64. Meepowpan, P.; Punyodom, W.; Molloy, R. Process for the Preparation of Liquid Tin(II) Alkoxides. U.S. Patent 9,637,507 B2, 2 May 2017.
65. Chaiwon, T.; Sriyai, M.; Meepowpan, P.; Molloy, R.; Nalampang, K.; Kaabbuathong, N.; Punyodom, W. Kinetic and Mechanistic Studies of Bulk Copolymerization of L-lactide and Glycolide Initiated by Liquid Tin(II) *n*-Butoxide. *Chiang Mai J. Sci.* **2021**, *48*, 489–505.
66. Sriyai, M.; Chaiwon, T.; Molloy, R.; Meepowpan, P.; Punyodom, W. Efficiency of Liquid Tin(II) *n*-Alkoxide Initiators in the Ring-Opening Polymerization of L-lactide: Kinetic Studies by Non-Isothermal Differential Scanning Calorimetry. *RSC Adv.* **2020**, *10*, 43566–43578. [[CrossRef](#)]
67. Sattayanon, C.; Sontising, W.; Jitonnorn, J.; Meepowpan, P.; Punyodom, W.; Kungwan, N. Theoretical Study on the Mechanism and Kinetics of Ring-Opening Polymerization of Cyclic Esters Initiated by Tin(II) *n*-Butoxide. *Comput. Theor. Chem.* **2014**, *1044*, 29–35. [[CrossRef](#)]
68. Dumklang, M.; Pattawong, N.; Punyodom, W.; Meepowpan, P.; Molloy, R.; Hoffman, M. Novel Tin(II) Butoxides for Use as Initiators in the Ring-Opening Polymerisation of  $\epsilon$ -Caprolactone. *Chiang Mai J. Sci.* **2009**, *36*, 136–148.

MDPI  
St. Alban-Anlage 66  
4052 Basel  
Switzerland  
Tel. +41 61 683 77 34  
Fax +41 61 302 89 18  
[www.mdpi.com](http://www.mdpi.com)

*Polymers* Editorial Office  
E-mail: [polymers@mdpi.com](mailto:polymers@mdpi.com)  
[www.mdpi.com/journal/polymers](http://www.mdpi.com/journal/polymers)





MDPI  
St. Alban-Anlage 66  
4052 Basel  
Switzerland  
Tel: +41 61 683 77 34  
[www.mdpi.com](http://www.mdpi.com)



ISBN 978-3-0365-7405-9